

Springer Series in Optical Sciences 161

Herbert Venghaus
Norbert Grote *Editors*

Fibre Optic Communication

Key Devices

2nd Edition

 Springer

founded by H.K.V. Lotsch

Editor-in-Chief: W.T. Rhodes, Boca Raton

Editorial Board: A. Adibi, Atlanta
T.W. Hänsch, Garching
F. Krausz, Garching
B.R. Masters, Cambridge
K. Midorikawa, Saitama
H. Venghaus, Berlin
H. Weber, Berlin
H. Weinfurter, München

Springer Series in OPTICAL SCIENCES

The Springer Series in Optical Sciences, under the leadership of Editor-in-Chief William T. Rhodes, Georgia Institute of Technology, USA, provides an expanding selection of research monographs in all major areas of optics: lasers and quantum optics, ultrafast phenomena, optical spectroscopy techniques, optoelectronics, quantum information, information optics, applied laser technology, industrial applications, and other topics of contemporary interest.

With this broad coverage of topics, the series is of use to all research scientists and engineers who need up-to-date reference books.

The editors encourage prospective authors to correspond with them in advance of submitting a manuscript. Submission of manuscripts should be made to the Editor-in-Chief or one of the Editors. See also www.springer.com/series/624

Please view available titles in *Springer Series in Optical Sciences* on series homepage <http://www.springer.com/series/624>

Herbert Venghaus • Norbert Grote
Editors

Fibre Optic Communication

Key Devices

Second Edition

 Springer

Editors

Herbert Venghaus
Fraunhofer Institute for
Telecommunications
Heinrich Hertz Institute
Berlin, Germany

Norbert Grote
Fraunhofer Institute for
Telecommunications
Heinrich Hertz Institute
Berlin, Germany

ISSN 0342-4111
Springer Series in Optical Sciences
ISBN 978-3-319-42365-4
DOI 10.1007/978-3-319-42367-8

ISSN 1556-1534 (electronic)
ISBN 978-3-319-42367-8 (eBook)

Library of Congress Control Number: 2017931567

Springer Cham Heidelberg New York Dordrecht London

© Springer International Publishing Switzerland 2012, 2017

This work is subject to copyright. All rights are reserved by the Publisher, whether the whole or part of the material is concerned, specifically the rights of translation, reprinting, reuse of illustrations, recitation, broadcasting, reproduction on microfilms or in any other physical way, and transmission or information storage and retrieval, electronic adaptation, computer software, or by similar or dissimilar methodology now known or hereafter developed.

The use of general descriptive names, registered names, trademarks, service marks, etc. in this publication does not imply, even in the absence of a specific statement, that such names are exempt from the relevant protective laws and regulations and therefore free for general use.

The publisher, the authors and the editors are safe to assume that the advice and information in this book are believed to be true and accurate at the date of publication. Neither the publisher nor the authors or the editors give a warranty, express or implied, with respect to the material contained herein or for any errors or omissions that may have been made.

Printed on acid-free paper

Springer is part of Springer Science+Business Media (www.springer.com)

Preface to the 2nd edition

Fibre optic communications continues to be a key enabler for industrial development, economic progress and the shaping of modern society. Despite the tremendous achievements over the past twenty years there is a strong demand for further advances. Overall data traffic will continue to grow strongly, optical communication technologies will move closer to the end user, optical technologies will take a central role in (intra) data centre information exchange. However today's communications and data centres already account for a few percent of the world's total usage of electrical energy and this is projected to continue increasing. Going forwards, the cost of optical communication has to go down and energy efficiency must improve. In order to achieve these goals, significant R&D effort is being spent on improving performance of key components as well as lowering device size and fabrication cost, and this trend is predicted to go on in the years to come.

As a consequence of the significant progress made in virtually all fields during the last few years, we considered a 2nd updated edition of the book *Fibre Optic Communication—Key Devices* appropriate some four years after the appearance of the 1st edition. We would like to recognise the great engagement of the many contributors and the publisher in making this revised book available. Existing chapters have been appropriately updated and a few new chapters have been added in appreciation of topics that have received particular attention and have made substantial progress during the past few years.

Spatial division multiplexing (SDM), including mode division multiplexing, is among the fields which have experienced rapid development recently. Its promise is to enable improved cost and energy efficiency, and its implementation requires specific device developments, in particular SDM fibres and dedicated fibre amplifiers and de/multiplexers. SDM is treated in a chapter in its own right and in SDM-related sections in the chapters on optical fibres and fibre amplifiers as well.

Higher order modulation (HOM) formats represent another topic which has witnessed tremendous advancement. Dedicated optical devices combined with extensive electronic signal processing have lead to spectral efficiencies in the tens of bit/s/Hz. As a result of the remarkable achievements related to HOM formats, the corresponding chapter has been rewritten rather than updating the respective chapter of the 1st edition.

Photonic integration is considered a promising approach towards realizing higher device functionality at lower cost and with lower power consumption, and various paths are currently being pursued:

Hybrid photonic integration, which is essentially an optical micro-assembly technology, has been pursued for about two decades already and has achieved remarkable results using different dielectric waveguide platforms, and therefore a new, dedicated chapter has been included in this 2nd edition.

A particular hot topic in photonics is ‘Silicon Photonics’, i.e. silicon-on-insulator (SOI) based chips with optical functionality. A large number of exciting results have been reported recently including improved performance of individual subcomponents as well as higher levels of integration. Promising applications have emerged in various fields, amongst them optical rack-to-rack-, chip-to-chip, and optical on-chip interconnects. The corresponding chapter of the 1st edition focusing on silicon photonic sources has been updated including a new section on modulators, and a new chapter addressing key passive devices and detectors has been added to the book.

A third path towards higher functionality and lower chip cost is monolithic integration using III–V semiconductors, primarily indium phosphide along with its lattice-matched ternary and quaternary compounds. In contrast to Si Photonics this approach enables the full monolithic integration of lasers and related device structures with detectors, modulators and passive functionalities. A newly written chapter is devoted to this integration platform, particularly highlighting generic fabrication of photonic integrated circuits following a foundry model.

“Optical switching” is a generic term which covers an extremely wide range of techniques and solutions, ranging from simple and slow network protection to all-optical switching. It is a topic which justifies corresponding books in their own right, and an in-depth treatment would have been beyond the scope of the present book. However, the range of devices treated in the 1st edition has been complemented by a new chapter on optical switches. The chapter covers generic aspects such as larger switching matrices and wavelength selective switches, and implementations including opto-mechanical-, liquid crystal-, planar lightwave- and in particular MEMS based switches. Beyond these expansions of the scope of the 1st edition, two topics have no longer been considered in the 2nd edition: optical signal processing for high-speed data transmission. In the editors’ opinion the corresponding concepts have not experienced major progress during the last few years, and there are no signs that such techniques may find practical applications in the near to medium future. The chapter on optical networks is also no longer included in the book, as there is currently significant development across multiple network domains, and it is difficult to do the subject justice in one chapter. Access networks are seeing new standardisation for NG-PON2, new concepts are emerging for SDM fibre, and increasing levels of software defined and data centric networking. Covering all these topics requires a book in its own right and so the editors have decided to leave this field out.

The overall structure will essentially be similar to that of the 1st edition: The introductory chapter on space division multiplexing is followed by a chapter on the

optical fibre, the fundamental building element of any fibre optic communication system. The chapter covers fundamentals, key properties of all relevant kinds of fibre and most recent developments for SDM applications as well.

The next three chapters focus on InP semiconductor based lasers. The first of them covers fundamental aspects and various kinds of 1.3–1.6 μm laser structures including recent results on vertical cavity surface emitting lasers (VCSELs), and a section on semiconductor optical amplifiers (SOA) as well. The latter replaces the SOA chapter of the 1st edition and takes advantage of many common aspects between lasers and SOAs. The following two laser related chapters treat ultrafast laser sources and widely tunable laser diodes.

A chapter on photodetectors as the key elements on the receiver side is followed by chapters on those elements which enable advanced fibre optic communication systems with highest spectral efficiency and transmission capacity: semiconductor-based modulators and higher order modulation formats.

The next few chapters are dedicated to wavelength filters, optical switches, passive devices including optical circulators and optical isolators, and fibre amplifiers. The four chapters focusing on photonic integration conclude the book.

Altogether, the book follows the same principles as in the case of the 1st edition: the treatment of the topics of the individual chapters start from the fundamental physics before moving on to generic devices and commercially available implementations, and covers solutions under current development before highlighting new research directions.

The editors would like to express their deepest thanks to all the renowned authors for their extreme engagement and their valuable time spent on writing the individual chapters. It is them who made it possible to edit a book covering such a wide range of diverse topics and presenting a high-level, up-to-date overview with the most recent accomplishments. We are also very grateful to the publisher Springer Verlag, and in particular Claus Ascheron, for their continuous support and encouragement.

Berlin, Germany

Herbert Venghaus
Norbert Grote

Contents

1	Spatial Division Multiplexing	1
	Haoshuo Chen and A.M.J. (Ton) Koonen	
1.1	Introduction	1
1.2	Why SDM?	3
1.2.1	Cost-Efficiency	4
1.2.2	Energy-Efficiency	4
1.3	State-of-the-Art	5
1.4	SDM Components	6
1.4.1	SDM Fiber	6
1.4.2	Spatial Multiplexers (SMUX)	9
1.4.3	Optical Amplifiers	20
1.4.4	Wavelength Selective Switches (WSS)	25
1.4.5	Fiber Splicers and Connectors	28
1.5	Digital Signal Processing	28
1.6	Commercialization	31
	Appendix	31
1.7.1	Economic Aspects of Mode Division Multiplexed Links	31
1.7.2	Conclusions	36
	References	37
2	Optical Fibers	49
	Pierre Sillard and Denis Molin	
2.1	Introduction	49
2.2	Fiber Basics	50
2.2.1	Principle of Light Propagation in Optical Fibers	50
2.2.2	Modal Theory of Light Propagation in Optical Fibers	51
2.2.3	Fiber Fabrication	54
2.2.4	Fiber Loss	55
2.2.5	Fiber Dispersion	56
2.3	Multimode Fibers	57

2.3.1	Key Characteristics	58
2.3.2	Different Types of Multimode Fibers	61
2.3.3	Standardization	65
2.4	Single-Mode Fibers	66
2.4.1	Key Characteristics	66
2.4.2	Standardization	68
2.4.3	Fiber Types	72
2.5	Optical Fiber Cables	78
2.5.1	Basic Elements of a Cable	78
2.5.2	Cable Environment and Cable Types	80
2.6	New Developments	81
2.6.1	Micro-Structured Optical Fibers	82
2.6.2	Bragg Fibers	83
2.6.3	Fibers Mixing Glass and Semiconductors	84
2.6.4	Fibers for Space Division Multiplexing	84
	References	90
3	Laser Components	103
	Norbert Grote, Martin Möhrle, and Markus Ortsiefer	
3.1	Introduction	103
3.2	Materials for “Long-Wavelength” Laser Diodes	104
3.3	Laser Diode Structures	106
3.3.1	Layer Structure	106
3.3.2	Lateral Structure	106
3.4	Active Medium	109
3.5	Fabry-Pérot Lasers	113
3.6	Gain Elements and Optical Amplifiers	117
3.7	Single-Mode Laser Diodes	119
3.7.1	Distributed Feedback (DFB) Lasers	120
3.7.2	Advanced Single-Mode Laser Structures	127
3.8	Surface-Emitting Laser Diodes	131
3.8.1	Vertical-Cavity Surface-Emitting Laser (VCSEL)	131
3.8.2	Horizontal Cavity Surface Emitting Laser Concepts	142
	References	144
4	Ultra-Fast Semiconductor Laser Sources	151
	Masahiro Aoki and Ute Troppenz	
4.1	Introduction	151
4.2	Ultra-Fast Directly-Modulated Laser Sources	153
4.2.1	High-Speed Characteristics of Directly-Modulated Lasers	153
4.2.2	Large-Signal Dynamic Analysis of Rate Equations	156
4.2.3	Chirp Characteristics of Directly Modulated Lasers	158
4.2.4	High-Gain Active Materials for Ultra-Fast Uncooled Lasers	158
4.2.5	Short-Cavity Ultra-Fast Lasers	163

- 4.3 Ultra-Fast, Low-Chirp Externally-Modulated Laser Sources . . . 168
 - 4.3.1 High-Speed Characteristics of Externally Modulated Lasers 169
 - 4.3.2 Chirp Characteristics of Externally Modulated Lasers . . 172
 - 4.3.3 Facet-Reflection Induced Chirp in Externally Modulated Lasers 173
 - 4.3.4 Transmission Simulation of Externally Modulated Lasers Considering Facet-Reflection Induced Chirp . . . 175
 - 4.3.5 Effect of Photo-Generated Current on Modulation Characteristics 179
 - 4.3.6 High-Speed Externally Modulated Lasers in System Use 182
 - 4.3.7 Uncooled, High-Speed, Low-Chirp Externally Modulated Lasers 184
- 4.4 New Challenges for Ultra-Fast Semiconductor Light Sources . . 187
 - 4.4.1 High-Speed Active/Passive Feedback Diode Lasers . . . 187
 - 4.4.2 Traveling-Wave EA Modulators 189
 - 4.4.3 Management of Chirp and Chromatic Dispersion Impairments in High Speed C- and L-Band Transmitters 191
- 4.5 Directly Modulated Transmitters in 100G/400G Applications . . 194
 - 4.5.1 High Speed 40/56 Gb/s 1.3 μm Transmitters 194
 - 4.5.2 Advanced Modulation Formats for Higher Spectral Efficiency in Short Reach Applications 198
- References 199
- 5 Widely Tunable Laser Diodes 209**

Hélène Debrégeas

 - 5.1 Basics of Current Injection Tuning, DBR Lasers 211
 - 5.1.1 Current Injection Tuning Mechanisms 211
 - 5.1.2 DBR Lasers: Principle of Operation 214
 - 5.2 Widely Tunable Lasers by Current Injection 219
 - 5.2.1 Sampled Gratings 219
 - 5.2.2 SG-DBR Lasers 220
 - 5.2.3 SSG-DBR Lasers 223
 - 5.2.4 Y-Lasers 224
 - 5.2.5 Multiple Peak Grating and Tunable Wide Filter Lasers (GCSR, DS-DBR) 224
 - 5.2.6 DBR-MMI 226
 - 5.3 Control Issues 226
 - 5.3.1 Control Algorithms 227
 - 5.3.2 Influence of Cavity Length and Non-linear Effects . . . 229
 - 5.3.3 Fast Tuning 232
 - 5.4 Other Wavelength Tunable/Selectable Lasers 232
 - 5.4.1 Thermally Tuned DFB Array 232
 - 5.4.2 Tunable Vertical Cavity Surface Emitting Lasers (VCSELs) 234

- 5.4.3 External Cavity Tunable Lasers 234
- 5.4.4 Tunable Lasers with Ring Resonators 236
- 5.5 Subsystems and Tunable Photonic Integrated Circuits 240
 - 5.5.1 Tunable Laser Integrated with Modulator 240
 - 5.5.2 Tunable Subsystems 242
- 5.6 Conclusion 243
- References 245
- 6 Photodetectors 249**
 - Andreas Beling and Joe C. Campbell
 - 6.1 Fundamentals 249
 - 6.2 Photodiode Types 253
 - 6.2.1 p–i–n Photodiode 253
 - 6.2.2 Metal-Semiconductor-Metal Photodetector 255
 - 6.2.3 Avalanche Photodiodes 257
 - 6.2.4 Advanced Photodiode Structures 262
 - 6.2.5 High-Speed Side-Illuminated Photodiodes 266
 - 6.2.6 Material Systems 274
 - 6.2.7 Germanium Photodiodes on Silicon 275
 - 6.2.8 Heterogeneously Integrated Photodiodes 276
 - 6.3 Summary 279
 - References 279
- 7 Higher-Order Modulation Formats – Concepts and Enabling Devices 291**
 - Wilfried Idler and Fred Buchali
 - 7.1 Introduction 291
 - 7.2 Coherent Transceiver 296
 - 7.2.1 Reinvention of Coherent Receiver Technology 296
 - 7.2.2 Coherent Optical Transceiver – Concepts and Building Blocks 297
 - 7.3 Higher-Order Modulation Formats 300
 - 7.3.1 Quadrature Amplitude Modulation 301
 - 7.3.2 Spectral Efficiency and Fiber Capacity 310
 - 7.3.3 High Bit Rate Transmission 314
 - 7.4 Forward Error Correction (FEC) 326
 - 7.4.1 Hard Decision FEC 326
 - 7.4.2 Soft Decision FEC 327
 - 7.5 Digital Signal Processing 329
 - 7.5.1 Transmitter Digital Signal Processing 329
 - 7.5.2 Receiver Digital Signal Processing 332
 - 7.6 Data Converters (DAC and ADC) 334
 - 7.6.1 Digital-to-Analogue Converters 335
 - 7.6.2 Analogue-to-Digital Converters 338
 - 7.7 Devices for Coherent Transceivers 342
 - 7.7.1 Dual Polarization IQ Modulators 343

7.7.2	Optical Receiver Frontend	345
7.7.3	ASIC Technologies	346
	References	349
8	Semiconductor-Based Modulators	359
	Hiroshi Yasaka and Yasuo Shibata	
8.1	Overview of the Methods to Generate a Digital Optical Signal	360
8.1.1	Direct Modulation of Semiconductor Lasers	361
8.1.2	Electroabsorption Modulators (EAMs)	363
8.1.3	Mach-Zehnder Interferometer (MZI) Modulators	366
8.2	Semiconductor-Based MZI Modulators	371
8.2.1	Fundamentals/Refractive Index Control of Semiconductor Materials	371
8.2.2	GaAs- and InP-Based MZI Modulators	377
8.3	High-Speed Modulator Design	379
8.4	Performance of Current MZI Modulators	384
8.4.1	n-i-n Structure MZI Modulators	384
8.4.2	Advanced MZI Modulator Modules	390
8.5	High-Performance Modulators for Advanced Modulation Formats	395
8.5.1	Optical Duobinary (ODB) Modulation	396
8.5.2	Optical DPSK Modulation	398
8.5.3	Semiconductor Optical DQPSK Modulators	402
8.5.4	Semiconductor Multilevel Modulators	406
8.6	Summary and Future Issues	407
	References	408
9	Wavelength Filters	417
	Herbert Venghaus	
9.1	Introduction	417
9.2	Phase Effects	419
9.2.1	General Considerations	419
9.2.2	Phase Characterisation Techniques	421
9.2.3	Typical Group Delay Characteristics	421
9.2.4	Group Delay Ripple	423
9.2.5	Systems Implications of Non-ideal Filter Characteristics	424
9.3	Fibre and Planar Directional Couplers	425
9.3.1	Basics of Coupled Mode Theory	425
9.3.2	Fabrication of Fibre Couplers	427
9.3.3	Characteristics of Fibre Coupler-Based Wavelength Filters	427
9.3.4	Applications Beyond Wavelength Channel Filters	428
9.3.5	Planar Polarization Splitters	429
9.4	Mach-Zehnder Interferometers	429
9.5	Diffraction Gratings	431
9.5.1	Planar Diffraction Gratings	431

9.5.2	Relevant Parameters of Diffraction Gratings	432
9.5.3	Diffraction Gratings Used in Fibre Optic Communication	433
9.5.4	Planar Echelle Gratings	435
9.6	Arrayed Waveguide Gratings	436
9.6.1	Basics of AWGs	436
9.6.2	AWGs in Silica-on-Silicon	440
9.6.3	AWGs in InP	443
9.6.4	AWGs in SOI	444
9.7	Fibre Bragg Gratings	444
9.7.1	Generic Properties	445
9.7.2	Types of Gratings	447
9.7.3	Apodization	447
9.7.4	Temperature and Strain Dependence	448
9.7.5	Chirped Gratings	448
9.7.6	Long-Period Fibre Bragg Gratings	449
9.7.7	Commercially Available Devices	449
9.8	Fabry-Pérot Interferometers	450
9.8.1	Multiple-Reflection Cavities	451
9.8.2	Wavelength/Frequency Characteristics	452
9.8.3	Implementations	453
9.8.4	Typical Performance Characteristics	454
9.8.5	Applications	454
9.9	Thin Film Filters	455
9.9.1	Generic Functionalities of TFFs	455
9.9.2	Fabrication of TFFs	457
9.9.3	Filters for Telecom Applications	458
9.9.4	Filter Modules	460
9.10	Microrings	463
9.10.1	Key Features of Microring Resonators	463
9.10.2	Polarization-Dependent Effects	465
9.10.3	Higher Order Filters	466
9.10.4	Microring-Based Filters with Extended FSR	468
9.10.5	Prospects and Further Developments of MR-Based Filters	468
9.11	Interleavers	468
9.11.1	Operation Principle	468
9.11.2	Interleaver Types	469
9.11.3	Characteristics of Commercially Available Interleavers	470
9.12	Acousto-Optic Tunable Filters	471
	References	472

10	Optical Switches	483
	Shifu Yuan and John E. Bowers	
10.1	General Concepts of Optical Switching	483
10.1.1	Introduction	483
10.1.2	Basics	484
10.1.3	Optical Matrix Switches	485
10.1.4	Wavelength Selective Switches (WSS)	487
10.2	Opto-Mechanical Switches	492
10.2.1	Fiber Collimators	492
10.2.2	Opto-Mechanical Actuators	493
10.2.3	1×1 , 1×2 , 2×2 and Small Port Count $N \times N$ Opto-Mechanical Switches	493
10.2.4	$1 \times N$ Opto-Mechanical Switches	494
10.2.5	Large Scale $N \times N$ Opto-Mechanical Switches with Robotic Arms	495
10.3	Liquid Crystal (LC)-Based Optical Switching	497
10.3.1	Operating Principles of Liquid Crystal Material for Optical Switches	497
10.3.2	Liquid Crystal Optical Matrix Switch: 1×2 , 2×2 , $N \times N$ and $1 \times N$ Switches	500
10.3.3	Wavelength Selective Switches Using Liquid Crystal Techniques	504
10.4	Waveguide-Based Optical Switches	509
10.4.1	Generic Aspects	509
10.4.2	Electro-Optic Waveguide Optical Switches	510
10.4.3	Waveguide-Based Thermo-Optic Switches	511
10.5	MEMS-Based Optical Switch Technologies	517
10.5.1	Generic Aspects	517
10.5.2	2D MEMS Switches	518
10.5.3	3D MEMS Switches	520
10.5.4	3D MEMS $N \times N$ Optical Switches	523
10.5.5	3D MEMS-Based Wavelength Selective Switches	529
10.6	Piezoelectric Optical Switches	532
10.7	Summary and Outlook	533
	References	533
11	Passive Devices	547
	Wolfgang Coenning and François Caloz	
11.1	Optical Connectors	548
11.1.1	Introduction	548
11.1.2	Connecting Different Types of Fibres	548
11.1.3	Basics of FO-Connectors	550
11.1.4	Relevant Standards for Optical Connectors	551
11.1.5	Optical Requirements for Single-Mode FO-Connectors	552
11.1.6	Mechanical and Climatic Requirements for FO-Connectors	554

- 11.1.7 Available Standard Connector Types 554
- 11.1.8 FO-Cables for Patch Cords 556
- 11.1.9 Connectors for Special Fibres or Special Use 557
- 11.1.10 Cleaning and Inspection 561
- 11.2 Fibre Optical Couplers 562
 - 11.2.1 Introduction 562
 - 11.2.2 Modelling of Optical Directional Couplers/Power Splitters 563
 - 11.2.3 Fibre Coupler Technologies 566
 - 11.2.4 Classification 567
 - 11.2.5 Star Couplers 568
- 11.3 Optical Circulators 569
- 11.4 Optical Isolators 571
 - 11.4.1 General Characteristics 571
 - 11.4.2 Polarisation-Independent Optical Isolators 573
 - 11.4.3 Two-Stage Isolators 575
 - 11.4.4 Commercially Available Optical Isolators 575
- 11.5 Planar Integrated Waveguide-Based Optical Isolators and Circulators 577
 - 11.5.1 Planar Integrated Optical Isolators 577
 - 11.5.2 Planar Optical Circulators 579
- References 581
- 12 Fiber Amplifiers 585**
 - Karsten Rottwitt
 - 12.1 The EDFA 586
 - 12.1.1 Energy Levels 587
 - 12.1.2 Rate Equations 588
 - 12.1.3 Signal Propagation 588
 - 12.1.4 Emission and Absorption Cross Sections 590
 - 12.1.5 Characteristics 591
 - 12.1.6 Amplifier Performance 592
 - 12.1.7 Recent Applications 595
 - 12.2 Raman Amplifiers 599
 - 12.2.1 Propagation Equations 600
 - 12.2.2 The Raman Gain Coefficient 602
 - 12.2.3 Characteristics 603
 - 12.2.4 Amplifier Performance 605
 - 12.2.5 System Considerations 608
 - 12.2.6 Recent Applications 610
 - 12.3 Parametric Amplifiers 613
 - 12.3.1 Propagation Equations 613
 - 12.3.2 Amplifier Gain Spectrum 615
 - 12.3.3 Characteristics 616
 - 12.3.4 Amplifier Performance 617

12.3.5	Application Issues	619
12.3.6	Recent Applications	620
12.4	Conclusion	622
	References	623
13	Hybrid Photonic Integration: Components and Technologies . . .	629
	Ziyang Zhang and Arne Leinse	
13.1	Introduction	629
13.2	Passive Photonic Components	630
13.2.1	Polymer Waveguides	630
13.2.2	TriPleX Waveguides	633
13.2.3	Fiber Attachment Grooves (U-Grooves)	636
13.3	New Hybrid Assembly Approach	637
13.4	Thin Film Elements	638
13.4.1	Wavelength Filters	638
13.4.2	Polarization Handling TFEs	641
13.5	Hybrid Integration with Active Components	643
13.5.1	Planar Photodiode Integration via 45° Mirrors	644
13.5.2	Butt-Joint Laser Diode Integration	648
13.5.3	Gain Chip Integration	649
13.5.4	TriPleX Hybrid Integration Method	651
13.6	Optical Subassemblies and Modules	652
13.6.1	Polymer AWG-Based OLTs	654
13.6.2	TriPleX AWGs	656
13.6.3	Colorless ONU	657
13.6.4	Dual-Polarization Switchable Tunable Laser	660
13.6.5	Colorless Dual-Polarization 90° Hybrid	662
13.6.6	TriPleX Microwave Beam-Former Assembly	664
13.6.7	TriPleX Optical Coherence Tomography Assembly	666
13.7	Conclusion	667
	References	668
14	Silicon Photonic Integrated Circuits	673
	Roel Baets, Wim Bogaerts, Bart Kuyken, Abdul Rahim, Günther Roelkens, Thijs Spuesens, Joris Van Campenhout, and Dries Van Thourhout	
14.1	Silicon Photonics as a Generic Photonic Integrated Circuit Platform	674
14.1.1	The Market Driver: Short Reach Data Links	675
14.1.2	The Physical Driver: High Index Contrast	676
14.1.3	The Technology Driver: The CMOS Fab	679
14.2	Basic Properties of Silicon High-Index-Contrast Waveguides	681
14.2.1	Strip Waveguides	682
14.2.2	Rib Waveguides	684
14.2.3	Slot Waveguides	687
14.3	Wavelength-Handling Components in Silicon Photonics	687

- 14.3.1 Introduction 687
- 14.3.2 Delay Line Based Spectral Filters 689
- 14.3.3 Spectral Filters Using Ring Resonators 695
- 14.4 Grating Coupling for Silicon Photonics 698
- 14.5 Edge Coupling for Silicon Photonics 702
- 14.6 Waveguide Ge Photodetectors on Si 707
 - 14.6.1 Introduction 707
 - 14.6.2 Design Aspects 707
 - 14.6.3 Integration Aspects 709
 - 14.6.4 State of the Art 710
 - 14.6.5 Impact and Outlook 713
- 14.7 Optical Isolators Integrated on a Silicon Photonics Platform . . . 715
- 14.8 Nonlinear Optics Based on Silicon Photonics 718
 - 14.8.1 Introduction 718
 - 14.8.2 Nonlinear Optical Interactions and Nonlinear Optical Materials 719
 - 14.8.3 Applications and Demonstrations 722
- 14.9 Design of Complex Silicon Photonic Integrated Circuits 727
- References 730
- 15 Silicon Lasers and Photonic Integrated Circuits 739**

Sudharsanan Srinivasan, Alan Y. Liu, Di Liang, and John E. Bowers

 - 15.1 Silicon as a Platform for PICs 739
 - 15.2 Lasers (Emitters) and Amplifiers on Silicon 742
 - 15.2.1 Low-Dimensional Silicon Approaches 744
 - 15.2.2 Raman Effect 749
 - 15.2.3 Monolithic Integration Approaches 752
 - 15.2.4 Quantum Dot and Quantum Well Lasers on Silicon 756
 - 15.2.5 Hybrid (Assembly-Level) Integration 762
 - 15.2.6 Heterogeneous (Wafer-Scale) Integration 763
 - 15.2.7 Industrial Development and Commercialization 769
 - 15.3 High-Speed Signal Processing in Silicon 781
 - 15.3.1 Silicon Optical Modulators 782
 - 15.3.2 Hybrid Silicon Modulators 783
 - 15.4 Summary 788
 - References 788
- 16 Photonic Integrated Circuits on InP 799**

Norbert Grote, Moritz Baier, and Francisco Soares

 - 16.1 Introduction 800
 - 16.2 Key Technological Challenges of Photonic Integration 801
 - 16.2.1 Vertical Integration 802
 - 16.2.2 Lateral Integration 805
 - 16.3 Recent Achievements 813
 - 16.4 Open Access to Integration Platforms: Adoption of Foundry Model 820

- 16.4.1 A Generic TxRx PIC Platform 821
- 16.4.2 Testing of PICs 828
- 16.4.3 Design Environment 830
- 16.4.4 Generic Packaging 834
- References 835
- Index** 841

Contributors

Masahiro Aoki Center for Technology Innovation, Research & Development Group, Hitachi Ltd., Hitachi-city, Ibaraki, Japan

Roel Baets Ghent University – imec, Photonics Research Group, Center of Nano- and Biophotonics (NB-Photonics), iGent Tower – Department of Information Technology (INTEC), Ghent University, Gent, Belgium

Moritz Baier Fraunhofer Institute for Telecommunications, Heinrich-Hertz-Institute, Berlin, Germany

Andreas Beling School of Engineering and Applied Science, Department of Electrical & Computer Engineering, University of Virginia, Charlottesville, VA, USA

Wim Bogaerts Ghent University – imec, Photonics Research Group, Center of Nano- and Biophotonics (NB-Photonics), iGent Tower – Department of Information Technology (INTEC), Ghent University, Gent, Belgium

John E. Bowers Electrical and Computer Engineering Department, University of California, Santa Barbara, CA, USA

Fred Buchali Nokia Bell Labs, Stuttgart, Germany

François Caloz Diamond SA, Losone, Switzerland

Joe C. Campbell School of Engineering and Applied Science, Department of Electrical & Computer Engineering, University of Virginia, Charlottesville, VA, USA

Haoshuo Chen Nokia Bell Labs, Holmdel, NJ, USA

Wolfgang Coenning Hochschule Esslingen, Esslingen, Germany

Hélène Debrégeas III–V Lab, Palaiseau, France

Norbert Grote Fraunhofer Institute for Telecommunications, Heinrich-Hertz-Institute, Berlin, Germany

Wilfried Idler Nokia Bell Labs, Stuttgart, Germany

A.M.J. (Ton) Koonen Technische Universiteit Eindhoven, Eindhoven, MB, The Netherlands

Bart Kuyken Ghent University–imec, Photonics Research Group, Center of Nano- and Biophotonics (NB-Photonics), iGent Tower–Department of Information Technology (INTEC), Ghent University, Gent, Belgium

Arne Leinse LioniX BV, Enschede, AL, The Netherlands

Di Liang Hewlett Packard Labs in Hewlett Packard Enterprise (HPE), Palo Alto, CA, USA

Alan Y. Liu Materials Department, University of California, Santa Barbara, CA, USA

Martin Moehrle Fraunhofer Institute for Telecommunications, Heinrich-Hertz-Institute, Berlin, Germany

Denis Molin Prysmian Group, Parc des Industries Artois Flandres, Haisnes Cedex, Billy Berclau, France

Markus Ortsiefer VERTILAS GmbH, Garching, Germany

Abdul Rahim Ghent University–imec, Photonics Research Group, Center of Nano- and Biophotonics (NB-Photonics), iGent Tower–Department of Information Technology (INTEC), Ghent University, Gent, Belgium

Günther Roelkens Ghent University–imec, Photonics Research Group, Center of Nano- and Biophotonics (NB-Photonics), iGent Tower–Department of Information Technology (INTEC), Ghent University, Gent, Belgium

Karsten Rottwitt DTU Fotonik, Department of Photonics Engineering, Technical University of Denmark, DTU, Kgs. Lyngby, Denmark

Yasuo Shibata NTT Electronics Corporation, Atsugi-shi, Kanagawa Pref., Japan

Pierre Sillard Prysmian Group, Parc des Industries Artois Flandres, Haisnes Cedex, Billy Berclau, France

Francisco Soares Fraunhofer Institute for Telecommunications, Heinrich-Hertz-Institute, Berlin, Germany

Thijs Spuesens Ghent University–imec, Photonics Research Group, Center of Nano- and Biophotonics (NB-Photonics), iGent Tower–Department of Information Technology (INTEC), Ghent University, Gent, Belgium

Sudharsanan Srinivasan Aurrion Inc., Goleta, CA, USA

Ute Troppenz Fraunhofer Institute for Telecommunications, Heinrich-Hertz-Institute, Berlin, Germany

Joris Van Campenhout imec, Heverlee, Belgium

Dries Van Thourhout Ghent University – imec, Photonics Research Group, Center of Nano- and Biophotonics (NB-Photonics), iGent Tower – Department of Information Technology (INTEC), Ghent University, Gent, Belgium

Herbert Venghaus c/o Fraunhofer Institute for Telecommunications, Heinrich-Hertz-Institute, Berlin, Germany

Hiroshi Yasaka Research Institute of Electrical Communication, Tohoku University, Sendai-shi, Miyagi Pref., Japan

Shifu Yuan Calient Technologies, Goleta, CA, USA

Ziyang Zhang Leibniz Institute for Astrophysics (AIP), Potsdam, Germany

Abbreviations

3DW	3-dimensional waveguide
ACC	automatic current control
ADC	analogue-to-digital converter
AMI	alternate mark inversion
AOTF	acousto-optic tunable filter
APC	angled physical contact connector
APC	automatic power control
APD	avalanche photodiode
AR	antireflection
ASE	amplified spontaneous emission
ASIC	application specific integrated circuit
ASK	amplitude-shift keying
AWG	arrayed waveguide grating
AWGN	additive white Gaussian noise
BB	building block
BCB	benzocyclobutene
BCH	Bose-Chaudhuri-Hocquenghem
BDP	beam displacing prism
BER	bit error rate, bit error ratio
BH	buried-heterostructure
BiCMOS	bipolar complementary metal-oxide semiconductor
BOX	buried oxide layer
BPSK	binary phase-shift keying
BR	buried ridge
B_{ref}	reference bandwidth
BRS	buried ridge stripe
BTC	block turbo code
BTJ	buried tunnel junction
BW	bandwidth

\hat{C}	Shannon capacity
C:YIG	Ce substituted yttrium iron garnet
CAGR	cumulated annual growth rate
CapEx	capital expenditure
CB	conduction band
CCD	charge-coupled device
CD	chromatic dispersion
CDL	core dependent loss
CDP	carrier density pulsation(s)
CFO	carrier frequency offset
CFP	compact form-factor pluggable (100G optical transceiver)
CIL	coupler insertion loss
CL	cylindrical lens
CLIPP	contactless integrated photonic probe
CMA	constant modulus algorithm
CMCF	coupled multi-core fibre
CML	chirp managed laser
CMOS	complementary metal oxide semiconductor
CMP	chemical mechanical polishing
CPE	carrier phase estimation
CRM	cylindrical reflective mirror
CRx	coherent receiver
CSDFB	curved stripe DFB (laser)
CTE	coefficient of thermal expansion
CVD	chemical vapour deposition
CW	continuous wave
CWDM	coarse wavelength division multiplexing
DA	data aided
DAC	digital-to-analogue converter
DBR	distributed Bragg reflector
DC	direct current
DCF	dispersion compensated/-ing fibre
DCG	dispersion-compensating (fibre Bragg) grating
DD	decision directed least mean square
DD	dual-drive
DDR	dual-depletion region (photodiode)
D-EML	dual-EML
DEMUX	demultiplexer
DER	dynamic extinction ratio
DFB	distributed feedback
DGD	differential group delay
DM	discrete mode
DMA	differential mode attenuation
DMD	differential mode delay

DMG	differential modal gain
DML	directly modulated laser
DMT	discrete multi-tone
DMX	de-multiplexing
DNL	differential nonlinearity
DoF	degree-of-freedom
DOS	digital optical switch
DP	dual polarization
DP-QPSK	dual polarization quadrature phase-shift keying
DPSK	differential phase-shift keying
DQPSK	differential quadrature phase shift keying
DR	distributed reflector
DRA	distributed Raman amplifier
DRC	design rule check
DS-DBR	digital supermode distributed Bragg reflector
DSF	dispersion shifted fibre
DSP	digital signal processing/processor
DUV	deep UV (lithography)
DVI	digital visual interface
DVS-BCB	divinylsiloxane-bis-benzocyclobutene
DWDM	dense wavelength division multiplexing
E/E	electrical/electrical
E/O	electrical/optical
EA	electroabsorption
EAM	electroabsorption modulator
E _b	energy per bit
EDFA	erbium-doped fibre amplifier
E-FEC	enhanced forward error correction
EIC	extended wavelength independent coupler
EL	electroluminescence
EMB	effective modal bandwidth
EMB _c	effective modal bandwidth, computed
EML	electroabsorption modulated laser
EML	externally modulated laser
ENOB	effective number of bits
EO	electro-optic
ER	extinction ratio
E _s	energy per symbol
e-XFP	extended XFP
EXNOR	exclusive-NOR
F-ADC	flash-analogue-to-digital converter
FBC	fused biconical coupler
FBG	fibre Bragg grating

FCA	free carrier absorption
FDE	frequency domain equalizer
FDM	frequency division multiplexing
FEC	forward error correction
FEM	finite element method
FIC	full range wavelength independent coupler
FIN	finesse
FIR	finite impulse response (filter)
FM	frequency-shift keying modulation
FMF	few-mode fibre
FO	fibre-optic
FOM	figure of merit
FP	Fabry-Pérot (cavity)
FPI	Fabry-Pérot interferometer
FPR	free propagation region
FRP	fibre glass reinforced plastic
FSR	free spectral range
FTT	fast Fourier transform
FTTH	fibre-to-the-home
FTTX, FttX	fibre-to-the-X, X = curb, building, home
FWHM	full width half maximum
GbE	Gigabit Ethernet
GC	gain chip
GCSR	grating-assisted codirectional coupled sampled grating reflector (laser)
GDR	group delay ripple
GE	Gigabit Ethernet
GFF	gain-flattening filter
GI	graded index
GI-POF	graded-index POF
GN	Gaussian noise
GRIN	graded index (lens)
GSG/GS	ground-signal-ground/ground-signal
GTI	Gires-Tournois interferometer
GVD	group velocity dispersion
HBT	heterojunction bipolar transistor
HCPS	hexagonal close-packed structure
HCSEL	horizontal cavity surface emitting laser
HD	hard decision
HDMI	high-definition multimedia interface
HFFR	halogen free fire retardant
HH	heavy hole
HNA	high numerical aperture (fibre)

HOM	higher order mode
HOM	higher order modulation
HPLD	high-power laser diode
HR	high reflection/reflectivity
HR-XRD	high-resolution X ray diffraction
HSEP	heterogeneous silicon evanescent platform
HWP	half-wave plate
I	in-phase
I ² E	impact ionization engineering
IA	implementation agreement
IC	integrated circuit
ICE	impedance control electrode
ICP	inductively coupled plasma (etching)
ICT	Information and Communication Technology
IDM	integratable discrete mode
IEC	International Electrotechnical Commission
IFB	integrated feedback
IIR	infinite impulse response (filter)
IL	insertion loss
IM	intensity modulation
INL	integral nonlinearity
IPDR	input power dynamic range
IQ	in-phase and quadrature, in-phase/quadrature
ISI	inter-symbol interference
ITLA	integrated tunable laser assembly
ITO	indium tin oxide
ITRS	International Technology Roadmap for Semiconductors
ITU	International Telecommunication Union
ITU-T	ITU- Telecommunication Standardisation Sector
LC	liquid crystal
LC	long cavity
LCoS	liquid crystal on silicon
LD	laser diode
LDPC	low density parity check code
LE	lumped element
LED	light emitting diode
LH	light hole
LISEL	lens integrated surface emitting laser
LIV	light-current-voltage
LMS	least mean square
LO	local oscillator
LP	linear(ly) polarized
LPCVD	low-pressure CVD

LPE	liquid phase epitaxy
LPG	long-period FBG
LPIN	lateral p-i-n (photodiode)
LR	low-reflectivity
LSB	least significant bit
LSZH	low smoke zero halogen
LTOPA	low-temperature oxygen plasma-assisted
LW	long-wavelength
LWPF	long wavelength pass filter
MAP	maximum-a-posteriori
MBE	molecular beam epitaxy
MCF	multi-core fibre
MCS	multi-cast switch
MC-SMF	multi-core single-mode fibre
MCVD	modified chemical vapour deposition
MDGD	modal differential group delay
MDL	mode-dependent loss
MEMS	micro-electro-mechanical system
MESFET	metal-semiconductor field-effect transistor
MFD	mode field diameter
MIMO	multiple-input-multiple-output
MLA	micro lens array
MMF	multimode fibre
MMI	multimode interference
MOF	micro-structured optical fibre
MOMBE	metal-organic MBE
MOVPE	metal-organic VPE
MPD	monitor photodiode
MPW	multi-project wafer
M-QAM	number of symbol (M)-quadrature amplitude modulation
MQW	multi-quantum well
MR	microring
MRR	microring resonator
MSA	multi-source agreement
MSB	most significant bit
MSK	minimum-shift keying
MSL	microstrip line
MSM	metal-semiconductor-metal
MUTC	modified uni-travelling-carrier (photodiode)
MUX	multiplexer
MWIR	mid-wave infrared/medium wavelength infrared
MWP	microwave photonics
MZ	Mach-Zehnder
MZDI	Mach-Zehnder delay interferometer

MZI	Mach-Zehnder interferometer
MZM	Mach-Zehnder modulator
NA	numerical aperture
NCG	net coding gain
NF	noise figure
NRZ	non-return-to-zero
NZDSF	non-zero dispersion-shifted fibre
O/E	opto/electrical
OADM	optical add-drop multiplexer
OBFN	optical beam-forming network
ODB	optical duobinary
OEIC	opto-electronic integrated circuit
OEO	opto-electronic-optical/optical-electrical-optical
OFDM	orthogonal (optical) frequency division multiplexing
OFE	optical front end
OFL	over-filled launch (condition)
OH	overhead
OIF	Optical Internetworking Forum
OLT	optical line terminal
OM _{<i>i</i>} (<i>i</i> = 1, 2, 3, 4)	special classes of multi-mode fibre
ONU	optical network unit
OOK	on-off keying
OPGW	optical ground wire
ORR	optical ring resonator
ORS	one-ring structure
OSNR	optical signal to noise ratio
OSNR _{RX}	optical signal to noise ratio receiver sensitivity
OSR	optical spectrum reshaper
OSSB	optical single-sideband
OTDR	optical time-domain reflectometry
OTN	optical transport network
OTU	optical transport unit
OVD	outside vapour deposition
PAM	pulse amplitude modulation
PAM4	4-level amplitude modulation
PAN	parallel aligned nematic
PBG	photonic bandgap
PBS	polarization beam splitter
PC	physical contact (-polished connector)
PCG	planar concave grating
PCI	peripheral component interconnect
PCVD	plasma chemical vapour deposition

PD	photodiode
PDA	partially-depleted-absorber (photodiode)
PDG	polarization dependent gain
PDK	process design kit
PDL	polarization dependent loss
PDM	polarization division multiplexing
PECVD	plasma-enhanced chemical vapour deposition
PER	polarization extinction ratio
P_F	fibre launch power
PFL	passive feedback laser
PIC	photonic integrated circuit
PI-IL	path-independent insertion loss
PL	photoluminescence
PL	pipeline
PLC	planar lightwave circuit
PM	polarization maintaining (fibre)
PMC	polarization multiplexing circuit
PMD	polarization mode dispersion
PMMA	polymethylmethacrylate
PM-QPSK	polarization-multiplexed QPSK
POF	plastic optical fibre
PON	passive optical network
P_{opt}	optimum fibre launch power
PRBS	pseudorandom bit/binary sequence
PS	polarization splitter
PS	polarization switch
PSK	phase-shift keying
PSM4	parallel single-mode 4-lane
PSTFE	polarization splitting thin film element
PVTEM	plain-view transmission electron microscope
PWC	printed wiring chip
PWG	passive waveguide
Q	quadrature
QAM	quadrature amplitude modulation
QCSE	quantum-confined Stark effect
QD	quantum dot
QPSK	quadrature phase-shift keying
QW	quantum-well
QWI	quantum-well intermixing
R&D	research and development
r.m.s.	root mean square
RAP	right angle prism
R_c	code rate

Rc	raised cosine
RCE	resonant cavity enhanced (photodetector)
RF	radio frequency
RFPD	refracting facet photodiode
RIE	reactive ion etching
RL	return loss
ROADM	reconfigurable optical add-drop multiplexer
RS	Reed Solomon
RS	ridge shape
Rs	symbol rate
RSOA	reflective semiconductor optical amplifier
RTA	rapid thermal annealing
RW	ridge waveguide
RWG	ridge waveguide
Rx	receiver
RZ	return-to-zero
RZ-DPSK	return-to-zero differential phase-shift keying
RZ-DQPSK	return-to-zero differential quadrature phase-shift keying
SACM	SAM APD including a charge layer
SAE	selective area epitaxy
SAG	selective area growth
SAM	separate absorption and multiplication (APD)
SAR	successive approximation register
SBS	stimulated Brillouin scattering
SCEEL	short-cavity edge-emitting laser
SC-FMF	single-core few-mode fibre
SD-FEC	soft decision forward error correction
SDM	space/spatial division multiplexing
SD _{SDM}	spatial density (of SDM fibre)
SE	spectral efficiency
SEM	scanning electron microscope
SER	symbol error rate (probability)
SFDR	spurious free dynamic range
SG	sampled grating
SG-DBR	sampled grating distributed Bragg reflector
SGGG	substituted gadolinium gallium garnet
SH	sample and hold
SHA	sample and hold amplifier
SI	semi-insulating
SI	step index
SINAD	signal-to-noise-and-distortion ratio
SLE	slope efficiency
SLM	spatial light modulator
SM	single mode

SMF	single-mode fibre
SMSR	side-mode suppression ratio
SNR	signal-to-noise ratio
SNR _b	signal-to-noise ratio per bit
SNR _s	signal-to-noise ratio per symbol
SO	split-off (valence band)
SOA	semiconductor optical amplifier
SOAG	semiconductor optical amplifier gate
SOI	silicon-on-insulator
SOP	state of polarization
SoS	silica-on-silicon
SR	serial ripple
SSB	single sideband
SSC	spot size converter
SSC	standard single-mode coupler
SSFM	split step Fourier method
SSG	super-structure grating
SSMF	standard single-mode fibre
SVD	singular value decomposition
SWIR	short wave/wavelength infrared
SWP	spatial walk-off polarizer
TE	transverse electric (polarized light)
TEC	thermally expanded core
TEC	thermoelectric cooler
TEM	transmission electron microscope
TFE	thin-film element
TFF	thin-film filter
TGG	terbium-gallium-garnet
THD	third harmonics distortion
TI	time interleaved
TI DMD	Texas Instruments digital micromirror device
TIA	Telecommunications Industry Association
TIA	transimpedance amplifier
TIR	total internal reflection
TLA	tunable DFB laser array
TM	transverse magnetic (polarized light)
TMC	thermometer coded
TN	twisted nematic
TO	thermo-optic
TOS	thermo-optic switch
TOSA	transmitter optical sub-assembly
TPA	two-photon absorption
TPS	two-pitch structure
Tx	transmitter

UMCF	uncoupled multi-core fibre
UTC	uni-travelling-carrier (photodiode)
VAD	vapour axial deposition
VB	valence band
VCSEL	vertical cavity surface emitting laser
VOA	variable optical attenuator
VPH	volume-phase holographic
VSL	variable stripe length (method)
WDL	wavelength-dependent loss
WDM	wavelength division multiplexing
WFC	wavelength flattened coupler
WG	waveguide
WGDP	waveguide-photodiode
WIC	wavelength independent coupler
WSS	wavelength selective switch
WSXC	wavelength-selective cross-connect
XFP	extra flat packaging (10 Gbit small form factor pluggable module)
XRD	X-ray diffraction
YIG	yttrium-iron-garnet

Chapter 1

Spatial Division Multiplexing

Haoshuo Chen and A.M.J. (Ton) Koonen

Abstract Spatial division multiplexing (SDM) by employing few-mode fiber or multi-core fiber is expected to efficiently enhance the capacity of optical networks and overcome the anticipated ‘capacity crunch’ due to fast increasing capacity demand. This chapter first introduces the advantages and state-of-the-art of SDM. Second, different SDM technologies and key building blocks such as spatial multiplexer, optical amplifier, wavelength selective switch, splicer, connector and digital signal processing block are thoroughly analyzed. Third, commercialized SDM-related components are summarized and discussed.

1.1 Introduction

The exploitation of the spatial domain, which is regarded as the last unexplored physical dimension in optical communication [1, 2], has come into spotlight recently and the corresponding technologies are designated as spatial division multiplexing (SDM).¹ While the utilization of spatial channels in order to enhance system capacity is still considered as innovative in the optical world, “SDM” has already

¹“SDM” is spelled out in the literature both as “spatial” and as “space” division multiplexing. SDM comprises various realization concepts: (1) Transmission based upon multiple parallel fibers, each with a separate cladding comprising one or more cores, without coupling between the fibers is one straightforward SDM concept. (2) Multi-channel transmission using fibers with a single few-moded or highly multi-moded core inside a cladding is designated to the point as mode-division multiplexing (MDM) although the designation SDM is also found in the literature for this case. (3) Transmission based upon multiple cores inside a single cladding where (i) each core may be single-moded without coupling between cores, (ii) each core may be multi-moded without coupling between the cores, (iii) there may be coupling between the cores of a multi-core fiber resulting in supermodes, is typically designated as SDM although MDM may also be comprised.

H. Chen (✉)
Nokia Bell Labs, 791 Holmdel Road, Holmdel, NJ 07733, USA
e-mail: haoshuo.chen@nokia-bell-labs.com

A.M.J. Koonen (✉)
Technische Universiteit Eindhoven, P.O. Box 513, 5600 MB, Eindhoven, The Netherlands
e-mail: a.m.j.koonen@tue.nl

been widely applied in the electronic and wire-less worlds, which influences our life unconsciously. PCI (Peripheral Component Interconnect) which refers to multiple parallel digital signal ports is widely used as a local computer bus. It interconnects mother boards with external functioning cards for video, sound and network. HDMI (High-Definition Multimedia Interface) and DVI (Digital Visual Interface), both characterized by a 2-dimensional digital port structure, support the transmission of high-quality videos from players to screens. Moreover, Wi-Fi empowered by multiple-input-multiple-output (MIMO) technology based on multiple antennas [3] is inevitable in our daily life to provide mobile Internet access.

In the optical domain, besides arranging more parallel optical fibers together as a fiber bundle, multiple modes co-propagating over few-mode fiber (FMF) and parallel-signal transmission over coupled or uncoupled multi-core fiber (MCF) are currently regarded as new-emerging SDM technologies to be exploited in optical communication. However, the origin of the concept to employ MCF and multiple modes co-propagating can be traced back to 1979 [4] and 1982 [5], respectively. However, only limited attention was paid to these SDM technologies during the past decades because capacity requirements of optical networks could nicely be satisfied by other, more cost-efficient technologies such as low-loss single-mode fiber (SMF) [6], optical amplifiers such as erbium-doped fiber amplifiers (EDFA) [7], wavelength division multiplexing (WDM) [8], quadrature (and higher order) multi-level modulation [9] and polarization division multiplexing (PDM) [10]. Figure 1.1 shows the evolution of the record transmission capacity and capacity demand of optical networks [2, 11]. Due to the fast growth of capacity requirement of optical networks, it has been foreseen that future bandwidth demands will exceed the maximum achievable capacity of SMF-based networks due to fiber nonlinear effects [12, 13]. The ‘capacity crunch’ [14] has been anticipated to happen around 2018, when commercial systems are expected to offer capacity per fiber in excess of 80 Tbit/s [15], which is almost the cap of SMF-based networks. As the last unexplored physical dimension, space [16, 17], and correspondingly SDM, is proposed to

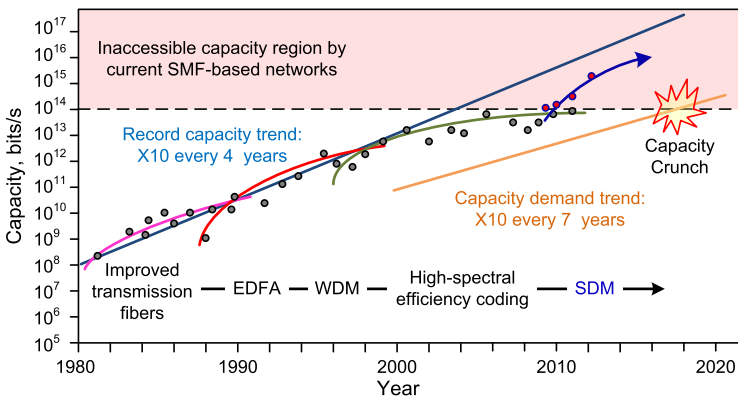


Fig. 1.1 The evolution of the record transmission capacity and capacity demand of optical networks

Table 1.1 System requirements for different optical networks

	Distance	Spectral efficiency	Component costs	Reliability
Submarine	<12.000 km	Highest	Highest	Highest
Long-haul	<4000 km	Higher	Higher	Higher
Regional	<1000 km	High	High	High
Metro	<200 km	High	High	High
Access	<100 km	Medium	Medium	Medium
Datacenter	<100 m	Low	Low	Low

bring a big leap forward in spectral efficiency per fiber so that the ‘capacity crunch’ is expected to be averted.

1.2 Why SDM?

The later 1970s witnessed the upspring of optical fiber based links and more recently copper cables have been rapidly replaced by optical fibers which offer a significant advantage in bandwidth distance product. The optical network development moved from long-haul to metro, access and nowadays to datacenter networks. Although datacenters have been the last where optical technologies have been introduced, SDM technologies have already been deployed in servers and super-computer interconnected networks due to their short distances, e.g. <100 m and strict requirements for low installation and maintenance costs. Vertical cavity surface emitting lasers (VCSELs), which are much cheaper than edge-emitting lasers and can be arranged as 2D arrays in a single wafer, along with low-cost PIN photodiodes have become key enabling components for the deployment of SDM in datacenters. SDM fibers such as MMF ribbons [18, 19] and MCFs with multi-mode cores [20–22] have been commercialized for datacenter and other short-reach applications in order to achieve high alignment tolerance, lower cabling costs and increasing cable density. 70 Gbit/s transmission over 100 m multi-mode 7-core UMCF was demonstrated by employing low-cost VCSELs [23]. A compact fiber link composed of a VCSEL array, MCF and a photodiode array can be a low cost and low power consumption solution for optical interconnects.

Datacenter development is mainly driven by cost, but in general any technology has to prove its reliability [24, 25] before its implementation starts in telecommunication networks ranging from access to submarine links as listed in Table 1.1. Moreover, the introduction of new technologies needs to be a smooth transition based upon existing infrastructure. For SDM technologies, the latter expectation cannot be fully satisfied since SMF links cannot be reused and new SDM fibers have to be deployed. Therefore the chance of SDM is expected to be primarily in new and upgraded optical networks for which new or more fibers have to be placed in order to meet the capacity demand. Under these circumstances, submarine networks can

be the first opportunity for SDM deployment since these networks are mostly influenced by fiber nonlinear effects due to the ultra-long length and will be confronted with a capacity crunch in the first position. Note that submarine networks also have the highest requirements on reliability, which means that the performance of SDM links has to be comparable to that of commercial SMF links. For the practical implementation, new-emerging SDM fibers such as FMF and MCF need to be verified with respect to their advantages in terms of cost-efficiency and energy-efficiency compared to simply arranging a number of parallel SMFs as a fiber bundle.

1.2.1 Cost-Efficiency

The development of SDM fibers such as MCF or FMF integrating multiple spatial channels over one fiber can be regarded as an extension of the integration trend in optical communication. Photonic integration enables fabrication of powerful photonic integrated circuits (PICs) composed of a large number of optical elements. Densely-integrated optical transmitters [26–28] and receivers [29, 30] have been demonstrated in support of WDM signals. The cost-efficiency of PICs through wafer-scale mass-production is more advantageous compared to the solutions employing discrete components, as the total number of components is getting larger. This is exactly the demand for SDM compatible optical transponders whose components' number is proportional to the spatial-channel number. Besides, SDM opens the possibility to integrate other key optical modules such as optical amplifiers [31, 32] and wavelength selective switch (WSS) based optical reconfigurable add/drop multiplexers (ROADMs) [33, 34]. SDM solutions provide the feasibility for network integration and therefore are able to lower the network cost per bit. Economic aspects of SDM are treated in more detail in the [Appendix \(Sect. 1.7\)](#).

1.2.2 Energy-Efficiency

It was pointed out [35, 36] that the energy efficiency of optical networks has been improving with a rate of about 15% annually, which can hardly be expected to be followed by simply deploying more SMFs. Considering a majority of power consumption comes from system management overheads [36], SDM which provides higher spectral efficiency is able to improve overall energy efficiency. For example, (1) a single cooling system can be used for a densely-integrated SDM transponder; (2) a cladding-pumped multi-mode EDFA by employing one multi-mode laser diode [31, 32] can amplify all spatial channels together with no need for a temperature controlling system (see also Chap. 12); (3) since spatially multiplexed signals over one specific wavelength are amplified and switched together, signals over one SDM fiber will experience common impairments which enables joint digital signal processing (DSP) to compensate the same impairments, e.g., frequency offset and

Table 1.2 Potential applications of SDM technologies and key components for different telecommunication networks and datacenters

	FMF or CMCF	UMCF	SDM amplifier	SDM ROADM
Submarine	✓	✓	✓	
Long-haul	✓	✓	✓	✓
Regional	✓	✓	✓	✓
Metro	✓	✓		
Access	✓	✓		
Datacenter		✓		

✓: high potential, applications without mark: less promising

phase distortions in coherent detection [37, 38]. Compared to independent multiple SMFs, power consumption at the receivers can be reduced due to lower computational complexity; (4) one overhead including routing and management information is enough for all spatially multiplexed signals and can be added into one spatial channel. In this case, the other channels can directly send data information. After a proof-point in submarine links has been reached, SDM can be passed down to terrestrial networks due to the aforementioned advantages in cost- and energy-efficiency. Table 1.2 gives expected potential applications of SDM technologies and key components for different telecommunication networks and datacenters. Transmission of multiple modes over FMF or coupled MCF (CMCF) and independent signal co-propagation over different cores of uncoupled MCF (UMCF) have their advantages and disadvantages, respectively, which also strongly depend on the development of related components, and fibers along with electronics in the future.

1.3 State-of-the-Art

In the past few years, a series of successful experiments employing SDM has been carried out in telecommunication networks. High capacity SDM, combined with WDM transmission trials are listed in Table 1.3 with an increasing transmission distance. 140.7 Tbit/s transmission [39] over a 7-core MCF of 7326 km length is a record SDM transmission distance. All state-of-the-art SDM system trials listed in the top half of the table have been realized by MDM over either FMF or multi-mode fiber (MMF). The highest achieved spectral efficiency per fiber core for MDM is 32 bit/s/Hz [40], almost 3 times larger than the maximum capacity that can be provided by an SMF over the same distance. The MDM demonstration over a conventional MMF [41] further enhances the possibility for practical applications of SDM since already deployed MMFs can be reused. By the end of December 2014, combined SDM and WDM trials with a transmission distance longer than 1000 km were only demonstrated with MCFs, listed in the bottom part of Table 1.3. Components for MCF based networks such as multi-core EDFA [42], MCF compatible reconfigurable optical add/drop (ROADM) [33] and MCF loop [43] were demonstrated through directly upgrading the existing SMF based ones. On the contrary to

Table 1.3 High capacity SDM combined with MDM transmission trials (SMUXs will be treated in detail below, see Sect. 1.4.2)

	Distance (km)	Capacity (Tbit/s)	Spectral efficiency (bit/s/Hz)	Fiber type	SMUX solution
[44]	119	73.7	12	3-mode FMF	Phase plate
[50]	120	7.68	9.6	3-mode FMF	Spot coupler
[40]	177	24.6	32	6-mode FMF	Photonic lantern
[51]	305	18	9	MMF	Photonic lantern
[52]	500	30	3.6	3-mode FMF	Phase plate
[49]	900	9.6	3	3-mode FMF	Photonic lantern
[52]	1000	3.5	1.8	3-mode FMF	Phase plate
[53]	1500	2×344	36.8	12-core MCF	Fiber bundle
[54]	1705	17.82	18	6-core CMCF	Photonic lantern
[55]	2688	7.5	15	7-core MCF	Fiber bundle
[56]	4200	1.2	4.8	3-core CMCF	Spot coupler
[42]	6160	28.8	14.4	7-core MCF	Fiber bundle
[43]	7326	140.7	28	7-core MCF	Fiber bundle

the MCF trials, although few-mode EDFA [44–46], few-mode re-circulation loop [47, 48] and low-loss mode coupler [49] were verified successfully, non-negligible mode-dependent loss (MDL) and coupler insertion loss (CIL) still exist in these components, which limit the distance, especially in an accumulated case such as loop measurements.

1.4 SDM Components

1.4.1 SDM Fiber

Figure 1.2 illustrates different optical fibers.

(1) SMF, see Fig. 1.2(a), is operating below the cut off frequency and guides the fundamental LP_{01} mode only. Therefore, SMF provides one spatial channel with two orthogonal polarization states.

(2) FMFs have a slightly bigger core, as shown in Fig. 1.2(b) which enables guiding a few fiber modes. Linearly polarized (LP) modes are well known and usually used to represent fiber modes. However, in SDM, especially MDM, spatial modes are used more often since the number of spatial modes is exactly that of the spatial channels, each of which has two orthogonal polarization states. For spatial modes, degenerate LP modes are considered as two different modes, in other words, two spatial channels. For example, the LP_{11} mode in LP mode definition is degenerate and has two spatial modes LP_{11a} and LP_{11b} . One rotated by 90 degrees with respect to the other, see Fig. 1.3(a).

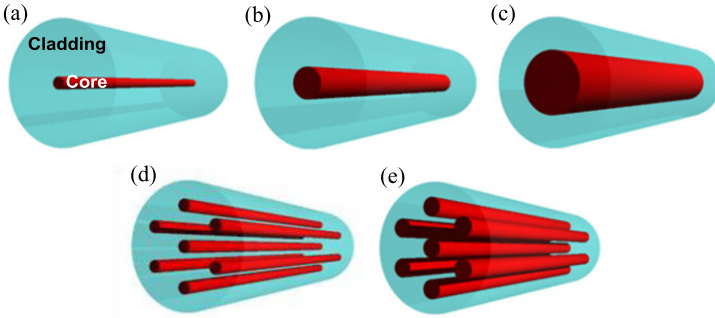


Fig. 1.2 Illustrations of different optical fibers: (a) SMF; (b) FMF; (c) MMF; (d) MCF and (e) multi-core FMF

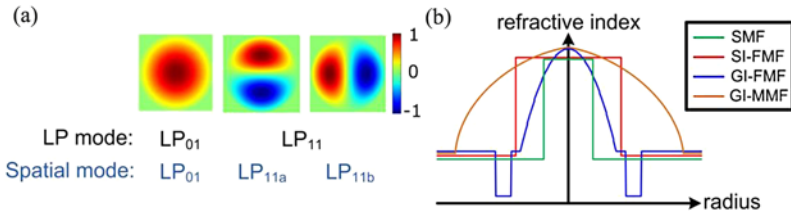
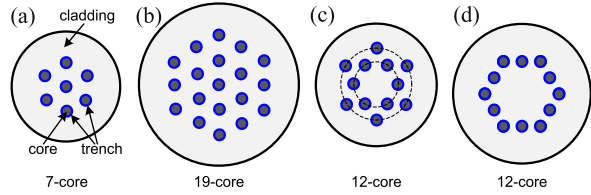


Fig. 1.3 (a) Relation between LP and spatial modes, and (b) index profiles for different fiber types. Color indicates relative phase of isolated modes

Both, step-index (SI) and graded-index (GI) FMFs, see Fig. 1.3(b), can be used in MDM transmission. The SI index profile enables to minimize mode coupling and achieve weakly-coupled FMFs [57, 58]. The differences of propagation velocities between different modes in SI-FMF are quite large, which makes it difficult to achieve a small modal differential group delay (MDGD) over long distance transmission, i.e., <20 ps/km. If there is negligible modal crosstalk and each mode can be individually detected, the complexity of multiple-input-multiple-output based receivers can be significantly reduced and MDGD is not an issue anymore. The practical application of this type of FMF requires precise fiber splicing along the fiber link and excellent FMF components such as spatial multiplexers (SMUXs) to selectively launch and detect each mode. The GI-FMF is generally designed with an index trench [58, 59] in order to minimize fiber bend loss, see Fig. 1.3(b). Low MDGMs within ps/km can be achieved by a well-designed GI index profile. Moreover, through combining FMF spools with positive and negative delays, the cascaded MDGDs can be fully compensated [50], which is beneficial for reducing the size of the MIMO equalizer in the receiver. The additional advantage is that no mode-selective SMUXs are required. Conventional MMFs are generally fabricated with a core size of $50 \mu\text{m}$ or $62.5 \mu\text{m}$ in a $125 \mu\text{m}$ cladding. A $50 \mu\text{m}$ GI-MMF, see Fig. 1.3(b), supports around 50 spatial modes in the wavelength regime around 1550 nm and has a maximum MDGD around 2 ns/km . Due to the modal disper-

Fig. 1.4 UMCF integrating (a) 7, (b) 19, (c, d) 12 cores in a single cladding



sion, MMF is mostly used for short-distance communication. Particular attention has been paid to explore the SDM possibilities of MMFs as an already installed fiber which supports MDM. It has been demonstrated that low order modes can be selectively launched and detected [41, 51] and >300 km MDM transmission over MMF is possible.

(3) Multi-core fiber is another type of SDM fiber, which integrates multiple cores in one cladding. MCF can be categorized into two groups depending on whether cores are coupled with each other or not: coupled-MCF (CMCF) and uncoupled-MCF (UMCF), respectively.

Each core of the UMCF can be regarded as an individual spatial channel. For long-distance (i.e., >10 km) optical networks, large capacity transmission over 7-core [39, 55, 60], 12-core [53, 61] and 19-core [62, 63] has been demonstrated. The 7-core, see Fig. 1.4(a) and 19-core, see Fig. 1.4(b) UMCFs are both based on a hexagonal close-packed structure (HCPS). In order to reduce the crosstalk between cores, trench-assisted [64] and hole-assisted [65, 66] structures have been proposed. The trenches and holes around cores have a smaller index which confines the electric field distribution in each core. Two kinds of 12-core MCFs, based on a two-pitch structure (TPS) [53] and a one-ring structure (ORS) [61], respectively, have also been demonstrated, see Fig. 1.4(c) and (d). The significant advantage of UMCF is that commercial polarization-diversity coherent receivers can be directly used for signal recovery. To support long-haul transmission, UMCF needs to achieve low fiber loss, a large effective area (A_{eff}) to reduce fiber nonlinear effects, small inter-core crosstalk, and a reasonable cladding diameter to guarantee mechanical reliability. Another remaining issue for its practical application is scalability. The 19-core UMCF has a cladding diameter around $200 \mu\text{m}$, which is already quite sensitive to fiber bending with a small radius [67]. If the cladding has to be enlarged in order to integrate more cores with negligible inter-core crosstalk, the fiber's mechanical reliability will be a serious issue.

Coupled MCF is the other type of MCF which can have strongly- or weakly-coupled cores [68]. For CMCFs, supermodes are generated at the coupled-core region where each supermode can be regarded as one spatial channel. Figures 1.5 and 1.6 show the schematics and simulated supermode profiles for a 3-core and 6-core CMCF, respectively. It is worthwhile to note that the phases of the isolated modes, the superposition of which results in the supermodes, are not always the same. This is indicated in Figs. 1.5 and 1.6 by the different colors which indicate the relative phases of the constituent isolated modes. In simulations, the index contrast and core diameter d for both fibers are 3×10^{-3} and $12 \mu\text{m}$, respectively. The circle radii, r , where cores are located, are $17 \mu\text{m}$ and $28 \mu\text{m}$, respectively. Compared to

Fig. 1.5 (a) Schematic of a 3-core CMCF and (b) simulated supermode profiles. *Color* indicates relative phase of isolated modes

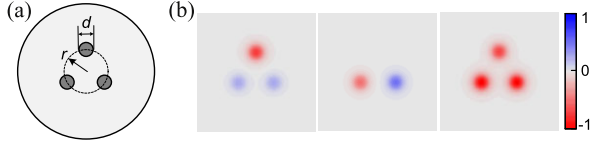


Fig. 1.6 (a) Schematic of a 6-core CMCF and (b) simulated supermode profiles. *Color* indicates relative phase of isolated modes

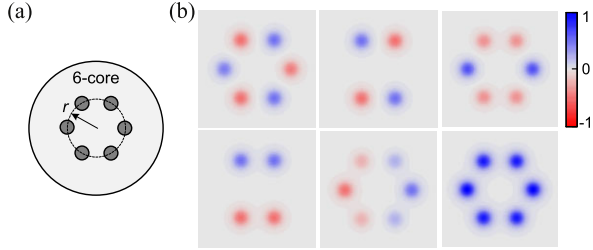


Table 1.4 Comparison between FMF and two types of MCFs

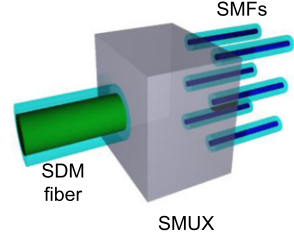
	Spatial utilization efficiency	DSP complexity	Nonlinearity tolerance [72]	Scalability
FMF/MMF	High	High	Medium	High
CMCF	Medium	Medium	Medium/High	Medium
UMCF	Low	Low (\approx SMF)	Low (\approx SMF)	Low

FMF, CMCF can be designed with larger A_{eff} and is therefore more tolerant to fiber nonlinearities [69, 70]. 4200 km and 1705 km combined SDM and WDM transmission have been achieved by 3-core and 6-core CMCF, respectively [54, 71], which is much longer than the maximum distance reached by 3-mode and 6-mode FMF. Moreover, the MDGD of CMCF increases in proportion to the square root of the fiber length [69, 70] instead of linearly as encountered in FMF. Similar to transmission over FMF, MIMO-based DSP is needed for CMCF to fully recover signals but with reduced computational complexity due to the smaller MDGD. Compared to UMCF, CMCF has a higher spatial utilization efficiency and can nicely fit into a standard 125 μm cladding. Table 1.4 gives the comparison between FMF and two types of MCFs. Chapter 2 gives a more detailed description of optical fibers.

1.4.2 Spatial Multiplexers (SMUX)

Figure 1.7 is a schematic diagram of an SMUX, whose basic functionality is to convert optical power from a bundle of SMFs into modes or separate cores of an SDM fiber [73]. SMUXs have evolved from bulky optics with large footprint to recent photonic integrated, 3-dimensional waveguide (3DW) and fiber-bundle based compact solutions. In principle, these solutions can be categorized into two groups.

Fig. 1.7 Schematic diagram of SMUX



One is based on multiple spots, which are generally Gaussian-distributed optical beams from SMFs or single-mode waveguides. In this chapter, these solutions are designated as spot-based SMUXs, which enable efficient coupling not only to MCF but to FMF as well. The second group is mode-selective based on creating similar mode profiles to FMF and therefore only suitable to realize MDM. In the following sections, different SMUX solutions such as bulk optics, photonic integration, fiber bundle and 3DW are discussed subsequently. The performance of SMUXs can be judged in terms of mode or core dependent loss (MDL or CDL) and coupler insertion loss (CIL). MDL is the loss difference between the best and worst modes and CDL is the counterpart for separate cores. CIL represents the average insertion loss for all spatial channels which can be modes or cores.

In order to simplify the model, matrices are utilized to represent the SMUX, as shown below:

$$\underbrace{\begin{bmatrix} M_1 \\ M_2 \\ \vdots \\ M_N \end{bmatrix}}_{M: \text{spatial channel field}} = \underbrace{\begin{bmatrix} \gamma_{1,1} & \gamma_{1,2} & \cdots & \gamma_{1,N} \\ \gamma_{2,1} & \gamma_{2,2} & \cdots & \gamma_{2,N} \\ \vdots & \vdots & \ddots & \vdots \\ \gamma_{N,1} & \gamma_{N,2} & \cdots & \gamma_{N,N} \end{bmatrix}}_{\Gamma: \text{SMUX transfer matrix}} \underbrace{\begin{bmatrix} I_1 \\ I_2 \\ \vdots \\ I_N \end{bmatrix}}_{I: \text{launch field}} \quad (1.1)$$

where the components of the vector I represent the launch fields from input SMFs, M is an array of the fields of spatial channels and N is the number of spatial channels in the SDM fiber. Γ is the transfer matrix of the SMUX, which can be quantified with an overlap integral at the SDM fiber facet. The overlap integral is calculated as:

$$\gamma_{i,j} = \frac{\int E_{\text{launch},i}^* \cdot H_{\text{spatial},j} dA}{\sqrt{\int E_{\text{launch},i}^* \cdot H_{\text{spatial},i} dA} \sqrt{\int E_{\text{mode},j}^* \cdot H_{\text{spatial},j} dA}} \leq 1 \quad (1.2)$$

where $E_{\text{launch},i}$ and $H_{\text{spatial},j}$ are the transverse electric field of the i th launch field at the SDM fiber facet and the transverse magnetic field of the j th spatial channel, respectively. A is the fiber cross-sectional area. The notation $*$ indicates the complex conjugate.

For MCF with uncoupled cores, (1.1) can be rewritten as a diagonal matrix Γ . CDL and CIL can be calculated immediately with the diagonal entries of Γ , which

are identical to singular values.

$$\begin{bmatrix} M_1 \\ M_2 \\ \vdots \\ M_N \end{bmatrix} = \begin{bmatrix} \gamma_{1,1} & 0 & \cdots & 0 \\ 0 & \gamma_{2,2} & \cdots & 0 \\ \vdots & \vdots & \ddots & \vdots \\ 0 & 0 & \cdots & \gamma_{N,N} \end{bmatrix} \begin{bmatrix} I_1 \\ I_2 \\ \vdots \\ I_N \end{bmatrix} \quad (1.3)$$

$$CDL = \max(\gamma_{n,n}^2) / \min(\gamma_{n,n}^2) \quad (1.4)$$

$$CIL = \sum(\gamma_{n,n}^2) / N \quad (1.5)$$

For FMF with spatial modes, Γ is diagonal only in the case of mode selective excitation. Singular value decomposition (SVD) is arranged for Γ to get N singular values λ_n ($n = 1$ to N). MDL and CIL can be calculated by:

$$MDL = \max(\lambda_n^2) / \min(\lambda_n^2) \quad (1.6)$$

$$CIL = \sum(\lambda_n^2) / N \quad (1.7)$$

1.4.2.1 Bulk Optics

(1) Spot-Based Excitation

For free space spot-based SMUXs, prisms [50, 74–76] and sharp-edge mirrors [56] have been applied to relocate multiple collimated optical beams closer to each other in a certain spot arrangement. Additional imaging optics is generally chosen to optimize the size of the parallel optical beams to match the SDM fiber. Due to optical reversibility, the same setup can also be used for demultiplexing. It is straightforward to design spot-based SMUXs for MCFs. In order to achieve decent coupling performance for FMFs which have a single core, specific spot arrangements are required as analyzed in [77, 78] (see Fig. 1.8) for unitary mode transitions.

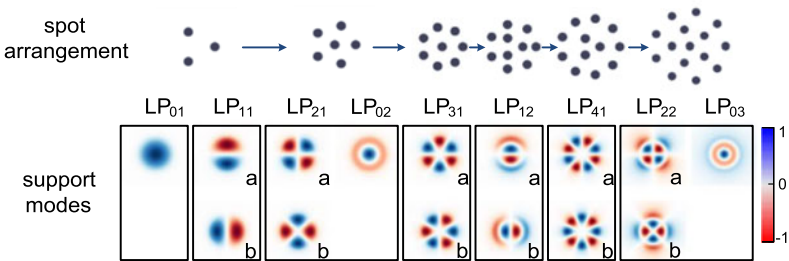


Fig. 1.8 Spot arrangements for supporting different spatial modes. *Color* indicates relative phase of isolated modes

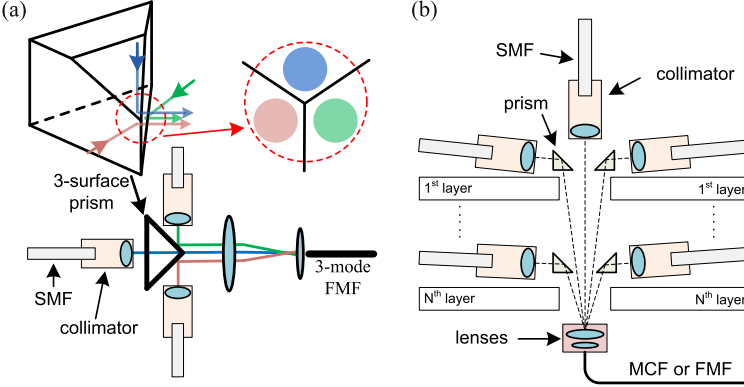


Fig. 1.9 (a) 3-spot SMUX for 3-mode FMF based on a single prism [50]; (b) scalable spot-based SMUX, designed for a 19-core UMCF [74]

Three spots located at the vertices of an equilateral triangle provide efficient mode multiplexing for the spatial LP_{01} , LP_{11a} and LP_{11b} modes, which was demonstrated by a 3-surface prism with small bevels in free space [50]. As shown in Fig. 1.9(a), two vertical surfaces of the prism are perpendicular to each other and the top surface is inclined by 45° with respect to the vertical. In order to ensure the optimal injection with optical beams along the optical axis, a telecentric lens setup is utilized to image spots into a 3-mode FMF. An ideal 3-spot SMUX can be approximated [77] by the equation given below with spot-profile optimization [79].

$$\begin{bmatrix} M_1 \\ M_2 \\ M_3 \end{bmatrix} = \begin{bmatrix} 1 & 1 & 1 \\ 1 & e^{j2\pi/3} & e^{-j2\pi/3} \\ 1 & e^{-j2\pi/3} & e^{j2\pi/3} \end{bmatrix} \begin{bmatrix} I_1 \\ I_2 \\ I_3 \end{bmatrix} \quad (1.8)$$

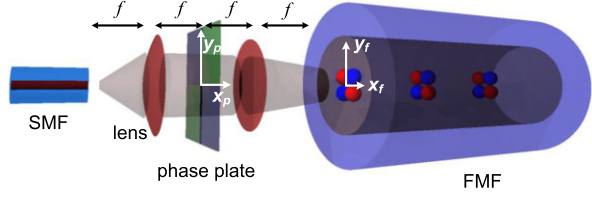
where M_1 , M_2 and M_3 represent the field profiles for the LP_{01} , LP_{11a} and LP_{11b} modes, respectively. The transfer matrix Γ is unitary, which means that both, MDL and CIL are zero.

The schematics of a scalable spot-based SMUX in free space is illustrated in Fig. 1.9(b) which was designed for coupling to a 19-core UMCF [74]. Fiber collimators and prisms are circularly arranged around the SMUX's central axis and more layers can be added as the number of spots increases.

(2) Mode-Selective Excitation

For the excitation of one specific spatial mode, the optical launch field should have the same field distribution as the mode of interest, which can be realized through spatially tailoring the collimated optical beam. Binary phase plates [44, 47, 80, 81], and spatial light modulators (SLM) [57, 82, 83] have been demonstrated for selectively exciting modes. SLMs are usually based on polarization-sensitive liquid

Fig. 1.10 Mode-selective excitation of LP_{21} mode



crystals. To support polarization multiplexed light, extra polarization separation and conversion setups are required [84, 85]. Phase plates can be made of glass and supporting both polarization states. A $4f$ setup is usually applied for mode-selective excitation. An example of LP_{21} mode excitation is illustrated in Fig. 1.10, where a phase plate is placed at the Fourier plane. x_p, y_p and x_f, y_f are spatial coordinates of the Fourier and the FMF input plane, respectively. At the Fourier plane, the collimated optical beam from the SMF is written as $I_P(x_p, y_p)$, and the transmittance of the phase plate is given by $t_P(x_p, y_p)$. The launch field at the back focal point of the 2nd lens can be described as the Fourier transform of the product of $t_P(x_p, x_p)$ and $I_P(x_p, x_p)$ [86, 87]:

$$U_F(x_f, y_f) = \mathcal{F}[I_P(x_p, y_p) \cdot t_P(x_p, y_p)] \quad (1.9)$$

where \mathcal{F} denotes the Fourier transform. Figure 1.11(a) gives the theoretical mode profiles (left to right: LP_{11a} , LP_{21a} and LP_{02} mode) of a 6-mode fiber. Figure 1.11(b) shows the schematics of binary phase plates which are employed to excite each spatial mode. The simulated launch field profiles at the FMF input plane corresponding to different phase plates are also given, which are simulated for the case that a Gaussian-distributed LP_{01} mode is the input beam. With a 90° rotation of the phase plate, the LP_{11b} mode can be excited. For the LP_{21b} mode, the phase plate needs to be rotated by 45° . Figure 1.12 gives the vertical cross-sections of the theoretical mode profiles of a 6-mode SI-FMF with a core diameter of $24.7 \mu\text{m}$ by the blue curves and the simulated launch field profiles are shown by the red curves. It can be seen that binary phase plates are able to create a similar optical field at the focal point to match the corresponding fiber mode [84].

In order to (de)multiplex N spatial modes, $N - 1$ lossy beam combiners need to be used, see Fig. 1.13. Assuming that each spatial mode is efficiently excited through an ideal phase plate and beam splitters with different splitting ratios are used to balance the insertion loss for different ports since different launch fields go through different numbers of beam splitters, the CIL is given by:

$$CIL = -1/N \quad (1.10)$$

CIL will be 10 dB for 10 spatial modes. The increasing CIL limits the scalability of phase-plate based SMUXs.

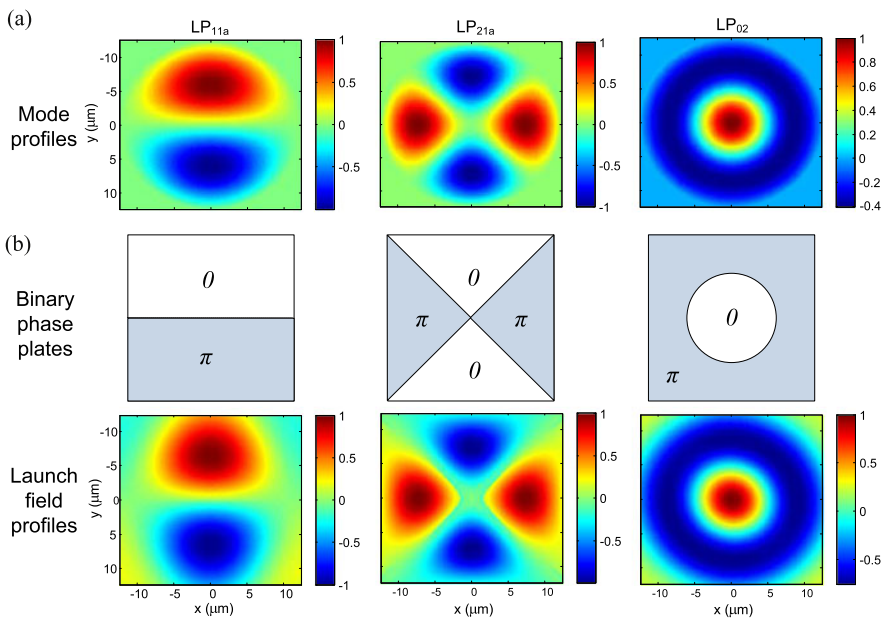


Fig. 1.11 (a) Theoretical mode profiles and (b) simulated launch field profiles of phase plates for LP₁₁, LP₂₁ and LP₀₂ modes. *Color* indicates relative phase of isolated modes

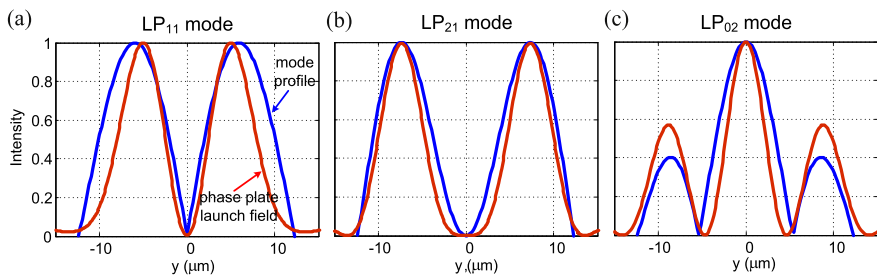
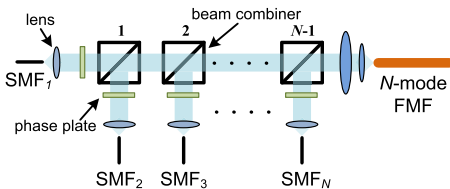


Fig. 1.12 Vertical cross-section of theoretical mode profiles (*blue curves*) and simulated launch field profiles of phase plates (*red curves*) for (a) LP₁₁, (b) LP₂₁ and (c) LP₀₂ mode

Fig. 1.13 Phase-plate based mode-selective SMUX



1.4.2.2 Photonic Integration

Photonic integration technology based on the silicon-on-insulator (SOI) [88, 89] and indium phosphide (InP) [90, 91] platforms enables the integration of passive and active optical functionalities on a single chip, which is more compact, reliable and potentially cheaper than the solution with discrete optical components. The SOI and InP platforms generally offer planar photonic integrated circuits (PICs), and fiber-chip coupling can be realized by edge coupling through spot-size converters [92], lensed or tapered fibers and top-coupling through grating couplers [93–96] or vertical mirrors [97, 98]. It is challenging for edge coupling to stack multiple waveguide layers together with a small spacing to realize 2D coupling for SDM, especially for coupling into FMFs, where 2D patterns need to be positioned with micron accuracy. Top coupling provides more freedom for vertical emitters in 2D arrangements. Figure 1.14(a) illustrates the schematics of a spot-based SMUX by employing three 1D grating couplers to couple to a 3-core MCF. Photonic integrated MCF transceivers were demonstrated in [22] where eight SOI-based grating couplers were employed for coupling to a 2×4 linear UMCF. A silicon photonic 7-core UMCF receiver was demonstrated in [99]. It has been demonstrated that 1.25 dB coupling loss to an SMF can be achieved for a 1D grating coupler which couples one polarization state into or out of the fiber [100]. The coupling loss increases to 3.2 dB for a 2D grating coupler which supports dual polarization states. As illustrated in Fig. 1.14(b), two orthogonal polarization states x and y are combined by a single 2D grating coupler, and three 2D grating couplers were employed to couple to a 3-mode FMF as a 3-spot SMUX [101].

Mode-selective excitation can also be achieved by 2D top-coupling. For instance, in order to create a bipolar field for exciting the LP_{11} mode, two grating couplers are driven in a push-pull configuration with a π phase difference [102–104], as illustrated in Fig. 1.15. By further extending this concept, a full 6-channel integrated mode-selective SMUX was demonstrated in [105], where one 2D grating coupler is placed at the center for launching or detecting the LP_{01} mode, and four grating couplers are distributed in an outer ring for the LP_{11a} and LP_{11b} modes. A scanning

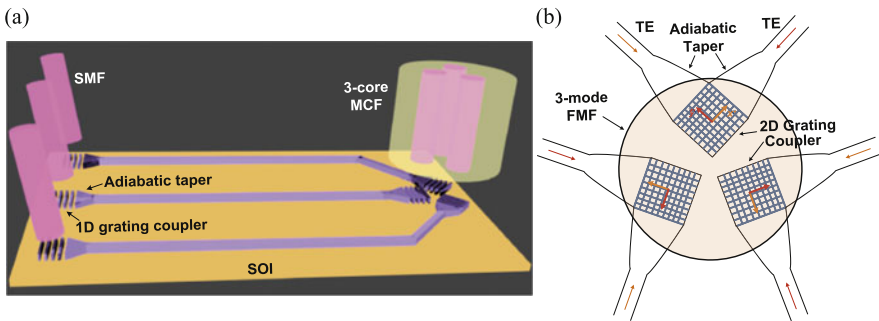


Fig. 1.14 (a) Schematics of spot-based SMUX employing 1D grating couplers, and (b) top-view of a 3-spot SMUX based on three 2D grating couplers coupling to a 3-mode FMF [101]

Fig. 1.15 Schematics of a push-pull based LP_{11} mode excitation scheme

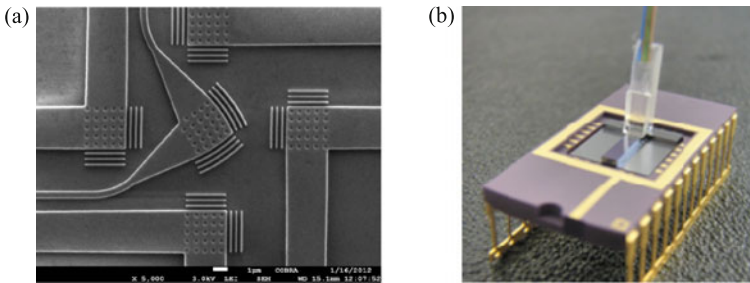
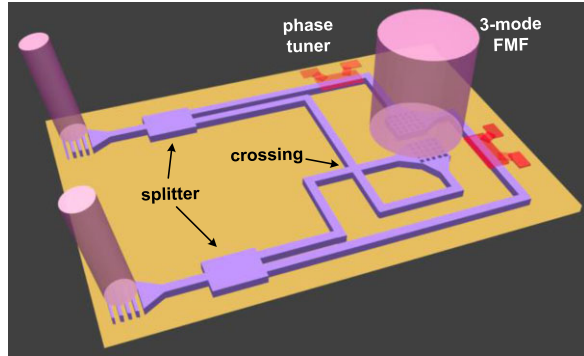


Fig. 1.16 (a) SEM image of region with five grating couplers and (b) image of packaged SOI-based SMUX

electron microscope (SEM) image of the region with all five grating couplers is given in Fig. 1.16(a). The integrated SMUX has been packaged with an SMF array for six SMF ports and wire-bonded to an electronic circuit for controlling the phases for selectively exciting the LP_{11} modes, see Fig. 1.16(b).

1.4.2.3 Fiber Bundle

A fiber bundle is an assembly of many optical fibers. Based on fiber bundles, both spot-based and mode-selective SMUXs have been demonstrated. It is straightforward to employ fiber bundles for coupling to MCFs. Figure 1.17(a) shows a design of a fiber-bundle SMUX for a UMCF [106, 107], where seven thin-cladding fibers are inserted into a glass capillary, stacked by curing adhesive and then polished mechanically. The cladding diameter of each fiber is around $45\ \mu\text{m}$, which is similar to the pitch of the 7-core UMCF. For fibers with larger cladding diameters, a tapering process can be applied to downsize the fiber bundle to match the size of the MCF, see Fig. 1.17(b) [108]. The SMUX for MCF is also designated as a fan-in/fan-out (FI/FO) device in some articles.

In order to selectively excite fiber modes, a fiber bundle is further down-tapered in such a way that a few-mode end guiding multiple supermodes is created, see

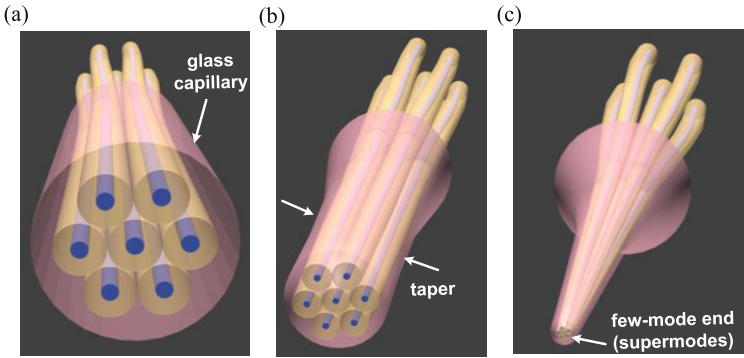


Fig. 1.17 Fiber bundle (a) without and (b) with down-tapering; (c) mode-selective SMUX based on tapered fiber bundle

Fig. 1.18 Image of 6-core photonic lantern coupling to a 50/125 μm GI-MMF [41]

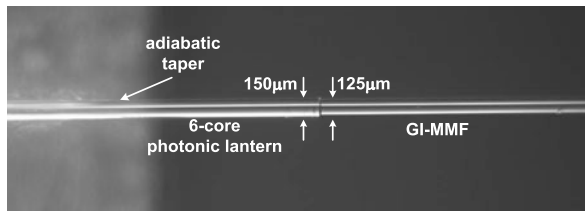


Fig. 1.17(c). This type of SMUX is also designated as a photonic lantern, which was originally proposed for applications in astrophotonics [109–111]. Figure 1.17(c) gives an example of a 6-mode mode-selective SMUX. Unlike the arrangement of fiber cores in a 7-core MCF, six fibers are positioned in the glass capillary according to the structure shown in Fig. 1.8 (see the arrangement of six spots for interfacing with LP_{01} , $LP_{11a/b}$, $LP_{21a/b}$ and LP_{02} modes) in order to support the six spatial modes [78]. In [49] and [112], respectively, 3-mode and 6-mode photonic-lantern SMUXs have been experimentally verified. It should be noted that if all fibers are identical, the photonic lantern cannot excite each spatial mode but creates supermodes which are the unitary combinations of the spatial modes [78]. In this chapter, this kind of SMUX is also classified as mode-selective since only desired spatial modes get excited. For instance, six fully mixed spatial modes were experimentally excited over a conventional 50/125 μm GI-MMF which guides more than 35 spatial modes by the fiber-bundle SMUX [41] and mode mixing was compensated by DSP. Figure 1.18 gives the image of a 6-core photonic lantern coupling to the 50/125 μm GI-MMF.

In order to selectively launch each spatial mode, dissimilar fibers are used to introduce degeneracy into the cores and create an asymmetric few-mode end. In this case, spatial modes can be individually excited through corresponding isolated input fibers [113–116].

1.4.2.4 3-Dimensional Waveguide (3DW)

The fabrication of 3-dimensional waveguide devices is enabled by femto-second laser pulses, which are focused inside a fused silica substrate. Both, the core and the cladding of the waveguides are made out of pure fused silica. This concept enables to locally modify the refractive index of a glass so that waveguides in 3D are created. Figure 1.19 gives a sketch of a 3DW SMUX for coupling to a 7-core MCF. The 3DW SMUX has seven single-mode waveguides arranged in a line at the one end, which enables the efficient connection to a standard SMF array with a pitch of 127 μm or 250 μm . Figure 1.20 shows the 3DW SMUX for coupling to a 6-mode FMF. Single-mode and few-mode waveguides can be written by multi-scan techniques [117, 118].

Laser-inscribed waveguides were investigated as early as 1996 [119]. More recently, laser-inscribed single-mode waveguides with small propagation loss around 0.3 dB/cm at 1550 nm [120] and low coupling loss to an SMF have been realized. However, refractive index changes induced by the laser inscription are constrained to a small volume. Higher index contrast, i.e., $\Delta n > 6 \times 10^{-3}$, has been achieved through an additional fabrication process [121, 122], but the uniformity and the scattering of the waveguides have not been thoroughly discussed/investigated. 3DW devices with low Δn can work properly for MCF coupling due to the single-mode operation, whereas for FMF, larger Δn is required for direct coupling between a 3DW SMUX and an FMF, especially in cases with a large number of modes [123]. As a means to overcome the design constraints of 3DW devices due to the limited

Fig. 1.19 3DW SMUX for coupling to 7-core MCF

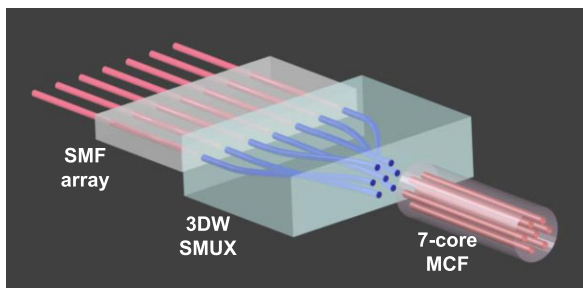


Fig. 1.20 3DW SMUX for coupling to 6-mode FMF

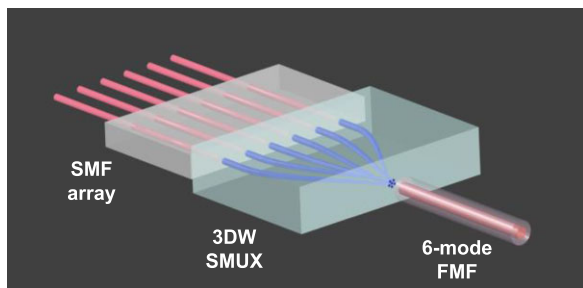
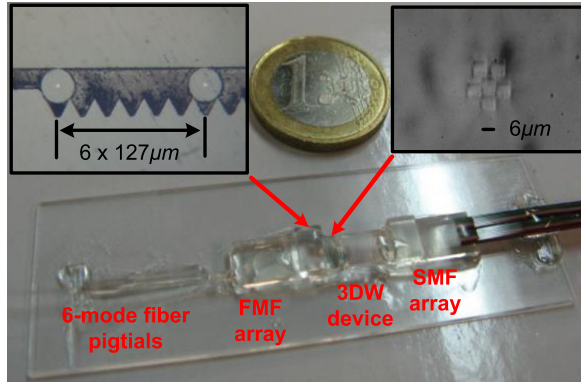


Fig. 1.21 Picture of packaged dual-channel 6-mode 3DW device with up-tapered 6-mode FMF array [123]



Δn , the employment of imaging optics [124] or up-tapering [123] has been proposed.

A dual-channel 6-mode 3DW device with two photonic-lantern SMUXs has been demonstrated as illustrated in Fig. 1.21 [123]. Two SMUXs can be used as mode multiplexer and demultiplexer, respectively. The left inset in Fig. 1.21 gives the microscope image of the FMF array facet where two adiabatically up-tapered 6-mode FMFs with a cladding of $175 \mu\text{m}$ diameter are positioned and assembled in a standard V-groove with a pitch of $127 \mu\text{m}$. The right inset in Fig. 1.21 gives the microscope image of the 3DW 6-core photonic-lantern structure. The SMF array, 3DW device, and FMF array are glued together using UV curing epoxy. Figure 1.21 shows the packaged 3DW device, which has a link CIL less than 8 dB and a double-pass MDL around 7 dB. Large capacity six spatial-mode multiplexed transmission demonstrations based on the fully packaged 3DW device have been published in [125].

1.4.2.5 Summary

Tables 1.5 and 1.6 list the measured results of a larger number of experimentally demonstrated SMUXs for coupling to different kinds of MCF and FMF/MMF, respectively. Decent performance of MCF SMUXs in terms of CIL and CDL is achieved by most of the applied technologies due to single-mode operation. For MDM applications, as shown in Table 1.6, spot-based and mode-selective solutions have both been shown to enable smooth mode transitions from multiple single modes to a group of spatial modes. Photonic lantern technology [78] based on fiber bundle or 3DW devices is the most promising solution to achieve efficient mode (de)multiplexing with low CIL and MDL. Moreover, photonic-lantern based 3DW SMUXs have also been exploited for few-mode MCFs [126, 127], which further demonstrates the photonic lantern's flexibility and robustness in 2D optical coupling.

Table 1.5 Experimentally demonstrated SMUXs for MCF

	Fiber type	Technology	CIL (dB)	CDL (dB)
[128]	7-core UMCF	Tapered fiber bundle	1.48	2.3
[107]	7-core UMCF	Thin-cladding fiber bundle	0.2	0.3
[129]	7-core UMCF	Stacked polymer waveguide	6	6
[75]	7-core UMCF	Prism based bulk optics	0.4	0.4
[130]	12-core UMCF	Ferrule with a hexagonal hole	0.64	1
[74]	19-core UMCF	Prism based bulk optics	1.22	0.4
[54]	6-core CMCF	3DW	4.5	

Table 1.6 Experimentally demonstrated SMUXs for MDM

	Fiber type	Technology	CIL (dB)	MDL (dB)
[80, 131]	3-mode FMF	Phase plate based bulk optics ^a	9	2.3
[132]	3-mode FMF	Sharp-edge mirror based bulk optics	3.8	<2
[50]	3-mode FMF	3-surface prism based bulk optics	3.5	<2
[102, 105]	3-mode FMF	Silicon integrated grating coupler ^a	22	5
[49]	3-mode FMF	Fiber based photonic lantern	<2	<1
[133]	3-mode FMF	Stacked polymer waveguide ^a	8	10
[134, 135]	6-mode FMF	Trench-assisted PLC ^a	5	9
[73, 123]	6-mode FMF	3DW	<4	<3.5
[136]	6-mode FMF	Multi-plane light conversion [137] ^a	3.6	1
[41]	50 μ m GI-MMF	Fiber based photonic lantern	2.5	4.5

^aMode selective excitation

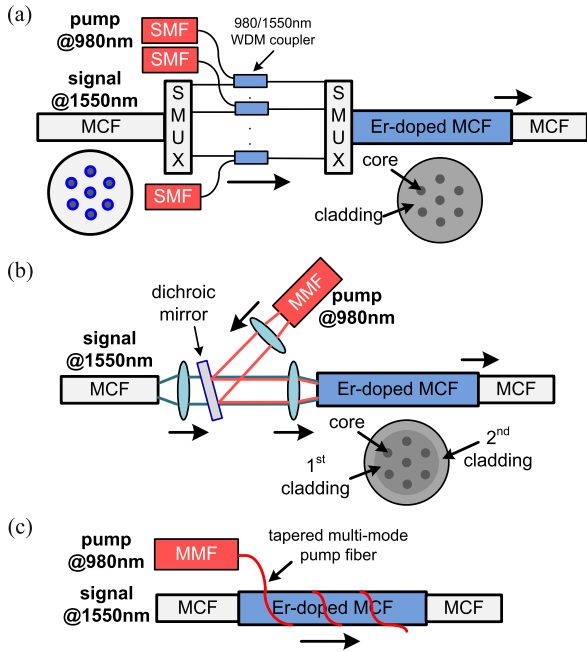
1.4.3 Optical Amplifiers

Although optical fibers nowadays can be manufactured with low attenuation loss around 0.2 dB/km, optical amplifiers such as erbium-doped fiber amplifiers and distributed Raman amplifiers are still inevitable to compensate connector and fiber losses of optical networks, especially for those with distances larger than 100 km.

1.4.3.1 MCF

A hybrid amplification scheme by employing both DRAs and EDFAs was demonstrated in [138], where 9–12 dB DRA gain and less than 1 dB noise figure (NF) were realized over a 75 km 7-core MCF. Extra SMF EDFAs were used to fully compensate the fiber loss. In order to achieve enough amplification gain, core-

Fig. 1.22 (a) Schematic of core-pumped EDFA with external WDM couplers; (b) cladding-pumped EDFA with multi-mode laser diode by end-coupling and (c) side-coupling



pumped and cladding-pumped EDFAs are both under investigation for MCF applications.

A schematic illustration of a core-pumped MCF EDFA [139–141] with external WDM couplers to combine the signal and pump is shown in Fig. 1.22(a) where the number of pump lasers and couplers is proportional to that of the core channels. It has been demonstrated that the performance of the core-pumped MCF amplifiers are comparable to that of conventional SMF EDFAs with 25 dB amplification gain and less than 4 dB NF [139, 142]. In order to lower the power consumption and downsize the optical amplifier, cladding-pumped MCF amplifiers have become more attractive and are under current investigation [143–146]. Instead of using discrete pump sources, it was demonstrated that a single multi-mode laser diode launched into the center core can be applied to pump all outer six cores in a 7-core MCF [143]. Cladding pumping enables the use of all cores as transmission channels, and a corresponding solution is illustrated in Fig. 1.22(b), where a dichroic mirror acts as a free space WDM coupler for end-coupling and combining signal and pump light. In order to confine the pump better, Er-doped MCFs are generally designed and fabricated with double claddings. Due to the small overlap between the cores and the pump light, double-cladding Er-doped MCFs operate over longer distances [144, 147] in order to increase pump absorption and pump all cores simultaneously. However, the long Er-doped MCFs result in a low gain spectrum and large NFs in the short wavelength regime of the C-band, e.g., 1530 nm [142, 148, 149], which limits the full C-band (1530–1565 nm) operation of cladding-pumped MCF amplifiers. In order to further minimize internal loss from free space coupling and downsize opti-

Table 1.7 Experimentally demonstrated MCF EDFAs

	MCF type	Pumping type	Length (m)	Gain (dB)	NF (dB)	Crosstalk (dB)
[139]	7-core (Er)	Core	15	25	4	< -25
[140]	7-core (Er)	Core	16	20	< 7	< -40
[141]	Bundled 7-core (Er)	Core	7.3	23	5.1	< -48.5
[143]	7-core (Er)	Cladding	50	20	6	
[144]	7-core (Er) ^a	Cladding	10	>14	<9	< -32.7
[147]	7-core (Er) ^a	Cladding	100	>15	<5.5	< -30
[146]	19-core (Er)	Cladding	7	<23.3	<7	
[145]	12-core (Er/Yb) ^a	Cladding	5	<18.3	<13	< -33
[32]	7-core (Er) ^b	Cladding	34	>20	<8	< -45

^aDouble-cladding^bSide-coupling

cal amplifiers, a side-coupled MCF EDFA has been proposed, see Fig. 1.22(c). All cores were pumped simultaneously by a side-coupled tapered multimode fiber [32], and more than 25 dB was obtained in each core over the full C-band. Besides gain and NF, core-to-core crosstalk is also essential and determines the maximum transmission length and capacity. A comprehensive list of demonstrated MCF EDFAs is given in Table 1.7.

1.4.3.2 FMF

Both DRAs and EDFAs for FMF applications have been experimentally demonstrated. Similar to the MCF case, an FMF DRA was applied together with SMF EDFAs due to the low DRA gain [150]. This hybrid FMF amplification scheme realized 5–8 dB DRA gain and <2 dB NF covering the full C-band for three spatial modes propagating over a 137 km FMF. Unlike the FMF DRA, an FMF EDFA is able to offer large amplification gain to fully compensate the fiber loss [151]. The FMF EDFA can be analyzed as a two-level model with total erbium ion concentration ρ . The power of the i th spatial mode at position z along the erbium-doped fiber can be calculated by:

$$\frac{dP_{s,i}(v_s, z)}{dz} = P_{s,i}(v_s, z) [\gamma_{e,i}(v_s, z) - \gamma_{a,i}(v_s, z)] \quad (1.11)$$

where v_s is the signal frequency, and $\gamma_{e,i}$ and $\gamma_{a,i}$ are the emission and absorption factors for the i th spatial mode, respectively.

$$\gamma_{e,i}(v_s, z) \propto \int n_2(z) I_{s,i}(z) dA \quad (1.12)$$

$$\gamma_{a,i}(\nu_s, z) \propto \int n_1(z) I_{s,i}(z) dA \quad (1.13)$$

where A is the fiber cross-sectional area and n_1 and n_2 are the erbium ion populations at the upper and lower energy level, respectively, and obeying the relation $n_1 + n_2 = \rho$. Note that amplified spontaneous emission (ASE) and mode mixing are omitted.

The factors $\gamma_{e,i}$ and $\gamma_{a,i}$ are determined by the overlap integrals between the i th spatial mode and the erbium ion populations.

In a steady state, n_1 and n_2 along the active fiber are fully determined by the intensity profiles of M pump modes $I_{p,j}$ ($j = 1$ to M) and N signal modes $I_{s,i}$ ($i = 1$ to N). Therefore, the erbium ion distribution and the intensity profiles of the pump and signal modes all play crucial roles in determining the gain of each spatial mode. A good FMF amplifier should offer a large average gain, small differential modal gain (DMG) and low NF. Assuming that the transmission FMF and the Er-doped active FMF have the same guided modes, a signal mode whose profile has a better match to the profiles of the pump intensity and the Er-doping will experience a larger gain. The DMG at the frequency ν_s can be calculated by:

$$DMG = \max[P_{s,i}(\nu_s, L)] / \min[P_{s,i}(\nu_s, L)] \quad (1.14)$$

where L is the length of the erbium-doped fiber.

In order to balance the DMG, different schemes for optimizing the pump and Er-doped FMF have been investigated. Active FMFs with different Er-doping profiles result in different gain for each mode. It has been demonstrated that through concatenating two active FMFs with different Er-doping profiles, it is possible to achieve DMG <6 dB for all six spatial modes over the full C-band using a single-mode pump [152, 153], see Fig. 1.23(a). Besides optimizing the Er-doping profiles, it is also beneficial to modify the transverse profile of the pump for achieving a lower DMG. Using a few-mode EDFA supporting five [154] or six [155] spatial modes and pumping a higher order mode, e.g. LP₂₁, DMG <2.5 dB has been demonstrated. As shown in Fig. 1.23(b), the LP₂₁ mode has been excited by employing phase plates in combination with bi-directional pumping. More details of these investigations, including various FMF EDFAs reported so far, are compiled in Table 1.8.

As the number of modes is scaled up, more pump power will be required to keep the same gain and NF for all modes, which means multiple single-mode pumps need to be combined and used together. Due to the availability of high-power multi-mode laser diodes, a cladding-pumped FMF EDFA has been proposed for simultaneous amplification of all modes in a more cost-efficient and simple way [31], see Fig. 1.23(c). A recent theoretical analysis aiming at minimizing the maximum DMG over all supported signal modes of cladding-pumped four-mode and six-mode-group EDFAs has shown that more than 20 dB gain per mode and less than 1 dB DMG across the whole C-band (1530–1565 nm) can be achieved for up to 10 spatial modes. The corresponding optimum EDFA design had a step index profile with up to four different doping levels in a circular arrangement [156]. Such active FMFs with ring-shaped doping (see Fig. 1.23(c)) have turned out to be advantageous in

Fig. 1.23 Schematics of different FMF EDFA concepts: (a) concatenated active FMFs to balance DMG, (b) bi-directional pumping with high-order pump mode, (c) cladding-coupling and ring-doped active FMF

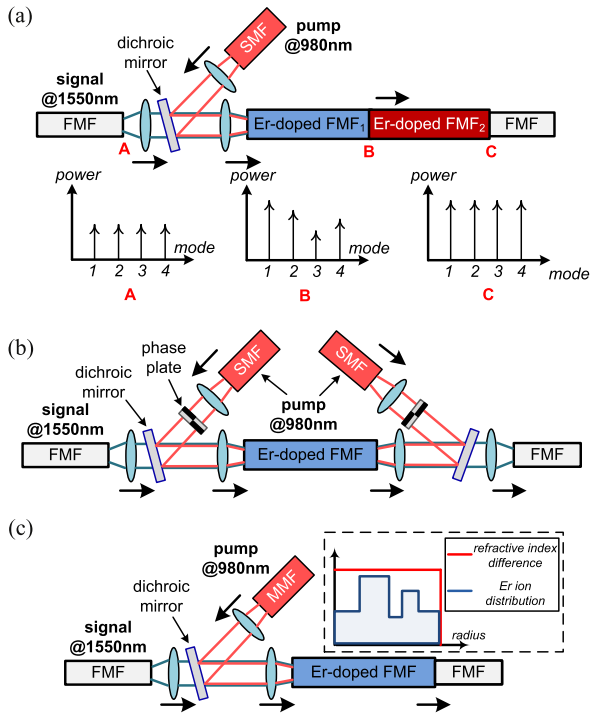


Table 1.8 Experimentally demonstrated FMF EDFAs

	FMF type	Pumping scheme	Gain (dB)	DMG (dB)	NF (dB)
[46]	3-mode	Core (offset pump)	>20	<5	
[152]	6-mode (concatenated)	Core (LP ₀₁ mode pump)	>18	<6	<7
[154]	5-mode (ring-doped)	Core (LP ₂₁ mode pump) ^a	>20	<2.5	
[155]	6-mode (ring-doped)	Core (LP ₂₁ mode pump) ^a	>20	<2	
[31]	6-mode (double-cladding)	Cladding (multi-mode pump)	>20	<4	

^aBi-directional pump

balancing the DMG [157, 158] and reducing performance degradation in macro-bending [159]. However, with conventional fiber fabrication processes such as modified chemical vapor decomposition (MCVD), the designed Er-doping profiles are hard to achieve mainly due to Er ion diffusion [160, 161]. It has been observed in [155, 160] that each doped section is more like Gaussian-shaped. In order to overcome this unwanted effect, a micro-structured core, which can be manufactured by the stack-and-draw process, has been proposed to approximate the ring geometry with moderate fabrication complexity [160].

1.4.4 Wavelength Selective Switches (WSS)

A wavelength selective switch (WSS) is a $1 \times N$ optical device which receives multiple wavelengths at one common input port and enables dynamic routing of any wavelength channel to any of N output ports (see also Chap. 10, Sect. 10.1.4). Its functionality can be used reversely to combine the wavelength channels. WSSs constitute a key component in reconfigurable optical add/drop multiplexers [162]. The schematic of an SMF WSS is illustrated in Fig. 1.24, which essentially consists of (1) a fiber and a micro-lens array as input/output section, (2) a diffraction grating which angularly disperses wavelength channels in a horizontal plane (the x - y plane in Fig. 1.24), (3) a Fourier lens which converts the angular shifts as beam displacements on a beam steering element, and (4) the beam steering element which can be a micro-electro-mechanical system (MEMS) [163, 164] or a liquid crystal-on-silicon (LCoS) [165] for vertical beam steering. Note that a polarization-diversity section and a beam expansion section have been omitted in Fig. 1.24.

In a conventional SMF WSS, each wavelength channel can be switched individually. Investigations trying to transfer this concept to SDM by switching spatial channels individually have shown that this approach is apparently limited due to crosstalk induced by mode mixing [166]. Moreover, it has been pointed out that MDM and WDM are two fundamentally different concepts [24]: crosstalk in WDM can be negligible while MDM exhibits severe linear crosstalk among parallel modes. With respect to performance requirements such as negligible crosstalk and high spectral resolution, all spatial channels at one wavelength should be regarded as one entity to be switched and should therefore jointly be routed over SDM compatible WSSs similar to the SMF case.

Fig. 1.24 Schematic of an SMF WSS

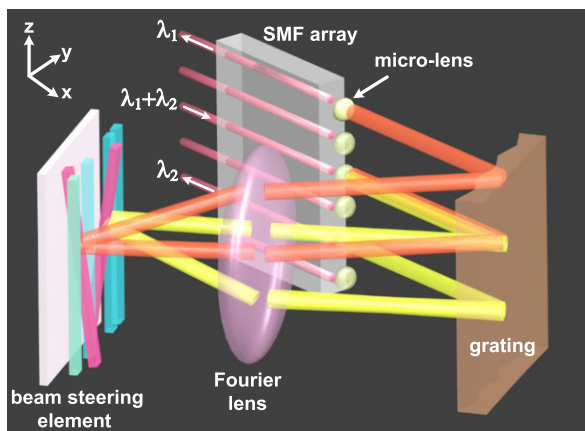


Table 1.9 Experimentally demonstrated SDM WSSs

	SDM type	SDM ports	SMUX usage	Remapping	Steering element
[33]	7-core MCF	1×2	Yes	No	MEMS
[167]	7-core MCF	1×2	Yes	Yes	MEMS
[34]	3-mode FMF	1×9	No	No	LCoS
[168]	3-mode FMF	1×2	No	No	LCoS
[169]	3-mode FMF	1×2	Yes	Yes	LCoS
[170]	3-mode FMF	1×11	Yes	No	LCoS

^aDouble-cladding^bSide-coupling

1.4.4.1 MCF WSS

In [33, 167] 7-core MCF WSSs have been demonstrated, where an SMUX is used to demultiplex a spatially-multiplexed signal into seven parallel ones over seven SMFs. The seven parallel signals are fed into a commercial WSS with more than 21 SMF ports ($7 \text{ cores} \times (1 \text{ common port} + 2 \text{ output ports})$), jointly steered to seven output SMF ports, which are multiplexed by another SMUX to a 7-core MCF. In order to minimize beam steering angle and crosstalk [171], it was proposed to add a remapping block between the SMUXs and the SMF input/output section which interleaves the signals from different spatial channels into neighboring single-mode ports [167]. A compilation of experimentally demonstrated SDM WSSs is presented in Table 1.9.

1.4.4.2 FMF WSS

Since spatial modes propagate together in one fiber core, it is feasible to replace the SMF array as shown in Fig. 1.24 directly by an FMF array to realize an FMF compatible WSS, as demonstrated in [34, 168] for three spatial modes. In contrast to the conversion of mode-multiplexed signals into single-mode operation by SMUXs [170], the port count of a WSS is not affected by the direct replacement [172]. However, due to different modal characteristics such as mode field diameter (MFD) [173, 174] and mode field profile, different modes exhibit mode-dependent spectral responses. Figure 1.25 gives the simulated 3×3 amplitude responses for 3 spatial modes versus the normalized wavelength. Different amplitude roll-offs can be observed at the passband edges in the diagonal plots (blue curves), which are for the case that the excitation and launch modes are the same. In the other plots (red curves), strong mode coupling can be found. Based on the 3×3 amplitude responses, Fig. 1.26 gives the simulated transmission and MDL as a function of normalized wavelength. It can be seen that the MDL curve is narrower than the transmission curve due to varying spectral responses of modes, which results in a narrower spectral passband [175, 176]. Therefore, this type of FMF WSS requires

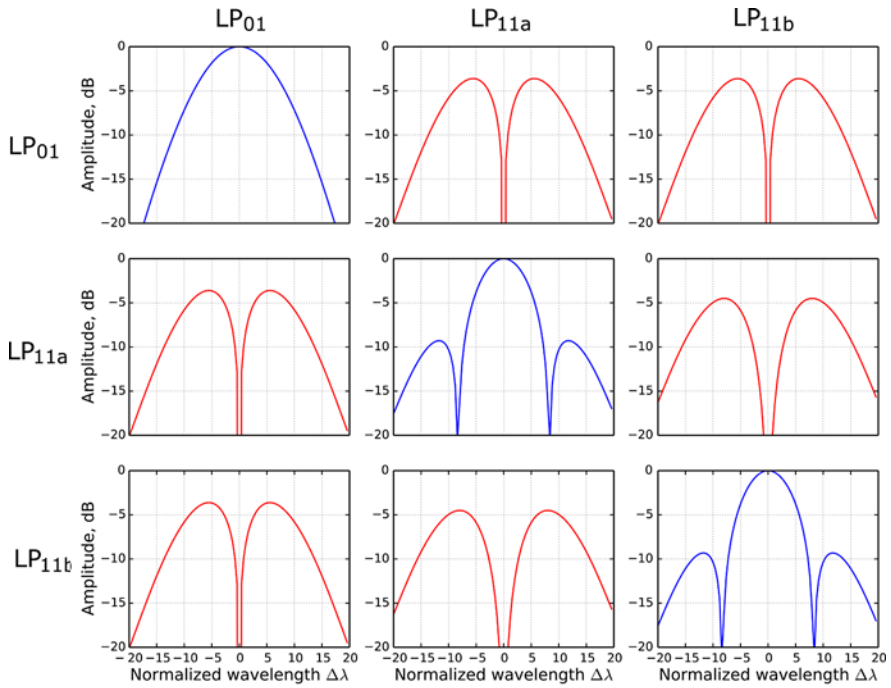
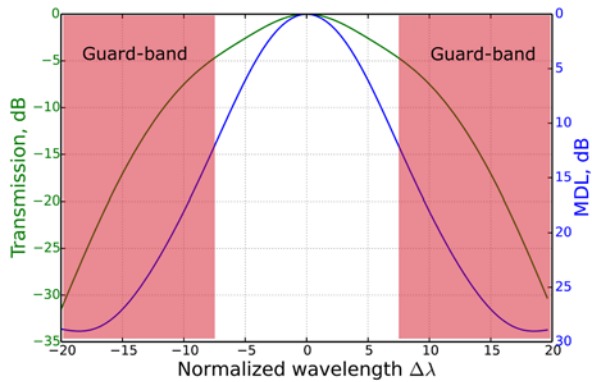


Fig. 1.25 Amplitude responses of FMF WSS for three spatial modes as a function of normalized wavelength

Fig. 1.26 Transmission and MDL of FMF WSS versus normalized wavelength



larger spectral guard-bands compared to the conventional SMF ones. Removal of the mode-dependencies, which at the same time minimizes the guard bands, has recently been demonstrated by employing a spatial-diversity scheme with an SMUX for demultiplexing the spatial modes into identical Gaussian beams and a remapping network for the proper arrangement and reshuffling of these beams [169].

1.4.5 Fiber Splicers and Connectors

Fiber splicers are used to join two fibers permanently through locally heating the fiber ends to melt and fuse them together. The functionality of fiber splicers is indispensable for the maintenance and installation of optical networks. Therefore, whether high-quality splicing for SDM fibers can be realized in an efficient way is a critical criterion to judge whether SDM will eventually become a practical solution. Since FMF and MMF have one single core inside a standard 125 μm cladding, conventional fiber fusion splicers empowered by either core or cladding alignment and fusion splice techniques using electric arcs or carbon dioxide (CO_2) lasers can still do the job with some fusion parameters optimization for specific FMFs or MMFs. The most popular fiber splicers based on electric arcs have shown decent performance in FMF [50, 177] and MMF [41] splicing. In terms of core-to-core misalignment induced splice losses, FMFs and MMFs for supporting MDM have higher requirements compared to the SMF case. Core-to-core misalignment does only cause power attenuation in SMF, but in fibers for MDM applications, MDL is also induced which limits transmission length and capacity. Numerical analyses show that the quality of fiber splicing determines the maximum reach of MDM systems [178], which is also valid for FMF mechanical connectors.

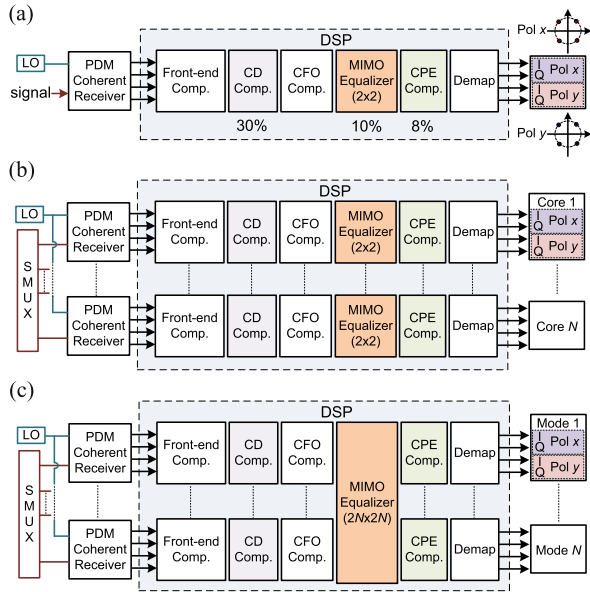
In order to align all fiber cores of MCFs simultaneously, MCF compatible splicers need to be capable of rotational alignment in addition to lateral alignment. It was demonstrated that both fiber side view [179] and end view [180] observation can enable rotational alignment. For side view observation, hollow-hole markers with large refractive index contrast have been added into a 7-core MCF to enhance visibility [179]. For end view observation, a camera has been used to monitor the two fiber ends, detect core positions and align corresponding cores [180], which is equivalent to the process for alignment of polarization maintaining fibers. Since MCFs generally have a larger cladding size, traditional fusion splice techniques cannot guarantee uniform heat distribution along the radial direction, which results in non-identical splice losses for different cores [181]. To create a sufficiently uniform discharge, a swing-electrode based fusion technique has been proposed to splice large cladding fibers such as MCFs.

A 7-core MCF connector with 0.13 dB average attenuation and < -45 dB average reflection has been developed by using a floating mechanism to eliminate the influence of deformation and physical contact to reduce the return loss [182]. The performance of the MCF connector is comparable to that of corresponding SMFs.

1.5 Digital Signal Processing

One important enabling factor of high capacity SDM systems especially with coupled spatial channels and essentially realized so far in lab trials only, is the tremendous development in electronics and DSP. For almost all demonstrations, optical coherent receivers and high-speed real-time oscilloscopes have been utilized for

Fig. 1.27 Schematics of optical receiver empowered by DSP for (a) SMF with DSP power dissipation distribution, (b) UMCF with N cores, and (c) CMCF or FMF guiding N spatial modes with a $2N \times 2N$ MIMO equalizer (LO: local oscillator)



detecting and sampling the received signals. The schematics of optical receivers supporting SMF, UMCF with N cores and CMCF or FMF supporting N spatial modes are all illustrated in Fig. 1.27. The optical receiver consists of optical polarization division multiplexing (PDM) coherent receivers and DSP blocks. In the digital domain, front-end impairments, chromatic dispersion (CD), timing offsets and carrier frequency offset (CFO) are compensated by DSP [183, 184]. Carrier phase estimation (CPE) is implemented after the time or frequency domain MIMO equalizer. For UMCF applications, as shown in Fig. 1.27(b), the DSP block for SMF can be duplicated to individually unravel the mixed PDM signals for each core. However, due to mode mixing, an MIMO equalizer with a larger matrix dimension is required for both, the CMCF and FMF cases, see Fig. 1.27(c).

The computational complexity of each digital module increases linearly with the number of spatial channels except for the bigger MIMO equalizers in the CMCF and FMF cases. Since all spatial channels at one wavelength are routed together, common-mode impairments can be expected and therefore joint signal recovery can be exploited. The joint CPE compensation has been demonstrated in both uncoupled [37] and coupled [38] spatial channels due to the phase fluctuations being correlated. Instead of employing N separate CPE compensation modules, one joint CPE scheme is sufficient.

One argument for coupled SDM applications is that the MIMO equalizer has to be applied to redo the coupling for recovering the signals, which results in higher computational complexity. Moreover, the size of the MIMO equalizer exhibits a quadratic growth with the number of spatial channels. For example, six spatial modes require a 12×12 MIMO equalizer which is 36-fold and 6-fold larger than

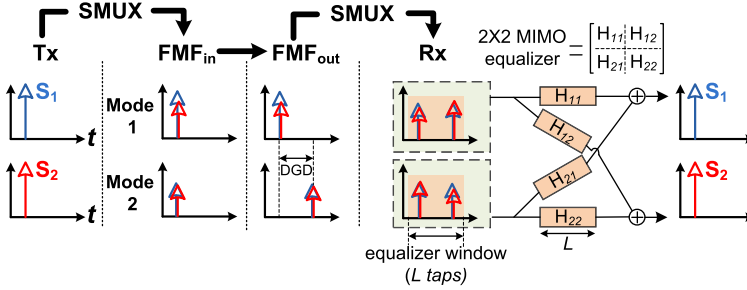


Fig. 1.28 Schematic of mode mixing and MDGD after FMF transmission (the MIMO equalizer has a wide equalizer window to handle MDGD)

the one for SMF and 10-core UMCF, respectively. Modal differential group delay (MDGD) is another effect which adds pressure on the DSP. Figure 1.28 shows a schematic diagram of mode mixing and MDGD after transmission of two spatial modes with one polarization. The MDGD is caused by the different propagation constants of the different modes. S_1 and S_2 in Fig. 1.28 represent two transmitted signals, and it is assumed that mode mixing occurs only in the multiplexing/demultiplexing stages. After transmission, the separation of two modes due to MDGD can be observed in the time domain. A 2×2 MIMO equalizer with a finite-impulse-response (FIR) filter in a butterfly structure can recover the mixed spatial channels. In order to cover the time delay between two modes, the equalizer window (in other words, the number of taps L) needs to be wider than the delay.

In early MDM demonstrations [44, 80], the time-domain data-aided (DA) least-mean-square (LMS) algorithm has been used for initializing the taps of the MIMO equalizer, and after convergence, decision-directed (DD) LMS or constant modulus algorithms (CMA) have been employed. To recover the optical PDM signals over N spatial modes, the MIMO equalizer requires a $2N \times 2N \times L$ FIR filter. Through applying frequency domain equalizers (FDE) [185, 186] with block-by-block processing and Fast Fourier Transform (FFT) implementation, a tremendous reduction in computational complexity [187] of MIMO processing for the handling of large MDGD has been demonstrated with the complexity becoming less dependent on MDGD [188]. Moreover, strong mode mixing shows its benefits in the reduction of DSP complexity [189]. In Fig. 1.27(a), the distribution of power dissipation for the different modules in the digital core of a 100 Gbit/s line card is given [190], where the CD compensation module consumes 30% power and the power dissipation of the MIMO equalizer consumes only 10% [187]. Therefore, the total DSP complexity of a coupled SDM system with six spatial channels, which can be a 6-mode FMF or a 6-core CMCF, only doubles compared to that of an uncoupled SDM system, which scales sublinearly with the SDM channel count.

1.6 Commercialization

SDM has not only received attention by academia, but by industry as well. SDM components such as corresponding fiber, SMUXs, optical amplifiers and splicers have been released into the market quickly following the research activities. Table 1.10 lists commercialized SDM components. It can be expected that more and more SDM components will be available from the shelf in the near future. In addition to the components, technical standards with respect to parameter definitions and component requirements, as well as standardized test procedures are also crucial for the further development of SDM technologies.

Table 1.10 Commercially available SDM components

SDM component	Manufacturer	Technology
FMF	OFS [191]	GI-FMF with depressed cladding [59]
MCF	OFS [192]	
MCF	YOFC [193]	
SMUX (FMF)	CAILabs [194]	Multi-plane light conversion [136, 137]
SMUX (MCF)	Chiral Photonics [195]	Fiber bundle [196, 197]
SMUX (FMF)	Kylia [198]	Free space optics [199]
SMUX (FMF)	Optoscribe [200]	3D waveguide [201]
SMUX (MCF)	Optoscribe [202]	3D waveguide [201]
Mode converter	Phoenix Photonics [203]	Mechanical grating [204, 205]
FMF EDFA	Phoenix Photonics [203]	
Fiber splicer	Fujikura [206]	Swing electrode [181]

Appendix

1.7.1 Economic Aspects of Mode Division Multiplexed Links

Next to the technical aspects of mode division multiplexed (MDM) systems, their economic aspects are also of major importance when deciding on the installation of new transmission links. An analysis has been made of the capital expenditure (CapEx) needed to install an MDM transmission link versus the CapEx for a traditional fiber division multiplexed (FDM¹) link, i.e. a link using a number of single-mode fiber links in parallel.

¹In electrical engineering the acronym FDM typically denotes frequency division multiplexing, i.e. multiplexing of frequency bands in the spectral domain. Here we use FDM to denote the multiplexing of fibers in the spatial domain.

Fiber Division Multiplexing

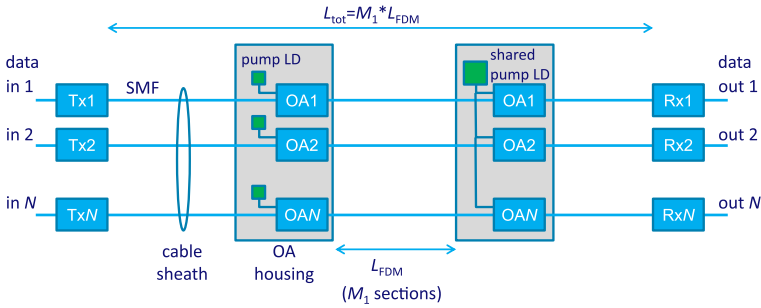


Fig. 1.29 Fiber division multiplexed transmission link using N single-mode fibers in parallel carrying N data channels

Mode Division Multiplexing

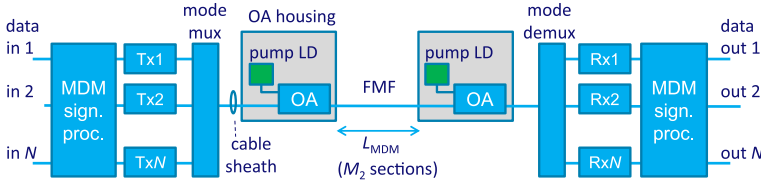


Fig. 1.30 Mode division multiplexed transmission link using a single few-moded fiber carrying N data channels

1.7.1.1 Cost Modeling

The system models used for this comparison are shown in Figs. 1.29 and 1.30.

The transmission link has to carry N data channels over a link total length L_{tot} which consists of M_1 single-mode fiber sections having a length L_{FDM} (or M_2 few-moded fiber sections of length L_{MDM}) with optical amplifiers (OAs) in between them. The N digital data channels are transmitted by N transmitters Tx_i ($i = 1..N$), and received by N receivers Rx_i ($i = 1..N$).

In the SDM link, the N data channels are carried over N single-mode fibers. N separate OAs are needed at each coupling between two sections; they may use N pump lasers or one shared powerful pump laser. The N OAs can be accommodated in a single housing. $(M_1 - 1)$ of these OA-sets are needed, where M_1 is the number of link sections. The N fibers are hosted in a single protective cable sheath, which is buried in a duct.

In the MDM link, the N data channels are carried over N mode channels in a single few-moded fiber. These mode channels are amplified together by a single multimode OA; $(M_2 - 1)$ of these OAs are needed, where M_2 is the number of link sections. The FMF is put in a protective cable sheath, which is buried in a duct. At the transmitter end of the link, a mode multiplexer couples the optical output signals of the N transmitters into the N mode channels of the FMF. At the receiver

end, a mode demultiplexer separates the N mode channels into the N receivers. Both at the transmitter end and at the receiver end digital signal processing is used for pre-conditioning the signals and counteracting the crosstalk incurred between them.

Based on these system models, the link CapEx costs for an FDM link, C_{FDM} , can be expressed as

$$C_{FDM} = N \cdot Tx + cable_{FDM} + (M_1 - 1)(N \cdot OA_{FDM} + housing_{OA}) + mode\ mux + mode\ demux + N \cdot Rx + 2 \cdot signal\ proc \quad (1.15)$$

where

$$cable_{FDM} = L_{FDM}(sheath + duct + N \cdot fibre_{FDM}) \quad (1.16)$$

and Tx , Rx , OA_{FDM} are the cost for a transmitter, a receiver, and an optical amplifier, respectively, $fibre_{FDM}$, $cable_{FDM}$, $sheath$, and $duct$ are the FDM fiber, FDM cable, sheath and duct cost per unit length, and $housing_{OA}$, $mode\ mux$, $mode\ demux$, and $signal\ proc$ are the unit cost for an OA housing, a mode multiplexer or mode demultiplexer, and signal processing, respectively.

In a similar way, the link CapEx costs for an MDM link, C_{MDM} , are

$$C_{MDM} = N \cdot Tx + cable_{MDM} + (M_2 - 1)(OA_{MDM} + housing_{OA}) + mode\ mux + mode\ demux + N \cdot Rx + 2 \cdot signal\ proc \quad (1.17)$$

where

$$cable_{MDM} = L_{MDM}(sheath + duct + fiber_{MDM}) \quad (1.18)$$

and all other quantities are defined for MDM fibers, devices, etc. corresponding to those in (1.15) and (1.16).

1.7.1.2 Assumptions

Table 1.11 shows preliminary cost assumptions for the three fiber types considered: standard SMF for the FDM case, and solid-core FMF (SC-FMF) and photonic bandgap FMF for the MDM case. Note that these numbers are approximative ones, taken for the sake of enabling a relative cost comparison of an MDM versus an FDM system.

Due to differential mode losses in the SC-FMF, the maximum section length in the MDM/SC-FMF case has been assumed to be somewhat smaller than for the FDM/SMF case. Due to the (expected) much lower losses in the photonic bandgap (PBG)-FMF, the maximum section length in the MDM/PBG-FMF case is considerably larger than in the other two cases. Because of the larger complexity (amongst others to achieve gain flatness among the modes) and the possibility of pump sharing among multiple OAs in the FDM case, the costs of a multimode OA needed in the MDM cases are assumed to be higher than for the MDM cases. The cable

Table 1.11 Cost assumptions for system elements

	Fiber cable (€/km)		Max. section length (km)	Optical Amplifier unit		Tx (€)	Rx (€)	Mode		Sign. proc. (€)
	Sheath	Duct instal.		Fiber	OA (€)			Housing (€)	mux (€)	
SMF	2000	1000	10	7000	10000	25000	35000			
SC-FMF	2000	1000	30	15000	10000	25000	35000	25000	25000	20000
PBG-FMF	2000	1000	50	15000	10000	25000	35000	25000	25000	20000

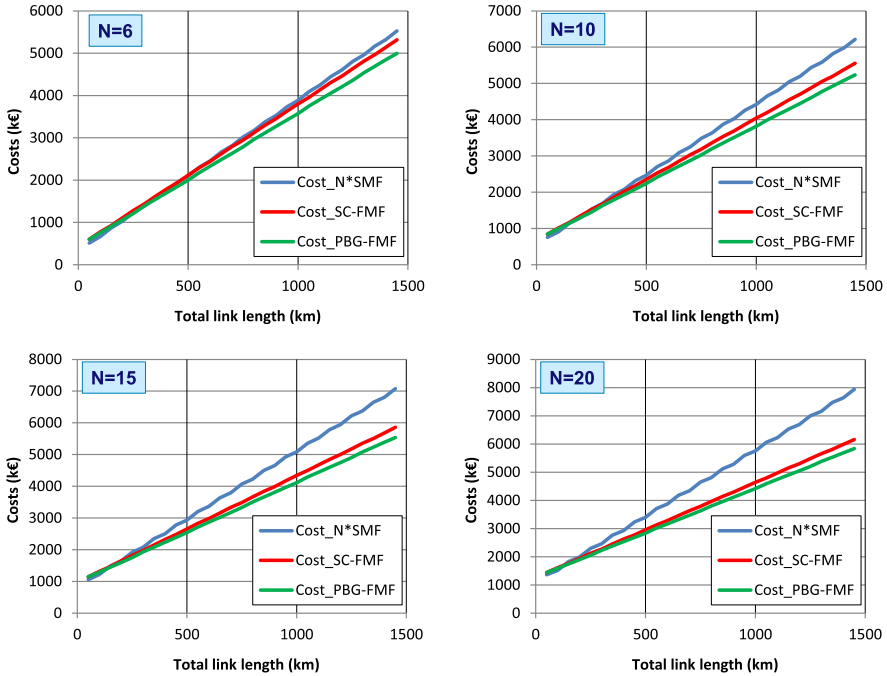


Fig. 1.31 Cost comparison between FDM case (N SMFs in parallel) and two MDM cases (solid core FMF, and photonic bandgap FMF), versus total link length and for different numbers N of multiplexed data channels

sheath, duct installation, OA housing, transmitter and receiver costs are expected to be (nearly) the same for the various cases.

1.7.1.3 Results

Figure 1.31 shows the costs calculated for the FDM case using N parallel SMFs and the two MDM cases using a single solid-core FMF using photonic bandgap FMF, respectively. The results indicate that MDM offers increasing cost advantages when the total link length grows, and when the number N of multiplexed data channels grows. Figure 1.32 indicates how the various cost items contribute to the total system costs for a total link length $L_{tot} = 1000$ km. The cost benefits of MDM are clearly due to the reduced OA costs, which outweigh the additional costs for the mode multiplexers and the signal processing. The contribution by the OA costs is reduced due to OA sharing in the MDM cases, and costs are further reduced due to the use of PBG-FMF because the section length increases and thus the number of OAs needed decreases.

Figure 1.33 summarizes the relative cost differences between MDM and FDM for the two MDM cases. It again shows that MDM offers cost advantages above

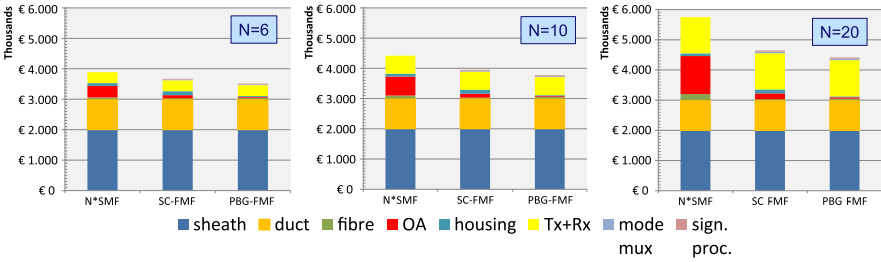


Fig. 1.32 Cost items for the FDM case (N SMFs in parallel) and two MDM cases (solid core FMF, and photonic bandgap FMF), for total link length $L_{tot} = 1000$ km and for different numbers N of multiplexed data channels

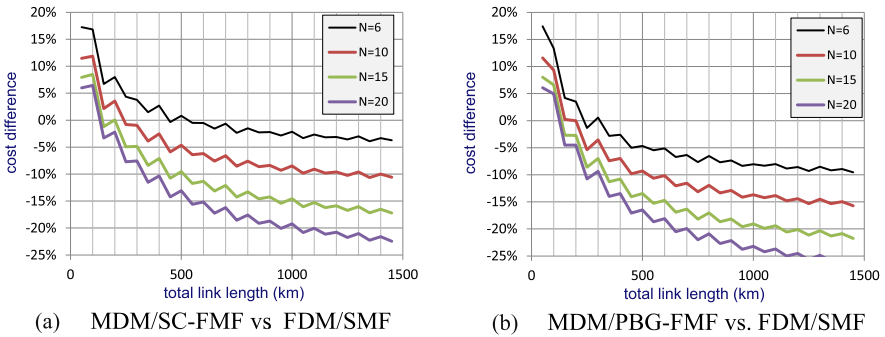


Fig. 1.33 Relative cost differences between MDM and FDM when using (a) solid-core FMF and (b) photonic bandgap FMF

FDM beyond a certain total link length. This break-even total link length decreases when the number of multiplexed data channels is increased, and when PBG-FMF is used instead of SC-FMF. For example, when using $N = 10$ channels MDM is advantageous beyond $L_{tot} = 250$ km for SC-FMF, and already beyond $L_{tot} = 150$ km for PBG-FMF. And for a link length $L_{tot} = 1000$ km, MDM with SC-FMF offers a cost reduction of 2.1% for $N = 6$ channels to 19.2% for $N = 20$ channels, and with PBG-FMF even a cost reduction of 8.1% for $N = 6$ to 23.2% for $N = 20$.

1.7.2 Conclusions

MDM offers clear CapEx cost reductions with respect to FDM for long link lengths where the total link length is sufficiently large (i.e. beyond 300 to 500 km), and when the number of multiplexed channels is large (i.e. beyond 10).

References

1. R.W. Tkach, Scaling optical communications for the next decade and beyond. *Bell Labs Tech. J.* **14**(4), 3–9 (2010)
2. D.J. Richardson, J.M. Fini, L.E. Nelson, Space-division multiplexing in optical fibers. *Nat. Photonics* **7**(5), 354–362 (2013)
3. G.J. Foschini, Layered space-time architecture for wireless communication in a fading environment when using multi-element antennas. *Bell Labs Tech. J.* **1**(2), 41–59 (2002)
4. S. Iano, T. Sato, S. Sentsui, T. Kuroha, Y. Nishimura, Multicore optical fiber, in *Opt. Fiber Commun. Conf. (OFC'79)*, Washington, DC, USA (1979), Techn. Digest, paper WB1
5. S. Berdagué, P. Facq, Mode division multiplexing in optical fibers. *Appl. Opt.* **21**(11), 1950–1955 (1982)
6. K. Nagayama, M. Kakui, M. Matsui, T. Saitoh, Y. Chigusa, Ultra-low-loss (0.1484 dB/km) pure silica core fibre and extension of transmission distance. *Electron. Lett.* **38**(20), 1168–1169 (2002)
7. E. Desurvire, J.R. Simpson, P.C. Becker, High-gain erbium-doped traveling-wave fiber amplifier. *Opt. Lett.* **12**(11), 888–890 (1987)
8. O.E. DeLange, Wide-band optical communication systems: Part II Frequency-division multiplexing. *Proc. IEEE* **58**(10), 1683–1690 (1970)
9. P.J. Winzer, R. Essiambre, Advanced optical modulation formats. *Proc. IEEE* **94**(5), 952–985 (2006)
10. B. Glance, Polarization independent coherent optical receiver. *J. Lightwave Technol.* **5**(2), 274–276 (1987)
11. D.J. Richardson, Filling the light pipe. *Science* **330**(6002), 327–328 (2010)
12. R.-J. Essiambre, G. Kramer, P.J. Winzer, G.J. Foschini, B. Goebel, Capacity limits of optical fiber networks. *J. Lightwave Technol.* **28**(4), 662–701 (2010)
13. A. Mecozzi, R.-J. Essiambre, Nonlinear Shannon limit in pseudolinear coherent systems. *J. Lightwave Technol.* **30**(12), 2011–2024 (2012)
14. A. Chraplyvy, The coming capacity crunch, in *Proc. 35th Europ. Conf. Opt. Commun. (ECOC'09)*, Vienna, Austria (2009), plenary paper
15. P.J. Winzer, Making spatial multiplexing a reality. *Nat. Photonics* **8**(5), 345–348 (2014)
16. “ModeGap,” Multi-mode capacity enhancement with PBG fiber. [Online]. Available: <http://modegap.eu>
17. T. Morioka, New generation optical infrastructure technologies: ‘EXAT initiative’ towards 2020 and beyond, in *OptoElectron. Commun. Conf. (OECC'09)*, Hong Kong SAR, China (2009), paper FT4
18. M.A. Taubenblatt, Optical interconnects for high-performance computing. *J. Lightwave Technol.* **30**(4), 448–457 (2012)
19. C. DeCusatis, Optical interconnect networks for data communications. *J. Lightwave Technol.* **32**(4), 544–552 (2014)
20. B. Rosinski, J.W.D. Chi, P. Grosso, J. Le Bihan, Multichannel transmission of a multicore fiber coupled with vertical-cavity surface-emitting lasers. *J. Lightwave Technol.* **17**(5), 807–810 (1999)
21. M.-J. Li, B. Hoover, V.N. Nazarov, D.L. Butler, Multicore fiber for optical interconnect applications, in *Proc. 17th OptoElectron. Commun. Conf. (OECC'12)*, Busan, South Korea (2012), pp. 564–565
22. T. Pinguet, P.M. De Dobbelaere, D. Foltz, S. Gloeckner, S. Hovey, Y. Liang, M. Mack, G. Masini, A. Mekis, M. Peterson, S. Sahni, J. Schramm, M. Sharp, D. Song, B.P. Welch, K. Yokoyama, S. Yu, Silicon photonics multicore transceivers, in *Proc. IEEE Photon. Soc. Summer Top. Meeting*, Seattle, WA, USA (2012), pp. 238–239
23. B. Zhu, T.F. Taunay, M.F. Yan, M. Fishteyn, G. Oulundsen, D. Vaidya, 70-Gb/s multicore multimode fiber transmissions for optical data links. *IEEE Photonics Technol. Lett.* **22**(22), 1647–1649 (2010)

24. P.J. Winzer, G.J. Foschini, Mode division multiplexed transmission systems, in *Opt. Fiber Commun. Conf. (OFC'14)*, San Francisco, CA, USA (2014), Techn. Digest, paper Th1J.1
25. P.J. Winzer, Energy-efficient optical transport capacity scaling through spatial multiplexing. *IEEE Photonics Technol. Lett.* **23**(13), 851–853 (2011)
26. R. Nagarajan, M. Kato, J. Pleumeekers, P. Evans, D. Lambert, A. Chen, V. Dominic, A. Mathur, P. Chavarkar, M. Missey, A. Dentai, S. Hurtt, J. Bäck, R. Muthiah, S. Murthy, R. Salvatore, C. Joyner, J. Rossi, R. Schneider, M. Ziari, H.-S. Tsai, J. Bostak, M. Kauffman, S. Pennypacker, T. Butrie, M. Reffle, D. Mehuys, M. Mitchell, A. Nilsson, S. Grubb, F. Kish, D. Welch, Large-scale photonic integrated circuits for long-haul transmission and switching. *J. Opt. Netw.* **6**(2), 102–111 (2007)
27. K. Lawniczuk, C. Kazmierski, J. Provost, M.J. Wale, R. Pyramidowicz, P. Szczepanski, M.K. Smit, X.J.M. Leijtens, InP-based photonic multiwavelength transmitter with DBR laser array. *IEEE Photonics Technol. Lett.* **25**(4), 352–354 (2013)
28. C. Zhang, H. Zhu, S. Liang, X. Cui, H. Wang, L. Zhao, W. Wang, Ten-channel InP-based large-scale photonic integrated transmitter fabricated by SAG technology. *Opt. Laser Technol.* **64**, 17–22 (2014)
29. R. Nagarajan, J. Rahn, M. Kato, J. Pleumeekers, D. Lambert, V. Lal, H.-S. Tsai, A. Nilsson, A. Dentai, M. Kuntz, R. Malendevich, J. Tang, J. Zhang, T. Butrie, M. Raburn, B. Little, W. Chen, G. Goldfarb, V. Dominic, B. Taylor, M. Reffle, F. Kish, D. Welch, 10 channel, 45.6 Gb/s per channel, polarization-multiplexed DQPSK, InP receiver photonic integrated circuit. *J. Lightwave Technol.* **29**(4), 386–395 (2011)
30. P. Dong, X. Liu, S. Chandrasekhar, L.L. Buhl, R. Aroca, Y.-K. Chen, Monolithic silicon photonic integrated circuits for compact 100 Gb/s coherent optical receivers and transmitters. *IEEE J. Sel. Top. Quantum Electron.* **20**(4), 150–157 (2014)
31. E.L. Lim, Y. Jung, Q. Kang, T.C. May-Smith, N.H.L. Wong, R. Standish, F. Poletti, J.K. Sahu, S. Alam, D.J. Richardson, First demonstration of cladding pumped few-moded EDFA for mode division multiplexed transmission, in *Opt. Fiber Commun. Conf. (OFC'14)*, San Francisco, CA, USA (2014), Techn. Digest, paper M2J.2
32. K.S. Abedin, J.M. Fini, T.F. Thierry, B. Zhu, M.F. Yan, L. Bansal, F.V. Dimarcello, E.M. Monberg, D.J. DiGiovanni, Seven-core erbium-doped double-clad fiber amplifier pumped simultaneously by side-coupled multimode fiber. *Opt. Lett.* **39**(4), 993–996 (2014)
33. M.D. Feuer, L.E. Nelson, K.S. Abedin, X. Zhou, T.F. Taunay, J.F. Fini, B. Zhu, R. Isaac, R. Harel, G. Cohen, D.M. Marom, ROADM system for space division multiplexing with spatial superchannels, in *Opt. Fiber Commun. Conf. and Nat. Fiber Opt. Eng. Conf. (OFC/NFOEC'13)*, Anaheim, CA, USA (2013), Techn. Digest, paper PDP 5B.8
34. R. Ryf, N.K. Fontaine, J. Dunayevsky, D. Sinefeld, M. Blau, M. Montoliu, S. Randel, C. Liu, B. Ercan, M. Esmaelpour, S. Chandrasekhar, A.H. Gnauck, S.G. Leon-Saval, J. Bland-Hawthorn, J.R. Salazar-Gil, Y. Sun, L. Grüner-Nielsen, R. Lingle, D.M. Marom, Wavelength-selective switch for few-mode fiber transmission, in *Proc. 39th Europ. Conf. Opt. Commun. (ECOC'13)*, London, UK (2013), paper PDI-C-4
35. S. Han, Moore's Law and energy and operations savings in the evolution of optical transport platforms. *IEEE Commun. Mag.* **48**(2), 66–69 (2010)
36. R. Tucker, Green optical communications-part I: energy limitations in transport. *IEEE J. Sel. Top. Quantum Electron.* **17**(2), 245–260 (2011)
37. M.D. Feuer, L.E. Nelson, X. Zhou, S.L. Woodward, R. Isaac, B. Zhu, T.F. Taunay, M. Fishteyn, J.M. Fini, M.F. Yan, Joint digital signal processing receivers for spatial superchannels. *IEEE Photonics Technol. Lett.* **24**(21), 1957–1960 (2012)
38. R.G.H. van Uden, C.M. Okonkwo, V.A.J.M. Sleiffer, M. Kuschnerov, H. de Waardt, A.M.J. Koonen, Single DPLL joint carrier phase compensation for few-mode fiber transmission. *IEEE Photonics Technol. Lett.* **25**(14), 1381–1384 (2013)
39. K. Igarashi, T. Tsuritani, I. Morita, Y. Tsuchida, K. Maeda, M. Tadakuma, T. Saito, K. Watanabe, K. Imamura, R. Sugizaki, M. Suzuki, Super-Nyquist-WDM transmission over 7,326-km seven-core fiber with capacity-distance product of 103 Exabit/s·km. *Opt. Express* **22**(2), 1220–1228 (2014)

40. R. Ryf, S. Randel, N.K. Fontaine, M. Montoliu, E. Burrows, S. Chandrasekhar, A.H. Gnauck, C. Xie, R.-J. Essiambre, P. Winzer, R. Delbue, P. Pupalaiakis, A. Sureka, Y. Sun, L. Grüner-Nielsen, R.V. Jensen, R. Lingle, 32-bit/s/Hz spectral efficiency WDM transmission over 177-km few-mode fiber, in *Opt. Fiber Commun. Conf. and Nat. Fiber Opt. Eng. Conf. (OFC/NFOEC'13)*, Anaheim, CA, USA (2013), Techn. Digest, paper PDP 5A.1
41. R. Ryf, N.K. Fontaine, H. Chen, B. Guan, S. Randel, N. Sauer, S.J.B. Yoo, A.M.J. Koonen, R. Delbue, P. Pupalaiakis, A. Sureka, R. Shubochkin, Y. Sun, R. Lingle, 23 Tbit/s transmission over 17-km conventional 50- μ m graded-index multimode fiber, in *Opt. Fiber Commun. Conf. (OFC'14)*, San Francisco, CA, USA (2014), Techn. Digest, paper Th5B.1
42. H. Takahashi, T. Tsuritani, E.L.T. de Gabory, T. Ito, W.R. Peng, K. Igarashi, K. Takeshima, Y. Kawaguchi, I. Morita, Y. Tsuchida, Y. Mimura, K. Maeda, T. Saito, K. Watanabe, K. Imamura, R. Sugizaki, M. Suzuki, First demonstration of MC-EDFA-repeated SDM transmission of 40×128 -Gbit/s PDM-QPSK signals per core over 6,160-km 7-core MCF. *Opt. Express* **21**(1), 789–795 (2013)
43. K. Igarashi, T. Tsuritani, I. Morita, Y. Tsuchida, K. Maeda, M. Tadakuma, T. Saito, K. Watanabe, K. Imamura, R. Sugizaki, M. Suzuki, 1.03-Exabit/s km super-Nyquist-WDM transmission over 7.326-km seven-core fiber, in *Proc. 39th Europ. Conf. Opt. Commun. (ECOC'13)*, London, UK (2013), paper PD3-E-3
44. V.A.J.M. Sleiffer, Y. Jung, V. Veljanovski, R.G.H. van Uden, M. Kuschnerov, H. Chen, B. Inan, L. Grüner-Nielsen, Y. Sun, D.J. Richardson, S.U. Alam, F. Poletti, J.K. Sahu, A. Dhar, A.M.J. Koonen, B. Corbett, R. Winfield, A.D. Ellis, H. de Waardt, 73.7 Tb/s ($96 \times 3 \times 256$ -Gb/s) mode-division-multiplexed DP-16QAM transmission with inline MM-EDFA. *Opt. Express* **20**(26), B428–B438 (2012)
45. Q. Kang, E.L. Lim, Y. Jung, F. Poletti, S. Alam, D.J. Richardson, Design of four-mode erbium doped fiber amplifier with low differential modal gain for modal division multiplexed transmissions, in *Opt. Fiber Commun. Conf. and Nat. Fiber Opt. Eng. Conf. (OFC/NFOEC'13)*, Anaheim, CA, USA (2013), Techn. Digest, paper OTu3G.3
46. Y. Jung, S. Alam, Z. Li, A. Dhar, D. Giles, I.P. Giles, J.K. Sahu, F. Poletti, L. Grüner-Nielsen, D.J. Richardson, First demonstration and detailed characterization of a multimode amplifier for space division multiplexed transmission systems. *Opt. Express* **19**(26), B952–B957 (2011)
47. E. Ip, M.-J. Li, Y.-K. Huang, A. Tanaka, E. Mateo, W. Wood, J. Hu, Y. Yano, K. Koreshkov, $146\lambda \times 6 \times 19$ -Gbaud wavelength-and mode-division multiplexed transmission over 10×50 -km spans of few-mode fiber with a gain-equalized few-mode EDFA, in *Opt. Fiber Commun. Conf. and Nat. Fiber Opt. Eng. Conf. (OFC/NFOEC'13)*, Anaheim, CA, USA (2013), Techn. Digest, paper PDP 5A.2
48. V.A.J.M. Sleiffer, Y. Jung, M. Kuschnerov, S.U. Alam, D.J. Richardson, L. Grüner-Nielsen, Y. Sun, H. de Waardt, Optical chopper-based re-circulating loop for few-mode fiber transmission. *Opt. Lett.* **39**(5), 1181–1184 (2014)
49. R. Ryf, N.K. Fontaine, M. Montoliu, S. Randel, B. Ercan, H. Chen, S. Chandrasekhar, A. Gnauck, S.G. Leon-Saval, J. Bland-Hawthorn, J.R. Salazar Gil, Y. Sun, R. Lingle, Photonic-lantern-based mode multiplexers for few-mode-fiber transmission, in *Opt. Fiber Commun. Conf. (OFC'14)*, San Francisco, CA, USA (2014), Techn. Digest, paper W4J.2
50. H. Chen, V. Sleiffer, F. Huijskens, R. van Uden, C. Okonkwo, P. Leoni, M. Kuschnerov, L. Grüner-Nielsen, Y. Sun, H. de Waardt, T. Koonen, Employing prism-based three-spot mode couplers for high capacity MDM/WDM transmission. *IEEE Photonics Technol. Lett.* **25**(24), 2474–2477 (2013)
51. R. Ryf, N.K. Fontaine, B. Guan, B. Huang, M. Esmaelpour, S. Randel, A.H. Gnauck, S. Chandrasekhar, A. Adamiecki, G. Raybon, R.W. Tkach, R. Shubochkin, Y. Sun, R. Lingle Jr., 305-km combined wavelength and mode-multiplexed transmission over conventional graded-index multimode fibre, in *Proc. 40th Europ. Conf. Opt. Commun. (ECOC'14)*, Cannes, France (2014), paper PD3.5
52. E. Ip, M.-J. Li, K. Bennett, Y.-K. Huang, A. Tanaka, A. Korolev, K. Koreshkov, W. Wood, E. Mateo, J. Hu, Y. Yano, $146\lambda \times 6 \times 19$ -Gbaud wavelength-and mode-division multiplexed

- transmission over 10×50 -km spans of few-mode fiber with a gain-equalized few-mode EDFA. *J. Lightwave Technol.* **32**(4), 790–797 (2014)
53. T. Kobayashi, H. Takara, A. Sano, T. Mizuno, H. Kawakami, Y. Miyamoto, K. Hiraga, Y. Abe, H. Ono, M. Wada, Y. Sasaki, I. Ishida, K. Takenaga, S. Matsuo, K. Saitoh, M. Yamada, H. Masuda, T. Morioka, 2×344 Tb/s propagation-direction interleaved transmission over 1500-km MCF enhanced by multicarrier full electric-field digital back-propagation, in *Proc. 39th Europ. Conf. Opt. Commun.* (ECOC'13), London, UK (2013), paper PD3-E-4
 54. R. Ryf, N.K. Fontaine, B. Guan, R.-J. Essiambre, S. Randel, A.H. Gnauck, S. Chandrasekhar, A. Adamiecki, G. Raybon, B. Ercan, R.P. Scotti, S.J. Ben Yoo, T. Hayashi, T. Nagatsuka, T. Sasaki, 1705-km transmission over coupled-core fibre supporting 6 spatial modes, in *Proc. 40th Europ. Conf. Opt. Commun.* (ECOC'14), Cannes, France (2014), paper PD3.2
 55. S. Chandrasekhar, A.H. Gnauck, X. Liu, P.J. Winzer, Y. Pan, E.C. Burrows, T.F. Taunay, B. Zhu, M. Fishteyn, M.F. Yan, J.M. Fini, E.M. Monberg, F.V. Dimarcello, WDM/SDM transmission of 10×128 -Gb/s PDM-QPSK over 2688-km 7-core fiber with a per-fiber net aggregate spectral-efficiency distance product of 40,320 km b/s/Hz. *Opt. Express* **20**(2), 706–711 (2012)
 56. R. Ryf, R.-J. Essiambre, A.H. Gnauck, S. Randel, M.A. Mestre, C. Schmidt, P.J. Winzer, R. Delbue, P. Pupalaiakis, A. Sureka, Space-division multiplexed transmission over 4200-km 3-core microstructured fiber, in *Opt. Fiber Commun. Conf. and Nat. Fiber Opt. Eng. Conf.* (OFC/NFOEC'12), Los Angeles, CA, USA (2012), Techn. Digest, paper PDP 5C.2
 57. C. Koebele, M. Salsi, L. Milord, R. Ryf, C. Bolle, P. Sillard, S. Bigo, G. Charlet, 40 km transmission of five mode division multiplexed data streams at 100 Gb/s with low MIMO-DSP complexity, in *Proc. 37th Europ. Conf. Opt. Commun.* (ECOC'11), Geneva, Switzerland (2011), paper Th.13.C.3
 58. P. Sillard, M. Bigot-Astruc, D. Molin, Few-mode fibers for mode-division-multiplexed systems. *J. Lightwave Technol.* **32**(16), 2824–2829 (2014)
 59. L. Grüner-Nielsen, Y. Sun, J.W. Nicholson, D. Jakobsen, K.G. Jespersen, R. Lingle, B. Palsdottir, Few mode transmission fiber with low DGD, low mode coupling, and low loss. *J. Lightwave Technol.* **30**(23), 3693–3698 (2012)
 60. K. Igarashi, K. Takeshima, T. Tsuritani, H. Takahashi, S. Sumita, I. Morita, Y. Tsuchida, M. Tadakuma, K. Maeda, T. Saito, K. Watanabe, K. Imamura, R. Sugizaki, M. Suzuki, 110.9-Tbit/s SDM transmission over 6,370 km using a full C-band seven-core EDFA. *Opt. Express* **21**(15), 18053–18060 (2013)
 61. S. Matsuo, Y. Sasaki, T. Akamatsu, I. Ishida, K. Takenaga, K. Okuyama, K. Saitoh, M. Koshihba, 12-core fiber with one ring structure for extremely large capacity transmission. *Opt. Express* **20**(27), 28398–28408 (2012)
 62. J. Sakaguchi, B.J. Puttnam, W. Klaus, Y. Awaji, N. Wada, A. Kanno, T. Kawanishi, K. Imamura, H. Inaba, K. Mukasa, 19-core fiber transmission of $19 \times 100 \times 172$ -Gb/s SDM-WDM-PDM-QPSK signals at 305 Tb/s, in *Opt. Fiber Commun. Conf. and Nat. Fiber Opt. Eng. Conf.* (OFC/NFOEC'12), Los Angeles, CA, USA (2012), Techn. Digest, paper PDP 5C-1
 63. J. Sakaguchi, B.J. Puttnam, W. Klaus, Y. Awaji, N. Wada, A. Kanno, T. Kawanishi, K. Imamura, H. Inaba, K. Mukasa, R. Sugizaki, T. Kobayashi, M. Watanabe, 305 Tb/s space division multiplexed transmission using homogeneous 19-core fiber. *J. Lightwave Technol.* **31**(4), 554–562 (2013)
 64. K. Takenaga, Y. Arakawa, S. Tanigawa, N. Guan, S. Matsuo, K. Saitoh, M. Koshihba, Reduction of crosstalk by trench-assisted multi-core fiber, in *Opt. Fiber Commun. Conf. and Nat. Fiber Opt. Eng. Conf.* (OFC/NFOEC'11), Los Angeles, CA, USA (2011), Techn. Digest, paper OWJ4
 65. C. Xia, R. Amezcua-Correa, N. Bai, E. Antonio-Lopez, D.M. Arrijoja, A. Schulzgen, M. Richardson, J. Liñares, C. Montero, E. Mateo, X. Zhou, G. Li, Hole-assisted few-mode multicore fiber for high-density space-division multiplexing. *IEEE Photonics Technol. Lett.* **24**(21), 1914–1917 (2012)
 66. A. Zioliwicz, M. Szymanski, L. Szostkiewicz, T. Tenderenda, M. Napierala, M. Murawski, Z. Holdynski, L. Ostrowski, P. Mergo, K. Poturaj, M. Makara, M. Slowikowski, K. Paw-

- lik, T. Stanczyk, K. Stepien, K. Wysokinski, M. Broczkowska, T. Nasilowski, Hole-assisted multicore optical fiber for next generation telecom transmission systems. *Appl. Phys. Lett.* **105**(8), 081106 (2014)
67. S. Matsuo, K. Takenaga, Y. Arakawa, Y. Sasaki, S. Taniagwa, K. Saitoh, M. Koshiha, Large-effective-area ten-core fiber with cladding diameter of about 200 μm . *Opt. Lett.* **36**(23), 4626–4628 (2011)
 68. R. Ryf, R.-J. Essiambre, S. Randel, M.A. Mestre, C. Schmidt, P.J. Winzer, Impulse response analysis of coupled-core 3-core fibers, in *Proc. 38th Europ. Conf. Opt. Commun. (ECOC'12)*, Amsterdam, The Netherlands (2012), paper Mo.1.F.4
 69. C. Xia, N. Bai, I. Ozdur, X. Zhou, G. Li, Supermodes for optical transmission. *Opt. Express* **19**(17), 16653–16664 (2011)
 70. S.O. Arik, J.M. Kahn, Coupled-core multi-core fibers for spatial multiplexing. *IEEE Photonics Technol. Lett.* **25**(21), 2054–2057 (2013)
 71. R. Ryf, R.-J. Essiambre, S. Randel, A.H. Gnauck, P.J. Winzer, T. Hayashi, T. Taru, T. Sasaki, MIMO-based crosstalk suppression in spatially multiplexed $3 \times 56\text{-Gb/s}$ PDM-QPSK signals for strongly coupled three-core fiber. *IEEE Photonics Technol. Lett.* **23**(20), 1469–1471 (2011)
 72. S. Mumtaz, R.-J. Essiambre, G.P. Agrawal, Nonlinear propagation in multimode and multi-core fibers: Generalization of the Manakov equations. *J. Lightwave Technol.* **31**(3), 398–406 (2013)
 73. H. Chen, N.K. Fontaine, R. Ryf, B. Guan, S.J.B. Yoo, T. Koonen, Design constraints of photonic-lantern spatial multiplexer based on laser-inscribed 3D-waveguide technology. *J. Lightwave Technol.* **33**(6), 1147–1154 (2015)
 74. W. Klaus, J. Sakaguchi, B.J. Puttnam, Y. Awaji, N. Wada, T. Kobayashi, M. Watanabe, Free-space coupling optics for multicore fibers. *IEEE Photonics Technol. Lett.* **24**(21), 1902–1905 (2012)
 75. Y. Tottori, T. Kobayashi, M. Watanabe, Low loss optical connection module for seven-core multicore fiber and seven single-mode fibers. *IEEE Photonics Technol. Lett.* **24**(21), 1926–1928 (2012)
 76. Y. Tottori, H. Tsuboya, T. Kobayashi, Multi functionality demonstration for multi core fiber fan-in/fan-out devices using free space optics, in *Opt. Fiber Commun. Conf. (OFC'14)*, San Francisco, CA, USA (2014), Techn. Digest, paper Th2A.44
 77. R. Ryf, N.K. Fontaine, R.-J. Essiambre, Spot-based mode couplers for mode-multiplexed transmission in few-mode fiber. *IEEE Photonics Technol. Lett.* **24**(21), 1973–1976 (2012)
 78. N.K. Fontaine, R. Ryf, J. Bland-Hawthorn, S.G. Leon-Saval, Geometric requirements for photonic lanterns in space division multiplexing. *Opt. Express* **20**(24), 27123–27132 (2012)
 79. M. Blau, D.M. Marom, Optimization of spatial aperture-sampled mode multiplexer for a three-mode fiber. *IEEE Photonics Technol. Lett.* **24**(23), 2101–2104 (2012)
 80. R. Ryf, S. Randel, A.H. Gnauck, C. Bolle, A. Sierra, S. Mumtaz, M. Esmaelpour, E.C. Burrows, R. Essiambre, P.J. Winzer, D.W. Peckham, A.H. McCurdy, R. Lingle, Mode-division multiplexing over 96 km of few-mode fiber using coherent 6×6 MIMO processing. *J. Lightwave Technol.* **30**(4), 521–531 (2012)
 81. S. Randel, R. Ryf, A. Sierra, P.J. Winzer, A.H. Gnauck, C.A. Bolle, R.-J. Essiambre, D.W. Peckham, A. McCurdy, R. Lingle, $6 \times 56\text{-Gb/s}$ mode-division multiplexed transmission over 33-km few-mode fiber enabled by 6×6 MIMO equalization. *Opt. Express* **19**(17), 16697–16707 (2011)
 82. C. Koebele, M. Salsi, D. Sperti, P. Tran, P. Brindel, H. Mardoyan, S. Bigo, A. Boutin, F. Verluise, P. Sillard, M. Astruc, L. Provost, F. Cerou, G. Charlet, Two mode transmission at $2 \times 100\text{ Gb/s}$, over 40 km-long prototype few-mode fiber, using LCOS-based programmable mode multiplexer and demultiplexer. *Opt. Express* **19**(17), 16593–16600 (2011)
 83. J. Carpenter, T.D. Wilkinson, Characterization of multimode fiber by selective mode excitation. *J. Lightwave Technol.* **30**(10), 1386–1392 (2012)
 84. H. Chen, T. Koonen, Single multi-mode mask for multi-channel mode division demultiplexing, in *Opt. Fiber Commun. Conf. and Nat. Fiber Opt. Eng. Conf. (OFC/NFOEC'13)*, Ana-

- heim, CA, USA (2013), Techn. Digest, paper OTh1B.4
85. H. Chen, T. Koonen, Scalable multi-segment phase mask for spatial power splitting and mode division demultiplexing, in *Proc. 39th Europ. Conf. Opt. Commun.* (ECOC'13), London, UK (2013), paper OTh1B.4
 86. J.W. Goodman, *Introduction to Fourier Optics*, 3rd edn. (Roberts, Greenwood Village, 2005)
 87. D.G. Voelz, *Computational Fourier Optics: A MATLAB® Tutorial* (SPIE, Bellingham, 2011)
 88. M.J.R. Heck, J.F. Bauters, M.L. Davenport, J.K. Doylend, S. Jain, G. Kurczveil, S. Srinivasan, Y. Tang, J.E. Bowers, Hybrid silicon photonic integrated circuit technology. *IEEE J. Sel. Top. Quantum Electron.* **19**(4), 6100117 (2013)
 89. D. Liang, J.E. Bowers, Recent progress in lasers on silicon. *Nat. Photonics* **4**(8), 511–517 (2010)
 90. M. Smit, X. Leijtens, E. Bente, J. van der Tol, H. Ambrosius, D. Robbins, M. Wale, N. Grote, M. Schell, Generic foundry model for InP-based photonics. *IET Optoelectron.* **5**(5), 187–194 (2011)
 91. F.M. Soares, K. Janiak, R.G. Broeke, N. Grote, Technology development towards a generic InP-based photonic-integration foundry, in *Internat. Conf. on Applications of Optics and Photonics* (2011). *Proc. SPIE*, vol. 8001, 800111. doi:[10.1117/12.892126](https://doi.org/10.1117/12.892126)
 92. D. D'Agostino, E. Kleijn, R. Santos, H.P.M.M. Ambrosius, M.K. Smit, A dense spot size converter array fabricated in a generic process on InP, in *Integrated Photonics: Materials, Devices, and Applications II* (2013). *Proc. SPIE*, vol. 8767, 87670Q. doi:[10.1117/12.2017307](https://doi.org/10.1117/12.2017307)
 93. F. Van Laere, T. Claes, J. Schrauwen, S. Scheerlinck, W. Bogaerts, D. Taillaert, L. O'Faolain, D. Van Thourhout, R. Baets, Compact focusing grating couplers for silicon-on-insulator integrated circuits. *IEEE Photonics Technol. Lett.* **19**(23), 1919–1921 (2007)
 94. F. Van Laere, W. Bogaerts, P. Dumon, G. Roelkens, D. Van Thourhout, R. Baets, Focusing polarization diversity gratings for silicon-on-insulator integrated circuits, in *5th IEEE Conf. Group IV Photonics*, Sorrento, Italy, 2008 (2008), paper ThB3
 95. X. Chen, C. Li, H.-K. Tsang, Fabrication-tolerant waveguide chirped grating coupler for coupling to a perfectly vertical optical fiber. *IEEE Photonics Technol. Lett.* **20**(23), 1914–1916 (2008)
 96. L. Chen, L. Zhang, C.R. Doerr, N. Dupuis, N.G. Weimann, R.F. Kopf, Efficient membrane grating couplers on InP. *IEEE Photonics Technol. Lett.* **22**(12), 890–892 (2010)
 97. A.J. Koonen, H.S. Chen, V.A.M. Sleiffer, R.G.H. van Uden, C.M. Okonkwo, Compact integrated solutions for mode (de-)multiplexing, in *Proc. OptoElectron. Commun. Conf. and Austral. Conf. Opt. Fibre Technol.* (OECC/ACOFT'14), Melbourne, Australia (2014), pp. 164–166
 98. S. Choi, A. Higo, M. Zaitzu, M.-J. Kwack, M. Sugiyama, H. Toshiyoshi, Y. Nakano, Development of a vertical optical coupler using a slanted etching of InP/InGaAsP waveguide. *IEICE Electron. Express* **10**(6), 20130116 (2013)
 99. C.R. Doerr, T.F. Taunay, Silicon photonics core-, wavelength-, and polarization-diversity receiver. *IEEE Photonics Technol. Lett.* **23**(9), 597–599 (2011)
 100. A. Mekis, S. Gloeckner, G. Masini, A. Narasimha, T. Pinguet, S. Sahni, P. De Dobbelaere, A grating-coupler-enabled CMOS photonics platform. *IEEE J. Sel. Top. Quantum Electron.* **17**(3), 597–608 (2011)
 101. N.K. Fontaine, C.R. Doerr, M.A. Mestre, R. Ryf, P.J. Winzer, L. Buhl, Y. Sun, X. Jiang, R. Lingle, Space-division multiplexing and all-optical MIMO demultiplexing using a photonic integrated circuit, in *Opt. Fiber Commun. Conf. and Nat. Fiber Opt. Eng. Conf.* (OFC/NFOEC'12), Los Angeles, CA, USA (2012), Techn. Digest, paper PDP 5B.1
 102. A.M.J. Koonen, H. Chen, H.P.A. Van den Boom, O. Raz, Silicon photonic integrated mode multiplexer and demultiplexer. *IEEE Photonics Technol. Lett.* **24**(21), 1961–1964 (2012)
 103. H. Chen, T. Koonen, B. Snyder, X. Chen, G.T. Reed, Packaged mode multiplexer based on silicon photonics, in *Proc. Asia Commun. Photon. Conf.*, Guangzhou, China, 2012 (2012), paper ATh2B.4
 104. Y. Ding, H. Ou, J. Xu, C. Peucheret, Silicon photonic integrated circuit mode multiplexer. *IEEE Photonics Technol. Lett.* **25**(7), 648–651 (2013)

105. H. Chen, V. Sleiffer, B. Snyder, M. Kuschnerov, R. van Uden, Y. Jung, C.M. Okonkwo, O. Raz, P. O'Brien, H. de Waardt, T. Koonen, Demonstration of a photonic integrated mode coupler with MDM and WDM transmission. *IEEE Photonics Technol. Lett.* **25**(21), 2039–2042 (2013)
106. K. Watanabe, T. Saito, Y. Tsuchida, K. Maeda, M. Shiino, Fiber bundle type fan-out for multicore Er doped fiber amplifier, in *Proc. 18th OptoElectron. Commun. Conf. and Photonics in Switching*, Kyoto, Japan, 2013 (2013), paper TuS1_5
107. K. Watanabe, T. Saito, K. Imamura, M. Shiino, Development of fiber bundle type fan-out for multicore fiber, in *Proc. 17th OptoElectron. Commun. Conf. (OECC'12)*, Busan, Korea (2012), pp. 475–476
108. H. Uemura, K. Takenaga, T. Ori, S. Matsuo, K. Saitoh, M. Koshiha, Fused taper type fan-in/fan-out device for multicore EDF, in *Proc. 18th OptoElectron. Commun. Conf. and Photonics in Switching*, Kyoto, Japan, 2013 (2013), paper TuS1_4
109. S.G. Leon-Saval, T.A. Birks, J. Bland-Hawthorn, M. Englund, Multimode fiber devices with single-mode performance. *Opt. Lett.* **30**(19), 2545–2547 (2005)
110. D. Noordegraaf, P.M. Skovgaard, M.D. Nielsen, J. Bland-Hawthorn, Efficient multi-mode to single-mode coupling in a photonic lantern. *Opt. Express* **17**(3), 1988–1994 (2009)
111. S.G. Leon-Saval, A. Argyros, J. Bland-Hawthorn, Photonic lanterns: a study of light propagation in multimode to single-mode converters. *Opt. Express* **18**(8), 8430–8439 (2010)
112. N.K. Fontaine, Photonic lantern spatial multiplexers in space-division multiplexing, in *Proc. IEEE Photon. Soc. Summer Top. Meeting*, Waikoloa, HI, USA (2013), pp. 97–98
113. N.K. Fontaine, S.G. Leon-Saval, R. Ryf, J.S. Gil, B. Ercan, J. Bland-Hawthorn, Mode selective dissimilar fiber photonic-lantern spatial multiplexers for few-mode fiber, in *Proc. 39th Europ. Conf. Opt. Commun. (ECOC'13)*, London, UK (2013), paper PD1-C-3
114. S. Yerolatsitis, T.A. Birks, Tapered mode multiplexer based on standard single-mode fibre, in *Proc. 39th Europ. Conf. Opt. Commun. (ECOC'13)*, London, UK (2013), paper PD1-C-1
115. S. Yerolatsitis, I. Gris-Sánchez, T.A. Birks, Adiabatically-tapered fiber mode multiplexers. *Opt. Express* **22**(1), 608–617 (2014)
116. S.G. Leon-Saval, N.K. Fontaine, J.R. Salazar-Gil, B. Ercan, R. Ryf, J. Bland-Hawthorn, Mode-selective photonic lanterns for space-division multiplexing. *Opt. Express* **22**(1), 1036–1044 (2014)
117. A.A. Said, M. Dugan, P. Bado, Y. Bellouard, A. Scott, J.R. Mabesa Jr., Manufacturing by laser direct-write of three-dimensional devices containing optical and microfluidic networks, in *Photon Processing in Microelectronics and Photonics III* (2004). *Proc. SPIE*, vol. 5339, pp. 194–204
118. Y. Nasu, M. Kohtoku, Y. Hibino, Low-loss waveguides written with a femtosecond laser for flexible interconnection in a planar light-wave circuit. *Opt. Lett.* **30**(7), 723–725 (2005)
119. K.M. Davis, K. Miura, N. Sugimoto, K. Hirao, Writing waveguides in glass with a femtosecond laser. *Opt. Lett.* **21**(21), 1729–1731 (1996)
120. S.M. Eaton, M.L. Ng, J. Bonse, A. Mermillod-Blondin, H. Zhang, A. Rosenfeld, P.R. Herman, Low-loss waveguides fabricated in BK7 glass by high repetition rate femtosecond fiber laser. *Appl. Opt.* **47**(12), 2098–2102 (2008)
121. S. Eaton, H. Zhang, P. Herman, F. Yoshino, L. Shah, J. Bovatsek, A. Arai, Heat accumulation effects in femtosecond laser-written waveguides with variable repetition rate. *Opt. Express* **13**(12), 4708–4716 (2005)
122. A. Arriola, S. Gross, N. Jovanovic, N. Charles, P.G. Tuthill, S.M. Olaizola, A. Fuerbach, M.J. Withford, Low bend loss waveguides enable compact, efficient 3D photonic chips. *Opt. Express* **21**(3), 2978–2986 (2013)
123. H. Chen, N.K. Fontaine, R. Ryf, B. Guan, S.J.B. Yoo, A.M.J. Koonen, A fully-packaged 3D-waveguide based dual-fiber spatial-multiplexer with up-tapered 6-mode fiber pigtailed, in *Proc. 40th Europ. Conf. Opt. Commun. (ECOC'14)*, Cannes, France (2014), paper We.1.1.4
124. N.K. Fontaine, R. Ryf, M.A. Mestre, B. Guan, X. Palou, S. Randel, Y. Sun, L. Grüner-Nielsen, R.V. Jensen, R. Lingle, Characterization of space-division multiplexing systems us-

- ing a swept-wavelength interferometer, in *Opt. Fiber Commun. Conf. and Nat. Fiber Opt. Eng. Conf. (OFC/NFOEC'13)*, Anaheim, CA, USA (2013), Techn. Digest, paper OW1K.2
125. Y. Chen, A. Lobato, Y. Jung, H. Chen, R.V. Jensen, Y. Sun, L. Grüner-Nielsen, D.J. Richardson, V. Sleiffer, M. Kuscherov, N.K. Fontaine, R. Ryf, I.P. Giles, R. Chen, V. Carcia-Munoz, A.M.J. Koonen, B. Lankl, N. Hanik, 41.6 Tb/s C-band MDM OFDM transmission through 12 spatial and polarization modes over 74.17 km few mode fiber, in *Proc. 40th Europ. Conf. Opt. Commun. (ECOC'14)*, Cannes, France (2014), paper Mo.3.3.3
 126. R. Ryf, N.K. Fontaine, M. Montoliu, S. Randel, S.H. Chang, H. Chen, S. Chandrasekhar, A. Gnauck, R.-J. Essiambre, P.J. Winzer, T. Taru, T. Hayashi, T. Sasaki, Space-division multiplexed transmission over 3×3 coupled-core multicore fiber, in *Opt. Fiber Commun. Conf. (OFC'14)*, San Francisco, CA, USA (2014), Techn. Digest, paper Tu2J.4
 127. R.G.H. van Uden, R.A. Correa, E.A. Lopez, F.M. Huijskens, C. Xia, G. Li, A. Schülzgen, H. de Waardt, A.M.J. Koonen, C.M. Okonkwo, Ultra-high-density spatial division multiplexing with a few-mode multicore fibre. *Nat. Photonics* **8**(11), 865–870 (2014)
 128. B. Zhu, T.F. Taunay, M. Fishteyn, X. Liu, S. Chandrasekhar, M.F. Yan, J.M. Fini, E.M. Monberg, F.V. Dimarcello, 112-Tb/s space-division multiplexed DWDM transmission with 14-b/s/Hz aggregate spectral efficiency over a 76.8-km seven-core fiber. *Opt. Express* **19**(17), 16665–16671 (2011)
 129. T. Watanabe, M. Hikita, Y. Kokubun, Laminated polymer waveguide fan-out device for uncoupled multi-core fibers. *Opt. Express* **20**(24), 26317–26325 (2012)
 130. Y. Abe, K. Shikama, S. Yanagi, T. Takahashi, Low-loss physical-contact-type fan-out device for 12-core multicore fiber, in *Proc. 39th Europ. Conf. Opt. Commun. (ECOC'13)*, London, UK (2013), paper P.1.7
 131. R. Ryf, S. Randel, A. Gnauck, C. Bolle, R. Essiambre, P.J. Winzer, D.W. Peckham, A. McCurdy, R. Lingle, Space-division multiplexing over 10 km of three-mode fiber using coherent 6×6 MIMO processing, in *Opt. Fiber Commun. Conf. and Nat. Fiber Opt. Eng. Conf. (OFC/NFOEC'11)*, Los Angeles, CA, USA (2011), Techn. Digest, paper PDP B10
 132. R. Ryf, M.A. Mestre, A. Gnauck, S. Randel, C. Schmidt, R. Essiambre, P.J. Winzer, R. Delbue, P. Pupalaiakis, A. Sureka, Y. Sun, X. Jiang, D. Peckham, A.H. McCurdy, R. Lingle, Low-loss mode coupler for mode-multiplexed transmission in few-mode fiber, in *Opt. Fiber Commun. Conf. and Nat. Fiber Opt. Eng. Conf. (OFC/NFOEC'12)*, Los Angeles, CA, USA (2012), Techn. Digest, paper PDP 5B.5
 133. T. Watanabe, Y. Kokubun, Stacked waveguide type mode-evolutional multi/demultiplexer for LP_{01} , LP_{11}^a and LP_{11}^b , in *Proc. 40th Europ. Conf. Opt. Commun. (ECOC'14)*, Cannes, France (2014), paper We.1.1.7
 134. K. Saitoh, T. Uematsu, N. Hanzawa, Y. Ishizaka, K. Masumoto, T. Sakamoto, T. Matsui, K. Tsujikawa, F. Yamamoto, PLC-based LP_{11} mode rotator for mode-division multiplexing transmission. *Opt. Express* **22**(16), 19117–19130 (2014)
 135. N. Hanzawa, K. Saitoh, T. Sakamoto, T. Matsui, K. Tsujikawa, M. Koshiba, F. Yamamoto, Mode multi/demultiplexing with parallel waveguide for mode division multiplexed transmission. *Opt. Express* **22**(24), 29321–29330 (2014)
 136. G. Labroille, B. Denolle, P. Jian, P. Genevaux, N. Treps, J.-F. Morizur, Efficient and mode selective spatial mode multiplexer based on multi-plane light conversion. *Opt. Express* **22**(13), 15599–15607 (2014)
 137. J.-F. Morizur, S. Armstrong, N. Treps, J. Janousek, H.-A. Bachor, Spatial reshaping of a squeezed state of light. *Eur. Phys. J. D* **61**(1), 237–239 (2011)
 138. H. Takara, H. Ono, Y. Abe, H. Masuda, K. Takenaga, S. Matsuo, H. Kubota, K. Shibahara, T. Kobayashi, Y. Miyamoto, 1000-km 7-core fiber transmission of 10×96 -Gb/s PDM-16QAM using Raman amplification with 6.5 W per fiber. *Opt. Express* **20**(9), 10100–10105 (2012)
 139. K.S. Abedin, T.F. Taunay, M. Fishteyn, M.F. Yan, B. Zhu, J.M. Fini, E.M. Monberg, F.V. Dimarcello, P.W. Wisk, Amplification and noise properties of an erbium-doped multicore fiber amplifier. *Opt. Express* **19**(17), 16715–16721 (2011)
 140. Y. Tsuchida, K. Maeda, K. Watanabe, T. Saito, S. Matsumoto, K. Aiso, Y. Mimura, R. Sugizaki, Simultaneous 7-core pumped amplification in multicore EDF through fibre based fan-

- in/out, in *Proc. 38th Europ. Conf. Opt. Commun. (ECOC'12)*, Amsterdam, The Netherlands (2012), paper Tu.4.F.2
141. M. Yamada, K. Tsujikawa, L. Ma, K. Ichii, S. Matsuo, N. Hanzawa, H. Ono, Optical fiber amplifier employing a bundle of reduced cladding erbium-doped fibers. *IEEE Photonics Technol. Lett.* **24**(21), 1910–1913 (2012)
 142. K.S. Abedin, J.M. Fini, T.F. Thierry, V.R. Supradeepa, B. Zhu, M.F. Yan, L. Bansal, E.M. Monberg, D.J. DiGiovanni, Multicore erbium doped fiber amplifiers for space division multiplexing systems. *J. Lightwave Technol.* **32**(16), 2800–2808 (2014)
 143. K.S. Abedin, T.F. Taunay, M. Fishteyn, D.J. DiGiovanni, V.R. Supradeepa, J.M. Fini, M.F. Yan, B. Zhu, E.M. Monberg, F.V. Dimarcello, Cladding-pumped erbium-doped multicore fiber amplifier. *Opt. Express* **20**(18), 20191–20200 (2012)
 144. S. Takasaka, H. Matsuura, W. Kumagai, M. Tadakuma, Y. Mimura, Y. Tsuchida, K. Maeda, R. Miyabe, K. Aiso, K. Doi, R. Sugizaki, Cladding-pumped seven-core EDFA using a multimode pump light coupler, in *Proc. 39th Europ. Conf. Opt. Commun. (ECOC'13)*, London, UK (2013), paper We.4.A.5
 145. H. Ono, K. Takenaga, K. Ichii, S. Matsuo, T. Takahashi, H. Masuda, M. Yamada, 12-core double-clad Er/Yb-doped fiber amplifier employing free-space coupling pump/signal combiner module, in *Proc. 39th Europ. Conf. Opt. Commun. (ECOC'13)*, London, UK (2013), paper We.4.A.4
 146. J. Sakaguchi, W. Klaus, B.J. Puttnam, J.M.D. Mendinueta, Y. Awaji, N. Wada, Y. Tsuchida, K. Maeda, M. Tadakuma, K. Imamura, R. Sugizaki, T. Kobayashi, Y. Tottori, M. Watanabe, R.V. Jensen, 19-core MCF transmission system using EDFA with shared core pumping coupled via free-space optics. *Opt. Express* **22**(1), 90–95 (2014)
 147. Y. Mimura, Y. Tsuchida, K. Maeda, R. Miyabe, K. Aiso, H. Matsuura, R. Sugizaki, Batch multicore amplification with cladding-pumped multicore EDF, in *Proc. 38th Europ. Conf. Opt. Commun. (ECOC'12)*, Amsterdam, The Netherlands (2012), paper Tu.4.F.1
 148. Y. Tsuchida, M. Tadakuma, R. Sugizaki, T. Yagi, Multicore EDFA for space division multiplexing, in *Proc. OptoElectron. Commun. Conf. and Photonics in Switching (OECC/PS'13)*, Kyoto, Japan (2013), paper TuS1_1
 149. M. Yamada, H. Ono, S. Matsuo, Multicore EDFA for long-distance transmission, in *Next-Generation Optical Communication: Components, Sub-systems, and Systems III* (2013). Proc. SPIE, vol. 9009, 90090N
 150. R. Ryf, A. Sierra, R. Essiambre, S. Randel, A.H. Gnauck, C. Bolle, M. Esmaelpour, P.J. Winzer, R. Delbue, P. Pupalakise, A. Sureka, D.W. Peckham, A. McCurdy, R. Lingle, Mode-equalized distributed Raman amplification in 137-km few-mode fiber, in *Proc. 37th Europ. Conf. Opt. Commun. (ECOC'11)*, Geneva, Switzerland (2011), paper Th.13.K.5
 151. N. Bai, E. Ip, T. Wang, G. Li, Multimode fiber amplifier with tunable modal gain using a reconfigurable multimode pump. *Opt. Express* **19**(17), 16601–16611 (2011)
 152. M. Salsi, D. Peyrot, G. Charlet, S. Bigo, R. Ryf, N.K. Fontaine, M.A. Mestre, S. Randel, X. Palou, C. Bolle, B. Guan, G. Le Cocq, L. Bigot, Y. Quiquempois, A six-mode erbium-doped fiber amplifier, in *Proc. 38th Europ. Conf. Opt. Commun. (ECOC'12)*, Amsterdam, The Netherlands (2012), paper Th.3.A.6
 153. G. Le Cocq, L. Bigot, A. Le Rouge, M. Bigot-Astruc, P. Sillard, C. Koebele, M. Salsi, Y. Quiquempois, Modeling and characterization of a few-mode EDFA supporting four mode groups for mode division multiplexing. *Opt. Express* **20**(24), 27051–27061 (2012)
 154. Y. Jung, Q. Kang, J.K. Sahu, B. Corbett, R. Winfield, F. Poletti, S.U. Alam, D.J. Richardson, Few-mode EDFA supporting 5 spatial modes with reconfigurable differential modal gain control, in *Proc. 39th Europ. Conf. Opt. Commun. (ECOC'13)*, London, UK (2013), paper We.4.A.2
 155. Y. Jung, Q. Kang, J.K. Sahu, B. Corbett, J. O'Callaghan, F. Poletti, S.-U. Alam, D.J. Richardson, Reconfigurable modal gain control of a few-mode EDFA supporting six spatial modes. *IEEE Photonics Technol. Lett.* **26**(11), 1100–1103 (2014)
 156. Q. Kang, E.-L. Lim, F.P.Y. Jung, C. Baskiotis, S. Alam, D.J. Richardson, Minimizing differential modal gain in cladding-pumped EDFAs supporting four and six mode groups. *Opt.*

- Express **22**(18), 21499–21507 (2014)
157. D. Askarov, J.M. Kahn, Design of transmission fibers and doped fiber amplifiers for mode-division multiplexing. *IEEE Photonics Technol. Lett.* **24**(21), 1945–1948 (2012)
 158. Q. Kang, E.-L. Lim, F. Poletti, Y. Jung, S. Alam, J.R. David, Minimizing differential modal gain in cladding pumped MM-EDFAs for mode division multiplexing in C and L bands, in *Proc. 7th Internat. Photon. Optoelectron. Meetings (POEM'14)*, Wuhan, China (2014), paper FTh4F.1
 159. Q. Kang, E. Lim, Y. Jun, X. Jin, F.P. Payne, S. Alam, D.J. Richardson, Gain equalization of a six-mode-group ring core multimode EDFA, in *Proc. 40th Europ. Conf. Opt. Commun. (ECOC'14)*, Cannes, France (2014), paper P.1.14
 160. G. Le Cocq, Y. Quiquempois, A. Le Rouge, G. Bouwmans, H. El Hamzaoui, K. Delplace, M. Bouazaoui, L. Bigot, Few mode Er^{3+} -doped fiber with micro-structured core for mode division multiplexing in the C-band. *Opt. Express* **21**(25), 31646–31659 (2013)
 161. G. Le Cocq, Y. Quiquempois, L. Bigot, Gradient descent optimization for few-mode Er^{3+} -doped fiber amplifiers with micro-structured core, in *Proc. IEEE Photon. Soc. Summer Top. Meeting*, Montreal, Quebec, Canada (2014), pp. 150–151
 162. W.I. Way, Next generation ROADM architectures, in *Proc. Asia Commun. Photon. Conf.*, Guangzhou, China, 2012 (2012), paper AS1G.3
 163. D.M. Marom, D.T. Neilson, D.S. Greywall, C.-S. Pai, N.R. Basavanahally, V.A. Aksyuk, D.O. Lopez, F. Pardo, M.E. Simon, Y. Low, P. Kolodner, C.A. Bolle, Wavelength-selective $1 \times K$ switches using free-space optics and MEMS micromirrors: theory, design, and implementation. *J. Lightwave Technol.* **23**(4), 1620–1630 (2005)
 164. S. Li, Z. Wan, J. Xu, S. Zhong, Y. Wu, Wavelength-selective switch based on a polarization-independent transmission grating and a high fill-factor micromirror array. *IEEE Photonics Technol. Lett.* **23**(17), 1249–1251 (2011)
 165. N. Collings, T. Davey, J. Christmas, D. Chu, W.A. Crossland, The applications and technology of phase-only liquid crystal on silicon devices. *J. Disp. Technol.* **7**(3), 112–119 (2011)
 166. H.S. Chen, A.M.J. Koonen, LP01 and LP11 mode division multiplexing link with mode crossbar switch. *Electron. Lett.* **48**(19), 1222–1223 (2012)
 167. L.E. Nelson, M.D. Feuer, K. Abedin, X. Zhou, T.F. Taunay, J.M. Fini, B. Zhu, R. Isaac, R. Harel, G. Cohen, D.M. Marom, Spatial superchannel routing in a two-span ROADM system for space division multiplexing. *J. Lightwave Technol.* **32**(4), 783–789 (2014)
 168. R.Y. Gu, E. Ip, M.-J. Li, Y.-K. Huang, J.M. Kahn, Experimental demonstration of a spatial light modulator few-mode fiber switch for space-division multiplexing, in *Frontiers in Optics (FiO'13)*, Orlando, FL, USA (2013), PDP FW6B.4
 169. N.K. Fontaine, R. Ryf, C. Liu, B. Ercan, J.R. Salazar Gil, S.G. Leon-Saval, J. Bland-Hawthorn, D.T. Neilson, Few-mode fiber wavelength selective switch with spatial-diversity and reduced-steering angle, in *Opt. Fiber Commun. Conf. (OFC'14)*, San Francisco, CA, USA (2014), Techn. Digest, paper Th4A.7
 170. J. Carpenter, S.G. Leon-Saval, J.R. Salazar-Gil, J. Bland-Hawthorn, G. Baxter, L. Stewart, S. Frisken, M.A.F. Roelens, B.J. Eggleton, J. Schröder, 1×11 few-mode fiber wavelength selective switch using photonic lanterns. *Opt. Express* **22**(3), 2216–2221 (2014)
 171. X. Jiang, R. Harel, G. Cohen, D.M. Marom, M.D. Feuer, Crosstalk in an ROADM supporting spatial superchannels for space division multiplexing, in *Conf. Lasers Electro-Opt./Sci. Innov. (CLEO'14)*, San Jose, CA, USA (2014), Techn. Digest, paper SW3J-8
 172. N.K. Fontaine, R. Ryf, D.T. Neilson, Fiber-port-count in wavelength selective switches for space-division multiplexing, in *Proc. 39th Europ. Conf. Opt. Commun. (ECOC'13)*, London, UK (2013), paper We.4.B.6
 173. K.-P. Ho, J.M. Kahn, J.P. Wilde, Wavelength-selective switches for mode-division multiplexing: Scaling and performance analysis. *J. Lightwave Technol.* **32**(22), 3724–3735 (2014)
 174. X. Chen, A. Li, J. Ye, A. Al Amin, W. Shieh, Demonstration of few-mode compatible optical add/drop multiplexer for mode-division multiplexed superchannel. *J. Lightwave Technol.* **31**(4), 641–647 (2013)

175. E. Ip, N. Cvijetic, T. Wang, Spatial light modulator-based few-mode fiber switches for space-division multiplexing applications, in *Proc. 39th Europ. Conf. Opt. Commun. (ECOC'13)*, London, UK (2013), paper Th.1.C.2
176. D.M. Marom, Wavelength-selective switches operating over space-division multiplexing, in *Proc. IEEE Photon. Soc. Summer Top. Meeting*, Montreal, Quebec, Canada (2014), pp. 160–161
177. V. Sleiffer, Y. Jung, V. Veljanovski, R. van Uden, M. Kuschnerov, Q. Kang, L. Grüner-Nielsen, Y. Sun, D. Richardson, S. Alam, F. Poletti, J. Sahu, A. Dhar, H. Chen, B. Inan, T. Koonen, B. Corbett, R. Winfield, A. Ellis, H. de Waardt, 73.7 Tb/s ($96 \times 3 \times 256$ -Gb/s) mode-division-multiplexed DP-16QAM transmission with inline MM-EDFA, in *Proc. 38th Europ. Conf. Opt. Commun. (ECOC'12)*, Amsterdam, The Netherlands (2012), paper Th.3.C.4
178. S. Warm, K. Petermann, Splice loss requirements in multi-mode fiber mode-division-multiplex transmission links. *Opt. Express* **21**(1), 519–532 (2013)
179. K. Watanabe, T. Saito, K. Imamura, Y. Nakayama, M. Shiino, Study of fusion splice for single-mode multicore fiber, in *Proc. 17th IEEE Microoptics Conf. (MOC'11)*, Sendai, Japan (2011), paper H-8
180. K. Yoshida, A. Takahashi, T. Konuma, K. Yoshida, K. Sasaki, Fusion splicer for specialty optical fiber with advanced functions. *Fujikura Tech. Rev.* **41**, 10–13 (2012)
181. Y. Amma, Y. Arakawa, A. Takahashi, K. Takenaga, S. Matsuo, Low-loss fusion splice technique for multicore fiber with a large cladding diameter, in *Proc. IEEE Photon. Soc. Summer Top. Meeting*, Waikoloa, HI, USA (2013), pp. 74–75
182. K. Sakai, R. Nagase, K. Watanabe, T. Saito, Connection characteristics of multicore fiber connector, in *Proc. OptoElectron. Commun. Conf. and Photonics in Switching (OECC/PS'13)*, Kyoto, Japan (2013), paper TuPS_1
183. M. Kuschnerov, F.N. Hauske, K. Piyawanno, B. Spinnler, A. Napoli, B. Lankl, Adaptive chromatic dispersion equalization for non-dispersion managed coherent systems, in *Opt. Fiber Commun. Conf. and Nat. Fiber Opt. Eng. Conf. (OFC/NFOEC'09)*, San Diego, CA, USA (2009), Techn. Digest, paper OMT1
184. A. Viterbi, Nonlinear estimation of PSK-modulated carrier phase with application to burst digital transmission. *IEEE Trans. Inf. Theory* **29**(4), 543–551 (1983)
185. M.S. Faruk, K. Kikuchi, Adaptive frequency-domain equalization in digital coherent optical receivers. *Opt. Express* **19**(13), 12789–12798 (2011)
186. N. Bai, G. Li, Adaptive frequency-domain equalization for mode-division multiplexed transmission. *IEEE Photonics Technol. Lett.* **24**(21), 1918–1921 (2012)
187. S. Randel, P.J. Winzer, M. Montoliu, R. Ryf, Complexity analysis of adaptive frequency-domain equalization for MIMO-SDM transmission, in *39th Europ. Conf. Opt. Commun. (ECOC'13)*, London, UK (2013), pp. 801–803, paper Th.2.C.4
188. P.J. Winzer, Spatial multiplexing: The next frontier in network capacity scaling, in *39th Europ. Conf. Opt. Commun. (ECOC'13)*, London, UK (2013), pp. 372–374, tutorial We.1.D.1
189. S.O. Arik, D. Askarov, J.M. Kahn, Effect of mode coupling on signal processing complexity in mode-division multiplexing. *J. Lightwave Technol.* **31**(3), 423–431 (2013)
190. M. Kuschnerov, T. Bex, P. Kainzmaier, Energy efficient digital signal processing, in *Opt. Fiber Commun. Conf. (OFC'14)*, San Francisco, CA, USA (2014), Techn. Digest, paper Th3E.7
191. OFS: Few-mode optical fiber series. [Online]. Available: <http://fiber-optic-catalog.ofsoptics.com/category/few-mode-optical-fiber-series>
192. OFS: Multi-core fiber. [Online]. Available: <http://www.ofsoptics.com/multicore.html>
193. YOFC: Photonic crystal fibre (PCF); Multi-core Fiber. [Online]. Available: <http://www.yofc.com.cn/Specialty/13/131.aspx>
194. CAILabs: Spatial multiplexer. [Online]. Available: <http://www.cailabs.com/products/spatial-multiplexer/>
195. Chiral Photonics: Multicore fiber fanout. [Online]. Available: http://www.chiralphotonics.com/Web/multicore_fiber_fanout.html

196. V.I. Kopp, A.Z. Genack, Chiral fibres: adding twist. *Nat. Photonics* **5**(8), 470–472 (2011)
197. V.I. Kopp, J. Park, M. Wlodawski, J. Singer, D. Neugroschl, A.Z. Genack, Pitch reducing optical fiber array for dense optical interconnect, in *Proc. IEEE Avion. Fiber-Opt. Photon. Technol. Conf. (AVFOP'12)*, Cocoa Beach, FL, USA (2012), pp. 48–49
198. Kyliia: Modal multiplexer/demultiplexer. [Online]. Available: <http://www.kyliia.com/modes.html>
199. V.A.J.M. Sleiffer, H. Chen, Y. Jung, P. Leoni, M. Kuschnerov, A. Simperler, H. Fabian, H. Schuh, F. Kub, D.J. Richardson, S.U. Alam, L. Grüner-Nielsen, Y. Sun, A.M.J. Koonen, H. de Waardt, Field demonstration of mode-division multiplexing upgrade scenarios on commercial networks. *Opt. Express* **21**(25), 31036–31046 (2013)
200. Optoscribe: 3D MMux photonic lantern. [Online]. Available: <http://optoscribe.com/products/3d-mmux-photonic-lantern/>
201. P. Mitchell, G. Brown, R.R. Thomson, N. Psaila, A. Kar, 57 Channel (19×3) spatial multiplexer fabricated using direct laser inscription, in *Opt. Fiber Commun. Conf. (OFC'14)*, San Francisco, CA, USA (2014), Techn. Digest, paper M3K.5
202. Optoscribe: 3D optofan series. [Online]. Available: <http://optoscribe.com/products/3d-optofan-series/>
203. Phoenix Photonics: SDM components. [Online]. Available: http://www.phoenixphotonics.com/website/products/spatial_division_multiplexing_SDM_products.htm
204. I. Giles, A. Obeysekara, R. Chen, D. Giles, F. Poletti, D.J. Richardson, All fiber components for multimode SDM systems, in *Proc. IEEE Photon. Soc. Summer Top. Meeting*, Seattle, WA, USA (2012), pp. 212–213
205. A. Li, A.A. Amin, X. Chen, S. Chen, G. Gao, W. Shieh, Reception of dual-spatial-mode CO-OFDM signal over a two-mode fiber. *J. Lightwave Technol.* **30**(4), 634–640 (2012)
206. Fujikura: Fusion splicers—specialty. [Online]. Available: <http://www.fujikura.co.uk/products/fusion-splicers-and-accessories/fusion-splicers-specialty/arcmaster-fsm-100mplus-and-100pplus/>

Haoshuo Chen received B.S. and M.S. degrees in electrical engineering from Shanghai University in 2007 and 2009, and the Ph.D. degree (cum laude) in electrical engineering from the Eindhoven University of Technology, Eindhoven, The Netherlands, in 2014. Supported by the European Union FP7 MODE-GAP Project, he investigated free space and photonic integrated spatial multiplexing solutions and demonstrated several large capacity few-mode fiber transmission trials. From September 2013 to March 2014, he was an intern at Bell Laboratories, Holmdel, NJ, USA, where he researched novel spatial multiplexers and wavelength selective switches. Since December 2014, he has been a member of the Advanced Photonic Research Department at Bell Laboratories, Holmdel, NJ.

His main research interests include spatial division multiplexing, photonic integration, digital signal processing, and wavelength selective switches. He received the Best Student Award in Asia Communications and Photonics Conference in 2012. He has also served as a peer reviewer for *IEEE Photonics Technology Letters*, *Journal of Lightwave Technology*, *OSA Optics Express*, *Optics Letters*, *Applied Optics* and *IET Optoelectronics*.

A.M.J. (Ton) Koonen is full professor in Eindhoven University of Technology since 2001. Since 2004 he is chairman of the group Electro-Optical Communication Systems and since 2012 vice-dean of the department Electrical Engineering. Before 2001, he worked for more than 20 years in applied research in industry, amongst others in Bell Labs—Lucent Technologies. He is Bell Labs Fellow (1998), IEEE Fellow (2007), OSA Fellow (2013), and Distinguished Guest Professor of Hunan University, Changsha, China (2014). In 2011 he received an Advanced Investigator Grant of the European Research Council. He (co-)authored more than 140 international journal papers, 10 book chapters, and 430 conference papers. His current research interests are spatial division multiplexed systems, access and in-building fiber networks, including high capacity POF networks, radio-over-fiber techniques, and wireless optics techniques.

Chapter 2

Optical Fibers

Pierre Sillard and Denis Molin

Abstract The chapter starts with the fundamentals of light propagation in optical fibers followed by the essentials of fiber fabrication. Subsequent sections focus on typical loss and dispersion characteristics of single-mode and multimode fibers including relevant information on standardization. The basic elements of fiber cables and cables for various applications constitute another topic followed by new developments such as micro-structured and Bragg fibers, hybrid devices combining glass fibers and semiconductors and fibers for space division multiplexing.

2.1 Introduction

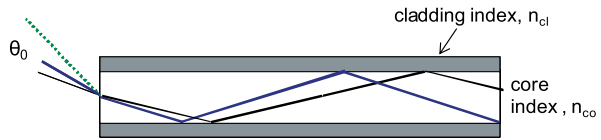
Within the past forty years optical fibers have evolved from a not-so-transparent glass tube to an extraordinarily efficient transmission medium, now acknowledged as a central element of modern telecommunication networks. Who could have imagined then, that by now several 100s million kilometers of fibers would have been installed worldwide, allowing today's highly sophisticated World Wide Web (WWW) to link the whole planet in real time? Since the first proposition of using glass fibers as a data transmission medium in 1966 [1], optical fibers have had an extremely dynamic development, always sustaining the evolution of transmission systems and the growing needs for bandwidth.

It is the purpose of this chapter to give the reader some basic knowledge about optical fibers: How are they fabricated? What are the key characteristics and what are the different optical fibers? What are the latest innovations? This chapter is thus organized as follows: The first paragraph includes some fiber basics to give the reader a very first insight on fiber propagation and to introduce the two main categories of optical fibers, that is single-mode and multimode fibers. The following

P. Sillard (✉) · D. Molin
Prysmian Group, Parc des Industries Artois Flandres, 644 Boulevard Est, 62092 Haisnes Cedex,
Billy Berclau, France
e-mail: pierre.sillard@prysmiangroup.com

D. Molin
e-mail: denis.molin@prysmiangroup.com

Fig. 2.1 Schematic of light propagation, based on geometrical optics



two paragraphs are dedicated specifically to multimode and single-mode telecom fibers, respectively. In each of those two paragraphs, we describe in detail key fiber characteristics, the different types of fibers that have been developed over the past few years and some standardization basics. The subsequent paragraph will shortly present fiber cables for telecom applications, and we will finish with the latest developments on novel optical fibers.

2.2 Fiber Basics

2.2.1 Principle of Light Propagation in Optical Fibers

An optical fiber is a thin cylindrical strand of silica glass, consisting of a central core surrounded by a cladding: the core has higher refractive index n_{co} than the surrounding cladding n_{cl} ($n_{co} > n_{cl}$), thus allowing light to be guided through internal reflection. Typical dimensions are from 10 to a few 10s of μm for the core diameter, depending on fiber type, and 125 μm for the cladding. The index difference between the core and the cladding is very small, ranging from ~ 5 to $\sim 30 \times 10^{-3}$, again depending on fiber type.

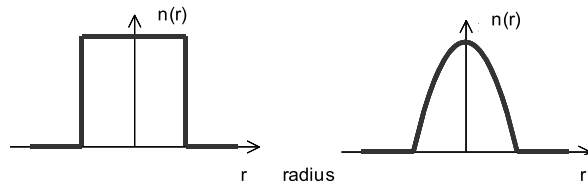
Geometrical optics is often used to get a first physical insight of light propagation. Indeed, light guidance can be simply described by a succession of total internal reflections at the core-cladding interface, with each optical path within the fiber corresponding to one ‘mode’ of propagation. This is illustrated in Fig. 2.1. Fibers allowing several modes to propagate are called multimode fibers (MMF), while fibers allowing only one mode to propagate are called single-mode.

Snell-Descartes’ law can be used in a straightforward way to derive the angle of acceptance, or critical angle θ_0 , which defines how much light is captured and guided through a multimode fiber. Any light coming into the fiber at an incident angle larger than θ_0 will not experience total internal reflection and will thus not be guided through the fiber. The following relation relates θ_0 to the fiber characteristics:

$$\sin \theta_0 = \sqrt{n_{co}^2 - n_{cl}^2} = NA \quad (2.1)$$

where NA is the numerical aperture. The larger NA , the larger the number of modes. Classical silica-based multimode fibers have NA ranging from 0.2 to 0.3. Again, geometrical optics cannot replace a full description based on electromagnetic theory and Maxwell’s equations. Basic principles will be given in the next section. Let’s also underline that total internal reflection is not the only mechanism that allows

Fig. 2.2 Step index profile (left) and parabolic index profile (right)



light to be guided. Over the past ten years, much research has been devoted to new fiber types that rely on different physical mechanisms to guide light. This will be described in the last Sect. 2.6 of this chapter.

We conclude this section with a few words about the refractive-index profile $n(r)$ that describes the change of index over the fiber cross-section. The index profile fully defines the properties of light propagating through the fiber. The most simple index profile consists of a step, i.e. a core with a constant index of refraction, but we will see in Sect. 2.4 that profile shapes have become increasingly complicated as fiber requirements have become more stringent. Figure 2.2 illustrates the two most common index profiles, that is the step and parabolic profiles. The parabolic shape, also called graded-index, is essentially used for multimode fibers while a large variety of shapes can be used for single-mode fibers, ranging from the simple step to more complex segmented structures.

2.2.2 Modal Theory of Light Propagation in Optical Fibers

Light propagation in optical fibers is governed by Maxwell's equations, like all electromagnetic phenomena. For a detailed theory, the reader can refer to well-established textbooks about optical fibers [2, 3]. In this section, we intend to give a short overview of the most important equations and to introduce the concept of modes from an electromagnetic perspective.

Recall that for an isotropic, non-conducting, non-magnetic medium, Maxwell's equations can be written as:

$$\nabla \times \mathbf{E} = -\frac{\partial \mathbf{B}}{\partial t} \quad (2.2)$$

$$\nabla \times \mathbf{H} = \frac{\partial \mathbf{D}}{\partial t} \quad (2.3)$$

$$\nabla \cdot \mathbf{D} = 0 \quad (2.4)$$

$$\nabla \cdot \mathbf{B} = 0 \quad (2.5)$$

where \mathbf{E} and \mathbf{H} are the electric and magnetic vectors, respectively, and \mathbf{D} and \mathbf{B} the corresponding flux densities. In a dielectric medium, they are related to field vectors by:

$$\mathbf{D} = \varepsilon \mathbf{E} \quad (2.6)$$

$$\mathbf{B} = \mu_0 \mathbf{H} \quad (2.7)$$

where $\varepsilon = \varepsilon_0 \varepsilon_r$ is the dielectric permittivity, ε_0 is the vacuum permittivity and ε_r is the relative permittivity, and μ_0 is the vacuum permeability.

The wave equation is obtained by combining the equations above to isolate the electric vector \mathbf{E} . Assuming that loss is low enough so that the permittivity ε is real and replacing ε by $\varepsilon_0 n^2$, where n is the refractive index profile, leads to the following wave equation:

$$\nabla^2 \mathbf{E} - \frac{n^2}{c^2} \cdot \frac{\partial^2 \mathbf{E}}{\partial t^2} = \nabla(\nabla \cdot \mathbf{E}) = -\nabla(\nabla(\ln n^2) \cdot \mathbf{E}) \quad (2.8)$$

We saw in the preceding section, that in optical fibers the index difference between the core and the cladding is small, on the order of $\sim 10^{-2}$. This feature allows to fully neglect the term on the right side of (2.8). This is called the ‘weakly-guiding approximation’ [4], which allows for a simpler description of guided wave propagation.

Cylindrical symmetry of the guiding structure is another important feature that allows to write any of the field components in cylindrical coordinates (r, θ) as:

$$E = F(r)G(\theta)e^{i(\omega t - \beta z)} \quad (2.9)$$

where ω is the angular frequency and β the propagation constant of the field propagating along the z -axis.

Inserting (2.9) into the wave equation (2.8) within the weakly guiding approximation yields the following important equations:

$$\begin{cases} \frac{d^2 F}{dr^2} + \frac{1}{r} \cdot \frac{dF}{dr} + \left(k^2 n^2 - \beta^2 - \frac{\nu^2}{r^2} \right) \cdot F = 0 \\ \frac{d^2 G}{d\theta^2} + \nu^2 G = 0 \end{cases} \quad (2.10)$$

Here, k is the wavenumber, equal to ω/c or $2\pi/\lambda$ and ν is the azimuthal number, that can only take integer values due to the 2π field periodicity.

In the case of a simple step-index profile, with constant index values in the core with radius a and in the cladding, the solution of (2.10) is well-known and takes the form of Bessel functions. In the case of more complicated index-profile shapes within the core, even though many strategies have been developed in the past to solve this scalar wave equation, numerical methods have to be applied.

There are many solutions to (2.10), each solution being called a mode and being defined by its propagation constant and field distribution. However, we are mainly interested in the guided modes, whose radial distributions should be finite at $r = 0$ and decay to 0 at infinity. It is then possible to show that all the guided modes have a propagation constant that obeys:

$$n_{cl} < \frac{\beta}{k} < n_{co} \quad (2.11)$$

where β/k is the effective refractive index n_{eff} , n_{co} is the maximum index within the core, and n_{cl} is the cladding index. In some cases, like for trench assisted profiles (described in Sect. 2.3.2), it may be necessary to take into account modes with complex propagation constant and field distribution that oscillates at infinity: the leaky modes. In the particular case of trench assisted profiles, the real part of the propagation constant of these modes typically follows:

$$n_- < \frac{real(\beta)}{k} < n_{cl} \quad (2.12)$$

where n_- is the lowest refractive index of the depressed area surrounded by the outer cladding of constant refractive index. These leaky modes are confined by the depressed index area within the core but leak out energy to the outer cladding by tunneling effect [5], even without bending. The leakage losses of the leaky modes, expressed in dB per unit of length, are a function of the imaginary part of the propagation constant:

$$Loss = \frac{20}{\ln 10} \cdot \text{Im}(\beta) \quad (2.13)$$

Whatever the index profile is, it is necessary to apply the boundary conditions, that is the electric field and its derivative are continuous at the core/cladding interface, leading to the well-known eigenvalue equation which only depends on the index profile, the wavelength, and the azimuthal number, and whose solution is the propagation constant β . Depending on the profile parameters and wavelength, this equation will have one or more solutions for each integer value ν . Each solution is labeled $\beta_{\nu\mu}$, (where $\mu = 1, 2 \dots$) and corresponds to a mode of propagation labeled $LP_{\nu\mu}$ whose optical field distribution is obtained from (2.10) knowing $\beta_{\nu\mu}$, where LP stands for Linearly Polarized. Indeed, it is possible to show that modes are nearly transverse. Figure 2.3 shows examples of radial distributions of different modes.

In a single-mode fiber profile parameters are chosen so that the only mode that propagates is the LP_{01} mode. As can be seen in Fig. 2.3, this mode is nearly Gaussian.

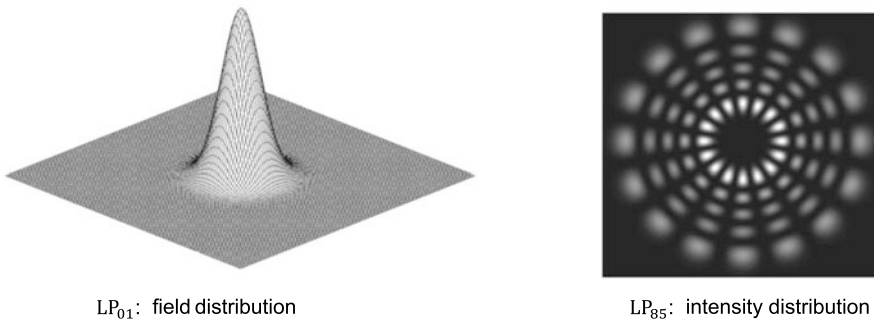


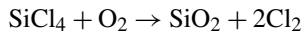
Fig. 2.3 Schematic of radial distribution of LP_{01} mode (left graph) showing a 3D computed plot, and LP_{85} mode (right) showing a computed cross-section of the intensity

2.2.3 Fiber Fabrication

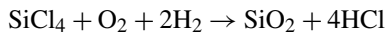
Over the past 40 years silica glass has proven to be the material of choice for optical fibers, combining both low loss and good reliability and being easy to process. Research is still going on to find alternative materials, but current interest is directed towards very specific applications in the field of nonlinear optics. In the case of silica glass the index profile can be tailored by the addition of a small quantity of dopants: Ge-P in some cases- to increase the index of refraction and F-B in some cases- to lower it. For example, changing the index of refraction by 1×10^{-3} with respect to silica requires about 1 wt% of Ge only.

Fiber manufacturing has become an extremely well-mastered process. Geometry is controlled to the μm level, while material purity is controlled to well below ppb levels.

Fiber manufacturing is a two-step process. The first step is the fabrication of a high-purity rod called preform. This rod has exactly the same composition and cross-sectional profile as the fiber but its diameter is a few centimeters. Because of its larger size it is possible to achieve a very good control of the index profile. Different techniques are currently used by fiber manufacturers to make preforms [6]: MCVD (Modified Chemical Vapor Deposition), PCVD (Plasma Chemical Vapor Deposition), VAD (Vapor Axial Deposition) and OVD (Outside Vapor Deposition). For all these methods glass is created from a high-temperature reaction between gases. In the case of MCVD, glass is formed layer after layer on the inner surface of a tube through the oxidation of SiCl_4 gas ($1400\text{ }^\circ\text{C}$ to $1600\text{ }^\circ\text{C}$).



The high temperature is usually obtained by a burner or a furnace. PCVD, as MCVD, is an inside deposition process but reactions occur within a microwave-generated plasma. For OVD and VAD, as opposed to MCVD and PCVD, soot is formed through hydrolysis:



Thus, both methods require an extra-step consisting of dehydration and vitrification in a heating furnace ($\sim 1500\text{ }^\circ\text{C}$) to eventually obtain glass. OVD is an external-deposition process, where soot layers are deposited one after another onto a starting rod. In the case of VAD, the rod is built vertically with core and cladding made at the same time.

The second step consists in drawing the preform rod into the $125\text{ }\mu\text{m}$ fiber, which becomes an exact smaller-size replica of the rod. This is usually done in a drawing tower, over 10 m high, that includes a high-temperature furnace at the top to melt down the preform and a spooling device at the bottom to wind the fiber. The end of the preform rod is thus heated in the furnace ($\sim 2000\text{ }^\circ\text{C}$) above the melting point to allow the fiber to be drawn by the winding device with a controlled bare-fiber tension. Fiber is also coated with polymer during the drawing process to ensure

mechanical protection. Two polymer coatings are generally applied onto the glass fiber: a first soft material to protect the fiber from lateral pressure when cabled, and a more rigid layer to provide mechanical protection. Coating is usually transparent, but color components can be directly added to the secondary layer, thus eliminating the need for an extra inking-process step before cabling. Final diameter of coated fiber is typically 250 μm .

2.2.4 Fiber Loss

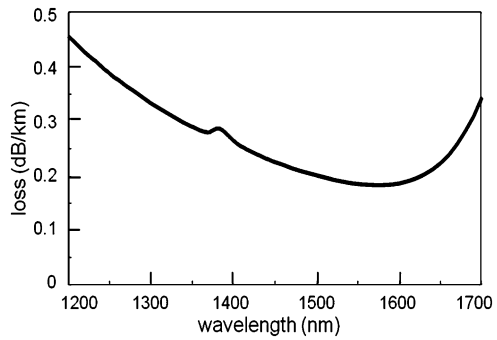
Fiber loss is a fundamental limiting factor as it reduces signal power propagating through the fiber. It is described by an attenuation coefficient (α) in dB/km. As for any material, loss is linked to either absorption or scattering mechanisms.

Pure silica absorbs in the ultraviolet (electronic transitions) and in the far-infrared region (molecular vibrations of SiO_2). Metallic impurities could give rise to additional absorption peaks [7], but the fiber fabrication process has improved to a point where impurities are no longer a significant concern, with much less than ppb levels and no impact on loss. Hydrogen is also one of the well-known impurities, which has to be avoided during fiber fabrication and once the fiber is installed. Hydrogen diffuses easily and can undergo chemical reactions with the network of silica glass, leading to the formation of numerous defects, the most detrimental one being SiOH. The SiOH vibration has a fundamental absorption peak at 2.73 μm and overtones at 1.38 μm and 0.95 μm , and a concentration of 1 ppm_w only leads to a few tens of dB/km attenuation at 1.38 μm [8]. From the early days of fiber fabrication much work has been devoted to the reduction of the so-called OH peak. Latest advances at the end of the 90's have allowed manufacturers to produce virtually OH-free fibers with additional loss of less than 0.1 dB/km at 1.38 μm . These fiber types are now very well described by standardization bodies and referred to as G.652.D for single-mode fibers.

Rayleigh scattering is the dominant scattering mechanism in silica fibers. It varies as λ^{-4} and is also dependent on fiber composition. In most cases, the higher the dopant concentration is, the higher the corresponding scattering is. In pure silica, the Rayleigh scattering coefficient is of the order of 0.6 to 0.8 dB $\mu\text{m}^4/\text{km}$ and depends on fabrication process and thermal history of the glass measured through its fictive temperature [9]. The influence of Ge doping on Rayleigh scattering has been extensively studied in the past and it can be considered to grow linearly with composition: Rayleigh scattering is doubled compared to pure silica at a germanium incorporation equivalent to a refractive index increase of about 25×10^{-3} [9]. Additional scattering can also be generated by any defects or small fluctuations at the core/cladding interface, also referred to as 'waveguide imperfection' [10]. This component is negligible for standard single-mode fibers, but can be significant for higher dopant contents [11].

When summing up all these contributions minimum loss is found around 1.55 μm where most of today's telecommunication systems operate. Figure 2.4 shows a typical loss spectrum for commercially available single-mode fibers with typical values

Fig. 2.4 Spectral loss of a commercial single-mode fiber



of 0.2 dB/km at 1.55 μm . In this wavelength range Rayleigh scattering is the main contribution. Even though these values are very close to the fundamental limit for silica, there is still some research to further reduce fiber loss with a record loss of 0.152 dB/km recently reported and achieved through careful profile design and fiber fabrication [12].

One important feature of optical fibers is that they can be bent. However, light is not guided as well in a bent fiber as it is in a straight fiber, it scatters away and loss occurs. The smaller the bending radius the higher is the loss. Also, when fibers are in cable form, they are pressed against a surface that is never perfectly smooth, thus generating random axial oscillations for the fibers and referred to as micro-bending. Both, macro- and micro-bend loss, will be further discussed in Sect. 2.4 as their control is important when designing fibers.

2.2.5 Fiber Dispersion

Dispersion is the other important limiting factor when considering data transmission. It is the mechanism that causes a light pulse to broaden as it propagates through the fiber and limits transmission capacity whether the system is digital or analog. Dispersion is very different in multimode and single-mode fibers.

In a multimode fiber it can be very well understood with the geometrical-optics description. Injected light is coupled to the different modes that the fiber can sustain (or part of them, depending on how injection is made). Modes have different paths, thus leading to different time-of-flight at the output of the fiber. This is called intermodal dispersion. Very simple geometrical-optics computations show that in a multimode step-index fiber it is of the order of 10s of ns/km. This is exactly why graded-index profiles have been developed: to decrease the intermodal dispersion and allow higher data rates to be transmitted. This will be further discussed in the next section dedicated to multimode fibers.

In a single-mode fiber intermodal dispersion does not occur because all the light is carried within one mode. However, pulse broadening is still present because any given source emits over a range of wavelengths, and different wavelengths travel at

a different speed. This is called intra-modal dispersion or chromatic dispersion. The chromatic dispersion coefficient is given in ps/(nm km). Chromatic dispersion exists in all dielectric materials and is intrinsically related to the wavelength dependence of refractive index. In fibers, dispersion can be computed easily when knowing the wavelength dependence of the effective index n_{eff} , through:

$$D = \frac{d\tau_g}{d\lambda} = -\frac{\lambda}{c} \cdot \frac{d^2 n_{eff}}{d\lambda^2} \quad (2.14)$$

where τ_g is the group delay. It can be shown that dispersion can be very well approximated by the sum of two contributions: that of silica itself, called ‘material dispersion’, and that of the guiding structure, called ‘waveguide dispersion’.

In the telecom wavelength range, silica dispersion increases with wavelength. It zeroes near 1.28 μm and is ~ 20 ps/(nm km) at 1.55 μm [13]. On the other hand, waveguide dispersion is negative over a broad spectral range. Waveguide dispersion depends on profile shape and can thus strongly modify material dispersion. Chromatic dispersion is a very important characteristic, and many fiber types have been developed with different dispersion properties. This will be further discussed in Sect. 2.4 devoted to single-mode fibers.

2.3 Multimode Fibers

Multimode fibers were the first fibers to be commercialized in the 1970’s, being used for both short and long distance telecommunications, operating mainly at 0.85 μm with LED (Light-Emitting Diode) sources. Single-mode fibers were of course recognized for their higher bandwidth, but there were no sources to couple light efficiently into the narrower core of single-mode fibers. At the beginning of the 80’s, research on sources resulted in reliable semiconductor lasers suited for smaller core single-mode fibers, which narrowed down the application of multimode fibers to short-distance systems.

Multimode fiber development has continued from the 1980’s up to now mainly in the framework of Ethernet dedicated to data communications that successively promoted bit rates from 10 Mbit/s to 10 Gbit/s (2002) and to future 100 Gbit/s. Multimode fibers have been able to follow this increase in bit rate thanks to process improvements and technological breakthroughs in sources that provided low-cost 10 Gbit/s sources at the end of the 90’s, in particular the Vertical Cavity Surface Emitting Laser (VCSEL) operating at 850 nm (see also Chap. 3).

Compared to single-mode fibers, multimode fibers offer much more relaxed connectorization tolerances between fibers and to sources.

2.3.1 Key Characteristics

2.3.1.1 Modal Bandwidth

Bandwidth is one of the main characteristics of multimode fibers: it quantifies the light carrying capacity, the higher, the better. It is generally normalized by the fiber length and thus expressed in MHz km, referring to the analog world, but a relation between maximum bit rate and modal bandwidth can be derived.

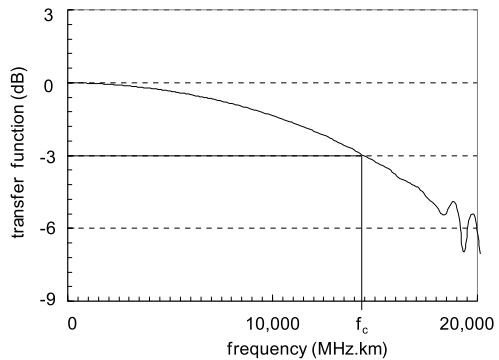
Fiber can be seen as a passive low-pass filter. Its bandwidth is then defined as the modulation frequency that is reduced by 3 dB as compared to the zero frequency (DC) response. This is illustrated in Fig. 2.5. Bandwidth can be measured either in the time or frequency domain [14]. In the time domain, it consists of measuring the temporal response of the fiber by injecting a short pulse. The transfer function $TF(f)$ can then be computed from the recorded input $s_{in}(t)$ and output $s_{out}(t)$ signals as the ratio of their respective fast Fourier transform $\tilde{s}_{in}(f)$ and $\tilde{s}_{out}(f)$:

$$TF(f) = 10 \cdot \log_{10} \left(\frac{\tilde{s}_{out}(f)}{\tilde{s}_{in}(f)} \right) \quad (2.15)$$

One of the main features of multimode fibers is that many of their characteristics depend on the way light is coupled, more commonly called the launching conditions. The launching condition defines which modes are excited or not, and what the corresponding power distribution is. However, the launching conditions provided by LEDs and VCSELs are very different, and very different even within the VCSELs family. LEDs usually excite almost all the guided modes, while VCSELs excite a smaller number of modes, which varies widely from one VCSEL to another.

So, in order to ensure consistent bandwidth measurements and enable a comparison of fibers on the same basis, bandwidth is measured under what is called the Over-Filled Launch (OFL) condition, which corresponds to a uniform excitation of all guided modes in the fiber. In practice, a mode scrambler is inserted between the laser and the fiber to provide a spatially, angularly and uniformly over-filled launch. Typical values of OFL modal bandwidth are several hundreds of MHz km, with the

Fig. 2.5 Computed transfer function of a multimode fiber (f_c : modal bandwidth)



best modern fibers exhibiting values over 10 GHz km at 850 nm. The OFL modal bandwidth renders fiber properties very well when fiber is coupled to an LED.

Modal bandwidth under VCSEL launch is called Effective Modal Bandwidth (EMB). Due to the plurality of VCSEL patterns, no standardized launching conditions have been defined, but dedicated measurement strategies have been developed to best characterize fiber performance. It mainly relies on differential mode delay measurements as explained in the next paragraph.

2.3.1.2 Differential Mode Delay

Differential Mode Delay (DMD) measurement is another way of characterizing the modal properties of multimode fibers. It is now widely used by fiber manufacturers to assess performance of fibers dedicated to high-speed networks operating at 10 Gbit/s and beyond and using VCSEL sources. Because VCSELs excite only a limited number of modes, OFL bandwidth is thus less relevant for such applications.

Examples of DMD measurements at 850 nm are shown in Fig. 2.6 for two different multimode fibers with a core radius of 50 μm . DMDs provide cartographies of modal dispersions across the fiber radius. Indeed, each line of this plot corresponds to the power evolution as a function of time when a short laser pulse (20 ps to 1 ns) is launched – through a single-mode fiber – at one specific position across the multimode fiber radius, called the ‘offset launch’ on the graph. The mode field diameter of the single-mode fiber is of the order of several μm – below the diameter of typical multimode fibers – so that it can only excite a sub-set of modes. A centered launch (offset launch equal to 0 μm) excites mainly the lowest order modes, while large-offset launches excite the highest order modes. Here, the fiber is scanned from its center to the edge of its core with 1 μm steps. The DMD plot depends on several settings such as the spot size used at the launching stage, the pulse duration, the fiber length and so on. In order to ensure consistent measurements, DMD measurements have been standardized in 2003 [15] for 50 μm -core multimode fibers.

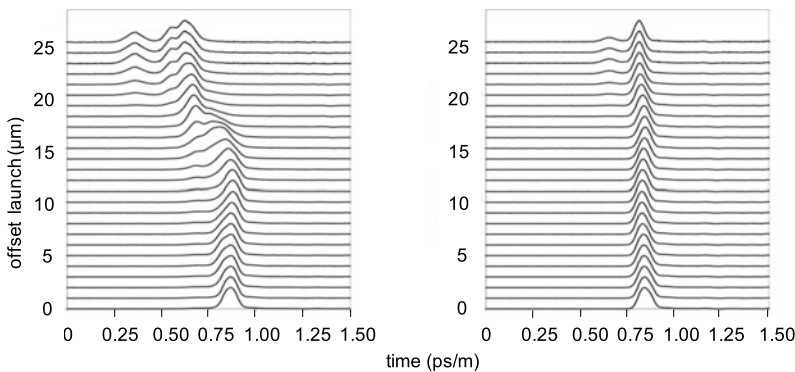


Fig. 2.6 Measured DMD plots of two different multimode fibers

The DMD plot on the left of Fig. 2.6 reveals that the highest order modes, those excited by the largest offset launches, travel faster than the lower order modes, excited by the lowest offset launches. This fiber thus exhibits a large modal dispersion, especially when compared to the fiber whose plot is on the right of Fig. 2.6. For this last fiber, group delays are well equalized.

In addition, the standards provide a set of tools dedicated to the analysis of the DMD plot: the DMD values, expressed in ps/m [15]. They roughly correspond to the delay between the fastest and the slowest pulses within a given sub-group of offset launches, also called templates. The standards define three DMD values with their respective templates and named inner, outer and an unofficially called sliding. For instance, the inner DMD value corresponds to offset launches between 5 μm and 18 μm only. The fibers of Fig. 2.6 have an inner DMD value of 0.141 ps/m (left) and 0.025 ps/m (right). As further developed in Sect. 2.3.3 (Standardization), specifications have been defined for those DMD values, to allow for a minimum EMB value.

The same standards also propose an alternative to the DMD values: the EMBc (Effective Modal Bandwidth, where “c” stands for computed), which has been defined to evaluate the worst effective modal bandwidth the fiber may exhibit when coupled to VCSELs [15]. Indeed, DMD plots also allow to simulate fiber response – that is the output pulse shape – from a linear combination of each individual trace. Standards define ten different sets of weights to compute this linear combination and to render the variety of VCSEL launches. EMB can then be computed from those 10 output pulses and the worst value is called EMBc. The fibers of Fig. 2.6 have EMBc values of 4,140 MHz km (left) and greater than 15,000 MHz km (right) with respective OFL modal bandwidth of 3,300 MHz km and greater than 14,000 MHz km.

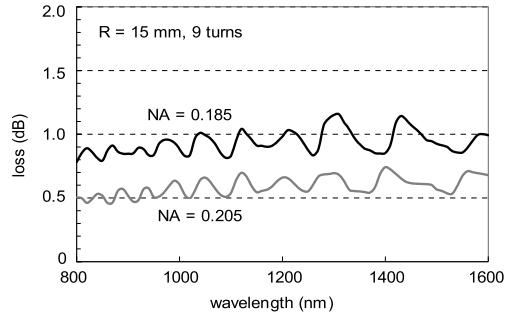
2.3.1.3 Loss

Loss in a multimode fiber may be more complex than in a single-mode fiber because each mode may experience different attenuation levels. This effect is called DMA (Differential Mode Attenuation). In practice, DMA is negligible in modern silica multimode fibers, and loss does not depend on the launching condition and linearly increases with fiber length. As for single-mode fibers, it is expressed in dB/km. Typical loss values of a 50 μm multimode fiber are about 2.2 dB/km at 850 nm and 0.5 dB/km at 1300 nm.

2.3.1.4 Bend Loss

Multimode fibers generally do not behave like single-mode fibers under bending. Each mode exhibits significantly different bend sensitivities: the highest order modes are weakly guided compared to the lowest order modes and thus far more sensitive to bending than the lowest order ones. As a consequence bend-loss level strongly depends on launching conditions: a launching condition that mainly excites

Fig. 2.7 Bend loss as a function of wavelength for two 50 μm -core multimode fibers with respective NA of 0.205 and 0.185 after 9 turns around a 15 mm radius mandrel



the highest order modes yields higher bend loss whereas injection that confines the light in the lowest order mode may exhibit a very good bend resistance. Another consequence is that bend loss of multimode fibers cannot be expressed in dB/turn or dB/m as for single-mode fibers. It is recommended to express them in dB for a given number of turns and a given launching condition [16].

Another very different feature of bend loss of multimode fibers compared to single-mode fibers is their spectral dependence. Indeed, bend loss does not exponentially increase with wavelength as it is the case with single-mode fibers, but, under the OFL condition, it oscillates around a fairly constant value over the whole spectrum, as shown in Fig. 2.7. The oscillations come from the cutoff of the highest order modes [17].

2.3.2 Different Types of Multimode Fibers

2.3.2.1 Silica Step-Index Multimode Fiber

Step-index multimode fibers were the first ones to be developed in the early days of optical communication. As briefly explained in Sect. 2.2.5, the difference of arrival times between the slowest mode and the fastest one can be written as:

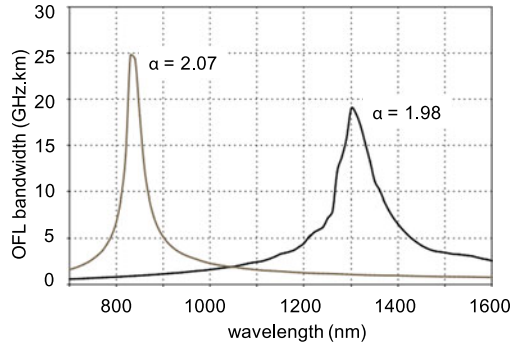
$$\Delta t = \frac{L \cdot NA^2}{2cn_{cl}} \quad (2.16)$$

where n_{cl} is the refractive index of the cladding, NA is the numerical aperture, L the fiber length and c the speed of light. Modal dispersion in such fibers depends on the square of the numerical aperture. OFL bandwidth of step-index multimode fibers usually does not exceed a few tens of MHz km, making these fibers definitively not suited for high-speed transmissions.

2.3.2.2 Silica Graded-Index Multimode Fiber

Graded-index multimode fibers were soon introduced to improve and reduce modal dispersion of step-index fibers [18]. The idea consists of equalizing the various op-

Fig. 2.8 Computed OFL modal bandwidth vs. wavelength for $\alpha = 2.07$ and $\alpha = 1.98$ for a 50 μm -core multimode fiber



tical paths followed by all rays of light by lowering the refractive index experienced by the longest paths. The core profile follows a power law parameterized by the α parameter:

$$n(r) = \begin{cases} n_{co} \cdot \sqrt{1 - 2\Delta \left(\frac{r}{a}\right)^\alpha} & r \leq a \\ n_{cl} & r \geq a \end{cases} \quad (2.17)$$

where n_{co} is the core maximum refractive index, n_{cl} is the cladding index, and a is the core radius and Δ is defined in (2.18).

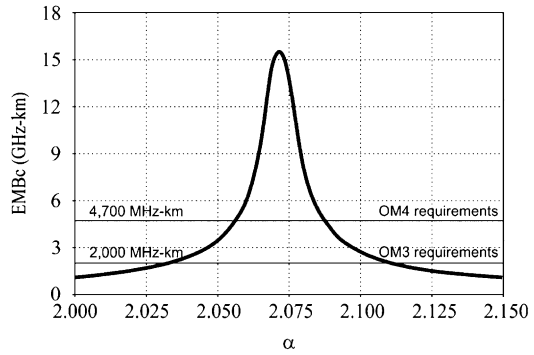
$$\Delta = \frac{n_{co}^2 - n_{cl}^2}{2n_{co}^2} \quad (2.18)$$

With such an α -parameterized profile and by a proper choice of the α parameter it is possible to maximize the OFL bandwidth at a given wavelength [19, 20]. Indeed, multimode fibers can be used either around 850 nm (LEDs or VCSELs) or around 1300 nm (LEDs). The α values typically used for maximizing the OFL bandwidth at wavelengths of 850 and 1300 nm are ~ 2.07 and ~ 1.98 , respectively, as shown in Fig. 2.8.

One can see from Fig. 2.8 that it is not easy to achieve very high bandwidths in a reproducible way because bandwidth strongly depends on the α value: a slight variation of less than 0.01 shifts the optimal wavelength by tens of nanometers. Also, any index profile deviation reduces the bandwidth. This indicates that the achievement of very high bandwidths requires an extremely accurate process control because a slight error on the refractive index profile leads to a dramatic decrease of fiber performance.

Nowadays, two classes of graded-index multimode fibers dominate: the 50 μm and the 62.5 μm multimode fibers that have 50 μm and $62.5 \pm 2.5 \mu\text{m}$ core diameters and numerical apertures of 0.200 and 0.275 ± 0.015 , respectively. The 50 μm multimode fiber is historically the first fiber that has been developed, followed very rapidly by the 62.5 μm type that is still the most widely installed multimode fiber in the world. This trend is about to reverse due to the advent of the VCSEL sources at the end of the 1990's, which are able to sustain the high modulation speeds required for multi-Gbit/s transmission. This breakthrough pushed the fiber manufac-

Fig. 2.9 Computed EMBc vs. α at 0.85 μm for a 50 μm core multimode fiber



turers to improve their process control in order to allow today’s mass production of the new class of 50 μm multimode (also known as OM3 and OM4 fibers and further explained in Sect. 2.3.3), that exhibits the high bandwidths required for 10 Gbit/s transmission. Their effective modal bandwidths at 850 nm are typically greater than 2,000 MHz km for OM3 and 4,700 MHz km for OM4, and their OFL modal bandwidth at 850 nm is typically greater than 1,500 MHz km and 3,500 MHz km, respectively, at this wavelength. As illustrated by Fig. 2.9, α tolerances of OM4 fibers are more than twice tighter than those of OM3 fibers.

Another aspect, that has recently been the center of attention, is the bending sensitivity of multimode fibers. The important rise of traffic in data centers, subject to harsh environments (massive cabling, plurality of connectors, reduced footprint), has spurred the development of a new type of multimode fibers: bend-resistant OM3 and OM4 fibers. These fibers typically exhibit macro-bending sensitivities that are about 10 times lower than those of legacy OM3 and OM4 fibers, with macro-bend losses below 0.2 dB for 2 turns at 7.5 mm bend radius at 850 nm. They all have a depressed-index area in the cladding, i.e. a trench near the graded-index core (see Fig. 2.10) that allows for better light confinement. These new trench-assisted graded-index multimode fibers are paving the way to more reliable cable managements in data centers, and to innovative and more compact cable designs [21, 22].

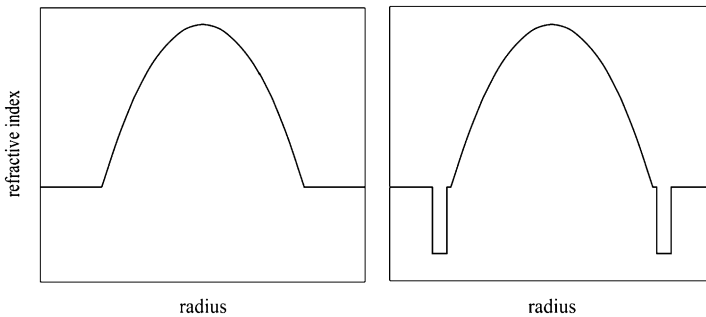


Fig. 2.10 Refractive index profiles of a regular (*left*) and a trench-assisted (*right*) 50 μm -core multimode fiber

Basically, the larger the trench is (in depth and width), the lower the macro-bend losses are. However, a too large trench favors the guidance of leaky modes that might be problematic from characterization, backward compatibility and transmission points of view. The trench design is thus a trade-off between macro-bend-loss improvement and leaky-mode resistance [21, 23]. The introduction of the trench also requires careful engineering to meet the DMD specifications of OM4 fibers because the trench influences the group velocity of the highest-order modes. There are several ways to deal with this issue either by optimizing the trench, the inner cladding between the core and the trench or the core-inner cladding interface. In the end, trench-assisted multimode fibers offer similar bandwidths to those of regular multimode fibers with a 10-fold macro-bend-loss improvement while maintaining backward compatibility [24, 25].

In order to meet the future increase of demand, the multimode fiber capacity will ultimately have to be increased [26]. The combination of wide-band multimode fibers [27, 28] and longer-wavelength VCSELs for multiple-wavelength operation appears today as the most promising option. In this context, the feasibility of wide-band multimode fibers with high bandwidths over a broad wavelength range is the most challenging issue (see Fig. 2.8). Recently, however, a trench-assisted wide-band multimode fiber with OM4 bandwidths over the 850 to 950 nm window has been demonstrated [29].

2.3.2.3 Plastic Optical Fibers

Plastic Optical Fibers (POF) are multimode fibers whose core and cladding are made out of plastic material. They usually have a larger core than silica fibers, up to the millimeter range, and can be operated down to the visible. POFs are easy to connect and easy to bend. They offer a cheap alternative to silica multimode fibers, but are limited to very short distances due to their inherent higher loss and lower bandwidth. POFs were first used in automation, mainly in the visible, but the past few years have witnessed a shift to the Ethernet world with operating wavelength of 850 and 1300 nm.

The original POF design consists of a step-index profile, also known as the standard POF, with a large core of 980 μm made of poly-methylmetacrylate surrounded by a thin 10 μm cladding of fluorinated polymer. The typical numerical aperture is about 0.5. This material exhibits high absorption of about 100 dB/km at 520 nm, 560 nm and 650 nm.

A graded-index profile is mandatory for higher transmission speed and/or distance. The early trials did not yield satisfactory loss results, but in the early 90's, thanks to the use of perfluorinated polymer, feasibility of low-loss graded-index plastic optical fibers (GI-POF) was demonstrated [30] and first fibers were commercialized in 2000. Nowadays, losses of GI-POF are kept below 20 dB/km over the 800–1300 nm range [31], and fibers with core sizes as small as 50 μm are available. They show good transmission capabilities and can provide OFL-bandwidths larger than 400 MHz km [32, 33].

2.3.3 Standardization

The concern for standardization has started at the early stage of fiber development. Several bodies are active: the Telecommunication Standardization Sector of the International Telecommunication Union (ITU-T), the International Electrotechnical Commission (IEC), the ISO/IEC jointly operated by the International Organization for Standardization and the IEC, and the Telecommunications Industry Association (TIA). The first ITU-T recommendation on multimode fibers has been published in 1984 (G.651).

One of the most common classifications is that of ISO/IEC, which defines four main multimode fiber classes known as OM1, OM2, OM3 and OM4 [34]. OM1 and OM2 define specifications for both 50 μm and 62.5 μm multimode fibers and known as A1a.1 for 50 μm and A1b for 62.5 μm in IEC [35], while OM3 and OM4 deals with 50 μm multimode fibers only and known as A1a.2 and A1a.3 in IEC, as shown in Table 2.1 published in 2002 and closely linked to the IEEE 802.3 10GbE Ethernet Standard released the same year. An OM4 fiber, when operated at 850 nm in combination with VCSEL sources, allows to bridge 400 m at 10 Gbit/s (10GbE links) and up to 100 m at 40/100 Gbit/s ((40/100)GbE links) in parallel solutions.

In the early 2000's, in the framework of the IEEE 802.3 standards, it was shown through extensive modeling that an error-free 10 Gbit/s transmission over 300 m requires an EMB larger than 2,000 MHz km. The OM3 standard translates this system requirement into specifications on the DMD values computed from the DMD plots, the definition of which has been given in Sect. 2.3.1.2 [36]. These specifications are summarized in Table 2.2. They include six different sets of DMD values. To be compliant, fibers need to fulfill one of the six sets only.

Since the introduction of the OM3 fiber, fiber manufacturers have developed a higher grade of laser optimized multimode fibers, with tighter DMD specifications intended to ensure EMB greater than 4,700 MHz km. Such a fiber could offer longer distances for the 10GbE, e.g. up to 550 m, or additional margins for Data Centers where more connectors are used. In November 2009, such fibers, labeled OM4, were added to the TIA 492AAAD. They provide point-to-point 40 and 100GbE links over 4 or 10 pairs of fibers up to 150 m (cf. IEEE 802.3ba-2010 standard) and 10GbE up to 400 m, extending the 300 m reach of OM3 fibers. These specifications are summarized in Table 2.3, which includes three different sets of DMD values. To be compliant, fibers need to fulfill one of the three sets only.

Table 2.1 OFL bandwidth specifications for OM1, OM2, OM3 and OM4 fibers

Fiber class ISO/IEC	Fiber type IEC	Core diameter (μm)	OFL-BW at 850 nm (MHz km)	EMB at 850 nm (MHz km)	OFL-BW at 1300 nm (MHz km)
OM1	A1b	62.5	>200	–	>500
OM2	A1a.1a & A1a.1b	50	>500	–	>500
OM3	A1a.2a & A1a.2b	50	>1,500	>2,000	>500
OM4	A1a.3a & A1a.3b	50	>3,500	>4,700	>500

Table 2.2 DMD specifications ensuring EMB higher than 2,000 MHz km

Specifications	Outer DMD (ps/m)	Inner DMD (ps/m)	Sliding DMD (ps/m)
1	≤ 0.33	≤ 0.33	≤ 0.25
2	≤ 0.27	≤ 0.35	≤ 0.25
3	≤ 0.26	≤ 0.40	≤ 0.25
4	≤ 0.25	≤ 0.50	≤ 0.25
5	≤ 0.24	≤ 0.60	≤ 0.25
6	≤ 0.23	≤ 0.70	≤ 0.25

Table 2.3 DMD specifications ensuring an EMB greater than 4,700 MHz km

Specifications	Outer DMD (ps/m)	Inner DMD (ps/m)	Sliding DMD (ps/m)
1	≤ 0.10	≤ 0.30	≤ 0.11
2	≤ 0.11	≤ 0.17	≤ 0.11
3	≤ 0.14	≤ 0.14	≤ 0.11

Finally, bend-resistant 50 μm -core multimode fibers have been standardized as A1a.1b for bend-resistant OM2, A1a.2b for bend-resistant OM3 and A1a.3b for bend-resistant OM4. The “b” suffix has been added to the former fiber type in IEC for the bend-resistance feature. The maximum macro-bend loss of these different fiber types are summarized in Table 2.4. Since macro-bend losses do not vary linearly with the number of turns, the macro-bend losses are expressed in dB per number of turns. The launch condition for the macro-bend-loss measurement shall fulfill that described in IEC 61280-4-1.

2.4 Single-Mode Fibers

Single-Mode Fibers (SMF) have replaced multimode fibers for long-distance transmissions in the early 1980’s, when semiconductor laser sources became available. Since then steady progress in transmission capacity has been made, with bit rates as high as several Tbit/s being now transmitted over several thousands of kilometers [37]. SMFs have kept evolving all along to fit the always more demanding system and capacity requirements, yielding several fiber types as we will see in this section.

2.4.1 Key Characteristics

We discuss here the main characteristics of single-mode fibers that are of importance to assess fiber performance with respect to given applications, that are loss,

Table 2.4 Maximum macro-bend loss of standardized 50 μm -core multimode fibers

Fiber type IEC	A1a.1a A1a.2a A1a.3a	A1a.1b A1a.2b A1a.3b
0.85 μm 37.5 mm bend radius 100 turns	0.5 dB	0.5 dB
0.85 μm 15 mm bend radius 2 turns	1.0 dB	0.1 dB
0.85 μm 7.5 mm bend radius 2 turns	–	0.2 dB
1.3 μm 37.5 mm bend radius 100 turns	0.5 dB	0.5 dB
1.3 μm 15 mm bend radius 2 turns	1.0 dB	0.3 dB
1.3 μm 7.5 mm bend radius 2 turns	–	0.5 dB

dispersion, cutoff wavelength, mode field diameter and effective area. Loss and dispersion have been described earlier in the fiber basics Sects. 2.2.4 and 2.2.5. Recall that loss is in the range of 0.20 dB/km at 1.55 μm for straight fibers. When a fiber is bent on a macro-scale or subject to micro-deformations causing micro-bends, light scatters away and loss occurs. Macro-bend loss mainly depends on the optical properties of the fiber, and proper profile design allows to make it negligible for bend radii around 15 mm or down to 5 mm for some applications (see sections below). Micro-bend loss depends on both optical and material properties of the fiber, and careful choice of both profile and coating renders it negligible when fiber is put into a cable or under compression or lateral stress. Extensive literature exists on both topics, starting from the early days of fiber optics history. The reader is referred to [2, 3] for a theoretical treatment.

Chromatic dispersion is especially important in single-mode fibers, because of its double impact on light pulse broadening and pulse distortions due to nonlinear effects. We have seen in Sect. 2.2.5, that chromatic dispersion can be made very different from that of silica, thanks to profile design. Indeed, all along fiber history, much research work has been done to tailor chromatic dispersion through proper design to best fit telecommunication systems requirements. Usually, dispersion characteristics are given in terms of zero-chromatic dispersion wavelength λ_0 , chromatic dispersion and dispersion slope (first derivative of chromatic dispersion with respect to wavelength) at the operating wavelength. Fibers with dispersion values ranging from 17 ps/(nm km) to well below -100 ps/(nm km) at 1.55 μm are now commercially available.

Another source of dispersion arises in single-mode fiber when circular symmetry is broken, yielding a slight birefringence and different group velocity for orthogonal modes of polarization. It is referred to as Polarization-Mode Dispersion (PMD) [38]. Because fiber birefringence is small and varies in a random fashion along the fiber, PMD is not linear with length, but is given in ps/ $\sqrt{\text{km}}$. PMD of recent single-mode fibers is well mastered and below 0.10 ps/ $\sqrt{\text{km}}$.

The cutoff wavelength characterizes the wavelength range above which a fiber is single-moded and carries only the fundamental LP₀₁ mode as seen in Sect. 2.2.2. In theory, each higher-order mode is allowed to propagate for wavelengths below its cutoff wavelength, so that the term ‘‘cutoff wavelength’’ refers to the longest cutoff wavelength of all higher-order modes, being in most cases that of the LP₁₁ mode. In practice, one speaks of fiber and cable cutoff wavelengths (μ_{cf} and λ_{cc} , respectively), which are measured by standardized methods (FOTP-80 EIA-TIA-455-80) and correspond to the wavelength above which higher-order modes can be neglected due to their high losses. Transmission fibers are specified with $\lambda_{cc} < 1.26 \mu\text{m}$ or $< 1.45 \mu\text{m}$, or even $< 1.53 \mu\text{m}$.

Two quantities are used to characterize the mode spatial extension: the Mode Field Diameter (MFD) in units of μm and the effective area A_{eff} in μm^2 :

$$MFD = 2 \sqrt{\frac{\int_0^\infty F(r)^2 r dr}{\int_0^\infty \frac{dF(r)^2}{dr} r dr}} \quad (2.19)$$

$$A_{eff} = 2\pi \cdot \frac{(\int_0^\infty |F(r)|^2 r dr)^2}{\int_0^\infty |F(r)|^4 r dr} \quad (2.20)$$

where F is the electric field as defined in Sect. 2.2.2.

The MFD definition was first proposed in 1983 [39] and is related to the r.m.s. width of the far-field intensity. It is commonly used to evaluate splice losses. On the other hand, the effective area is used as a measure of non-linear effects that might occur in fibers. The larger the effective area, the more effectively can non-linear effects be avoided since they are proportional to the signal intensity through the non-linear index n_2 [40, 41]. Transmission fibers have A_{eff} ranging from ~ 50 to $\sim 150 \mu\text{m}^2$ and n_2 ranging from 2.5 to $2.7 \times 10^{-20} \text{ m}^2/\text{W}$.

2.4.2 Standardization

As it is the case with multimode fibers, standardization bodies have always been very active in following closely or even anticipating fiber developments. The most common classification is that of the Telecommunication Standardization Sector of the International Telecommunication Union (ITU-T) defining a range of fiber values for each recommendation or fiber type. They are named G.652, G.653 and so on.

2.4.2.1 ITU-T Recommendation for Standard Single-Mode Fibers (G.652)

This recommendation describes what is also called the “Standard” Single-Mode Fiber (SSMF), whose main feature is a zero chromatic dispersion wavelength around 1.31 μm . This recommendation was released in 1984, and at that time fiber was optimized for 1.31 μm operation. The recommendation has been updated several times, again to follow the latest advances in fiber development, essentially regarding loss and PMD. Concerning this latter parameter, the manufacturer shall supply a PMD link design value, PMDQ, that serves as a statistical upper bound for the PMD coefficient of the concatenated optical fiber cables within a defined possible link of M cable sections. The upper bound is defined in terms of a small probability level, Q, which is the probability that a concatenated PMD coefficient value exceeds PMDQ (see Table 2.5).

By now, this fiber is mostly operated at 1.55 μm and it is the most widely installed fiber in the world. Overall, these fibers have chromatic dispersion curves very close to that of silica with values around 17 ps/(nm km) at 1.55 μm . There is no need for complicated fiber design in that case, and a simple step-index profile is used, with typical core-cladding index difference of $\sim 5 \times 10^{-3}$ and core diameter of $\sim 9 \mu\text{m}$.

2.4.2.2 ITU-T Recommendations for Dispersion-Tailored Fibers (G.653, G.655 and G.656)

Recommendation G.652 was soon followed by G.653 in 1988, describing Dispersion-Shifted Fibers (DSFs) with the zero-dispersion wavelength λ_0 shifted to 1.55 μm instead of previous 1.31 μm , intended to be used for single-channel operation at 1.55 μm and thus to benefit of the lowest-loss window of silica fibers.

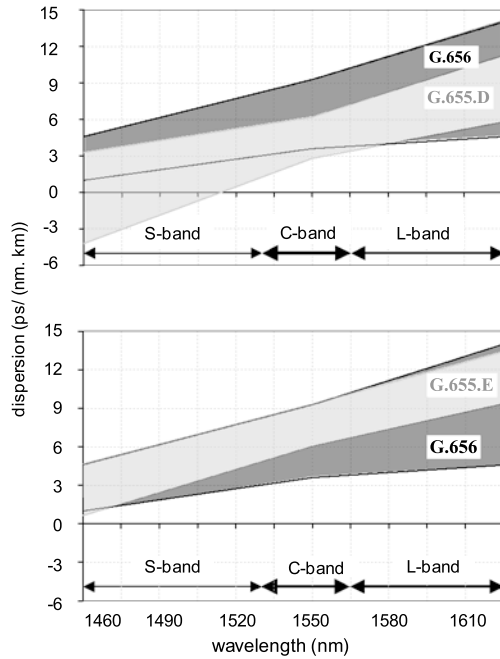
At the same time, however, the discovery of Erbium Doped Fiber Amplifiers (EDFAs) made possible the amplification of signals within a whole band around 1.55 μm (the C-band from 1.53 to 1.565 μm) and paved the way for multiple wavelength channel transmission, well known as Wavelength-Division Multiplexing (WDM) systems. It was soon recognized that DSFs favored deleterious inter-channel non-linear effects and were thus not suited for WDM transmission. As a consequence Non-Zero Dispersion-Shifted Fibers (NZDSFs) have been developed featuring a zero-dispersion wavelength (λ_0) between ~ 1.4 and $\sim 1.6 \mu\text{m}$ and a small but non-zero chromatic dispersion value at 1.55 μm .

The ITU-T recommendation G.655 was first released in 1996 to cover NZDSFs. G.655 fibers have an absolute value of chromatic dispersion between 0.1 and 6 ps/(nm km) over the C-band. Over the past few years it was amended twice, and now includes five different sub-types: G.655.A (the original description); G.655.B and G.655.C to allow the maximum absolute value of dispersion to reach 10 ps/(nm km) over the C-band, further handling parasitic inter-channel nonlinear effects for Dense WDM (DWDM); G.655.D and G.655.E to better account for the wavelength dependence of dispersion over the S-, C- and L-bands, ranging from 1.46 to 1.625 μm , as depicted in Fig. 2.11.

Table 2.5 G.652, G.G57.A and G.657.B attributes

		G.652		G.657		G.657.B3		
		G.652.B	G.652.D	G.657.A1	G.657.A2	G.657.B2		
Cable cutoff wavelength		<1260 nm						
MFD	Nominal value at 1310 nm	8.6–9.5 μm						
	Tolerance	± 0.4 μm						
Macrobend loss	Radius (mm)	30	15	10	7.5	15	10 7.5	
	Number of turns	100	10	1	1	10	1 1	
	Max. at 1550 nm (dB)		0.25	0.75	0.03	0.1	0.5	0.03
	Max. at 1625 nm (dB)	0.1	1	1.5	0.1	0.2	1	0.1
Dispersion	λ_0	1300–1324 nm						
	Slope	<0.092 ps/nm ² km at λ_0						
Proof test	Minimum	0.69 GPa						
Cladding diameter	Nominal	125						
	Tolerance	± 0.7 μm						
Core concentricity error	Maximum	0.6 μm						
	Minimum	0.5 μm						
Cladding non-circularity	Maximum	1%						
	Minimum	0.4 dB/km						
Attenuation (cable)	Max. at 1310 nm	0.4 dB/km						
	Max. at 1550 nm	0.35 dB/km						
	Max. at 1625 nm	0.4 dB/km						
	Max. 1310–1625 nm	0.4 dB/km						
PMD (cable)	Max. at 1383 nm	<0.092 ps/nm ² km at λ_0						
	M	20 cables						
	Q	0.01%						
	Max. PMD _Q	0.2 ps/km ^{0.5}						
Dispersion	Minimum	0.69 GPa						
	Nominal	125						
	Tolerance	± 0.7 μm						
	Maximum	0.5 μm						
Cladding non-circularity	Maximum	1%						
	Minimum	0.4 dB/km						
Attenuation (cable)	Max. at 1310 nm	0.4 dB/km						
	Max. at 1550 nm	0.35 dB/km						
	Max. at 1625 nm	0.4 dB/km						
	Max. 1310–1625 nm	0.4 dB/km						
PMD (cable)	Max. at 1383 nm	<0.092 ps/nm ² km at λ_0						
	M	20 cables						
	Q	0.01%						
	Max. PMD _Q	0.2 ps/km ^{0.5}						
Dispersion	Minimum	0.69 GPa						
	Nominal	125						
	Tolerance	± 0.7 μm						
	Maximum	0.5 μm						
Cladding non-circularity	Maximum	1%						
	Minimum	0.4 dB/km						
Attenuation (cable)	Max. at 1310 nm	0.4 dB/km						
	Max. at 1550 nm	0.35 dB/km						
	Max. at 1625 nm	0.4 dB/km						
	Max. 1310–1625 nm	0.4 dB/km						
PMD (cable)	Max. at 1383 nm	<0.092 ps/nm ² km at λ_0						
	M	20 cables						
	Q	0.01%						
	Max. PMD _Q	0.2 ps/km ^{0.5}						
Dispersion	Minimum	0.69 GPa						
	Nominal	125						
	Tolerance	± 0.7 μm						
	Maximum	0.5 μm						
Cladding non-circularity	Maximum	1%						
	Minimum	0.4 dB/km						
Attenuation (cable)	Max. at 1310 nm	0.4 dB/km						
	Max. at 1550 nm	0.35 dB/km						
	Max. at 1625 nm	0.4 dB/km						
	Max. 1310–1625 nm	0.4 dB/km						
PMD (cable)	Max. at 1383 nm	<0.092 ps/nm ² km at λ_0						
	M	20 cables						
	Q	0.01%						
	Max. PMD _Q	0.2 ps/km ^{0.5}						
Dispersion	Minimum	0.69 GPa						
	Nominal	125						
	Tolerance	± 0.7 μm						
	Maximum	0.5 μm						
Cladding non-circularity	Maximum	1%						
	Minimum	0.4 dB/km						
Attenuation (cable)	Max. at 1310 nm	0.4 dB/km						
	Max. at 1550 nm	0.35 dB/km						
	Max. at 1625 nm	0.4 dB/km						
	Max. 1310–1625 nm	0.4 dB/km						
PMD (cable)	Max. at 1383 nm	<0.092 ps/nm ² km at λ_0						
	M	20 cables						
	Q	0.01%						
	Max. PMD _Q	0.2 ps/km ^{0.5}						

Fig. 2.11 Ranges of dispersion values allowed across the S-, C- and L-bands for: (top) G.656 dark-grey shaded area and G.655.D, light-grey shaded area; (bottom): G.656 dark-grey shaded area and G.655.E, light-grey shaded area



The last recommendation, G.656, was introduced in 2004 and covers NZDSFs optimized for wideband operation in the S-, C- and L-band. The zero-chromatic dispersion wavelength λ_0 is below 1.46 μm , thus reducing inter-channel nonlinear effects compared to G.655-only compliant NZDSFs and allowing for efficient multiple-wavelengths Raman pumping. This recommendation was also updated in 2006 by expressing the chromatic dispersion requirements as a pair of bounding curves versus wavelength from 1.46 to 1.625 μm . Note that G.655.E fibers are also G.656 compliant, which is not the case for G.655.D fibers (see Fig. 2.11).

All these categories allow for longer λ_{cc} (up to 1.45 μm) than those specified in G.652. This can offer higher margins in profile designs (see Sect. 2.4.3) but at the expense of losing 1.31 μm applicability.

2.4.2.3 ITU-T Recommendation for Bend-Optimized Fibers (G.657)

Over the past few years, fiber penetration deeper into the network – that is for Fiber-to-the-X (FtX, X = curb, building, home, ...) applications – has spurred the development of fibers with reduced bending sensitivity compared to that of G.652 fibers. Increased resistance against bending is needed for such applications because of a greater risk of encountering incidental bends, sharp bends when installed in corners or when stapling the cable along a wall.

These bend-insensitive fibers are described in recommendation G.657, released in 2006. The first version included two classes: G.657.A is G.652 compliant and

exhibits a reduced bending sensitivity; G.657.B shows further reduced bending sensitivity, but it is not G.652 compliant because it contains a wider range of characteristics, especially concerning chromatic dispersion parameters (see Table 2.5). For both categories, the cable cutoff wavelength is specified to be below 1.26 μm to ensure single mode operation in the O-band, ranging from 1.26 to 1.36 μm . In 2009, this recommendation was updated to include 2 new subclasses G.657.A1 (former G.657.A) & G.657.A2, and G.657.B2 (former G.657.B) & G.657.B3 with bend-loss specifications at bend radii down to 5 mm. And in 2012, the MFD, chromatic dispersion and attenuation parameters were also revised, resulting in specifications closer to those of G.652 (see Table 2.5).

2.4.3 Fiber Types

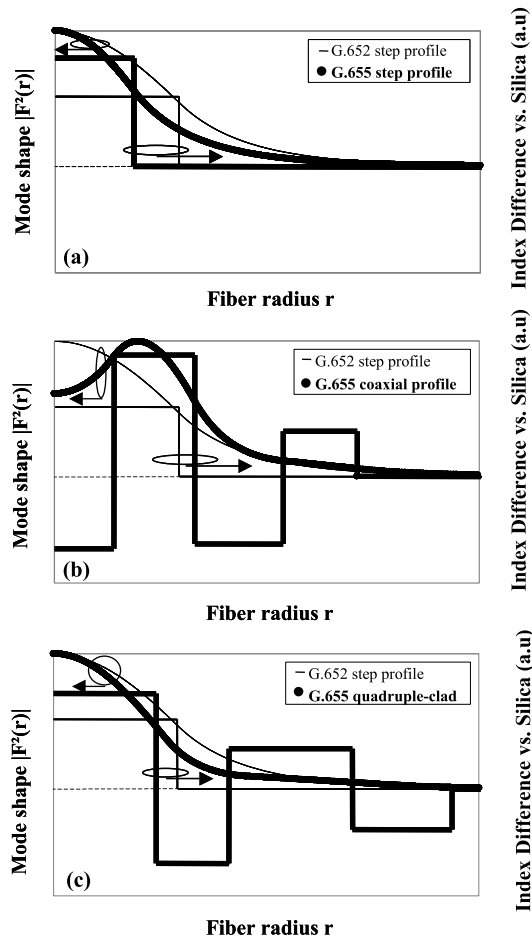
2.4.3.1 Dispersion-Tailored Transmission Fibers

As outlined earlier, the shift to the 1.55 μm transmission wavelength region in order to benefit from the lowest-loss window of silica fibers and the subsequent advent of WDM systems have both triggered much research to design dispersion-optimized fibers. However, other parameters such as the MFD or effective area (the larger the better) and the dispersion slope (the smaller the better) are also important, and depending on system constraints an optimum compromise has to be found.

For those fiber types, step-index profiles offer limited possibilities only: a higher index difference (from ~ 6 to $\sim 10 \times 10^{-3}$) and a smaller diameter (from ~ 8 to $\sim 5 \mu\text{m}$) are required to lower chromatic dispersion, yielding small A_{eff} ($\leq 50 \mu\text{m}^2$ at 1.55 μm) for standard dispersion slopes ($\sim 0.055 \text{ ps}/(\text{nm}^2 \text{ km})$ at 1.55 μm), as illustrated in Fig. 2.12(a).

To overcome such a problem multi-layered core index structures have been proposed quite early in the history of optical fibers [42]. Larger A_{eff} are then obtained at the expense of more complicated profile structures and, sometimes, longer λ_{cc} . For a given profile family, A_{eff} is unfortunately proportional to the dispersion slope thus leading to trade-offs: a large A_{eff} with a relatively high dispersion slope or a small dispersion slope with a small A_{eff} [43, 44]. Two profile families are of particular interest: the coaxial family, which includes a depressed center (negative index difference with respect to cladding) surrounded by one or several rings; and the multiple-clad family, which includes a central step surrounded by rings with alternate negative and positive index differences, as illustrated in Figs. 2.12(b) and 2.12(c), respectively. Figure 2.12(c) shows a quadruple-clad design. Coaxial profiles offer very large A_{eff} for acceptable dispersion slopes ($> 95 \mu\text{m}^2$ for ~ 0.060 to $0.070 \text{ ps}/(\text{nm}^2 \text{ km})$ at 1.55 μm [45, 46]) but exhibit relatively large loss ($> 0.21 \text{ dB km}$) because of their unusual shape. Multiple-clad profiles offer low dispersion slopes for acceptable A_{eff} ($< 0.030 \text{ ps}/(\text{nm}^2 \text{ km})$ for ~ 45 to $55 \mu\text{m}^2$ at 1.55 μm [47–49]) and loss around 0.20 dB/km .

Fig. 2.12 G.655 fibers, index profiles and mode shapes at 1.55 μm . **(a)** Step profile with $A_{\text{eff}} \sim 45 \mu\text{m}^2$ and slope $\sim 0.050 \text{ ps}/(\text{nm}^2 \text{ km})$ and $\lambda_{\text{cc}} < 1.1 \mu\text{m}$; **(b)** coaxial profile with $A_{\text{eff}} \sim 105 \mu\text{m}^2$ and slope $\sim 0.060 \text{ ps}/(\text{nm}^2 \text{ km})$ and $\lambda_{\text{cc}} \sim 1.375 \mu\text{m}$ [46]; **(c)** quadruple-clad profile $A_{\text{eff}} \sim 50 \mu\text{m}^2$ and slope $\sim 0.010 \text{ ps}/(\text{nm}^2 \text{ km})$ and $\lambda_{\text{cc}} \sim 1.395 \mu\text{m}$ [48], all compared to G.652 step profile with $A_{\text{eff}} \sim 80 \mu\text{m}^2$ and slope $\sim 0.058 \text{ ps}/(\text{nm}^2 \text{ km})$ and $\lambda_{\text{cc}} \sim 1.18 \mu\text{m}$



2.4.3.2 Ultra-Long Haul Transmission Fibers

For ultra-long-haul WDM terrestrial or submarine networks the picture is somewhat different. Research has focused on the two factors that directly limit optical transmission: loss with the early demonstration of record loss values [50], and, more recently in the early 2000's, non-linear effects. In this context, fibers with low loss (from 0.17 to 0.18 dB/km at 1.55 μm) and large A_{eff} ($> 100 \mu\text{m}^2$ at 1.55 μm) have been developed [51–58] and dispersion is dealt with using newly developed and high-performance DCFs, either in modules or in cables (see Sect. 2.4.3.4), or using advanced coherent detection and digital signal processing techniques.

Complicated index profiles are not needed and simple step-index profiles with small index difference (around 4×10^{-3}) and a large diameter (around 12 μm) can be used, contrary to NZDSFs. The drawback of this option, however, is that smaller fractions of the modes propagate in the cladding, yielding larger chromatic dispersion ($\sim 20 \text{ ps}/(\text{nm km})$ at 1.55 μm) and longer λ_{cc} compared to those of standard

G.652 step-index fibers. These fibers are called cutoff-shifted and are described in the ITU-T recommendation G.654 that specifies $\lambda_{cc} < 1.53 \mu\text{m}$.

To limit this λ_{cc} increase without jeopardizing the macro- and micro-bending performances, a slightly depressed cladding can be added next to the step core. In this way, A_{eff} around $105 \mu\text{m}^2$ at $1.55 \mu\text{m}$ was demonstrated in the beginning of the 2000s [51–53] and more recently A_{eff} of $134 \mu\text{m}^2$ has been demonstrated [56]. An alternative to these depressed-cladding structures has been presented in [54]. It consists in using a trench in the cladding. As will be seen in the next section, the trench can be used to reduce the bending sensitivity of fibers while keeping the same MFD (or A_{eff}) and the same λ_{cc} as those of G.652 step-index fibers. Here, the trench is used to enlarge A_{eff} and to control λ_{cc} while slightly improving macro- and micro-bending performance compared to those of G.652 step-index fibers. With such a profile A_{eff} of around $155 \mu\text{m}^2$ at $1.55 \mu\text{m}$ has recently been demonstrated [58].

2.4.3.3 Bend-Insensitive Fibers

As mentioned in Sect. 2.4.3.2, the reduction of bend losses is mandatory for FttX networks. For a given bend radius, macro-bend losses are proportional to the power fraction of the mode propagating after the radiation caustic. As explained in [59], the radiation caustic is the radius for which the effective index of the mode (see Sect. 2.2.2) intersects the index of the cladding of a tilted index profile representing the bent fiber.

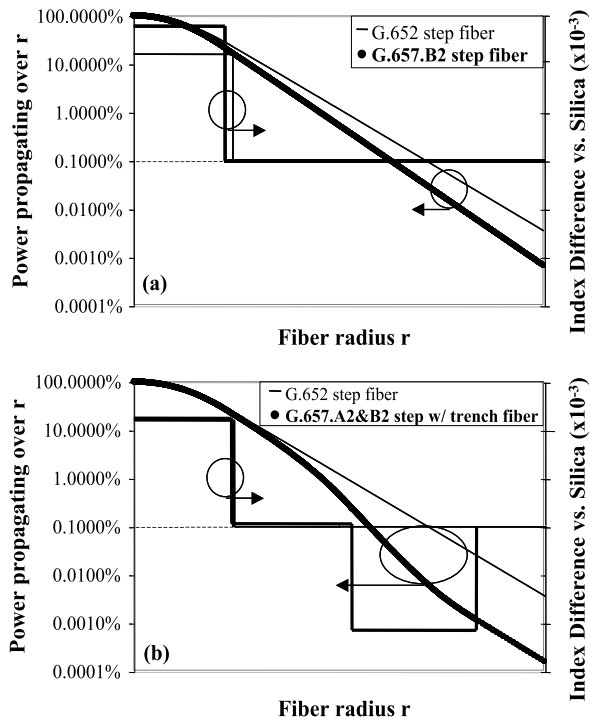
One way to reduce the bending sensitivity is to decrease this power fraction without changing the shape of the power profile. For step-index profiles this means to use a higher index difference and/or a larger diameter than those of G.652 fibers. This results in smaller MFDs and/or larger λ_{cc} , which might be a problem when splicing to G.652 fibers. This is illustrated in Fig. 2.13(a) which shows a step-index fiber that is G.657.B2 compliant except for the MFD that has a small value of $8.0 \mu\text{m}$ at $1.31 \mu\text{m}$. This value is also much smaller than the typical MFD value of $9.1 \mu\text{m}$ for SSMFs. Finally, the bend loss levels remain significantly high when applying incidental kinks with radii in the order of 1 to 10 mm.

The alternative and much more efficient way to reduce the bending sensitivity is to change the shape of the power profile for a given set of MFD and λ_{cc} . For this purpose new index profile types have to be used. The common feature of these profiles is a trench (either made with solid down-doped silica or with random voids or holes) that is added in the cladding close to the core [60–64]. The trench confines the tail of the mode without modifying its intrinsic nature, as illustrated in Fig. 2.13(b). MFD, λ_{cc} and chromatic dispersion characteristics are kept unchanged. As a consequence, bend loss can be significantly reduced by a factor of ~ 100 compared to SSMFs while ensuring full compliance with G.652 attributes.

2.4.3.4 Dispersion-Compensating Fibers

The demonstration that fibers can exhibit very negative dispersion at $1.55 \mu\text{m}$ was soon recognized in the development of optical fibers [65]. Its application to compen-

Fig. 2.13 Power distribution and index profiles of bend-insensitive fibers. (a) G.657.B2-compliant fiber except for the MFD: step profile with MFD $\sim 8.0 \mu\text{m}$ at $1.31 \mu\text{m}$ and $\lambda_{cc} < 1.26 \mu\text{m}$; (b) G.657.A2 and G.657.B2 fiber: step with trench profile with MFD $\sim 8.9 \mu\text{m}$ at $1.31 \mu\text{m}$ and $\lambda_{cc} \sim 1.21 \mu\text{m}$ [9] both compared to G.652 step profile with MFD $\sim 9.0 \mu\text{m}$ at $1.31 \mu\text{m}$ and $\lambda_{cc} \sim 1.18 \mu\text{m}$



sate the dispersion accumulated over already-installed SSMFs started in the early 90’s [66, 67] and allowed upgrades of existing infrastructure to 10 Gbit/s. Currently there are two different kinds of Dispersion Compensating Fibers (DCF), whether the fiber is put inside a module at the amplifier location or into a cable as part of the transmission link. Because of the increase in data rates compensating dispersion for all fiber types (SSMF or NZDSF) has become mandatory.

DCF design is similar to NZDSF design (a triple clad index profile is most commonly used) only more extreme: the fraction of the mode that propagates in the cladding becomes so huge, in order to get very large waveguide dispersion and negative chromatic dispersion, that the mode is only weakly guided. This is achieved with cores with very high index differences ($>15 \times 10^{-3}$) and small diameters ($<5 \mu\text{m}$). As a result, DCFs suffer from small A_{eff} ($<30 \mu\text{m}^2$ at $1.55 \mu\text{m}$), high loss ($>0.25 \text{ dB/km}$ at $1.55 \mu\text{m}$) and high bending sensitivities. DCFs characteristics are also more sensitive to small core index variations and to core ovalities than SSMFs or NZDSFs. Fiber manufacturing has to be done extremely carefully to tightly control longitudinal and radial core homogeneities and thus chromatic dispersion and PMD of the DCF [68].

When used in modules that are not part of the transmission distance, the extra loss introduced by DCFs depends on fiber loss but also on length. A commonly used Figure Of Merit (FOM) for such DCFs is the ratio of the absolute value of chromatic dispersion to fiber loss, measured in $\text{ps}/(\text{nm dB})$. Considerable work has been per-

formed to improve this parameter and DCFs with values ranging from 200 to more than 300 ps/(nm dB) for chromatic dispersions between -100 and -200 ps/(nm km) at 1550 nm are now available [54, 69–71]. $A_{eff} \sim 20 \mu\text{m}^2$ and PMD ~ 0.10 ps/ $\sqrt{\text{km}}$ at 1.55 μm are generally associated with such features. When used in cables that are part of the transmission distance, the situation is different [72]. Loss of spans consisting of transmission fibers and DCFs should be minimized and high FOM DCFs are no longer the optimum. Chromatic dispersion around -40 ps/(nm km) with loss around 0.25 dB/km at 1.55 μm proves to be better suited for such applications [51–53]. In addition, larger A_{eff} ($\sim 30 \mu\text{m}^2$) and smaller PMD (~ 0.06 ps/ $\sqrt{\text{km}}$) can be obtained.

To achieve optimum WDM performance, DCFs must not only compensate for chromatic dispersion at a given wavelength but also over the whole range of wavelengths used. This implies that both chromatic dispersion and dispersion slope should be negative. Simple step-index profiles are again insufficient for such a purpose. Adding a depressed cladding next to the core provides a better control of the wavelength dependence of the waveguide dispersion, and negative dispersion slope can be obtained [67]. A ring surrounding the depressed region can also be included to improve bending sensitivities. In the last few years, DCFs with negative chromatic dispersions and negative dispersion slopes that match those of all types of transmission fibers have been introduced [44, 69, 70].

Chromatic dispersion, however, does not vary linearly as a function of wavelength, and chromatic dispersion and dispersion slope are insufficient to describe how well a DCF matches a transmission fiber within a wide bandwidth (> 30 nm). Variations of the dispersion slope have to be considered. These variations are responsible for the chromatic dispersion excursion, or residual dispersion, that remains in the waveband after the compensation. This residual dispersion has a direct impact on WDM performance and depends on the transmission fiber type that is used [73].

Figures 2.14 and 2.15 show the two extreme cases of DCFs adapted to compensate for G.652 fibers and for large- A_{eff} G.655.D fibers (with chromatic dispersion of 4 ps/(nm km), dispersion slope of 0.080 ps/(nm² km) and $A_{eff} \sim 70 \mu\text{m}^2$ at 1.55 μm) [74]. The typical chromatic dispersion spectrum of a DCF can be described as follows [69]: first, the chromatic dispersion starts to decrease with wavelength and passes through an inflection point where the dispersion slope can be made \sim constant over a certain waveband; then it reaches its minimum (where the dispersion slope is null), and finally it increases. What is noticeable is that the inflection point of G.652 DCFs is inside, or below, the C-band and that it moves away from this band when the chromatic dispersion value at 1.55 μm decreases (see Fig. 2.14(a)). On the contrary, the inflection point of large- A_{eff} G.655.D DCFs is always above the C-band, which imposes high variations of the dispersion slope in this band whatever the chromatic dispersion value might be at 1.55 μm (see Fig. 2.14(a)). As a consequence, for G.652 DCFs the residual dispersion in the C-band is relatively small and it increases when the chromatic dispersion value at 1.55 μm decreases (see Fig. 2.14(b)), whereas for large- A_{eff} G.655.D DCFs the residual dispersion is intrinsically high and almost independent of the chromatic dispersion value at 1.55 μm (see Fig. 2.15(b)). For

Fig. 2.14 G.652: Chromatic dispersion spectra of DCFs for different dispersion values at 1.55 μm detailed on each curve (a); residual dispersion of the compensated links (b); indicated dispersion values given in ps/(nm km)

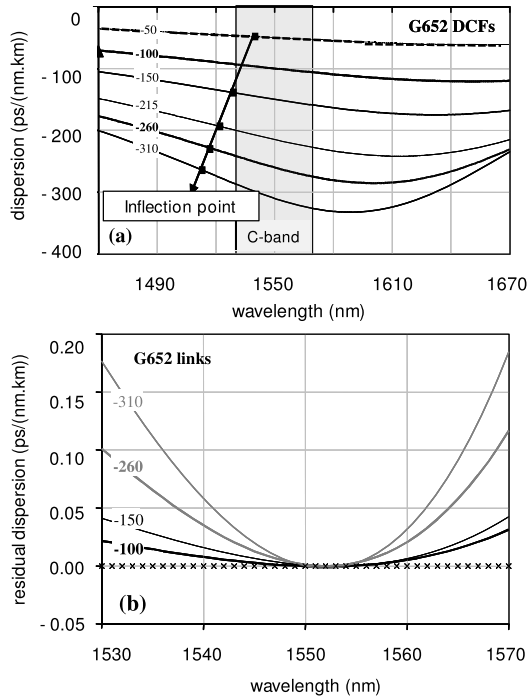
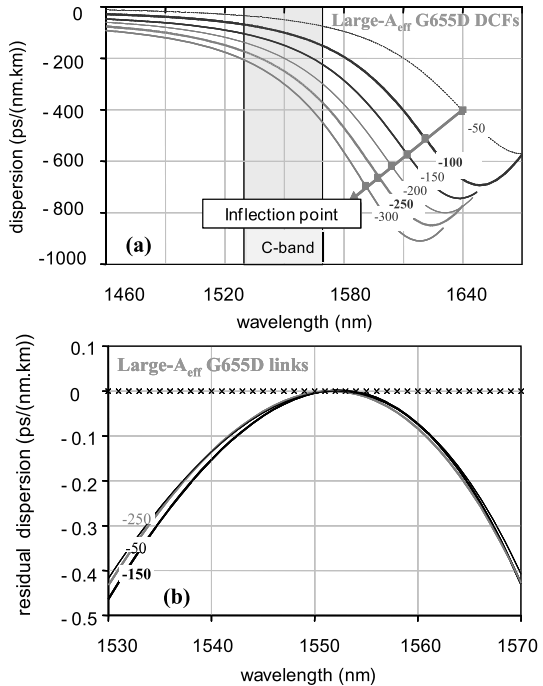


Fig. 2.15 Large- A_{eff} G.655.D: Chromatic dispersion spectra of DCFs for different dispersion values at 1.55 μm detailed on each curve (a); residual dispersion of the compensated link (b); indicated dispersion values given in ps/(nm km)



G.655.E and G.656 DCFs, the situation is in-between these two cases: the residual dispersion is slightly larger than that of G.652 DCFs but the impact of the chromatic dispersion value at 1.55 μm is smaller.

These considerations help to choose the appropriate DCF for a dedicated application. Note that within a given residual dispersion limit DCFs with high negative chromatic dispersion are often preferable because they limit the impact of loss and non-linearity [69, 71, 75], thereby improving the performance of optical networks [74, 75].

2.5 Optical Fiber Cables

We have seen in the previous sections the different kinds of optical fibers for telecommunication. For this application, fibers will eventually be installed and operated in many different environments: they can be buried underground or undersea, strung aerially between poles, or running through intricate paths within buildings, and so on. Cabling is then the packaging of optical fibers that will protect them from anything that may damage them. And the list is long and diverse: rodents attacks, lightning, more gradual degradation mechanisms like long-term exposure to moisture, heat and extreme temperatures, crush, and of course tensile strength when cables are installed. Cables also allow for easier handling and grouping of optical fibers.

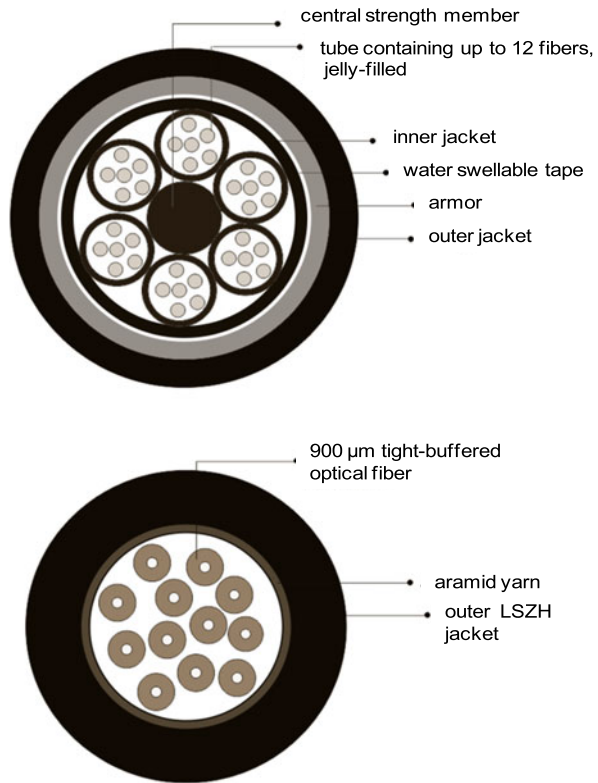
There is a large variety of cables due to the differing environments and requirements they must fulfill. The simplest cable includes one fiber at its center and has a diameter of a few millimeters, while the most complex cables can include up to several hundreds of fibers, and their diameter can be as large as several centimeters. In this section, we will briefly review some cable basics, that is the key elements of an optical cable, the different types of environments and associated cables. The interested readers can refer to some textbooks dedicated to cables [6, 76].

2.5.1 *Basic Elements of a Cable*

As stated above, cables can be very different to fit the diverse environments they encounter. However, their design always comes down to the same few basic elements. There are four basic cable constructions: loose tube, micro-module, tight-buffered and ribbon. Cables that include a large number of fibers are built-up in a modular structure, starting from those basic elements. For example, a 96-fiber cable can be made from eight loose tube modules containing 12 fibers each.

A loose tube simply consists of a larger tube, containing several $\sim 250 \mu\text{m}$ coated optical fibers. Fiber length is slightly longer than that of the tube, so that the fiber can adjust itself within the tube, thus nearly eliminating micro-bend losses. The loose-tube construction is widely used for outdoor applications, but can also be found for

Fig. 2.16 Schematic of cables, the upper part (a) shows a loose tube construction consisting of 6×12 -fiber tubes stranded around the central strength member, the lower part (b) shows a tight-buffered construction including 12 tight-buffered optical fibers



indoor applications. Figure 2.16(a) shows an example of a cable which is based on a loose-tube construction.

The micro-module structure consists of several fibers, typically 12, which are put together and covered by a thin and flexible plastic layer. This structure allows to build high-count fiber cables in a very compact and flexible way. They are also easy to handle within splice boxes.

Tight-buffered cables, as the name implies, only contain tight-buffered fibers, and are mainly used for indoor applications. A tight-buffered fiber consists of a 250 μm fiber with an additional layer of plastic extruded on top of it. The resulting element is typically 900 μm in diameter and can be easily terminated with connectors. This forms also the basic element of patchcords, which only include one or two additional protective layers. Figure 2.16(b) depicts a tight-buffered cable.

At last, ribbon is manufactured by aligning several fibers (from 4 to 24) side by side and binding them together using a UV-curable matrix. This structure is quite popular in the USA. Ribbons ensure that fibers are precisely located so that splicing can be automated easily with dedicated splicers. Mass splicing is seen as one of the key advantages of ribbons.

A key role of cables is to protect fibers from longitudinal stress, for example when the cable is pulled during installation. A strength member, made out of metal

or hard plastic like FRP (Fiber glass Reinforced Plastic) and located at the center of the cable is then used to isolate the fibers from stress and cable is built by stranding the fiber-containing-tubes around the strength member. For further protection, one or more layers can be added. For smaller count and smaller size cables, glass-yarns or aramid-yarns protective layers insure a good tensile strength. Finally, crush resistance is accomplished by adding protective layers of metal or hard plastic material. Metal is also a good protection against rodents that can chew away cables.

Water protection is another key feature for cables. Water causes micro-cracking in the glass that can weaken the fiber significantly and eventually break it. Water protection is especially relevant for outdoor cables. The moisture can enter the cable in two ways, radially if the sheath is damaged during installation or longitudinally when moisture can enter through the unprotected ends of the cables. Several strategies have been deployed all along, mainly including hydrophobic gel-filling of tubes or using water swelling tape.

Layers of metal conductors can also be included in fiber-optic cables when electrical power is needed. This is especially true for submarine applications, in order to supply power to the repeaters.

As described above, cables can include one or more of the basic structures containing the fibers, which, for large-count cables, are stranded around a strength member or loosely stranded in a bigger tube. Then one or more layers are added to ensure protection against crush, water, rodents, etc., until the last outer jacket or sheath. Several materials can be used for outer jacketing: polyethylene, which is most widely used and which offers a good durability, but also PVC, polypropylene, and others. For some applications, essentially indoor, special fire-code requirements have to be fulfilled and specific classes of materials have to be used: LSZH (Low Smoke Zero Halogen) or HFFR (Halogen Free Fire Retardant) that retard fire and avoid toxic fumes to be released.

2.5.2 Cable Environment and Cable Types

Cables are especially designed for each environment to withstand particular conditions. As it is the case with fibers, cable specifications and characterization are standardized (CENELEC EN 187 000 and IEC 60794). The range of cable characteristics is very broad and diverse, including tensile performance, kinking, cable crush, but also temperature cycling, water penetration, flame propagation, and so on.

It is customary to classify the cables between outdoor and indoor applications. For outdoor cable, there is a further sub-classification mainly depending on the final resting place: outdoor direct-burial cables, outdoor ducted cables, outdoor aerial, and undersea cables.

Outdoor direct-burial cables usually contain a large number of SMFs. They are designed with very extensive waterproofing, strength members and often armoring to protect against gnawing by all kind of rodents. This is illustrated schematically in the upper part of Fig. 2.16(a).

Outdoor ducted cables are installed in plastic ducts buried underground. Very often, it is a large main duct that includes smaller sub-ducts (called micro ducts) for progressive installation. Those cables are installed by pulling or blowing. Corresponding cables are usually lighter and smaller and they need to combine good flexibility, high tensile strength and a good friction factor.

Outdoor aerial cables have been developed to benefit from the existing pole infrastructure, thus avoiding the need to dig roads to bury cables of new ducts. They can be either directly suspended between the poles or lashed to a messenger wire that runs between poles and takes the stress outside of the fiber cable. Aerial cables have to sustain environmental extremes (ice and wind loadings, solar radiation, lightning, ...) and need heavy strength membering, both central and radial. When lightning is a hazard, they do not include any metal. There is a special subset of aerial cables, called OPGW (Optical Ground Wire), which is included in the earth wire of a high voltage electrical system.

The most sophisticated undersea cables are the transoceanic ones that run thousands of kilometers between continents. Long-distance cables have to protect fibers from strain during cable laying and repair, from pressure in the ocean depth and from water. They do not include such a large number of fibers, from 12 to 24 generally, but include a large number of protective layers of all kinds and as mentioned earlier a conductor to carry power for repeaters that lie undersea. Cables that are intended to operate over short distances are essentially rugged and water-proof versions of direct burial cables. Those cables can either be buried in the sea floor or just laid, but with extra armoring to account for any damages due to shipping or fishing activities.

There is a large variety of indoor cables as well, and with the advent of FTTH, a lot of activities have been devoted to develop optimized cable structures over the past few years. One of the main requirements for indoor cables is flexibility and compactness. Indoor cables usually include a smaller number of fibers and there is less need for waterproofing and armoring, but some protection from rats is still needed. In addition, cable materials have to be chosen following fire-code requirements. A typical indoor cable structure would then consist of a number of 900 μm tight-buffered elements wrapped either around a central strength member or within a yarn-based layer surrounded by an outer jacket made out of HFFR or LSZH material, as depicted in the right part of Fig. 2.16(b).

2.6 New Developments

Research in the area of silica-based optical fiber is very active. In this section, we give a brief overview of innovative research works on micro-structured optical fibers (Sect. 2.6.1), Bragg fibers (Sect. 2.6.2), fibers mixing glass and semiconductors (Sect. 2.6.3) and fibers for space division multiplexing (Sect. 2.6.4).

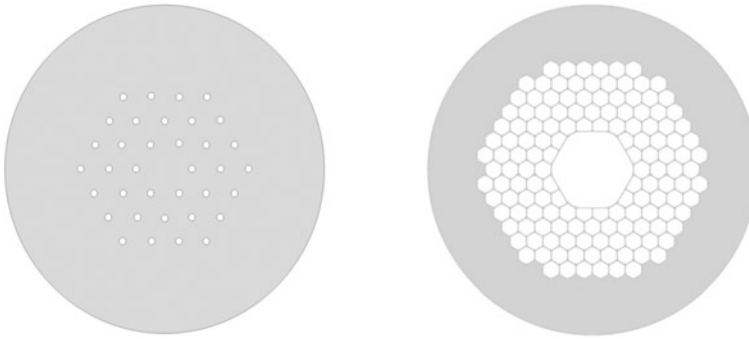


Fig. 2.17 Schematic of micro-structured optical fiber, *left*: TIR-MOF, *right*: PGF-MOF

2.6.1 Micro-Structured Optical Fibers

A Micro-structured Optical Fiber (MOF) contains an arrangement of air holes that run along its length. Light is guided using modified Total Internal Reflection (TIR) or the Photonic-Band-Gap (PBG) effect. In TIR-MOFs, holes act to lower the index in the cladding so that light is confined in the solid core that has a higher index, similarly to conventional solid fibers [77]. In PBG-MOFs, the holes that define the cladding are arranged on a periodic lattice and a hole that breaks the periodicity of the cladding acts as the core. As a result, certain ranges of propagation constants are forbidden in the cladding and allowed in the core [78]. These fibers are usually made by stacking an array of hollow silica rods to form the preform, which is then drawn into a fiber. Figure 2.17 shows a schematic of both fiber types.

TIR-MOFs exhibit novel optical properties. Broadband single-mode guidance was the first one to be experimentally demonstrated in 1997 [79]. At long wavelengths, TIR-MOFs act as solid fibers, i.e. higher-order modes are cut off because they are less confined in the solid core and their propagation constants decrease and become equal to that of the cladding (see Sect. 2.4.1). At short wavelengths, unlike solid fibers, higher-order modes are cut off because they are more confined in the silica regions and avoid the holes, thus raising the effective propagation constant of the cladding that becomes equal to theirs. Eventually, the single-mode range is extended. These “endlessly single-mode” TIR-MOFs have been used to transmit WDM signals in the 1 μm region [80]. Such transmissions have also been possible thanks to an impressive work on loss reduction [81, 82]: from a few 100 dB/km in the late 90’s down to 0.18 dB/km in 2007 [82].

TIR-MOFs are also attractive because of the high index difference between silica and air that cannot be achieved with solid fibers. This specific feature can be used to design bend-optimized fibers (also called hole-assisted fibers) for which air holes in the cladding act as a trench that confines light at bends (see Sect. 2.4.3.3). It also offers more degrees of freedom when tailoring the waveguide dispersion that can become very negative (similarly to solid DCFs but in a more extreme way) with values below -1000 ps/(nm km) at 1.55 μm [83], or very positive thus shifting λ_0 below

1 μm [84]. Unlike solid fibers, anomalous dispersion arises because a large fraction of the mode propagates in the holes. This latter feature is used to extend generations of supercontinua or soliton techniques to shorter wavelengths [85, 86]. Tailoring the mode area to reach extremely small or large A_{eff} (ranging from a few μm^2 to more than 500 μm^2) is also possible. This leads to highly nonlinear fibers [87, 88] used for all-optical signal processing, Raman amplification and broadband sources, or to large mode area fibers [89, 90] used for high power applications (delivery, amplifier or laser).

PBG-MOFs offer even more unusual features because light propagates in a “hollow core”. This opens the door to ultra-low nonlinearity and thus to high power deliveries [91], but also to new spectral regions both in terms of dispersion and loss characteristics [92]. Concerning loss, some mechanisms are common to solid fibers (see Sect. 2.2.4), but roughness of the hole surfaces also causes scattering loss. This can be of importance for some TIR-MOFs for which modes overlap with the holes, however, it is a fundamental limit for PBG-MOFs for which 1.2 dB/km obtained at 1.62 μm [93] might be close to the ultimate lower limit [94]. Finally, filling the core with gas leads to sustainable light interactions with gas over long lengths and enables applications such as gas sensing [95].

All these new features make possible a wide array of applications. Practical realizations, however, remain critical. Issues such as loss, bending sensitivity, polarization effects, splices, and mechanical strength are still subject to intense research.

2.6.2 Bragg Fibers

There are three types of PBG fibers: hollow-core PBG-MOFs, described in the previous section, where the cladding is composed of two-dimensional arrays of holes; solid versions of these structures where the core is made of doped or non-doped silica and the cladding holes are replaced by high-index rods [96–98]; and one-dimensional PBG fibers where a low-index core is surrounded by a cladding made of cylindrical layers with alternating high and low indices, also called Bragg fibers [99]. Bragg fibers were first demonstrated using all-dielectric structures (for CO_2 laser transmission) in 1999 [100], closely followed by all-silica [101] and air-silica [102] realizations.

All-silica Bragg fibers are of particular interest because they offer the unique properties of PBG fibers with the advantage of solid cores that can be used to write Bragg gratings or can be doped to realize fiber amplifiers or lasers. In addition, Bragg fibers have one-dimensional structures that allow for low index differences [98] that can easily be made with standard CVD techniques [101, 103, 104] (see Sect. 2.2.3) thus avoiding the inherent drawbacks of holey structures.

Such Bragg fibers can be designed to exhibit large mode areas together with good bending sensitivities making them suitable for high power applications [104].

Many theoretical studies have also investigated the potential of Bragg fibers for chromatic dispersion tailoring, but most examples concern air-core structures that

are difficult to realize [105, 106]. Few examples of all-silica structures have been reported [107–109], among which one experimental demonstration of a large- A_{eff} Bragg fiber with chromatic dispersion below -1000 ps/(nm km) at 1.48 μm , obtained at the expense of high loss (> 100 dB/km) [109].

Bragg fibers were first proposed in the 1970's [99], but it is only recently that they have received more attention. Experimental demonstrations and applications are in their early stages and many researches have still to be made to exploit the full potential of such fibers.

2.6.3 Fibers Mixing Glass and Semiconductors

Modern telecommunications do not only use 100s of millions of optical fiber km to transmit light but also 100s millions of semiconductor devices to generate, control and detect the light. Nowadays, these two technologies are heterogeneously interfaced using costly and complex optical-electronic conversion techniques.

Recently, efforts have been made to combine these two technologies [110–113], the ultimate goal being the realization of fiber-integrated optical-electronic devices that bring together capabilities to manipulate photons and electrons. Silica glass and crystalline semiconductors, however, have different properties at high temperature and cannot be drawn together into a fiber. To overcome this difficulty, research has focused on MOFs (see Sect. 2.6.1) that offer the possibility to embed semiconductors into their capillary holes. Traditional chemical vapor deposition methods for the formation of semiconductors cannot efficiently be applied to such a confined space; as a consequence new techniques such as high-pressure micro-fluidic chemical deposition have been developed [112].

With these processes, realizations of hybrid devices have been reported. In-fiber silicon wires have proved to function as field-effect transistors and light waveguides [112], and all-optical modulation of light has been demonstrated in amorphous silicon-filled MOFs [113].

This new field of research exploits the design capabilities of both technologies but fundamental materials science has still to be developed to fully realize its promises.

2.6.4 Fibers for Space Division Multiplexing

2.6.4.1 Introduction

Space-Division Multiplexing (SDM) [114, 115] is currently subject to intense research due to its ability to increase by more than a tenfold the current 10s of Tbit/s capacity of Single-Core Single-Mode (SC-SM) systems and thus avoid the foreseen capacity crunch [116, 117].

Significant efforts have been spent to develop Multi-Core Single-Mode Fibers (MC-SMFs), Single-Core Few-Mode Fibers (SC-FMFs) and MC-FMFs adapted to SDM transmissions [118]. These fibers can be classified into 3 categories depending on the way the crosstalk issue is addressed. In the 1st, weakly-coupled category [119–151], the crosstalk is minimized so that each (group of) SDM channel(s) is separately detected without using complex Multiple-Input-Multiple-Output Digital Signal Processing (MIMO-DSP). In the 2nd, low-Differential-Group-Delay (low-DGD) category [152–180], the DGDs between all the SDM channels are minimized so that they can be simultaneously detected at reception and that MIMO-DSP can efficiently compensate for crosstalk. The 3rd category [181–191] is a hybrid category in which low-DGD SDM channels are arranged in weakly-coupled groups.

One way to compare their performance is to use the spatial density parameter that is a measure of the space efficiency. The generalized form of the Spatial Density (SD) of an SDM fiber [183] depends on the number of SDM channels (cores and modes), the A_{eff} and the glass diameter (D), and is normalized to the spatial density of the standard SC-SMF as follows:

$$SD_{SDM} = \left[\sum_{c=1}^C \sum_{m=1}^M (A_{effc,m}) / \left(\frac{\pi}{4} D^2 \right) \right] / SD_{\text{standard SC-SMF}} \quad (2.21)$$

where C is the number of cores, M is the number of spatial modes and

$$SD_{\text{standard SC-SMF}} = A_{eff} / \left(\frac{\pi}{4} D^2 \right) = 80 \mu\text{m}^2 / \left(\frac{\pi}{4} (125 \mu\text{m})^2 \right) \quad (2.22)$$

2.6.4.2 Weakly-Coupled Fibers

Single-Core Few-Mode Fibers

Orbital-angular-momentum fibers [130–132] and ring fibers [133–135] belong to this category because of their potential great resistance to mode coupling. But these fibers are still in their early stages and 1st prototypes are only few km long and have high attenuations (>1 dB/km at 1550 nm).

Standard SC-FMFs [119–129] can be made with usual manufacturing processes that allow for large-scale productions. 2-LP-mode [120, 124, 125, 127] and 4-LP-mode [122, 127] fibers (3 and 6 SDM channels, respectively) have already been reported with attenuations of ~ 0.20 to ~ 0.22 dB/km at 1550 nm. To increase the number of SDM channels supported by these SC-FMFs, the A_{eff} have to be decreased to maintain sufficiently high effective index differences, Δn_{eff} , between the LP modes to limit crosstalk [126]. This has a direct impact on spatial density. If it increases from 5 [120] (3 SDM channels) to 9.5 [122] (6 SDM channels), as illustrated in Fig. 2.18, and to 17 (12 SDM channels for an optimized step-index SC 7-LP-mode fiber with $\min |A_{eff}| = 90 \mu\text{m}^2$ and $\min |\Delta n_{eff}| = 1 \times 10^{-3}$ between the LP modes), it then decreases to 15 despite the 15 SDM channels of 15 (SC 9-LP-mode fiber) because of a much smaller $\min |A_{eff}|$ of $70 \mu\text{m}^2$ ($\min |\Delta n_{eff}| = 1 \times 10^{-3}$) [126]. The

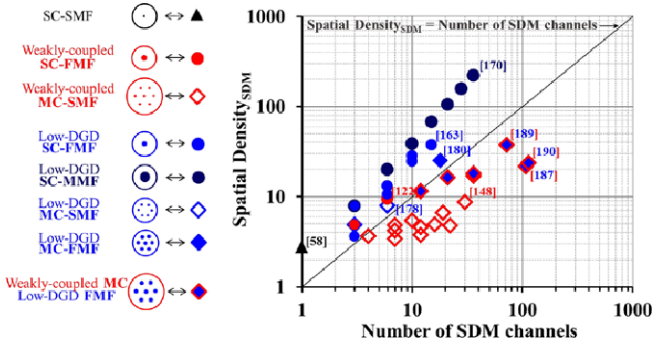


Fig. 2.18 Normalized Spatial Density vs. number of SDM channels for the different fiber categories

spatial density is, nevertheless, high for this type of fiber thanks to SDM channels that spatially overlap and that allow to keep D at 125 μm .

This is an advantage for spatial density but this is a drawback for crosstalk. The SC 4-LP-mode fiber of [9] with $\min |\Delta n_{\text{eff}}| = 0.8 \times 10^{-3}$ has a crosstalk of -33 dB/km. It has recently been used to transmit 5 SDM channels at 100 Gbit/s at 1550 nm over 80 km with a mid-span few-mode amplifier [128] and 6 SDM channels at 1 Gbit/s at 1310 nm in a 20 km PON [129]. Further increasing the number of SDM channels to 12 or 15 is likely to degrade the crosstalk and consequently to decrease the achievable distance. Indeed, taking -25 dB as an overall upper limit for crosstalk in order to maintain low optical signal-to-noise ratio penalties without MIMO-DSP (≤ 0.5 dB for QPSK and 16 QAM modulation formats) [192] means that only few 10s of km can be achieved.

Weakly-coupled SC-FMFs with their high spatial densities and relatively high crosstalks and are thus more adapted to short-reach applications.

Multi-Core Single-Mode Fibers

Contrary to SC-FMFs, MC-SMFs have spatially separated SDM channels, i.e. cores, which naturally allows for low crosstalk. This is why most MC-SMFs [136–151] belong to this category, for which attenuations of ~ 0.20 dB/km and ~ 0.17 dB/km [140] at 1550 nm with germanium-doped-core and pure-silica-core structures, respectively, have been demonstrated. The crosstalk is much smaller (< -45 dB/km) than that of weakly-coupled SC-FMFs. It increases, however, with the number of SDM channels. This increase is due to the mechanical reliability constraint that limits D to ~ 225 μm [138] and that imposes a closer positioning of the higher number of SDM channels. Trenches [140] around the cores and specific core arrangements (circular [144], dual ring [33] and heterogeneous [148] structures) have nevertheless allowed to reach crosstalk ≤ -60 dB/km for 7, 19 and 30 SDM channels which permits to achieve several 1000s of km without MIMO-DSP. This has notably allowed to demonstrate a record capacity \times distance

of 1.031 Ebit/s \times km with 7 SDM channels (140.7 Tbit/s over 7326 km) [145]. A record capacity of 2.15 Pbit/s with 22 SDM channels over 31 km [151] has also recently been reported, but the 22-core SMF used in the experiment had a D of 260 μm , which questions its mechanical reliability.

These low crosstalks have been obtained at the expense of spatial density (see Fig. 2.18). It is much smaller than that of SC-FMFs. The increase of spatial density with the number of SDM channels is also much more moderate, from 4.8 [140] (7 SDM channels) to 6.5 [144] (19 SDM channels) and 8.7 [148] (30 SDM channels), primarily because of the increase of D to ~ 225 μm . Going to a 37-core structure with A_{eff} of 80 μm^2 and D of 225 μm would allow to reach 11.4, but this would eventually increase the crosstalk to values > -55 dB/km, preventing from reaching more than several 100s of km.

Weakly-coupled MC-SMFs, with moderate spatial densities and very low crosstalk, are thus very well adapted to long-haul applications, but their limits in term of space efficiency are close by. It is also worth noting that, so far, they have been fabricated by drilling or stack-and-draw processes [143] that are not fully adapted to large-scale productions.

2.6.4.3 Low-DGD Fibers

Single-Core Few-Mode Fibers

Hollow-core-phonic-bandgap fibers can be classified into this category. These fibers, however, still have high attenuations (>1 dB/km at 1550 nm) and exhibit high DGDs (>1 ns/km) that prevent from achieving long distances [171, 172]. Ring fibers, designed to exhibit strong coupling between their low order LP modes in order to reduce the DGDs [173], also fall into this category.

Regarding standard SC-FMFs [152–170], 2-LP-mode [152, 153, 156, 162], 4-LP-mode [155, 162], 6-LP-mode [158, 159] and 9-LP-mode [163, 164] fibers (3, 6, 10 and 15 SDM channels, respectively) have been reported with attenuations ≤ 0.22 dB/km at 1550 nm. Recently, an SC-MMF with a standard core diameter of 50 μm and for which the 20 lowest-order LP modes (36 SDM channels) can be selectively excited and detected for SDM use [168, 169], has also been reported [170]. For this low-DGD category, the main concern is not the crosstalk but the DGD that increases with the number of SDM channels, and the increased MIMO complexity that goes with it. The $\max|\text{DGD}|$ between the LP modes increases from less than 10 ps/km for 2 LP modes [156] to 73 ps/km for 6 LP modes [159] and 153 ps/km for 9 LP modes [163]. These relatively high DGDs are mainly due to the high sensitivity of the SC-FMFs to process variability that prevents from reaching the minimum theoretical values (that can be one order of magnitude lower) [123]. The SC-MMF, being less sensitive thanks to its large core diameter of 50 μm , has lower DGDs than those of SC-FMFs: 115 ps/km for 9 LP modes, 127 ps/km for 12 LP modes and 160 ps/km for 20 LP modes [170]. One way to further reduce these values is to concatenate fibers with DGDs with opposite signs and thus realize DGD-compensated

links. Values of ~ 1 ps/km for 2-LP-mode links [153], ~ 6 ps/km for 4-LP-mode links [157] and ~ 25 ps/km for 6-LP-mode links [159] have been reported. Calculations show that values < 50 ps/km can realistically be obtained for 9-LP-mode links [163], which would allow to achieve long distances with 30×30 MIMO-DSP with few 10s of ns memory. For 12-LP-mode links (21 SDM channels), tighter process control might be required to reduce the ~ 100 ps/km for practical use, while for 20-LP-mode links (36 SDM channel), made with SC-MMFs, values are expected to be < 70 ps/km.

These low-DGD SC-FMFs have much larger A_{eff} than those of weakly-coupled SC-FMFs ($\min |A_{eff}| \geq 90 \mu\text{m}^2$ for 2- to 12-LP-mode fibers) mainly because there is no constraint on crosstalk and thus on Δn_{eff} . This ensures small nonlinearity and high spatial density. These fibers also benefit from the spatial overlapping of the SDM channels and the resulting D of $125 \mu\text{m}$. Values of ~ 8 [156, 162] (3 SDM channels), 9.5 [155] (6 SDM channels), 28 [158] (10 SDM channels) and 38 [163] (15 SDM channels) have been obtained (see Fig. 2.18). These latter results have notably allowed to demonstrate a record spectral efficiency of 43.6 bit/s/Hz for the low-DGD category with 15 SDM channels over 22.8 km [164] and a record capacity of 115.2 Tbit/s for a SC fiber with 10 SDM channels over 87 km [167]. Spatial densities of 55 could then be reached with 21 SDM channels (12-LP-modes fibers) [126] but, as previously mentioned, the increase of DGDs might prevent from reaching the levels required for ultra-long-haul transmissions with MIMO-DSP. SC-MMFs can be interesting because they have much larger A_{eff} that allow to reach much higher spatial densities of 67 for 9 LP modes, 105 for 12 LP modes and 220 for 20 LP modes [170] (see Fig. 2.18).

Low-DGD SC-FMFs and SC-MMFs with high spatial densities are thus very promising for long-haul applications if MIMO-DSP complexity can be contained thanks to careful fiber design and tight controls of the manufacturing processes.

Multi-Core Fibers

Some MCFs [174–180] also belong to this low-DGD category. Their main advantage compared to weakly-coupled MC-SMFs is that they have higher spatial densities thanks to cores that can be put closer together because there is no more crosstalk constraint. Spatial densities are, however, smaller than those of low-DGD SC-FMFs because cores are separated and have smaller A_{eff} than those of the higher-order LP modes (see Fig. 2.18).

In the single-mode version, spatial densities of 4.8 [176] (3 SDM channels) and 8 [178] (6 SDM channels) have been reported with attenuations of ~ 0.19 to 0.24 dB/km at 1550 nm (see Fig. 2.18). Further increasing the number of SDM channels to 19 and 37 would give spatial densities of 28 and 34 , respectively, for $D = 125 \mu\text{m}$. Then, D has to be increased to accommodate the higher number of cores, and a value of 38 could be obtained for a 61-core SMF. Another key advantage of this fiber type is that lower DGDs than those of low-DGD SC-FMFs can be obtained. Indeed, the DGDs now scale with the square-root of distance

thanks to the strong coupling resulting from the close positioning of the cores [176]. A max|DGD| of 515 ps over 31 km has been reported for the 6-core SMF [178] (6 SDM channels) without using DGD-compensating techniques, which allowed to demonstrate a record capacity \times distance of 0.031 Ebit/s \times km for the low-DGD category (18 Tbit/s over 1705 km).

In the few-mode version [174, 177, 180], the spatial densities are even higher because D can be kept at 125 μm and because SDM channels that strongly overlap, i.e. higher-order modes, are now used. A moderately-coupled 6-core 2-LP-mode fiber [180] (18 SDM channels) with a spatial density of 25 has recently been reported (see Fig. 2.18). A spatial density of 80 could then be reached with a 7-coupled-core 4-LP-mode fiber (42 SDM channels). In principle, very low DGD can also be obtained, but this still needs further investigations and experimental validations. If this was the case, these fibers would be very promising because they could provide very high spatial densities without scarifying DGD. Note, however, that because of their multi-core structures, they have to be made with non-standard manufacturing processes.

2.6.4.4 Hybrid Weakly-Coupled and Low-DGD Fibers

MC-FMFs, that can have standard attenuations of $\sim 0.20\text{--}0.23$ dB/km at 1550 nm, preferably belong to this category [181–190] (low-DGD LP modes inside weakly-coupled cores). MC-SMFs, in which low-DGD cores are arranged in weakly-coupled groups, also belong to this category [191].

Similarly to weakly-coupled MC-SMFs, crosstalk between (groups of) cores, that has to be minimized to avoid complex MIMO-DSP, increases with the number of SDM channels because of the $D < \sim 225$ μm boundary condition. It increases from -66 dB/km for a 12-core 2-LP-mode [188] (36 SDM channels) to -47 dB/km for a 12-core 4-LP-mode [189] (72 SDM channels) fibers. Both fibers use optimized trenches and heterogeneous square lattice core arrangements to minimize the crosstalk. For the same number of SDM channels, this category exhibits lower crosstalks than those of weakly-coupled MC-SMFs because of the use of more-densely-packed low-DGD SDM channels, i.e. modes. As for the low-DGD SC-FMFs, the DGDs of the different cores increases with the number of LP modes, going from 63 ps/km for the 2 LP modes [188] to 430 ps/km for the 4 LP modes [189]. These values are higher than those of SC-FMFs and SC-MMFs for the same number of LP modes because DGDs have to be minimized for all the cores of the structure which, given the high sensitivity to process variability, is much more challenging.

Not surprisingly, spatial density is in between those of the weakly-coupled MC-SMFs and of the low-DGD SC-FMFs (see Fig. 2.18). Spatial densities of 18 and 37 have been demonstrated with a 12-core 2-LP-mode fiber [188] (36 SDM channels) and a 12-core 4-LP-mode fiber [189] (72 SDM channels), respectively. This has allowed to demonstrate a record spectral efficiency of 247.9 bit/s/Hz for a fiber with $D < \sim 225$ μm (12 cores with 2 LP modes) over 40.4 km [185]. The spatial

density can then be further increased by using more cores and/or more LP modes. But, as for the weakly-coupled category, these structures might suffer from high crosstalks (> -55 dB/km) if D is kept $< \sim 225$ μm . Recently, 2 such MC-FMFs have been reported but with $D > 300$ μm which led to smaller spatial densities (< 30): a 36-core 2-LP-mode fiber (108 SDM channels) with $D = 306$ μm [187], and a 19-core 4-LP-mode structure (114 SDM channels) with $D = 318$ μm [190], the latter allowing to demonstrate a record spectral efficiency of 456 bit/s/Hz over 9.8 km.

2.6.4.5 Conclusion

SDM fibers can be classified in different categories, depending on the way crosstalk is dealt with. Weakly-coupled and hybrid fibers, that minimize crosstalk, have already allowed to significantly improve spectral efficiency, capacity and capacity \times distance. But they might soon reach their limits in term of space efficiency. Low-DGD fibers, that use MIMO-DSP to compensate for crosstalk, have a greater potential in terms of space efficiency. They have already offered important improvements in terms of spectral efficiency and capacity, but they still have to demonstrate their ability to reach high capacity \times distance, the main issue being to maintain low DGDs to allow for efficient MIMO-DSP.

The active research to develop ever improved SDM fibers might soon meet the remaining challenges and allow for practical deployments.

Acknowledgements The authors are very much indebted to Pascale Nouchi who made significant contributions to the book chapter of the 1st edition, which has been taken as the basis for the current updated and expanded text. Unfortunately, the successful cooperation could not be continued due to a major change in responsibilities and scientific focus of Pascale.

References

1. C.K. Kao, G.A. Hockham, Dielectric fiber surface waveguides for optical frequencies. *Proc. IEE* **113**, 1151–1158 (1966)
2. D. Marcuse, *Theory of Dielectric Optical Waveguides*, 2nd edn. (Academic Press, San Diego, 1991)
3. A.W. Snyder, J.D. Love, *Optical Waveguide Theory* (Chapman and Hall, New York, 1983)
4. D. Gloge, Weakly guiding fibers. *Appl. Opt.* **10**, 2252–2258 (1971)
5. S.R. Bickham, S.C. Garner, O. Kogan, T.A. Hanson, Theoretical and experimental studies of macrobend losses in multimode fibers, in *Proc. 58th Intern. Wire & Cable Symposium (IWCS'09)*, Charlotte, NC, USA, 13-3 (2009), pp. 450–457
6. H. Murata, *Handbook of Optical Fibers and Cables*, 2nd edn. (Marcel Dekker, New York, 1996)
7. P.C. Schultz, Optical absorption of the transition elements in vitreous silica. *J. Am. Ceram. Soc.* **57**, 309–313 (1974)
8. O. Humbach, H. Fabian, U. Grzesik, U. Haken, W. Heitmann, Analysis of OH absorption bands in synthetic silica. *J. Non-Cryst. Solids* **203**, 19–26 (1996)

9. K. Tsujikawa, K. Tajima, K. Shiraki, I. Sankawa, Method for predicting Rayleigh scattering loss of silica-based optical fibers. *J. Lightwave Technol.* **25**, 2122–2128 (2007)
10. M.E. Lines, W.A. Reed, D.J. Di Giovanni, J.R. Hamblin, Explanation of anomalous loss in high delta single-mode fibres. *Electron. Lett.* **35**, 1009–1010 (1999)
11. P. Guenot, P. Nouchi, B. Poumellec, Influence of drawing temperature on light scattering properties of single-mode fibers, in *Opt. Fiber Commun. Conf. (OFC'99)*, San Diego, CA, USA (1999), Techn. Digest, paper ThG2
12. K. Nagayama, M. Kakui, M. Matsui, I. Saitoh, Y. Chigusa, Ultra-low-loss (0.1484 dB/km) pure silica core fibre and extension of transmission distance. *Electron. Lett.* **38**, 1168–1169 (2002)
13. J.W. Fleming, Dispersion in GeO₂–SiO₂ glasses. *Appl. Opt.* **23**, 4486–4493 (1984)
14. CEI/IEC recommendation 60793-1-41 (2003)
15. TIA recommendation TIA-455-220-A (2003)
16. ITU-T recommendation G.651.1 (2007)
17. D. Molin, P. Matthijsse, G. Kuyt, P. Sillard, Reduced bend sensitivity of multimode fibers in FttX applications, in *Proc. 56th Intern. Wire & Cable Symposium (IWCS'07)*, Lake Buena Vista, FL, USA (2007), 10-1
18. D. Gloge, A.J. Marcattili, Multimode theory of graded-core fibers. *Bell Syst. Tech. J.* **52**, 1563–1579 (1973)
19. R. Olshansky, D.B. Keck, Pulse broadening in graded-index multimode fibers. *Appl. Opt.* **15**, 483–491 (1976)
20. M. Horiguchi, Y. Ohmori, H. Takata, Profile dispersion characteristics in high-bandwidth graded-index multimode fibers. *Appl. Opt.* **19**, 3159–3167 (1980)
21. D. Molin, M. Bigot-Astruc, K. de Jongh, P. Sillard, Trench-assisted bend-resistant OM4 multi-mode fibers, in *Proc. 36th Europ. Conf. Opt. Commun. (ECOC'10)*, Torino, Italy (2010), paper P1.11
22. M.-J. Li, P. Tandon, D.C. Bookbinder, S.R. Bickham, K.A. Wilbert, J.S. Abbott, D.A. Nolan, Designs of bend-insensitive multimode fibers, in *Opt. Fiber Commun. Conf. and Nat. Fiber Opt. Eng. Conf. (OFC/NFOEC'11)*, Los Angeles, CA, USA (2011), Techn. Digest, paper JThA3
23. D. Molin, M. Bigot-Astruc, P. Sillard, Leaky modes in trench-assisted bend-insensitive MMFs, in *Opt. Fiber Commun. Conf. and Nat. Fiber Opt. Eng. Conf. (OFC/NFOEC'13)*, Anaheim, CA, USA (2013), Techn. Digest, paper OTh3K
24. L. Provost, D. Molin, H. Maerten, L. Galkovsky, F. Achten, G. Kuyt, P. Sillard, Connectivity and compatibility performance of bend-insensitive multimode fibers, in *Proc. 60th Intern. Wire & Cable Symposium (IWCS'11)*, Charlotte, NC, USA (2011), p. 176
25. D. Molin, M. Bigot-Astruc, P. Sillard, Chromatic dispersion compensation in regular and bend-insensitive multimode fibers, in *Opt. Fiber Commun. Conf. and Nat. Fiber Opt. Eng. Conf. (OFC/NFOEC'12)*, Los Angeles, CA, USA (2012), Techn. Digest, paper OM2D.3
26. D. Molin, G. Kuyt, M. Bigot-Astruc, P. Sillard, Recent advances in MMF technology for data networks, in *Opt. Fiber Commun. Conf. and Nat. Fiber Opt. Eng. Conf. (OFC/NFOEC'11)*, Los Angeles, CA, USA (2011), Techn. Digest, paper OWJ6
27. F.J. Achten, M.P.M. Jetten, G.-J. Krabshuis, G. Kuyt, P. Matthijsse, M.J.N. van Stralen, New generation of broad wavelength window multimode fibers, in *Proc. 30th Europ. Conf. Opt. Commun. (ECOC'04)*, Stockholm, Sweden (2004), paper Th.3.3.3
28. R. Shubochkin, K. Balemarthy, Y. Sun, J. Kim, R. Lingle Jr., D.S. Vaidya, J. Kamino, Trends in datacom optical links, in *Proc. 62th Intern. Wire & Cable Symposium (IWCS'13)*, Charlotte, NC, USA (2013), 13-3
29. D. Molin, F. Achten, M. Bigot, A. Amezcua-Correa, P. Sillard, WideBand OM4 multi-mode fiber for next-generation 400 Gbps data communications, in *Proc. 40th Europ. Conf. Opt. Commun. (ECOC'14)*, Cannes, France (2014), paper P.1.6
30. T. Ishigure, E. Nihei, Y. Koiye, Graded-index polymer optical fiber for high speed data communication. *Appl. Opt.* **33**, 4261–4266 (1994)

31. Y. Koike, T. Ishigure, High-bandwidth plastic optical fiber for fiber to the display. *J. Lightwave Technol.* **24**, 4541–4553 (2006)
32. N. Yoshihara, Y. Watanabe, T. Onishi, T. Tsukamoto, Transmission trials of perfluorinated GI-POF, in *Opt. Fiber Commun. Conf. (OFC'00)*, Baltimore, MD, USA (2000), Techn. Digest, paper ThR2-1
33. W.R. White, L.L. Blyler Jr., R. Ratnagiri, M. Park, Manufacture of perfluorinated plastic optical fibers, in *Opt. Fiber Commun. Conf. (OFC'04)*, Los Angeles, CA, USA (2004), Techn. Digest, paper ThC3
34. ISO/IEC recommendation 11801 (2002)
35. IEC 60793-2-10/Ed5 (2015)
36. P. Pepeljugoski, M.J. Hackert, J.S. Abbott, S.E. Swanson, S.E. Golowich, A.J. Ritger, P. Kolesar, Y.C. Chen, P. Pleunis, Development of system specification for laser-optimized 50 μm multimode fiber for multigigabit short-wavelength LANs. *J. Lightwave Technol.* **21**, 1256–1275 (2003)
37. G. Charlet, M. Salsi, H. Mardoyan, P. Tran, J. Renaudier, S. Bigo, M. Astruc, P. Sillard, L. Provost, F. Cérou, Transmission of 81 channels at 40 Gbit/s over a transpacific-distance, Erbium-only link, using PDM-BPSK modulation, coherent detection, and a new large effective area fibre, in *Proc. 34th Europ. Conf. Opt. Commun. (ECOC'08)*, Bruxelles, Belgium (2008), paper Th3.E.3
38. G.J. Forschini, C.D. Poole, Statistical theory of polarization dispersion in single mode fibers. *J. Lightwave Technol.* **9**, 1439–1456 (1991)
39. K. Petermann, Constraints for fundamental-mode spot size for broadband dispersion-compensated single-mode fibres. *Electron. Lett.* **19**, 712–714 (1983)
40. G.P. Agrawal, *Nonlinear Fiber Optics*, 3rd edn. (Academic Press, San Diego, 2001)
41. P. Sillard, P. Nouchi, J.-C. Antona, S. Bigo, Modeling the non-linear index of optical fibers, in *Opt. Fiber Commun. Conf. (OFC'05)*, Anaheim, CA, USA (2005), Techn. Digest, paper OFH4
42. V.A. Bhagavatula, M.S. Spatz, D.E. Quinn, Uniform waveguide dispersion segmented-core designs for dispersion-shifted single mode fibers, in *Opt. Fiber Commun. Conf. (OFC'84)*, New Orleans, LA, USA (1984), Techn. Digest, paper MG2
43. P. Nouchi, Maximum effective area for non-zero dispersion-shifted fiber, in *Opt. Fiber Commun. Conf. (OFC'98)*, San Jose, CA, USA (1998), Techn. Digest, paper ThK3
44. P. Nouchi, L.-A. de Montmorillon, P. Sillard, New transmission fibers for future networks, in *Proc. 30th Europ. Conf. Opt. Commun. (ECOC'04)*, Stockholm, Sweden (2004), paper Th3.3.1
45. S. Matsuo, K. Aikawa, N. Shimida, S. Tanigawa, K. Himeno, K. Harada, Non-linearity suppressed fiber link of large-effective area medium dispersion fiber and dispersion compensation, in *Proc. 28th Europ. Conf. Opt. Commun. (ECOC'02)*, Copenhagen, Denmark (2002), paper 3.2.4
46. L. Expert, L.-A. de Montmorillon, P. Guénot, M. Gorlier, L. Fleury, D. Molin, P. Sillard, V. Salles, P. Nouchi, Low nonlinearity medium-dispersion fiber-based link, in *Proc. 29th Europ. Conf. Opt. Commun. (ECOC'03)*, Rimini, Italy (2003), paper Th2.3.6
47. N. Kumano, K. Mukasa, S. Matsushita, T. Yagi, Zero-dispersion slope NZDSF with ultra wide bandwidth over 300 nm, in *Proc. 28th Europ. Conf. Opt. Commun. (ECOC'02)*, Copenhagen, Denmark (2002), paper PD1.4
48. D. Molin, L. Fleury, M. Gorlier, F. Beaumont, L. Expert, L.-A. de Montmorillon, P. Sillard, P. Nouchi, Ultra-low slope medium-dispersion fiber for wide-band terrestrial transmissions, in *Opt. Fiber Commun. Conf. (OFC'03)*, Atlanta, GA, USA (2003), Techn. Digest, paper TuB2
49. L.A. de Montmorillon, P. Sillard, M. Astruc-Bigot, B. Dany, P. Nouchi, B. Lavigne, E. Balmefrezol, J.-C. Antona, O. Leclerc, Transmission fiber optimized for metro optical network, in *Opt. Fiber Commun. Conf. (OFC'05)*, Anaheim, CA, USA (2005), Techn. Digest, paper OFH1
50. H. Yokota, H. Kanamori, Y. Ishiguro, G. Tanaka, S. Tanaka, H. Takada, M. Watanabe, S. Suzuki, K. Yano, M. Hoshikawa, H. Shimba, Ultra-low-loss pure-silica-core single-mode

- fiber and transmission experiment, in *Opt. Fiber Commun. Conf. (OFC'86)*, Atlanta, GA, USA (1986), Techn. Digest, paper PD3-1
51. M. Tsukitani, T. Kato, E. Yanada, M. Hirano, M. Nakamura, Y. Ohga, M. Onishi, E. Sasoaka, Y. Makio, M. Nishimura, Low-loss dispersion-flattened hybrid transmission lines consisting of low-nonlinearity pure silica core fibers and dispersion compensating fibers. *Electron. Lett.* **36**, 64–66 (2000)
 52. W.D. Cornwell, O.E. Edwards, N.H. Taylor, D.S. Lotay, S.A. Smith, S. Hamidi, Comparison of 64×10 Gbit/s NRZ and RZ transmission over 6,000 km using a dispersion-managed fiber solution, in *Opt. Fiber Commun. Conf. (OFC'02)*, Anaheim, CA, USA (2002), Techn. Digest, paper WP4
 53. S.N. Knudsen, B. Zhu, L.E. Nelson, M.O. Pederson, D.W. Peckham, S. Stultz, 420 Gbit/s (42×10 Gbit/s) WDM transmission over 4000 km of UltraWave fiber with 100 km dispersion-managed spans and distributed Raman amplification. *Electron. Lett.* **37**, 965–967 (2001)
 54. M. Bigot-Astruc, F. Gooijer, N. Montaigne, P. Sillard, Trench-assisted profiles for large-effective-area single-mode fibers, in *Proc. 34th Europ. Conf. Opt. Commun. (ECOC'08)*, Brussels, Belgium (2008), paper Mo.4.B.1
 55. S. Chandrasekhar, X. Liu, B. Zhu, D.W. Peckham, Transmission of a 1.2 Tbps 24-carrier no-guard-interval coherent OFDM superchannel over 7200 km of ultra-large-area fiber, in *Proc. 35th Europ. Conf. Opt. Commun. (ECOC'09)*, Vienna, Austria (2009), paper PD2.6
 56. Y. Yamamoto, M. Hirano, K. Kuwahara, T. Sasaki, OSNR-enhancing pure-silica-core fiber with large effective area and low attenuation, in *Opt. Fiber Commun. Conf. and Nat. Fiber Opt. Eng. Conf. (OFC/NFOEC'11)*, Los Angeles, CA, USA (2011), Techn. Digest, paper OTu12
 57. J.D. Downie, J. Hurley, J. Cartledge, S. Ten, S. Bickham, S. Mishra, X. Zhu, A. Kobayakov, 40×112 Gbps transmission over an unrepeated 365 km effective area-managed span comprised of ultra-low loss optical fiber, in *Proc. 36th Europ. Conf. Opt. Commun. (ECOC'10)*, Torino, Italy (2010), paper We.7.C.5
 58. M. Bigot-Astruc, L. Provost, G. Krabshuis, P. Dhenry, P. Sillard, 125 μm glass diameter single-mode fiber with A_{eff} of 155 μm^2 , in *Opt. Fiber Commun. Conf. and Nat. Fiber Opt. Eng. Conf. (OFC/NFOEC'11)*, Los Angeles, CA, USA (2011), Techn. Digest, paper OTuJ2
 59. D. Marcuse, Influence of curvature on the losses of doubly clad fibers. *Appl. Opt.* **21**, 4208–4213 (1982)
 60. K. Himeno, S. Matsuo, N. Guan, A. Wada, Low-bending-loss single-mode fibers for Fiber-to-the-Home. *J. Lightwave Technol.* **23**, 3494–3499 (2005)
 61. L.-A. de Montmorillon, P. Matthijsse, F. Gooijer, D. Molin, F. Achten, X. Meerssemann, C. Legrand, Next generation SMF with reduced bend sensitivity for FTTH networks, in *Proc. 32nd Europ. Conf. Opt. Commun. (ECOC'06)*, Cannes, France (2006), paper Mo3.3.2
 62. T. Hasegawa, T. Saitoh, D. Nishika, E. Sasaoka, T. Hosoya, Bend-insensitive single-mode holey fiber with SMF-compatibility for optical wiring applications, in *Proc. 29th Europ. Conf. Opt. Commun. (ECOC'03)*, Rimini, Italy (2003), paper We2.7.3
 63. Y. Tsuchida, K. Saitoh, M. Koshiba, Design and characterization of single-mode holey fibers with low bending losses. *Opt. Express* **13**, 4770–4779 (2005)
 64. M.-J. Li, P. Tandon, D.C. Bookbinder, S.R. Bickham, M.A. McDermott, R.B. Desorcie, D.A. Nolan, J.J. Johnson, K.A. Lewis, J.J. Englebert, Ultra-low bending loss single-mode fiber for FTTH, in *Opt. Fiber Commun. Conf. and Nat. Fiber Opt. Eng. Conf. (OFC/NFOEC'08)*, San Diego, CA, USA (2008), Techn. Digest, paper PDP10
 65. S. Sudo, H. Itoh, Efficient non-linear optical fibres and their applications. *Opt. Quantum Electron.* **22**, 187–212 (1990)
 66. J.M. Dugan, A.J. Price, M. Ramadan, D.L. Wolf, E.F. Murphy, A.J. Antos, D.K. Smith, D.W. Hall, All optical, fiber-based 1550 nm dispersion compensation in a 10 Gbit/s, 150 km transmission experiment over 1310 nm optimized fiber, in *Opt. Fiber Commun. Conf. (OFC'92)*, San Jose, CA, USA (1992), Techn. Digest, paper PDP14
 67. A.M. Vengsarkar, A.E. Miller, W.A. Reed, Highly efficient single-mode fiber for broadband dispersion compensation, in *Opt. Fiber Commun. Conf. (OFC'93)*, San Jose, CA, USA

- (1993), Techn. Digest, paper PD13
68. P. Nouchi, H. Laklalech, P. Sansonetti, J. von Wirth, J. Ramos, F. Bruyère, C. Brehm, J.-Y. Boniort, B. Perrin, Low-PMD dispersion-compensating fibers, in *Proc. 21st Europ. Conf. Opt. Commun.* (ECOC'95), Brussels, Belgium (1995), paper TuP04
 69. L. Grüner-Nielsen, M. Wandel, P. Kristensen, C. Jorgensen, L. Vilbrad Jorgensen, B. Edvold, B. Palsdotir, D. Jakobsen, Dispersion-compensating fibers. *J. Lightwave Technol.* **23**, 3566–3579 (2005)
 70. M.J. Li, Recent progress in fiber dispersion compensators, in *Proc. 27th Europ. Conf. Opt. Commun.* (ECOC'01), Amsterdam, The Netherlands (2001), paper ThM1.1
 71. T. Sasaki, K. Makihara, M. Hirano, T. Haruna, T. Kashiwada, S. Hagihara, M. Onishi, Novel dispersion compensating fiber with fluorine-doped cladding for simultaneous realization of high dispersion compensation efficiency and low attenuation, in *Opt. Fiber Commun. Conf.* (OFC'06), Anaheim, CA, USA (2006), Techn. Digest, paper OThA2
 72. K. Mukasa, Y. Akasaka, Y. Suzuki, T. Kamiya, Novel network fiber to manage dispersion at 1.55 μm with combination of 1.3 μm zero dispersion single-mode fiber, in *Proc. 23rd Europ. Conf. Opt. Commun.* (ECOC'97), Edinburgh, UK (1997), vol. 1, pp. 127–130
 73. J.-C. Antona, P. Sillard, S. Bigo, Impact of imperfect wideband dispersion compensation on the performance of WDM transmission systems at 40 Gbps, in *Proc. 32nd Europ. Conf. Opt. Commun.* (ECOC'06), Cannes, France (2006), paper Th1.6.4
 74. P. Sillard, J.-C. Antona, S. Bigo, Optimized chromatic dispersion of DCMs in WDM transmission systems at 40 Gbps, in *Conf. and Nat. Fiber Opt. Eng. Conf.* (OFC/NFOEC'08), San Diego, CA, USA (2008), Techn. Digest, paper JWA13
 75. J.-C. Antona, P. Sillard, Relationship between the achievable distance of WDM transmission systems and criterion of quality for DCM. in *Opt. Fiber Commun. Conf.* (OFC'06), Anaheim, CA, USA (2006), Techn. Digest, paper OWJ2
 76. B. Elliott, M. Gilmore, *Fiber Optic Cabling*, 2nd edn. (Newnes, Oxford, 2002)
 77. J.C. Knight, T.A. Birks, P.S.J. Russell, D.M. Atkin, Pure silica single-mode fiber with hexagonal photonic crystal cladding, in *Opt. Fiber Commun. Conf.* (OFC'96), San Jose, CA, USA (1996), Techn. Digest, paper PD3
 78. J.C. Knight, J. Broeng, T.A. Birks, P.S.J. Russell, Photonic band gap guidance in optical fibers. *Science* **282**, 1476–1478 (1998)
 79. T.A. Birks, J.C. Knight, P.S.J. Russell, Endlessly single-mode photonic crystal fibers. *Opt. Lett.* **22**, 961–963 (1997)
 80. K. Kurukawa, T. Yamamoto, K. Tajima, A. Aratake, K. Suzuki, T. Kurashima, High capacity WDM transmission in 1.0 μm band over low PCF using supercontinuum source, in *Opt. Fiber Commun. Conf. and Nat. Fiber Opt. Eng. Conf.* (OFC/NFOEC'08), San Diego, CA, USA (2008), Techn. Digest, paper OMH5
 81. L. Farr, J.C. Knight, B.J. Mangan, P.J. Roberts, Low loss photonic crystal fibre, in *Proc. 28th Europ. Conf. Opt. Commun.* (ECOC'02), Copenhagen, Denmark (2002), paper PD1.3
 82. K. Tajima, Low loss PCF by reduction of hole surface imperfection, in *Proc. 33rd Europ. Conf. Opt. Commun.* (ECOC'07), Berlin, Germany (2007), paper PDP 2.1
 83. B.J. Mangan, F. Couny, L. Farr, A. Langford, P.J. Roberts, D.P. Williams, M. Banham, M.W. Mason, D.F. Murphy, E.A.M. Brown, H. Sabert, T.A. Birks, J.C. Knight, P.S.J. Russell, Slope-matched dispersion-compensating photonic crystal fiber, in *Conf. Lasers Electro-Opt.* (CLEO'04), Baltimore, MD, USA (2004), paper CPDD3
 84. P.J. Bennett, T.M. Monro, N.G.R. Broderick, D.J. Richardson, Towards practical holey fiber technology: fabrication, splicing and characterization, in *Proc. 25th Europ. Conf. Opt. Commun.* (ECOC'99), vol. I, Nice, France (1999), pp. 20–23
 85. K.J. Ranka, S.R. Windeler, A.J. Stentz, Visible continuum generation in air-silica microstructure optical fibers with anomalous dispersion at 800 nm. *Opt. Lett.* **25**, 25–27 (2000)
 86. K. Kurukawa, K. Tajima, K. Nakajima, 10 GHz 0.5 ps pulse generation in 1000 nm band in PCF for high speed optical communication, in *Proc. 32nd Europ. Conf. Opt. Commun.* (ECOC'06), Cannes, France (2006), paper PDP5

87. P. Petropoulos, T.M. Monro, W. Belardi, K. Furusawa, J.H. Lee, D.J. Richardson, 2R-regenerative all-optical switch based on a highly nonlinear holey fiber. *Opt. Lett.* **26**, 1233–1235 (2001)
88. G. Mélin, L. Provost, A. Fleureau, S. Lempereur, X. Rejeaunier, A. Bourova, L. Gasca, Innovative design for highly non-linear microstructured fibers, in *Proc. 30th Europ. Conf. Opt. Commun. (ECOC'04)*, Stockholm, Sweden (2004), paper Th4.3.2
89. W.S. Wong, X. Peng, J.M. McLaughlin, L. Dong, Breaking the limit of maximum effective area for robust single-mode operation in optical fibers. *Opt. Lett.* **30**, 2855–2857 (2005)
90. J.M. Fini, Bend-resistant design of conventional and micro-structure fibers with very large mode area. *Opt. Express* **14**, 69–81 (2006)
91. J. Shephard, J. Jones, D. Hand, G. Bouwmans, J. Knight, P. Russell, B. Mangan, High energy nanosecond laser pulses delivered single-mode through hollow-core PBG fibers. *Opt. Express* **12**, 717–723 (2004)
92. C.J.S. de Matos, J.R. Taylor, T.P. Hansen, K.P. Hansen, J. Broeng, All-fiber chirped pulse amplification using highly-dispersive air-core photonic bandgap fiber. *Opt. Express* **11**, 2832–2835 (2003)
93. P.J. Roberts, F. Couny, H. Sabert, B.J. Mangan, D.P. Williams, L. Farr, M.W. Mason, A. Tomlinson, T.A. Birks, J.C. Knight, P.S.J. Russell, Ultimate low loss of hollow-core photonic crystal fibres. *Opt. Express* **13**, 236–244 (2005)
94. T.A. Birks, Reducing losses in photonic crystal fibers, in *Opt. Fiber Commun. Conf. (OFC'06)*, Anaheim, CA, USA (2006), Techn. Digest, paper OFC7
95. T. Ritari, J. Tuominen, H. Ludvigsen, J. Petersen, T. Sørensen, T.P. Hansen, H.R. Simonsen, Gas sensing using air-guiding photonic bandgap fibers. *Opt. Express* **12**, 4080–4087 (2004)
96. N.M. Litchinitser, S.C. Dunn, B. Usner, B.J. Eggleton, T.P. White, R.C. McPhedran, C. Martijn de Sterke, Resonances in microstructured optical waveguides. *Opt. Express* **11**, 1243–1251 (2003)
97. A. Agyros, T.A. Birks, S.G. Leon-Saval, C.M.B. Cordeiro, F. Luan, P.S.J. Russell, Photonic bandgap with an index step of one percent. *Opt. Express* **13**, 309–314 (2005)
98. G. Bouwmans, L. Bigot, Y. Quiquempois, F. Lopez, L. Provino, M. Douay, Fabrication and characterization of an all-solid 2D photonic bandgap fiber with a low-loss region (<20 dB/km) around 1550 nm. *Opt. Express* **13**, 8452–8459 (2005)
99. P. Yeh, A. Yariv, E. Marom, Theory of Bragg fiber. *J. Opt. Soc. Am.* **68**, 1196–1201 (1978)
100. Y. Fink, D.J. Ripin, S. Fan, C. Chen, J.D. Joannopoulos, E.L. Thomas, Guiding optical light in air using an all-dielectric structure. *J. Lightwave Technol.* **17**, 2039–2041 (1999)
101. F. Brechet, P. Roy, J. Marcou, D. Pagnoux, Single-mode propagation into depressed-core-index photonic bandgap fiber designed for zero-dispersion propagation at short wavelengths. *Electron. Lett.* **36**, 514–515 (2000)
102. G. Vienne, Y. Xu, C. Jakobsen, H.J. Deyerl, T.P. Hansen, B.H. Larsen, J.B. Jensen, T. Sørensen, M. Terrel, Y. Huang, M.R.K. Lee, N.A. Mortensen, H. Simonsen, A. Bjarklev, A. Yariv, First demonstration of air-silica Bragg fiber, in *Opt. Fiber Commun. Conf. (OFC'03)*, Atlanta, GA, USA (2003), Techn. Digest, paper PDP25
103. C. Baskiotis, D. Molin, G. Bouwmans, F. Gooijer, P. Sillard, Y. Quiquempois, M. Douay, Bend-induced transformation of the transmission window of a large-mode-area Bragg fiber, in *Proc. 34th Europ. Conf. Opt. Commun. (ECOC'08)*, Brussels, Belgium (2008), paper Mo.4.B.2
104. D. Gapanov, P. Roy, S. Février, M.E. Likhachev, S.L. Semjonov, M.M. Bubnov, E.M. Dianov, M.Yu. Yashkov, V.F. Khopin, M.Yu. Salganskii, A.N. Guryanov, High-power photonic bandgap fiber laser, in *Proc. 33rd Europ. Conf. Opt. Commun. (ECOC'07)*, Berlin, Germany (2007), paper PD 3.9
105. G. Ouyang, Y. Xu, A. Yariv, Theoretical study on dispersion compensation in air-core Bragg fibers. *Opt. Express* **10**, 889–908 (2002)
106. T. Engeness, M. Ibanescu, S. Johnson, O. Weisberg, M. Skorobogatiy, S. Jacobs, Y. Fink, Dispersion tailoring and compensation by modal interactions in OmniGuide fibers. *Opt. Express* **11**, 1175–1196 (2003)

107. J. Marcou, F. Brechet, Ph. Roy, Design of weakly guiding Bragg fibers for chromatic dispersion shifting towards short wavelengths. *J. Opt. A, Pure Appl. Opt.* **3**, 144–153 (2001)
108. N. Yi, Z. Lei, G. Chong, J. Shu, P. Jiangde, A novel design for all-solid silica Bragg fiber with zero-dispersion wavelength at 1550 nm. *Opt. Express* **12**, 4602–4607 (2004)
109. F. Gérôme, S. Février, A.D. Pryamikov, J.L. Auguste, R. Jamier, J.M. Blondy, M.E. Likhachev, M.M. Bubnov, S.L. Semjonov, E.M. Dianov, Highly dispersive large mode area photonic bandgap fiber. *Opt. Lett.* **32**, 1208–1210 (2007)
110. M. Fokine, L.E. Nilsson, A. Claesson, D. Berlemont, L. Kjellberg, L. Krummenacher, W. Margulis, Integrated fiber Mach-Zehnder interferometer for electro-optic switching. *Opt. Lett.* **27**, 1643–1645 (2002)
111. M. Bayindir, F. Sorin, A.F. Abouraddy, J. Viens, S.D. Hart, J.D. Joannopoulos, Y. Fink, Metal-insulator-semiconductor optoelectronic fibers. *Nature* **431**, 826–829 (2004)
112. P.J.A. Sazio, A. Amezcu-Correa, C.E. Finlayson, J.R. Hayes, T.J. Scheidemantel, N.F. Baril, B.R. Jackson, D.-J. Won, F. Zhang, E.R. Margine, V. Gopalan, V.H. Crespi, J.V. Badding, Microstructured optical fibers as high-pressure microfluidic reactors. *Science* **311**, 1583–1586 (2006)
113. D.J. Won, M.O. Ramirez, H. Kang, V. Gopalan, N.F. Baril, J. Calkins, J.V. Badding, P.J.A. Sazio, All-optical modulation of laser light in amorphous silicon filled microstructured optical fibers. *Appl. Phys. Lett.* **91**, 161112 (2007)
114. S. Inao, T. Sato, S. Senstui, T. Kuroha, Y. Nishimura, Multicore optical fiber, in *Opt. Fiber Commun. Conf. (OFC'79)*, Washington, DC, USA (1979), Techn. Digest, paper WB1
115. S. Berdagué, P. Facq, Mode division multiplexing in optical fibers. *Appl. Opt.* **21**, 1950–1955 (1982)
116. R.-J. Essiambre, G.J. Foschini, P.J. Winzer, G. Kramer, Capacity limits of fiber-optic telecommunication systems, in *Opt. Fiber Commun. Conf. and Nat. Fiber Opt. Eng. Conf. (OFC/NFOEC'09)*, San Diego, CA, USA (2009), Techn. Digest, paper OThL1
117. R.W. Tkach, Network traffic and system capacity: scaling for the future, in *Proc. 36th Europ. Conf. Opt. Commun. (ECOC'10)*, Torino, Italy (2010), paper We.7.D.1
118. P. Sillard, Next-generation fibers for space-division-multiplexed transmissions. *J. Lightwave Technol.* **33**, 1092–1099 (2015)
119. N. Hanzawa, K. Saitoh, T. Sakamoto, T. Matsui, S. Tomita, M. Koshiha, Demonstration of mode-division multiplexing transmission over 10 km two-mode fiber with mode coupler, in *Opt. Fiber Commun. Conf. and Nat. Fiber Opt. Eng. Conf. (OFC/NFOEC'11)*, Los Angeles, CA, USA (2011), Techn. Digest, paper OWA4
120. A. Li, A.A. Amin, X. Chen, W. Shieh, Reception of mode and polarization multiplexed 107 Gbps CO-OFDM signal over a two-mode fiber, in *Opt. Fiber Commun. Conf. and Nat. Fiber Opt. Eng. Conf. (OFC/NFOEC'11)*, Los Angeles, CA, USA (2011), Techn. Digest, paper PDPB8
121. M. Salsi, C. Koebele, D. Sperti, P. Tran, P. Brindel, H. Mardoyan, S. Bigo, A. Boutin, F. Verluise, P. Sillard, M. Bigot-Astruc, L. Provost, F. Cerou, G. Charlet, Transmission at 2×100 Gbps, over two-modes of 40 km-long prototype few-mode fiber, using LCOS-based mode multiplexer and demultiplexer, in *Opt. Fiber Commun. Conf. and Nat. Fiber Opt. Eng. Conf. (OFC/NFOEC'11)*, Los Angeles, CA, USA (2011), Techn. Digest, paper PDPB9
122. P. Sillard, M. Bigot-Astruc, D. Boivin, H. Maerten, L. Provost, Few-mode fiber for uncoupled mode-division multiplexing transmissions, in *Proc. 37th Europ. Conf. Opt. Commun. (ECOC'11)*, Geneva, Switzerland (2011), paper Tu.5.LeCervin.7
123. P. Sillard, M. Bigot-Astruc, D. Molin, Few-mode fibers for mode-division-multiplexed systems. *J. Lightwave Technol.* **32**, 2824–2829 (2014)
124. T. Mori, T. Sakamoto, M. Wada, T. Yamamoto, F. Yamamoto, Experimental evaluation of modal crosstalk in two-mode fibre and its impact on optical MIMO transmission, in *Proc. 40th Europ. Conf. Opt. Commun. (ECOC'14)*, Cannes, France (2014), paper Th.1.4.4.
125. C. Xia, N. Chand, A.M. Velázquez-Benítez, X. Liu, J.E. Antonio Lopez, H. Wen, B. Zhu, F. Effenberger, R. Amezcu-Correa, G. Li, Demonstration of world's first few-mode GPON, in *Proc. 40th Europ. Conf. Opt. Commun. (ECOC'14)*, Cannes, France (2014), paper PD.1.5

126. P. Sillard, Scalability of few-mode fibers for mode-division-multiplexed systems, in *Proc. IEEE Photon. Conf. (IPC'14)*, San Diego, California, USA (2014), paper WG4.2
127. R. Maruyama, N. Kuwaki, S. Matsuo, M. Ohashi, Experimental investigation of relation between mode-coupling and fiber characteristics in few-mode fibers, in *Opt. Fiber Commun. Conf. (OFC'15)*, Los Angeles, CA, USA (2015), Techn. Digest, paper M2C.1
128. C. Simonneau, Ph. Genevaux, G. Le Cocq, Y. Quiquempois, L. Bigot, A. Boutin, M. Bigot-Astruc, P. Sillard, G. Charlet, 5-Mode amplifier with low modal crosstalk for spatial mode multiplexing transmission with low signal processing complexity, in *Proc. 41st Europ. Conf. Opt. Commun. (ECOC'15)*, Valencia, Spain (2015), Paper We.2.4.2
129. H. Wen, C. Xia, A.M. Velázquez-Benítez, N. Chand, J.E. Antonio-Lopez, B. Huang, H. Liu, H. Zheng, P. Sillard, X. Liu, F. Effenberger, R. Amezcua-Correa, G. Li, First demonstration of 6-mode PON achieving a record gain of 4 dB in upstream transmission loss budget. *J. Lightwave Technol.* **34**, 1990–1996 (2016)
130. N. Bozinovic, Y. Yue, Y. Ren, M. Tur, P. Kristensen, A.E. Willner, S. Ramachandran, Orbital angular momentum (OAM) based mode division multiplexing (MDM) over a km-length fiber, in *Proc. 37th Europ. Conf. Opt. Commun. (ECOC'12)*, Amsterdam, The Netherlands (2012), paper Th.3.C.6
131. C. Brunet, P. Vaity, Y. Messaddeq, S. LaRochelle, L.A. Rusch, Design, fabrication and validation of an OAM fiber supporting 36 states. *Opt. Express* **22**, 26117–26127 (2014)
132. S. Ramachandran, P. Gregg, P. Kristensen, S.E. Golowich, On the scalability of ring fiber designs for OAM multiplexing. *Opt. Express* **23**, 3721–3730 (2015)
133. X.Q. Jin, R. Li, D.C. O'Brien, F.P. Payne, Linearly polarized mode division multiplexed transmission over ring-index multimode fibers, in *Proc. IEEE Summer Topical Meeting 2013*, Waikoloa, Hawaii, USA (2013), paper TuC4.3
134. M. Kasahara, K. Saitoh, T. Sakamoto, N. Hanzawa, T. Matsui, K. Tsujikawa, F. Yamamoto, Design of three-spatial-mode ring-core fiber. *J. Lightwave Technol.* **32**, 1337–1343 (2014)
135. F. Feng, G.S. Gordon, X. Jin, D. O'Brien, F. Payne, Y. Jung, Q. Kang, J.K. Sahu, S.U. Alam, D.J. Richardson, T.D. Wilkinson, Experimental characterization of a graded-index ring-core fiber supporting 7 LP mode groups, in *Opt. Fiber Commun. Conf. (OFC'15)*, Los Angeles, CA, USA (2015), Techn. Digest, paper TU2D.3
136. J. Sakaguchi, Y. Awaji, N. Wada, A. Kanno, T. Kawanishi, T. Hayashi, T. Taru, T. Kobayashi, M. Watanabe, 109 Tbps ($7 \times 97 \times 172$ Gbps SMD/WDM/PDM) QPSK transmission through 16.8 km homogeneous multi-core fiber, in *Opt. Fiber Commun. Conf. and Nat. Fiber Opt. Eng. Conf. (OFC/NFOEC'11)*, Los Angeles, CA, USA (2011), Techn. Digest, paper PDPB6
137. B. Zhu, T.F. Taunay, M. Fishteyn, X. Liu, S. Chandrasekhar, M.F. Yan, J.M. Fini, E.M. Monberg, F.V. Dimarcello, Space-, wavelength-, polarization-division multiplexed transmission of 56 Tbps over 76.8 km seven-core fiber, in *Opt. Fiber Commun. Conf. and Nat. Fiber Opt. Eng. Conf. (OFC/NFOEC'11)*, Los Angeles, CA, USA (2011), Techn. Digest, paper PDPB7
138. S. Matsuo, K. Takenaga, Y. Arakawa, Y. Sasaki, S. Taniagwa, K. Saitoh, M. Koshihba, Large-effective-area ten-core fiber with cladding diameter of about 200 μm . *Opt. Lett.* **36**, 4626–4628 (2011)
139. J. Sakaguchi, B.J. Puttnam, W. Klaus, Y. Awaji, N. Wada, A. Kanno, T. Kawanishi, K. Imamura, H. Inaba, K. Mukasa, R. Sugizaki, T. Kobayashi, M. Watanabe, 19-core fiber transmission of $19 \times 100 \times 172$ Gbps SDM-WDM-PDM-QPSK signals at 305 Tbps, in *Opt. Fiber Commun. Conf. and Nat. Fiber Opt. Eng. Conf. (OFC/NFOEC'12)*, Los Angeles, CA, USA (2012), Techn. Digest, paper PDP5C.1
140. T. Hayashi, T. Taru, O. Shimakawa, T. Sasaki, E. Sasaoka, Low-loss and large- A_{eff} multi-core fiber for SNR enhancement, in *Proc. 38th Europ. Conf. Opt. Commun. (ECOC'12)*, Amsterdam, The Netherlands (2012), paper Mo.1.F.3
141. H. Takara, A. Sano, T. Kobayashi, H. Kubota, H. Kawakami, A. Matsuura, Y. Miyamoto, Y. Abe, H. Ono, K. Shikama, Y. Goto, K. Tsujikawa, Y. Sasaki, I. Ishida, K. Takenaga, S. Matsuo, K. Saitoh, M. Koshihba, T. Morioka, 1.01 Pbps (12SDM/222WDM/456 Gbps) crosstalk-managed transmission with 91.4 bps/Hz aggregate spectral efficiency, in *Proc. 38th Europ. Conf. Opt. Commun. (ECOC'12)*, Amsterdam, The Netherlands (2012), paper Th.3.C.1

142. H. Takahashi, T. Tsuritani, E.L.T. de Gabory, T. Ito, W.R. Peng, K. Igarashi, K. Takeshima, Y. Kawaguchi, I. Morita, Y. Tsuchida, Y. Mimura, K. Maeda, T. Saito, K. Watanabe, K. Imamura, R. Sugizaki, M. Suzuki, First demonstration of MC-EDFA-repeated SDM transmission of 40×128 Gbps PDM-QPSK signals per core over 6,160 km 7-core MCF, in *Proc. 38th Europ. Conf. Opt. Commun.* (ECOC'12), Amsterdam, The Netherlands (2012), paper Th.3.C.3
143. I. Ishida, T. Akamatsu, Z. Wang, Y. Sasaki, K. Takenaga, S. Matsuo, Possibility of stack and draw process as fabrication technology for multi-core, in *Opt. Fiber Commun. Conf. and Nat. Fiber Opt. Eng. Conf.* (OFC/NFOEC'13), Anaheim, CA, USA (2013), Techn. Digest, paper OTu2G.1
144. J. Sakaguchi, W. Klaus, B.J. Puttnam, J.-M.D. Mendinueta, Y. Awaji, N. Wada, Y. Tsuchida, K. Maeda, M. Tadakuma, K. Imamura, R. Sugizaki, T. Kobayashi, Y. Totori, M. Watanabe, R.V. Jensen, 19-Core MCF transmission system using EDFA with shared core pumping coupled in free-space optics, in *Proc. 39th Europ. Conf. Opt. Commun.* (ECOC'13), London, UK (2013), paper Th.1.C.6
145. K. Igarashi, T. Tsuritani, I. Morita, Y. Tsuchida, K. Maeda, M. Tadakuma, T. Saito, K. Watanabe, K. Imamura, R. Sugizaki, M. Suzuki, 1.03 Ebps km super-Nyquist-WDM transmission over 7,326 km seven-core fiber, in *Proc. 39th Europ. Conf. Opt. Commun.* (ECOC'13), London, UK (2013), paper PD3.E.3
146. I. Ishida, Y. Amma, K. Hirakawa, H. Uemura, Y. Sasaki, K. Takenaga, N. Itou, K. Osato, S. Matsuo, Multicore-fiber cable with core density of 6 cores/mm², in *Opt. Fiber Commun. Conf.* (OFC'14), San Francisco, CA, USA (2014), Techn. Digest, paper W4D.3
147. K. Takeshima, T. Tsuritani, Y. Tsuchida, K. Maeda, T. Saito, K. Watanabe, T. Sasa, K. Imamura, R. Sugizaki, K. Igarashi, I. Morita, M. Suzuki, 51.1-Tbit/s MCF transmission over 2,520 km using cladding pumped 7-core EDFAs, in *Opt. Fiber Commun. Conf.* (OFC'15), Los Angeles, CA, USA (2015), Techn. Digest, paper W3G.3
148. Y. Amma, Y. Sasaki, K. Takenaga, S. Matsuo, J. Tu, K. Saitoh, M. Koshihara, T. Morioka, Y. Miyamoto, High-density multicore fiber with heterogeneous core arrangement, in *Opt. Fiber Commun. Conf.* (OFC'15), Los Angeles, CA, USA (2015), Techn. Digest, paper Th4C.4
149. T. Matsui, T. Sakamoto, Y. Goto, K. Saito, K. Nakajima, F. Yamamoto, T. Kurashima, Design of 125 μ m cladding multi-core fiber with full-band compatibility to conventional single-mode fiber, in *Proc. 41st Europ. Conf. Opt. Commun.* (ECOC'15), Valencia, Spain (2015), paper We.1.4.5
150. M. Arikawa, T. Ito, E. Le Taillandier de Gabory, K. Fukuchi, Crosstalk reduction using bidirectional signal assignment over square lattice structure 16-core fiber for gradual upgrade of SSMF-based lines, in *Proc. 41st Europ. Conf. Opt. Commun.* (ECOC'15), Valencia, Spain (2015), paper Th.1.2.3
151. B.J. Puttnam, R.S. Luís, W. Klaus, J. Sakaguchi, J.-M. Delgado Mendinueta, Y. Awaji, N. Wada, Y. Tamura, T. Hayashi, M. Hirano, J. Marcianti, 2.15 Pbps transmission using a 22 core homogeneous single-mode multi-core fiber and wideband optical comb, in *Proc. 41st Europ. Conf. Opt. Commun.* (ECOC'15), Valencia, Spain (2015), paper PDP3.1
152. R. Ryf, S. Randel, A.H. Gnauck, C. Bolle, R.-J. Essiambre, P.J. Winzer, D.W. Peckham, A. McCurdy, R. Lingle Jr., Space-division multiplexing over 10 km of three-mode fiber using coherent 6×6 MIMO processing, in *Opt. Fiber Commun. Conf. and Nat. Fiber Opt. Eng. Conf.* (OFC/NFOEC'11), Los Angeles, CA, USA (2011), Techn. Digest, paper PDPB10
153. R. Ryf, S. Randel, M.A. Mestre, C. Schmidt, A.H. Gnauck, R.-J. Essiambre, P.J. Winzer, R. Delbue, P. Pupalais, A. Sureka, Y. Sun, X. Jiang, A.H. McCurdy, D.W. Peckham, R. Lingle Jr., 209 km single-span mode- and wavelength-multiplexed transmission over hybrid few-mode fiber, in *Proc. 38th Europ. Conf. Opt. Commun.* (ECOC'12), Amsterdam, The Netherlands (2012), paper Tu.1.C.1
154. V.A.J.M. Sleiffer, Y. Jung, V. Veljanovski, R.G.H. van Uden, M. Kuschnerov, Q. Kang, L. Grüner-Nielsen, Y. Sun, D.J. Richardson, S. Alam, F. Poletti, J.K. Sahu, A. Dhar, H. Chen, B. Inan, A.M.J. Koonen, B. Corbett, R. Winfield, A.D. Ellis, H. de Waardt, 73.7 Tbps ($96 \times 3 \times 256$ Gbps) mode-division-multiplexed DP-16QAM transmission with inline MM-EDFA,

- in *Proc. 38th Europ. Conf. Opt. Commun.* (ECOC'12), Amsterdam, The Netherlands (2012), paper Th.3.C.4
155. T. Mori, T. Sakamoto, M. Wada, T. Yamamoto, F. Yamamoto, Low DMD four LP mode transmission fiber for wide-band WDM-MIMO system, in *Opt. Fiber Commun. Conf. and Nat. Fiber Opt. Eng. Conf.* (OFC/NFOEC'13), Anaheim, CA, USA (2013), Techn. Digest, paper OTh3K.1
 156. E. Ip, M.-J. Li, K. Bennett, Y.-K. Huang, A. Tanaka, A. Korolev, K. Koreshkov, W. Wood, E. Mateo, J. Hu, Y. Yano, $146\lambda \times 6 \times 19$ -Gbaud wavelength- and mode-division multiplexed transmission over 10×50 -km spans of few-mode fiber with a gain-equalized few-mode EDFA, in *Opt. Fiber Commun. Conf. and Nat. Fiber Opt. Eng. Conf.* (OFC/NFOEC'13), Anaheim, CA, USA (2013), Techn. Digest, paper PDP5A.2
 157. R. Ryf, S. Randel, N.K. Fontaine, X. Palou, E. Burrows, S. Corteselli, S. Chandrasekhar, A.H. Gnauck, C. Xie, R.-J. Essiambre, P.J. Winzer, R. Delbue, P. Pupalaiakis, A. Sureka, Y. Sun, L. Grüner-Nielsen, R.V. Jensen, R. Lingle Jr., 708 km combined WDM/SDM transmission over few-mode fiber supporting 12 spatial and polarization modes, in *Proc. 39th Europ. Conf. Opt. Commun.* (ECOC'13), London, UK (2013), paper We.2.D.1
 158. P. Sillard, D. Molin, M. Bigot-Astruc, H. Maerten, D. Van Ras, F. Achten, Low-DMGD 6-LP-mode fiber, in *Opt. Fiber Commun. Conf.* (OFC'14), San Francisco, CA, USA (2014), Techn. Digest, paper M3F.2
 159. T. Mori, T. Sakamoto, M. Wada, T. Yamamoto, F. Yamamoto, Six-LP-mode transmission fiber with DMD of less than 70 ps/km over C + L band, in *Opt. Fiber Commun. Conf.* (OFC'14), San Francisco, CA, USA (2014), Techn. Digest, paper M3F.3
 160. Y. Chen, A. Lobato, Y. Jung, H. Chen, R.V. Jensen, Y. Sun, L. Grüner-Nielsen, D.J. Richardson, V.A.J.M. Sleiffer, M. Kuschnerov, N.K. Fontaine, R. Ryf, I.P. Giles, R. Chen, V. Carcia-Munoz, A.M.J. Koonen, B. Lankl, N. Hanik, 41.6 Tbps C-band SDM OFDM transmission through 12 spatial and polarization modes over 74.17 km few mode fiber, in *Opt. Fiber Commun. Conf.* (OFC'14), San Francisco, CA, USA (2014), Techn. Digest, paper Mo.3.3.3
 161. R. Ryf, N.K. Fontaine, M. Montoliu, S. Randel, B. Ercan, H. Chen, S. Chandrasekhar, A.H. Gnauck, S.G. Leon-Saval, J. Bland-Hawthorn, J.R. Salazar-Gil, Y. Sun, R. Lingle Jr., Photonic lantern-based mode multiplexers for few-mode-fiber transmission, in *Opt. Fiber Commun. Conf.* (OFC'14), San Francisco, CA, USA (2014), Techn. Digest, paper W4J.2
 162. L. Grüner-Nielsen, Y. Sun, R.V. Jensen, J.W. Nicholson, R. Lingle Jr., Splicing of few mode fibers, in *Proc. 40th Europ. Conf. Opt. Commun.* (ECOC'14), Cannes, France (2014), paper P.1.15
 163. P. Sillard, D. Molin, M. Bigot-Astruc, K. de Jongh, F. Achten, Low-differential-mode-group-delay 9-LP-mode fiber, in *Opt. Fiber Commun. Conf.* (OFC'15), Los Angeles, CA, USA (2015), Techn. Digest, paper M2C.2
 164. N.K. Fontaine, R. Ryf, H. Chen, A. Velazquez-Benitez, J.E. Antonio-Lopez, R. Amezcua-Correa, B. Guan, B. Ercan, R.P. Scott, S.J. Ben Yoo, L. Grüner-Nielsen, Y. Sun, R. Lingle Jr., 30×30 MIMO transmission over 15 spatial modes, in *Opt. Fiber Commun. Conf.* (OFC'15), Los Angeles, CA, USA (2015), Techn. Digest, paper Th5C.1
 165. R. Ryf, N.K. Fontaine, H. Chen, A.H. Gnauck, Y. Jung, Q. Kang, J.K. Sahu, S.U. Alam, D.J. Richardson, Y. Sun, X. Jiang, L. Grüner-Nielsen, R.V. Jensen, R. Lingle Jr., 72 Tbps transmission over 179-km all-fiber 6-mode span with two cladding pumped in-line amplifiers, in *Proc. 41st Europ. Conf. Opt. Commun.* (ECOC'15), Valencia, Spain (2015), paper Tu.3.2.2
 166. R. Ryf, M. Esmaelpour, N.K. Fontaine, H. Chen, A.H. Gnauck, R.-J. Essiambre, J. Toulouse, Y. Sun, R. Lingle Jr., Distributed Raman amplification based transmission over 1050-km few-mode fiber, in *Proc. 41st Europ. Conf. Opt. Commun.* (ECOC'15), Valencia, Spain (2015), paper Tu.3.2.3
 167. R. Ryf, H. Chen, N.K. Fontaine, A.M. Velazquez-Benitez, J. Antonio-Lopez, C. Jin, B. Huang, M. Bigot-Astruc, D. Molin, F. Achten, P. Sillard, R. Amezcua-Correa, 10-Mode mode-multiplexed transmission over 125 km single-span multimode fiber, in *Proc. 41st Europ. Conf. Opt. Commun.* (ECOC'15), Valencia, Spain (2015), paper PDP3.3

168. T. Mori, T. Sakamoto, T. Yamamoto, F. Yamamoto, Wideband WDM coherent optical MIMO transmission over 50 μm -core GI-MMF using selective mode excitation technique. *Opt. Fiber Technol.* **19**, 658–664 (2013)
169. R. Ryf, N.K. Fontaine, H. Chen, B. Guan, B. Huang, M. Esmaeelpour, A.H. Gnauck, S. Randel, S.J.B. Yoo, A.M.J. Koonen, R. Shubochkin, Y. Sun, R. Lingle Jr., Mode-multiplexed transmission over conventional graded-index multimode fibers. *Opt. Express* **23**, 235–246 (2015)
170. P. Sillard, D. Molin, M. Bigot-Astruc, A. Amezcua-Correa, K. de Jongh, F. Achten, 50 μm multimode fibers for mode division multiplexing, in *Proc. 41st Europ. Conf. Opt. Commun. (ECOC'15)*, Valencia, Spain (2015), paper Mo.4.1.2
171. J. Xu, J. Kristian Lyngsø, L. Leick, J. Carpenter, T.D. Wilkinson, C. Peucheret, Mode division multiplexing exploring hollow-core photonic bandgap fibers, in *Proc. 15th Internat. Conf. Transparent Optical Netw. (ICTON)*, Cartagena, Spain (2013), paper We.B6.2
172. Y. Jung, V.A.J.M. Sleiffer, N. Baddela, M.N. Petrovich, J.R. Hayes, N.V. Wheeler, D.R. Gray, E. NumkamFokoua, J.P. Wooler, N.H.-L. Wong, F. Parmigiani, S.U. Alam, J. Surof, M. Kuschnerov, V. Veljanovski, H. de Waardt, F. Poletti, D.J. Richardson, First demonstration of a broadband 37-cell hollow core photonic bandgap fiber and its application to high capacity mode division multiplexing, in *Opt. Fiber Commun. Conf. (OFC'14)*, San Francisco, CA, USA (2014), Techn. Digest, paper PDP5A.3
173. N.K. Fontaine, R. Ryf, M. Hirano, T. Sasaki, Experimental investigation of crosstalk, accumulation in a ring-core fiber, in *Proc. IEEE Summer Topical Meeting 2013*, Waikoloa, Hawaii, USA (2013), paper TuC4.2
174. C. Xia, N. Bai, I. Ozdur, X. Zhou, G. Li, Supermodes for optical transmission. *Opt. Express* **19**, 16653–16664 (2011)
175. R. Ryf, R.-J. Essiambre, S. Randel, A.H. Gnauck, P.J. Winzer, T. Hayashi, T. Taru, T. Sasaki, MIMO-based crosstalk suppression in spatially multiplexed 3×56 Gbps PDM-QPSK signals for strongly coupled three-core fiber. *IEEE Photonics Technol. Lett.* **23**, 1469–1471 (2011)
176. R. Ryf, R.-J. Essiambre, A.H. Gnauck, S. Randel, M.A. Mestre, C. Schmidt, P.J. Winzer, R. Delbue, P. Pupalais, A. Sureka, T. Hayashi, T. Taru, T. Sasaki, Space-division multiplexed transmission over 4200 km of 3-core micro-structured fiber, in *Opt. Fiber Commun. Conf. and Nat. Fiber Opt. Eng. Conf. (OFC/NFOEC'12)*, Los Angeles, CA, USA (2012), Techn. Digest, paper PDP5C.2
177. S.O. Arik, J.M. Khan, Coupled-core multi-core fibers for spatial multiplexing. *IEEE Photonics Technol. Lett.* **25**, 2054–2057 (2013)
178. R. Ryf, N.K. Fontaine, B. Guan, R.-J. Essiambre, S. Randel, A.H. Gnauck, S. Chandrasekhar, A. Adamiecki, G. Raybon, B. Ercan, R.P. Scott, S.J. Ben Yoo, T. Hayashi, T. Nagashima, T. Sasaki, 1705 km transmission over coupled-core fiber supporting 6 spatial modes, in *Proc. 40th Europ. Conf. Opt. Commun. (ECOC'14)*, Cannes, France (2014), paper PD.3.2
179. H. Chen, N.K. Fontaine, R. Ryf, R.-J. Essiambre, L. Wang, Y. Messaddeq, S. LaRochelle, T. Hayashi, T. Nagashima, T. Sasaki, Transmission over coupled six-core fiber with two in-line cladding-pumped six-core EDFAs, in *Proc. 41st Europ. Conf. Opt. Commun. (ECOC'15)*, Valencia, Spain (2015), paper We.1.4.2
180. T. Sakamoto, T. Mori, T. Yamamoto, M. Wada, F. Yamamoto, Moderately coupled 125 μm cladding 2 LP-mode 6-core fiber for realizing low MIMO-DSP and high spatial density, in *Proc. 40th Europ. Conf. Opt. Commun. (ECOC'14)*, Cannes, France (2014), paper Tu.4.1.3
181. C. Xia, R. Amezcua-Correa, N. Bai, E. Antonio-Lopez, D. May-Arrijoa, A. Schulzgen, M. Richardson, J. Liñares, C. Montero, E. Mateo, X. Zhou, G. Li, Low-crosstalk few-mode multi-core fiber for high-mode-density space-division multiplexing, in *Proc. 38th Europ. Conf. Opt. Commun. (ECOC'12)*, Amsterdam, The Netherlands (2012), paper Mo.1.F.5
182. Y. Sasaki, K. Takenaga, N. Guan, S. Matsuo, K. Saitoh, M. Koshiba, Large-effective-area uncoupled few-mode multi-core fiber, in *Proc. 38th Europ. Conf. Opt. Commun. (ECOC'12)*, Amsterdam, The Netherlands (2012), paper Tu.1.F.3
183. K. Takenaga, Y. Sasaki, N. Guan, S. Matsuo, M. Kasahara, K. Saitoh, Large effective-area few-mode multicore fiber. *IEEE Photonics Technol. Lett.* **24**, 1941–1944 (2012)

184. Y. Sasaki, Y. Amma, K. Takenaga, S. Matsuo, K. Saitoh, M. Koshihara, Trench-assisted low-crosstalk few-mode multicore fiber, in *Proc. 39th Europ. Conf. Opt. Commun.* (ECOC'13), London, UK (2013), paper Mo.3.A.5
185. T. Mizuno, T. Kobayashi, H. Takara, A. Sano, H. Kawakami, T. Nakagawa, Y. Miyamoto, Y. Abe, T. Goh, M. Oguma, T. Sakamoto, Y. Sasaki, I. Ishida, K. Takenaga, S. Matsuo, K. Saitoh, T. Morioka, 12-core \times 3-mode dense space division multiplexed transmission over 40 km employing multi-carrier signals with parallel MIMO equalization, in *Opt. Fiber Commun. Conf.* (OFC'14), San Francisco, CA, USA (2014), Techn. Digest, paper Th5B.2
186. R.G.H. van Uden, R. Amezcua Correa, E. Antonio-Lopez, F.M. Huijskens, G. Li, A. Schulzgen, H. de Waardt, A.M.J. Koonen, C.M. Okonkwo, 1 km hole-assisted few-mode multi-core fiber 32QAM WDM transmission, in *Opt. Fiber Commun. Conf.* (OFC'14), San Francisco, CA, USA (2014), Techn. Digest, paper Mo.3.3.4
187. J. Sakaguchi, W. Klaus, J.-M.D. Mendinueta, B.J. Puttnam, R.S. Luis, Y. Awaji, N. Wada, T. Hayashi, T. Nakanishi, T. Watanabe, Y. Kokubun, T. Takahata, T. Kobayashi, Realizing a 36-core, 3-mode fiber with 108 spatial channels, in *Opt. Fiber Commun. Conf.* (OFC'15), Los Angeles, CA, USA (2015), Techn. Digest, paper Th5C.2
188. K. Shibahara, T. Mizuno, H. Takara, A. Sano, H. Kawakami, D. Lee, Y. Miyamoto, H. Ono, M. Oguma, Y. Abe, T. Kobayashi, T. Matsui, R. Fukumoto, Y. Amma, T. Hosokawa, S. Matsuo, K. Saito, H. Nasu, T. Morioka, Dense SDM (12-core \times 3-mode) transmission over 527 km with 33.2 ns mode-dispersion employing low-complexity parallel MIMO frequency-domain equalization, in *Opt. Fiber Commun. Conf.* (OFC'15), Los Angeles, CA, USA (2015), Techn. Digest, paper Th5C.3
189. T. Sakamoto, T. Matsui, K. Saitoh, S. Saitoh, K. Takenaga, S. Matsuo, Y. Tobita, N. Hanzawa, K. Nakajima, F. Yamamoto, Few-mode multi-core fibre with highest core multiplicity factor, in *Proc. 41st Europ. Conf. Opt. Commun.* (ECOC'15), Valencia, Spain (2015), paper We.1.4.3
190. D. Soma, K. Igarashi, Y. Wakayama, K. Takeshima, Y. Kawaguchi, N. Yoshikane, T. Tsuritani, I. Morita, M. Suzuki, 2.05 Pbps super-Nyquist-WDM SDM transmission using 9.8 km 6-mode 19-core fiber in full C band, in *Proc. 41st Europ. Conf. Opt. Commun.* (ECOC'15), Valencia, Spain (2015), paper PDP3.2
191. R. Ryf, N.K. Fontaine, M. Montoliu, S. Randel, S.H. Chang, H. Chen, S. Chandrasekhar, A.H. Gnauck, R.-J. Essiambre, P.J. Winzer, T. Taru, T. Hayashi, T. Sasaki, Space-division multiplexed transmission over 3×3 coupled-core multicore fiber, in *Opt. Fiber Commun. Conf.* (OFC'14), San Francisco, CA, USA (2014), Techn. Digest, paper Tu2J.4
192. P.J. Winzer, Spatial multiplexing: The next frontier in network capacity scaling, in *Proc. 39th Europ. Conf. Opt. Commun.* (ECOC'13), London, UK (2013), paper We.1.D.1

Pierre Sillard received the engineering diploma of the Ecole Nationale Supérieure des Télécommunications, Télécom ParisTech, in 1994, and the Ph.D. degree in Optics from the University of Paris VI in 1998, in collaboration with Thales Research & Technology, on the subject of non-linear interactions in laser resonators.

He has been working in the field of optical fibers since 1999, and he is now leading the Fiber Product R&D group in Prysmian Group in Haisnes, France. His research interests include modeling and characterizing optical fibers and systems.

He has published more than 200 papers and has been granted more than 65 patents. In 2004, he received the TR35 innovator award from MIT Technology Review for the design of fibers now being used in high-capacity communications. He is a member of the OSA and IEEE societies and he serves as a reviewer and committee member of several journals and conferences.

Denis Molin received the engineering diploma of the Ecole Supérieure d'Optique, now Institut d'Optique Graduate School, in 2000, and the Ph.D. degree in Optics from the University of Lille-1 in 2016 on multimode fibers for data networks.

He joined the System Design Team in Corvis-Algety the same year and the Fiber Optic R&D Unit in Alcatel in 2001 where he worked on modeling long-haul WDM transmissions. He is now with Prysmian Group, Marcoussis, France, working on single-mode & multi-mode fibers and systems modeling for communications and data applications. His research interests include modeling and characterizing optical fibers and system with a particular interest on multimode fibers and data communications. He supports new developments in International Standardization bodies. He has authored and co-authored more than 60 papers and holds more than 40 patents.

Chapter 3

Laser Components

Norbert Grote, Martin Möhrle, and Markus Ortsiefer

Abstract The chapter covers InP based laser diodes (1.3–1.6 μm wavelength range) deployed as transmitter devices in today's optical communication systems. Only discrete directly modulated devices are considered in this chapter which is followed by two other laser related articles dealing specifically with ultra-fast and wavelength-tunable devices. In the first part a description of basic laser structures and technology, of relevant gain materials and their impact on lasing properties is given. This is followed by summarizing fundamental characteristics of Fabry-Pérot devices. Recent achievements on the derivative semiconductor optical amplifiers (SOA) will then be addressed which are no longer treated in a dedicated chapter in this re-edited book. The second part is devoted to single-wavelength lasers focusing on design aspects and various implementations. Essentially distributed feedback (DFB) devices are treated but other options like so-called “discrete mode” laser diodes will also be outlined. The third part of this chapter is devoted to surface emitting laser diodes, mainly vertical cavity surface emitting lasers (VCSEL) are also including horizontal cavity DFB structures designed for surface emission.

3.1 Introduction

Semiconductor laser diodes used as optical transmitters represent one of the principal components in any fiber based communication system. Laser diodes are used because these devices can be directly current modulated with modulation rates of up to several tens of Gb/s being achievable today, they are extremely small in size

N. Grote (✉) · M. Möhrle

Photonic Components Dept., Fraunhofer Institute for Telecommunications,
Heinrich-Hertz-Institute, Einsteinufer 37, 10587 Berlin, Germany
e-mail: norbert.grote@hhi.fraunhofer.de

M. Möhrle

e-mail: martin.moehrle@hhi.fraunhofer.de

M. Ortsiefer

VERTILAS GmbH, Daimlerstrasse 11d, 85748 Garching, Germany
e-mail: ortsiefer@vertilas.com

and power efficient, and can be made at very low cost due to the use of semiconductor wafer batch fabrication. Nowadays market prices of state-of-the-art Fabry-Perot (multi-wavelength) laser chips are well below 1 US\$ in high volumes, and even the more demanding single-wavelength diodes have reached the lower single-digit US\$ range. The first functioning semiconductor laser devices came into existence as early as in 1962 [1, 2], and a major breakthrough was achieved in 1969 [3, 4] by demonstrating a heterojunction design which was honored recently with the year 2000 Nobel prize. Those laser diodes were based on Ga(Al)As generating laser emission in the wavelength window around 850 nm. This spectral range is still prevailing for short reach (<300 m) data communications (data centers, local area and storage area networks, office communication, etc.) using multimode fibers (MMF) and GaAs based laser diodes in the form of VCSELs (vertical cavity surface emitting laser). In the telecommunications arena and for longer datacom transmission distances, however, the 1.3–1.6 μm infrared wavelength range is dominating due to optimal transmission properties (attenuation, dispersion) of the optical fiber, as outlined in the previous chapter. Laser diodes covering this spectral range are made on InP, rather than on GaAs, more specifically using the compounds InGaAsP and InGaAlAs. Development of InGaAsP/InP lasers commenced already in the mid of the mid-1970's, for example [5, 6]. Although more than 40 years have passed since then, development efforts are continuously strong worldwide targeting the optimization of specific laser parameters to meet enhanced and new systems requirements without compromising the wide range of other relevant properties. Wavelength tunability, enhancement of modulation capability, and uncooled operation up to 85 °C and above, and lower power consumption are in the focus of current developments, not to forget the never ending call for cost reduction.

In this article, we focus on laser diodes for the “long-wavelength” range (1.3–1.6 μm). In the first part some basics including material aspects and device structures will be addressed. A more in-depth description of the fundamentals of laser diodes may be found in distinct text books, for example [7]. In the second part of this chapter, a review of single-mode laser diodes will be presented. Finally, we will deal with surface-emitting lasers, mainly VCSELs but also variants building on horizontal-cavity structures. Two special topics of high relevance, namely wavelength-tunable and very high bit-rate laser devices, will be treated in the subsequent separate Chaps. 4 and 5.

3.2 Materials for “Long-Wavelength” Laser Diodes

To create semiconductor laser diodes two basic requirements have to be fulfilled: The semiconductor needs to possess a *direct* band structure to efficiently generate laser light, and allow the band gap energy to be adjusted to the desired emission wavelength. For the wavelength range of interest here, the material of choice are the III–V semiconductor InP and the related quaternary compounds InGaAsP and InGaAlAs illustrated in the “bandgap vs lattice constant” diagram in Fig. 3.1. The

Fig. 3.1 Band gap vs lattice constant diagram for “long wavelength” III–V compound semiconductors (*solid line*: direct bandgap; *broken line*: indirect bandgap; *dotted vertical line* between InGaAs and InP/InAlAs: lattice-matched quaternary compositions

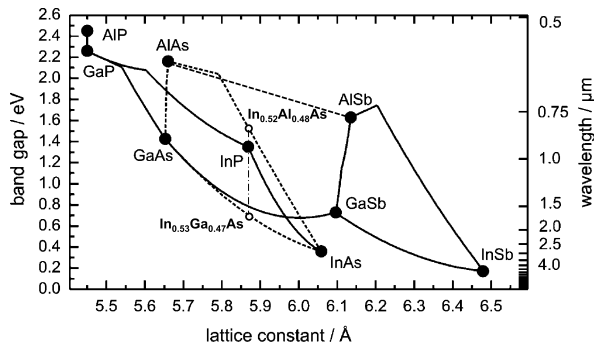
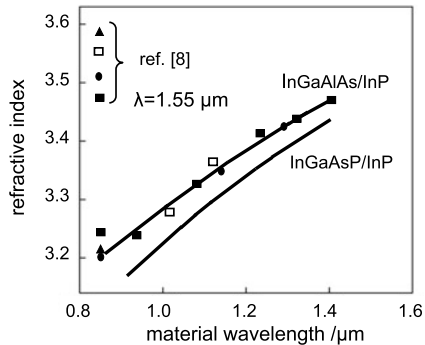


Fig. 3.2 Dependence of optical refraction index on material composition of InGaAsP and InGaAlAs lattice-matched to InP at 1.55 μm wavelength (taken from [8] and references therein; relationship for InGaAsP after [9])



binary semiconductors, such as GaAs and InP, are characterized by a naturally given band gap and a fixed lattice constant. By mixing binaries, i.e. by replacing a fraction of the group (III) and/or group (V) elements, generally any ternary and quaternary composition can be adjusted within the area spanned between the binaries concerned. In practice, such composites are deposited as crystalline layers onto a binary substrate wafer utilizing well established epitaxial techniques, and to achieve layers of high crystal quality virtually perfect lattice matching (<0.1% deviation) is required.

Hence, starting from InP, only layers can be stacked that have a composition which is defined by a vertical line through the InP point. Thus restricted, only those InGaAsP materials covering the compositional range between InP and the ternary end constituent In_{0.53}Ga_{0.47}As can be used, associated with a band gap span from 1.35 eV to 0.75 eV, or—in terms of wavelengths—from 920 nm to 1650 nm. Another InP related material family is InGaAlAs ranging from In_{0.52}Al_{0.48}As (1.48 eV, 840 nm) to again In_{0.53}Ga_{0.47}As. The optical index of refraction, which is a crucial parameter for optical waveguiding properties (Fig. 3.2), varies along with the band gap.

The indicated band gap values refer to room temperature but change with temperature, roughly by—in terms of wavelengths—0.5 nm/K. This means a variation of the order of 60 nm over the full temperature range of practical interest for fiber optics components, i.e. from -40 to +85 °C in the extreme case. This behavior has

substantial implications for the design and operation of laser diodes, in particular regarding wavelength stability and adjustment.

There is one important exception to the stringent lattice-match requirement: Below a certain layer thickness, which is dependent on the mismatch in lattice constant and referred to as the critical thickness, the layer may be elastically strained by purposely introducing lattice mismatch without affecting crystalline integrity. The figure-of-merit here is the “thickness \times strain” product which as a rule of thumb should not exceed the critical value of around 20 nm%, with the strain, ε , representing the percentage of relative lattice-mismatch to the unstrained materials. The lattice deformation is associated with a modification of the band structure which is beneficially exploited in strained multi-quantum well layer structures widely employed as the active medium in laser diodes today.

3.3 Laser Diode Structures

3.3.1 Layer Structure

To build a real laser diode, the lasing layer is embedded between layers of higher band gap and thus lower refractive index. In this way an optical waveguide is formed in which the light traveling back and forth within the laser cavity is vertically confined. Concurrently, the injected carriers interact with the optical wave to generate stimulated light emission. Such a layer stack design is called a double-heterostructure comprised of inner quaternary layers and n- and p-doped InP cladding layers to create a pn-diode. The quaternary layers may also be lightly doped. By applying an electrical forward current to the diode hole and electron carriers are injected from the doped InP layers into the active layer where they are electrically confined and converted into photons by recombination. Once the carrier densities have reached critical levels to yield so-called population inversion in the conduction and valence band light amplification can occur by the process of stimulated emission. A basic layer structure is sketched in Fig. 3.3.

The highly doped InGaAs cap layer facilitates formation of ohmic p-contacts of very-low resistivity ($\sim 10^{-6} \Omega\text{cm}^2$) which is essential for achieving high modulation bandwidth and for minimizing heat dissipation. Additional layers may be inserted for performance or fabrication reasons (e.g., etch stop layer). Altogether, advanced lasers may contain even more than 20 different layers yielding a total thickness of about 3 to $>5 \mu\text{m}$. Mainly n-type InP substrates are used but inverted designs building on a p-doped substrate (Zn doped) are being employed as well [10]. Substrate wafers of 2- and 3-inch diameter are common.

3.3.2 Lateral Structure

Whereas in the vertical direction the laser waveguide is defined by the layer stack, structural measures have to be taken that define the waveguide in the lateral direction

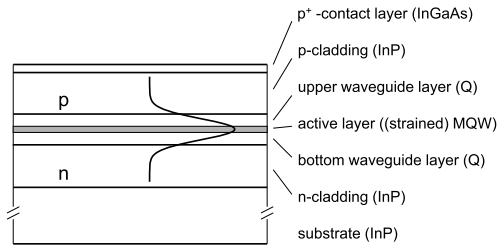


Fig. 3.3 Basic layer structure of an InP based double-heterostructure laser diode; inserted profile schematically indicating vertical intensity distribution of laser light propagating along the laser cavity (*MQW* multi quantum well (refer to Sect. 3.4); *Q* quaternary composition)

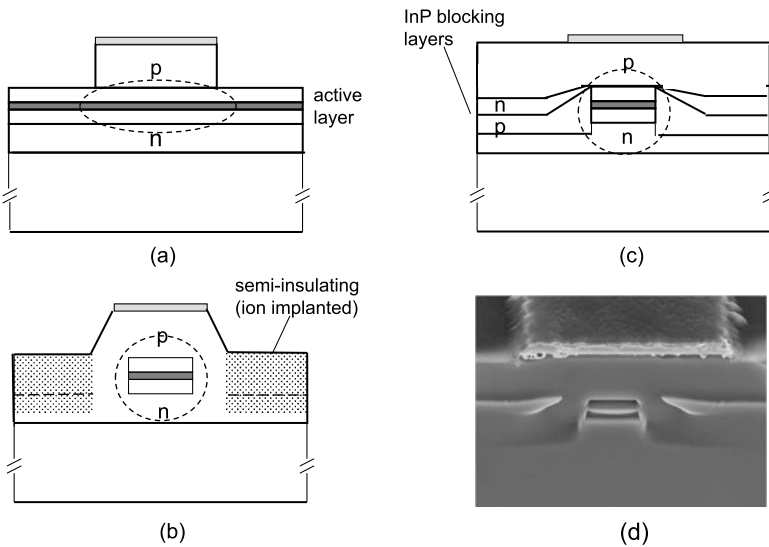


Fig. 3.4 Schematic cross-section of basic configurations of InP laser diodes: (a) ridge waveguide (RW); (b) buried ridge (BR) structure; (c) buried heterostructure (BH) with pn current blocking layers; (d) scanning electron microscopy (SEM) image of real BH cross-section; *dotted ellipse* and *circle* illustrate near-field profile (not drawn to scale) of laser beam

too. Simultaneously carrier injection needs to be efficiently restricted to this active region which is typically $\sim 2 \mu\text{m}$ wide to guarantee monomode waveguiding. In actual lasers two fundamentally different designs are used (Fig. 3.4(a)–(d)): (a) ridge waveguide (RW) and (b) buried-heterostructure (BH). In the former, a mesa ridge is etched into the upper layers along the laser cavity resulting in a lower effective refractive index outside the ridge and thus lateral optical confinement. The p-contact is applied to the ridge area, thereby confining the current flow. Because of lateral current spreading and unavoidable lateral diffusion of carriers inside the active layer, current-dependent broadening of the lasing region occurs, and this outdiffusion effect causes a certain portion of carriers to no longer contribute to lasing.

In BH-type laser diodes the active region is fully surrounded by InP thus creating a well-defined buried waveguide. This is achieved by a special selective regrowth process of InP layers at both sides of the previously etched active stripe. Because these layers are n-p doped to provide a built-in reverse-biased junction, current flow is effectively blocked such that it is completely funneled into the active stripe. Out-diffusion of carriers is suppressed by the energetic barrier between the lower band gap of the active material and the higher band gap of the adjacent InP. As opposed to the RW design, the upper InP cladding layer extends over the full structure. Therefore the p-contact can be made significantly wider implying lower series resistance.

While BH lasers with pn current-blocking layers are the most common, there are other variants that are being successfully used. Instead of pn blocking layers semi-insulating InP has been employed the high resistivity ($\sim 10^8 \Omega \text{ cm}$ at room temperature) of which is achieved by doping with Fe (conc. $\sim 10^{17} \text{ cm}^{-3}$). Such semi-insulating layers are advantageous regarding parasitic capacitance and therefore for high-speed laser devices. However, the specific resistivity decreases by almost three orders of magnitude between 20 °C and 85 °C, and Fe diffusion effects may raise reliability concerns. Another version is the so-called buried ridge stripe laser (BRS) which may be considered a hybrid of the RW and BH structure. Here the etched laser ridge is conformally overgrown with the p-InP cladding layer. Whereas most of this layer is rendered electrically insulating by means of ion implantation, parasitic current flow through the small remaining conductive InP regions adjacent to the active part is suppressed due to the higher built-in voltage at the InP pn junction.

Generally, the overall performance of BH-type lasers is superior to their RW counterparts: lower threshold current, better high-temperature output power and high-frequency characteristics, and almost circular rather than elliptical beam profile. Conversely, fabrication of RW lasers is less complex and hence more cost-efficient, thanks to fewer epitaxial steps. If high performance is required, the majority of the long-wavelength lasers made today are BH devices.

The RW design is, however, still preferred today when any Al containing layers are involved. This is particularly the case with 1.3 μm uncooled 10 Gb/s lasers widely deployed in datacom networks, as well as for even higher bit rate devices including externally modulated lasers, EML (see Chap. 4), the latter benefiting from the better electroabsorption behavior of InGaAlAs structures. The issue encountered with BH lasers is that InGaAlAs materials are prone to surface oxidation when exposed to air, an effect that is practically unavoidable in the fabrication process. Any residual oxide on the regrown BH interface may introduce nonradiative recombination centers and may be a potential source for lifetime issues with these lasers. There have been several approaches for fabricating InGaAlAs-BH laser diodes in the past: Among them is the use of narrow-stripe selective-area growth whereby the InGaAlAs MQW layers are buried in-situ with an InP layer [11]. Primarily, however, studies were focused on cleaning the oxidized surface with an etching gas inside the epitaxy reactor. Using such a measure achievement of reliable 1.3 μm devices was already claimed some ten years ago [12]. Apparently, however, that achievement did not yet lead to the technology maturity required for industrial commercialization, and only incremental progress was made since then. Only recently significant

progress was made employing in-situ thermal desorption as the presently preferred process. As a result low threshold currents and superior temperature dependence compared to InGaAsP-BH devices, and most importantly long-term stability of laser operation have been accomplished and published [13, 14].

3.4 Active Medium

In its simplest form the active medium of the laser diode consists of a bulk layer made of InGaAsP. Basically, the lasing transitions occur between the conduction and the valence band edges to generate laser wavelengths corresponding to the composition-dependent band gap, E_g . However such “bulk” lasers exhibit comparably high threshold currents because of moderate material gain resulting in low output power and poor high temperature performance.

InGaAsP and InGaAlAs Based Quantum-Well Layers More advantageous are the so-called quantum-well (QW) structures. In such a structure a thin well layer is sandwiched between two barrier layers of higher band gap. If the thickness of the embedded well layer is smaller than the De Broglie wavelength of the electrons and holes in this material, quantization of the electron and hole energy levels occurs. The optical transitions then take place between the quantized electron and hole levels in the QW rather than between the virtual conduction and valence band (Fig. 3.5). The well/barrier (QW) layer stack is either made of InGaAsP or InGaAlAs but mixed InGaAsP/InGaAlAs-QW’s have also been employed and have shown distinct benefits for enhancing the modulation bandwidth (30 GHz [15]). Typical well and barrier thicknesses range from 4–8 nm and from 7–15 nm for the well and barrier layer, respectively. The former thickness has a substantial effect on the emission wavelength

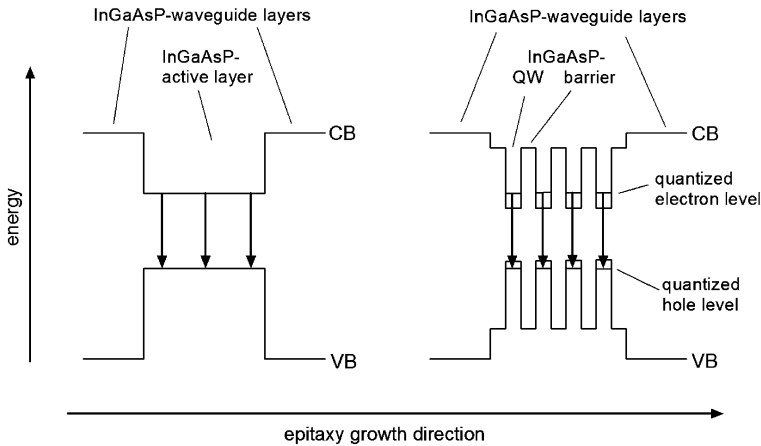


Fig. 3.5 Schematic energy band structure and corresponding optical transitions in a bulk (*left*) and a multi-quantum-well structure (*right*); CB = conduction band; VB = valence band

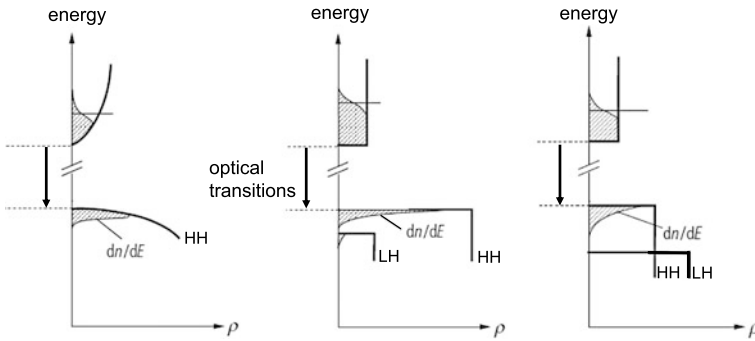


Fig. 3.6 Schematic representation of density of states and corresponding spectral carrier density dn/dE at transparency condition for (a) bulk, (b) lattice-matched quantum well structure, and (c) compressive strained quantum-well structure (LH = light hole; HH = heavy hole; n = carrier density; E = band energy)

which increases with decreasing well width. Commonly, a series of QW layers is vertically stacked to result in multi-quantum-well (MQW) structures.

Physically the advantage of QWs originates from the density of states. As a consequence of the quantized electron and hole states the respective energy dependence of the density of states in the conduction (CB) and valence band (VB) changes from parabolic curves in case of a bulk layer to step-like functions with QW-layers. If electrically pumped these carrier states are filled according to Boltzmann's thermal occupation statistics resulting in spectral carrier densities, dn/dE , as depicted in Fig. 3.6(a), (b). Due to the fact that, as a first approximation, the optical gain of semiconductor material for a specific optical transition is proportional to the product of the respective spectral carrier densities in the conduction and the valence band, it is obvious that QW-structures exhibit higher optical gain than their bulk counterparts (Fig. 3.6(b)). MQW-structures therefore show lower threshold current densities and accordingly superior temperature behavior and high-frequency characteristics.

Strained QWs By incorporating strain into the quantum wells the gain characteristics can be further improved considerably. Typical strain values used here range from -1.5% (tensile strain) to $+1.5\%$ (compressive strain). The main physical effect of strain in the quantum wells is the breakup of the energy degeneration of the heavy hole (HH) and light hole (LH) valence bands at $k = 0$ and corresponding significant changes in the shape of the respective in-plane energy dependence (Fig. 3.7). By applying compressive strain in the quantum well the in-plane HH mass is reduced and the density of states in the HH valence band decreased. Accordingly, band filling at the same electrical pumping level increases to yield lower threshold current densities and also higher differential gain values. Furthermore the effect of optical intraband losses due to absorption between the HH- and the split-off- (SO) valence band at the optical transition energy is substantially reduced. The benefit of strained layer MQW laser was recognized already at the end of the 1980's [16], and nowadays commercial laser diodes are commonly designed this way using compres-

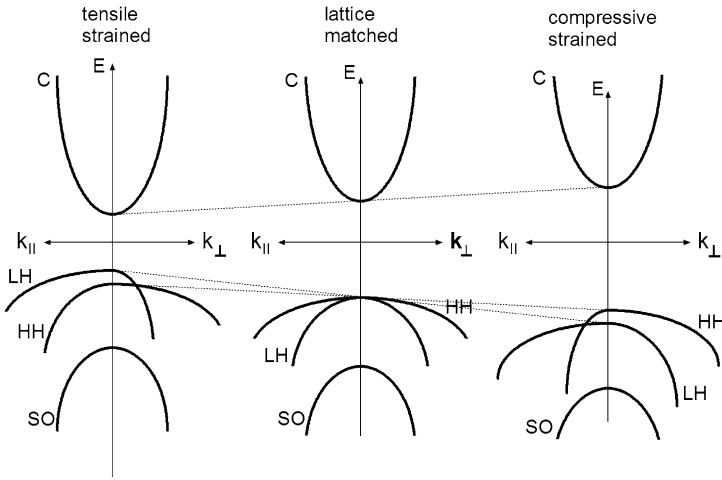


Fig. 3.7 Schematic energy band structure of strained InGaAsP-material on InP for the cases: tensile-strained (*left*), lattice-matched (*middle*), and compressive-strained (*right*)

sively strained wells in the MQW structures. 1% of compressive strain was discovered to be optimal [17]. The barrier layers may be tensile-strained for (partial) strain compensation to allow for implementing higher period MQW structures without exceeding the critical thickness. It should be noted that unstrained and compressively strained QWs strongly support TE polarized laser emission whereas tensile strain results in TM polarization. This behavior is exploited e.g. in semiconductor optical amplifiers (SOA) to balance TE/TM gain [18] and has to be taken into account with vertically emitting lasers where TE gain is needed.

For many applications the high-temperature performance of laser diodes is of crucial importance. Optical datacom links and fiber-to-the-home (FTTH) networks demand uncooled operation up to ambient temperatures of $+85^{\circ}\text{C}$. At higher temperatures the optical gain reduces due to thermal broadening of the energetic band filling distribution of the carrier resulting in smaller dn/dE values at a specific energy. Material inherent optical losses such as Auger absorption also increase with increasing temperature. Both effects lead to an increase of laser threshold current and a decrease of external power vs. current efficiency (slope efficiency) with increasing temperature. This is also true for the electrical pumping efficiency of an MQW-structure which tends to get lower at higher temperatures. This is because carriers may be thermally released from the well into the adjacent barrier and waveguide layers (referred to as carrier leakage). Due to their lower mass this mechanism mainly affects electron injection and is largely dependent on the conduction band discontinuity between well and barrier layer (Fig. 3.8). In InGaAsP/InGaAsP MQW-structures the conduction band discontinuity makes up only some 40% of the band gap difference, ΔE_g , of the layers involved. More advantageous with respect to this carrier overflow issue are InGaAlAs/InGaAlAs-MQWs and also the combination InGaAsP/InGaAlAs. Here the conduction band discontinuity amounts

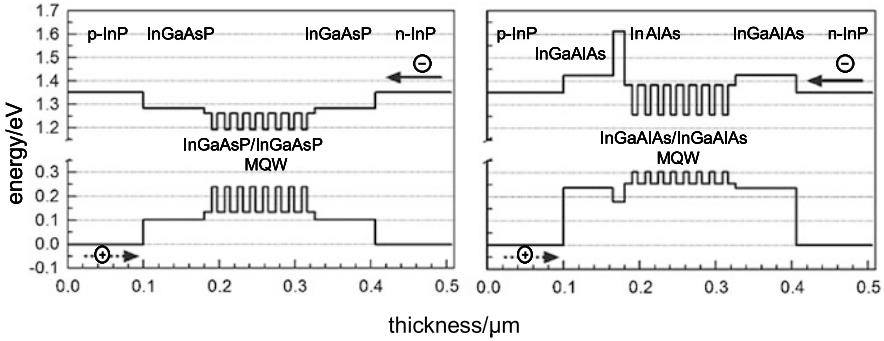


Fig. 3.8 Schematic energy band structure of a typical InGaAsP/InGaAsP- (*left*) and InGaAlAs/InGaAlAs-MQW-structure (*right*); quantization effects are not regarded for the sake of clarity. Note the “inverted” MQW band structure

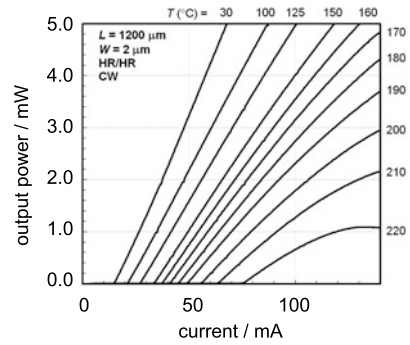
to 72% and 80% of ΔE_g , respectively. To further avoid electron leakage into the surrounding optical waveguide regions, an additional very thin InAlAs layer is often inserted into the laser layer stack to serve as an electron stopper.

Another advantage of the Al containing QW option is related to the modulation capability. The lower valence band discontinuity, in accordance with a higher conduction band discontinuity, of InGaAlAs/InGaAlAs-MQW-structures favors the hole transport in and out of the quantum wells allowing for significantly faster high-frequency response and thus larger modulation bandwidth compared to InGaAsP/InGaAsP. In accordance with this, a higher number of QWs can be uniformly pumped with holes. Uncooled 1.3 μm lasers with 10 Gb/s modulation capability which are receiving greatest attention today for 10 Gb/s datacom links are commonly relying on InGaAlAs technology (refer to Chap. 4).

Quantum Dots Quantum-dot (QD) materials have attracted a lot of attention in recent years as a novel active laser medium. QD are tiny pyramidal nanocrystals of about 10–20 nm footprint that are embedded in host layers. Formation of such QD structures is accomplished using highly lattice mismatched material (e.g. InAs) deposited at dedicated epitaxial growth conditions. QD feature δ -function-like density of states functions and thus much higher maximum gain values than QW structures. Ideally, they offer unique lasing properties, such as ultra-low threshold current density, high temperature stability, zero chirping, low noise, and ultrahigh frequency capability. In reality, however, the hitherto unavoidable size dispersion of the QD particles and their low total active volume to a great deal inhibit these features to become into effect.

The bulk of QD research has been devoted to GaAs based lasers and has produced a range of impressive single laser parameters, for instance threshold densities approaching 10 A cm^{-2} at $\lambda = 1.22 \mu\text{m}$ emission [19] and low temperature dependence of output power and threshold current, even negative To-values were observed [20]. A special feature of GaAs-based QD lasers is that their emission wavelengths can be shifted into the 1.3 μm range thus competing with

Fig. 3.9 Output characteristics of a GaAs based quantum dot laser emitting at 1300 nm. Laser operation is achieved even at $>220\text{ }^{\circ}\text{C}$



laser diodes on InP in this wavelength domain. In particular, such devices have shown laser operation at $>220\text{ }^{\circ}\text{C}$ (Fig. 3.9) [21] and are commercially available [www.qdlaser.com]. The same is true for such long-wavelength laser diodes specifically designed for high optical output power (pump lasers), emitting $>250\text{ mW}$ of fiber coupled power [www.innolume.com]. Regarding achievable laser wavelengths, however, 1300 nm appears to represent a practical upper limit for QD laser devices on GaAs; all attempts to significantly raise the emission wavelengths virtually failed.

On InP quantum-dot structures appear to be more challenging to grow, and quantum dashes rather than dots may be generated depending on growth conditions. The basic laser properties achieved until today generally do not outperform those of QW lasers. Among the apparent advantages of QD lasers, also encompassing so-called “quantum dash” material, is their improved noise behavior exploited in superior mode-locked lasers and all-optical clock recovery devices [22]. The QD size distribution resulting in an excessively broad gain spectrum has been exploited to create so-called comb lasers [23]. Specific advantages of QD based optical amplifiers have been well recognized. A unique future application may be as active medium for single photon sources for quantum cryptography applications. Despite these achievements QD technology may be claimed to enhance specific laser parameters but has not led to revolutionize semiconductor laser technology.

3.5 Fabry-Pérot Lasers

The simplest form of a laser diode is the Fabry-Pérot (FP) type. The laser cavity length is defined by cleaving, and the resonator mirrors are simply provided by the resulting crystal facets. Assuming an effective refraction index of the laser material of $n_l = 3.5$ the resulting mirror reflectivity against air ($n = 1$) amounts to some 30%. By applying optical reflection coatings to the facets other values can be easily adjusted. In particular, using a high-reflectivity (HR) coating at the back-facet and a low-reflectivity (LR) one at the front facet the optical output power from either facet can be made highly asymmetric. This way, compared to symmetrical mirror condi-

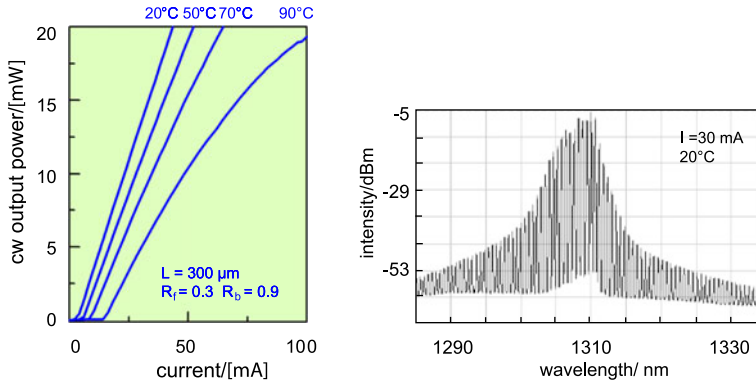


Fig. 3.10 Representative P – I curves (left) and emission spectrum (right) of an InGaAsP/InP MQW BH-FP laser. These characteristics are basically similar for any other emission wavelengths in the accessible 1.3–1.6 μm range (R_f , R_b = reflectivity at front and back facet, resp.)

tions, the optical power from the front-side may almost be doubled at the expense of the power from the backside. The latter is commonly exploited for optical power control by means of a monitor photodiode for which an only moderate intensity is sufficient.

For the reflection coating the wafer needs to be cleaved into bars several tens of which can be simultaneously coated by evaporation or (ion beam) sputtering, one run for either facet. Due to the large handling effort involved this process is rather costly. The coating films consist of periodic pairs of quarter-wavelength dielectric layers of different refractive index, e.g. SiO_2 and TiO_2 . Care has to be taken to minimize undesirable spilling on the surface and backside of the laser chips. Besides their optical function the coatings also serve to protect the facets against detrimental environmental effects. Following the coating process individual laser chips are singulated by a scribe-and-break process. To ease this process and the previous bar cleaving the full processed wafer is thinned to a thickness of only some 100 μm . The dimensions of a representative laser chip used for optical data transmission has a cavity length of 200–400 μm and a width of 250–400 μm , to some extent depending on the targeted bit rate.

A typical emission spectrum of an InP based FP laser diode is represented in Fig. 3.10. Since the gain spectrum of the laser material is fairly broad ($\gtrsim 30 \text{ nm}$ full width at half maximum) and the reflectivity of the facet mirrors practically wavelength independent, multiple emission wavelengths appear reflecting the longitudinal Eigen modes of the cavity.

Taking into account the chromatic dispersion of optical fibers the width of the emission spectrum is crucial for the maximum achievable transmission length at a given bit rate. A measure for the spectral width is the RMS-value which is a weighted quantity according to (3.1) considering all modes (i) with intensities p_i within the -20 dB range relative to the prevailing one (λ_c):

$$\lambda_{RMS} = \sqrt{\frac{M}{I}} = \sqrt{\frac{\sum p_i \cdot (\lambda_i - \lambda_c)^2}{\sum p_i}}; \quad \lambda_c = \frac{\sum p_i \cdot \lambda_i}{\sum p_i} \quad (3.1)$$

Typical RMS values are in the 1–2 nm range, with 3 nm representing a specified upper limit for e.g. 1.3 μm 10 Gb/s FP lasers at any operational condition.

Also shown in Fig. 3.10 are optical power vs current characteristics of a BH-FP transmitter laser diode at various temperatures. Threshold currents in the <5–10 mA region and optical output power well exceeding 40 mW are representative for those lasers at room temperature. Due to physical effects outlined in the previous section, the output power tends to significantly decrease with increasing temperature (T) whereas the threshold current (I_{th}) increases exponentially according to the empirical equation (3.2) (T_r = reference temperature, e.g. 20 °C):

$$I_{th}(T) = I_{th}(T_r) \exp[(T - T_r)/T_o] \quad (3.2)$$

Here T_o denotes the so-called characteristic temperature which for InP laser diodes comprising an active InGaAsP MQW region ranges from ~ 40 to ~ 60 K, depending on active volume, cavity length and facet reflectivity. Using InGaAlAs instead higher values up to some 80 K are achievable. These values hold for operation up to some 60 °C but tend to be lower beyond that point. Altogether, compared to Ga(Al)As the temperature behavior of InP based laser diodes proves to be substantially worse which largely impacts practical applications and has demanded large R&D efforts in recent years to accomplish uncooled laser operation.

As opposed to other laser systems the output beam of semiconductor lasers is highly divergent due to optical diffraction. The far-field of the laser beam is essentially determined by the design of the laser waveguide. RW lasers exhibit a pronounced elliptical intensity profile whereas the one of BH structures is fairly circular. The circular shape is highly desirable because it matches well to single mode fibers for the benefit of efficient optical coupling. The far-field pattern is often characterized by the divergence angle, taken as the full angle at half intensity maximum (FWHM angle). The following values (vertical \times lateral) may be considered representative for transmitter laser diodes: $45^\circ \times 20^\circ$ for RW, and $>30^\circ \times 30^\circ$ for BH structures.

To accomplish lower values so-called tapered lasers have been developed. A simple yet efficient method is to gradually narrow the active stripe in the lateral direction towards the front facet, as illustrated in Fig. 3.11(left). As optical guiding becomes weaker the more the waveguide narrows, the optical mode broadens accordingly to result in lower beam divergence. This design does not require any extra process steps but is applicable to BH structures only. Depending on the taper design the far-field angle can be nearly halved to angles down to as small as 15° by this means. An example is depicted in Fig. 3.11(right), with the FWHM angle amounting to some 20° in this case. In [24] it is shown that such a reduction leads to an improvement in coupling efficiency by 6 dB when directly butt-coupled to a flat SMF, comparing tapered and non-tapered laser diode of otherwise the same design. Other taper techniques that provide even smaller far-fields have been published but these involve a much higher fabrication complexity [25], including selective area growth [26]. It

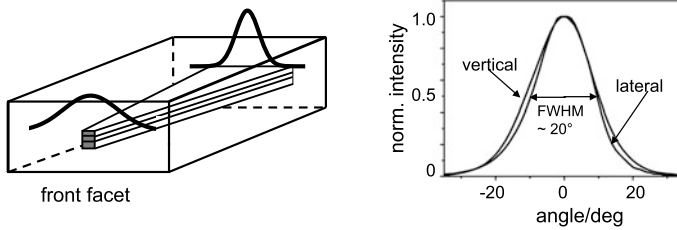


Fig. 3.11 Schematic representation of a tapered laser diode exploiting the concept of a laterally tapered active stripe leading to mode expansion due to weaker optical guidance (*left*); optical far-field pattern of a tapered BH laser in vertical and lateral direction (*right*): the value of 20° has to be compared to $>30^\circ$ for non-tapered structures

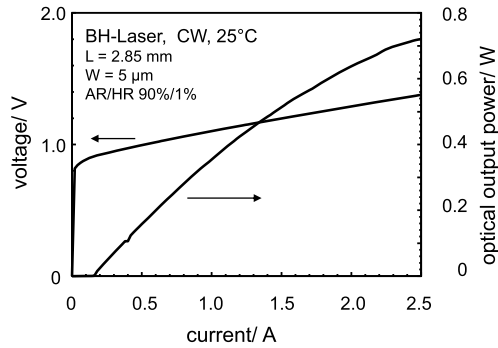
should be noted that VCSELs (see Sect. 3.8.1) inherently provide a circular-shaped far-field of low divergence angles which is one of their great advantages.

For efficient laser-fiber coupling tapered lasers are advantageous but not really mandatory because low-cost lenses can be used. They are, however, extremely helpful in hybrid integration technology where such diodes are to be directly coupled to optical waveguides without any beam shaping optics. In addition to the enhanced coupling efficiency they also provide larger alignment tolerances.

High-Power Laser Diodes The main application of FP lasers in optical communications has been for uplink transmission (1310 nm) in FTTH passive optical networks. Generally, the relative importance of FP lasers has been decreasing in recent years, mainly because of the spectral bandwidth related restrictions in transmission bit rate and distance, and because of the drastic price decay of their superior DFB counterparts (refer to Sect. 3.7). One prominent application area, however, is high-power laser diodes (HPLD), either in the form of (spatially) single mode or broad-area devices. The design of such laser diodes which are normally operated in cw (continuous wave) or pulsed mode is substantially different from transmitter lasers. Key to achieving high output power is to minimize series resistance and internal optical losses. The former issue mainly requires optimizing doping profiles and layer transitions whereas the latter aspect relates to the waveguide design. One has to bestow great care on keeping the portion of the optical intensity profile penetrating into the lossy p-doped waveguide region low. This leads to an asymmetric waveguide design associated with a relatively small confinement factor of the active region. To compensate for this the HPLDs are built excessively long ($\sim 2\text{--}3$ mm). Reported optical output power of 1460 nm HPLD lasers emitting in the fundamental mode has exceeded the 1 W level at room temperature [27].

Figure 3.12 shows the optical power/current curve of a BH-type HPLD delivering about 700 mW @ 1480 nm of ex-facet output power which may be regarded more as state-of-the-art. Such lasers are mainly used as pump sources for Er doped fiber amplifiers (pump wavelength: 1480 nm) and for Raman fiber amplification (14xx nm wavelengths) [28]. Besides that there are diverse applications outside the telecom field, e.g. for LIDAR (light detection and ranging). To date, leading edge

Fig. 3.12 Optical output power characteristic of a BH-HPLD emitting at 1480 nm (source: Fraunhofer HHI)



research results of single-emitter broad-area HPLDs in this spectral range, typically made with a stripe width of 100 μm , are characterized by ~ 6 W (at 18 A) of optical output power in cw operation [29] associated with maximum power conversion efficiency of $>40\%$, and on bar level (1 cm) by 50–72 W, depending on cooling conditions [30]. Commercial products typically deliver up to around 5 W.

3.6 Gain Elements and Optical Amplifiers

As discussed before, for making an active medium lase optical feedback is required which in the case of the FP lasers is provided by the (coated) front and rear facet serving as broadband mirrors. If these facets—or at least one of them—are non-reflecting and no other feedback mechanism present, the device only supports amplification of light. In this configuration the devices are called gain chips (GC) and semiconductor optical amplifiers (SOA), respectively. The former term is mainly used when such elements are employed as “gain provider” inside the cavity of more complex laser components, for example in wavelength-tunable lasers with external-cavity or hybridly integrated designs (refer to Chaps. 5 and 13). As SOAs they are capable of covering diverse functions: pre-amplification in conjunction with detectors; post-amplification (booster) in laser devices; in-line amplification in optical fiber links; on-chip amplification in photonic integrated circuits (see Chap. 16); optical switching, and functions exploiting non-linear effects, like frequency conversion.

It is obvious that there is no single established GC/SOA design, instead for each application an optimized structure will have to be adapted. For instance, whereas for laser related applications (GC, booster) only TE polarization needs to be taken into account most of the others demand coping with random polarizations and, hence, need polarization-insensitive active regions. Extremely low reflectivity of the AR coated facet(s) is a must for both GC and SOA devices. To this end, angled facets ($\sim 5^\circ \dots 9^\circ$ off) are commonly used making residual reflectivities down to the 0.01% range feasible. Tapered inputs and outputs, e.g. as sketched in Fig. 3.11, are beneficial to reduce fiber-coupling losses.

Semiconductor optical amplifiers have been extensively treated in a chapter on its own in the 1st edition of this book. Here we will limit ourselves to show current

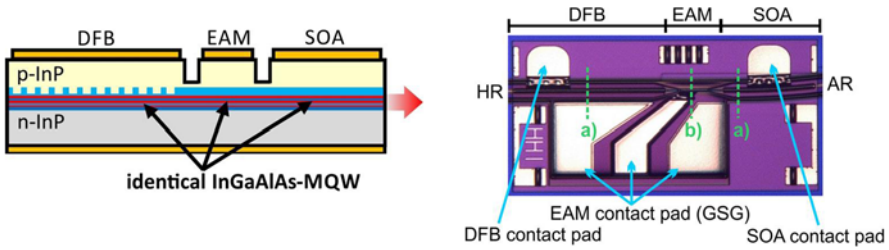


Fig. 3.13 Schematic structure and chip image of an electro-absorption modulated DFB laser (EML) with integrated booster SOA. The same active layer is used for the DFB, the modulator (EAM), and the SOA section. The AR coated output facet is tilted to enhance suppression of back-reflection [32]

trends and achievements. In earlier years, SOAs were believed to have the potential of becoming the standard linear optical amplifier component in fiber optical networks, superseding fiber optical amplifiers (see Chap. 12). However, until to date this did not happen because SOAs haven't reached comparable overall performance yet. However, in recent years application areas have emerged where GC/SOAs play a significant role, especially in the framework of photonic integration.

SOAs have been widely used in monolithic tunable lasers to boost the output power (e.g. [31]). More recently, this measure was also successfully adopted to electro-absorption modulated laser devices (EML). This type of transmitter (see Chap. 4) exhibits unrivaled speed capability but concurrent achievement of modulated optical output power proves to be challenging. Additional integration of a SOA section helps overcome this restriction. Starting from a fairly simple EML structure with identical active region a SOA section was added as a third section, again exploiting the same layer structure [32]. Figure 3.13 shows the scheme of such a device along with a photograph of a fabricated chip. Although SOA operation is often believed to be limited to data rates of 10–20 Gb/s region those SOA enhanced EMLs were capable of generating 56 Gb/s signals with fiber-coupled optical power of 7.8 dBm (1574 nm).

In recent years, WDM-PON systems have been the subject of comprehensive R&D activities worldwide. One of the concepts uses a so-called reflective-SOA (RSOA) as upstream “colourless” transmitter placed in each optical network unit (ONU) at the subscriber end. In these devices, the rear facet is HR-coated, and the input facet AR coated. Unmodulated light with an assigned wavelength is generated in the central office and sent to the respective ONU where it is amplified and reflected by the RSOA and concurrently encoded with the data of the subscriber. The main advantage of this scheme is that the wavelength generation and control is concentrated in the central office. RSOA devices that have been deployed could be readily modulated up to 2.5 Gb/s. Operation at 10 Gb/s was also demonstrated, however, at the expense of involving complex electronics as well as degraded performance [33]. This issue could be mitigated by introducing RSOAs that are integrated with an electro-absorption modulator (EAM, see also Chap. 4). In this component, named R-EAM-SOA, modulation takes place in the EAM section whereas

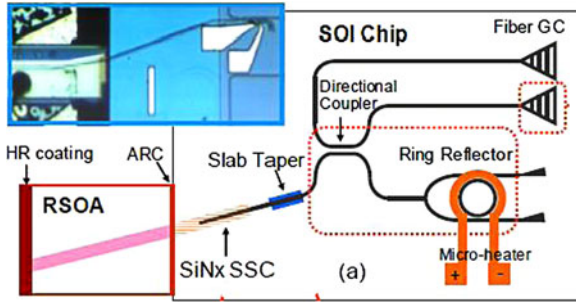


Fig. 3.14 Gain chip (here denoted as RSOA) hybridly integrated with a silicon-on-insulator (SOI) chip carrying a thermally tunable ring reflector to form a tunable laser (adapted from [35]). The 1 mm long angled (7°) gain chip is edge-coupled via a SiN_x spot-size converter (SSC) providing mode-matching between the SOI waveguide and the gain chip (note: GC in this image means grating coupler to fiber)

the SOA “only” acts as reflecting amplifier. High-quality 10 Gb/s operation with added functionalities was achieved using such “colourless” devices in WDM-PON systems [34].

Recently, various hybrid solutions have emerged for implementing tunable lasers. In those builds the gain chip forms the optical gain section, and its HR coated facet the back-mirror of the laser. Wavelength tunability is accomplished by tunable filter structures acting as the wavelength-selective front mirror. Various integrated waveguide platforms made of silicon-on-insulator (SOI), polymers, silica (SiO_2), and siliconoxynitride (SiON) have been used. For the tunable reflector both Bragg gratings and ring resonator structures have been applied. Figure 3.14 shows a tunable laser component based on SOI [35].

SOAs are also very attractive for fast optical switching devices because they not only offer large dynamic extinction ratio and switching speed in the nanosecond regime but concurrently allow for loss-less switching components or even components with built-in gain. In [36] a high-radix photonic switch array is shown which is comprised of SiN_x waveguides on Si with embedded flip-chipped angled SOA sub-arrays. In contrast to the device shown in Fig. 3.14 two-sided waveguide coupling is required in this hybridized concept. To meet the tight fabrication tolerance of the SOA lengths these devices were etched rather than cleaved thus guaranteeing lithographic dimensional precision. A monolithic 8×8 optical switch matrix has been reported in [37]. It incorporates 64 SOAs in its switching and features on-chip gain between 4 and 8 dB for all of the optical paths.

3.7 Single-Mode Laser Diodes

To cope with the effect of optical fiber dispersion which restricts achievable bit rate and transmission distance transmitter lasers are demanded that emit a single rather than multiple wavelengths. Typically residual side wavelengths need to be

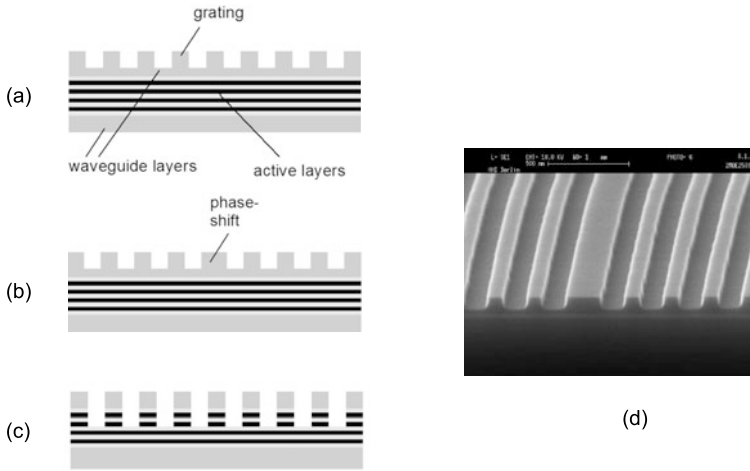


Fig. 3.15 Schematic views of DFB gratings: (a) uniform real index coupling, (b) index coupled grating with integrated $\lambda/4$ phase shift, and (c) complex coupling. Not drawn are the upper cladding layers which are grown on top for completing the laser structure. In part (d) a SEM image of a real $\lambda/4$ phase shifted DFB grating is depicted made by electron beam lithography and subsequent reactive ion etching. The grating period (1st order) for a 1550 nm DFB laser amounts to some 220 nm only

suppressed by at least 35 dB, commonly referred to as side-mode suppression ratio (SMSR). Various types of single mode laser diode devices are well known including distributed feedback (DFB) lasers, distributed Bragg reflector (DBR) lasers, external cavity lasers, coupled cavity lasers, discrete mode lasers (Sect. 3.7.2), and vertical cavity surface emitting lasers (VCSEL, Sect. 3.8.1).

3.7.1 Distributed Feedback (DFB) Lasers

DFB lasers the concept of which was already introduced some 45 years ago [38] have become the most established single-wavelength laser type. The key structural element of such lasers diodes is the so-called DFB grating providing a periodic change of the effective optical index of refraction along the laser cavity and thereby partial reflection at each index step (real or complex) to generate distributed optical feedback by constructive interference. This mechanism is strongly wavelength-selective to support longitudinal single mode operation. The DFB grating is realized by etching a “washboard”-like structure into the optical waveguide stack of the laser heterostructure (Fig. 3.15) which is subsequently overgrown with the p-cladding/contact layers. This way the DFB coupling relies on the periodic variation of the *real* part of the refractive index which represents the commonly used solution. Alternative embodiments, though less often applied, are gratings that are formed in the substrate, i.e. below the active region; in the sidewalls of the ridge of RW laser structures; and metal gratings placed aside this ridge [39].

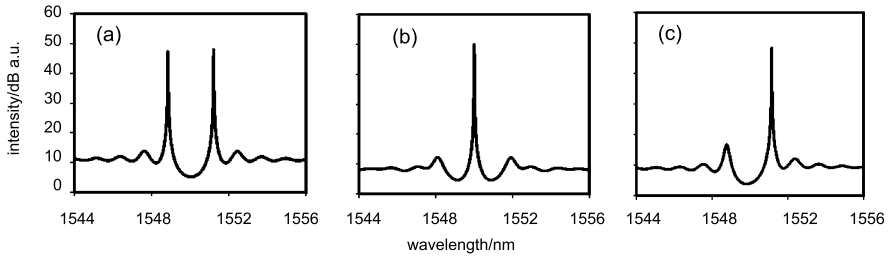


Fig. 3.16 Typical spectra at laser threshold (simulation) of an (a) uniformly index coupled, (b) $\lambda/4$ -phase shifted index coupled, and (c) complex coupled DFB structure with both facets AR-coated ($L = 300 \mu\text{m}$, $\kappa = 50 \text{ cm}^{-1}$)

In order to obtain longitudinal mode selection the grating period Λ has to fulfill the so-called Bragg condition:

$$\Lambda = \lambda \cdot m / (2 \cdot n_{eff}) \quad (3.3)$$

where Λ denotes the grating period, λ the emission wavelength, n_{eff} the effective refractive index of the laser structure, and m the grating order ($m = 1, 2, \dots$). 1st order gratings ($m = 1$) have the advantage that virtually all the light is reflected back and forth only in the direction of the waveguide thus resulting in very efficient optical feedback. In case of higher order gratings part of the light is vertically coupled out of the waveguide causing excess optical loss for the laser. Therefore 1st order gratings are predominantly utilized, whereas 2nd order gratings have been exploited in special surface-emitting DFB laser designs (see Sect. 3.8.2), and higher order gratings in high-power DFB devices owing to their particularly long cavity. Mathematically DFB lasers can be described and simulated by the well-proven coupled mode and transmission line model, respectively. Both theoretical models are thoroughly described e.g. in [40].

Basic DFB Design In order to fully exploit the longitudinal mode selection mechanism of the DFB grating any back-reflections from the facets have to be avoided. This is commonly achieved by applying anti-reflection (AR) coating layers to either end facet. Index-coupled DFB lasers with AR-coated facets (Fig. 3.15(a)) however show a two-mode spectrum at the Bragg grating stop band, as depicted in Fig. 3.16(a). To achieve true single-mode operation an additional $\lambda/4$ phase shift in the center part of the grating can be implemented (Fig. 3.15(b)). In that case single mode operation at the Bragg wavelength (3.3) is obtained (Fig. 3.16(b)). Alternatively multiple phase shifts distributed along the DFB grating can be used here [41]. Another means to obtain single-mode operation is to use so-called complex coupling in which case an additional imaginary index (gain or absorption) coupling component adds to the real index coupling. As a result single-wavelength emission is obtained that corresponds to the “red” (gain) or “blue” (absorption) side stop band mode (Fig. 3.16(c)). In reality, as one approach, such complex coupling is accomplished by etching the DFB grating further into the active layer (Fig. 3.15(c)).

Fig. 3.17 Dependence of threshold gain \cdot length product, $g_{th} \cdot L$, on the coupling coefficient \cdot length product, $\kappa \cdot L$, for $\lambda/4$ -phase shifted DFB-lasers with AR-coated facets (optical losses neglected). L denotes the length of the DFB-grating

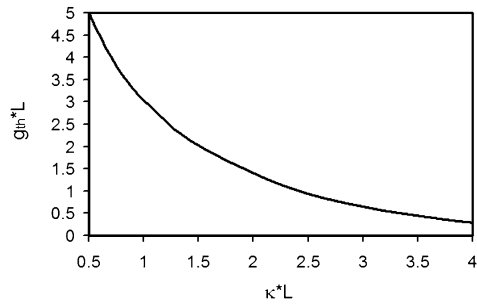
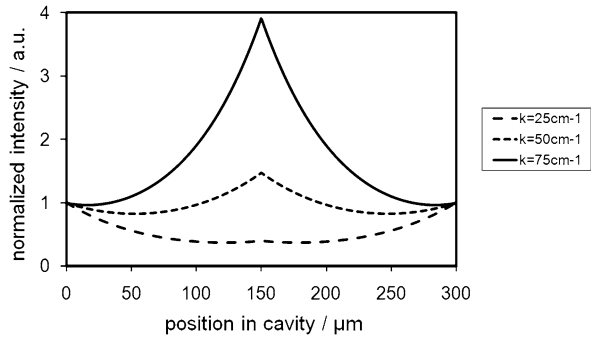


Fig. 3.18 Normalized intensity distribution along the DFB cavity at laser threshold for different coupling coefficients κ ($L = 300 \mu\text{m}$, both facets AR-coated)



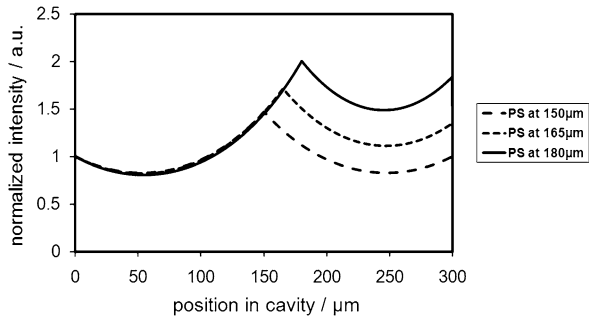
Though there have been concerns about reliability of such DFB structures it could be demonstrated that good lifetime behavior is achievable if the fabrication is done properly. Because of the oxidation issue (see Sect. 3.3.2), however, this “active layer etching” approach is hardly applicable to Al-containing layer structures.

A key parameter in the design of DFB lasers is the coupling strength of the DFB grating, denoted by the coupling coefficient κ and defined as the fraction of light intensity reflected back at each periodical index step. κ depends on the amount of light confined in the grating layer, i.e. on the grating depth and on the effective refractive index difference between the materials that compose the grating. The value of κ largely impacts, amongst others, the threshold current of a DFB laser. Figure 3.17 exemplarily shows the dependency of the threshold gain, g_{th} , on the coupling strength κ for a $\lambda/4$ phase shifted DFB laser.

Another effect governed by the κ -coefficient is the intensity distribution inside the DFB laser structure. This is illustrated in Fig. 3.18 where the resulting optical intensity profile along the cavity is drawn for different κ -values in case of a $300 \mu\text{m}$ long phase shifted DFB device. Strong coupling leads to pronounced intensity peaking at the phase shift position that may cause local depletion of the optical gain in that region of the cavity, also known as spatial hole burning [42]. As a consequence the side mode suppression will get deteriorated and the lasers will tend to become spectrally multi-mode. For this reason strong index coupling is generally avoided; mostly, $\kappa \cdot L$ product values between 1 and 2 are used.

DFB laser devices with AR-coated facets generate equal optical output power from both cavity sides (Fig. 3.18). In most practical applications, however, asym-

Fig. 3.19 Normalized intensity distribution at laser threshold along the DFB cavity for different positions of the $\lambda/4$ phase shift ($L = 300 \mu\text{m}$, $\kappa = 50 \text{ cm}^{-1}$, both facets AR-coated)



metrical output power distribution is desired to increase the usable power from the front facet at the expense of the light emission from the rear facet, the latter commonly utilized to feed a monitor photodiode. This can be accomplished in two alternative ways. The first one is to implement gratings with an off-center phase shift (Fig. 3.19). By this means the optical intensity can be lifted such as to yield higher values at the front facet, and accordingly increased output power. However, as a trade-off side-mode suppression tends to decrease with increasing phase shift displacement from the center position of the DFB grating. Typically a front/back optical power ratio up to 2–3 can be achieved using this method.

The second solution is to employ a cleaved ($R = 30\%$) or high reflection (HR, $R \sim 60\text{--}90\%$) coated back facet. Depending on the chosen HR value the optical output, or in other terms the external slope efficiency ($SLE = \Delta P / \Delta I$), at the front facet can almost be doubled, associated with a very high front-to-back asymmetry factor. However, this cavity design again largely affects the statistical single-mode yield which tends to drop significantly as a consequence of the random phase value of the reflective back facet relative to the DFB grating. Laser facets are created by a cleaving process the positional precision of which is limited to values between $\pm 5 \mu\text{m}$ to $\pm 10 \mu\text{m}$, unless special demanding technological measures are taken. In any case, it is impossible to perform the cleaving so as to result in a facet with a well-defined phase value relative to the DFB grating. This would require nanometer scale accuracy.

The strong influence of the back facet phase condition on the single-mode behavior is illustrated in Fig. 3.20. Here the optical output spectra at laser threshold of a $\lambda/4$ phase shifted DFB laser are depicted for different phase values. Their strong effect on the onset of the competing DFB modes is clearly visible. At phase 0° the lasers behave purely single-moded whereas at 180° they emit at the Bragg grating stop band modes (see Fig. 3.15). As a consequence, assuming an even phase distribution such lasers typically exhibit a single-mode yield of around 50% only, depending on the specified SMSR limit. Along with this a statistical fluctuation of the output power occurs.

To conclude, with traditional DFB laser designs there is a distinct trade-off between SM yield and achievable optical output power/slope efficiency: Two-sided AR coated devices give high SM yield (virtually 100%) but limited SLE values (typical $\sim 0.25 \text{ mW/mA}$). With AR/HR coated DFB lasers, on the other hand, the

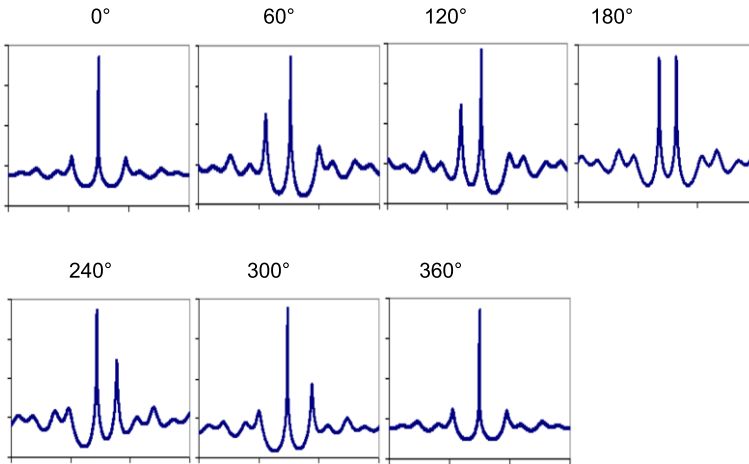


Fig. 3.20 Normalized calculated optical output spectra at laser threshold of a $\lambda/4$ phase shifted DFB laser ($L = 300 \mu\text{m}$, $\kappa = 50 \text{ cm}^{-1}$, AR/60% facet coating) for different phase values at the back facet

SM yield is significantly reduced to the 50% range but high SLE values are achievable ($>0.4 \text{ mW/mA}$). For commercial applications actually both high SM yield and high slope efficiency are desired for obvious reasons.

DFB lasers are widely deployed in wavelength-division-multiplex (WDM) networks. To this end special demands are posed on the accuracy of emission wavelength. With dense WDM (DWDM) precisely defined transmission wavelength channels with optical frequency spacing down to 50 GHz of optical frequency (equivalent to 0.4 nm at 1550 nm) are used. Respective DFB devices have to be assigned by selection. Due to the temperature dependence of the material refractive index the wavelength of a DFB laser changes with temperature at a rate of about $+0.1 \text{ nm/K}$, i.e. by a factor of 5 smaller than the gain spectrum ($\sim 0.5 \text{ nm/K}$) shifts. For DWDM lasers precise temperature adjustment and stabilization using a Peltier cooler is therefore mandatory to match the specified DWDM wavelengths (“ITU grid”). For such temperature controlled conditions DFB lasers have been commodity items for up to 10 Gb/s modulation rates for many years. More recently, there has been a strong trend to deploy wavelength tunable transmitter devices (see Chap. 5) rather than fixed wavelength devices to avoid costly selection and to reduce inventory costs.

Clearly, uncooled laser operation is desirable to eliminate cooling power and cooler costs. This is particularly true for access applications like FTTH PON networks. In the extreme case those lasers need to operate in the range from $-40 \text{ }^\circ\text{C}$ to $+85 \text{ }^\circ\text{C}$. To support WDM technologies though coarse WDM (CWDM) schemes have been introduced which typically feature a channel spacing of $\Delta\lambda = 20 \text{ nm}$. Nonetheless, quite a challenging fabrication tolerance of the lasing wavelength of only $\pm 2.5 \text{ nm}$ has to be met to stay within a specified transmission window of 12.5 nm over the temperature range from 0–75 $^\circ\text{C}$. To compensate for the lower

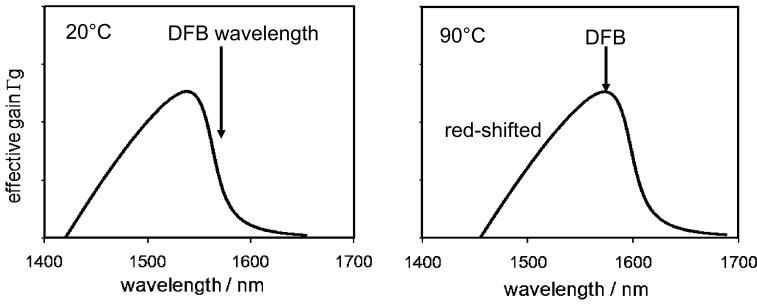


Fig. 3.21 Schematic illustration of wavelength detuning of DFB lasers to optimize laser characteristics at high operation temperatures (90 °C). The drawn *curve* represents the gain profile, and the *arrow* the position of the emission wavelength as defined by the DFB grating

gain at higher temperature—at least to a certain degree—the difference in temperature shift of spectral gain and DFB wavelength is exploited to optimize DFB laser diodes for high temperature operation, as illustrated in Fig. 3.21.

At room temperature the DFB wavelength is intentionally positioned on the long-wavelength side of the optical gain spectrum by adjusting the DFB grating accordingly. This design measure is referred to as “wavelength detuning”. With increasing temperature, differently from FP lasers, the emission wavelength shifts to the gain peak region to benefit from the higher gain and hence to assure still low threshold currents even at high operation temperatures. In this case the resulting effective T_0 -value is no longer related to material properties alone but is also detuning dependent.

In applications where cooled operation is used wavelength detuning can also be applied to optimize modulation parameters. If the DFB wavelength is detuned to the short-wavelength side left of the gain peak, an increase in differential gain and thus a higher modulation bandwidth can be achieved (for further reading see Chap. 4). This design measure is limited by the associated increase of the threshold current with increasing distance from the gain peak. However, this effect may be compensated for by adjustment of the grating coupling strength or use of suitable HR back facet coating [43]. Along with the increase of the differential gain also the Henry (or α -) factor tends to decrease which has a decisive impact on the static and dynamic spectral linewidth of the emission wavelength. The static linewidth is crucial for coherent detection schemes requiring a local oscillator laser of very narrow linewidth whereas the dynamic one characterized by linewidth broadening under modulation (“chirp effect”) largely affects dispersion related transmission properties.

Performance of DFB Lasers Representative output power characteristics are shown in Fig. 3.22 for an AR/HR coated BH-DFB transmitter laser based on InGaAsP/InP and designed for uncooled operation. Room temperature threshold currents around 5 mA and optical output power levels even exceeding 50 mW are obtainable with elaborated designs and today’s highly developed fabrication techno-

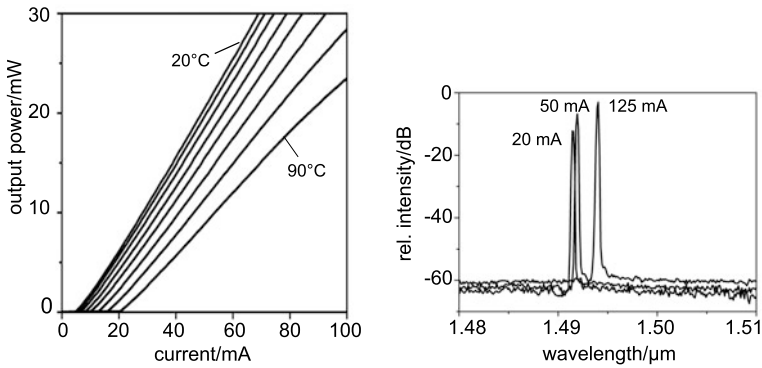


Fig. 3.22 Representative P – I curves of a 1490 nm BH-DFB laser diode designed for uncooled operation, 10 K temperature steps (*left*), and current dependent emission spectra taken at 20 °C (*right*)

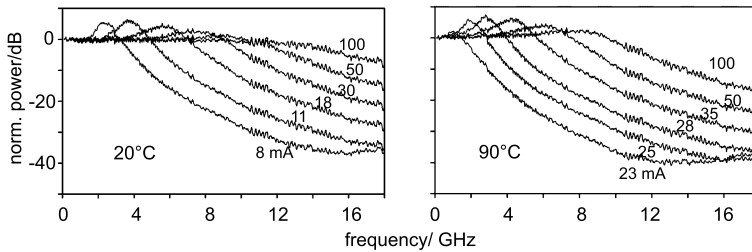


Fig. 3.23 Small-signal modulation curves of a InGaAsP/InP BH-DFB-laser diode at 20 °C and 90 °C; indicated bias currents including threshold currents

logy. Inherent to InP laser diodes is the relatively large material related degradation of maximum output power and slope efficiency with increasing temperature. SMSR values >50 dB are readily achievable. It may not be taken for granted, however, that such values are maintained over the full operational current and temperature range. Instead, the single-mode behavior may get worse and even out-of-specification which is of particular concern in the low-temperature regime.

The frequency performance can be characterized by small-signal modulation curves, as shown in Fig. 3.23 for a device similar to the one demonstrated in Fig. 3.22. The characteristic -3 dB cut-off frequency is well known to increase with increasing bias current until a saturation limit is reached. At high operation temperature the maximum modulation bandwidth tends to diminish rendering it hard to modulate uncooled InGaAsP/InP DFB devices at 10 Gb/s, at least at practical current conditions. InGaAlAs/InP based lasers provide superior performance in this respect, thanks to their “inverse” QW band structure (Sect. 3.3), and are therefore prevailing for uncooled 10 Gb/s applications and mandatory for even higher bit rates (see also Chap. 4)

3.7.2 Advanced Single-Mode Laser Structures

From the previous section it becomes apparent that ordinary DFB lasers do not meet all the requirements that the fiber optics industry desires. Hence much effort has been spent over the recent years on achieving improved performance.

Complex-Coupled DFB Lasers One approach has been the introduction of complex-coupled DFB lasers [44], already introduced above (see Fig. 3.15). Using this concept in conjunction with a reflective back facet the single-mode yield indeed tends to substantially increase, compared to the conventional purely real index coupled DFB devices. Another benefit is their reduced optical feedback sensitivity [45]. Optical feedback in fact represents a major issue with DFB lasers: When laser light is reflected back from any external reflection site this light, depending on the phase conditions, may render the laser to become multi-mode and even chaotic. Feedback sensitivity—described by the threshold ratio of reflected-to-emitted intensity at which multi-mode behavior starts to occur—as high as possible is desired to avoid the use of an optical isolator. In most cases, such an optical isolator placed in front of the laser is needed to sufficiently eliminate this detrimental feedback effect. In spite of these advantages complex-coupled DFB variants seemingly play an only minor role yet in commercial applications because of the more challenging fabrication technology and potentially larger reliability risks although good lifetime results have indeed been demonstrated [46].

Curved Stripe DFB Laser An alternative innovative concept relying on conventional index coupling has been introduced recently, named Curved Stripe DFB (CS-DFB) [47]. Initially designed to realize a tapered DFB diode by pursuing an implementation similar to the one sketched in Fig. 3.11 it turned out that the CSDFB structure offers additional features overcoming drawbacks of traditional DFB lasers. A schematic view of such a device is shown in Fig. 3.24. Inherent to the design is a curved active BH stripe tapered towards the front side. The resulting angled front facet provides an effective AR behavior enabling these lasers to emit single mode even without any anti-reflection coating on the front facet. The purpose of the curved active stripe is as follows: Due to the tapered design the effective index n_{eff} of the laser structure decreases in longitudinal direction towards the front facet, and the Bragg condition (3.3) varies accordingly along the cavity. Rather than using a DFB

Fig. 3.24 Schematic top view of a Curved Stripe DFB laser indicating the basic architecture (AC = as-cleaved; AR = anti-reflection; HR = high reflection, as-cleaved (30%) or coated)

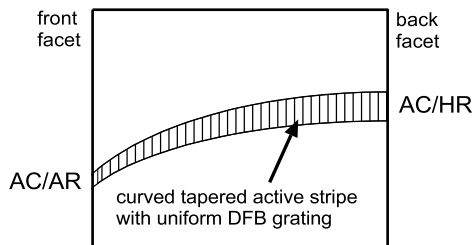
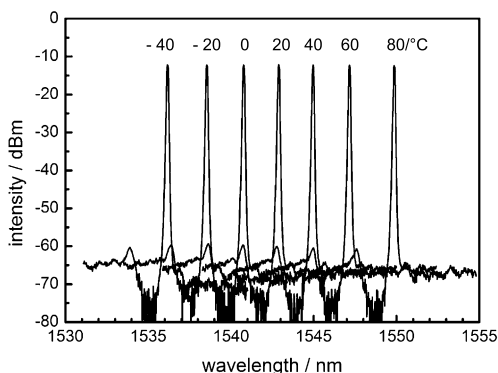


Fig. 3.25 Emission spectra of a CSDFB laser diode in the temperature range from $-40\text{ }^{\circ}\text{C}$ to $+80\text{ }^{\circ}\text{C}$



grating with a gradually varying period which would be quite expensive to implement the required spatial effective index variation is created by a properly designed curvature in conjunction with a constant period grating. This way, established techniques for grating formation can be utilized, such as the inexpensive UV interference exposure technique.

The combined effect of decreasing optical gain and index coupling strength towards the front facet and the bending of the active stripe consistently leads to an efficient suppression of the short-wavelength Bragg mode. This feature is of special advantage if tight wavelength tolerances are required. Calculations similar to those depicted in Fig. 3.16 clearly indicate that the adverse effect of the phase variation at the as-cleaved (or HR) back facet on the single-mode yield is significantly reduced in CSDFB structures. As a consequence these lasers were found to exhibit a single-mode yield in the higher 90% range even in the absence of any facet coating [47].

The apparently superior mode stability becomes manifest also when regarding the single-mode behavior over the operating temperature range. It has been verified

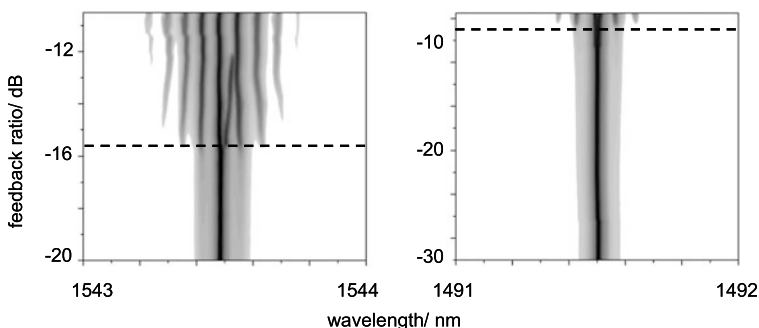


Fig. 3.26 Comparative optical feedback measurements on conventional (*straight stripe*) and complex-coupled curved stripe DFB laser of otherwise comparable design but slightly different wavelengths (measurements according to IEEE Standard 802.3aeTM-2002, 1 mW in fiber); *dashed lines* indicate onset of multimode emission depicted by the lobes; note the different scale of the feedback ratio (= reflected/launched optical power)

that stable single-mode emission is well maintained particularly in the lower range ($<0\text{ }^{\circ}\text{C}$). An example is given in Fig. 3.25.

Another evidence is the fact that CSDFB lasers prove to be less sensitive to optical feedback effects. Comparative measurements on CSDFB and straight structures of otherwise comparable design indicated enhanced immunity against optical feedback by a factor of more than 3 dB [48]. By combining the CSDFB laser concept with complex coupling further improvement by 3–4 dB could be achieved [49], as illustrated in Fig. 3.26.

Discrete Mode Laser Diode Discrete mode (DM) laser diodes are single longitudinal and spatial mode laser diodes based on ridge waveguide Fabry-Perot (FP) laser diodes [50]. DM laser diodes are produced by etching reflective defects (slots) into the ridge of a ridge waveguide FP laser diode. The etched slots have a small overlap with the transverse field profile of the optical mode and act as refractive index discontinuities in the laser cavity which introduce a perturbation to the optical mode in the laser. By judicious placement of a sequence of low-loss slots with respect to the facets pre-selected FP modes are significantly enhanced leading to robust single-frequency lasing with narrow linewidth and wide temperature stability [51]. These slots cause a selective reflectivity at a certain predetermined wavelength causing strong feedback at this wavelength, while including a low scattering loss to all wavelengths. The total round trip gain can be expressed as shown in (3.4) and has an internal loss component including slot scattering loss, and also a mirror loss term which includes the enhanced reflectivity which is strongly wavelength dependent due to the slot period.

$$1 = \exp[(\Gamma g(\lambda) - \alpha_i)L]R(\lambda) \quad (3.4)$$

This additional wavelength dependent reflectivity determines which longitudinal mode of the cavity experiences higher total round trip gain and therefore reaches threshold at a lower laser bias current. The placement, etch depth and distance between slots all play a role in the strength, and wavelength position of the single-mode peak in the DM spectrum. As the slots add additional scattering loss to all longitudinal modes of the cavity, the lasing threshold is slightly higher than that of a FP cavity, while the efficiency is slightly lower. The slots are etched only into the upper cladding of the waveguide therefore they do not impact on the Al containing layers of the QW and barrier regions meaning there are no additional lifetime and failure issues with DM lasers over conventional FP lasers. Figure 3.27 shows a schematic representation of a DM laser diode with a scanning electron microscope (SEM) image of a typical slot pattern.

In DM lasers the mechanism used to achieve single-mode operation relies on a combination of the slot reflectivity and the facet reflectivity, however integratable discrete mode (IDM) type lasers are also available which rely on the slots in their entirety for feedback from the front of the cavity. These type of lasers are used when cleaving of one facet is not possible or when the laser is to be monolithically integrated with other photonics components in i.e. laser integrated with electro-absorption modulator (EAM), or a laser array integrated with multi-mode interference (MMI) coupler for single output of many wavelengths.

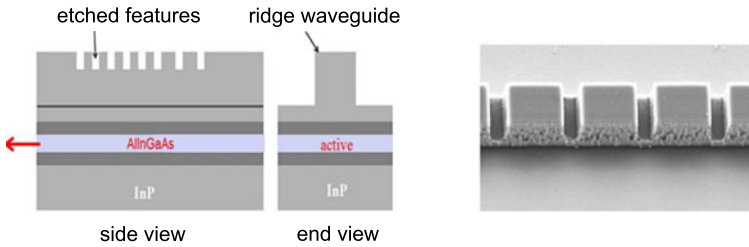


Fig. 3.27 Schematic representation of a DM laser diode (*left*), and SEM image of a typical slot pattern etched into the ridge of a DM laser diode (the slots are typically a few μm apart)

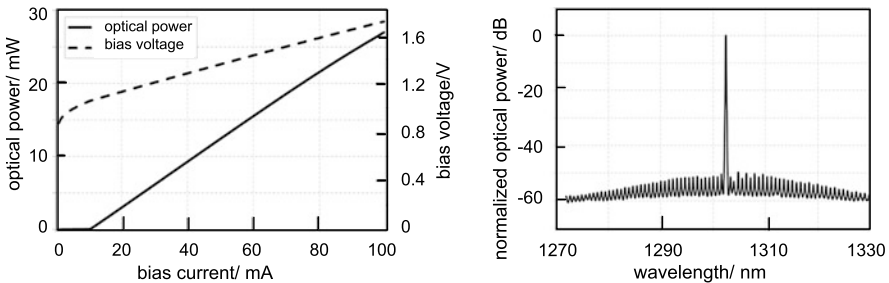


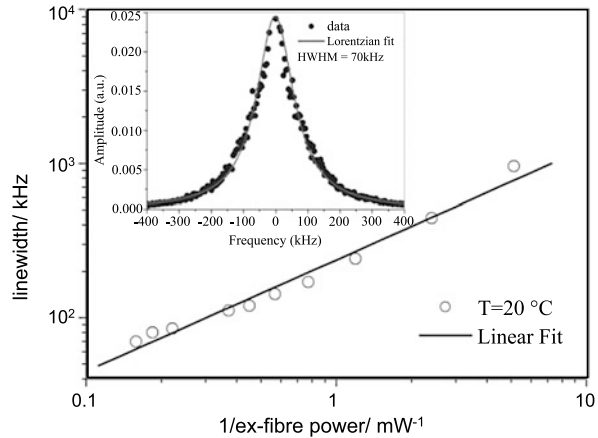
Fig. 3.28 Typical 1310 nm DM LIV at 25 °C and optical spectrum at 40 mA, 25 °C

Both DM and IDM lasers are fundamentally different to DFB type single-frequency lasers. DM lasers are used extensively for similar applications to DFB lasers in optical communications at 2.5 and 10 Gb/s direct modulation. Many of the previously mentioned techniques for achieving good temperature and modulation bandwidth for DFB lasers hold true for DM lasers, not least in detuning the DM peak from the gain peak for -40 to 85 °C uncooled operation. Mode-hop free operation over this temperature range is readily available for most DM laser diode wavelength ranges.

A typical LIV (light-current-voltage) curve at 25 °C and an optical spectrum at 40 mA, 25 °C for a at 1302 nm DM are shown in Fig. 3.28 below, with typical values of threshold current of 10 mA, slope efficiency of 0.28 W/A and SMSR close to 50 dB.

Due to the relative ease of processing compared with DFB lasers, DM lasers require only a single epitaxial growth step and no regrowth steps and as such have a significant cost reduction for low and high volume production. DM lasers can access regions that have been historically difficult for DFB lasers such as in the 400–750 nm spectral range due to the grating dimensions and problems associated with manufacture of Al containing materials. DM lasers have no such issues and as such have been developed over an extremely wide wavelength range from 650 nm to 2450 nm, using the material systems GaInP, GaAs, InGaAlAs and InGaAsSb, grown on GaAs, InP and GaSb substrates [52]. Single mode lasers at particular wavelengths over this wide wavelength range are required for multi-species gas detection where

Fig. 3.29 Extracted linewidth versus inverse optical power at $T = 20\text{ }^{\circ}\text{C}$ for a DM laser diode at 1550 nm. *Inset* delayed self-heterodyne spectrum at 400 mA with Lorentzian fit linewidth = 70 kHz



many molecular species have strong absorption lines in this range, such as oxygen, methane, carbon dioxide and water vapor among many others.

DM laser diodes have also been fabricated that have excellent linewidth characteristics, with linewidths down below 100 kHz, while maintaining good optical power and single mode behavior as shown in Fig. 3.29 [53, 54]. This behavior is achieved by waveguide design coupled with custom epitaxial design whereby the optical loss is reduced and the cavity length is increased.

3.8 Surface-Emitting Laser Diodes

3.8.1 Vertical-Cavity Surface-Emitting Laser (VCSEL)

The concept for a vertical-cavity surface-emitting laser (VCSEL) was first published in the late 1970s [55]. One decade later, a significant breakthrough occurred with the first demonstration of VCSELs operating continuous-wave at room temperature [56]. Since the mid 1990s, VCSELs became commercially available, with main applications in optical sensing and interconnects ranging from the laser mouse to Ethernet modules. These devices are usually designed for 850 nm emission wavelength and based on GaAs. A detailed overview on the fundamentals, technology and applications of VCSELs can be found in [57]. The importance of VCSELs today is reflected by the fact that they are on the way to reach or even have passed the largest production volume among all types of lasers exceeding many tens of million of units per year.

The impressive success of VCSELs is mainly due to a number of unique advantages for this laser type as compared to conventional edge emitting lasers. The most important features of VCSELs include low beam divergence associated with circular beam profile leading to relaxed fiber alignment tolerances; sharply reduced power consumption with threshold currents around 1 mA; excellent capability for

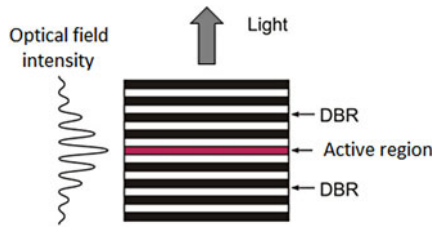


Fig. 3.30 Schematic VCSEL structure with top and bottom DBR, active region and illustration of the internal field intensity. The propagation of the light output is perpendicular to the wafer plane. The reflectivity of each DBR can be tailored by the number of mirror pairs and is typically well above 99%

high speed modulation; integration into one and two dimensional laser arrays; complete on-wafer testability with enormous cost reduction compared to edge-emitters; and high reliability. High performance, cost effectiveness and low power consumption as a step towards “green photonics” are fundamental prerequisites for most applications and can be ideally served by VCSELs.

While GaAs-based VCSELs with emission wavelengths below 1 μm have reached a remarkable maturity and widespread applications, the development of their long-wavelength counterparts designed for emission wavelengths at 1.3 μm and beyond has been severely delayed. Application capability and commercialization has only been achieved recently with highly advanced device concepts. This aspect is even more astonishing since huge efforts in industry and academia have been made and significant market potentials exist for such devices. Since all above mentioned advantages also hold for long-wavelength VCSELs, low power consumption single-mode VCSELs with long emission wavelengths are highly attractive devices for numerous applications in optical communications and sensing. The following sections address the specific aspects and needs of such lasers and present innovative state-of-the-art device concepts allowing for superior device performance.

VCSEL Fundamentals As opposed to conventional edge emitting laser diodes, the optical beam of a VCSEL is perpendicular to the wafer plane. The laser resonator as shown in Fig. 3.30 consists of two Distributed Bragg Reflector (DBR) mirrors parallel to the wafer surface with an active region in between. A multi-quantum-well structure is typically used for laser light generation. The planar DBR-mirrors consist of layers with alternating high and low refractive indices. The thickness of each layer corresponds to a quarter of the laser wavelength in the material.

Like with other laser types, lasing in a vertical cavity is enabled when the gain in the active region balances the losses. The latter ones are given by reflection losses in the mirrors and internal losses (α_i) by free-carrier absorption, potential scattering and diffraction. With $R_{t,b}$ as reflectivities for top and bottom mirror, Γ_r as relative confinement factor, g_{th} as net gain in the active region, d_a as active region length and L_{eff} as effective cavity length defined as the inner distance between the two

Bragg reflectors plus a penetration depth of the optical field into the reflectors, the round trip condition for lasing threshold becomes

$$R_t R_b \exp\{2[\Gamma_r g_{th} d_a - \alpha_i (L_{eff} - d_a)]\} = 1 \quad (3.5)$$

The relative confinement factor Γ_r (or gain enhancement factor) describes the overlap of the active layers of total thickness d_a with the standing-wave pattern of the optical field $E(z)$ and is defined by

$$\Gamma_r = \frac{L \int_{d_a} |E(z)|^2 dz}{d_a \int_L |E(z)|^2 dz} \quad (3.6)$$

Equation (3.6) can be regarded as average intensity in the active layers normalized to that in the inner cavity. While the theoretical limit of Γ_r is 2, typical values of Γ_r amount to 1.8 when the quantum wells are properly placed in an antinode of the standing-wave pattern. By exploiting the standing-wave effect, the optical amplification can therefore be almost doubled. Since optical losses are also locally varying in the resonator, the absorption coefficient α_i in (3.5) should be regarded as an average value weighted with the intensity profile.

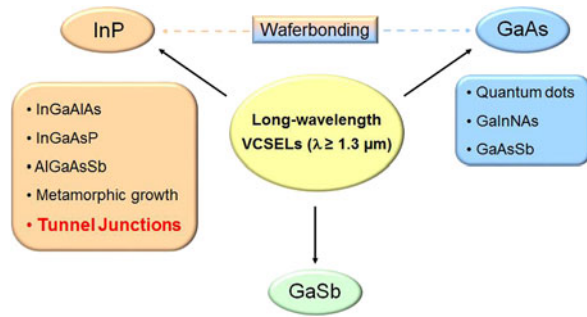
Compared to edge emitting lasers where the resonator length is usually equivalent to the length of the gain section and typically amounts to some hundreds of micrometers, the axial length of the gain section in a vertical cavity structure where the light passes through amounts only to a few tens of nanometers. Even for a high material gain coefficient of 1000 cm^{-1} that can be achieved in semiconductor quantum wells, the mirror reflectivities have to exceed 99% in order to fulfill (3.5). To achieve such high values, a multilayer DBR is commonly used in VCSELs the layer thicknesses of which are designed such that the reflections at the different interfaces are all in phase. In a VCSEL DBR, two alternating materials with different refractive indices are used where each layer thickness equals a quarter of the optical wavelength in the material ($n_1 d_1 = n_2 d_2 = \lambda/4$). Assuming a plane wave without any diffraction and absorption losses in the DBR, the reflectivity R of a DBR consisting of N pairs of layers with refractive indices n_1, n_2 is expressed by

$$R = \left[\frac{1 - \frac{n_t}{n_i} \left(\frac{n_1}{n_2}\right)^{2N}}{1 + \frac{n_t}{n_i} \left(\frac{n_1}{n_2}\right)^{2N}} \right]^2 \quad (3.7)$$

n_i, n_t indicate the refractive indices for the medium of incidence (i.e. medium from which light enters the DBR) and the medium of transmission (i.e. medium in which light propagate after passing the DBR), respectively.

Challenges of Long-Wavelength VCSELs Despite the very first VCSEL prototypes were demonstrated on InP-based material and intensive efforts paid also in the aftermath to realize VCSELs for emission wavelengths beyond $1.3 \mu\text{m}$, the development of application suitable devices has been significantly delayed particularly in comparison to their short-wavelength counterparts. Long-wavelength VCSEL research mainly has to cope with the inferior intrinsic properties of the material systems that are principally available for this wavelength regime. A major drawback is that mature active region materials such as InGaAsP or InGaAlAs cannot

Fig. 3.31 Overview of different concepts for long-wavelength VCSELs and possible realization schemes divided by substrate/material systems



be grown together with GaAlAs layers on GaAs substrates with adequate crystal quality needed for lasing action. While GaAs-based VCSELs benefit from the large refractive index difference between GaAs and AlAs that are almost lattice matched and enable high-reflective DBRs even with relatively small numbers of layer pairs, the long-wavelength VCSELs based on InP suffer from almost by a factor of two smaller index contrast of the InGaAsP or InGaAlAs mirror layers [58]. Accordingly, larger numbers of layer pairs are required for achieving reasonable mirror reflectivity. Together with the larger layer thicknesses due to the longer wavelength, the epitaxial mirror stacks of the InP-based VCSELs become rather thick. Considering further the small thermal conductivity of the ternary/quaternary layers being about an order of magnitude smaller than with GaAs and AlAs [59], the thermal resistance of equally reflecting epitaxial mirrors for the InP-based long-wavelength VCSELs is 20–40 times larger. Using AlAsSb lattice-matched on InP, the index contrast can—in principle—be increased up to about the same magnitude as in the GaAs-based material system. However, the small thermal conductivity still prevents effective heat dissipation through the corresponding epitaxial mirrors. The enhanced self-heating caused by high thermal resistances is even more critical with respect to increased temperature sensitivity of the optical gain of commonly used InP-based active regions. Due to gain saturation, stronger electrical pumping leads to unacceptable internal temperature rise which in turn deteriorates the radiative recombination efficiency. Furthermore, the perfected lateral steam oxidation technique to create insulating films from AlAs that represents an effective and well-established method in the GaAs-based devices for self-adjusted current and photon confinement [60] is not available in the InP-based material systems. In principal, steam oxidation can be applied onto AlAsSb, which can be grown lattice-matched on InP [61]. However, the performance of the oxidized regions has not yet proven to be sufficient for the realization of InP-based devices.

The fundamental approaches for long-wavelength VCSELs can be classified by the substrate used, as shown in Fig. 3.31. For the classical optical telecommunication wavelengths from 1.3–1.6 μm , InP-based materials show the highest maturity for the design of active regions whereas superior thermal and optical characteristics are found for GaAs-based layers. While emission with high optical quality on GaAs substrates is somewhat limited to 1.3 μm employing diluted nitrogen containing InGaAs quantum wells or quantum dot layers as active region, the en-

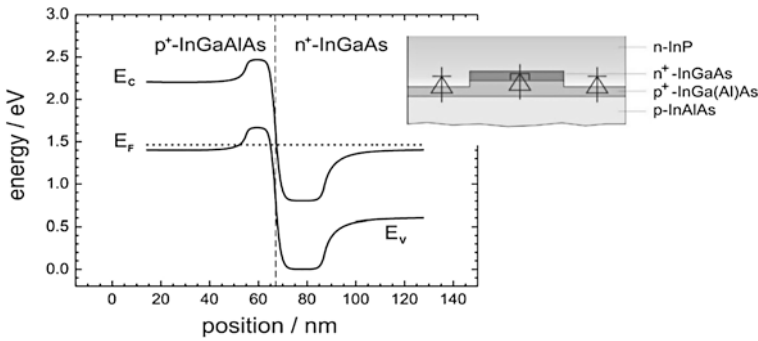


Fig. 3.32 Band diagram of a p^+ -InGa(Al)As/ n^+ -InGaAs tunnel junction. High doping on both sides in conjunction with small band gaps leads to a very small depletion region enhancing tunneling of charge carriers to result in ohmic behavior under applied bias

tire communications wavelength range can be served by straightforward combination of InP-based active regions and GaAs-based mirrors by means of wafer bonding [62]. The incorporation of tunnel junctions when using InP-based active regions has shown to be of paramount importance for the achievement of high-performing long-wavelength VCSELs and will be addressed in detail in the following section.

For the sake of completeness, GaSb-based VCSELs have already been demonstrated for wavelengths beyond $2 \mu\text{m}$ and offer some inherent advantages similar to those of their GaAs-based counterparts [63]. While wavelengths in the mid infrared range would allow for ultra-low attenuation in fluoride fibers, these still suffer from high cost and fragility which makes them less suited compared to silica fibers.

InP-Based Buried Tunnel Junction (BTJ) VCSELs Following the outline above, an indispensable precondition for long-wavelength VCSELs to be highly performing and to be practically applicable aims at a reduction of internal device heating. In this context, minimization of both the thermal resistance and the excess heat generation must be achieved. The latter one is significantly reduced by Buried Tunnel Junctions (BTJ) [64]. Low-bandgap and highly-doped materials based on InP are particularly well suited and show contact resistances of only some $10^{-6} \Omega \text{cm}^2$. Accordingly, only a very small voltage drop occurs in the tunnel junction itself. With the substitution of highly resistive p-doped layers by low-resistance n-doped material, however, a significantly reduced series resistance in the spreading layers becomes possible. The BTJ approach also supports lateral current injection in conjunction with electrically insulating dielectric or undoped epitaxial mirrors. Figure 3.32 shows the band structure of an InP-based tunnel junction and its incorporation in a VCSEL structure. Taking into account the high absorption of the tunnel junction layers and for avoiding excessive loss, they have to be placed in a node of the standing wave pattern. Buried Tunnel Junctions are fabricated by laterally etching the uppermost n^+ -layer outside of a well defined mesa and subsequent regrowth with moderately n-doped material. As shown in the inset of Fig. 3.32, this results in an ohmic tunnel junction region in the non-etched center region and a reverse biased

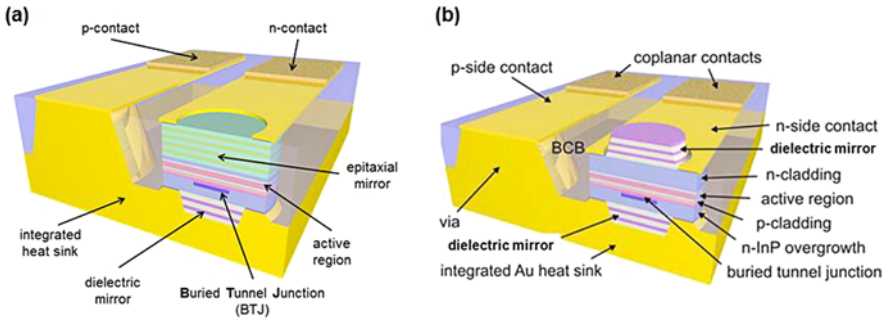


Fig. 3.33 Schematic cross-section of InP-based BTJ-VCSEL incorporating an (a) epitaxial output mirror for long-cavity VCSELs or (b) dielectric output mirror for short-cavity VCSELs with ultra-high speed modulation capability

$p^+ - n$ junction in the etched region. The current flow is therefore restricted to the tunnel junction area with several orders of magnitude of current density difference between these two regions. In addition to the strong current confinement, the differing optical lengths in the etched and non-etched regions lead to self-aligned and strong index-guiding, comparable to oxide confined GaAs-based VCSEL [65].

While excessive heating can be significantly reduced by a buried tunnel junction, the reduction of the thermal resistance is accomplished by the build of the VCSEL chip, as shown in Fig. 3.33 [66]. The upside-down arrangement incorporates a hybrid dielectric/gold back reflector. By selecting proper material combinations with high refractive index difference of the alternating quarter-wave layers, only 2–3 mirror layer pairs are needed for achieving reflectivities of around 99.9%. The dielectric layers are made of insulating and amorphous materials such as fluorides and sulphides. In conjunction with a thermally high-conductive InP heat spreading layer for the tunnel junction regrowth and an integrated Au heatsink, the structure allows for highly efficient heatsinking. The bottom plated Au layer also serves to provide mechanical stability since the former InP-substrate on top is completely removed exposing the epitaxial layers which can be used in the front mirror irrespective of their poor thermal conductivity. Small diameter pillars are etched and planarized with benzocyclobutene (BCB) to feature a low parasitic capacitance structure and to enable high modulation rates.

As shown in Fig. 3.33, two different configurations are commonly used for high-speed capability which differ in the type of output mirror. In the first approach, also referred to long-cavity (LC) design, an epitaxial mirror with typically 30–40 layer pairs, depending on wavelength, is used. Due to the small index difference of only 0.2–0.3 in the mirror layers, the optical field intensity penetrates to a large extent in this epitaxial DBR leading to an increased effective cavity length. By substituting the epitaxial DBR by a dielectric DBR, the effective cavity length can be significantly reduced allowing for shorter photon lifetimes and enhanced modulation characteristics. This short cavity (SC) design is particularly useful for ultra-high speed VCSELs with modulation rates of 25 Gb/s and beyond [67].

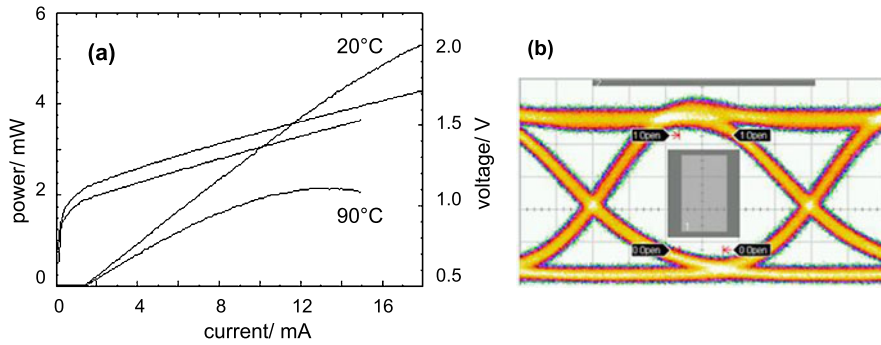


Fig. 3.34 (a) Representative temperature dependent *LIV*-characteristics of 1.3 μm LC-BTJ-VCSELs, (b) eye diagram at 10 Gb/s, 90 $^{\circ}\text{C}$, and extinction ratio of ~ 5 dB

Figure 3.34 shows the light-current-voltage (*LIV*) characteristics of a 1.3 μm LC-BTJ-VCSEL. Optical output powers of more than 5 mW and 2 mW are achieved at 20 $^{\circ}\text{C}$ and 90 $^{\circ}\text{C}$, respectively. A single-mode emission spectrum with side-mode suppression ratios around 40 dB is obtained over the whole current and temperature range. The incorporation of mostly n-doped material yields very small series resistance of only 30–40 Ω even for single-mode aperture diameters of 5–6 μm . Thanks to their low electrical resistance and parasitics, BTJ-VCSELs as shown in Fig. 3.33 are ideal for high-speed modulation even at high temperatures [68, 69]. As an example, Fig. 3.34(b) shows an eye diagram for a 1.3 μm LC-BTJ-VCSEL at a modulation rate of 10 Gb/s and heat sink temperature of 90 $^{\circ}\text{C}$. The rectangular mask for SONET STM64/OC192 has no mask hits even at 15% mask margin.

The improved dynamic performance of SC-VCSELs is demonstrated in Fig. 3.35. The maximum modulation bandwidth as given by the 3 dB cut-off frequency, and the maximum resonance frequency can be seen to amount to 18 GHz and 20 GHz, respectively. By analyzing the small-signal response, one can deduce a theoretical maximum internal bandwidth of 32 GHz assuming no parasitics to be present. Accordingly, even higher modulation bandwidths are anticipated when parasitics may be further reduced. Figure 3.35(b) shows eye diagrams at different modulation rates at room temperature. The eyes were recorded under standard on-off keying condition and extinction ratios between 3–5 dB.

VCSEL-Based Wavelength Division Multiplexing The increasing demand of bandwidth in optical backbone networks as well as in data centers favors wavelength division multiplexing (WDM) techniques in combination with compact integration of light sources for delivering scalable and flexible optical data links with low power consumption, high data throughput, longer transmission distance, and the cost effectiveness needed to efficiently cope with present and future stringent bandwidth requirements. With respect to light sources, VCSELs offer an attractive combination of high bit rates, low power consumption and array integration that, along with their tuning capabilities, make them highly suitable for compact and wideband optical interconnects.

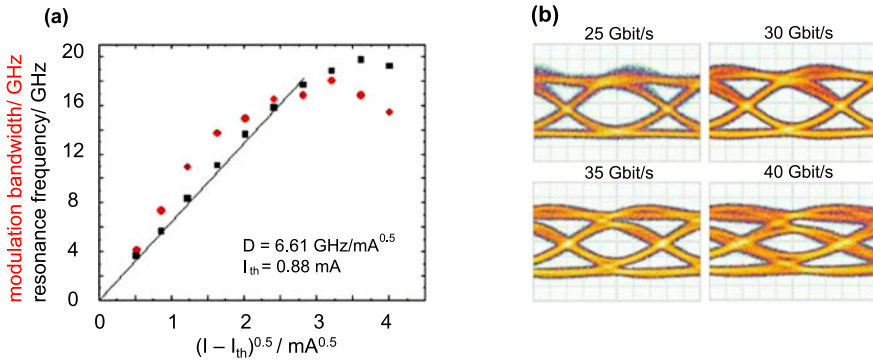


Fig. 3.35 Modulation characteristics of a 1.55 μm SC-BTJ-VCSEL (a) 3 dB cut-off frequency and resonance frequency, (b) eye diagrams for different modulation rates at 25 $^{\circ}\text{C}$

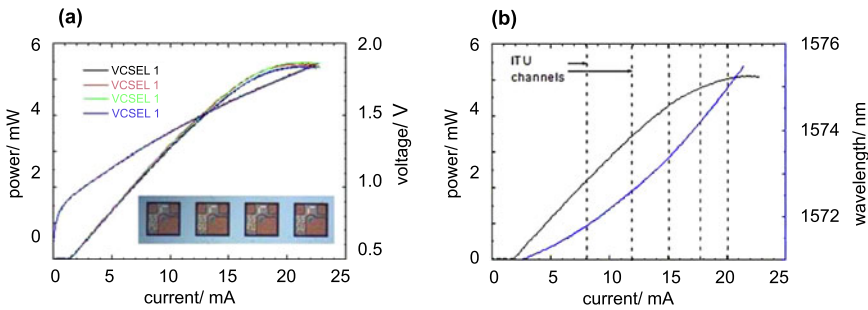
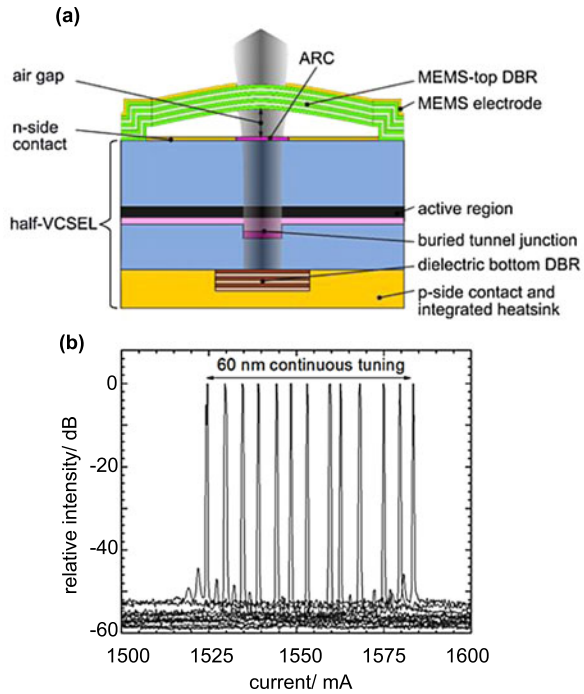


Fig. 3.36 (a) Light-current-voltage characteristics of a 1×4 BTJ-VCSEL array at 20 $^{\circ}\text{C}$. (b) current tuning characteristics of single VCSEL. The vertical lines represent ITU channels with a 100 GHz separation

Wavelength tuning in VCSELs can be accomplished by different means. The very small active region and resonator volume is associated with a high thermal load under electrical pumping and leads to a significantly higher efficiency of current tuning via internal heating as compared to edge emitters. Figure 3.36(a) shows the stationary characteristics of a monolithic 1×4 BTJ-VCSEL array with an emission wavelength around 1.57 μm . A representative current tuning curve for each of these VCSELs is depicted in Fig. 3.36(b). From this, a typical current tuning coefficient of 0.2–0.3 nm/mA is derived. In a VCSEL array with stabilized temperature, the emission wavelength can thus be simply tuned to the desired WDM channel by adjusting the bias current to each of the VCSELs within the array [70]. On the other hand, the wavelength is not affected when operating the VCSELs under GHz modulation since transient heat effects are too slow. While controlling the wavelength by bias current proves to be a simple method, an issue may arise from the different output powers associated with the different wavelength of each of the VCSELs. A system specification usually includes the minimum power level, data rate and

Fig. 3.37 (a) Schematic cross-section of a widely tunable MEMS-VCSEL, (b) optical spectra for different MEMS actuation



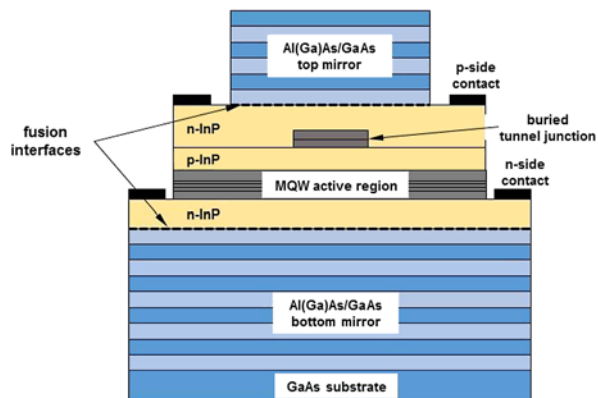
channel spacing. By setting a minimum output power of 2 mW, the VCSELs as shown in Fig. 3.36 can still achieve 10 Gb/s at the lowest channel around 8 mA bias current and up to 4 channels with 100 GHz spacing can be addressed. One solution to simultaneously achieve uniform output powers at different wavelengths is to use altering cavity lengths. For BTJ-VCSELs as shown in Fig. 3.33, this can be realized by controlled etching of semiconductor material or different thicknesses of dielectric mirror layers. New approaches include the application of a high-contrast grating (SWG) as front mirror which also inherently provides polarization pinning. A multi-wavelength VCSEL-array for WDM applications can be realized by varying the grating period and duty cycle [71].

While the approach described above is usually limited to several nanometers of tuning range in practical applications, significantly larger tuning ranges have been demonstrated by combining VCSELs with micro-electro-mechanical system (MEMS) mirrors. The basic idea is to use a high-reflective DBR which can be deflected to change the length of an air gap between the lower “half-VCSEL” and the upper MEMS-DBR. Figure 3.37(a) shows the design of a widely tunable VCSEL based on the BTJ-concept. The MEMS DBR consists of micro-machined dielectric SiO/SiN layers. A thin electrode on top of this DBR enables heating which leads to an upward bending to increase the air gap. Accordingly, the cavity length and the emission wavelength increase. An alternative to thermal actuation consists in electrostatic deflection with downward bending of the MEMS DBR. The maximum achievable tuning speed for the latter method is faster and can reach to the kHz

range. Figure 3.37(b) shows 60 nm tuning of a C-band BTJ-MEMS-VCSEL. Over the entire tuning range, the spectra exhibit high side-mode-suppression ratios of at least 40 dB. In addition, 10 Gb/s modulation is also feasible over the whole tuning range. Record tuning ranges of more than 100 nm have been achieved for electrically pumped non high-speed BTJ-MEMS-VCSELs [72]. A distinct advantage of widely tunable MEMS-VCSELs compared to widely tunable edge emitting solutions is the truly continuous tuning behavior over the free spectral range without any mode hops occurring in between.

Long-Wavelength VCSELs Using Wafer Bonding The basic idea of wafer bonded long-wavelength VCSELs is to combine an InP-based active region offering high optical gain with the superior optical and thermal properties of Al(Ga)As/GaAs Bragg mirrors. Since both material systems have strongly different lattice constants with a mismatch of around 3.7%, no relaxation-free combination of both crystal structures can be grown by regular epitaxy methods. For this reason, the layer stacks of the DBR mirrors and of the active region are first grown independently on GaAs and InP-substrates, respectively, and subsequently bonded to a uniform structure using high temperature and pressure conditions. During this process, covalent bonds are formed across the material interfaces. Figure 3.38 shows a wafer bonded LW-VCSEL with two fused interfaces. Both the top and the bottom mirror are formed by GaAs-based DBRs which are wafer bonded to an InP-based central region including the active region. Using a double intracavity contacting scheme, undoped DBR mirrors can be implemented allowing for very small optical losses along with low electrical device resistance. Furthermore, this contacting scheme avoids current flow across the bonded interfaces which may exhibit rather poor electrical characteristics. For current confinement, a BTJ aperture is incorporated. If bottom and top DBR are grown independently with a different number of mirror pairs, the entire structure needs however 4 epitaxial growths on three different wafers. While these wafer-fused VCSELs need higher epitaxial and processing efforts compared to other types of VCSELs, the concept allows for advantageous device parameters such as low optical loss and very good thermal characteristics. High single-mode optical

Fig. 3.38 Schematic cross-section of a double-fused long-wavelength VCSEL combining GaAs-based top and bottom mirror and an InP-based active region



output powers of 6.7 mW at 20 °C and 1.5 mW at 100 °C have been demonstrated on wafer fused long-wavelength VCSELs around 1.55 μm wavelength. In addition, such VCSELs at 1.3 μm have shown 10 Gb/s operation up to 100 °C [73, 74].

GaAs-Based VCSELs with Extended Emission Wavelength For obvious reasons, a straightforward approach would be to preserve the advantages of the proven GaAs-based technology and just extend the emission wavelength from values below 1 μm to longer regimes. In this context, emission wavelengths around 1.3 μm appear of special interest for many applications in optical communications. Usually, a value of 1.3 μm cannot be achieved with conventional strained GaInAs quantum wells since the increasing compressive strain acts as a limiting factor and only allows emission wavelengths up to approximately 1.1 μm . The reason of unacceptable crystalline strain at long wavelengths also holds for GaAsSb quantum wells [75]. As a consequence, alternative materials have been extensively studied. A widely investigated material consists of GaInNAs quantum wells (dilute nitrides) [76]. In principal, this alloy allows lattice matching to GaAs substrates by adjusting the amount of indium and nitrogen. For example, emission around 1.3 μm can be obtained with only 1.5–2% of nitrogen in conjunction with 35–38% of indium content. VCSELs incorporating such dilute nitrides have shown high output powers of several milliwatt with good temperature stability and modulation speeds up to 10 Gb/s [77–79]. While most of the research activities on GaInNAs active material have shown lasers with emission wavelengths shortly below 1.3 μm , accomplishment of longer wavelengths appears to increasingly suffer from degrading optical gain properties. For applications such as optical links based on the IEEE 40GBASE-LR4 specification including four wavelengths from 1270–1330 nm with 20 nm spacing, the consistent utilization of GaAs-based technology seems unlikely. Further, long-term stability still seems to represent a major issue.

Another approach to extend the emission wavelength of GaAs-based VCSELs is to use self-assembled In(Ga)As quantum dots (QD) [80]. In theory, the zero-dimensional quantum dot system promises unique material gain properties. In practice, however, QD-based VCSELs suffer from the small active volume limiting the total achievable gain. Because of this restriction, achievement of ultra-high modulation speeds requiring high gain conditions is challenging [81]. It remains therefore rather questionable whether QD technology may eventually represent the technology of choice for the realization of long-wavelength VCSEL devices.

For even longer wavelengths, e.g. 1.55 μm , all of the above mentioned concepts prove to be more and more complicated [82, 83]. For example, it proves to be very difficult to incorporate a higher content of nitrogen whilst maintaining high photoluminescence efficiency. Owing to a miscibility gap of dilute nitrides, they also tend to decompose under stress conditions such as high current densities. The latter conditions are, however, typical for VCSELs particularly for achieving high modulation speeds which require high carrier and photon densities to boost the relaxation oscillation frequency. Therefore, high speed performance and reliability often turn out to represent contradicting features. Nevertheless, innovative concepts for implementing novel active materials are still subject to intensive research, and the quality of such materials has seen a significant progress in recent years.

3.8.2 Horizontal Cavity Surface Emitting Laser Concepts

There have been several approaches recently to combine surface emission with “normal” laser structures, that is lasers with horizontal cavities. The aim of these developments is to benefit from the laser performance of those lasers whilst simultaneously retaining the economical advantages (e.g. on-wafer testability) of VCSEL devices. Like VCSELs, horizontal cavity surface-emitting lasers are also attractive light sources for hybrid integration technology as surface-mount devices on optical waveguide boards. In fact, nowadays they are considered an option for source lasers for silicon integrated photonic circuits.

Surface Emitting Lasers with Turning Mirrors This laser type, known under the acronym HCSEL, is basically an edge-emitting laser comprising a 45° mirror facet for vertical out-coupling of the laser-beam, as represented in Fig. 3.39. Both FP and DFB embodiments are feasible. The characteristics of HCSELs, including output power, beam shape, polarization stability and wavelength precision, are basically the same as with their edge-emitting counterparts, whereas full on-wafer processing and on-wafer testability, packaging cost, and monolithic 2D-array fabrication are advantages that are shared with VCSELs. Further, epitaxial growth and manufacturing processes are identical to those utilized in mature edge-emitter technology, apart from the additional etching process needed to form the 45° turning mirror. HCSELs can outperform VCSELs regarding specific advantages of edge-emitters, like higher output power and the possibility of monolithically integrating further devices in the horizontal plane, namely a monitor photodiode as indicated in Fig. 3.39. Conversely, HCSELs exhibit higher power consumption and larger beam divergence than VCSELs. Nonetheless, recent HCSEL developments have led to achieving appreciably low laser currents [84] which eventually may allow for employing the low-power laser driver circuits used with VCSEL.

Recently, a concept similar to HCSELs was realized but with the 45° turning mirror formed such as to direct the output beam downwards through the substrate.

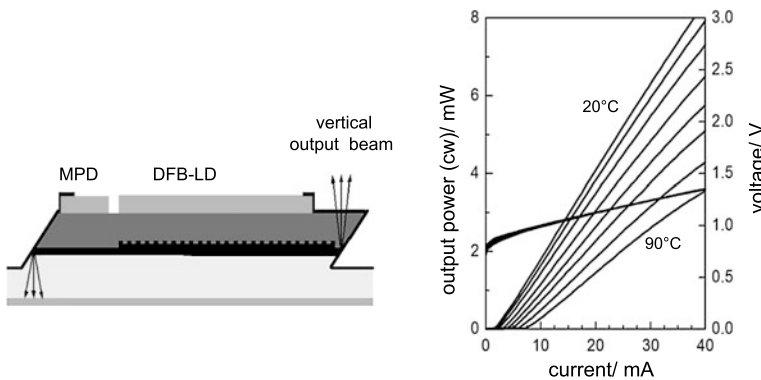
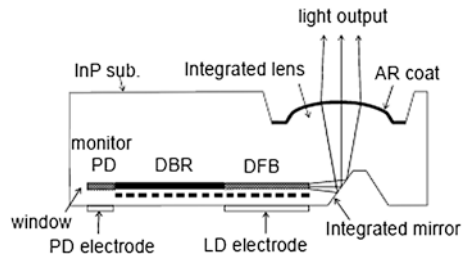


Fig. 3.39 Schematic structure of a single-mode (DFB) HCSEL integrated with a monitor photodiode (MPD, left) and optical output characteristics (right)

Fig. 3.40 Schematic cross-section of a facet-free 1.3- μm LISEL DFB laser diode [87]



At the backside of the substrate, a collimating lens was formed by etching to result in a very low beam divergence of only 2.5° [85]. Using a $1.3\ \mu\text{m}$ InGaAlAs/InP RW laser structure, 25 Gb/s direct modulation up to 100°C was demonstrated on such lasers [86], called LISEL (lens integrated surface emitting laser). Thanks to the substrate-side emission they could be flip-chip mounted directly on high-frequency coplanar lines. This concept was taken further to create a surface-emitting laser device claimed to be facet-free. At the rear side of a DFB laser a DBR grating along with a monitor photodiode and a window section has been implemented to provide a residual reflection-less back-side mirror. At the front side there is also a transparent window section separating the active DFB part from the integrated turning mirror. Laser parameters were reported to be very similar to those of comparable conventional DFB laser diodes [87]. The absence of facet coating in the lasing path is regarded advantageous with respect to non-hermetic packaging [88].

Surface-Emitting Lasers with 2nd Order Grating Another approach for surface-emitting lasers relies on exploiting 2nd order DFB gratings to generate vertical emission. In contrast to 1st order gratings providing optical feedback only in longitudinal direction, with 2nd order designs a substantial portion of the light is reflected into vertical direction. Both 2nd order DBR [89, 90] and DFB structures [91] have been demonstrated. In the former case one laser facet is replaced by a DBR grating, enabling longitudinal mode selection, optical feedback into the laser resonator as well as vertical out-coupling of the laser light. In SE-DFB lasers the 2nd order grating can provide surface emission in the center of the DFB-resonator [91] and can be designed to shape the optical output beam of the laser. It is, for instance, possible to focus the output beam into one or more spots or to optimize the beam quality [90]. Compared to HCSELs the challenge in manufacturing is shifted from the formation of a smooth 45° plane to lithographically defining complex high precision gratings with nano-scale accuracy. Despite the existent advantages such 2nd order grating deflection devices have not been commercialized so far.

In this chapter we have covered the basics of InP based long-wavelength semiconductor laser diodes, including material options, laser structures and related technologies, multi- and single-mode emitting lasers, and different variants of surface-emitting laser devices. Many of these components are commercially available today, nonetheless continuous efforts are made to improve on their overall performance and on specific parameters, and to reduce fabrication costs. Reliability issues have

been largely overcome but need to be revalidated whenever structural and technology changes are introduced. The different laser diodes addressed essentially are capable of up to 10 Gb/s modulation, at least at room temperature conditions. However, there is a strong market demand these days to push this limit to much higher values – 25 Gb/s, and 40 Gb/s, and 56 Gb/s and even more (or GBaud when applying more sophisticated modulation schemes)—to enable 100–400 Gb/s transmitter implementations. Those developments are dealt with in the next chapter. A second major focus is on wavelength tunability which will be the subject of a third laser related article, Chap. 5.

References

1. R.N. Hall, G.E. Fenner, J.D. Kingsley, T.J. Soltys, R.O. Carlson, Coherent light emission from GaAs p–n junctions. *Phys. Rev. Lett.* **9**, 366–368 (1962)
2. M.I. Nathan, W.P. Dumke, G. Burns, F.H. Dill, G.J. Lasher, Stimulated emission of radiation from GaAs p–n junction. *Appl. Phys. Lett.* **1**, 62–64 (1962)
3. Z.I. Alferov, V.M. Andreev, V.I. Korolkov, E.L. Portnoi, D.N. Tretyakov, Injection properties of n-Al_xGa_{1-x}As p-GaAs heterojunctions. *Sov. Phys. Semicond.* **2**, 843 (1969)
4. I. Hayashi, M.B. Panish, P.W. Foy, A low threshold room temperature injection laser. *IEEE J. Quantum Electron.* **5**, 210–211 (1969)
5. J.J. Hsieh, Room temperature operation of GaInAsP/InP double heterostructure diode lasers emitting at 1.1 μm. *Appl. Phys. Lett.* **28**, 283–285 (1976)
6. T. Yamamoto, K. Sakai, S. Akiba, Y. Suematsu, In_{1-x}Ga_xAs_yP_{1-y}/InP DH lasers fabricated on InP(100) substrates. *IEEE J. Quantum Electron.* **14**, 95–98 (1978)
7. G.H.B. Thompson, *Physics of Semiconductor Laser Devices* (Wiley, New York, 1980). ISBN 0471276855
8. N. Grote, The III–V materials for Infra-red devices, in *Materials for Optoelectronics*, ed. by M. Quillec (Kluwer Academic, Amsterdam, 1996), pp. 153–183. ISBN 0-7923-9665-0
9. K. Utaka, K. Kobayashi, Y. Suematsu, Lasing characteristics of 1.5–1.6 μm GaInAsP/InP integrated twin-guide lasers with first-order distributed Bragg reflectors. *IEEE J. Quantum Electron.* **17**, 651–658 (1981)
10. K. Kadoiwa, K. Ono, H. Nishiguchi, K. Matsumoto, Y. Ohkura, T. Yagi, P-substrate partially inverted buried heterostructure distributed feedback laser diode performance improvement by inserting Zn diffusion-stopping layer. *Jpn. J. Appl. Phys.* **45**, 7704–7708 (2006)
11. W. Feng, J.Q. Pan, L.F. Wang, J. Bian, B.J. Wang, F. Zhou, X. An, L.J. Zhao, H.L. Zhu, W. Wang, Fabrication of InGaAlAs MQW buried heterostructure lasers by narrow stripe selective MOVPE. *J. Phys. D, Appl. Phys.* **40**, 361–365 (2007)
12. H. Sato, T. Tsuchuya, T. Kitatani, N. Takahashi, K. Oouchi, K. Nakahara, M. Aoki, Highly reliable 1.3 μm InGaAlAs buried heterostructure laser diode for 10 GbE, in *Proc. 16th Intern. Conf. on InP and Related Materials (IPRM'04)*, Kagashima, Japan (2004), pp. 731–733
13. K. Nakamura, Y. Wakayama, T. Kitatani, T. Fukamachi, Y. Sakuma, S. Tanaka, 56-Gb/s direct modulation in InGaAlAs BH-DFB lasers at 55 °C, in *Conf. Opt. Fiber Commun. Conf. and Nat. Fiber Opt. Eng. Conf. (OFC/NFOEC'14)*, San Francisco, CA, USA (2014), Techn. Digest, paper Th3A.1
14. Y. Matsui, T. Pham, T. Sudo, G. Carey, B. Young, 112-Gb/s WDM link using two Directly Modulated Al-MQW BH DFB Lasers at 56 Gb/s, in *Conf. Opt. Fiber Commun. (OFC'15)*, Los Angeles, USA (2015), Postdeadline papers, Th5B.6
15. Y. Matsui, H. Murai, S. Arahira, Y. Ogawa, A. Suzuki, Enhanced modulation bandwidth for strain-compensated InGaAlAs–InGaAsP MQW lasers. *IEEE J. Quantum Electron.* **34**, 1970–1978 (1998)

16. P.J.A. Thijs, E.A. Montie, T. van Dongen, Structures for improved 1.5 μm wavelength lasers grown by LP-OMVPE; InGaAs–InP strained-layer quantum wells a good candidate. *J. Cryst. Growth* **107**, 731–740 (1991)
17. P.J.A. Thijs, J.J.M. Binsma, L.F. Tiemejer, T. van Dongen, Improved performance 1.5 μm wavelength tensile and compressively strained InGaAs–InGaAsP quantum well lasers, in *17th Europ. Conf. Optical Communication (ECOC'91)*, Paris (1991), vol. **2**, pp. 31–38, Techn. Digest
18. M.A. Newkirk, B.I. Miller, U. Koren, M.G. Young, M. Chien, R.M. Jopson, C.A. Burrus, 1.5 μm multi quantum-well semiconductor optical amplifier with tensile and compressively strained wells for polarization-independent gain. *IEEE Photonics Technol. Lett.* **5**, 406–408 (1993)
19. D.G. Deppe, K. Shavritranuruk, G. Ozgur, H. Chen, S. Freisem, Quantum dot laser diode with low threshold and low internal loss. *Electron. Lett.* **45**, 54–56 (2009)
20. T.J. Badcock, H.Y. Liu, K.M. Groom, C.Y. Jin, M. Gutierrez, M. Hopkinson, D.J. Mowbray, M.S. Skolnick, 1.3 μm InAs/GaAs quantum-dot laser with low-threshold current density and negative characteristic temperature above room temperature. *Electron. Lett.* **42**, 922–923 (2006)
21. T. Kageyama, K. Takada, K. Nishi, M. Yamaguchi, R. Mochida, Y. Maeda, H. Kondo, K. Takemasa, Y. Tanaka, T. Yamamoto, M. Sugawara, Y. Arakawa, Long-wavelength quantum dot FP and DFB lasers for high temperature applications, in *SPIE Photonics West 2012*, San Francisco, CA, USA (2012), 8277-11
22. G.H. Duan, A. Shen, A. Akrouf, F. van Dijk, F. Lelarge, F. Pommereau, O. Le-Gouezigou, J.G. Provost, H. Gariah, High performance InP-based quantum dash semiconductor mode-locked lasers for optical communications. *Bell Labs Tech. J.* **14**, 63–84 (2009)
23. C.S. Lee, W. Guo, D. Basu, P. Bhattacharya, High performance tunnel injection quantum dot comb laser. *Appl. Phys. Lett.* **96**, 101107 (2010)
24. M. Moehrl, H. Roehle, A. Sigmund, A. Suna, F. Reier, High-performance all-active tapered 1550 nm InGaAsP BH-FP lasers, in *Proc. 14th Intern. Conf. on InP and Related Materials (IPRM'02)*, Stockholm (2002), pp. 27–30
25. S.W. Park, J.H. Han, Y.T. Han, S.S. Park, B.Y. Yoon, B.K. Kim, H.K. Sung, J.I. Song, Two-step laterally tapered spot-size converter 1.55 μm laser diode having a high slope efficiency. *IEEE Photonics Technol. Lett.* **18**, 2138–2140 (2006)
26. H. Kobayashi, M. Ekawa, N. Okazaki, O. Aoki, S. Ogita, H. Soda, Tapered thickness MQW waveguide BH MQW lasers. *IEEE Photonics Technol. Lett.* **6**, 1080–1081 (1994)
27. A. Guermache, V. Voiriot, N. Bouche, F. Lelarge, D. Locatelli, R.M. Capella, J. Jacquet, 1 W fibre coupled power InGaAsP/InP 14xx pump laser for Raman amplification. *Electron. Lett.* **40**, 1535–1536 (2004)
28. M. Haverkamp, G. Kochem, K. Boucke, E. Schulze, H. Roehle, 1.1 W four-wavelength Raman pump using BH lasers, in *Opt. Fiber Commun. Conf. (OFC/NFOEC'07) Anaheim USA (2007)*, Techn. Digest, paper OMK7
29. T. Tanbun-Ek, R. Pathak, Z. Wang, H. Winhold, S. Kim, High power and high efficiency 14xx nm wavelength Fabry-Perot lasers. *Proc. SPIE* **8965**, 896511 (2014)
30. J. Telkkälä, J. Boucart, M. Krejci, T. Crum, N. Lichtenstein, High power laser diodes at 14xx nm wavelength range for industrial and medical applications. *Proc. SPIE* **8965**, 896510 (2014)
31. A.J. Ward, D.J. Robbins, G. Busico, E. Barton, L. Ponnampalam, J.P. Duck, N.D. Whitbread, P.J. Williams, D.C.J. Reid, A.C. Carter, M.J. Vale, Widely tunable DS-DBR laser with monolithically integrated SOA: design and performance. *IEEE J. Sel. Top. Quantum Electron.* **11**, 149–156 (2006)
32. M. Theurer, G. Przyrembel, A. Sigmund, W.-D. Molzow, U. Troppenz, M. Möhrle, 56 Gb/s L-band InGaAlAs ridge waveguide electroabsorption modulated laser with integrated SOA. *Phys. Status Solidi A* **213**, 970–974 (2016)
33. A. Borghesani, I.F. Lealman, A. Poustie, D.W. Smith, R. Wyatt, High temperature, colourless operation of a reflective semiconductor optical amplifier for 2.5 bit/s upstream transmission

- in a WDM-PON, in *Proc. 33rd Europ. Conf. on Optical Communication (ECOC'07)*, Berlin (2007), paper We.6.4.1
34. Q.T. Nguyen, G. Vaudel, O. Vaudel, L. Bramerie, P. Besnard, A. Garreau, C. Kazmierski, A. Shen, G.H. Duan, P. Chanclou, J.C. Simaon, Multi-functional R-EAM-SOA for 10-Gb/s WDM access, in *Opt. Fiber Commun. Conf. and Nat. Fiber Opt. Eng. Conf. (OFC/NFOEC'11)*, Los Angeles (USA) (2011), Techn. Digest, paper OThG7
 35. J.H. Lee, I. Shubin, J. Yao, J. Bickford, Y. Luo, S. Lin, S.S. Djordjevic, H.D. Tucker, J.E. Cunningham, K. Raj, X. Zheng, A.V. Krishnamoorthy, High power and widely tunable Si hybrid external-cavity laser for power efficient Si photonics WDM links. *Opt. Express* **22**, 7678–7685 (2014)
 36. L. Schares, R. Budd, D. Kuchta, F. Doany, C. Schow, M. Möhrle, A. Sigmund, W. Rehbein, Etched-facet semiconductor optical amplifiers for gain-integrated photonic switch fabrics, in *Proc. 41st Europ. Conf. on Optical Communication (ECOC'15)*, Valencia, Spain (2015), paper Mo-3.2.1
 37. Q. Cheng, A. Wonfor, J.L. Wei, R.V. Penty, I.H. White, Low-energy, high-performance loss-less 8×8 SOA switch, in *Opt. Fiber Commun. Conf. (OFC'15)*, Los Angeles, USA (2015), paper Th4E.6
 38. H. Kogelnik, C.V. Shank, Coupled-wave theory of distributed feedback lasers. *J. Appl. Phys.* **43**, 2327–2335 (1972)
 39. M. Kamp, J. Hofmann, F. Schaefer, M. Reinhard, M. Fischer, T. Bleuel, J.P. Reithmeier, A. Forchel, Lateral coupling—a material independent way to complex coupled DFB lasers. *Opt. Mater.* **17**, 19–25 (2001)
 40. H. Burkhard, S. Hansmann, Transmitters, in *Fibre Optic Communication Devices*, ed. by N. Grote, H. Venghaus (Springer, Berlin, 2001), pp. 71–116. ISBN 3-540-66977-9
 41. G.P. Agrawal, A.H. Bobeck, Modeling of distributed-feedback semiconductor lasers with axially-varying parameters. *IEEE J. Quantum Electron.* **24**, 2407–2414 (1988)
 42. A.J. Lowery, A. Keating, C.N. Murtonen, Modeling the static and dynamic behavior of quarter-wave-shifted DFB lasers. *IEEE J. Quantum Electron.* **28**, 1874–1883 (1992)
 43. A.K. Verma, M. Steib, Y.L. Ha, T. Sudo, 25 Gbps 1.3 μm DFB laser for 10–25 km transmission in 100 GbE systems, in *Opt. Fiber Commun. Conf. (OFC'09)*, San Diego, USA (2009), Techn. Digest, paper OThT2
 44. G.P. Li, T. Makino, R. Moore, N. Puetz, K.-W. Leong, H. Lu, Partly gain-coupled 1.55 μm strained-layer multi-quantum-well DFB laser. *IEEE J. Quantum Electron.* **29**, 1736–1742 (1993)
 45. J. Kreissl, W. Brinker, E. Lenz, T. Gaertner, W. Rehbein, S. Bauer, B. Sartorius, Isolator-free directly modulated complex-coupled DFB lasers for low cost applications, in *Opt. Fiber Commun. Conf. (OFC'05)*, Anaheim, USA (2005), vol. 4, pp. 3–4, Techn. Digest
 46. J. Kreissl, U. Troppenz, W. Rehbein, T. Gaertner, P. Harde, M. Radziunas, 40 Gbit/s directly modulated passive feedback laser with complex-coupled DFB section, in *Proc. 33rd Europ. Conf. on Optical Commun. (ECOC'07)*, Berlin (2007), paper We.8.1.4
 47. M. Moehrle, A. Sigmund, A. Suna, L. Moerl, W. Fuerst, A. Dounia, W.D. Molzow, High single-mode yield, tapered 1.55 μm DFB lasers for CWDM applications, in *Proc. 31st Europ. Conf. on Optical Commun. (ECOC'05)*, Glasgow, UK (2005), paper Tu 4.5.4
 48. L. Moerl, M. Moehrle, W. Brinker, A. Sigmund, N. Grote, Tapered 1550 nm DFB lasers with low feedback sensitivity, in *Proc. 32nd Europ. Conf. on Optical Commun. (ECOC'06)*, Cannes, France (2006), paper Mo3.4.3
 49. M. Moehrle, W. Brinker, C. Wagner, G. Przyrembel, A. Sigmund, W.D. Molzow, First complex coupled 1490 nm CSDFB lasers: high yield, low feedback sensitivity, and uncooled 10 Gb/s modulation, in *Proc. 35th Europ. Conf. on Optical Commun. (ECOC'09)*, Vienna, Austria (2009), paper We 8.1.2
 50. C. Herbert, D. Jones, A. Kaszubowska, B. Kelly, M. Rensing, J. O'Carroll, P.M. Anandarajah, P. Perry, L.P. Barry, J. O'Gorman, Discrete mode lasers for communication applications. *IET J. Optoelectron.* **3**, 1–17 (2009)

51. R. Phelan, B. Kelly, J. O'Carroll, C. Herbert, A. Duke, J. O'Gorman, $-40\text{ }^\circ\text{C} < T < 95\text{ }^\circ\text{C}$ mode-hop-free operation of uncooled AlGaInAs-MQW discrete-mode laser diode with emission at $\lambda = 1.3\text{ }\mu\text{m}$. *Electron. Lett.* **45**, 43–45 (2009)
52. J. O'Carroll, D. Byrne, B. Kelly, R. Phelan, F.C.G. Gunning, P.M. Anandarajah, L.P. Barry, Dynamic characteristics of InGaAs/InP multiple quantum well discrete mode laser diodes emitting at $2\text{ }\mu\text{m}$. *Electron. Lett.* **50**, 948–950 (2014)
53. B. Kelly, R. Phelan, D. Jones, C. Herbert, J. O'Carroll, M. Rensing, J. Wendelboe, C.B. Watts, A. Kaszubowska-Anandarajah, P. Perry, C. Guignard, L.P. Barry, J. O'Gorman, Discrete mode laser diodes with very narrow linewidth emission. *Electron. Lett.* **43**, 1282–1283 (2007)
54. J. O'Carroll, R. Phelan, B. Kelly, D. Byrne, L.P. Barry, J. O'Gorman, Wide temperature range $0 < T < 85\text{ }^\circ\text{C}$ narrow linewidth discrete mode laser diode for coherent communications applications. *Opt. Express* **19**, 18–22 (2011)
55. H. Soda, K. Iga, C. Kitahara, Y. Suematsu, GaInAsP/InP surface emitting injection lasers. *Jpn. J. Appl. Phys.* **18**, 2329–2330 (1979)
56. F. Koyama, S. Kinoshita, K. Iga, Room-temperature continuous wave lasing characteristics of GaAs vertical cavity surface-emitting laser. *Appl. Phys. Lett.* **55**, 221–222 (1989)
57. R. Michalzik, *Fundamentals, Technology and Applications of Vertical-Cavity Surface-Emitting Lasers*. Springer Series in Optical Sciences (2013)
58. S. Adachi, *Physical properties of III–V semiconductor compounds* (Wiley, Chichester, 1992)
59. S. Adachi, Lattice thermal resistivity of III–V compound alloys. *J. Appl. Phys.* **54**, 1844–1848 (1983)
60. D.L. Huffaker, D.G. Deppe, K. Kumar, T.J. Rogers, Native-oxide defined ring contacts for low threshold vertical-cavity lasers. *Appl. Phys. Lett.* **65**, 97–99 (1994)
61. S. Mathis, K. Lau, A. Andrews, E. Hall, G. Almuneau, E. Hu, J. Speck, Lateral oxidation kinetics of AlAsSb and related alloys lattice matched to InP. *J. Appl. Phys.* **89**, 2458 (2001)
62. A. Black, A. Hawkins, N. Margalit, D. Babic, A. Holmes, Y. Chang, P. Abraham, J. Bowers, E. Hu, Wafer fusion: materials issues and device results. *IEEE J. Sel. Top. Quantum Electron.* **3**, 927–936 (1997)
63. A. Bachmann, K. Kashani-Shirazi, S. Arafin, M.-C. Amann, GaSb-based VCSEL with buried tunnel junction for emission around $2.3\text{ }\mu\text{m}$. *IEEE J. Sel. Top. Quantum Electron.* **15**, 933–940 (2009)
64. M. Ortsiefer, R. Shau, G. Böhm, F. Köhler, G. Abstreiter, M.-C. Amann, Low-resistance InGa(Al)As tunnel junctions for long-wavelength vertical-cavity surface-emitting lasers. *Jpn. J. Appl. Phys.* **39**, 1727–1729 (2000)
65. G. Hadley, K. Lear, M. Warren, K. Choquette, J. Scott, S. Corzine, Comprehensive numerical modeling of vertical-cavity surface-emitting lasers. *IEEE J. Quantum Electron.* **32**, 607–616 (1996)
66. R. Shau, M. Ortsiefer, J. Roskopf, G. Böhm, C. Lauer, M. Maute, M.-C. Amann, Long-wavelength InP-based VCSELs with buried tunnel junction: Properties and applications. *Proc. SPIE* **5364**, 1–15 (2004)
67. M. Müller, P. Wolf, C. Grasse, M.P.I. Dias, M. Ortsiefer, G. Böhm, E. Wong, W. Hofmann, D. Bimberg, M.C. Amann, $1.3\text{ }\mu\text{m}$ short-cavity VCSELs enabling error-free transmission at 25 Gbps over a 25 km fiber link. *Electron. Lett.* **48**, 1487–1489 (2012)
68. M. Ortsiefer, B. Kögel, J. Roskopf, M. Görblich, Y. Xu, C. Gréus, C. Neumeyr, Long wavelength high speed VCSELs for long haul and data centers, in *Opt. Fiber Commun. Conf. (OFC'14)*, San Francisco, CA, USA (2014), paper W4C.2
69. C. Xie, S. Spiga, P. Dong, P. Winzer, A. Gnauck, C. Gréus, M. Ortsiefer, C. Neumeyr, M. Müller, M.C. Amann, Generation and transmission of 100-Gb/s PDM 4-PAM using directly modulated VCSELs and coherent detection, in *Opt. Fiber Commun. Conf. (OFC'14)*, San Francisco, CA, USA (2014), paper Th3K.2
70. J. Estarán, R. Rodes, T.T. Pham, M. Ortsiefer, C. Neumeyr, J. Roskopf, I. Tafur Monroy, Quad 14 Gbps L-band VCSEL-based system for WDM migration of 4-lanes 56 Gbps optical data links, in *38th Europ. Conf. on Optical Commun. (ECOC'12)*, (2012), Th.2.B.3

71. C.J. Chang-Hasnain, W. Yang, High-contrast gratings for integrated optoelectronics. *Adv. Opt. Photonics* **4**, 379–440 (2012)
72. C. Gierl, T. Gründl, P. Debernardi, K. Zogal, C. Grasse, H.A. Davani, G. Böhm, S. Jatta, F. Küppers, P. Meissner, M.-C. Amann, Surface micromachined tunable 1.55 μm -VCSEL with 102 nm continuous single-mode tuning. *Opt. Express* **19**, 17336–17343 (2011)
73. A. Caliman, A. Mereuta, G. Suruceanu, V. Iakovlev, A. Sirbu, E. Kapon, 8 mW fundamental mode output of wafer-fused VCSELs emitting in the 1550-nm band. *Opt. Express* **19**, 16996–17001 (2011)
74. A. Mereuta, G. Suruceanu, A. Caliman, V. Iakovlev, A. Sirbu, E. Kapon, 10-Gb/s and 10-km error-free transmission up to 100 °C with 1.3- μm wavelength wafer-fused VCSELs. *Opt. Express* **17**, 12981–12986 (2009)
75. P. Dowd, S.R. Johnson, S.A. Field, M. Adamcyk, S.A. Chaparro, J. Joseph, K. Hilgers, M.P. Horning, K. Shiralagi, Y.H. Zhang, Long wavelength GaAsP/GaAs/GaAsSb VCSELs on GaAs substrates for communication applications. *Electron. Lett.* **39**, 978–988 (2003)
76. M. Kondow, T. Kitatani, S. Nakatsuka, M.C. Larson, K. Nakahara, Y. Yazawa, M. Okai, K. Uomi, GaInNAs, A novel material for long-wavelength semiconductor lasers. *IEEE J. Sel. Top. Quantum Electron.* **3**, 719–730 (1997)
77. H. Riechert, A. Ramakrishnan, G. Steinle, Development of InGaAsN-based 1.3 μm VCSELs. *Semicond. Sci. Technol.* **17**, 892–897 (2002)
78. Y. Onishi, N. Saga, K. Koyama, H. Doi, T. Ishizuka, T. Yamada, K. Fujii, H. Mori, J. Hashimoto, M. Simazu, A. Yamaguchi, T. Katsuyama, Long-wavelength GaInNAs VCSEL with buried tunnel junction current confinement structure. *SEI Tech. Rev.* **68**, 40–43 (2009)
79. J. Jewell, L. Graham, M. Crom, K. Maranowski, J. Smith, T. Fanning, M. Schnoes, Commercial GaInNAs VCSELs grown by MBE. *Phys. Status Solidi C* **5**, 2951–2956 (2008)
80. R. Mirin, J. Ibbetson, K. Nishi, A. Gossard, J. Bowers, 1.3 μm photoluminescence from InGaAs quantum dots on GaAs. *Appl. Phys. Lett.* **67**, 3795–3797 (1995)
81. M. Laemmlin, G. Fiol, M. Kuntz, F. Hopfer, A. Mutig, N. Ledentsov, A.R. Kovsh, C. Schubert, A. Jacob, A. Umbach, D. Bimberg, Quantum dot based photonic devices at 1.3 μm : direct modulation, mode-locking, SOAs and VCSELs. *Phys. Status Solidi C* **3**, 391–394 (2006)
82. M.A. Wistey, S.R. Bank, H.B. Yuen, L.L. Goddard, J.S. Harris, Monolithic GaInNAsSb VCSELs at 1.46 μm on GaAs by MBE. *Electron. Lett.* **39**, 1822–1823 (2003)
83. N. Yamamoto, K. Akahane, S. Gozu, A. Ueta, N. Ohtani, 1.55 μm -waveband emissions from Sb-based quantum-dot vertical-cavity surface-emitting laser structures fabricated on GaAs substrate. *Jpn. J. Appl. Phys.* **45**, 3423–3426 (2006)
84. M. Moehrl, J. Kreissl, W.D. Molzow, G. Przyrembel, C. Wagner, A. Sigmund, L. Moerl, N. Grote, Ultra-low 1490 nm surface-emitting BH-DFB laser diode with integrated monitor photodiode, in *Proc. 22nd Intern. Conf. on InP and Related Materials (IPRM'10)*, Takamatsu, Japan (2010), pp. 55–58
85. K. Adachi, K. Shinoda, T. Fukamachi, T. Shiota, T. Kitatani, K. Hosomi, Y. Matsuoka, T. Sugawara, M. Aoki, A 1.3 μm lens-integrated horizontal-cavity surface-emitting laser with direct and highly efficient coupling to optical fibers, in *Opt. Fiber Commun. Conf. (OFC'09)*, San Diego, USA (2009), Techn. Digest, paper JThA31
86. K. Adachi, K. Shinoda, T. Shiota, T. Fukamachi, T. Kitatani, K. Hosomi, Y. Matsuoka, T. Sugawara, M. Aoki, 100 °C, 25 Gbit/s direct modulation of 1.3 μm surface emitting laser, in *Conference on Lasers and Electro-Optics (CLEO/QELS'10)*, San Jose, USA (2010), Techn. Digest, paper CME4
87. K. Adachi, T. Suzuki, T. Ohtoshi, K. Nakahara, M. Sagawa, A. Nakanishi, K. Naoe, S. Tanaka, Facet-free surface-emitting 1.3- μm DFB laser, in *41st Europ. Conf. on Optical Communication (ECOC'15)*, Valencia, Spain (2015), paper We 1.5.4
88. T. Suzuki, K. Adachi, A. Takei, Y. Wakayama, A. Nakanishi, K. Naoe, K. Nakahara, S. Tanaka, K. Uomi, Capability of high optical-feedback tolerance and non-hermetic-packaging for low-cost interconnections using lens-integrated surface-emitting laser, in *Opt. Fiber Commun. Conf. (OFC'15)*, Los Angeles, CA, USA (2015), paper M3B.4

89. L. Vaissie, O.V. Smolski, A. Mehta, E.G. Johnson, High efficiency surface-emission laser with subwavelength antireflection structure. *IEEE Photonics Technol. Lett.* **17**, 732–734 (2005)
90. P. Modh, J. Backlund, J. Bengtsson, A. Larsson, N. Shimada, T. Suhara, Multifunctional gratings for surface-emitting lasers: design and implementation. *Appl. Opt.* **42**, 4847–4854 (2003)
91. G. Witjaksono, S. Li, J.L. Lee, D. Botez, W.K. Chan, Single-lobe, surface-normal beam surface emission from second-order distributed feedback lasers with half-wave grating phase. *Appl. Phys. Lett.* **83**, 5365–5367 (2003)

Norbert Grote received the Dipl. Phys. and Dr. degree in physics from the Technical University of Aachen (RWTH), Germany, in 1974 and 1977, respectively. At the RWTH he was working on III–V (GaInP, GaAlP) based light emitting diodes and GaAs DFB lasers and related liquid phase epitaxial growth processes. In 1980 he joined the Heinrich-Hertz-Institute in Berlin where he was among the first to help establish the Integrated Optics Division having the mission of developing components for optical telecommunication systems. He was engaged with InP epitaxy and the development of various photonic and also electronic (HBT) devices on InP basis. Until mid of 2015, he was deputy head of the Photonic Components department, renamed after HHI became a member institute of the Fraunhofer Association in 2003. In this position he was supervising different R&D groups working on InP materials technology, laser devices, and polymer based waveguide devices. In recent years his R&D focus was mainly on photonic integration encompassing both monolithic InP photonic integrated circuits and hybrid integration technology on a polymer platform. Currently he is working for HHI in an advisory position. Over the years he was extensively involved in the initiation and coordination of public and industrial R&D programmes/projects. Amongst others, he coordinated the EC funded FP6 project MEPHISTO, and was engaged with the FP7 IP projects EuroPIC and PARADIGM, both addressing generic monolithic optical integration technology and photonic integrated circuits. He is (co)author of more than 140 papers and conference contributions. He (co)-chaired various national and European workshops, and in 2011 he was Conference Chair of the prestigious “International Conference on Indium Phosphide and Related Materials” (23rd IPRM) for which he subsequently served as chairman of the International Steering Committee from 2011–2013.

Martin Möhrle received his diploma degree in physics (M.S.) from the University of Stuttgart in 1988, and the Ph.D. degree from the Technical University of Berlin in 1992. In 1988, he joined the Fraunhofer Institute for Telecommunications, Heinrich-Hertz-Institute. He has more than twenty years experience and expertise in modeling, design, technology, development and fabrication of a large variety of semiconductor FP- and DFB-lasers, tunable lasers, surface emitting lasers, electroabsorption modulated lasers, optical amplifiers, flip-chip compatible devices and monolithically integrated devices. At HHI he is head of the laser development group and manages projects with national and international partners. He holds several patents on laser devices and is author/coauthor of more than 100 papers.

Markus Ortsiefer was born in Cham, Germany, in 1970. He received his diploma degree in physics in 1997 and the doctoral degree in 2001, both from the Technical University of Munich. During his Ph.D. work, he studied novel concepts for long wavelength VCSELs and pioneered the InP-based buried tunnel junction (BTJ)-VCSEL. In 2001, he co-founded VERTILAS where he was managing director from 2001 to 2003. Since 2003, he is Chief Technology Officer and responsible for the company’s production and research activities. Markus Ortsiefer has authored or coauthored more than 150 publications in scientific journals, conference proceedings and books and filed several patents on optoelectronic devices. In 2004, he was awarded the Karl-Heinz-Beckurts price together with Prof. Dr.-Ing. M.-C. Amann for the realization and commercialization of the breakthrough concept for long-wavelength VCSELs. Over the past years, he has been strongly involved in national and international R&D programs as well as collaborative projects with academic and industrial partners for the development of advanced applications and systems in optical communications and sensing. Dr. Ortsiefer is a member of the German Physical Society (DPG).

Chapter 4

Ultra-Fast Semiconductor Laser Sources

Masahiro Aoki and Ute Troppenz

Abstract The chapter focuses on ultra-fast light sources for achieving small footprint and lower-power-consumption optical transceivers and covers various important light sources such as directly-modulated diode lasers with high optical-gain materials, low chirp externally-modulated diode lasers, and ultra-fast diode lasers with new structure and modulation scheme. The chapter starts with an in-depth theoretical treatment of key characteristics and dependences, illustrates typical realizations of ultra-fast diode lasers and integrated laser-modulators, and includes relevant operation and performance characteristics as well. In response to strong demand for datacom and access network applications selected variants of edge emitting transmitters are presented with particular emphasis on spectral and bandwidth efficiency.

4.1 Introduction

Since the recovery from the ‘dot-com bubble’ (or ‘information technology bubble’) that occurred at the beginning of this century, demand for highly efficient transmission of huge amounts of data has soared with the explosive growth of broadband/broadgather data networks. Core/edge routers, switches, and data servers are now essential for the information and communications technology (ICT) that provides the infrastructure for our daily lives and our business activities in today’s ICT-based society. High-end ICT equipment depends heavily on fast optical data transmission technologies. Such technologies are essential not only in communication networks (for both telecommunications and mobile backhaul communication), but also in storage networks (so-called fiber channels) as well as in local area networks.

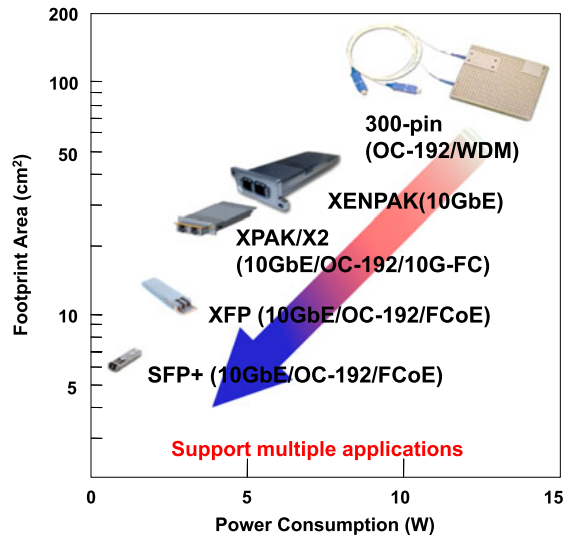
M. Aoki

Center for Technology Innovation, Research & Development Group, Hitachi Ltd., 1-1, Omika 7, Hitachi-city, Ibaraki, Japan
e-mail: masahiro.aoki.ev@hitachi.com

U. Troppenz (✉)

Fraunhofer Institute for Telecommunications, Heinrich-Hertz-Institute, Einsteinufer 37, 10587 Berlin, Germany
e-mail: ute.troppenz@hhi.fraunhofer.de

Fig. 4.1 Footprint area and power consumption of 10 Gbit/s optical transceivers



Common technological keys enable high data throughput, high port densities and at the same time cost effectiveness. The total system performance depends heavily both on the data throughput of each channel port and on the integration density determined by the assembly size and power consumption of the components. That is why gigabit-per-second (Gbit/s) class optical transceivers with low power consumption and small footprints are so important. An example of the technology trend of optical transponders used for 10 Gbit/s systems is shown in Fig. 4.1, which plots the relationship between module footprint and total power consumption for several types of standard transceiver modules.

The standard 10 Gbit/s optical transceivers started with 300 pins in 2000 [1] with a large footprint (ca. 100 cm²) and high power consumption (ca. 15 to 20 W). To meet the demands for reduced size and power consumption, several types of de facto standard 10 Gbit/s transceiver packages, XENPAK [2], XPAK [3] X2 [4], XFP [5], and SFP+ [6] have been developed and, as a result, the footprint and power consumption have been reduced in rapid succession. Moreover, the optical connector has changed from a pigtail to a receptacle to simplify the assemblies. Currently, the members of the CFP Multi-Source Agreement (MSA) group are defining CFP, CFP2 and CFP4 form factors for the next generation 100G/400G transceiver packages [7] to support ultra-high bandwidth requirements of data communications and telecommunication networks.

10 Gbit/s components are insufficient to meet current and, in particular, future system requirements, and therefore 40- and 100 Gbit/s optical transceivers have been developed. In mid 2010 a new standard (IEEE 802.3ba [8]) for 40G- and 100G-Ethernet was approved relying on wavelength-multiplexed 4×10 Gbit/s, and 10×10 Gbit/s and 4×25 Gbit/s transmission schemes. For the latter scheme, laser sources with specified emission wavelengths around 1.3 μm (four wavelengths with 800 GHz spacing, referred to as LAN-CWDM) are required that are capable of gen-

erating 25 Gbit/s bit streams. To achieve 400 Gbit/s transmission serial 50 Gbit/s and 100 Gbit/s lanes are under development for the next generation of 400 Gigabit Ethernet (400GbE) with a new standard expected in 2017 [9]. For the implementation of respective multi-lane transmitter modules lasers for bit rates up to 56 Gbit/s will be needed as key building blocks.

In order to reduce the size and power consumption of optical modules, lower-current/voltage drivability is crucial, and the elimination of thermo-electric coolers is highly desired. The keys to meeting these requirements are high-speed, uncooled semiconductor laser sources with small drive current/voltage. This chapter reviews recent technological progress in ultra-fast light sources for achieving small footprints and lower-power-consumption optical transceivers. We will address several important light source devices such as directly-modulated diode lasers with high-optical gain materials, externally-modulated diode lasers, ultra-fast diode lasers exploiting new structures and modulation schemes, and, in response to strong demand for datacom and access network applications, selected variants of edge emitting transmitters with particular emphasis on spectral and bandwidth efficiency.

4.2 Ultra-Fast Directly-Modulated Laser Sources

4.2.1 High-Speed Characteristics of Directly-Modulated Lasers

The small-signal frequency response $R(f)$ of a diode laser can be derived from the rate equations that describe the interaction between the carrier density N and the photon density S in the active medium of a laser [10]. Above the threshold condition, these are expressed as

$$\frac{dN}{dt} = \frac{I}{eV} - v_g \frac{dg}{dN} (1 - \varepsilon S)(N - N_T)S - \frac{N}{\tau_N}, \quad (4.1)$$

$$\frac{dS}{dt} = v_g \frac{dg}{dN} (N - N_T)(1 - \varepsilon S)S - \frac{S}{\tau_P} + \xi\beta \frac{N}{\tau_N}, \quad (4.2)$$

where I is the current injected into the active region of total volume V , e the electron charge, v_g the group velocity of light in the laser medium, dg/dN the differential gain, ε the gain saturation coefficient, N_T the transparency carrier density, τ_N the carrier life time, τ_P the photon life time, ξ the optical confinement factor, and β is the spontaneous emission fraction for lasing. Assuming small signal current modulation, i.e., $I(t) = I_0 + \delta I_1 e^{j\omega t}$, $R(f)$ is expressed as

$$R(f) = \frac{f_r^4}{(f^2 - f_r^2)^2 + f^2 \Gamma^2 / (2\pi)^2} \cdot \frac{1}{1 + (2\pi C_{ld} R_{ld} f)^2}, \quad (4.3)$$

where f_r is the relaxation oscillation frequency, Γ the damping constant, and $C_{ld} R_{ld}$ is the laser parasitic constant (the index 'ld' denotes laser diode). f_r and Γ are expressed as

$$f_r = \frac{1}{2\pi} \sqrt{v_g \frac{dg}{dN} (1 - \varepsilon S) \eta_i \frac{\xi}{eV} (I - I_{th})}, \quad (4.4)$$

$$\Gamma = \frac{1}{\tau_N} + v_g \frac{dg}{dN} S + \frac{\varepsilon S}{\tau_P} = \frac{1}{\tau_N} + K f_r^2, \quad (4.5)$$

where η_i is the internal quantum efficiency. K is called the nonlinear K -factor and is expressed as

$$K = \frac{4\pi^2}{v_g} \left(\frac{\varepsilon}{\frac{dg}{dN}} + \frac{1}{\alpha_m + 2\alpha_{th}} \right), \quad (4.6)$$

with α_m and α_{th} being the mirror loss and lasing threshold gain, respectively.

It is apparent from (4.3), that in order to achieve high-speed lasers, it is important to enhance the relaxation oscillation frequency f_r or to reduce the laser parasitic constant $C_{ld}R_{ld}$ and the damping constant Γ . The quantitative effects of these factors on the high-speed performance are discussed below.

Reduction of Laser Parasitic Constant $C_{ld}R_{ld}$ From (4.3), the CR- (capacitance-resistance) limited frequency bandwidth f_{3dB}^{CR} , where f_{3dB} is the 3-dB-down bandwidth, is expressed as

$$f_{3dB}^{CR} = \frac{1}{2\pi C_{ld}R_{ld}}. \quad (4.7)$$

With today's device/process techniques in III-V semiconductor-based optoelectronics, laser capacitances C_{ld} can be designed to be less than a few hundred femto-Farad (fF). Moreover, the laser series resistance R is in the range from several Ohm to several tens of Ohm (Ω). If we assume $C_{ld} = 400$ fF and $R_{ld} = 10 \Omega$, then the calculated value of f_{3dB}^{CR} is 40 GHz. This simply means that 40 Gbit/s direct modulation is theoretically feasible in terms of laser parasitics.

Enhancement of Relaxation Oscillation Frequency f_r By solving

$$R(f_{3dB}^{fr}) = 1/2$$

for the condition $C_{ld}R_{ld} = 0$, $\Gamma = 0$, we get

$$f_{3dB}^{fr} = \sqrt{1 + \sqrt{2}} \cdot f_r \cong 1.55 \cdot f_r. \quad (4.8)$$

The relaxation oscillation frequency f_r is governed by the resonant oscillation behavior between carriers and photons that occurs in a laser resonator, and the laser light output can never respond to a rapidly changing electrical input signal any faster than f_r . In other words, f_r is the essential parameter that determines the dynamic limit of semiconductor diode lasers.

Reduction of Damping Constant Γ Damping is known to originate from nonlinear gain saturation, and it adversely affects the laser dynamics. It does not only lower the resonant peak in $R(f)$, but also reduces the frequency bandwidth, especially in the high frequency range above 20 GHz.

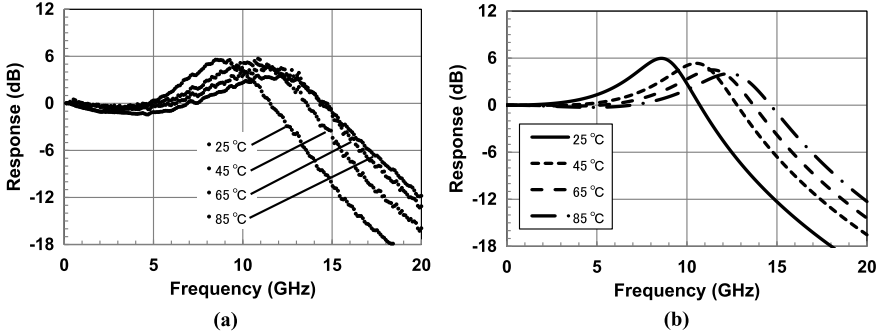


Fig. 4.2 (a) Example of small-signal frequency responses $R(f)$ measured for a 1.3 μm wavelength range diode laser [11] compared with (b) fitted responses calculated using (4.3)

Again, by solving $R(f_{3dB}^K) = 1/2$ for $C_{ld}R_{ld} = 0$, $f_r = \infty$, we get

$$f_{3dB}^K = 2\sqrt{2\pi}/K. \tag{4.9}$$

In fact, the nonlinear K -factor is typically 0.3 ns for InGaAsP/InP-based quantum well lasers, and the corresponding f_{3dB}^K is calculated to be about 30 GHz. This essentially implies that the effect of damping can never be neglected in ultra-fast diode lasers modulated in the range of a few tens of GHz.

An example of small-signal frequency responses ($R(f)$) measured for a 1.3 μm wavelength range diode laser [11] is shown in Fig. 4.2(a).

The laser has an active region composed of InGaAlAs (see Sect. 4.2.4 and also Chap. 3) formed on an InP substrate. It is designed with a 300 μm long cavity and a ridge waveguide as the striped structure. Data for $R(f)$ measured at various temperatures ranging from 25 to 85 °C are plotted in Fig. 4.2(a). By fitting the measured $R(f)$ using (4.3), the temperature dependence of f_r and the nonlinear K -factor were both extracted; they are plotted in Fig. 4.3.

Fitted responses calculated using these data as parameters are drawn in Fig. 4.2(b). The results clearly reveal the good agreement between measured and fitted curves,

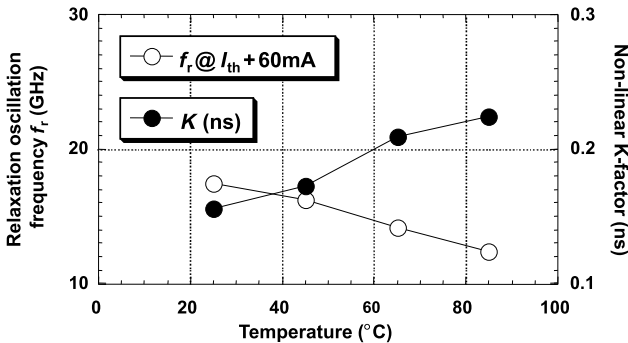


Fig. 4.3 Temperature dependence of f_r and nonlinear K -factor

evidencing the correctness and accuracy of the laser dynamics modeling provided by (4.3).

Lastly, it is important to note here that there could be significant contributions of carrier injection and carrier transport that occur inside or in the vicinity of the active region other than the above limiting factors of the laser dynamics; i.e., the parasitic constant, the relaxation oscillation frequency and the damping factor. Slow carrier transport or poor carrier injection efficiency into quantum wells easily deteriorate the high-speed modulation performance, leading to low frequency roll-off and excess increase of damping. These negative effects can be diminished, and by employing a proper active region design the inherent high-speed capability can be retained [12, 13].

4.2.2 Large-Signal Dynamic Analysis of Rate Equations

Assuming digital modulation of laser sources, large-signal analysis has been performed to understand the dynamic behavior of a laser, which is closely related to fiber transmission performance [14–17]. The large-signal modulation was simulated to obtain the temporal variations in optical intensity $S(t)$ and carrier density $N(t)$. The rate equations (4.1) and (4.2) were solved numerically using the time-developed Runge-Kutta method. A drive-waveform with a maximum 32-bit non-return-to-zero (NRZ) pseudo-random pattern was used in this calculation. A bit sequence of “01010111” was used to simulate dynamic changes in $S(t)$ and $N(t)$. The electrical circuit model of the parasitic is shown in Fig. 4.4.

The laser drive current waveform with a trapezoidal pattern (meaning finite rise and fall times) was filtered to account for the parasitics of the modulator and assemblies. The model includes laser capacitance C_{ld} , internal resistance R_{ld} , wiring inductance L , and a termination resistor to match the impedance of the radio frequency (RF) signal lines with a standard characteristic impedance of $50\ \Omega$. In the computation procedures, a signal rate of 10 Gbit/s was used to investigate the feasibility of 10 Gbit/s direct intensity modulation. Most of the parameters used in the computation were extracted from experiment data [11]. As mentioned earlier, the active material was assumed to be an InGaAlAs/InP-based multiple quantum well

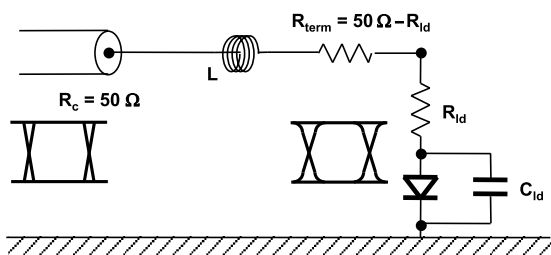


Fig. 4.4 Electrical circuit model of laser parasitics. C_{ld} : laser parasitic capacitance (5.0 pF) R_{ld} : laser internal resistance (15 Ω); R_c : characteristic impedance of RF line (50 Ω); R_{term} : termination resistance (50 $\Omega - R_{ld}$); L : wiring inductance (0.4 nH)

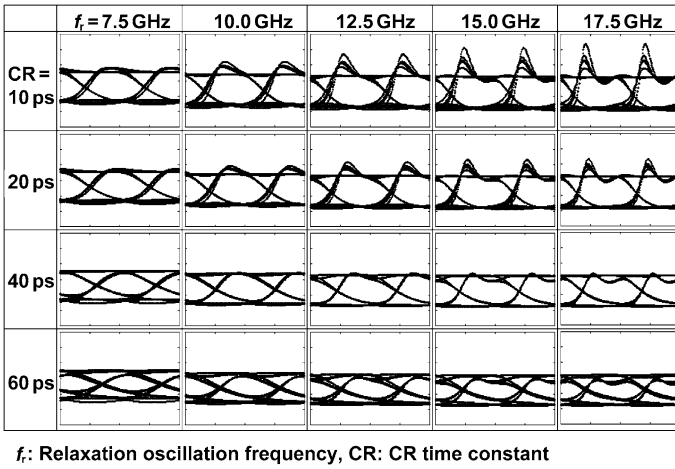


Fig. 4.5 Calculated eye diagrams for 10 Gbit/s modulation at various values of relaxation oscillation frequency f_r and CR parasitic constant

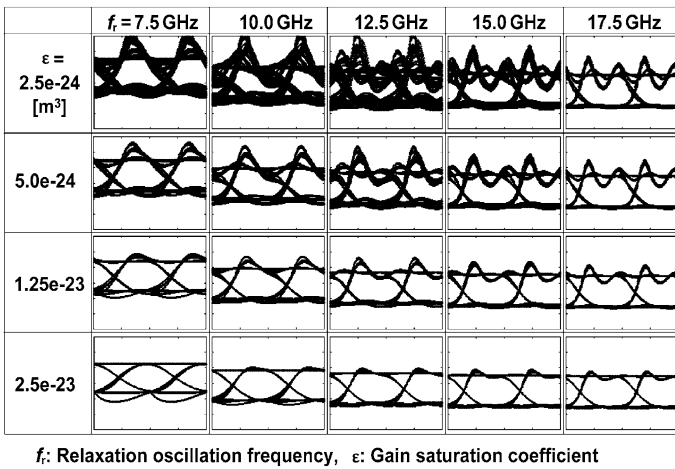


Fig. 4.6 Calculated eye diagrams for 10 Gbit/s modulation with various values of relaxation oscillation frequency f_r and gain saturation coefficient

(MQW). Calculated eye diagrams for 10 Gbit/s modulation with various values of relaxation oscillation frequency f_r , CR parasitic, and gain saturation coefficient ϵ are shown in Figs. 4.5 and 4.6.

The results directly indicate the importance of a higher f_r and a smaller CR constant for obtaining better eye opening. Moreover, note here as well that a too small value of ϵ results in large peaking in the leading edge of the optical waveform. This implies that the nonlinear gain in high-speed lasers acts to reshape the waveforms through damping effects.

4.2.3 Chirp Characteristics of Directly Modulated Lasers

In optical fiber transmission systems, the transmission distance and the transmission capacity of a single-channel data stream are mainly limited by the optical loss as well as by the chromatic dispersion of the fiber medium. The latter limiting factor is linked to the spectral purity of the modulated light source, which is known as dynamic spectrum linewidth or chirp. This chirp is closely related to the broadening that an optical pulse suffers as it propagates over long-distance dispersive fibers. In long-haul transmission systems, fiber-inline amplifiers such as erbium-doped fiber amplifiers (EDFAs) are commonly used to compensate for the accumulated propagation loss. This makes the chirp-induced pulse broadening to severely limit the bit rate and maximum transmission distance [17]. The chirp observed in directly intensity-modulated diode lasers is characterized by the spectral linewidth enhancement factor, also simply known as the α parameter (α_{ld}), which is described by

$$\alpha_{ld} = -\frac{4\pi}{\lambda} \cdot \frac{\frac{dn}{dN}}{\frac{dg}{dN}}, \quad (4.10)$$

where dn/dN is the differential index in the laser medium and λ is the wavelength of the laser light. The numerator in (4.10) denotes the changes in refractive index in the laser cavity, i.e. the wavelength/frequency fluctuation. On the other hand, the denominator dg/dN , the differential gain, expresses the degree of intensity modulation. So the α -parameter of a laser diode, α_{ld} , can be regarded as the ratio of frequency modulation depth to amplitude modulation depth.

Calculation results showing how the maximum fiber transmission distance (L_{\max}) is limited by α_{ld} are presented in Figs. 4.7(a) and (b). We assumed a Gaussian-shaped optical signal pulse propagating through a normal single-mode fiber line. Two different signal wavelengths in the 1.3 and 1.55 μm range were used, referring to Figs. 4.7(a) and (b), respectively. We found, as appears reasonable, that L_{\max} strongly depends on α_{ld} . Note that α_{ld} of typical directly modulated lasers operated in a single longitudinal mode is within a range between 2 to 8 depending mainly on the active material. This limits the maximum transmission distance at 10 Gbit/s, for example, to 10 km in Fig. 4.7(b). The figure also shows that the distance is severely restricted by the transmission data rate. These results directly indicate the importance of ultra-fast, low-chirp light sources for longer-reach transmission. For achieving maximum transmission distances, it is apparent that reduction of α_{ld} is crucial. In general, the use of a laser direct modulation scheme is limited to shorter-reach applications, while external modulation is utilized to enhance the link distance. Chirp suppression is very important for this purpose, and the use of external modulators is discussed in Sect. 4.3.

4.2.4 High-Gain Active Materials for Ultra-Fast Uncooled Lasers

In present long-reach optical fiber communication systems, different types of light sources are used in the 1.3- and 1.55 μm wavelength windows where the optical

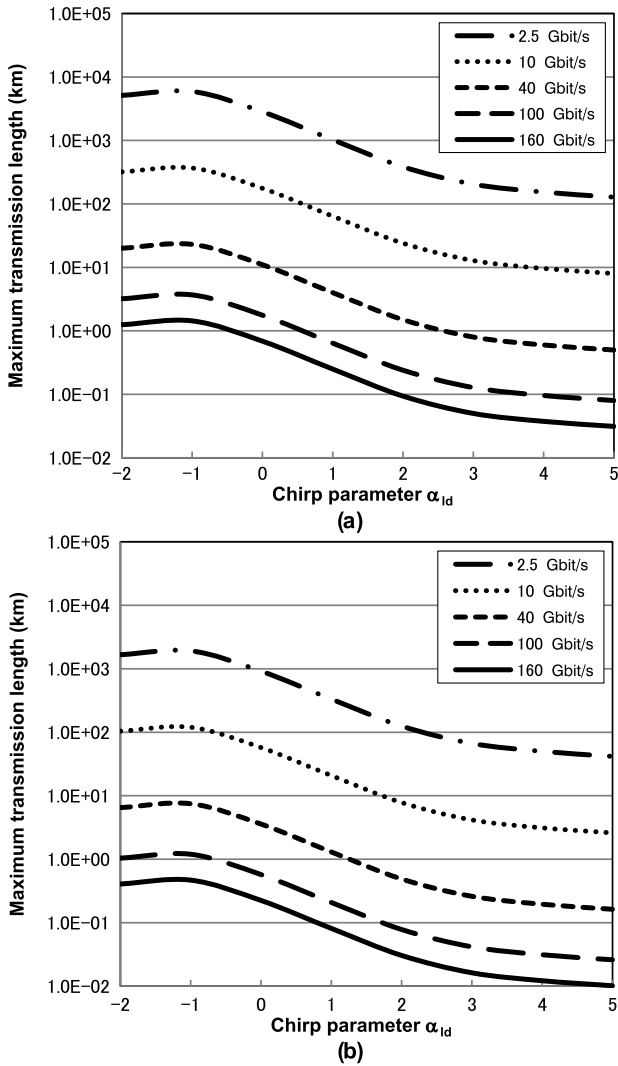


Fig. 4.7 Calculated results showing how the maximum fiber transmission distance is limited by α_{id} . (a) 1.3 μm range transmission (with chromatic dispersion of 6.5 ps/(nm km)) and (b) 1.55 μm range transmission (with chromatic dispersion of 20 ps/(nm km))

loss or effect of fiber chromatic dispersion is minimum. If we focus on the III–V compound materials used for these laser sources, we see that InGaAsP grown on a standard InP substrate has been the most widely used material. This is because it can provide 1.3/1.55 μm range operation along with the superior long-term stability (more than a decade) required for the communication infrastructure. Initially, bulk InGaAsP-based laser sources were used, and these were assembled on thermoelectric coolers to compensate for their poor temperature stability. Recently, wide-

temperature range or so-called uncooled operation has been demonstrated with this material system through the use of MQWs which are a new artificial form of material (see also Chap. 3). In particular, strained-layer MQWs have been successful in producing uncooled InGaAsP diode lasers [18–26]. However, with the wide and rapid spread of optical fiber links, faster operation at 10 Gbit/s or beyond has become essential. Besides, cost effectiveness is naturally important from the commercial perspective. That is why new high-speed, and hopefully uncooled, diode lasers are key devices and therefore in the focus of current component developments.

It is apparent from (4.4) that higher differential gain dg/dN is very effective for faster direct modulation. In general, the optical gain g of an optically active material is determined by the electric dipole moment $|M_b|^2$, the reduced density of states ρ_{red} , and the Fermi-Dirac functions of carriers in the conduction and valence bands f_c and f_v , respectively. It is written as

$$g(E) = \frac{\pi e^2 \hbar}{nm_0^2 \epsilon_0 c E} |M_b|^2 \rho_{red}(E) [f_c(E) - f_v(E)], \quad (4.11)$$

where n is the refractive index of the laser medium, m_0 the electron mass, ϵ_0 the permittivity of free space, c the velocity of light in vacuum, \hbar Planck's constant, and E is the photon energy. It is important to note that the band structure in active materials has a strong impact on the laser gain g . The three factors, i.e., $|M_b|^2$, ρ_{red} , and $[f_c - f_v]$, in (4.11) are dominated by the quantum size effect in the active materials we use. By introducing the quantum size effect using low-dimensional nano-scale structures such as quantum wells, we can greatly enhance ρ_{red} due to the step-like density of states. Furthermore, the transition probability between electrons and heavy holes is enhanced since degenerate heavy holes and light holes are split in the quantum wells. This directly increases the dipole moment $|M_b|^2$, leading to greater optical gain. Quantitatively, the quantum size effect can be described by the energy depth of the potentials in both the conduction and valence bands, which correspond to the confinement of electrons and holes, respectively. Band diagrams of the quantum well structures for three types of material systems are schematically illustrated in Fig. 4.8 for (a) InGaAsP/InP, (b) InGaAlAs/InP, and (c) GaInNAs/GaAs,

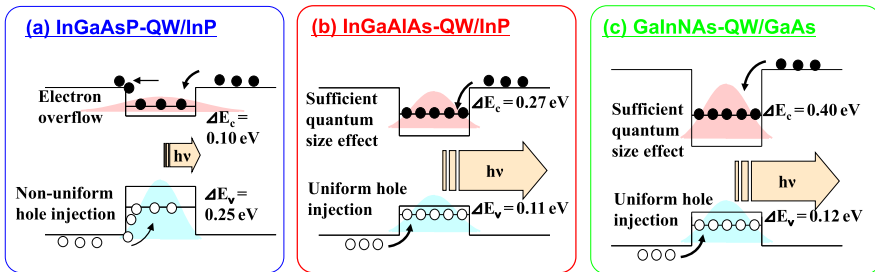
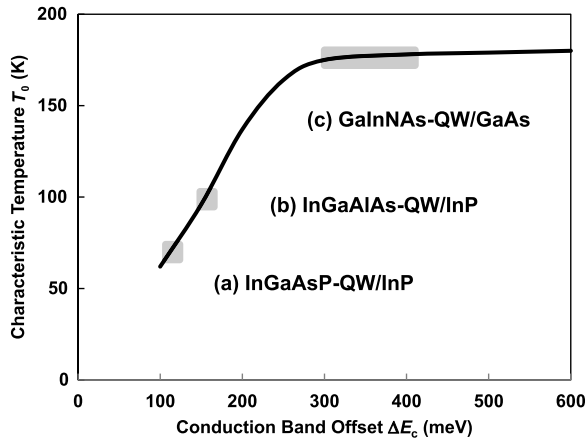


Fig. 4.8 Band diagrams of quantum well structures for three types of material systems. (a) InGaAsP/InP, (b) InGaAlAs/InP, and (c) GaInNAs/GaAs. ΔE_c , and ΔE_v are the typical band-offsets for the respective material

Fig. 4.9 Calculated characteristic temperature as a function of conduction band offset [27]



all designed for 1.3 μm range light emission. Note that in the latter case GaAs is used as substrate material.

The important band offset numbers between quantum wells and barriers are presented for each of the cases in the figures. The conventional InGaAsP/InP system (a) has a small conduction band offset ΔE_c for electrons of about 100 meV and a large valence band offset ΔE_v for heavy holes of about 250 meV, meaning an inconvenient band structure. Since electrons are much lighter than holes, ΔE_c should be greater than ΔE_v in order to achieve strong quantum confinement of electrons. A small ΔE_v is desired for simultaneously achieving smooth heavy hole injection.

On the other hand, InGaAlAs/InP (b) and GaInNAs/GaAs (c) both possess distinctly superior band diagrams in these respects. In particular, GaInNAs/GaAs has a large ΔE_c of 300 meV to 500 meV, which should efficiently suppress electron leakage/overflow from the quantum wells. The calculated temperature stability of diode lasers made from these materials is shown in Fig. 4.9 [27].

The diagram indicates how the characteristic temperature T_0 depends on ΔE_c . Here T_0 is employed as a figure-of-merit for high-temperature stability of the threshold current of a diode laser. Using T_0 the temperature dependence of the threshold current $I_{th}(T)$ is expressed as: $I_{th}(T) = I_{th}(0) \exp(T/T_0)$, with T being the absolute temperature. The calculation is based on the thermo-ionic emission model developed by Suemune [28]. Quasi-Fermi levels for electrons were assumed to be 50 meV and 70 meV at 300 K and 360 K, respectively. For deep quantum wells ($\Delta E_c > 400$ meV), the calculated T_0 has a very high value of 180 K, meaning that electron leakage from the wells can be largely neglected.

To illustrate the effectiveness of using a high-gain active material, high-temperature/high-speed characteristics of a GaInNAs diode laser operated at 1.3 μm are presented in Fig. 4.10. This GaInNAs laser [27, 29] was grown on a (100)-oriented n-type GaAs substrate by molecular beam epitaxy (MBE) with the nitrogen atoms supplied in the form of radicals. The nitrogen flux was produced by an RF discharge in an appropriate nitrogen radical cell. The laser comprises three GaInNAs quantum wells (TQW) separated by GaAs barriers. The important quantities ΔE_c

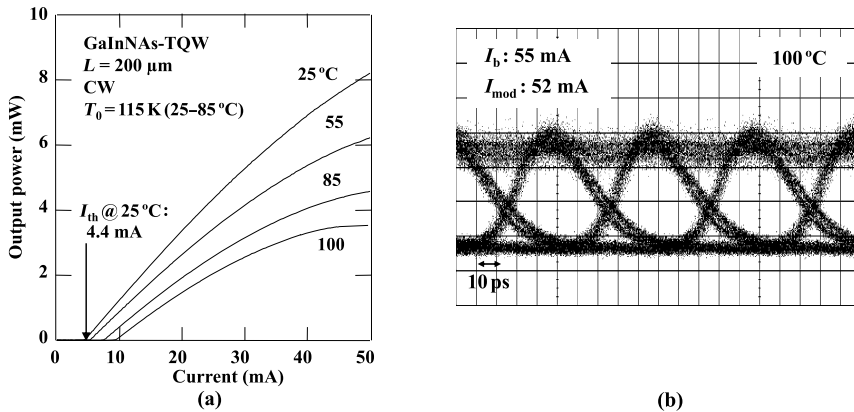


Fig. 4.10 (a) Light output power versus current characteristics of GaInNAs RWG laser and (b) 10 Gbit/s directly modulated waveform at 100 °C

and ΔE_v amount to 400 meV and 150 meV, respectively. To characterize its high temperature stability due to the superior band structure, a high T_0 of over 100 K, uncooled 10 Gbit/s direct modulation at 100 °C, and even 40 Gbit/s direct modulation were obtained [29]. However, with GaInNAs lasers it proves very difficult to extend the emission wavelength significantly above 1.3 μm whilst retaining good lasing properties, and lifetime issues are still existing.

As discussed earlier, the InGaAlAs MQW structure also possesses fairly large ΔE_c and small ΔE_v ($\Delta E_c : \Delta E_v = 7 : 3$). Accordingly, sufficient electron confinement in the conduction band and uniform hole injection are expected with this class of material too, again leading to high differential gain and good high-temperature performance.

After the initial demonstration of narrow linewidth InGaAs/InAlAs MQW lasers operating in the 1.55 μm range [30], superior uncooled operation of 1.3 μm range InGaAlAs MQW ridge waveguide (RWG) lasers was demonstrated [31]. Experimental studies have evidenced that the differential gain of InGaAlAs lasers was distinctly higher than that for InGaAsP lasers. With the explosive growth of Internet traffic, 10 Gbit/s InGaAlAs MQW RWG distributed feedback (DFB) lasers have been actively developed and demonstrated by various groups [11, 31–37]. In 10 Gbit/s DFB lasers with InGaAlAs active medium, the maximum operating temperature and bit rate have reached 115 °C at 12.5 Gbit/s [26, 34] and 120 °C at 10 Gbit/s [35], while those for InGaAsP appear to be limited to near 100 °C at 10 Gbit/s [24]. These results provide direct evidence that InGaAlAs offers pronounced advantages with respect to high-temperature and high-speed operation. On the basis of these superior material characteristics, 1.3 μm DFB lasers have been successfully demonstrated for use in de facto standard 10 Gbit/s small form factor transceiver modules like SFP+ or XFP. A photograph of an XFP module (10 Gbit/s form factor module pluggable) incorporating a 1.3 μm InGaAlAs-based DFB laser is shown in Fig. 4.11. As a result of the high-gain properties of InGaAlAs a clearly

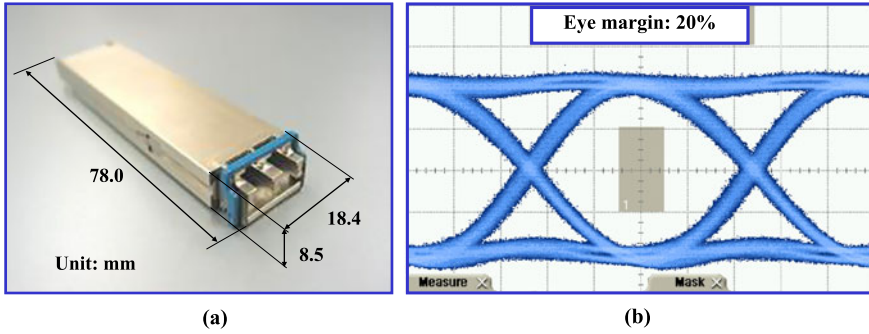


Fig. 4.11 (a) XFP transponder module incorporating a 1.3 μm InGaAlAs DFB laser (Opnext, TRF5010/TRF5020) and (b) 10 Gbit/s optical waveform

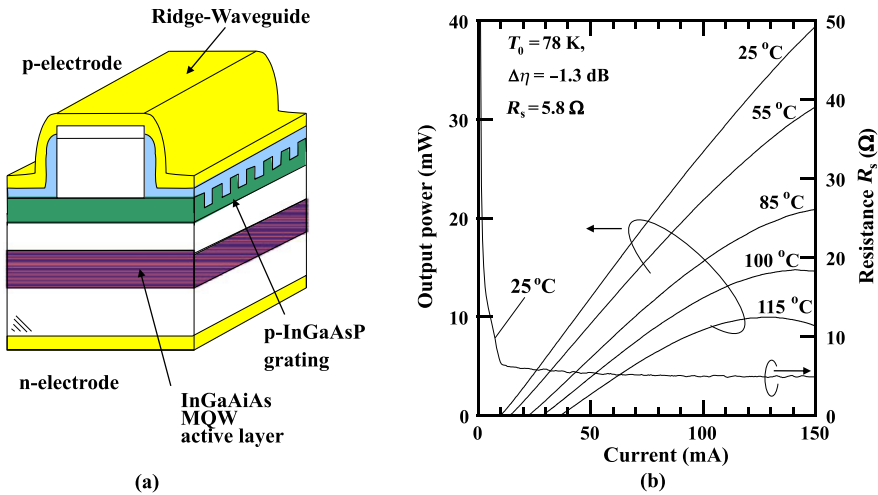


Fig. 4.12 (a) Device structure and (b) light-current curves of a 1.3 μm InGaAlAs DFB laser [34, 35]

opened eye diagram was obtained at 10 Gbit/s modulation. The structure of the InGaAlAs-based laser chip and light-current characteristics measured at elevated temperatures of up to 115 $^{\circ}\text{C}$ are depicted in Fig. 4.12 [34, 35].

4.2.5 Short-Cavity Ultra-Fast Lasers

This section discusses how the downsizing of the laser cavity has a positive effect on the laser dynamics. At a first glance, (4.4) would suggest that the relaxation oscillation frequency f_r can be raised by minimizing the total volume V of the laser

active region. In reality, however, the gain saturation and strong damping in a small active region severely limit the high-speed performance. To explore the optimum design of the laser cavity for higher-speed characteristics, analytical expressions for the optical gain and carrier life time are used.

The optical gain generated in an active quantum well laser region can be empirically written using the injection current density J as [38]

$$g = G_0 \ln\left(\frac{J}{N_w J_0}\right), \quad (4.12)$$

where G_0 , N_w , and J_0 denote the gain coefficient, the number of MQWs, and the transparency current density. Here, $J = I/W_a/L_c$, where W_a and L_c are the lateral width and the length of the laser active region, respectively. The first term of the rate equation for the carriers, (4.1), denotes the number of injected carriers, and it can be rewritten using the carrier density N as

$$\frac{I}{eV} = \frac{JW_aL_c}{eV} = AN + BN^2 + CN^3, \quad (4.13)$$

where A , B , and C are coefficients that describe non-radiative and radiative recombination, and the Auger process. Using (4.12) and (4.13), the differential gain dg/dN is then calculated as

$$\frac{dg}{dN} = \frac{dg}{dJ} \frac{dJ}{dN} = G_0 \frac{A + 2BN + 3CN^2}{AN + BN^2 + CN^3}. \quad (4.14)$$

Using (4.14) and (4.4), we can derive the current efficiency of f_r , indicated by η_{f_r} , as

$$\eta_{f_r} = \frac{f_r}{\sqrt{I - I_{th}}} \propto \sqrt{\frac{dg}{dN} \frac{\alpha_i + \alpha_m}{\alpha_m} \frac{1}{L_c}}. \quad (4.15)$$

Here, I_{th} is the threshold current for lasing, α_m the mirror loss at the laser facets, and α_i the internal loss of the laser cavity. In the case of Fabry-Pérot-type lasers, α_m is a function of R_f and R_r , which describe the mirror power reflectivities at the end facets, and it is given by

$$\alpha_m = \frac{1}{2L_c} \ln\left(\frac{1}{R_f R_r}\right). \quad (4.16)$$

By solving the lasing condition

$$\Gamma N_w g = \alpha_i + \alpha_m, \quad (4.17)$$

we can calculate dg/dN at the threshold to determine η_{f_r} .

The calculated η_{f_r} is shown in Fig. 4.13 as a function of laser cavity length L_c . The parameters used in this simulation, which are indicated in the figure caption, are typical for InGaAlAs-based 1.3 μm diode lasers used in recent 10 Gbit/s systems. First, η_{f_r} for a 200 μm long InGaAlAs laser is calculated and used as a reference. The ratio $\eta_{f_r}(L_c)/\eta_{f_r}(200 \mu\text{m})$ (for $L_c < 200 \mu\text{m}$) illustrates the positive effect of a short-cavity design. The calculation was performed for several sets

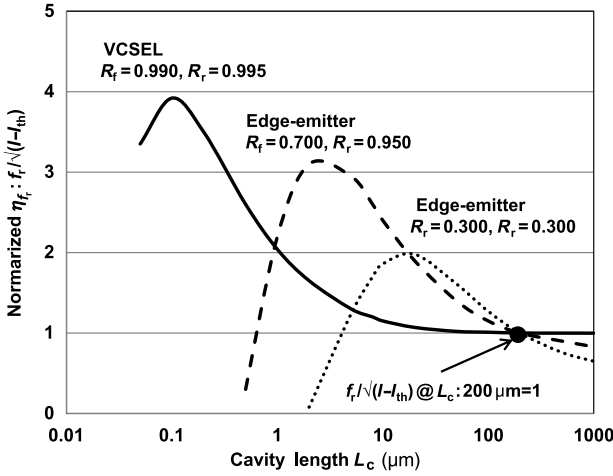


Fig. 4.13 Calculated η_f as a function of laser cavity length L_c . Parameters are: $G_0 = 850 \text{ cm}^{-1}$, $J_0 = 1254 \text{ A/cm}^{-2}$, $\alpha_i = 20 \text{ cm}^{-1}$, $\Gamma = 0.1$, $d = 0.1 \text{ }\mu\text{m}$, $A = 9.5 \times 10^7 \text{ sec}^{-1}$, $B = 7.7 \times 10^{-17} \text{ m}^3/\text{s}$ and $C = 1.1 \times 10^{-40} \text{ m}^6/\text{s}$

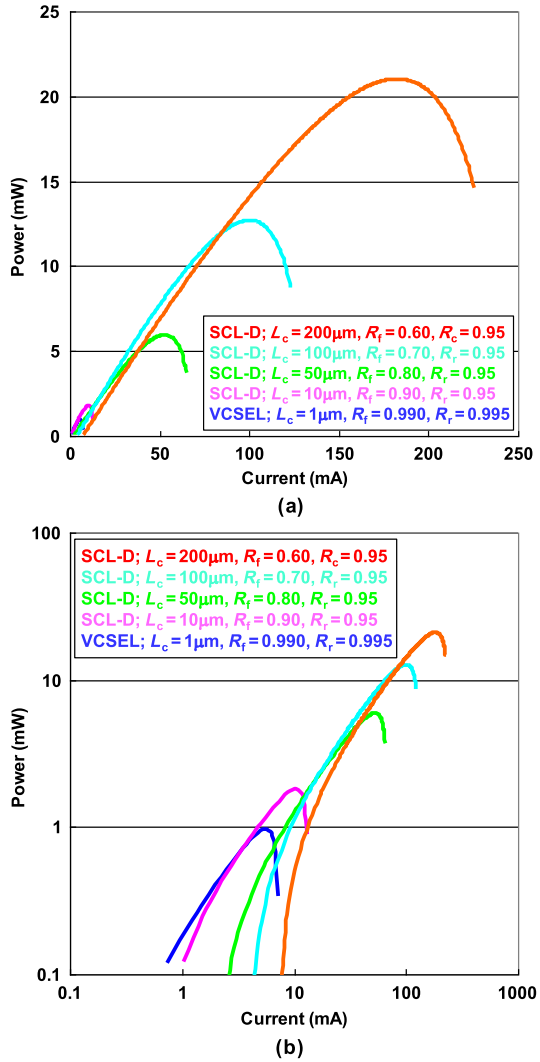
of R_f and R_r to fairly well compare short-cavity edge-emitting lasers (SCEELs) and vertical cavity surface emitting laser (VCSELs) versus “normal-length” cavity edge-emitting lasers. The results show that η_f is definitely enhanced by shortening L_c . We also find that the optimum L_c strongly depends on facet reflectivity; i.e., stronger facet reflection is essential for shorter L_c in order to compensate for the increased mirror loss factor of $1/2L_c \ln(1/R_f R_r)$. For example, for $R_f = 70\%$ and $R_r = 95\%$, the optimum L_c was calculated to be $5 \text{ }\mu\text{m}$ with a resultant $\eta_f(L_c)/\eta_f(200 \text{ }\mu\text{m})$ enhancement ratio of about 3. It is noteworthy that in the case of a VCSEL ($R_f = 99.0\%$ and $R_r = 99.5\%$) the optimum L_c lies naturally within the submicrometer range, and $\eta_f(L_c)/\eta_f(200 \text{ }\mu\text{m})$ enhancement turns out to be close to 4.

The above findings indicate the potential of achieving faster diode lasers by employing short cavity designs. However, since thermal effects were neglected in the above model, we next simulated light-current curves of these short-cavity diode lasers taking into account the electrical resistance R_{ld} and thermal resistance Θ_{ld} . When a short-cavity laser is used, both resistances adversely affect the static laser performance. Typical $I-L$ curves for a range of short-cavity devices are drawn in Figs. 4.14(a) and (b), which have linear and logarithmic vertical scales (light power), respectively.

It is obvious that severe power saturation is encountered with short-cavity devices. This suggests that the maximum f_r should saturate due to this thermal saturation as well. Taking this effect into account, we have calculated the maximum f_r as a function of L_c . The results are shown in Fig. 4.15.

It is apparent from this figure that there is an optimum L_c to suit the drivable laser current swings (I_f). For example, if we assume a drive current swing of 20 mA, the

Fig. 4.14 Typical I - L curves for a range of short-cavity devices on (a) linear scale and (b) logarithmic scale



best f_r of 13 GHz would be achieved with a short L_c of about 40 μm . It is interesting to note that this maximum f_r for the SCEEL is much higher than those for VCSELS ($L_c < 1\mu\text{m}$). This simply underlines the promising future potential for very higher speed operation of SCEELS.

Results calculated using (4.3), (4.4), and (4.5) are shown in Fig. 4.16. They show the requirements for the parameters f_r and K which essentially govern laser dynamics. The combination of the two parameters was computed using the three equations so that they achieved certain levels of $f_{3\text{dB}}$, as indicated in the figure. To highlight the capability of 40 Gbit/s direct modulation, the bold line indicates the criterion for reaching $f_{3\text{dB}} = 40\text{ GHz}$. Moreover, 40 Gbit/s eye diagrams were simulated for

Fig. 4.15 Maximum f_r calculated as a function of L_c considering thermal effects and with respect to limits of current driver swing I_f

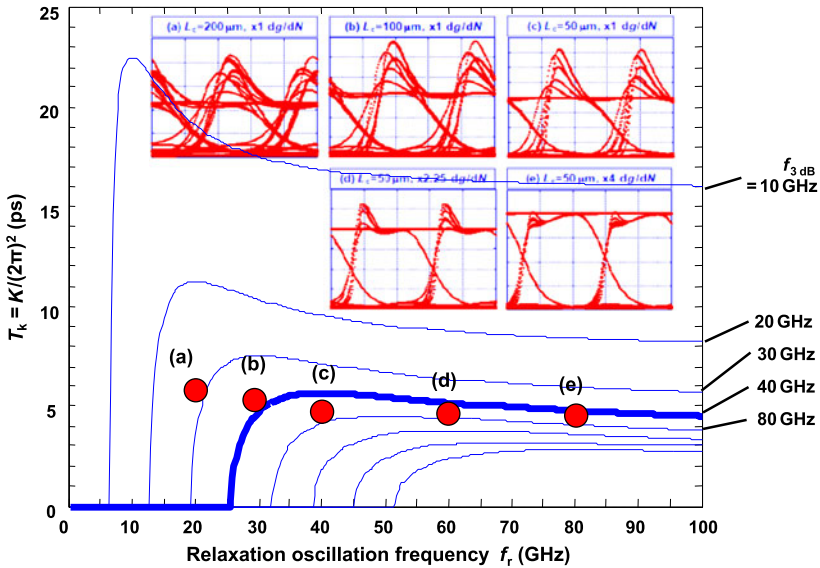
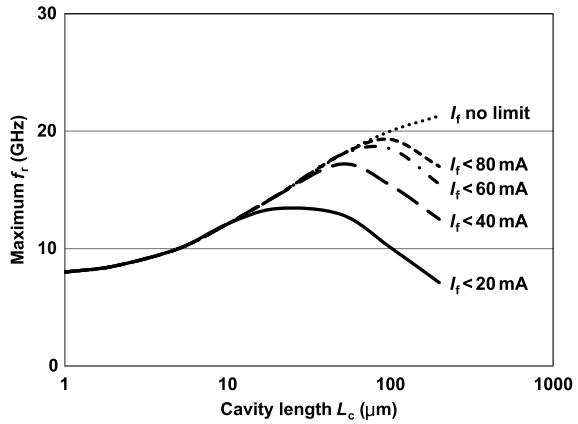
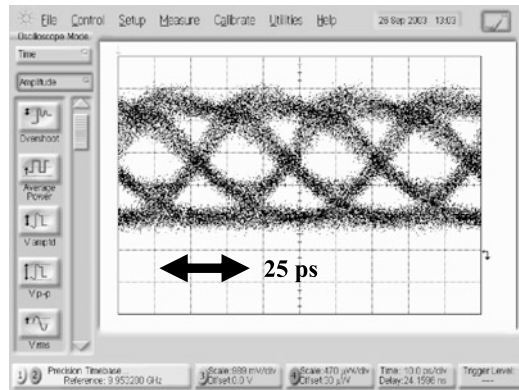


Fig. 4.16 Calculated results indicating the capability of 40 Gbit/s direct modulation

several sets of L_c and dg/dN using the method described in Sect. 4.2.2. The results directly indicate that a high f_r value of at least close to 40 GHz is necessary to accomplish 40 Gbit/s opened eyes with a small amount of jitter caused by inter-symbol interference. Also evidenced is the effectiveness of a shorter laser cavity via f_r enhancement. The results of successful 40 Gbit/s direct modulation of an SCEEL [39] designed in accordance with the rules given above are shown in Fig. 4.17.

The corresponding 1.3 μm range InGaAlAs laser had a 100 μm long short cavity realized by using a conventional cleaving technique. The short-cavity length of 100 μm only led f_r to increase to 28 GHz, and this enhancement successfully

Fig. 4.17 Successful 40 Gbit/s direct modulation achieved with a 100 μm long SCEEL



resulted in room temperature 40 Gbit/s modulation capability as demonstrated by the eye-opened optical waveforms represented in Fig. 4.17. Since then appreciable progress has been achieved with such directly modulated short-cavity laser diodes. The practical fabrication difficulties associated with cleaving and handling such devices was essentially overcome by incorporating passive waveguide sections by butt-joint growth to extend the physical device length. A DFB laser designed in such a way featured a 3-dB bandwidth of 28 GHz at 60 °C and a bias current of 45 mA only enabling 40 Gbit/s operation at that temperature with well opened eyes [40]. In another structure a waveguide based Bragg mirror has been formed at either side of the short-cavity DFB laser section to increase feedback to the active region and thus to reduce the threshold gain [41]. A buried heterostructure- (BH-) design using semi-insulating blocking layers was successfully adopted despite the Al containing active medium. A relaxation oscillation frequency f_r well beyond 25 GHz was obtained at 25 °C, and still some 20 GHz even at 70 °C. Threshold currents were as low as 4 mA at 25 °C, and below 10 mA at 70 °C. These values enabled error-free 40-Gbit/s transmission over 5 km of SMF even at the higher temperature. These recent developments appear to be quite promising, nonetheless it needs to be seen how competitive such directly modulated ultra high-speed lasers will be with respect to alternative transmitter devices to be discussed in the following.

4.3 Ultra-Fast, Low-Chirp Externally-Modulated Laser Sources

With the development of high-performance Er-doped fiber amplifiers (EDFA), the loss-limited transmission distance in multi-gigabit optical-fiber communication systems could be increased dramatically [42]. In high-speed long-haul transmission systems employing such inline fiber amplifiers, the transmission distance is no longer limited by the optical loss in the fiber but by the chirp of the light source. With chirp-limited transmission, the key requirements include high-modulation-speed and spectrum-stabilized transmitter light sources operating at a wavelength

of 1.55 μm . Therefore, to overcome the problem of chirp-induced pulse broadening, intensive efforts have been made to produce various types of external optical modulators (see Chap. 7, Sect. 7.1). Using these modulators substantially helps to avoid the large wavelength chirping that occurs with conventional laser diodes under direct current modulation. The impact of chirp (α) reduction on the extended fiber transmission distance was discussed earlier with reference to Fig. 4.7.

Among the various kinds of optical modulators, MQW optical modulators consisting of III/V compound semiconductors are promising candidates. MQW modulators can operate at high frequencies with low chirp and low drive voltage [43–50]. These favorable properties arise from the large field-induced variations in the absorption coefficient (or refractive index) resulting from the quantum-confined Stark effect (QCSE) [51, 52]. In particular, QCSE-based electroabsorption (EA) modulators have a high potential for practical use because of the simplicity of their device physics as well as the good structural feasibility of monolithically integrating them with laser diodes [53–63]. Monolithic laser integration not only reduces size and cost but also improves performance. The light output, for example, increases substantially because the insertion loss is very low compared with that of discrete modulators, and the long-term reliability is also improved because the packaging is more robust.

Most of the 1.55 μm band EA modulators developed so far use MQW structures with InGaAsP or InGaAlAs quaternary wells and barriers. Note that in these MQW modulators, barrier materials with optimized well/barrier band discontinuities are chosen to achieve sufficient quantum confinement for enhancing the QCSE as well as for better high-power capacity. The latter requirement is related to the sweep-out of photo-generated carriers outside the quantum wells, which is very important, especially when the light source is monolithically integrated with the modulator.

One major difficulty in fabricating photonic integrated circuits has been to reproducibly produce good optical waveguide coupling between the functional elements. Although the modulators and lasers are fabricated in the same way, it has still been difficult to create a nanometer-sized smooth high-quality crystal interface between the components. Nowadays, several monolithic integration methods are available to solve this issue (see also Chap. 16). An in-plane bandgap energy control integration technique based on selective area growth [55, 56, 61, 62] and a butt-joint integration technique [53, 54, 57–59, 63], in which each functional element is implemented separately by selective etching followed by epitaxial regrowth are now widely used. These methods enable the integration of different MQW structures, and, as a result, the performance of both the modulator and the laser has been dramatically improved through the exploitation of the quantum size effect in MQW structures.

4.3.1 High-Speed Characteristics of Externally Modulated Lasers

This section focuses mainly on modulators integrated with a light source rather than on the solitary modulator itself. After describing the basics of EA modulators, the

important technical issues associated with laser integration, such as modulator/laser interactions, are discussed. A more general description of external modulators is given in Chap. 8.

The small-signal frequency response $R(f)$ of an external modulator can be expressed in a much simpler way than that of directly-modulated diode lasers. Basically, it is determined by the parasitics and the transport/sweep-out time of photo-generated carriers. Here, we assume a lumped element model in which the modulator is regarded as being much smaller in size than the wavelength of the microwave signal driving the modulator. We also assume that the photo-generated carriers are swept out of the quantum wells so fast that they do not influence the modulator dynamics. A device structure model and an electrical circuit model of an EA-modulator integrated with a DFB laser (EA/DFB laser) are depicted in Fig. 4.18.

The EA/DFB device structure is composed of an EA-modulator and a DFB-laser with an automatically aligned optical axis. The optical coupling efficiency between them is defined as C_{out} . As with the standard DFB-laser, several crucial optical pa-

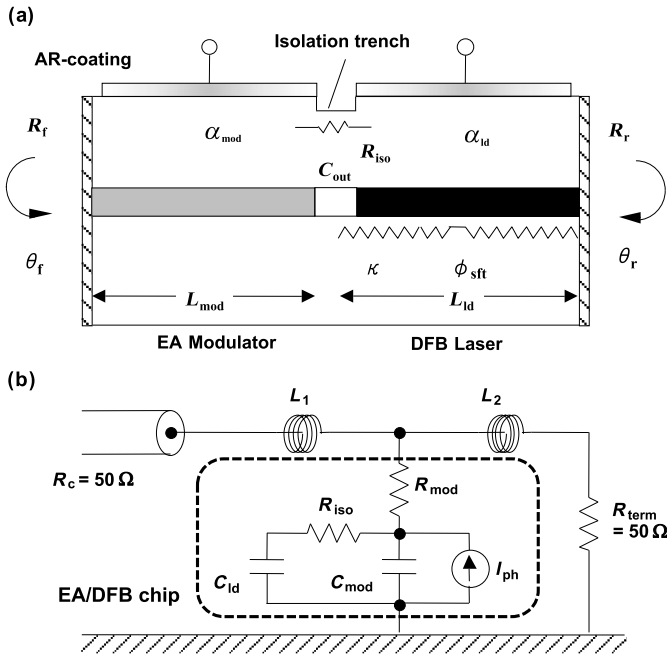


Fig. 4.18 (a) Physical model of an EA/DFB structure. C_{out} : optical coupling efficiency, C_{ld} : laser parasitic capacitance, R_f : front facet reflectivity, R_r : rear facet reflectivity, θ_f : front facet phase, θ_r : rear facet phase, L_{mod} : modulator length, L_{ld} : laser length, κ : coupling efficiency in grating, ϕ_{sft} : phase shift in grating, α_{mod} : α -parameter of the modulator, α_{ld} : α -parameter of the laser. (b) Electrical circuit model of assembled EA/DFB laser. C_{mod} : modulator parasitic capacitance, C_{ld} : laser parasitic capacitance, R_{mod} : modulator internal resistance, R_{iso} : laser/modulator isolation resistance, R_c : characteristic impedance of RF line, R_{term} : termination resistance, L_1 : wiring inductance 1, L_2 : wiring inductance 2, I_{ph} : photo-generated current

rameters such as facet reflectivity along with the optical phase with respect to the DFB grating have to be considered. The electrical circuit model starts with standard modulator parameters, namely capacitance C_{mod} , internal resistance R_{mod} , wiring inductances L_1 and L_2 , and a 50Ω termination resistor R_{term} for matching the impedance of RF signal lines with the characteristic impedance of 50Ω . Newly added in this model are the laser capacitance C_{ld} connected via an isolation resistor R_{iso} and a constant current source. During operation of the EA/DFB laser, a photo-generated current I_{ph} always flows in the modulator section. I_{ph} is treated as a constant current source, as indicated in the figure because it seriously degrades the electric reflection properties. This effect of I_{ph} on the modulation characteristics is discussed in the next section.

If we neglect the effects of I_{ph} and wiring inductances, the frequency response $R(f)$ is simply expressed as

$$R(f) = \frac{1}{1 + \{\pi C_{mod}(R_{mod} + R_{term}/2) \cdot f\}^2} = \frac{1}{1 + \{\pi C_{mod}(R_{mod} + 25 \Omega) \cdot f\}^2}. \quad (4.18)$$

By solving $R(f_{3dB}) = 1/2$, we get

$$f_{3dB} = \frac{1}{\pi C_{mod}(R_{mod} + 25 \Omega)}. \quad (4.19)$$

The light extinction ratio (on/off ratio) ER of the EA-modulator is proportional to the modulator length L_{mod} and the field-induced change in the absorption coefficient $\Delta\alpha_{abs}$ and is given by

$$ER(\text{dB}) = 4.34 \cdot \xi_{MQW} \Delta\alpha_{abs} L_{mod}, \quad (4.20)$$

where ξ_{MQW} is the optical confinement factor of the MQW absorption layer.

It is apparent from (4.19) that in order to achieve higher-speed externally modulated lasers, it is important to reduce the capacitance C_{mod} and the internal resistance R_{mod} of the modulator. As with high-speed diode lasers, shorter modulator lengths are effective in lowering C_{mod} for this purpose. However, since shortening L_{mod} has a direct adverse impact on R_{mod} and the amount of light absorption (and hence light extinction), there is a trade-off between high-speed characteristics and the operating voltage needed to achieve a given extinction ratio. Thus, a simple figure of merit (FOM) of the modulator can be formulated as f_{3dB}/V_m (or inversely V_m/f_{3dB}), where V_m is the modulation voltage swing. A more accurate FOM is defined in [64]; it considers the amount of modulation drive power $P = V_m^2/R_{term}$. It should be emphasized that a clear trade-off exists between f_{3dB} and V_m for all kinds of modulators reported so far [64].

Regarding high-speed limitations associated with the mobility of photo-generated carriers, related effects can be expected to be strongly dependent on their density and on the band discontinuities in the quantum wells. Similar to the case of directly-modulated lasers, a small valence band offset ΔE_v is important for achieving smooth sweep-out of heavy holes under higher light power operation [65–67]. This will be of particular concern when a light-source laser is monolithically integrated.

4.3.2 Chirp Characteristics of Externally Modulated Lasers

External modulation techniques can provide high-speed, low-chirp optical signals that are suitable for high-bit-rate long-haul trunk communication. These techniques can avoid the large chirp generated by carrier fluctuations in directly modulated lasers.

As in the case of the latter devices, the chirp observed in external intensity modulators is characterized by an α -parameter for modulators, which is expressed as

$$\alpha_{mod} = \frac{4\pi}{\lambda} \cdot \frac{\frac{dn}{dE}}{\frac{d\alpha_{abs}}{dE}} \quad (4.21)$$

where the numerator dn/dE in (4.21) represents the electric-field-induced variation of the refractive index in the modulator medium which is associated with a phase change in the light signals. On the other hand, the denominator $d\alpha_{abs}/dE$ expresses the degree of intensity modulation by light absorption. Like the α -parameter for diode lasers α_{ld} given in (4.10), α_{mod} corresponds to the ratio of two modulation depths, but in this case to the ratio of phase modulation depth to amplitude modulation depth. More importantly, α_{mod} for EA-modulators is typically within the range between -0.5 and $+1.0$, which is much smaller than the α -parameter of directly modulated lasers of typically 2 to 8 (as noted in Sect. 4.2.3). The simple reason for the smaller EA-modulator chirp is that the field-induced change in refractive index ($dn/dE \cdot \Delta E$) is much smaller than the carrier-induced refractive index change ($dn/dN \cdot \Delta N$) in (4.10). This is the primary advantage of EA-modulators over directly modulated diode lasers. In the case of laser-integrated EA-modulators, however, careful attention must be paid to any interactions (or signal crosstalk) between the modulator and the laser which may induce an additional chirp factor. In general, the possible physical origins of those interactions may be electrical, optical, and thermal crosstalk effects. Among these, electrical interaction can be efficiently eliminated by state-of-the-art electrical isolation techniques. For example, isolation (separation) resistance (R_{iso}) between the two device elements can be increased to more than 20 k Ω by forming a shallow isolation trench in the cladding layer. If the modulator voltage swing V_{pp} is assumed to be 2 to 3 V, this value of R_{iso} corresponds to a leakage modulation current I_{pp} to the laser section of less than 150 μ A which is sufficiently small compared to the laser driving current of several tens of milliamperes. Thermal interaction may also be neglected because of the slow response of thermal effects in the order of milliseconds. Keep in mind that a normally applied NRZ pseudo-random modulation with a $2^{31} - 1$ bit sequence corresponds to a lowest modulation frequency of several hundreds of kilohertz.

The remaining interaction effect, optical crosstalk, in fact represents a serious factor in achieving reproducible low-chirp operation. This is why the reduction of modulator facet reflection has been an issue. Any optical reflection at the modulator facet could produce an undesirable fluctuation in the lasing mode leading to considerable optical feedback-induced excess chirp produced in the laser section. Although, qualitatively, this phenomenon is quite well understood, only few attempts

have been made to quantitatively clarify the influence of optical feedback-induced chirp on the performance of high-bit-rate transmission over long-distance dispersive fibers [68–70]. In this section an outline is given how fiber transmission can numerically be simulated by taking into account the optical feedback-induced excess chirp. The simulation results allow for designing robust low-chirp EA/DFB lasers. Eye distortion and the resulting transmission penalties are derived as a function of the residual modulator facet reflectivity, and these characteristics are shown to be consistent with experimental results. In getting the required system performance, it is found that not only the modulator facet reflection but also the chirping parameters (α -parameters) in both the laser (α_{ld}) and the modulator section (α_{mod}) as well as the optical coupling coefficient in the DFB cavity are critical parameters that need to be well controlled.

Another possible interference is associated with the impact of laser power-induced photo-generated current on modulator performance. Although this effect has been widely neglected and studied very little only, it appears to be of great importance in practical applications. In particular, if the modulator driver circuit and the EA-modulator are DC-coupled, a photo-generated current might flow in the driver circuit which would directly deteriorate the drivability. This type of interference will therefore be quantitatively analyzed and discussed in Sect. 4.3.5.

4.3.3 Facet-Reflection Induced Chirp in Externally Modulated Lasers

The model that accounts for the facet-reflection induced chirp is shown in Fig. 4.18(a). It shows an EA/DFB structure with a corrugation and a phase shifter in the middle of the laser cavity. The laser parameters are the cavity length L_{ld} , coupling coefficient of the corrugation κ , facet reflectivity R_r at the laser rear end, relative phase θ_r (with respect to the corrugation phase) at the laser rear end, and the period of the corrugation Λ . The main parameters of the modulator part are the modulator length L_{mod} , the relative corrugation phase θ_f , and the facet reflectivity (R_f) at the modulator front end.

The calculation of the facet-reflection induced chirp is based on coupled-mode and rate equations, respectively. The facet-reflection induced chirp under DC conditions (static chirp) is calculated by solving the coupled-mode equations of a modified DFB cavity with a variable front facet [68–70]. The EA-modulator section is modeled simply as a piece of waveguide that has variable loss and a propagation constant according to digital modulation. Since the waveguide is directly attached to the front end of the DFB-laser section, it can be regarded as a reflector with variable reflectivity and phase.

The static chirp $\Delta\lambda_{s_chirp}$ (also designated as adiabatic chirp) was calculated as follows: The static chirp corresponds to the amount of wavelength variation that occurs between the on- and off-states when the EA-modulator is driven by DC signals.

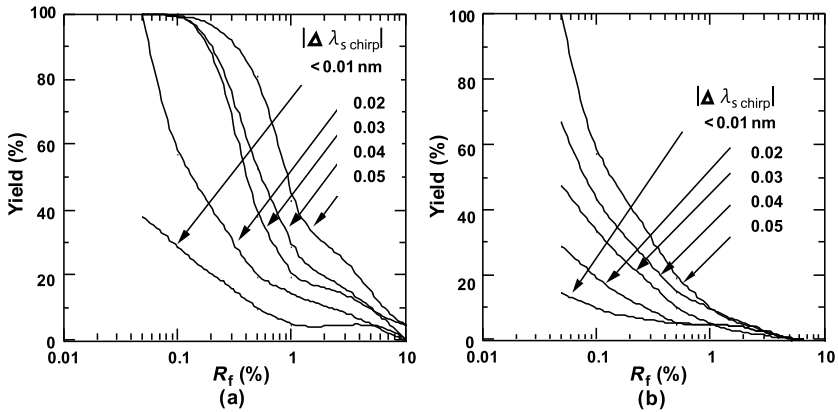


Fig. 4.19 Comparison of the static chirp yield between bulk- and MQW-based devices. (a) $\lambda/4$ -shifted DFB structure with an MQW active region ($\alpha_{ld} = 3$, $\kappa L_{ld} = 2$, $\Delta\alpha_{th}L_{ld} > 0.3$) and (b) $\lambda/4$ -shifted DFB structure with a bulk active region ($\alpha_{ld} = 8$, $\kappa L_{ld} = 2$, $\Delta\alpha_{th}L_{ld} > 0.3$)

To obtain the static chirp, we solve the time-independent rate equation ($d/dt = 0$). The 16×16 combinations of phase at the front (θ_f) and rear (θ_r) facets are varied in $\pi/8$ steps with respect to the grating. The dependence of the calculated $\Delta\lambda_{s_chirp}$ yield on R_f for $\kappa L_{ld} = 2.0$ is shown in Fig. 4.19.

Here, κL_{ld} expresses the amount of distributed Bragg reflection occurring in the DFB-laser cavity, and it corresponds to the Q -factor in the laser resonator. The calculation was performed for two α_{ld} values: $\alpha_{ld} = 3$ (Fig. 4.19(a), the case for an MQW active region) and $\alpha_{ld} = 8$ (Fig. 4.19(b), the case for a bulk active region). The figures clearly indicate that for both α_{ld} cases any increase in R_f leads to a poorer yield in obtaining a certain level of $\Delta\lambda_{s_chirp}$. This is reasonably understood from the enhanced perturbation in the lasing mode induced by the fraction of modulated light that is reflected at the modulator front facet back into the laser cavity. The figures also show that the $\Delta\lambda_{s_chirp}$ yield depends strongly on α_{ld} , which is another important parameter that governs the chirp behavior in EA/DFB lasers. It can be clearly seen from the figures that the $\Delta\lambda_{s_chirp}$ yield for $\alpha_{ld} = 3$ is much higher than that for $\alpha_{ld} = 8$. This tendency can be understood more naturally if we consider the fact that facet-reflection induced chirp is produced in the laser medium, and not in the modulator. The above results directly indicate that not only reduction of the modulator chirp α_{mod} but also of the laser chirp α_{ld} is essential in obtaining low-chirp EA/DFB lasers. The reduction of α_{ld} can be achieved in several ways, for instance by introducing strained MQWs [71–73] combined with negative wavelength detuning [74] of the DFB-laser structure. Indeed, MQW active regions offer a superior robust design for achieving low $\Delta\lambda_{s_chirp}$ operation of an EA/DFB laser. Furthermore, it can be concluded from the obtained results that a small α_{ld} value is essential for suppressing facet-reflection induced chirp even though the device is based on an external modulation scheme.

4.3.4 Transmission Simulation of Externally Modulated Lasers Considering Facet-Reflection Induced Chirp

The dynamic chirp of EA/DFB lasers was analyzed by combining the coupled-mode and the rate equations [70]. Again as with directly modulated diode lasers, large signal analysis was performed using the time-developed Runge-Kutta method to obtain the temporal variations in the optical intensity and phase. A trapezoidal drive waveform with a 32-bit 2.5 Gbit/s NRZ pseudo-random pattern was filtered to account for the parasitics of the modulator and assembly. Most of the parameters for devices and fiber transmission (Table 4.1) were extracted from experiment data.

Table 4.1 List of device and transmission parameters used to simulate the impact of facet-reflection induced chirp on fiber transmission performance

Parameter	Symbol	Unit	Value
Laser parameters			
Wavelength	λ	μm	1.557
Optical confinement factor	ξ	–	0.027
Carrier lifetime	τ_N	ns	0.22
Photon lifetime	τ_P	ns	variable
Differential gain	dg/dN	m^2	5×10^{-12}
Laser chirp parameter	α_{ld}	–	3.0
Gain saturation coefficient	ε	m^3	5×10^{-23}
Cavity length	L_{ld}	μm	400
Active region width	W_{act}	μm	1.5
Well number	N_w	–	7
Coupling coefficient	κ_L	–	1.5
Rear facet reflectivity	R_r	%	90
Rear facet phase	θ_r	–	variable
Modulator parameters			
Modulator chirp parameter	α_{mod}	–	0.4
Front facet reflectivity	R_f	%	variable
Rear facet phase	Θ_f	–	variable
Modulator length	L_{mod}	μm	200
Extinction ratio	ER	dB	16
Parasitic capacitance	C_{mod}	pF	1.0
Driver impedance	R_z	Ω	50
Transmission parameters			
Bit rate	B	Gbit/s	2.5
Fiber dispersion	D	ps/(nm km)	17
Fiber loss	L	dB/km	0.2
Nonlinear coefficient	n_2	m^2/W	2.6×10^{-20}
Fiber input power	P_{in}	dBm	10

Assuming InGaAsP/InP-based MQW material, the important chirp parameters for the modulator and laser, α_{mod} and α_{ld} , were taken to be 0.4 and 3.0, respectively. The 8×8 combinations of phases at the front and rear facets with respect to the grating were varied in steps. The transmission behavior over normal-dispersion (17 ps/nm/km) single-mode fibers was analyzed using the model given in [75, 76], with receiver parameters adjusted to the ones used in the experiments. The calculation was done for different front facet reflectivity values (R_f) ranging from 0% to 2% while the rear facet reflectivity (R_r) was kept constant at 90%.

Simulated modulation waveforms and dynamic wavelength shifts (total chirp) occurring in an AR-HR coated device are shown in Fig. 4.20.

The optical feedback was calculated for (a) $R_f = 0\%$, (b) $R_f = 0.001\%$, (c) $R_f = 0.01\%$, and (d) $R_f = 0.1\%$. The rise and fall times used in the computation were 80 ps, and the facet phase combination (θ_f, θ_r) was $(0, \pi)$. This facet phase combination yielded the largest chirp, i.e. corresponds to the worst-case chirp calculation. As is clearly seen in Fig. 4.20(d), for $R_f = 0.1\%$ the time-resolved chirp represents a relaxation oscillation which arises from the dynamic nature of the laser.

It was also found that a reduction in R_f leads to lower oscillation peaking. Here, the peak-to-peak height of the dynamic chirp is defined as $\Delta\lambda_{d_chirp}$. The residual $\Delta\lambda_{d_chirp}$ that exists even at $R_f = 0\%$ (Fig. 4.20(a)) is due to the phase chirp caused by the refractive index modulation in the modulator medium. This modulation is determined by the modulator chirp parameter α_{mod} . It is interesting to note that when R_f is less than about 0.01%, $\Delta\lambda_{d_chirp}$ is not determined by α_{mod} rather than R_f . This might indicate that, with this chirp combination of α_{ld} and α_{mod} , R_f of 0.01% is low enough to eliminate the effect of facet reflection on the hybrid chirp behavior. Simulation results showing how the eye diagrams before and after transmission through 125 km, 250 km, 375 km and 500 km-long fibers depend on R_f are presented in Fig. 4.21.

Facet phase combinations (θ_f, θ_r) of (a) $(0\pi, 0\pi)$ and (b) $(\pi/2, \pi/2)$ were chosen as examples. The results clearly indicate serious eye distortion caused by the optical feedback chirp when R_f is larger than 0.5%. To determine the criterion for R_f , the simulated transmission power penalty (P_d) was plotted against R_f for all 64 facet phase combinations. The calculation was performed for transmission through 125 km, 250 km, and 500 km lengths of normal fibers. The results are plotted in Fig. 4.22, which illustrates the R_f criteria for achieving 2.5 Gbit/s transmission with reproducibly low P_d values.

Figure 4.22 suggests that the R_f values that reproducibly allow $P_d < 1$ dB are roughly 0.3%, 0.1%, and 0.04% for 125 km, 250 km, and 500 km transmission distances, respectively. A linear dispersion limit of 0.4 is also indicated at about 500 km. This means that the maximum transmission distance is no longer limited by R_f but by α_{mod} itself when R_f is less than 0.04%. This finding is in qualitative agreement with the R_f dependence of the dynamic chirp shown in Fig. 4.20.

Next, the measured eye patterns before and after transmission over 120 km and 240 km long fibers are compared with the simulated ones using the facet phases as fitting parameters. This comparison is shown in Fig. 4.23(a) for a device with a large R_f of about 2%.

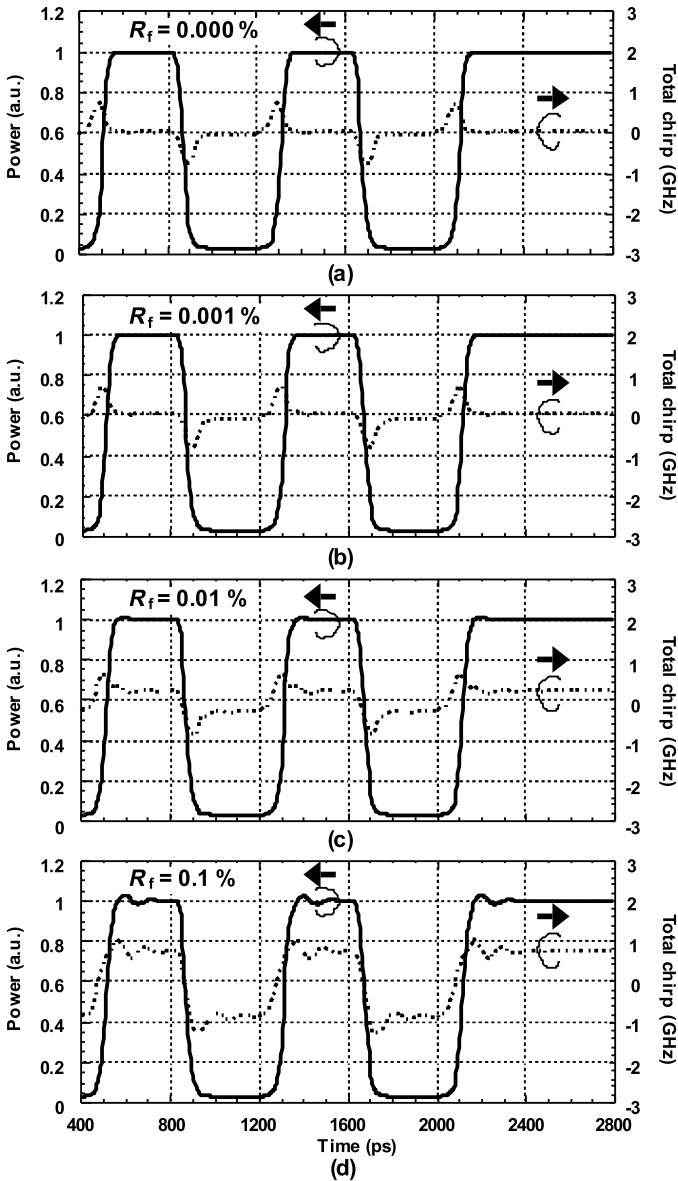


Fig. 4.20 Calculated modulation waveforms and corresponding dynamic chirp under 2.5 Gbit/s digital modulation for various values of modulator facet reflectivity

By roughly choosing facet phases with an accuracy of $\pi/4$, close correspondences were obtained. This provides a reasonable explanation of the inter-symbol interference shown in Fig. 4.23(a), where faster propagation of the energy at the leading edge caused by the blue chirp is seen. This behavior is very similar to that

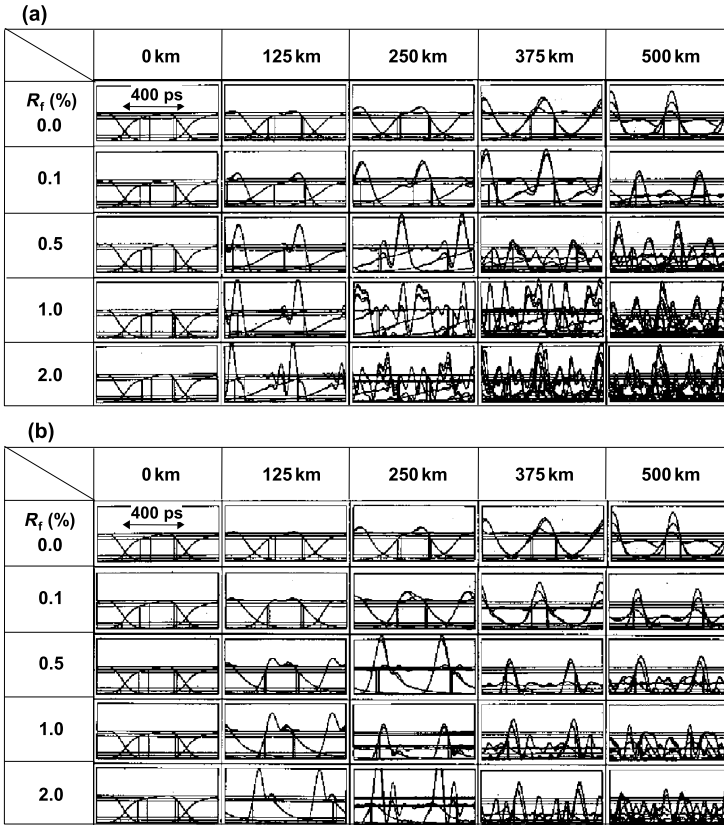


Fig. 4.21 Calculated transmitted eye diagrams at a signal rate of 2.5 Gbit/s for various values of modulator facet reflectivity: (a) $\theta_f = 0$, $\theta_r = 0$, (b) $\theta_f = \theta_r = \theta/2$, $\pi_f = \pi_r = \theta/2$. π_f and θ_r denote the relative corrugation phases at the front and rear facet, respectively

Fig. 4.22 Criteria for modulator facet reflectivity to achieve 2.5 Gbit/s long-distance fiber transmission

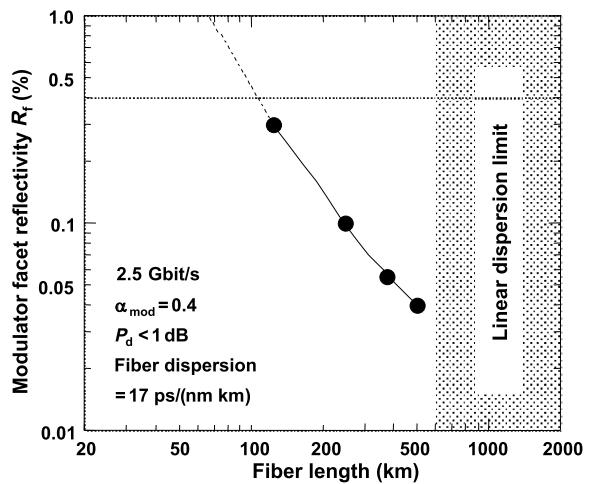


Fig. 4.23 Comparison of eye-diagrams between experiment and simulation for: (a) $R_f = 2\%$ and (b) $R_f = 0.02\%$

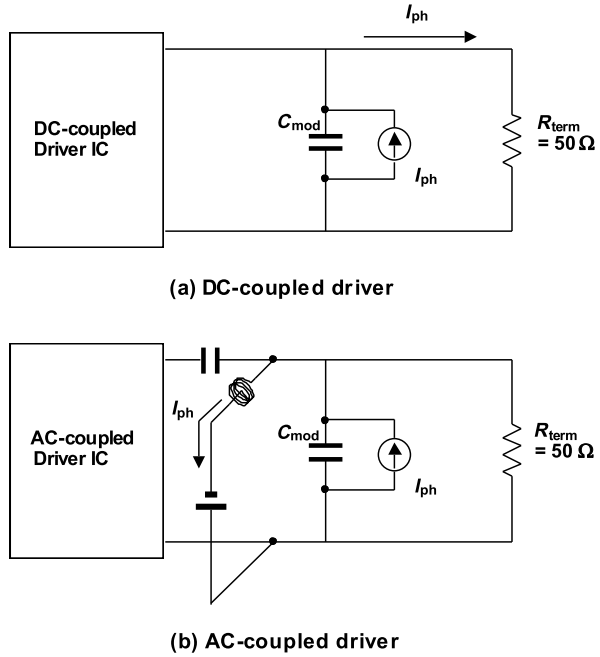
	(a)			
	exp.	P_d	sim.	P_d
0 km		-		-
120 km		2.3 dB		2.1 dB
240 km		floor		3.2 dB
	(b)			
	exp.	P_d	sim.	P_d
0 km		-		-
120 km		2.3 dB		2.1 dB
240 km		floor		3.2 dB

of directly modulated lasers [76, 77]. It is important to note, however, that the sign of the excess chirp is determined randomly by the facet phase combination, which is difficult to control deliberately. This means that reduction of R_f is essential to reproducibly attain low-chirp operation independently of the facet phases. Figure 4.23(b) shows the same results for a device with a lower R_f ($\sim 0.02\%$) achieved through the combination of a window structure and/or multilayer antireflection coating techniques. In this case, good agreement was obtained between the experiment and simulation for all 16 combinations of the facet phases, suggesting that R_f of 0.02% is small enough for 240 km transmission, in agreement with the theoretical prediction made above.

4.3.5 Effect of Photo-Generated Current on Modulation Characteristics

When the EA/DFB laser is under operation, photo-generated current I_{ph} is produced due to light absorption in the EA-modulator section. This continuous current may flow in the assembly circuits, which adversely affects the modulator perfor-

Fig. 4.24 Electrical circuit model of an EA/DFB laser combined with
 (a) a DC-coupled and
 (b) an AC-coupled driver IC.
 C_{mod} : modulator capacitance,
 R_{term} : termination resistance



mance. Circuit models of high-speed EA/DFB lasers considering I_{ph} are shown in Fig. 4.24.

The DC-coupled scheme corresponds to the normal EA/DFB assembly method. I_{ph} can flow in a 50Ω impedance-matching resistor along with the bias current of $I_{matching} = V_{mod}/50 \Omega$ induced by the modulator bias voltage V_{mod} because the driver circuit of the modulator is usually designed to have high impedance. This extra I_{ph} flow into the resistor can severely affect RF reflection. The scattering parameters S_{11} and S_{21} of the EA/DFB laser, taking into account the existence of I_{ph} flow, are modeled in Fig. 4.24 and given by the following equations [77]:

$$S_{21}(\omega) = 10 \log_{10} \left| \frac{H(\omega)}{H(0)} \right|^2 \text{ [dB]}, \quad (4.22)$$

where

$$H(\omega) = \frac{\{kR_{mod} + (1+k)(R_{term} + j\omega L_2)\}/j\omega C_{mod}}{(R_c + j\omega L_1)\{(R_{mod} + 1/j\omega C_{mod}) + (R_{term} + j\omega L_2)\} + (R_{term} + j\omega L_2)[R_{mod} + (1+k)/j\omega C_{mod}]}. \quad (4.23)$$

with $k = R_{term}I_{ph}/V_{mod}$, and

$$S_{11}(\omega) = 10 \log_{10} \left| \frac{G(\omega)}{G(0)} \right|^2 \text{ [dB]}, \quad (4.24)$$

with

$$G(\omega) = j\omega L_1 + \frac{(R_{term} + j\omega L_2)\{R_{mod} + (1+k)/j\omega C_{mod}\}}{(R_{mod} + 1/j\omega C_{mod}) + (R_{term} + j\omega L_2)}. \quad (4.25)$$

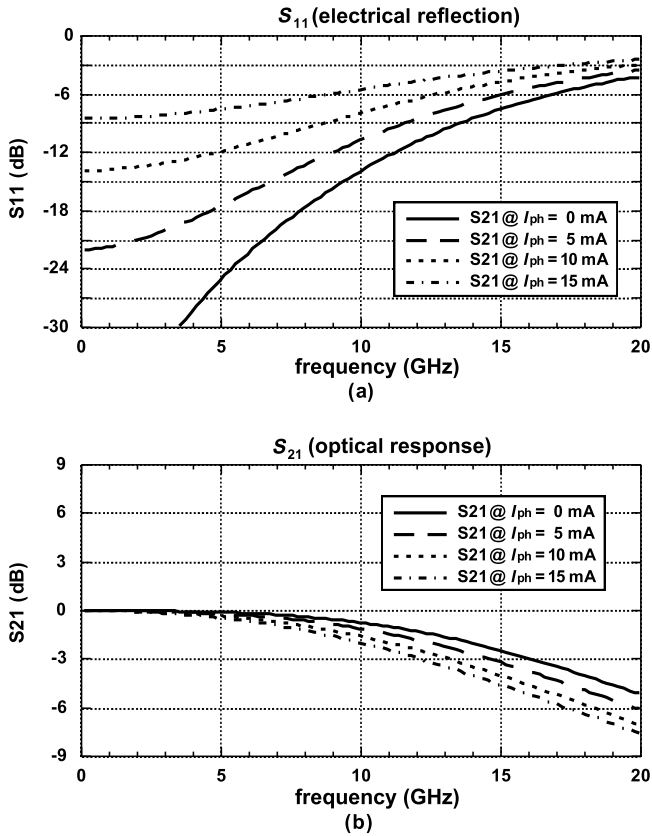


Fig. 4.25 Calculated frequency responses of (a) S_{11} and (b) S_{21} parameters for several photo-currents

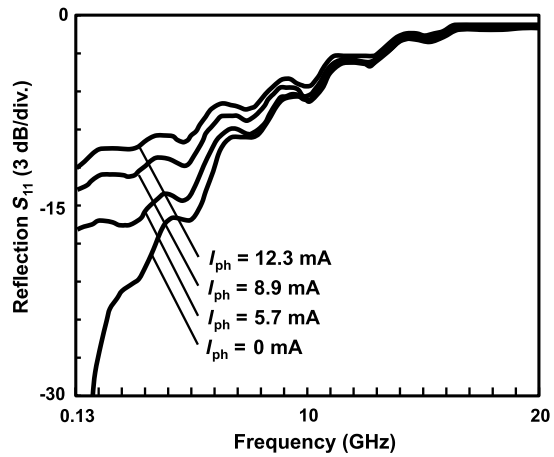
Here, the parameter k as defined is a constant that represents I_{ph} . Calculated frequency responses of the S_{11} and S_{21} parameters for several values of I_{ph} are shown in Fig. 4.25.

The calculated S_{11} parameter largely decreases with increasing I_{ph} . The measured frequency dependence of S_{11} for various values of I_{ph} is shown in Fig. 4.26, and the response curves can be seen to be similar to those of the theoretical results illustrated in Fig. 4.25(a).

It is meaningful to qualitatively explain the S_{11} dependence. In the circuit model in Fig. 4.24(a), any current I_{ph} that flows in the $50\text{-}\Omega$ matching resistor reduces the voltage at the input port. This voltage reduction leads to a deviation in the actual terminal resistance R_{term} from the ideal value of $50\ \Omega$. Under DC conditions ($f = 0\text{ Hz}$), R_{term} is given by

$$R_{term}(\Omega) = \frac{50\ \Omega}{1 + \frac{50\ \Omega \cdot I_{ph}}{V_{mod}}}, \tag{4.26}$$

Fig. 4.26 S_{11} parameters measured at several photo-currents



(4.26) indicates that R_{term} becomes smaller than 50Ω once a photo-current is generated, and that this reduction of R_{term} can directly deteriorate S_{11} . Fortunately, as shown in Fig. 4.25, the measured S_{11} at 5 GHz under the worst condition (i.e., $I_{ph} > 10$ mA) is at least 10 dB. Such an S_{11} value does not cause a critical problem at a data rate of 2.5 Gbit/s. However, it must be improved if higher bit rate transmission as used in 10- to 40 Gbit/s systems are envisaged. The curves in Fig. 4.25(b) reveal the I_{ph} sensitivity of S_{21} . When I_{ph} amounts to 15 mA, the 3-dB-down bandwidth is reduced by about 20%. This reduction should also be taken into account in the design of higher speed EA/DFB lasers.

Another vital issue is the I_{ph} -induced reduction of the effective modulation voltage swing of EA-driver ICs. A non-negligible amount of I_{ph} can flow in the driver circuit when this circuit is directly connected to the modulator (DC-coupled scheme, Fig. 4.24(a)). This leakage current easily produces a voltage drop in the output signal swing of the driver, and this reduces the dynamic extinction ratio. This indicates that careful attention should be paid to this voltage drop when designing RF-signal connections between EA/DFB lasers and driver circuits. One simple solution for this could be to introduce a bypass line for I_{ph} , as shown in Fig. 4.24(b). If this bypass circuit is integrated into the driver IC, most of the I_{ph} flow will take this path to effectively suppress the adverse effects of I_{ph} on modulator performance.

4.3.6 High-Speed Externally Modulated Lasers in System Use

An example of a high-speed low-chirp EA/DFB laser that operates in the $1.55 \mu\text{m}$ wavelength range [78, 79] is shown in Fig. 4.27(a).

43 Gbit/s operation and 2 km transmission over a standard single-mode fiber has been demonstrated employing those devices. Note that an extended data rate of up to

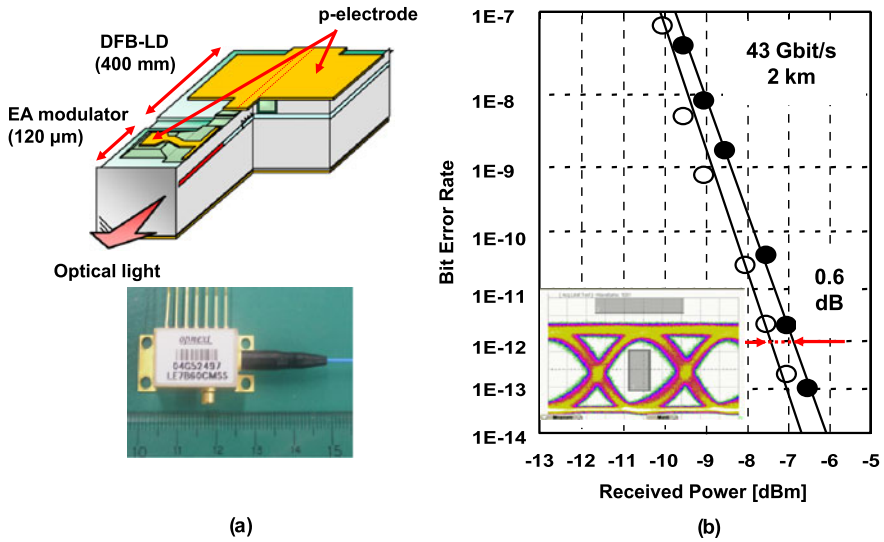


Fig. 4.27 Example of a 43 Gbit/s low-chirp EA/DFB laser in the 1.55 μm range [79]. (a) Chip schematic and module photograph and (b) 43 Gbit/s, 2 km transmission performance over standard single-mode fiber

43 Gbit/s is needed to meet the system demands for forward error correction (FEC). The reported device consists of a short InGaAsP MQW-based EA-modulator monolithically integrated with a DFB-laser light source made of the same material. It was bonded onto a chip carrier with a 50- Ω termination resistor and then packaged in a high-speed module involving lenses, a thermo-electric cooler, a thermistor, and a high-speed standard electrical connector. The module was hermetically sealed for reliability reasons. Evidencing the small parasitics in EA/DFB chips and assemblies, a 3-dB-down bandwidth of over 40 GHz was measured on this device, and 43 Gbit/s operation was successfully demonstrated at a modulator voltage swing V_{pp} of 2.5 V (Fig. 4.27(b)). Currently, 40 Gbit/s EA/DFB lasers are mainly deployed in so-called very-short-reach router-to-router interconnections and/or client interfaces in communications.

Devices capable of even 50 Gbit/s modulation have been developed recently which may be used as building blocks in future >100 Gbit/s multi-lane transmitters, e.g. for 400GbE-applications [80], and 50 Gbit/s does by far not yet represent an upper speed limit of EA/DFB devices. In fact, the world's first serial 100 Gbit/s lumped-element EA/DFB laser, shown in Fig. 4.28, was already introduced a few years ago [81]. This particular component contained an InGaAlAs-based 10-quantum-well absorption layer structure that was buried by a low-capacitance semi-insulating buried heterostructure. Using a 50 μm short modulator co-assembled with a very-high-speed driver IC 100 Gbit/s open eye diagrams could be successfully accomplished at such an ultrahigh bit rate for the first time.

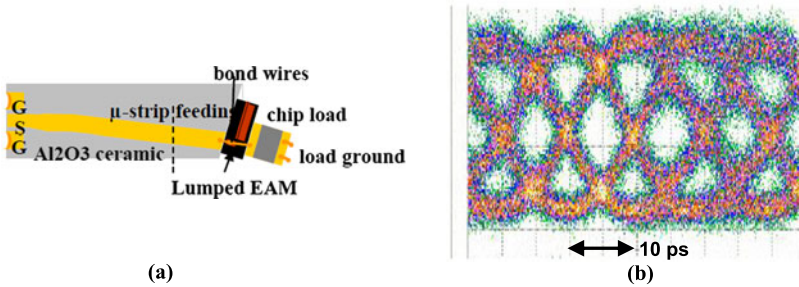
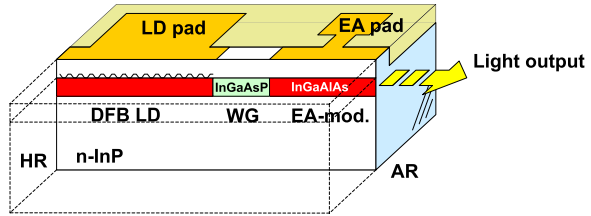


Fig. 4.28 World's first serial 100 Gbit/s EA/DFB laser [81]. (a) EA/DFB laser assembled on a high-speed carrier and (b) 100 Gbit/s optical waveform

4.3.7 Uncooled, High-Speed, Low-Chirp Externally Modulated Lasers

EA/DFB lasers have been playing an important role in telecommunication networks owing to their distinctly advantageous features, namely ultrahigh speed capability, low chirp, low power consumption, and compactness. With the explosive spread of broadband services, power consumption is becoming more and more critical, and one of the key issues of related photonics/electronics is to find ways to reduce it. Focusing on the environmental temperature of these components, most directly modulated diode lasers have been evolving from temperature-stabilized (cooled) devices to temperature robust (uncooled) ones. Uncooled operation of directly modulated diode lasers in short-link applications has successfully eliminated the electric power consumed by thermo-electric coolers. Accordingly, cooler-free operation has been strongly desired also for EA/DFB lasers deployed in modules for long-distance transmission. However, this goal proves to be highly challenging, the main reason being that EA/DFB lasers behave very sensitive to changes in operating temperature. This fact essentially arises from the large mismatch in the temperature coefficients of the electroabsorption peak wavelength (typically 0.7 nm/K) and the DFB-lasing wavelength (typically 0.1 nm/K). The phenomenon is widely known, and the mismatch has often been compensated for by controlling the DC bias voltage applied to EA-modulators [82, 83]. In most cases, the DC bias has been adapted to the operating temperature set for tuning the DFB wavelength to a targeted wavelength-division-multiplexing (WDM) grid channel [83]. This technique has also been applied to extending the operating temperature range of the device [82]. An uncooled EA/DFB laser for short-reach (10 km) applications has been proposed using this voltage-offset method [84]. When the offset DC-bias applied to the EA modulator was adjusted to suit the temperature variation, the device was able to handle the mismatch in wavelength shift over a wide temperature range. One key issue involved is how to keep the detuning parameter (i.e. the difference between the DFB lasing and the electroabsorption peak wavelength) nearly constant. In addition to this, careful attention must be paid to the increase in optical loss and the change in chirp when applying an offset bias. As to the optical loss, any increment of the applied bias

Fig. 4.29 Schematic chip structure of the first 1.55 μm uncooled EA/DFB laser [85]



voltage as well as of the temperature is certain to lead to increasing light absorption. Whereas this would be unlikely to occur in case of an ideal step-function-shaped absorption spectrum, in reality it will occur because of the existing tail-shaped absorption spectrum. For these reasons, a properly designed detuning parameter is so important from a practical viewpoint to keep the optical loss within a tolerable range. It should be noted here that the device reported in [84] was designed for short-reach transmission in the 1.3 μm wavelength range where chirping virtually does not matter so much. For 1.55 μm range long-reach applications, however, there have been serious difficulties in managing the severe trade-off between the extinction ratio and optical loss plus chirp. This renders 1.55 μm uncooled EA/DFB lasers much more difficult to achieve compared to their 1.3 μm counterparts.

The first successfully accomplished uncooled high-speed, low-chirp EA/DFB laser operating in the 1.55 μm range is schematically illustrated in Fig. 4.29 [85].

The device comprised a temperature-robust InGaAlAs EA-modulator, an InGaAsP DFB laser, and an InGaAsP bridge waveguide in between, monolithically integrated on an InP substrate. As with directly modulated diode lasers, the InGaAlAs material effectively enhances the temperature tolerance of the EA-modulator owing to its favorable band structure. The large ΔE_c associated with InGaAlAs is beneficial for the extinction ratio at low temperatures by effectively maintaining the QCSE under the high electric field applied to the quantum wells. On the other hand, a small valence band offset ΔE_v supports prompt sweep-out of photo-generated holes over shallow valence band barrier walls, implying high optical power robustness.

Measured eye diagrams obtained under 10 Gbit/s, $2^{31} - 1$ PRBS modulation are shown in Fig. 4.30 for 15 $^{\circ}\text{C}$ and 95 $^{\circ}\text{C}$. Clearly opened eye diagrams were obtained at both operating temperatures even after transmission through an 80 km long normal dispersion fiber. The measured error-free bit error rate (BER) performance after 80 km transmission with power penalty (P_d) of less than 2 dB and dynamic extinction ratio (DER) of greater than 9 dB are sufficient for practical use in 10 Gbit/s intermediate-reach (40 km) and long-reach (80 km) applications [86–88].

Another emerging application of high-speed EA/DFB lasers is 100-Gigabit Ethernet (100GbE) [89] which has become the high-speed network standard to meet the explosive increase in network traffic [8]. The world's first standard-compliant 100GbE transceiver module using EA/DFB light sources operating in the 1.3 μm range is shown in Fig. 4.31.

Four sets of 25 Gbit/s-driven EA/DFB lasers are integrated inside a 100GbE compact form-factor pluggable (CFP) module ($144 \times 78 \times 13.6 \text{ mm}^3$) [7]. The four

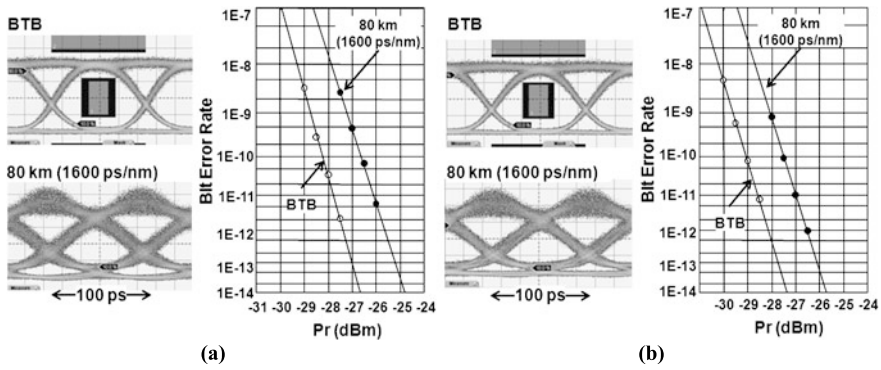
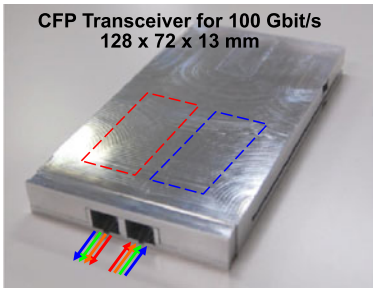
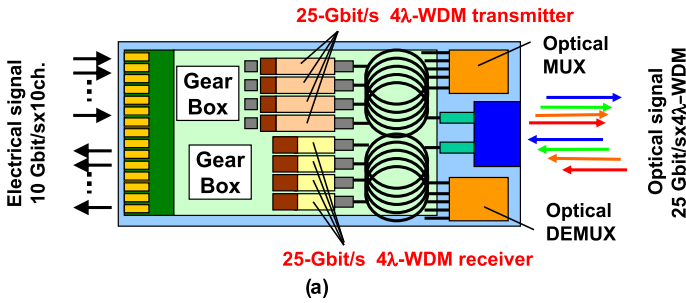


Fig. 4.30 10 Gbit/s, 80 km (1600 ps/nm) single-mode fiber transmission characteristics using an uncooled 1.55 μm EA/DFB. (a) 15 $^{\circ}\text{C}$: DER = 9.8 dB, $P_d = 1.7$ dB, and (b) 95 $^{\circ}\text{C}$: DER = 10.9 dB, $P_d = 1.5$ dB



(b)

Ch1; $\lambda = 1290$ nm, NRZ, $2^{31}-1$ PRBS

Temp.	0 $^{\circ}\text{C}$	85 $^{\circ}\text{C}$
DER	9.85 dB	9.61 dB
V_{OH}	-1.5 V	-0.65 V
BTB		
SMF 12 km		

(c)

Fig. 4.31 First parallel 100 Gbit/s transceiver using 25 Gbit/s 4 λ -WDM EA/DFB light sources. (a) Schematic structure of a 100GbE transponder, (b) 100 Gbit/s CFP transceiver, and (c) 25 Gbit/s optical waveform for uncooled operation

25 Gbit/s EA/DFB lasers arranged in a 4 λ -WDM channel assignment yielded a total data rate of 100 Gbit/s. Moreover, 25.8 Gbit/s 12 km single-mode-fiber transmission over a wide temperature range from 0 $^{\circ}\text{C}$ to 85 $^{\circ}\text{C}$ was also achieved, which is attractive for low-power 100GbE systems. This module is a promising candidate for

cost-effective 100GbE client-side technology. A 40 Gbit/s uncooled EA/DFB laser using similar technologies has also been successfully demonstrated [88]. Ideally, the four laser devices and the wavelength multiplexer needed in the above 4-lane transmitter configuration would be monolithically integrated on one chip to reduce packaging expenditures and to enable the use of small-size packages. Such a transmitter chip incorporating four monolithic EA/DFB devices, emitting at four different wavelengths ranging from 1.297 μm to 1.309 μm (LAN-CWDM grid), and a multi-mode interference (MMI) coupler to form the multiplexer was realized and successfully tested for 100GbE applications at semi-cooled conditions [90].

4.4 New Challenges for Ultra-Fast Semiconductor Light Sources

4.4.1 High-Speed Active/Passive Feedback Diode Lasers

The physical limit of the modulation speed of semiconductor diode lasers could be artificially controlled by the modulation scheme employed. In 1985, K. Iga made a clear theoretical prediction for improving laser dynamics [91]. He showed that instead of modulating the injection current into a diode laser, one could alternatively modulate the optical gain, loss, or photon lifetime. He pointed out that the maximum modulation frequency for gain and photon lifetime (cavity Q -factor) modulation can exceed the relaxation oscillation frequency f_r . The degree to which the small signal response $R(f)$ is improved, for example, by Q -factor modulation (i.e., photon lifetime modulation) or by gain modulation is illustrated in Fig. 4.32 [91]. This figure clearly points out the possibility of achieving faster response in diode lasers by a factor of more than ten through Q -factor/gain modulation.

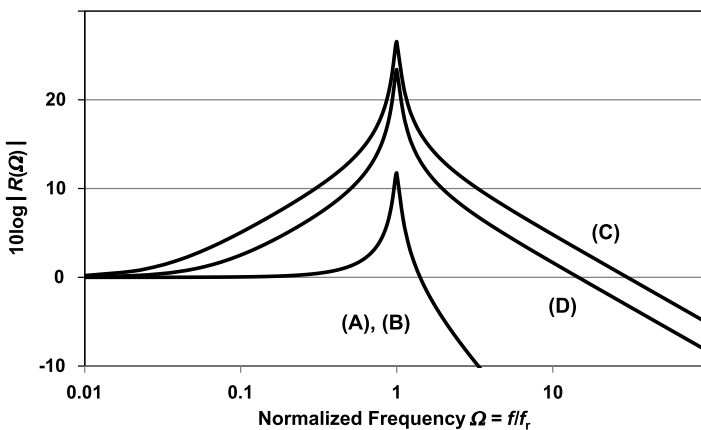
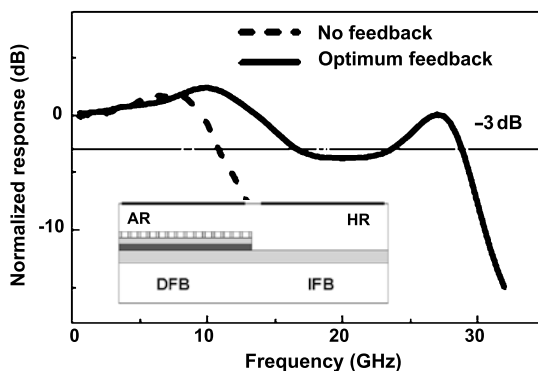


Fig. 4.32 Calculated responses for various modulation schemes [91]. (A) injection current modulation, (B) carrier loss modulation, (C) gain modulation, (D) cavity Q modulation

Fig. 4.33 Effect of optical feedback on small-signal response (*inset: laser structure*) [107]

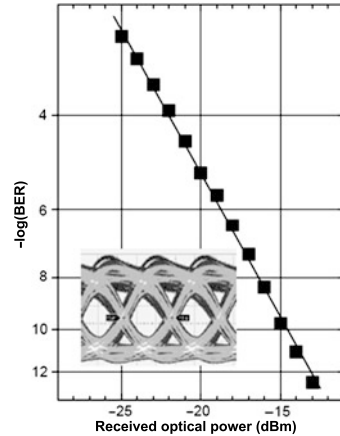


Based upon this suggestion, there have been several practical approaches for applying alternative modulation schemes to high-speed diode lasers. These include optical injection locking [92–97], gain switching [98–100], and multi-section waveguide lasers including an active/passive feedback mechanism [101–107].

Here, we focus on active/passive feedback lasers. The high-speed characteristics of diode lasers can be improved by optical feedback to the laser cavity or, in other terms, by modulating the mirror reflectivity [105]. The high-speed operability relies on an enhanced frequency bandwidth achieved by photon lifetime modulation. The relatively slow response associated with carrier-photon interaction that governs the relaxation oscillation in diode lasers is replaced by photon-photon interaction. This effect leads to an additional photon-photon resonance peak at frequencies that potentially exceed the usual carrier-photon resonance frequency several times. Using the passive-feedback DFB laser depicted in Fig. 4.33, 40 Gbit/s direct current modulation at an emission wavelength of 1.55 μm could be demonstrated for the first time [107]. The basic laser structure is an active/passive monolithic two-section laser with a standard section length of a few hundred micrometers. AR and HR (>90%) coatings were applied to the DFB and integrated feedback (IFB) facets, respectively.

When the optical modulation response was recorded under different IFB biasing, a strong change in the modulation bandwidth was observed. The feedback effect is shown in more detail in Fig. 4.33. Without any support from the feedback section (absorbing IFB section, dashed line) the behavior was found to be similar to that of a single-section DFB laser, the modulation bandwidth of which is limited by the carrier-photon resonance frequencies of typically 8 to 12 GHz. On the other hand, a drastically enhanced modulation bandwidth of about 30 GHz was measured under optimum feedback conditions, thus exceeding the normal relaxation oscillation frequency limit by a factor of 3. Figure 4.34 illustrates successful large signal modulation at 40 Gbit/s achieved with no bit errors when measured for $2^7 - 1$ PRBS data streams for NRZ signals [107]. The passive feedback DFB laser exhibited high modulation bandwidth >30 GHz for 1.5 μm and 1.3 μm ridge waveguide lasers [108]. It should be emphasized that 40 Gbit/s operation was accomplished with low-gain active material, InGaAsP, at a moderate current level of 40 mA. With a similar concept and the support of well designed photon-photon resonances au-

Fig. 4.34 Results of back-to-back BER measurements for 40 Gbit/s large-signal modulation [107]



thors in [109] could even realize the record 3-dB modulation bandwidth of 55 GHz. Their laser device comprises a particular DBR structure having a 50 μm DFB gain section of InGaAlAs MQWs and 200 μm DBR grating section. The 1.3 μm laser was successfully applied for serial 112 Gbit/s PAM-4 transmission over 2.2 km SMF.

4.4.2 Traveling-Wave EA Modulators

As discussed in the previous sections, the EA-modulated laser is currently one of the most promising candidates for high-speed compact light sources for use in long-distance communications. The present EA-modulators are based on lumped element designs and models (see Fig. 4.18(b)), and their high-speed capability is limited by the CR time constant $C_{mod}(R_{mod} + R_{term}/2)$, as expressed in (4.19). Here again, C_{mod} , R_{mod} , and R_{term} denote modulator capacitance, modulator internal resistance, and a 50- Ω termination resistor, respectively. With this conventional technology, EA/DFB lasers operating at 40 Gbit/s driven by signals with a voltage swing of 2 to 3 V_{pp} have been deployed in practical subsystems. These values result in a figure of merit of roughly 17 to 20 GHz/V. It will be difficult to further improve this FOM significantly in a practical way by simply exploiting conventional schemes because the reduction of C_{mod} by using even shorter modulator structures leads to poor extinction ratio and hence high driving voltage. It should also be mentioned by the way that even if a higher-speed EA-modulator, for example a 100 Gbit/s EA-modulator, is realized, we will still face the inherent fiber dispersion limitation. According to the data discussed in Sect. 4.3.2, the maximum transmission distance of 100 Gbit/s, 1.3 μm range signals produced by the EA-modulator will be a few km. To extend the high-speed limitation of lumped EA modulators, structures featuring “traveling-wave” designs have been demonstrated to overcome the RC-limitation [110–113]. The aim in the traveling-wave is to reach very-high-speed intensity modulation by

exploiting the electrical/optical velocity matching effect. With traveling-wave EA-modulators, the lumped short electrode is replaced by a relatively long transmission-line electrode. This approach was initially developed for Mach-Zehnder interferometer modulators formed on lithium-niobate (LiNbO_3) (see Chap. 8, Sect. 8.1.3), and on III–V compounds (GaAs [114, 115]) as well as InP [116–118]). In the traveling wave design, the electrical drive signal propagates in the same direction as the optical modulated signal. Ideally, both signals run at the same speed, permitting the light modulation to accumulate monotonically as they propagate together, which could, in principle, lead to non-RC-limited operation, irrespective of the operating frequency. In reality, however, it is not very easy to perfectly match the velocities of the two waves. This causes a walk-off between the electrical and optical signal waves, which tends to severely degrade the high-speed capability. It can be readily shown that the frequency response $R(f)$ of an idealized traveling-wave modulator is expressed as [114]

$$R(f) = \left[\frac{\sin\left(\frac{\pi f |n_{opt} - n_{ele}| L_{mod}}{c}\right)}{\frac{\pi f |n_{opt} - n_{ele}| L_{mod}}{c}} \right]^2, \quad (4.27)$$

where n_{opt} and n_{ele} denote the optical and electrical effective refractive indices, respectively, and L_{mod} is the modulator length (being equal to the length of the traveling-wave electrodes). From (4.27), the 3-dB-bandwidth can be derived:

$$f_{3dB}^{TW} = \frac{1.39c}{\pi |n_{opt} - n_{ele}| L_{mod}}. \quad (4.28)$$

Because of the negative dependence on L_{mod} , the bandwidth and drive voltage can be traded for in the same way as with lumped element (LE) modulators; thus, the bandwidth-voltage FOM is equally applicable [114]. In the case of traveling-wave EA modulators, however, there is a large mismatch between n_{opt} and n_{ele} , which inevitably makes their characteristic impedance small, $\sim 25 \Omega$, about half of the standard $50\text{-}\Omega$ RF connections. This difference is likely to seriously degrade the optical waveforms owing to large electrical reflection. In response, several velocity/impedance matching techniques have been developed for improving conventional low-impedance traveling-wave EA-modulators.

Such a refined traveling-wave EA-integrated laser [113] is shown in Fig. 4.35(a). To compensate for the inherently low characteristic impedance of EA-modulators, a high-impedance transmission line is integrated with a low-impedance traveling-wave EA-modulator. This simple method is quite successful in achieving quasi-impedance matching between the modulator and driver circuit, which greatly enhances the high-frequency performance (Fig. 4.35(b)), and this kind of artificial impedance control electrode (ICE) was found to be very effective in achieving a compact low-power-consumption 40 Gbit/s EA/DFB laser. A packaged device with an InP/InGaAs hetero-bipolar-transistor (HBT) based IC driver was able to provide 40 Gbit/s, 2 km single-mode-fiber transmission with a 0.3 dB penalty [113].

Another important advanced traveling-wave EA-modulator [112] is shown in Fig. 4.36(a). Here a segmented transmission-line electrode was used. This solution enabled us to design a traveling-wave EA-modulator with a characteristic

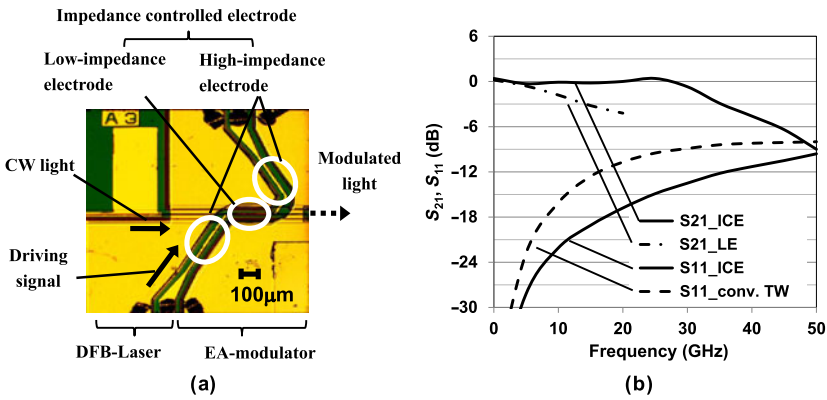


Fig. 4.35 Improved traveling-wave EA-integrated laser [113]. (a) View of an EA/DFB laser with an impedance controlled electrode and (b) improved frequency responses compared to lumped-element (LE) and conventional traveling-wave (TW) designs

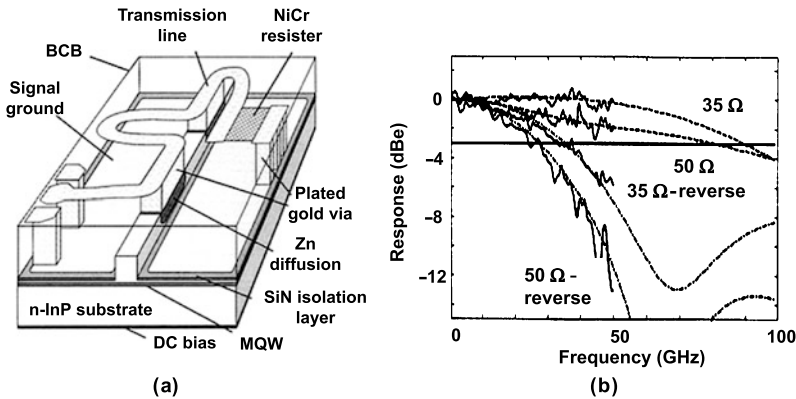


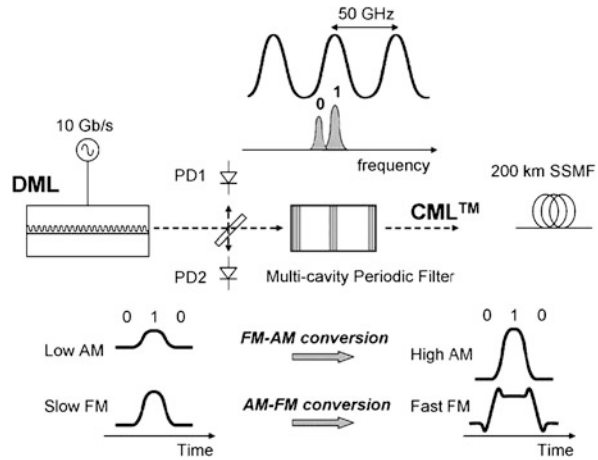
Fig. 4.36 (a) Device structure and (b) optical small-signal frequency responses of a segmented transmission-line EA-modulator [112]

impedance close to 50 Ω. The device exhibits low electrical reflection (return loss: > 15 dB) and excellent frequency response up to 50 GHz. A maximum 3 dB electrical bandwidth of 90 GHz was obtained by modeling-based extrapolation of experimental data (Fig. 4.36(b)).

4.4.3 Management of Chirp and Chromatic Dispersion Impairments in High Speed C- and L-Band Transmitters

As demonstrated in Sects. 4.2.3 and 4.3.2 to 4.3.4 a positive chirp factor (α) [119]) of directly modulated lasers (DML) and EA/DFBs (also designated as electroab-

Fig. 4.37 Operation scheme of 10 Gbit/s chirp managed laser (CML) [123]



sorption modulated lasers, EMLs) causes a significant reduction of link lengths in uncompensated systems. Signals of ≥ 10 Gbit/s from transmitters with operation wavelengths away from the zero-dispersion wavelength (~ 1310 nm) experience pronounced pulse broadening due to chromatic dispersion. Typical alpha factors of DMLs in the range from 2 to 8 (α_{ld} , see (4.10)) limit the transmission of typical 10 Gbit/s C-band lasers to about 10 km in standard single mode fibers (see Sect. 4.2.1). In order to alleviate or even overcome the negative impact of chromatic dispersion, different approaches have been investigated. The most straightforward way is to reduce the alpha factor. A particularly low alpha value of $\alpha_{ld} \sim 1$ has been reported for a DML with the structure of a passive feedback laser (PFL) as described in Sect. 4.4.1 [120]. Reduction of the alpha factor was achieved by an appropriate setting of the phase of the internal optical feedback. This chirp is almost comparable to typical chirp values of EA/DFBs which allows a 40 Gbit/s transmission reach up to 2 km (see Fig. 4.7), and it is also interesting to note that such laser chirp tuning has been successfully employed for the demonstration of the phase coding format DPSK as well [121].

A different concept for increasing link distances in systems with chromatic dispersion is using ‘chirped managed lasers’ (CML) [122, 123]. A CML comprises a directly modulated DFB laser in combination with a multi-cavity etalon filter serving as an optical spectrum reshaper (OSR). Figure 4.37 shows the schematic of a CML and the operation principle [123].

A conventional high-speed DFB laser is biased high above threshold and modulated directly. This results in intensity modulation (IM) with a low ER (approx. 2 dB) and, in parallel, the DFB laser generates frequency-shift keying modulation (FM) and adiabatic chirp.

The adiabatic chirp $\Delta\lambda_{s_chirp}$ is proportional to the modulated power and causes ‘1’ bits to experience a blue shift of the signal relative to the ‘0’ bits. The laser emission is aligned to the transmission of the OSR filter in such a way that the blue shifted ‘1’ bits pass almost unaffected while the red shifted 0 bits are attenuated. This FM-IM conversion can increase the ER at the output of the OSR filter to

> 10 dB. Furthermore, the operation conditions of CMLs are typically chosen such that the peak-to-peak adiabatic chirp of the DFB laser corresponds to half the bit rate frequency, e.g. 5 GHz chirp for a 10 Gbit/s signal, known as the minimum-shift keying (MSK) condition. By passing the OSR filter the chirped waveform is converted into flat-top chirped pulses with abrupt transitions at the intensity minima of isolated '0' bits. This constant phase envelope of the optical signal with an abrupt π change at a '0' bit is the decisive feature of CML's dispersion tolerance. After propagation through dispersive fiber, two '1' bits which are separated by only one '0' bit will interfere destructively. They remain well separated and produce an open eye and a low bit error rate (BER). The CML concept enables record lengths of NRZ transmission without optical dispersion compensation (e.g. 250 km at 10 Gbit/s have been reported in [122]). An extension of the CML concept to bit rates > 10 Gbit/s requires an adjustment of the FM and OSR filter characteristics. CML operation was recently demonstrated in combination with a 25 nm tunable C-band laser. The fully integrated hybrid III-V/SOI (silicon-on-insulator) CML chip uses SOI-based ring resonators for the functionality of the optical reshaper and a 10 Gbit/s directly modulated tunable laser. The compact chip has been realized using wafer bonding technology [124].

Besides taking advantage of their dispersion tolerance, the phase-coding property of CMLs has been used to demonstrate generation and transmission of alternative formats like return-to-zero alternate mark inversion (RZ-AMI) and RZ differential phase-shift keying (DPSK) [125, 126].

The output power of EA/DFBs is inherently lower than for directly modulated lasers, however, their low alpha values $\alpha_{mod} \leq 1$ (see (4.21)) make EA/DFBs superior to DMLs as far as modulation bandwidth and extinction ratio are concerned, and enable C- and L-band transport with bit rates ≥ 40 Gbit/s. At the typical EAM operation point, characterized by the highest slope of output power as a function of EAM voltage, the chirp parameter α_{mod} is in the range of 0.3 to 1. Under these EAM bias conditions the 40 Gbit/s NRZ transmission distance of 1.55 μm EA/DFB transmitters is limited to about 2 km SSMF. However, zero or even negative alpha values as needed for improved transmission properties, require significantly higher negative (reverse) EAM bias, and this causes an increased absorption by the EA modulator and a further reduction of the overall optical output power.

One obvious means to overcome low output power is the integration of an SOA section in front of the EAM, and this EML device concept has been investigated by different researchers. In [127] the authors investigated C-band devices and focused on the optimization of SOA length and driving conditions for low power consumption under 45 °C operation temperature. With a 50 μm long SOA section they could transmit 40 Gbit/s NRZ signals over an increased link distance of 5 km. The EMLs have been operated with a dynamic extinction of 8 dB and an average optical power of 5 dBm. The implementation of an SOA section in front of the EAM works well also for designing low chirp and high speed L-band transmitters. Due to a larger impact of chromatic dispersion for longer wavelengths low chirp operation will be of particular importance for L-band transmitters. In [128] the concept of an integrated SOA was applied to an L-band EML comprising one common active layer for the

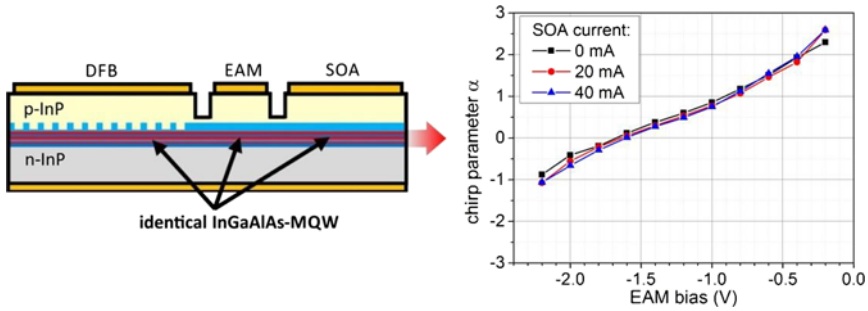


Fig. 4.38 Low chirp and high output power operation of high speed L-band EML based on common active layer: device schematic (*left*) and chirp parameter α_{mod} as function of EAM bias (*right*) (after [128])

DFB, EAM, and SOA-sections (see Fig. 4.38). The operation point of the EAM was chosen close to zero chirp while driving the amplifier up to 40 mA enabled an average optical power >4 dBm. Successful 40 Gbit/s NRZ signal transmission was demonstrated for up to 3 km link distance.

Dual-EMLs (D-EML) operate in a way similar to CMLs and constitute another EA/DFB variety which enables increased transmission distances in dispersive systems [129]. D-EMLs consist of a DFB laser with an integrated EAM section as in conventional EA/DFBs. However, the operation conditions of the D-EML differ. Both the DFB laser and the EAM are modulated separately by a dual RF signal. The laser works in a high FM regime and the EAM under high IM conditions. In this way optical single-sideband (OSSB) signals are generated for NRZ modulation formats. The right choice of IM and FM parameters allows to suppress one of the harmonic sidebands and results in a flat channel response of the OSSB. The D-EML concept relies, similar to the CML approach, on the appropriate amount of FM that has to be adjusted to half the bit rate. In case of D-EMLs the FM to IM conversion is realized by the EAM transfer function and can be controlled by properly setting the DC and RF operation points of the EAM. Using a D-EML, 40 Gbit/s NRZ transmission over 12 km SSMF without compensation for chromatic dispersion effects has been demonstrated in [129].

4.5 Directly Modulated Transmitters in 100G/400G Applications

4.5.1 High Speed 40/56 GBd 1.3 μm Transmitters

The technical recommendations for 100 Gbit/s transmitters and receivers have been fixed in the Ethernet standard IEEE 802.3ba, agreed in 2010 [130]. The standard defines four parallel bit streams with symbol rate of 25.8 GBd in optical systems with link distances of 10 km (LR – ‘long reach’) and 40 km (ER – ‘extended reach’) single mode fibers. The bit streams are wavelength division multiplexed (WDM)

with lanes specified at 1295.56 nm, 1300.05 nm, 1304.58 nm and 1309.14 nm for the 100GBASE-LR4 and 100GBASE-ER4 standards. The demand for an extinction ratio of 8 dB for 40 km links makes EML transmitters the preferred choice. A much lower extinction ratio of 4 dB is requested for the 10 km solutions (LR4) and can be achieved also by directly modulated lasers.

4.5.1.1 Short Cavity DMLs with BH Type Laser Structure

Active layers based on InGaAlAs QWs represent the preferred material solution for components designed for uncooled or semi-cooled operation. The Al containing MQW stack enables the operation of optical components at high ambient temperatures (see Chap. 3, Sect. 3.4) which is the key to decrease power consumption of TEC controllers and hence reduce the overall power budget. A further objective of DML development is the reduction of driving currents and voltages. The reduced level of laser current is accompanied by a smaller value of DC power consumption. The more significant effect, however, is expected with respect to RF power consumption of the driver ICs which require lower input power as the modulation output swing of the RF circuits gets lower.

For that reason novel high speed DML designs take advantage of buried heterostructure type lasers. A high lateral confinement of BH lasers (see Chap. 3, Sect. 3.3) enables low threshold currents as well as low driving currents. However, the growth of BH type lasers using Al in the active layer stack is rather challenging. The exposure of Al-containing layers to an oxygen containing atmosphere causes surface oxidation and requires additional technological effort for subsequent overgrowth. Consequently, after forming the active laser stripe a well-developed surface passivation of the InGaAlAs layers is mandatory prior to the growth of blocking layers. Several groups have successfully demonstrated technological progress with high speed DFB-BH lasers based on InGaAlAs-MQWs active layers. A selection is presented in the following paragraph.

The authors of [131] describe the performance of a 1.3 μm DFB-distributed reflector (DR) laser which is applicable for symbol rates up to 50 GBd [132]. The InGaAlAs lasers are built on semi-insulating InP comprising 12 QWs in the active layer, and the longitudinal laser design is based on a DFB section embedded in between DBR sections at the front and the rear side as well. The operation of such lasers was also investigated in a monolithic 4-array structure [131]. With wavelengths fitting to the Ethernet channels the individual lasers have been tested at 25.8 GBd and an ambient temperature of 50 °C. Driving the lasers at a low DFB bias current of 30 mA with a modulation swing of 20 mA resulted in an extinction ratio of 5 dB. Other authors reported 25.8 GBd BH-DFB lasers operating at temperatures up to 85 °C where the 200 μm long BH laser consisted of a 150 μm long DFB section and an integrated passive waveguide section at the front side of the laser [133].

More recently DMLs enabling symbol rates as high as 56 GBd at 45 °C and even higher temperatures have been reported. One example utilizes a ‘ridge shaped’ (RS)

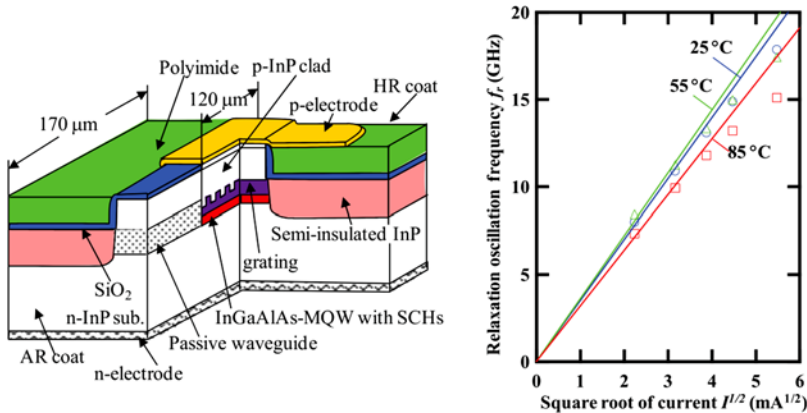


Fig. 4.39 High speed DML with ridge shape RS-BH design: device structure (*left*) and relaxation oscillation frequency versus square root of current above threshold (*right*) [134]

type BH laser as schematically shown in Fig. 4.39(left) [134]. The authors claim that their RS-BH laser design allows a reduced lateral leakage current and a higher confinement factor compared to conventional BH lasers. The longitudinal design in [134] consists, similar to the example in [133], of an active DFB part in combination with an integrated passive section. The overall device length is 170 μm and combines the 120 μm long laser section with a passive InGaAsP waveguide in front, embedding the Al-containing layers. At 85 $^{\circ}\text{C}$ the DML still exhibits a modulation bandwidth of 22 GHz. Figure 4.39(right) shows the relaxation oscillation frequency versus the square of the current above threshold for the RS-BH laser at different temperatures. The slope yields the efficiency η_{fr} according to (4.15) which can be taken as a figure-of-merit for high speed DMLs. For the laser in [134] a high η_{fr} of $3.2 \text{ GHz}/(\text{mA})^{1/2}$ was obtained at 85 $^{\circ}\text{C}$.

A further DML variant supporting 56 Gbit/s NRZ signals has been described in [135]. The device scheme and the large signal eye diagram are depicted in Fig. 4.40. The BH laser has been fabricated with conventional pn-blocking layers. The overall device with a length of 200 μm comprises a 150 μm long DFB section and a butt-joint coupled passive waveguide section. Driving the laser with a moderate current of 60 mA resulted in a 3 dB modulation bandwidth of 30 GHz at 55 $^{\circ}\text{C}$ device temperature. These properties allowed extinction ratios of 4.5 dB and higher at symbol rates of 56 GBd.

Reliability has also been investigated and reported in [135]: Accelerated ageing at 85 $^{\circ}\text{C}$ over 7000 hours resulted in 2% reduction of output power only for a constant current of 60 mA.

The results of different research groups indicate similar approaches for the implementation of 28/56 GBd DMLs. For single mode fiber based Ethernet and data-com applications the focus is on DFB lasers with a BH type lateral structure and active layers based on InGaAlAs MQWs. In accordance with the SCEEL concept (see Sect. 4.2.5) the length of DFB lasers is typically in the range from 100 μm

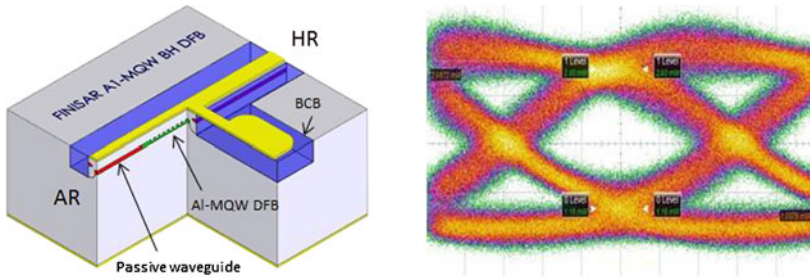


Fig. 4.40 BH laser structure with pn-blocking layers (left) and 56 Gbit/s NRZ eye pattern at $T = 55\text{ }^{\circ}\text{C}$ (right) [135]

to $150\text{ }\mu\text{m}$ integrated with a short Al-free passive waveguide section at the output facet completing the chip to an overall length of about $200\text{ }\mu\text{m}$. The passive section is beneficial for chip handling, however, it is also helpful in order to protect the Al-containing active layers. The novel lasers allow NRZ signals up to 56 Gbit/s at typical driving currents of 60 mA and lower, the output power of the DFB lasers is about 10 mW, and these high speed edge emitting lasers are characterized by an $\eta_{fr} > 3\text{ GHz}/(\text{mA})^{1/2}$ and operation temperatures up to $85\text{ }^{\circ}\text{C}$.

4.5.1.2 Arrays of EA/DFB (EML) Transmitters

Despite the success in increasing the modulation bandwidth of DMLs for the application of NRZ modulation formats up to 56 GBd, EA/DFBs (EMLs) are still the components with the higher modulation bandwidth and an unsurpassed high extinction ratio. Recent trends in the development of EML transmitters focused on cost effective fabrication technologies, high output power and, in particular, on the implementation of monolithic EML arrays. As for DMLs the design relies on Al-containing quantum wells allowing semi-cooled or uncooled operation. Highest modulation bandwidths $\geq 50\text{ GHz}$ that could be demonstrated in single EAMs are currently under investigation for integrated versions. The simplest laser integration concept based upon a common active layer stack and the formation of separate laser and modulator sections, is advantageous in terms of processing technology and yield [136]. Such EML devices enable small chip size, and even NRZ bit rates as high as 70 Gbit/s in a single lane have been achieved with on chip impedance matching to overcome the RC limitation of the absorber structure [137].

Integrated chips with 4-fold or even 8-fold EML arrays are of interest for future 400G-systems and have already been demonstrated. The success of monolithic integration of EMLs in array-structures in combination with multiplexer devices is shown in [138, 139]. The authors demonstrated a total of 400 Gbit/s with a single chip carrying an array of eight 50 Gbit/s modulators. The channel spacing was 800 GHz. The whole chip including integrated monitor diodes and the 8:1 MMI multiplexer was prepared for flip-chip technology and could be successfully mounted into a transmitter package [140].

4.5.2 *Advanced Modulation Formats for Higher Spectral Efficiency in Short Reach Applications*

In contrast to coherent systems where an increase of spectral efficiency can be achieved by various advanced modulation schemes, short reach systems require low cost optical components and favor direct detection. Novel DSP supported solutions for transmitters and receivers allow higher numbers of bits per symbol. Since the same bit rate can be realized with a lower symbol rate, the bandwidth requirements for electronic and opto-electronic components can be relaxed. On the other hand, higher order modulation formats help reducing the number of optical channels and relaxing the bandwidth requirements resulting in cost savings of the systems. Preferred higher order modulation formats in IM/DD systems are the discrete multi-tone (DMT) and the m-fold pulse amplitude modulation (PAM-M) concepts. They are under intensive discussion for the next generation of short reach 400GbE-systems (see e.g. [141]). DMT is a version of orthogonal frequency division multiplexing (OFDM) technology in the baseband (see [142]) which transmits optical data using the intensity domain only and does not use the phase domain. DMT is a water-filling technique that allocates optimal power and modulation order to each subcarrier. The spectral efficiency is improved by assigning a high modulation level to “high quality” subcarriers while low modulation levels are assigned to “low quality” ones. In this way the transfer characteristics of the transmitter can be used very efficiently, even if the modulation response is not flat. By utilizing bit-loading, DMT has the unique ability to maximize the capacity of a frequency-selective channel [143]. Compared to conventional NRZ modulation an improvement of spectral efficiency by a factor of 4 is possible [144]. With DMT schemes applied to DML transmitters bit rates of 100 Gbit/s and higher have already been demonstrated in a single optical channel [145].

The spectral efficiency for PAM modulation can be increased by a factor of 2 in the case of PAM-4 or by a factor of 3 in case of PAM-8, respectively (see Chap. 7, Sect. 7.3.1). For the same bit rate PAM-4 modulation needs higher transmitter bandwidth than DMT coding but much lower power consumption by IC drivers is expected [146].

The progress of DML development paved the way for novel high speed lasers for 56 Gbit/s implementation using PAM-4 modulation. The first demonstration of a 50 Gbit/s PAM based signal exploiting a DML transmitter was shown in [147] with four intensity levels generated by 3×12 mA current swing around a 70 mA bias current. Although the total extinction ratio (taken from the power of the lowest and highest intensity levels) was lower than 3 dB, well separated amplitude levels have been achieved. With a higher total *ER* of 4.7 dB an optical 56 Gbit/s PAM-4 has been shown in [135], the respective eye diagram is presented in Fig. 4.41 (left). With its high bandwidth of 55 GHz the DML introduced in [109] allowed the PAM-4 modulation with clearly separated levels even at symbol rates of 56 GBd.

More than four intensity levels, e.g., PAM-8 or PAM-16 formats, based on DML transmitters look rather challenging for symbol rates of ≥ 28 GBd.

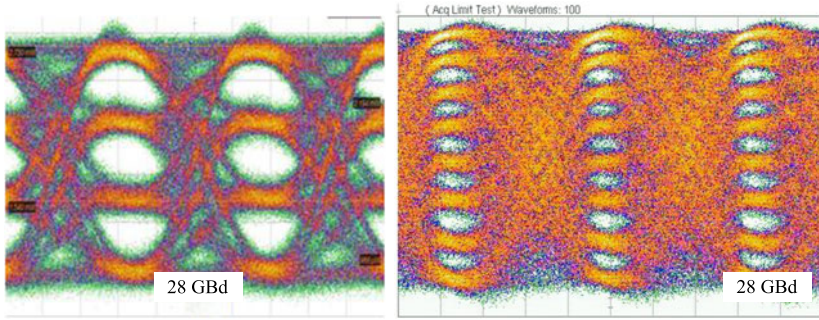


Fig. 4.41 Optical eye diagrams (back to back) of 1.3 μm signals from PAM-4 modulated 56 Gbit/s DML [135] (*left*) and PAM-8 modulated 84 Gbit/s EML [148] (*right*) at symbol rate of 28 GBd

The situation is different for the use of EML transmitters. As they offer higher modulation bandwidth and higher achievable *ERs*, EMLs are particularly suited as directly modulated optical sources for PAM-*M* formats. If the electronic ICs allow flexible level spacings, the impact of nonlinearities of the *e/o* transfer function can be mitigated and their high total *ER* can be taken advantage of. By working with EMLs even PAM-8 schemes for symbol rates of 28 GBd and above look realistic. Figure 4.41(right) shows the PAM-8 optical signal of a 1.3 μm EML transmitter chip at 28 GBd [148] where eight well separated intensity levels can be seen. It demonstrates the potential of PAM-8 based modulation of EMLs for the realization of higher spectral efficiency in future IM/DD schemes.

The implementation of a single carrier 100G solution based upon a PAM-4 modulated 56 GBd EML was successfully demonstrated in [149] and [150]. The flip-chip version of EMLs in [149] with bandwidth >50 GHz was realized for emission at 1.3 μm and enabled equalizer free transmission of 56 GBd and 112 GBd PAM-4 signals over a 10 km fiber link [151, 152]. With a 1.55 μm EML as part of a transmitter module a 112 Gbit/s PAM-4 transmission over 2 km with only a 3 tap digital equalizer (for details see Chap. 7, Sect. 7.5) and without any optical amplification has been reported in [150].

In conclusion, PAM-4 and PAM-8 as well as DMT are very promising techniques that enable cost effective 100 Gbit/s transmission in a single optical channel. Progress and applications of corresponding DML- and EML transmitters will depend to a significant extent on the further development of high speed electronic ICs such as drivers, DAC/ADC components, and DSP chips.

References

1. <http://www.300pinmsa.org/>
2. <http://www.xenpak.org/>
3. <http://www.xpak.org/>
4. <http://www.x2msa.org/>

5. <http://www.xfpmsa.org/>
6. SFF-8431 specifications for enhanced 8.5 and 10 Gigabit small form factor pluggable module "SFP+". Revision 2.1, 30 August 2007
7. <http://www.cfp-msa.org/>
8. <http://www.ieee802.org/3/ba/index.html>
9. http://www.ieee802.org/3/bs/timeline_3bs_0915.pdf
10. H. Stutz, G. de Mars, in *Quantum Electronics*, ed. by C.H. Townes (Columbia Univ. Press, New York, 1960), p. 530
11. M. Aoki, T.K. Sudo, T. Tsuchiya, D. Takemoto, S. Tsuji, 85 °C 10-Gbit/s operation of 1.3- μm InGaAlAs MQW-DFB laser, in *Proc. 26th Europ. Conf. Opt. Commun. (ECOC'00)*, Munich, Germany (2000), vol. **1**, pp. 123–124
12. M. Ishikawa, R. Nagarajan, T. Fukushima, J.G. Wasserbauer, J.E. Bowers, Long wavelength high-speed semiconductor lasers with carrier transport effects. *IEEE J. Quantum Electron.* **28**, 2230–2241 (1992)
13. K. Uomi, T. Tsuchiya, H. Nakano, M. Aoki, M. Suzuki, N. Chinone, High-speed and ultralow-chirp 1.55 μm multiquantum well $\lambda/4$ -shifted DFB lasers. *IEEE J. Quantum Electron.* **27**, 1705–1713 (1991)
14. D. Marcuse, T.H. Wood, Time-dependent simulation of a laser-modulator combination. *IEEE J. Quantum Electron.* **30**, 2743–2755 (1994)
15. D. Marcuse, T.H. Wood, Simulation of a laser modulator driven by NRZ pulses. *J. Lightwave Technol.* **14**, 860–866 (1996)
16. P.J. Corvini, T.L. Koch, Computer simulation of high-bit-rate optical fiber transmission using single-frequency lasers. *J. Lightwave Technol.* **LT-5**, 1591–1595 (1987)
17. F. Koyama, Y. Suematsu, Analysis of dynamic spectral width of dynamic-single-mode (DSM) lasers and related transmission bandwidth of single-mode fibers. *IEEE J. Quantum Electron.* **QE-21**, 292–297 (1985)
18. H. Temkin, N.K. Dutta, T. Tanbun-Ek, R.A. Logan, A.M. Sergent, InGaAs/InP quantum well lasers with sub-mA threshold current. *Appl. Phys. Lett.* **57**, 1610–1612 (1990)
19. P.J.A. Thijs, L.F. Tiemeijer, P.I. Kuindersma, J.J.M. Binsma, T. van Dongen, High-performance 1.5 μm InGaAs–InGaAsP strained quantum well lasers and amplifiers. *IEEE J. Quantum Electron.* **27**, 1426–1439 (1991)
20. E. Zah, R. Bhat, F.J. Favire, S.G. Menocal, N.C. Andreakis, K.W. Cheung, D.D. Hwang, M.A. Koza, T.P. Lee, Low-threshold 1.5 μm compressive-strained multiple-and single-quantum-well lasers. *IEEE J. Quantum Electron.* **27**, 1440–1450 (1991)
21. T. Namegaya, A. Kasukawa, N. Iwai, T. Kikuta, High temperature operation of 1.3 μm GaInAsP/InP GRINSCH strained-layer quantum well lasers. *Electron. Lett.* **29**, 392–393 (1992)
22. J.S. Osinski, P. Grodzinski, Y. Zou, P.D. Dapkus, Z. Karim, A.R. Tanguay, Low threshold current 1.5 μm buried heterostructure lasers using strained quaternary quantum wells. *IEEE Photonics Technol. Lett.* **4**, 1313–1315 (1992)
23. T. Tsuchiya, M. Komori, K. Uomi, A. Oka, T. Kawano, A. Oishi, Investigation of effect of strain on low-threshold 1.3 μm InGaAsP strained-layer quantum well lasers. *Electron. Lett.* **30**, 788–789 (1994)
24. K. Kojima, O. Mizuhara, L.J.P. Ketelsen, I. Kim, R.B. Bylisma, 1.3- μm uncooled DFB lasers for 10 Gb/s transmission over 50 km of non-dispersion-shifted fiber, in *Opt. Fiber Commun. Conf. (OFC'96)*, San Jose, CA, USA (1996), Techn. Digest, paper PDP11-2
25. R. Paoletti, M. Agresti, G. Burns, G. Berry, B. Bertone, P. Charles, P. Crump, A. Davies, R.Y. Fang, R. Ghin, P. Gotta, M. Holm, C. Kompocholis, G. Magnetti, J. Massa, G. Meneghini, G. Rossi, P. Ryder, A. Taylor, P. Valenti, M. Meliga, 100 °C 10 Gb/s directly modulated InGaAsP DFB lasers for uncooled Ethernet applications, in *Proc. 27th Europ. Conf. Opt. Commun. (ECOC'01)*, Amsterdam, The Netherlands (2001), PD 84–85
26. G. Sakaino, Y. Hisa, K. Takagi, T. Aoyagi, T. Nishimura, E. Omura, Uncooled and directly modulated 1.3 μm DFB laser diode for serial 10 Gb/s Ethernet, in *Proc. 26th Europ. Conf. Opt. Commun. (ECOC'00)*, Munich, Germany (2000), vol. **1**, pp. 125–126

27. M. Kondow, K. Uomi, A. Niwa, T. Kitatani, S. Watahiki, Y. Yazawa, GaInNAs: A novel material for long-wavelength-range laser diodes with excellent high-temperature performance. *Jpn. J. Appl. Phys.* **35**, 1273–1275 (1996)
28. I. Suemune, Theoretical estimation of leakage current in II–VI heterostructure lasers. *Jpn. J. Appl. Phys.* **31**, 95–98 (1992)
29. T. Kitatani, J. Kasai, K. Nakahara, K. Adachi, M. Aoki, High-performance GaInNAs long-wavelength lasers, in *Conf. Indium Phosphide Relat. Mater. (IPRM'07)*, Matsue, Japan (2007), Techn. Digest, pp. 354–357
30. Y. Matsushima, K. Utaka, K. Sakai, Narrow spectral linewidth of MBE-grown GaInAs/AlInAs MQW lasers in the 1.55 μm range. *IEEE J. Quantum Electron.* **25**, 1376–1380 (1989)
31. C.E. Zah, R. Bhat, B.N. Pathak, F. Favire, W. Lin, M.C. Wang, N.C. Andreadakis, D.M. Hwang, M.A. Koza, T.P. Lee, Z. Wang, D. Darby, D. Flanders, J.J. Hsieh, High-performance uncooled 1.3- μm Al_xGa_yIn_{1-x-y}As/InP strained layer quantum-well lasers for subscriber loop applications. *IEEE J. Quantum Electron.* **30**, 511–522 (1994)
32. T.K. Sudoh, D. Takemoto, T. Tsuchiya, M. Aoki, S. Tsuji, Highly reliable 1.3- μm InGaAlAs MQW DFB lasers, in *17th IEEE Internat. Semicond. Laser Conf. (ISLC'00)*, Monterey, CA, USA (2000), Conf. Digest, paper TuB6
33. T. Takiguchi, Y. Hanamaki, T. Kadowaki, T. Tanaka, C. Watatani, M. Takemi, Y. Mhashi, E. Omura, 1.3 μm uncooled AlGaInAs-MQW DFB laser with $\lambda/4$ -shifted Grating, in *Opt. Fiber Commun. Conf. (OFC'02)*, Anaheim, CA, USA, 2002. Techn. Digest (2002), paper ThF3
34. K. Nakahara, T. Tsuchiya, S. Tanaka, T. Kitatani, K. Shinoda, T. Taniguchi, T. Kikawa, E. Nomoto, S. Fujisaki, M. Kudo, M. Sawada, T. Yuasa, M. Mukaikubo, 115 °C, 12.5-Gb/s direct modulation of 1.3- μm InGaAlAs-MQW RWG DFB laser with notch-free grating structure for datacom applications, in *Opt. Fiber Commun. Conf. (OFC'03)*, Atlanta, GA, USA (2003), Techn. Digest, paper PD-40
35. K. Nakahara, T. Tsuchiya, T. Kitatani, K. Shinoda, T. Kikawa, F. Hamano, S. Fujisaki, T. Taniguchi, E. Nomoto, M. Sawada, T. Yuasa, 12.5-Gb/s direct modulation up to 115 °C in 1.3- μm InGaAlAs-MQW RWG DFB lasers with notch-free grating structure. *J. Lightwave Technol.* **25**, 159–165 (2004)
36. S. Shirai, Y. Tatsuoka, C. Watatani, T. Ota, K. Takagi, T. Aoyagi, E. Omura, N. Tomita, 120 °C uncooled operation of direct modulated 1.3- μm AlGaInAs-MQW DFB laser diodes for 10-Gb/s telecom applications, in *Opt. Fiber Commun. Conf. (OFC'04)*, Los Angeles, CA, USA (2004), Techn. Digest, paper ThD2
37. Y. Muroya, T. Okuda, R. Kobayashi, K. Tsuruoka, Y. Ohsawa, T. Kouji, T. Tsukuda, T. Nakamura, K. Kobayashi, 100 °C, 10-Gb/s direct modulation with a low operation current of 1.3- μm AlGaInAs buried heterostructure DFB laser diodes, in *Opt. Fiber Commun. Conf. (OFC'03)*, Atlanta, GA, USA (2003), Techn. Digest, paper FG6
38. P.M. Ilroy, A. Kurobe, Y. Uematsu, Analysis and application of theoretical gain curves to the design of multi-quantum-well lasers. *IEEE J. Quantum Electron.* **QE-21**, 1958–1963 (1985)
39. K. Nakahara, T. Tsuchiya, T. Kitatani, K. Shinoda, T. Taniguchi, T. Kikawa, M. Aoki, 40-Gb/s direct modulation in 1.3- μm InGaAlAs-MQW RWG DFB lasers, in *Conf. Lasers Electro-Opt. (CLEO'07)/Pacific Rim*, Seoul, South Korea (2007), OSA Techn. Digest, paper ThA3_2
40. T. Tadokoro, W. Kobayashi, T. Fujisawa, T. Yamanaka, F. Kano, High-speed modulation lasers for 100GbE applications, in *Opt. Fiber Commun. Conf. and Nat. Fiber Opt. Eng. Conf. (OFC/NFOEC'11)*, Los Angeles, CA, USA (2011), Techn. Digest, paper OWD1
41. T. Simoyama, M. Matsuda, S. Okumura, M. Ekawa, T. Yamamoto, 40-Gbps transmission using direct modulation of 1.3- μm AlGaInAs MQW distributed-reflector lasers up to 70 °C, in *Opt. Fiber Commun. Conf. and Nat. Fiber Opt. Eng. Conf. (OFC/NFOEC'11)*, Los Angeles, CA, USA (2011), Techn. Digest, paper OWD3
42. Optical amplifiers, *J. Lightwave Technol.* **9**, 145–296 (1991) (Special Issue)
43. T.H. Wood, Multiple quantum well waveguide modulators. *J. Lightwave Technol.* **6**, 743–757 (1988)

44. K. Wakita, I. Kotaka, O. Mitomi, H. Asai, Y. Kawamura, M. Naganuma, High-speed InGaAs/InAlAs multiple quantum well optical modulators with bandwidths in excess of 40 GHz at 1.55 μm , in *Conf. Lasers Electro-Opt.* (CLEO'90), Baltimore, MD (1990), Techn. Digest, paper CtuC6
45. H. Sano, H. Inoue, H. Nakamura, K. Ishida, J.M. Glinski, Low loss single-mode InGaAs/InAlAs multiquantum well electroabsorption modulator, in *Opt. Fiber Commun. Conf.* (OFC'90), San Francisco, CA, USA (1990), Techn. Digest, paper WM15
46. U. Koren, B.I. Miller, T.L. Koch, G. Eisenstein, R.S. Tucker, I. Bar-Joseph, D.S. Chemla, Low-loss InGaAs/InP MQW optical electroabsorption waveguide modulator. *Appl. Phys. Lett.* **51**, 1132–1134 (1987)
47. F. Devaux, E. Bigan, B. Rose, M. Mckee, F. Huet, M. Carré, High-speed, InGaAsP/InP multiple quantum 1.55 μm single mode modulator. *Electron. Lett.* **27**, 1926–1927 (1991)
48. F. Devaux, E. Bigan, A. Ougazzaden, B. Pierre, F. Huet, M. Carré, A. Carenco, InGaAsP/InGaAsP multiple quantum well modulator with improved saturation intensity and bandwidth over 20-GHz. *IEEE Photonics Technol. Lett.* **4**, 720–722 (1992)
49. H. Sano, H. Inoue, S. Tsuji, K. Ishida, InGaAs/InAlAs MQW Mach-Zehnder optical modulator for 10-Gbit/s long-haul transmission systems, in *Opt. Fiber Commun. Conf.* (OFC'92), San Jose, CA, USA (1992), Techn. Digest, paper ThG4
50. J.E. Zucker, K.L. Jones, B.I. Miller, M.G. Young, U. Koren, B. Tell, K. Brown-Goebeler, Interferometric quantum well modulators with gain. *J. Lightwave Technol.* **10**, 924–932 (1992)
51. D.A.B. Miller, D.S. Chemla, T.C. Damen, A.C. Gossard, W. Wiegmann, T.H. Wood, C.A. Burrus, Electric field dependence of optical absorption near the band gap of quantum well structures. *Phys. Rev. B* **32**, 1043–1060 (1985)
52. K. Wakita, Y. Kawamura, Y. Yoshikuni, H. Asahi, Electroabsorption on room-temperature excitons in InGaAs/InGaAlAs multiple quantum-well structures. *Electron. Lett.* **21**, 338–340 (1985)
53. Y. Kawamura, K. Wakita, Y. Yoshikuni, Y. Itaya, H. Asahi, Monolithic integration of a DFB laser and an MQW optical modulator in the 1.5- μm wavelength range. *IEEE J. Quantum Electron.* **27**, 915–918 (1991)
54. H. Soda, K. Sato, H. Sudo, S. Takeuchi, H. Ishikawa, Ultralow-chirp characteristics of monolithic electroabsorption modulator/DFB laser light source, in *Proc. 17th Europ. Conf. Opt. Commun.* (ECOC'91), Paris, France (1991), paper WeB7-1
55. T. Kato, T. Sasaki, N. Kida, K. Komatsu, I. Mito, Novel MQW DFB laser diode modulator integrated light source using bandgap energy control epitaxial growth technique, in *Proc. 17th Europ. Conf. Opt. Commun.* (ECOC'91), Paris, France (1991), paper WeB7-2
56. M. Aoki, H. Sano, M. Suzuki, M. Takahashi, K. Uomi, A. Takai, Novel structure MQW electroabsorption-modulator/DFB-laser-integrated device fabricated by selective area MOCVD growth. *Electron. Lett.* **27**, 2138–2140 (1991)
57. M. Suzuki, H. Tanaka, H. Taga, S. Yamamoto, Y. Matsushima, $\lambda/4$ -Shifted DFB laser/electroabsorption modulator integrated light source for multigigabit transmission. *J. Lightwave Technol.* **10**, 90–94 (1992)
58. K. Wakita, I. Kotaka, H. Asai, M. Okamoto, Y. Kondo, M. Naganuma, High-speed and low-drive-voltage monolithic multiple quantum well modulator/DFB laser light source. *IEEE Photonics Technol. Lett.* **4**, 16–18 (1992)
59. U. Koren, B. Gance, B.I. Miller, M.G. Young, M. Chien, T.H. Wood, L.M. Ostar, T.L. Koch, R.M. Jopson, J.D. Evankow, G. Raybon, C.A. Bums, P.D. Magill, K.C. Reichmann, Widely tunable distributed Bragg reflector laser with an integrated electroabsorption modulator, in *Opt. Fiber Commun. Conf.* (OFC'92), San Jose, CA, USA (1992), Techn. Digest, paper WG5
60. M. Aoki, N. Kikuchi, K. Sekine, S. Sasaki, M. Suzuki, T. Taniwatari, Y. Okuno, T. Kawano, A. Takai, Low-drive-voltage and low-chirp integrated electroabsorption modulator/DFB-laser for 2.5 Gbit/s 200-km normal fiber transmission. *Electron. Lett.* **29**, 1983–1984 (1993)
61. K.C. Reichmann, P.D. Magill, G. Raybon, Y.K. Chen, T. Tanbun-Ek, R.A. Logan, A. Tate, A.M. Sergent, K.W. Wecht, P.F. Sciortino Jr., Long-distance transmission experiment at

- 2.5 Gbit/s using an integrated laser/modulator grown by selective-area MOVPE, in *Opt. Fiber Commun. Conf. (OFC'94)*, San Jose, CA, USA (1994), Techn. Digest, paper ThM-4
62. K. Komatsu, T. Kato, M. Yamaguchi, T. Sasaki, S. Takano, H. Shimizu, N. Watanabe, M. Kitamura, DFB-LD/modulator integrated light sources fabricated by band-gap-energy-controlled selective MOVPE with stable fiber transmission characteristics, in *Opt. Fiber Commun. Conf. (OFC'94)*, San Jose, CA, USA (1994), Techn. Digest, paper TuC-3
 63. B. Clesca, S. Gauchard, V. Rodrigues, D. Lesterlin, E. Kuhn, A. Bodere, H. Haisch, K. Satzke, J.F. Vinchant, 2.5 Gbit/s, 1291-km transmission over nondispersion-shifted fiber using an integrated electroabsorption modulator/DFB laser module, in *Proc. 21st Europ. Conf. Opt. Commun. (ECOC'95)*, Brussels, Belgium (1995), paper Th.A.3.8
 64. K. Wakita, I. Kotaka, O. Mitomi, H. Asai, Y. Kawamura, M. Naganuma, High-speed InGaAlAs/InAlAs multiple quantum well optical modulators. *J. Lightwave Technol.* **8**, 1027–1032 (1990)
 65. A.M. Fox, D.A.B. Miller, G. Livescu, J.E. Cunningham, J.E. Henry, W.Y. Jan, Quantum well carrier sweep out: relation to electroabsorption and exciton saturation. *IEEE J. Quantum Electron.* **27**, 2281–2295 (1991)
 66. T.H. Wood, T.Y. Chang, J.Z. Pastalan, C.A. Burrus Jr., N.J. Sauer, B.C. Johnson, Increased optical saturation intensities in GaInAs multiple quantum wells by the use of AlGaInAs barriers. *Electron. Lett.* **27**, 257–259 (1991)
 67. T. Ido, H. Sano, S. Tanaka, H. Inoue, Frequency-domain measurement of carrier escape times in MQW electro-absorption optical modulators. *IEEE Photonics Technol. Lett.* **7**, 1421–1423 (1995)
 68. D. Marcuse, DFB laser with attached external intensity modulator. *IEEE J. Quantum Electron.* **26**, 262–269 (1990)
 69. Y. Kotaki, H. Soda, Analysis of static and dynamic wavelength shifts in modulator-integrated DFB lasers, in *Proc. 19th Europ. Conf. Opt. Commun. (ECOC'93)*, Montreux, Switzerland (1993), paper WeP8.6
 70. M. Aoki, S. Takashima, Y. Fujiwara, S. Aoki, New transmission simulation of EA-modulator integrated DFB-lasers considering the facet reflection-induced chirp. *IEEE Photonics Technol. Lett.* **9**, 380–382 (1997)
 71. R. Adams, Band-structure engineering for low-threshold high-efficiency semiconductor lasers. *Electron. Lett.* **22**, 249–250 (1986)
 72. E. Yablonoivitch, E.O. Kane, Reduction of lasing threshold current density by the lowering of valence band effective mass. *J. Lightwave Technol.* **LT-4**, 504–506 (1986)
 73. T. Ohtoshi, N. Chinone, Linewidth enhancement factor in strained quantum well lasers. *IEEE Photonics Technol. Lett.* **1**, 117–119 (1989)
 74. K. Kamite, H. Sudo, M. Yano, H. Ishikawa, H. Imai, Ultra-high-speed InGaAsP/InP DFB lasers emitted at 1.3 μm wavelength. *IEEE J. Quantum Electron.* **QE-23**, 1054–1058 (1987)
 75. P.J. Corvini, T.L. Koch, Computer simulation of high-bit-rate optical fiber transmission using single-frequency lasers. *J. Lightwave Technol.* **LT-5**, 1591–1595 (1987)
 76. K. Uomi, A. Murata, S. Sano, R. Takeyari, A. Takai, Advantages of 1.55 μm InGaAs/InGaAsP MQW-DFB lasers for 2.5 Gbit/s long-span normal fiber transmission. *IEEE Photonics Technol. Lett.* **4**, 657–660 (1992)
 77. M. Aoki, Monolithically-integrated laser diodes for optical telecommunications by selective area growth technologies. Ph.D. Dissertation, Department of Electrical and Electronic Engineering, Tokyo Institute of Technology, Tokyo, Japan (1999)
 78. N. Sasada, K. Naoe, Y. Sakuma, K. Motoda, T. Kato, M. Akashi, J. Shimizu, T. Kitatani, M. Aoki, M. Okayasu, K. Uomi, 1.55- μm 40-Gbit/s electro-absorption modulator integrated DFB laser modules for very short reach transmission, in *10th OptoElectronics Commun. Conf. (OECC'05)*, Seoul, Korea (2005), Techn. Digest, paper 6F2-1
 79. K. Naoe, N. Sasada, Y. Sakuma, K. Motoda, T. Kato, M. Akashi, J. Shimizu, T. Kitatani, M. Aoki, M. Okayasu, K. Uomi, 43-Gbit/s operation of 1.55- μm electro-absorption modulator integrated DFB laser modules for 2-km transmission, in *Proc. 31st Europ. Conf. Opt. Commun. (ECOC'05)*, Glasgow, UK (2005), paper Th 2.6.4

80. T. Fujisawa, K. Tahahat, W. Kobayashoi, T. Tadokoro, N. Fujiwara, S. Kanazawa, F. Kano, 1.3- μm , 50-Gbit/s EADFB lasers for 400GbE, in *Opt. Fiber Commun. Conf. and Nat. Fiber Opt. Eng. Conf. (OFC/NFOEC'11)*, Los Angeles, CA, USA (2011), Techn. Digest, paper OWD4
81. C. Kazmierski, A. Konczykowska, F. Jorge, F. Blache, M. Riet, C. Jany, A. Scavennec, 100 Gb/s operation of an AlGaInAs semi-insulating buried heterojunction EML, in *Opt. Fiber Commun. Conf. and Nat. Fiber Opt. Eng. Conf. (OFC/NFOEC'09)*, San Diego, CA, USA (2009), Techn. Digest, paper OTHT7
82. H. Tanaka, M. Horita, Y. Matsushima, Temperature dependence of InGaAsP electro-absorption modulator module, in *Conf. Indium Phosphide Relat. Mater. (IPRM'95)*, Hokkaido, Japan (1995), Techn. Digest, paper ThP45
83. B. Clesca, S. Gauchard, E. Lantoine, V. Rodrigues, F. Giraud, D. Lesterlin, 3.2 nm wavelength tuning via temperature control for integrated electroabsorption modulator/DFB laser with high tolerance to chromatic dispersion. *Electron. Lett.* **32**, 927–929 (1996)
84. M.R. Gokhale, P.V. Studenkov, J. Ueng-McHale, J. Thomson, J. Yao, J. van Saders, Uncooled, 10 Gb/s 1310 nm electroabsorption modulated laser, in *Opt. Fiber Commun. Conf. (OFC'03)*, Atlanta, GA, USA (2003), Techn. Digest, paper PDP-42
85. S. Makino, K. Shinoda, T. Kitatani, T. Tsuchiya, M. Aoki, Wide temperature range (0 to 85 °C), 40-km SMF transmission of a 1.55 μm , 10-Gbit/s InGaAlAs electroabsorption modulator integrated DFB laser, in *Opt. Fiber Commun. Conf. (OFC'05)*, Anaheim, CA, USA (2005), Techn. Digest, paper PDP-14
86. S. Makino, K. Shinoda, T. Shiota, T. Kitatani, T. Fukamachi, M. Aoki, N. Sasada, K. Naoe, K. Uchida, H. Inoue, Wide temperature (15 °C to 95 °C), 80-km SMF transmission of a 1.55- μm , 10-Gbit/s InGaAlAs electroabsorption modulator integrated DFB laser, in *Opt. Fiber Commun. Conf. and Nat. Fiber Opt. Eng. Conf. (OFC/NFOEC'07)*, Anaheim, CA, USA (2007), Techn. Digest, paper OMS-1
87. N. Sasada, K. Naoe, Y. Sakuma, K. Okamoto, R. Washino, D. Nakai, K. Motoda, S. Makino, M. Aoki, Un-cooled operation (10 °C to 85 °C) of a 10.7-Gbit/s 1.55- μm electro-absorption modulator integrated DFB laser for 40-km transmission, in *Opt. Fiber Commun. Conf. and Nat. Fiber Opt. Eng. Conf. (OFC/NFOEC'07)*, Anaheim, CA, USA (2007), Techn. Digest, paper We8.1.5
88. H. Hayashi, S. Makino, T. Kitatani, T. Shiota, K. Shinoda, S. Tanaka, M. Aoki, N. Sasada, K. Naoe, A first uncooled (25 to 85 °C) 43-Gbps light source based on InGaAlAs EA/DFB laser technology, in *Proc. 34th Europ. Conf. Opt. Commun. (ECOC'08)*, Brussels, Belgium (2008), paper We.3.C.3
89. S. Makino, K. Shinoda, T. Kitatani, H. Hayashi, T. Shiota, S. Tanaka, M. Aoki, N. Sasada, K. Naoe, High-speed electroabsorption modulator integrated DFB laser for 40 Gbps and 100 Gbps application, in *Conf. Indium Phosphide Relat. Mater. (IPRM'09)*, Newport Beach, CA, USA (2009), Techn. Digest, paper ThB1.1
90. T. Fujisawa, S. Kanazawa, N. Nunoya, H. Ishii, Y. Kawaguchi, A. Ohki, H. Fujiwara, K. Takahat, R. Iga, F. Kano, H. Oohashi, 4×25 -Gbit/s, 1.3- μm , monolithically integrated light source for 100-Gbit/s Ethernet, in *Proc. 36th Europ. Conf. Opt. Commun. (ECOC'10)*, Turino, Italy (2010), paper Th.9.D.1
91. K. Iga, Modulation limit of semiconductor lasers by some parametric modulation scheme. *Trans. Inst. Electron. Commun. Eng. Jpn.* **E-68**, 417–420 (1985)
92. R. Lang, Injection locking properties of a semiconductor-laser. *IEEE J. Quantum Electron.* **QE-18**, 976–983 (1982)
93. A. Tager, K. Petermann, High-frequency oscillations and self-mode locking in short external-cavity laser diodes. *IEEE J. Quantum Electron.* **30**, 1553–1561 (1994)
94. P. Even, K.A. Ameer, G.M. Stephan, Modeling of an injected gas laser. *Phys. Rev. A* **55**, 1441–1453 (1997)
95. E.G. Lariontsev, I. Zolotoverkh, P. Besnard, G.M. Stephan, Injection locking properties of a microchip laser. *Eur. Phys. J. D* **5**, 107–117 (1999)

96. X.J. Meng, T. Chau, M.C. Wu, Improved intrinsic dynamic distortions in directly modulated semiconductor lasers by optical injection locking. *IEEE Trans. Microw. Theory Tech.* **47**, 1172–1176 (1999)
97. L. Chrostowski, X. Zhao, C.J. Chang-Hasnain, R. Shau, M. Ortsiefer, M.-C. Amann, 50 GHz optically injection-locked 1.55- μm VCSELs. *IEEE Photonics Technol. Lett.* **18**, 367–369 (2006)
98. T. Sogawa, Y. Arakawa, M. Tanaka, H. Sakaki, Observation of a short optical pulse (<1.3 ps) from a gain switched quantum well laser. *Appl. Phys. Lett.* **53**, 1580–1582 (1988)
99. D. Bimberg, K. Ketterer, E.H. Böttcher, E. Scholl, Gain modulation of unbiased semiconductor lasers: ultrashort light-pulse generation in the 0.8 μm –1.3 μm wavelength range. *Int. J. Electron.* **60**, 23–45 (1986)
100. H.F. Liu, M. Fukazawa, Y. Kawai, T. Kamiya, Gain-switched picosecond pulse (<10 ps) generation from 1.3 μm laser diodes. *IEEE J. Quantum Electron.* **25**, 1417–1425 (1989)
101. O. Kjebon, R. Schatz, S. Lourudoss, S. Nilsson, B. Stalnacke, L. Backborn, 30 GHz direct modulation bandwidth in detuned loaded InGaAsP DBR lasers at 1.55 μm . *Electron. Lett.* **33**, 488–489 (1997)
102. L. Bach, W. Kaiser, J.P. Reithmaier, A. Forchel, T.W. Berg, B. Tromborg, Enhanced direct-modulated bandwidth of 37 GHz by a multi-section laser with a coupled cavity-injection-grating design. *Electron. Lett.* **39**, 1592–1593 (2003)
103. J.P. Reithmaier, W. Kaiser, L. Bach, A. Forchel, M. Gioannini, I. Montrosset, T.W. Berg, B. Tromborg, Modulation speed enhancement by coupling to higher order resonances: A road towards 40 GHz bandwidth lasers on InP, in *Conf. Indium Phosphide Relat. Mater. (IPRM'05)*, Glasgow, UK (2005), Techn. Digest, paper 05CH37633C
104. S. Bauer, O. Brox, M. Biletzke, J. Kreissl, M. Radziunas, B. Sartorius, H.J. Wünsche, Speed potential of active feedback lasers, in *Conf. Lasers Electro-Opt. (CLEO'03)*, Europe (2003), OSA Techn. Digest, p. 176
105. B. Sartorius, M. Möhrle, Mirror modulated lasers: a concept for high speed transmitters. *Electron. Lett.* **32**, 1781–1782 (1996)
106. M. Radziunas, A. Glitzky, U. Bandelow, M. Wolfram, U. Troppenz, J. Kreissl, W. Rehbein, Improving the modulation bandwidth in semiconductor lasers by passive feedback. *IEEE J. Sel. Top. Quantum Electron.* **13**, 136–142 (2007)
107. U. Troppenz, J. Kreissl, W. Rehbein, C. Bornholdt, T. Gaertner, M. Radziunas, A. Glitzky, U. Bandelow, M. Wolfram, 40 Gb/s directly modulated InGaAsP passive feedback DFB laser, in *Proc. 32nd Europ. Conf. Opt. Commun. (ECOC'06)*, Cannes, France (2006), paper Th4.5.5
108. U. Troppenz, J. Kreissl, M. Möhrle, C. Bornholdt, W. Rehbein, B. Sartorius, I. Woods, M. Schell, 40 Gbit/s directly modulated lasers: physics and application. *Proc. SPIE* **79530**, 79530F1 (2011). doi:[10.1117/12.876137](https://doi.org/10.1117/12.876137)
109. Y. Matsui, T. Pham, W.A. Ling, R. Schatz, G. Carey, H. Daghighian, T. Sudo, C. Roxlo, 55-GHz bandwidth short-cavity distributed reflector laser and its application to 112-Gb/s PAM-4, in *Opt. Fiber Commun. Conf. (OFC'16)*, Anaheim, CA, USA (2016), Techn. Digest, paper Th5B.4
110. Y.-J. Chiu, H.-F. Chou, V. Kaman, P. Abraham, J.E. Bowers, High extinction ratio and saturation power traveling-wave electroabsorption modulator. *IEEE Photonics Technol. Lett.* **14**, 792–794 (2002)
111. Y. Akage, K. Kawano, S. Oku, R. Iga, H. Okamoto, Y. Miyamoto, H. Takeuchi, Wide bandwidth of over 50 GHz traveling wave electrode electroabsorption modulator integrated DFB lasers. *Electron. Lett.* **37**, 299–300 (2001)
112. R. Lewén, S. Irmscher, U. Westergren, L. Thylén, U. Eriksson, Segmented transmission-line electroabsorption modulators. *J. Lightwave Technol.* **LT-2**, 172–179 (2002)
113. M. Shirai, H. Arimoto, K. Watanabe, A. Taike, K. Shinoda, J. Shimizu, H. Sato, T. Ido, T. Tsuchiya, M. Aoki, S. Tsuji, N. Sasada, S. Tada, M. Okayasu, 40 Gbit/s electroabsorption modulators with impedance controlled electrodes. *Electron. Lett.* **39**, 734–735 (2003)
114. R.G. Walker, High-speed semiconductor intensity modulators. *IEEE J. Quantum Electron.* **QE-7**, 654–667 (1991)

115. S.R. Sakamoto, A. Jackson, N. Dagli, Substrate removed GaAs/AlGaAs Mach-Zehnder electro-optic modulators for ultra wide bandwidth operation, in *Internat. Top. Meeting Microw. Photon.* (1999), pp. 13–16
116. L. Mörl, D. Hoffmann, K. Matzen, C. Bornholdt, G.G. Mekonnen, F. Reier, Traveling wave electrodes for 50 GHz operation of opto-electronic devices based on InP, in *Conf. Indium Phosphide Relat. Mater.* (IPRM'99), Davos, Switzerland (1999), Techn. Digest, paper WeA1-3
117. S. Akiyama, S. Hirose, T. Watanabe, M. Ueda, S. Sekiguchi, N. Morii, T. Yamamoto, A. Kuramata, H. Soda, Novel InP-based Mach-Zehnder modulator for 40 Gb/s integrated lightwave source, in *18th IEEE Internat. Semicond. Laser Conf.* (ISLC'02), Garmisch-Partenkirchen, Germany (2002), Conf. Digest, paper TuC1
118. K. Tsuzuki, H. Shibata, N. Kikuchi, M. Ishikawa, T. Yasui, H. Ishii, H. Yasaka, 10-Gbit/s, 200 km duobinary SMF transmission using a full C-band tunable DFB laser array co-packaged with InP Mach-Zehnder modulator, in *21st IEEE Int. Semicond. Laser Conf.* (ISLC'08), Sorrento, Italy (2008), Conf. Digest, paper MB6
119. F. Koyama, K. Iga, Frequency chirping in external modulators. *J. Lightwave Technol.* **6**(1), 87–93 (1988)
120. J. Kreissl, V. Vercesi, U. Troppenz, T. Gaertner, W. Wenisch, M. Schell, Up to 40 Gb/s directly modulated laser operating at low driving current: buried-heterostructure passive feedback laser (BH-PFL). *IEEE Photonics Technol. Lett.* **24**, 362–364 (2012)
121. S. Karar, Y. Gao, K.P. Zhong, J.H. Ke, J.C. Cartledge, Generation of DPSK signals using a directly modulated passive feedback laser, in *Proc. 38th Europ. Conf. Opt. Commun.* (ECOC'12), Amsterdam, The Netherlands (2012), paper Tu.4.A.1
122. D. Mahgerefteh, Y. Matsui, C. Liao, B. Johnson, D. Walker, X. Zheng, Z.F. Fan, K. McCallion, P. Tayebati, Error-free 250 km transmission in standard fibre using compact 10 Gbit/s chirp-managed directly modulated lasers (CML) at 1550 nm. *Electron. Lett.* **41**(9), 543–544 (2005)
123. D. Mahgerefteh, Y. Matsui, X. Zheng, K. McCallion, Chirp managed laser and applications. *IEEE J. Sel. Top. Quantum Electron.* **16**(5), 1126–1139 (2010)
124. A. Shen, G. Levaufre, A. Accard, J. Decobert, N. Lagay, J.-G. Provost, D. Make, G.-H. Duan, 50 km error free transmission of fully integrated chirp-managed 10 Gb/s directly modulated C-band tunable III–V/SOI hybrid lasers, in *Opt. Fiber Commun. Conf.* (OFC'16), Anaheim, CA, USA (2016), Techn. Digest, paper M2C.5
125. W. Jia, J. Xu, Z. Liu, K.-H. Tse, C.-K. Chan, Generation and transmission of 10-Gb/s RZ-DPSK signals using a directly modulated chirp-managed laser. *IEEE Photonics Technol. Lett.* **23**(3), 173–175 (2011)
126. W. Jia, Y. Matsui, D. Mahgerefteh, I. Lyubomirsky, C.-K. Chan, Generation and transmission of 10-Gbaud optical 3/4-RZ-DQPSK signals using a chirp-managed DBR laser. *J. Lightwave Technol.* **30**(21), 3299–3305 (2012)
127. W. Kobayashi, M. Arai, T. Fujisawa, T. Sato, T. Ito, K. Hasebe, S. Kanazawa, Y. Ueda, T. Yamanaka, H. Sanjoh, Novel approach for chirp and output power compensation applied to a 40-Gbit/s EADFB laser integrated with a short SOA. *Opt. Express* **23**(7), 9533–9542 (2015)
128. M. Theurer, G. Przyrembel, A. Sigmund, W.-D. Molzow, U. Troppenz, M. Möhrle, 56 Gb/s L-band InGaAlAs RW electroabsorption modulated laser with integrated SOA. *Phys. Status Solidi A* **213**(4), 970–974 (2016)
129. D. Erasme, T. Anfray, M.E. Chaibi, K. Kechaou, J. Petit, G. Aubin, K. Merghem, C. Kazmieriski, J.-G. Provost, P. Chanclou, C. Aupetit-Berthelemot, The dual-electroabsorption modulated laser, a flexible solution for amplified and dispersion uncompensated networks over standard fiber. *J. Lightwave Technol.* **32**(21), 4068–4078 (2014)
130. <https://standards.ieee.org/findstds/standard/802.3ba-2010.html>
131. M. Matsuda, A. Uetake, T. Simoyama, S. Okumura, K. Takabayashi, M. Ekawa, T. Yamamoto, Simultaneous 40-Gbps direct modulation of 1.3- μm wavelength AlGaInAs distributed-reflector laser arrays on semi-insulating InP substrate, in *Conf. Indium Phosphide Relat. Mater.* (IPRM'13), Kobe, Japan (2013), Techn Digest, paper TuD2-2

132. M. Matsuda, A. Uetake, T. Simoyama, S. Okumura, K. Takabayashi, M. Ekawa, T. Yamamoto, High-speed directly modulated distributed-reflector lasers, in *24th IEEE Int. Semicond. Laser Conf. (ISLC'14)*, Palma de Mallorca, Spain (2014), Conf. Digest, paper TUA.01
133. N. Nakamura, M. Shimada, G. Sakaino, T. Nagira, H. Yamaguchi, Y. Okunuki, A. Sugitatsu, M. Takemi, 25.8 Gbps direct modulation AlGaInAs DFB lasers of low power consumption and wide temperature range operation for data center, in *Opt. Fiber Commun. Conf. (OFC'15)*, Los Angeles, CA, USA (2015), Techn. Digest, paper W2A.53
134. K. Nakahara, Y. Wakayama, T. Kitatani, T. Taniguchi, T. Fukamachi, Y. Sakuma, S. Tanaka, Direct modulation at 56 and 50 Gb/s of 1.3 μm InGaAlAs ridge-shaped-BH DFB lasers. *IEEE Photonics Technol. Lett.* **27**(5), 534–536 (2015)
135. Y. Matsui, T. Pham, T. Sudo, G. Carey, B. Young, 112-Gb/s WDM link using two directly modulated Al-MQW BH DFB lasers at 56 Gb/s, in *Opt. Fiber Commun. Conf. (OFC'15)*, Los Angeles, CA, USA (2015), Techn. Digest, paper Th5B.6
136. M. Moehrle, H. Klein, C. Bornholdt, G. Przyrembel, A. Sigmund, W.-D. Molzow, U. Troppenz, H.-G. Bach, InGaAlAs RW-based electro-absorption-modulated DFB-lasers for high speed applications, in *Semicond. Lasers Laser Dynam. VI*, Brussels, Belgium. Proc. SPIE, vol. 9134 (2014), pp. 913419–913428. doi:[10.1117/12.2053772](https://doi.org/10.1117/12.2053772)
137. H. Klein, C. Bornholdt, G. Przyrembel, A. Sigmund, W.-D. Molzow, H.-G. Bach, M. Moehrle, 56 Gbit/s InGaAlAs-MQW 1300 nm electroabsorption-modulated DFB-lasers with impedance matching circuit, in *Proc. 39th Europ. Conf. Opt. Commun. (ECOC'13)*, London, UK (2013), paper Th.1.B.5
138. T. Fujisawa, K. Takahata, W. Kobayashi, T. Tadokoro, N. Fujiwara, S. Kanazawa, F. Kano, 1.3- μm , 50-Gbit/s EADFB lasers for 400 GbE, in *Opt. Fiber Commun. Conf. and Nat. Fiber Opt. Eng. Conf. (OFC/NFOEC'11)*, Los Angeles, CA, USA (2011), Techn. Digest, paper OWD4
139. S. Kanazawa, T. Fujisawa, N. Nunoya, A. Ohki, K. Takahata, H. Sanjoh, R. Iga, H. Ishii, Ultra-compact 100 GbE transmitter optical sub-assembly for 40-km SMF transmission. *J. Lightwave Technol.* **31**, 602–608 (2015)
140. S. Kanazawa, T. Fujisawa, K. Takahata, H. Sanjoh, R. Iga, Y. Ueda, W. Kobayashi, H. Ishii, 400-Gb/s operation of flip-chip interconnection EADFB laser array module, in *Opt. Fiber Commun. Conf. (OFC'15)*, Los Angeles, CA, USA (2015), Techn. Digest, paper T3I.1
141. B. Teipen, Considerations on baud rate and lane number for 400 Gigabit Ethernet optical interfaces. IEEE 802.3bs 400 Gb/s Ethernet Task Force, Interim Meeting, May 2014. http://www.ieee802.org/3/bs/public/14_05/teipen_3bs_01a_0514.pdf
142. T. Tanaka, T. Takahara, J.C. Rasmussen, Discrete multi-tone technology for 100G Ethernet (100GbE). IEEE P802.3bm 40 Gb/s and 100 Gb/s Fiber Optic Task Force, Interim Meeting, September 2012. http://www.ieee802.org/3/bm/public/sep12/tanaka_01_0912_optx.pdf
143. J. Lee, P. Dong, N. Kaneda, Y.-K. Chen, Discrete multi-tone transmission for short-reach optical connections, in *Opt. Fiber Commun. Conf. (OFC'16)*, Anaheim, CA, USA (2016), Techn. Digest, paper Th1G.1
144. T. Takahara, T. Tanaka, M. Nishihara, Z. Tao, L. Li, J.C. Rasmussen, Can discrete multi-tone reduce the cost for short reach systems? in *Opt. Fiber Commun. Conf. (OFC'15)*, Los Angeles, CA, USA (2015), Techn. Digest, paper W4H.5
145. T. Takahara, T. Tanaka, M. Nishihara, Y. Kai, L. Li, Z. Tao, J.C. Rasmussen, Discrete multi-tone for 100 Gb/s optical access networks, in *Opt. Fiber Commun. Conf. (OFC'14)*, San Francisco, CA, USA (2014), Techn. Digest, paper M2I.1
146. S. Bhoja, F. Chang, PAM modulation for 400G SMF. IEEE P802.3bm 400 Gb/s Ethernet Task Force, Interim Meeting, May 2014. http://www.ieee802.org/3/bs/public/14_05/bhoja_3bs_01_0514.pdf
147. W. Kobayashi, T. Fujisawa, S. Kanazawa, H. Sanjoh, 25 Gbaud/s 4-PAM (50 Gbit/s) modulation and 10 km SMF transmission with 1.3 μm InGaAlAs-based DML. *Electron. Lett.* **50**(4), 299–300 (2014)
148. U. Troppenz, M. Narodovitch, C. Kottke, G. Przyrembel, W.-D. Molzow, A. Sigmund, H.-G. Bach, M. Moehrle, 1.3 μm electroabsorption modulated lasers for PAM4/PAM8 single

- channel 100 Gb/s, in *Conf. Indium Phosphide Relat. Mater. (IPRM'14)*, Montpellier, France (2014), Techn. Digest, paper Th-B2-5
149. S. Kanazawa, T. Fujisawa, K. Takahata, T. Ito, Y. Ueda, W. Kobayashi, H. Ishii, H. Sanjoh, Flip-chip interconnection lumped-electrode EADFB laser for 100-Gb/s/ λ transmitter. *IEEE Photonics Technol. Lett.* **27**(16), 1699–1701 (2015)
 150. C. Caillaud, M.A. Mestre Adrover, F. Blache, F. Pommereau, J. Decobert, F. Jorge, P. Charbonnier, A. Konczykowska, J.-Y. Dupuy, H. Mardoyan, K. Mekhazni, J.-F. Paret, M. Faugeron, F. Mallecot, M. Achouche, Low cost 112 Gb/s InP DFB-EAM for PAM-4 2 km transmission, in *Proc. 41st Europ. Conf. Opt. Commun. (ECOC'15)*, Valencia, Spain (2015), paper PDP.1.5
 151. S. Kanazawa, T. Fujisawa, K. Takahata, Y. Nakanishi, H. Yamazaki, Y. Ueda, W. Kobayashi, Y. Muramoto, H. Ishii, H. Sanjoh, 56-Gbaud 4-PAM (112-Gbit/s) operation of flip-chip interconnection lumped-electrode EADFB laser module for equalizer-free transmission, in *Opt. Fiber Commun. Conf. (OFC'16)*, Anaheim, CA, USA (2016), Techn. Digest, paper W4J.1
 152. S. Kanazawa, H. Yamazaki, Y. Nakanishi, T. Fujisawa, K. Takahata, Y. Ueda, W. Kobayashi, Y. Muramoto, H. Ishii, H. Sanjoh, Transmission of 214-Gbit/s 4-PAM signal using an ultra-broadband lumped-electrode EADFB laser module, in *Opt. Fiber Commun. Conf. (OFC'16)*, Anaheim, CA, USA (2016), Techn. Digest, paper Th5B.3

Masahiro Aoki received the B.E., M.E., and Ph.D. degrees in physical electronics from the Tokyo Institute of Technology, Tokyo, Japan, in 1987, 1989, and 1999, respectively. In 1989, he joined the Central Research Laboratory, Hitachi, Ltd., Tokyo, Japan, where he has been engaged in the research, development and commercialization of semiconductor lasers and related monolithic/hybrid integrated components/modules for telecommunications/data communications, information, and industry applications. From 1999 to 2000, he was a Visiting Researcher at Heinrich-Hertz-Institute, Berlin, Germany, where he was engaged in the advanced monolithic integration of Indium Phosphide-based photonic ICs. Since 2006, he had been heading a Nano-Electronics R&D team and his interest extended to new materials and new functional devices such as organic electronics, power electronics, and Micro Electro Mechanical Systems (MEMS), and related sub-systems. Since 2013, he had been with the Center for Technology Innovation-Materials, Hitachi, Ltd. and his focus was extended to the field of functional materials and their applications. He is now heading the Center for Technology Innovation, Hitachi, Ltd., taking care of R&D for advanced social infrastructure, such as IT/ICT, energy, water, transportation and medical/healthcare.

Dr. Aoki is a member of the Japan Society of Applied Physics and the Institute of Electronics, Information and Communication Engineers (IEICE) of Japan. He received Best Paper Awards from the Third Optoelectronics Conference in 1990, the Second Optoelectronics and Communication Conference in 1997, and the Seventh Optoelectronics and Communication Conference in 2004. He also received the Scientific Encouragement Award in 1994, the Excellent Paper Award in 1995, and the Achievement Award in 2007, all from IEICE, the R&D100 Award in 1996, and the IPRM 10th Anniversary Paper Award in 1998 from the IEEE Lasers and Electro-Optics Society.

Ute Troppenz received the Ph.D. degree in physics from the Humboldt University in Berlin. She joined HHI in 1992 where, since 2000, she is working in the research field of InP based passive and active photonic components for telecommunication and THz systems. Her current research focus is the development of optical transmitters for Datacom application comprising the simulation, design and characterization work on laser components and modules. A particular emphasis is placed on high speed directly modulated lasers and electro-absorption modulated lasers for highest symbol rates and multi-level modulation formats.

Chapter 5

Widely Tunable Laser Diodes

Hélène Debrégeas

Abstract The chapter provides a comprehensive overview over widely tunable laser diodes and includes a description of the different tuning mechanisms and relevant implementations: sampled grating- and superstructure grating-DBR lasers, Y-lasers, multiple peak grating- and widely tunable filter lasers. The treatment covers fundamentals of the various solutions, typical performance characteristics and control issues as well. The focus is primarily on edge emitting semiconductor lasers, however, VCSELs and external cavity tunable lasers, integrated tunable laser-modulators, and tunable laser subsystems are also contained.

Widespread deployment of dense wavelength division multiplex (DWDM) systems calls for transmitter lasers that can emit with extreme accuracy at any WDM specific wavelength, as defined by the ITU (International Telecommunication Union) standardization body. Predominantly these wavelengths cover the whole C-band (1525–1565 nm), but will eventually extend over the L-band (1570–1610 nm) as well. A basic approach consists in using standard DFB lasers, the emission wavelength of which is determined by the Bragg grating pitch, fixed by fabrication. Any DFB laser can be slightly thermally tuned over a small range of typically 4 nm with 0.1 nm/°C tuning efficiency, thus covering a limited number of WDM transmission channels only. A largely superior and preferred solution is to employ widely tunable lasers which allow adjusting the laser wavelength to any ITU channel within the transmission bands. Such tunable laser devices are mandatory for a large range of applications today.

In long distance networks, tunable lasers are either used as spare source to replace any failing DFB laser, or as a universal source dramatically reducing maintenance and inventory management costs. Today, 50% of newly deployed long-distance transmitters comprise tunable lasers, and deployment is expected to reach 90% within the next 10 years.

Tunable lasers provide both flexibility and adaptability in long-distance and metropolitan networks. They represent a key element of Reconfigurable Optical

H. Debrégeas (✉)
III-V Lab, 1 Avenue Augustin Fresnel, 91767 Palaiseau, France
e-mail: helene.debregeas@3-5lab.fr

Add and Drop Multiplexers (ROADMs) – components that can extract or insert any wavelength to dynamically reconfigure wavelength allocation according to traffic evolution. They are used for all-optical routing without the need for optic – electronic – optic conversion, ensuring independence from protocols and bit rates. In packet switching transmission schemes they would allow for real-time network reconfiguration with packet granularity, demanding extremely fast wavelength tuning within the guard time of the optical packets (~ 100 ns).

In future WDM-based access networks, each end user may be equipped with a receiver configured for a specific wavelength. This wavelength can be used as an address to route traffic to the desired user. Tunable lasers are foreseen at the optical line terminal in order to rapidly tune the data for routing to the final users.

For all these applications, performance data similar to standard DFB lasers are required such as 13 dBm coupled output power, more than 40 dB side-mode suppression ratio (SMSR), low noise, linewidths below 5 MHz, wavelength accuracy compliant with the ITU standard, and others. In addition, however, they must be capable of wavelength tuning over the whole 40 nm C-band (48 channels, 100 GHz spaced), and in coming years over the full C + L band (1525–1610 nm). For real mass deployment in DWDM systems, the cost premium compared to fixed wavelength lasers has to remain below 20% which imposes the following general design requirements:

- To reach high industrial production yield, the tuning mechanism must be based on robust, fabrication tolerant processes.
- Power, wavelength and SMSR feedback loops must be simple enough to ensure fast characterization and reliable servo-control algorithms.

Monolithic integration can be advantageous for avoiding costly alignment procedures and multiple bulky mechanical elements. In particular, for metro and access applications the laser must fit into a TOSA type module (Transmitter Optical Sub-Assembly) that is compatible with low-cost e-XFP modules (extended eXtra Flat Packaging). Last but not least, the possibility to integrate additional functionalities like external modulation, variable optical attenuation, optical gating, and fast tuning capability are important assets too. They enable compatibility with different network configurations and reductions in system costs.

Tunable lasers have been studied for several decades, leading to a wide variety of technology solutions based on thermal, mechanical, and current injection tuning mechanisms [1]. Several types of devices are commercially available now while research strongly continues to further improve performance, increase functionalities, and reduce costs.

Tunable lasers based on current injection tuning allow for monolithic integration with additional functionalities, including fast tuning. Derived from Distributed Bragg Reflector lasers (DBR), solutions incorporating several gratings with multiple peak reflections can provide more than 40 nm wavelength tuning and are widely used in today's networks. Yet, control complexity remains the main drawback, and many studies have been dedicated to propose simpler tuning methods and robust

feedback algorithms. Recently, photonic integration has even led to the demonstration of complete sub-systems monolithically integrated on InP that comprise tunable lasers, modulators, photodiodes, and optical amplifiers (see Sect. 5.5).

Other approaches rely on the selection of a laser from an array of thermally tuned lasers or use an external cavity with a moveable Bragg grating. These device structures are, however, not fully integrable in semiconductor technology, and they are not suited for fast tuning or integrated modulation. Nonetheless, as they are based on robust technologies and use simple control mechanisms, they may be commercially competitive with applications requiring less sophisticated laser functions.

5.1 Basics of Current Injection Tuning, DBR Lasers

5.1.1 Current Injection Tuning Mechanisms

All tunable laser structures relying on current injection integrate a section with a p-i-n junction containing an intrinsic layer made of quaternary passive material (typically InGaAsP with 1450 nm photoluminescence wavelength, in the following referred to as Q1.45). Under carrier injection, the non-equilibrium excess carrier concentration creates variations of the index of refraction in this quaternary material via three main mechanisms: free-carrier absorption, band filling, and band gap shrinkage [2]. Physically, these effects are the consequence of a modification of material absorption $\alpha(E)$ over the whole spectrum which can be linked via the Kramers-Krönig relation to the index variation at the operating energy E_0 :

$$\Delta n(E_0) = \frac{\hbar c}{\pi} \text{Princ} \int_0^\infty \frac{\Delta \alpha(E)}{E^2 - E_0^2} dE \quad (5.1)$$

where Princ means principal value of the integral. The effects are represented schematically in Fig. 5.1 and detailed below.

Free Carrier Absorption This intra-band mechanism illustrated in Fig. 5.1(a) corresponds to the absorption of a photon by a free carrier (electron or hole), raising its energy within the conduction (or valence) band. Conservation of the wavevector k is ensured by the interaction with a phonon or an impurity. This absorption at very low energies implies a free-carrier related decrease of the refractive index given by [2]:

$$\Delta n_{fc} = -\frac{e^2 \lambda^2}{8\pi^2 c^2 \varepsilon_0 n} \left(\frac{N}{m_e} + \frac{P}{\frac{m_{hh}^{3/2} + m_{lh}^{3/2}}{m_{hh}^{1/2} + m_{lh}^{1/2}}} \right) \quad (5.2)$$

with n denoting the effective refractive index, m_e , m_{hh} and m_{lh} the effective masses of electrons, heavy and light holes, respectively, P the hole density, and N the electron density, and ε_0 the permittivity of free space. As $m_e \ll m_{lh, hh}$, the effect is dominated by electron absorption in the conduction band.

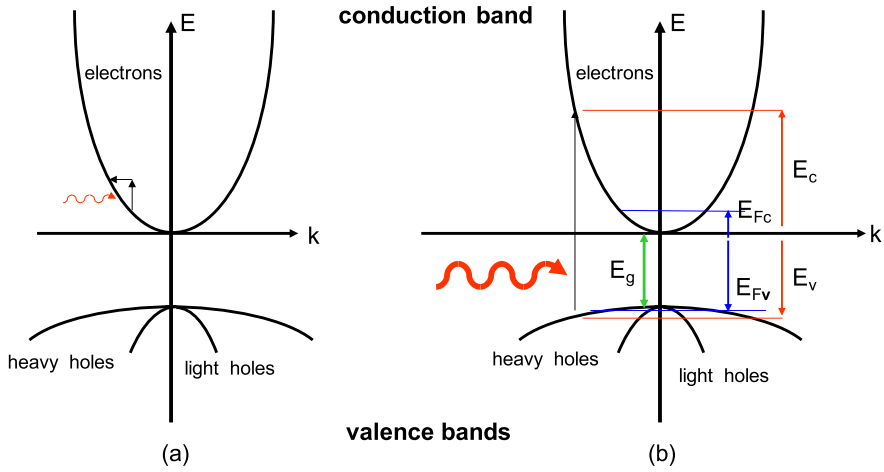


Fig. 5.1 Schematic representation of the different types of absorption relevant under current tuning (a) intra-band free-carrier absorption, (b) inter-band absorption (E = carrier energy; indices c and v refer to the conduction and valence band, respectively, and E_{Fc} and E_{Fv} represent the Fermi level of the conduction and valence bands, respectively)

Band-filling Assuming a parabolic approximation for the band diagram and using the notations of Fig. 5.1(b), absorption without carrier injection $\alpha(E)$ at an energy E close to the band gap, E_g , is given by [2]:

$$\alpha(E) = \frac{C}{E} \sqrt{E - E_g} \quad \text{if } E \geq E_g \quad \text{and} \quad \alpha(E) = 0 \quad \text{otherwise} \quad (5.3)$$

where C is a material dependent constant (given in $\text{cm}^{-1} \text{eV}^{1/2}$).

Under current injection electrons and holes fill conduction and valence band states at low energy levels (Fig. 5.2(a)). Now photon absorption at energy E , with electron transfer occurring from the valence band energy E_v to the conduction band energy E_c , is possible only if firstly $E = E_v + E_c$, and secondly if level E_v is occupied and level E_c vacant. Then (5.3) must be expanded to take into account the occupation probability of either energy state:

$$\alpha(E) = \frac{C}{E} \sqrt{E - E_g} [f_v(E_v) - f_c(E_c)] \quad \text{if } E \geq E_g, \quad (5.4)$$

$$\alpha(E) = 0 \quad \text{otherwise}$$

Here $f_v(E_v)$ and $f_c(E_c)$ indicate the probability that valence band level E_v and conduction band level E_c , respectively, are occupied by an electron. They are expressed by Fermi-Dirac distributions:

$$f_c(E_c) = \frac{1}{1 + e^{(E_c - E_{Fc})/kT}}, \quad f_v(E_v) = \frac{1}{1 + e^{(E_v - E_{Fv})/kT}} \quad (5.5)$$

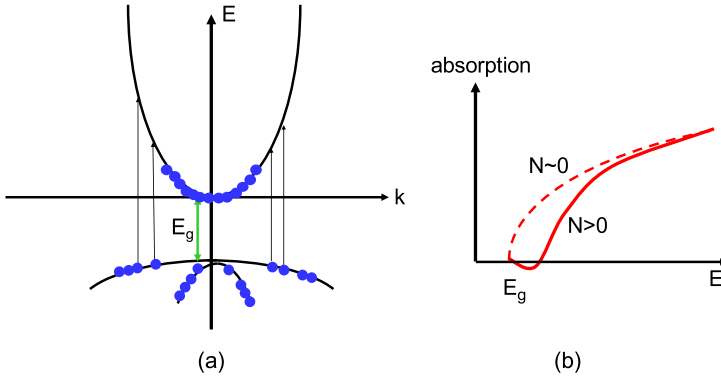


Fig. 5.2 Illustration of band-filling: (a) band diagram under current injection, and (b) impact on absorption spectrum. $N \sim 0$ and $N > 0$ correspond to the case without and with current injection, respectively

where E_{Fc} and E_{Fv} represent the Fermi levels in the conduction and valence band. Under carrier injection, the energy values of the Fermi quasi-levels tend to increase. For energies E slightly larger than E_g , $f_c(E_c)$ becomes non-zero and $f_v(E_v)$ becomes lower than unity. Absorption is no longer possible, and injected carriers can even create gain by stimulated emission as shown in Fig. 5.2(b) (negative absorption).

Band Gap Shrinkage Injected carriers occupy bands of lower energy levels, and their wavefunctions overlap. They repel each other (electrons–electrons, and holes–holes) due to Coulomb forces and for statistical reasons when their spins are identical. These repulsions screen the electric field built in the semiconductor crystal network, and as a consequence the band gap energy E_g is reduced. An approximate model gives [2]:

$$\Delta E_g = -\frac{e}{2\pi\epsilon_0\epsilon}\left(\frac{3N}{\pi}\right)^{1/3} \quad (5.6)$$

where ϵ represents the dielectric constant of the semiconductor material.

Cumulative Impact on Refractive Index Variation The index variation due to carrier injection corresponds to the sum of the three effects. Simulations of index variation as a function of wavelength are presented in Fig. 5.3 for a bulk layer of Q1.45 composition. For the data shown in Fig. 5.3 the factor C in (5.3), which determines the absorption coefficient, has been extrapolated from experimental values [3] to be $2.82 \times 10^4 \text{ cm}^{-1} \text{ eV}^{1/2}$. Band diagrams are derived from effective electron and hole masses [4] ($m_e = 0.065 m_0$, $m_{hh} = 0.49 m_0$ and $m_{lh} = 0.07 m_0$, with $m_0 = 9.1095 \times 10^{-31} \text{ kg}$ being the free electron mass), the refractive index n is 3.49, and the dielectric constant ϵ is 13.8.

Band-filling and band gap renormalization result in a modification of the absorption behavior close to the band gap energy. Due to the denominator $E^2 - E_0^2$

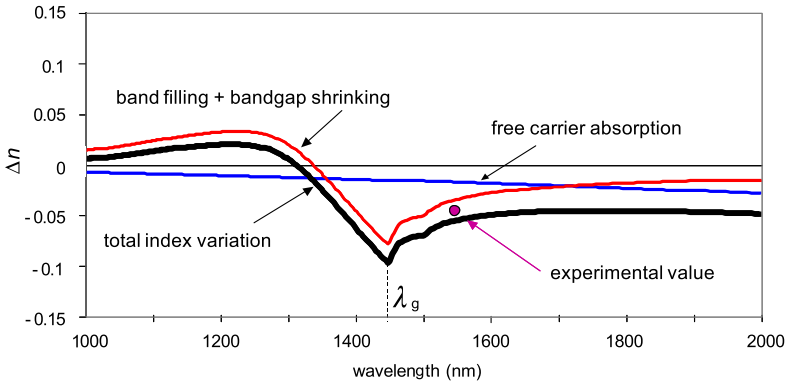


Fig. 5.3 Index variation calculated as a function of wavelength for $\text{Ga}_{0.35}\text{In}_{0.75}\text{As}_{0.74}\text{P}_{0.26}$ (Q1.45) at $N = 3 \times 10^{18} \text{ cm}^{-3}$. An experimental value at 1550 nm is indicated by the dot and λ_g represents the bandgap equivalent wavelength

in the Kramers-Krönig relation (see (5.1)), they generate a maximum index variation around E_g . On the contrary, the free-carrier plasma leads to an increase of absorption at energies much smaller than the band gap energy: the impact on index variation around wavelengths corresponding to the band gap is very weakly dependent on energy. At a typical operation wavelength of 1550 nm free carrier absorption accounts approximately for one third of the overall index variation, and band filling and band gap shrinkage for two thirds. A typical experimental value at 1550 nm is $\Delta n \sim -0.05$, plotted in Fig. 5.3 for comparison.

5.1.2 DBR Lasers: Principle of Operation

DBR Cavity and Mode Selection Exploiting index variation under carrier injection, the first current injection tunable laser was the DBR laser, proposed in the 1970's and subsequently optimized by many laboratories [5–7]. A typical DBR laser, as shown in Fig. 5.4, comprises three different monolithically integrated sections each controlled by separate currents: one active and two passive sections, the

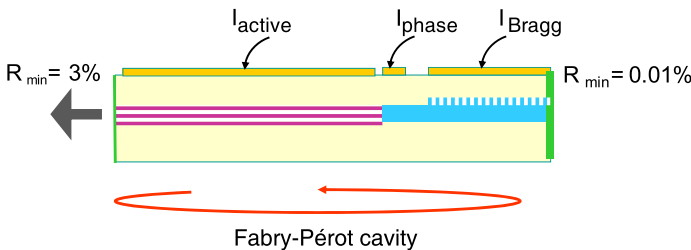
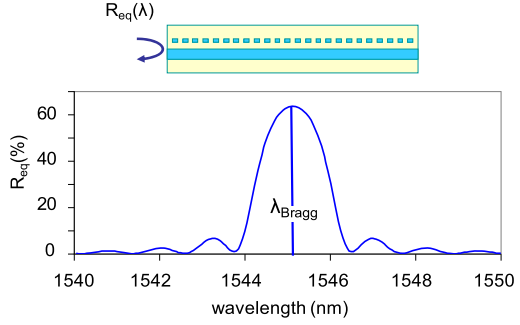


Fig. 5.4 Schematic cross-section of a DBR laser

Fig. 5.5 Equivalent reflectivity R_{eq} of a Bragg grating as a function of wavelength ($\kappa = 40 \text{ cm}^{-1}$, $L = 300 \mu\text{m}$, loss = 15 cm^{-1})



latter called Bragg and phase section, respectively. The rear facet is antireflection coated and the front facet provides low reflectivity ($\sim 3\%$) to create a Fabry-Pérot (FP) cavity between the front facet and the mirror formed by the Bragg section. The active section has a Multi Quantum Well (MQW) vertical structure. Injecting the current I_{active} gives rise to gain around 1550 nm and generates an FP comb.

The Bragg section is made of bulk Q1.45 material and contains a Bragg grating. This section acts as a wavelength selective mirror with maximum reflectivity at the Bragg wavelength λ_{Bragg} given by

$$\lambda_{Bragg} = 2n_{eff} \Lambda \quad (5.7)$$

where n_{eff} is the effective waveguide index of the Bragg section and Λ the grating pitch. For $\sim 1550 \text{ nm}$ emission, n_{eff} values are typically 3.2, which yields a pitch of around $0.24 \mu\text{m}$. The reflection bandwidth and its maximum value are closely related to the length of the grating and to the coupling coefficient κ , defined as the grating reflectivity per unit length and expressed in cm^{-1} . For a rectangular grating it is given by:

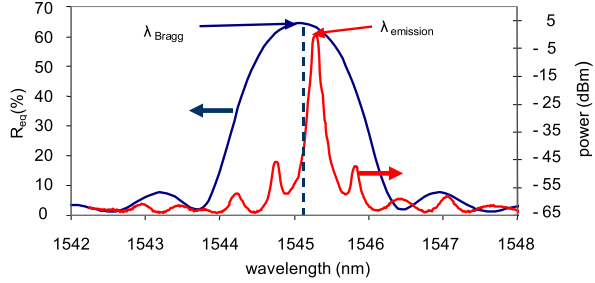
$$\kappa = \frac{2\Delta n_{eff}}{\lambda} \quad (5.8)$$

where Δn_{eff} represents the effective index difference between the mark and space regions of the grating. Figure 5.5 shows the calculated equivalent reflectivity spectrum for a $300 \mu\text{m}$ long Bragg grating, assuming $\kappa = 40 \text{ cm}^{-1}$ and 15 cm^{-1} material loss.

We define an effective penetration length, L_{eff} , into the Bragg grating corresponding to the penetration distance at which the optical power is decreased by a factor e . For high κ values L_{eff} is equal to $1/(2\kappa)$. A laser cavity of length $L_{cavity} = L_a + L_{ph} + L_{eff}$ generates a comb of FP modes separated by a Free Spectral Range (FSR) according to:

$$FSR = \frac{\lambda^2}{2n_g L_{cavity}} \quad (5.9)$$

Fig. 5.6 FP mode selection by a Bragg grating



Here n_g indicates the group index that takes into account the wavelength dependent dispersion of n_{eff} :

$$n_g = n_{eff}(\lambda) - \lambda \left. \frac{dn_{eff}}{d\lambda} \right|_{\lambda} \quad (5.10)$$

The Bragg filter selects the FP mode nearest to λ_{Bragg} that benefits from lowest cavity losses, and as a result monomode emission occurs at $\lambda_{emission}$ (Fig. 5.6).

DBR Coarse Tuning with Bragg Section In a DFB laser the Bragg grating is inside the active section. Above threshold, injected carriers are almost totally consumed by stimulated photon emission so that the carrier density is clamped. Therefore the effective index cannot be varied through the carrier related effect anymore, and the only index variation occurs via heating due to current injection, typically leading to a maximum 3 to 4 nm tuning range. The possibility to tune λ_{Bragg} is specific to DBR lasers. As the Bragg section is made of passive material and separated from the gain section, the carrier density is no longer clamped. When injecting a current I_{Bragg} , the carrier density increases and the effective index n_{eff} is reduced via the processes presented in Sect. 5.1.1. This gives rise to a decrease of λ_{Bragg} with a relationship derived from (5.7):

$$\Delta\lambda_{Bragg} = 2\Delta n_{eff} \Lambda \quad (5.11)$$

Maximal achievable n_{eff} variation by current injection is in the range of 4×10^{-2} , allowing up to 16 nm tuning. When the Bragg filter is tuned by I_{Bragg} , FP modes are successively selected, but this selection leads to tuning characteristics which exhibit mode hops (Fig. 5.7). Apart from those mode hops the SMSR remains higher than 40 dB, corresponding to the case where adjacent FP modes are situated on both sides of the Bragg reflectivity spectrum.

DBR Fine Tuning with Phase Section The FP modes in the DBR cavity are defined by the phase condition

$$2(n_{eff,a}L_a + n_{eff,ph}L_{ph} + n_{eff,B}L_{eff}) = m\lambda, \quad m \in \mathbb{N} \quad (5.12)$$

where $n_{eff,a}$, $n_{eff,ph}$ and $n_{eff,B}$ are the effective indices in the active, phase, and Bragg section, respectively. When a current I_{ph} is injected into the passive phase section,

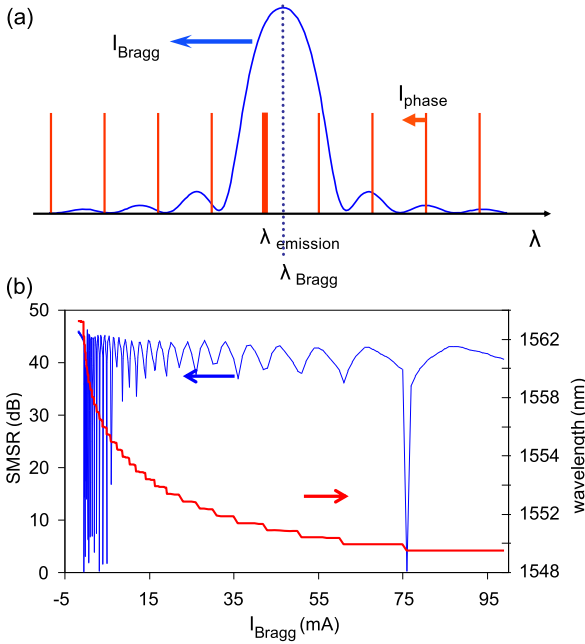


Fig. 5.7 (a) DBR tuning mechanism, where FP modes are successively selected with decreasing wavelength by injecting current I_{Bragg} , (b) example of experimental tuning characteristics illustrating emission wavelength and SMSR as a function of I_{Bragg}

$n_{\text{eff},ph}$ decreases due to the same mechanisms as in the Bragg section. By taking the derivative of (5.12) we obtain:

$$\frac{\Delta\lambda_{FP}}{\lambda} = \frac{\Delta n_{\text{eff},ph} L_{ph}}{n_{g,a} L_a + n_{g,ph} L_{ph} + n_{g,B} L_{\text{eff}}} \quad (5.13)$$

with $n_{g,a}$, $n_{g,ph}$ and $n_{g,B}$ denoting the group indices of the three sections. The FP comb can be continuously shifted to lower wavelengths as illustrated in Fig. 5.7, and the position of the mode hops in the DBR tuning curve can be finely adjusted along the tuning curve. In this way, emission at any wavelength λ in the tuning range can be achieved with high accuracy and high SMSR by adjusting I_{Bragg} in order to align λ_{Bragg} with λ , and I_{ph} to align an FP mode with λ .

Overall DBR Performance The design of a DBR laser requires multiple compromises in order to simultaneously reach a wide tuning range, high output power, and high SMSR. The tuning range, given by (5.11), can be rewritten as:

$$\Delta\lambda_{\text{Bragg}} = 2\Gamma_Q \frac{dn_Q}{dN} \Delta N \Lambda \quad (5.14)$$

where Γ_Q is the mode's optical confinement factor in the undoped quaternary Q1.45 waveguide material of the Bragg section into which carriers are injected, dn_Q/dN

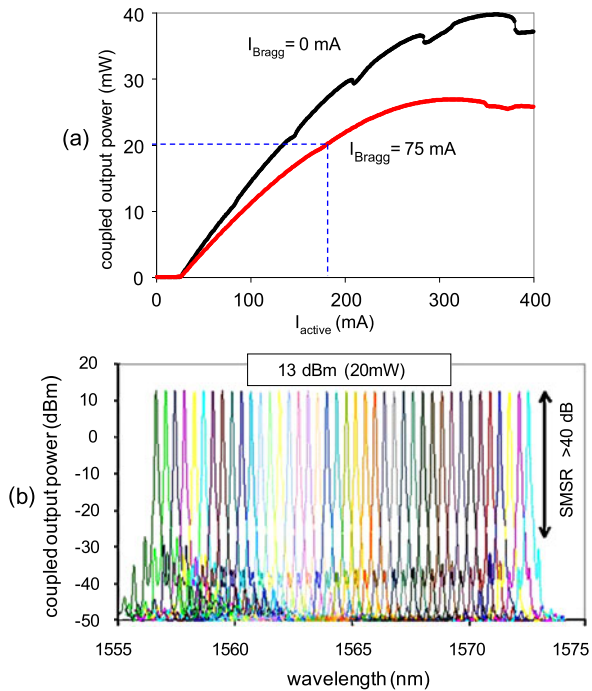
is the quaternary index variation with changing carrier density (negative value), and ΔN represents the increase of carrier density with current injection. In order to maximize the tuning range, one aims at achieving:

- high Γ_Q by using a thick bulk quaternary guiding layer
- large dn_Q/dN by using a quaternary material in the Bragg section which has a band gap wavelength close to the emission wavelength where the band filling effect is particularly pronounced (Fig. 5.3)
- high ΔN by reducing current leakage and by reducing the Bragg section length to limit radiative recombination through amplified spontaneous emission

In order to reach high output power the following targets must be reached at the same time:

- maintaining a high mode overlap between active and passive sections
- using a quaternary material in the Bragg section with a band gap wavelength sufficiently shorter than the emission wavelength so that absorption at low I_{Bragg} or carrier consumption at high I_{Bragg} by stimulated emission is limited
- increasing fiber coupling efficiency via a spot-size converter in the active section
- maximizing κ in the Bragg section to ensure high Bragg mirror reflectivity while keeping mode selectivity sufficiently high
- optimizing the length of the active section regarding the trade-off between a long section ensuring low current threshold density and low thermal effects, and a

Fig. 5.8 (a) Coupled output power versus I_{active} for minimum (0 mA) and maximum (75 mA) I_{Bragg} values, (b) superimposed spectra, each at well adjusted current conditions, for I_{active} , I_{phase} and I_{Bragg} , covering a tuning range of 16 nm with 20 mW constant coupled output power and more than 40 dB SMSR



moderate section length to retain a sufficiently high FSR for efficient Bragg mirror selectivity.

Typical optimized parameters are

- for the passive sections: 0.42 μm thick Q1.45 material providing $\Gamma_Q \sim 75\%$, with $\kappa \sim 45 \text{ cm}^{-1}$, $L_{\text{Bragg}} \sim 300 \mu\text{m}$, and $L_{\text{ph}} \sim 50 \mu\text{m}$
- for the active section: six 8 nm thick Q1.55 quantum wells with Q1.18 barriers sandwiched between two 100 nm thick Q1.18 confinement heterostructures, providing 96% overlap between active and passive section modes.

Such DBR lasers can emit at any ITU channel over a 16 nm tuning range with SMSR > 40 dB and 20 mW of constant coupled output power, as illustrated in Fig. 5.8 [7]. The output power decreases with increasing I_{ph} or I_{Bragg} (Fig. 5.8(a)) because of free carrier absorption, but constant output power can be ensured by adjusting I_{active} for each channel (see Fig. 5.8(b)).

5.2 Widely Tunable Lasers by Current Injection

DBR lasers represent basic current-injection-tunable laser devices that exploit a rather simple operation principle relying on the selection of an FP mode with a tunable filter and fine wavelength adjustment by means of a phase section. Their tunability, directly correlated to the limited achievable effective index variation, is limited to around 16 nm, that is nearly half of the C band. To further increase the tuning range and in particular to cover the whole 40 nm C-band with a monolithic device involving current injection, several approaches have been proposed by different laboratories. Basically, these are utilizing the same principle as DBR lasers, but the Bragg section is replaced by two independently controlled passive sections designed with more complex Bragg gratings. The wavelength tunable selective mirror is the result of the interaction between these two section gratings, thereby widely enhancing the tuning range.

5.2.1 Sampled Gratings

The most widely used grating design for such devices is the Sampled Grating (SG), illustrated in Fig. 5.9. As explained in detail in [8], it consists in a grating with periodically sampled pitch Λ , leading to grating burst lengths Z_G at a sampling period Z_S . The resulting reflectivity spectrum is the convolution of the reflectivity of an equivalent Bragg grating with pitch Λ and the reflectivity of a periodic square function of length Z_G and period Z_S . As a consequence, the reflectivity spectrum shows several reflectivity peaks, centered at $\lambda_{\text{Bragg}} = 2n_{\text{eff}}\Lambda$ and separated by:

$$\Delta\lambda = \lambda^2/2n_g Z_S \quad (5.15)$$

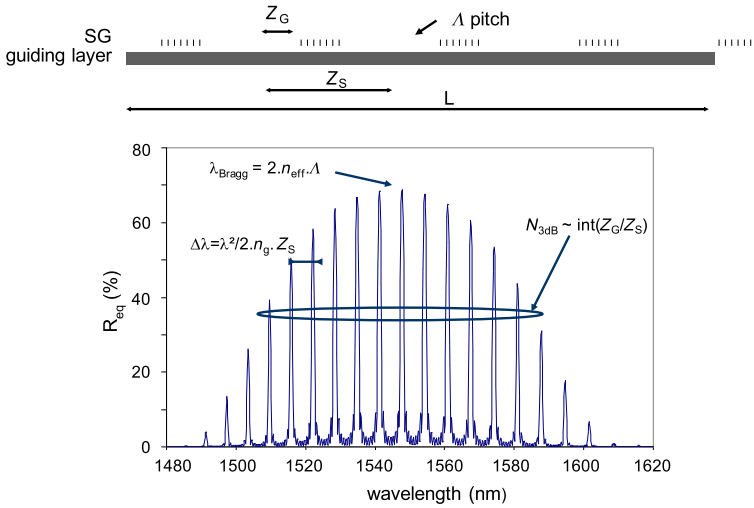


Fig. 5.9 Sampled grating scheme and calculated reflectivity spectrum ($L = 580 \mu\text{m}$, $Z_S = 58 \mu\text{m}$, $Z_G = 6 \mu\text{m}$, $\kappa = 300 \text{ cm}^{-1}$, losses = 15 cm^{-1})

Each reflectivity peak number n ($n = 0$ corresponds to the central peak) is equivalent to the reflectivity of an unsampled Bragg grating with SG length L , but with a coupling coefficient $\kappa(n)$ given by:

$$\kappa(n) = \kappa_0 \frac{Z_G}{Z_S} \frac{\sin(\pi n Z_G / Z_S)}{\pi n Z_G / Z_S} \exp\left(\frac{-i\pi n Z_G}{Z_S}\right) \quad (5.16)$$

Thus the peaks are not phase-matched, and they correspond to a smaller coupling coefficient than that of the central peak which is given by $\kappa(0) = \kappa_0 Z_G / Z_S$. The envelope of the reflectivity peaks widens when the duty cycle Z_G / Z_S is reduced, and the number of peaks in the 3 dB envelope can be approximated by:

$$N_{3\text{dB}} = \text{int}\left(\frac{Z_G}{Z_S}\right) \quad (5.17)$$

To obtain a large number of peaks, the duty cycle must be reduced which necessitates a higher κ_0 in order to retain a sufficiently large $\kappa(n)$ -value for the required reflectivities. Such SGs typically use κ_0 as high as 300 cm^{-1} , with a 10% Z_G / Z_S duty cycle.

5.2.2 SG-DBR Lasers

The first device incorporating dual passive grating sections is the SG-DBR structure, initially developed at the University of California at Santa Barbara [8]. It is composed of an active section and an adjacent phase section, sandwiched between

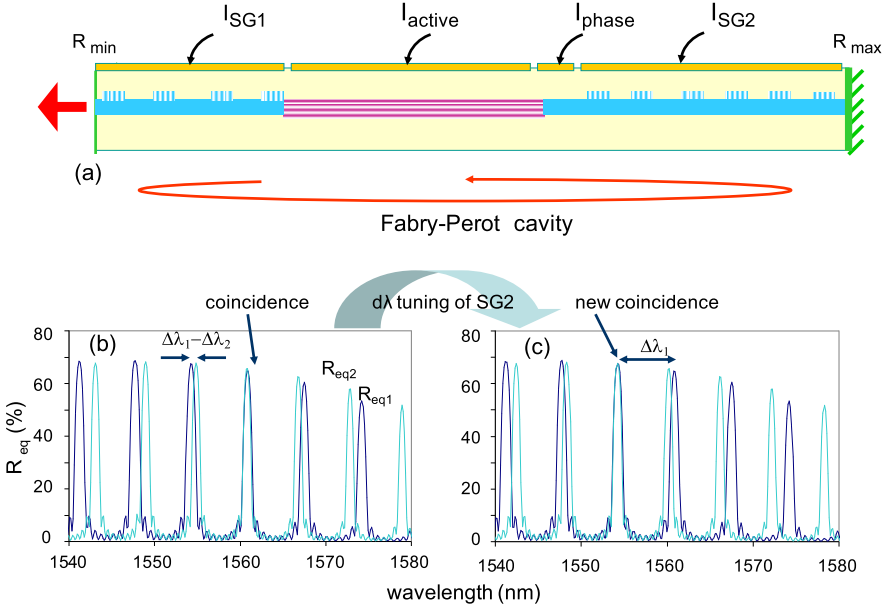


Fig. 5.10 SG-DBR laser structure: (a) schematic cross-section, (b, c) superimposed SG spectra providing Vernier effect

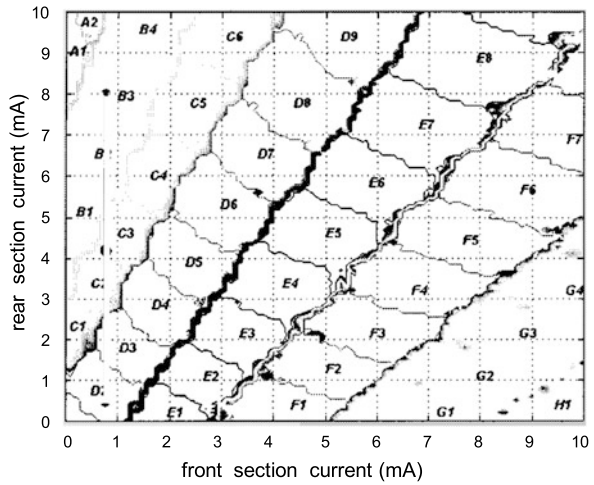
two SGs (Fig. 5.10(a)). The laser cavity itself is delimited by the two SGs: the reflectivity for the FP modes is given by the multiplication of the two SG reflectivities. Both SGs have the same pitch Λ , but their sampling periods Z_{S1} and Z_{S2} are slightly different, thus generating different spacings, $\Delta\lambda_1$ and $\Delta\lambda_2$, between the respective reflectivity peaks. By an appropriate choice of Z_{S1} and Z_{S2} one can ensure that only two peaks are in coincidence between the two zeros of the spectrum envelope. This coincidence leads to a higher reflectivity for the specific FP modes and selects the lasing mode (Fig. 5.10(b)).

By injecting current for example into SG₂ corresponding to the smaller $\Delta\lambda$, the associated reflectivity comb shifts to lower wavelengths by $\delta\lambda = \lambda \Delta n_{eff2} / n_g$ according to (5.11). When $\delta\lambda$ reaches $\Delta\lambda_1 - \Delta\lambda_2$, the coincidence shifts to adjacent peaks to the left-side. Tuning one SG by $\delta\lambda = \Delta\lambda_1 - \Delta\lambda_2$ thus generates a shift of the maximum reflectivity by $\Delta\lambda_1$. This behavior is called Vernier effect and leads to a tuning enhancement given by:

$$F = \frac{\Delta\lambda_1}{\Delta\lambda_1 - \Delta\lambda_2} \tag{5.18}$$

By applying the same current density simultaneously to both SGs, the two reflectivity spectra shift equally. Coincidence can be kept on the same peaks, simply tuned by $\delta\lambda = \lambda \Delta n_{eff1,2} / n_g$, all wavelengths within the reflections' envelope can be reached by an appropriate coincidence.

Fig. 5.11 Two-dimensional tuning map of an SG-DBR laser (after [9])



Sampled grating DBR lasers are hence characterized by two-dimensional tuning curves $\lambda = f(I_{SG1}, I_{SG2})$ as illustrated in Fig. 5.11. If the currents in the front and rear sampled grating areas (I_{SG1} and I_{SG2} , respectively) are changed essentially in the same way (corresponding to a movement along a $+45^\circ$ diagonal in Fig. 5.11), SG coincidences remain the same and hops occur between FP cavity modes, designated by a number. On the other hand, if the current of only one of the sampled gratings is changed (I_{SG1} or I_{SG2}), “super-mode hops” occur, due to a change of SG coincidences (corresponding to a horizontal or vertical movement in Fig. 5.11). Different super-modes are designated by different capital letters.

In order to precisely reach any ITU channel, currents are injected into SG_1 and SG_2 to position the emission wavelength in the middle of a mode-hop free area of the 2D tuning curves. Subsequently the FP wavelength is finely tuned by current injection into the phase section. SG-DBR type tunable lasers demand a precise design in order to simultaneously guarantee stable modal behavior, high SMSR, and a 40 nm tuning range required for covering the whole C-band. To ensure full coverage, the reflection peak spacings $\Delta\lambda_{1,2}$ are typically chosen to be around 5 nm, leading to SG periods $Z_{S1,2}$ of some 60 μm . The overall tuning range is limited by the wavelength spacing between two coincidences, which is given by the enhancement factor F multiplied by the spacing difference $\Delta\lambda_1 - \Delta\lambda_2$ between the SG reflectivity peaks. To reach 40 nm, this difference must be kept very small, entailing each reflectivity peak to be extremely narrow in order to avoid SMSR degradation by adjacent channels. This design requirement leads to quite extended SG sections with lengths of around 600 μm and many grating bursts (about 10). Such an optimized design is presented in [10]. There a front grating was applied comprising $10 \times 6 \mu\text{m}$ bursts and a 58 μm long sampling period, a rear grating with $11 \times 6 \mu\text{m}$ bursts and a 64 μm long sampling period, and a κ of 300 cm^{-1} . Such a device provides a tuning enhancement factor F of 10, and 50 nm tuning range with SMSR $> 35 \text{ dB}$.

With the laser light being emitted through the front SG, a Semiconductor Optical Amplifier (SOA) structure (see also Chap. 3) can be inserted between that SG section and the front facet as a booster to enhance the output power. The emitted light is amplified by a single pass through the SOA, while the FP cavity is kept unaffected. Given a typical SOA gain of 15 dB, an input power of 1 mW into the SOA is sufficient to achieve more than 20 mW of optical output power from the laser. Under these conditions, the SOA is operated in the saturation regime: the carrier density in the SOA is low, leading to reduced amplified spontaneous emission and high signal-to-noise ratio. A tilted output and a high quality 10^{-4} antireflection coating are necessary to avoid creating any parasitic cavity between the output facet and the Bragg section, and to ensure a low noise level [10, 11].

5.2.3 SSG-DBR Lasers

The overall envelope of the reflectivity peaks represents one of the limitations of SG-DBRs, as it reduces reflectivity far from the central wavelength. To overcome this restriction, it was proposed to replace one or both SGs by more complex gratings, so-called Super-Structure Gratings (SSG), that consist of periodically repeated gratings with varying pitch (Fig. 5.12). Numerically calculated optimal pitch variations within one period can generate a reflection spectrum with a square envelope [12]. As an example, a device has been designed with a rear SSG to provide uniform reflectivity peaks, and a short front SG to minimize free carrier absorption of the emitted light. In this way more than 18 mW of output power and 40 dB SMSR over a 30 nm tuning range have been achieved. Even more than 45 mW could be obtained with an integrated booster SOA [13].

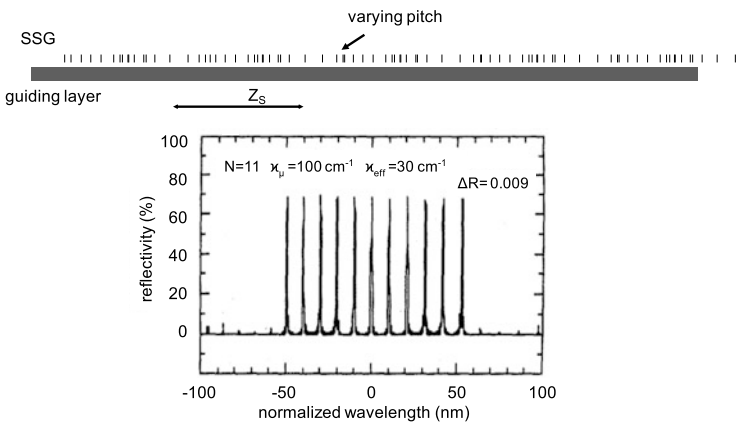
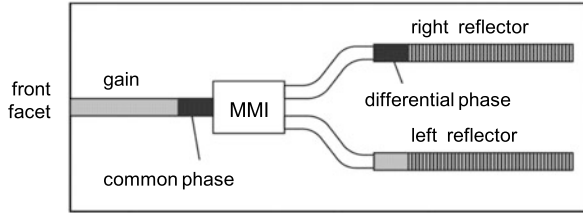


Fig. 5.12 Super-structure grating scheme and calculated reflectivity spectrum for optimum grating pitch variations [12]

Fig. 5.13 Schematic structure of a Y-laser (after [14])



5.2.4 Y-Lasers

Another approach very close to the SG-DBR variant consists in using a Y-coupler in order to place the two SGs parallel on the same side of the active section (Fig. 5.13) rather than on either side of the active gain section. Likewise, the Vernier effect is exploited to reach 40 nm tuning, but contrary to SG-DBR lasers, the reflectivity for the FP modes is given by the vector sum of the SG reflectivities, instead of multiplication. Waveguides need to be carefully designed in order to adjust the differential phase between both SGs and to get opposite phase conditions between competing adjacent channels, and to improve super-mode selection. Such a device can deliver an output power of more than 10 mW with more than 40 dB SMSR over a 40 nm tuning range [14, 15].

5.2.5 Multiple Peak Grating and Tunable Wide Filter Lasers (GCSR, DS-DBR)

There are other sophisticated solutions that use an active and a phase section sandwiched between a multiple peak grating (SG or SSG) and a tunable wide filter section. Instead of making use of the Vernier effect, the wide filter simply selects one of the reflectivity peaks. The first example of this kind was the Grating-assisted Codirectional coupled Sampled grating Reflector (GCSR) laser [16]. The filter is formed by a vertical coupler composed of two waveguides with a long-period grating. The tunability is given by:

$$\Delta\lambda = \lambda \frac{\Delta n_1}{n_{g1} - n_{g2}} \quad (5.19)$$

where Δn_1 represents the refractive index change of the upper waveguide due to current injection, and n_{g1}, n_{g2} the group indices of the upper and lower waveguide, respectively. Using an optimized coupler design and a specially tailored reflector grating, wavelength tuning over 32 nm was demonstrated, along with SMSR higher than 40 dB and 25 mW output power [17]. This concept has been taken further more recently by employing a grating assisted codirectional coupler filter that is formed by laterally rather than vertically arranged asymmetric waveguides [18]. It was claimed that the adiabatic coupling conditions at the input and output of this

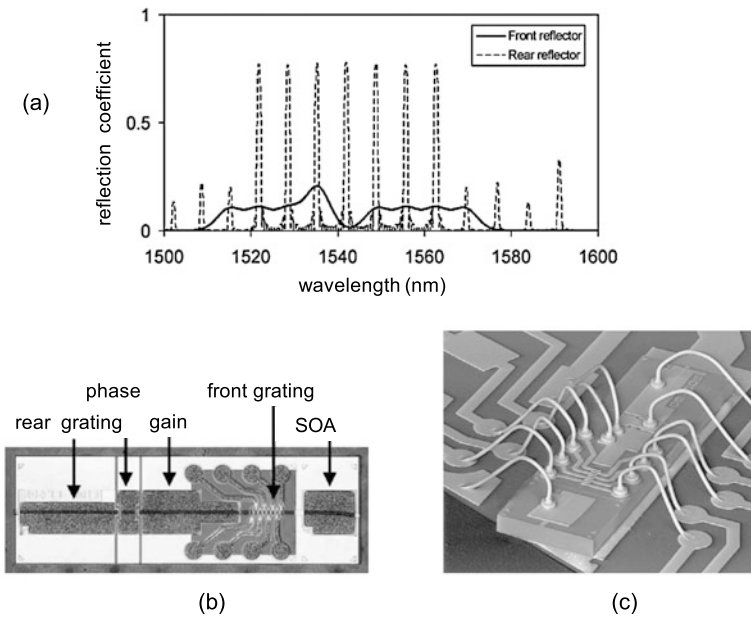


Fig. 5.14 DS-DBR (-SOA) structure: (a) tuning mechanism, (b) top view, (c) photo image of a mounted device [19]

filter variant provided more stable characteristics. A very wide quasi-continuous tuning range of 65 nm (1510 nm to 1575 nm) with SMSR >35 dB was obtained at 50 °C and appreciably low operating currents.

Furthermore, the Digital Supermode DBR (DS-DBR) has been proposed which involves an SSG grating, and a series of eight short Bragg gratings with slightly different pitches (Fig. 5.14) to provide the filter function. Each Bragg grating section is controlled by an individual current. Without current injection, they generate a sequence of reflection peaks separated by 5 nm to result in a wide weak reflectivity spectrum. When current is applied to Bragg section i , its reflectivity shifts from λ_i to lower wavelengths and adds to the reflectivity at λ_{i-1} of the adjacent Bragg section $i - 1$ with lower pitch. As a result, the SG peak closest to λ_{i-1} will be preferentially selected (Fig. 5.14(a)). Although such a device requires many electrodes, it may be simpler to control than SG-DBR type lasers because it is not relying on the critical Vernier effect, and the currents controlling the short Bragg sections are digitally fixed at 0 or ~ 5 mA. The drawback of this structure is the poor selectivity of the multiple Bragg peaks. The uniformity of the rear SSG peaks has to be very carefully optimized to ensure efficient peak selectivity. Again, more than 40 nm tuning together with SMSR better than 40 dB has been demonstrated. As with SG-DBR designs a booster SOA has been incorporated in front of the multiple gratings giving 14 dBm fiber coupled power [19].

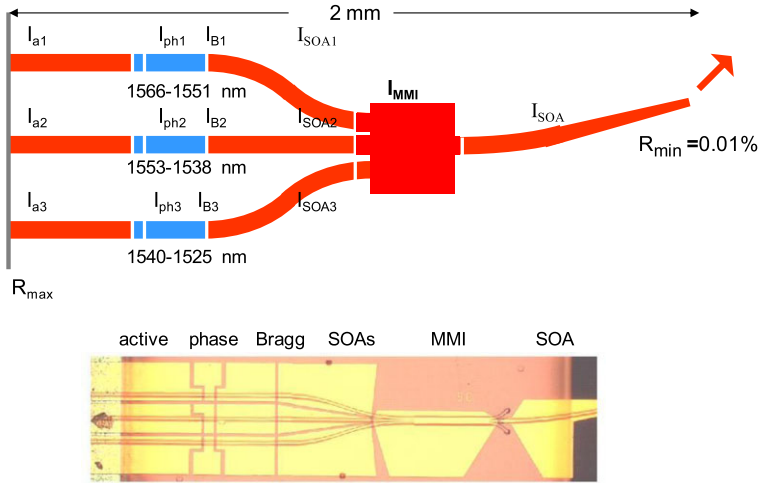


Fig. 5.15 Wavelength tunable laser design (*top*) employing three selectable DBR structures combined by an MMI coupler, and fabricated device chip (*bottom*). Only one of the three branches is operated at the same time

5.2.6 DBR-MMI

Another means to increase the tuning range consists in using 3 DBR lasers in parallel, each of them covering one third of the C-band. A Multi-Mode Interference (MMI) coupler combines the three outputs, while a common SOA section guarantees high output power (Fig. 5.15). This device requires quite a few electrodes, on the other hand the tuning scheme proves to be fairly simple. Only one DBR is operated at the same time, and the tuning characteristics are determined by only one Bragg current rather than the two currents simultaneously feeding the grating sections in the afore-mentioned designs. A total tuning range of 40 nm has been demonstrated whilst maintaining the SMSR level above 40 dB [20].

5.3 Control Issues

All current injection based tunable lasers described above are very attractive because they are monolithically integrated on InP-based semiconductors, offering small footprint and packaging costs, and compatibility even with e-XFP modules. They are also well suited for fast tuning applications as the tuning speed is limited intrinsically only by carrier lifetime (~ 1 ns). From a practical perspective, however, the major challenge with all these approaches arises from control measures needed to guarantee constant output power, extremely precise emission wavelength, and to avoid any SMSR degradation or even mode-hopping. Control accuracy has to be maintained during the full time of operation when the laser is kept running, and

when the laser is turned on after a period without operation. To this end tunable laser components require exhaustive and complex initial characterization to precisely define the optimum operating conditions and feedback loop parameters. Changes in performance and settings due to ageing effects are demanded to be limited to levels as low as possible but nonetheless to be well controlled in order to ensure stability over the entire life cycle. These constraints lead to limited fabrication yield and high characterization costs.

5.3.1 Control Algorithms

Tunable lasers are operated at constant temperature, monitored on submount by means of a temperature-dependent resistive probe, and controlled by a Peltier element. Commonly, a tap coupler is positioned between the front facet and the fiber coupling optics to extract a small amount of light for monitoring purposes. This light is split by a second tap and received by a photodiode PD_1 in the one axis and by another photodiode PD_2 in the other axis after passing a Fabry-Pérot etalon (Fig. 5.16(a)). PD_1 monitors the output power, which is controlled by the drive current of the active laser section or of the booster SOA via a feedback loop. The signal received by PD_2 varies periodically with wavelength, with a period equal to the etalon's free spectral range (typically the 100 GHz ITU spacing, i.e. 0.8 nm at C-band wavelengths). By adjusting the FP etalon transmission characteristic such that the positions of maximum slope coincide with the ITU channels, the ratio I_{PD2}/I_{PD1} can be normalized to unity and used to monitor the position of the emitted wavelength relative to an ITU channel (Fig. 5.16(b)): if $I_{PD2}/I_{PD1} > 1$ then $\lambda_{emission}$ will be $> \lambda_{ITU}$, whereas $I_{PD2}/I_{PD1} < 1$ indicates $\lambda_{emission}$ to be $< \lambda_{ITU}$. In this way the emission wavelength of the tunable laser is finely tuned to be precisely aligned to the ITU wavelength, controlled by the phase section current in conjunction with a feedback loop.

The major difficulty is to avoid both SMSR degradation and mode hops. For adjusting and maintaining maximum SMSR it is necessary to extract a monitoring parameter that can easily be measured inside the module. SMSR is optimized when

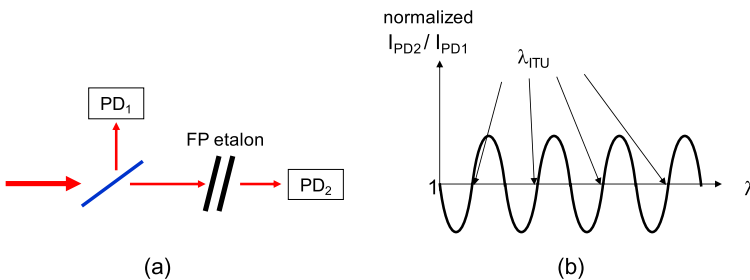


Fig. 5.16 (a) Scheme of wavelength and power locker inside the module, (b) ratio I_{PD2}/I_{PD1} vs wavelength characteristic

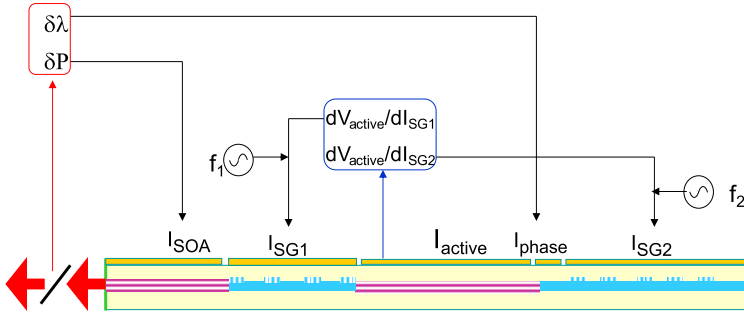


Fig. 5.17 Servo-control loops for controlling an SG-DBR laser

an FP mode matches a maximum of cavity reflectivity, corresponding to the center of mode-hop-free areas in the 1D or 2D tuning curves. This situation is characterized by minimal loss in the cavity, and accordingly yields minimum threshold current. Then, the voltage at the active section, V_{active} , will exhibit a local minimum and the output power a local maximum.

The method used to avoid mode hops in DBRs consists in superimposing a small and slow dithering signal on the current I_{Bragg} . Then dP/dI_{Bragg} (or dV_{active}/dI_{Bragg}) is measured at the same frequency, and maintained on a local extremum by controlling I_{Bragg} via a feedback loop. In the case of tunable lasers comprising simultaneously controlled multiple Bragg sections (SG-DBR, Y-laser, or GCSR), the individual currents are dithered at different frequencies, leading to double monitoring of e.g. dP/dI_{SG1} and dP/dI_{SG2} , involving two feedback loops [21].

Dedicated algorithms are applied to adjust the servo control loops and to ensure stable behavior. But these loops, schematically illustrated in Fig. 5.17 for an SG-DBR-SOA, are interdependent. For example, when I_{SG} is increased to maintain maximum SMSR, the effective refractive index in the SG section is reduced, thus causing the FP modes to shift towards lower wavelengths: the emitted wavelength is decreased. Likewise, when increasing I_{phase} or I_{SG} , cavity losses tend to increase due to free-carrier absorption, and the output power decays. If the power is adjusted by increasing the active current accordingly, the associated heating shifts FP modes and SG reflectivity peaks to higher wavelengths.

Adjusting the optical power by using an SOA is advantageous since the SOA is located outside the FP cavity. Any heating effects do not impact the emitted FP mode wavelength. The SOA requires an additional control current, however I_{active} can be set to a constant value (e.g. 50 mA) sufficient for lasing. Hence the number of adjustable currents is kept unchanged. Moreover, the SOA can fulfill the needed functionality of optical gating: when tuning from one wavelength to another, or when turning on the laser, light is emitted on adjacent channels during the transition interval, which is unacceptable for WDM networks. The SOA can be switched off during those transition time slots and turned on only once the laser is fully stabilized.

Aiming at simplifying the servo-control of SG-DBR type lasers, a Tunable Twin Guide laser (TTG) has been proposed [22]. In this approach the sampled gratings

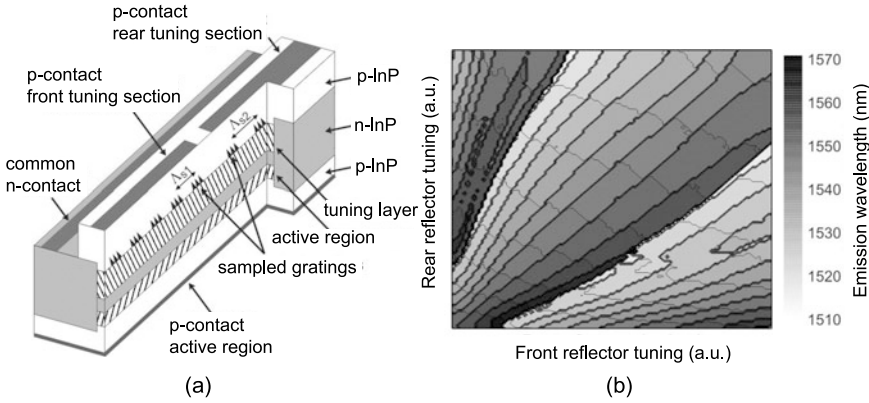


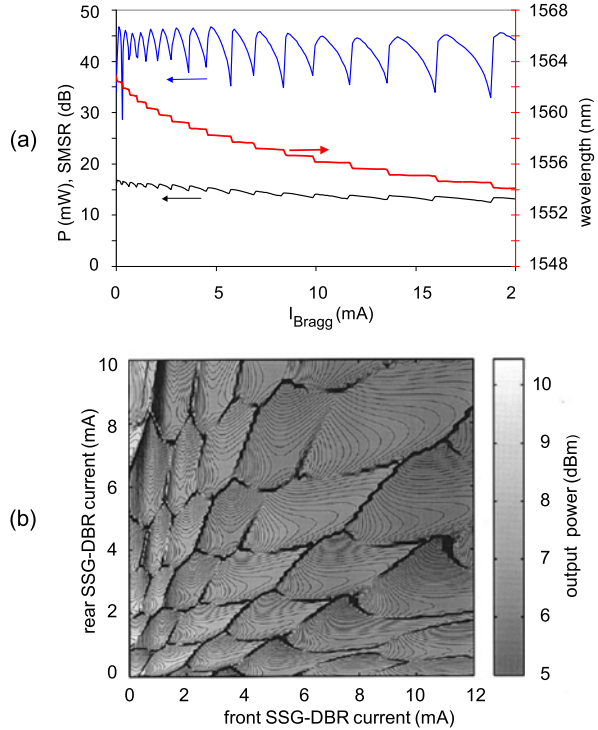
Fig. 5.18 (a) Scheme of a TTG laser and (b) 2D tuning characteristics: the *thin solid lines* within the supermodes indicate 1 nm spaced iso-wavelength contours for visual aid [22]

SG₁ and SG₂ are incorporated in a passive waveguide layer which is placed above the active waveguide (Fig. 5.18(a)). The phase section can be omitted, because SG₁ + SG₂ cover the whole cavity length. When SG₁ and SG₂ are simultaneously tuned such that coincidence is retained for the same reflectivity peaks, the FP comb will be tuned similarly and the FP mode remains aligned to this coincidence. Continuous mode-hop free wavelength tuning up to 8 nm is achievable within the supermodes (Fig. 5.18(b)). The difficulty to be solved in such devices is to achieve efficient, independent current injection into the two overlaying active and passive p-i-n junctions.

5.3.2 Influence of Cavity Length and Non-linear Effects

The complexity of the control mechanisms is strongly influenced by two factors: the FP cavity length of the tunable laser structure and non-linear intra-cavity effects. The free spectral range represents the width of a mode-hop-free area in the tuning characteristics in the center of which the emission wavelength must be kept. According to (5.9) the FSR is inversely proportional to the cavity length. Therefore, tunable laser designs aim at reducing the cavity length to allow for larger tolerances of the current settings and for more tolerant control algorithms with reduced mode hops risks. As an example, for a DBR laser the total cavity length $L_{cavity} = L_{active} + L_{phase} + L_{eff}$ amounts to $\sim 400 \mu\text{m} + 50 \mu\text{m} + 150 \mu\text{m} = 650 \mu\text{m}$. With a typical value of 3.8 for n_g , this yields an FSR value of $\sim 0.5 \text{ nm}$. For widely tunable lasers, on the other hand, such as SG-DBR lasers, the respective length is defined by the active and the phase section, and by the two sampled grating sections, which leads to $L_{cavity} = L_{active} + L_{phase} + 2L_{eff,SG} \sim 500 \mu\text{m} + 100 \mu\text{m} + 2 \times 400 \mu\text{m} = 1400 \mu\text{m}$. Effective lengths in SGs are long due to the reduction of coupling coefficient by the

Fig. 5.19 (a) Tuning characteristics of DBR laser: Emission wavelength (*red curve*), SMSR (*blue curve*), and output power (*black curve*). SMSR and output power exhibit a sequence of maxima around 45 dB and 15 mW, respectively, shifted to the left side (lower Bragg current) of mode hop-free areas (after [20]). (b) Output power characteristics of SSG-DBR laser as a function of current in rear and front SSG-DBR sections. Mode hop-free areas have maximum power away from the center or even no power maximum [21]



sampling effect (5.16). The width of mode-hop-free areas is thus reduced to about 0.23 nm.

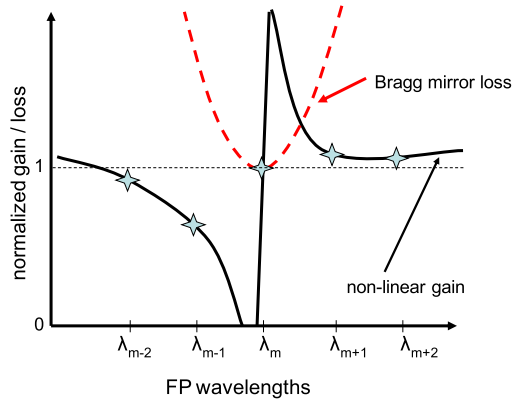
The other drawback associated with long cavities is the occurrence of non-linear effects. When experimentally observing SMSR or power maxima on tuning characteristics, they appear not to occur at the center of mode-hop free areas but to shift towards a higher wavelength mode. Sometimes, maxima even tend to move outside this area which renders SMSR monitoring impossible (Fig. 5.19). A hysteresis effect may be noticed as well: the currents corresponding to mode hops are different depending on whether the Bragg current is increased or decreased.

This phenomenon was thoroughly studied in [23] and has been attributed to the non-linear Four Wave Mixing (FWM) effect. As detailed in [24], the beating of FP modes generates modulation of the carrier density and carrier energies within the conduction or valence bands at a frequency determined by:

$$\Delta\nu = \frac{c}{\lambda^2} FSR \quad (5.20)$$

For tunable lasers, where the FSR remains within 0.2 to 0.5 nm, $\Delta\nu$ is in the 25 to 60 GHz range. At these frequencies, the dominant effect turns out to be Carrier

Fig. 5.20 Normalized gain/loss behavior at the different FP wavelengths around the m th emitted mode, taking into account the carrier density pulsation (CDP) effect



Density Pulsation (CDP), whereas intra-band effects like spectral hole burning or carrier heating can be neglected. CDP generates an asymmetric gain modification around the emission wavelength [24], as illustrated in Fig. 5.20.

In a tunable laser, assuming the m th FP mode to be emitted, the gain characteristics behave asymmetrically, centered at λ_m , in that the gain of mode $m + 1$ at $\lambda_{m+1} > \lambda_m$ is larger than the gain of mode $m - 1$ at $\lambda_{m-1} < \lambda_m$. Mode hopping towards decreasing wavelengths is then impeded, while mode hopping towards higher wavelength is favored. This explains why SMSR and power maxima always tend to shift towards the higher wavelength sides, as mentioned above. When a mode hop occurs, the center of the asymmetric gain characteristics shifts to the new mode and generates an abrupt change in the gain. This results in SMSR or power discontinuities (Fig. 5.19) and causes the hysteresis phenomenon. Indeed, initial gain values for the FP modes are different depending on the initial lasing mode, i.e. whether the Bragg current is being increased or decreased.

Aiming at reducing these non-linear effects to get regular tuning characteristics with clear power maxima, it proves necessary to shorten the cavity length to increase the spacing of the FP modes and reduce their beating. Secondly, the intra-cavity power should be reduced. In this respect the integration of an output SOA is another benefit in that, by providing external amplification, the requirements for the emission power from the cavity itself are highly relaxed. The current driving the active section as well as the section length can be reduced, typically from 600 μm in a DBR to 400 μm for a DBR with SOA. This measure immediately damps non-linear effects and leads to more regular hysteresis-free characteristics.

Despite all these difficulties, simultaneous control of optical power, wavelength and SMSR is possible via interleaved feedback loops on control currents of the different sections. This is done at the cost of extremely precise measurements, electronics, and algorithms. Some companies have developed sufficiently reliable algorithms to obtain stable behavior despite ageing or variation of external conditions (e.g. [25]), and to eventually meet Telcordia qualification standards.

5.3.3 Fast Tuning

The transmission of individual packets at different wavelengths leads to very high granularity and offers high flexibility for coping with fast traffic fluctuations in metropolitan or access networks. For such emerging applications to become reality the laser tuning speed should be shorter than the 50 ns packet guard time. Current-injection tunable lasers are the only possible candidates for such applications due to the intrinsic fast tuning mechanism, limited only by carrier lifetime (~ 1 ns). Studies on widely tunable lasers such as SG-DBR or DS-DBR lasers with optimized electrical current signals have indeed shown extremely fast tuning [9, 26]. Practically however, the wavelength switching period must also encompass the time needed for precise stabilization of the output power and of the emission wavelength onto the ITU grid including sufficiently good single-mode behavior (SMSR).

The altered injection currents enabling tuning give also rise to transient heating effects, and these are very slow processes. As a consequence the effective tuning speed for this type of lasers is limited by the servo control feedback loops. The efficiency of these loops, i.e. the possibility to run them very fast without mode-hop risk, is closely related to the robustness of the tuning mechanisms and to the tolerance with respect to control current variations. With extremely fast electronics, 50 ns tuning with 3 GHz wavelength accuracy has been demonstrated on GCSR lasers [27].

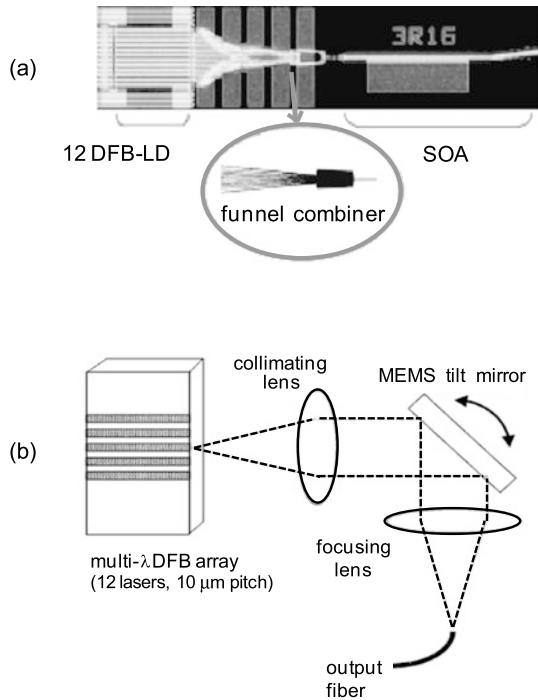
5.4 Other Wavelength Tunable/Selectable Lasers

Monolithically integrated tunable lasers based on current injection are attractive as they offer low cost potential, reduced footprint and fast tuning, and various kinds of such lasers have been introduced into current commercial systems. This has become possible thanks to a large effort on design, process development, characterization and electronics that led to devices meeting Telcordia specifications (extrapolated lifetime of 25 years with stable performance) and an industrial yield compatible with commercially viable production. Researchers and manufacturers have suggested many other approaches including lasers with mechanical or thermal tuning. In general, these devices tend to be larger but in exchange they offer relaxed control mechanisms. Depending on their design, they can provide even larger tuning ranges, e.g. over the complete C + L bands, very high output powers, or record low spectral linewidth.

5.4.1 Thermally Tuned DFB Array

A very simple and efficient approach is an array of typically 12 DFB lasers with a stripe-to-stripe wavelength spacing of about 3 nm obtained by an appropriate vari-

Fig. 5.21 (a) DFB array with funnel combiner and output SOA [29], and (b) DFB array with MEMS tilt mirror [30]



ation of the grating pitch. For operation only one of the lasers is selected and electrically turned on while the array temperature is varied within a range of 30 °C to finely tune to the desired wavelength. This solution benefits from an extremely simple control scheme, absence of mode hops, and from the high performance, maturity and reliability of standard DFB lasers. On the other hand, fabrication of such lasers requires a high level of process control to meet yield requirements. Especially single-mode behavior must be guaranteed for each laser device on the array (see also Chap. 3). In addition, thermal tuning requires a large operation temperature range and is not compatible with fast tuning applications.

One option for selecting any of the DFB lasers is to use a monolithically integrated coupler, such as an MMI [28], or alternatively and preferably a funnel combiner (Fig. 5.21(a)) [29] which relaxes fabrication tolerances. With an integrated output SOA to compensate for around 15 dB coupler losses, achievement of up to 40 mW coupled output power has been demonstrated over the C-band. Another alternative is to make use of an external Micro Electro-Mechanical System (MEMS) tilt mirror placed at the focal plane of a collimating lens (Fig. 5.21(b)) [30]. The InP chip is simplified, losses of the passive combiner are suppressed, and packaging remains simple thanks to an electronic fine alignment of the mirror. Today, this solution has found widespread use in DWDM systems.

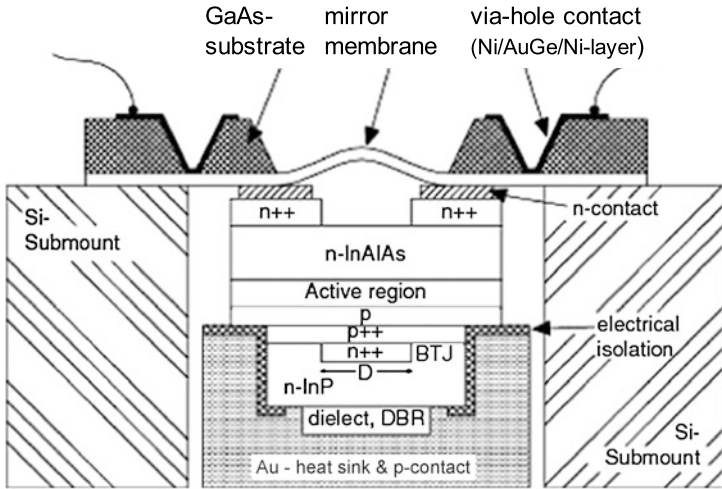


Fig. 5.22 Tunable VCSEL with a movable top mirror membrane [31] (see also Sect. 3.7.1)

5.4.2 Tunable Vertical Cavity Surface Emitting Lasers (VCSELs)

Another very simple-to-control solution is a VCSEL composed of an active structure sandwiched between a bottom Bragg mirror and a movable mirror membrane on top [31], as sketched in Fig. 5.22. Due to the extremely short cavity, only one FP mode exists in the wavelength range where gain is available. This FP mode can be continuously tuned by changing the cavity length accomplished by moving the top mirror. Electrically pumped devices were realized featuring a 76 nm tuning range albeit the output power remained limited to a few mW only.

5.4.3 External Cavity Tunable Lasers

External cavity tunable lasers consist of a long cavity built from discrete elements, including an InP chip as the gain medium (basically an anti-reflection coated FP laser) and wavelength-selective mirrors. These long cavities have the advantage of enabling fairly small linewidths compared to integrated solutions but at the same time they generate extremely dense FP combs. As a consequence the laser design must incorporate solutions which assure that both, the FP modes and the wavelength selective mirror(s), can automatically be tuned in a correlated fashion so that uncontrolled mode hops are avoided.

Design with Diffraction Grating An InP gain chip is placed within a cavity delimited by a fixed mirror and a wavelength tunable external grating. A first example is the Littman/Metcalf cavity configuration depicted in Fig. 5.23(a) [32]. The beam

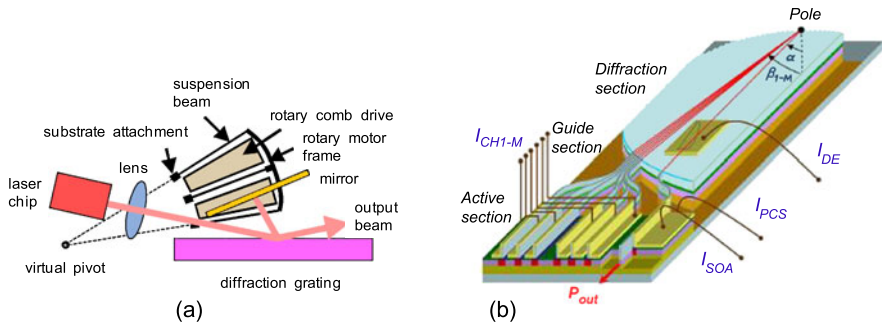


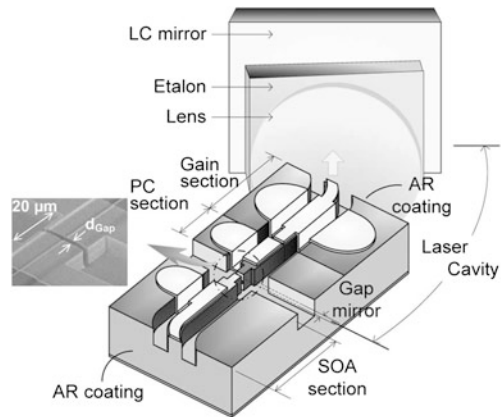
Fig. 5.23 Designs of external cavity tunable lasers: (a) with rotating Bragg grating [32], and (b) with integrated vertical concave grating and dispersive element for fine tuning [33]; I_{DE} , I_{PCS} , I_{SOA} , and I_{CH1-M} denote the currents of the dispersive element, phase-controlled section, optical amplifier, and of the active elements (channel 1- M), respectively

emerging from a diode with a rear high-reflection coating is collimated by a lens and then diffracted by a grating. A voltage is applied to an MEMS actuator, thereby rotating the grating plane to allow a particular wavelength to be coupled back into the laser diode. The first order diffracted beam is used to automatically adjust the actuator voltage. By careful choice of the Bragg grating rotation with respect to the pivot point an equal shift of the cavity FP modes and Bragg grating can be achieved during tuning, and thereby continuous mode-hop free tuning over 40 nm along with 55 dB SMSR.

A widely tunable multichannel grating cavity laser is another variant which has been proposed more recently [33]. The laser operates in a Littrow configuration and comprises: a number of active sections arranged in parallel to each other and all lasing at different wavelengths, an output SOA, a phase-controlled section, a current-tunable dispersive element, and an etched vertical diffraction grating, all monolithically integrated on a single InP chip (Fig. 5.23(b)) [33]. The cavity is formed by the front facets of the active elements and the rear diffraction grating (the center of which is designated by “pole”). Coarse wavelength tuning is accomplished by selecting an appropriate active element while fine tuning is managed by modifying the angle of the back-reflected beam in that the effective refractive index in the dispersive element is varied via current injection. More than 50 nm tuning without mode hops has already been demonstrated. Nonetheless, the design still needs further improvements so that the output power can be raised above its present values which range from -5 to 0 dBm.

Design with Fabry-Pérot Etalon In another concept an FP etalon is placed inside the cavity. Its maximum transmittance is adjusted to the ITU wavelengths so that these are the only possible wavelengths to be emitted from the cavity. A widely tunable filter selects the desired ITU channel and again a phase section is used to finely align a cavity mode. In principle, this approach is very similar to the DS-DBR laser, except that the multiple peak grating is replaced by an FP etalon.

Fig. 5.24 External cavities based on an FP etalon and an LC tunable mirror [34]



A more advanced device consists of a chip with active and phase section and a front SOA section separated by an on-chip mirror (a deeply etched gap). Light emitted from the active section is collimated by a lens into an FP etalon and reflected by a Liquid Crystal (LC) based widely tunable mirror (Fig. 5.24) [34] the reflectivity of which is tuned to the desired transmission peak of the etalon. The phase current is used for fine tuning in the established way. With the SOA section arranged outside the cavity, external modulation or Variable Optical Attenuator (VOA) functionalities are feasible, and more than 100 mW output power is achievable over the whole C-band.

Some companies have proposed an external cavity containing two thermally tuned FP etalons of slightly different wavelength periodicity such that tuning is obtained by the Vernier effect between the two FP etalons.

Design with Polymer Waveguide Gratings Another type of tunable external cavity laser comprises a thermo-optically tunable waveguide grating that is based on polymer material and coupled to an InP based gain chip by means of a collimating lens [35] or in a hybrid integration fashion [36, 37]. Such devices offer the potential of very cost-efficient fabrication. Tuning over more than 26 nm was reported [36].

5.4.4 Tunable Lasers with Ring Resonators

A microring (MR) coupled to a waveguide represents a microring resonator (MRR) which exhibits periodic high transmission peaks. Their periodicity (FSR for Free Spectral Range) is determined by the effective refractive index of the MR waveguide and the diameter of the microring (see also Chap. 9, Sect. 9.10.1). The behavior of such an MRR is similar to that of an FP etalon, and therefore an MRR can also be used for locking laser emission wavelengths to predetermined channels.

In the case of widely tunable lasers it is advantageous to combine an MRR, which transmits channels with narrow spacing, with another element for coarse wavelength

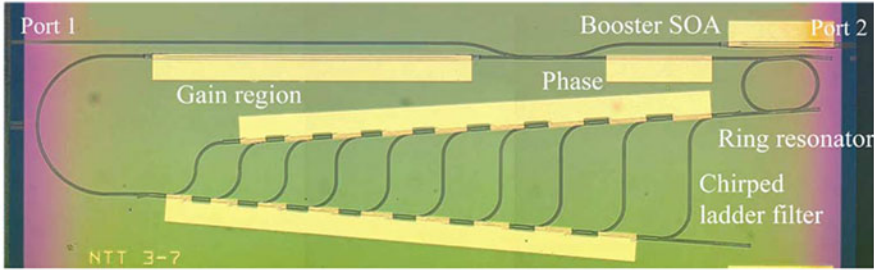


Fig. 5.25 Ring resonator type monolithically integrated tunable laser with ring resonator and ladder filter [38]

selection. One such example is shown in Fig. 5.25 [38]. The monolithic laser structure comprises a gain section, a phase section, a ring resonator, a ladder filter for coarse wavelength selection, and an output booster SOA. The diameter of the ring resonator has been chosen in such a way that the transmission maxima coincide with ITU channels. The ladder filter consists of an input and an output waveguide plus a number of interconnecting waveguides coupled via multimode interference (MMI) couplers. The ladder filter is conceptually equivalent to an Arrayed Waveguide Grating (AWG, see also Chap. 9). It may either exhibit periodic peaks with equal transmission [39] or, alternatively, a single transmission peak can be made significantly more pronounced than all the others by chirping (more than 5.4 dB are reported in [38]) so that the coarse wavelength selection is improved. Tuning of this single transmission peak is accomplished by varying the effective refractive index of the input or output waveguide by means of current injection. In essence, the tuning involves three steps: the transmission maximum of the ladder filter assures wide wavelength tuning, the ring resonator selects an ITU channel, and the phase section finely tunes the corresponding cavity mode. A total tuning range of 38 nm and 9 dBm output power thanks to the booster SOA have been demonstrated with this device.

Another embodiment, recently developed by multiple teams as a simple solution to provide even larger tuning ranges, combines an SOA gain section with two or three rings inside a cavity. The device can only lase on wavelengths corresponding to maxima of the rings transmission characteristics, operating as a succession of selective narrow filters. By using rings with slightly different FSRs, only one wavelength can be selected within the cavity, corresponding to the coincidence of transmission maxima of the complete sequence of rings. Tuning is obtained via the Vernier effect between the rings, and the individual transmission characteristics are swept by means of thin metal heaters. Multiple technological combinations of an InP-SOA and rings have been explored for widely tunable lasers: hybrid integration of SOAs with silica or silicon rings, or monolithic integration with InP rings.

An example of hybrid solution with silica rings is illustrated Fig. 5.26 [40]. Due to the small index contrast of SiON/SiO₂ waveguides (typically 2 to 4%), ring diameters have to be above hundreds of microns, leading to FSRs about 100 GHz maximum. Three rings are therefore necessary to ensure sufficient wavelength selectivity

Fig. 5.26 Multiple rings tunable laser with three successive SiON/SiO₂ rings [40]

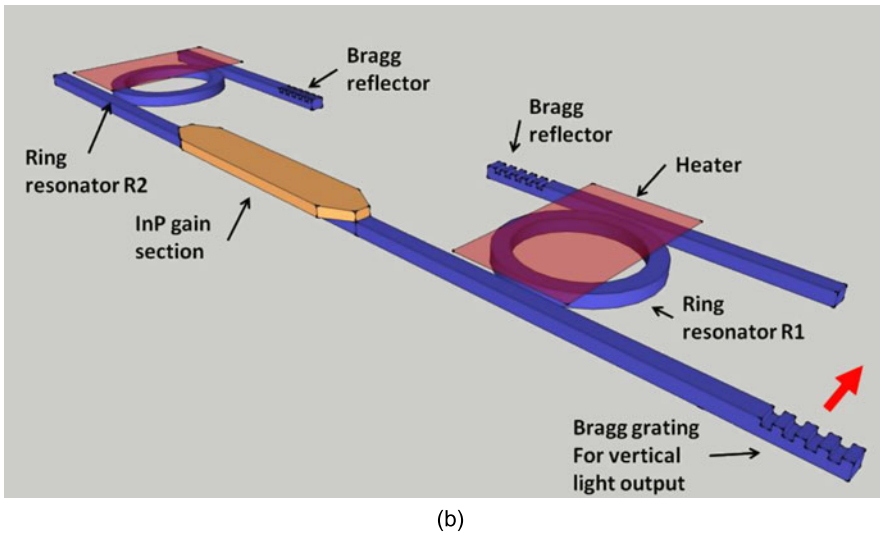
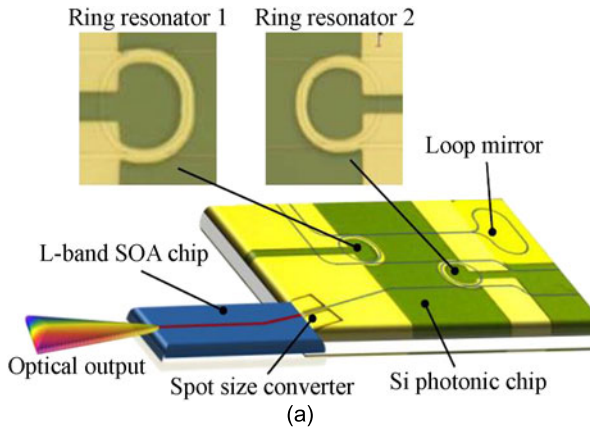
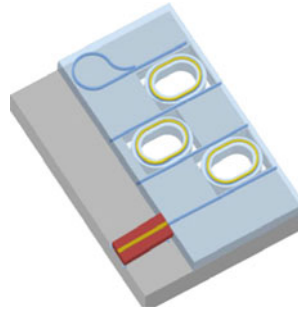


Fig. 5.27 Schematic views of widely tunable lasers using two Si-photonic rings, by butt-joint integration of SOA (a) [41], by wafer-bonding of SOA on top of Si waveguide (b) [44]

among the cavity. In this example, one ring with 100 GHz peak spacing acts as an ITU etalon, the second ring with 101.25 GHz periodicity provides coarse tuning, and the third ring with 78.95 GHz peak separation the fine tuning. Cavity is limited by a loop mirror with 3 dB coupler and the SOA back facet where light is coupled into a fiber. Ring thermal tuning efficiency is increased by etching Si around the waveguides, resulting in an air-bridge structure with high thermal resistance. Such a device delivers C-band tuning with 45 dB SMSR and more than 16 dBm coupled output power.

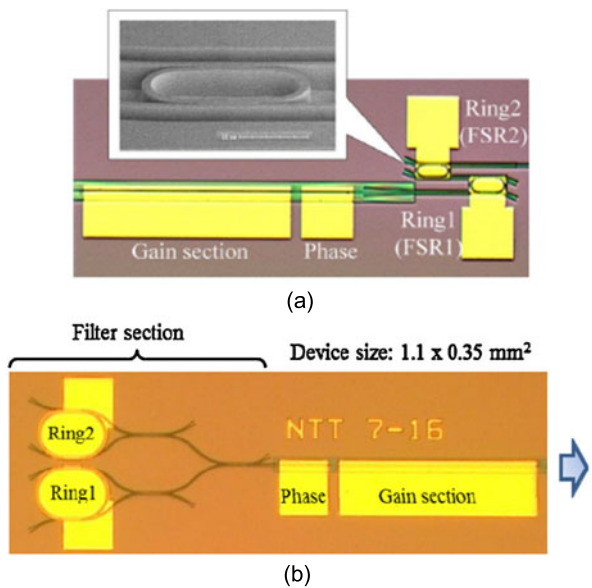
Silicon photonic or monolithic integrated solutions on InP have attracted much interest owing to their strong index contrast that enables small rings with FSRs as large as 500 GHz. Only two rings are sufficient within the cavity to ensure single mode operation, leading to simpler control and smaller footprint.

For Si photonics, one first approach is shown in Fig. 5.27(a). It is a hybrid device with an SOA directly butt-jointed in front of a Si photonic chip [41, 42]. A more recent implementation relies on hybrid multi-chip integration by passive alignment which enables high reliability and low cost, and a chip with integrated booster SOA exhibited >100 mW fiber coupled output power over the whole C-band [43].

A second approach, illustrated in Fig. 5.27(b), consists in direct wafer bonding of active InP material on top of SOI waveguides [44]. Adiabatic tapers at both edges of the SOA enable to transfer light from the gain material to the passive Si waveguides [44, 45].

The same design can be implemented by monolithic integration as shown Fig. 5.28(a) [46], with two serial rings inside the laser cavity, using a deep etch process in the passive sections to reach high FSRs for the rings. A solution based on parallel rings (Fig. 5.28(b) [47]) takes advantage of phase opposition between the

Fig. 5.28 Photography of monolithically integrated widely tunable lasers using two InP-rings serial [46] or parallel [47]



coincidences of adjacent rings, in the same way as Y-lasers with sampled gratings presented in Sect. 5.2.4 compared to serial SG-DBR of Sect. 5.2.2.

All these ring-based tunable lasers can at least cover the whole C-band with high SMSR. Some of them reach up to 40 mW output power. Based on thermal tuning rather than current injection, they benefit from linear and predictable tuning characteristics, leading to a simple control procedure. These solutions are particularly adapted to be used for coherent transmission systems as sources or local oscillators, owing to their narrow linewidths. Indeed light is trapped for multiple paths inside the rings, leading to long equivalent cavities. Si photonics or InP devices reach about 100 kHz linewidths, and SiO₂ solutions with equivalent cavity lengths up to a few centimeters even demonstrate record 2 kHz linewidths [48].

5.5 Subsystems and Tunable Photonic Integrated Circuits

Tunable lasers covering the C-band have now become commercially available, and as a next development step various approaches aim at expanding the tuning range to the C + L bands in order to reduce cost and simplify control. In addition, a large amount of current work focuses on the integration of tunable lasers with other optoelectronic devices in order to improve performance and provide new functionalities, apart from cost aspects.

One option is to introduce hybrid integration in optical packaging. For example, an InP Mach-Zehnder modulator mounted between collimating lenses has been successfully added to the DFB array with selective MEMS of Fig. 5.21(b), and to the DS-DBR-SOA of Fig. 5.14, to implement a 10 Gbit/s transmitter capable of low chirp and adaptable to a small form factor optical module. To further reduce footprint and packaging costs, additional optoelectronic devices may be monolithically integrated with the tunable laser chip, leading to so-called Photonic Integrated Circuits (PICs). Each device requires a different material band edge according to its functionality, whether it is an active section with gain, a passive tuning section, a photodetector, an electro-absorption modulator, and maybe others. Different optical integration schemes exist such as butt-joint coupling, selective area growth, and quantum-well intermixing (QWI) [49] so that material of different composition can be epitaxially grown on the same wafer. The University of Santa Barbara in California appears to be the most active group in the field of widely tunable PICs. They have focused on the QWI technique and have applied it to demonstrate various PICs around their widely tunable SG-DBR design (see e.g. [49]).

5.5.1 Tunable Laser Integrated with Modulator

Direct modulation of tunable lasers has been investigated using several designs but the maximum achievable transmission distances remained limited to around 10 km

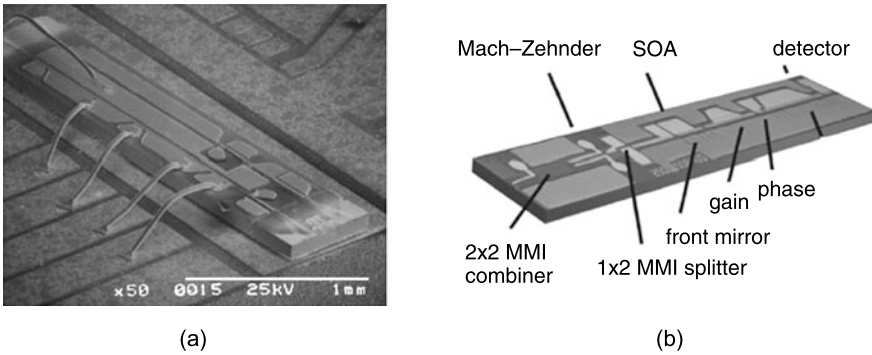


Fig. 5.29 (a) Photo image of a mounted SG-DBR-SOA-EAM [50], and (b) schematic structure of an SG-DBR-SOA-MZ [51]

at 10 Gbit/s due to laser chirp. Improved transmission distances and modulation bit rates can be expected if an external modulator is integrated with a widely tunable laser, similar to the concept of integrating DFB lasers with a modulator.

One example in this respect is an SG-DBR-SOA integrated with a 40 Gbit/s Electro-Absorption Modulator (EAM) as shown in Fig. 5.29(a) [50]. The EAM bandgap is detuned to 1500 nm by QWI and provides more than 20 dB static extinction ratio for SG-DBR emission ranging between 1540 nm and 1560 nm. 1 V peak-to-peak voltage has been sufficient to provide a clear 40 Gbit/s eye diagram with 8 dB dynamic extinction ratio. However, the integration of EAMs with widely tunable lasers remains critical because the operation of EAMs relies on the Quantum Confined Stark Effect (QCSE) which is a band edge effect and therefore highly dependent on the detuning between the lasing wavelength and the (photoluminescence) wavelength of the EAM. As a consequence it is necessary to adapt the driving voltages to the emitted wavelengths, and the performance in terms of power, peak-to-peak voltage, chirp, etc. varies considerably over the whole tuning range.

Mach-Zehnder modulators (MZM), which are based upon the interference between two phase-modulated arms (see also Chap. 8), intrinsically provide almost wavelength-independent characteristics and their chirp can be adjusted arbitrarily, allowing for longer reach, virtually penalty-free transmission. The disadvantages of Mach-Zehnder modulators are more stringent processing specifications, higher complexity with monolithic integration, and larger device size. An example of a successful integration is shown in Fig. 5.29(b) [51] featuring 300 μm long MZ arms, more than 10 GHz bandwidth, and 20 dB static extinction for less than 5 V operation voltage. Higher bandwidth and lower driving voltages can be obtained if the MZM is operated in push-pull configuration and traveling wave electrodes are used on the MZ arms. Clear eye diagrams have been demonstrated at 40 Gbit/s over a tuning range of 34 nm with 3.2 V drive voltage [52].

Finally, the device illustrated in Fig. 5.27(b) has also been monolithically integrated with an EAM on silicon operating in the 1.55 μm wavelength regime. Wavelength tunability of the integrated device was limited to 10 nm because the laser and

the EAM had the same layer structure, and the dynamic extinction ratio amounted to 6 to 10 dB with 1 V_{pp} drive voltage [53], however, the device concept is promising with respect to the large volume and low cost perspectives of silicon photonics.

5.5.2 Tunable Subsystems

Monolithic integration can be pushed even further so that complete widely tunable subsystems are obtained as shown in Fig. 5.30(a) for example [54]. The transmitter is composed of an SG-DBR laser integrated with a 125 μm long EAM and an output booster SOA that provides 3 dB penalty only for 40 Gbit/s transmission over 5 km. The tuning range exceeds 30 nm and the driving voltages are as low as 1.5 to 2.5 V. The receiver consisted of two SOAs and a Uni-Traveling-Carrier (UTC) type photodiode yielding -20 dBm sensitivity at 40 Gbit/s.

A 40 Gbit/s tunable all-optical wavelength converter for packet-switched optical networks is illustrated in Fig. 5.30(b) [55]. The input signal pulses are split into two arms with a relative delay of 10 ps, then amplified by two linear SOAs, and subsequently they generate time delayed carrier depletion in the non-linear SOAs of the MZ interferometer. The corresponding phase changes lead to a short time window during which the MZ interferences are constructive. Because the continuous wave (cw) signal emitted by the SG-DBR tunable laser is coupled into both MZ arms and recombined at the output, the resulting signal is a replica of the input pulses, however, converted to the cw wavelength. In this device QWI for implementing the SG-DBR sections and linear SOAs is combined with butt-joint technology for integrating non-linear SOAs containing highly confined bulk material. Very low jitter

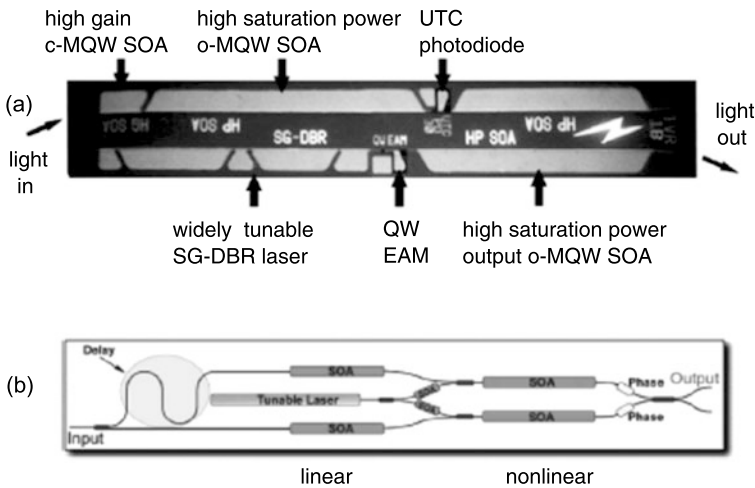


Fig. 5.30 (a) Complex monolithically integrated 40 Gbit/s components: tunable transceiver [54], and (b) wavelength converter [55]

and more than 12 dB output extinction ratio have been obtained at 40 Gbit/s with less than 1 dB penalty across the whole C-band.

5.6 Conclusion

Research has been carried out for more than a decade to achieve widely tunable lasers for DWDM systems featuring high performance, reduced footprint, simple control, and cost-efficient fabrication. This topic is extremely rich in terms of overall design innovation, and an impressive variety of approaches have been pursued. None of them, however, appears to be a universal solution so far, instead there may be optimum designs for different specific applications.

Designs like the SG-DBR or DS-DBR lasers appear to be the prevailing solutions for metropolitan networks and for ROADMs. DFB arrays are widely used solutions that are commercially available. This is especially true for long distance transmission based upon coherent modulation formats (like QPSK or QAM) where both amplitude and phase are modulated and the signals decoded by interference with a local oscillator (see also Chap. 7). A narrow linewidth is mandatory for these applications in order to assure low phase noise at the detection site.

Tuning can be accomplished thermally, mechanically and by current injection. The lasers can be monolithically integrated on InP or made of discrete elements. Many embodiments are fundamentally based on the same principles. Most of them comprise an FP cavity and require alignment of a cavity mode to the desired wavelength via a phase section current or via cavity length adjustment (in an external cavity). Coarse tuning relies essentially on three generic concepts and elements:

- Use of highly-selective tunable filters. Examples are the current injection tuned Bragg section in a DBR or a Bragg grating with tunable angle in an external cavity.
- Use of the Vernier effect between multiple peak elements. Multiple peak elements can be multiple peak gratings such as sampled gratings and superstructure gratings in SG-DBR, SSG-DBR or TTG lasers. Alternatively, they can be formed by Fabry-Pérot etalons in external cavities with dual FPs or by ring resonators in ring reflector lasers.
- Use of a multiple peak element and a widely tunable coarse filter. For example, in DS-DBR lasers a super structure grating and multiple Bragg gratings are utilized, in an external cavity laser an FP etalon and a liquid crystal type mirror are employed, and a tunable ring laser involves a ring resonator and a ladder filter.

The main approaches for widely tunable lasers are summarized in Table 5.1, which includes the tuning principles and mechanisms, and state-of-the-art pros and cons for each device.

Some of these tunable lasers are commercially available and deployed in DWDM systems to a varying degree where they offer enhanced flexibility (SG-DBR-, SSG-DBR-, Y-, DS-DBR-, DFB array + Funnel-, DFB array + MEMs-, and External Cavity + FP etalon + LC mirror laser). Other innovative solutions are still in the

Table 5.1 Summary of main tunable lasers approaches, including their tuning characteristics and their state-of-the-art pros and cons. Devices marked with an * are commercially available

Device	References (companies)	Tuning mechanism	Tuning principle	Pros	Cons
SG-DBR*	[8, 10, 12–14]	Current	Vernier	Monolithic integration	Complex control Large linewidth
SSG-DBR Y-laser*	JDS-Uniphase, Syntune				
DS-DBR*	[16, 17, 19]	Current	Multiple peaks + wide filter	ID tuning No phase section	Complex injection
GCSR	Oclaro	Current	One filter		
DBR-MMI	[20]	Current	Vernier	Simple control	Slow tuning
TTG	[22]	Current	Vernier		
DFB array + Funnel*	[28, 29] NTT	Thermal	Selection	Simple control Vertical emission	Footprint Slow tuning
DFB array + MEMS*	[30] Santur	Thermal	Selection		
VCSEL	[31]	Voltage	Single FP mode	Low linewidth	Low power
Ext. cavity + Bragg	[32]	Mechanical	One filter	Complex alignment Large footprint	Slow tuning
Ext. cavity + Bragg (integ. solution)	[33]	Current	One filter	Low linewidth Monolithic integration	Slow tuning Low power
Ext. Cavity + FP etalon + LC mirror	[34]	Voltage	Multiple peaks + wide filter	Low linewidth High power	Large footprint
Ext. cavity + 2 FP etalons		Thermal	Vernier	Low linewidth	Control Slow tuning
Ladder laser	[38]	Current	Multiple peaks + wide filter	Monolithic integration Simple control Fast tuning	Critical processing High power
Ring reflector laser	[40, 42, 44–47]	Thermal	Vernier	Hybrid integration C + L bands or monolithic C-band	Control Slow tuning

laboratory stage, and these include lasers based upon an external cavity with monolithically integrated concave mirror, with an FP etalon and an LC mirror, and more recent developments based upon multiple ring resonators. These innovations are expected to further improve performance, e.g. by offering tuning across the full C + L band, allowing for faster switching in future WDM PON access networks, reaching very low linewidths, or fitting to very cost-efficient assemblies.

Another important research target is the extension of tunable lasers to photonic integrated circuits to eventually arrive at complete monolithically integrated subsystems. This opens the way towards multiple combinations of various subcomponents and to a wide range of future devices and system functionalities.

References

1. J. Buus, M.-C. Amann, D.J. Blumenthal, *Tunable Laser Diodes and Related Optical Sources*, 2nd edn. (Wiley, Hoboken, 2005). ISBN-13 978-0-471-20816-7
2. B.R. Bennett, R.A. Soref, J.A. Del Alamo, Carrier-induced change in refractive index of InP, GaAs, and InGaAsP. *IEEE J. Quantum Electron.* **30**, 113–122 (1994)
3. J.-P. Weber, Optimization of the carrier-induced effective index change in InGaAsP waveguides – application to tunable Bragg filters. *IEEE J. Quantum Electron.* **30**, 1801–1816 (1994)
4. S.L. Chuang, *Physics of Optoelectronic Devices*, 2nd edn. (Wiley Interscience, Hoboken, 2009)
5. A. Yariv, M. Nakamura, Periodic structures for integrated optics. *IEEE J. Quantum Electron.* **QE-13**, 233–253 (1977)
6. T.L. Koch, U. Koren, B.I. Miller, High-performance tunable 1.5 μm InGaAs/InGaAsP multiple quantum well distributed Bragg reflector lasers. *Appl. Phys. Lett.* **53**, 1036–1088 (1988)
7. H. Debrégeas-Sillard, A. Vuong, F. Delorme, J. David, V. Allard, A. Bodéré, O. Legouezigou, F. Gaborit, J. Rotte, M. Goix, V. Voiriot, J. Jacquet, DBR module with 20 mW constant coupled output power over 16 nm (40 channels 50 GHz spaced). *IEEE Photonics Technol. Lett.* **13**, 4–6 (2001)
8. V. Jayaraman, Z.-M. Chuang, L.A. Coldren, Theory, design, and performance of extended tuning range semiconductor lasers with sampled gratings. *IEEE J. Quantum Electron.* **29**, 1824–1834 (1993)
9. R. O’Dowd, S. O’Duill, G. Mulvihill, N. O’Gorman, Y. Yu, Frequency plan and wavelength switching limits for widely tunable semiconductor transmitters. *IEEE J. Sel. Top. Quantum Electron.* **7**, 259–269 (2001)
10. B. Mason, J. Barton, G.A. Fish, L.A. Coldren, S.P. DenBaars, Design of sampled grating DBR lasers with integrated semiconductor optical amplifier. *IEEE Photonics Technol. Lett.* **12**, 762–764 (2000)
11. H. Debrégeas-Sillard, C. Fortin, A. Accard, O. Drisse, E. Derouin, F. Pommereau, C. Kazmieriski, Non-linear effects analysis in DBR lasers: applications to DBR-SOA and new double Bragg-DBR. *IEEE J. Sel. Top. Quantum Electron.* **13**, 1142–1149 (2007)
12. H. Ishii, H. Tanobe, F. Kano, Y. Tohmori, Y. Kondo, Y. Yoshikuni, Quasicontinuous wavelength tuning in super-structure-grating (SSG) DBR lasers. *IEEE J. Quantum Electron.* **32**, 433–441 (1996)
13. M. Gotoda, T. Nishimura, Y. Tokuda, Widely tunable SOA-integrated DBR laser with combination of sampled-grating and superstructure grating, in *19th Internat. Semicond. Laser Conf. (ISLC’04)*, Matsue, Japan (2004), Conf. Digest, paper SaA5

14. M. Schilling, W. Idler, E. Kühn, G. Laube, H. Schweizer, K. Wünstel, O. Hildebrand, Integrated interferometric injection laser. Novel fast and broad-band tunable monolithic light source. *IEEE J. Quantum Electron.* **27**, 1616–1624 (1991)
15. J.O. Wesström, G. Sarlet, S. Hammerfeldt, L. Lundqvist, P. Szabo, P.-J. Rigole, State-of-the-art performance of widely tunable modulated grating Y-branch lasers, in *Opt. Fiber Commun. Conf. (OFC'04)*, Los Angeles, CA, USA (2004), Techn. Digest, paper TuE2
16. M. Öberg, S. Nilsson, K. Streubel, J. Wallin, L. Bäckbom, T. Klinga, 74 nm wavelength tuning range of an InGaAsP/InP vertical grating assisted codirectional coupler laser with rear sampled grating reflector. *IEEE Photonics Technol. Lett.* **5**, 735–738 (1993)
17. Y. Gustafsson, S. Hammerfeldt, J. Hammersberg, M. Hassler, T. Hörman, M. Isaksson, J. Karlsson, D.E. Larsson, O.D. Larsson, L. Lundqvist, T. Lundström, M. Rask, P.-J. Rigole, E. Runeland, A. Saavedra, G. Sarlet, R. Siljan, P. Szabo, L. Tjemplund, O. Träskman, H. de Vries, J.-O. Wesström, C. Ögren, Record output power (25 mW) across C-band from widely tunable GCSR lasers without additional SOA. *Electron. Lett.* **39**, 292–293 (2003)
18. T. Suzuki, H. Arimoto, T. Kitatani, A. Takei, T. Taniguchi, K. Shinoda, S. Tanaka, S. Tsuji, Wide-tuning (65 nm) semi-cooled (50 °C) operation of a tunable laser based on a novel widely tunable filter, in *Opt. Fiber Commun. Conf. and Nat. Fiber Opt. Eng. Conf. (OFC/NFOEC'11)*, Los Angeles, CA, USA (2011), Techn. Digest, paper OWD7
19. A.J. Ward, D.J. Robbins, G. Busico, E. Barton, L. Ponnampalam, J.P. Duck, N.D. Whitbread, P.J. Williams, D.C.J. Reid, A.C. Carter, M.J. Vale, Widely tunable DS-DBR laser with monolithically integrated SOA: design and performance. *IEEE J. Sel. Top. Quantum Electron.* **11**, 149–156 (2005)
20. H. Debrégeas-Sillard, C. Fortin, F. Pommereau, D. Dugeon, Y. Gottesman, O. Drisse, E. Derouin, N. Lagay, B. Rousseau, F. Martin, J. Landreau, C. Kazmierski, More than 40 nm tuning DBR-MMI-SOA with only one Bragg current control compatible with fast switching, in *Proc. 33rd Europ. Conf. Opt. Commun. (ECOC'07)*, Berlin, Germany (2007), paper 9.2.4
21. G. Sarlet, G. Morthier, R. Baets, Wavelength and mode stabilization of widely tunable SG-DBR and SSG-DBR lasers. *IEEE Photonics Technol. Lett.* **11**, 1351–1353 (1999)
22. R. Todt, T. Jacke, R. Meyer, J. Adler, R. Laroy, G. Morthier, M.-C. Amann, Sampled grating tunable twin-guide laser diodes with over 40 nm electronic tuning range. *IEEE Photonics Technol. Lett.* **17**, 2514–2516 (2005)
23. G. Sarlet, Tunable laser diodes for WDM communication – methods for control and characterisation. PhD thesis, University of Ghent and INTEC, Belgium (2001)
24. A. Uskov, J. Mørk, J. Mark, Wave mixing in semiconductor laser amplifiers due to carrier heating and spectral-hole burning. *IEEE J. Quantum Electron.* **30**, 1769–1781 (1994)
25. M.C. Larson, M. Bai, D. Bingo, N. Ramdas, S. Penniman, G.A. Fish, L.A. Coldren, Mode control of widely-tunable SG-DBR lasers, in *Proc. 28th Europ. Conf. Opt. Commun. (ECOC'02)*, Copenhagen, DK (2002), poster P2.04
26. L. Ponnampalam, N.D. Whitbread, R. Barlow, G. Busico, A.J. Ward, J.P. Duch, D.J. Robbins, Dynamically controlled channel-to-channel switching in a full-band DS-DBR laser. *IEEE J. Quantum Electron.* **42**, 223–230 (2006)
27. J.E. Simsarian, L. Zhang, Wavelength locking a fast-switching tunable laser. *IEEE Photonics Technol. Lett.* **16**, 1745–1747 (2004)
28. H. Hatakeyama, K. Kudo, Y. Yokoyama, K. Naniwae, T. Sasaki, Wavelength-selectable microarray light sources for wide-band DWDM applications. *IEEE J. Sel. Top. Quantum Electron.* **8**, 1341–1348 (2002)
29. H. Ishii, K. Kasaya, H. Oohashi, Y. Shibata, H. Yasaka, K. Okamoto, Widely wavelength-tunable DFB laser array integrated with funnel combiner. *IEEE J. Sel. Top. Quantum Electron.* **13**, 1089–1094 (2007)
30. B. Pezeshki, E. Vail, J. Kubicky, G. Yoffe, S. Zou, J. Heanue, P. Epp, S. Rishton, D. Ton, B. Faraji, M. Emanuel, X. Hong, M. Sherback, V. Agrawal, C. Chipman, T. Razazan, 20 mW widely tunable laser module using DFB array and MEMS selection. *IEEE Photonics Technol. Lett.* **14**, 1457–1459 (2002)

31. S. Jatta, B. Kögel, M. Maute, K. Zogal, F. Riemenschneider, G. Böhm, M.-C. Amann, P. Meißner, Bulk-micromachined VCSEL at 1.55 μm with 76 nm single-mode continuous tuning range. *IEEE Photonics Technol. Lett.* **21**, 1822–1824 (2009)
32. J.D. Berger, Y. Zhang, J.D. Grade, H. Lee, S. Hrinya, H. Jerman, Widely tunable external cavity diode laser based on a MEMS electrostatic rotary actuator, in *Opt. Fiber Commun. Conf. (OFC'01)*, Anaheim, CA, USA (2001), Techn. Digest, paper TuJ2
33. O.K. Kwon, J.H. Kim, K.H. Kim, E.D. Sim, K.R. Oh, Widely tunable multichannel grating cavity laser. *IEEE Photonics Technol. Lett.* **18**, 1699–1701 (2006)
34. M.L. Nielsen, S. Sudo, K. Mizutani, T. Okamoto, K. Tsuruoka, K. Sato, K. Kudo, Integration of functional SOA on the gain chip of an external cavity wavelength tunable laser using etched mirror technology. *IEEE J. Sel. Top. Quantum Electron.* **13**, 1104–1111 (2007)
35. S.H. Oh, K.S. Kim, M. Kim, K.H. Yoon, D.K. Oh, Y.O. Noh, H.J. Lee, Tunable external cavity laser employing uncooled superluminescent diode. *Opt. Express* **17**, 10189–10194 (2009)
36. G. Jeong, J.H. Lee, M.Y. Park, C.Y. Kim, S.H. Cho, W. Lee, B.W. Kim, Over 26-nm wavelength tunable external cavity laser based on polymer waveguide platforms for WDM access networks. *IEEE Photonics Technol. Lett.* **18**, 2102–2104 (2006)
37. F.M. Soares, Z. Zhang, G. Przyrembel, M. Lauer mann, M. Moehrl, N. Metzbach, C. Zawadzki, B. Zittermann, N. Keil, N. Grote, Hybrid photonic integration of InP-based laser diodes and polymer PLCs, in *Conf. Indium Phosphide Relat. Mater. (IPRM'11)*, Berlin, Germany (2011), Techn. Digest, paper Th-8.1.3
38. S. Matsuo, S.-H. Jeong, T. Segawa, H. Okamoto, Y. Kawaguchi, Y. Kondo, H. Suzuki, Y. Yoshikuni, Tunable laser using chirped ladder filter. *IEEE J. Sel. Top. Quantum Electron.* **13**, 1122–1128 (2007)
39. S. Matsuo, Y. Yoshikuni, T. Segawa, Y. Ohiso, H. Okamoto, A widely tunable optical filter using ladder-type structure. *IEEE Photonics Technol. Lett.* **15**, 1114–1116 (2003)
40. T. Matsumoto, A. Suzuki, M. Takahashi, S. Watanabe, S. Ishii, K. Suzuki, T. Kaneko, H. Yamazaki, N. Sakuma, Narrow spectral linewidth full band tunable laser based on waveguide ring resonators with low power consumption, in *Opt. Fiber Commun. Conf. and Nat. Fiber Opt. Eng. Conf. (OFC/NFOEC'10)*, San Diego, CA, USA (2010), Techn. Digest, paper OThQ5
41. T. Kita, K. Nemoto, H. Yamada, Narrow spectral linewidth and high output power Si photonic wavelength tunable laser diode, in *10th IEEE Internat. Conf. Group IV Photonics*, Seoul, Korea (2013), paper FB4
42. T. Kita, K. Nemoto, H. Yamada, Silicon photonic wavelength-tunable laser diode with asymmetric Mach-Zehnder interferometer. *IEEE J. Sel. Top. Quantum Electron.* **20**(4), 8201806 (2014)
43. K. Sato, N. Kobayashi, M. Namiwaka, K. Yamamoto, S. Watanabe, T. Kita, H. Yamada, H. Yamazaki, Demonstration of silicon photonic hybrid ring-filter external cavity wavelength tunable lasers, in *Proc. 41st Europ. Conf. Opt. Commun. (ECOC'15)*, Valencia, Spain (2015), paper We. 2.5.4
44. G.-H. Duan, C. Jany, A. Le Liepvre, A. Accard, M. Lamponi, D. Make, P. Kaspar, G. Levaufre, N. Girard, F. Lelarge, J.-M. Fedely, A. Descos, B. Ben Bakir, S. Messaoudene, D. Bordel, S. Menezo, G. de Valicourt, S. Keyvaninia, G. Roelkens, D. Van Thourhout, D.J. Thomson, F.Y. Gards, G.T. Reed, Hybrid III–V on silicon lasers for photonic integrated circuits on silicon. *IEEE J. Sel. Top. Quantum Electron.* **20**(4), 6100213 (2014)
45. J.C. Hulme, J.K. Doylend, J.E. Bowers, Widely tunable Vernier ring laser on hybrid silicon. *Opt. Express* **21**(17), 19718–19722 (2013)
46. S. Matsuo, T. Segawa, Microring-resonator-based widely tunable lasers. *IEEE J. Sel. Top. Quantum Electron.* **15**, 545–554 (2009)
47. T. Segawa, T. Sato, R. Iga, S. Matsuo, R. Takahashi, A novel tunable laser with flat-output wideband tuning based on parallel ring resonators, in *Internat. Conf. Photonics in Switching*, Ajaccio, France (2012), paper Fr-S36-O14, Online ISBN: 978-2-9123-2861-8
48. H. Debrégeas, C. Ferrari, M.A. Cappuzzo, F. Klemens, R. Keller, F. Pardo, C. Bolle, C. Xie, M.P. Earnshaw, 2 kHz linewidth C-band tunable laser by hybrid integration of reflective SOA

- and SiO₂ PLC external cavity, in *Internat. Semicond. Laser Conf. (ISLC'14)*, Palma de Mallorca, Spain (2014), Conf. Digest, pp. 50–51
49. E.J. Skogen, J.W. Raring, G.B. Morrison, C.S. Wang, V. Lal, M.L. Mašanović, L.A. Coldren, Monolithically integrated active components: a quantum-well intermixing approach. *IEEE J. Sel. Top. Quantum Electron.* **11**, 343–355 (2005)
 50. J.W. Raring, L.A. Johansson, E.J. Skogen, M.N. Sysak, H.N. Poulsen, S.P. DenBaars, L.A. Coldren, 40 Gb/s widely tunable low-drive-voltage electroabsorption-modulated transmitters. *J. Lightwave Technol.* **25**, 239–248 (2007)
 51. J.S. Barton, E.J. Skogen, M.L. Mašanović, S.P. DenBaars, L.A. Coldren, A widely tunable high-speed transmitter using an integrated SGDBR laser-semiconductor optical amplifier and Mach-Zehnder modulator. *IEEE J. Sel. Top. Quantum Electron.* **9**, 1113–1117 (2003)
 52. J.S. Barton, M.L. Mašanović, A. Tauke-Pedretti, E.J. Skogen, L.A. Coldren, Monolithically-integrated 40 Gb/s widely-tunable transmitter using series push-pull Mach-Zehnder modulator SOA and sampled-grating DBR laser, in *Opt. Fiber Commun. Conf. (OFC'05)*, Anaheim, CA, USA (2005), Techn. Digest, paper OTuM3
 53. X. Pommarede, N. Girard, S. Olivier, S. Malhouitre, A. Accard, G. Levaufre, A. Shen, D. Make, R. Brenot, F. Lelarge, J.-G. Provost, G.-H. Duan, Transmission over 50 km at 10 Gb/s with a hybrid III–V on silicon integrated tunable laser and electro-absorption modulator, in *Opt. Fiber Commun. Conf. (OFC'16)*, Anaheim, CA, USA (2016), Techn. Digest, paper M2C.7
 54. J.W. Raring, L.A. Johansson, E.J. Skogen, M.N. Sysak, H.N. Poulsen, S.P. DenBaars, L.A. Coldren, Single-chip 40 Gb/s widely-tunable transceivers with integrated SG-DBR laser. QW EAM, UTC photodiode, and low confinement SOA, in *Internat. Semicond. Laser Conf. (ISLC'06)*, Kohala Coast, HI, USA (2006), Conf. Digest, paper TuA1
 55. V. Lal, M.L. Mašanović, J.A. Summers, G. Fish, D.J. Blumenthal, Monolithic wavelength converters for high-speed packet-switched optical networks. *IEEE J. Sel. Top. Quantum Electron.* **13**, 49–57 (2007)

Hélène Debrégeas was born in France in 1972. She received the engineer degree from the Ecole Nationale Supérieure des Télécommunications (ENST) of Paris in 1994, and passed the aggregation of Mathematics in 1995. She joined Alcatel in 1997, where she focused on design, simulations and characterizations of semiconductor InP telecommunications components. She was first in charge of 10 Gb/s Electro-Absorption Modulator Lasers until an industrial transfer to Alcatel Optronics in 1999. Then she worked on tunable lasers within the joined laboratory Alcatel Thales III–V Lab, and passed her Ph.D. on that topic in 2006. She was involved within Bell Labs France and Bell Labs US in research on photonic integrated circuits, either monolithic on InP, or based on hybrid integration with PLCs. She spent 2 years in Bell Labs US to optimize hybrid integration. In this domain, she developed a 10 × 10 Gb/s hybrid transmitter and a widely tunable hybrid laser with ring resonators.

Chapter 6

Photodetectors

Andreas Beling and Joe C. Campbell

Abstract In optical communication systems semiconductor photodetectors are used for the optoelectronic conversion of the modulated light signal into the electrical domain. This chapter focuses on p–i–n, metal-semiconductor-metal (MSM), and avalanche photodiodes. The basic concepts of the light receiving process as well as advanced high-speed high-power photodiode types are introduced. Photodetectors based on group III–V materials and Silicon/Germanium are described.

6.1 Fundamentals

The light absorption process in a semiconductor photodetector for photogeneration of electron-hole-pairs is based on the internal photoelectric effect and requires the photon energy $h\nu$ to be at least equal to the bandgap energy E_g (bandgap equivalent wavelength: λ_g) of the absorber material. Only then is the available energy of one photon sufficient to excite an electron from the valence band to the conduction band leaving a hole in the valence band. For this band-to-band transition, the upper wavelength limit for photon absorption is given by:

$$\lambda_g [\mu\text{m}] = \frac{1.24}{E_g [\text{eV}]} \quad (6.1)$$

Under the influence of an electric field, that is established by an applied bias voltage, electrons and holes are swept across the absorber which results in a flow of photocurrent in the external circuit [1]. The external quantum efficiency η_{ext} quantifies the ability of the photodiode (PD) to transform light into an electrical current

A. Beling (✉) · J.C. Campbell
School of Engineering and Applied Science, Department of Electrical & Computer Engineering,
University of Virginia, 351 McCormick Rd., PO Box 400743, Charlottesville, VA 22904, USA
e-mail: andreas@virginia.edu

J.C. Campbell
e-mail: jcc7s@virginia.edu

and is defined as the number of charge carrier pairs generated per incident photon:

$$\eta_{ext} = \frac{I_{pd}}{q} \cdot \frac{h\nu}{P_{opt}} \tag{6.2}$$

where I_{pd} is the photogenerated current by the absorption of the optical input power P_{opt} at frequency ν , and q is the elementary charge (-1.602×10^{-19} C). Ideally $\eta_{ext} = 1$, that is each photon generates one electron hole pair. However, it will be shown below that in practice photodiodes usually exhibit $\eta_{ext} < 1$ because of several effects including finite absorber thickness, carrier recombination, optical reflections and coupling losses. A common figure of merit is the responsivity R_{pd} , defined as the ratio of photocurrent to optical input power. Based on (6.2) we write:

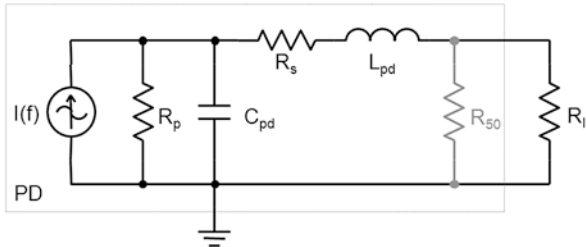
$$R_{pd} = \frac{I_{pd}}{P_{opt}} = \frac{\eta_{ext}\lambda \text{ [\mu m]} A}{1.24 W} \tag{6.3}$$

Using (6.3), $\eta_{ext} = 1$, and a wavelength of $\lambda = 1.55 \mu\text{m}$ we find that the maximum achievable responsivity is $R_{pd} = R_{ideal} = 1.25 \text{ A/W}$. Whenever R_{pd} depends on the state of polarization of the incoming light, the definition of the polarization dependent loss is useful:

$$PDL = 10 \log \left(\frac{R_{max}}{R_{min}} \right) \text{ [dB]} \tag{6.4}$$

Here, R_{max} and R_{min} are the maximum and minimum responsivities for all states of polarization. In telecommunication systems photodiodes are required to detect optical signals modulated at high data rates. Thus, another important figure of merit is the opto-electrical 3 dB bandwidth, which is defined as the frequency range from DC to the cut-off frequency f_{3dB} . The latter is the frequency at which the electrical output power has dropped by 3 dB below the power value at very low frequency. The RC-time constant and the carrier transit times are the two crucial bandwidth limitations of a photodiode. Considering the RC-effect, Fig. 6.1 shows a simple equivalent circuit of a lumped element photodetector for which the device length is much shorter than the electrical signal wavelength. The photodiode is described as an ideal current source $I(f)$ in parallel with the junction capacitance, C_{pd} , and resistance, R_p , and a series resistance, R_s . R_l is the external load resistor and is usually 50Ω . In order to achieve a matched transition to the load impedance, R_l , an optional termination resistor, R_{50} ($= 50 \Omega$), may be implemented close to the

Fig. 6.1 Equivalent circuit of a lumped element photodetector



photodiode. Thus, the effective load is reduced to 25Ω , but at the expense of losing half the output current. In most cases the parallel leakage current is small compared to the photocurrent and therefore R_p becomes very high and can be omitted. The inductance L_{pd} may originate from electrical interconnections or air bridges. It is usually in the pH-range and can be neglected in photodetectors with bandwidths up to 20 GHz. With these simplifications the RC-limited 3 dB cut-off frequency is calculated from the equivalent circuit as

$$f_{RC} = \frac{1}{2\pi R_{eff} C_{pd}} \quad (6.5)$$

with $R_{eff} = R_s + R_l R_{50}/(R_l + R_{50})$.

The second bandwidth constraint is the carrier transit time, which is the time a photogenerated electron or hole takes to travel through the active region prior to being collected by the contacts. Assuming uniform photogeneration in an absorber with thickness d_{abs} , the transit time-limited bandwidth, f_t , can be well estimated using [2]:

$$f_t \approx \frac{3.5\bar{v}}{2\pi d_{abs}} \quad (6.6)$$

where \bar{v} is the averaged carrier velocity. The resulting 3 dB bandwidth is given by the expression:

$$f_{3\text{ dB}} \approx \sqrt{\frac{1}{\frac{1}{f_{RC}^2} + \frac{1}{f_t^2}}} \quad (6.7)$$

Taking the product of the bandwidth (6.7) and quantum efficiency (6.2) one can define the bandwidth-efficiency product in units of [GHz]. As will be shown in the following paragraphs, the bandwidth-efficiency product of photodiodes is generally limited.

In the absence of light the photodiode's dark or leakage current dominates. Generally several effects contribute to the dark current with their actual magnitudes depending on the bias voltage, material properties, and detector design. The current that is common to all junction diodes is the diffusion current. However, in most photodiodes the diffusion current is considerably smaller than the generation current [3, 4], which originates in the depleted absorption layer from impurities within the bandgap and can be reduced by improving material quality. Additionally, tunneling and impact ionization currents can be observed once the electric field exceeds 100 kV/cm. While the tunneling current is generally undesirable, impact ionization can be used to provide an internal gain mechanism to amplify the photocurrent. Photodiodes that exploit impact ionization effects are referred to as avalanche photodiodes (APD) and will be discussed in Sect. 6.2.3.

Photocurrent and dark current generate shot noise, which, together with thermal noise, degrades the sensitivity of the photodiode. Shot noise accompanies any generated current within a photodetector and is related to the statistical nature of the

carrier transport and the photon detection process. The mean square noise current of shot noise for a photodiode is given by

$$\langle i_{shot}^2 \rangle = 2q(I_{pd} + I_d)\Delta f \quad (6.8)$$

I_{pd} is the photocurrent, I_d the dark current and Δf is the bandwidth.

The thermal noise or Johnson noise is due the thermal motion of electrons in conductors and is generated in all resistances of the photodiode. The mean square thermal noise current of a resistor R for a given bandwidth Δf is given by the expression

$$\langle i_{th}^2 \rangle = \frac{4kT\Delta f}{R} \quad (6.9)$$

where k is Boltzmann's constant and T is the temperature. It is worth noting that $\langle i_{th}^2 \rangle$ does not depend on the photocurrent and dark current whereas $\langle i_{shot}^2 \rangle$ does. Since shot noise and thermal noise are uncorrelated, the total noise is found from adding individual noise contributions as sums of squares. Once the total noise in a photodiode is known, the signal-to-noise ratio, SNR, can be determined. The electrical SNR is defined as the ratio of signal power to noise power and can be computed for a given average photocurrent, I_{pd} , using the relation

$$SNR = \frac{I_{pd}^2}{\langle i_{shot}^2 \rangle + \langle i_{th}^2 \rangle} \quad (6.10)$$

which assumes that the power varies as the square of the current.

An important measure in digital communication systems is the bit-error rate (BER) given by the probability of false identification of a bit by the decision circuit in the receiver. The decision circuit compares the sampled signal to a reference value, the decision threshold. If the signal is greater than the decision threshold, it indicates that a "1" was detected, otherwise a "0". As in binary systems there are only two possible signal levels, that for a "1", I_1 , and that for a "0", I_0 . Each of these signal levels may have a different average noise associated with it. In order to calculate the overall probability of a bit error, the SNRs of both signal levels have to be taken into account which leads to the definition of the Q -factor:

$$Q = \frac{I_1 - I_0}{\sqrt{\langle i_1^2 \rangle} + \sqrt{\langle i_0^2 \rangle}} \quad (6.11)$$

In this expression I_1 , I_0 , and $\langle i_1^2 \rangle$, $\langle i_0^2 \rangle$ are the photocurrents and the Gaussian mean square noise currents associated with the received bits "1" and "0", respectively. Assuming a constant but optimum threshold level in the decision circuit, the BER is related to the Q -factor by the following equation:

$$BER = \frac{1}{2} \operatorname{erfc} \left(\frac{Q}{\sqrt{2}} \right) \approx \frac{\exp(-Q^2/2)}{Q\sqrt{2\pi}} \quad (6.12)$$

where erfc represents the complementary error function. The approximate form of (6.12) is accurate for $Q > 3$. A bit-error rate of 10^{-12} or a Q -factor of 7 corresponds to a probability of $1 : 10^{12}$ that a bit is identified incorrectly and is commonly called “error-free” reception.

The receiver sensitivity is a common figure in optical communication systems. It is the minimum received average optical power P_{rec} that is necessary to achieve error-free detection at a given bitrate. Considering on-off modulated signals with optical power P_1 and P_0 in bits “1” and “0”, respectively, the average power is $0.5(P_1 + P_0)$. Here we consider a more general case, that is $P_0 \neq 0$. The fact that some optical power is received during “0” bits is common to most fiber links and is quantified by the extinction ratio, $r_e = P_0/P_1$. Using (6.3) and (6.11), the receiver sensitivity can be approximated as:

$$P_{rec} = \left(\frac{1 + r_e}{1 - r_e} \right) \frac{Q}{2R} \left(\sqrt{\langle i_1^2 \rangle} + \sqrt{\langle i_0^2 \rangle} \right) \approx \left(\frac{1 + r_e}{1 - r_e} \right) \frac{Q}{R} \sqrt{\langle i_{ih}^2 \rangle} \quad (6.13)$$

where shot noise from I_{pd} and I_d has been neglected.

It should be noted, that the sensitivity is usually used to characterize the entire optical front-end including photodiode and electrical amplifiers. This requires modification of (6.13) in order to include noise contributions from the amplifier. Similarly, if the receiver contains an optical pre-amplifier, the amplifier’s noise figure has to be taken into account. In this case P_{rec} is typically referred to the optical power before amplification.

The ultimate detection limit of an ideal receiver (i.e. no thermal noise, no dark current, 100% quantum efficiency, and $r_e = 0$) is given by the quantum limit. Assuming an ideal receiver, the sensitivity for a BER of 10^{-12} is given by [5]:

$$P_{min}^* \approx 13.5 \cdot h\nu \cdot B \quad (6.14)$$

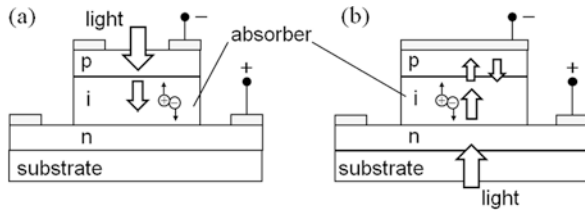
where $h\nu$ is the photon energy, B is the bitrate and 13.5 is the average number of photons per bit. For example, at a bitrate of 40 Gbit/s and an optical signal wavelength of 1.55 μm , the quantum limited sensitivity P_{min}^* is -42 dBm.

6.2 Photodiode Types

6.2.1 p-i-n Photodiode

In order to achieve a high optoelectronic conversion efficiency and high bandwidth the p-i-n photodiode is widely used. The p-i-n PD consists of an intrinsic absorber, sandwiched between highly doped n^+ - and p^+ -layers which give rise to a space charge region. Compared to a simple p-n-junction, this design allows for a lower junction capacitance and provides an additional degree of freedom in designing the thickness of the depleted high-field region. In contrast to a homojunction PD where

Fig. 6.2 (a) Top and (b) back illuminated p–i–n photodiode



the p-, i-, and n-layers have the same bandgap, a heterostructure p–i–n PD potentially provides higher speed, as slow diffusion photocurrents arising from carriers generated in undepleted material are suppressed. In this design the contact layers exhibit bandgap energies higher than the photon energy and are consequently transparent at the operation wavelength. In order to avoid slow carrier trapping effects at the heterojunction interfaces grading of the bandgap can be employed to smooth the discontinuities in the band structure [6].

A schematic of a top-illuminated p–i–n photodiode is shown in Fig. 6.2(a); this simple structure has become a standard commercial product. For high-speed operation the device is reverse biased by an externally applied voltage to completely deplete the absorber and create an electric field to facilitate carrier transport. Once an electron-hole-pair is created, the carriers drift at their saturation velocities in opposite directions toward the electrodes and contribute to the photocurrent. The device responsivity can be written as

$$R_{pd} = R_{ideal}(1 - R_0)(1 - e^{-\alpha d_{abs}}) \quad (6.15)$$

where α is the absorption coefficient, d_{abs} is the absorber thickness and R_0 is the reflectance at the air-semiconductor interface. Assuming negligible carrier trapping at energy band discontinuities the bandwidth is well approximated by (6.7).

It is well known that for this device structure there is a performance trade-off between quantum efficiency and bandwidth associated with the thickness of the absorber region. As thicker absorption layer provides higher quantum efficiency this also results in longer carrier transit time which reduces the bandwidth. A second bandwidth constraint is due to the photodiode RC time constant. Since the resistance is usually governed by the fixed load resistor (50 Ω), reducing the RC time constant is achieved by decreasing the device capacitance. In a p–i–n photodiode this can be achieved by minimizing the active junction area ($C_{pd} \sim A$) and maximizing the depleted absorber thickness ($C_{pd} \sim d^{-1}$), which, in turn, results in longer transit times. As a result of these considerations, the bandwidth-efficiency-product of normal-incidence p–i–n photodiodes is limited to approximately 20 GHz [7], which enables operation up to 40 Gbit/s. However, due to device miniaturization, integration of matching circuits on chip and improvements in the vertical layer structure, several very high-speed vertically-illuminated p–i–n photodiodes with acceptable quantum efficiencies have been demonstrated. Wey et al. achieved a 3 dB bandwidth of 110 GHz with a back-illuminated p–i–n PD [6]. Even though a thin absorber (200 nm) was employed the external quantum efficiency was 30% as an en-

hanced efficiency was obtained by “double pass” of the light from the top electrode (Fig. 6.2(b)). To increase the resistance-capacitance (RC)-bandwidth limitation a matched resistor (50Ω) was integrated on chip. Hence, the effective load was reduced to 25Ω , however, since the resistor forms a current divider with the load, half the output current was lost which resulted in a 6-dB reduction in output power at low frequencies. If a reduced spectral width can be accepted, the resonant cavity enhanced (RCE) photodetector represents another solution. With the integration of mirrors at the top and bottom of the structure multi-pass absorption can be achieved, leading to doubled quantum efficiency as reported in [8].

6.2.2 Metal-Semiconductor-Metal Photodetector

A metal-semiconductor-metal (MSM) photodetector consists of an undoped semiconductor absorption layer on which two interdigitated metal electrodes have been deposited. Hence, it can be basically described as two Schottky diodes connected back-to-back. For operation a voltage has to be applied to the electrodes to completely deplete the absorber and generate an electric field within the absorber (Fig. 6.3). Since one of the diodes is in reverse bias while the other is forward biased, the MSM detector exhibits symmetric current-voltage and capacitance-voltage characteristics. Figure 6.4 shows the simplified band structure of an MSM detector under bias condition. Due to the Schottky barriers, Φ_n and Φ_p , formed at the metal-semiconductor interfaces, carriers are prevented from entering the semiconductor from the metal contacts which lowers the dark current. This is in contrast to photoconductors which consist of Ohmic metal-semiconductor contacts. Under illumination photogenerated carriers drift to the electrodes and contribute to the photocurrent. Compared to p-i-n PDs this type of planar photodetector generally exhibits lower capacitance, a simple fabrication process, and is well suited for monolithic integration with metal-semiconductor field-effect transistors (MESFET) [9]. However, the responsivity of top-illuminated MSM photodetectors is significantly lower

Fig. 6.3 MSM photodetector

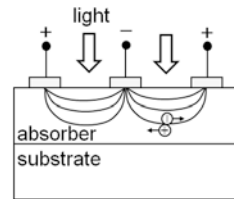
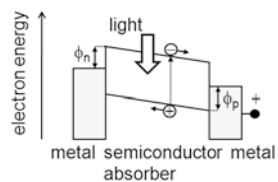


Fig. 6.4 Schematic band diagram of MSM PD



compared to p-i-n PDs due to shadowing of the electrode fingers. This issue has been addressed by using either semitransparent electrodes made, for example, from cadmium tin oxide [10] or thin metal [11], or by back-illumination [12, 13]. Using back-illumination through the substrate, the responsivity can be at least doubled [13]. Similar to p-i-n photodiodes the bandwidth of an MSM photodetector is generally governed by RC- and carrier transit time effects. Since the MSM PD has lower capacitance per unit area compared to PDs based on p-n junctions, its bandwidth is usually determined by carrier transit times. Although the optical radiation propagates perpendicular to the direction of the charge carrier transport (Fig. 6.3), the MSM PD suffers from a trade-off between the quantum efficiency and bandwidth: In order to increase the quantum efficiency of a front-illuminated MSM detector the absorber has to be made thicker and the electrode finger spacing needs to be enlarged, which, in turn, leads to an increase in carrier transit times and hence lower bandwidth. Back-illuminated MSM photodetectors are even more adversely affected by longer transit times since the carriers are predominantly generated further away from the high electric field regions near the top electrodes. Compared to their front-illuminated counterparts they achieve lower bandwidths. In some cases the bandwidth reduction is as great as 50% [13].

In the last three decades, high-performance GaAs-based MSM photodetectors operating in the 0.85 μm -wavelength window have been extensively studied. Owing to their large Schottky barrier of 0.7 eV, these MSM photodetectors have achieved low dark currents and high speed [14]. For operation at the longer telecommunication wavelengths MSM photodetectors with a narrow-bandgap InGaAs absorber are required. However, as the Schottky barrier height of undoped InGaAs is only 0.2 eV, the direct deposition of the electrode on the InGaAs results in unacceptably large leakage currents at low bias voltage. To solve this problem a thin undoped barrier-enhancement layer (GaAs, InAlAs or InP) has been introduced between the electrode and the absorption layer [9]. Since the resulting bandgap discontinuity may be responsible for some performance degradation due to charge pile-up at the interface, additional compositionally graded layers or a graded superlattice region have been placed between the hetero-interfaces to improve device performance [15].

Due to the low capacitance of the MSM structure very large area detectors with notable bandwidth have been reported. In [16] a $350 \times 350 \mu\text{m}^2$ MSM detector with 0.4 A/W responsivity and 900 MHz bandwidth has been achieved. A $1 \times 1\text{-mm}^2$ area MSM photodetector with 1.02 A/W responsivity at 1.53 μm wavelength and 210 MHz bandwidth was reported in [17]. To reduce carrier transit times and thus achieve higher speed the electrode finger widths and gaps were further downscaled into the sub-micron range. By applying direct electron beam lithography, front-illuminated InGaAs MSM photodetectors with 0.2 μm feature size finger electrodes with 70 GHz bandwidth have been demonstrated [18]. Recently, a compact MSM waveguide-integrated Germanium-on-insulator photodetector with 10 fF capacitance and operating speed sufficient to support data rates at 40 Gbit/s was demonstrated in [19]. The barrier height and the dark current of a 30- μm long photodetector at 1 V bias voltage were determined to be 0.08 eV and 90 μA , respectively.

6.2.3 Avalanche Photodiodes

Unlike the previously described photodiode structures, the avalanche photodiode (APD) can achieve substantially better sensitivity due to an internal gain mechanism. In an APD the photogenerated carriers are accelerated in a high-field drift region to such an extent that they generate new electron-hole pairs by impact ionization. Thus, a single photon is able to produce multiple electron-hole pairs. The multiplication factor M quantifies the photocurrent enhancement and is typically between 10 and 100 for fiber optic receivers. Although APDs require more complex epitaxial wafer structures and bias circuits, they have been successfully deployed in optical receivers that operate up to 10 Gbit/s. Due to their gain APDs provide higher sensitivity in optical receivers (PD + amplifier) than p-i-n photodiodes [20–23]. This advantage, however, applies only to thermal-noise-limited receivers since the gain mechanism is accompanied by an excess noise which depends on the carrier multiplication statistics. The excess noise also affects the speed of an APD through the avalanche build-up time which gives rise to the gain-bandwidth product of an APD.

The multiplication region of an APD plays a critical role in determining its performance, specifically the gain, the multiplication noise, and the gain-bandwidth product. According to McIntyre's local-field avalanche theory [24–26], both the noise and the gain-bandwidth product of APDs are determined by the electron-, α , and hole-, β , ionization coefficients of the semiconductor in the multiplication region, or more specifically, the ionization coefficient ratio, $k = \beta/\alpha$ if $\beta < \alpha$ and $k = \alpha/\beta$ if $\beta > \alpha$. The shot noise current for mean gain M is given by

$$\langle i_{shot,APD}^2 \rangle = 2qM^2(I_{pd} + I_d)F(M)\Delta f \quad (6.16)$$

where $F(M)$ is the excess noise factor, which arises from the random nature of impact ionization. Under the conditions of uniform electric fields and injection of the carrier with the highest ionization coefficient, the excess noise factor is

$$F(M) = kM + (1 - k) \left(2 - \frac{1}{M} \right) \quad (6.17)$$

Equation (6.17) has been derived under the condition that the ionization coefficients are in local equilibrium with the electric field, hence, the designation “local field” model. This model assumes that the ionization coefficients at a specific position are determined solely by the electric field at that position. It is clear from (6.17) that lower noise is achieved when $k \ll 1$. The gain-bandwidth product results from the time required for the avalanche process to build up or decay; the higher the gain, the higher the associated time constant and, thus, the lower the bandwidth. Emmons [27] has shown that the frequency-dependent gain can be approximated by the expression

$$M(2\pi f) = \frac{M_0}{\sqrt{1 + (2\pi f M_0 k \tau)^2}} \quad (6.18)$$

where M_0 is the DC gain and τ is approximately (within a factor of ~ 2) the carrier transit time across the multiplication region. It follows from this expression that for $M_0 > 1/k$ the frequency response is characterized by a constant gain bandwidth-product that increases as k decreases.

There are three documented methods to achieve low excess noise in an avalanche photodiode. The best-known approach is to select a material with low-noise characteristics, i.e., $k \ll 1$, such as Si [28–31]. Si APDs were widely used in first-generation optical fiber communication systems which operated in the wavelength range 800 nm to 900 nm [32]. Since the attenuation and dispersion characteristics of optical fibers favor operation in the now standard telecommunication wavelength range of 1.3 μm to 1.6 μm , subsequent generations employed materials appropriate for longer wavelength operation, primarily those lattice-matched to InP. One such material, $\text{In}_{0.53}\text{Ga}_{0.47}\text{As}$ (referred to in the following as InGaAs), which has a bandgap energy of 0.75 eV, is widely used as the absorbing layer in a wide range of telecommunication detectors. However, the narrow bandgap, which enables high responsivity in the short wavelength infrared (SWIR) spectrum also results in excessive dark current due to tunneling at the high electric fields required for impact ionization in InGaAs homojunctions [33, 34]. This led to the development of separate absorption and multiplication (SAM) APD structures [35]. In these APDs the p–n junction and thus the high-field multiplication region is located in a wide bandgap semiconductor such as InP where tunneling is insignificant and absorption occurs in an adjacent InGaAs layer. By properly controlling the charge density in the multiplication layer, it is possible to maintain a high enough electric field to achieve good avalanche gain while keeping the field low enough to minimize tunneling and impact ionization in the InGaAs absorber. However, the frequency response of SAM APDs, as originally implemented, was very poor owing to accumulation of photo-generated holes at the absorption/multiplication heterojunction interface [36]. To eliminate the slow release of trapped holes a transition region consisting of one or more lattice-matched, intermediate-bandgap InGaAsP layers was introduced [37, 38]. A second modification to the original SAM APD structure has been the inclusion of a high-low doping profile in the multiplication region [39–41]. In this structure the wide-bandgap multiplication region consists of a lightly doped layer where the field is high, and an adjacent, doped charge layer or field control region. This type of APD, which is frequently referred to as the SACM structure with the “C” representing the charge layer, decouples the thickness of the multiplication region from the charge density constraint in the SAM APD. Most of the initial work on InP/InGaAsP/InGaAs SAM and SACM APDs utilized mesa structures owing to their fabrication simplicity and reproducibility. However, the consensus that planar structures can effectively suppress edge breakdown spurred their development. Figure 6.5 shows a schematic cross section of an InP/InGaAsP/InGaAs SACM APD with a double diffused floating guard ring [42]. The adjacent graph shows the electric field profile normal to the surface and illustrates how the charge layer is used to tailor the relative fields in the multiplication and absorption layers.

Low excess noise and high gain-bandwidth product have also been achieved by submicron scaling of the thickness of the multiplication region, w_m . This is somewhat counterintuitive since it appears to contradict the local field model. As w_m

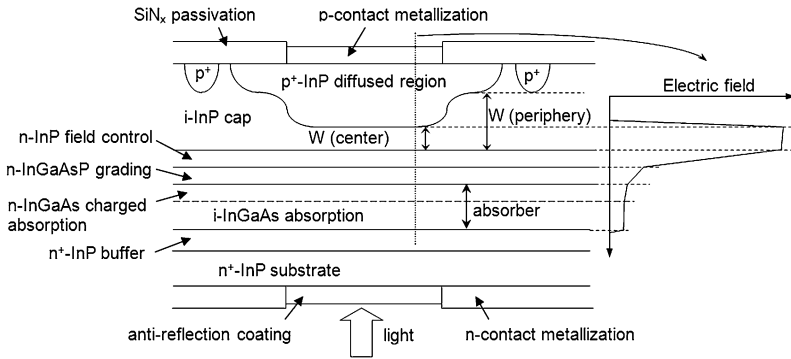


Fig. 6.5 Schematic cross section of InP/InGaAsP/InGaAs SACM APD with double-diffused floating guard ring configuration [42]

is reduced, in order to maintain the same gain, the electric field intensity must increase in order to reduce the distance between ionization events. However, for high electric fields the electron and hole ionization coefficients tend to merge so that k approaches unity. Consequently, based on the excess noise expression in (6.17), higher excess noise would be expected for the same gain. However, in contrast to the basic assumption of the local-field model, it is well known that impact ionization is non-local in that carriers injected into the high field region are “cool” and require a certain distance to attain sufficient energy to ionize [43]. This also applies to carriers immediately after ionization because their final states are typically near the band edge. The distance in which essentially no impact ionization occurs is frequently referred to as the “dead space”. If the multiplication region is thick, the dead space can be neglected and the local field model provides an accurate description of APD characteristics. However, for thin multiplication layers the non-local nature of impact ionization has a profound impact as the ionization process becomes more deterministic. Several models [44–50] have successfully been developed to accurately include the effect of the dead space. Practical noise reduction in thin APDs has been demonstrated for a wide range of materials [51–53]. Figure 6.6 shows the excess noise figure versus gain for GaAs APDs with w_m in the range from 0.1 μm to 0.8 μm [46]. The dashed lines are plots of (6.17) for $k = 0.2$ to 0.5. These lines are not representative of the actual k values; they are presented solely for reference because the k value has become a widely used indirect figure of merit for excess noise. For constant gain, it is clear that the excess noise falls significantly with decreasing w_m .

While shrinking the multiplication region thickness is an effective approach to noise reduction, it should be noted that this is relative to the characteristic noise of the bulk (thick) material. Thus, it appears that lower noise can be achieved by beginning with “low-noise” semiconductors. For this reason, InAlAs, which can be grown lattice-matched on InP substrates, is an attractive candidate for telecommunications APDs. Watanabe et al. [54] measured the ionization coefficients for InAlAs and found that $k = \beta/\alpha \sim 0.3$ to 0.4 for electric fields in the range from

Fig. 6.6 Comparison of calculated noise curves (*solid lines*) with experimental data for GaAs homojunction APD of different thickness 0.1 μm (\bullet), 0.2 μm (\blacksquare), 0.5 μm (\blacktriangle), and 0.8 μm (\blacktriangledown) [46]

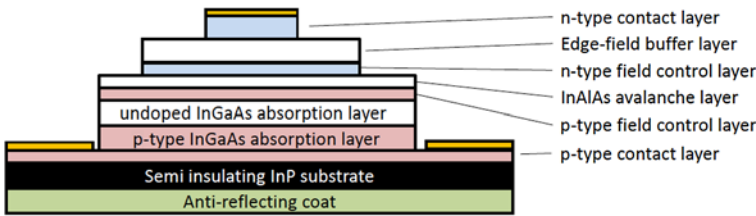
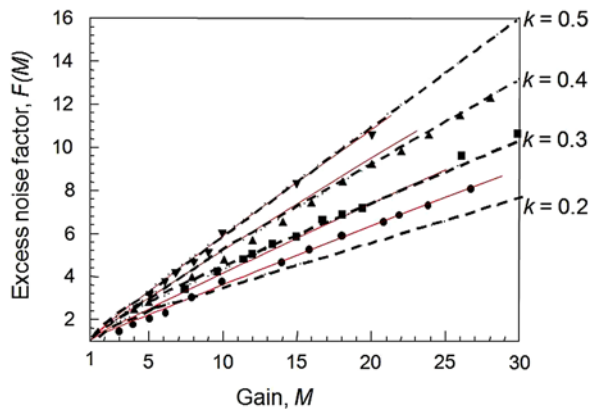


Fig. 6.7 Schematic cross-sectional view of an inverted InAlAs/InGaAs p-down APD with triple-mesa structure [59]

400 to 650 kV/cm which compares favorably with $k = \alpha/\beta \sim 0.4$ to 0.5 for InP. Thin layers of InAlAs have also been incorporated into the multiplication region of SACM APDs. Ning Li et al. [55] reported that mesa-structure undepleted-absorber InAlAs APDs with 180 nm-thick multiplication regions exhibited excess noise equivalent to $k = 0.15$ and a gain-bandwidth product of 160 GHz. Several planar InAlAs/InGaAs SACM APDs have also been developed. An AlInAs/InGaAs planar SACM APD without a guard ring has achieved gain >40 , high external quantum efficiency (88%), 10 GHz low-gain bandwidth, and a gain-bandwidth product of 120 GHz [56, 57]. Higher operating bandwidth and gain-bandwidth product have been achieved with a triple mesa p-down InAlAs/InGaAs APD. A schematic cross section of the structure is shown in Fig. 6.7. In order to optimize the transit time, the InGaAs absorber is partially depleted similar to that in partially depleted absorber UTC-type photodiodes [58]. The 100 nm InAlAs multiplication layer enabled a gain-bandwidth product of 235 GHz [59]. A triple-mesa configuration is employed to eliminate edge breakdown by reducing the electric field at the periphery of the device [60]. Devices designed for 25 Gbit/s have achieved 72% external quantum efficiency, bandwidths of 18.5 GHz and 23 GHz at gains of $M = 10$ and 4.47, respectively, and an excess noise factor corresponding to $k = 0.2$. A four channel receiver utilizing these APDs demonstrated 100GbE over 50 km; all channels achieved receiver sensitivities better than -20 dBm at 10^{-12} BER [59].

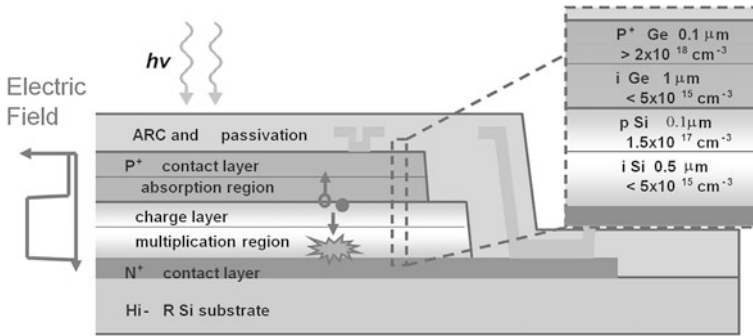
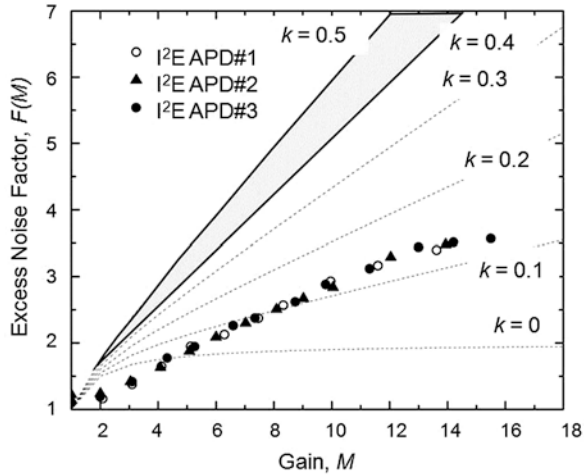


Fig. 6.8 Schematic cross section of a Ge/Si SACM APD [64]

The low noise of Si APDs has motivated several approaches to merge Si multiplication regions with long-wavelength absorbers. Si/InGaAs APDs have been fabricated by wafer bonding [61–63]. These APDs have achieved low dark current (4×10^{-5} A/cm² @ $M = 50$) [62], excess noise levels comparable to Si homojunction devices ($k \sim 0.02$) and bandwidths up to 4.8 GHz [61]. However, these APDs have not displaced InP/InGaAs SACM APDs owing to materials issues related to the bonded interface between InGaAs and Si. The SACM structure has been successfully applied to a monolithically grown Ge/Si APD in which light absorption and carrier multiplication occur inside Ge and Si, respectively [64]. A schematic cross-section of the device structure is shown in Fig. 6.8. A 1 μm -thick Ge absorber was grown on the Si multiplication layer (0.5 μm) by chemical vapor deposition. A Si charge layer was used to maintain a low electric field at the SiGe interface. Of particular note, these APDs achieved gain-bandwidth product of 340 GHz, which is two to three times higher than InP/InGaAs APDs. The effective noise factor, k , was only 0.09. Optical receivers built with these APDs demonstrated a sensitivity of -28 dBm at 10 Gbit/s and a bit error rate (BER) of 10^{-12} [64]. Using a similar structure, M. Huang et al. reported 18 GHz at a gain of 8, responsivity = 0.55 A/W at 1310 nm, and successful operation at 25 Gbit/s; the receiver sensitivity was -20 dBm [65].

It has been shown that the noise of APDs with thin multiplication regions can be reduced even further by incorporating new materials and impact ionization engineering (I²E) with appropriately designed heterostructures [66–73]. Structurally, I²E is similar to a truncated multiple quantum well, however, operationally there is a fundamental difference in that these APDs do not invoke heterojunction band discontinuities. Their function relies instead on the differences in threshold energies for impact ionization between adjacent wide-bandgap and narrower-bandgap materials. The structures that have achieved the lowest excess noise to date, utilize multiplication regions in which electrons are injected from a wide bandgap semiconductor into adjacent low bandgap material. Recently, InGaAlAs/InP implementations that operate at the telecommunications wavelengths have been reported. Using both a single-well structure and a pseudo-graded bandgap based on InAlAs/InGaAlAs materials Wang et al. [72] demonstrated excess noise equivalent to $k \sim 0.12$ and dark

Fig. 6.9 Excess noise factor, $F(M)$, versus gain for an SACM APD with I^2E $\text{In}_{0.52}\text{Ga}_{0.15}\text{Al}_{0.33}\text{As}/\text{In}_{0.52}\text{Al}_{0.48}\text{As}$ multiplication region [73]



current comparable to that of homojunction InAlAs APDs. Duan et al. have incorporated a similar I^2E multiplication region into an MBE-grown InGaAlAs I^2E SACM APD [73]. Based on Monte Carlo simulations of similar $\text{GaAs}/\text{AlGaAs}$ I^2E APDs [69], it can be inferred that there are relatively few ionization events in the $\text{In}_{0.52}\text{Al}_{0.48}\text{As}$ layer, owing to the combined effects of “dead space” and the higher threshold energy in $\text{In}_{0.52}\text{Al}_{0.48}\text{As}$. Figure 6.9 shows the excess noise factor, $F(M)$, versus gain. The dotted lines in Fig. 6.9 are plots of $F(M)$ for $k = 0$ to 0.5. For $M \leq 4$, it appears that $k < 0$, which is unphysical and simply reflects the inapplicability of the local field model for this type of multiplication region. At higher gain, the excess noise is equivalent to a k value of ~ 0.12 . For reference, the excess noise factor for $\text{InP}/\text{In}_{0.53}\text{Ga}_{0.47}\text{As}$ SACM APDs is shown as the shaded region in Fig. 6.9.

Interest in extending the transmission of optical communications into the $2\ \mu\text{m}$ band has been stimulated by the development of hollow core photonic bandgap fibers. Detectors that operate in the mid-wave infrared (MWIR) spectrum are not as advanced as those in the SWIR. A promising candidate for $2\ \mu\text{m}$ APDs utilizes InAs as the gain material. InAs APDs have also demonstrated $k \sim 0$ with moderately low dark current at room temperature [74, 75]. InAs APDs employing $10\ \mu\text{m}$ -thick intrinsic regions and AlAsSb blocking layer to suppress electron diffusion current achieved gain as high as ~ 300 at $15\ \text{V}$ bias. The gain-bandwidth product was $> 500\ \text{GHz}$, however, the bandwidth was transit-time limited in the range 2 to 3 GHz independent of gain owing to the thick depletion width required to minimize the tunneling component of the dark current.

6.2.4 Advanced Photodiode Structures

Driven by the requirements of coherent fiber optic links and high-speed analogue systems there has been increased interest in high-speed photodiodes that achieve the

requisite bandwidths without sacrificing responsivity, linearity, or output power signal levels [76–78]. In analogue fiber optic links high output photocurrent levels help to minimize the noise figure and hence increase the dynamic range [79, 80]. However, there are several physical mechanisms that impact saturation in photodiodes, including space-charge screening [81, 82], and thermal [83, 84] effects. The space charge effect has its origin in the spatial distribution of the photogenerated carriers as they transit the depletion layer. At high current densities, as electrons and holes travel in opposite directions, an internal space-charge field is generated that opposes the bias electric field. For sufficiently high optical input power levels, the space-charge induced electric field can be strong enough to make the bias electric field collapse, which will result in reduced carrier drift velocities, longer transit times, and hence RF photocurrent compression [85]. Higher applied voltages help to mitigate these effects, however, eventually the added Joule heating increases junction temperatures which can cause device failure. The thermal limit is determined by the heat dissipation characteristics of the constituent semiconductor layers, the photodiode geometry, and by the heat sink design. Joule heating can result in temperatures as high as 500 °C in the depletion region [84] which can cause device thermal and/or electrical failure. When large output photocurrent is delivered to the load, the voltage drop across the load and the device series resistance can effectively remove the available voltage bias from the depletion region and thus negatively impact the photodiode saturation. A measure of the photodiode saturation is the saturation current which is defined as the average photocurrent at which the electrical output power at the cut-off frequency deviates by -1 dB from an ideal current-power relation at the load resistor.

To address the space-charge effect several photodiode structures have been developed including the dual-depletion region (DDR) photodiode [86], the uni-traveling carrier (UTC) photodiode [87, 88] and the partially-depleted-absorber (PDA) photodiode [89].

The DDR PD is characterized by a transparent drift layer between the intrinsic absorber and the n-type contact layer (Fig. 6.10(a)). Compared to a p–i–n PD with the same depleted absorber thickness it allows for a reduced junction capacitance for the same hole transit time. In the structure the photogenerated holes transit only the InGaAs absorbing layer whereas the electrons travel across both the absorbing layer and the InP drift layer. Since electrons are faster than holes, the overall bandwidth in otherwise RC-limited devices can be reasonably increased when the layer thicknesses are designed properly. To date, DDR PDs with bandwidths up to 50 GHz and 0.7 A/W responsivity have been published [90]. Using a graded-index (GRIN) lens for uniform illumination, which mitigates the space-charge effect [81], saturation photocurrents of 45 mA at 10 GHz were achieved [91].

The band diagram of the UTC PD is schematically shown in Fig. 6.10(b). The active part of the UTC PD consists of a p-type narrow-bandgap light absorption layer and an undoped, wide-bandgap (transparent) depleted carrier-collection layer. The photogenerated minority electrons in the neutral absorption layer are transported by diffusion and/or drift into the depleted collection layer. In order to accelerate the electron diffusion process, a built-in electric field can be generated in the p-doped

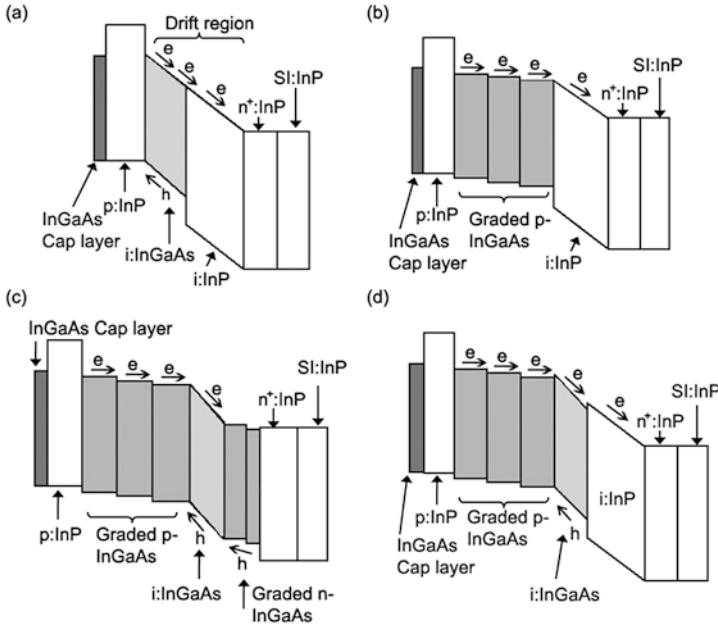


Fig. 6.10 Schematic band diagrams of (a) DDR PD, (b) UTC PD, (c) PDA PD and (d) MUTC PD with InGaAs absorbing layers and InP contact layers on semi-insulating (SI) InP substrate. The transit paths of photogenerated electrons (e) and holes (h) are indicated

absorber by well-controlled bandgap- or doping-grading. Once the electrons reach the high-field collection layer, they drift toward the n-contact at a high saturation velocity. On the other hand, since the absorption layer is quasi-neutral, photogenerated majority holes respond very fast within the dielectric relaxation time by their collective motion. This is an essential difference from the conventional p–i–n PD, in which both electrons and holes contribute to the response current and the low-velocity hole-transport dominates the speed performance and exacerbates the space-charge effect [92]. Since electrons maintain their high velocity at relatively low electric fields, the UTC PD can achieve high speed and high saturation output photocurrent even at low bias voltage [93].

In the UTC PD the transit time for electrons has two components corresponding to the undepleted absorber and the drift region with widths W_A , and W_C , respectively. The total transit-time is [94]:

$$\tau_i = \frac{W_C}{3.5\bar{v}} + \left[\frac{W_A^2}{3D_e} + \frac{W_A}{v_{th}} \right] \tag{6.19}$$

where D_e is the electron diffusion coefficient and v_{th} is the electron thermal velocity. $W_A^2/3D_e$ is the diffusion transit time and W_A/v_{th} is the correction factor associated with the finite thermal velocity.

The reduction of absorber and drift region widths and the miniaturization of the active area has led to UTC photodiodes that achieved high saturation current and

very high-speed. Shimizu et al. reported a $20\text{-}\mu\text{m}^2$ back-illuminated UTC PD with a 3 dB bandwidth of 152 GHz, an output peak voltage of 0.7 V, and 13% external quantum efficiency [95]. A UTC PD with bandwidth of 220 GHz at $25\ \Omega$ effective load and 0.13 A/W was presented in [96]. In addition, the carrier transit time in UTC photodiodes can be further reduced by exploiting the velocity overshoot of electrons in the depletion layer [97]. By introducing an additional p-type charge layer between collector and n-contact layer, the electric field inside the structure can be adjusted to benefit from the electron velocity overshoot [98]. Using this structure Wu et al. have reported a $64\ \mu\text{m}^2$ device having a 3 dB bandwidth of 120 GHz at $25\ \Omega$ effective load. The back-illuminated PD with an integrated micro-lens on the substrate showed a responsivity of 0.15 A/W [98]. Recently, a similar device flip-chip bonded onto an AlN substrate for improved heat sinking achieved a saturation photocurrent of 37 mA [99].

In [58] Li et al. proposed a structure where a thin InGaAs depletion layer was combined with undepleted InGaAs absorbers to increase responsivity (Fig. 6.10(c)). This structure is called a partially-depleted-absorber (PDA) photodiode and provides higher responsivity than a UTC PD with the same undepleted absorber thickness. Balancing the hole and electron densities within the depletion region was previously suggested as a technique for minimizing the space charge effect and for increasing photocurrents [85]. In the PDA, photodiode charge balance is accomplished by the p-doped absorber and an n-doped absorber on each side of the i-region. The p-doped absorber injects electrons into the i-region while the n-doped absorber injects holes. In the implementation, electron injection is stronger than that of holes due to the different thicknesses of the absorbers on each side of the i-layer. Since thin depletion layers are essential to obtain high currents, the PDA PD was designed with a thinned i-layer (250 nm) which reduces space-charge screening and minimizes thermal effects across the depletion layer [92]. Due to the poor thermal conductivity of InGaAs high-power InP/InGaAs PDs need to avoid thick InGaAs depletion layers to prevent thermally-induced degradation and potential device failure at high optical photocurrents [85]. The measured compression photocurrent of a back-illuminated $8\ \mu\text{m}$ -diameter PDA PD was 24 mA at 48 GHz with responsivity of 0.6 A/W [58].

A hybrid structure of UTC and PDA has been proposed by Jun et al. in [100]. This structure, called a modified UTC (MUTC), is formed by inserting an undoped i-InGaAs layer between the p-type InGaAs absorber and the InP drift layer (Fig. 6.10(d)). Thus the MUTC PD provides an additional design parameter which allows higher responsivity and higher bandwidth when the layer design is optimized [101]. The epitaxial layer structure of an MUTC PD that reached very high saturation current is shown in Fig. 6.11 [102]. The InGaAs absorber region was comprised of a 150 nm-thick depleted layer and 700 nm step-graded p-doped layers. The latter create a quasioelectric field that enhances the electron diffusion toward the drift region [95]. The 900 nm InP electron drift layer was slightly n-type doped for space charge compensation [103]. The incorporated positive charges pre-distort the electric field to partially compensate the field change caused by the space charge in the presence of high photocurrents. A “cliff” layer was incorporated between

Layer	Material	Doping (cm^{-3})	Thickness (nm)
p-contact	InGa _{0.47} As _{0.53}	p ⁺ doping, 2×10^{19}	50
Block layer	InP	p ⁺ doping, 1.5×10^{18}	100
Quaternary layer	InGaAsP, Q 1.1	p ⁺ doping, 2×10^{18}	15
Quaternary layer	InGaAsP, Q 1.4	p ⁺ doping, 2×10^{18}	15
Graded doped absorber	InGa _{0.47} As _{0.53}	p ⁺ doping, $5 \times 10^{17} \sim 2 \times 10^{18}$	700
Depleted absorber	InGa _{0.47} As _{0.53}	n ⁻ doping, 1×10^{16}	150
Quaternary layer	InGaAsP, Q 1.4	n ⁻ doping, 1×10^{16}	15
Quaternary layer	InGaAsP, Q 1.1	n ⁻ doping, 1×10^{16}	15
Cliff layer	InP	n doping, 1.4×10^{17}	50
Drift layer	InP	n ⁻ doping, 1×10^{16}	900
n-contact	InP	n ⁺ doping, 1×10^{19}	1000
Substrate	InP, semi-insulating, double side polished		

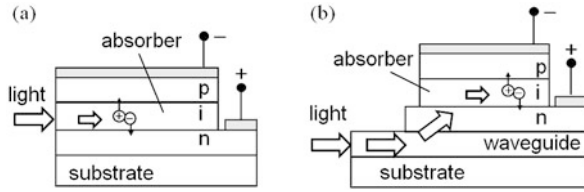
Fig. 6.11 Epitaxial layer structure of charge-compensated MUTC photodiode [102, 106]. Q 1.1 (1.4) represents quaternary GaInAsP with 1.1 (1.4) μm bandgap equivalent wavelength

the absorber and charge-compensated transparent drift layers to enhance the electric field in the depleted absorber layer [104, 105]. To improve thermal dissipation these MUTC-PDs were flip-chip bonded onto high-thermal conductivity submounts. Using a Au–Au thermo-compression bonding process the maximum dissipated DC power ($I_{pd} \times V_{bias}$) of the photodiodes was increased by up to 90% as the result of flip-chip bonding onto an AlN substrate [106]. Even higher values were obtained when using diamond substrates. Photodiodes with diameters of 28 μm and 50 μm achieved RF output powers of 26 dBm at 25 GHz, and 32.7 dBm at 10 GHz, respectively, the average photocurrent reached 300 mA [102]. Recently, device miniaturization and optimization of the on-chip microwave transmission lines enabled MUTC PDs with 3-dB bandwidths up to 65 GHz and 16 dBm RF output power [107]. In this design an air-bridge connected the photodiode to a high-impedance transmission line ($\sim 85 \Omega$) which was also the bond pad in the flip-chip bonding process. As the transmission line was designed to provide slight inductive peaking, the bandwidth was expanded by 30% beyond the conventional RC-limitation.

6.2.5 High-Speed Side-Illuminated Photodiodes

To overcome the bandwidth-efficiency trade-off side-illuminated waveguide-photodiodes (WGPD) have been developed for p–i–n [108, 109], MSM [18, 19], UTC [110–113], PDA [114], and APD photodiodes [115–118]. WGPD structures are illustrated in Fig. 6.12. The primary benefit of this type of photodetector is that

Fig. 6.12 Side-illuminated
 (a) WGPD and
 (b) evanescently-coupled
 WGPD



high efficiency and short carrier transit times can be achieved simultaneously [119]. Waveguide-photodiodes utilize an input optical waveguide with embedded absorbing layer. The photogenerated carriers transit only the thin absorption/depletion region perpendicular to the epitaxial layers which enables high bandwidths. Since electrical and optical transports are not collinear, the carrier transit times are determined by the thickness of the absorber while the length of the detector primarily controls the responsivity. Assuming a single mode WGPD, the responsivity is given by [7]:

$$R_{WGPD} = R_{ideal}(1 - R_0)\eta_c[1 - \exp(-\Gamma_{xy}\alpha l_{abs})] \quad (6.20)$$

Here, η_c is the input coupling efficiency determined from the overlap integral between the optical fields of the input (fiber) and WGPD, Γ_{xy} is the confinement factor in the xy -plane (perpendicular to the propagation direction) which quantifies the fraction of power confined within the absorbing layer, and l_{abs} is the PD length. For high-speed WGPDs with thin absorbers ($<1 \mu\text{m}$) either η_c or Γ_{xy} is <1 . This is because the diameter of the fiber input light spot, even when focused by lenses, is no less than $2 \mu\text{m}$, while the optical field distribution well confined within the absorbing layer is narrower than $1 \mu\text{m}$. On the other hand, having a wider optical field distribution in the WG-PD improves η_c , however, at the expense of a reduced Γ_{xy} .

Using a double core, i.e. large multimode optical cavity, Kato et al. presented a WGPD with a record bandwidth-efficiency product of 55 GHz in 1994 [120]. The $12 \mu\text{m}$ -long p-i-n WGPD achieved a quantum efficiency as high as 50%. The mushroom mesa approach developed for this photodiode yielded low resistance (10Ω) while minimizing the p-n junction area to realize very low capacitance ($\sim 15 \text{ fF}$) which enabled an RC-limited bandwidth of 110 GHz.

The disadvantages of WGPDs are the limited high-power capability due to non-uniform carrier distribution along the optical path and the low tolerance to lateral and vertical displacement of the input signal. The latter implies the use of additional optics or a tapered fiber in order to efficiently illuminate the small active region. Thus, in general, a low tolerance to lateral and vertical displacement of the input signal is obtained which makes the fiber-chip coupling more crucial and complex. Recently, coupling tolerances at 1 dB extra loss of $\pm 0.85 \mu\text{m}$ and $\pm 1.3 \mu\text{m}$ in the vertical and horizontal direction, respectively, were reported for a $5 \mu\text{m}$ -wide tapered waveguide photodiode [121]. This photodiode had an absorption layer of only 100 nm thickness embedded within thicker depleted transparent layers to reduce capacitance and balance electron and hole drift times. The reported bandwidth was 42 GHz with a responsivity of 1.08 A/W. In another approach Fukano et al.

proposed the edge-illuminated refracting facet photodiode (RFPD) in which the incident light that is parallel to the top surface is refracted at an angled facet and transmits the absorption layer with a certain refracted angle [122]. With this design, the fiber-chip -1 dB-misalignment tolerances in the horizontal and vertical direction were as large as $13.4\ \mu\text{m}$ and $3.3\ \mu\text{m}$, respectively. Furthermore, since this design leads to an increased absorption length compared to a vertically-illuminated photodiode, a high responsivity of $1\ \text{A/W}$ with <0.3 dB polarization dependent loss (PDL) was measured for a p-i-n RFPD with a $1\text{-}\mu\text{m}$ thick absorber [123]. Applying the UTC structure to the RFPD and further downscaling of the active area has led to high-speed, high-power UTC PDs with 3 dB bandwidths up to 310 GHz (at $12.5\ \Omega$ effective load) [124]. In [125] a refracting-facet UTC PD module with responsivity of $0.21\ \text{A/W}$ and 0.5 dB PDL for the detection of 100 and 160 Gbit/s return-to-zero (RZ) data rates was reported. Similar detector modules have been further optimized for W-band (75–110 GHz) [126], F-band (90–140 GHz) [127] and D-band (110–170 GHz) [128] operation; the latter exhibited a maximum RF output power of 2 dBm at 150 GHz.

In contrast to these side-illuminated devices the evanescently-coupled WGPD consists of a photodiode located on top of a passive waveguide. In the structure shown in Fig. 6.12(b) the light couples evanescently from a single mode input waveguide to the PD mesa which ensures a more uniform absorption along the device length and leads to an improved high-power capability [129]. This WGPD is well-suited for the monolithic integration with additional components, such as planar lightwave circuits resulting in advanced detector structures with increased functionality or photonic integrated circuits [130]. Furthermore, independent of the active device, a mode field transformer (taper) can be integrated in order to improve the fiber-chip coupling efficiency. This enables the use of a cleaved fiber instead of a tapered/lensed fiber, which simplifies the fiber-chip coupling process and also provides large alignment tolerances of $\pm 2.5\ \mu\text{m}$ and $\pm 3.5\ \mu\text{m}$ in the vertical and horizontal directions, respectively [108]. A highly efficient waveguide-integrated p-i-n photodetector was reported in [131]. The photodetector chip comprised a p-i-n photodiode with an active area of $5 \times 20\ \mu\text{m}^2$ and an InGaAsP/InGaAs heterostructure absorption layer stack, a vertically tapered mode field transformer, a biasing network, and a $50\ \Omega$ load resistor. An optimized impedance of the electrical output line of the detector led to an increase of the cut-off frequency to >100 GHz. Figure 6.13 shows (a) a schematic of this photodiode structure, (b) the p-i-n layer stack, and (c) the monolithically integrated bias circuitry. The chip was assembled into a package equipped with a 1 mm coaxial output connector and a fiber pigtail (Fig. 6.14, inset). Figure 6.14 shows the calibrated frequency response of the photodetector module at -2 V bias. A 3 dB bandwidth of 100 GHz with a maximum RF output power of -7 dBm was measured with an optical heterodyne setup [132]. The responsivity was $0.73\ \text{A/W}$.

Similar PD modules have been evaluated in several back-to-back transmission experiments [133]. Figure 6.15 shows the received electrical 80 Gbit/s return-to-zero (RZ) eye patterns at different optical input power levels using a 70 GHz-sampling oscilloscope. All measured eye patterns exhibit wide opening with a peak voltage up

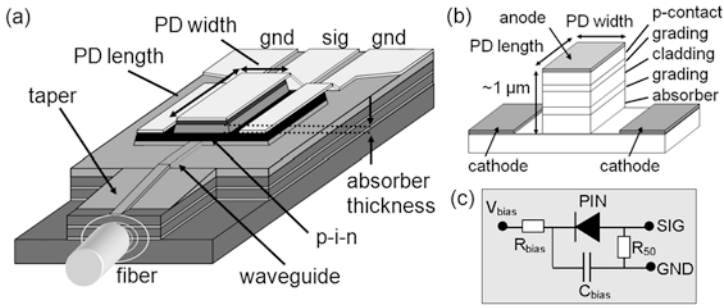


Fig. 6.13 (a) Evanescently-coupled WGPD, (b) p-i-n mesa, and (c) monolithically integrated bias circuitry [131]

Fig. 6.14 Relative frequency response of the PD module (+2.3 dBm optical input power), *inset*: photograph of the PD module [132]

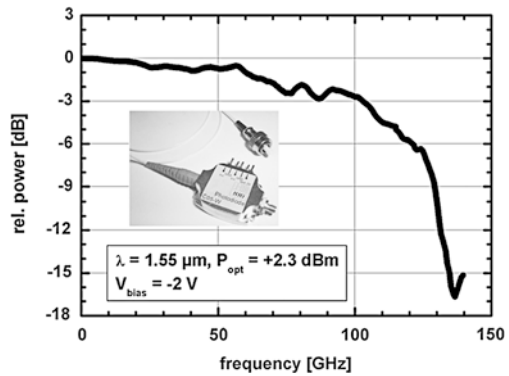
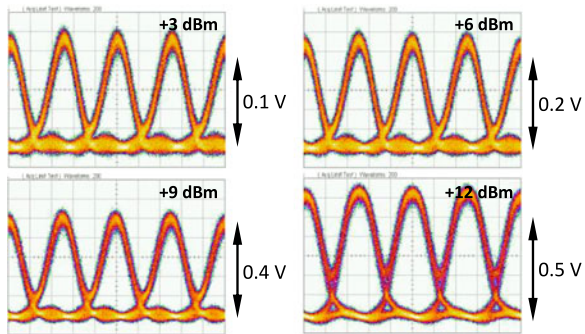


Fig. 6.15 Electrical 80 Gbit/s return-to-zero (RZ) eye pattern at 3, 6, 9 and 12 dBm optical input power detected by the PD module at -2.5 V bias (x: 5ps/div) [133]



to 0.6 V revealing only negligible saturation effects at +12 dBm. Figure 6.16 shows the detected 160 Gbit/s RZ data stream at +12 dBm optical input power. Due to the insufficient bandwidth of the sampling head and the PD module an RZ-to-NRZ conversion can be observed. Nevertheless, the eye amplitude is still notable and the inner eye opening reached 160 mV.

Fig. 6.16 Detected eye pattern under 160 Gbit/s RZ excitation [133]

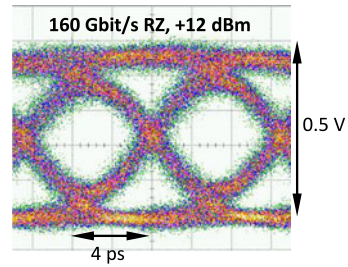
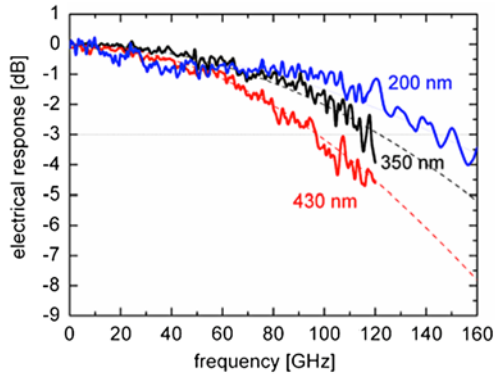


Fig. 6.17 Measured frequency responses for $5 \times 7 \mu\text{m}^2$ p-i-n photodiodes with 430 nm, 350 nm, and 200 nm thick absorbers



A fully packaged photodiode of this type capable of providing a flexible DC offset voltage at its RF output achieved a bandwidth of 90 GHz. The on-chip bias network of this photodetector was modified to supply a voltage to the postamplifier or demux IC without the need of an external bias tee [134]. The responsivity of the photodetector module was 0.53 A/W with a PDL of only 0.1 dB.

The reduction of absorber thickness and PD length allowed to further enhance the bandwidth of similar p-i-n photodiodes in [135, 136]. By downscaling the PD length to $7 \mu\text{m}$ the reduced capacitance enabled transit-time limited bandwidths at 25Ω effective load of 100 GHz, 120 GHz and 145 GHz for 430 nm-, 350 nm- and 200 nm-thick absorbers, respectively (Fig. 6.17). Owing to an optimized evanescent coupling scheme the fiber-coupled responsivities were 0.51 A/W, 0.48 A/W and 0.35 A/W, respectively. To avoid a decrease in responsivity, which generally follows the reduction in PD length, the n-contact layer was extended by a well-defined length L toward the single mode input waveguide (Fig. 6.18). Since both, the PD mesa and the protruding section L form multimode waveguides, mode beating effects can be exploited in order to facilitate an efficient coupling from the single mode waveguide into the absorber [137, 138], and thus increase Γ_{xy} . Since Γ_{xy} is a function of z (in propagation direction) and L , the responsivity of the evanescently coupled WGPLD, R_{eWGPLD} , can be estimated using the relation:

$$R_{eWGPLD} = R_{ideal}(1 - R_0)\eta_c \left[1 - \exp\left(-\alpha \int_0^{l_{abs}} \Gamma_{xy}(z, L) dz\right) \right] \quad (6.21)$$

Fig. 6.18 Responsivity vs. PD length. Each *circle* displays experimental data for a different device from a previously fabricated wafer with $L = 2 \mu\text{m}$. The *star* indicates the optimized design with $L = 7 \mu\text{m}$ [140]

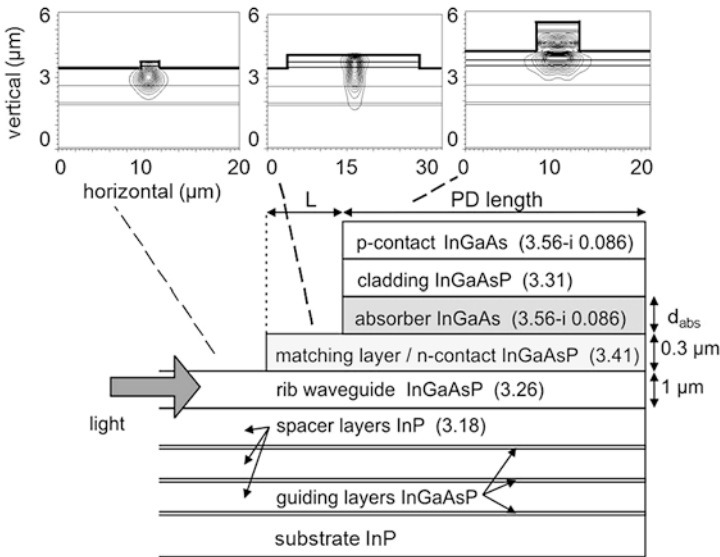
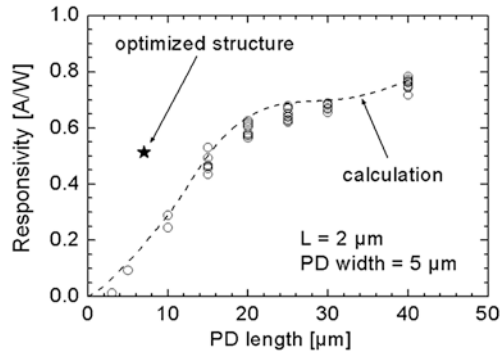
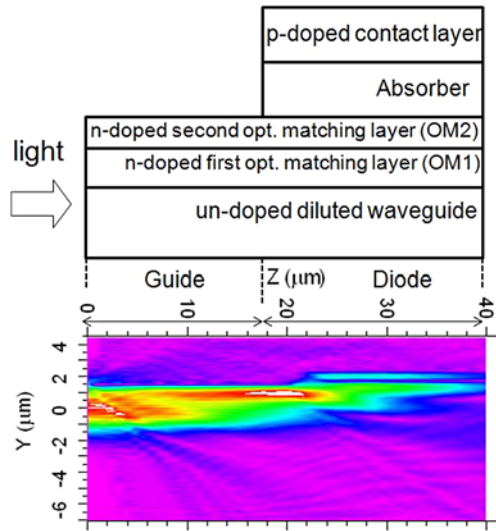


Fig. 6.19 Cross-sectional view of the PD with extended n-contact layer (matching layer). All refractive indices at $1.55 \mu\text{m}$ wavelength. The light is injected from the left into the mode field transformer (not shown) and couples evanescently from the semi-insulating waveguide into the p-i-n mesa. The *insets* depict the optical 2D field intensity profiles calculated in the single mode waveguide (*left*), multimode matching layer (*center*) and multimode PD mesa (*right*) [140]

where the input waveguides are assumed to be lossless. It should be noted that designing a WGPD with a non-constant confinement factor can be beneficial for high-power applications [139]. To achieve a more uniform absorption profile and thus current density the confinement factor should increase toward the end of the WGPD.

Numerical simulations of the optimized structure showed that illumination, and thus absorption, are strong in the first few microns of the absorber (Fig. 6.19, insets) [140]. For maximum responsivity the protrusion length L can be estimated from the beat length of the two most prominent modes in the multimode structure reduced by

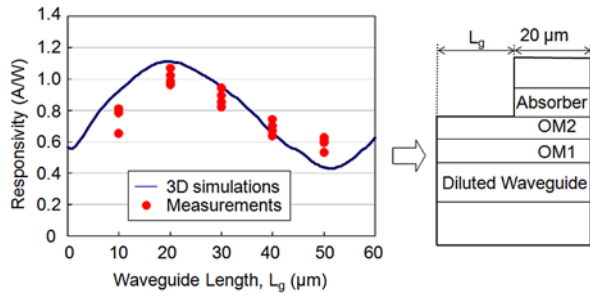
Fig. 6.20 Schematic of photodiode with planar multimode input waveguide and two optical matching layers. The *lower image* is the simulated optical intensity as light propagates through the integrated waveguide/PD structure [142]



the PD length. Experimentally $L = 7 \mu\text{m}$ was found for a $7 \mu\text{m}$ -long PD which is in good agreement with the calculation using a numerically determined beat length of $13 \mu\text{m}$. Compared to previous devices with $L = 2 \mu\text{m}$ a twofold responsivity increase to 0.51 A/W was reached with the optimized structure (Fig. 6.18).

It has been shown that high fiber-coupled efficiencies can be achieved without the need of a mode field transformer if a short multimode input waveguide is used [141]. The photodiode in [142] utilized a planar diluted input waveguide and two optical matching layers designed to provide a gradual increase of the optical refractive index from the diluted waveguide to the absorbing layer which resulted in a significant enhancement in the quantum efficiency. Figure 6.20 depicts a schematic of an evanescently-coupled photodiode that utilizes a planar diluted waveguide and two optical matching layers. The diluted waveguide is a stack of 10-periods of un-doped InP/InGaAsP ($1.1\text{-}\mu\text{m}$ bandgap equivalent wavelength) layers. The number of periods was optimized to achieve high coupling efficiency with an input fiber and low TE/TM polarization dependence. The two optical matching layers are n-doped InGaAsP with bandgaps corresponding to $1.1 \mu\text{m}$ and $1.4 \mu\text{m}$ for the first and second optical matching layers, respectively. For this approach, since the waveguide to photodiode coupling is based on mode beating effects, the coupling efficiency oscillates along the propagation direction. The solid line in Fig. 6.21 presents the responsivity simulation of $20\text{-}\mu\text{m}$ long photodiodes versus the input waveguide length. Oscillations related to inter-modal interferences are clearly visible in this figure. In agreement with the modeling, the responsivity was 1.07 A/W for an optimal input waveguide length when using a lensed fiber. The reported bandwidth was 48 GHz . It has been demonstrated that the length of the planar multimode waveguide can be controlled precisely by dry etching of the waveguide input facet. In addition, it was found that etching a lensed facet improved horizontal fiber-chip 1-dB alignment tol-

Fig. 6.21 Responsivity of photodiode with planar multimode input waveguide versus guide length for a 20- μm long active region: the solid line is the simulated responsivity and the filled circles are measurements [142]



erances to $>20 \mu\text{m}$ [143]. The reported lensed facet waveguide UTC PDs achieved 0.55 A/W and a bandwidth of $>50 \text{ GHz}$ [144].

Lateral tapering of diluted input waveguides was demonstrated in [145] using an asymmetric twin-waveguide technology [146]. In this PD the incident light is collected by a single mode diluted waveguide and transferred via a taper to a thinner coupling waveguide from where it couples evanescently into the absorber. Using a lensed fiber for input coupling a responsivity of $\sim 1 \text{ A/W}$ and a bandwidth 42 GHz were demonstrated. Using a similar waveguide taper Rouvalis et al. reported UTC waveguide PDs with a bandwidth of 110 GHz and 0.32 A/W [147]. The PD active area and absorber thickness were $4 \times 15 \mu\text{m}^2$ and 70 nm, respectively. For sub-THz applications similar PDs with traveling wave electrodes and integrated resonant antennas achieved a maximum extracted power of 150 μW around 460 GHz.

The WGPD approach has also been applied to APDs. Demiguel et al. [148] have reported an evanescently coupled $\text{In}_{0.52}\text{Al}_{0.48}\text{As}/\text{In}_{0.53}\text{Ga}_{0.47}\text{As}$ SACM APD having a planar short multimode input waveguide. A schematic cross section of this APD is shown in Fig. 6.22. The input diluted waveguide is similar to that reported for p-i-n PDs in [142]. The photocurrent, dark current, and gain versus reverse bias are plotted in Fig. 6.23. The breakdown occurred at $\sim 18.5 \text{ V}$ and the dark current at 90% of the breakdown was in the range 100 to 500 nA. The responsivity was 0.62 A/W with a PDL $<0.5 \text{ dB}$. Figure 6.24 shows the bandwidth versus gain; at low gain the maximum bandwidth was 35 GHz and the high-gain response exhibits a gain-bandwidth product of 160 GHz. Nakata et al. [116] have reported an edge-coupled $\text{InAlAs}/\text{InGaAs}$ APD that achieved 0.73 A/W responsivity, low-gain bandwidth of

Fig. 6.22 Schematic cross section of evanescently-coupled $\text{InAlAs}/\text{InGaAs}$ waveguide APD [148]

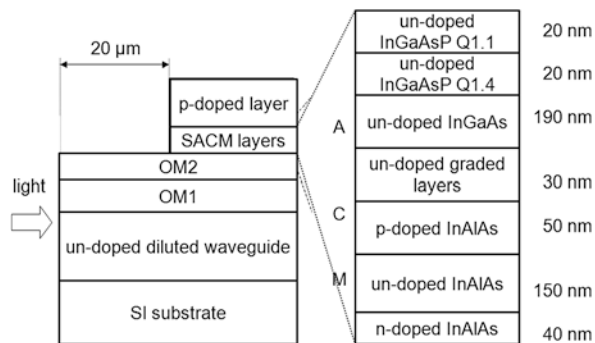


Fig. 6.23 Photocurrent, dark current, and gain versus reverse bias of evanescently-coupled InAlAs/InGaAs waveguide APD [148]

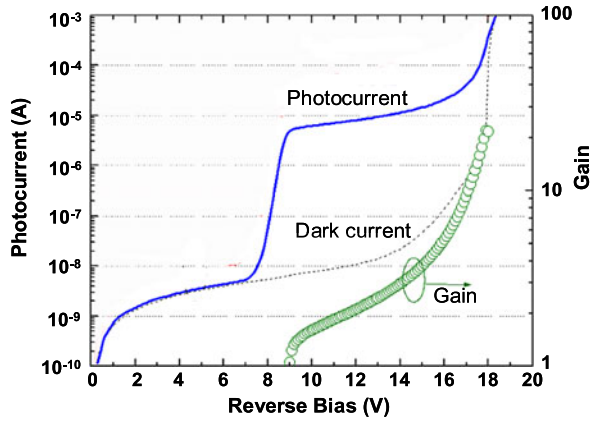
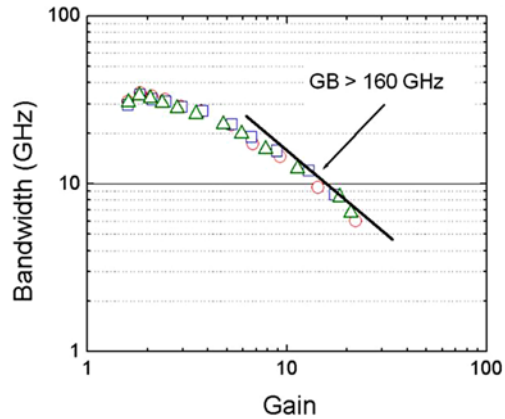


Fig. 6.24 Bandwidth versus gain of evanescently-coupled InAlAs/InGaAs waveguide APD. GB: gain-bandwidth product



35 GHz, and 140 GHz gain-bandwidth product. A similar waveguide APD with a gain-bandwidth product of 170 GHz and a minimum received power of -19.6 dBm at 40 Gbit/s (for BER of 10^{-9}) was recently reported in [149].

6.2.6 Material Systems

The group III–V semiconductor InP with its lattice-matched compounds continues to be a leading material system for the fabrication of high-performance photodiodes in the C and L bands. Owing to its high absorption efficiency, high carrier drift velocities, and good material quality (low dark current) the InGaAs/InP PD has become a standard solution for today’s high-speed applications.

Varying compositions of the alloys (bandgap engineering) allow the bandgap to be varied between 0.75 eV ($1.65 \mu\text{m}$) and 1.35 eV ($0.92 \mu\text{m}$). Thus the material system allows a composition of highly absorbing and transparent layers at telecommunication wavelengths. Another advantage of the InP material system arises from

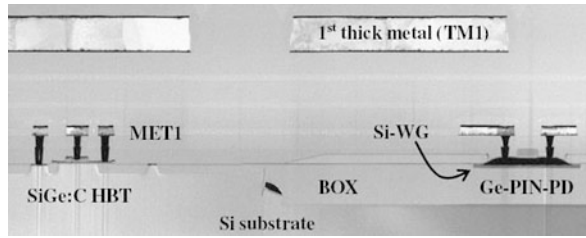
the potential for monolithic integration. To date monolithic integration of all active and passive optical functions and electronic devices has been demonstrated. Hence, InP is a leading platform for photonic integrated circuits (PICs) which have the potential to enhance performance, reduce footprint, and decrease packaging costs of complex photonic devices. Due to steady progress in the field of components and manufacturing, large-scale PICs have reached sufficient reliability for deployment in optical networks [150].

However, with the rapid progress in Silicon photonics there has been increased research effort toward Si-compatible waveguide photodiodes that operate at the telecommunication wavelengths. Although Si is transparent at wavelengths $> 1.1 \mu\text{m}$ numerous approaches have been reported to enable efficient light detection at $1.55 \mu\text{m}$ wavelength, including ion-implanted all-silicon [151], InGaAs/GaAs growth on Si [152, 153], polycrystalline Ge films [154, 155], Si-Ge hetero-epitaxy [156–158], and III–V on Si bonding [159].

6.2.7 Germanium Photodiodes on Silicon

Since Ge can be grown on silicon substrates, this approach ultimately promises large-scale photonic-electronic integration using the available CMOS infrastructure [160–162]. To reduce defect densities arising from the $\sim 4\%$ lattice mismatch between Ge and Si various growth techniques including the deposition of graded SiGe buffer layers [163], high/low temperature growth [157], area-selective growth [164, 165], and cyclic annealing have been successfully developed [166]. In [161], surface-normal PDs with a bandwidth of 36 GHz and 0.47 A/W responsivity achieved a low dark current of $< 100 \text{ nA}$. Using a two-step MBE growth technique consisting of a silicon buffer followed by a very thin Ge virtual substrate grown at low temperature for lattice mismatch accommodation low-dark-current, high-speed photodiodes were demonstrated in [167]. These n–i–p photodiodes with $10 \mu\text{m}$ -diameter achieved a high bandwidth of 49 GHz and 0.05 A/W responsivity at 2 V. The absorption coefficient of Ge depends on the growth conditions, and typical values range between 1000 cm^{-1} and 4000 cm^{-1} at $1.55 \mu\text{m}$ wavelength [168, 169]. Thus, when compared to InGaAs/InP photodiodes, surface-normal Ge photodiodes typically exhibit lower bandwidth-efficiency products. Waveguide structures have the potential to achieve larger bandwidth-efficiency products and to date several high-performance Ge waveguide PDs have been demonstrated [170, 171]. Due to their nature, they have become key devices in silicon-on-insulator (SOI) photonic integrated circuits [172]. In [19], a high-speed CMOS-compatible evanescently-coupled Ge MSM waveguide photodetector was reported. In this device a 150 nm -thick Ge layer served as the absorption layer and the MSM detector was formed by implementing 150 nm -wide inter-digitated metal fingers on top of the waveguide. The dark current and the internal responsivity at $1.3 \mu\text{m}$ wavelength were $90 \mu\text{A}$ and 0.42 A/W at 1 V, respectively. The bandwidth was 40 GHz due to the detector's small active area of $0.7 \times 20 \mu\text{m}^2$ [19]. An even higher 3 dB bandwidth of 45 GHz

Fig. 6.25 TEM cross section of a Ge-photodiode on SOI and a SiGe:C HBT fabricated in an adjacent bulk region [180]



was achieved with an n–i–p Ge waveguide photodiode with an active area of only $1.3 \times 4 \mu\text{m}^2$ in [173]. The dark current and responsivity were 3 nA at 1 V and 0.6 A/W at 1.55 μm , respectively. Recently, a lateral Ge photodetector with a large cross-section SOI waveguide was demonstrated in [174]. In this design an intrinsic Ge layer with a width of 650 nm was butt-coupled to a tapered SOI waveguide that enabled low-loss input coupling to the fiber. The demonstrated photodiode reached a bandwidth of 32 GHz and responsivity of 0.8 A/W at 1.55 μm wavelength. The dark current was 1.3 μA at 1 V. In [175], Vivien et al. reported a butt-coupled lateral p–i–n photodiode with >110 GHz bandwidth. At zero bias the measured responsivity was 0.8 A/W. The device was fabricated using a silicon recess etch followed by a selective Ge-regrowth. Dopants were implanted to form a horizontal p–i–n junction with a nominal intrinsic Ge width of 500 nm. Recently, Liow et al. demonstrated a waveguide photodiode with a high responsivity of 1.3 A/W at 1.61 μm wavelength [176]. In their experiments they applied a bias voltage of 9 V to achieve a moderate amount of multiplication gain. The dark current and bandwidth were 1.3 μA and 27 GHz, respectively.

It should be mentioned that much of the recent development has been focused on CMOS-compatible processing techniques of Ge photodiodes [177, 178] including the thermal budget of Ge epitaxy and post-growth annealing [179]. To reduce the dislocation density it is often required to anneal the Ge at very high temperatures ($\geq 900 \text{ }^\circ\text{C}$). However, this anneal can degrade the CMOS-device performance if the Ge photodiode layers are integrated after the formation of the CMOS electronics. In another approach Knoll et al. recently used a BiCMOS process to develop a waveguide Ge p–i–n photodiode on SOI waveguide [180]. The PD had a low dark current of 50 nA at 1 V and an internal responsivity of more than 0.6 A/W at 1.55 μm wavelength. The device showed a bandwidth of 35 GHz and was integrated with a high-performance SiGe:C HBT that was designed for 25 Gbit/s data detection (Fig. 6.25).

6.2.8 Heterogeneously Integrated Photodiodes

To integrate group III–V material based active devices onto SOI waveguides several hybrid and heterogeneous integration schemes have been developed. While these approaches are particularly interesting for transmitters on silicon [181], they also led to low dark current photodiodes with high efficiencies beyond 1.55 μm . Furthermore, heterogeneous integration has the potential to fully exploit bandgap engineering available in III–V materials to design more complex detector heterostructures.

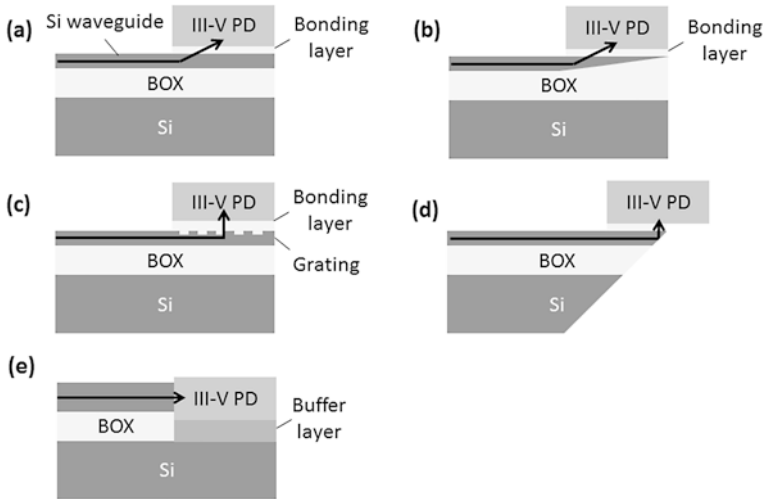


Fig. 6.26 Coupling schemes for III–V photodiodes on SOI waveguide: (a) evanescent, (b) adiabatic taper, (c) vertical coupling grating, (d) 45° polished facet or mirror, and (e) butt-coupling

There have been five documented optical coupling schemes reported for III–V photodiodes on SOI waveguides (Fig. 6.26).

In [182], Park et al. demonstrated evanescently-coupled waveguide photodiodes utilizing an absorber consisting of both compressively and tensile strained AlGaInAs quantum wells wafer-bonded onto an SOI waveguide (Fig. 6.26(a)). The photodiode layers were grown on an InP substrate and then transferred to the patterned silicon wafer using a low temperature oxygen assisted bonding process. The photodetector had low dark current of 100 nA at 2 V and fiber-coupled responsivities of 0.31 A/W and 0.23 A/W at 1.55 μm and 1.65 μm wavelengths, respectively. In [183] it was demonstrated that a similar bonding process can be used for selective area bonding to integrate two different III–V epitaxial layers on a silicon chip simultaneously. The demonstrated chip comprised an InGaAs/InP p–i–n photodiode and an AlInGaAs MQW laser that were part of a triplexer. Using a similar wafer bonding technology, Xie et al. recently demonstrated InP-based MUTC PDs on SOI waveguides for high-power high-speed applications [184]. The structure was adopted from a normal-incidence InGaAsP/InP MUTC photodiode that had previously achieved high saturation current and high linearity [185]. A schematic of the layer stack is shown in Fig. 6.27. The demonstrated bandwidth was 48 GHz and at 6.5 V bias the photodiode delivered more than 12 dBm RF output power at 40 GHz. Typical dark currents were below 10 nA at 5 V reverse bias voltage, and the internal responsivities were as high as 0.95 A/W at 1.55 μm wavelength. In [186] Piels et al. showed that InGaAs/InP p–i–n photodiodes can also be integrated on low-loss Si_3N_4 waveguides. The III–V material was wafer-bonded onto an intermediate silicon layer that, due to its lateral tapering, facilitated adiabatic coupling between the Si_3N_4 waveguide and the photodiode (Fig. 6.26(b)). A photodiode with $4 \times 30 \mu\text{m}^2$ active area had a fiber-coupled responsivity of 0.36 A/W and 30 GHz

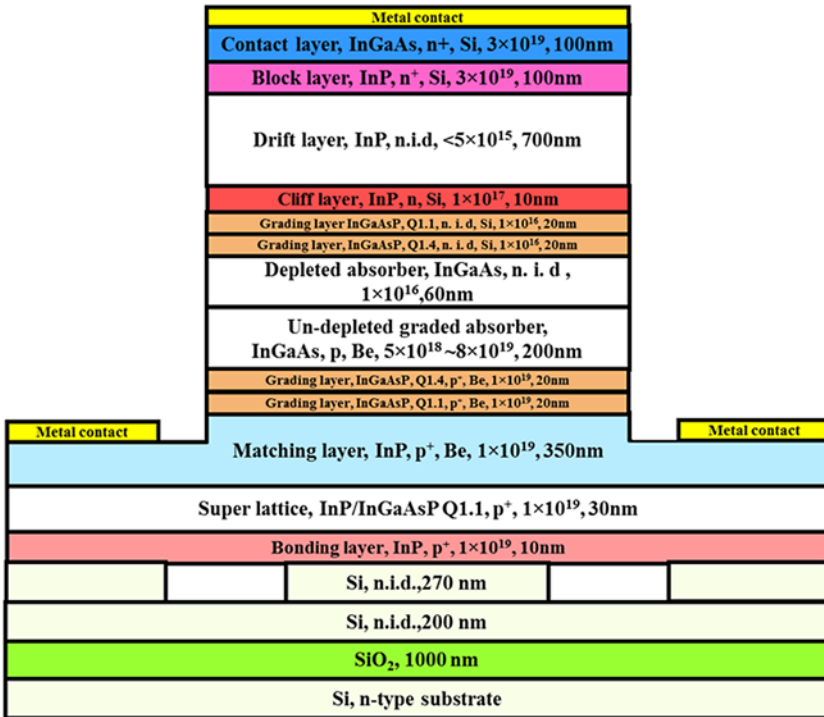


Fig. 6.27 Layer stack of heterogeneously integrated MUTC PD on SOI waveguide. Doping concentrations in cm^{-3} [184]

bandwidth. Using a tapered InP membrane input waveguide to couple light out of a Si photonic wire on the SOI wafer, Binetti et al. demonstrated a p–i–n PD with a bandwidth of 33 GHz in [187]. Heterogeneous integration on SOI was achieved by direct molecular bonding of InP dies using a 300-nm-thick SiO₂ interface layer. For a photodiode with a mesa area of 50 μm^2 the responsivity and dark current were 0.45 A/W and 2 nA at 4 V, respectively. In [188], Roelkens et al. demonstrated a grating coupler to diffract light from an SOI waveguide into an InP/InGaAsP photodiode (Fig. 6.26(c)). The InP die was bonded onto the SOI waveguide structure using adhesive bonding with benzocyclobutene (BCB) as a bonding layer. Since this vertical coupling scheme allows thicker bonding layers ($\sim 3 \mu\text{m}$), the requirements on roughness, flatness, and cleanliness of the two wafers that have to be joined, were somewhat relaxed. The measured dark current at 1 V and the responsivity at 1.55 μm were 0.3 nA and 0.02 A/W, respectively. The low responsivity was mainly attributed to the thin InGaAsP absorber that was only 120 nm. Recently, the same wafer bonding technology was also used to integrate GaInAsSb photodiodes onto SOI waveguides for detection in the SWIR range [189]. At 2.3 μm wavelength, photodiodes using evanescent coupling exhibited a responsivity of 1.4 A/W and devices utilizing a grating coupler achieved a responsivity of 0.4 A/W. The dark current was 4 μA at 1 V at room temperature.

In another approach shown in Fig. 6.26(d) the photodiode chip is integrated onto the silicon chip surface, where an etched or polished reflective mirror redirects the light beam to the detector surface [190]. Using a 45° polished facet, Zimmermann et al. demonstrated that high-speed vertically illuminated photodiodes can be assembled on the waveguide using epoxy [191]. Typical insertion loss and photodiode bandwidth were 5 dB and 28 GHz, respectively.

Geng et al. studied InGaAs pin photodiodes that were butt-coupled to SOI waveguides (Fig. 6.26(e)) in [192]. The authors used a selective-area MOCVD technique to grow the photodiodes on 2.6 μm -thick InP/GaAs buffers on Si. Photodiodes with an area of 64 μm^2 had a dark current of 400 μA and a bandwidth of 15 GHz at 5 V.

6.3 Summary

The continuing demand for higher and higher speed and the need for photonic integration have spurred the development of UTC-type structures and waveguide photodiodes. To date, high-efficiency evanescently coupled waveguide PDs with bandwidths well above 100 GHz have been demonstrated. Recently, there has been increased emphasis in achieving similar performance goals in photonic integrated circuits on Si. This has required novel column IV and III–V compound materials efforts, process developments, and optimized device designs. While significant progress has been achieved, challenges to reduce dark current and increase bandwidth-efficiency products in combination with achieving process compatibility with existing CMOS remain.

References

1. S. Ramo, Currents induced by electron motion. *Proc. IRE* **27**, 584–585 (1939)
2. K. Kato, S. Hata, K. Kawano, A. Kozen, Design of ultrawide-band, high-sensitivity p–i–n photodetectors. *IEICE Trans. Electron. E* **76–C**, 214–221 (1993)
3. W. Shockley, W.T. Read, Statistics of the recombination of holes and electrons. *Phys. Rev.* **87**, 835–839 (1952)
4. R.N. Hall, Electron-hole recombination in germanium. *Phys. Rev.* **87**, 387–391 (1952)
5. G.P. Agrawal, *Fiber-Optic Communication Systems* (Wiley, New York, 2002)
6. Y.-G. Wey, K. Giboney, J. Bowers, M. Rodwell, P. Silvestre, P. Thiagarajan, G. Robinson, 110-GHz GaInAs/InP double heterostructure p–i–n photodetectors. *J. Lightwave Technol.* **13**, 1490–1499 (1995)
7. K. Kato, Ultrawide-band/high-frequency photodetectors. *IEEE Trans. Microw. Theory Tech.* **47**, 1265–1281 (1999)
8. I. Kimukin, N. Biyikli, B. Butun, O. Aytur, S.M. Ünlü, E. Ozbay, InGaAs-based high performance p–i–n photodiodes. *IEEE Photonics Technol. Lett.* **14**, 366–368 (2002)
9. V. Hurm, W. Benz, M. Berroth, W. Bronner, G. Kaufel, K. Köhler, M. Ludwig, E. Olander, B. Raynor, J. Rosenzweig, 20 Gbit/s fully integrated MSM-photodiode AlGaAs/GaAs-HEMT optoelectronic receiver. *Electron. Lett.* **32**, 638–685 (1996)

10. W. Gao, A.-S. Khan, P.R. Berger, R.G. Hunsperger, G. Zyzdik, H.M. O'Bryan, D. Sivco, A.Y. Cho, In_{0.53}Ga_{0.47}As metal-semiconductor-metal photodiodes with transparent cadmium tin oxide Schottky contacts. *Appl. Phys. Lett.* **65**, 1930–1932 (1994)
11. M.A. Matin, K.C. Song, B.J. Robinson, J.G. Simmons, D.A. Thompson, F. Gouin, Very low dark current InGaP/GaAs MSM photodetector using semi-transparent and opaque contacts. *Electron. Lett.* **32**, 766–767 (1996)
12. J.H. Kim, T. Griem, R.A. Friedman, E.Y. Chan, S. Ray, High-performance back-illuminated InGaAs/InAlAs MSM photodetector with a record responsivity of 0.96 A/W. *IEEE Photonics Technol. Lett.* **4**, 1241–1243 (1992)
13. M.C. Hargis, S.E. Ralph, J. Woodall, D. McInturff, A.J. Negri, P.O. Haugsjaa, Temporal and spectral characteristics of back-illuminated InGaAs MSM photodetectors. *IEEE Photonics Technol. Lett.* **8**, 110–112 (1996)
14. J. Burm, K.I. Litvin, D.W. Woodard, W.J. Schaff, P. Mandeville, M.A. Jaspan, M.M. Gitin, L.F. Eastman, High-frequency, high-efficiency MSM photodetectors. *IEEE J. Quantum Electron.* **31**, 1504–1509 (1995)
15. Y.G. Zhang, A.Z. Li, J.X. Chen, Improved performance of InAlAs–InGaAs–InP MSM photodetectors with graded superlattice structure grown by gas source MBE. *IEEE Photonics Technol. Lett.* **8**, 830–832 (1996)
16. F. Hieronymi, E.H. Böttcher, E. Dröge, D. Kuhl, D. Bimberg, High-performance large-area InGaAs MSM photodetectors. *IEEE Photonics Technol. Lett.* **5**, 910–913 (1993)
17. J. Kim, W.B. Johnson, S. Kanakaraju, L.C. Calhoun, C.H. Lee, Improvement of dark current using InP/InGaAsP transition layer in large-area InGaAs MSM photodetectors. *IEEE Trans. Electron Devices* **51**, 351–356 (2004)
18. E. Dröge, E.H. Böttcher, D. Bimberg, O. Reimann, R. Steingrüber, 70 GHz InGaAs MSM photodetectors for polarization-insensitive operation. *Electron. Lett.* **34**, 1421–1422 (1998)
19. S. Assefa, F. Xia, S.W. Bedell, Y. Zhang, T. Topuria, P.M. Rice, Y.A. Vlasov, CMOS-integrated high-speed MSM germanium waveguide photodetector. *Opt. Express* **18**, 4986–4999 (2010)
20. S.D. Personick, Receiver design for digital fiber-optic communication systems, Parts I and II. *Bell Syst. Tech. J.* **52**, 843–886 (1973)
21. R.G. Smith, S.D. Personick, Receiver design for optical fiber communications systems, in *Semiconductor Devices for Optical Communication*, ed. by H. Kressel (Springer, New York, 1980). Chap. 4
22. S.R. Forrest, Sensitivity of avalanche photodetector receivers for high-bit-rate long-wavelength optical communication systems, in *Semiconductors and Semimetals*, ed. by W.T. Tsang. Lightwave Communications Technology, vol. 22 (Academic Press, Orlando, 1985). Chap. 4
23. B.L. Kasper, J.C. Campbell, Multigigabit-per-second avalanche photodiode lightwave receivers. *J. Lightwave Technol.* **LT-5**, 1351–1364 (1987)
24. R.J. McIntyre, Multiplication noise in uniform avalanche diodes. *IEEE Trans. Electron Devices* **13**, 154–158 (1966)
25. R.J. McIntyre, The distribution of gains in uniformly multiplying avalanche photodiodes: theory. *IEEE Trans. Electron Devices* **ED-19**, 703–713 (1972)
26. R.J. McIntyre, Factors affecting the ultimate capabilities of high speed avalanche photodiodes and a review of the state-of-the-art, in *Internat. Electron Devices Meeting*, Washington, D.C., USA (1973), Techn. Digest, vol. **19**, pp. 213–216
27. R.B. Emmons, Avalanche-photodiode frequency response. *J. Appl. Phys.* **38**, 3705–3714 (1967)
28. C.A. Lee, R.A. Logan, R.L. Batdorf, J.J. Kleimack, W. Weigmann, Ionization rates of holes and electrons in silicon. *Phys. Rev.* **134**, A761–A773 (1964)
29. J. Conradi, The distributions of gains in uniformly multiplying avalanche photodiodes: experimental. *IEEE Trans. Electron Devices* **ED-19**, 713–718 (1972)
30. W.N. Grant, Electron and hole ionization rates in epitaxial silicon at high electric fields. *Solid-State Electron.* **16**, 1189–1203 (1973)

31. T. Kaneda, H. Matsumoto, T. Yamaoka, A model for reach-through avalanche photodiodes (RAPD's). *J. Appl. Phys.* **47**, 3135–3139 (1976)
32. H. Melchior, A.R. Hartman, D.P. Schinke, T.E. Seidel, Planar epitaxial silicon avalanche photodiode. *Bell Syst. Tech. J.* **57**, 1791–1807 (1978)
33. S.R. Forrest, M. DiDomenico Jr., R.G. Smith, H.J. Stocker, Evidence of tunneling in reverse-bias III–V photodetector diodes. *Appl. Phys. Lett.* **36**, 580–582 (1980)
34. H. Ando, H. Kaaba, M. Ito, T. Kaneda, Tunneling current in InGaAsP and optimum design for InGaAs/InP avalanche photo-diodes. *Jpn. J. Appl. Phys.* **19**, 1277–1280 (1980)
35. K. Nishida, K. Taguchi, Y. Matsumoto, InGaAsP heterojunction avalanche photodiodes with high avalanche gain. *Appl. Phys. Lett.* **35**, 251–253 (1979)
36. S.R. Forrest, O.K. Kim, R.G. Smith, Optical response time of In_{0.53}Ga_{0.47}As avalanche photodiodes. *Appl. Phys. Lett.* **41**, 95–98 (1982)
37. J.C. Campbell, A.G. Dentai, W.S. Holden, B.L. Kasper, High-performance avalanche photodiode with separate absorption, grading, and multiplication regions. *Electron. Lett.* **18**, 818–820 (1983)
38. Y. Matsushima, A. Akiba, K. Sakai, K. Kushirn, Y. Node, K. Utaka, High-speed response InGaAs/InP heterostructure avalanche photodiode with InGaAsP buffer layers. *Electron. Lett.* **18**, 945–946 (1982)
39. F. Capasso, A.Y. Cho, P.W. Foy, Low-dark-current low-voltage 1.3–1.6 μm avalanche photodiode with high-low electric field profile and separate absorption and multiplication regions by molecular beam epitaxy. *Electron. Lett.* **20**, 635–637 (1984)
40. P. Webb, R. McIntyre, J. Scheibling, M. Holunga, A planar InGaAs APD fabricated using Si implantation and regrowth techniques, in *Opt. Fiber Commun. Conf. (OFC'90)*, New Orleans, LA (1990), Tech. Digest, paper WQ32
41. L.E. Tarof, Planar InP–InGaAs avalanche photodetectors with n-multiplication layer exhibiting a very high gain-bandwidth product. *IEEE Photonics Technol. Lett.* **2**, 643–645 (1990)
42. M.A. Itzler, K.K. Loi, S. McCoy, N. Codd, N. Komaba, Manufacturable planar bulk-InP avalanche photodiodes for 10 Gb/s applications, in *Ann. Meeting IEEE Lasers & Electro-Optics Soc (LEOS'99)*, San Francisco, CA, USA (1999), Conf. Digest, pp. 748–749
43. Y. Okuto, C.R. Crowell, Ionization coefficients in semiconductors: a nonlocalized property. *Phys. Rev. B* **10**, 4284–4296 (1974)
44. M.M. Hayat, B.E.A. Saleh, M.C. Teich, Effect of dead space on gain and noise of double-carrier multiplication avalanche photodiodes. *IEEE Trans. Electron Devices* **39**, 546–552 (1992)
45. R.J. McIntyre, A new look at impact ionization—part I: a theory of gain, noise, breakdown probability and frequency response. *IEEE Trans. Electron Devices* **48**, 1623–1631 (1999)
46. X. Li, X. Zheng, S. Wang, F. Ma, J.C. Campbell, Calculation of gain and noise with dead space for GaAs and Al_xGa_{1-x}As avalanche photodiodes. *IEEE Trans. Electron Devices* **49**, 1112–1117 (2002)
47. B. Jacob, P.N. Robson, J.P.R. David, G.J. Rees, Fokker-Planck model for nonlocal impact ionization in semiconductors. *J. Appl. Phys.* **90**, 1314–1317 (2001)
48. A. Spinelli, A.L. Lacaita, Mean gain of avalanche photodiodes in a dead space model. *IEEE Trans. Electron Devices* **43**, 23–30 (1996)
49. G.M. Dunn, G.J. Rees, J.P.R. David, S.A. Plimmer, D.C. Herbert, Monte Carlo simulation of impact ionization and current multiplication in short GaAs p⁺–i–n⁺ diodes. *Semicond. Sci. Technol.* **12**, 111–120 (1997)
50. S.A. Plimmer, J.P.R. David, D.S. Ong, K.F. Li, A simple model for avalanche multiplication including deadspace effects. *IEEE Trans. Electron Devices* **46**, 769–775 (1999)
51. K.F. Li, S.A. Plimmer, J.P.R. David, R.C. Tozer, G.J. Rees, P.N. Robson, C.C. Button, J.C. Clark, Low avalanche noise characteristics in thin InP p⁺–i–n⁺ diodes with electron initiated multiplication. *IEEE Photonics Technol. Lett.* **11**, 364–366 (1999)
52. M.A. Saleh, M.M. Hayat, P.O. Sotirelis, A.L. Holmes, J.C. Campbell, B. Saleh, M. Teich, Impact-ionization and noise characteristics of thin III–V avalanche photodiodes. *IEEE Trans. Electron Devices* **48**, 2722–2731 (2001)

53. C.H. Tan, J.C. Clark, J.P.R. David, G.J. Rees, S.A. Plimmer, R.C. Tozer, D.C. Herbert, D.J. Robbins, W.Y. Leong, J. Newey, Avalanche noise measurements in thin Si p⁺-i-n⁺ diodes. *Appl. Phys. Lett.* **76**, 3926–3928 (2000)
54. T. Watanabe, K. Torikai, K. Makita, T. Fukushima, T. Uji, Impact ionization rates in (100) Al_{0.48}In_{0.52}As. *IEEE Electron Device Lett.* **11**, 437–439 (1990)
55. N. Li, R. Sidhu, X. Li, F. Ma, X. Zheng, S. Wang, G. Karve, S. Demiguel, A.L. Holmes Jr., J.C. Campbell, InGaAs/InAlAs avalanche photodiode with undepleted absorber. *Appl. Phys. Lett.* **82**, 2175–2177 (2003)
56. E. Yagyu, E. Ishimura, M. Nakaji, T. Aoyagi, Y. Tokuda, Simple planar structure for high-performance AllnAs avalanche photodiodes. *IEEE Photonics Technol. Lett.* **18**, 76–78 (2006)
57. E. Yagyu, E. Ishimura, M. Nakaji, T. Aoyagi, K. Yoshiara, Y. Tokuda, Investigation of guardring-free planar AllnAs avalanche photodiodes. *IEEE Photonics Technol. Lett.* **18**, 1264–1266 (2006)
58. X. Li, S. Demiguel, N. Li, J.C. Campbell, D.L. Tulchinsky, K.J. Williams, Backside illuminated high saturation current partially depleted absorber photodetectors. *Electron. Lett.* **39**, 1466–1467 (2003)
59. M. Nada, Y. Muramoto, H. Yokoyama, T. Toshimatsu, H. Matsuzaki, High-speed avalanche photodiodes for 100-Gb/s systems and beyond, in *Proc. 40th Europ. Conf. Opt. Commun. (ECOC'14)*, Cannes, France (2014), paper We.2.4.3
60. M. Nada, Y. Muramoto, H. Yokoyama, T. Ishibashi, H. Matsuzaki, Triple-mesa avalanche photodiode with inverted p-down structure for reliability and stability. *J. Lightwave Technol.* **32**(81), 1543–1548 (2014)
61. A.R. Hawkins, T.E. Reynolds, D.R. England, D.I. Babic, M.J. Mondry, K. Streubel, J.E. Bowers, Silicon heterointerface photodetector. *Appl. Phys. Lett.* **70**, 303–305 (1996)
62. Y. Kang, P. Mages, A.R. Clawson, P.K.L. Yu, M. Bitter, Z. Pan, A. Pauchard, S. Hummel, Y.H. Lo, Fused InGaAs–Si avalanche photodiodes with low-noise performances. *IEEE Photonics Lett.* **14**, 1593–1595 (2002)
63. M. Bitter, Z. Pan, S. Kristjansson, L. Boman, R. Gold, A. Pauchard, InGaAs-on-Si photodetectors for high-sensitivity detection, in *Infrared Tech. and Applications XXX* (2004), *Proc. SPIE*, vol. 5406, pp. 1–12
64. Y. Kang, H.-D. Liu, M. Morse, M.J. Paniccia, M. Zadka, S. Litski, G. Sarid, A. Pauchard, Y.-H. Kuo, H.-W. Chen, W.S. Zaoui, J.E. Bowers, A. Beling, D.C. McIntosh, X. Zheng, J.C. Campbell, Monolithic germanium/silicon avalanche photodiodes with 340 GHz gain-bandwidth product. *Nat. Photonics* **3**, 59–63 (2008)
65. M. Huang, T. Shi, P. Cai, L. Wang, S. Li, W. Chen, C. Hong, D. Pan, 25 Gb/s normal incident Ge/Si avalanche photodiode, in *Proc. 40th Europ. Conf. Opt. Commun. (ECOC'14)*, Cannes, France (2014), paper We.2.4.4
66. P. Yuan, S. Wang, X. Sun, X.G. Zheng, A.L. Holmes Jr., J.C. Campbell, Avalanche photodiodes with an impact-ionization-engineered multiplication region. *IEEE Photonics Technol. Lett.* **12**, 1370–1372 (2000)
67. O.-H. Kwon, M.M. Hayat, S. Wang, J.C. Campbell, A.L. Holmes Jr., B.E.A. Saleh, M.C. Teich, Optimal excess noise reduction in thin heterojunction Al_{0.6}Ga_{0.4}As–GaAs avalanche photodiodes. *IEEE J. Quantum Electron.* **39**, 1287–1296 (2003)
68. C. Groves, C.K. Chia, R.C. Tozer, J.P.R. David, G.J. Rees, Avalanche noise characteristics of single Al_xGa_{1-x}As (0.3 < x < 0.6)–GaAs heterojunction APDs. *IEEE J. Quantum Electron.* **41**, 70–75 (2005)
69. S. Wang, R. Sidhu, X.G. Zheng, X. Li Sun, A.L. Holmes Jr., J.C. Campbell, Low-noise avalanche photodiodes with graded impact-ionization-engineered multiplication region. *IEEE Photonics Technol. Lett.* **13**, 1346–1348 (2001)
70. S. Wang, F. Ma, X. Li, R. Sidhu, X.G. Zheng, X. Sun, A.L. Holmes Jr., J.C. Campbell, Ultra-low noise avalanche photodiodes with a ‘centered-well’ multiplication region. *IEEE J. Quantum Electron.* **39**, 375–378 (2003)

71. M.M. Hayat, O.-H. Kwon, S. Wang, J.C. Campbell, B.E.A. Saleh, M.C. Teich, Boundary effects on multiplication noise in thin heterostructure avalanche photodiodes: theory and experiment. *IEEE Trans. Electron Devices* **49**, 2114–2123 (2002)
72. S. Wang, J.B. Hurst, F. Ma, R. Sidhu, X. Sun, X.G. Zheng, A.L. Holmes Jr., J.C. Campbell, A. Huntington, L.A. Coldren, Low-noise impact-ionization-engineered avalanche photodiodes grown on InP substrates. *IEEE Photonics Technol. Lett.* **14**, 1722–1724 (2002)
73. N. Duan, S. Wang, F. Ma, N. Li, J.C. Campbell, C. Wang, L.A. Coldren, High-speed and low-noise SACM avalanche photodiodes with an impact-ionization engineered multiplication region. *IEEE Photonics Technol. Lett.* **17**, 1719–1721 (2005)
74. A.R.J. Marshall, P. Vines, P.J. Ker, J.P.R. David, C.H. Tan, Avalanche multiplication and excess noise in InAs electron avalanche photodiodes at 77 K. *IEEE J. Quantum Electron.* **47**(6), 858–864 (2011)
75. W. Sun, S.J. Maddox, S.R. Bank, J.C. Campbell, Record high gain from InAs avalanche photodiodes at room temperature, in *72nd Device Research Conference (DRC'14)*, Santa Barbara, CA, USA (2014), Techn. Digest, pp. 47–48
76. J. Klamkin, Y.-C. Chang, A. Ramaswamy, L.A. Johansson, J.E. Bowers, S.P. DenBaars, L.A. Coldren, Output saturation and linearity of waveguide untraveling-carrier photodiodes. *IEEE J. Quantum Electron.* **44**, 354–359 (2008)
77. M. Chtioui, A. Enard, D. Carpentier, S. Bernard, B. Rousseau, F. Lelarge, F. Pommereau, M. Achouche, High-power high-linearity uni-traveling-carrier photodiodes for analog photonic links. *IEEE Photonics Technol. Lett.* **20**, 202–204 (2008)
78. A. Beling, H. Pan, H. Chen, J.C. Campbell, Linearity of modified uni-traveling carrier photodiodes. *J. Lightwave Technol.* **26**, 2373–2378 (2008)
79. K.J. Williams, L.T. Nichols, R.D. Esman, Photodetector nonlinearity on a high-dynamic range 3 GHz fiber optic link. *J. Lightwave Technol.* **16**, 192–199 (1998)
80. A.J. Seeds, K.J. Williams, Microwave photonics. *J. Lightwave Technol.* **24**, 4628–4641 (2006)
81. K.J. Williams, R.D. Esman, Design considerations for high-current photodetectors. *J. Lightwave Technol.* **17**, 1443–1454 (1999)
82. K.J. Williams, R.D. Esman, M. Dagenais, Effects of high space-charge fields on the response of microwave photodetectors. *IEEE Photonics Technol. Lett.* **6**, 639–641 (1994)
83. J. Paslaski, P.C. Chen, J.S. Chen, C.M. Gee, N. Bar-Chaim, High-power microwave photodiode for improving performance of RF fiber optic links, in *Photonics and Radio Frequency*, Denver, CO, USA (1996), Proc. SPIE, vol. 2844, pp. 110–119
84. N. Duan, X. Wang, N. Li, H.-D. Liu, J.C. Campbell, Thermal analysis of high-power InGaAs–InP photodiodes. *IEEE J. Quantum Electron.* **42**, 1255–1258 (2006)
85. K.J. Williams, Comparison between dual-depletion-region and uni-travelling-carrier p–i–n photodetectors. *IEE Proc. Optoelectron.* **149**, 131–137 (2002)
86. F.J. Effenberger, A.M. Joshi, Ultrafast, dual-depletion region, InGaAs/InP p–i–n detector. *J. Lightwave Technol.* **14**, 1859–1864 (1996)
87. G.A. Davis, R.E. Weiss, R.A. LaRue, K.J. Williams, R.D. Esman, A 920–1650 nm high current photodetector. *IEEE Photonics Technol. Lett.* **8**, 1373–1375 (1996)
88. T. Ishibashi, N. Shimizu, S. Kodama, H. Ito, T. Nagatsuma, T. Furuta, Uni-traveling-carrier photodiodes. in: *Ultrafast Electronics and Optoelectronics, 1997*. Opt. Soc. America, Washington, DC, 1997. OSA Trends in Optics and Photonics Series, vol. 13 (1997), paper UC3
89. X. Li, N. Li, X. Zheng, S. Demiguel, J.C. Campbell, D. Tulchinsky, K.J. Williams, High-speed high-saturation-current InP/InGaAs photodiode with partially depleted absorber, in *Opt. Fiber Commun. Conf. (OFC'03)*, Atlanta, GA, USA (2003), Techn. Digest, vol. 1, pp. 338–339
90. A.M. Joshi, X. Wang, DC to 50 GHz wide bandwidth InGaAs photodiodes and photo-receivers, in *Reliability of Optical Fibers and Optical Fiber Systems* (1999), Proc. SPIE, vol. CR73, pp. 181–196

91. A.M. Joshi, D. Becker, GRIN lens-coupled top-illuminated photodetectors for high-power applications, in *IEEE Internat. Topical Meeting: Microwave Photonics*, Victoria, BC, Canada (2007), pp. 18–20
92. T. Furuta, H. Ito, T. Ishibashi, Photocurrent dynamics of uni-traveling-carrier and conventional pin photodiodes. *Inst. Phys. Conf. Ser.* **166**, 419–422 (2000)
93. H. Ito, T. Furuta, S. Kodama, T. Ishibashi, Zero-bias high-speed and high-output-voltage operation of cascade-twin uni-travelling-carrier photodiode. *Electron. Lett.* **36**, 2034–2036 (2000)
94. T. Ishibashi, T. Furtua, H. Fushimi, H. Ito, Photoresponse characteristics of uni-traveling-carrier photodiodes, in *Physics and Simulation of Optoelectronic Devices IX (2001)*, *Proc. SPIE*, vol. 4283, pp. 469–479
95. N. Shimizu, N. Watanabe, T. Furuta, T. Ishibashi, InP-InGaAs uni-traveling-carrier photodiode with improved 3 dB bandwidth of over 150 GHz. *IEEE Photonics Technol. Lett.* **10**, 412–414 (1998)
96. H. Ito, T. Furuta, S. Kodama, N. Watanabe, T. Ishibashi, InP/InGaAs uni-travelling-carrier photodiode with 220 GHz bandwidth. *Electron. Lett.* **35**, 1556–1557 (2004)
97. T. Ishibashi, High speed heterostructure devices, in *Semiconductors and Semimetals*, vol. 41, ed. by R. Willardson, R. Kiehl, T.G. Sollner, A. Beer, E. Weber (Academic Press, San Diego, 1994), Chap. 5
98. Y.-S. Wu, J.-W. Shi, Dynamic analysis of high-power and high-speed near-ballistic untravelling carrier photodiodes at W-band. *IEEE Photonics Technol. Lett.* **20**, 1160–1162 (2008)
99. J.-W. Shi, F.-M. Kuo, C.-J. Wu, C.L. Chang, C.-Y. Liu, C.Y. Chen, J.-I. Chyi, Extremely high saturation current-bandwidth product performance of a near-ballistic uni-traveling-carrier photodiode with a flip-chip bonding structure. *IEEE J. Quantum Electron.* **46**, 80–86 (2010)
100. D.-H. Jun, J.-H. Jang, I. Adesida, J.-I. Song, Improved efficiency-bandwidth product of modified uni-traveling carrier photodiode structures using an undoped photo-absorption layer. *Jpn. J. Appl. Phys.* **45**, 3475–3478 (2006)
101. X. Wang, N. Duan, H. Chen, J.C. Campbell, InGaAs/InP photodiodes with high responsivity and high saturation power. *IEEE Photonics Technol. Lett.* **19**, 1272–1274 (2007)
102. X. Xie, Q. Zhou, K. Li, Y. Shen, Q. Li, Z. Yang, A. Beling, J.C. Campbell, High-power high-power-conversion-efficiency modified uni-traveling carrier photodiode flip-chip bonded on diamond submount. *Optica* **1**, 429–435 (2014)
103. N. Li, X. Li, S. Demiguel, X. Zheng, J.C. Campbell, D.A. Tulchinsky, K.J. Williams, T.D. Isshiki, G.S. Kinsey, R. Sudharsansan, High saturation-current charge-compensated InGaAs–InP uni-traveling-carrier photodiode. *IEEE Photonics Technol. Lett.* **16**, 864–866 (2004)
104. N. Shimizu, N. Watanabe, T. Furuta, T. Ishibashi, Improved response of uni-traveling-carrier photodiodes by carrier injection. *Jpn. J. Appl. Phys.* **37**, 1424–1426 (1998)
105. Y.-S. Wu, J.-W. Shi, P.-H. Chiu, Analytical modeling of a high-performance near-ballistic uni-traveling-carrier photodiode at a 1.55- μm wavelength. *IEEE Photonics Technol. Lett.* **18**, 938–940 (2006)
106. E. Rouvalis, F.N. Baynes, X. Xie, K. Li, Q. Zhou, T.M. Fortier, S.A. Diddams, A.G. Stefan, A. Beling, J.C. Campbell, High-power and high-linearity photodetector modules for microwave photonic applications. *IEEE J. Lightwave Technol.* **32**, 3810–3816 (2014)
107. Q. Zhou, A.S. Cross, A. Beling, Y. Fu, Z. Lu, J.C. Campbell, High-power V-band InGaAs/InP photodiodes. *IEEE Photonics Technol. Lett.* **25**, 907–909 (2013)
108. A. Umbach, D. Trommer, R. Steingrüber, S. Seeger, W. Ebert, G. Unterbörsch, Ultrafast, high-power 1.55 μm side-illuminated photodetector with integrated spot size converter, in *Opt. Fiber Commun. Conf. (OFC'00)*, Baltimore, MD, USA (2000), Techn. Digest, pp. 117–119
109. T. Takeuchi, T. Nakata, K. Makita, T. Torikai, High-power and high-efficiency photodiode with an evanescently coupled graded-index waveguide for 40 Gb/s applications, in *Opt. Fiber Commun. Conf. (OFC'01)*, Anaheim, CA, USA (2001), Techn. Digest, vol. 3, paper WQ2-1-3

110. Y.-S. Wu, P.-H. Chiu, J.-W. Shi, High-speed and high-power performance of a dual-step evanescently-coupled uni-traveling-carrier photodiode at 1.55 μm wavelength, in *Opt. Fiber Commun. Conf. and Nat. Fiber Opt. Eng. Conf. (OFC/NFOEC'07)*, Anaheim, CA, USA (2007), Techn. Digest, paper OThG1
111. M. Achouche, V. Magnin, J. Harari, F. Lelarge, E. Derouin, C. Jany, D. Carpentier, F. Blanche, D. Decoster, High performance evanescent edge coupled waveguide unitraveling-carrier photodiodes for >40 Gb/s optical receivers. *IEEE Photonics Technol. Lett.* **16**, 584–586 (2004)
112. Y. Muramoto, K. Kato, M. Mitsuhashi, O. Nakajima, Y. Matsuoka, N. Shimizu, T. Ishibashi, High output voltage, high speed, high efficiency uni-travelling carrier waveguide photodiode. *Electron. Lett.* **34**, 122–123 (1998)
113. C.C. Renaud, D. Moodie, M. Robertson, A.J. Seeds, High output power at 110 GHz with waveguide uni-travelling carrier photodiode, in *Ann. Meeting IEEE Lasers & Electro-Optics Soc. (LEOS'07)*, Lake Buena Vista, FL, USA (2007), Techn. Digest, pp. 782–783
114. S. Demiguel, X. Li, N. Li, H. Chen, J.C. Campbell, J. Wei, A. Anselm, Analysis of partially depleted absorber waveguide photodiodes. *J. Lightwave Technol.* **23**, 2505–2512 (2005)
115. C. Cohen-Jonathan, L. Giraudet, A. Bonzo, J.P. Praseuth, Waveguide AlInAs/GaAlInAs avalanche photodiode with a gain-bandwidth product over 160 GHz. *Electron. Lett.* **33**, 1492–1493 (1997)
116. T. Nakata, T. Takeuchi, K. Maliita, Y. Amamiya, T. Kalo, Y. Suzuki, T. Torikai, High-sensitivity 40-Gbit/s receiver with a wideband InAlAs waveguide avalanche photodiode, in *Proc. 28th Europ. Conf. Opt. Commun. (ECOC'02)*, Copenhagen, Denmark (2002), paper 10.5.1
117. G.S. Kinsey, J.C. Campbell, A.G. Dentai, Waveguide avalanche photodiode operating at 1.55 μm with a gain-bandwidth product of 320 GHz. *IEEE Photonics Technol. Lett.* **13**, 842–844 (2001)
118. J. Wei, F. Xia, S.R. Forrest, A high-responsivity high-bandwidth asymmetric twin-waveguide coupled InGaAs–InP–InAlAs avalanche photodiode. *IEEE Photonics Technol. Lett.* **14**, 1590–1592 (2002)
119. J.E. Bowers, C.A. Burrus, High-speed zero-bias waveguide photodetectors. *Electron. Lett.* **22**, 905–906 (1986)
120. K. Kato, A. Kozen, Y. Muramoto, Y. Itaya, T. Nagatsuma, M. Yaita, 110-GHz, 50%-efficiency mushroom-mesa waveguide p–i–n photodiode for a 1.55- μm wavelength. *IEEE Photonics Technol. Lett.* **6**, 719–721 (1994)
121. W. Park, High-responsivity and high-speed waveguide photodiode with a thin absorption region. *IEEE Photonics Technol. Lett.* **22**, 975–977 (2010)
122. H. Fukano, A. Kozen, K. Kato, O. Nakajima, Edge-illuminated refracting-facet photodiode with high responsivity and low-operation voltage. *Electron. Lett.* **32**, 2346–2347 (1996)
123. H. Fukano, Y. Matsuoka, A low-cost edge-illuminated refracting-facet photodiode module with large bandwidth and high responsivity. *J. Lightwave Technol.* **18**, 79–83 (2000)
124. H. Ito, T. Furuta, S. Kodama, T. Ishibashi, InP/InGaAs uni-travelling-carrier photodiode with 310 GHz bandwidth. *Electron. Lett.* **36**, 1809–1810 (2000)
125. Y. Muramoto, K. Yoshino, S. Kodama, Y. Hirota, H. Ito, T. Ishibashi, 100 and 160 Gbit/s operation of uni-travelling-carrier photodiode module. *Electron. Lett.* **40**, 378–379 (2004)
126. H. Ito, T. Furuta, T. Ito, Y. Muramoto, K. Tsuzuki, K. Yoshino, T. Ishibashi, W-band uni-travelling-carrier photodiode module for high-power photonic millimeter-wave generation. *Electron. Lett.* **38**, 1376–1377 (2002)
127. H. Ito, T. Ito, Y. Muramoto, T. Furuta, T. Ishibashi, Rectangular waveguide output unitraveling-carrier photodiode module for high-power photonic millimeter-wave generation in the F-band. *J. Lightwave Technol.* **21**, 3456–3462 (2003)
128. H. Ito, T. Ito, Y. Muramoto, T. Furuta, T. Ishibashi, Rectangular waveguide output unitraveling-carrier photodiode module for high-power photonic millimeter-wave generation in the F-band. *J. Lightwave Technol.* **21**, 3456–3462 (2003)

129. G. Unterborsch, D. Trommer, A. Umbach, R. Ludwig, H.-G. Bach, High-power performance of a high-speed photodetector, in *Proc. 24th Europ. Conf. Opt. Commun. (ECOC'98)*, Madrid, Spain (1998), pp. 67–68
130. H.-G. Bach, A. Matiss, C.C. Leonhardt, R. Kunkel, D. Schmidt, M. Schell, A. Umbach, Monolithic 90° hybrid with balanced PIN photodiodes for 100 Gbit/s PM-QPSK receiver applications, in *Opt. Fiber Commun. Conf. and Nat. Fiber Opt. Eng. Conf. (OFC/NFOEC'09)*, San Diego, CA, USA (2009), Techn. Digest, paper OMK5
131. H.-G. Bach, A. Beling, G.G. Mekonnen, R. Kunkel, D. Schmidt, W. Ebert, A. Seeger, M. Stollberg, W. Schlaak, InP-based waveguide-integrated photodetector with 100-GHz bandwidth. *IEEE J. Sel. Top. Quantum Electron.* **10**, 668–672 (2004)
132. A. Beling, H.-G. Bach, G.G. Mekonnen, T. Eckhardt, R. Kunkel, D. Schmidt, C. Schubert, Highly efficient PIN photodetector module for 80 Gbit/s and beyond, in *Opt. Fiber Commun. Conf. (OFC'05)*, Anaheim, CA, USA (2005), Techn. Digest, paper OFM1
133. A. Beling, PIN photodiode modules for 80 Gbit/s and beyond, in *Opt. Fiber Commun. Conf. (OFC'06)*, Anaheim, CA, USA (2006), Techn. Digest, paper OFI1
134. H.-G. Bach, R. Kunkel, G.G. Mekonnen, R. Zhang, A. Sigmund, D. Schmidt, C. Sakkas, D. Pech, C. Schubert, Novel 107 Gb/s bias-feeding photodetector OEIC for efficient low-cost photoreceiver co-packaging, in *Proc. 35th Europ. Conf. Opt. Commun. (ECOC'09)*, Vienna, Austria (2009), paper PD1.8
135. A. Beling, H.-G. Bach, G.G. Mekonnen, R. Kunkel, D. Schmidt, Miniaturized waveguide-integrated p–i–n photodetector with 120-GHz bandwidth and high responsivity. *IEEE Photonics Technol. Lett.* **17**, 2152–2154 (2005)
136. A. Beling, H.-G. Bach, G.G. Mekonnen, R. Kunkel, D. Schmidt, High-speed miniaturized photodiode and parallel-fed traveling-wave photodetectors based on InP. *IEEE J. Sel. Top. Quantum Electron.* **13**, 15–21 (2007)
137. R.J. Hawkins, R.J. Deri, O. Wada, Optical power transfer in vertically integrated impedance-matched waveguide/photodetectors: physics and implications for diode-length reduction. *Opt. Lett.* **16**, 470–472 (1991)
138. R.J. Deri, W. Döldissen, R.J. Hawkins, R. Bhat, J.B.D. Soole, L.M. Schiavone, M. Seto, N. Andreadakis, Y. Silberberg, M.A. Koza, Efficient vertical coupling of photodiodes to InGaAsP rib waveguides. *Appl. Phys. Lett.* **58**, 2749–2751 (1991)
139. J. Klamkin, S.M. Madison, D.C. Oakley, A. Napoleone, F. O'Donnell, J. Frederick, M. Sheehan, L.J. Missaggia, J.M. Caissie, J.J. Plant, P.W. Juodawlkis, Uni-traveling-carrier variable confinement waveguide photodiodes. *Opt. Express* **19**, 10199–10205 (2011)
140. A. Beling, InP-based 1.55 μm waveguide-integrated photodetectors for high-speed applications, in *Integr. Optics: Dev., Mater., Technol. X*, San Jose, CA, USA (2006), Proc. SPIE, vol. 6123, 61230K
141. M. Achouche, V. Magnin, J. Harari, D. Carpentier, E. Derouin, C. Jany, F. Blanche, D. Decoster, Design and fabrication of a p–i–n photodiode with high responsivity and large alignment tolerances for 40 Gb/s applications. *IEEE Photonics Technol. Lett.* **18**, 556–558 (2006)
142. S. Demiguel, N. Li, X. Li, X. Zheng, J. Kim, J.C. Campbell, H. Lu, A. Anselm, Very high-responsivity evanescently coupled photodiodes integrating a short planar multimode waveguide for high-speed applications. *IEEE Photonics Technol. Lett.* **15**, 1761–1763 (2003)
143. M. Achouche, C. Cuisin, E. Derouin, F. Pommereau, J.Y. Dupuy, F. Blache, P. Berdaguer, M. Riet, H. Gariah, S. Vuye, D. Carpentier, 43 Gb/s balanced photoreceiver using monolithic integrated lensed facet waveguide dual-UTC photodiodes, in *Proc. OptoElectron. Commun. Conf. and Austral. Conf. Opt. Fibre Technol. (OECC/ACOFT'08)*, Sydney, Australia (2008), paper WeC-3
144. G. Glastre, D. Carpentier, F. Lelarge, B. Rousseau, B. Blache, M. Achouche, High-linearity and high responsivity UTC photodiodes for multi-level formats applications, in *Proc. 35th Europ. Conf. Opt. Commun. (ECOC'09)*, Vienna, Austria (2009), paper 9.2.5
145. F. Xia, J.K. Thomson, M.R. Gokhale, P.V. Studenkov, J. Wei, W. Lin, S.R. Forrest, An asymmetric twin-waveguide high-bandwidth photodiode using a lateral taper coupler. *IEEE Photonics Technol. Lett.* **13**, 845–847 (2001)

146. V.M. Menon, F. Xia, S.R. Forrest, Photonic integration using asymmetric twin-waveguide (ATG) technology: part II – devices. *IEEE J. Sel. Top. Quantum Electron.* **11**, 30–42 (2005)
147. E. Rouvalis, C.C. Renaud, D.G. Moodie, M.J. Robertson, A.J. Seeds, Traveling-wave uni-traveling carrier photodiodes for continuous wave THz generation. *Opt. Express* **18**, 11105–11110 (2010)
148. S. Demiguel, X.-G. Zheng, N. Li, X. Li, J.C. Campbell, J. Decobert, N. Tschertpner, A. Anselm, High-responsivity and high-speed evanescently-coupled avalanche photodiodes. *Electron. Lett.* **39**, 1848–1849 (2003)
149. K. Makita, K. Shiba, T. Nakata, E. Mizuki, S. Watanabe, Recent advances in ultra-high-speed waveguide photodiodes for optical communications. *IEICE Trans. Electron.* **E 92-C**, 922–927 (2009)
150. F.A. Kish et al., Current status of large-scale InP photonic integrated circuits. *IEEE J. Sel. Top. Quantum Electron.* **17**, 1470–1489 (2011)
151. M.W. Geis, S.J. Spector, M.E. Grein, R.T. Schulein, J.U. Yoon, D.M. Lennon, S. Deneault, F. Gan, F.X. Kaertner, T.M. Lyszczarz, CMOS-compatible all-Si high-speed waveguide photodiodes with high responsivity in near-infrared communication band. *IEEE Photonics Technol. Lett.* **19**, 152–154 (2007)
152. M. Zirngibl, J.C. Bischoff, M. Ilegems, J.P. Hirtz, B. Bartenian, P. Beaud, W. Hodel, High speed 1.3 μm InGaAs/GaAs superlattice on Si photodetector. *Electron. Lett.* **26**, 1027–1029 (1990)
153. Y. Gao, Z. Zhong, S. Feng, Y. Geng, H. Liang, A.W. Poon, K.M. Lau, High-speed normal-incidence p–i–n InGaAs photodetectors grown on silicon substrates by MOCVD. *IEEE Photonics Technol. Lett.* **24**, 237–239 (2012)
154. G. Masini, L. Colace, F. Galluzzi, G. Assanto, Advances in the field of poly-Ge on Si near infrared photodetectors. *Mater. Sci. Eng. B* **69**, 257–260 (2000)
155. L. Colace, G. Masini, A. Altieri, G. Assanto, Waveguide photodetectors for the near-infrared in polycrystalline germanium on silicon. *IEEE Photonics Technol. Lett.* **18**, 1094–1096 (2006)
156. S. Luryi, A. Kastalsky, J. Bean, New infrared detector on a silicon chip. *IEEE Trans. Electron Devices* **31**, 1135–1139 (1984)
157. L. Colace, G. Masini, F. Galluzzi, G. Assanto, G. Capellini, L. Di Gaspare, E. Palange, F. Evangelisti, Metal-semiconductor-metal near-infrared light detector based on epitaxial Ge/Si. *Appl. Phys. Lett.* **72**, 3175–3178 (1998)
158. J. Osmond, G. Isella, D. Chrastina, R. Kaufmann, M. Acciarri, H.V. Kanel, Ultralow dark current Ge/Si(100) photodiodes with low thermal budget. *Appl. Phys. Lett.* **94**, 201106:1–201106:3 (2009)
159. D. Liang, G. Roelkens, R. Baets, J.E. Bowers, Hybrid integrated platforms for silicon photonics. *Materials* **3**, 1782–1802 (2010)
160. G. Masini, G. Capellini, J. Witzens, C. Gunn, High-speed, monolithic CMOS receivers at 1550 nm with Ge on Si waveguide photodetectors, in *Ann. Meeting IEEE Lasers & Electro-Optics Soc (LEOS'07)*, Lake Buena Vista, FL, USA (2007), Techn. Digest, pp. 848–849, paper ThU1
161. S. Klinger, M. Berroth, M. Kaschel, M. Oehme, E. Kasper, Ge-on-Si p–i–n photodiodes with a 3-dB bandwidth of 49 GHz. *IEEE Photonics Technol. Lett.* **21**, 920–922 (2009)
162. D. Liang, J.E. Bowers, Photonic integration: Si or InP substrates? *Electron. Lett.* **45**, 578–581 (2009)
163. Z. Huang, J. Oh, J.C. Campbell, Back-side-illuminated high-speed Ge photodetector fabricated on Si substrate using thin SiGe buffer layers. *Appl. Phys. Lett.* **85**, 3286–3289 (2004)
164. H.-Y. Yu, J.-H. Park, A.K. Okyay, K.C. Saraswat, Selective-area high-quality germanium growth for monolithic integrated optoelectronics. *IEEE Electron Device Lett.* **33**, 579–581 (2012)
165. H.-C. Luan, D.R. Lim, K.K. Lee, K.M. Chen, J.G. Sandland, K. Wada, L.C. Kimerling, High-quality Ge epilayers on Si with low threading-dislocation densities. *Appl. Phys. Lett.* **75**, 3286–3289 (2004)

166. D. Suh, S. Kim, J. Joo, G. Kim, 36-GHz high-responsivity Ge photodetectors grown by RPCVD. *IEEE Photonics Technol. Lett.* **21**, 672–674 (2009)
167. S.J. Koester, J.D. Schaub, G. Dehlinger, J.O. Chu, Germanium-on-SOI infrared detectors for integrated photonic applications. *IEEE J. Sel. Top. Quantum Electron.* **12**, 1489–1502 (2006)
168. J. Liu, D.D. Cannon, K. Wada, Y. Ishikawa, S. Jongthammanurak, D.T. Danielson, J. Michel, L.C. Kimerling, Tensile strained Ge p–i–n photodetectors on Si platform for C and L band telecommunications. *Appl. Phys. Lett.* **87**, 011110 (2005)
169. D. Ahn, C.-Y. Hong, J. Liu, W. Giziewicz, M. Beals, L.C. Kimerling, J. Michel, J. Chen, F.X. Kärtner, High performance, waveguide integrated Ge photodetectors. *Opt. Express* **15**, 3916–3921 (2007)
170. T. Yin, R. Cohen, M.M. Morse, G. Sarid, Y. Chetrit, D. Rubin, M.J. Paniccia, 31 GHz Ge n–i–p waveguide photodetectors on silicon-on-insulator substrate. *Opt. Express* **15**, 13965–13971 (2007)
171. D. Feng, W. Qian, H. Liang, B.J. Luff, M. Asghari, High-speed receiver technology on the SOI platform. *IEEE J. Sel. Top. Quantum Electron.* **19**, 38100–38108 (2013)
172. S. Assefa, F. Xia, S.W. Bedell, Y. Zhang, T. Topuria, P.M. Rice, Y.A. Vlasov, CMOS-integrated 40 GHz germanium waveguide photodetector for on-chip optical interconnects, in *Opt. Fiber Commun. Conf. and Nat. Fiber Opt. Eng. Conf. (OFC/NFOEC'09)*, San Diego, CA, USA (2009), Techn. Digest, paper OMR4
173. C.T. DeRose, D.C. Trotter, W.A. Zortman, A.L. Starbuck, M. Fisher, M.R. Watts, P.S. Davids, Ultra compact 45 GHz CMOS compatible germanium waveguide photodiode with low dark current. *Opt. Express* **19**, 24897–24904 (2011)
174. D. Feng, S. Liao, P. Dong, N.-N. Feng, H. Liang, D. Zheng, C.-C. Kung, J. Fong, R. Shafiqi, J. Cunningham, A.V. Krishnamoorthy, M. Asghari, High-speed Ge photodetector monolithically integrated with large cross-section silicon-on-insulator waveguide. *Appl. Phys. Lett.* **95**, 261105-03 (2009)
175. L. Vivien, A. Polzer, D. Marris-Morini, J. Osmond, J.M. Hartmann, P. Crozat, E. Cassan, C. Kopp, H. Zimmermann, J.M. Fédéli, Zero-bias 40 Gbit/s germanium waveguide photodetector on silicon. *Opt. Express* **20**, 1096–1101 (2012)
176. T.-Y. Liow, A. Eu-Jin Lim, N. Duan, M. Yu, G.-Q. Lo, Waveguide germanium photodetector with high bandwidth and high L-band responsivity, in *Opt. Fiber Commun. Conf. and Nat. Fiber Opt. Eng. Conf. (OFC/NFOEC'13)*, Anaheim, CA, USA (2013), Techn. Digest, paper OM3K.2
177. P. De Dobbelaere, B. Analui, E. Balmater, D. Guckenberger, M. Harrison, R. Koumans, D. Kucharski, Y. Liang, G. Masini, A. Mekis, S. Mirsaidi, A. Narasimha, M. Peterson, T. Pinguet, D. Rines, V. Sadagopan, S. Sahni, T.J. Sleboda, Y. Wang, B. Welch, J. Witzens, J. Yao, S. Abdalla, S. Gloeckner, G. Capellini, Demonstration of first WDM CMOS photonics transceiver with monolithically integrated photo-detectors, in *Proc. 34th Europ. Conf. Opt. Commun. (ECOC'08)*, Brussels, Belgium (2008), paper Tu. 3.C.1
178. K.-W. Ang, T.-Y. Liow, M.-B. Yu, Q. Fang, J. Song, G.-Q. Lo, D.-L. Kwong, Low thermal budget monolithic integration of evanescent-coupled Ge-on-SOI photodetector on Si CMOS platform. *IEEE J. Sel. Top. Quantum Electron.* **16**, 106–113 (2010)
179. S.J. Koester, C.L. Schow, L. Schares, G. Dehlinger, J.D. Schaub, F.E. Doany, R.A. John, Ge-on-SOI-detector/Si-CMOS-amplifier receivers for high-performance optical-communication applications. *J. Lightwave Technol.* **25**, 46–57 (2007)
180. D. Knoll, S. Lischke, L. Zimmermann, B. Heinemann, D. Micusik, P. Ostrovskyy, G. Winzer, M. Kroh, R. Barth, S. Grabolla, K. Schulz, M. Fraschke, M. Lisker, J. Drews, A. Trusch, A. Krüger, S. Marschmeyer, H.H. Richter, O. Fursenko, Y. Yamamoto, B. Wohlfeil, K. Petermann, A. Beling, Q. Zhou, B. Tillack, Monolithically Integrated 25 Gbit/sec receiver for 1.55 μm in photonic BiCMOS technology, in *Opt. Fiber Commun. Conf. (OFC'14)*, San Francisco, CA, USA (2014), Techn. Digest, paper Th4C.4
181. H. Park, M.N. Sysak, H.-W. Chen, A.W. Fang, D. Liang, L. Liao, B.R. Koch, J. Bovington, Y. Tang, K. Wong, M. Jacob-Mitos, R. Jones, J.E. Bowers, Device and integration technology

- for silicon photonic transmitters. *IEEE J. Sel. Top. Quantum Electron.* **17**, 671–688 (2011)
182. H. Park, A.W. Fang, R. Jones, O. Cohen, O. Raday, M.N. Sysak, M.J. Paniccia, J.E. Bowers, A hybrid AlGaInAs–silicon evanescent waveguide photodetector. *Opt. Express* **15**, 6044–6052 (2007)
 183. H.-H. Chang, Y.-H. Kuo, H.-W. Chen, R. Jones, A. Barkai, M.J. Paniccia, J.E. Bowers, Integrated triplexer on hybrid silicon platform, in *Opt. Fiber Commun. Conf. and Nat. Fiber Opt. Eng. Conf. (OFC/NFOEC'10)*, San Diego, CA, USA (2010), Techn. Digest, paper OThC4
 184. X. Xie, Q. Zhou, E. Norberg, M. Jacob-Mitos, Y. Chen, A. Ramaswamy, G. Fish, J.E. Bowers, J. Campbell, A. Beling, Heterogeneously integrated waveguide-coupled photodiodes on SOI with 12 dBm output power at 40 GHz, in *Opt. Fiber Commun. Conf. (OFC'15)*, Los Angeles, CA, USA (2015), Techn. Digest, PDP Th5B.7
 185. H. Pan, Z. Li, A. Beling, J.C. Campbell, Measurement and modeling of high-linearity modified uni-traveling carrier photodiode with highly-doped absorber. *Opt. Express* **17**, 20221–20226 (2009)
 186. M. Piels, J.F. Bauters, M.L. Davenport, M.J.R. Heck, J.E. Bowers, Low-loss silicon nitride AWG demultiplexer heterogeneously integrated with hybrid III–V/silicon photodetectors. *J. Lightwave Technol.* **32**, 817–823 (2014)
 187. P.R.A. Binetti, X.J.M. Leijtens, T. de Vries, Y.S. Oei, L. Di Cioccio, J.-M. Fédéli, C. Laguna, J. Van Campenhout, D. Van Thourhout, P.J. van Veldhoven, R. Nötzel, M.K. Smit, InP/InGaAs photodetector on SOI photonic circuitry. *IEEE Photonics J.* **2**, 299–305 (2010)
 188. G. Roelkens, J. Brouckaert, D. Taillaert, P. Dumon, W. Bogaerts, D. Van Thourhout, R. Baets, Integration of InP/InGaAsP photodetectors onto silicon-on-insulator waveguide circuits. *Opt. Express* **13**, 10102–10108 (2005)
 189. A. Gassenq, N. Hattasan, L. Cerutti, J.B. Rodriguez, E. Tournié, G. Roelkens, Study of evanescently-coupled and grating-assisted GaInAsSb photodiodes integrated on a silicon photonic chip. *Opt. Express* **20**, 11665–11672 (2012)
 190. B.T. Smith, H. Lei, C.-C. Kung, D. Feng, J. Yin, H. Liang, Integrated silicon photonic circuit: monolithic 8-channel modulator, tap, vertical coupler, and flip-chip mounted photodetector array, in *Silicon Photonics*. San Jose, CA, USA (2006), Proc. SPIE, vol. 6125, 61250I
 191. L. Zimmermann, M. Kroh, K. Voigt, G. Winzer, H. Tian, L. Stampoulidis, B. Tillack, K. Petermann, Hybrid integration of coherent receivers for Terabit Ethernet on SOI waveguide PLC, in *9th IEEE Conf. Group IV Photonics*, San Diego, CA, USA (2012), Techn. Digest, pp. 153–155
 192. Y. Geng, S. Feng, A.W.O. Poon, K.M. Lau, High-speed InGaAs photodetectors by selective-area MOCVD toward optoelectronic integrated circuits. *IEEE J. Sel. Top. Quantum Electron.* **20**, 36–42 (2014)

Andreas Beling received the Dipl.-Phys. degree (M.S.) in physics from the University of Bonn, Germany, in 2000 and the Dr.-Ing. degree (Ph.D.) in electrical engineering from Technical University Berlin, Germany, in 2006. He was a staff scientist in the photonics division at the Heinrich-Hertz-Institute in Berlin in 2001–2006, a Research Associate in the Department of Electrical and Computer Engineering at the University of Virginia in 2006–2008, and has two years of industry experience as a project manager working on 100-GHz photodiodes and coherent receivers. He returned to University of Virginia and became Assistant Professor in the Department of Electrical and Computer Engineering in 2013. His research interests include high-speed optoelectronic devices, photonic integrated circuits, microwave photonics, and optical communications. Andreas Beling has authored or co-authored more than 110 technical papers, two book chapters, and four patents. He has served on the technical program committee of the Optical Fiber Communication (OFC) Conference (2010–2012), the International Conference on Indium Phosphide and Related Materials (2014), and the Microwave Photonics Conference (2015) and was a Technical Program Subcommittee Chair for Subcommittee 8 (Optoelectronic Devices) at OFC in 2013. Since 2014 Dr. Beling is an Associate Editor of the IEEE/OSA Journal of Lightwave Technology.

Joe C. Campbell received the B.S. Degree in Physics from the University of Texas at Austin in 1969, and the M.S. and Ph.D. degrees in Physics from the University of Illinois at Urbana-Champaign in 1971 and 1973, respectively. From 1974 to 1976 he was employed by Texas Instruments. In 1976 he joined the staff of AT&T Bell Laboratories in Holmdel, New Jersey. In 1989 he accepted Cockrell Family Regents Chair in Engineering at the University of Texas at Austin. Professor Campbell joined the faculty of the University of Virginia in Charlottesville as the Lucian Carr, III Chair in the School of Engineering and Applied Science in 2006. At present he is actively involved in single-photon-counting APDs, Si-based optoelectronics, high-speed low-noise avalanche photodiodes, high-power high-linearity photodiodes, and ultraviolet avalanche photodiodes. To date he has coauthored 10 book chapters, 420 articles for refereed technical journals, and more than 300 conference presentations.

Chapter 7

Higher-Order Modulation Formats – Concepts and Enabling Devices

Wilfried Idler and Fred Buchali

Abstract The chapter gives a general introduction to higher-order modulation (HOM) formats and reviews the current status of concepts of coherent transceivers applied in optical fiber communications. The chapter presents an overview on the major enablers of HOM formats in optical transmission: forward error correction, digital signal processing, data converter, DP-IQ modulator, receiver frontend and application-specific integrated circuit (ASIC) technology. Based on the examples of current and future 400 Gbit/s and 1 Tbit/s transceivers the chapter illustrates feasible transmission capacities and transmission reach with HOM formats based on EDFA repeated C-band transmission over dispersion uncompensated standard single mode fiber.

7.1 Introduction

Over the past 20 years the worldwide Internet traffic has grown exponentially and cumulated annual growth rates (CAGRs) have been of the order of 100% during the period from 1995 to 2000, and even after the “burst of the bubble” impressive ~40% CAGRs have been achieved up to 2013, primarily driven by data-centric users. This growth in traffic has been enabled by tremendous increments of transport capacity of the fiber optical networks, and this development is still going on. Latest forecasts in 2016 [1] predict that until 2020 the global Internet traffic will still continue to grow worldwide with a CAGR of about 22%.

Figure 7.1 shows the progress and status of single fiber capacities on the optical C-band and transmission bit rate achievements in research and product implementations from 1988 until 2014, and Fig. 7.1 also illustrates a CAGR trend of 22% (grey arrow) for the fiber capacity utilization between 2014 and 2020.

In DWDM fiber networks the capacity of a single fiber has been increased from 1 Gbit/s with a single carrier modulated with 1 Gbit/s NRZ in the mid-1980s to al-

W. Idler (✉) · F. Buchali
Nokia Bell Labs, Lorenzstraße 10, 70435 Stuttgart, Germany
e-mail: wilfried.idler@nokia-bell-labs.com

F. Buchali
e-mail: fred.buchali@nokia-bell-labs.com

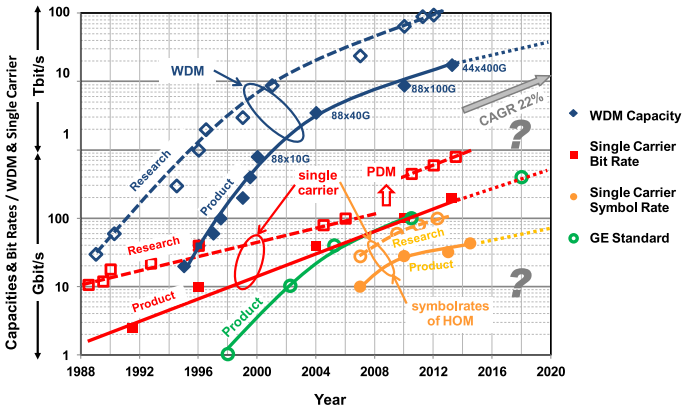


Fig. 7.1 C-band fiber capacities and increase of bit rates over the years in research and products

most 1 Tbit/s by 2000. Based upon progress in TDM technology single carrier bit rates have been raised from 1 Gbit/s to 2.5 Gbit/s and 10 Gbit/s NRZ, and in combination with the introduction of WDM technology in 1995 [2], five years later in 2000, 880 Gbit/s total capacity was achieved on a single fiber with 10 Gbit/s \times 88 channels in the C-band on the 50 GHz standard grid. Determined by the optical bandwidth of EDFA repeaters we are considering throughout this chapter 4.4 THz optical bandwidth (~ 35 nm) for the C-band and the supported single fiber capacities.

In order to further increase the capacity from 10 Gbit/s towards the next transport hierarchy of 40 Gbit/s, research has focused on modulation formats other than NRZ which spectrally fit into the 50 GHz grid. First 40 Gbit/s WDM products started in 2004 and were based on optical duobinary (ODB) and differential quaternary phase shift keying (DQPSK) for Metro applications with direct detection receivers. They achieved spectral efficiencies (SE) of 0.8 bit/s/Hz and enabled up to 3.5 Tbit/s fiber transport capacity in 2004. DQPSK was the first product implementation in optical transport with a multi-level higher order modulation (HOM) format, modulating 4 phase levels. Six years earlier a multi-level format on the basis of 4 amplitude modulated levels (4ASK), also denoted as 4PAM (pulse amplitude modulation), had been proposed in research as an early solution for 40 Gbit/s bit rates [3] based on 20 GBd symbol rate electronics. Recently the 4PAM format became of high interest for 400 Gigabit Ethernet (GE) transport [4]. All 40 Gbit/s direct detection Metro and long haul transport systems have been challenged with fiber polarization mode dispersion (PMD) as well as the need for a further increase of the SE by including polarization division multiplexing (PDM). A major breakthrough of reaching SE beyond 1 bit/s/Hz and the mitigation of issues related to PMD and PDM has been achieved after 2008 with coherent receiver technology and the implementation of 100 Gbit/s systems based on PDM or dual-polarization (DP) and QPSK modulation formats in 2010. The key of the rediscovery of coherent receiver technology and the key enabler for the effective use of HOMs were the introduction of analogue-to-digital data

converters (ADCs) and digital signal processing (DSP) in optical communication enabled by the continuous progress of complementary metal-oxide semiconductor (CMOS) technology.

In recent years complex HOM formats based on quadrature amplitude modulation (QAM) became indispensable in all digital communication areas in order to increase transmission bit rates over existing infrastructures by increasing spectral efficiency and capacity [5]. In telephone modems or at cable based digital video broadcast (DVB-C2) very high constellation sizes of 4096QAM are applied. However, in optical communication the transmission bit rates are significantly higher and signal-to-noise-ratio values at optical receivers are significantly lower, and therefore constellation sizes applicable for optical communication products are significantly lower. Nevertheless, constellation sizes as high as 1024QAM [6] and even 2048QAM [7] have been demonstrated in optical communication research, requiring very narrow linewidth lasers and Raman amplification for transmission demonstration.

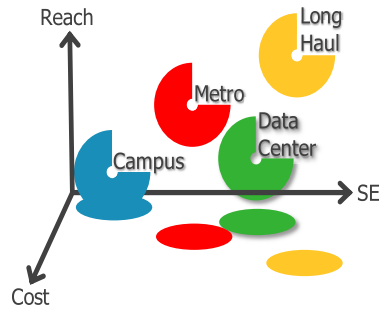
100 Gbit/s based on DP-QPSK with coherent detection became a preferred solution [8] as it can be applied on existing 50 GHz grid fiber infrastructure, operating with 28 GBd symbol rate. QPSK is encoding two bits/symbol and together with PDM four bits are encoded on each symbol. Since the first commercial deployment of 100 Gbit/s line cards with DP-QPSK on a single carrier in 2010, about 300,000 line cards [9] have already been deployed until mid 2016. According to [10], until 2020 the demand for 100 Gbit/s (and higher) line cards will grow with a CAGR of about 120%. On the other hand, 40 Gbit/s line card deployments are continuously dropping, they became less than 10% of 100 Gbit/s line card shipments in 2016 [9], as many operators apparently move from 10 Gbit/s directly to 100 Gbit/s systems.

The most recent bit rate hierarchy started in 2014 with 400 Gbit/s systems based on 200 Gbit/s and the DP-16QAM HOM format with an SE of 4 bit/s/Hz. Including frequency division multiplexing (FDM) by combining two sub-carriers, 2×200 Gbit/s can also be transported over the 50 GHz grid capturing two frequency slots of 50 GHz. Thus the C-band capacity of a single fiber with 4.4 THz bandwidth reaches ~ 18 Tbit/s.

The use of HOM formats together with orthogonal frequency division multiplexing (OFDM) has been intensively investigated for optical transmission applications. OFDM is somewhat less spectrally efficient than the corresponding single carrier schemes can be when they are modulated with the same HOM formats, due to cyclic prefix, pilot, and training symbol overhead requirements [11]. Furthermore, as OFDM uses a rather high number of sub-carriers and low symbol rates, OFDM is severely impaired by inter-channel and intra-channel fiber non-linear effects, especially at dispersion managed transmission. The latter is dominated by strong self-phase modulation (SPM) due to the narrow spectral width of the individually modulated carriers as SPM tolerance is increasing with the symbol rate [12]. This is one reason why OFDM systems have not yet been deployed and will not be considered further in this chapter.

Recently, HOM formats together with discrete multitone transmission (DMT) using directly modulated lasers and direct detection have been proposed as a low cost alternative for 100 Gbit/s [13] and for 400 Gbit/s [14] short reach transmission (see

Fig. 7.2 Applications triangle



also Chap. 4, Sect. 4.5.2). DSP in direct detection DMT is comparable with OFDM but DMT rejects the complex part of the received signal. However, even if a high constellation size such as 128QAM [13] is applied, DMT is not spectrally efficient for DWDM networks due to the poor frequency stability of directly modulated and uncooled DFB lasers, and therefore the proposed application area of DMT is short reach CWDM [15] with 20 nm channel spacing. Similar to OFDM, DMT does also apply a very high number of sub-carriers (> 1000) and symbol rates per sub-carrier in the few Mbd regime. Therefore DMT does also suffer from SPM so that its application space is limited to short reach or intra campus applications. As OFDM, DMT will also not be treated in this chapter.

The application areas of optical transmission systems have different requirements on capacity (spectral efficiency), the supported transmission distance (reach) and cost per transported bit, as depicted in Fig. 7.2. Application areas we will focus on in this chapter are intra data center, Metro and long haul. Connections between data centers (inter) are usually point-point long haul transmission links. Depending on country and continent the required distances for Metro and long haul are different but can roughly be separated: Metro below 500 km fiber distances and long haul between 500 km and 1000 km in Europe and up to 3000 km in North America. Intra data center distances are typically well below 50 km. Except for campus and access applications, for intra data center, Metro and long haul high spectral efficiencies are required but with different sensitivities to cost.

The application areas and corresponding capacity limits of HOM formats are determined by their OSNR (optical signal to noise ratio) constraints or sensitivities and the fiber infrastructure. Taking long haul fiber infrastructures for comparison, capacities can be increased by 150% by including L-band transmission [16], implementation of new fiber types with lower insertion loss and higher effective area [17], or including Raman amplification. Finally, depending on the development progress and future cost of regenerators, the use of high constellation sizes for 3R-regenerators could become very attractive for shifting the application boundaries of HOM formats towards higher constellation sizes.

If only widely deployed C-band transmission with standard single mode fibers (SMF) and EDFA repeaters are taken into account, the capacity limits per fiber of long haul networks in the order of 15 to 20 Tbit/s are reached with 8QAM and 16QAM, respectively. Metro network backbones supported by HOM formats can reach 35 Tbit/s with DP-64QAM, potentially implementable before 2020. Further

increments of the spectral efficiency and capacities up to 40 or 50 Tbit/s are feasible by 128QAM or 256QAM, but due to increasing OSNR constraints with increasing the constellation size of HOMs, regeneration for long haul transmission will be required or potential future application areas are limited to short reach, access and data centers.

SDM [18] has been proposed as the only way-out of potential future capacity bottlenecks for long haul and Metro networks and significant research has been performed in the past few years with amazing results (see also Chap. 1). Recently, very high spectral efficiencies above 300 bit/s/Hz [19] have already been demonstrated with transmission over a 19 core fiber where six modes appear coupled. Multiple-input and multiple-output (MIMO) DSP has become an essential element of wireless communication as a method for multiplying the capacity of a radio link using multiple transmit and receive antennas to exploit multipath propagation. In optical transmission research MIMO has been successfully demonstrated in multimode fiber transmission or in transmission of multi-core fibers where modes can also be coupled. The highest MIMO complexity has been reported with transmission over 15 coupled spatial modes in MMF by massive 30×30 MIMO processing [20]. However, from today's perspective, the potential market maturity and implementation start of SDM are unknown as these are determined by many factors, mainly driven by future capacity requirements of operators' backbone and by the performance and cost of the new SDM technology.

A perpetual question is the degree of capacity utilization of operations backbone and when investments are needed for new technologies and higher fiber capacities. Today it appears very uncertain by what time single fiber capacities higher than 35 Tbit/s will be required and when SDM technologies will be needed or alternatively transmission including the optical L-band will be favored or regenerators for HOM formats become available or Raman amplification will be further pushed for implementation. Fiber utilization and capacity requirements vary significantly between applications, countries and operators, and neither analyst studies can provide reliable predictions of future developments. One often reported message is that 0.88 Tbit/s capacity per fiber is utilized and that operators had begun in 2014 already a capacity upgrade moving directly from 10G to 100G launching for a future completion of an 8.8 Tbit/s capacity. The arrow (CAGR 22%) in Fig. 7.1 indicates an optimistic case that with 3.6 Tbit/s capacity (e.g.: 88×40 Gbit/s) already utilized in operators' Metro fiber backbone in 2014 and a 22% increase per year the capacity requirements will be ~ 10 Tbit/s in 2020. Thus operators may not require single fiber capacities of 35 Tbit/s in earlier than 2020.

This chapter reviews the current status of concepts and enabling devices for HOM formats in optical transmission, comprised in current and future coherent transceivers: DP-MQAM formats are generated with transmitter DSP, digital-analogue converters (DACs) and IQ modulators and received with a coherent receiver frontend followed by ADCs and DSP. This chapter will be organized as follows: In Sect. 7.2 on optical transceivers we will highlight coherent receiver technology concepts and building blocks. In Sect. 7.3 we will focus on HOM formats suitable for three application areas (intra data center, Metro and long haul)

and analyze the transmission performance for the case without optical dispersion compensation and analyze achievable fiber transmission capacities versus application areas. In the following three sections we will present an overview on the key electronic concepts, the major enablers of HOM formats in optics: forward error correction (Sect. 7.4), digital signal processing (Sect. 7.5) and data converters (Sect. 7.6). Section 7.7 will focus on the enabling optical devices for HOM formats: DP-IQ modulator, receiver frontend and application-specific integrated circuit (ASIC) technology, including data converter and DSP, as the key components for the realization and implementation of QAM formats and reception for very high bit rate transmission.

7.2 Coherent Transceiver

7.2.1 *Reinvention of Coherent Receiver Technology*

In optical fiber communication, coherent receivers with free running local oscillator (LO) lasers, which exploit information in amplitude and phase, were extensively studied in the late eighties and early nineties of the last century [21–24]. This receiver concept was called “Intradyn Receiver” to be distinguished from a heterodyne receiver where the transmit laser frequency and the LO frequency can differ by more than the signal bandwidth.

Basically, we distinguish between three different coherent receiver concepts:

Homodyne: the optical signal spectrum is converted to the electrical baseband and a single common laser source is used for the transmitter (Tx) and as LO.

Intradyn: the optical signal spectrum is converted to the electrical baseband and two independent lasers for Tx and LO corresponding to the same channel number are applied but any frequency offset must be significantly smaller than the electrical baseband.

Heterodyne: the converted optical signal spectrum is converted outside the electrical baseband as the offset between Tx and LO lasers is larger than the signal bandwidth or the symbol rate.

Coherent detection of amplitude and phase is performed by mixing the modulated carrier signal with an LO into the baseband, a technique widely used in RF wireline and wireless telecommunication systems. The baseband signal is amplified by the LO and subsequently down-converted including appropriate filtering.

With the emergence of the EDFA in the early nineties of the last century, the advantage of higher receiver sensitivity of a coherent receiver compared to direct detection vanished and coherent receiver technology disappeared for more than 10 years. Since 2006 coherent optical systems are rediscovered as an area of very high interest again [25] and have revolutionized long haul and high-speed optical communication systems. Corresponding R&D activities were significantly pushed by Si hardware, in particular as high speed ADCs and electronic signal processors have become mature. In optical communications digital signal processing at the optical receiver has been commercialized at bit rates of 10 Gbit/s at first and coherent receivers at 40 Gbit/s later. Due to further progress in CMOS technologies until to-

day, data converters and DSP can now be realized by a single chip for 100 Gbit/s and 400 Gbit/s transceivers.

By coherent detection, all optical field parameters (amplitude, phase and polarization) become available in the electrical domain. Therefore the demodulation schemes are not limited to the detection of phase differences as for directly detected DPSK or DQPSK formats, but arbitrary modulation formats and modulation constellations including polarization multiplexed signals can be analyzed. The preservation of the temporal phase enables electronic compensation of linear transmission impairments such as chromatic dispersion [26, 27], and polarization mode dispersion (PMD), and even fiber nonlinearities can be partly mitigated at the electrical baseband. Many limitations and obstacles which existed in the past for the deployment of coherent detection have now been overcome: Carrier linewidth requirements become relaxed with increasing channel data and symbol rates so that standard commercial communication lasers can be used [28]. In addition, high-speed digital signal processing allows to perform fast polarization tracking, channel equalization, frequency and phase recovery, all processed in the electronic domain, which lifts the main barriers which have so far prevented to exploit the advantages of coherent detection.

7.2.2 Coherent Optical Transceiver – Concepts and Building Blocks

After a start of coherent system implementations with 40 Gbit/s in 2008, single carrier 100 Gbit/s DP-QPSK coherent systems have been shipped since 2010 [29]. In 2010 various modulation format options had been proposed for 100 Gbit/s applications [30], however, in the following years the optical transport market has rapidly accepted DP-QPSK with coherent reception due to its superior performance: Until today DP-QPSK had been massively deployed, it has reached a market share of more than 80%, and this is still growing.

The major driver of the 100G coherent transceiver commercialization was the OIF, which had initiated the “100G Ultra Long Haul DWDM Framework Document” [8] and component related documents [31, 32], with the intention of pushing interoperability and cost reduction by various implementation agreements in which the main building blocks of optical transceivers are described.

After 40 Gbit/s, 100 Gbit/s has been the 2nd bit rate hierarchy where client GE bit rates of 100GE [33] met optical transport client bit rates. The first commercially available 100 Gbit/s DP-QPSK transceiver operates at ~ 112 Gbit/s transmission line rate or gross rate and ~ 28 Gbd symbol rate or baud rate. Line rate and symbol rate are related via the modulation efficiency of 4 bits/symbol for DP-QPSK. The exact line rate is defined by the OTU4 line rate = 111.809973 Gbit/s given in G.709 [34], and the maximum net rate is defined by the 100GE rate [35]: 103.125 Gbit/s. The difference to the OTU4 line rate includes protocol overhead (OH) and 7% forward error correction (FEC) OH. If transceivers work on the OTU4 line rate, there is no

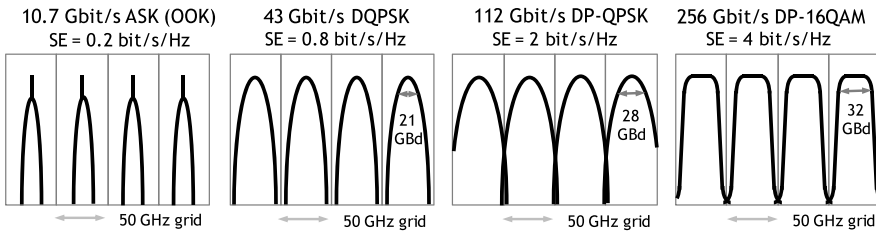


Fig. 7.3 Channel allocation of bit rate hierarchies, showing *line rates* per carrier and modulation formats: four channels at 10.7 Gbit/s, 43 Gbit/s, 112 Gbit/s and 256 Gbit/s

capacity available for further bits potentially required for training sequences, for more details see Sect. 7.5.2, and the coherent receiver has to operate with blind adaptation. Transceivers from different suppliers operating on the OTU4 line rate are potentially interoperable if they include the same FEC encoding.

The 3rd hierarchy where GE rates meet transport bit rates will be 400 Gbit/s. It is targeted for 2018 and will support future 400GE rates [35] with a true net rate of 412.5 Gbit/s. 400 Gbit/s transceivers based on dual-carrier frequency division multiplexing (FDM) and DP-16QAM modulation format (8 bits/symbol) have been developed and entered the optical transport market in 2014 already. 16QAM modulation plus the higher line rate causes a degradation of about 10 dB in OSNR compared to 100 Gbit/s transceivers. In order to mitigate this penalty more powerful FEC has been developed (i.e. SD-FEC) leading to the 3rd FEC generation [36] (Sect. 7.4.2). The consequence of 400 Gbit/s transmission was the need for higher FEC overhead of $\sim 25\%$ resulting in higher transmission line rates of 512 Gbit/s (2×256 Gbit/s FDM sub-carriers). The latter are based on 32 GBd symbol rate and can cope with bit error ratios (BER) before SD-FEC of 0.04.

The diagram most to the right in Fig. 7.3 shows the spectral characteristics of 400 Gbit/s transmitters based upon two FDM sub-carriers. For comparison purposes Fig. 7.3 also illustrates the spectral characteristics of commercially available 10 Gbit/s, 40 Gbit/s and 100 Gbit/s transceivers, from left to right, all on the 50 GHz channel grid. Figure 7.3 includes the respective spectral efficiencies, the line rates, the modulation formats, the symbol rates (GBd) in case of HOM formats (at 40 Gbit/s we exemplarily selected DQPSK), and the respective spectral efficiencies. The spectral efficiency is generally related to the information bit rate or net rate and the channel spacing (W). Spectral shaping or spectral pre-emphasis (cf. Section 7.5.1) has been applied for the 256 Gbit/s/32 GBd signals while the other signals in Fig. 7.3 are not spectrally pre-shaped.

Current 400 Gbit/s and next generations of optical coherent transceivers are based on the indispensable concepts of: HOM formats, polarization division multiplexing, FEC, digital-analogue and analogue-digital conversion, and DSP.

Polarization division multiplexing means transmission of data in both optical polarizations, thus PDM or dual polarization operation doubles the modulation efficiency and the spectral efficiency of any HOM format. DP operation of HOM became a common method together with coherent technology as fast and reliable

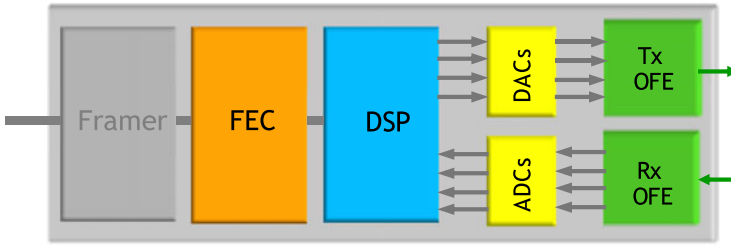


Fig. 7.4 Block diagram of a coherent transceiver

polarization demultiplexing became feasible by coherent detection and the following DSP.

A single carrier or FDM based optical transceiver with coherent detection as shown in Fig. 7.4 comprises four electronics and two optical building blocks: (1) the data framer as interface to client data structures, (2) FEC for data encoding and decoding, (3) the large DSP block including the HOM format generation and various algorithmic processing steps, (4) four DACs and four ADC data converters which support modulation and reception of the four tributaries: I_x , I_y , Q_x and Q_y , (5) the transmitter optical frontend (Tx-OFE) including linear amplification and modulation of light of a C-band tunable laser, and finally (6) the optical receiver frontend (Rx-OFE) consisting of a local oscillator (C-band tunable) and a coherent optical frontend.

A *Client data framer* realizes the mapping (multiplexing/demultiplexing) of variable length, higher-layer client signals (today mostly IP) over a circuit switched transport network like OTN [34]. Client interface considerations are beyond the scope of this chapter and will not be discussed further.

Forward Error Correction (FEC): Transmitted data are encoded on an FEC encoder and the received and processed data are verified and corrected in an FEC decoder. FEC became inevitable in coherent transceivers as (a) error free transmission with BERs below 10^{-15} cannot be achieved with coherent receivers and (b) high coding gain is required with high pre-FEC BERs above 10^{-2} ensuring post-FEC BERs $<10^{-15}$. Due to the need and inclusion of SD-FEC, the FEC requires a significant part of the transceiver complexity and power consumption. More details about SD-FEC are reported in Sect. 7.4.

Digital Signal Processing (DSP): DSP together with data converters are the key enablers of coherent technology. DSP comprises the implementation of all necessary algorithmic processing steps to recover single carrier related transmission impairments of a single fiber. However, space division multiplexing and transmission over multi-core fibers requiring massive $M \times M$ MIMO algorithm implementations [18], related to M spatial coupled fiber modes and M polarization modes, will not be treated further in this chapter (but it is covered in detail in Chap. 1). Transmission over a single fiber on a single carrier with two polarizations reduces the MIMO space to a 2×2 MIMO as applied at the polarization demultiplexing algorithm.

At the transmitter side the algorithms include encoding of bits onto HOM formats, spectral equalization and pre-emphasis which has become an important con-

cept for optimization of spectral efficiency. More details are given in Sects. 7.5.1 and 7.5.2. At the receiver side the most important algorithms required are: chromatic dispersion compensation, timing recovery, polarization demultiplexing, channel equalization, frequency and phase estimation adapted to HOM formats. Chromatic dispersion compensation requires high complexity at the receiver DSP due to the very high amount of dispersion of typically 35,000 ps/nm to be compensated. More details about the transceiver DSP are given in Sect. 7.5.

High Speed Data Converters: DACs and ADCs have enabled digital modulation and digital detection and have become inevitable interfaces to the optical frontends (OFE) of coherent transceivers. Due to the very high bit rates and the required complexity of DACs and ADCs, the digital revolution arrived in fiber optics several years later than in other technologies. More details on architectures and technologies of data converters are given in Sects. 7.6 and 7.7.3.

Optical Frontends (OFE) including the data modulator and polarization diversity receiver will be described in Sect. 7.7.

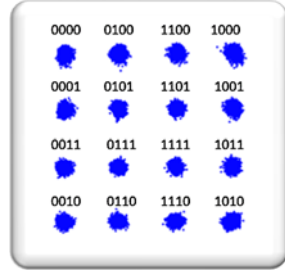
7.3 Higher-Order Modulation Formats

In electrical communication technologies very high constellation sizes up to 4096 ($m = 12$) became standard applications but in optical communication the bit rates are significantly higher and the noise at the receiver is significantly lower and thus feasible constellation sizes for optical communication products are significantly smaller. However, a constellation size as high as 2048QAM including transmission over 150 km of fiber has already been demonstrated in fiber optics research [7]. The main challenges of applying high constellation sizes are laser phase noise and OSNR constraints, thus smaller constellations potentially up to 64QAM might be implementable in real systems in the near future and potentially up to 256QAM might be expected in about five to ten years. In this chapter we include constellation sizes up to 1024QAM for the comparison of HOM formats.

The main objective of HOM formats is to raise the spectral efficiency by increasing the bit rate together with keeping or reducing the modulation symbol rate and its signal spectral width. HOM formats are defined by their number of encoded bits on transmitted symbols. While in the standard NRZ modulation format 1 bit is encoded per symbol and the symbol rate corresponds to the bit rate, with HOM formats more bits are encoded per symbol so that the symbol rate and thus the spectral width of the modulated signal becomes significantly smaller than the bit rate.

Figure 7.5 shows exemplarily a 16QAM ($M = 16$ symbols) constellation diagram of one polarization measured with a dual carrier DP-16QAM 512 Gbit/s transceiver. With 16QAM constellations 4 bits are encoded per symbol, as depicted in Fig. 7.5 with Gray mapped bits. Gray mapping [37] is a commonly applied mapping scheme that minimizes the number of bit errors between neighboring symbols as only 1 bit out of 4 is changed.

Fig. 7.5 Measured 16QAM constellation diagram with Gray mapped bits



7.3.1 Quadrature Amplitude Modulation

The most commonly applied HOM formats are MQAM (multiple-quadrature-amplitude-modulation) formats, where M symbols have specific amplitude and phase states or in-phase (I) and quadrature (Q) components in the electric field as defined by their complex constellation diagram. The I and Q states have 90° phase difference and are modulated independently onto the same carrier.

According to information theory [38] the mapping of m bits onto the M symbols of HOM formats is referred to as coded modulation. The number M is the total number of symbols and determines the constellation size of an MQAM format. The number m of bits carried by each symbol is determined by:

$$m = R_C \times \log_2(M) \text{ [bits/symbol]} \tag{7.1}$$

R_C represents the encoding rate or code rate which satisfies $0 < R_C \leq 1$. The channel encoder is adding a redundancy or a code OH to a stream of bits like forward error correction OH. The code overhead, usually given in percentage, is defined as:

$$\text{OH} = (1 - R_C)/R_C \tag{7.2}$$

In the absence of coding (code rate $R_C = 1$) the total number of M different symbols is determined by:

$$M = 2^m \text{ [symbols]} \tag{7.3}$$

Each symbol is transmitted in a time slot $T_S = 1/R_S$, and the symbol rate R_S is related to the bit rate B following Hartley’s law [39]:

$$R_S = B/m \text{ [GBd]} \tag{7.4}$$

In (7.4) m represents a nominal spectral efficiency and determines the maximum number of bits per symbol, m is also denoted as modulation efficiency which is determined by the ratio of the bit rate B and the symbol rate R_S . We denote a modulation format as HOM format if more than only 1 bit is encoded per symbol, e.g. QPSK or “4QAM” encodes 2 bits/symbol.

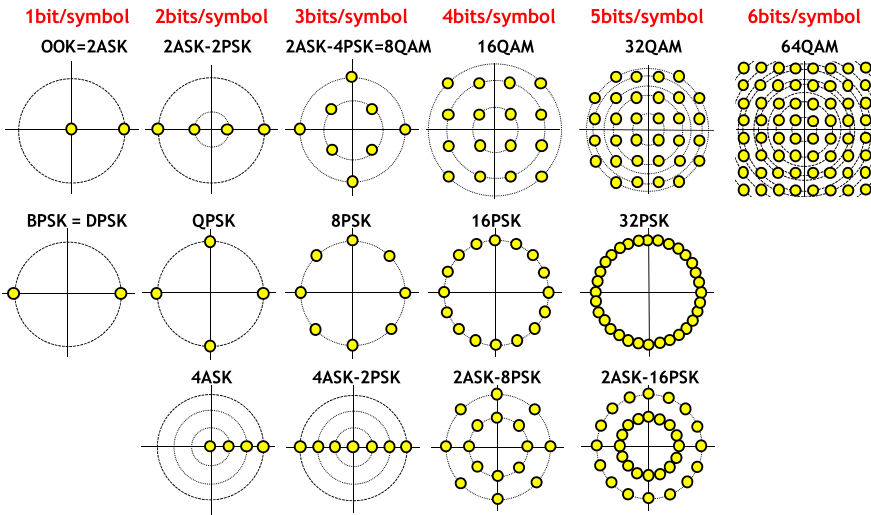


Fig. 7.6 Examples of constellation diagrams, the columns indicate respective numbers of bits/symbol

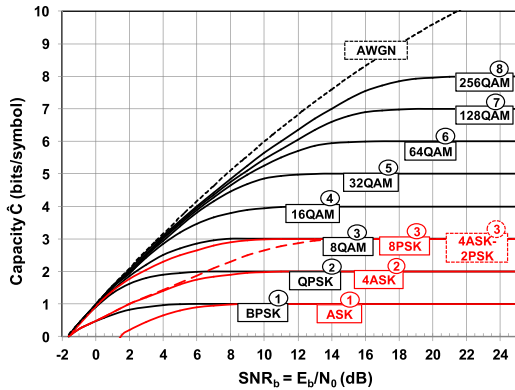
7.3.1.1 Constellation Diagrams

Figure 7.6 illustrates examples of QAM constellation diagrams including pure ASK (OOK) options (OOK and 4ASK) and various pure PSK formats, ASK-PSK combinations and MQAM options up to 64QAM. The columns indicate the modulation efficiencies by the number of m bits encoded per symbol. While a few examples of constellations consider only the real part or in-phase of the electric field, most constellations use the real and imaginary part, or in-phase (I) and quadrature (Q) of the electric field.

The first row of Fig. 7.6 starts with only one amplitude value modulated: this is standard NRZ-OOK or binary ASK or 2ASK encoding 1 bit/symbol ($m = 1$). By adding a second amplitude and a second phase shifted by 180° we obtain 2ASK-2PSK which encodes 2 bits/symbol: as 00, 01, 10, 11. In the following constellation 2ASK-4PSK, corresponding to the conventional 8QAM format, 3 bits/symbol are encoded. The next constellations are square-16QAM, 32QAM and square-64QAM which were introduced in 1962 [40] and which encode 4, 5 and 6 bits/symbol, respectively.

The constellations of the second row of Fig. 7.6 show purely phase modulated signals. They all have one constant amplitude ring. Only the first two are of practical interest: BPSK (DPSK) and (D)QPSK which encode 1 and 2 bits/symbol, respectively. The following constellations from 8PSK to 32PSK are included here for illustration purposes only. The Euclidian distance or minimum distance between the symbols is a measure for the robustness of the constellations to noise, thus from left to right, especially visible for the constellations in row two, sensitivity to noise in-

Fig. 7.7 Capacity in bits/symbol versus SNR_b for AWGN channels (Shannon limit) and for various modulation formats, numbers indicate maximum modulation efficiencies (bits/symbol). (Dashed red curve corresponds to 4ASK-2PSK)



creases significantly, so that BPSK has the highest robustness and 32PSK the lowest robustness to noise.

The constellation examples of the third row have up to four amplitudes and up to eight phase values. By 4ASK or Quaternary-ASK or 4PAM, 2 bits are encoded per symbol. All constellations of row three have significantly lower Euclidian distances than the constellations of the first row for corresponding modulation efficiencies.

7.3.1.2 Shannon Capacity Limit

HOM formats, that have widely been used in wireless and wireline and optical communication systems are square-MQAM formats, where the symbols are arranged in a square, leading to optimized Euclidean distances between the symbols which determine sensitivity performance or robustness versus noise.

According to Shannon [38] increasing the spectral efficiency by using higher constellation sizes of any HOM format comes at the price of higher signal to noise ratio (SNR) requirements. The Shannon-Hartley theorem describes that the ultimate capacity (limit) \hat{C} versus SNR_S (SNR per symbol) is given by a complex additive white Gaussian noise (AWGN) channel in the simple form of (7.5): For the same SNR_S , the capacity of any HOM format cannot be higher than the capacity of the AWGN channel.

$$\hat{C} = \log_2(1 + SNR_S) \text{ [bits/symbol]} \tag{7.5}$$

The Shannon capacity \hat{C} expresses error free transmission for the case of ideal channel coding and appears in the dimension of bits/symbol, as modulation efficiency. Figure 7.7 illustrates the Shannon capacity for the AWGN channel (limit) and includes the maximum achievable capacity (upper bound) of most HOM formats from Fig. 7.6, but including up to 256QAM formats versus SNR_b (per bit) according to [41, 42]. The difference between SNR_S and SNR_b is obtained by a comparison of (7.6) and (7.7), below.

Error free transmission is achieved in all cases if the SNR_b exceeds -1.59 dB. As shown in Fig. 7.7, for sufficiently high SNR_b all formats saturate at their theoretical

maximum spectral efficiency, e.g. 4 bit/s/Hz for 16QAM, and at their theoretical maximum modulation efficiency of $\log_2(M)$ bits per symbol. Comparison of formats with the same maximum capacity reveals that the formats modulating in one dimension only (4ASK) reach their maximum capacity at higher SNR_b than formats with modulation in both dimensions (QPSK). A comparison of 8QAM with 8PSK (red line) shows that 8QAM achieves higher capacity at lower SNR_b , in agreement with the observation of higher Euclidian distances of the constellation points of 8QAM compared to 8PSK.

It is interesting to note the following observation in Fig. 7.7: A specific target capacity, e.g. 5 bit/symbol, can be achieved with 32QAM at a high $\text{SNR}_b > 12$ dB. Alternatively, one might use constellations larger than 32QAM and encode them with the appropriate code rate or redundancy to achieve a lower SNR requirement (~ 9 dB) for the same capacity. This is in contrast to the BER performance without coding, described in the following section where larger constellations sizes always require higher SNR than smaller constellations.

By including the nonlinear properties of the transmission fiber the theoretical maximum capacity of a fiber channel modulated with an HOM format is reduced as analyzed in [43]. These capacities have been denoted as the lower bound capacities.

7.3.1.3 BER Performance

According to communication theory [42] error probabilities can be calculated in terms of signal to noise ratio (SNR), which may be the SNR per bit (SNR_b) or per symbol (SNR_S), represented by (7.6) and (7.7):

$$\text{SNR}_S = E_S/N_0 \quad (7.6)$$

$$\text{SNR}_b = E_b/N_0 \quad (7.7)$$

with

$$E_b = E_S/m \quad (7.8)$$

E_S and E_b are the energies per symbol and per information bit, respectively, and N_0 is the corresponding noise power.

Figure 7.8 represents the theoretical electrical sensitivity performance of dedicated HOM formats in terms of their symbol error probability (SER) versus SNR_S , left diagram, and bit error probability or bit error ratio (BER) versus SNR_b , right diagram. Note, that the BER curves shown in Fig. 7.8 hold for the absence of coding ($R_C = 1$).

BER versus SNR_b represents the more realistic case compared to SER versus SNR_S , as SNR_b takes into account how many bits are comprised and transported by a given symbol. For MQAM constellations and BER values smaller than 0.08 a good approximation for BER versus SNR_b can be found in [42] and is given by (7.9)

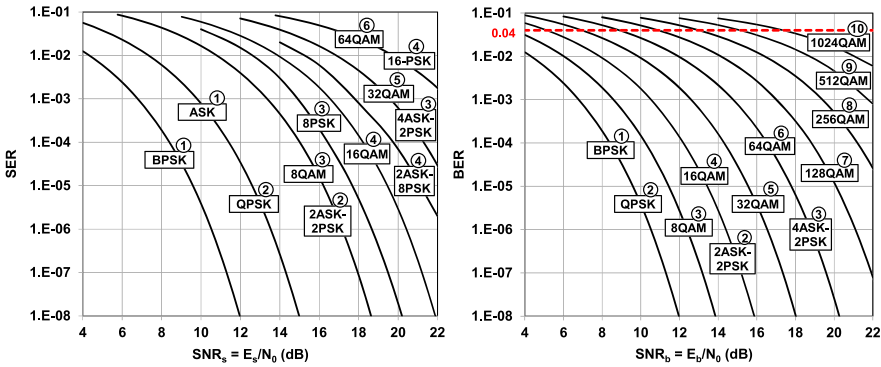


Fig. 7.8 SER vs. SNR per symbol (*left*) and BER vs. SNR per bit (*right*) of various constellation diagrams, including the number m of modulation efficiency

$$BER = \frac{\sqrt{M} - 1}{\sqrt{M} \log_2(M)} \operatorname{erfc} \left(\sqrt{\left(\frac{3 \log_2(M)}{2(M-1)} \right) SNR_b} \right) \quad (7.9)$$

At first we compare the various HOM formats of Fig. 7.6 with respect to their symbol Euclidian distances in Fig. 7.8, left diagram, and focus on formats with equal modulation efficiency:

- (1) BPSK significantly outperforms ASK by about 3 dB lower SNR_b ,
- (2) QPSK outperforms 2ASK-2PSK,
- (3) 8QAM outperforms 8PSK and more significantly 4ASK-2PSK, as 8QAM has higher Euclidian distances between symbols, and
- (4) square-16QAM outperforms 2ASK-8PSK (star 16QAM).
- (5) A comparison of 64QAM with 16PSK, which perform both with similar Euclidian distances and SER versus SNR_s , demonstrates that 64QAM has a significant advantage as it encodes 2 bits/symbol more than 16PSK.

If we look into the diagram of BER versus SNR_b (right diagram of in Fig. 7.8) and take into account the number of bits (m) each symbol is carrying, we can conclude that for the same SNR_b value square-MQAM formats perform with twofold higher modulation efficiencies compared to formats transporting symbols in a single state only: QPSK (2) versus BPSK (1); 16QAM (4) versus 2ASK-2PSK (2), and 64QAM (6) versus 4ASK/2PSK (3).

The main outcome of Fig. 7.8 is that the highest modulation efficiencies together with the best SNR_b performance are obtained with quasi square-MQAM constellation diagrams which outperform star-QAM and alternative ASK-PSK formats. Thus, MQAM formats became standard HOM formats and have received highest interest for optical transmission systems.

In order to compare the system sensitivities of HOM formats, their respective SNR_b at one common pre-FEC BER (e.g. of 0.04) can be used, as shown by the dashed red line in Fig. 7.8, right side. The BER of 0.04 is considered as an imple-

Table 7.1 Signal to noise ratio per bit (SNR_b) and OSNR values at 128 Gbit/s line rate versus number of bits per symbol (m) of MQAM formats, required for 0.04 pre-FEC BER, SNR_b values at theoretical limit of pre-FEC BER

m (bits/symbol)		2	3	4	5	6	7	8	9	10	
$SNR_b = E_b/N_0$ (dB)	@ pre-FEC BER	limit	1.1	2.6	4.2	5.9	7.7	9.6	11.5	13.5	15.6
		0.04	1.8	3.4	5.2	7.0	8.9	10.9	13.0	15.2	17.4
OSNR (dB) @ 128 Gbit/s		0.04	8.9	10.5	12.3	14.1	16.0	18.0	20.1	22.3	24.5

mentable pre-FEC BER of HOM formats with 25% SD-FEC OH with margin with respect to a theoretical limit, as described in more detail in Sect. 7.4.2.

The use of pre-FEC thresholds in case of SD-FEC has been questioned in [44] and generalized mutual information (GMI) has been suggested as a better predictor. However, for an SD-FEC OH of 25% which we consider throughout this chapter, it was also shown in [44] that deviations of pre-FEC BERs required in order to obtain a specific post-FEC BER appear to be rather small and are within the errors of SNR data which are summarized in Table 7.1.

Table 7.1 summarizes the required uncoded $SNR_b(E_b/N_0)$ values versus the number m of bits/symbol of QPSK and square-MQAM formats related to a pre-FEC BER of 0.04 and at the theoretical limit of pre-FEC BER related to SD-FEC with 25% OH. Note, that the corresponding coded SNR_b values with 25% of OH would be 0.96 dB smaller. The estimated accuracy of the SNR values given in Table 7.1 is ± 0.1 dB up to $m = 6$ (64QAM) and ± 0.2 dB for m between 6 and 10 (1024QAM).

The lower SNR_b values for the theoretical limits of per-FEC BER are apparently more optimistic compared to the higher SNR_b values at a constant pre-FEC BER of 0.04. For further comparison of HOM formats in this chapter we will consider only the SNR_b values at constant pre-FEC BER of 0.04. The differences or penalty steps of formats between QPSK ($m = 2$) and 1024QAM ($m = 10$) are about 2 dB, more precisely between 1.6 dB and 2.2 dB.

In optical communication, the optical signal to noise ratio (OSNR) is the parameter corresponding to the electrical parameter SNR_b [43] given by (7.10). The OSNR data are in reference to the gross bit rate or the line rate B_L including the coding with 25% of OH and the considered SNR_b values are, according to Table 7.1, the uncoded values at a BER of 0.04.

$$OSNR = B_L / (2 \times B_{ref}) \times SNR_b \quad (7.10)$$

B_{ref} is the reference bandwidth, usually expressed as a 12.5 GHz (0.1 nm) bandwidth. The relation (7.10) is valid for single polarization as well as for dual polarization operation. For HOM formats with constant line rates, e.g. with constant FEC-OH, the OSNR penalties are identical to the SNR_b penalties and increase between the HOM formats roughly also in steps of 2 dB.

Table 7.1 includes the corresponding OSNR required for 128 Gbit/s line rate. The 8.9 dB of OSNR at 128 Gbit/s DP-QPSK will serve as OSNR reference throughout this chapter. The penalty of 15.6 dB between QPSK ($m = 2$) and 1024QAM ($m = 10$) is the price for the five-fold higher modulation efficiency.

7.3.1.4 Dual-Polarization MQAM

Polarization division multiplexing means transmitting data in two orthogonal optical polarizations (x and y) which doubles the modulation efficiency and the spectral efficiency of any HOM format. PDM or dual polarization operation of HOM formats in combination with coherent technology has become a commonly applied method after coherent receivers have enabled fast and reliable digital polarization demultiplexing.

For the investigation of bit rates beyond 100 Gbit/s on a single carrier and multiple carriers as well we will focus in the following on standard HOM formats and will generally include PDM. Dual polarization operation simply multiplies the modulation efficiency according to $m_{DP} = 2 \times m$, and the granularity of m_{DP} for standard DP-MQAM formats appears in steps of 2 bits/symbol. Corresponding to this granularity, the theoretical OSNR penalty is usually considered to vary in steps of 2 dB. OSNR sensitivities determine the application area as 2 dB OSNR penalty results in 2 dB lower transmission distance. However, in practice the OSNR penalties are even higher than the theoretical OSNR predictions as HOM formats are usually associated with implementation penalties.

Table 7.2 illustrates the DP-BPSK and the DP-MQAM constellations up to DP-64QAM formats, including their modulation efficiencies m_{DP} expressed by the number of encoded bits per symbol. Table 7.2 includes the theoretical OSNR penalties of the DP-MQAM formats with BPSK and QPSK taken as a reference, for the case of SD-FEC with 25% OH and a pre-FEC BER of 0.04. The OSNR penalties versus HOM formats correspond to the SNR_b penalties according to (7.10) with the assumption of constant line-rate for all formats. The DP-MQAM formats illustrated in Table 7.2 are considered to be the most attractive ones for current and future generations of long haul and Metro transmission distances.

For transceivers operating with flexible adaption of the modulation format the 2 bits/symbol granularity of standard HOM formats is not always an optimum choice, and depending on the application finer granularities can be advantageous. Time domain hybrid modulation formats (TDHM) have been proposed [45–47] by generating so-called supersymbols with standard HOM format constellations alternating in the time domain. With this approach finer granularities can be obtained, e.g. 0.5 bits/symbol [48] and superior transmission performance has been demonstrated including filtering of Reconfigurable Optical Add Drop Multiplexers (ROADMs).

Table 7.2 Dual-polarization BPSK and higher order modulation MQAM formats: DP-modulation efficiency m_{DP} (bits/symbol), constellations illustrated on both polarizations, OSNR penalties referenced versus DP-QPSK



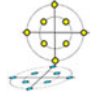
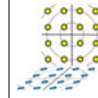
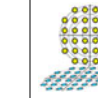
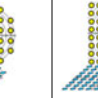
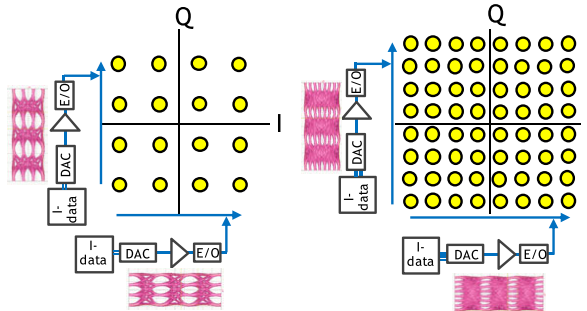
	HOM format					
	DP-BPSK	DP-QPSK	DP-8QAM	DP-16QAM	DP-32QAM	DP-64QAM
m_{DP} (bits/symbol)	2×1	2×2	2×3	2×4	2×5	2×6
DP-constellation						
OSNR penalty (dB)	0	0	1.6	3.4	5.2	7.2

Fig. 7.9 16QAM generation with 4 level modulator driving signals (*left*) and 64QAM generation with 8 level modulator driving signals using a single IQ modulator



7.3.1.5 Principle of DP-MQAM Modulation and Reception

A 16QAM signal in optical transmission by modulating a single IQ modulator with a 4-level drive signal (4PAM signal) has been demonstrated in 2008 [49] and together with a 6-bit DAC in 2010 [50], and a 64QAM signal has been generated with an 8-level drive signal (8PAM signal) using a DAC with only 3 bit resolution [51].

The examples in Fig. 7.9 depict the principle of generating e.g. 16QAM or 64QAM constellations by a 2-bit DAC ($2^2 = 4$ signal levels) or by a 3-bit DAC ($2^3 = 8$ signal levels), respectively, with a single polarization IQ modulator as E/O converter. The levels or number of states of the electrical driving signals correspond to the number of projections of the symbols onto the in-phase and the quadrature axis. The I/O modulator acts as a PAM to QAM converter. Each symbol of the complex electrical output field of the transmitter is addressable, provided that the chain DAC-driver-modulator is highly linear.

With one IQ modulators per polarization, the I and Q components of both, the optical x - and y -polarization, can be generated at the transmitter output resulting in a quasi 4D modulation format by 4 different optical fields [52].

High speed DACs implemented in ASICs (see Sect. 7.7.3) of deployed optical transceivers have a limited resolution between 6 and 8 bits and support sampling rates between 32 and 64 GSamples/s, and very recently up to 92 GSamples/s. For

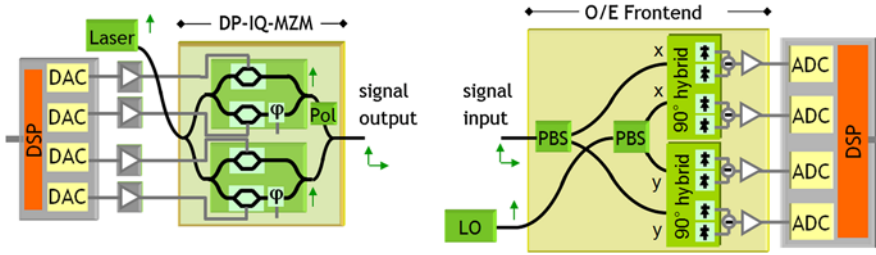


Fig. 7.10 Transmitter and receiver setup with IQ modulator and receiver details (schematic), φ : 90° phase shifter; PBS: polarization beam splitter

measurement equipment DACs with 10 bit and more are available which support sampling rates up to a few GSamples/s. The effective number of bits (ENOB) is typically 1 to 3 bits lower than the theoretical resolution. In the case of SiGe based 6 bit DACs the ENOB is ~ 5 bits and for CMOS based 8 bit DACs the ENOB is in the range of 4.5 to 6 bits. Table 7.3 compiles the analogue modulation levels of the DAC output and the minimum DAC resolution required to encode various standard HOM formats. The modulation efficiency m_{DP} (bits/symbol) includes polarization multiplexing or dual-polarization operation.

Figure 7.10 shows the schematics of a state-of-the-art DP-MQAM transmitter and a coherent receiver. The transmitter includes DSP, four DACs for four tributaries and a dual polarization I/O modulator on the basis of two nested Mach-Zehnder modulators (MZM) per polarization, described in more detail in Sect. 7.7.1. The transmitter includes a C-band tunable laser in an integrated tunable laser assembly (ITLA).

Four parallel linear amplifiers are required after the DAC to amplify their output of typically 1V differential to $\sim 6V_{pp}$ ($\sim 2V_{\pi}$) single ended as required at the modulator input.

An MZM has sinusoidal electrical field modulation characteristics and not linear as required for PAM to QAM conversion. Two alternative approaches are applied to compensate or counteract the shortcomings of the MZM characteristics: (a) pre-compensation of the multi-level driving signals with DACs and modulation with non-equidistant levels, (addressed in Sect. 7.5.1), or (b) modulation with lower amplitude of $\sim V_{\pi}$ or even less, so that the MZM is operated in the quasi linear regime. This approach results in higher insertion loss as the lowest insertion loss under modulation is obtained only when the modulator is driven with the full $2V_{\pi}$ modulation amplitude.

The receiver also shown in Fig. 7.10 includes an LO laser and the polarization diversity O/E frontend. Key elements of the latter are polarization beam splitters (PBS) and optical 90° hybrids which enable interference of the signal, in phase and quadrature components in x - and y -polarization, with the light of the LO laser, and four balanced photodiodes which convert the received signal spectrum to the electrical baseband, linear TIAs, (for more details see Sect. 7.7.2), and four ADCs for conversion of the four tributaries followed by the receiver DSP, to be discussed in more detail in Sect. 7.6.2.

7.3.2 Spectral Efficiency and Fiber Capacity

After 2009, with the availability of high resolution high speed DACs, significant progress in research has been made with the demonstration of HOM formats and constellation sizes of 16QAM and beyond targeting very high spectral efficiencies and very high capacities on a single fiber. By using DP-16QAM an SE of 6.4 bit/s/Hz and a very high fiber transmission capacity of 69.1 Tbit/s was demonstrated [16], and with DP-36QAM, a non “standard” HOM format which has a non integer modulation efficiency by encoding 10.34 bits/symbol, the SE was increased to 8 bit/s/Hz and the demonstrated fiber transmission capacity was 64 Tbit/s [53]. In both experiments the SE was supported by appropriate wavelength interleavers and a WDM crosstalk penalty was tolerated. Finally, the high capacities were achieved including L-band transmission.

With DP-64QAM [54, 55] the spectral efficiency has been further increased and including FDM 10 bit/s/Hz has been reported [56]. A transmission capacity of 45 Tbit/s using the C-band only has been achieved including spectral shaping to minimize the linear WDM crosstalk. By moving to DP-128QAM, a spectral efficiency of 11 bit/s/Hz has been demonstrated and an extremely high fiber transmission capacity of 101.7 Tbit/s including L-band transmission was reported. In all high capacity WDM transmission experiments mentioned above an HD (hard decision) -FEC with 7% OH has been included.

Even higher constellation sizes and spectral efficiencies have been achieved by DP-256QAM enabling a spectral efficiency of 11.8 bit/s/Hz [57], by DP-512QAM resulting in a spectral efficiency of 13.2 bit/s/Hz [58], by DP-1024QAM with 13.8 bit/s/Hz SE [6] and finally by DP-2048QAM with the record spectral efficiency in optical transmission of 15.3 bit/s/Hz [7] without use of SDM. The highest constellation sizes have been obtained using arbitrary waveform generators (AWG) including DACs with 10 bit theoretical resolution operated at 12 GSamples/s. These DACs support low symbol rates (~ 6 GBd) only and thus very narrow linewidth lasers are required as well. As these narrow linewidth lasers are available only for a limited number of wavelengths, no DWDM experiments and no new record capacities could be demonstrated so far based upon the highest constellation sizes. In the transmission experiments with particularly high constellation sizes the OSNR constraints were mitigated by Raman amplification. Table 7.4 summarizes selected high capacity experiments with modulation formats between DP-16QAM and DP-128QAM [59] and compiles the various parameters for comparison: the modulation efficiency m_{DP} , the spectral efficiency SE, the total fiber transmission capacity achieved, the line rate (B_L), the applied number of sub-carriers for the case of FDM, the symbol rates (R_S), the net rate (B_N), the channel spacing (W), the bandwidth efficiency η (described below by (7.13)) and the corresponding C- and L-band fiber bandwidths.

For the selected experiments in Table 7.4 the modulation efficiency and spectral efficiency, the bit rates and symbol rates, the number of sub-carriers and the C- and the L-band bandwidths vary significantly. Only the FEC OH remains constant and the bandwidth efficiency η remains comparable.

Table 7.3 DAC output levels and minimum required DAC resolution versus HOM formats

	HOM format									
	DP-QPSK	DP-8QAM	DP-16QAM	DP-32QAM	DP-64QAM	DP-128QAM	DP-256QAM	DP-512QAM	DP-1024QAM	
m_{DP} (bits/symbol)	4	6	8	10	12	14	16	18	20	
Analogue modulation levels	2	4	4	6	8	12	16	24	32	
Minimum resolution (bit)	1	2	2	2.6	3	3.6	4	4.6	5	

Table 7.4 Overview of high capacity experiments with key performance parameters for comparison

Format	m_{DP} (bits/symbol)	SE (bit/s/Hz)	Cap. (Tbit/s)	B_N (Gbit/s)	B_L (Gbit/s)	FEC OH (%)	no sub- carriers	R_s (GBd)	Grid W (GHz)	η (GBd/GHz)	C-band (THz)	L-band (THz)	Ref.
DP16QAM	8	6.4	69.1	160	171	7	1	21.66	25	0.87	4.3	6.7	[16]
DP-36QAM	10.34	8	64	100	107	7	1	10.7	12.5	0.86	4.0	4.2	[53]
DP-64QAM	12	10	45.2	500	538	7	8	5.6	50	0.90	4.5	0.0	[56]
DP-128QAM	14	11	101.7	275	294	7	4	5.25	25	0.84	4.8	4.6	[59]

In the following part of this section we will compare potential spectral efficiencies and total fiber capacities of HOM formats for an optical C-band fiber bandwidth of 4.4 THz and exclude L-band transmission. We will not discuss potential application areas and consider constellation sizes between DP-QPSK and DP-1024QAM, we will include throughout 25% OH for SD-FEC, to counteract OSNR constraints of HOM. Our transmission line rates are generally 28% higher than the net rates, e.g. 128 Gbit/s and 100 Gbit/s, respectively while the true net rates are always $\sim 3\%$ above our depicted net rates, as we include GE rates of e.g. 103.125 Gbit/s. As we consider 25% of FEC OH, the SE will be correspondingly smaller than achievable with 7% OH only.

Symbol rates and bit rates of HOM formats are linked via Hartley's law (7.4) and using modulation efficiencies in dual polarization operation (m_{DP}) symbol rates R_S as given by (7.4) are modified by:

$$R_S = B_L/m_{DP} \quad (7.11)$$

B_L is the transmission line rate and the transported net rates B_N and the channel spacing (W) determine the spectral efficiencies (SE) according to:

$$SE = W/B_N \quad (7.12)$$

In DWDM transmission the channel allocation scenarios are described by the bandwidth efficiency parameter η given by:

$$\eta = R_S/W \quad (7.13)$$

According to [60] DWDM channel allocation scenarios are distinguished and designated as:

- (1) $\eta > 0.2$: legacy WDM or coarse WDM
- (2) $0.2 > \eta > 0.83$: common DWDM
- (3) $0.83 > \eta > 1.0$: quasi Nyquist WDM
- (4) $\eta = 1$: Nyquist WDM
- (5) $\eta > 1$: super-Nyquist-WDM (faster than Nyquist)

For the fiber capacity discussion in this chapter we will focus on three different cases of DWDM bandwidth efficiency with the following terminology:

$$\eta \approx 0.64: \text{ "far Nyquist DWDM"} \quad (7.14)$$

$$\eta \approx 0.85: \text{ "near Nyquist DWDM"} \quad (7.15)$$

$$\eta = 1: \text{ "Nyquist DWDM"} \quad (7.16)$$

For example, "far Nyquist" DWDM (7.14) corresponds to a 50 GHz channel grid with a transmitted format of 32 GBd symbol rate, e.g. using 128 Gbit/s DP-QPSK, as also illustrated in Fig. 7.11, left side. The center and right side of Fig. 7.11 represent "near Nyquist" DWDM (7.15) cases with 32 GBd symbol rate on a 37.5 GHz grid

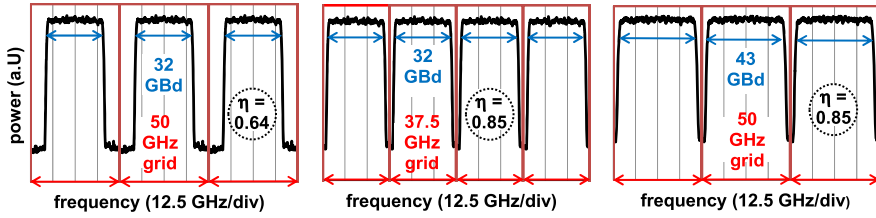


Fig. 7.11 Illustration of “far-Nyquist DWDM” (*left*) and “near Nyquist DWDM” (*center and right*) with 32 GBd and 43 GBd of symbol rates

and with 43 GBd on a 50 GHz grid, respectively. 50 GHz is the standard ITU-T channel grid and 37.5 GHz an example of a flexible channel grid with a granularity of 12.5 GHz [61]. In all three examples of Fig. 7.11 the signals are spectrally pre-shaped and show no linear crosstalk, more details will be given in Sect. 7.5.1.1.

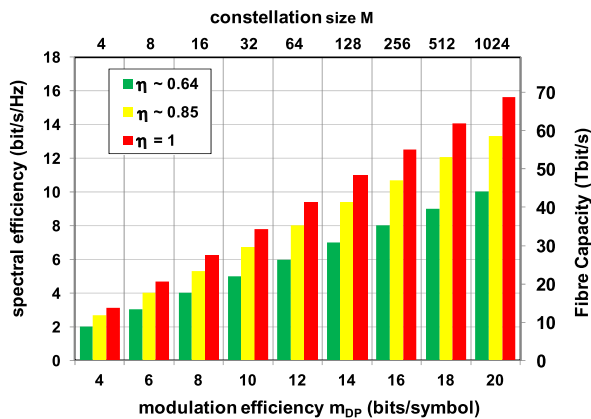
The gain of spectral efficiency and capacity by going from “far-” to “near Nyquist DWDM” and to “Nyquist DWDM” are 33% and 56%, respectively. Further capacity advantages potentially feasible with “faster than Nyquist” ($\eta > 1$) approaches will not be considered here.

The bandwidth efficiency is a very sensitive measure for the routing capabilities of transmitted formats and determines the acceptable number of ROADMs included in a transmission link [48]. In case of $\eta \approx 0.64$ many ROADMs (> 10) can be passed, while for $\eta \approx 0.85$, only a few (< 4) can be included.

Figure 7.12 illustrates the full range of spectral efficiencies and maximum single fiber transmission capacities in the optical C-band (4.4 THz) available with DP-MQAM formats, indicated versus constellation size M or modulation efficiency m_{DP} . The SE and capacity data are bit rate independent and can be considered for single carrier solutions as well as for FDM or superchannel solutions [60].

At far Nyquist DWDM ($\eta \sim 0.64$) the SE (capacity) increases with the constellation size from 2 bit/s/Hz (8.8 Tbit/s) to 10 bit/s/Hz (44 Tbit/s) with DP-QPSK and DP-1024QAM, respectively. At Nyquist DWDM ($\eta = 1$), the SE (capacity) in-

Fig. 7.12 Spectral efficiency and C-band fiber capacity versus M or m_{DP} of DP-MQAM formats with bandwidth efficiencies of $\eta \sim 0.64$ (*green-*), $\eta \sim 0.85$ (*yellow-*) and $\eta = 1$ (*red bars*)



creases from 3.1 bit/s/Hz (13.8 Tbit/s) to 15.6 bit/s/Hz (69 Tbit/s), and at the intermediate case of near Nyquist DWDM ($\eta \sim 0.85$), the SE (capacity) increases from 2.7 bit/s/Hz (11.7 Tbit/s) to 13.3 bit/s/Hz (59 Tbit/s).

Any future gain of spectral efficiency and fiber capacity which may be potentially realized in the future with “faster than Nyquist” will scale with the achieved bandwidth efficiency. If transmission within the L-band is also included, the total fiber transmission capacity of HOM formats can be further increased, as illustrated by three experimental demonstrations included in Table 7.4, with as much as about 150% capacity increase reported in [16].

7.3.3 High Bit Rate Transmission

According to Hartley’s law (7.4) implementation of HOM formats is a promising approach for achieving very high bit rates (line rates) provided sufficiently fast electronics are available. Table 7.5 is a compilation of research demonstrators from the last few years where symbol rates beyond 40 GBd have enabled to achieve the highest line rates realized on a single carrier so far. The examples include different formats and modulation efficiencies (m_{DP}), different DAC approaches and technologies, different net rates and spectral efficiencies, different FEC OH and different experimentally achieved OSNR values for the given FEC thresholds.

Table 7.5 shows that significant progress in research has been achieved to obtain single carrier line rates of 400 Gbit/s [62] and beyond in order to approach the 1 Tbit/s net rate which has finally been achieved in 2015 with a line rate of 1.24 Tbit/s reported in [63]. However, this result may be questioned to be a true single carrier 1 Tbit/s demonstration as the Nyquist shaped 124 GBd signal has been synthesized from four 32.5 GHz spectral sub-bands (spectral slices) merged into a 125 GHz frequency slot.

The two research demonstrators in Table 7.5 using a “DAC resolution” of 2 bits were applying a passive combination of binary data to obtain a 4PAM signal for the 16QAM generation [64, 65]. The demonstrator in Table 7.5 with a 3-bit DAC applies an InP based power-DAC [66]. The demonstrators in Table 7.5 close to products including high resolution DACs with more than 6 bits theoretical resolution are: 552 Gbit/s transmission [67] with 46-GBd DP-64QAM using 65-GSample/s DACs with 8 bit theoretical resolution in CMOS technology, 864 Gbit/s transmission [68] with 72-GBd DP-64QAM with a SiGe DACs, and finally the 1240 Gbit/s demonstrator with 124 GBd DP-32QAM using also the 65-GSamples/s DACs with 8 bit theoretical resolution in CMOS technology, but required in total 16 DACs while a true single carrier and single sub-band transceivers would include only 4 DACs for the 4 tributaries.

Single-carrier 1 Tbit/s solutions combine high constellation sizes [73] together with ultimate symbol rates [74], while few carriers 1 Tbit/s solutions [69–74] are based upon the superchannel concept [60] targeting the use of two, three or four FDM sub-carriers, that the requests on constellation size or symbol rate become

less demanding. The first commercially available 100 Gbit/s transceiver introduced in 2009 uses a two sub-carrier FDM solution based on the first 40 Gbit/s coherent receiver technology using the DP-QPSK modulation format. Current 400 Gbit/s transceivers introduced in 2014 also use two sub-carrier FDM but with DP-16QAM modulation format providing a 2-fold higher spectral efficiency than DP-QPSK which raises the SE from 2 bit/s/Hz to 4 bit/s/Hz.

The superchannel or FDM concept cannot provide higher spectral efficiencies than single carrier solutions and therefore superchannels are considered as an intermediate stage only. The final target is a single carrier transceiver which will be more cost-effective and will have less components and lower power consumption. The higher symbol rates of single carrier implementations match better with the granularity and the spectral properties of optical routing components. While the first single carrier 100G transceiver was available only one year after the two sub-carrier FDM product, the product maturity of a single carrier 400G transceiver e.g. based on DP-16QAM with 64 GBd symbol rate will require a longer development time. The development of a single carrier 1 Tbit/s transceiver is significantly more demanding, as the symbol rate or the modulation efficiency has to be 2.5 times higher than for a 400G single carrier solution.

In the following part of this section we will investigate potential future 400 Gbit/s single carrier product implementations, address the particular challenge of 1 Tbit/s single carrier options, and compare the performance of 400 Gbit/s solutions with dual and single carrier(s) in detail, and finally depict realistic scenarios for 1 Tbit/s few carrier product options.

7.3.3.1 400G and 1T Single Carrier Options

Table 7.6 illustrates the symbol rate correlation and OSNR penalties of MQAM HOM formats for 400 Gbit/s net rate, based upon 512 Gbit/s line rate with 25% SD-FEC OH. Symbol rates supported by corresponding transceivers are mainly limited by the data converters (DACs and ADCs) and to a lower extent by the O/E converters as modulators and receivers have already been demonstrated to operate at symbol rates higher than 64 GBd [71]. The MQAM constellation sizes shown range from QPSK (4 bits/symbol) up to the 1024QAM (20 bits/symbol), and dual-polarization operation is generally included.

As already indicated in Table 7.1 for SNR_b , the OSNR penalty for 512 Gbit/s or any other constant bit rate exhibits a difference of about 2 dB between adjacent standard MQAM formats. The colors at the symbol rates in Table 7.6 indicate the probability of the data converter availability within the next 5 to 10 years (red: unlikely, orange: likely; green: currently available). Symbol rates up to 32 GBd are supported by current DAC and ADC technologies implemented in commercial 100 Gbit/s and 400 Gbit/s transceivers. DAC technologies available in 2015 [75] support symbol rates of at least 43 GBd, but symbol rates above 70 GBd appear to be very challenging for data converters with more than 6 bits of theoretical resolution. Apparently, the current main development targets of the data converter industry are to reduce

Table 7.5 Examples of high line rate transmission experiments with symbol rates >40 GBd

Line rate (Gbit/s)	Format	Symbol rate (GBd)	DAC res. (bits)	m_{DP} (bits/symbol)	Net-rate (Gbit/s)	SE (bit/s/Hz)	FEC OH (%)	FEC thresh. (BER)	OSNR exp. (dB)	WDM chs (no.)	Reach (km)	Ref.
428	DP-QPSK	107	-	4	400	2.9	7	0.0038	19.2	8	5600	[62]
516	DP-64QAM	43	3	12	400	8	20	0.02	27.5	20	600	[66]
552	DP-64QAM	46	8	12	334	6.7	58	0.09	21.5	153	2000	[67]
640	DP-16QAM	80	2	8	520	5.2	23	0.03	22.3	10	3200	[64]
856	DP-16QAM	107	2	8	713	5.9	20	0.019	26	5	200	[65]
864	DP-64QAM	72	6	8	640	6.4	35	0.04	27.5	1	400	[68]
1240	DP-32QAM	124	8	10	1000	8	24	0.042	31.5	1	660	[63]

Table 7.6 Combinations of HOM formats and symbol rates enabling 512 Gbit/s line rate on a single carrier; colors at symbol rates indicate (expected) data converter availability: red: unlikely within next 5–10 years, orange: likely; green: available. OSNR penalties given with 128 Gbit/s DP-QPSK as reference

	HOM format									
	512 Gbit/s – 1 carrier									
m_{DP} (bits/symbol)	DP-QPSK	DP-8QAM	DP-16QAM	DP-32QAM	DP-64QAM	DP-128QAM	DP-256QAM	DP-512QAM	DP-1024QAM	
Symbol rate (GBd)	128	85	64	51	43	37	32	28	26	
OSNR penalty (dB) ^a	6.0	7.6	9.4	11.2	13.1	15.1	17.2	19.4	21.6	
	Longhaul									Metro
										Data center
										???

^a 128 Gbit/s DP-QPSK

power consumption of DACs and ADCs while to increase their sampling speed has lower priority.

On the other hand, in research significantly higher symbol rates such as 80 to 107 GBd [74] have already been reported from experiments in which a passive combination of binary data have enabled to obtain 100 GBd four level signals. For commercial products high resolution DACs become mandatory in order to optimize the spectral efficiency by pulse shaping which requests additional 2 to 3 bits of DAC resolution (for details see Sect. 7.5.1).

As an example, we will compare two DP-MQAM format options which both enable 400 Gbit/s on a single carrier. According to Table 7.6 these are 64 GBd symbol rate with 16QAM or 32 GBd symbol rate with 256QAM, and they differ by a factor of two in modulation efficiency and capacity: DP-16QAM with 8 bits/symbol and DP-256QAM with 16 bits/symbol. The second option has about 8 dB higher OSNR requirement and in addition a 3 dB lower robustness to SPM [12] due to half the symbol rate compared to the first option. The price for the 2-fold higher capacity is about 11 dB penalty in transmission performance or more than 90% of transmission reach reduction. Therefore the second option might be attractive for shorter reach and future data center communication while the first option is an attractive 400G single carrier transceiver solution for longer reach applications. Finally we will shortly look on the very challenging 1 Tbit/s options on a single carrier, as depicted in Table 7.7. The realization of 1 Tbit/s on a single carrier and with a single sub-band might be feasible only with the three HOM options highlighted in orange, however, by what time or whether at all will primarily depend on the future progress of data converters. Moreover, as these options have significant OSNR penalty, they are expected to be suitable for short reach applications only.

7.3.3.2 Transmission Reach of 400 Gbit/s Single Carrier and Dual Carrier FDM

In this section we will analyze the transmission reach performance of 400 Gbit/s single and dual carrier FDM options (2×200 Gbit/s) over dispersion uncompensated fiber. As in the previous section the line rate will be kept constant at 512 Gbit/s with 25% FEC OH, and the symbol rates will vary with the HOM formats. As a reference we will take again the performance of 2nd generation 100 Gbit/s transceivers with 128 Gbit/s line rate and 32 GBd DP-QPSK including 25% OH, related to a pre-FEC BER of 0.04.

We will limit the maximum constellation size to 256QAM and consider transmission over dispersion uncompensated fiber links where the statistics of HOM can be described by Gaussian noise (GN) [76]. We will also assume that differences in nonlinear impairments from constellation sizes can be neglected and that the transmission performance can be described by the GN [77] or the enhanced GN model [78].

Independent of the transmission format and optical fiber type, transmission distances achievable with EDFA repeaters over N spans of fiber are determined by

Table 7.7 Combinations of HOM formats and symbol rates for 1280 Gbit/s line rate on a single carrier; colors at symbol rates indicate (expected) data converter availability: red: unlikely (during the next 5 to 10 years), orange: likely; OSNR penalties are given relative to those of 128 Gbit/s DP-QPSK

	HOM format 1280 Gbit/s – 1 carrier									
	DP-QPSK	DP-8QAM	DP-16QAM	DP-32QAM	DP-64QAM	DP-128QAM	DP-256QAM	DP-512QAM	DP-1024QAM	
m_{DP} (bits/symbol)	4	6	8	10	12	14	16	18	20	
Symbol rate (GBd)	320	213	160	128	107	91	80	71	64	
OSNR penalty (dB) ^a	10.0	11.6	13.4	15.2	17.1	19.1	21.2	23.4	25.6	

^a 128 Gbit/s DP-QPSK

amplified spontaneous emission (ASE) noise accumulation and the received OSNR. Measured with 0.1 nm resolution bandwidth, OSNR is for instance given by [79]:

$$OSNR (0.1 \text{ nm}) [\text{dB}] = P_F - \alpha_F - NF - 10 \log(N) + 58 \text{ dB} \quad (7.17)$$

Equation (7.17) assumes constant fiber launch power (P_F) into each fiber span, constant fiber attenuation (α_F) of each span, and constant noise figure (NF) of each repeater amplifier. In order to achieve a targeted BER (e.g. of 0.04) after transmission with a specific modulation format over a specific type of fiber, the achievable transmission distance D_N (7.18) or the number of spans N are determined only by the OSNR receiver sensitivity ($OSNR_{RX}$) and the optimum fiber launch power (P_{opt}) into each transmission fiber span N :

$$D_N [\text{dB}] = 10 \log(N) \propto P_{opt} - OSNR_{RX} \quad (7.18)$$

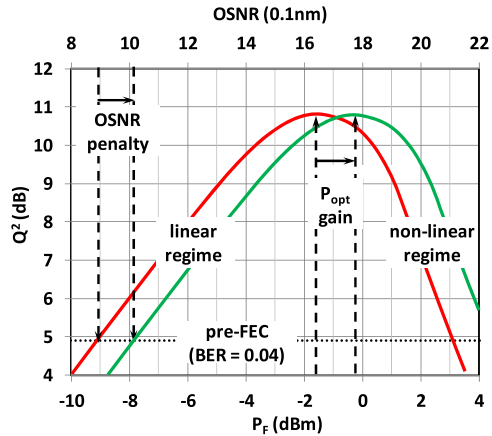
The required OSNR sensitivities (penalties) scale with the bit rates according to (7.10) and with the constellation size of HOM formats, as e.g. shown in Table 7.6 for 400 Gbit/s net rate. The optimum launch power for dispersion uncompensated transmission with HOM formats is dominated by intra-channel nonlinear effects [12]. These depend on the spectral shape and the spectral width of the transmitted symbol rate. In a simplified picture we assume that P_{opt} doubles (3 dB P_{opt} gain) if the symbol rate is doubled. According to (7.18) we simply can express the transmission reach penalty by the OSNR penalty and the P_{opt} penalty or gain. Inter-channel nonlinear effects at uncompensated transmission are not negligible but of minor importance and will not be considered in this chapter.

In Fig. 7.13 we illustrate the transmission performance over a few spans of dispersion uncompensated SMF fiber at two different bit rates (red and green curves) by their respective Q^2 factor versus P_F and OSNR. The Q^2 factors are calculated from the BERs according to [79] and the OSNR is related to P_F according to (7.17). In both cases we have significant Q^2 factor margins above $Q^2 \sim 4.9$ dB as BERs are lower than the targeted pre-FEC BER of 0.04. In the low P_F regime (below -4 dBm) both cases perform in the linear transmission regime where the Q^2 factor increases linearly with P_F . The linear increase of the Q^2 versus OSNR represents the back-to-back performance of the case with $OSNR_{RX}$ obtained at $Q^2 \sim 4.9$ dB ($BER = 0.04$). In the high P_F regime (above +3 dBm) both cases perform in the non-linear transmission regime where the Q^2 factor decreases with P_F . Optimum transmission performance is obtained in between where P_{opt} at highest Q^2 factors (lowest BERs) are obtained, respectively. The two cases show different $OSNR_{RX}$ and different P_{opt} , but their differences in terms of OSNR penalty and P_{opt} gain appear comparable. Thus both cases perform with comparable transmission reach.

In the following part of this section we will analyze 400 Gbit/s and 1 Tbit/s options of HOM formats with respect to their transmission reach penalty (reach reduction) versus our reference format 128 Gbit/s DP-QPSK.

A comparison of the single carrier performances at 200 Gbit/s (a) and 400 Gbit/s (b) at the same HOM format shows: (a) has 3 dB lower OSNR sensitivity compared to (b), while (b) supports 3 dB higher launch power compared to (a) due to the

Fig. 7.13 Q^2 factor versus fiber launch power (P_F) for two different bit rates cases (red and green curves) with respective OSNR penalty and P_{opt} gain

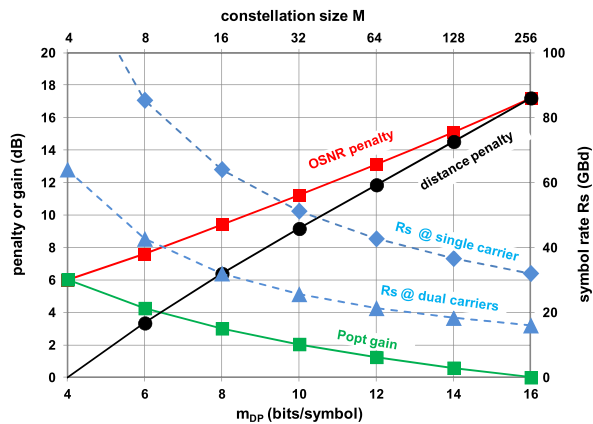


twofold higher symbol rate and spectral width as well. Thus both solutions have the same transmission reach, and the same reach is obtained also for 2×200 Gbit/s as a dual carrier FDM option for 400 Gbit/s is compliant with 2×200 Gbit/s DWDM channels.

The dual carrier FDM option has the same OSNR sensitivity and the same P_{opt} as the single carrier 400 Gbit/s option because the bit rate and the total power P_{opt} are identical. As a consequence distance penalties of HOM formats are independent of the transmission bit rate and independent of the number of FDM sub-carriers. In Fig. 7.14 we display OSNR penalty, P_{opt} gain and reach penalty of single and dual carrier 400 Gbit/s options together with their symbol rates as a function of the constellation size of the MQAM HOM format. 128 Gbit/s DP-QPSK with 32 GBd symbol rate is taken as the reference for the penalty values shown.

Compared to the previously introduced SNR_b and OSNR penalty versus constellation size which increases by steps of ~ 2 dB between the standard MQAM formats ($\Delta m_{DP} = 2$), the reach penalty increases more significantly between the

Fig. 7.14 Reach penalty, OSNR penalty, P_{opt} gain and symbol rates per carrier versus constellation size for single and dual carrier 400 Gbit/s solutions, penalty and gain values given relative to those of 128 Gbit/s DP-QPSK (32 GBd)



standard MQAM formats by steps of ~ 3 dB due to the optical gain (P_{opt}) which varies by steps of ~ 1 dB.

The reach penalty is the main tribute to be paid for the capacity advantage of HOM formats. A 3 dB reach penalty reduces the transmission reach by 50% when going from one standard MQAM format to the next higher one ($\Delta m_{DP} = 2$). These 3 dB steps express a significant granularity of transmission penalty. Transceivers operating with TDHM formats which reduce the step size of the modulation efficiency to e.g. $\Delta m_{DP} = 0.5$ [48] are advantageous as they reduce at the same time the transmission penalty between the TDHM formats to 0.75 dB (16% transmission reach reduction) according to the slope of the reach penalty curve in Fig. 7.14 of 1.5 dB/bits/symbol.

A significant transmission reach advantage can be expected using probabilistically shaped HOM formats instead of standard HOM formats as probabilistically shaped constellations perform closer to the Shannon limit. In [80] a reach advantage of 35% has been demonstrated using a probabilistically shaped 64QAM format versus a standard 16QAM format.

The OSNR performance and reach penalty data presented in Fig. 7.14 are theoretical values and unfortunately real world OSNR values are coming with “implementation penalties” which are related to hardware limitations depending on constellation size and symbol rate. Minimum implementation penalties in the order of about 2 dB are observed for 32 GBd DP-QPSK, the penalties increase to about 3 dB for 32 GBd DP-16QAM, and they may reach more than 4 dB, as experimentally demonstrated for 21 GBd [81]. In general implementation penalties increase with the constellation size, however, this penalty can partly be overcome by coding gain improvements brought by empowered FEC.

7.3.3.3 Channel Grid for 400 Gbit/s Single Carrier and Dual Carrier FDM

In the following paragraph we will compare the 400 Gbit/s single with the dual-carrier option (2×200 Gbit/s) with respect to channel grid allocations at far (7.14) and near Nyquist (7.15) DWDM with bandwidth efficiencies of $\eta \sim 0.64$ and $\eta \sim 0.85$, respectively. As in the previous section, we will include constellation sizes such as 128QAM and 256QAM as potential options for future short reach data center applications. Figure 7.15 illustrates the different channel spacing options of HOM formats including the corresponding symbol rates (blue bars), and the left and right parts of the figure correspond to 200 Gbit/s and 400 Gbit/s channel net rates (line rates in brackets), respectively. Green and red bars indicate the far and near Nyquist cases. The solid, colored bars show applications on the flexible grid with a frequency grid granularity of 12.5 GHz, according to the ITU-T standard [61]. The open colored bars show applications not covered by the flexible grid. We designate these as open grid applications as they do not match with the frequency grid granularity of 12.5 GHz and are not compliant with the ITU-T standard [61].

Due to the 2-fold higher symbol rate at 400 Gbit/s, the flexible grid granularity with 12.5 GHz appears to be sufficient up to high constellation sizes as a compar-

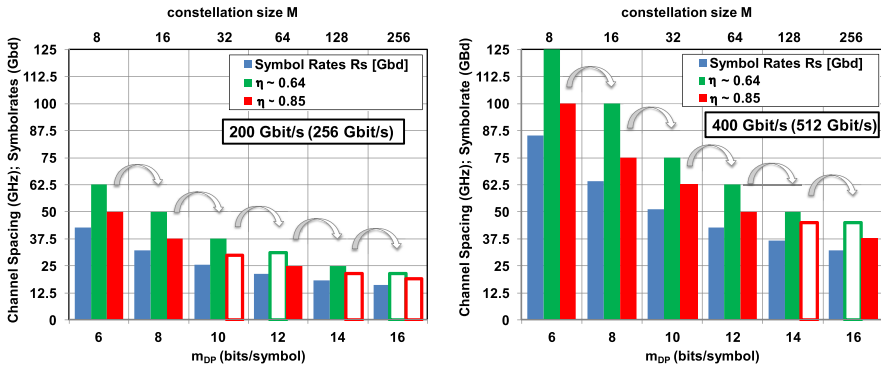


Fig. 7.15 Channel spacings of HOM formats at 200 Gbit/s (left) and 400 Gbit/s (right), corresponding to $\eta \sim 0.64$ and $\eta \sim 0.86$ for flexible (solid green and red bars) and open grid allocation (open green and red bars)

ison of the solid and open bars in Fig. 7.15 demonstrates. At 200 Gbit/s, the flexible grid granularity is apparently rather insufficient as it is limited to DP-16QAM only. For example, DP-32QAM on a 37.5 GHz flexible grid ($\eta \sim 0.64$) does not offer any spectral efficiency advantage compared to DP-16QAM for $\eta \sim 0.86$, as DP-32QAM with $\eta \sim 0.86$ is on the open grid. If compliance with the flexible grid is requested, a further spectral efficiency gain would be provided only by DP-64QAM with $\eta \sim 0.86$ on the 25 GHz flexible grid.

At 200 Gbit/s the use of hybrid modulation formats [48] would increase the spectral efficiency granularity and make it fit into the flexible grid granularity but for 400 Gbit/s hybrid modulation formats are not required in this respect. As already mentioned, the highest constellation sizes of the standard HOM formats, 128QAM and 256 QAM, are only suited for short reach (intra data center) applications where no flexible grid standard is targeted.

7.3.3.4 1 Tbit/s Few Sub-carriers FDM Options

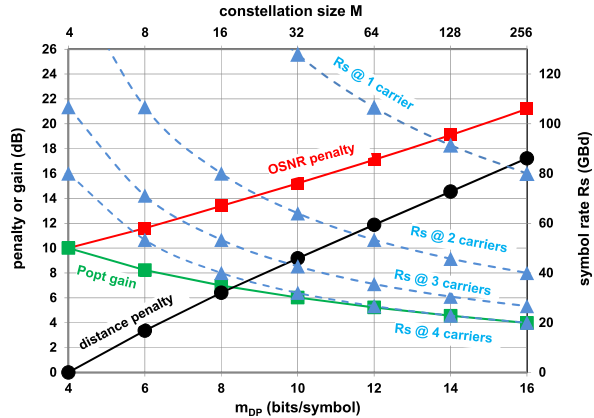
In the past few years, significant research has been performed on the development of 1 Tbit/s transceivers, and the focus has mainly been on FDM. Like the first 100 Gbit/s and first 400 Gbit/s solutions, also future first 1 Tbit/s solution will be based upon FDM and the superchannel concept and the number of sub-carriers and the applied symbol rates will be determined by the available converter technologies.

Table 7.8 shows single carrier and superchannel (FDM) options for the realization of 1 Tbit/s net rate and 1.28 Tbit/s line rate. As for 100 Gbit/s and 400 Gbit/s net rates, the true net rates include GE client rates and the line rates include 25% OH for SD-FEC. As in the case of Table 7.6 and Table 7.7, the color codes chosen for the symbol rates indicate the availability of the required digital converter technology within the next 5–10 years. Red (orange) indicates unlikely (likely) availability

Table 7.8 1 Tbit/s single carrier and superchannel (FDM) options: Symbol rates and constellation sizes for given number of sub-carriers. Colors at symbol rates indicate probability of converter availability within the next 5 to 10 years (see text)

Symbol rate (GBd)		43	53	71	40	53	80	32	64	128	53	107	46	91	40	80	36	71	32	64	
Net rate (Gbit/s)	Line rate (Gbit/s)	8																			
	const. Size M	16																			
1000	m_{DP} (bits/symbol)	6																			
	no. of sub-carriers	5	4	3	4	3	2	4	2	1	2	1	2	1	2	1	2	1	2	1	2
		1280																			
		8																			
		32																			
		10																			
		12																			
		64																			
		128																			
		14																			
		128																			
		256																			
		16																			
		18																			
		512																			
		20																			

Fig. 7.16 Reach penalty, OSNR penalty, P_{opt} gain and symbol rates per carrier versus constellation size for single and multiple carrier 1.28 Tbit/s options, penalty and gain values given relative to those of 128 Gbit/s DP-QPSK (32 GBd)



while DACs and ADCs required for the symbol rates highlighted in green are already available.

With current converter technology, which supports symbol rates of about 43 GBd, a 1 Tbit/s transceiver requires four sub-carriers e.g. together with DP-16QAM at 40 GBd or two sub-carriers e.g. together with DP-128QAM at 46 GBd, respectively. With future converter technologies which may support symbol rates up to ~ 70 GBd or even 80 GBd, attractive two sub-carrier solutions can be based upon DP-64QAM with 53 GBd or on DP-32QAM with 64 GBd or even on DP-16QAM with 80 GBd.

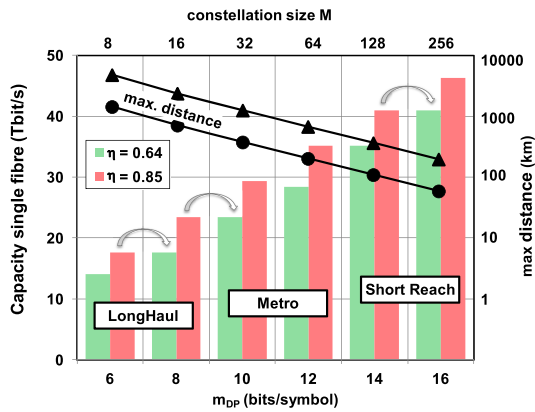
Similar to the 400 Gbit/s case shown in Fig. 7.14, Fig. 7.16 illustrates various 1 Tbit/s options (1.28 Tbit/s line rate) including: the development of OSNR penalty, fiber launch power (P_{opt}) gain, and the reach penalty versus constellation size of the MQAM HOM formats with 128 Gbit/s DP-QPSK (32 GBd) taken as a reference. Figure 7.16 includes the symbol rates required for potential single carrier options and for two, three, and four sub-carrier FDM options.

The ten-fold higher bit rate compared to 128 Gbit/s DP-QPSK leads to 10 dB higher OSNR (penalty) at 1.28 Tbit/s DP-QPSK but comes together with 10 dB P_{opt} gain due to ten times broader spectral width. The resulting 0 dB reach penalty is in accordance with the case of 10×128 Gbit/s DWDM as the spectral efficiency remains unchanged. If the spectral efficiency is increased by the constellation size, the OSNR penalty and the P_{opt} gain scale bit rate independently as in the case of 400 Gbit/s options shown in Fig. 7.14: the reach penalty increases in steps of 3 dB between the standards MQAM formats or with a slope of 1.5 dB/bits/symbol.

7.3.3.5 Transmission Reach Versus Capacity

Figure 7.17 summarizes the trade-off between maximum fiber capacities in the C-band for different constellation sizes of standard HOM formats and the maximum transmission reach over terrestrial SMF links with EDFA repeater and without dis-

Fig. 7.17 Maximum single fiber capacities for dedicated application areas and maximum fiber (SMF) transmission distances (triangles: optimistic, points: pessimistic case) versus HOM formats for far Nyquist DWDM: $\eta \sim 0.64$ (green bars) and near Nyquist DWDM: $\eta \sim 0.85$ (red bars)



person compensation. Potential application areas are indicated. A distinction between flexible and open grid has not been made here. The capacity as well as the maximum transmission data are bit rate independent and hold for 200 Gbit/s, 400 Gbit/s or even 1 Tbit/s on a single carrier and are also valid for multiple carrier FDM solutions.

The maximum distance values designated as “pessimistic” correspond to the 1,500 km product performance of 112 Gbit/s DP-QPSK, data labeled “optimistic” correspond to 10,000 km research performance, and 14,000 km reach has been demonstrated with 128 Gbit/s DP-QPSK for EDFA repeated SMF transmission [82].

The advantage of pulse shaping together with HOM formats can be seen in Fig. 7.17 (similar to Fig. 7.12), as indicated by the arrows: by pulse shaping ($\eta \sim 0.85$, red bars) the same channel spacing, spectral efficiency, and capacity can be obtained as that achieved by the next higher HOM format without pulse shaping ($\eta \sim 0.64$, green bars), i.e., pulse shaping enables a modulation efficiency increase by 2 additional bits/symbol.

From today’s perspective the maximum single fiber capacities in the optical C-band feasible with standard HOM formats are ~ 24 Tbit/s, 35 Tbit/s and 46 Tbit/s for long haul, Metro and short reach applications, respectively. The corresponding spectral efficiencies are 5.3, 8, and 10.7 bit/s/Hz achieved by DP-16QAM, DP-64QAM, and DP-256QAM, respectively. If the optical L-band is included, the available fiber bandwidths increase from 4.4 THz up to 11 THz [16], and the single fiber capacities can reach ~ 60 Tbit/s, 87 Tbit/s, and 115 Tbit/s, respectively.

The application limitations visible in Fig. 7.17 can still be shifted significantly. For example, DP-64QAM may become an option for long-haul transmission by including (a) Raman amplification, so that the OSNR constraints and penalties of high constellation sizes become relaxed or (b) 3R regeneration, depending on the future cost development of coherent transceivers.

Recently probabilistically shaped DP-64QAM constellations [83] have been proposed for reach extensions. It has also been demonstrated [83], at same spectral efficiencies that probabilistically shaped DP-16QAM and DP-64QAM constellations

constellations perform with longer reach than regular DP-16QAM and DP-64QAM formats.

In submarine transmission configurations with gridless channel allocations, the channel spacing chosen and bandwidth efficiencies η are usually closer to Nyquist: $0.85 < \eta < 1$, enabled by the use of very low signal roll-off factors (< 0.1) resulting in respective higher spectral efficiencies.

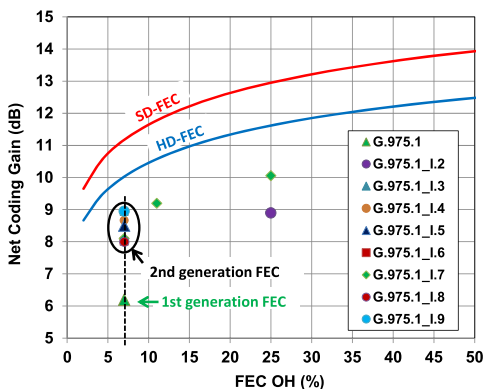
7.4 Forward Error Correction (FEC)

7.4.1 *Hard Decision FEC*

FEC has a long history in optical communication systems. It has been introduced in 2.5 Gbit/s OOK systems first and has become indispensable in today's coherent transmission systems. In 1995, the first FEC, using Reed-Solomon block codes, was applied in optical transport to bridge submarine transmission distances. In 10 Gbit/s NRZ terrestrial DWDM long-haul systems, the well-known Reed Solomon RS(255,239) block code was widely implemented as described by ITU-T recommendations G.975.1 [84] and G.709 [85] and was classified as first generation FEC. This RS(255,239) code requires an OH of 6.7% and corrects a pre-FEC-BER of 2×10^{-4} to post-FEC-BER $< 10^{-15}$, corresponding to a net coding gain (NCG) of 6.2 dB. During the development of 40 Gbit/s systems system engineers were looking for stronger FECs with higher NCG to compensate the 6 dB higher OSNR required by the new 40 Gbit/s bit rate systems compared to the installed 10 Gbit/s solutions. Most of the improved FEC schemes applied concatenated product codes [86] with e.g. inner-RS and outer-RS codes. More precisely, a bit stream is first encoded by an inner algorithmic code, code words are jointly interleaved, and after partitioning the product is encoded a second time by an outer algorithmic code. These codes achieve very good performance and low error floors with limited implementation complexity. The inner and outer codes of such schemes are often BCH (Bose-Chaudhuri-Hocquenghem) and/or RS codes. The advantage of BCH codes is that very efficient closed-form solutions exist for computing the error locations at the decoder [87]. Keeping the OH at 7%, the NCG could be improved significantly with these new FEC schemes, also denoted as enhanced FEC (E-FEC), summarized in G.975.1 [84]. These E-FEC codes have been classified as second generation FEC schemes, they provide NCG between ~ 8 dB and ~ 9 dB, and correct pre-FEC-BERs between 10^{-3} and 3.8×10^{-3} to post-FEC-BER $< 10^{-15}$.

Figure 7.18 summarizes the NCG of different realized versions [84] of 2nd generation FEC including the NCG of 6.2 dB for the 1st generation FEC. Both generations are so-called hard decision FECs, as "0-1" decisions are performed. Figure 7.18 also includes the NCG of further implemented HD-FEC schemes with 11% and 25% FEC OH [84].

Fig. 7.18 Net coding gain (NCG) of 1st and 2nd generation HD-FEC codes and theoretical limit of HD-FEC and SD-FEC schemes versus FEC OH



7.4.2 Soft Decision FEC

Since the first implementations of 100G transponders which used second generation HD-FEC, there has been intensive research to develop even more powerful FEC codes with NCG beyond 10 dB by soft-decision [88, 89] but also allowing higher OH than 7% only. Soft-decision means that no “0-1” decisions are made prior to FEC decoding but all information coming from the DSP is exploited. If hard “0-1” decisions are made at an early stage of signal processing, information is lost which could otherwise be used to improve the FEC performance.

Figure 7.18 includes the theoretical limit of NCG for HD-FEC and SD-FEC depending on the FEC OH, which has been described by Shannon’s second theorem [38]. A performance gain between 1 and 1.5 dB is observed for SD-FEC compared to HD-FEC in the range between 2% and 50% of OH, respectively. For example, the ultimate NCG limit for SD-FEC with 25% OH is 12.9 dB which we will consider in this chapter for the comparison of HOM formats.

SD-FEC schemes are designated as third generation FEC, they are significantly more complex and consume significantly more power than the first and second generation HD-FEC schemes, at the encoder as well as at the decoder side but they also allow higher flexibility. In general, for HD-FEC less information needs to be transferred between the receiver DSP and the FEC decoder. In the case of SD-FEC the data flow is significantly higher and a fast interface is required between SD-FEC and the coherent receiver DSP, thus both have to be implemented together in one ASIC. Since the introduction of 35 nm CMOS technology this became feasible and has been realized with reasonable power consumption. Second generation 100 Gbit/s transponders already include SD-FEC with $\sim 25\%$ OH and a small amount (typically $\sim 3\%$) of HD-FEC to correct for error-floors [90].

Two competing classes of SD-FEC are currently investigated for 100 Gbit/s systems and beyond. The first class uses block turbo codes (BTC) and is in principle an extension of second generation concatenated codes and applies so-called iterative soft-decision decoding [91]. BTC decoders are highly parallelizable while keeping the internal decoder data flow low, they converge rather fast and require a small

number of decoding iterations only. The main disadvantage of these codes is their relatively large block length leading to larger delays. Further disadvantages include inflexibility with respect to varying frame sizes and overheads.

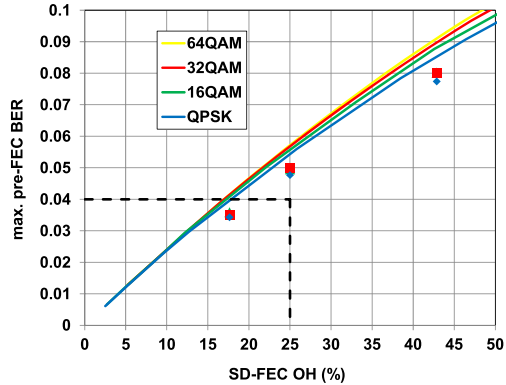
The second class are low-density parity-check (LDPC) codes applying maximum a posteriori (MAP) soft-decision decoding. LDPC codes have been invented in 1963 [92] and were rediscovered in the 90ies of the last century and are applied in wireless (WLAN, IEEE 802.11, DVB-S2) and powerline communication (IEEE 1901) and 10G Ethernet (IEEE 802.3). The first LDPC code implemented in optics was an HD-FEC scheme included in the second generation FEC scheme in G.975.1. Latest developments of LDPC codes for future optical communication systems are given in [93]. Compared to BTC schemes LDPC codes have relatively simple algorithms allowing a high degree of flexibility as there exists no common design rule. Various algorithms have been proposed for 100G and beyond systems with advantages and disadvantages. The target design is a code that yields high coding gain, fast convergence and that is implementable in the considered CMOS technology with reasonable power consumption. LDPC codes usually suffer from an error floor at BERs between 10^{-6} and 10^{-10} . Therefore, modern FEC systems are typically constructed using an SD-LDPC inner code which reduces the BER to a level of 10^{-3} to 10^{-5} and an HD outer code which pushes the post FEC-BER to levels well below 10^{-12} , as proposed in [94]. With the latest generation of LPCD codes floorless error correction [95] is achieved so that no additional HD-FEC is required.

For the application of HOM formats which come along with increasing OSNR sensitivity constraints, improved FEC performance becomes more and more essential. One option to meet this challenge is to trade off part of the modulation efficiency of HOM formats against higher overhead and thus for stronger SD-FEC so that the higher OSNR demands can at least partially be relieved.

The curves in Fig. 7.19 show the theoretically maximum correctable pre-FEC BER (pre-FEC threshold) as a function of OH for SD-FEC for four examples of HOM formats. The use of pre-FEC threshold as theoretical limit in the case of SD-FEC has been questioned [44] and the generalized mutual information has been claimed to be a better predictor. However, at an SD-FEC OH of 25% under consideration here it was also pointed out in [44] that the differences for the pre-FEC in order to obtain a required post-FEC are very small and become significant only for much higher OH.

Realistically achievable values of maximum pre-FEC BERs with SD-FEC were confirmed for different OH and different HOM formats as illustrated by the points in Fig. 7.19. These maximum pre-FEC BER values were obtained for a class of spatially coupled LDPC codes [96], currently one of the best known schemes for SD-FEC. This class of codes has been successfully verified in various transmission experiments, e.g., for high spectral-efficiency ultra long-haul submarine transmission [97]. It can be seen that this class of codes allows one to operate close to the theoretical limits, shown by the curves in Fig. 7.19 where a dependency on HOM formats can be observed. These theoretical limits of pre-FEC BER at 25% OH appear to be in the range between 0.054 and 0.057 for QPSK and 64QAM, respectively. Extrapolation to 1024QAM suggests that the maximum pre-FEC BER should

Fig. 7.19 Maximum tolerable pre-FEC BER vs. SD-FEC overhead for QPSK, 16QAM and 32QAM, curves show theoretical performance, points show simulated SD-FEC decoder performance



not exceed 0.059 at 25% OH. The use of a single common pre-FEC BER of 0.04 at 25% OH for the comparison of HOM formats appears pessimistic according to Fig. 7.19 and therefore we conclude that the performance of very high constellation sizes appears to be slightly underestimated compared to low constellation sizes.

7.5 Digital Signal Processing

7.5.1 Transmitter Digital Signal Processing

If DACs and DSPs are included in a transmitter, a single transceiver with enormous flexibility is obtained. The DSP and DAC allow for the generation of HOM formats together with spectral pre-shaping which becomes a mandatory feature for the optimization of the spectral efficiency of near Nyquist shaped flat top signal spectra. In addition, the modulation format of the transceiver can be dynamically changed on the fly by the DSP if the routed signal path is changed and transmission impairments vary. Besides standard HOM, modulation formats with different FEC codes can also be included [98]. Furthermore, hybrid HOM formats like time domain hybrid modulation formats can be included to further increase the granularity of standard HOM [47, 48], to better adapt for targeted transmission distances. Finally, a variety of equalization functions can be addressed in addition to spectral pre-shaping (pulse shaping): (a) equalization of the frequency modulation response given by the concatenation of the DAC, the driver, and the modulator, (b) compensation of the sinusoidal modulation characteristics of the MZM, (c) dispersion pre-compensation, (d) SPM pre-compensation etc. Thus software defined transceivers can be implemented if DACs and transmitter DSP are included.

As reported in Sect. 7.3.1.5, high speed DACs implemented in ASICs for optical transceivers have a limited available resolution, determined by the ENOB, typically between 4 and 6 bits, and the degree of realizable equalization functionality is determined by the target constellation size. Apparently there is a trade-off between

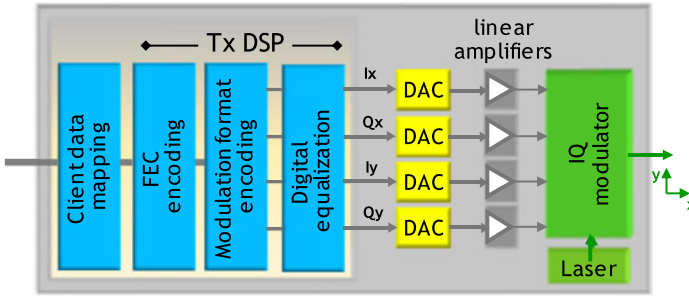


Fig. 7.20 Transmitter building blocks

the desired constellation size and the realizable equalization [99]. For example, as shown in Table 7.3, if DP-64QAM is targeted with DACs and if an ENOB of 5 bits is assumed, there are two bits available for equalization functions. In [100] it has been estimated that pulse shaping requires 1 bit in effective resolution, and 1 additional bit is required for equalization of the frequency modulation response, as a consequence, the application of 64QAM is possible in that example.

Figure 7.20 shows the main transmitter building blocks, consisting of Tx DSP and four DACs which convert the digital representations of the four tributaries I_x , Q_x , I_y and Q_y to multi-level analogue signals. These are subsequently amplified by linear amplifiers and launched to a DP-IQ modulator. In the following discussion we will restrict ourselves to the Tx DSP block consisting of client data mapping, FEC encoding, modulation format encoding, and digital equalization.

Data Mapping: At the input of a transceiver so-called client signals arrive. Since the GE Ethernet and optical transport hierarchy met with 100GE and 100 Gbit/s (OTU-4) standards in 2010, the client data are mostly GE based. Including synchronization and data skewing, these data are mapped onto the four tributaries I_x , Q_x , I_y , and Q_y , where I and Q are the in-phase (I) and quadrature (Q) components of the signal in x and y polarization, respectively.

FEC Encoding includes encoding of data by HD-FEC or by SD-FEC. If only SD-FEC is used, the applied LDPC code must allow for error floor free performance at the receiver side. More details on FEC were summarized in Sect. 7.4.2.

Modulation Encoding includes the mapping of the FEC encoded bits onto the desired HOM format. Depending on the available resolution, modulation encoding potentially includes the equalization of the MZM sinusoidal characteristics by adapting the digital representation of the amplitude and phase levels to the symbol constellations.

Digital Equalization at the transmitter side uses fixed static none adaptive equalizers usually implemented by time-domain FIR filters. The equalization includes the equalizing function shown above. The equalization of the frequency response of DAC, driver, and modulator is performed with the target of achieving a flat top output spectrum which is achieved by signal pulse shaping.

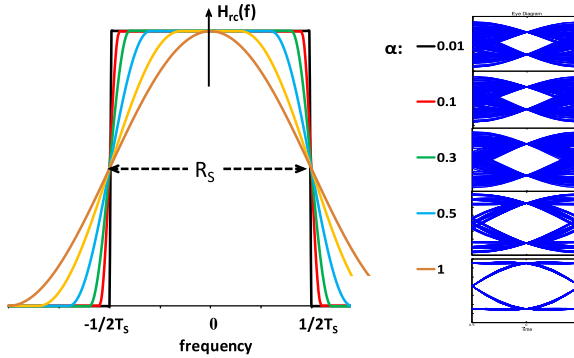


Fig. 7.21 Raised-cosine filter response (spectrum) and eye-diagrams for various roll-off factors α

7.5.1.1 Spectral Pre-shaping

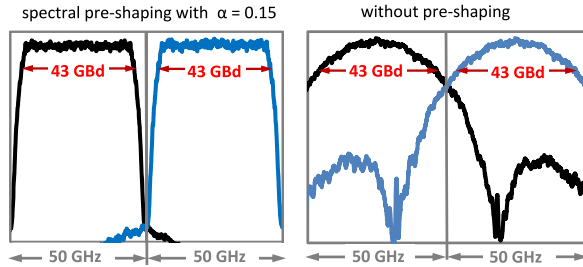
The key motivations for spectral pre-shaping or Nyquist pulse shaping are (a) raising the spectral efficiency in order to maximize the fiber capacity (see Sect. 7.3.2) by appropriate control of the transmitter signal spectrum, (b) minimizing intersymbol interferences (ISI) and (c) increasing the nonlinear tolerance of the transmitted signal. A widely used filter function is the raised cosine (rc) function $H_{rc}(f)$ given by (7.19)

$$H_{rc}(f) \begin{cases} 1; & |f| < \frac{1-\alpha}{2T_S} \\ \cos^2\left(\frac{\pi T_S}{2\alpha} \left(|f| - \frac{1-\alpha}{2T_S}\right)\right); & \frac{1-\alpha}{2T_S} < |f| < \frac{1+\alpha}{2T_S} \\ 0; & \text{else} \end{cases} \quad (7.19)$$

and filtering is typically implemented in such a way that the filtering is shared between the transmitter and the receiver. The corresponding filter function at both sides is a root raised cosine filter $H_{rrc}(f)$ with $T_S = 1/R_S$ ($R_S =$ symbol rate) and α as the roll-off factor. Figure 7.21 represents the rc filter function (spectrum) with variable roll-off factors between 0.01 and 1. The function $H_{rc}(f)$ acts as an ideal low pass filter for the case of $\alpha = 0$ and it eliminates all undesired out of band signal contributions. The full width at half maximum (FWHM) of the spectrum corresponds to the symbol rate R_S for all roll-off factor cases. Figure 7.21 includes simulated binary eye-diagrams with rc modulation and the corresponding roll-off factor. As a compromise between remaining eye-opening and spectral properties, actually implemented roll-off factors are usually between 0.1 and 0.2 for terrestrial transmission applications.

Figure 7.22 shows a comparison of the spectral characteristics of two 43 GBd (DP-16QAM modulated) signals on the 50 GHz grid with bandwidth efficiency of $\eta \sim 0.85$ (near Nyquist DWDM), one with and the other without spectral pre-shaping. Spectral pre-shaping (left channel pair) provides significantly better channel separation and significantly lower linear crosstalk than what can be obtained without pre-shaping (right channel pair), measured crosstalk penalties are less than

Fig. 7.22 Spectral characteristics of 43 GBd DP-16QAM signal pairs for 50 GHz channel spacing; *left side*: with spectral pre-shaping with $H_{rc}(f)$ and $\alpha = 0.15$, *right side*: no spectral pre-shaping



0.2 dB and more than 2 dB, respectively. If targeting without pre-shaping together with less than 0.2 dB cross talk penalty between neighboring channels, the channel spacing must be higher and the spectral efficiency becomes 30 to 40% lower. In addition, higher nonlinear tolerance of pre-shaped signals has been demonstrated in [101].

7.5.2 Receiver Digital Signal Processing

In general there are two different approaches for the receiver signal processing: either signal processing using training sequences or signal processing using full blind adaptation; in this section we will concentrate on full blind adaptation. Figure 7.23 shows the building blocks of the coherent receiver. The four analogue tributaries (I_x , Q_x , I_y , and Q_y) received from the phase and polarization diversity receiver frontend are linearly amplified and digitized by four high speed ADCs and fed to the receiver DSP. The DSP comprises the following stages: timing recovery, frontend corrections, dispersion equalizer, polarization recovery, frequency recovery, phase recovery, FEC and modulation decoding & decision, and Client mapping.

Timing Recovery is the first DSP building block to resample/synchronize the oversampling ratio of the signal to a 2-fold ratio. In favor of that the phase of the received signal has to be estimated using the Gardner timing recovery [102] or the square timing recovery [103]. Due to operating the system in the digital domain

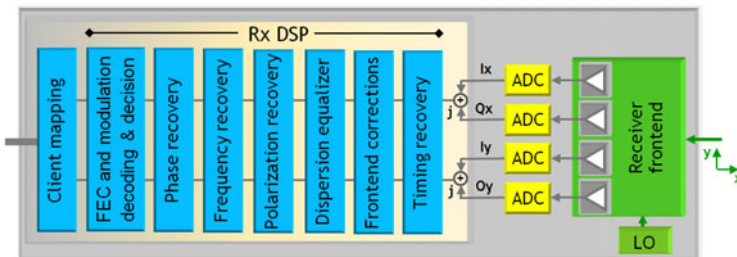


Fig. 7.23 Coherent receiver building blocks

without closed feedback loop a full synchronous sampling is impossible. Therefore any phase offset has to be compensated by an interpolation filter. In order to minimize the offset the phase estimation may be used to adjust the ADC's sampling frequency.

Frontend Corrections are applied to compensate for quadrature imbalances that may originate from imperfect phase reception of the optical 90° hybrid. Quadrature imbalance compensation is well known in wireless communication and has been proposed to be used in optical communications as well [104]. A detailed example of $I-Q$ imbalance compensation is reported in [105] by measuring and minimizing the cross correlation between the in-phase (I) and quadrature (Q) components of the received signal, employing a feedback structure. The $I-Q$ output results from a linear combination of the received $I-Q$ signals.

Chromatic Dispersion Compensation is performed in two steps: at first by static dispersion equalization with slow update rates for compensation of high chromatic dispersion values while fast residual dispersion compensation by an adaptive equalization is performed in the following polarization recovery part. The target filter function is a simple all pass filter for the compensation of differential group delay. The number of required filter taps for compensation of the CD increases linearly with the dispersion and therefore linearly with fiber length.

A static equalizer [106, 107] can be implemented either in the time [108] or in the frequency domain [109] with different degrees of complexity which rises proportional to N or $\log_2 N$, respectively, where N is the number of filter taps. The number of taps is typically large and suitable for the compensation of the CD of a few 1000 km of SMF. Therefore an implementation of the CD filter in the frequency domain is advantageous. The tap weights are complex numbers in the time domain implementation, while the tap weights in the frequency domain implementation are complex numbers with modulus 1.

Polarization Recovery including PMD Compensation is typically performed in a 2×2 MIMO configuration [107]. Also designated as a butterfly structure including four independent adaptive filters partitioned into three parts: The actual FIR filter bank, error estimation, and calculation of updated filter coefficients [110].

The actual filter bank consists of simple FIR filters. At this point in the processing chain the carrier frequency and the phase are not yet estimated nor compensated. At the polarization recovery output the constellations are still rotating in the complex plain. Therefore decision directed adaptation schemes are more difficult to implement for polarization recovery including PMD compensation.

A very popular blind adaptation scheme for error estimation is the constant modulus algorithm (CMA) [111] which optimizes deviations of the amplitude of the equalized signal from a desired fixed value. In the case of rotating symbols the unit circle is used as adaptation target. The standard CMA is optimally suited for purely PSK modulated signals, including QPSK, with all symbols on a ring corresponding to constant intensity (constant modulus). For HOM formats multi-modulus algorithms (MMA) have been proposed [112] although the standard CMA is applicable for HOMs too. The most widely used implementation for the calculation of filter coefficient updates is the least-mean-squares algorithm [113]. The idea of the LMS

algorithm is to estimate the gradient of the error by partial derivatives of the mean squared error with respect to the filter coefficients. The exact formulation of this algorithm and a comparison with a decision feedback structure can be found for instance in [114]. The update of the filter coefficients and the resulting convergence speed must be fast enough for the compensation of the fastest expected polarization changes. On the other hand the filters must also be long enough to simultaneously compensate for the maximum expected polarization dependent delays. These are determined by the maximum differential group delay (DGD) expected for the transmission link at the end of which the transceiver is expected to operate. The filter acts as a channel equalizer, too. If $H_{rc}(f)$ pulses are applied with very low roll-off factors, the long impulse response of the channel equalizer may dominate the filter length. At the filter input oversampled data are applied, and at the output baud rate sampled data are required for further processing.

Carrier Frequency Recovery or Frequency Offset Compensation: The frequency offset between the Tx laser and the LO determines the rotation frequency of the whole constellation in the $I-Q$ plane and can be estimated in the frequency domain. A common method is using the M th power nonlinearity in order to find the frequency with the maximum power in the Fourier transform of the residual signal after the modulation has been removed [115]. The estimated carrier frequency is used to downconvert the signal into the baseband by one complex multiplication.

Carrier Phase Recovery is required to finally remove phase differences or phase walk-off between the Tx and LO carriers by either using a joint-polarization approach [116], feed-forward M th power phase estimation [117] or a Viterbi-Viterbi algorithm [118]. More details can be found in [119]. After application of the M th power of the symbols the modulation is removed, the carrier phase can be estimated, and one more complex multiplication finally compensates the carrier phase. At the output of the carrier phase recovery the symbols are regenerated completely.

Modulation Decoding and FEC Decoding: The modulation has to be decoded depending on the Tx encoding scheme in order to regenerate the binary data, and these data are finally FEC decoded according to the applied FEC scheme.

7.6 Data Converters (DAC and ADC)

Enabled by the progress on integration of Si technology, first high speed DAC and ADC technologies have been implemented in 10 Gbit/s direct detection systems [120, 121] supporting sampling rates of ~ 20 GSamples/s, and the target was the compensation of chromatic dispersion in the electronic domain by pre-compensation or by post-compensation, respectively. Initially coherent 40G and 100G transponders required ADCs at the receiver only but DACs at the transmitter side became the key enabler for HOM formats and DACs enabled flexible adaptation of formats, equalization of components frequency response and spectral pre-shaping in order to optimize spectral efficiencies.

Several DAC and ADC concepts or architectures are known today, and their suitability for a specific application is determined by: physical size, power consumption,

resolution, speed, accuracy and cost. While the architectures of high-speed DACs and high speed ADCs are significantly different, the common attributes of both are: effective resolution, linearity, maximum sampling rate, total harmonic distortions, noise floor, clock speed, jitter, bandwidth, suitability for integration with the DSP and power dissipation.

The realization of data converters for first generation and current state-of-the-art coherent transceivers is summarized in Sect. 7.7.3 on ASIC technologies.

7.6.1 Digital-to-Analogue Converters

In this section we will describe the main parameters which characterize DACs and summarize the principles of typical high speed DAC architectures that have been realized for optical communication. We will focus here on high speed DACs with a minimum resolution of 6 bits that can be applied for ASICs including transmitter DSP in commercial transceiver implementations.

7.6.1.1 DAC Performance Parameters

DACs are characterized by static and dynamic parameters as described in detail below. Dynamic performance measurements are based on spectral analysis: The DAC is loaded with a digital image of a single or multi-tone sine-wave signal with frequency smaller than the Nyquist frequency (half the maximum sampling frequency of the DAC) and the DAC's output spectrum is measured with a spectrum analyzer.

Two static parameters characterize the DAC's linearity: the differential non-linearity (DNL) and the integral nonlinearity (INL). Both parameters are measures of the linearity of the level transitions of the converter and both affect the converter's quantization performance, so that due to the effects of DNL and INL the static effective number of bits is already less than the theoretically expected resolution. The basic dynamic DAC parameters are: the 3 dB electrical bandwidth, the maximum sampling rate, the signal-to-noise ratio without harmonics, the signal to total harmonic distortion ratio (THD), the signal to noise and distortion ratio (SINAD), the spurious free dynamic range, and finally the dynamic number of bits, as explained below.

DAC Resolution: The resolution of a DAC is determined by the number (n) of bits of possible output levels (2^n) the DAC is designed to reproduce. For instance, a 1 bit DAC is designed to reproduce only 2 (2^1) levels while an 8 bit DAC is designed for 256 (2^8) levels. This designed resolution corresponds to a theoretical resolution, and in reality the quantization of a signal with higher resolution leads to an unavoidable quantization error [99].

Maximum Sampling Rate: A measurement of the maximum speed at which the DAC's circuitry can operate and still produce the correct analogue output.

Signal-to-Noise-and-Distortion Ratio (SINAD or SNDR): SINAD is a good indication of the overall dynamic performance of a DAC because it includes all components which contribute to noise and distortion. Signal-to-noise-and-distortion (SINAD, or $S/(N + D)$) is the ratio of the signal amplitude to all other spectral components, including noise and harmonics while SNR and THD are the signal to noise and signal to distortion ratios, respectively.

$$SINAD = 20 \log \left(\frac{S}{N + D} \right) = 20 \log \sqrt{(10^{-SNR/20})^2 + (10^{-THD/20})^2} \quad (7.20)$$

Effective Number of Bits (ENOB): A measure of the actual resolution of a DAC is ENOB which is generally smaller than the theoretical or designed resolution of a DAC. ENOB is frequency dependent and usually decreases towards the highest sampled frequency. ENOB (7.21) is calculated from SINAD measurements using the relationship for the theoretical SNR of an ideal n -bit DAC or ADC: $SNR = 6.02n + 1.76$ dB [122]. The equation is solved for n , and the value of SINAD is substituted for SNR:

$$ENOB = \frac{SINAD \text{ (dB)} - 1.76}{6.02} \quad (7.21)$$

Spurious Free Dynamic Range (SFDR): The SFDR is the ratio of the rms value of the signal to the rms value of the worst spurious signal regardless of where it occurs in the frequency spectrum. The worst spurious signal may or may not be a harmonic of the original signal. SFDR is an important specification in communication systems because it represents the smallest value of signal that can be distinguished from a large interfering signal (blocker). SFDR can be specified with respect to full-scale (dBFS) or with respect to the actual signal amplitude (dBc).

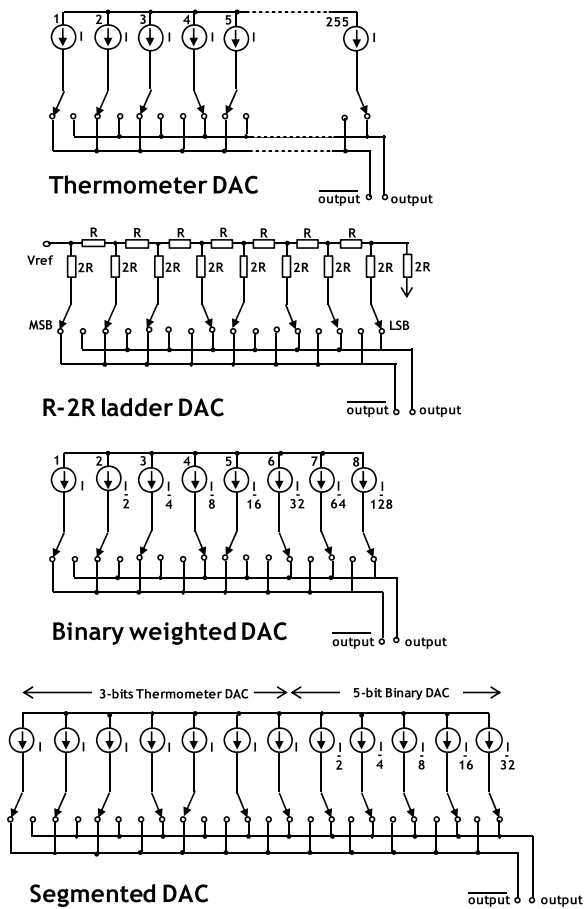
7.6.1.2 DAC Architectures

During the past 10 years four different DAC concepts have been considered, all based on current steering logic and differential analogue output [122], thermometer-coded, R-2R resistor ladder, binary weighted, or segmented DAC. Figure 7.24 shows the architectures of these DACs, all in an 8-bit theoretical resolution configuration.

Thermometer-Coded DAC (TMC-DAC): The TMC-DAC, or “fully decoded DAC”, in a version with active current sources, contains $2^n - 1$ identical current-source segments, one segment for each possible value of DAC output, i.e. 257 elements in the case of an 8 bit DAC. Thermometer-coded DACs require decoder logic and are very large but are fast and ensure very high monotonicity.

R-2R Resistor Ladder DAC (R-2R-DAC): The R-2R-DAC is based on an R and 2R resistor ladder network with two resistors with ratio of 2:1 per stage. An n -bit DAC requires $2n$ resistors. In this architecture, all stages have identical devices and matched resistors which can be trimmed easily. The output impedance of the DAC is equal to R (relatively low). A distinct advantage is that only a 2:1 resistor ratio

Fig. 7.24 Principles of various DACs all 8-bit resolution



is required regardless of the resolution. This architecture requires no decoding logic but dissipates significant power (mainly in the internal resistors), and high resolution converters perform slowly due to increasingly large RC-constants for each added R-2R link.

Binary-Weighted DAC (BW-DAC): A BW-DAC with n -bit resolution contains n individual current sources. These precise currents are weighted with powers of two ($1 : 2 : 4 : 8 : \dots : 2^{n-1}$) and sum up to the correct output value. This is a very fast conversion method but it suffers from poor accuracy because of the high precision required for each individual voltage or current. Such high-precision components are expensive, and therefore this type of converter is usually limited to 8-bit resolution or less, it dissipates less power than R-2R-DACs, requires smaller area, however, glitching (transients) is an issue.

Segmented DAC (SEG-DAC): An SEG-DAC or hybrid DAC uses combinations of the techniques explained above in a single converter. If a DAC with a specific performance is required, a single architecture is often not ideal, therefore most DACs

Table 7.9 Advantages and disadvantages of various DAC concepts

DAC concept	Advantages	Disadvantages
TMC-DAC	identical stages, monotonicity	$2n$ current sources, decoding logic, large area
R-2R-DAC	only 2 resistor values, identical stages, no decoding logic	power dissipation of resistors
BW-DAC	n current sources, no decoding logic	large current ratios
SEG-DAC	overshoot reduction	additional logic

are of segmented type in response to the challenge to achieve low cost together with high speed and high resolution in one device. A segmented DAC is divided into two sub-DACs including e.g. one thermometer-coded DAC for the most significant bits (MSBs) and one binary weighted DAC for the least significant bits (LSBs). Segmentation allows higher-resolution DAC implementations at the cost of additional logic. Finally, transients are also reduced significantly by this method.

Table 7.9 summarizes the advantages and disadvantages of the DAC concepts.

7.6.2 Analogue-to-Digital Converters

Fast ADCs followed by DSP are the key concept and enabler of coherent receivers. In this section we will discuss the main parameters characterizing ADCs and summarize the architectures of typical high speed ADCs [123] applied in optical communication.

7.6.2.1 ADC Performance Parameters

ADCs have similar static and dynamic parameters as DACs and dynamic characterization is also performed by spectral analysis [124]. If an ADC operates at a sampling rate greater than twice the bandwidth of the signal, then a reliable digital reproduction of an analogue signal is possible according to the Nyquist sampling theorem, provided the ADC can be considered ideal and quantization errors can be neglected. In contrast to DACs, ADCs require sampling and hold of the analogue input signal as ADCs cannot perform an instantaneous conversion. The input value must be held constant during the time in which the converter performs a conversion. An input circuit called a sample-and-hold or a sample-and-hold amplifier (SHA) performs this task, e.g. a capacitor plus a gate. SHAs are affected by noise, distortions, and aperture jitter.

The static parameters DNL and the INL characterize the ADC linearity. The dynamic parameters are: 3 dB electrical bandwidth, signal to noise ratio and distortion ratio, sampling rate, aliasing, jitter, and the effective number of bits.

ADC Resolution: The resolution of n bits of an ADC indicates the number of 2^n discrete values or voltage levels it can produce. The minimum change in voltage

required to guarantee a change in the output code level is called the least significant bit (LSB) voltage, corresponding to the resolution of the ADC according to (7.22)

$$LSB = E_{FSR}/2^n \quad (7.22)$$

where n is the ADC's resolution in bits and E_{FSR} is the full scale voltage range (also called span).

Sampling Rate of ADC: The sampling rate (GSamples/s) of ADCs defines the rate at which digital values are sampled from the analogue signal.

Effective Number of Bits (ENOB): Similar to the case of DACs, the ADC can resolve a signal to a certain number of bits of resolution only (ENOB, see (7.21)) and the resolution of the ADC is limited mainly by the SNR of the digitized signal. One effective bit of resolution changes the SNR by a factor of 2^1 or by 6 dB in voltage. TIAs in front of an ADC introduce further noise and may further reduce the ENOB. A non-ideal sampling clock or aperture including unavoidable clock jitter will result in additional recorded noise that will also reduce the ENOB. As for ADCs the ENOB of DACs is frequency dependent as illustrated e.g. by the so-called Walden plot [125] which shows the ENOB versus ADC input frequency.

Aperture Jitter is phase noise of the sampling clock. Care must be taken to minimize this sampling jitter on the sampling clock in the sample-and-hold circuit. Aperture jitter limits the sampling rate and also the ENOB.

Signal to Noise and Distortion Ratio (SINAD or SNDR): If aperture jitter is the only determining factor, the SNDR [126] is given by

$$SNDR \text{ (dB)} = -20 \log(2\pi f t_j) \quad (7.23)$$

where f is the analogue input frequency and t_j is the rms aperture jitter of the ADC.

Signal-to-Quantization-Noise Ratio (SQNR): Quantization error is the noise introduced by “quantization” in an ideal ADC. The resolution determines the magnitude of the quantization error and therefore determines the maximum possible average signal to noise ratio. For an ideal ADC the SQNR can be calculated by:

$$SQNR \text{ (dB)} = 20 \log 2^n \sim 6.02n \quad (7.24)$$

where n is the number of quantization bits or the bit resolution. For example, an 8-bit ADC has a maximum signal-to-noise ratio of $6.02 \times 8 = 48.16$ dB, and thus the quantization error is 48.16 dB below the maximum level. Quantization error is distributed from DC to the Nyquist frequency. If part of the ADC's bandwidth is not used, as in the case of oversampling, some of the quantization error will fall out of band which effectively improves the SQNR. In an oversampled system, noise shaping can be used to further increase the SQNR by forcing more quantization error out of the band.

Aliasing: If sampling above the Nyquist rate (i.e. more than twice the highest frequency) is possible, then all frequencies in the signal can be reconstructed (oversampling). Sampled frequencies above half the Nyquist rate are incorrectly detected compared to lower frequencies, and this process is designated as aliasing. In order

to avoid aliasing, the input of an ADC can be low-pass filtered which removes frequencies above half the sampling rate. Such a filter is called an anti-aliasing filter and is essential for ADC systems that are designed for analogue signals with higher frequency content.

7.6.2.2 ADC Architectures

As already mentioned, ADC and DAC architectures are significantly different and ADCs can be implemented in various ways with different pros and cons. The most popular high speed ADCs for DSP applications are flash-, successive approximation register-, pipelined-, ripple-, and time-interleaved ADC architectures. Various concepts of ADCs that have been considered and realized for optical coherent receivers will be summarized in the following section. The corresponding ADC architectures are shown in Fig. 7.25, all in 8-bit theoretical resolution configuration.

Flash ADC (F-ADC): Direct-conversion or parallel or flash ADCs have a large number ($2^n - 1$) of comparators which sample the input signal in parallel. The comparators are separated by resistors which reduce the reference voltages by 1 LSB voltage between comparators. Each comparator is followed by a logic circuit which generates a code for each voltage range. This kind of a direct conversion is very fast, capable to operate at Gb/s sampling rates, but has limited resolution of ~ 8 bits or fewer, due to the high number of comparators and resistors needed, e.g. a 8-bit flash ADC requires $2^8 - 1 = 255$ comparators. ADCs of this type have a large die size and high power dissipation.

Successive Approximation Register ADC (SAR-ADC): An SAR-ADC executes conversion on demand based on SHAs and comparators. The approximation is stored in a successive approximation register after each comparator step, fed back to a DAC, and compared again until the desired resolution is reached. The overall accuracy and linearity is determined by the DAC. Bit by bit, the SAR-ADC is successively narrowing the range of input voltages from the MSB voltage down to the LSB voltage. An n -bit conversion takes n steps. This serial operating procedure of an SAR-ADC limits its operating speed.

Pipeline ADC (PL-ADC): PL-ADCs or sub-ranging ADCs combine the advantages of SAR- and flash-ADCs. After the SHA a first flash ADC works on 4 bits and results in a coarse conversion, the difference between that value and the input signal is determined with a DAC (4 bit resolution) and then converted finer by a further flash-ADC. A pipeline ADC enables higher resolution and has lower power consumption than a pure flash ADC.

Serial Ripple ADC (SR-ADC): SR-ADCs are converting with a cascade of one stage per bit. Each of the n stages has a bit output and a residue output. The residue output of one stage is the input to the following stage. Finally, the LSB is detected with a single comparator as shown in Fig. 7.25. This architecture is slightly slower than the flash topology. It is a simple architecture since the number of amplifiers and flip-flops is equal to the resolution. However, propagation delay through each stage is critical.

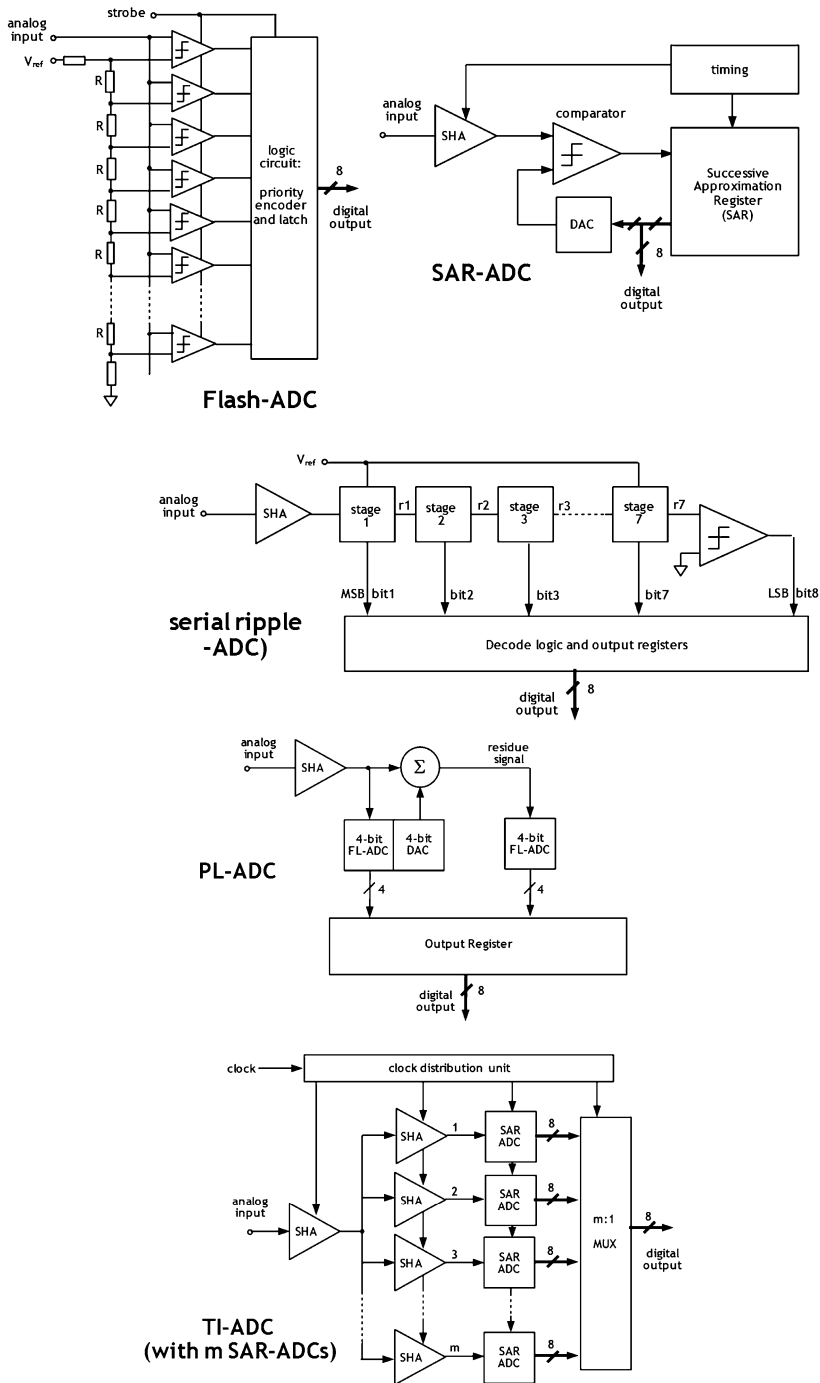


Fig. 7.25 Various ADC architectures (all with 8-bit resolution)

Table 7.10 Strengths and weaknesses of ADC concepts

Concept	Speed	Latency	Accuracy	Area
FL-ADC	++	++	++	--
SAR-ADC	–	--	+	++
PL-ADC	+	++	+	0
SR-ADC	+	0	0	–
TI-SAR-ADC	++	+	+	0

Time-interleaved SAR ADC (TI-ADC): TI-ADCs use m parallel sub-ADCs where each sub-ADC samples data every m th cycle of the effective sampling clock. Thus, each sub-ADC needs to manage an m -times lower sampling rate only which results in a very high aggregate throughput. The sub-ADCs in the time-interleaved approach are usually SAR ADCs. The challenges of TI-SAR ADCs are the clock distribution and the handling of mismatch and de-skew between the sub-ADCs. The time-interleaving concept enables the use of lower speed CMOS circuits for ADCs with multi-G sampling rates [25]. The input bandwidth of the TI-SAR ADC is determined by the first set of SHAs.

Table 7.10 indicates where the different ADC concepts have particular strengths (++ or +), weaknesses (– or --) or exhibit neutral performance (0).

ADCs and DACs for optical communication have been realized by different technologies and their performance will be discussed in the section on ASIC technologies (Sect. 7.7.3).

7.7 Devices for Coherent Transceivers

As mentioned above IQ modulators are particularly suited for square-QAM formats due to the regular structure of the constellation projected onto the in-phase and quadrature axis. Various alternative modulator and transmitter structures with separate amplitude and phase modulator stages to better support the modulation of various ASK-PSK modulation formats and which are suited for direct detection (DD) have been discussed in detail in [127]. In addition, a variety of hybrid optical structures for coherent and DD receivers have also been treated in [127].

The laser phase noise issue, one of the biggest problems of coherent systems in the past, has been overcome by the implementation of better frequency and phase correction algorithms. As laser phase noise scales with the symbol rate, the use of high symbol rates relaxes phase noise issues even further. By continuously increasing sampling rates of DACs and ADCs, the symbol rate of transmission systems has been increased significantly compared to the first coherent transceivers operating at 40 Gbit/s with symbol rates of 10 GBd. The pessimistic picture of laser phase noise given in [127] had been derived from the idea of applying HOM formats at 40 Gbit/s on a single polarization which would have resulted in symbol rates well

below 10 GBd, e.g. 6.4 GBd for 16QAM. Finally, low linewidth lasers for coherent transceivers with 100 kHz linewidth and even 4 kHz lasers [128] have become commercially available.

In the following section we will concentrate on dual-polarization IQ modulators and coherent receiver frontends for coherent detection for a single and for dual sub-carrier FDM solutions. Beyond the OE frontends, the ASIC technology requirements and limitations for the realization of data converters and DSP are addressed and recent ASIC chips realized for optical communications are summarized.

7.7.1 Dual Polarization IQ Modulators

We will focus on the ideal modulator for square-QAM operated in a dual polarization mode. This is the dual polarization IQ modulator which has become commercially available in 2009, and the package and performance parameters of this DP-IQ modulator have been specified by the OIF Implementation Agreement (IA) [31] in 2010. Initially the OIF-IA was intended to specifically address 100G DP-QPSK applications including FEC and supporting symbol rates up to 32 GBd.

7.7.1.1 Single and Dual Carrier IQ Modulators

Figure 7.10 of Sect. 7.3.1.5 illustrated the generic structure of a DP-IQ modulator for the modulation of a single carrier wavelength in x and y polarization by two separate nested or mother MZM structures. We call this structure version 1 (v1). A potential future integrated 2nd version (v2) of a DP-IQ modulator is shown in Fig. 7.26 (left side), including integrated lasers, either monolithically integrated on InP or hybridly integrated on GaAs or Si. Another important feature is related to the driving path from the DAC to the modulator. The modulator requires voltages which cannot be delivered fully by the converter itself. Therefore driver-less operation or an integrated driver option are important alternatives to save volume and reduce power consumption. Figure 7.26 also includes a future two sub-carrier FDM modulator which has significantly higher complexity.

Each IQ mother MZM consists of two child MZMs, the I- and Q-MZM, and a 90° phase shifter ($\pi/2$). The OIF-IA specifies four single ended GPPO modulation inputs per child MZM while all DC bias segments are usually implemented differentially (n and p) at the bias segments of both child and the mother MZM. This is in contrast to the principle shown in Fig. 7.26 where only one branch of the mother MZM includes the 90° phase shift element. Laser light is injected via a polarization maintaining fiber and split and separately modulated by the mother MZMs. The modulated output of one mother MZM is polarization rotated and combined with the second in a polarization beam combiner resulting in two modulated signals having two polarizations orthogonal to each other.

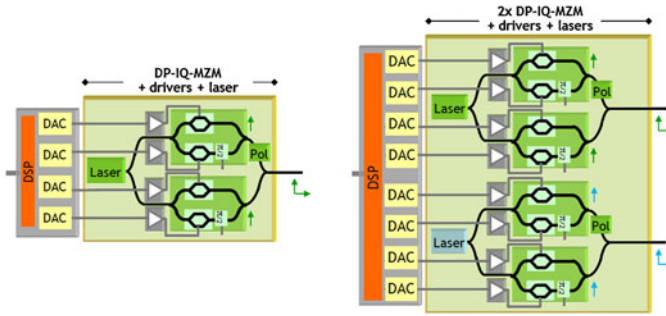


Fig. 7.26 Single and dual sub-carrier (FDM) dual-polarization IQ modulator structures in future (potentially integrated) version (v2). Pol: polarization rotator, φ : 90° phase shifter

In order to modulate BPSK or MQAM signals, the DC bias voltages of all four child MZMs are set to the minimum transmission point $V_{bias} = V_{\pi}$, and the modulation swing is chosen to be $V_{mod} = V_{2\pi}$. Modulators with low V_{π} are desirable in order to minimize driver voltages and power consumption. A major design issue of MZMs is the trade-off between achieving low V_{π} and high modulation bandwidth at the same time. The main performance parameters of DP-IQ modulators are: total minimum insertion loss, modulation voltage V_{π} at 1 GHz, modulation bandwidth, minimum extinction ratio including all child and mother MZMs, and skewing of the four modulation paths I_x , Q_x , I_y , and Q_y . The minimum insertion loss is measured when all modulators are biased at maximum transmission. Extinction ratios are measured between bias at maximum and minimum transmission corresponding to the individual child or mother MZM.

The first commercially available DP-IQ modulator was based upon a LiNbO₃ z-cut modulator structure and since 2013, InP- and GaAs technology based dual-polarization IQ modulators compliant with the OIF-IA have also become commercially available which have the advantage of enabling significantly smaller form factors. The same holds for Si-based modulators [129] which have already been integrated together with a coherent frontend [130].

In [127] modulation voltages V_{π} specified for various LiNbO₃ modulators have been summarized, and they vary between 4 V and 7.5 V so that a four child DP-IQ MZM requires four channel drivers with 4×8 V and 4×15 V, respectively. None of these drivers is available today. However, due to an attractive V_{π} value reported in [131] (reduced to ~ 3 V) in combination with attractive volume prices of dual polarization modulators, thousands of LiNbO₃ DP-IQ modulators have been shipped since 2010 and have been implemented in most 100G transceivers.

The first 400G transceivers which include two sub-carrier FDM DP-16QAM have been implemented using two separate DP-IQ modulators with two separate four channel modulator drivers. Since 2015 a LiNbO₃ modulator package is commercially available which includes two DP-IQ modulators and also eight integrated channel modulator drivers to be connected with $8 \times$ G3PO connectors for modula-

tion of the eight child MZMs. Figure 7.26 includes a future two sub-carrier FDM DP-IQ modulator with integrated laser and drivers.

1 Tbit/s two sub-carrier FDM transceivers require symbol rates of 53 GBd or 64 GBd together with DP-64QAM or DP-32QAM modulation, respectively, as shown in Table 7.8.

7.7.1.2 Multiple Carrier IQ Modulators

The first integrated multiple sub-carrier IQ modulators have been based upon InP technology with a monolithically integrated PIC [132] implemented in FDM transmitters. The PIC comprises 10 IQ modulators, 10 tuneable DFB lasers and an arrayed waveguide grating (AWG) serving as wavelength combiner. InP PIC chips were also incorporated in coherent FDM transceivers including 10-fold QPSK modulations.

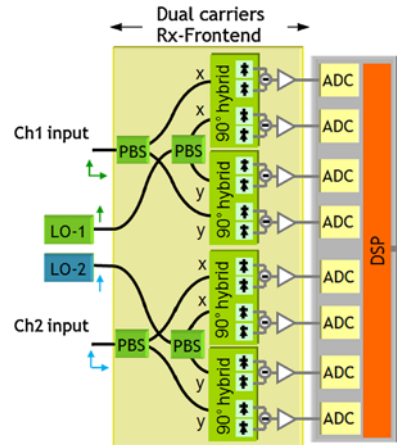
These FDM transmitters did not include DACs and focused on binary modulation only, as a transceiver with 40 DACs and ADCs can hardly be realized due to power consumption issues. Thus, these FDM transmitters with a high number of sub-carriers have no potential for the optimization of the spectral efficiency by higher constellation MQAM formats including shaping.

7.7.2 Optical Receiver Frontend

Similar to the modulator case, component providers agreed also on a preferred solution for a polarization diversity coherent receiver frontend. In 2010 the OIF published the implementation agreement for an integrated intradyne coherent receiver also suitable for 100 Gbit/s DP-QPSK systems up to symbol rates of 32 GBd.

The basic structure of the frontend was shown in Fig. 7.10 (Sect. 7.3.1.5). Figure 7.27 includes a potential future integrated two sub-carrier FDM solution on Si with hybridly integrated local oscillator lasers. The chip has two input fibers allowing highest flexibility. For each single carrier path the received signal (coupled in from a standard fiber) is split by a polarization beam splitter, and the x and y polarization components of the signal interfere with the light of the LO laser in 2×2 90° hybrids. The splitting of the LO light by another PBS is shown schematically but in reality the separated polarization components of the information signal exhibit the same linear polarization state at the PBS outputs, and it is therefore sufficient that the LO light, the polarization of which must be aligned to the polarization of the signal at the two PBS outputs, is equally split by a 3 dB coupler. The output signals of the 2×2 90° hybrids are detected by four pairs of balanced photodiodes and amplified by linear TIAs. The outputs of the O/E frontend provide the in-phase and quadrature photocurrents of both polarization components: I_x , Q_x , I_y , and Q_y for both carriers, digitally converted by four ADCs and then further processed by

Fig. 7.27 Future two sub-carrier FDM frontend



digital signal processing. A two sub-carrier receiver simply doubles the components and complexity.

The key elements of the receivers are SMF input fibers for each sub-carrier which allow highest flexibility at the Rx, PM fiber inputs for external local oscillator lasers, 90° hybrids, balanced photodetectors, linear TIAs, all channels selectable with manual or automatic gain control, and coplanar RF input interfaces.

7.7.3 ASIC Technologies

The first DACs and ADCs were implemented in fiber optic communication in 10 Gbit/s intensity modulated and direct detection (IM-DD) systems in 2005. The purpose was the compensation of linear transmission distortions such as chromatic dispersion in the electronic domain. The first ADC chip supported over-sampling with 20 GSamples/s and 3-bit resolution, and was applied at the receiver side together with a digital equalizer (DEQ) chip for electronic dispersion post-compensation. In a multi-chip transceiver the ADC was implemented based upon 200 GHz SiGe bipolar technology while the DEQ chip based on a Viterbi decoder was realized by 130 nm CMOS technology. The first dual DAC supporting sampling with 22 GSamples/s and 5-bit resolution integrated in a single ASIC together with the transmitter DSP with FIR filter taps for electronic pre-compensation, was realized by 130 nm SiGe BiCMOS [133] technology.

Silicon technologies underwent significant progress by doubling the transistor count every two years. Between the introduction of digital converters and DSP in optical communication in 2005 and 2015 the number of gates and functionalities realized and implemented in application-specific integrated circuits has been increased very significantly. It is worthwhile to note that Moore’s law is still alive but applies to the chip density and not anymore to transistor speed, and 16 nm CMOS

technology reaches four times higher density than 28 nm CMOS technology applied in the 2014 generation of optical transceiver ASICs.

High-speed data converters have been realized in CMOS- or in SiGe-based bipolar technology. Due to a high degree of parallelization, CMOS favors high-sampling rate designs while SiGe bipolar supports higher bandwidth. Dual-chip solutions with a SiGe-based data converter and DSP in CMOS technology provide converters with optimum frequency response and allow the use of advanced CMOS technology for the DSP part. Unfortunately, this dual-chip approach leads to significant challenges with respect to high volume data transfer between the data converter ASIC and the DSP ASIC, and with respect to the resolution and sampling rate requirements of current and future 400G implementations, it becomes mandatory to co-integrate converters with the DSP. For example, in the 28 nm CMOS ASIC generation for optical transceivers, four DACs, each performing at least theoretically with 8-bit resolution and 92 GSamples/s maximum sampling rate, require a total transfer rate between DAC and DSP of $4 \times 8 \times 92 = 2.944$ Tbit/s. This can only be handled in a single CMOS ASIC chip solution.

In the first coherent transceiver generation the FEC was not fully integrated with DSP ASIC chips while in 2015 commercial coherent transceiver products comprise fully customized CMOS ASICs which offer best performance and lowest power consumption, however, at the expense of complexity and costly design cycles. DSP and FEC require purely digital functions and can be realized best in CMOS technology. Data converters include analogue and digital functions and are therefore also called ‘mixed signal’ circuits. Because of the stringent requirements concerning sampling speed, bandwidth, and signal integrity, they require a different design methodology than DSP and FEC. Typically, a full custom design procedure is implemented for the design of data converters and sampling speeds considered for symbol rates beyond 32 GBd. For analogue parts and even critical digital parts, the circuit layout is done manually and parasitic extraction is performed to augment the circuit simulation with more realistic models. In latest generation 28 nm CMOS technology, SD-FEC as well as Tx DSP and Rx DSP, eight DACs and eight ADCs required for a 400 Gbit/s transceiver with two sub-carriers can be implemented in a single ASIC chip. Single ASICs for 1 Tbit/s transceivers with up to five sub-carriers and twenty DACs and twenty ADCs are not expected to pose major problems arising from the number of supported carriers per ASIC chip if the ASIC is fabricated using the newest 16 nm CMOS technology, however, how to get the signals out of the ASIC package will probably be a demanding task.

Tables 7.11 and 7.12 summarize technologies which are used in optical communication and the focus is on data converters and integration (yes or no) with DSP functions. The tables indicate converter concepts, their maximum sampling rate and theoretical resolution, the die size, and power consumption. For most recent CMOS based DACs and ADCs the integration of DSP became mandatory and the applied concepts are usually segmented DACs and time-interleaved SAR ADCs. The tables also show the progress in sampling speed and power consumption obtained by CMOS technologies. Attractive high sampling speed has been achieved with

Table 7.11 Evolution and key parameters of DACs applied in optical transceiver ASICs or instrumentation

Source	Technology	Year	Tx-DSP integr.?	DAC Concept	Resolution (bits)	Max. Sampling Rate (GSamples/s)	Die size (mm ²)	Power (W)	Ref.
Nortel	13C-nm SiGe BiCMOS	2005	Yes	SEG (TM&R-2R)	6	22	2.5 × 1.8	1.2	[134]
NTT	1- μ m InP HBT	2009	No	R-2R	6	32	3 × 3	1.4	[135]
IHP	250-nm SiGe BiCMOS	2008	No	SEG (TM&R-2R)	8	20	2 × 3	2.5	[136]
Micram	SiGe BiCMOS	2010	No	BW	6	34	5 × 5	0.4	[137]
Nortel	65-nm CMOS	2011	Yes	SEG (TM&BW)	6	56	0.6 × 0.4	0.75	[138]
NTT	0.5- μ m InP HBT	2011	No	R-2R	6	60	3 × 3	1.8	[139]
Fujitsu	40-nm CMOS	2012	Yes	SEG	8	65	–	0.75	[140]
Tek	SiGe BiCMOS	2013	–	–	10	25	–	–	[141]
Fujitsu	28-nm CMOS	2014	Yes	SEG	8	92	–	–	[75]

Table 7.12 Evolution and key parameters of ADCs applied in optical transceiver ASICs or instrumentation

Source/Foundry	Technology	Year	Rx-DSP integr.?	ADC Concept	Resolution (bits)	Max. Sampling Rate (GSamples/s)	Die Size (mm ²)	Power (W)	Ref.
Agilent	180-nm CMOS	2003	No	PL	8	35	14 × 14	9	[142]
Nortel/STM	130-nm SiGe BiCMOS	2006	No	FL	5	22	1.8 × 2.5	3	[143]
Alcatel-Lucent	180-nm SiGe BiCMOS	2008	No	FL	5	24	2.6 × 3.3	3.3	[144]
Nortel	90-nm CMOS	2008	Yes	TI-SAR	6	24	4 × 4	1.2	[145]
Micram	SiGe HBT/BiCMOS	2010	Yes	SR	6	34	1 × 2.6	2	[137]
Ciena	65-nm CMOS	2010	Yes	TI-SAR	6	40	4 × 4	1.5	[138]
Fujitsu	65-nm CMOS	2010	Yes	TI-SAR	8	56	–	2	[146]
Fujitsu	40-nm CMOS	2012	Yes	TI-SAR	8	65	–	1.2	[147]
Fujitsu	28-nm CMOS	2013	Yes	TI-SAR	8	92	–	<1	[148]

CMOS and the power consumption has been continuously decreased with technology progress. Even higher sampling rates than 100 GSamples/s are probably feasible with CMOS but the current trend of ASIC design is to further reduce the power consumption instead of increasing the sampling speed.

References

1. www.cisco.com/c/en/us/solutions/collateral/service-provider/ip-ngn-ip-next-generation-network/white_paper_c11-481360.html
2. R.W. Tkach, Scaling optical communications for the next decade and beyond. *Bell Labs Tech. J.* **14**(4), 3–10 (2010)
3. B. Wedding, W. Idler, B. Franz, W. Pöhlmann, E. Lach, 40 Gbit/s quaternary dispersion supported transmission over 31 km of standard single mode fibre without optical dispersion compensation, in *Proc. 24th Europ. Conf. Opt. Commun.* (ECOC'98), Madrid, Spain (1998), paper WdCO8
4. C. Xie, S. Spiga, P. Dong, P. Winzer, M. Bergmann, B. Koegel, C. Neumeyr, M. Amann, 400-Gb/s PDM-4PAM WDM system using a monolithic 2×4 VCSEL array and coherent detection. *J. Lightwave Technol.* **33**(3), 670–677 (2015)
5. J.M. Kahn, K. Ho, Spectral efficiency limits and modulation/detection techniques for DWDM systems. *IEEE J. Sel. Top. Quantum Electron.* **10**, 259–279 (2004)
6. Y. Koizumi, K. Toyoda, M. Yoshida, M. Nakazawa, 1024 QAM (60 Gbit/s) single-carrier coherent optical transmission over 150 km. *Opt. Express* **20**(11), 12508–12514 (2012)
7. S. Beppu, K. Kasai, M. Yoshida, N. Nakazawa, 2048 QAM (66 Gbit/s) single-carrier coherent optical transmission over 150 km with a potential SE of 15.3 bit/s/Hz. *Opt. Express* **23**(4), 4960–4969 (2015)
8. Optical internetworking document: 100G ultra long haul DWDM framework document. OIF-FD-100G-DWDM-01.0.pdf
9. Dell'Oro Group, Optical transport market report 2Q16, Market summary and vendor information **18**(2), O1A
10. <http://www.lightwaveonline.com/articles/2016/01/100g-200g-wdm-to-drive-optical-transport-sales-growth-through-2020-delloro.html>
11. S.L. Jansen, I. Morita, K. Forozesh, S. Randel, D. van den Borne, H. Tanaka, Optical OFDM, a hype or is it for real? in *Proc. 24th Europ. Conf. Opt. Commun.* (ECOC'98), Madrid, Spain (1998), paper Mo.3.E.3
12. A. Bononi, N. Rossi, P. Serena, Transmission limitations due to fibre nonlinearity, in *Opt. Fiber Commun. Conf. and Nat. Fiber Opt. Eng. Conf.* (OFC/NFOEC'11), Los Angeles, CA, USA (2011), Techn. Digest, paper OWO7
13. W. Yan, T. Tanaka, B. Liu, M. Nishihara, L. Li, T. Takahara, Z. Tao, J.C. Rasmussen, T. Drenski, 100 Gb/s optical IM-DD transmission with 10G-class devices enabled by 65 GSamples/s CMOS DAC core, in *Opt. Fiber Commun. Conf. and Nat. Fiber Opt. Eng. Conf.* (OFC/NFOEC'13), Anaheim, CA, USA (2013), Techn. Digest, paper OM3H1
14. T. Tanaka, M. Nishihara, T. Takahara, W. Yan, L. Li, Z. Tao, M. Matsuda, K. Takabayashi, J.C. Rasmussen, Experimental demonstration of 448-Gbps DMT transmission over 30-km SMF, in *Opt. Fiber Commun. Conf.* (OFC'14), San Francisco, CA, USA (2014), Techn. Digest, paper M2I5
15. ITU-T recommendation G.694.2, Spectral grids for WDM applications: CWDM wavelength grid, published 12/2003
16. A. Sano, H. Masuda, T. Kobayashi, M. Fujiwara, K. Horikoshi, E. Yoshida, Y. Miyamoto, M. Matsui, M. Mizoguchi, H. Yamazaki, Y. Sakamaki, H. Ishii, 69.1-Tb/s (432×171 -Gb/s) C- and extended L-band transmission over 240 km using PDM-16-QAM modulation and

- digital coherent detection, in *Opt. Fiber Commun. Conf. and Nat. Fiber Opt. Eng. Conf.*, (OFC/NFOEC'10), San Diego, CA, USA (2010), Techn. Digest, paper PDPB7
17. S. Makovejs, C.C. Roberts, F. Palacios, H.B. Matthews, D.A. Lewis, D.T. Smith, P.G. Diehl, J.J. Johnson, J.D. Patterson, C.R. Towery, S.Y. Ten, Record-low (0.1460 dB/km) attenuation ultra-large A_{eff} optical fiber for submarine applications, in *Opt. Fiber Commun. Conf.* (OFC'15), Los Angeles, CA, USA (2015), Techn. Digest, PDP Th5A2
 18. S. Randel, Space-division multiplexed transmission, in *Opt. Fiber Commun. Conf. and Nat. Fiber Opt. Eng. Conf.* (OFC/NFOEC'13), Anaheim, CA, USA (2013), Techn. Digest, paper OW4F1
 19. K. Igarashi, D. Souma, Y. Wakayama, K. Takeshima, Y. Kawaguchi, T. Tsuritani, I. Morita, M. Suzuki, 114 space-division-multiplexed transmission over 9.8-km weakly-coupled-6-mode uncoupled-19-core fibers, in *Opt. Fiber Commun. Conf.* (OFC'15), Los Angeles, CA, USA (2015), Techn. Digest, PDP Th5C.4
 20. N.K. Fontaine, R. Ryf, H. Chen, A. Velazquez Benitez, J.E. Antonio-Lopez, R. Amezcua-Correa, B. Guan, B. Ercan, R.P. Scott, S.B. Yoo, L. Grueuner-Nielsen, Y. Sun, R. Lingle, 30×30 MIMO transmission over 15 spatial modes, in *Opt. Fiber Commun. Conf.* (OFC'15), Los Angeles, CA, USA (2015), Techn. Digest, PDP Th5C.1
 21. T.J. Xia, G. Wellbrock, B. Basch, S. Kotrla, W. Lee, T. Tajima, K. Fukuchi, M. Cvijetic, J. Sugg, Y. Ma, B. Turner, C. Coole, C. Urricariet, End-to-end native IP data 100G single carrier real time DSP coherent detection transport over 1520-km field deployed fiber, in *Opt. Fiber Commun. Conf. and Nat. Fiber Opt. Eng. Conf.* (OFC/NFOEC'10), San Diego, CA, USA (2010), Techn. Digest, paper PDP D4
 22. P.W. Hooijmans, *Coherent Optical System Design* (Wiley, Chichester, 1994)
 23. L.G. Kazovsky, R. Welter, A.F. Elrefaie, W. Sessa, Wide-linewidth phase diversity homodyne receivers. *J. Lightwave Technol.* **6**, 1527–1536 (1988)
 24. S. Norimatsu, K. Iwashita, K. Noguchi, An 8 Gb/s QPSK optical homodyne detection experiment using external-cavity laser diodes. *IEEE Photonics Technol. Lett.* **4**, 765–767 (1992)
 25. L.G. Kazovsky, G. Kalogerakis, W.T. Shaw, Homodyne phase-shift-keying systems: past, challenges and future opportunities. *J. Lightwave Technol.* **24**, 4876–4884 (2006)
 26. J.H. Winters, Equalization in coherent lightwave systems using a fractionally spaced equalizer. *J. Lightwave Technol.* **8**, 1487–1491 (1990)
 27. B. Spinnler, P.M. Krummrich, E.-D. Schmidt, Chromatic dispersion tolerance of coherent optical communication systems with electrical equalization, in *Opt. Fiber Commun. Conf.* (OFC'06), Anaheim, CA, USA (2006), Techn. Digest, paper OWB2
 28. T. Pfau, S. Hoffmann, R. Peveling, S. Bhandare, S.K. Ibrahim, O. Adamczyk, M. Pormann, R. Noé, Y. Achiam, First real-time data recovery for synchronous QPSK transmission with standard DFB lasers. *IEEE Photonics Technol. Lett.* **18**, 1907–1909 (2006)
 29. www.lightwaveonline.com, *Lightwave*, **27**(1) and **27**(2) (2010)
 30. E. Lach, W. Idler, Modulation formats for 100G and beyond. *Opt. Fiber Technol.* **17**(5), 377–386 (2011)
 31. Optical Internetworking Forum (OIF): Implementation agreement for integrated polarization multiplexed quadrature modulated transmitters, doc. IA # OIF-PMQ-TX-01.0, March, 2010
 32. Optical Internetworking Forum (OIF): Implementation agreement for integrated dual polarization intradyne coherent receivers, doc. IA#OIF-DPC-RX-01.1, Sept. 2011
 33. IEEE Standard 802.3ba-2010, Amendment 4: Media access control parameters, physical layers and management parameters for 40 Gb/s and 100 Gb/s operation, June 2010
 34. ITU-T recommendation G.709: Interfaces for the optical transport network (OTN), published Dec. 2009
 35. J. D'Ambrosia, 100 Gigabit Ethernet and beyond. *IEEE Commun. Mag.* **48**(3), S6–S13 (2010)
 36. Optical Internetworking Forum (OIF) document, 100G forward error correction, White Paper, May 2010, OIF-FEC-100G-01.0
 37. F. Gray, Pulse code communication, US Patent 2632058, 1953

38. C.E. Shannon, A mathematical theory of communication. *Bell Syst. Tech. J.* **27**, 379–423 and 623–656 (1948)
39. R. Hartley, Transmission of information, in *Intern. Congress on Telegraphy and Telephony*, Como, Italy (1927)
40. C.N. Campopiano, B.G. Glazer, A coherent digital amplitude and phase modulation system. *IRE Trans. Commun. Syst.* **CS-10**, 90–95 (1962)
41. G. Ungerboeck, Channel coding with multilevel/phase signals. *IEEE Trans. Inf. Theory* **28**(1), 55–67 (1982)
42. J.G. Proakis, *Digital Communications*, 4th edn. (McGraw–Hill, Singapore, 2001)
43. R.J. Essiambre, G. Kramer, P. Winzer, G. Foschini, B. Goebel, Capacity limits of optical fiber networks. *J. Lightwave Technol.* **28**(4), 662–701 (2010)
44. A. Alvarado, E. Agrell, D. Lavery, P. Bayvel, LDPC codes for optical channels: is the FEC limit a good predictor of post-FEC BER? in *Opt. Fiber Commun. Conf. (OFC'15)*, Los Angeles, CA, USA (2015), Techn. Digest, paper Th3E.5
45. W.R. Peng, I. Morita, H. Tanaka, Hybrid QAM transmission techniques for single-carrier ultra-dense WDM systems, in *Optoelectron. Commun. Conf. (OECC 2011)*, Taiwan, (2011), Techn. Digest, paper 8D2-4
46. Q. Zhuge, X. Xu, M. Morsy-Osman, M. Chagnon, M. Qiu, D.V. Plant, Time domain hybrid QAM based rate-adaptive optical transmissions using high speed DACs, in *Opt. Fiber Commun. Conf. and Nat. Fiber Opt. Eng. Conf. (OFC/NFOEC'13)*, Anaheim, CA, USA (2013), Techn. Digest, paper OTh4E6
47. F. Buchali, L. Schmalen, K. Schuh, W. Idler, Optimization of time-division hybrid-modulation and its application to rate adaptive 200 Gb transmission, in *Proc. 40th Europ. Conf. Opt. Commun. (ECOC'14)*, Cannes, France (2014), paper Tu.4.3.1
48. W. Idler, F. Buchali, L. Schmalen, K. Schuh, H. Buelow, Hybrid modulation formats outperforming 16QAM and 8QAM in transmission distance and filtering with cascaded WSS, in *Opt. Fiber Commun. Conf. (OFC'15)*, Los Angeles, CA, USA (2015), Techn. Digest, paper M3G4
49. P.J. Winzer, A.H. Gnauck, 112-Gb/s polarization-multiplexed 16-QAM on a 25-GHz WDM grid, in *Proc. 34th Europ. Conf. Opt. Commun. (ECOC'08)*, Brussels, Belgium (2008), PDP Th3.E.5
50. M. Nölle, J. Hilt, M. Seimetz, R. Freund, 8×224 Gb/s PDM 16QAM WDM transmission with real-time signal processing at the transmitter, in *Proc. 36th Europ. Conf. Opt. Commun. (ECOC'10)*, Torino, Italy (2010), paper We.8.C.4
51. A.H. Gnauck, P.J. Winzer, A. Konczykowska, F. Jorge, J. Dupuy, M. Riet, G. Charlet, B. Zhu, D.W. Peckham, Generation and transmission of 21.4 Gbaud PDM 64 QAM using a high power DAC driving a single I/Q modulator, in *Opt. Fiber Commun. Conf. and Nat. Fiber Opt. Eng. Conf. (OFC/NFOEC'11)*, Los Angeles, CA, USA (2011), Techn. Digest, paper PDPB2
52. H. Buelow, X. Lu, L. Schmalen, A. Klekamp, F. Buchali, Experimental performance of 4D optimized constellation – alternatives for PM-8QAM and PM-16QAM, in *Opt. Fiber Commun. Conf. and Nat. Fiber Opt. Eng. Conf. (OFC/NFOEC'14)*, San Francisco, CA, USA (2014), Techn. Digest, paper M2A.6
53. X. Zhou, J. Yu, M.-F. Huang, Y. Shao, T. Wang, L. Nelson, P. Magill, M. Birk, P.I. Borel, D.W. Peckham, R. Lingle, 64-Tb/s (640×107 -Gb/s) PDM-36QAM transmission over 320 km using both pre- and post-transmission digital equalization, in *Opt. Fiber Commun. Conf. and Nat. Fiber Opt. Eng. Conf. (OFC/NFOEC'10)*, San Diego, CA, USA (2010), Techn. Digest, paper PDPB9
54. A. Sano, T. Kobayashi, A. Matsuura, S. Yamamoto, S. Yamanaka, E. Yoshida, Y. Miyamoto, M. Matsui, M. Mizoguchi, T. Mizuno, 100×120 -Gb/s PDM 64-QAM transmission over 160 km using linewidth-tolerant pilotless digital coherent detection, in *Proc. 36th Europ. Conf. Opt. Commun. (ECOC'10)*, Torino, Italy (2010), paper PD2.4
55. A. Sano, T. Kobayashi, K. Ishihara, H. Masuda, S. Yamamoto, K. Mori, E. Yamazaki, E. Yoshida, Y. Miyamoto, T. Yamada, H. Yamazaki, 240-Gb/s polarization-multiplexed 64-

- QAM modulation and blind detection using PLC-LN hybrid integrated modulator and digital coherent receiver, in *Proc. 35th Europ. Conf. Opt. Commun.* (ECOC'09), Vienna, Austria (2009), paper PD2.2
56. T. Kobayashi, A. Sano, A. Matsuura, Y. Miyamoto, K. Ishihara, High-order QAM transmission for spectrally-efficient and high-capacity transport, in *Opt. Fiber Commun. Conf. and Nat. Fiber Opt. Eng. Conf.* (OFC/NFOEC'12), Los Angeles, CA, USA (2012), Techn. Digest, paper OM2A3
 57. M. Nakazawa, S. Okamoto, T. Omiya, K. Kasai, M. Yoshida, 256 QAM (64 Gbit/s) coherent optical transmission over 160 km with an optical bandwidth of 5.4 GHz, in *Opt. Fiber Commun. Conf. and Nat. Fiber Opt. Eng. Conf.* (OFC/NFOEC'10), San Diego, CA, USA (2010), Techn. Digest, paper OMJ5
 58. S. Okamoto, K. Toyoda, T. Omiya, K. Kasai, M. Yoshida, M. Nakazawa, 512 QAM (54 Gb/s) coherent optical transmission over 150 km with an optical bandwidth of 4.1 GHz, in *Proc. 36th Europ. Conf. Opt. Commun.* (ECOC'10), Torino, Italy (2010), paper PD2.3
 59. D. Qian, M.-F. Huang, E. Ip, Y.-K. Huang, Y. Shao, J. Hu, T. Wang, 101.7-Tb/s (370×294 -Gb/s) PDM-128QAM-OFDM Transmission over 3×55 -km SSMF using pilot-based phase noise mitigation, in *Opt. Fiber Commun. Conf. and Nat. Fiber Opt. Eng. Conf.* (OFC/NFOEC'11), Los Angeles, CA, USA (2011), Techn. Digest, paper PDPB5
 60. X. Liu, S. Chandrashekar, Superchannel for next-generation optical networks, in *Opt. Fiber Commun. Conf.* (OFC'14), San Francisco, CA, USA (2014), Techn. Digest, tutorial WH1.5
 61. ITU-T recommendation G.694.1: Spectral grids for WDM applications: DWDM frequency grid, published 2012
 62. G. Raybon, A.L. Adamiecki, P. Winzer, C. Xie, A. Konczykowska, F. Jorge, J.-Y. Dupuy, L.L. Buhl, S. Chandrashekar, S. Draving, M. Grove, K. Rush, Single-carrier 400G interface and 10-channel WDM transmission over 4,800 km using all-ETDM 107-Gbaud PDM-QPSK, in *Opt. Fiber Commun. Conf. and Nat. Fiber Opt. Eng. Conf.* (OFC/NFOEC'13), Anaheim, CA, USA (2013), Techn. Digest, paper PDP5A.5
 63. R. Rios-Müller, J. Renaudier, P. Brindel, H. Mardoyan, P. Jennevé, L. Schmalen, G. Charlet, 1-Terabit/s net data-rate transceiver based on single-carrier Nyquist-shaped 124 GBaud PDM-32QAM, in *Opt. Fiber Commun. Conf.* (OFC'15), Los Angeles, CA, USA (2015), Techn. Digest, PDP Th5B.1
 64. G. Raybon, A. Adamiecki, P. Winzer, S. Randel, L. Salamanca, A. Konczykowska, F. Jorge, J. Dupuy, L. Buhl, S. Chandrashekar, C. Xie, S. Draving, M. Grove, K. Rush, R. Urbanke, High symbol rate coherent optical transmission systems: 80 and 107 Gbaud. *J. Lightwave Technol.* **32**(4), 824–831 (2014)
 65. G. Raybon, A. Adamiecki, P.J. Winzer, M. Montoliu, S. Randel, A. Umbach, M. Margraf, J. Stephan, S. Draving, M. Grove, K. Rush, All-ETDM 107-Gbaud PDM-16QAM (856-Gb/s) transmitter and coherent receiver, in *Proc. 39th Europ. Conf. Opt. Commun.* (ECOC'13), London, UK (2013), paper PD2D3
 66. O. Bertran-Pardo, J. Renaudier, H. Mardoyan, P. Tran, R. Rios-Muller, A. Konczykowska, J.-Y. Dupuy, F. Jorge, M. Riet, B. Duval, J. Godin, S. Randel, G. Charlet, S. Bigo, Transmission of 50-GHz-spaced single-carrier channels at 516 Gb/s over 600 km, in *Opt. Fiber Commun. Conf. and Nat. Fiber Opt. Eng. Conf.* (OFC/NFOEC'13), Anaheim, CA, USA (2013), Techn. Digest, paper OTH4E2
 67. J. Renaudier, R. Rios-Muller, L. Schmalen, M. Salsi, P. Tran, G. Charlet, S. Bigo, 1-Tb/s transceiver spanning over just three 50-GHz frequency slots for long-haul systems, in *Proc. 39th Europ. Conf. Opt. Commun.* (ECOC'13), London, UK (2013), paper PD2D5
 68. S. Randel, O. Bertran-Pardo, H. Mardoyan, P. Tran, G. Charlet, S. Bigo, A. Konczykowska, J.-Y. Dupuy, F. Jorge, M. Riet, J. Godin, Spectral efficiency long-haul transmission of 22 Tb/s using 40-Gbaud PDM-16QAM with coherent detection, in *Opt. Fiber Commun. Conf.* (OFC'14), San Francisco, CA, USA (2014), Techn. Digest, paper OW4C.2
 69. J. Renaudier, R. Rios-Muller, L. Schmalen, M. Salsi, P. Tran, G. Charlet, S. Bigo, Spectrally efficient 1-Tb/s transceivers for long-haul optical systems. *J. Lightwave Technol.* **33**(7), 1452–1458 (2015)

70. F. Buchali, K. Schuh, L. Schmalen, W. Idler, E. Lach, A. Leven, 1-Tbit/s dual-carrier DP-64QAM transmission at 64 GBaud with 40% overhead soft-FEC over 320 km SMF, in *Opt. Fiber Commun. Conf. and Nat. Fiber Opt. Eng. Conf.* (OFC/NFOEC'13), Anaheim, CA, USA (2013), Techn. Digest, paper Th4E.3
71. G. Raybon, S. Randel, A. Adamieki, P. Winzer, L. Salamance, R. Urbanke, S. Chandrasekhar, A. Konczykowska, F. Jorge, J. Dupuy, L. Buhl, M. Grove, K. Rush, 1-Tb/s dual-carrier 80-Gbaud PDM-16QAM WDM transmission at 5.2 b/s/Hz over 3200 km, in *Proc. Photon. Conf.* (IPC'12) (2012). doi:[10.1109/IPCCon.2012.6359319](https://doi.org/10.1109/IPCCon.2012.6359319)
72. W. Idler, F. Buchali, K. Schuh, N. Cameron, T. Brast, S. Schmid, A. Steffan, 1 Tb/s – 4 × 343 Gb/s subcarriers on 50 GHz grid – transmission over 480 km SMF with 22 GHz bandwidth semiconductor modulator, in *Opt. Fiber Commun. Conf.* (OFC'14), San Francisco, CA, USA (2014), Techn. Digest, paper Th4F.2
73. R. Dischler, L. Schmalen, Transmission of a 1.1 Tb/s super channel in 100 GHz optical bandwidth based on PM-256 QAM and spatially coupled FEC, in *Proc. 40th Europ. Conf. Opt. Commun.* (ECOC'14), Cannes, France (2014), paper We. 1.C.1
74. G. Raybon, A. Adamiecki, S. Randel, P.J. Winzer, Single-carrier and dual-carrier 400-Gb/s and 1.0-Tb/s transmission systems, in *Opt. Fiber Commun. Conf.* (OFC'14), San Francisco, CA, USA (2014), Techn. Digest, paper Th4F1
75. Fujitsu, OOLA 55-92 GSa/s 8-bit DAC family; online: www.fujitsu.com/cn/en/products/devices/semiconductor/fsp/asic/asic/ipmacro/networkingips/
76. A. Carena, G. Bosco, V. Curri, P. Poggiolini, M. Tapia Taiba, F. Forghieri, Statistical characterization of PM-QPSK signals after propagation in uncompensated fiber links, in *Proc. 36th Europ. Conf. Opt. Commun.* (ECOC'10), Torino, Italy (2010), paper P4.07
77. P. Poggiolini, G. Bosco, A. Carena, V. Curri, Y. Jiang, F. Forghieri, The GN-model of fiber non-linear propagation and its applications. *J. Lightwave Technol.* **32**(4), 694–721 (2014)
78. A. Carena, G. Bosco, V. Curri, Y. Jiang, P. Poggiolini, F. Forghieri, EGN model of non-linear fiber propagation. *Opt. Express* **22**(13), 16335–16362 (2104)
79. ITU-T supplement 39 of G-Series: Optical system design and engineering considerations; published Sept. 2012
80. F. Buchali, G. Böcherer, W. Idler, L. Schmalen, P. Schulte, F. Steiner, Experimental demonstration of capacity increase and rate adaptation by probabilistically shaped 64-QAM, in *Proc. 41st Europ. Conf. Opt. Commun.* (ECOC'15), Cannes, France (2015), paper PDP 3.4
81. P.J. Winzer, A.H. Gnauck, A. Konczykowska, F. Jorge, J.-Y. Dupuy, Penalties from in-band crosstalk for advanced optical modulation formats, in *Proc. 37th Europ. Conf. Opt. Commun.* (ECOC'11), Geneva, Switzerland (2011), paper Tu. 5.B.7
82. F. Buchali, W. Idler, L. Schmalen, K. Schuh, H. Buelow, Performance and advantages of 100 Gb/s QPSK/8QAM hybrid modulation formats, in *Opt. Fiber Commun. Conf.* (OFC'15), Los Angeles, CA, USA (2015), Techn. Digest, paper Th2A.16
83. F. Buchali, F. Steiner, G. Boecherer, L. Schmalen, P. Schulte, W. Idler, Rate adaptation and reach increase by probabilistically shaped 64-QAM: an experimental demonstration. *J. Lightwave Technol.* **34**(7), 1599–1609 (2016)
84. ITU-T recommendation G.975.1, Forward error correction for high bit-rate DWDM submarine systems, published Feb. 2004
85. ITU-T recommendation G.709, Interfaces for the Optical Transport Network (OTN), published Dec. 2009
86. G.D. Forney, *Concatenated Codes* (MIT Press, Cambridge, 1966)
87. T.K. Moon, *Error Correction Coding: Mathematical Methods and Algorithms* (Wiley, New York, 2005)
88. I.B. Djordjevic, M. Arabaci, L.L. Minkov, Next generation FEC for high capacity communication in optical transport network. *J. Lightwave Technol.* **27**(16), 3518–3530 (2009)
89. Y. Miyata, K. Sugihara, W. Matsumoto, K. Onohara, T. Sugihara, K. Kubo, H. Yoshida, T. Mizuochi, A triple-concatenated FEC using soft-decision decoding for 100 Gb/s optical transmission, in *Opt. Fiber Commun. Conf. and Nat. Fiber Opt. Eng. Conf.* (OFC/NFOEC'10), San Diego, CA, USA (2010), Techn. Digest, paper OThL3

90. Optical Internetworking Forum (OIF) document, 100G forward error correction. White Paper, May 2010. OIF-FEC-100G-01.0
91. R. Pyndiah, Near optimum decoding of product codes: block turbo codes. *IEEE Trans. Commun.* **46**(8), 1003–1010 (1998)
92. R.G. Gallager, *Low-Density Parity-Check Codes* (MIT Press, Cambridge, 1963). www.ldpc-codes.com/papers/Robert_Gallager_LDPC_1963.pdf
93. A. Leven, L. Schmalen, Status and recent advances on forward error correction technologies for lightwave systems. *J. Lightwave Technol.* **32**(16), 2735–2750 (2014)
94. Y. Miyata, K. Kubo, H. Yoshida, T. Mizuoch, Proposal for frame structure of optical channel transport unit employing LDPC codes for 100 Gb/s FEC, in *Opt. Fiber Commun. Conf. and Nat. Fiber Opt. Eng. Conf.* (OFC/NFOEC'09), San Diego, CA, USA (2009), Techn. Digest, paper NThB2
95. L. Schmalen, D. Suikat, D. Rösener, A. Leven, Evaluation of left-terminated spatially coupled LDPC codes for optical communications, in *Proc. 40th Europ. Conf. Opt. Commun.* (ECOC'14), Cannes, France (2014), paper Th.2.3.4
96. L. Schmalen, V. Aref, J. Cho, D. Suikat, D. Roesener, A. Leven, Spatially coupled soft-decision error correction for future lightwave systems. *J. Lightwave Technol.* **33**(5), 1109–1116 (2015)
97. A. Ghazisaeidi, L. Schmalen, I.F. de Jauregui Ruiz, P. Tran, C. Simonneau, P. Brindel, G. Charlet, Transoceanic transmission systems using adaptive multi-rate FECs. *J. Lightwave Technol.* **33**(7), 1479–1487 (2015)
98. J.X. Cai, Y. Sun, H.G. Batshon, M. Mazurczyk, H. Zhang, D.G. Foursa, A.N. Pilipetski, 54 Tb/s transmission over 9,150 km with optimized hybrid Raman-EDFA amplification and coded modulation, in *Proc. 40th Europ. Conf. Opt. Commun.* (ECOC'14), Cannes, France (2014), paper PD.3.3
99. W.R. Bennett, Spectra of quantized signals. *Bell Syst. Tech. J.* **27**, 446–472 (1948). <https://archive.org/details/bstj27-3-446>
100. F. Buchali, A. Klekamp, L. Schmalen, T. Drenski, Implementation of 64QAM at 42.66 GBaud using 1.5 samples per symbol DAC and demonstration of up to 300 km fiber transmission, in *Opt. Fiber Commun. Conf.* (OFC'14), San Francisco, CA, USA (2014), Techn. Digest, paper M2A.1
101. W. Idler, F. Buchali, D. Roesener, E. Lach, A. Leven, Spectral pre-distortion with FPGA and DAC at 448-Gb/s DP-16QAM improving nonlinear threshold power (NLT), in *Opt. Fiber Commun. Conf. and Nat. Fiber Opt. Eng. Conf.* (OFC/NFOEC'13), Anaheim, CA, USA (2013), Techn. Digest, paper Oth3C.1
102. F.M. Gardner, A BPSK/QPSK timing-error detector for sampled receivers. *IEEE Trans. Commun.* **COM-34**, 423–429 (1986)
103. M. Oerder, H. Meyr, Digital filter and square timing recovery. *IEEE Trans. Commun.* **COM-36**, 605–612 (1988)
104. I. Fatadin, S. Savory, D. Ives, Compensation of quadrature imbalance in an optical QPSK coherent receiver. *IEEE Photonics Technol. Lett.* **20**(20), 1733–1735 (2008)
105. A. Leven, L. Schmalen, Implementation aspects of coherent transmit and receive functions in application-specific integrated circuits, in *Optical Fibre Telecommunications VIA, Systems and Networks*, 6th edn., vol. 15 (Elsevier, Amsterdam, 2013), pp. 555–585
106. M. Kuschnerov, F.N. Hauske, K. Piyawanno, B. Spinnler, E.-D. Schmidt, B. Lankl, Joint equalization and timing recovery for coherent fiber optic receivers, in *Proc. 34th Europ. Conf. Opt. Commun.* (ECOC'08), Brussels, Belgium (2008), paper Mo3D3
107. S.J. Savory, Compensation of fibre impairments in digital coherent systems, in *Proc. 34th Europ. Conf. Opt. Commun.* (ECOC'08), Brussels, Belgium (2008), paper Mo3D1
108. B. Spinnler, Equalizer design and complexity for digital coherent receivers. *IEEE J. Sel. Top. Quantum Electron.* **16**(5), 1180–1192 (2010)
109. G. Clark, S. Parker, S. Mitra, A unified approach to time- and frequency-domain realization of FIR adaptive digital filters. *IEEE Trans. Acoust. Speech Signal Process.* **31**, 1073–1083 (1983)

110. S.J. Savory, G. Gavioli, R.I. Killey, P. Bayvel, Transmission of 42.8 Gbit/s polarization multiplexed NRZ-QPSK over 6400 km of standard fiber with no optical dispersion compensation, in *Opt. Fiber Commun. Conf. and Nat. Fiber Opt. Eng. Conf.* (OFC/NFOEC'07), Anaheim, CA, USA (2007), Techn. Digest, paper OTuA1
111. D. Godard, Self-recovering equalization and carrier tracking in two-dimensional data communication systems. *IEEE Trans. Commun.* **28**, 1867–1875 (1980)
112. I. Fatadin, D. Ives, S.J. Savory, Blind equalization and carrier phase recovery in a 16-QAM optical coherent system. *J. Lightwave Technol.* **27**(15), 3042–3049 (2009)
113. B. Widrow, Thinking about thinking: the discovery of the LMS algorithm. *IEEE Signal Process. Mag.* **22**, 100–106 (2005)
114. S.J. Savory, Digital filters for coherent optical receivers. *Opt. Express* **16**, 804–810 (2008)
115. A. Leven, N. Noriaki, U.V. Koc, Y.-K. Chen, Frequency estimation in intradyne reception. *IEEE Photonics Technol. Lett.* **19**(6), 366–368 (2007)
116. M. Kuschnerov, D. Van den Borne, K. Piyawanno, F.N. Hauske, C.R.S. Fludger, T. Duthel, T. Wuth, J.C. Geyer, C. Schulien, B. Spinnler, E.-D. Schmidt, B. Lankl, Joint-polarization carrier phase estimation for XPM-limited coherent polarization-multiplexed QPSK transmission with OOK-neighbors, in *Proc. 34th Europ. Conf. Opt. Commun.* (ECOC'08), Brussels, Belgium (2008), paper Mo4D2
117. J.D. Proakis, M. Salehi, *Digital Communications*, 5th edn. (McGraw Hill, Singapore, 2008). ISBN 978-0-07-295716-7
118. A.J. Viterbi, A.M. Viterbi, Nonlinear estimation of PSK-modulated carrier phase with application to burst digital transmission. *IEEE Trans. Inf. Theory* **29**, 543–551 (1983)
119. E. Ip, J. Kahn, Feedforward carrier recovery for coherent optical communications. *J. Lightwave Technol.* **25**(9), 2675–2692 (2007)
120. C. Laperle, A. Savchenko, C. Li, G. Mak, M. O'Sullivan, 5120 km RZ-DPSK transmission over G.652 fiber at 10 Gb/s with no optical dispersion compensation, in *Opt. Fiber Commun. Conf. and Nat. Fiber Opt. Eng. Conf.* (OFC/NFOEC'05), Anaheim, CA, USA (2005), Techn. Digest, paper PDP27
121. T. Kupfer, C. Schulien, Maximum likelihood sequence estimation at 10 Gb/s, from concept to implementation, in *18th Ann. Meeting IEEE Lasers & Electro-Optics Soc.* (LEOS'05), Sydney, Australia (2005), Techn. Digest, paper THU4
122. W. Kester, *Analog-Digital Conversion, Analog Devices* (2004), Chap. 2. Also available as *The Data Conversion Handbook* (Elsevier/Newnes, 2005), ISBN 0-7506-7841-0. Online: www.analog.com/library/analogDialogue/archives/39-06/data_conversion_handbook.html
123. W. Kester, *Analog-Digital Conversion, Analog Devices* (2004), Chap. 3. Also available as *The Data Conversion Handbook* (Elsevier/Newnes, 2005), ISBN 0-7506-7841-0. Online: www.analog.com/library/analogDialogue/archives/39-06/data_conversion_handbook.html
124. Standard for terminology and test methods for analog-to-digital converters, IEEE Std 1241-2000, 2001
125. R.H. Walden, Performance trends for analog-to-digital converters. *IEEE Commun. Mag.* **37**(2), 96–101 (1999)
126. W. Kester, Aperture time, aperture jitter, aperture delay time – removing the confusion, *Analog Devices*, Tutorial MT-07 (2009), online: www.analog.com/static/imported-files/tutorials/MT-007.pdf
127. Y. Achiam, A.M. Kaplan, M. Seimetz, Systems with higher order modulation, in *Fibre Optic Communication*, ed. by H. Venghaus, N. Grote (Springer, Berlin, 2012), Chap. 8
128. H.T. Quynhanh, A. Suzuki, M. Yoshida, T. Hirooka, M. Nakazawa, A $\lambda/4$ -shifted distributed-feedback laser diode with a fiber ring cavity configuration having an OSNR of 85 dB and a linewidth of 7 kHz. *J. Lightwave Technol.* **20**(18), 1578–1580 (2008)
129. P. Dong, C. Xie, L. Chen, L.L. Buhl, Y.-K. Chen, 112-Gb/s monolithic PDM-QPSK modulator in silicon. *Opt. Express* **20**(26), 624–629 (2012)
130. C. Doerr, L. Chen, D. Vermeulen, T. Nielsen, S. Azemati, S. Stulz, G. McBrien, X.-M. Xu, B. Mikkelsen, M. Givchchi, C. Rasmussen, S.-Y. Park, Single-chip silicon photonics

- 100-Gb/s coherent transceiver, in *Opt. Fiber Commun. Conf. (OFC'14)*, San Francisco, CA, USA (2014), Techn. Digest, paper Th5C.1
131. Fujitsu introduces World's first DP-QPSK LN modulator for 100 Gbps optical networks (Sept. 2009), www.fujitsu.com/jp/group/foc/en/resources/news/press-releases/2009/0914.html
 132. S. Corzine, P. Evans, M. Kato, G. He, M. Fisher, M. Raburn, A. Dentai, I. Lyubomirsky, A. Nilsson, J. Rahn, R. Nagarajan, C. Tsai, J. Stewart, D. Christini, M. Missey, V. Lal, H. Dinh, A. Chen, J. Thomson, W. Williams, P. Chavarkar, S. Nguyen, D. Lambert, S. Agashe, J. Rossi, P. Liu, J. Webjorn, T. Butrie, M. Reffle, R. Schneider, M. Ziari, C. Joyner, S. Grubb, F. Kish, D. Welch, 10-Channel \times 40 Gb/s per channel DQPSK monolithically integrated InP-based transmitter PIC, in *Opt. Fiber Commun. Conf. and Nat. Fiber Opt. Eng. Conf. (OFC/NFOEC'08)*, San Diego, CA, USA (2008), Techn. Digest, paper PDP18
 133. P. Schvan, A 22 GS/s 5-b ADC in 0.13 μ m SiGe BiCMOS, in *Proc. IEEE Internat. Solid-State Circ. Conf. (ISSCC'06)*, San Francisco, CA, USA (2006), pp. 572–573
 134. P. Schvan, D. Pollex, T. Bellingrath, A 22 GS/s 6b DAC with integrated digital ramp generator, in *Proc. IEEE Internat. Solid-State Circ. Conf. (ISSCC'05)*, San Francisco, CA, USA (2005), pp. 122–123
 135. M. Nagatani, H. Nosaka, S. Yamanaka, K. Sano, K. Murata, A 32-GS/s 6-bit double-sampling DAC in InP HBT technology, in *Proc. IEEE Compound Semicond. Integr. Circuits Symp.*, Greensboro, NC, USA (2009), [10.1109/csics.2009.5315628](https://doi.org/10.1109/csics.2009.5315628)
 136. S. Halder, H. Gustat, C. Scheytt, A. Thiede, A 20 GS/s 8-bit current steering DAC in 0.25 μ m SiGe BiCMOS technology, in *Proc. Eur. Microw. Integr. Circuits Conf.*, Amsterdam, The Netherlands (2008), pp. 147–150
 137. T. Ellermeyer, R. Schmid, A. Bielik, J. Rupeter, M. Möller, DA and AD converters in SiGe technology: speed and resolution for ultra high data rate applications, in *Proc. 36th Europ. Conf. Opt. Commun. (ECOC'10)*, Torino, Italy (2010), paper Th.10.A.6
 138. Y.M. Greshishchev, D. Pollex, S.-C. Wang, M. Besson, P. Flemeke, S. Szilagy, J. Aguirre, C. Falt, N. Ben-Hamida, R. Gibbins, P. Schvan, A 56 GS/s 6b DAC in 65 nm CMOS with $256 \times 6b$ memory, in *Int. Solid-State Circ. Conf. (ISSCC'11)*, San Francisco, CA, USA (2011), pp. 194–196, Techn. Digest
 139. M. Nagatani, H. Nosaka, K. Sano, K. Murata, K. Kurishima, M. Ida, A 60-GS/s 6-bit DAC in 0.5 μ m InP HBT technology for optical communication systems, in *Proc. Comp. Semicond. Integr. Circ. Symp. (CSICS'11)*, Waikoloa, HI, USA (2011), Techn. Digest, paper G.3
 140. Fujitsu. Digital to analog converter. (Mar. 2012). [Online]. Available: www.fujitsu.com/downloads/MICRO/fme/documentation/c60.pdf
 141. Tektronix. Tektronix announces world's fastest 10-bit commercial DAC. (Mar. 2013) <http://component-solutions.tek.com/news-library/Tektronix%20Component%20Solutions%20Announces%20Worlds%20Fastest%2010-bit%20Commercial%20DAC%20-%2020031813.pdf>
 142. K. Poulton, R. Neff, B. Setterberg, B. Wuppermann, T. Kopley, R. Jewett, J. Pernillo, C. Tan, A. Montijo, A 20 GS/s 8b ADC with a 1 MB memory in 0.18 μ m CMOS, in *Proc. Int. Solid-State Circuits Conf. (ISSCC'03)*, San Francisco, CA, USA (2003), pp. 318–319
 143. P. Schvan, D. Pollex, S.-C. Wang, C. Falt, N. Ben-Hamida, A 22 GS/s 5b ADC in 0.13 μ m SiGe BiCMOS, in *Proc. IEEE Internat. Solid-State Circ. Conf. (ISSCC'06)*, San Francisco, CA, USA (2006), pp. 572–573
 144. J. Lee, J. Weiner, P. Roux, A. Leven, Y.-K. Chen, A 24 GS/s 5-b ADC with closed-loop THA in 0.18 μ m SiGe BiCMOS, in *Proc. IEEE Custom Integr. Circ. Conf. (CICC'08)*, San Jose, CA, USA (2008), pp. 313–316
 145. P. Schvan, J. Bach, C. Falt, P. Flemke, R. Gibbins, Y. Greshishchev, N. Ben-Hamida, D. Pollex, J. Sitch, S.-C. Wang, J. Wolczanski, A 24 GS/s 6b ADC in 90 nm CMOS, in *Proc. IEEE Internat. Solid-State Circ. Conf. (ISSCC'08)*, San Francisco, CA, USA (2008), pp. 544–545
 146. I. Dedic, 56 GS/s ADC: enabling 100GbE, in *Opt. Fiber Commun. Conf. and Nat. Fiber Opt. Eng. Conf. (OFC/NFOEC'10)*, San Diego, CA, USA (2010), Techn. Digest, paper OThT6

147. Fujitsu, Factsheet LUKE-ES55 – 65 GSa/s 8 bit ADC. Online: www.fujitsu.com/downloads/MICRO/fme/documentation/c63.pdf
148. Fujitsu, ROTTA 37-92 GSa/s 8-bit ADC family. Online: www.fujitsu.com/cn/en/products/devices/semiconductor/fsp/asic/asic/ipmacro/networkingips/

Wilfried Idler received the Diploma degree in Physics from University of Stuttgart in 1987. Between 1987 and 1996 he was at the Alcatel O/E components research division in Stuttgart, engaged in design and characterization of high speed DFB lasers, tunable lasers and wavelength converter structures and was involved in DFB laser technology transfers to Alcatel Optronics in France. Since 1996 he is with the Optical Networks Division of Alcatel and Alcatel-Lucent Bell Labs in Stuttgart. He was contributing to the world-wide first 40 Gb/s field trials and to various $N \times 40$ Gb/s multi-Terabit transmission experiments and the related postdeadline papers at OFC and ECOC. Subsequently he was engaged at the 40 Gb/s and the 100 Gb/s product development of Alcatel-Lucent. His current research interest are coherent few carrier 1 Tb/s systems. Following his long standing experience on optical transmission systems, optical components and subsystems he was representing Alcatel-Lucent at the ITU-T study group 15 for a 10 years period. As expert on modulation formats and he was program committee member of OFC and regularly serves as referee for various journals. He published more than 100 journal and conference papers and holds numerous patent applications.

Fred Buchali received the diploma degree in electrical engineering in 1988 and the Ph.D. degree in 1991 from Humboldt-University Berlin. During his Ph.D. he worked on InGaAs/InP p–i–n photodiodes for fiber-optic communication. In 1991 he joined Duisburg University where he was involved in the research on InAlAs/InGaAs HFET and MSM-detectors. 1992 Fred Buchali joined Alcatel-Lucent Germany, where he was part of the optoelectronics components research department. There he worked on optimized pin photodiode processes for 10 Gb/s application. In 1999 he joined the optical transmission systems group, where he started research on optical and electrical impairment mitigation techniques at 10 and 40 Gb/s by analog electrical and optical techniques. During emerging coherent transmission technology he substantially contributed to the discovery of OFDM in optics. His current research interests cover coherent few carrier systems for 1 Tb/s and beyond using higher order modulation formats including the transmission aspects of the optical fiber and the digital signal processing. Fred Buchali was member of the OFC technical program committee and contributed continuously as reviewer for various journals. He published more than 100 journal and conference papers and holds more than 30 patent applications.

Chapter 8

Semiconductor-Based Modulators

Hiroshi Yasaka and Yasuo Shibata

Abstract The chapter starts with a comparison of methods to generate digital optical signals: direct laser modulation, electroabsorption and Mach-Zehnder interferometer modulators. Next follows an in-depth treatment of physical effects which are utilized for semiconductor-based modulators (plasma-, Franz-Keldysh-, quantum-confined Stark-, and electro-optic (Pockels) effect), and their exploitation for InP- and GaAs-based modulators with specific emphasis on aspects of high-speed modulator design. Modulator characteristics including eye diagrams obtained for different implementations and various operation conditions illustrate the current state-of-the-art, and the chapter concludes with a section on modulators for higher order modulation formats.

Semiconductor-based modulators are particularly promising for applications in fiber optic communication systems owing to various characteristics which include compactness, low power consumption, and the potential for monolithic integration with other devices.

Key features of semiconductor-based modulators and typical performance parameters will be the topic of this chapter, and it is organized as follows: First, general methods for digital optical signal generation by using semiconductor photonic devices and their features are described (Sect. 8.1). In Sect. 8.2, fundamentals and features of semiconductor-based Mach-Zehnder interferometer (MZI) modulators are elucidated. The way for designing a high-speed semiconductor MZI modulator is discussed in Sect. 8.3. Properties of current semiconductor-based MZI modulators and high performance modulators for future optical fiber transmission systems are shown in Sects. 8.4 and 8.5, and a general summary is given in the final Sect. 8.6.

H. Yasaka (✉)

Research Institute of Electrical Communication, Tohoku University, 2-1-1 Katahira, Aoba-ku, Sendai-shi, Miyagi Pref., 980-8577, Japan
e-mail: yasaka@riec.tohoku.ac.jp

Y. Shibata

NTT Electronics Corporation, 3-1 Wakamiya, Morinosato, Atsugi-shi, Kanagawa Pref., 243-0198, Japan
e-mail: shibata-yasuo@ntt-el.com

8.1 Overview of the Methods to Generate a Digital Optical Signal

The generation of high-speed intensity modulated digital optical signals is one of the key functions in fiber optic communication systems. Digital optical signals can either be generated by directly modulating single-mode semiconductor lasers, or by using external intensity modulators, and the characteristics of such signals after transmission through spans of single mode optical fibers (SMFs) significantly depend on the way the digital optical signals had been generated. This will be discussed in more detail below.

The transmission distance of digital optical signals through an SMF is limited by the group velocity (chromatic) dispersion of the SMF and the amount of spectral broadening (spectral width) of the digital optical signal. In principle, the optical spectrum is broadened when the optical intensity is coded by a high-speed digital signal. The spectrum is additionally broadened by the instantaneous frequency change of the signal light, a phenomenon normally designated as “chirp”. The amount of chirp is expressed by using a chirp parameter α_{cp} , and the parameter is defined by [1]

$$\alpha_{cp} = \Delta n / \Delta n', \quad (8.1)$$

where Δn and $\Delta n'$ are the relative changes in the real part and the imaginary part of the complex refractive index, respectively. The imaginary part of the complex refractive index n' is related to the propagation loss or gain of the material. In this chapter, the character n with no subscript or superscript is used as the real part of the complex refractive index and also the term “refractive index” expresses the real part of the complex refractive index in all cases unless otherwise stated. In an external modulation scheme, an instantaneous frequency change due to a phase change is obtained by using a time differential of the phase:

$$\Delta\omega = -\partial\phi/\partial t, \quad (8.2)$$

where ω and ϕ are the angular frequency and the phase of the light, respectively. The phase change is derived by using α_{cp} according to [2]

$$\frac{d\phi}{dt} = \left(\frac{\alpha_{cp}}{2}\right) \left(\frac{1}{S}\right) \left(\frac{dS}{dt}\right), \quad (8.3)$$

where S is the intensity of the light. The chirp parameter varies over a certain range depending on the modulation methods used for the digital optical signal generation.

The waveform after SMF transmission can be calculated by using a split step Fourier method (SSFM) [3]. Using this technique, the Fourier component having an instantaneous angular frequency ω at the position z , $U(z, \omega)$, is expressed by using the chromatic dispersion coefficient D of the SMF:

$$U(z, \omega) = U(0, \omega) \times \exp\left(-j \frac{\lambda^2}{4\pi \cdot c} D \omega^2 z\right), \quad (8.4)$$

where λ and c are the signal light wavelength and the velocity of light, respectively. The chromatic dispersion coefficient of conventional SMFs takes a value around 17 ps/(nm km) at 1550 nm wavelength.

In the following, we will focus on three ways to generate high-speed digital optical signals: (i) direct modulation of semiconductor lasers, (ii) external modulation with electroabsorption modulators and (iii) external modulation using Mach-Zehnder modulators. We will illustrate characteristics such as waveform, chirp, etc., but we will also discuss features related to SMF transmission such as waveform distortions, eye opening penalties, dispersion tolerances and so forth.

8.1.1 Direct Modulation of Semiconductor Lasers

In directly modulated single-mode semiconductor lasers, the mode of chirping is slightly different from that in external modulation schemes expressed by (8.2). The lasing wavelength (i.e., the lasing optical frequency) itself changes when the output light intensity is directly modulated with high-speed digital signals superimposed on the injection current. The wavelength change is due to the fact that the carrier density in the laser cavity changes dynamically, and as a consequence, the refractive index in the laser cavity also changes through the plasma effect (see Sect. 8.2.1.1). The chirp parameter α_{cp} for a semiconductor laser is defined as

$$\alpha_{cp} \equiv \frac{4\pi}{\lambda} \times \frac{dn/dN}{dg/dN}, \quad (8.5)$$

where n , g , and N are the real part of the refractive index of the laser cavity, the modal gain of the laser, and the carrier density in the laser cavity, respectively. The parameter α_{cp} is well-known as the linewidth enhancement factor for semiconductor lasers (see also Chap. 4, Sect. 4.2.3), and it typically takes values around 3 to 5 for conventional single-mode semiconductor lasers. The optical frequency change $\Delta\nu$ due to a carrier density change ΔN can be expressed by using the chirp parameter:

$$\Delta\nu = \frac{c}{4\pi \cdot n} \times \alpha_{cp} \times \Gamma_{oc} \times A_g \times \Delta N, \quad (8.6)$$

where Γ_{oc} and A_g are the optical confinement factor of the laser cavity and the differential gain coefficient of the laser material, respectively. ΔN can be derived by using the well-known semiconductor laser rate equations for the carrier density and the photon density of the laser under the condition that the injection current is modulated by a high-speed digital signal.

Figure 8.1 shows the calculated waveforms for injected and generated pulses with 100 ps width, which corresponds to one bit of a 10 Gbit/s non-return-to-zero (NRZ) signal. Figure 8.1(a) represents the pulse shape of the input electrical signal with limited bandwidth of some tens of GHz. Figure 8.1(b) illustrates the corresponding optical output signal from the laser. The waveform is distorted due to the

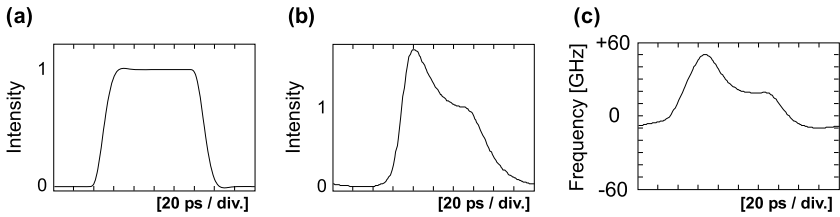


Fig. 8.1 Calculated output waveforms for a directly modulated semiconductor laser. (a) Input electrical signal with pulse width of 100 ps, (b) output waveform from the laser, (c) optical frequency change of the laser under modulation

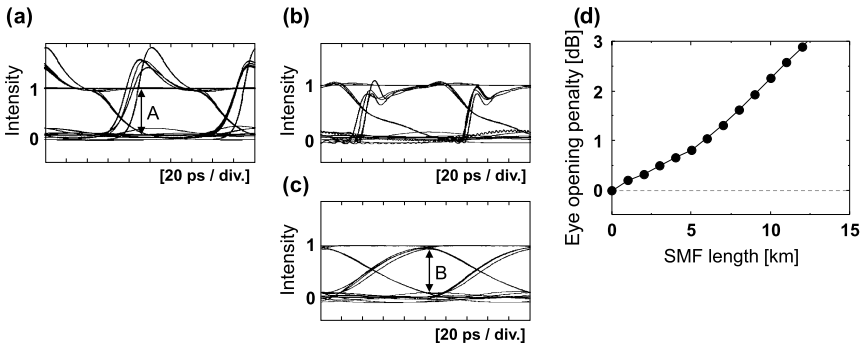
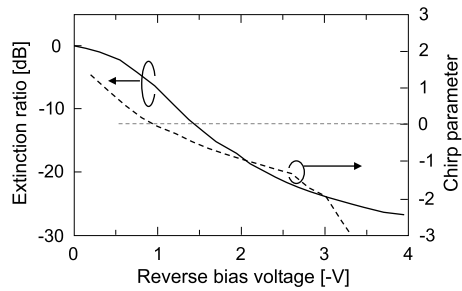


Fig. 8.2 Calculated characteristics of semiconductor laser output under 10 Gbit/s NRZ signal operation. (a) Output eye diagram from the laser under direct modulation, (b, c) eye diagrams after 6 km SMF transmission for 1550 nm wavelength (total dispersion ~ 100 ps/nm) without and with low-pass filter, (d) calculated eye opening penalty as a function of SMF transmission length

well-known relaxation oscillations. Finally, Fig. 8.1(c) shows the optical frequency change. In the calculation, a value of three has been used for the chirp parameter. The changes of the optical frequency and that of the optical intensity are correlated by the dynamic carrier density change in the laser cavity. Based on these results, eye diagrams before and after SMF transmission are calculated for a 10 Gbit/s NRZ signal using the semiconductor laser rate equations and the SSFM.

Figure 8.2(a) represents an eye diagram for the laser output under modulation where relaxation oscillations and pattern effects are clearly visible. Figures 8.2(b), (c) are the eye diagrams after 6 km SMF transmission for a 1550 nm wavelength signal without and with a low-pass filter (4th order Bessel-Thomson low-pass filter with cut-off frequency f_0 of 7.5 GHz). The total amount of fiber chromatic dispersion is around 100 ps/nm. A pronounced waveform distortion is observed even after a fairly short SMF transmission distance such as 6 km. Figure 8.2(d) is the calculated eye opening penalty as a function of SMF length. The chromatic dispersion coefficient is approximated to be 17 ps/(nm km). The eye opening penalty, which is used to

Fig. 8.3 Extinction ratio (solid line) and chirp parameter (dotted line) of an EAM as a function of applied reverse bias



quantitatively discuss the waveform distortion, is calculated by using

$$\text{Eye opening penalty} = -10 \times \log_{10} \left(\frac{B}{A} \right), \quad (8.7)$$

where A and B are the eye openings of the eye diagrams before (actually, for the filtered eye diagram) and after SMF transmission as shown in Figs. 8.2(a), (c). The penalty increases drastically as the SMF transmission distance gets longer, while the penalty remains below 1 dB only as long as the SMF transmission distance is shorter than 6 km. This means that a 10 Gbit/s NRZ optical signal generated from a directly modulated single-mode semiconductor laser has a dispersion tolerance of about 100 ps/nm only. As a consequence, directly modulated single-mode semiconductor lasers are mainly used in systems that operate in the 1300 nm wavelength band where the chromatic dispersion of an SMF is almost zero.

8.1.2 Electroabsorption Modulators (EAMs)

Electroabsorption modulators (EAMs) utilize the property of semiconductors that the band-edge wavelength changes under the influence of an applied electric field. The phenomenon is called Franz-Keldysh effect in the case of bulk material [4, 5] and the quantum-confined Stark effect (QCSE) for multi-quantum well (MQW) structured materials [6–13]. Until now, the latter one is commonly used for EAMs because the change in the photoabsorption coefficient is steeper for the QCSE compared to the Franz-Keldysh effect, and large optical extinction ratios can be obtained in MQW-EAMs with low bias voltages. Because the EAMs are operated at the band-edge wavelengths, they have large wavelength dependences. Moreover, EAMs also exhibit chirp caused by the refractive index change due to the applied bias voltage. The changes of the refractive index and that of the absorption under the influence of the applied voltage are related to each other by the Kramers-Kronig relations [14, 15]. Figure 8.3 shows an example of the measured extinction of an MQW-EAM as a function of reverse bias voltage.

The absorption rises rapidly as the reverse bias voltage increases. The chirp parameter measured by utilizing the fiber response method [16, 17] is also shown in

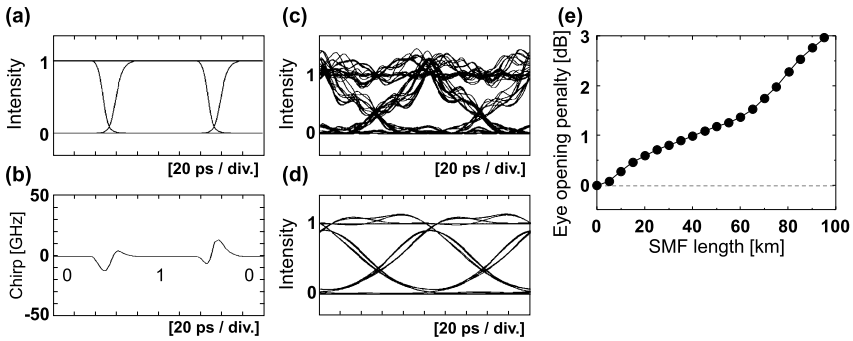


Fig. 8.4 Calculated characteristics of EAM output under 10 Gbit/s NRZ signal operation. (a) Output eye diagram from the EAM, (b) calculated chirp for fixed 010 pattern, (c, d) eye diagrams after 50 km SMF transmission without and with low-pass filter, (e) calculated eye opening penalty as a function of SMF transmission length

the figure. The chirp parameter decreases gradually as the reverse bias voltage increases, and it takes negative values when the reverse bias voltage exceeds 1 V.

The waveforms for a 10 Gbit/s NRZ signal are calculated by using the characteristics shown in Fig. 8.3, and corresponding results are illustrated in Fig. 8.4. In this calculation, the DC bias and modulation voltages are set to -1.3 V and $2V_{p-p}$, respectively. The operation wavelength is assumed to be 1550 nm and therefore the chromatic dispersion coefficient is set to 17 ps/(nm km). Figure 8.4(a) shows the intensity modulated output eye diagram from the EAM. Due to the nonlinear extinction characteristic, the cross-point of the eye diagram becomes low which is one of the drawbacks of EAMs. The instantaneous frequency chirp for a fixed 010 pattern is also calculated and the result is shown in Fig. 8.4(b). Pronounced chirp due to the phase change in the EAM can be observed at the leading and falling edges of the pattern. Figures 8.4(c), (d) are the eye diagrams after 50 km SMF transmission without and with a low-pass filter, respectively. The total amount of fiber dispersion is calculated to be 850 ps/nm. Waveform distortion due to chromatic dispersion is observed, but the eye is still open. Figure 8.4(e) is the calculated eye opening penalty as a function of propagation distance along the SMF. As expected, the penalty rises as the SMF transmission distance gets longer. Less than 1 dB penalty can be obtained as long as the SMF transmission distance is shorter than 40 km. This means that a 10 Gbit/s NRZ optical signal generated by an EAM has around 800 ps/nm dispersion tolerance. Research has been devoted to increase the dispersion tolerance. Recently, EAMs having a dispersion tolerance of around 1600 ps/nm have been developed for 10 Gbit/s NRZ optical signals [18–20]. Here, the amount of stress or strain and the thicknesses of the well and barrier layers in the EAM core are designed strictly to make the chirp parameters to have negative values. Moreover, core layers are also fabricated in the InGaAlAs material system in order to enlarge the dispersion tolerance and improve the temperature-dependent characteristics. A DFB laser monolithically integrated with a traveling-wave EAM

has recently been operated even at 100 Gbit/s, however, no information on chirp nor on maximum transmission distances has been given so far [21].

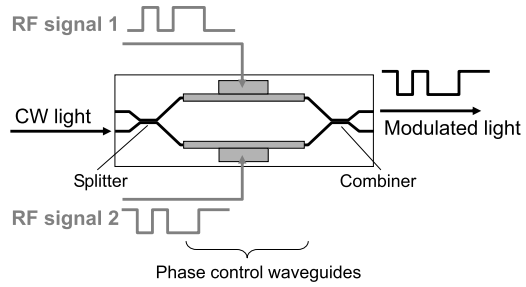
Research on raising the operation speed of lumped electrode EAMs integrated with DFB lasers has been performed and 56 Gbit/s operation at 1305 nm has been demonstrated [22]. In this integrated light source an identical InGaAlAs MQW core in the DFB laser and the EAM section was introduced, and a 50- Ω matching circuit was fabricated on the chip simultaneously which contributed to an enhancement of the 3 dB bandwidth of the EAM to 39.4 GHz. The EAM integrated light source emitted a fiber coupled output power of +5 dBm at an operation temperature of 45 °C. Four channel arrays of EAMs with integrated DFB lasers have also been realized which offer the potential to be used in small size transponders for future 100G Ethernet systems [23–25]. The EAMs operated at a bit rate higher than 25 Gbit/s, and the total capacity of the light sources was more than 100 Gbit/s which is sufficient for 100G Ethernet systems.

Transmitters in PONs should enable long reach (up to \sim 100 km), high bit rate operation and low power consumption, and reaching these targets by tailoring the chirp is one focus of current EAM development [26, 27]. Low (or negative) chirp is favorable in this respect, and such chirp values can be achieved by raising the bias voltage applied to the EAM as illustrated in Fig. 8.3. However, as already mentioned, the absorption increases under these conditions, and one possibility to compensate for the reduced output power is to monolithically integrate a semiconductor optical amplifier (SOA) to the EAM [26]. A negative chirp of -1.4 provided a net power gain after fiber transmission and also extended the available modulation bandwidth (\sim 6.7 GHz after 100 km reach). As a result, a 23 Gbit/s OFDM signal with 6-GHz bandwidth and fixed 16-QAM format reached the FEC limit in the range of 60 \sim 100-km fiber transmission without any need of adaptive bit- and power-loading.

In an alternative approach the chirp of an EAM was canceled by a short cavity SOA monolithically integrated with the EAM and a DFB laser [27]. The carrier density of a saturated SOA changes when the power of the incoming light power varies, and therefore the refractive index of the SOA also changes. This index change gives rise to a chirp of the optical signal, which is opposite in sign to the chirp induced by the EAM. As a consequence the total chirp at the output of the integrated device is significantly reduced [28]. In addition, the integrated SOA-EA-DFB laser device has been designed in such a way that its total power consumption was lower than that of a comparable stand-alone EAM integrated with a laser, and it was successfully used for transmitting a 40 Gbit/s signal over 5 km SMF.

Single side band (SSB) optical signal generation was also demonstrated by using an EAM integrated with a DFB laser [29]. In this trial, the EAM was used as an intensity modulator while the DFB laser was used for phase modulation by direct injection current modulation. 11.11 Gbit/s SSB optical signal generation has been demonstrated, and successful transmission over 200 km SMF has also been achieved.

Fig. 8.5 Schematic structure of an MZI modulator



8.1.3 Mach-Zehnder Interferometer (MZI) Modulators

Mach-Zehnder interferometer (MZI) modulators are very versatile devices which can be used for many purposes, for example, high-speed modulation or the realization of advanced modulation formats (see also Chap. 7, Sect. 7.3), and they have been fabricated in various material systems including III–V semiconductors (to be covered in more detail below), in LiNbO_3 and based upon electro-optic polymers as well [30, 31].

The generic structure of an MZI modulator is that of a symmetric Mach-Zehnder interferometer as schematically shown in Fig. 8.5.

The electric field of an incoming CW light, E_{in} , can be represented by

$$E_{in}(z, t) = E_0 \exp[-j(\beta z - \omega t)] \quad (8.8)$$

with the propagation constant β defined by

$$\beta = \frac{2\pi n_{eff}}{\lambda}, \quad (8.9)$$

and n_{eff} and λ being the effective refractive index of the medium in which the wave propagates (dielectric waveguide for example) and the propagating light's wavelength in vacuum, respectively. Light is assumed to propagate along the z -direction. The incoming electromagnetic field is equally split into both interferometer arms by a splitter. After traveling along the two branches, it is recombined by a combiner and the output electromagnetic field E_{out} at the cross-port output is given by

$$E_{out}(z, t) = -j \frac{E_0}{2} [\exp(-j\beta_u L) + \exp(-j\beta_l L)], \quad (8.10)$$

where β_u and β_l are the propagation constants along the upper and lower MZI branches, respectively. (The factor $(-j)$ reflects the fact that the output signal from the cross-port is advanced by 90° with respect to the through-port signal.)

For the following considerations, it is useful to rewrite the propagation constants as

$$\beta_{u,l} = \beta + \Delta\beta_{u,l}, \quad (8.11)$$

where $\Delta\beta_{u,l}$ may be positive or negative as well (see below). According to (8.9), $\Delta\beta_{u,l}$ can be directly related to a change in the effective refractive index, Δn_{eff} , and as outlined in detail in Sect. 8.2, different physical effects can be used to induce effective refractive index changes Δn_{eff} by a voltage V_{RF} applied to the waveguide arms of the MZI.

Intensity-modulated optical signals are generated by modulating the refractive indices of the two interferometer branches differently, i.e.,

$$\Delta\beta_u \neq \Delta\beta_l, \quad (8.12)$$

which results in a corresponding phase difference between the two light waves interfering at the MZI output. The interferometer branches can thus be designated as phase control waveguides and modulation is normally realized by applying a radio frequency (RF) signal to one or both phase control waveguides of the MZI modulator.

The following cases are of particular interest:

(i) A modulation voltage is applied to one of the MZI arms only (“single arm operation”):

$$\beta_u = \beta + \Delta\beta \quad \text{and} \quad \beta_l = \beta \quad (8.13)$$

and under these operation conditions, the output electric field becomes

$$E_{out} = -j E_0 \cos\left(\frac{\Delta\beta L}{2}\right) \times \exp\left[-j\left(\beta + \frac{\Delta\beta}{2}\right)L\right]. \quad (8.14)$$

E_{out} is characterized by a sinusoidal intensity variation plus an additional $\Delta\beta$ -induced phase change (given by the second term in (8.14)), i.e., the output signal exhibits chirp.

(ii) A voltage of equal amplitude but different sign (designated as the “push-pull operation”) is applied to the two MZI arms, i.e.,

$$\Delta\beta_u = +\frac{1}{2}\Delta\beta \quad \text{and} \quad \Delta\beta_l = -\frac{1}{2}\Delta\beta. \quad (8.15)$$

Inserting (8.15) into (8.10) and taking (8.11) into account yields

$$E_{out}(z, t) = -j E_0 \cos\left(\frac{\Delta\beta L}{2}\right) \times \exp(-j\beta L). \quad (8.16)$$

This operation mode is characterized by a $\Delta\beta$ -dependent sinusoidal variation of the output signal without any modulation-induced chirp. In addition, it is worthwhile to note that the required propagation constant change $\Delta\beta/2$ (which is proportional to the driving voltage swing for each differential RF signal) in the differential drive scheme is half of that needed in the single arm operation scheme, $\Delta\beta$.

Figure 8.6 illustrates the output intensity of an MZI modulator which changes sinusoidally as a function of applied bias voltage (black solid curve).

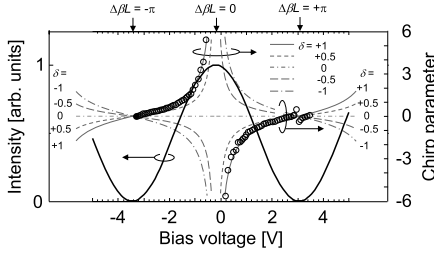


Fig. 8.6 Output intensity dependence of an MZI modulator as a function of bias voltage applied to phase control waveguide (*black solid curve*). Chirp parameter measured (*black open circles*) and calculated for a differential drive MZI modulator (*grey lines*) for various values of δ (see text)

One parameter which characterizes MZI modulators is the so-called half-wavelength voltage V_π , which corresponds to an applied voltage resulting in a π -phase difference between the lightwaves in both phase modulation waveguides. Hence the half-wavelength voltage V_π is defined by the voltage needed to change the output power of MZI modulators from the maximum to the minimum value. In Fig. 8.6, the half-wavelength voltage V_π is ~ 3 V.

The measured chirp parameter under the single arm operation conditions, shown by the black open circles in Fig. 8.6, depends on the bias voltage. The chirp vanishes when the output intensity becomes zero and it diverges when the output intensity gets close to the maximum value. The sign of the chirp parameter depends on the sign of the extinction slope, $d(\text{Intensity})/dV$. When the slope is positive, the chirp parameter takes positive values, and the parameter becomes negative when the slope is negative.

Another specific advantage of the differential drive scheme for an MZI modulator is that the chirp of the output optical signal can be freely controlled by adjusting the ratio of the modulation voltages of the differential RF signals. The chirp under unbalanced differential drive conditions can be discussed by introducing an unbalance parameter δ into (8.11) as

$$\beta_u = \beta + (1 + \delta) \times \Delta\beta/2, \quad (8.17)$$

$$\beta_l = \beta - (1 - \delta) \times \Delta\beta/2 \quad (8.18)$$

with $-1 \leq \delta \leq +1$. The single arm (i) and balanced differential drive (ii) operation conditions discussed above are described by setting the parameter δ to $+1$ and to zero, respectively. By inserting (8.17) and (8.18) into (8.10), we get

$$E_{out} = -jE_0 \cos(\Delta\beta L/2) \times \exp(-j(\beta + \delta \times \Delta\beta/2)L). \quad (8.19)$$

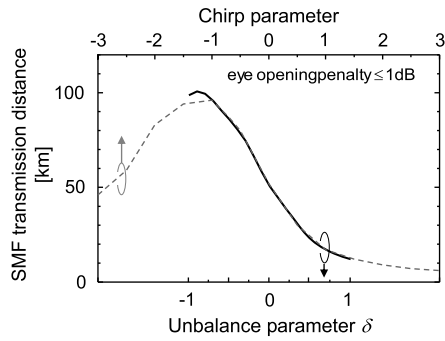
The output intensity S_{out} and its phase change $\Delta\phi$ can now be expressed by

$$S_{out} = E_0^2 \cos^2(\Delta\beta L/2) \quad (8.20)$$

with

$$\Delta\phi = (\Delta\beta L/2) \times \delta. \quad (8.21)$$

Fig. 8.7 Calculated maximum SMF transmission distance for eye opening penalty of < 1 dB as a function of an MZI modulator’s unbalance parameter δ (black solid curve) and modulated optical signal’s chirp parameter (grey dotted curve)



It is worthwhile to note that the output intensity does not depend on the unbalance parameter δ and remains constant if the parameter δ is changed, while the phase varies linearly with δ . The chirp parameter for the MZI modulator defined by (8.3) can be derived by using (8.20) and (8.21) as

$$\alpha_{cp} = 2S \frac{\Delta\phi}{\Delta S} = -\frac{2 \cos^2(\Delta\beta L/2)}{\sin(\Delta\beta L)} \times \delta = -\tan^{-1}(\Delta\beta L/2) \times \delta. \quad (8.22)$$

The calculated chirp parameters for various values of δ are shown in Fig. 8.6 as grey curves. The horizontal axis of the calculated chirp parameter is adjusted by fitting the measured and calculated output intensity curves. The calculated chirp parameter for $\delta = +1$ agrees quite well with the measured one displayed by black open circles. As one can see, that the chirp parameter and hence the amount of phase change can be controlled by an appropriate choice of the unbalance parameter δ and hence by adjusting the ratio of the modulation swing voltages of the differential RF signals. However, the chirp parameter depends on the bias voltage as well ($\Delta\beta \sim V_{RF}$), and hence, in a complicated way, on the output intensity of the MZI modulator. Chirpless operation ($\alpha_{cp} = 0$) can be obtained by setting the parameter δ to zero as shown by the dash-dotted line in the figure and also indicated by (8.21).

Calculated SMF transmission characteristics of 10 Gbit/s NRZ optical signals generated by an MZI modulator are illustrated in Figs. 8.7, 8.8 and 8.9. In this calculation, the operation wavelength is set to 1550 nm. The calculated maximum SMF transmission distance for an eye opening penalty of less than 1 dB is shown by the solid black curve in Fig. 8.7 as a function of the unbalance parameter δ .

The transmission distance increases (decreases) as the unbalance parameter decreases (increases) related to a corresponding change of the chirp parameter as shown in Fig. 8.6. Commonly, the SMF transmission characteristics of digital intensity modulated optical signals are discussed by using the approximation that the chirp parameter is constant when changing the optical intensities (see [2, 3]), which helps to clarify the SMF transmission characteristics easily and simply using the parameter α_{cp} and the simple relation between the phase change and the optical intensity change given in (8.3). When one adopts the constant chirp parameter approximation to the output from the MZI modulator, the slight distortion of the optical signal waveform in E/O conversion with an MZI modulator caused by the nonlinear

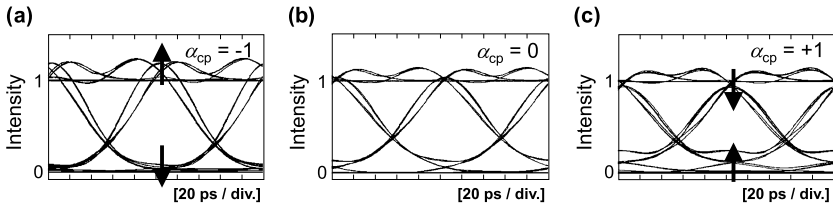


Fig. 8.8 Calculated eye diagrams after 50 km SMF transmission for various chirp parameter values, (a) $\alpha_{cp} = -1$, (b) $\alpha_{cp} = 0$, (c) $\alpha_{cp} = +1$

transfer function (8.16) and the complicated relation between the chirp parameter and the propagation constant change $\Delta\beta L$ (see (8.17) and (8.18)) are ignored. In order to find out the validity range of the constant chirp parameter approximation, the dependence of the transmission distance on the unbalance parameter δ is fitted by calculated results using the constant chirp parameter approximation. The calculated transmission distances for intensity modulated optical signals with constant chirp parameter are given in Fig. 8.7 by the grey dotted curve. The horizontal axes for these results are adjusted in order to get optimum agreement between the two calculated curves which turns out to be quite good. The change in the unbalance parameter δ from -1 to $+1$ is approximately equivalent to a change of the chirp parameter of the modulated optical signal from -1.4 to $+1.4$. It indicates that the SMF transmission characteristics of the MZI modulator's output can be discussed to a good approximation by using the intensity modulated signal with constant chirp parameter α_{cp} in the range from -1.4 to $+1.4$. To generalize the discussions below, the SMF transmission characteristics for the MZI modulator outputs are discussed by using the chirp parameter α_{cp} . Here, the chirp parameter is defined for the modulated optical signal and is assumed to be constant. One can see from the figure that a slightly negative value of the chirp parameter (around -1) enlarges the SMF transmission distance and raises the chromatic dispersion tolerance. Figure 8.8 shows the eye diagrams of modulated optical signals with various chirp parameter α_{cp} values after 50 km SMF transmission.

The eye opening is enhanced when $\alpha_{cp} = -1$ (Fig. 8.8(a)) compared to the case of $\alpha_{cp} = 0$ (Fig. 8.8(b)). On the other hand, it is reduced when $\alpha_{cp} = +1$, as shown in Fig. 8.8(c). In this case, strong intersymbol interference occurs, which determines the maximum SMF transmission distance. Figure 8.9 summarizes the characteristics of the MZI modulator output having a chirp parameter of -1 .

Figure 8.9(a) shows the intensity modulated output eye diagram from the MZI modulator. The instantaneous frequency chirp for a fixed 010 pattern is shown in Fig. 8.9(b). Clear chirp due to the phase change in the MZI modulator can be observed at the leading and falling edges of the pattern. Figures 8.9(c), (d) are the eye diagrams after 100 km SMF transmission without and with a low-pass filter, respectively. The total amount of the fiber dispersion is 1700 ps/nm. Waveform distortion due to chromatic dispersion is observed, but the eye is still open. Figure 8.9(e) is the calculated eye opening penalty as a function of SMF transmission length with a chromatic dispersion coefficient of 17 ps/(nm km). The results suggest that less than 1 dB penalty can be obtained as long as the SMF transmission distance is shorter

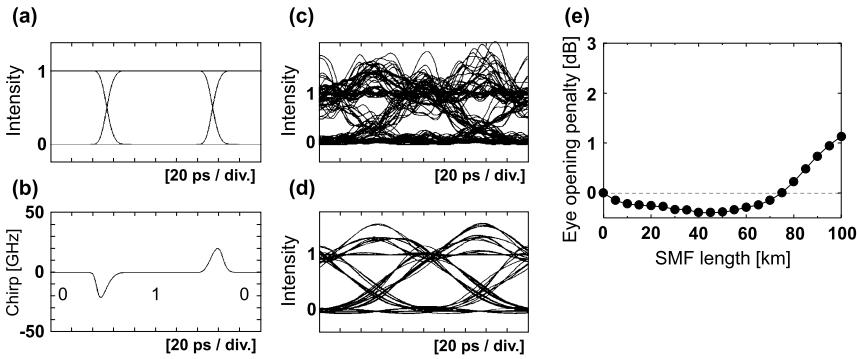


Fig. 8.9 Calculated characteristics of MZI modulator output with chirp parameter of -1 under 10 Gbit/s NRZ signal operation. (a) Output eye diagram from MZI modulator, (b) calculated chirp for fixed 010 pattern, (c, d) eye diagrams after 100 km SMF transmission without and with low-pass filter, (e) calculated eye opening penalty as a function of SMF transmission length

than 96 km, and this means that a 10 Gbit/s NRZ optical signal generated by an MZI modulator has a dispersion tolerance of more than 1600 ps/nm if the modulator is operated under proper driving conditions.

8.2 Semiconductor-Based MZI Modulators

Semiconductor-based MZI modulators offer various advantages including their small size, low driving voltage, and absence of DC drift problems. In addition, they have been investigated and developed in the GaAs- [32–44] and in the InP-material system as well [45–52]. In this section, fundamentals and relevant features of semiconductor MZI modulators are summarized. The refractive index control methods for semiconductor materials are explained in Sect. 8.2.1. In particular, the plasma (Sect. 8.2.1.1), Franz-Keldysh (Sect. 8.2.1.2), quantum-confined Stark (Sect. 8.2.1.3), and electro-optic (Sect. 8.2.1.4) effects are described. In Sect. 8.2.2, features of GaAs- and InP-based MZI modulators utilizing the effects mentioned above are described.

8.2.1 Fundamentals/Refractive Index Control of Semiconductor Materials

Intensity modulation with an MZI modulator is realized by varying the refractive indices of the two phase control waveguides in the MZI modulator. The refractive index of semiconductor materials can be changed in various ways: by injecting carriers through the plasma effect or by applying electric fields via the Franz-Keldysh, the quantum-confined Stark, or the electro-optic effect. The features of these effects are summarized below.

8.2.1.1 Plasma Effect

Free carriers in semiconductor materials change the refractive index of these materials. Following the Drude model, the refractive index n of a material can be expressed as

$$n \approx 1 - \frac{\omega_p^2}{2(\omega^2 + \Gamma_d^2)}, \quad (8.23)$$

$$\omega_p = \sqrt{\frac{N_d \times q^2}{\varepsilon_0 \times m}},$$

where, ω_p is the plasma angular frequency, and N_d , q , m , ε_0 , ω , Γ_d are density, charge, and mass of carrier, permittivity of free space, angular frequency of light, and damping constant, respectively. From the equations, one can see that the plasma frequency ω_p increases (decreases) when the carrier density N_d increases (decreases), so the refractive index of the material n decreases (increases). The change in the refractive index for semiconductor material is derived in [53, 54] and can be expressed as

$$\Delta n = -\frac{e^2 \cdot \lambda^2}{8\pi^2 c^2 \varepsilon_0 n} \times \left(\frac{N}{m_e} + \frac{P}{m_h} \right), \quad (8.24)$$

where e , λ , c , n , m_e , m_h , N and P are electron charge, incident light wavelength, velocity of light, refractive index, electron effective mass, hole effective mass, electron density, and hole density, respectively. The hole effective mass, m_h , in (8.24) includes contributions of heavy and light holes. But as the light hole mass is usually much smaller than the heavy hole mass, the hole effective mass is mainly determined by the heavy hole. A precise expression including heavy and light hole masses is given in (21) in [54]. According to (8.24), the refractive indices of semiconductors can be varied by changing the amount of free carriers by injection. However, the refractive index change is accompanied by a large increase in free carrier absorption. The absorption coefficient α_{fc} (in cm^{-1}), for example, has the following dependence on the electron (N in cm^{-3}) and hole (P in cm^{-3}) densities for GaAs material [55]:

$$\alpha_{fc} \approx 3 \times 10^{-18} \times N + 7 \times 10^{-18} \times P. \quad (8.25)$$

8.2.1.2 Franz-Keldysh Effect

When an electric field is applied to a bulk semiconductor, the band structure of the semiconductor is modified and the tails of the electron and hole wave functions penetrate into the forbidden band which is equivalent to a bandgap shrinkage (or a long-wavelength shift of the bandgap-equivalent wavelength) [4, 5]. The refractive

index change of the semiconductor material is related to a change in the corresponding absorption spectra, and the following relation between the complex refractive index $n_c(\omega)$, the real part of the complex refractive index $n(\omega)$ and the absorption coefficient $\alpha(\omega)$ holds

$$n_c(\omega) = n(\omega) + j \frac{c \times \alpha(\omega)}{2\omega}. \quad (8.26)$$

The change in the real part of the complex refractive index $\Delta n(\omega)$ can be derived by using the absorption coefficient change $\Delta\alpha(\omega)$, following the Kramers-Kronig relations [14, 15, 56]

$$\begin{aligned} \Delta n(\omega) &= \frac{2c}{e^2} \times P_v \int_0^\infty \frac{\Delta\alpha(\omega')}{\omega'^2 - \omega^2} d\omega' \\ &\equiv \frac{2c}{e^2} \lim_{\delta \rightarrow 0} \left(\int_0^{\omega-\delta} \frac{\Delta\alpha(\omega')}{\omega'^2 - \omega^2} d\omega' + \int_{\omega+\delta}^\infty \frac{\Delta\alpha(\omega')}{\omega'^2 - \omega^2} d\omega' \right), \end{aligned} \quad (8.27)$$

where P_v denotes taking the Cauchy principal value. Thus, (8.27) illustrates how the refractive index of a semiconductor can be changed by applying an electric field through the Franz-Keldysh effect. The Franz-Keldysh effect exhibits a pronounced wavelength dependence because it is a band-edge related phenomenon.

8.2.1.3 Quantum-Confined Stark Effect (QCSE)

The nonlinear electroabsorption characteristics in quantum wells have been studied theoretically and experimentally since the 1980s [6–11]. The absorption spectrum of a multiquantum-well (MQW) structured semiconductor material shifts to longer wavelengths when an electric field is applied perpendicularly to the MQW structure. The shift, called the Stark shift, is analogous to the energy shift of a hydrogen atom under applied electric fields [6]. In the absorption spectrum of MQW structures, resonance peaks appear at the absorption edge, which are due to electron-hole pairs held together by the Coulomb attraction between the opposite charges and which are designated as Wannier excitons. The exciton resonances can be observed even at room temperature due to the confining potential of the barrier material surrounding the quantum wells. The presence of the exciton absorption and its shift in low-dimensional semiconductor systems is referred to as the quantum-confined Stark effect (QCSE). If the applied electric field is weak [12, 13, 54, 57], the bandgap energy shift Δ_{shift} can be expressed as

$$\Delta_{shift} = \frac{\pi^2 - 15}{24\pi^4 \hbar^2} (m_e + m_h) \times e^2 \times E^2 \times W^4, \quad (8.28)$$

where E and W are the applied electric field and the thickness of the well layer, given in units of V/m for E and in m for W . Δ_{shift} is then given in J, which can be converted to eV by applying the following relation: $1 \text{ eV} = 1.6022 \times 10^{-19} \text{ J}$. The shift is proportional to the square of the applied electric field E and the fourth

power of well width W . The change of the refractive index of the MQW semiconductor material is accompanied by a change in the absorption spectrum through the Kramers-Kronig relations as given by (8.27). The electric-field induced change in the absorption is much steeper for the QCSE than that due to the Franz-Keldysh effect, and as a consequence, almost all electroabsorption modulators and some semiconductor MZI modulators utilize the QCSE. However, similar to the Franz-Keldysh effect, the QCSE also exhibits a strong wavelength dependence as it is also a band-edge related phenomenon.

8.2.1.4 Electro-Optic (Pockels) Effect

The refractive index of semiconductors also changes via the electro-optic (or Pockels) effect when an electric field is applied to the material [58–60]. In anisotropic materials like crystals, an electric displacement field D_{0i} can be expressed by using the electric field components E_j as

$$D_{0i} = \sum_{j=1}^3 \varepsilon_{ij} \times E_j, \quad (8.29)$$

where ε_{ij} is the dielectric constant having the form of a symmetric tensor of rank two. Generally, the tensor is expressed as an ellipsoid according to

$$\sum_{i=1}^3 \sum_{j=1}^3 \varepsilon_{ij} \times x_i \times x_j = 1, \quad (8.30)$$

where x_i and x_j ($i, j = 1, 2, 3$) denote three axes of a rectangular coordinate system. It can be converted into the following standard expression by choosing an appropriate rectangular coordinate system

$$\varepsilon_x \times x^2 + \varepsilon_y \times y^2 + \varepsilon_z \times z^2 = 1. \quad (8.31)$$

This expression is formally equal to the following index ellipsoid whose principal values of the refractive indices are n_x , n_y , and n_z , that is,

$$\frac{x^2}{n_x^2} + \frac{y^2}{n_y^2} + \frac{z^2}{n_z^2} = 1. \quad (8.32)$$

The relation between the electric displacement field and the electric field can also be written as

$$E_i = \sum_{j=1}^3 b_{ij} \times D_{0j} \quad (8.33)$$

using coefficients b_{ij} defined as

$$b_{ij} = \frac{\partial E_i}{\partial D_{0j}}. \quad (8.34)$$

For the case of an electric field applied to a material, the following relation holds with respect to the reciprocal dielectric constant and the electric field:

$$b_{ij} = b_{ij}^0 + \sum_{k=1}^3 \gamma_{ijk} \times E_k + \frac{1}{2} \sum_{k=1}^3 \sum_{l=1}^3 Q_{ijkl} \times E_k \times E_l + \dots, \quad (8.35)$$

where γ_{ijk} and Q_{ijkl} are called the coefficients of the Pockels and Kerr effect, respectively. The quantity b_{ij}^0 is the reciprocal dielectric constant without electric field. The Pockels (or linear electro-optic) effect gives rise to a change in the refractive index which is linearly proportional to the electric field. The Pockels effect requires inversion asymmetry, and thus it is only observed in certain crystalline solids. On the other hand, in the case of the Kerr (or quadratic electro-optic) effect, the change in the refractive index is proportional to the square of the electric field and all materials exhibit the Kerr effect, but it is generally much weaker than the Pockels effect. Thus, electro-optic modulators are usually made from crystals exhibiting the Pockels effect.

III–V semiconductor materials such as GaAs and InP exhibit the Pockels effect. They have zincblende crystal structure with space group of T_d^2 – $F\bar{4}3m$. The index ellipsoid of this type of crystal structure with no external electric field is a sphere whose principal values of the refractive indices n_x , n_y , and n_z are equal, which will be designated as n_0 in the following. The crystal structure has determinants for the tensors of rank 2, 3, and 4 and these are given by (8.36)–(8.38) [58–60]. For the tensor of rank 2 (the reciprocal dielectric constant tensor),

$$b_{ij}^0 = \begin{bmatrix} b_{11} & 0 & 0 \\ 0 & b_{11} & 0 \\ 0 & 0 & b_{11} \end{bmatrix} \quad (8.36)$$

holds, for the tensor of rank 3 (coefficient for the linear electro-optic effect) is given by

$$\gamma_{ijk} = \begin{bmatrix} 0 & 0 & 0 \\ 0 & 0 & 0 \\ 0 & 0 & 0 \\ \gamma_{41} & 0 & 0 \\ 0 & \gamma_{41} & 0 \\ 0 & 0 & \gamma_{41} \end{bmatrix}, \quad (8.37)$$

while the tensor of rank 4 (coefficient for the quadratic electro-optic effect) is

$$Q_{ijkl} = \begin{bmatrix} Q_{11} & Q_{12} & Q_{12} & 0 & 0 & 0 \\ Q_{21} & Q_{11} & Q_{12} & 0 & 0 & 0 \\ Q_{21} & Q_{21} & Q_{11} & 0 & 0 & 0 \\ 0 & 0 & 0 & Q_{44} & 0 & 0 \\ 0 & 0 & 0 & 0 & Q_{44} & 0 \\ 0 & 0 & 0 & 0 & 0 & Q_{44} \end{bmatrix}. \quad (8.38)$$

Here, the subscripts for higher rank tensors are expressed as $\{11\} \rightarrow \{1\}$, $\{22\} \rightarrow \{2\}$, $\{33\} \rightarrow \{3\}$, $\{23\}$, $\{32\} \rightarrow \{4\}$, $\{31\}$, $\{13\} \rightarrow \{5\}$, and $\{12\}$, $\{21\} \rightarrow \{6\}$.

It is interesting to note that the principal values of the refractive indices keep the value n_0 even when an electric field $\mathbf{E} = (E_x, E_y, E_z)$ is applied, i.e.,

$$b_{11} = \frac{1}{n_0^2} \quad (8.39)$$

holds. This is due to the fact that the components γ_{11} , γ_{22} and γ_{33} in (8.37) are equal to 0, and the components b_{ij} in (8.36) are equal to b_{11} only when i is equal to j (moreover, the Kerr effect has been assumed to be negligible).

For the case of an applied electric field, the index ellipsoid can be expressed as

$$\frac{1}{n_0^2}(x^2 + y^2 + z^2) + 2\gamma_{41}(yz \times E_x + zx \times E_y + xy \times E_z) = 1. \quad (8.40)$$

Here, a rectangular coordinate system has been chosen with the x -, y -, and z -axes oriented along the (100), (010), and (001) crystal axes, respectively.

If an electric field is applied parallel to the (100) direction, which is the standard direction of epitaxial growth of semiconductor material and hence the direction perpendicular to the epitaxial layers, E_y and E_z in (8.40) become zero and (8.40) reduces to

$$\frac{1}{n_0^2}(x^2 + y^2 + z^2) + 2\gamma_{41} \times yz \times E_x = 1, \quad (8.41)$$

which means that the Pockels effect does not contribute to the refractive index change when the input light propagates along the z - or y -axis because this configuration corresponds to $y = 0$ or $z = 0$. From the discussion it becomes clear that the maximum refractive index change is obtained for light propagating at an angle of 45° from the y - and z -axis, that is, along the (011) or the (0 $\bar{1}$ 1) direction. By rotating the y - and the z -axis to the (011) (new y' -axis) and (0 $\bar{1}$ 1) direction (new z' -axis), (8.41) can be converted into

$$\frac{x^2}{n_0^2} + \left(\frac{1}{n_0^2} + \gamma_{41} \times E_x \right) \cdot y'^2 + \left(\frac{1}{n_0^2} - \gamma_{41} \times E_x \right) \cdot z'^2 = 1. \quad (8.42)$$

For the refractive index of a semiconductor under the influence of an electric field and for light propagating along the y' direction,

$$n_{y'} = \left(\frac{1}{n_0^2} + \gamma_{41} \times E_x \right)^{-(1/2)} \quad (8.43)$$

holds and for light propagating along the z' direction, one gets

$$n_{z'} = \left(\frac{1}{n_0^2} - \gamma_{41} \times E_x \right)^{-(1/2)}. \quad (8.44)$$

By assuming small changes of the refractive index due to the applied electric field, these equations can be expressed as

$$n_{y'} \approx n_0 - \frac{1}{2} n_0^3 \times \gamma_{41} \times E_x, \quad (8.45)$$

$$n_{z'} \approx n_0 + \frac{1}{2} n_0^3 \times \gamma_{41} \times E_x. \quad (8.46)$$

According to (8.45) and (8.46), the refractive index exhibits opposite changes if the light propagation direction is along the y' and the z' directions, while input light having an electric field component parallel to the (100) axis is not affected by the Pockels effect. Thus, semiconductor electro-optic modulators exhibit a strong polarization dependence.

The parameter γ_{41} for III–V semiconductors takes values around -1.0 to -2.0×10^{-12} m/V, while the parameter for LiNbO_3 is 10 to 30×10^{-12} m/V, which is about 20 times larger than that of semiconductor material. However, the larger refractive index in semiconductors helps to raise the Pockels effect ($n_{\text{LiNbO}_3} \sim 2.2$, $n_{\text{GaAs}} \sim 3.4$, $n_{\text{InP}} \sim 3.2$) because the refractive index change is proportional to the third power of the refractive index itself. Moreover, the small dimensions of waveguide structures in semiconductor devices are also favorable for getting a strong electric field at the waveguide core region. Thus, one can obtain a comparable or even larger refractive index change in semiconductor electro-optic modulators compared to the change achievable in LiNbO_3 waveguide devices.

8.2.2 GaAs- and InP-Based MZI Modulators

In long haul optical fiber transmission systems, the 1550 nm wavelength region is widely used due to the small propagation loss of optical fibers (see Chap. 2). GaAs-based MZI modulators operating in that wavelength region utilize the Pockels effect to control the refractive index and to modulate the optical phase. This is because the GaAs material has a bandgap-equivalent wavelength of 870 nm which is far from the operation wavelength. So band-edge related effects such as the QCSE cannot be applied. On the other hand, InP-based MZI modulators can utilize both, the

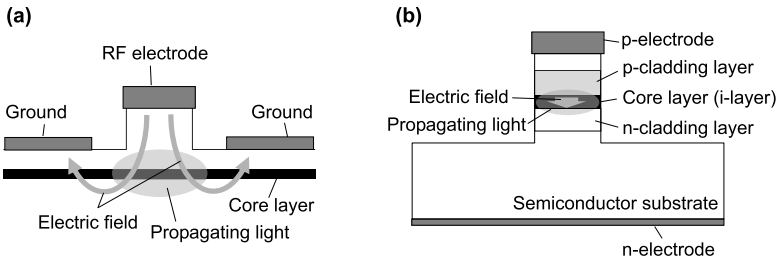


Fig. 8.10 (a) Schematic structure of Schottky electrode waveguide, and (b) p-i-n structure waveguide

QCSE and the Pockels effect as well. The core layer of InP-based modulators is composed of quaternary materials such as InGaAsP, InGaAlAs, and so forth, whose bandgap wavelength can be set close to the operation wavelength range. Particularly low driving voltages in InP-based MZI modulators can be obtained by utilizing the QCSE, however, this is achieved at the expense of a strong wavelength dependence. Moreover, an increasing optical absorption under the influence of an applied electric field, which distorts the output optical signal waveform, is also a problem. In order to reduce the wavelength dependence and the optical absorption change in InP-based modulators, it is desirable to only utilize the Pockels effect to control the refractive index of the modulators.

Two types of structures have found widespread use in semiconductor-based MZI modulators in order to efficiently apply the electric field to the core layer and prevent unwanted current flow at the same time.

One solution is a Schottky electrode structure [35–42] as schematically shown in Fig. 8.10(a), where a Schottky barrier between a metal electrode and the semiconductor material blocks the unwanted current flow. This option is primarily used for GaAs-based traveling-wave electrode modulators (see Sect. 8.3). A drawback of the structure is that the strength of the electric field applied to the core layer is lower compared to a p-i-n structure (see below) due to the low optical confinement to the core layer and a long distance between the RF electrode and the ground. The second alternative is a p-i-n structure [34, 45–49, 51]. It is schematically shown in Fig. 8.10(b). A thin insulating (i) layer (core layer) is sandwiched between p-type and n-type cladding layers. The structure blocks the current flow as a reverse biased diode. The strength of the electric field at the core layer is very high because the electric field is concentrated at the very thin i-layer. This is one of the reasons why p-i-n structure modulators can be made very compact. The electric field applied to the core layer of a p-i-n structure modulator is more than 100 times stronger than in LiNbO₃ modulators because the waveguide width is $\sim 1/4$ and the thickness of the core layer is less than $\sim 1/30$ compared to those of LiNbO₃ devices. Drawbacks of the p-i-n structure are:

1. Large absorption loss in the p-doped cladding layer, and
2. A large parasitic capacitance due to the thin i-layer.

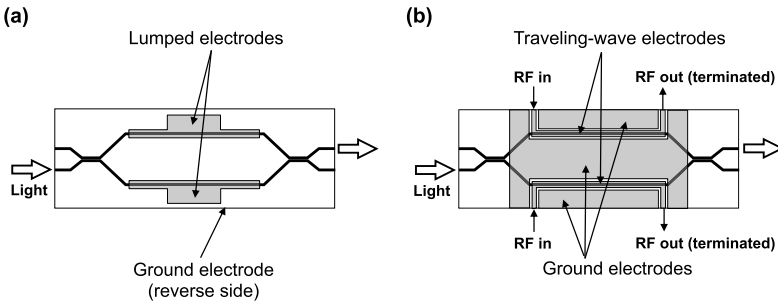


Fig. 8.11 Schematic structure of electrodes formed on MZI modulators. (a) Lumped electrode structure, (b) traveling-wave electrode structure

The p-type cladding layer has ~ 20 times larger absorption loss than an n-type one due to intervalence band absorption [61, 62]. The resistivity of the p-type cladding layer is also one or two order(s) of magnitude larger than that of n-type layers. Therefore, it is difficult to use sufficiently long traveling-wave electrodes which would meet the velocity and impedance matching conditions in p-i-n structure modulators. The large capacitance due to the thin i-layer is also unfavorable for extending the length of traveling-wave electrodes, and thus lumped electrodes are often used with p-i-n structure modulators, although the maximum achievable operation speed is limited for such designs.

8.3 High-Speed Modulator Design

Two types of electrode structures are essentially used with semiconductor MZI modulators, as mentioned above. One is the lumped electrode structure which is schematically shown in Fig. 8.11(a).

The core and cladding layers of the modulator's waveguide are sandwiched between the lumped electrode and the ground electrode which is located at the reverse (substrate) side of the chip, and an electric field is applied between the two. The structure is very simple and can be easily fabricated. The operation speed of the modulator with a lumped electrode structure is usually limited by the parasitic capacitance (CR time constant) of the electrode. The modulation efficiency of the modulator can be increased by extending the length of the phase control waveguide in the MZI modulator. However, a long electrode causes a large parasitic capacitance and the operation speed becomes low, i.e., it is limited to less than 10 Gbit/s for almost all MZI modulators with lumped electrode structure [45, 47, 48].

The other MZI modulator variant is illustrated schematically in Fig. 8.11(b): high-speed operation at low driving voltage is enabled by a coplanar traveling-wave structure where the RF drive signal is applied to one side of the electrode and exits from the other side. The output side of the electrode is usually terminated by a terminator resistance which prevents that the RF signal is reflected from the output end. Figure 8.12 shows the principle of the traveling-wave electrode.

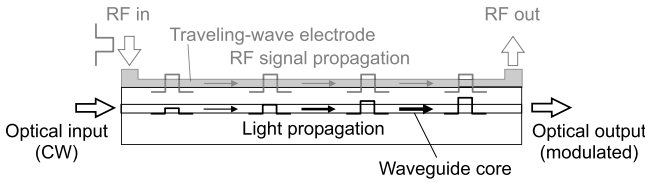


Fig. 8.12 Principle of a traveling-wave electrode

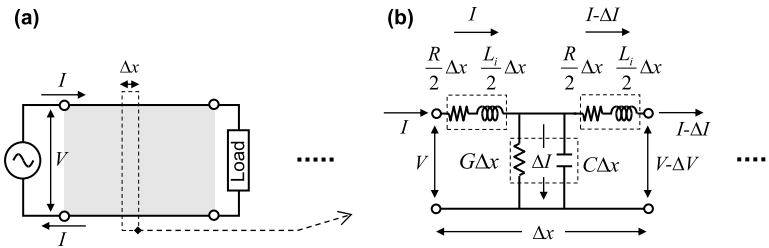


Fig. 8.13 (a) Schematic of transmission line, and (b) equivalent circuit segment for a small portion in the transmission line with a very short length of Δx

The RF signal, which propagates along the electrode, influences the light propagating along the waveguide core. When the velocity of the light is equal to that of the RF signal, the RF signal affects the propagating light all along the modulator and the efficiency is highest. Because the change of the refractive index, induced by the electro-optic effect, is smaller than that introduced by the QCSE, it is important to raise the modulation efficiency of the MZI modulator by using the traveling-wave electrode structure. This concept is free from the RC time constant limitation of the electrode, and one can, at least in principle, increase the modulation efficiency by extending the electrode length of the phase control waveguides in the MZI modulator without reducing the bandwidth.

Important requirements when designing traveling-wave electrodes are:

1. Impedance matching between the electrodes and the driving equipment (Z_0)
2. Velocity matching between the electrical signal and the propagating light (β), and
3. Sufficiently low transmission loss of the electrode (α_0).

The characteristics of a traveling-wave electrode can be discussed conveniently by using a transmission line (distributed element) model based on Maxwell’s equations [63] as illustrated schematically in Fig. 8.13(a).

The transmission line is divided into small sections and an equivalent circuit segment for a small section with a very short length of Δx is illustrated in Fig. 8.13(b). In this figure, R , L_i , G and C denote resistance, inductance, conductance and capacitance of the electrode, respectively, and the parameters are expressed in values per unit length. These parameters depend on the structure of the electrode (electrode

width, gap width between the electrode and ground, etc.), the dielectric constant of the semiconductor material the waveguides are made of, and so forth.

It is assumed that the voltage V , applied to the equivalent circuit segment, drops to $V - \Delta V$ due to the resistances $(R/2)\Delta x$ and the inductances $(L_i/2)\Delta x$ while the current I , flowing along the equivalent circuit segment, reduces to $I - \Delta I$ due to the leakage current ΔI through the conductance $G\Delta x$ and the capacitance $C\Delta x$. ΔV and ΔI are assumed to be small.

The voltage drop ΔV in the equivalent circuit segment is given by

$$\begin{aligned}\Delta V &= \left(\frac{R}{2} + j\omega\frac{L_i}{2}\right) \times I \times \Delta x + \left(\frac{R}{2} + j\omega\frac{L_i}{2}\right) \times (I - \Delta I) \times \Delta x \\ &= (R + j\omega L_i) \times I \times \Delta x - \left(\frac{R}{2} + j\omega\frac{L_i}{2}\right) \times \Delta I \times \Delta x \\ &\approx (R + j\omega L_i) \times I \times \Delta x = Z \times I \times \Delta x,\end{aligned}\tag{8.47}$$

where Z is the impedance per unit length of the equivalent circuit segment. The final result in (8.47) has been obtained by neglecting the second order product of small terms $\Delta I \Delta x$. It is straightforward to derive

$$\frac{dV}{dx} = Z \times I\tag{8.48}$$

from (8.47).

Analogous to (8.47), the decrease of the current along the equivalent circuit segment, ΔI , is given by

$$\begin{aligned}\Delta I &= (G + j\omega C) \times \left(V - \frac{\Delta V}{2}\right) \times \Delta x \\ &= (G + j\omega C) \times V \times \Delta x - (G + j\omega C) \times \frac{\Delta V}{2} \times \Delta x \\ &\approx (G + j\omega C) \times V \times \Delta x = Y \times V \times \Delta x,\end{aligned}\tag{8.49}$$

where Y is the admittance per unit length of the equivalent circuit segment. Once again, the final result in (8.49) has been obtained by neglecting the second order product of small terms $\Delta V \Delta x$, and (8.49) immediately yields

$$\frac{dI}{dx} = Y \times V.\tag{8.50}$$

The combination of (8.48) and (8.50) leads to

$$\frac{d^2V}{dx^2} = Z \times Y \times V\tag{8.51}$$

and the general solution of (8.51) is

$$V(x) = V_1 e^{\gamma_e \times x} + V_2 e^{-\gamma_e \times x},\tag{8.52}$$

where V_1 and V_2 are arbitrary values, and γ_e is given by

$$\gamma_e = \sqrt{Z \times Y} = \sqrt{(R + j\omega L_i) \times (G + j\omega C)}. \quad (8.53)$$

The complex parameter γ_e is normally called the propagation constant, and it is commonly expressed by using an attenuation constant α_0 and a phase constant β_e :

$$\gamma_e = \alpha_0 + j\beta_e. \quad (8.54)$$

Substitution of (8.52) into (8.48) leads to the following equation for the current I :

$$I(x) = \sqrt{\frac{Y}{Z}}(V_1 e^{\gamma_e x} - V_2 e^{-\gamma_e x}) = \frac{1}{Z_0}(V_1 e^{\gamma_e x} - V_2 e^{-\gamma_e x}), \quad (8.55)$$

where Z_0 is called the characteristic impedance given by

$$Z_0 = \sqrt{\frac{Z}{Y}} = \sqrt{\frac{R + j\omega L_i}{G + j\omega C}}. \quad (8.56)$$

The characteristic impedance and the propagation constant can be controlled by the parameters L_i , R , C , and G . In case that G is negligibly small and $R \ll \omega L_i$, the characteristic impedance Z_0 can be approximated by

$$Z_0 = \sqrt{\frac{L_i}{C} - j\frac{R}{\omega C}} \approx \sqrt{\frac{L_i}{C}} \times \left(1 - j\frac{R}{2\omega L_i}\right) \approx \sqrt{\frac{L_i}{C}} \quad (8.57)$$

while

$$\gamma_e \approx j\omega\sqrt{L_i C} \times \left(1 - j\frac{R}{2\omega L_i}\right) \approx j\omega\sqrt{L_i C}. \quad (8.58)$$

This represents a good approximation for the propagation constant γ_e and in this case,

$$\alpha_0 = \frac{R}{2} \times \sqrt{\frac{C}{L_i}} \approx 0 \quad (8.59)$$

and

$$\beta_e = \omega\sqrt{L_i C} \quad (8.60)$$

hold for the attenuation constant α_0 and the phase constant β_e , respectively. Thus, if the assumptions “small G and $R \ll \omega L_i$ ” are justified, the characteristic impedance Z_0 and the propagation constant γ_e are only determined by the parameters L_i and C .

From the discussions above, it is obvious that reducing the resistance R and the conductance G of the electrode in designing and fabricating traveling-wave electrodes of high-speed modulators is of prime importance. In addition, the characteristic impedance of the traveling-wave electrode should be matched to that of the driving equipment such as driver ICs and so forth. Usually, the impedance of the

driving equipment is 50Ω . Under these circumstances, the characteristic impedance of the traveling-wave electrode should also be set to 50Ω .

The phase velocity of the electrical signal in the transmission line is given by

$$v_p = \frac{\omega}{\beta_e} = \frac{1}{\sqrt{L_i C}} \quad (8.61)$$

and the phase velocity is approximately equal to the group velocity if the losses (R and G) of the transmission line are negligible. If the losses cannot be neglected, the group velocity is given by

$$v_g = \frac{\partial \omega}{\partial \beta_e} = v_p + \beta_e \times \frac{d(v_p)}{d\beta_e} \quad (8.62)$$

The following discussion will be based upon the assumption that the losses of the transmission line can be neglected and the phase velocity is equal to the group velocity, which is a good approximation for usual semiconductor MZI modulators with low loss electrodes.

The group velocity of light, v_o , in a medium with effective refractive index, n_{eff} , is given by

$$v_o = \frac{c}{n_{eff}}, \quad (8.63)$$

where c is the velocity of light in vacuum. A match as good as possible between the two velocities, v_p and v_o , is of key importance for modulators with traveling-wave electrode structure. The dielectric constants of GaAs and InP are around 12.5 and 12.4. Thus, v_p is normally larger than v_o in semiconductor-based modulators, and as a consequence, reducing the electrical group velocity v_p becomes important. In order to reduce the velocity v_p of GaAs-based MZI modulators with Schottky electrodes, the so-called slow-wave electrode structure has been proposed [34–42]. In this structure, the capacitance can be increased efficiently while the corresponding inductance change remains small, and as a result, the velocity v_p of the electrode can be reduced. Using this structure, high-speed GaAs MZI modulators operating up to 40 Gbit/s have been developed [41]. The length of the phase control section of the MZI modulator was 10 mm and the half wavelength voltage was 16.8 V for 1550 nm operation wavelength. Alternatively, a capacitively loaded coplanar strip electrode structure has also been proposed, and corresponding high-speed and low driving voltage MZI modulators on GaAs and InP substrates have been reported [32, 33, 43, 44, 52].

In p–i–n structure MZI modulators, the characteristic impedance of the electrodes becomes small because the modulators have thin i-layers and the capacitances are correspondingly large. In order to increase the characteristic impedance, a segmented electrode structure has been introduced to an InP-based MZI modulator [49]. The phase modulator section of the MZI modulator was divided into small sections, and these have been connected in a series by small capacitance Au electrodes. By introducing the novel structure, 40 Gbit/s operation of the p–i–n InP-MZI

modulator has been demonstrated with 5.3 V_{p-p} driving voltage. Thanks to the high electric field in the p–i–n structure, the chip was only 5.27 mm long.

Another InP-MZI modulator was designed with a unique electrode configuration as a quasi-traveling-wave type modulator with accelerator like segmented electrodes directly driven by CMOS RF driver ICs [64, 65]. 80 km transmission of a 10 Gbit/s signal over the full C-band was demonstrated by using the InP-MZI modulator [64]. The modulator was also used for arbitrary waveform generation (multilevel signal generation) [65]. In this trial, a 3-bit voltage-mode digital-to-analog converter (DAC) was introduced which can be operated at 10 Gsymbol/s, and one of the in-line centipede electrodes in the modulator was driven by the DAC. Generation of an 8-level ramp waveform was successfully demonstrated by using the device.

Another development direction has been the reduction of modulator power consumption, and an assembly comprising a low, non-standard impedance MZM with particularly low drive voltage V_π and a co-designed SiGe driver has been demonstrated for 32 Gbit/s OOK signal generation at 185 mW power consumption only [66], which is sufficiently low for being used as a compact modulator module for CFP4 applications.

The traveling-wave electrode technology has also been applied to EAMs and it enabled the increase in operation speed of EAMs [67, 68].

8.4 Performance of Current MZI Modulators

In this section, specific high performance semiconductor MZI modulators are described which are based upon a novel n–i–n isotype structure in phase control waveguides. Advanced MZI modulator modules are also described in which the novel structure MZI modulators are installed.

8.4.1 n–i–n Structure MZI Modulators

The high-speed semiconductor MZI modulators treated in Sect. 8.3 are designed with a rather complicated electrode structure and their fabrication is difficult. Thus, a simpler structure is much more promising for practical applications, provided the following requirements can be fulfilled simultaneously:

1. Simple electrode structure for easy fabrication
2. Capability to apply high electric fields to the core region of the modulator waveguide (similar to the situation with p–i–n waveguides), and
3. Sufficiently low loss of the upper waveguide cladding layer, both for optical and electrical signals.

Fig. 8.14 Schematic structure of the n-i-n waveguide

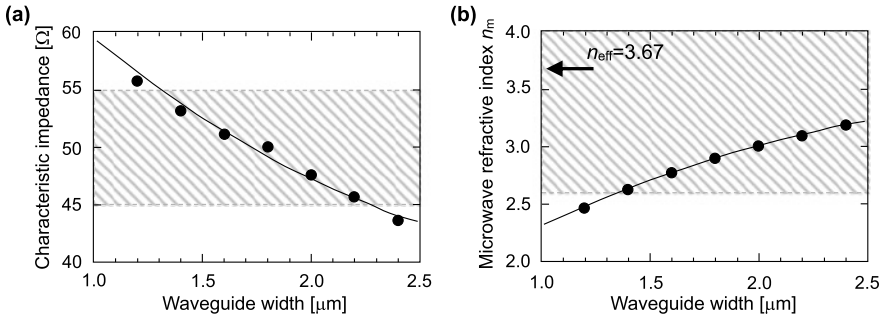
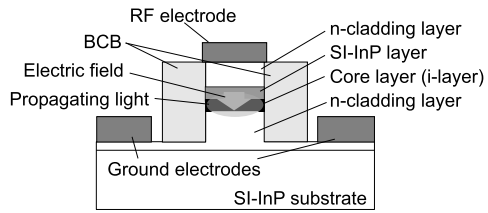


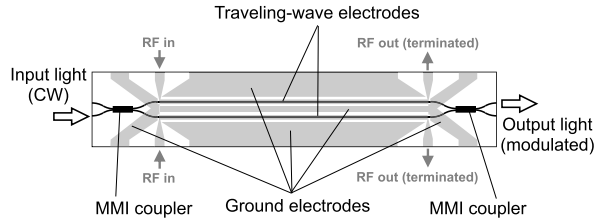
Fig. 8.15 (a) Calculated results for characteristic impedance and (b) microwave effective refractive index n_m of the n-i-n structure waveguide with a traveling-wave electrode as a function of waveguide width

An n-i-n isotype MZI modulator structure, which meets these requirements, has been fabricated and is described in [50]. The waveguide structure is schematically illustrated in Fig. 8.14.

A coplanar RF electrode is formed on a high-mesa optical waveguide buried by benzocyclobutene (BCB). The high-mesa optical waveguide consists of an n-doped lower cladding layer, an undoped core layer, an Fe-doped semi-insulating (SI) InP layer, and an n-doped upper cladding layer. The structure is grown on an SI-InP substrate. The waveguide has an n-i-n isotype heterostructure, and since there is no p-doped upper cladding layer, the typically large optical and electrical losses of a p-doped cladding layer are avoided. The concept does not only enable the modulator to operate at high speed, but also at low driving voltage by extending the lengths of the traveling-wave electrode and the phase control waveguide. The SI-InP layer is inserted in order to serve two purposes: as a potential barrier against electrons, it assures blocking of unwanted current flow and, in addition, it assures that a strong electric field is applied to the core layer of the waveguide. The characteristic impedance of the electrodes can be easily controlled by appropriately choosing the thickness of the core and the SI-InP layers, and the width of the high-mesa waveguide, thus determining the parasitic capacitance. Figure 8.15(a) is an example of the calculated characteristic impedance as a function of the waveguide width.

The calculation is done by using the commercially available high frequency 3-D structure simulator (HFSSTM) [69]. In this case, the thicknesses of the core and the SI-InP layers are set to 0.3 μm and 1.0 μm, respectively.

Fig. 8.16 Schematic view of n - i - n structure MZI modulator



A characteristic impedance of $50 \pm 5 \Omega$, corresponding to the hatched area, can be realized by setting the waveguide widths between $1.3 \mu\text{m}$ and $2.3 \mu\text{m}$, i.e., the acceptable waveguide width tolerance is fairly large and consequently the characteristic impedance control is rather straightforward in the case of the n - i - n structure.

In the case of insufficient velocity matching, the electrical bandwidth Δf of the traveling-wave electrode can be approximated by [33]

$$\Delta f \approx \frac{1.4 \times c}{\pi \times |n_{\text{eff}} - n_m| \times L}, \quad (8.64)$$

where c is the velocity of light, n_{eff} and n_m are the optical and microwave effective refractive indices, and L is the length of the electrode, respectively. According to (8.61), the microwave effective refractive index n_m is given by

$$n_m = \frac{c}{v_g} = \frac{c}{v_p} = \frac{c \times \beta_e}{\omega} = c \times \sqrt{L_i C}. \quad (8.65)$$

In n - i - n structure MZI modulators, a strong electric field can be applied to the core layer and enough efficiency can be obtained even with short phase control waveguides. Thus, L is set to 3 mm in the following discussion.

If 40 GHz bandwidth is required, the refractive index difference $|n_{\text{eff}} - n_m|$ must be lower than 1.1 according to (8.64), and for a calculated value $n_{\text{eff}} = 3.67$ of the optical effective refractive index of the n - i - n structure waveguide, this is equivalent to acceptable microwave effective indices within the range from 2.57 to 4.77. Figure 8.15(b) is an example of the calculated microwave effective refractive index n_m as a function of the waveguide width. The required range of n_m for realizing 40 GHz bandwidth is shown by the hatched area. The demands can be seen to be very relaxed, and velocity matching does apparently only require waveguide widths of more than $1.4 \mu\text{m}$. Impedance- and velocity-matching of the traveling-wave electrode with the simple structure can thus be realized at the same time by having the width of the n - i - n structure phase control waveguide between $1.4 \mu\text{m}$ and $2.3 \mu\text{m}$. In agreement with these results, the waveguide width has been chosen to be $2 \mu\text{m}$ in the fabricated n - i - n structure MZI modulator. Figure 8.16 shows the schematic structure of the n - i - n structure MZI modulator.

Input CW light is fed into a 2×2 multimode interference (MMI) coupler [70], and passed into two phase control waveguides with equal length. Two traveling-wave electrodes are located on the phase control waveguides. The refractive indices and hence the phases of the light traveling in the two phase control waveguides are

Fig. 8.17 DC extinction ratio of n-i-n structure MZI modulator as a function of bias voltage applied to a phase control waveguide

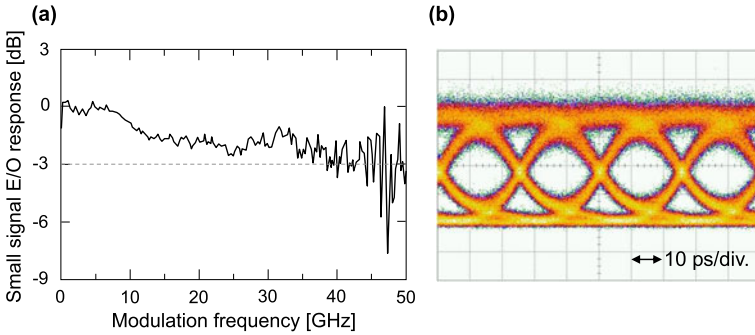
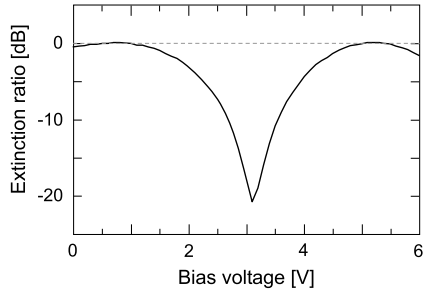


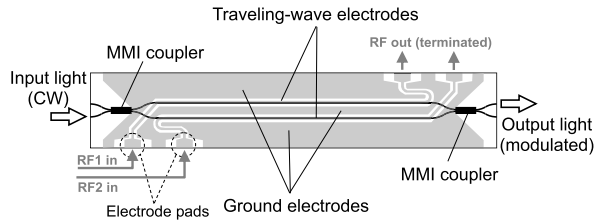
Fig. 8.18 (a) Small signal E/O response of n-i-n structure MZI modulator, (b) output eye diagram of n-i-n structure MZI modulator operated by 40 Gbit/s NRZ signal with PRBS of $2^{31} - 1$. Waveform measured with a single electrode only driven by the RF signal

modulated by RF signals applied to the two traveling-wave electrodes individually. Finally, light from both waveguides is recombined by another MMI coupler with the light interfering at the MMI coupler’s output. The length of the phase control waveguide is 3 mm, and the total size of the MZI modulator chip is 4.5 mm × 0.8 mm. Figure 8.17 shows the DC extinction ratio of an n-i-n structure MZI modulator as a function of the bias voltage applied to one phase control waveguide. The input wavelength is 1550 nm.

A maximum extinction of more than 20 dB is obtained. The half-wavelength voltage, V_{π} , is measured to be 2.3 V. It is worthwhile to note that there is no increase in the optical loss, even at the bias voltage of $2V_{\pi}$ (around a bias voltage of 5.2 V). Such behavior could not be obtained with the p-i-n structure MZI modulators utilizing the QCSE effect. The small signal Electrical/Optical (E/O) response of the n-i-n modulator is shown in Fig. 8.18(a).

The 3 dB bandwidth is measured to be 40 GHz, and a clear eye diagram is obtained for a 40 Gbit/s NRZ signal with pseudo random binary sequence (PRBS) of $2^{31} - 1$ (Fig. 8.18(b)). For measuring the eye diagram, an RF signal with $2.4 V_{p-p}$ driving voltage has been applied to one electrode of the modulator. This modulator exhibits strong potential for high-speed operation with low driving voltage. How-

Fig. 8.19 Schematic structure of differential-drive InP-MZI modulator



ever, packaging is difficult because of the two input RF electrode pads placed at opposite sides of the modulator chip.

A differential-drive MZI modulator is very important for generating chirp-less or chirp-controlled digital optical signals. It is also useful for the generation of phase modulated optical signals which will be utilized in next generation optical transmission systems. To operate the MZI modulator in a differential drive (push-pull) mode, it is important to equalize the RF signal phases, and hence to equalize the lengths of the two electrodes from the chip edge to the two phase control waveguides. In addition, the two electrode pads for the input RF signals should be placed on the same side of the chip for easy connection with differential output driver ICs [71]. A differential-drive InP-MZI modulator is shown schematically in Fig. 8.19.

Such a modulator has already been fabricated successfully [72], and the design is based upon the n - i - n modulator discussed earlier (Fig. 8.16) with additional microstrip lines (MSLs). The length of the phase control waveguides is 3 mm, and the electrode pads for the input RF signals are both placed on one side (lower side of the figure) of the chip. The pads for the output are placed on the other side (upper side of the figure). MSLs are used in order to equalize the electrode lengths from the pads to the phase control waveguides. The MSLs exhibit small electrical losses only, even when they have bends with small curvature radius. The chip size of the differential-drive InP-MZI modulator is 4.5 mm \times 0.8 mm, which is the same as that of the modulator shown in Fig. 8.16. Thus, the MSLs have been added without a need to extend the chip dimensions.

Measurements of the extinction ratio have shown that the same symmetric extinction characteristics can be obtained over the complete C-band if only the DC bias is adjusted linearly as the operation wavelength increases. The results of these experiments are shown in Fig. 8.20(a).

It is important to note that no adjustment of the RF voltage swing has been necessary and only the linear change of the DC voltage V_b shown in Fig. 8.20(b) had to be made.

The experimentally determined small signal Electrical/Electrical (E/E) response for both RF electrodes including traveling-wave electrodes (as shown in Fig. 8.21) exhibits a 6 dB E/E bandwidth (transmittance S_{21}) of 46 GHz for both electrodes and reflectance values S_{11} of less than -18 dB for all modulation frequencies up to 50 GHz.

The characteristics are almost the same for the two electrodes. This indicates that differential-drive InP-MZI modulators can be realized without degradation of the high-speed performance even when MSLs are introduced.

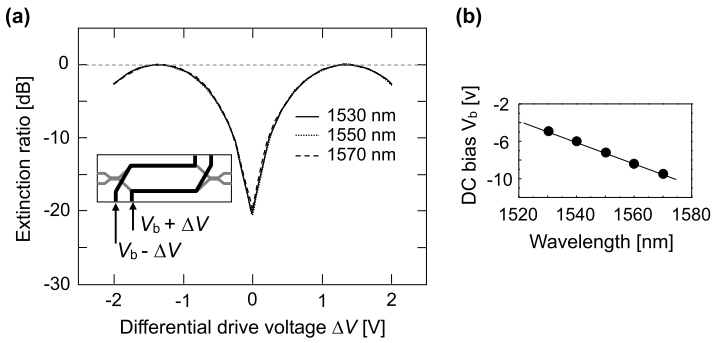


Fig. 8.20 (a) Extinction characteristics of differential-drive InP-MZI modulator. (b) Applied DC bias V_b as a function of operation wavelength

Fig. 8.21 Small signal E/E response of differential-drive InP-MZI modulator as a function of modulation frequency. S_{21} and S_{11} are E/E transmittance and reflectance, respectively

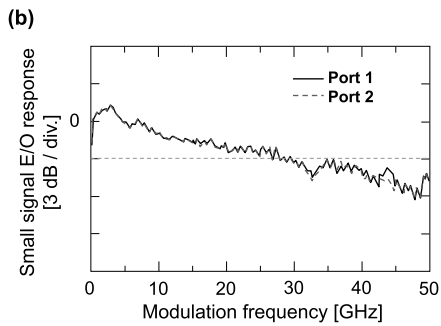
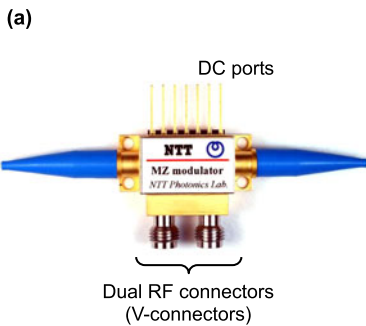
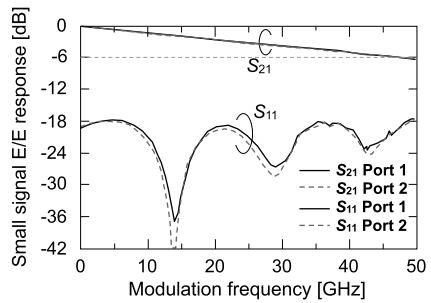


Fig. 8.22 (a) Photograph of a differential-drive InP-MZI modulator module, (b) small signal E/O response of the module

By mounting the MZI modulator in a package, a compact differential-drive InP-MZI modulator module has been fabricated [72]. Figure 8.22(a) shows a photograph of the module.

The module is 21 mm (L) × 17 mm (W) × 8 mm (H) in size, and its footprint is the same as that of commercially available conventional DFB lasers and EA-DFB lasers in butterfly-type packages. Two RF connectors for differential electrical

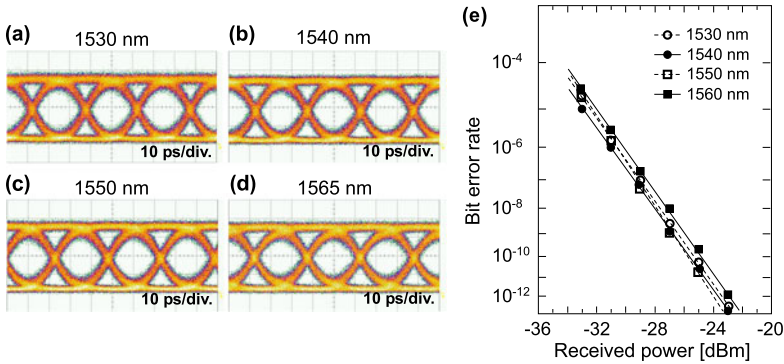


Fig. 8.23 (a–d) Eye diagrams, and (e) bit-error-rate performance of a differential-drive InP-MZI modulator module for 40 Gbit/s NRZ signals and various operation wavelengths

signals are placed at one side of the package while pins for DC bias and other control signals are placed at the opposite side of the package. The module contains $50\text{-}\Omega$ terminations and bias-tees for both RF electrodes in the package, and the fiber-to-fiber insertion loss of the module is 7 dB.

The E/O response of the module measured for both RF ports is illustrated in Fig. 8.22(b). Both curves are essentially the same and the 3dB E/O bandwidth of the module turns out to be 28 GHz which is sufficiently large for 40 Gbit/s operation. Experiments with differential 40 Gbit/s NRZ signals, PRBS of $2^{31} - 1$, and 1.3 V_{p-p} drive voltage swing applied to both RF connectors yielded the output eye diagrams shown in Figs. 8.23(a)–(d) for various operation wavelengths covering the complete C-band.

Clear eye opening can be observed for all operation wavelength channels. The dynamic extinction ratios are more than 10 dB. The bit error rate (BER) performance for the 40 Gbit/s NRZ signals have been measured in a back-to-back configuration, and the results are shown in Fig. 8.23(e) as a function of received power. The performance is essentially the same for all wavelength channels, no error floors could be observed, and error free operation of the modulator module can be concluded.

8.4.2 Advanced MZI Modulator Modules

8.4.2.1 Surface-Mountable Mini 10G MZI Modulator Module

Compact MZI modulator modules operating at 10 Gbit/s are desirable for reducing the size of optical transponders and optical transceivers. Semiconductor MZI modulators are promising candidates for that purpose due to their compactness. Although the MZI modulator module shown in Fig. 8.22(a) is very small compared to commercially available LiNbO_3 MZI modulator modules, a further reduction of the module size is desired, and thus very small surface-mountable differential-drive

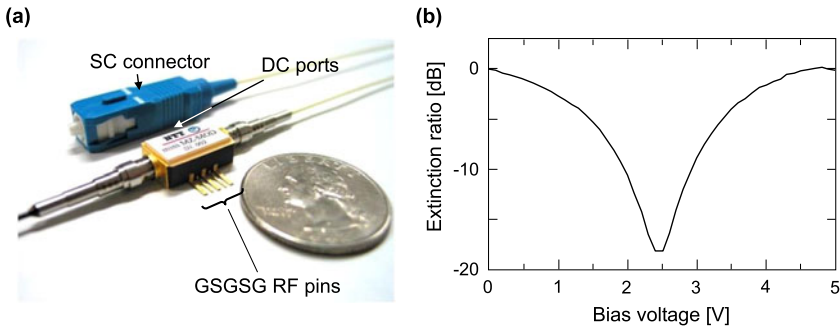
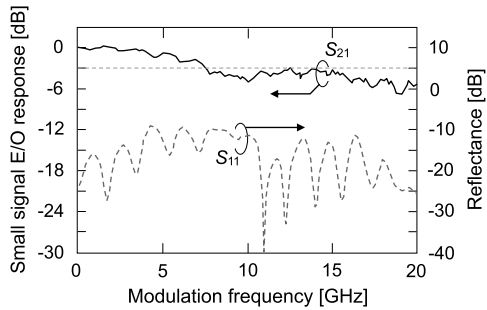


Fig. 8.24 (a) Photograph of surface-mountable mini 10G MZI modulator module, and (b) DC extinction ratio of the module as a function of bias voltage. An SC connector (blue box behind the module in the photograph) is also shown as a reference

Fig. 8.25 Small signal E/O response S_{21} and reflectance S_{11} of mini 10G MZI modulator module

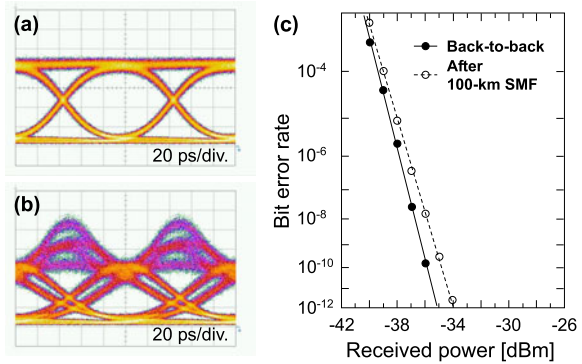


InP-MZI modulator modules have been developed [73]. A photograph of a corresponding mini 10G MZI modulator module is shown in Fig. 8.24(a).

The module is only 13.8 mm (L) × 8.9 mm (W) × 4.9 mm (H) in size, and it consists of an inexpensive ceramic-based package. The RF and DC lead pins are located at the bottom of the package in order to enable its direct mounting onto a printed circuit board. The two RF lead pins for differential drive are located on one side of the package with G–S–G–S–G configuration for high-speed operation. High-speed transmission lines are formed in the wall of the ceramic package to connect the signal (S) lead pins and the two RF electrode pads of the MZI modulator. These lines are designed to have 50-Ω impedance and the lengths are adjusted to be equal. Figure 8.24(b) shows the DC extinction ratio of the module as a function of bias voltage. The half-wavelength voltage V_{π} is estimated to be 2.4 V, and there is no increase in the optical loss even at a bias voltage of $2V_{\pi}$. The measured small signal E/O response S_{21} for the module is shown in Fig. 8.25.

The 3 dB E/O bandwidth is 7.5 GHz which is enough for 10 Gbit/s NRZ signal operation. Reflectance is also shown in the figure. It is less than -9 dB, including the reflection from the response measurement equipment. The module is operated by a 10 Gbit/s NRZ signal with PRBS of $2^{31} - 1$. The voltage swing of the differential RF signals applied to the two phase control waveguides is $2.0 V_{p-p}$ and $0.1 V_{p-p}$, respec-

Fig. 8.26 (a) Eye diagrams of 10 Gbit/s NRZ signal from mini 10G MZI modulator module for back-to-back, and (b) after 100 km SMF transmission; (c) corresponding bit-error-rate performance



tively. Under these conditions, the output modulated signal is negatively chirped. The input CW light wavelength has been set to 1550 nm. Figure 8.26(a) shows the eye diagram of the output 10 Gbit/s NRZ signal from the module in a back-to-back configuration.

Clear eye opening is observed. Figure 8.26(b) shows the eye diagram after 100 km SMF transmission. The eyes are still clearly open. The observed pattern agrees quite well with the calculated results shown in Fig. 8.9(c). Measured BER characteristics for back-to-back configuration and after 100 km SMF transmission are shown in Fig. 8.26(c). No error floor can be observed in both cases. The sensitivity degradation after 100 km SMF transmission is measured to be 1.1 dB (@BER = 10^{-12}).

8.4.2.2 Tunable Transmitter Modules with Semiconductor MZI Modulators

In tunable transmitters and transponders, wavelength tunable laser diodes are used together with MZI modulators. When semiconductor-based MZI modulators are utilized, monolithic [74–79] or hybrid [80–83] integration technologies enable particular compact transmitters, while such compact transmitters cannot be realized with LiNbO₃-based modulators because the thermal expansion coefficients for semiconductor materials ($\sim 4.9 \times 10^{-6}/\text{K}$ for InP) and LiNbO₃ ($\sim 15.0 \times 10^{-6}/\text{K}$) are quite different from each other. So laser diodes and LiNbO₃ modulators cannot be mounted on the same metal package, whose thermal expansion coefficient is set equal to that of the semiconductor material.

Monolithically integrated, wavelength-tunable transmitters utilize distributed Bragg reflector (DBR) lasers, while those based upon hybrid integration technology have been reported using various sources including a DBR laser [80], a widely tunable DFB laser array (TLA) [81], a tunable laser with external liquid crystal mirror [82], or a DFB laser array with a micro-electromechanical system (MEMS) switch [83]. All wavelength tunable transmitters cover the complete C-band.

The performance of various compact tunable transmitter modules is discussed in more detail in the following sections. Figure 8.27(a) illustrates a particularly

Fig. 8.27 Tunable transmitter module with InP-MZI modulator.
 (a) Photograph of module,
 (b) schematic structure

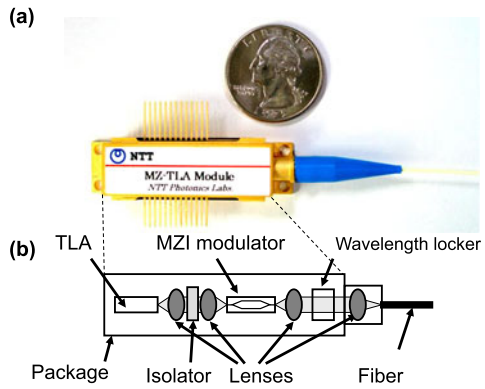
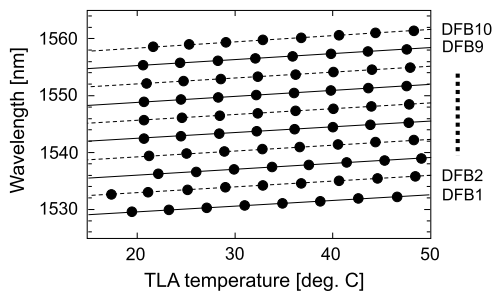


Fig. 8.28 Output wavelength of the module as a function of TLA temperature



compact module with actual package dimensions of

$$41 \text{ mm (L)} \times 13 \text{ mm (W)} \times 9 \text{ mm (H)}.$$

The transmitter consists of a widely tunable DFB laser array (TLA) [84, 85] comprising ten DFB lasers hybridly integrated with an InP-MZI modulator and a wavelength locker. This is schematically shown in Fig. 8.27(b). The TLA and the MZI modulator are mounted on the same metal carrier and a Peltier cooler. They are coupled by using lenses and include an optical isolator. The modulated output from the MZI modulator is coupled to an optical fiber after passing through the wavelength locker. The wavelength locker has a free-spectral range (FSR) of 50 GHz and assures locking of the output wavelength to any channel of the International Telecommunication Union (ITU) frequency grid defined for wavelength division multiplexing (WDM) systems. The output wavelengths of the transmitter shown can be tuned to 81 channels of the WDM grid with 50 GHz spacing by selecting an appropriate DFB laser for the desired channel from the 10 DFB lasers and setting the TLA chip temperature precisely to the appropriate temperature in the 15 to 50 °C range as shown in Fig. 8.28.

The output power of the module is more than +2 dBm for all channels. Figure 8.29 shows the extinction characteristics of the module for output wavelengths in the range from 1530 to 1560 nm as a function of bias voltage of the MZI modulator. The half-wavelength voltage V_{π} is around 2.5 V for all wavelengths.

Fig. 8.29 Extinction characteristics of the module for various output wavelengths

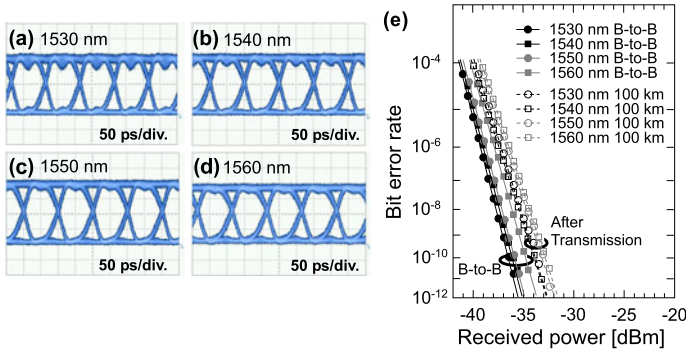
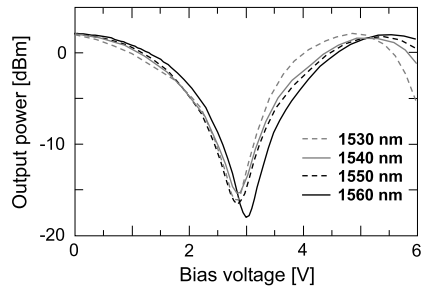


Fig. 8.30 (a)–(d) Eye diagrams of 10 Gbit/s NRZ signals for various output wavelengths, and (e) corresponding bit-error-rate performance for back-to-back and after 100 km SMF transmission. Modulator driving conditions were fixed for all wavelength channels

The module is driven by a 10 Gbit/s NRZ signal with PRBS of $2^{31} - 1$. The bias conditions for the MZI modulator have been kept constant during the measurement, even when the output wavelength has been switched. The bias voltages to the MZI modulator’s two phase control waveguides were set to -3.3 and -2.8 V, and the driving voltage swing applied to the two waveguides had been fixed to 0.75 and $2.25 V_{p-p}$ for push-pull operation. Under these conditions, the output signal is negatively chirped. Figures 8.30(a)–(d) show the eye diagrams for various output wavelengths.

The eyes are clearly open for all wavelengths, even under fixed modulation conditions. Figure 8.30(e) shows the bit-error-rate performance of the module measured for back-to-back and after 100 km SMF transmission for output wavelengths ranging from 1530 to 1560 nm. No error floors are observed under all conditions. The power penalties resulting from the transmission are less than 3 dB for all wavelength channels.

Another hybridly integrated light source is a co-packaged laser and MZI modulator prototype [86]. The narrow linewidth tunable laser with dual output ports served as transmitter and local oscillator. The output was coupled to an InP dual IQ modulator, and output occurred via a micro-optic polarization multiplexer. The device is intended to be used as a very small 100 Gbit/s transponder for digital coherent systems. Another recently reported light source is a DSDBR laser module

hybridly integrated with an InP dual IQ DP-QPSK modulator [87]. The modulator had a segmented electrode design and 28 Gbaud DP-16QAM operation has been demonstrated.

The size of laser sources can be reduced by monolithic integration of InP MZI modulators with wavelength tunable laser diodes, and corresponding research has been reported in the literature [74–79]. An early integrated light source has been realized by integrating a SG-DBR laser with an MZI modulator [74–76] and 10 Gbit/s NRZ [74], 40 Gbit/s NRZ [75] and 10 Gbit/s duobinary [76] operations have been demonstrated. One example of more recent progress in monolithically integrated light sources is a four channel DBR laser array with four MZI modulators and an AWG filter [77]. The device operated in the 1550 nm wavelength region, and the channel spacing was set to 100 GHz. The chip size was $4 \times 6 \text{ mm}^2$ and the length of the phase sections used for the MZI modulators was 1 mm. Output power coupled to an optical fiber was up to 4 dBm/channel, and 12.5 Gbit/s per transmission channel (total throughput was 50 Gbit/s) was demonstrated. An InP-MZI modulator-based QPSK modulator integrated with an SG-DBR laser was also demonstrated [78]. The bandwidth of the modulator was 8 GHz. 20 Gbit/s QPSK operation over a wavelength range of 20 nm has been demonstrated. The half-wavelength voltage V_π of the modulator was in the 3.5 V to 5 V range over the whole operation wavelength region. A monolithically integrated DS-DBR laser with an MZI modulator was also reported [79] to meet the demands for SFP+ TOSA applications. The chip length was 5.2 mm (2 mm for the DS-DBR laser and 3.2 mm for the MZI modulator). In these investigations the refractive index of the phase control section in the MZI modulator was controlled through the QCSE instead of the EO effect to reduce V_π . The modulator's V_π was in the range from 2.6 V to 3.8 V over the full wavelength tuning range. The wavelength tuning range was extended to $\sim 40 \text{ nm}$ and 11.3 Gbit/s operation at a chip temperature of 60°C has been achieved.

8.5 High-Performance Modulators for Advanced Modulation Formats

The maximum transmission distance of standard high-speed digital optical signals is limited by various factors, and one of particular relevance is the chromatic dispersion of the optical fiber (see Sect. 8.1 and also Chap. 2, Sect. 2.2.5). Thus, systems performance is expected to be improved if modulation formats are introduced which are less sensitive to chromatic dispersion. The optical duobinary (ODB) [88–93] format is such a solution. Coherent transmission systems are another option where the information is also carried by the optical phase and improvements in sensitivity are expected [94, 95]. It has already been a research topic of high interest in the 1980s and 1990s. Formats that have been investigated include optical phase-shift keying (PSK) and differential phase-shift keying (DPSK) [94, 96–99], differential quadrature phase-shift keying (DQPSK) [100–116] and even multilevel modulation formats such as multi-quadrature amplitude modulation (QAM) [117–121]. A more

detailed coverage of advanced modulation formats within the present book is given in Chap. 7.

Transmitters for advanced modulation formats must enable optical amplitude and phase modulation as well, and MZI modulators can be used for that purpose. In the following section, various advanced modulation formats and the applicability of semiconductor MZI modulators for their generation will be discussed.

8.5.1 Optical Duobinary (ODB) Modulation

Optical duobinary (ODB) signals can be generated by using MZI modulators driven with a three-level electrical signal as shown in Fig. 8.31, signal (a-E), which is generated by using the sequence shown in Fig. 8.32.

Fig. 8.31 Principle of optical duobinary signal generation. (a-E) Duobinary encoded three-level electrical signal, and (a-O) generated optical duobinary signal. (b-E) Eye diagram of electrical duobinary signal, and (b-O) eye diagram of optical duo-binary signal

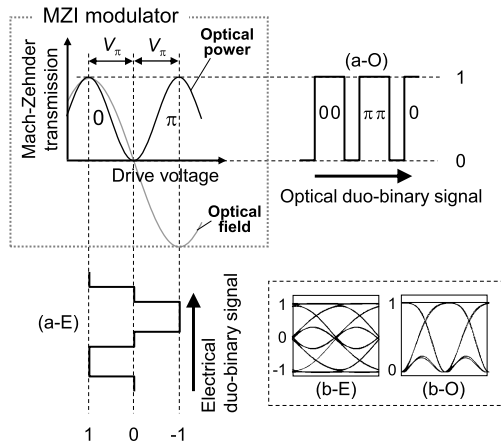
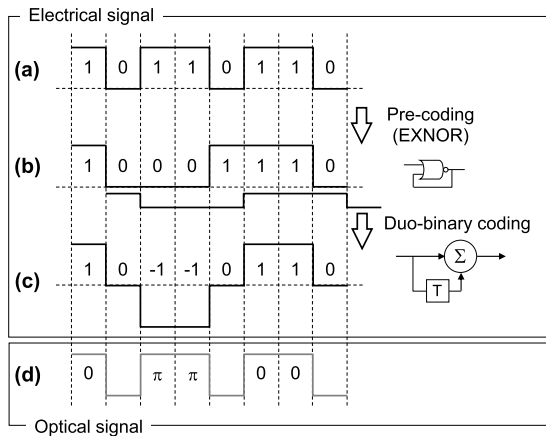


Fig. 8.32 (a–c) Principle of duobinary encoding, and (d) generated optical duobinary signal



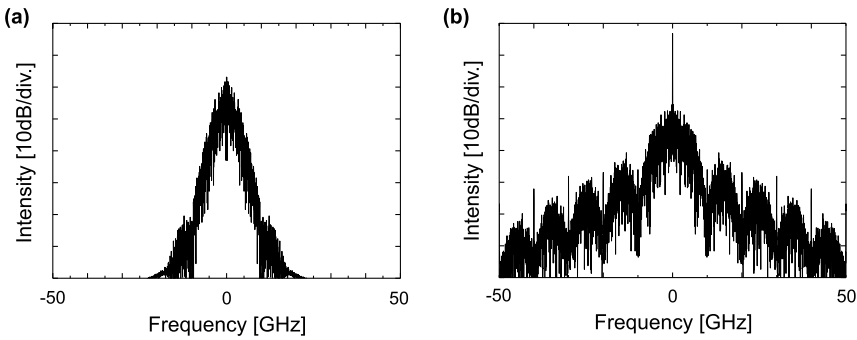


Fig. 8.33 Calculated optical spectra for (a) 10 Gbit/s optical duobinary signal and (b) 10 Gbit/s NRZ signal

First, a bit sequence with NRZ format (Fig. 8.32(a)) is precoded using an EXNOR operator. The converted bit sequence (Fig. 8.32(b)) is then duobinary coded by adding the bit sequence with one bit delay to the original one (Fig. 8.32(c)). The final duobinary encoded signal has three levels of $+1$, 0 , and -1 . By comparing the original bit pattern (Fig. 8.32(a)) with the encoded pattern (Fig. 8.32(c)), one can see that the absolute value of the encoded signal is equal to the original NRZ signal. When the three-level electrical duobinary encoded signal is applied to an MZI modulator, the bias voltages for the $+1$, 0 , and -1 levels are set in such a way that they correspond to the first maximum transmission point, the null point and the second maximum transmission point of the MZI modulator, respectively (see Fig. 8.31). The bias voltage differences from $+1$ to 0 and from 0 to -1 are V_π , and thus $2V_\pi$ total voltage swing is required for using an MZI modulator for ODB modulation. The resulting optical signals are shown in Fig. 8.31, signal (a-O), and Fig. 8.32(d). The phases of the modulated optical signals corresponding to the first ($+1$) and the second (-1) maximum transmission points have a phase difference of π . Thus, the ODB signal has the same intensity pattern as the original NRZ signal, but the ‘mark’ signals have two optical phases, 0 and π . ODB signals are detectable with conventional NRZ receivers because the intensity modulated bit pattern of the ODB signal (Fig. 8.32(d)) is identical to that of the corresponding NRZ bit pattern (Fig. 8.32(a)).

For completeness, eye diagrams for 10 Gbit/s input electrical three-level duobinary, signal (b-E), and corresponding ODB (b-O) signals are also shown in Fig. 8.31. Furthermore, Fig. 8.33(a) shows the calculated optical spectrum for the 10 Gbit/s ODB signal and as a reference, the calculated optical spectrum for a 10 Gbit/s NRZ signal as well (Fig. 8.33(b)).

The spectral broadening for the ODB signal is small compared to that of the NRZ signal, and there is no carrier frequency component in the spectrum for the ODB signal. These results clearly indicate that ODB signals are superior to NRZ signals with respect to chromatic dispersion tolerance of an optical fiber.

Differential-drive InP-based MZI modulators are particularly promising for ODB signal generation [73]. They can be operated at low driving voltage, chirp-less modulation can be achieved under differential drive conditions, and the increase in trans-

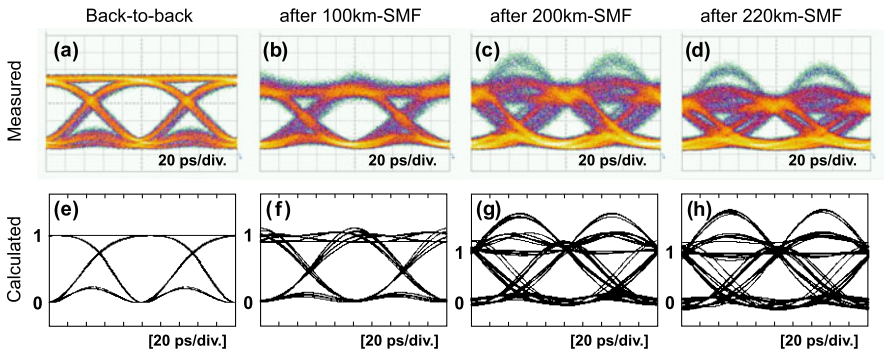


Fig. 8.34 Measured 10 Gbit/s eye diagrams for (a) generated optical duobinary signal, and after SMF transmission of (b) 100 km, (c) 200 km, and (d) 220 km, respectively. Lower figures are calculated eye diagrams for (e) generated optical duobinary signal, and after SMF transmission of (f) 100 km, (g) 200 km, and (h) 220 km, respectively

mission loss is negligibly low even if the driving voltage is raised above $2V_{\pi}$ (see for example Fig. 8.20 and Fig. 8.24). The last feature is important for the generation of ODB signals without waveform distortion because the signals require $2V_{\pi}$ drive voltage swing. Eye diagrams of 10 Gbit/s ODB signals measured with $2.3 V_{p-p}$ drive voltage swing are shown in Fig. 8.34(a).

The large tolerance of ODB signals with respect to chromatic dispersion is illustrated by eye diagrams measured after 100 km, 200 km, and 220 km transmission over standard SMF at 1550 nm operation wavelength as shown in Figs. 8.34(b)–(d). Clear eye openings are observed in all cases. Figures 8.34(e)–(h) are the calculated eye diagrams for the ODB signals at back-to-back (Fig. 8.34(e)), after 100 km (Fig. 8.34(f)), 200 km (Fig. 8.34(g)), and 220 km (Fig. 8.34(h)) SMF transmission. The calculated curves are in good agreement with the measured data in Figs. 8.34(a)–(d). These results indicate that the differential-drive InP-MZI modulator does not add any extra chirp nor any additional signal distortion. Figure 8.35 illustrates the measured bit-error-rate performance as a function of received power.

An error floor starts to develop after 240 km SMF transmission while error-free transmission can be achieved up to about 220 km transmission distance. The sensitivity degradation is less than 1.7 dB (@BER = 10^{-12}), even when the transmission distance is 220 km. These results indicate that the differential-drive InP-MZI modulator is suited as a compact and low drive voltage ODB signal generator.

8.5.2 Optical DPSK Modulation

In the optical phase-shift keying (PSK) format, bit information of digital optical signals is carried by optical phases. In coherent PSK systems [94, 96–99], an absolute phase reference is required at the receiver in order to read out the bit information. On the other hand, the optical differential PSK (DPSK) format utilizes the optical

Fig. 8.35 Measured bit-error-rate performance of 10 Gbit/s optical duobinary signal as a function of received power

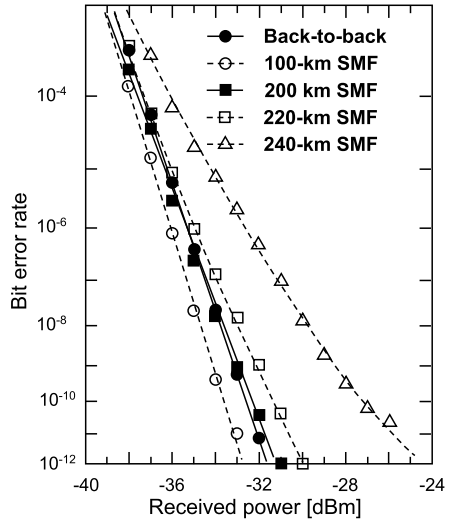
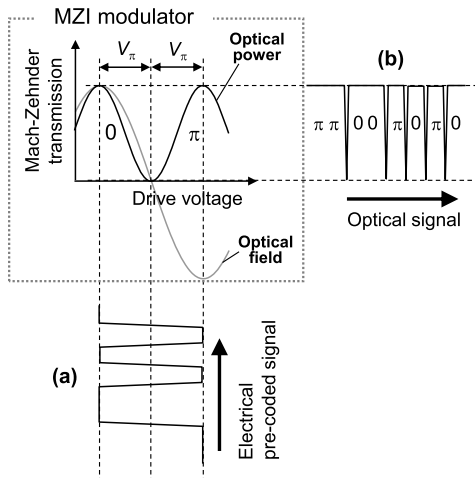


Fig. 8.36 Principle of optical DPSK signal generation using an MZI modulator. (a) Electrical pre-coded signal, (b) generated optical DPSK signal

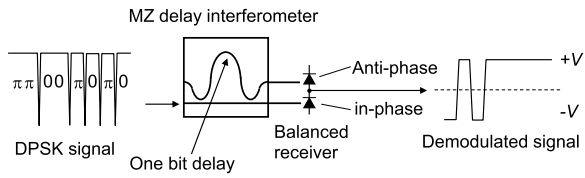


phase change to recognize the bit information and uses the phase of the preceding bit as a phase reference. The DPSK format offers several benefits such as low bit-pattern-dependent nonlinear effects, high sensitivity and large tolerance for tight optical filtering.

Optical DPSK signals can be generated by using a phase modulator or an MZI modulator, where the latter option is superior to the former with respect to chirping characteristics and reshaping of the electrical signal [110]. The method to generate DPSK signals by using an MZI modulator will be discussed in the following and Fig. 8.36 illustrates the concept.

The precoded electrical signal (a) in Fig. 8.36, generated by a precoder, is applied to an MZI modulator. The drive voltage swing of the precoded electrical signal is

Fig. 8.37 Principle of demodulation of optical DPSK signal using a Mach-Zehnder delay interferometer and a balanced receiver



set to twice the half-wavelength voltage ($2V_{\pi}$), while the DC bias is set to the null point of the MZI modulator. Under these conditions, the MZI modulator is operated between the first (phase 0) and the second (phase π) maximum transmission points, and the output signal of the MZI modulator is the optical DPSK signal as shown in Fig. 8.36(b). The intensity dip observed in the optical DPSK signal when the phase changes does not significantly affect the decoded signal at the receiver. The concept illustrated in Fig. 8.36 can also be modified in such a way that an additional intensity modulator is used as a pulse carver so that a return-to-zero (RZ) DPSK signal is generated which is more tolerant to optical fiber nonlinearities [122].

DPSK signal demodulation can be accomplished by using a Mach-Zehnder delay interferometer (MZDI) and a balanced receiver as shown in Fig. 8.37.

The MZDI has an asymmetric MZI structure with one arm of the MZI being longer than the other one, where the time needed by the optical signals to travel the extra length corresponds to exactly one bit. As a consequence, two subsequent bits of the DPSK signal interfere at the output of the MZDI, i.e., the preceding bit acts as a phase reference to demodulate the DPSK encoded optical signal. The MZDI has two output ports and the interfering signals yield a nonzero output in one of these outputs depending on their relative phase. When subsequent bits are in-phase (anti-phase), a nonzero optical signal leaves the MZDI from the lower (upper) port as illustrated in Fig. 8.37. (It should be noted that, due to the MZDI's asymmetric nature, one can achieve (by precisely controlling the device temperature) that CW light either leaves the MZDI from the cross port or from the through port. The latter is the case for the device shown in Fig. 8.37, and this is different from the behavior of symmetric MZIs (cf. Fig. 8.5).) The output signals are detected by means of a balanced detector, and because the demodulated electrical output signal of the balanced detector is twice as large as for conventional direct detection, a 3 dB sensitivity improvement of the signal-to-noise ratio (SNR) is expected in DPSK systems compared to conventional on-off keying (OOK).

Figure 8.38 compiles the calculated eye diagrams and optical spectra for three modulation formats, NRZ, DPSK, and RZ-DPSK, for 10 Gbit/s. Figures 8.38(a), (c), (e) are the generated optical waveforms for NRZ, DPSK, and RZ-DPSK formats. The mark ratio is 0.5, ~ 1 , and 0.5 when the original electrical signals have a mark ratio of 0.5. In the diagrams in Figs. 8.38(c), (e), the optical power is the same for each bit while the diagrams of the bits of the NRZ signal (Fig. 8.38(a)) is random, where the latter is due to the fact that in the case of NRZ signals, bits are easily affected by neighboring bits (pattern effect). Figure 8.38(b) represents the eye diagram of directly detected NRZ signals using a low-pass filter having a bandwidth of 0.7 times the bit rate. Figures 8.38(d), (f) are the eye diagrams of demodulated DPSK and RZ-DPSK signals with a low-pass filter. Figures 8.38(g)–(i)

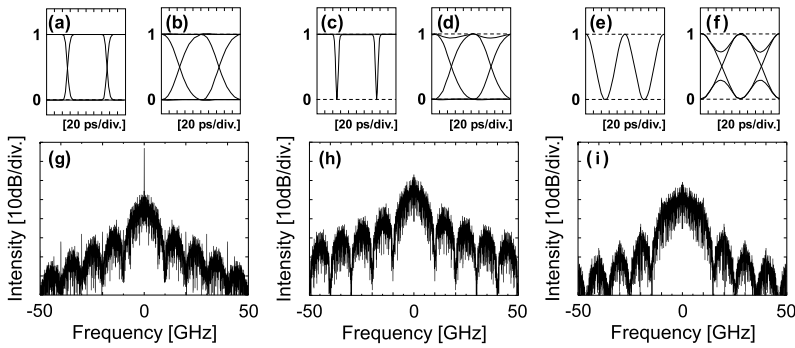


Fig. 8.38 Calculated 10 Gbit/s eye diagrams and optical spectra for (a, b, g) NRZ, (c, d, h) optical DPSK, and (e, f, i) optical RZ-DPSK signals. (a) Eye diagram for generated NRZ signal. (b) Eye diagram of directly detected NRZ signal with low-pass filter. (c, e) Eye diagrams for generated optical DPSK and RZ-DPSK signals. (d, f) Eye diagrams of demodulated DPSK and RZ-DPSK signals with low-pass filter, and calculated optical spectra for (g) NRZ, (h) DPSK, and (i) RZ-DPSK signals

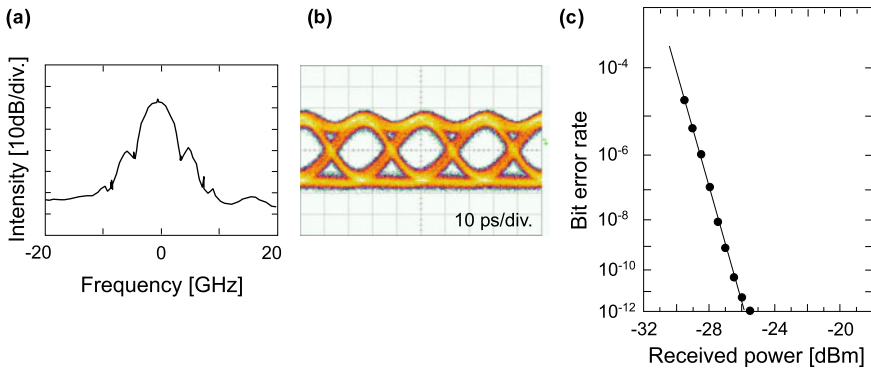


Fig. 8.39 Measured results for differential-drive InP-MZI modulator under 40 Gbit/s DPSK operation. (a) Optical spectrum for generated optical DPSK signal. (b) Eye diagram for demodulated optical DPSK signal, and (c) corresponding bit-error-rate performance

are the calculated optical spectra for NRZ, DPSK, and RZ-DPSK signals, and the comparison of Figs. 8.38(g), (h) demonstrates that the carrier frequency component of the spectrum for DPSK (Fig. 8.38(h)) is well suppressed in contrast to the case of the NRZ-related spectrum (Fig. 8.38(g)). The carrier frequency component of the RZ-DPSK spectrum (Fig. 8.38(i)) is also suppressed, but a slight spectral broadening is observed.

Finally, Fig. 8.39 compiles experimental data illustrating the performance of a differential-drive InP-MZI modulator operated in a 40 Gbit/s DPSK system.

Figure 8.39(a) represents the measured optical spectrum of the 40 Gbit/s DPSK signal. The carrier frequency component is well suppressed. Figures 8.39(b), (c) are the demodulated eye diagram and the bit-error-rate performance, respectively.

Clear eye opening can be observed in the demodulated optical signal (Fig. 8.39(b)), and Fig. 8.39(c) illustrates that error-free operation can be obtained with 40 Gbit/s DPSK signals generated by a differential-drive InP-MZI modulator, and it clearly demonstrates the potential of MZI modulators in high-speed DPSK systems. Similar results obtained with an InP-based InGaAlAs-InAlAs n-i-n modulator have been reported in [123].

8.5.3 Semiconductor Optical DQPSK Modulators

Differential quadrature PSK (DQPSK) is a modulation format slightly more complex than DPSK and the principle can be explained by using the constellation diagrams shown in Fig. 8.40.

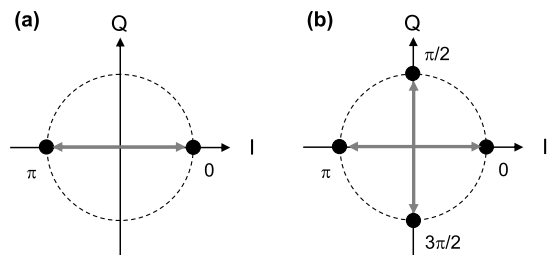
The intensity of all signals is unity, and in the case of DPSK, Fig. 8.40(a), there are two possible states corresponding to the phase either being 0 or π on the I-axis. On the other hand, DQPSK signals, Fig. 8.40(b), may take four phase values: 0 or π on the I-axis and $\pi/2$ or $3\pi/2$ on the Q-axis to express a two-bit signal. The benefits of the DQPSK modulation format compared with DPSK format are:

1. The symbol rate becomes half compared to that of the DPSK format for the same data rate because the bit rate in the DQPSK format is twice that of the symbol rate
2. Spectral broadening becomes smaller which results in higher chromatic dispersion tolerance and reduction of the bandwidth needed for transmitters and receivers, and
3. An increase in spectral efficiency can also be expected.

As outlined in more detail in Chap. 7, Sect. 7.3, a DQPSK transmitter and a corresponding receiver can be designed as illustrated in Fig. 8.41.

The modulator consists of two parallel sub-MZI modulators and a $\pi/2$ phase shifter which are arranged in two branches of a Mach-Zehnder interferometer. The input CW light is divided equally into the two branches, both branches are DPSK-modulated by the two sub-MZI modulators (in-phase (I) MZI modulator and quadrature-phase (Q) MZI modulator), and the $\pi/2$ phase shifter in the Q-arm ensures that the signal obtained after recombining both branches exhibits four different points in the constellation diagram.

Fig. 8.40 Signal constellations for (a) DPSK signal and (b) DQPSK signal



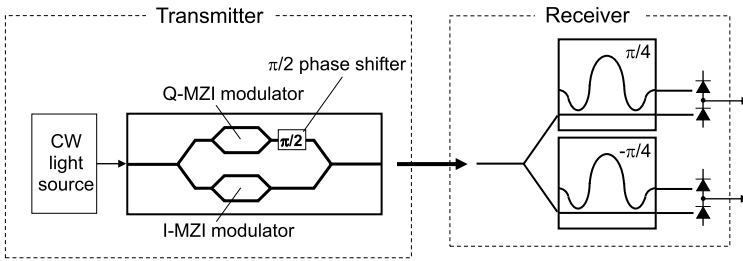


Fig. 8.41 Conventional optical DQPSK transmitter with a DQPSK modulator and receiver for optical DQPSK signals

DQPSK signals can be detected by two MZDIs and two balanced receivers as shown at the right side of Fig. 8.41. The phase differences in the delay lines of the two MZDIs are set to $+\pi/4$ and $-\pi/4$ [110, 112, 116]. Alternatively, novel 90° hybrids with delay lines are proposed and demonstrated as DQPSK receivers [111, 113–115], see also Chap. 7.

Optical DQPSK systems utilize the optical phase, so the spectral linewidth (phase noise) of the CW light sources discussed in [1] affects the performance of the system, and the requirements for the linewidth of the CW light sources are rather demanding as discussed in more detail in [109].

Semiconductor-based DQPSK modulators have been realized on GaAs [124, 125] and on InP substrates as well [126–133].

GaAs: A GaAs/AlGaAs DQPSK modulator reported in [124] has a chip size of $52 \text{ mm} \times 3.5 \text{ mm}$ and uses microwave slow-wave electrodes to achieve wide bandwidth with low driving voltage. The modulator exhibits a half-wavelength voltage V_π of 3.5 V, and 10 Gbit/s ($5 \text{ Gbit/s} \times 2$) operation has been demonstrated. Higher bit rates have been recently achieved with a GaAs-based IQ modulator array for OFDM-PON applications [125], where the bandwidth of the MZI modulators was more than 22 GHz and the half-wavelength voltage V_π was 3 V, which is suitable for a 100 km reach, 40 Gbit/s OFDM-PON supporting up to 1024 users.

InP: Most of the DQPSK modulators reported so far correspond to IQ modulators with two sub-MZI modulators at the branches of the main MZI [127–133], while an alternative solution is a three-arm-interferometer structure with two EAMs [126] where four DQPSK signal phase levels are produced by turning the EAMs on and off. 107 Gbit/s operation has been demonstrated by the very compact chip ($1500 \mu\text{m} \times 250 \mu\text{m}$ in size) but a drawback of the modulator is its large insertion loss of $\sim 34 \text{ dB}$ (excluding fiber coupling loss).

The InP-based DQPSK modulator reported in [127] integrates differential-drive InP-MZI modulators as I and Q modulators. The structure is shown in Fig. 8.42.

Two parallel differential-drive InP-MZI modulators (sub-MZI modulators) and two $\pi/2$ phase shifters are monolithically integrated at the branches of the main Mach-Zehnder interferometer. The two sub-MZI modulators are used for the generation of two optical DPSK signals, and the $\pi/2$ phase shifters are used to adjust the phase difference of the two DPSK signals to $\pi/2$. The length of the

Fig. 8.42 Photograph of InP-DQPSK modulator chip. The size is 7.5 mm × 1.3 mm

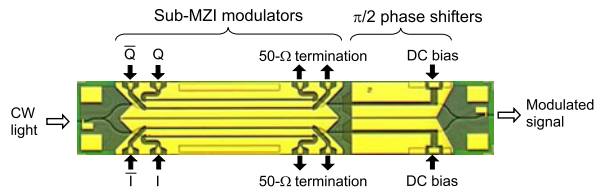


Fig. 8.43 Small signal E/E response S_{21} and reflectance S_{11} of an electrode of the InP-DQPSK modulator

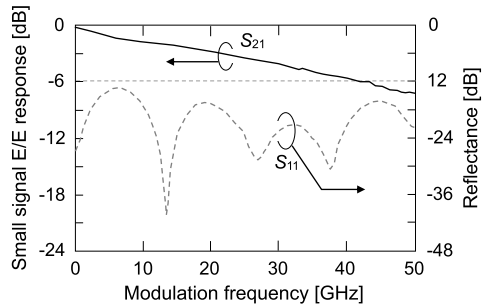
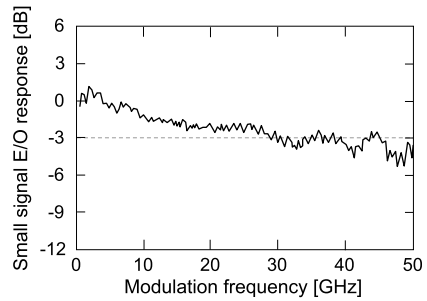


Fig. 8.44 Small signal E/O response of a sub-MZI modulator



phase control waveguides of the sub-MZI modulators is 3 mm, and the length of the $\pi/2$ phase shifters is 1.5 mm. The chip is only 7.5 mm × 1.3 mm in size. It is small enough for being installed into a small package such as a conventional 14-pin butterfly package [128] or into compact modules normally used for mounting conventional lasers and having RF connectors in addition to the standard electrical contacts [129]. Moreover, such InP-based n-p-i-n MZ modulators have also been co-packaged with a widely tunable laser into a transmitter module which enabled full C-band 40 Gbit/s DPSK operation [130]. The waveguide in the InP-DQPSK modulator is realized by introducing a novel n-p-i-n structure where a thin p-doped layer (chosen instead of the SI layer in the corresponding n-i-n structure) acts as a potential barrier against electron carriers. For the integration with semiconductor photonic active devices such as laser diodes, this new structure is more suitable than an n-i-n structure. Figure 8.43 shows the small signal E/E response S_{21} and reflectance S_{11} of a traveling-wave electrode on the modulator.

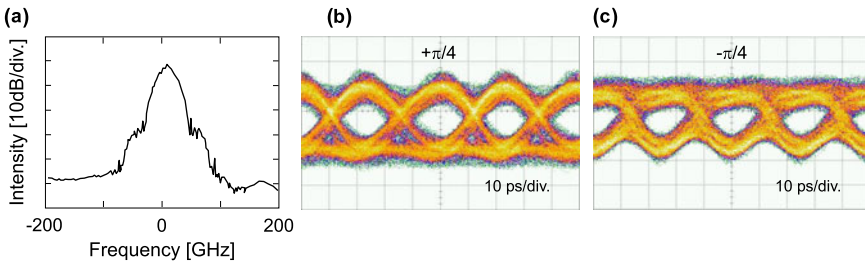


Fig. 8.45 Measured results of InP-DQPSK modulator under 80 Gbit/s operation. (a) Optical spectrum of 80 Gbit/s optical DQPSK signal, (b, c) demodulated signals' eye diagrams

The 6 dB E/O bandwidth exceeds 40 GHz, and the reflectance is below -14 dB up to 50 GHz. Figure 8.44 shows the small signal E/O response of the sub-MZI modulator. The 3 dB E/O bandwidth is measured to be 30 GHz. Thus, the modulator is sufficiently fast for 80 Gbit/s ($40 \text{ Gbit/s} \times 2$) operation, and the results also indicate that the sub-MZI modulators in the InP-DQPSK modulator have essentially the same characteristics as solitary differential-drive InP-MZI modulators. The 80 Gbit/s optical DQPSK signal generation by using the InP-DQPSK modulator is illustrated in Fig. 8.45.

The I and Q modulators are operated at 40 Gbit/s, and the phases of the generated signals are controlled by the $\pi/2$ phase shifters. Figure 8.45(a) shows the optical spectrum for an 80 Gbit/s optical DQPSK signal. The carrier frequency component is well suppressed, and the spectrum corresponds quite well to that of the 40 Gbit/s optical DPSK signal shown in Fig. 8.39(a). This is a clear indication that the 80 Gbit/s optical DQPSK signal has indeed a large chromatic dispersion tolerance. Figures 8.45(b), (c) are the demodulated eye diagrams of the 80 Gbit/s optical DQPSK signal, obtained by using two MZDIs and balanced receivers. The eyes are clearly open, and these results indicate that the InP-DQPSK modulator has high potential for being utilized in future high-speed, highly functional optical communication systems.

The InP-based IQ modulator reported in [131] has been developed for use in a very small pluggable module for coherent 100 Gbit/s systems. Capacitively loaded traveling wave electrodes enabled a 3 dB bandwidth of 40 GHz, V_π was 2.2 V, and an insertion loss of less than 6.5 dB and more than 27 dB extinction ratio have been achieved over the full C-band. A dual IQ modulator module has also been realized for DP-QPSK modulation with polarization multiplexing function [132]. V_π of the modulator was 1.8 V only, the module with a footprint of $34.0 \text{ mm} \times 16.5 \text{ mm}$ included packaged driver ICs, and 128 Gbit/s DP-QPSK operation has successfully been demonstrated. Another InP DP-IQ modulator module has been developed for application within a 100 Gbit/s digital coherent CFP transceiver [133]. 840 km transmission of a 127.2 Gbit/s signal over SMF has been achieved by using forward error correction (FEC) technology.

8.5.4 Semiconductor Multilevel Modulators

Multilevel modulation formats are considered as one promising option for improving the spectral efficiency of optical communication systems and raising the total single channel transmission capacity towards 100 Gbit/s and beyond (see also Chap. 4, Sect. 4.5.2). 16 quadrature amplitude modulation (16QAM) is one format which has received specific current interest and corresponding transmitters have already been realized in different ways, including a monolithic dual-drive (DD) InP Mach-Zehnder modulators [134–139]. The device reported in [134] used an EAM at one arm of the DD MZM as a 6 dB amplitude attenuator. By driving the two arms of the DD MZM with two different 4ASK signals, two QPSK signal are generated and are coupled with 6-dB power difference in the polar coordinates system. This results in the 16QAM format and 50 Gbit/s (12.5 Gsymbol/s \times 4 bit/symbol) signal generation was successfully demonstrated. The same group also realized a 16QAM modulator by integrating an InP twin IQ modulator chip on a silica-based planar lightwave circuit with polarization multiplexing circuit (PLC-PMC) [135]. The chip size was 50 mm \times 13 mm which is about half that of a comparable LiNbO₃-based modulator. Successful generation of 86 Gbit/s by polarization division multiplexing 16QAM signals and successful 240 km transmission has been achieved. A monolithically integrated dual IQ Mach-Zehnder modulator chip, designed for operation in a transmitter optical sub-assembly within a CFP2 pluggable module, has been reported in [136]. Key characteristics are 36 mm \times 10 mm chip size, $V_\pi \approx 2.5$ V and more than 25 dB extinction ratio. The bandwidth was ~ 15 GHz but the response had a linear and uniform roll-off suitable for 16QAM, 32 Gbaud operation using simple pre-emphasis by digital signal processing and enabling 256 Gbit/s total bit rate for dual polarization transmission. Demonstration of 16QAM signal generation was also reported in [137] by using a packaged module including a dual IQ modulator. The modulator chip was the same as previously used for DP-QPSK signal generation [132], however, by using more advanced driver ICs, 224 Gbit/s (dual polarization, 28 Gbaud) generated with a differential driving voltage of 2.5 V_{p-p} have been demonstrated. And the authors also confirmed that the module exhibited a bit-error-rate performance similar to that of commercially available LiNbO₃-based modulators in back-to-back operation.

64QAM signals have also been generated by using GaAs- [138] and InP-based [139] IQ modulators as well. In the case of the GaAs-based IQ modulator [138] V_π was 3 V and the modulation bandwidth exceeded 30 GHz due to the low loss coplanar waveguide configuration and excellent velocity matching. The symbol rate was limited to 25 Gbaud and led to a total data rate of 150 Gbit/s. 64QAM signal generation was also demonstrated by using an InP-based IQ modulator [139]. By compensating the IQ modulator response using a Mach-Zehnder extinction compensator and asymmetry compensators, 336 Gbit/s dual polarization (DP) 64QAM signal generation was successfully demonstrated.

Multilevel optical signal generation was also demonstrated by using a unique optical modulator [140–142]. It consisted of 1 \times 2 and 2 \times 1 MMI couplers as demultiplexer and multiplexer of light, two parallel waveguides (WG) connecting the

MMI couplers with an EA modulator and a phase shifter in each WG. Furthermore, a DFB laser was monolithically integrated with the modulator and the output from the DFB laser was split into two waveguides by the 1×2 MMI coupler, traveled along the WGs and was finally recombined by the 2×1 MMI coupler. The phase shifters were operated in such a way that the phase difference between two waveguides was set to π , and the EA modulators were operated as high speed variable optical attenuators. Driving the EA modulators with two binary signals enabled 20 Gbaud optical DPSK signal generation, and successful 40 km transmission over SSMF has been demonstrated [140]. This novel modulator integrated with the DFB laser was also used to generate multilevel optical signals by applying multilevel electrical signals to the EA modulators, and 224 Gbit/s PDM-2ASK-2PSK signal generation has been achieved [141]. By setting the phase difference between two waveguides to arbitrary angles, non-quadrature intensity modulation signal generation was successfully demonstrated [142] by this “integrated non-quadrature intensity modulation transmitter”.

8.6 Summary and Future Issues

Semiconductor MZI modulators offer a number of advantages such as small size, low driving voltage, and the capability of high-speed operation. Their key properties and recent progress in the development of semiconductor MZI modulators have been described in this chapter. The performance of the semiconductor MZI modulators is expected to improve even further, and they will be deployed in commercial optical communication systems in the near future.

Semiconductor-based MZI modulators can be monolithically integrated with other semiconductor active/passive optoelectronic devices on the same substrate. In this respect, InP-based MZI modulators have an advantage because the laser diodes for optical communication systems are made in the InGaAsP material system using InP substrates (see Chaps. 3–5). Monolithically integrated InP-MZI modulators with tunable lasers are corresponding examples [74–79]. High performance InP-MZI modulators have also been integrated with semiconductor optical amplifiers (SOAs) and very promising performance has been demonstrated [143, 144]. High performance modulators for advanced modulation formats including multilevel modulation have also been investigated energetically to apply them to future very compact transponders for digital coherent systems [77–79, 86, 87, 126, 131–133, 135–142]. Highly functional semiconductor photonic devices will rely on semiconductor MZI modulators and semiconductor phase modulators, and increasingly complex monolithic photonic integrated circuits comprising modulators will be an R&D topic of high relevance in the years to come.

Acknowledgements The authors thank Drs. Ken Tsuzuki and Nobuhiro Kikuchi in the NTT Laboratories, NTT Corporation for their work on the semiconductor modulators and for their fruitful discussions.

References

1. C.H. Henry, Theory of the phase noise and power spectrum of a single mode injection laser. *IEEE J. Quantum Electron.* **QE-19**, 1391–1397 (1983)
2. F. Koyama, K. Iga, Frequency chirping in external modulators. *J. Lightwave Technol.* **6**, 87–93 (1988)
3. G.P. Agrawal, *Nonlinear Fiber Optics* (Academic Press, New York, 1989)
4. K. Tharmalingham, Optical absorption in the presence of a uniform field. *Phys. Rev.* **130**, 2204–2206 (1963)
5. B.O. Seraphin, N. Bottoka, Franz-Keldysh effect of the refractive index in semiconductors. *Phys. Rev.* **139**, A560–A565 (1965)
6. D.A.B. Miller, D.S. Chemla, T.C. Damen, A.C. Gossard, W. Wiegmann, T.H. Wood, C.A. Burrus, Electric field dependence of optical absorption near the band gap of quantum-well structures. *Phys. Rev. B* **32**, 1043–1060 (1985)
7. D.A.B. Miller, D.S. Chemla, D.J. Eilenberger, P.W. Smith, A.C. Gossard, W.T. Tsang, Large room-temperature optical nonlinearity in GaAs/Ga_{1-x}Al_xAs multiple quantum well structures. *Appl. Phys. Lett.* **41**, 679–681 (1982)
8. D.S. Chemla, D.A.B. Miller, P.W. Smith, A.C. Gossard, W. Wiegmann, Room temperature excitonic nonlinear absorption and refraction in GaAs/AlGaAs multiple quantum well structures. *IEEE J. Quantum Electron.* **QE-20**, 265–275 (1984)
9. D.A.B. Miller, D.S. Chemla, S. Schmitt-Rink, Relation between electroabsorption in bulk semiconductors and in quantum wells: the quantum-confined Franz-Keldysh effect. *Phys. Rev. B* **33**, 6976–6982 (1986)
10. D.A.B. Miller, J.S. Weiner, D.S. Chemla, Electric-field dependence of linear optical properties in quantum well structures: waveguide electroabsorption and sum rules. *IEEE J. Quantum Electron.* **QE-22**, 1816–1830 (1986)
11. S. Schmitt-Rink, D.S. Chemla, W.H. Knox, D.A.B. Miller, How fast is excitonic electroabsorption. *Opt. Lett.* **15**, 60–62 (1990)
12. D.A.B. Miller, D.S. Chemla, T.C. Damen, A.C. Gossard, W. Wiegmann, T.H. Wood, C.A. Burrus, Electric field dependence of optical absorption near the band gap of quantum-well structures. *Phys. Rev. B* **32**, 1043–1060 (1985)
13. T.H. Wood, C.A. Burrus, D.A.B. Miller, D.S. Chemla, T.C. Damen, A.C. Gossard, W. Wiegmann, High-speed optical modulation with GaAs/AlGaAs quantum wells in a p-i-n diode structure. *Appl. Phys. Lett.* **44**, 16–18 (1994)
14. R. de L. Kronig, On the theory of dispersion of X-rays. *J. Opt. Sci. Am. Rev. Sci. Instrum.* **12**, 547–558 (1926)
15. H.A. Kramers, La diffusion de la lumière par les atomes. *Atti Cong. Intern. Fis. Como* **2**, 545–557 (1927)
16. F. Devaux, Y. Sorel, J.F. Kerdiles, Chirp measurement and transmission experiment at 10 Gbit/s with Wannier-Stark modulator. *Electron. Lett.* **29**, 814–816 (1993)
17. F. Devaux, Y. Sorel, J.F. Kerdiles, Simple measurement of fiber dispersion and of chirp parameter of intensity modulated light emitter. *J. Lightwave Technol.* **11**, 1937–1940 (1993)
18. Y. Miyazaki, T. Yamatoya, K. Matsumoto, K. Kuramoto, K. Shibata, T. Aoyagi, T. Ishikawa, High-power ultralow-chirp 10-Gb/s electroabsorption modulator integrated laser with ultrashort photocarrier lifetime. *IEEE J. Quantum Electron.* **42**, 357–362 (2006)
19. S. Makino, K. Shinoda, T. Shiota, T. Kitatani, T. Fukamachi, M. Aoki, N. Sasada, K. Naoe, K. Uchida, H. Inoue, Wide temperature (15 °C to 90 °C), 80-km SMF transmission of a 1.55- μ m, 10-Gbit/s InGaAlAs electroabsorption modulator integrated DFB laser, in *Opt. Fiber Commun. and Nat. Fiber Opt. Eng. Conf. (OFC/NFOEC'07)*, Anaheim, CA, USA (2007), Techn. Digest, paper OMS1
20. 10 Gbit/s EML (Electroabsorption modulator integrated lasers), NTT Electronics Corporation, http://www.ntt-electronics.com/en/products/photonics/10Gbps_EML-TOSA.html (as for December, 2014)

21. M. Chacinski, U. Westergren, B. Stoltz, R. Driad, R.E. Makon, V. Hurm, J. Rosenzweig, J. Li, A.G. Steffan, Transceiver modules utilizing travelling-wave electro-absorption modulator, in *Opt. Fiber Commun. and Nat. Fiber Opt. Eng. Conf. (OFC/NFOEC'10)*, San Diego, CA, USA (2010), Techn. Digest, paper OWN4
22. H. Klein, C. Bornholdt, G. Przyrembel, A. Sigmund, W.-D. Molzow, H.-G. Bach, M. Moehrle, 56 Gbit/s InGaAlAs-MQW 1300 nm electroabsorption-modulated DFB-Lasers with impedance matching circuit, in *Proc. 39th Europ. Conf. Opt. Commun. (ECOC'13)*, London, UK (2013), Techn. Digest, paper Th.1.B.5
23. S. Kanazawa, T. Fujisawa, A. Ohki, H. Ishii, N. Nunoya, Y. Kawaguchi, N. Fujiwara, K. Takahata, R. Iga, F. Kano, H. Oohashi, A compact EADFB laser array module for a future 100-Gb/s Ethernet transceiver. *IEEE J. Sel. Top. Quantum Electron.* **17**, 1191–1197 (2011)
24. S. Ristic, M. Florjanczyk, M. Leby, Optoelectronic integrated circuits (OEICs) for 100G Ethernet and coherent networks based on multi-guide vertical integration platform, in *Opt. Fiber Commun. Conf. (OFC'14)*, San Francisco, CA, USA (2014), Techn. Digest, paper Tu3H.6
25. K. Hasebe, T. Sato, K. Takeda, T. Fujii, T. Kakitsuka, S. Matsuo, 50-Gbit/s operation of lateral pin diode structure electro-absorption modulator integrated DFB laser, in *Proc. 40th Europ. Conf. Opt. Commun. (ECOC'14)* Cannes, France (2014), Techn. Digest, paper Mo.4.4.2
26. K.-C. Chang, S.-W. Shen, M.-C. Hsu, Y.-J. Chiu, C.-C. Wei, C.-K. Lee, Negative-chirped EAM-SOA for distance-insensitive optical OFDM transmission in long-reach OFDMA PONs, in *Opt. Fiber Commun. Conf. (OFC'14)*, San Francisco, CA, USA (2014), Techn. Digest, paper Tu3H.4
27. W. Kobayashi, M. Arai, T. Fujisawa, Y. Shibata, T. Sato, T. Ito, K. Hasebe, T. Yamanaka, H. Sanjoh, 40-Gbit/s EADFB laser integrated with short cavity SOA improving chirp characteristics with low power consumption, in *Proc. 40th Europ. Conf. Opt. Commun. (ECOC'14)*, Cannes, France (2014), Techn. Digest, paper Mo.4.4.5
28. T. Watanabe, N. Sakaida, H. Yasaka, F. Kano, M. Koga, Transmission performance of chirp-controlled signal by using semiconductor optical amplifier. *J. Lightwave Technol.* **18**, 1069–1077 (2000)
29. M.E. Chaibi, T. Anfray, K. Kechaou, C. Gosset, L.A. Neto, G. Aubin, C. Kazmierski, P. Chanclou, C. Aupetit-Berthelemot, D. Erasme, Dispersion compensation-free IM/DD SSB-OFDM transmission at 11.11 Gb/s over 200 km SSMF using dual EML. *IEEE Photonics Technol. Lett.* **25**, 2271–2273 (2013)
30. R. Thapliya, S. Nakamura, T. Kikuchi, High speed electro-optic polymeric waveguide devices with low switching voltages and thermal drift, in *Opt. Fiber Commun. and Nat. Fiber Opt. Eng. Conf. (OFC/NFOEC'08)*, San Diego, CA, USA (2008), Techn. Digest, paper OMJ1
31. J. Mallari, C. Wei, D. Jin, G. Yu, A. Barklund, E. Miller, P. O'Mathuna, R. Dinu, A. Motafakker-Fard, B. Jalali, 100 Gbps EO polymer modulator product and its characterization using a real-time digitizer, in *Opt. Fiber Commun. and Nat. Fiber Opt. Eng. Conf. (OFC/NFOEC'10)*, San Diego, CA, USA (2010), Techn. Digest, paper OThU2
32. R.G. Walker, I. Bennion, A.C. Carter, Low-voltage, 50 Ω , GaAs/AlGaAs travelling-wave modulator with bandwidth exceeding 25 GHz. *Electron. Lett.* **25**, 1549–1550 (1989)
33. R.G. Walker, High-speed III–V semiconductor intensity modulators. *IEEE J. Quantum Electron.* **27**, 654–667 (1991)
34. J.S. Cites, P.R. Ashley, High-performance Mach-Zehnder modulators in multiple quantum well GaAs/AlGaAs. *J. Lightwave Technol.* **12**, 1167–1173 (1992)
35. N.A.F. Jaeger, Z.K.F. Lee, Slow-wave electrode for use in compound semiconductor electrooptic modulators. *IEEE J. Quantum Electron.* **28**, 1778–1784 (1992)
36. R. Spickermann, N. Dagli, Experimental analysis of millimeter wave coplanar waveguide slow wave structures on GaAs. *IEEE Trans. Microw. Theory Tech.* **42**, 1918–1924 (1994)
37. S.R. Sakamoto, R. Spickermann, N. Dagli, Narrow gap coplanar slow wave electrode for travelling wave electro-optic modulators. *Electron. Lett.* **31**, 1183–1185 (1995)

38. R. Spickermann, N. Dagli, M.G. Peters, GaAs/AlGaAs electro-optic modulator with bandwidth >40 GHz. *Electron. Lett.* **31**, 915–916 (1995)
39. N.A.F. Jaeger, F. Rahmatian, H. Kato, R. James, E. Berolo, Z.K.F. Lee, Velocity-matched electrodes for compound semiconductor traveling-wave electrooptic modulators: experimental results. *IEEE Microw. Guided Wave Lett.* **6**, 82–84 (1996)
40. R. Spickermann, M.G. Peters, N. Dagli, A polarization independent GaAs–AlGaAs electrooptic modulator. *IEEE J. Quantum Electron.* **32**, 764–769 (1996)
41. R. Spickermann, S.R. Sakamoto, M.G. Peters, N. Dagli, GaAs/AlGaAs travelling wave electro-optic modulator with an electrical bandwidth >40 GHz. *Electron. Lett.* **32**, 1095–1096 (1996)
42. H.R. Khazaei, E. Berolo, F. Ghannouchi, High-speed slow-wave coplanar strip GaAs/AlGaAs electro-optic laser modulator. *Microw. Opt. Technol. Lett.* **19**, 184–186 (1998)
43. L. Mörli, C. Bornholdt, D. Hoffmann, K. Matzen, G.G. Mekonnen, F.W. Reier, A travelling wave electrode Mach-Zehnder 40 Gb/s demultiplexer based on strain compensated GaInAs/AlInAs tunnelling barrier MQW structure, in *Internat. Conf. Indium Phosphide Relat. Mater.* (IPRM'98), Tsukuba, Japan (1998), Techn. Digest, paper WA3-4
44. Y. Cui, P. Berini, Modeling and design of GaAs traveling-wave electrooptic modulators based on capacitively loaded coplanar strips. *J. Lightwave Technol.* **24**, 544–554 (2006)
45. C. Rolland, R.S. Moore, F. Shepherd, G. Hiller, 10 Gbit/s, 1.56 μm multiquantum well InP/InGaAsP Mach-Zehnder optical modulator. *Electron. Lett.* **29**, 471–472 (1993)
46. M. Fetterman, C.-P. Chao, S.R. Forrest, Fabrication and analysis of high-contrast InGaAsP–InP Mach-Zehnder modulators for use at 1.55 μm wavelength. *IEEE Photonics Technol. Lett.* **8**, 69–71 (1996)
47. D.M. Adams, C. Rolland, N. Puetz, R.S. Moore, F.R. Shepherd, H.B. Kim, S. Bradshaw, Mach-Zehnder modulator integrated with a gain-coupled DFB laser for 10 Gbit/s, 100 km NDSF transmission at 1.55 μm . *Electron. Lett.* **32**, 485–486 (1996)
48. O. Leclerc, C. Duchet, P. Brindel, M. Goix, E. Grard, E. Maunand, E. Desurvire, Polarisation-independent InP push-pull Mach-Zehnder modulator for 20 Gbit/s soliton regeneration. *Electron. Lett.* **34**, 1011–1013 (1998)
49. S. Akiyama, S. Hirose, T. Watanabe, M. Ueda, S. Sekiguchi, N. Morii, T. Yamamoto, A. Kuramata, H. Soda, Novel InP-based Mach-Zehnder modulator for 40 Gb/s integrated light-wave source, in *18th IEEE Int. Semicond. Laser Conf.* (ISLC'02), Garmisch-Partenkirchen, Germany (2002), Conf. Digest, paper 57-58
50. K. Tsuzuki, T. Ishibashi, T. Ito, S. Oku, Y. Shibata, R. Iga, Y. Kondo, Y. Tohmori, 40 Gbit/s n - i - n InP Mach-Zehnder modulator with a π voltage of 2.2 V. *Electron. Lett.* **39**, 1464–1466 (2003)
51. I. Betty, M.G. Boudreau, R.A. Griffin, A. Feckes, An empirical model for high yield manufacturing of 10 Gb/s negative chirp InP Mach-Zehnder modulators, in *Opt. Fiber Commun. Conf.* (OFC'05), Anaheim, CA, USA (2005), Techn. Digest, paper OWE5
52. S. Akiyama, H. Itoh, T. Takeuchi, A. Kuramata, T. Yamamoto, Low-chirp 10 Gbit/s InP-based Mach-Zehnder modulator driven by 1.2 V single electrical signal. *Electron. Lett.* **41**, 40–41 (2005)
53. C.H. Henry, R.A. Logan, K.A. Bertness, Spectral dependence of the change in refractive index due to carrier injection in GaAs lasers. *J. Appl. Phys.* **52**, 4457–4461 (1981)
54. B.R. Bennett, R.A. Soref, J.A. del Alamo, Carrier-induced change in refractive index of InP, GaAs, and InGaAsP. *IEEE J. Quantum Electron.* **26**, 113–122 (1990)
55. H.C. Casey Jr., M.B. Panish, *Heterostructure Lasers* (Academic Press, New York, 1978)
56. H.M. Nussenzweig, *Causality and Dispersion Relations* (Academic Press, New York, 1972)
57. T. Hiroshima, R. Lang, Well size dependence of Stark shifts for heavy-hole and light-hole levels in GaAs/AlGaAs quantum wells. *Appl. Phys. Lett.* **49**, 639–641 (1986)
58. S. Namba, Electro-optical effect of zincblends. *J. Opt. Soc. Am.* **51**, 76–79 (1961)
59. J.F. Nye, *Physical Properties of Crystals* (Oxford University Press, New York, 1975)
60. A. Yariv, P. Yeh, *Optical Waves in Crystals* (Wiley, New York, 1984)

61. C.H. Henry, R.A. Logan, H. Temkin, F.R. Merritt, Absorption, emission, and gain spectra of 1.3 μm InGaAsP quaternary lasers. *IEEE J. Quantum Electron.* **QE-19**, 947–952 (1983)
62. H.C. Casey Jr., P.L. Carter, Variation of intervalence band absorption with hole concentration in p-type InP. *Appl. Phys. Lett.* **44**, 82–83 (1984)
63. B.C. Wadell, *Transmission Line Design Handbook* (Artec House, Norwood, 1991)
64. T. Kato, M. Sato, T. Yamase, K. Sato, H. Noguchi, 10-Gb/s-80-km operation of full C-band InP MZ modulator with linear-accelerator-type tiny in-line centipede electrode structure directly driven by logic IC of 90-nm CMOS process, in *Opt. Fiber Commun. and Nat. Fiber Opt. Eng. Conf.* (OFC/NFOEC'11), Los Angeles, CA, USA (2011), Techn. Digest, paper OThP4
65. T. Yamase, M. Sato, H. Noguchi, K. Sato, T. Kato, Low-power multi-level modulation of InP MZM with in-line centipede structure directly driven by CMOS IC, in *18th OptoElectron. Commun. Conf.* (OECC'13), Kyoto, Japan (2013), Techn. Digest, paper WK2-3
66. K.-O. Velthaus, N. Wolf, J.H. Choi, L. Yan, P. Harati, M. Gruner, B.G. Saavedra, M. Rausch, H.-G. Bach, M. Schell, Impedance-engineered low power MZM/driver assembly for CFP4-size pluggable long haul and metro transceiver, in *Proc. 40th Europ. Conf. Opt. Commun.* (ECOC'14), Cannes, France (2014), Techn. Digest, paper Tu.1.1.1
67. Y.-J. Chiu, T.-H. Wu, W.-C. Cheng, F.J. Lin, J.E. Bowers, Enhanced performance in traveling-wave electroabsorption modulators based on undercut-etching the active-region. *IEEE Photonics Technol. Lett.* **17**, 2065–2067 (2005)
68. H. Fukano, T. Yamanaka, M. Tamura, Design and fabrication of low-driving-voltage electroabsorption modulators operating at 40 Gb/s. *J. Lightwave Technol.* **25**, 1961–1969 (2007)
69. HFSSTM – Simulation software for high-performance electronic design, Ansys Inc., <http://www.ansys.com/Support/Platform+Support/Ansoft+Products+14.0> (as for December, 2014)
70. L.B. Soldano, E.C.M. Pennings, Optical multi-mode interference devices based on self-imaging: principles and applications. *J. Lightwave Technol.* **13**, 615–627 (1995)
71. K. Tsuzuki, K. Sano, N. Kikuchi, N. Kashio, E. Yamada, Y. Shibata, T. Ishibashi, M. Tokumitsu, H. Yasaka, 0.3 V_{pp} single-drive push-pull InP Mach-Zehnder modulator module for 43-Gbit/s systems, in *Opt. Fiber Commun.* (OFC'06), Anaheim, CA, USA (2006), Techn. Digest, paper OWC2
72. K. Tsuzuki, H. Kikuchi, E. Yamada, H. Yasaka, T. Ishibashi, 1.3- V_{pp} push-pull drive InP Mach-Zehnder modulator module for 40 Gbit/s operation, in *Proc. 31st Europ. Conf. Opt. Commun.* (ECOC'05), Glasgow, Scotland, UK (2005), Techn. Digest, paper Th2.6.3
73. K. Tsuzuki, N. Kikuchi, Y. Shibata, W. Kobayashi, H. Yasaka, Surface mountable 10-Gb/s InP Mach-Zehnder modulator module for SFF transponder. *IEEE Photonics Technol. Lett.* **20**, 54–56 (2008)
74. Y.A. Akulova, G.A. Fish, P. Koh, P. Kozodoy, M. Larson, C. Schow, E. Hall, H. Marchand, P. Abraham, L.A. Coldren, 10 Gb/s Mach-Zehnder modulator integrated with widely-tunable sampled grating DBR Laser, in *Opt. Fiber Commun. Conf.* (OFC'04), Los Angeles, CA, USA (2004), Techn. Digest, paper TuE4
75. A. Tauke-Pedretti, M.N. Sysak, J.S. Barton, J.W. Raring, L. Johansson, L.A. Coldren, 40-Gb/s series-push-pull Mach-Zehnder transmitter on a dual-quantum-well integration platform. *IEEE Photonics Technol. Lett.* **18**, 1922–1924 (2006)
76. L.A. Johansson, L.A. Coldren, P.C. Koh, Y.A. Akulova, G.A. Fish, Transmission of 10 Gbps duobinary signals using an integrated laser-Mach Zehnder modulator, in *Opt. Fiber Commun. and Nat. Fiber Opt. Eng. Conf.* (OFC/NFOEC'08), San Diego, CA, USA (2008), Techn. Digest, paper OThC4
77. K. Ławniczuk, C. Kazmierski, J.-G. Provost, M.J. Wale, R. Piramidowicz, P. Szczepański, M.K. Smit, X.J.M. Leijtens, InP-based photonic multiwavelength transmitter with DBR laser array. *IEEE Photonics Technol. Lett.* **25**, 352–354 (2013)
78. S.B. Estrella, L.A. Johansson, M.L. Mašanović, J.A. Thomas, J.S. Barton, First monolithic widely tunable photonic coherent transmitter in InP. *IEEE Photonics Technol. Lett.* **25**, 641–643 (2013)

79. A.J. Ward, V. Hill, R. Cush, S.C. Heck, P. Firth, Y. Honzawa, Y. Uchida, Monolithic integration of AlInGaAs DS-DBR tunable laser and AlInGaAs MZ modulator with small footprint, low power dissipation and long-haul 10 Gb/s performance, in *Proc. 39th Europ. Conf. Opt. Commun.* (ECOC'13), London, UK (2013), Techn. Digest, paper P.2.14
80. R.A. Griffin, B. Pugh, J. Fraser, I.B. Betty, K. Anderson, G. Busico, C. Edge, T. Simmons, Compact, high power, MQW InP Mach-Zehnder transmitters with full-band tunability for 10 Gb/s DWDM, in *Proc. 31st Europ. Conf. Opt. Commun.* (ECOC'05), Glasgow, Scotland, UK (2005), Techn. Digest, paper Th2.6.2
81. K. Tsuzuki, N. Kikuchi, H. Sanjoh, Y. Shibata, K. Kasaya, H. Oohashi, H. Ishii, K. Kato, Y. Tohmori, H. Yasaka, Compact wavelength tunable laser module integrated with n-i-n structure Mach-Zehnder modulator, in *Proc. 32nd Europ. Conf. Opt. Commun.* (ECOC'06), Cannes, France (2006), Techn. Digest, paper Tu3.4.3
82. M.L. Nielsen, K. Tsuruoka, T. Kato, T. Morimoto, S. Sudo, T. Okamoto, K. Mizutani, K. Sato, K. Kudo, Demonstration of 10-Gb/s C + L-band InP-based Mach-Zehnder modulator. *IEEE Photonics Technol. Lett.* **20**, 1270–1272 (2008)
83. Tunable transmitter component, NeoPhotonics TLMZ, <http://www.santurcorp.com/products/productss.aspx?typeid=12> (as for December, 2014)
84. H. Oohashi, Y. Shibata, H. Ishii, Y. Kawaguchi, Y. Kondo, Y. Yoshikuni, Y. Tohmori, 46.9-nm wavelength-selectable arrayed DFB lasers with integrated MMI coupler and SOA, in *Internat. Conf. Indium Phosphide Relat. Mater.* (IPRM'01), Nara, Japan (2001), Techn. Digest, paper FB1-2
85. H. Oohashi, H. Ishii, K. Kasaya, Widely tunable DFB laser array (TLA), in *Proc. Internat. Conf. Optical Internet and Next Gen. Network* (COIN-NGNCON'06), Jeju, Korea (2006), Techn. Digest, paper TuB1-2
86. W. Forsysiak, Progress in InP-based photonic components and sub-systems for digital coherent systems at 100 Gbit/s and beyond, in *Proc. 39th Europ. Conf. Opt. Commun.* (ECOC'13), London, UK (2013), Techn. Digest, paper Mo. 3.C.2
87. R.A. Griffin, InP-based high-speed transponder, in *Opt. Fiber Commun. Conf.* (OFC'14), San Francisco, CA, USA (2014), Techn. Digest, paper W3B.7
88. M. Rocks, Calculation of duobinary transmission systems with optical waveguides. *IEEE Trans. Commun.* **COM-30**, 2464–2470 (1982)
89. S. Kuwano, K. Yonenaga, K. Iwashita, 10 Gbit/s repeaterless transmission experiment of optical duobinary modulated signal. *Electron. Lett.* **31**, 1359–1361 (1995)
90. X. Gu, S.J. Dodds, L.C. Blank, D.M. Spirit, S.J. Pycock, A.D. Ellis, Duobinary technique for dispersion reduction in high capacity optical systems – modelling, experiment and field trial. *IEE Proc. Optoelectron.* **143**, 228–236 (1996)
91. K. Yonenaga, S. Kuwano, Dispersion-tolerant optical transmission system using duobinary transmitter and binary receiver. *J. Lightwave Technol.* **15**, 1530–1537 (1997)
92. M. Shtائف, A.H. Gnauck, The relation between optical duobinary modulation and spectral efficiency in WDM systems. *IEEE Photonics Technol. Lett.* **11**, 712–714 (1999)
93. Y. Miyamoto, K. Yonenaga, A. Hirano, H. Toba, K. Murata, H. Miyazawa, 100 GHz-spaced 8 × 43 Gbit/s DWDM unrepeated transmission over 163 km using duobinary-carrier-suppressed return-to-zero format. *Electron. Lett.* **37**, 1395–1396 (2001)
94. R.A. Linke, B.L. Kasper, N.A. Olsson, R.C. Alferness, Coherent lightwave transmission over 150 km fiber lengths at 400 Mb/s and 1 Gb/s data rates using phase modulation. *Electron. Lett.* **22**, 30–31 (1986)
95. K. Emura, S. Yamazaki, S. Fujita, I. Mito, K. Minemura, Over 300 km transmission experiment on a optical FSK heterodyne dual filter detection system. *Electron. Lett.* **22**, 1096–1097 (1986)
96. A.H. Gnauck, R.A. Linke, B.L. Kasper, K.J. Pollock, K.C. Reichmann, R. Valenzuela, R.C. Alferness, Coherent lightwave transmission at 2 Gbit/s over 170 km of optical fiber using phase modulation. *Electron. Lett.* **23**, 286–287 (1987)
97. S. Yamazaki, S. Murata, K. Komatsu, Y. Koizumi, S. Fujita, K. Emura, 1.2 Gbit/s optical DPSK heterodyne detection transmission system using monolithic external-cavity DFB LDs.

- Electron. Lett. **23**, 860–862 (1987)
98. T. Chikama, T. Naitou, H. Onaka, T. Kiyonaga, S. Watanabe, M. Suyama, M. Seino, H. Kuwahara, 1.2 Gbit/s, 201 km optical DPSK heterodyne transmission experiment using a compact, stable external fiber cavity DFB laser module. *Electron. Lett.* **24**, 636–637 (1988)
 99. T. Chikama, S. Watanabe, T. Naito, H. Onaka, T. Kiyonaga, Y. Onoda, H. Miyata, M. Suyama, M. Seino, H. Kuwahara, Modulation and demodulation techniques in optical heterodyne PSK transmission system. *J. Lightwave Technol.* **8**, 309–322 (1990)
 100. H. Kim, P.J. Winzer, Robustness to laser frequency offset in direct-detection DPSK and DQPSK systems. *J. Lightwave Technol.* **21**, 1887–1891 (2003)
 101. M. Serbay, C. Wree, W. Rosenkranz, Implementation of differential precoder for high-speed optical DQPSK transmission. *Electron. Lett.* **40**, 1288–1289 (2004)
 102. Y. Han, G. Li, Impact of RZ pulse carver phase errors on optical DQPSK, in *Opt. Fiber Commun. Conf. (OFC'05)*, Anaheim, CA, USA (2005), Techn. Digest, paper OThO4
 103. I. Morita, N. Yoshikane, Merits of DQPSK for ultrahigh capacity transmission, in *Proc. 18th Annual Meeting of the IEEE Lasers & Electro-Optics Society (LEOS'05)*, Sydney, Australia (2005), Techn. Digest, paper WE5
 104. H.G. Weber, S. Ferber, M. Kroh, C. Schmidt-Langhorst, R. Ludwig, V. Marembert, C. Boerner, F. Futami, S. Watanabe, C. Schubert, Single channel 1.28 Tbit/s and 2.56 Tbit/s DQPSK transmission. *Electron. Lett.* **42**, 178–179 (2006)
 105. A. Sano, H. Masuda, Y. Kisaka, S. Aisawa, E. Yoshida, Y. Miyamoto, M. Koga, K. Hagimoto, T. Yamada, T. Furuta, H. Fukuyama, 14-Tb/s (140 × 111-Gb/s PDM/WDM) CSRZ-DQPSK transmission over 160 km using 7-THz bandwidth extended L-band EDFAs, in *Proc. 32nd Europ. Conf. Opt. Commun. (ECOC'06)*, Cannes, France (2006), Techn. Digest, paper Th4.1.1
 106. A.H. Gnauck, P.J. Winzer, L.L. Buhl, T. Kawanishi, T. Sakamoto, M. Izutsu, K. Higuma, 12.3-Tb/s C-band DQPSK transmission at 3.2 b/s/Hz spectral efficiency, in *Proc. 32nd Europ. Conf. Opt. Commun. (ECOC'06)*, Cannes, France (2006), Techn. Digest, paper Th4.1.2
 107. C. Fürst, J.-P. Elbers, M. Camera, H. Wernz, H. Griesser, S. Herbst, F. Cavaliere, A. Ehrhardt, D. Breuer, D. Frizsche, S. Vorbeck, M. Schneiders, W. Weiershausen, R. Leppla, J. Wendler, M. Schrödel, T. Wuth, C. Fludger, T. Duthel, B. Milivojevic, C. Schulien, 43 Gb/s RZ-DQPSK DWDM field trial over 1047 km with mixed 43 Gb/s and 10.7 Gb/s channels at 50 and 100 GHz channel spacing, in *Proc. 32nd Europ. Conf. Opt. Commun. (ECOC'06)*, Cannes, France (2006), Techn. Digest, paper Th4.1.4
 108. A.H. Gnauck, G. Charlet, P. Tran, P.J. Winzer, C.R. Doerr, J.C. Centanni, E.C. Burrows, T. Kawanishi, T. Sakamoto, K. Higuma, 25.6-Tb/s WDM transmission of polarization-multiplexed RZ-DQPSK signals. *J. Lightwave Technol.* **26**, 79–84 (2008)
 109. S. Savory, A. Hadjifotiou, Laser linewidth requirements for optical DQPSK systems. *IEEE Photonics Technol. Lett.* **16**, 930–932 (2004)
 110. A.H. Gnauck, P.J. Winzer, Optical phase-shift-keyed transmission. *J. Lightwave Technol.* **23**, 115–130 (2005)
 111. C.R. Doerr, D.M. Gill, A.H. Gnauck, L.L. Buhl, P.J. Winzer, M.A. Cappuzzo, A. Wong-Foy, E.Y. Chen, L.T. Gomez, Monolithic demodulator for 40-Gb/s DQPSK using a star coupler. *J. Lightwave Technol.* **24**, 171–174 (2006)
 112. G. Bosco, P. Poggiolini, On the joint effect of receiver impairments on direct-detection DQPSK systems. *J. Lightwave Technol.* **24**, 1323–1333 (2006)
 113. C.R. Doerr, L. Zhang, S. Chandrasekhar, L.L. Buhl, Monolithic DQPSK receiver in InP with low polarization sensitivity. *IEEE Photonics Technol. Lett.* **19**, 1765–1767 (2007)
 114. M. Oguma, Y. Nasu, H. Takahashi, H. Kawakami, E. Yoshida, Single MZI-based 1 × 4 DQPSK demodulator, in *Proc. 33rd Europ. Conf. Opt. Commun. (ECOC'07)*, Berlin, Germany (2007), Techn. Digest, paper 10.3.4
 115. H. Kawakami, E. Yoshida, Y. Miyamoto, M. Oguma, T. Itoh, Simple phase offset monitoring technique for 43 Gbit/s optical DQPSK receiver. *Electron. Lett.* **44**, 437–438 (2008)

116. I. Lyubomirsky, C.-C. Chien, Y.-H. Wang, Optical DQPSK receiver with enhanced dispersion tolerance. *IEEE Photon. Technol. Lett.* **20**, 511–513 (2008)
117. N. Chand, L. Bakker, D. van Veen, R.D. Yadavish, Significant performance advantage of electroabsorption modulator integrated distributed feedback laser (EML) transmitter in transporting multicarrier QAM signals. *J. Lightwave Technol.* **19**, 1462–1468 (2001)
118. M. Ohm, J. Speidel, Quaternary optical ASK-DPSK and receivers with direct detection. *IEEE Photonics Technol. Lett.* **15**, 159–161 (2003)
119. X. Liu, X. Wei, Y.-H. Kao, J. Leuthold, C.R. Doerr, Y. Su, L.F. Mollenauer, Return-to-zero quaternary differential-phase amplitude-shift-keying for long-haul transmission, in *Optical Fiber Commun. Conf. (OFC'04)*, Los Angeles, CA, USA (2004), Techn. Digest, paper FN2
120. K. Sekine, N. Kikuchi, S. Sasaki, S. Hayase, C. Hasegawa, T. Sugawara, 40 Gbit/s, 16-ary (4 bit/symbol) optical modulation/demodulation scheme. *Electron. Lett.* **41**, 430–432 (2005)
121. M. Yoshida, H. Goto, K. Kasai, M. Nakazawa, 64 and 128 coherent QAM optical transmission over 150 km using frequency-stabilized laser and heterodyne PLL detection. *Opt. Express* **16**, 829–840 (2008)
122. J.-X. Cai, C.R. Davidson, D.G. Foursa, L. Liu, Y. Cai, B. Bakhshi, G. Mohs, W.W. Patterson, P.C. Corbett, A.J. Lucero, W. Anderson, H. Li, M. Nissov, A.N. Pillpetskii, N.S. Bergano, Experimental comparison of the RZ-DPSK and NRZ-DPSK modulation formats, in *Opt. Fiber Commun. Conf. (OFC'05)*, Anaheim, CA, USA (2005), Techn. Digest, paper OTHo1
123. Y. Shibata, N. Kikuchi, K. Tsuzuki, W. Kobayashi, H. Yasaka, 40 Gbit/s DPSK modulation using an InGaAlAs–InAlAs MQW n–i–n Mach-Zehnder modulator. *Electron. Lett.* **44**, 1269–1271 (2008)
124. R.A. Griffin, Integrated DQPSK transmitters, in *Opt. Fiber Commun. Conf. (OFC'05)*, Anaheim, CA, USA (2005), Techn. Digest, paper OWE3
125. L. Stampoulidis, E. Giacomidis, M.F. O'Keefe, I. Aldaya, R.G. Walker, Y. Zhou, N. Cameron, E. Kehayas, A. Tsokanos, I. Tomkos, N.J. Doran, L. Zimmermann, Cost-effective broadband GaAs IQ modulator array for long-reach OFDM-PONs, in *Proc. 39th Europ. Conf. Opt. Commun. (ECOC'13)*, London, UK (2013), Techn. Digest, paper We.1.F.4
126. C.R. Doerr, L. Zhang, P.J. Winzer, J.H. Sinsky, A.L. Adamiecki, N.J. Sauer, G. Raybon, Compact high-speed InP DQPSK modulator. *IEEE Photonics Technol. Lett.* **19**, 1184–1186 (2007)
127. N. Kikuchi, H. Sanjoh, Y. Shibata, K. Tsuzuki, T. Sato, E. Yamada, T. Ishibashi, H. Yasaka, 80-Gbit/s InP DQPSK modulator with an n–p–i–n structure, in *Proc. 33rd Europ. Conf. Opt. Commun. (ECOC'07)*, Berlin, Germany (2007), Techn. Digest, paper 10.3.1
128. N. Kikuchi, K. Tsuzuki, Y. Shibata, M. Ishikawa, T. Yasui, H. Ishii, H. Oohashi, T. Ishibashi, T. Akeyoshi, H. Yasaka, F. Kano, Full L-band 40-Gbit/s operation of compact InP-DQPSK modulator module with low constant driving voltage of $3.5 V_{pp}$, in *Proc. 34th Europ. Conf. Opt. Commun. (ECOC'08)*, Brussels, Belgium (2008), Techn. Digest, paper Mo.3.C.4
129. N. Kikuchi, K. Tsuzuki, T. Kurosaki, Y. Shibata, H. Yasaka, High-speed, low-driving voltage dual-drive InP-based Mach-Zehnder modulator. *IEICE Trans. Electron.* **E92-C**, 205–211 (2009)
130. E. Yamada, A. Ohki, N. Kikuchi, Y. Shibata, T. Yasui, K. Watanabe, H. Ishii, R. Iga, H. Oohashi, Full C-band 40-Gbit/s DPSK tunable transmitter module developed by hybrid integration of tunable laser and InP n–p–i–n Mach-Zehnder modulator, in *Opt. Fiber Commun. and Nat. Fiber Opt. Eng. Conf. (OFC/NFOEC'10)*, San Diego, CA, USA (2010), Techn. Digest, paper OWU4
131. E. Rouvalis, C. Metzger, A. Charpentier, T. Ayling, S. Schmid, M. Gruner, D. Hoffmann, M. Hamacher, G. Fiol, M. Schell, A low insertion loss and low V_{π} InP IQ modulator for advanced modulation formats, in *Proc. 40th Europ. Conf. Opt. Commun. (ECOC'14)*, Cannes, France (2014), Techn. Digest, paper Tu.4.4.1
132. N. Kono, T. Kitamura, H. Yagi, N. Itabashi, T. Tatsumi, Y. Yamauchi, K. Fujii, K. Horino, S. Yamanaka, K. Tanaka, K. Yamaji, C. Fukuda, H. Shoji, Compact and low power DP-QPSK modulator module with InP-based modulator and driver ICs, in *Opt. Fiber Commun. and*

- Nat. Fiber Opt. Eng. Conf. (OFC/NFOEC'13)*, Anaheim, CA, USA (2013), Techn. Digest, paper OW1G.2
133. S. Yamanaka, H. Uzawa, T. Ohara, T. Saida, T. Akashi, K. Mori, O. Takeuchi, H. Onaka, K. Takei, K. Terada, S. Aisawa, O. Ishida, 100 Gb/s CFP coherent transceiver enabled by power-optimized DSP, in *19th OptoElectron. Commun. Conf. (OECC'14)*, Melbourne, Australia (2014), Techn. Digest, paper THPDP1-4
 134. E. Yamada, Y. Shibata, K. Watanabe, T. Yasui, A. Ohki, H. Mawatari, S. Kanazawa, R. Iga, H. Ishii, Demonstration of 50 Gbit/s 16QAM signal generation by novel 16QAM generation method using a dual-drive InP Mach-Zehnder modulator, in *Opt. Fiber Commun. and Nat. Fiber Opt. Eng. Conf. (OFC/NFOEC'11)*, Los Angeles, CA, USA (2011), Techn. Digest, paper OMU1
 135. E. Yamada, N. Kikuchi, A. Sano, T. Kobayashi, Y. Shibata, H. Ishii, Y. Miyamoto, 86 Gbit/s PDM 16-QAM signal transmission using InP optical IQ modulator. *Electron. Lett.* **48**, 1486–1487 (2012)
 136. S.C. Heck, S.K. Jones, R.A. Griffin, N. Whitbread, P.A. Bromley, G. Harris, D. Smith, L.N. Langley, T. Goodall, Miniaturized InP dual I&Q Mach Zehnder modulator with full monitoring functionality for CFP2, in *Proc. 40th Europ. Conf. Opt. Commun. (ECOC'14)*, Cannes, France (2014), Techn. Digest, paper Tu.4.4.2
 137. T. Tatsumi, N. Itabashi, T. Ikagawa, N. Kono, M. Seki, K. Tanaka, K. Yamaji, Y. Fujimura, K. Uesaka, T. Nakabayashi, H. Shoji, S. Ogita, A compact low-power 224-Gb/s DP-16QAM modulator module with InP-based modulator and linear driver ICs, in *Opt. Fiber Commun. Conf. (OFC'14)*, San Francisco, CA, USA (2014), Techn. Digest, paper Tu3H.5
 138. D. Korn, P.C. Schindler, C. Stamatidis, M.F. O'Keefe, L. Stampoulidis, R. Schmogrow, P. Zakyntinos, R. Palmer, N. Cameron, Y. Zhou, R.G. Walker, E. Kehayas, I. Tomkos, L. Zimmermann, K. Petermann, W. Freude, C. Koos, J. Leuthold, First monolithic GaAs IQ electro-optic modulator, demonstrated at 150 Gbit/s with 64-QAM, in *Opt. Fiber Commun. and Nat. Fiber Opt. Eng. Conf. (OFC/NFOEC'13)*, Anaheim, CA, USA (2013), Techn. Digest, paper PDP5C.4
 139. N. Kikuchi, R. Hirai, Y. Wakayama, High-speed optical 64QAM signal generation using InP-based semiconductor IQ modulator, in *Opt. Fiber Commun. Conf. (OFC'14)*, San Francisco, CA, USA (2014), Techn. Digest, paper M2A.2
 140. C. Kazmierski, D. Carrara, K. Ławniczuk, G. Aubin, J.-G. Provost, R. Guillet, 12.5 GB operation of a novel monolithic 1.55 μm BPSK source based on prefixed optical phase switching, in *Opt. Fiber Commun. and Nat. Fiber Opt. Eng. Conf. (OFC/NFOEC'13)*, Anaheim, CA, USA (2013), Techn. Digest, paper OW4J.8
 141. G. de Valicourt, M.A. Mestre, P. Jennevé, H. Mardoyan, J.C. Antona, S. Bigo, O. Bertran-Pardo, C. Kazmierski, N. Chimot, F. Blache, A. Garreau, Ultra-compact monolithic integrated InP transmitter at 224 Gb/s with PDM-2ASK-2PSK modulation, in *Opt. Fiber Commun. Conf. (OFC'14)*, San Francisco, CA, USA (2014), Techn. Digest, paper Th5C.3
 142. G. de Valicourt, M.A. Mestre, J.C. Antona, P. Jennevé, H. Mardoyan, S. Bigo, C. Kazmierski, N. Chimot, F. Blache, Integrated non-quadrature intensity modulation transmitter based on prefixed optical phases and intensity modulations, in *Proc. 40th Europ. Conf. Opt. Commun. (ECOC'14)*, Cannes, France (2014), Techn. Digest, paper Tu.4.4.3
 143. T. Yasui, Y. Shibata, K. Tsuzuki, N. Kikuchi, M. Ishikawa, Y. Kawaguchi, M. Arai, H. Yasaka, 10-Gb/s 100-km SMF transmission using InP Mach-Zehnder modulator monolithically integrated with semiconductor optical amplifier. *IEEE Photonics Technol. Lett.* **20**, 1178–1180 (2008)
 144. T. Yasui, Y. Shibata, N. Kikuchi, K. Tsuzuki, Y. Kawaguchi, M. Arai, H. Yasaka, 10-Gbit/s optical duobinary transmission using lossless InP n-p-i-n Mach-Zehnder modulator with semiconductor optical amplifier, in *Internat. Conf. Indium Phosphide Relat. Mater. (IPRM'08)*, Versailles, France (2008), Techn. Digest, paper ThA1.2

Hiroshi Yasaka received the B.S. and M.S. degrees in physics from Kyushu University in 1983 and 1985, and Ph.D. degree in Electronics Engineering from Hokkaido University in 1993. In 1985 he joined Atsugi Electrical Communication Laboratories, Nippon Telegraph and Telephone Corporation (NTT). Since then to 2008, he engaged in research and development on semiconductor photonic devices for optical fiber communication systems. In 2008 he joined Research Institute of Electrical Communication (RIEC) at Tohoku University as a professor and has been engaging in research on highly functional semiconductor photonic devices and their monolithically integrated devices. Professor Yasaka is a member of the Institute of Electronics, Information and Communication Engineers (IEICE), the Japan Society of Applied Physics (JSAP), the Physical Society of Japan (JPS), and IEEE/ Photonics.

Yasuo Shibata received the B.E. and M.E. degrees in electrical engineering, and Ph.D. degree in integrated design engineering from Keio University in 1985, 1987 and 2010, respectively. In 1987, he joined NTT Optoelectronics Laboratories, Nippon Telegraph and Telephone Corporation (NTT), Kanagawa, Japan, where he has been engaged in research on optical switches, optical filters and integrated devices. In 2014 he joined NTT Electronics Corporation. Dr. Shibata is a member of the Institute of Electronics, Information and Communication Engineers (IEICE), the Japan Society of Applied Physics (JSAP) and IEEE/Photonics.

Chapter 9

Wavelength Filters

Herbert Venghaus

Abstract The chapter reviews all relevant filters (to be) used in fibre optic communication and covers generic filter structures including fibre coupler filters and Mach-Zehnder interferometers, diffraction-, arrayed waveguide-, and fibre Bragg gratings, Fabry-Pérot interferometers, thin film- and microring filters, interleavers, and acousto-optic filters. The presentations include the underlying generic physical concepts, implementations as stand-alone filters or subcomponents of optoelectronic integrated circuits, and filter modules. Typical performance data are given in the wavelength and frequency domain, relevant phase properties are discussed as well, and attention is also given to system implications of the various device properties.

9.1 Introduction

The transmission capacity of a single optical fibre is in the range of several ten Tera-bit/s, and in order to make best use of it various concepts have been implemented in the past. One development path has been to raise the bit rate in a single channel. 10 Gbit/s systems using simple on-off keying and direct detection have already been widely deployed. However, device performance at the transmitter and at the receiver side including electronics plus signal degradation during propagation along the optical fibre prevent the extension of this straightforward concept to significantly higher bit rates, so that 100 Gbit/s links are typically realized as coherent systems using dual polarization-quadrature phase shift keying (DP-QPSK, see also Chap. 7), and even higher bit rates are likely to depend on the implementation of higher symbol rates [1].

A second approach in parallel to raising bit rates has been and still is transmitting different wavelengths along a single fibre where each wavelength carries information independently from all other wavelengths. The corresponding technique is called wavelength division multiplexing (WDM), and it has been pursued from the early days of fibre optic communication already [2, 3]. WDM has experienced a

H. Venghaus (✉)
c/o Fraunhofer Institute for Telecommunications, Heinrich-Hertz-Institute, Einsteinufer 37,
10587 Berlin, Germany
e-mail: herbert.venghaus@hhi.fraunhofer.de

particularly strong development push by the availability of the erbium-doped fibre amplifier (EDFA, cf. Chap. 12) in the 90-ies of the last century. The parallel transmission of up to several ten WDM channels represents the current state-of-the-art, significantly more channels have already been transmitted in parallel along a single fibre in different laboratories [4], and flexible grid transmission (i.e. going beyond the fixed ITU grid) enables to further raise the total transmission capacity per fibre.

More recently space division multiplexing (SDM) has received increasing attention as an additional means to raise the transmission capacity per fibre (see also Chap. 1), and by combining SDM with WDM 2.15 Pbit/s have already been transmitted over 31 km (using a 22 core homogeneous single-mode multi-core fibre) [5], or 105.1 Tbit/s over a trans-oceanic distance of 14,350 km (using a 12-core fibre) [6].

WDM systems do on the one hand need wavelength-selective transmitters (see Chaps. 3 and 5), but they also require wavelength filters which enable the selection, adding/dropping, and routing of individual wavelengths or wavelength bands as key elements, and these filters will be the topic of the current chapter.

The demands on wavelength filters depend strongly on their functionality and the respective system specifications, and a variety of different types of wavelength filters have been developed in the past and are continuously being further improved. Wavelength filters include adaptations of previously known concepts to the specific requirements of fibre optics (e.g. diffraction and transmission gratings or thin-film filters), planar integrated optics devices (such as arrayed waveguide gratings (AWGs) or microring filters), or they may be closely related to the optical fibre itself (such as fibre coupler filters, fibre Bragg gratings (FBGs), or fibre Fabry-Pérot filters). Filters are normally developed for the spatial separation of a larger number of wavelength channels. However, filters can also be designed with periodic response in such a way that a sequence of incoming wavelength channels is sequentially directed towards 2^N ($N = 1, 2, \dots$) outputs resulting in 2^N data streams with 2^N -times larger channel spacing than the original one. Such devices are called interleavers and enable a cost-efficient upgrading of WDM systems (see Sect. 9.11).

All filters mentioned above will be covered in more detail in the following sections. The treatment will include short summaries of relevant physical principles, the technological realisation of the different filters, and typical performance parameters as well. In accordance with the overall focus of the present book the treatment will be restricted to filters which are relevant for the 1.3 to 1.6 μm wavelength region, and we will consider linear passive optical filters only.

Filters used in WDM-systems can be classified as band-pass-, notch-, low-pass-, high-pass-, and all-pass filters which exhibit the following generic characteristics:

Band-pass filters transmit optical power within a certain wavelength window only while all other wavelengths are reflected or redirected elsewhere. In the case of a single optical channel the role of a band-pass filter is the rejection of noise at all wavelengths other than the optical channel. In multi-wavelength systems band-pass filters are key components for multiplexing and demultiplexing different wavelengths.

Low-pass and high-pass filters provide a sharp cut-off either above or below a particular wavelength and are therefore used for selecting (or rejecting) specific wavelength regions. A low-pass filter transmits long wavelength radiation while short wavelengths are reflected, and for a high-pass filter it is the other way round. **Notch filters** reflect a specific wavelength or narrow wavelength band and exhibit high transmission elsewhere.

Power-equalization filters ensure that wavelength channels in WDM systems have equal optical power. Adding and dropping of channels, non-uniform gain of optical amplifiers, power inequalities of laser sources are among the causes making channel power unequal. Power variations may be small after one span, however, they tend to accumulate and lead to large variations after a number of spans, and therefore power equalization is of high relevance.

All-pass filters transmit a complete wavelength band without any wavelength-dependent attenuation, but they induce a specific wavelength-dependent phase change. Such filters can, for example, be designed to compensate group velocity dispersion.

9.2 Phase Effects

Wavelength filters are fully characterized by their complex wavelength-dependent response, i.e. how the intensity and the phase of transmitted and/or reflected radiation is modified by the filter.

Filters used in fibre optics have traditionally been described primarily with respect to their wavelength-dependent intensity characteristics while the associated phase variations have received significantly less attention. This has been adequate for sufficiently large channel separations and moderate bit rates. However, as the separations between adjacent channels in WDM systems come down to as low as 25 GHz or even less (100 GHz \equiv 0.8 nm wavelength separation at 1.55 μ m) while the bit rates are raised at the same time, the phase characteristics of wavelength filters can no longer be ignored in leading-edge fibre optic systems. Phase-related effects get the more pronounced the narrower the respective filters are, and in addition, the narrower the filters are the closer the channel wavelengths come to the filter edges where phase effects tend to be strongest.

In most cases phase effects are unwanted although the phase characteristics can sometimes be taken advantage of, one corresponding example are fibre Bragg gratings tailored for dispersion compensation.

9.2.1 General Considerations

Filters are described mathematically (see e.g. [7, 8]) in a convenient fashion by means of a complex transfer function $H(\omega) = |H(\omega)| \exp[i\varphi(\omega)]$. If the angular

frequency ω is replaced by the complex variable $z = \exp(i\omega)$, designated as ‘ z -transform’, the new transfer function of digital filters, $H_z(z)$, can be represented as a ratio of polynomials which is true for the filters under consideration in this chapter. Depending on the location of the zeros and poles with respect to the unit circle ($|z| = 1$) filters fall into the two categories of ‘minimum-phase’ and ‘non-minimum-phase’ filters.

A minimum-phase filter results if all zeros are located inside the unit circle, and if a filter is minimum-phase, its amplitude and phase are correlated and can be inferred from each other by a relation analogue to the Kramers-Kronig relation (which links the real and imaginary parts of the dielectric function). The phase and amplitude of minimum-phase filters are said to constitute a Hilbert transform pair [7, 8].

On the other hand, non-minimum-phase filters do not obey the Kramers-Kronig relation. The property of a filter being minimum-phase or not is of high relevance in fibre optics for the following reason: In many cases filters should be narrow, have steep edges, and at the same time the corresponding filters should exhibit negligible dispersion. Non-minimum-phase filters can in principle meet this demand. However, if a filter is minimum-phase, these features cannot be optimized at the same time since steep roll-off implies strong dispersion due to the very nature of Hilbert transform pairs.

Interference filters such as Fabry-Pérot and thin-film filters (TFF) are inherently minimum phase while generalized Mach-Zehnder filters including AWGs are in general not minimum phase. However, the latter statement does only hold for ‘ideal’, i.e. loss-less AWGs, while ‘real’ AWGs which exhibit a certain amount of loss satisfy the minimum-phase condition. Grating filters are minimum-phase in transmission, but this is not always the case when they are used in reflection [8–10]. One possibility to reconcile the conflicting demands for steep filter band edges and flat dispersion at the same time even for minimum-phase filters is the combination of a minimum-phase filter with an appropriate all-pass filter which compensates the filter-induced dispersion [11].

The local slope of the phase response is called the group delay τ_g , and it is defined as the negative derivative of the phase response with respect to the angular frequency ω

$$\tau_g = -d\varphi/d\omega \quad (9.1)$$

(Note: the definition of the group delay is also found with positive sign in the literature, and it is a consequence of the choices of the sign for the phase in the definition of the transfer function and that of the time dependence in the complex representation of the electric field.)

The derivative D of the group delay with respect to wavelength

$$D = d\tau_g/d\lambda \quad (9.2)$$

is called the filter dispersion, typically given in ps/nm. The dispersion slope of filters, $dD/d\lambda$, (given in ps/nm²), does normally also have a significant impact on the performance of high-bit-rate optical networks (see Sect. 9.2.4) and has therefore

to be compensated (designated commonly as “third-order compensation”). In addition, it might be worthwhile to note that the dispersion of optical fibres is generally normalized with respect to length, and the corresponding units are [ps/(nm·km)].

9.2.2 Phase Characterisation Techniques

The dispersion of passive optical devices can be determined in different ways. One experimental method to derive the dispersion of optical components including optical fibres and wavelength filters is the so-called modulation phase-shift or simply phase-shift method [8, 12, 13]. Corresponding experiments provide the group delay τ_g , and the dispersion has to be derived from τ_g by differentiation. The method has two limitations: First, there is an averaging effect due to the fact that the two sidebands of the amplitude-modulated signal probe the dispersion of the device at two different wavelengths and this is a fundamental issue. Second, it might be difficult to numerically differentiate the measured curves in the case of noisy experimental data. The need for numerical differentiation can be overcome by application of the “differential phase-shift technique” which adds a low-speed modulation of the laser wavelength to the otherwise unchanged phase-shift measurement set-up, and this approach enables a direct determination of the dispersion of the device under investigation (fibre, wavelength filter, ...) [14].

Another option for determining the dispersion of optical components including filters is low-coherence interferometry [15], and the so-called dispersion offset method is a further technique, which has initially been proposed for the characterisation of optical fibres and has later been extended to the determination of the dispersion of wavelength filters [16], however, it is not much used in practice.

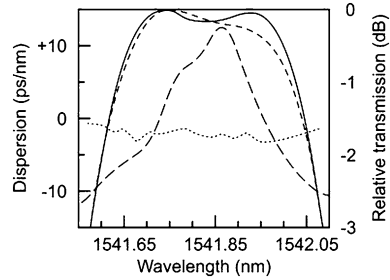
Finally, dual-wavelength heterodyne measurements have also been shown to directly provide the spectral phase and therefore the chromatic dispersion of optical filters with high precision, and the concept has been illustrated for the case of fibre Bragg gratings and thin-film filters as well [17].

9.2.3 Typical Group Delay Characteristics

In the following a few examples of experimental results will illustrate the dispersion characteristics of various filter types (AWG, FBG, TFF, volume phase holographic grating).

Standard AWGs exhibit Gaussian passbands and ideally have zero dispersion ([7, Sect. 4.4.2], [8, Sect. 2.4.4]). Flat top AWGs, which have a passband shape with more favourable properties for system applications (see Sect. 9.6.1.2), may have residual dispersion in the order of a few ps/nm only [18], however, experimentally observed values can be significantly higher. One corresponding example is illustrated in Fig. 9.1. A flat-top silicon-on-insulator- (SOI-)based AWG exhibited

Fig. 9.1 Comparison of dispersion and transmission across passband of AWG without and with phase-error correction. *Long-dashes*: dispersion, no correction; *dotted*: dispersion with correction; *short-dashed*: transmission, no correction; *full curve*: transmission with correction; after [19]



fairly large dispersion initially (long dashes) which turned out to be essentially due to a systematic phase error of the waveguides. After removing this phase error the dispersion appeared significantly improved (and the filter transmission has become more symmetric as well).

The relative group delay (measured using the phase-shift technique with 2 GHz modulation frequency) of two commercial-grade apodized fibre Bragg gratings designed for 100 GHz and 50 GHz channel separation is shown in Fig. 9.2.

The significantly higher group delay observed for the narrower filter is in agreement with expectation.

FBGs are routinely optimized towards two completely different goals: On the one hand, FBGs are designed for operation as filters reflecting a single band. For that purpose dispersion should be as small as possible, and residual dispersion of a few ps/nm has already been reported [20]. On the other hand, one key application of FBGs is for dispersion compensation, and for that purpose FBGs are designed to exhibit very large dispersion as treated in more detail in Sects. 9.7.5 and 9.7.7.

The group delay and related chromatic dispersion of a thin film “4-skip-1” filter (see Sect. 9.9.4) is shown in Fig. 9.3, which elucidates the strong increase of the group delay towards the filter band edges and the corresponding increase of the chromatic dispersion as well. 100 GHz thin film filters are typically specified with 30 ps/nm dispersion while this value increases to about 60 ps/nm for TFFs with an enlarged flat top region (see Sect. 9.9.3.1).

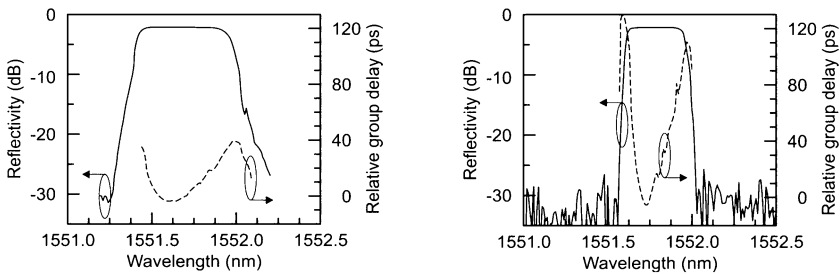


Fig. 9.2 Experimentally determined reflectivity and group delay of apodized fibre Bragg gratings designed for 100 GHz and 50 GHz channel separation (*left* and *right*, respectively, after [8])

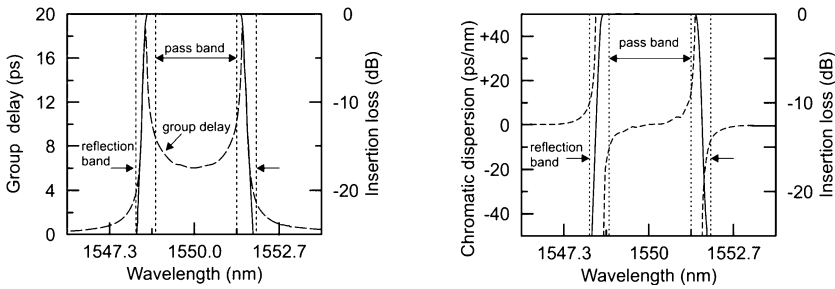
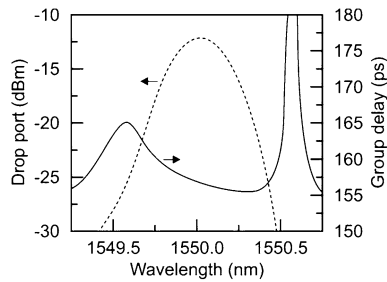


Fig. 9.3 Group delay (*left*) and chromatic dispersion (*right*) of thin-film 4-skip-1 filter [21]

Fig. 9.4 Group delay (*full line*) and drop port intensity (*broken line*) of a tunable volume phase holographic grating (after [22])



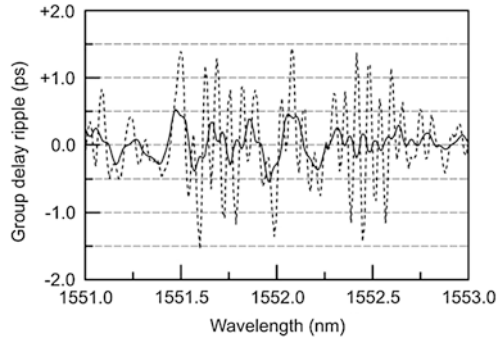
Finally, measurements of the group delay of volume phase holographic gratings (see Sect. 9.5.3) [22] reveal group delay variations of a few ps across the reflected channel, and the results do also illustrate a strong increase of the dispersion towards the passband edges which is the more pronounced the steeper the passband roll-off is (Fig. 9.4).

9.2.4 Group Delay Ripple

WDM filters, in particular gain flattening and dispersion compensating filters based upon thin-film and fibre-grating technologies, do typically exhibit in-band time delay ripples, (“group delay ripple(s)”, GDR) which can equivalently be characterized by the corresponding dispersion, the group delay, or the phase spectrum. Figure 9.5 illustrates (as an example) the GDR of an FBG-based gain flattening filter [23].

Sources of GDR may be design compromises and imperfections such as spurious reflections at the grating ends of FBGs which can be reduced by appropriate apodization [24] (see Sect. 9.7.3). On the other hand, GDR may be due to manufacturing imperfections/variations. Correspondingly, the ripple amplitude of cascaded gain flattening filters (GFF) was found to correspond essentially to the square root of the sum of individual ripple amplitudes squared, indicating that the GDR was not systematic in the GFFs investigated but varied randomly from one GFF to another [23, 25, 26].

Fig. 9.5 Group delay ripple of an FBG-based gain flattening filter; as measured (*broken line*) and averaged over 100 pm (*solid line*), after [23]



A more careful inspection (e.g. by Fourier analysis of the GDR) reveals that a number of different frequency components contribute to the total GDR, and they have different consequences. The low frequency ripple gives essentially rise to a broadening of the input pulse while high frequency ripple tends to create leading and trailing edge satellite pulses.

9.2.5 Systems Implications of Non-ideal Filter Characteristics

The estimation or evaluation of the adverse effects which non-ideal filter phase characteristics have on system performance, is in general a challenging task, and it is not only the filter characteristics itself which matters, but other effects may also be important. For example, (i) filters in real systems are not perfectly aligned (in contrast to re-circulating loop experiments), and (ii) the channel wavelengths of the transmitters are not perfectly aligned to the filter centre wavelengths. As a consequence the filter characteristics off the band centre become more important, and this is particularly relevant for higher bit rates and smaller channel separations. (iii) Signal distortions do not only occur due to passband dispersion [27], but in the case of add-drop multiplexers filter dispersion may also affect signals outside the filter bandwidth [28], in particular those adjacent to the channel selected by the filter.

Investigations (e.g. [28–30]) have further proven that it is not only the filter dispersion itself but the dispersion slope or even higher derivatives of the dispersion, and in particular the group delay ripple which can and normally do significantly degrade network performance.

The influence of GDR on system performance is extremely complex and consequently difficult to assess in a generic fashion. In addition to the GDR-induced broadening of signal bits or the creation of additional spurious spikes, a large number of other dependences have been reported in the literature. Higher GDR amplitudes tend to have larger detrimental effects, and therefore it is generally attempted to make the GDR amplitude as small as possible. The period of the GDR is also of high relevance, and adverse effects are particularly pronounced if the GDR period is close to that of the bit rate (i.e. corresponds to 10 or 40 Gbit/s, which is equivalent to 80 and 320 pm periodicity, respectively). The relative position of the ripple amplitudes with respect to the transmitted bits is important as well [31], and the system

impact of GDR depends on the modulation format used [25, 32], on the specific combination of modulation and signal detection scheme [33], and on pulse shape. The GDR related penalty is also affected by interactions between phase ripples and fibre nonlinearities, and as a consequence the maximum transmission distance decreases with increasing input power to the fibre [34]. Finally, all-optical 2R signal regeneration experiments performed in order to correct pulse distortions introduced by GDR, have demonstrated a dependence of the achievable results on the concept of 2R regeneration applied: Four-wave-mixing based regenerators achieved better performance than their self-phase modulation based counterparts [35].

9.3 Fibre and Planar Directional Couplers

9.3.1 Basics of Coupled Mode Theory

Directional couplers constitute one of the basic components in fibre optical communication [36, 37]) and are primarily implemented as fibre couplers but may be planar devices as well (see Sect. 9.3.5). Fibre couplers can serve different purposes in fibre optic networks. They can be used for passive functionalities as outlined in Chap. 11, and they do also exhibit wavelength-dependent characteristics which can be exploited to fabricate wavelength filters, and this will be the topic of the following section.

If two dielectric waveguides (WG) are located close enough to each other so that the evanescent fields of the modes guided in one of the WGs overlap with the core of the other WG, this arrangement is called a directional coupler, and an appropriately designed directional coupler constitutes a wavelength multiplexer/demultiplexer (MUX/DEMUX) as explained below. More detailed descriptions based on coupled-mode theory are found in many textbooks (e.g. [36–38]), and we will summarize here the most relevant results only.

Let us designate the upper WG in the insert of Fig. 9.6 (leading from port 1 to port 3) as WG ‘*a*’ and the lower WG as ‘*b*’ and represent the electric fields propagating along WG *a* and *b* as

$$E(x, y, z) = E^{(a)}(x, y)a(z) \quad \text{and} \quad E(x, y, z) = E^{(b)}(x, y)b(z) \quad (9.3)$$

where $E^{(i)}(x, y)$ (with $i = a, b$) characterizes the modal distribution of the electric fields in the x, y -plane.

(Please note that in standard S-parameter terminology ‘b’ normally represents back-reflected power, which is different from the definition convention used here!)

For the amplitudes $a(z)$ and $b(z)$ we assume

$$a(z) = a_0 \exp(i\beta_a z) \quad \text{and} \quad b(z) = b_0 \exp(i\beta_b z) \quad (9.4)$$

where β_i ($i = a, b$) are the propagation constants (see also (9.26), below). The total field of the coupled mode $E(z)$ is given by

$$E(x, y, z) = a(z)E^{(a)}(x, y) + b(z)E^{(b)}(x, y) \quad (9.5)$$

and the amplitudes $a(z)$ and $b(z)$ satisfy

$$\frac{d}{dz}a = i\beta_a a + i\kappa_{ab}b \quad \text{and} \quad \frac{d}{dz}b = i\kappa_{ba}a + i\beta_b b \quad (9.6)$$

Since we are not interested in the x, y -dependence but the coupling between the WGs only, we will omit the x, y -dependence in the following, and we will further assume that the electric field intensity has been normalized to 1. If we then make the substitution

$$\begin{bmatrix} a(z) \\ b(z) \end{bmatrix} = \begin{bmatrix} A \\ B \end{bmatrix} \exp(i\beta z) \quad (9.7)$$

assume symmetric coupling, i.e. $\kappa_{ab} = \kappa_{ba} = \kappa$, convert (9.6) into a matrix equation, and solve for non-trivial solutions of the corresponding determinant, we get

$$\beta = \frac{\beta_a + \beta_b}{2} \pm q \quad (9.8)$$

or, rewriting the two solutions of (9.8),

$$\beta_+ = \frac{\beta_a + \beta_b}{2} + q \quad \text{and} \quad \beta_- = \frac{\beta_a + \beta_b}{2} - q \quad (9.9)$$

with

$$q = \sqrt{\Delta^2 + \kappa^2} \quad \text{and} \quad \Delta = \frac{\beta_a - \beta_b}{2} \quad (9.10)$$

The two modes corresponding to the propagation constants β_+ and β_- are designated as “even” and “odd” modes. After finding the eigenvectors corresponding to β_+ and β_- , the general solution for the guided waves can be expressed as

$$\begin{bmatrix} a(z) \\ b(z) \end{bmatrix} = \mathbf{S}(z) \begin{bmatrix} a(0) \\ b(0) \end{bmatrix} \quad (9.11)$$

where the matrix $\mathbf{S}(z)$ is given by

$$\mathbf{S} = \begin{bmatrix} \cos(qz) + i\frac{\Delta}{q}\sin(qz) & i\frac{\kappa}{q}\sin(qz) \\ i\frac{\kappa}{q}\sin(qz) & \cos(qz) - i\frac{\Delta}{q}\sin(qz) \end{bmatrix} \exp(i\varphi z) \quad (9.12)$$

with

$$\varphi = \frac{\beta_a + \beta_b}{2} \quad (9.13)$$

If the input power is launched into the upper waveguide (designated as ‘ a ’), we have

$$a(0) = 1 \quad \text{and} \quad b(0) = 0 \quad (9.14)$$

and for the variation of the electric field amplitudes in the waveguides and the corresponding guided power in the case of identical WGs ($\beta_a = \beta_b$) we get

$$a(z) = \cos(\kappa z) \exp(i\beta z), \quad b(z) = \sin(\kappa z) \exp(i\beta z) \quad (9.15)$$

and

$$P_a = \cos^2(\kappa z), \quad P_b = \sin^2(\kappa z) \quad (9.16)$$

Equations (9.15) and (9.16) represent a periodic power transfer between the two WGs, and the distance after which complete coupling occurs for the first time is called the coupling length L_c , given by

$$L_c = \frac{\pi}{2\kappa} \quad (9.17)$$

The coupling constant κ depends on the distribution of the propagating fields (in particular their evanescent tails), and κ can be considered (to a good approximation) being proportional to $1/\lambda$. As a consequence, the output power in each port of the directional coupler varies periodically as a function of frequency/wavelength if the length of the directional coupler is fixed.

9.3.2 Fabrication of Fibre Couplers

Fibre couplers are most frequently realized as fused biconical taper couplers. Fabrication of the fibre couplers starts with a removal of the cladding in the region where the coupling is intended to occur, and the next fabrication steps are essentially a heating, stretching, and tapering of the two fibres. Due to stretching the fibre core diameters get smaller in the coupling region and as a consequence the confinement of the guided radiation is reduced which enables stronger coupling. The coupling region is typically multimode in contrast to the single-mode characteristics in the feeding branches of the coupler, and therefore it is a key issue in designing and fabricating directional couplers – beyond assuring the proper wavelength-dependent coupling – to make sure that essentially no power is coupled from the fundamental mode to higher order ones in the coupling region as this would give rise to unwanted losses [39, 40].

9.3.3 Characteristics of Fibre Coupler-Based Wavelength Filters

The typical parameters of optical fibres exhibit moderate wavelength-dependent variations, and as a consequence standard fibre coupler filters operate for rather large channel separations. Fibre couplers are commercially available for demultiplexing the 1.3 μm and 1.55 μm channels, demultiplexing a 1625 nm monitoring channel from the 1.3 μm or 1.55 μm band, as pump wavelength combiners for erbium-doped fibre amplifiers (980 nm/1550 nm, 1480 nm/1550 nm, 1054 nm/1550 nm, and 1065 nm/1550 nm multiplexers), and as 1017 nm/1300 nm multiplexers for Pr-doped fibre amplifiers. In addition, fibre-coupler based wavelength filters are offered for CATV or various measurement applications (see also Chap. 11, Sect. 11.2 and Fig. 11.16).

Fig. 9.6 *Upper part:* Schematic presentation of a directional coupler, *lower part:* wavelength-dependent transmission of a fibre coupler (1550/1625 nm MUX/DEMUX) [41]

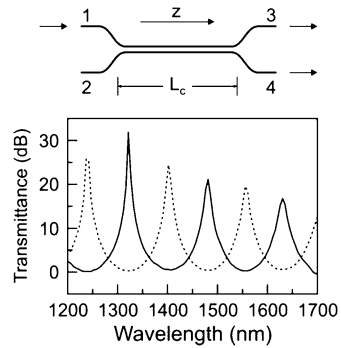


Figure 9.6 illustrates the periodic characteristics of a fibre coupler which has been designed and specified as a 1550/1625 nm MUX/DEMUX, and it also illustrates that the wavelength characteristics of standard fibre couplers do not enable high wavelength discrimination over a larger wavelength range (a crosstalk of the order of 20 dB is a typical requirement). One means to improve performance and in particular to achieve better crosstalk is cascading, and cascaded 1310/1550 nm fibre couplers with crosstalk better than 40 dB have already been demonstrated [42].

9.3.4 Applications Beyond Wavelength Channel Filters

Fibre couplers also enable the splitting of the guided power into any ratio desired. Power splitters or tap couplers are typically offered with splitting ratios ranging from 50:50 to 99:1, and such splitters can be fabricated for any wavelength wanted [43, 44], see also Chap. 11, Sect. 11.2.4. Figure 9.7 illustrates the generic wavelength dependence of different types of power splitters: single wavelength, wavelength flattened and broadband. The example chosen is for 1300 nm and 1550 nm as operation wavelengths and 10:90 splitting ratio, however, the wavelength dependence for other splitting ratios is very much the same.

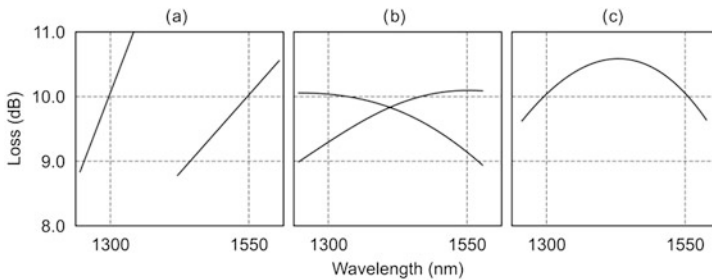


Fig. 9.7 Wavelength-dependence of fibre-coupler based power splitters. (a) Single wavelength, (b) wavelength flattened, (c) broadband [43]

Furthermore, fibre couplers can be designed as pump combiners which enable the combination of two different pump waves into a single fibre or alternatively combining two orthogonally polarized pumps at the same wavelength, and finally, fibre couplers can be designed as gain flattening filters (cf. also thin film filters, Sect. 9.9.1.4) which ensure gain flatness from 1530 nm to 1560 nm with less than ± 0.25 dB deviation from the target value [44].

9.3.5 Planar Polarization Splitters

In planar directional couplers the propagation constants for TE- and TM-polarized modes are in general different, and as a consequence the coupling lengths for the TE- and TM-modes become also different, i.e. planar directional couplers are typically polarization-dependent. By an appropriate choice of the device parameters this feature can be taken advantage of, e.g. by ensuring that TM-polarized waves leave a planar directional coupler via the cross port while TE-modes are guided to the bar port. Corresponding polarization splitters can serve as subcomponents in monolithic integrated polarization diversity chips, in particular in silicon photonics, and highly compact devices based upon Si wires have already been reported. In a two-Si-wire coupler structure of only $7 \times 16 \mu\text{m}^2$ size about 15 dB polarization extinction ratio (PER) has been demonstrated, and the PER could be raised to about 20 dB by adding a second coupler stage [45]. More recently a Si wire based bridged WG coupler (i.e. a structure with three parallel WGs in the central coupling region) exhibited >20 dB polarization extinction ratio and about 2 dB insertion loss over the complete C-band [46]. Alternative designs and references to other implementations can be found in [47].

9.4 Mach-Zehnder Interferometers

Planar Mach-Zehnder interferometers (MZI) constitute an important generic building block for a number of integrated optic devices including couplers, add-drop multiplexers, modulators, switches, routers, interleavers (see Sect. 9.11), polarization beam splitters, or sensors. The basic structure is schematically illustrated in Fig. 9.8, both, as symmetric (left) and asymmetric MZI (right part of figure).

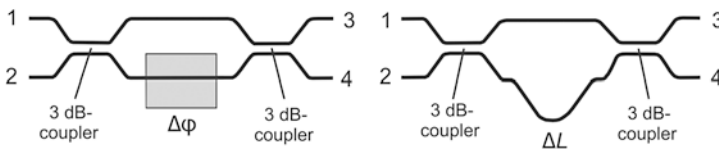


Fig. 9.8 Symmetric (left) and asymmetric Mach-Zehnder interferometer (right), schematic

The intensities at the MZI output ports are related to the input intensities by

$$P_3 = P_1 \sin^2 \frac{\Delta\varphi}{2} + P_2 \cos^2 \frac{\Delta\varphi}{2} \quad (9.18)$$

$$P_4 = P_1 \cos^2 \frac{\Delta\varphi}{2} + P_2 \sin^2 \frac{\Delta\varphi}{2} \quad (9.19)$$

with P_i being the signal power in port i .

The phase difference $\Delta\varphi$ experienced by two waves propagating along the two interferometer arms corresponds to an optical path difference of the two arms, and this path difference may be generated by external means such as an applied voltage (provided the WG material exhibits an electrooptic effect), by carrier injection, by adhesion of molecules in the case of MZI-based sensors, or $\Delta\varphi$ can simply be due to a geometrical path difference due to different WG shape or length (as illustrated in Fig. 9.8, right side).

Single stage MZIs are attractive for high-speed modulation (see Chap. 8) while a combination of two or larger numbers of nested MZIs enables IQ modulation or higher order modulation, respectively (see Chap. 7). Corresponding devices have been developed in various materials systems and have become commercially available for a variety of applications including and going beyond high-speed or IQ modulation (LiNbO₃ [48], SoS [49], InP [50, 51], GaAs [52]).

An (asymmetric) MZI does also constitute a generic filter structure although for most filter applications the transmission characteristics of a single MZI is insufficient due to the limited passband width, passband shape, and insufficient crosstalk properties. However, essentially any filter function can be approximated by cascaded MZIs with properly chosen delays and appropriately chosen coupling constants of the individual MZIs (i.e. the input and output couplers are no longer 3-dB couplers but may have any coupling ratio), and this concept has been used e.g. for the implementation of interleavers ([53], see also Sect. 9.11). Even larger flexibility is achieved by cascading general MZI structures in combination with MRRs [7], see also Sect. 9.10.3.

A large number of advanced components comprising MZIs have been reported in the literature, and recently reported devices include e.g. a wavelength tunable filter based upon MZIs only [54, 55], an MZI-based, cyclic and flat-top MUX/DEMUX for optical sub-carrier multi/demultiplexing in multi-carrier transceivers [56], or an 8×8 switching fabric realised in InAlGaAs/InAlAs on InP, comprising a total of 28 MZI 2×2 switches with switching accomplished by carrier injection into 220 μm long phase shifting sections [57].

Finally, MZIs as polarization beam splitters have also been reported including splitters in the GaInAsP/InP material system [58] and on SOI as well [59, 60] and > 10 dB polarization extinction ratio in the 1.54 to 1.58 μm wavelength range have been demonstrated [60].

9.5 Diffraction Gratings

9.5.1 Planar Diffraction Gratings

A diffraction grating is an arrangement of reflecting (or transmitting) elements separated by a distance comparable to the wavelength of the light (or more general: electromagnetic radiation) under investigation. Typical structures under discussion in the subsequent section are two-dimensional collections of parallel transparent slits or reflecting grooves on an optical surface while fibre Bragg gratings will be discussed in Sect. 9.7.

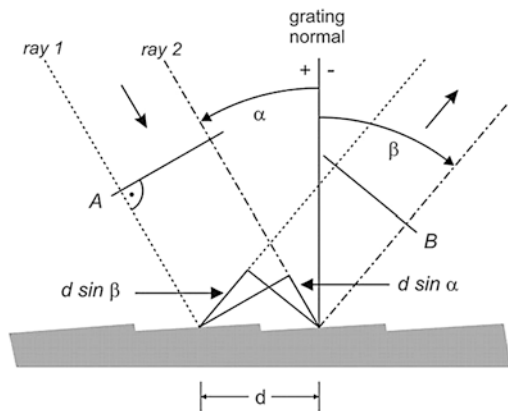
The characteristic property of a diffraction grating is its ability to diffract light into different, wavelength dependent directions. As a consequence, different wavelengths of an incoming beam are angularly separated, and this constitutes the basis for many kinds of spectroscopic investigations and for the fabrication of wavelength filters as well.

Diffraction gratings have been manufactured for more than 200 years, starting with the fabrication of the first diffraction grating by the American astronomer David Rittenhouse in 1785 and spurred by the pioneering work of Joseph von Fraunhofer at the beginning of the 19th century, so that by the end of that century diffraction gratings had become distinctly superior to prisms and interferometers for spectroscopic applications. In the early days the periodic structures had been grooves scratched on a blank surface while different grating variants have emerged subsequently. Gratings can be operated from the UV over the visible range until far into the IR regime, they are used in many different areas of science, and more recently diffraction gratings have found applications in fibre optic communication systems where they serve as wavelength MUX/DEMUX in WDM systems.

The operation of a reflection grating is illustrated in Fig. 9.9 (see e.g. [61–63]).

Ray 1 and ray 2 correspond to light diffracted from adjacent grooves separated by a distance d , and constructive interference occurs (i.e. these rays are in-phase) if their path difference after diffraction is an integral number of wavelengths. This

Fig. 9.9 Diffraction of planar wave fronts from a reflection grating (schematic). A planar wave front is represented by parallel rays such as “ray 1” and “ray 2”. Angles measured (counter-) clockwise are defined as negative (positive). Lines labelled “A” and “B” represent incoming and diffracted wave fronts, respectively



relationship is expressed by the grating equation

$$m\lambda = d(\sin \alpha + \sin \beta) \quad (9.20)$$

(please note that $\sin \beta$ is negative since $\beta < 0$). m is an integer and is called the diffraction order, and $m = 0$ is the special case of normal reflection. A frequently used configuration corresponds to $\alpha = \beta$, i.e. light is diffracted back into the direction where it came from, and this is called the *Littrow configuration*.

9.5.2 Relevant Parameters of Diffraction Gratings

The range of wavelengths for a given diffraction order without any superposition of light from adjacent orders is called the free spectral range (FSR). For telecom applications the FSR of diffraction gratings (typically operated in the first diffraction order) is much larger than the range of all wavelengths used in WDM systems, and thus there is no unwanted coincidence of any telecom channel/wavelength with higher orders of other wavelengths.

The diffraction efficiency of a grating into different orders m exhibits a pronounced wavelength dependence, and as a consequence, the efficiency is also strongly wavelength dependent for a given diffraction order. The efficiency of reflection gratings is particularly high if the directions of the incident and diffracted rays correspond to specular reflection from the grating facets. The corresponding angle θ_{bl} which satisfies the condition

$$m\lambda_{bl} = 2d \sin \theta_{bl} \quad (9.21)$$

is called the *blaze angle* and λ_{bl} is called the *blaze wavelength*, and diffraction gratings are normally designed/chosen in such a way that λ_{bl} corresponds to the centre of the wavelength range the diffraction grating is expected to cover in the application under consideration.

Diffraction gratings do also exhibit strong polarization dependence, however, this dependence can be kept acceptably low over a limited range of wavelengths by an appropriate design. States of polarization are normally designated as s- and p-polarized, however, there are two different definitions: The most widely accepted one is that s- and p-polarization correspond to radiation having the electric field vector orthogonal and parallel to the plane of incidence, respectively. However, s- and p-polarization are also defined as orthogonal and parallel to the grooves of the diffraction grating, and the latter definition is just the opposite of the former for the common configuration where the plane of incidence is orthogonal to the plane of the grooves. If the plane of incidence is not orthogonal to the grooves, there is no relation at all between the two definitions. We will use the former definition throughout this chapter, although the latter is the one more frequently used with diffraction gratings. Alternatively, s- (and p-) polarization are also called TE- (TM-) polarization.

The *resolving power* R or ability of a grating to resolve two closely spaced wavelengths is given by

$$R = \frac{\lambda}{\Delta\lambda} = |m|N \tag{9.22}$$

with m being the diffraction order and N the total number of illuminated grooves (see e.g. [61]). A slightly different expression for the maximum attainable resolving power R_{max} is derived in [62]:

$$R_{max} = \frac{2Nd}{\lambda} \tag{9.23}$$

where Nd is simply the width of the ruled area. Equation (9.23) holds for $|\alpha| \approx 90^\circ$ and $|\alpha| \approx |\beta|$, i.e. for grazing incidence in the Littrow configuration, and it is interesting to note that (9.23) does not depend on the diffraction order m .

9.5.3 Diffraction Gratings Used in Fibre Optic Communication

Diffraction gratings used in fibre optics fall into two categories: surface relief gratings and volume phase (holographic) gratings. Figure 9.9 is an example of a surface relief grating operated in reflection. Such gratings are typically composed of a substrate material, e.g. glass with low thermal expansion coefficient, an epoxy or photoresist structured in such a way as to exhibit the desired surface profile, and a metallic highly reflecting coating on top. Multiplexers and demultiplexers based upon reflection gratings have become commercially available for the C-, the L-, and the C + L-bands with 50, 100 or 200 GHz channel spacing, channel numbers ranging from 8 to 96, and polarization dependent loss <0.3 dB. The characteristics of a corresponding grating-based 40-channel 100 GHz multiplexer is shown in Fig. 9.10.

Another variety of surface relief gratings are surface relief transmission gratings. They are used in many different areas because they can be operated from about

Fig. 9.10 Transmission of diffraction-grating based 40-channel 100 GHz MUX [64]

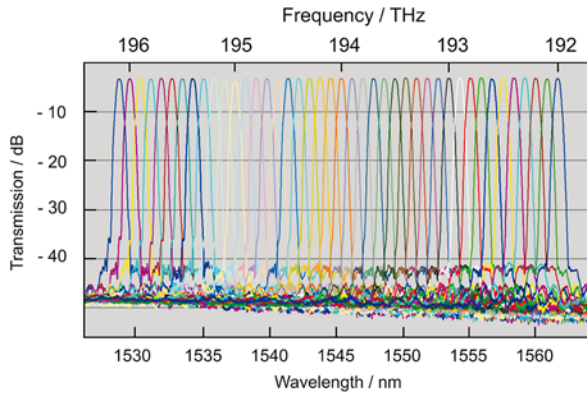
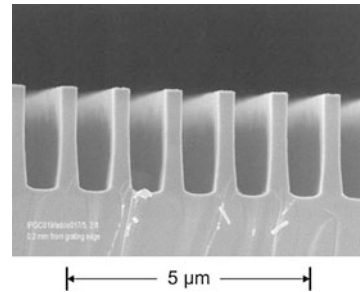


Fig. 9.11 SEM picture of fused silica surface relief transmission grating [65]



200 nm (or even 157 nm) into the mid-IR, exhibit very low absorption loss, are particularly stable with respect to environmental influences, can tolerate high temperature (up to 1000 °C) and high input power of the light to be dispersed, and there are specific designs for telecom applications as well.

A surface relief transmission grating designed for operation in the C-band (1525 to 1575 nm) is shown in Fig. 9.11.

MUX/DEMUXs based upon surface relief transmission gratings have already achieved >97% efficiency and <0.05 dB polarization dependent loss (PDL) all over the C-band, and more than 99% efficiency has been predicted theoretically [65]. Specific details, however, depend on customer requirements and on the overall design and implementation of the MUX/DEMUX.

A third type of diffraction gratings are volume-phase holographic (VPH) gratings consisting of a thin layer with modulated refractive index sandwiched between two glass substrates which makes such gratings particularly rugged. VPH gratings for telecom applications may be fabricated by optically replicating a previously recorded interference pattern, or alternatively, each grating may be an original where a thin film of dichromated gelatine is exposed to a laser interference pattern and laminated with a protective glass cover after proper processing of the film. VPH gratings encapsulated between parallel glass plates may additionally be sandwiched between two precision prisms in such a way that the beam cross-section is enhanced at the grating (providing higher resolution) and the Bragg condition is fulfilled for a particular wavelength, e.g. 1550 nm for telecom applications. VPH gratings are commercially available optimized for operation in the C-, L-, or the S-band [66, 67]. A diffraction-limited resolution of 12.5 GHz all over the C-band has been achieved already, and L- and S-band performance is comparable. Thus VPH gratings can be used in DWDM systems for combining/demultiplexing channels with separations as low as 25 GHz.

Other relevant characteristics of VPH gratings are 0.3 dB PDL, 1 dB uniformity over the complete wavelength range covered, and the total insertion loss may amount to a few dB but can be reduced to as low as 1 dB only if required. Angular resolution at around 1550 nm is typically in the range from 0.1 to 0.3 degrees/nm. VPH gratings exhibit a temperature dependence which is essentially that of the substrate. Zero expansion material, which is well suited for reflection gratings, is insufficient for transmission gratings with respect to optical clarity and homogeneity.

Better (and common) choices are fused silica with a coefficient of thermal expansion $\text{CTE}_{\text{SiO}_2} = 0.5 \times 10^{-6}/\text{K}$ or BK7 ($\text{CTE}_{\text{BK7}} = 7.5 \times 10^{-6}/\text{K}$) where the latter is obviously less favourable, however, significantly less expensive.

Volume phase holographic gratings can also be used for optical channel monitoring, and devices are commercially available covering the complete C or L bands and enabling channel monitoring with 50 GHz channel separation. For such applications the grating as the spectral dispersive element is typically combined with an extremely sensitive detector array (e.g. GaInAs, [66]).

9.5.4 Planar Echelle Gratings

Echelle gratings are a specific type of planar diffraction grating which have a blazing angle optimized for operating the grating in very high diffraction orders, and they usually have larger groove/reflecting facet separation compared to ‘standard’ diffraction gratings. Echelle gratings are encountered in various fields including astronomical instrumentation, and planar echelle gratings are attractive as wavelength-dispersive subcomponents in photonic integrated circuits (PICs).

Echelle gratings have been fabricated in the InP-material system, e.g. as part of multi-wavelength lasers [68] or as demultiplexer in integrated channel monitors [69–71], and they have been developed in silica-on-silicon (SoS) [72], and in particular in the SOI platform [73, 74]. Planar echelle gratings rely on multi-path interference similar to AWGs (see Sect. 9.6), however, in contrast to AWGs, where the light propagates along the arrayed waveguides, light in echelle gratings propagates freely in a light-guiding slab and is eventually reflected by a series of facets [75]. The fact that the crucial region, where dispersion typically accumulates, is a slab waveguide or free-space region without laterally confining waveguides makes echelle gratings the least sensitive to process variations among all filters used in SOI.

Echelle gratings can be designed in different ways, including different variants for the reflecting facets which constitute particularly crucial elements [76, 77]. Device footprint, insertion loss, channel crosstalk, and channel uniformity depend on the specific design, but the following recently reported characteristics of echelle gratings can be considered to represent the current state-of-the-art: 8 channels with 3.2 nm (400 GHz) separation and $250 \times 200 \mu\text{m}^2$ footprint [77] or 30 channels, again with 400 GHz separation, and 0.5 mm^2 footprint [78]. Adjacent channel crosstalk is typically around 20 dB, and insertion loss may be in the 3 to 4 dB range but 1 to 2 dB have also been reported [75]. Planar echelle gratings are strongly polarization dependent and the design is normally made for TE-polarization. A generic shortcoming of echelle gratings for MUX/DEMUX applications is the fact that they exhibit Gaussian passbands [79] whereas a flat top shape would generally be preferred. Despite these limitations echelle gratings can be considered to be superior to AWGs and constituting a good choice for low resolution (CWDM) small channel number monolithic integrated devices [75] with channel separations ranging from a few nm ($\equiv 400 \text{ GHz}$, e.g.) to 20 nm.

9.6 Arrayed Waveguide Gratings

Arrayed waveguide gratings are planar (lightwave) structures based upon an array of waveguides which exhibit both imaging and dispersive properties. The field of an input WG is imaged onto an array of output WGs in such a way that different input wavelengths are imaged onto different output WGs. AWGs were first reported by Smit [80], followed by Takahashi [81] and Dragone [82]. Besides “AWG” other names such as phased array (PHASAR) and waveguide grating router have also been proposed but AWG has become the most commonly used designation.

AWGs are fabricated in various material systems. Silica-on-silicon- (SoS-) based AWGs are the most relevant ones, they are commercially available since 1994 and can be considered to represent by far the best technology for MUX/DEMUX applications in high-channel-count (D)WDM systems. They offer lowest cost per channel, highest uniformity, and lowest loss (<0.05 dB/cm propagation loss and about 0.1 dB fibre chip coupling loss for appropriately chosen parameters, see below). AWGs are available for a wide range of channel spacings with a strong focus on 50 GHz and 100 GHz, and most effort has been (and still is) spent on devices for the 1.5 μm wavelength range although AWGs have been reported for the visible [83] and mid-IR [84] regimes as well.

In addition to AWGs as stand-alone components they have also attracted particular, continuously rising interest as subcomponents of complex integrated ICs, both in the InP- [see Sect. 9.6.3] and the SOI- [see Sect. 9.6.4 and also Chap. 14] material system. Finally, a number of other material systems have also been used for the fabrication of AWGs, e.g. polymer [85, 86], Si_3N_4 [87], and PLZT ((Pb, La)(Zr, Ti) O_3) [88].

9.6.1 Basics of AWGs

9.6.1.1 Operation Principle

A schematic of an AWG demultiplexer is shown in Fig. 9.12, and its operation can be understood as follows [89, 90]: After entering the AWG by the input WG, light propagates across the initial free propagation region (FPR) without lateral guidance so that the incoming intensity gets evenly distributed at the input aperture of the waveguide array before it propagates along the individual WGs towards the output aperture.

The waveguide array is designed in such a way that the optical path difference between adjacent WGs is equal to an integer multiple of the AWG’s (vacuum) centre wavelength (λ_c), and this is equivalent to

$$\Delta L = m \frac{\lambda_c}{n_{eff}} \quad (9.24)$$

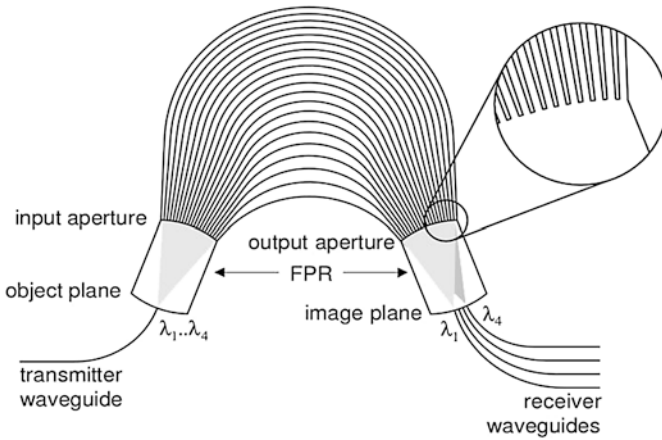


Fig. 9.12 AWG (schematic, after [90]). FPR: free propagation region

Here ΔL is the length difference between adjacent waveguides, the integer m is called the order of the array, n_{eff} is the effective refractive (phase) index of the guided mode. For the operation wavelength λ_c , the fields at the exit of the individual WGs have identical phase (mod 2π) and as a consequence the field distribution at the output aperture is a reproduction of that at the input aperture. Thus the divergent beam at the input aperture is transformed into a convergent beam at the output aperture, and the input field at the entrance of the input FPR gives rise to an image at the exit of the output FPR, i.e. the array behaves like a lens. If the operation wavelength λ is varied, the length increment ΔL of the array gives rise to a phase difference $\Delta\phi$ according to

$$\Delta\phi = \Delta\beta\Delta L \tag{9.25}$$

where

$$\beta = 2\pi\nu n_{eff}/c \tag{9.26}$$

is the propagation constant in the waveguides, $\nu = c/\lambda$ the frequency of the propagating waves, λ their (vacuum) wavelength, and c the vacuum speed of light. The wavelength-dependent phase difference $\Delta\phi$ causes a wavelength-dependent tilt of the outgoing wave front, and this leads to a wavelength-dependent shift of the focal point along the image plane.

The horizontal shift ds of the image point per unit frequency interval $d\nu$ is called the AWG's spatial dispersion D_{sp} and it is given by (as outlined in more detail in [91])

$$D_{sp} = \frac{ds}{d\nu} = \frac{1}{\nu_c} \frac{n_g}{n_{FPR}} \frac{\Delta L}{\Delta\alpha} \tag{9.27}$$

Here ν_c is the frequency corresponding to the centre (vacuum) wavelength, n_{FPR} is the slab mode index in the free propagation region, $\Delta\alpha$ is the divergence angle

between the array waveguides in the fan-in and the fan-out sections, and n_g is the group refractive index of the waveguide mode given by

$$n_g = n_{eff} + v \frac{dn_{eff}}{dv} \quad (9.28)$$

If the change of the input wavelength introduces a phase difference of $\Delta\phi = 2\pi$ between adjacent waveguides, the transfer characteristics of the AWG will be the same as before, i.e. the response is periodic or cyclic. The period is called the free spectral range (FSR). From

$$\Delta\beta = \frac{d\beta}{dv} \Delta v = \frac{2\pi}{c} \frac{d}{dv} (vn_{eff}) \Delta v \quad (9.29)$$

and

$$\frac{d}{dv} (vn_{eff}) = n_{eff} + v \frac{dn_{eff}}{dv} = n_g \quad (9.30)$$

we get

$$\Delta\beta = \frac{2\pi}{c} \left(n_{eff} + v \frac{dn_{eff}}{dv} \right) \Delta v = \frac{2\pi}{c} n_g \Delta v \quad (9.31)$$

and $\Delta\beta \Delta L = 2\pi$ in combination with (9.24) and (9.31) leads to

$$FSR = \frac{vc}{m} \left(\frac{n_{eff}}{n_g} \right) \quad (9.32)$$

Crosstalk problems with adjacent orders are avoided if the FSR is chosen larger than the whole frequency range covered by all channels. As an example, for a demultiplexer with 8 channels and 200 GHz channel spacing, the FSR should amount to at least 1600 GHz. For $\lambda_c \approx 1550$ nm, (9.32) suggests that the order of the array should be about 120 (with $n_{eff}/n_g \approx 0.975$ for the SoS- and $n_{eff}/n_g \approx 0.9$ for the InP-material system, respectively).

The design shown in Fig. 9.12 is the generic structure of a wavelength multiplexer/demultiplexer. AWGs may have more input channels than simply one, and $N \times N$ AWGs are of specific interest for routing applications (see below). Another, particularly compact and space saving AWG variant are reflection type devices. Key characteristics are a single free propagation region, straight arrayed WGs, and reflecting mirrors terminating each WG. Corresponding AWGs have been realized in the InP material system with reflecting facets implemented by lithography plus metal coating of the facets [92], and more recently in the SOI platform with photonic crystal reflectors [93], or Bragg mirror reflectors [94].

9.6.1.2 Passband Shape

The passband shape of standard AWGs is Gaussian. This is not optimum for optical networks where signals typically pass a certain number of wavelength filters and the

effective width of cascaded Gaussian filters becomes fairly narrow. Consequently AWGs are also designed with so-called “flat-top” characteristics, which can be accomplished in different ways. Recent implementations are reported in [95, 96] and references to earlier solutions are given in these publications as well. 1 dB (3 dB) passband width of flat-top AWGs is typically about 50% (75%) of the channel separation compared to 25% (50%) for Gaussian AWGs. The enhanced passband width goes along with an additional insertion loss which depends on the concept chosen. It may be as low as 1 dB [95] but it is typically about 2.5 dB for commercial products [49, 97].

The transmission bands of AWGs do normally exhibit sidelobes which can be attributed to various phenomena including finite array aperture sizes [91], phase errors due to fabrication imperfections [98], coupling between array waveguides [99], propagation of higher-order modes [100], and polarization rotation in the AWG [101]. By proper design and appropriate technology control sidelobe levels can be reduced to about -40 dB (see also Fig. 9.13).

Finally, birefringence (and consequently polarization dependence) and temperature-dependent behaviour may impair AWG performance, and different approaches have been developed to cope with these phenomena [90].

9.6.1.3 Applications

AWGs can serve a wide range of different purposes in fibre optic networks. The most straightforward functionality is combining different wavelengths in multi-wavelength sources or combining and/or separating different wavelength channels in fixed or reconfigurable optical add-drop multiplexers (OADM or ROADM, respectively). (R)OADMs have been designed in many different ways, and various architectures are explained in more detail in [90, 102]. AWGs are a particularly favourable choice for (R)OADMs designed for handling larger numbers of channels (>8).

Moreover, passive optical networks (PONs) can be upgraded by the use of AWGs as they support the overlay of additional WDM channels [90, 103], AWGs enable flexible and dynamic path optical networks [104]. They may be the wavelength dispersive element in optical channel monitoring modules [49], enable optical dispersion compensation [105], and AWGs can be contained in integrated multi-wavelength lasers [106] or multichannel modulators [107].

Finally, cyclic $N \times N$ AWGs allow the routing of an optical signal from any input port to any output by selecting an appropriate signal frequency (e.g. by means of a tunable laser). This routing capability enables the implementation of optical cross-connects, and one area of specific interest in this respect are high performance computing systems and data centres. Their huge bandwidth requirements for processor-to-processor or processor-to-memory interconnects will be in the Tera-byte/s range, and these demands are increasingly difficult to meet on the basis of electrical interconnects. Therefore, optical solutions are considered as a way to overcome these limitations, and AWG-router based concepts are a topic of current research [108, 109].

9.6.2 AWGs in Silica-on-Silicon

As already mentioned, SoS-based AWGs are the variety most widely used in today's fibre optic communication networks. These AWGs are typically fabricated on crystalline flat silicon wafers having 6" or 8" diameter, and this size offers the possibility to fabricate multiple devices on a single wafer and favours cost efficient processing. Fabrication of AWGs is essentially a sequence of glass and silica layer deposition combined with horizontal structuring, i.e. standard pattern transfer based on optical lithography and etching. For depositing the glass and silica layers two different processes are primarily used: flame hydrolysis and chemical vapour deposition (CVD) including low pressure CVD (LPCVD) and plasma enhanced CVD (PECVD) [90].

One key design (and fabrication) parameter of AWGs is the refractive index contrast Δn between the WG core and the cladding. The higher Δn the more compact an AWG can be made as bend radii can be made smaller without unacceptably high (bending) losses. However, larger Δn implies stronger confinement of the guided waves with two unfavourable consequences: (i) scattering losses due to WG side-wall roughness increase, and (ii) the size difference of modes guided in the AWG and in standard single-mode fibre (SMF) gets more pronounced which leads to narrower fibre-chip coupling tolerances and larger fibre-chip coupling losses (unless tapers are used for improving the coupling).

Commercially available AWGs are essentially designed and fabricated with the following different choices of refractive index contrast:

- $\Delta n = 0.30\%$ ($8 \times 8 \mu\text{m}^2$ WG core size and 25 mm minimum bend radius) and
- $\Delta n = 0.45\%$ ($7 \times 7 \mu\text{m}^2$ WG core size and 15 mm minimum bend radius).

Corresponding WGs enable very good coupling to standard SMF and have shown losses as low as 0.017 dB/cm [110], but these favourable characteristics go along with rather large total device size.

- $\Delta n = 0.75\%$ ($6 \times 6 \mu\text{m}^2$ WG core dimension and 5 mm minimum bend radius) represents a good compromise between fairly compact overall device size, relatively low propagation loss (0.035 dB/cm [111]) and still relatively good fibre-chip coupling characteristics. It can therefore be considered the "standard" choice. Typical AWG chip sizes are $30 \times 50 \text{ mm}^2$ for 40 channel-, $25 \times 40 \text{ mm}^2$ for 16 channel-, and $20 \times 20 \text{ mm}^2$ for 4×4 channel devices (*private communication Enablence Technologies Inc.* [112]).
- AWGs with $\Delta n = 1.5$ to 2% (4.5×4.5 to $3 \times 3 \mu\text{m}^2$ WG core size and 2 mm minimum bend radius) can be made really compact but efficient fibre-chip coupling requires tapers and propagation losses are about 0.1 dB/cm.

9.6.2.1 Polarization Dependence

Although WGs are normally designed with square cross section, different thermal expansion coefficients of glass and silicon induce compressive stress in the AWG

structures so that the propagation constants for TE- and TM-polarized waves get different ($\beta_{TE} \neq \beta_{TM}$). As a consequence a wavelength separation $\Delta\lambda$ between the peak transmission for TE- and TM-polarized waves is observed which is given by

$$\Delta\lambda = \frac{1}{m} \Delta L(n_{TE} - n_{TM}) \quad (9.33)$$

where n_{TE} and n_{TM} are the effective refractive indices for TE- and TM polarization, respectively. A typical value for the polarization-dependent peak transmission difference of SoS AWGs is about 30 GHz which is too high for standard channel separations (100 GHz or even smaller) and consequently various concepts have been reported to compensate unwanted birefringence so that <2.5 GHz variation can be ensured [90].

9.6.2.2 Temperature Dependence

The centre wavelength of any output WG of standard SoS AWGs exhibits a temperature-dependent shift $d\lambda/dT \approx -1.5$ GHz/K, and this variation is primarily due to the temperature dependence of the refractive index of the silica glass ($dn/dT = 1.1 \times 10^{-5}/\text{K}$). In order to avoid temperature-dependent adverse effects on system performance several options exist:

AWGs may be operated with a temperature control using either a Peltier cooler or a heater. This is a proven concept, however, specific equipment and electrical power at the site of the AWG is needed.

So-called ‘athermal’ AWGs need no extra equipment nor electrical power, and as a consequence athermal AWGs are attractive for long-haul, METRO, and for WDM-PON applications as well. In order to be suited for outdoor applications, athermal AWGs are required to work in a temperature range from -30 °C to $+70$ °C. Athermal behaviour has been obtained by various means, e.g. by fabricating part of the AWG using a material with refractive index variation $dn/dT < 0$ [113], or by mechanically compensating the temperature drift of the grating [114].

9.6.2.3 Commercially Available AWGs

SoS-based AWGs are commercially available from various suppliers worldwide. They are offered for operation in all wavelength bands (O-, E-, S-, C-, L-band), but there is a clear focus on the 1.55 μm range (C-band). The channel count ranges from 4 to about 80, and up to 128 channels are available on customer demand. Most commercial products are offered for 50, 100, and 200 GHz channel separation although other variants (down to 12.5 GHz) are also on sale, and the passband shape is most frequently Gaussian or flat top. An example of the wavelength characteristics of a commercial 40 channel AWG is shown in Fig. 9.13.

Commercial AWGs do normally require active temperature control, but athermal AWGs are also commercially available.

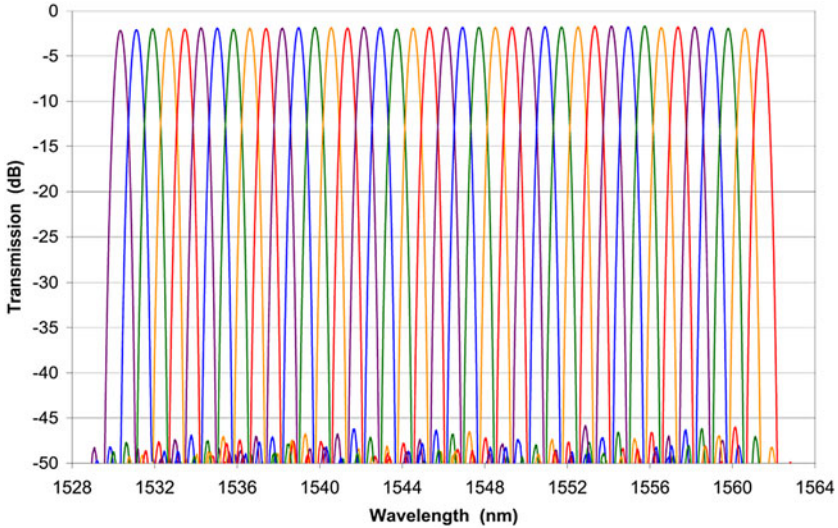


Fig. 9.13 Wavelength characteristics of a 40 channel AWG with Gaussian passband [112]

The cyclic behaviour of AWGs enables the fabrication of so-called ‘colourless’ AWGs. The design of these AWGs is made in such a way that the FSR exactly matches the channel separation times the number of output channels. If a sequence of evenly spaced channels enters a colourless AWG with m output ports, the first m channels leave the AWG via output channels no. 1 to m , and in general the k th channel leaves the AWG via output port $k \pmod{m}$. In practice, colourless AWGs are mostly designed having eight output- and one or two input ports.

The high interest in colourless AWGs comes from cost saving arguments: The complete C-band can accommodate about 96 channels with 50 GHz spacing, however, such a large number of channels is normally not installed at once. Instead, carriers start with a single band comprising eight channels and add more bands as traffic demand grows. If an appropriately designed colourless AWG is available, the same type of AWG can be taken for multiplexing/demultiplexing the individual channels of any of these bands, and thus inventory cost is significantly reduced.

The transmission of a colourless AWG with eight output ports and 50 GHz channel separation is illustrated in Fig. 9.14, where the cyclic characteristics with an 8-channel periodicity can be clearly seen.

Additional typical parameters of commercial AWGs not mentioned so far include 0.2 dB PDL, < 10 ps/nm chromatic dispersion, and 0.5 ps differential group delay. 3 dB can be considered a typical total insertion loss value, and it is also worthwhile to note that the insertion loss varies across the output ports by an amount of 2 to 3 dB, referred to as ‘non-uniformity’.

Beyond $1 \times N$ AWGs as MUX/DEMUX, commercial products also comprise AWG-based optical channel monitors for up to 80 wavelengths [112], as well as $N \times N$ AWG router modules with $N = 4, 8, 16, 24, \text{ or } 32$.

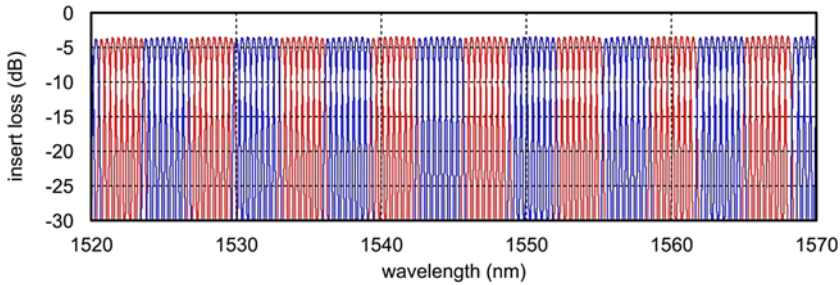


Fig. 9.14 Wavelength characteristics of colourless AWG with 50 GHz channel separation and 400 GHz free spectra range [115]

9.6.2.4 Non-commercial AWGs

Various types of AWGs have been reported in the literature with performance characteristics significantly exceeding those of commercial devices. Examples are AWGs with channel count as high as 400 in a single stage [116] or even 4200 channels in two stage configurations [117]. AWGs have further been developed for coarse WDM (CWDM) applications with 10 or 20 nm channel separation [118], and on the other hand an AWG with 1 GHz channel spacing operating in $m = 11,818$ grating order has also been reported [119].

9.6.3 AWGs in InP

InP-based AWGs constitute, besides SoS-based ones, another relevant variety. Compared to SoS, InP-based waveguides exhibit a significantly higher refractive index contrast, which enables very compact structures so that InP-based AWGs are about two orders of magnitude smaller than SoS-AWGs.

The first AWG fabricated in the GaInAsP material system has been reported in 1992 already [120], but AWGs have not received greater importance as stand-alone components due to inferior performance compared to SoS devices. However, they have attained an ever increasing relevance as subcomponents of higher complexity PICs. Corresponding progress has become particularly impressive during the last few years after the generic building block approach [121] had paved the way for significant progress in monolithic photonic integration.

A large number of PICs comprising AWGs has been developed since 1992 [122] which include multi-wavelength receivers [123], and -lasers [124] polarization demultiplexers [125], optical cross-connects [126], optical switches [127], integrated tunable filters [128], optical routers [129], monolithic multi-channel transmitters [130–132], and a four-channel monolithic polarization-diversity dual-quadrature coherent receiver with balanced detection in InP [133]. In the latter case the key element is a chirped AWG designed in such a way that four wavelength channels are

(i) wavelength- and (ii) polarization demultiplexed and (iii) for each of these channels four AWG output signals are generated, equivalent to the four outputs of a 90° hybrid. The design avoids any waveguide crossings and 4×43 Gbit/s QPSK transmission has been demonstrated. For more details and additional examples of PICs see [134] and also Chaps. 13, 14, and 16.

9.6.4 AWGs in SOI

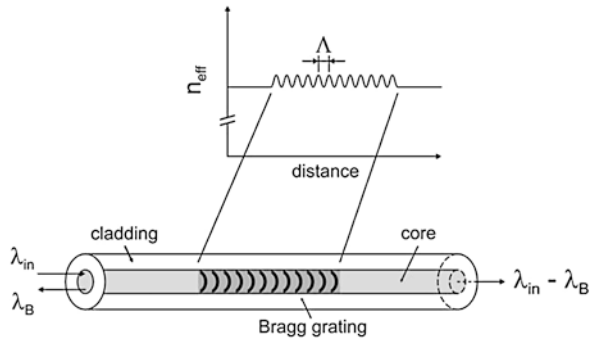
Silicon-on-insulator (SOI) is another material system which enables monolithic photonic integration (frequently designated as “Silicon Photonics”). The key advantage of this approach is the fact that well established CMOS technology can be taken advantage of, and that the high index contrast of this material system enables extremely small device dimensions (although in general at the expense of higher propagation loss and higher sensitivity to phase errors). During the last few years significant progress has been made with respect to the quality and technological reproducibility of individual devices, and at the same time there has been a significant increase of the number of different subcomponents which have been fabricated, both hybrid source structures (lasers, amplifying sections) and passives, and these topics are covered in depth in Chaps. 14 and 15, respectively.

AWGs are among the subcomponents which have successfully been fabricated in Silicon Photonics, most of them as “standard” AWGs but as reflective device as well [135]. As AWGs can be characterized by technical parameters such as channel separation, number of channels, FSR, foot print, etc., material parameters, and performance parameters such as insertion- and polarization dependent loss, crosstalk, etc., and because these parameters typically have interdependencies [136], it is therefore difficult to compile “typical” parameters. Nevertheless, the following should give a reasonable overview: Channel separations reported are frequently in the 100 GHz, 200 GHz, 400 GHz range but separations up to 24 nm or even 32 nm have also been realized [75]. On-chip insertion loss is typically about 1 dB to 3 dB, and crosstalk in the range from 15 dB to 25 dB [137]. Total channel count may be as low as 4 channels only but a 40 channels \times 100 GHz device has also been reported [138], as well as birefringence compensated AWGs [139] and AWGs with flattened response [96]. Finally, dimensions are typically in the several $100 \mu\text{m} \times$ several $100 \mu\text{m}$ regime.

9.7 Fibre Bragg Gratings

In 1978 Hill, Kawasaki and coworkers reported the discovery of photosensitivity of germanium doped optical fibre [140], later it was found that intense UV irradiation of photosensitive fibres created permanent index changes [141], and this spurred the development of fibre Bragg gratings which have found widespread applications since then, in particular in sensing, fibre lasers, and in fibre optic communication as well.

Fig. 9.15 Fibre Bragg Grating (schematic)



9.7.1 Generic Properties

An FBG is essentially a piece of single mode optical fibre with a periodic variation of the core refractive index. In the most simple case the planes of equal refractive index are parallel to the longitudinal axis of the optical fibre, and the index variations have constant period as illustrated in Fig. 9.15.

Light guided by the core and propagating along the FBG will be scattered by each of the grating planes, and in general light scattered from different planes will add up out of phase and will eventually cancel out. On the other hand, if

$$\lambda_B = 2n_{eff} \Lambda \tag{9.34}$$

holds, (where λ_B is the “Bragg wavelength”, n_{eff} is the (mean) effective refractive index experienced by an optical wave propagating along the fibre, and Λ is the period of the index modulation), the small amounts of light scattered from each plane add up constructively and give rise to a back scattered wave. The Bragg condition (9.34) is a straightforward consequence of energy and momentum conservation [142] and leads to a characteristic pit in the transmission spectrum as well as a peak in the reflection spectrum around λ_B .

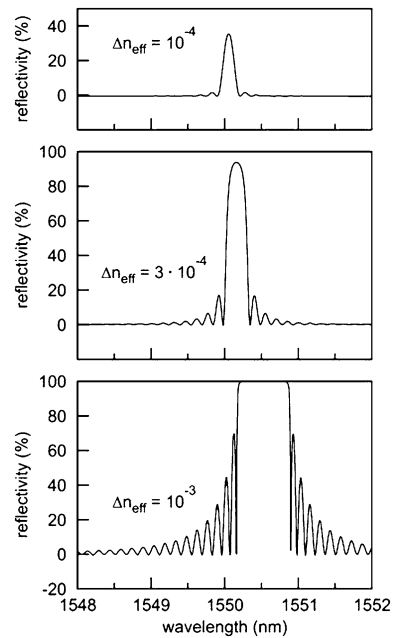
Typical reflection spectra of fibre Bragg gratings are illustrated in Fig. 9.16. The different spectra correspond to different values of refractive index contrast (ranging from 10^{-4} to 10^{-3}), the grating is 5.4 mm long, and $\lambda_B = 1500$ nm [143].

One characteristic and important parameter of any FBG is the width of the reflection band, and neglecting the fact that the detailed characteristics of FBGs depend on various design parameters in a complex manner [142], a good approximation for the full-width at half maximum of the reflection band, $\Delta\lambda_{FWHM}$, is given by [144]

$$\Delta\lambda_{FWHM} = \lambda_B S \sqrt{\left(\frac{\Delta n}{2n_{eff}}\right)^2 + \left(\frac{1}{N}\right)^2} \tag{9.35}$$

where Δn is the variation of the effective refractive index n_{eff} , N is the number of grating planes and S is a parameter varying between 0.5 for weak and 1.0 for strong gratings.

Fig. 9.16 (Calculated) reflectance of 5.4 mm long FBG with different refractive index contrast [143]



A number of key characteristics of FBGs are illustrated by Fig. 9.16: (i) the reflectance increases with higher index contrast, and essentially 100% reflectance can be achieved with appropriate contrast and sufficiently long gratings, (ii) the reflectance curve can be made flat-top as well by these means. (iii) Uniform gratings exhibit pronounced side lobes next to the main reflectance maximum. These side lobes are unwanted for many applications, in particular for channel selection in telecom applications, however, the side lobes can be removed by appropriate grating design as outlined in Sect. 9.7.3. (iv) The shift of the reflectance to longer wavelengths as Δn_{eff} increases is essentially a consequence of the correspondingly larger average effective index in the grating region.

Furthermore, (9.35) suggests that FBG filters get the narrower the longer the gratings are (as long as the index variation is sufficiently weak). This is in principle equivalent to the fact that the resolving power of a diffraction grating rises with increasing number of illuminated grooves. For higher index variation this is no longer true because a wave entering a high index contrast grating region is already completely reflected before reaching the end of the grating so that only a fraction of the grating planes determines the spectral shape of the reflected wave.

The fundamental characteristics of FBGs are a consequence of coupling between modes propagating in the forward direction with back reflected ones. However, the forward propagating mode can also couple to radiation modes, and this effect gives rise to dips in the transmission spectrum on the short-wavelength side of the main transmission minimum without corresponding spectral features in the reflected spectrum [142], but these dips are very much reduced in appropriately designed state-of-the-art FBGs.

Another phenomenon is coupling to cladding modes, which is particularly pronounced in long-period gratings and will be discussed in Sect. 9.7.6.

9.7.2 Types of Gratings

Fibre Bragg gratings are fabricated from fibres with different photosensitivity conditioning, and different inscription procedures are also being used. As a result different types of FBGs are obtained which are normally classified as type I, IA, II, and IIA. For details and additional references see [142, 147].

Type I gratings are generated in normal photosensitive fibres with moderate illumination intensities. The transmission and reflection spectra are complementary, i.e. type I FBGs do not exhibit unwanted loss. They are thermally stable up to about 200 °C and represent the most common variant of FBGs.

Type IA gratings are typically formed after relatively long UV exposure in hydrogenated germanosilicate fibre. The index change, attributed to the creation of colour centres, is particularly strong and gives rise to a pronounced red shift of the Bragg wavelength. Type IA are the least stable FBGs.

The formation of type IIA gratings builds upon the type I inscription process and eventually results in gratings due to material compaction in the grating region [145] so that these gratings are stable up to about 500 °C.

Finally, the refractive index changes giving rise to IIA FBGs are introduced by single excimer laser light pulses of $>0.5 \text{ J/cm}^2$ fluence [147]. The index changes are rather large (up to about 10^{-2}) and are attributed to localized fusion in the fibre core region. Wavelengths longer than λ_B are transmitted by type IIA gratings essentially unaffected while for $\lambda < \lambda_B$ strong coupling to cladding modes occurs associated with pronounced attenuation. The grating structure is stable beyond 800 °C which makes these gratings a particularly good choice for high ambient temperature applications.

9.7.3 Apodization

The strong side lobes observed in the reflectance spectra of FBGs with uniform gratings (Fig. 9.16) can be efficiently reduced by ‘apodization’. Apodized gratings are characterized by a short period index variation (with period length Λ , cf. (9.34)) plus a long-range variation which may have different shape (e.g. Gaussian or ‘raised-cosine’ [146]), and the local variation of the average effective refractive index may be zero or non-zero. Two schematic examples of apodized FBGs are illustrated in Fig. 9.17, one with raised index profile and one without change of the average refractive index. The efficient side lobe suppression is obvious in both cases.

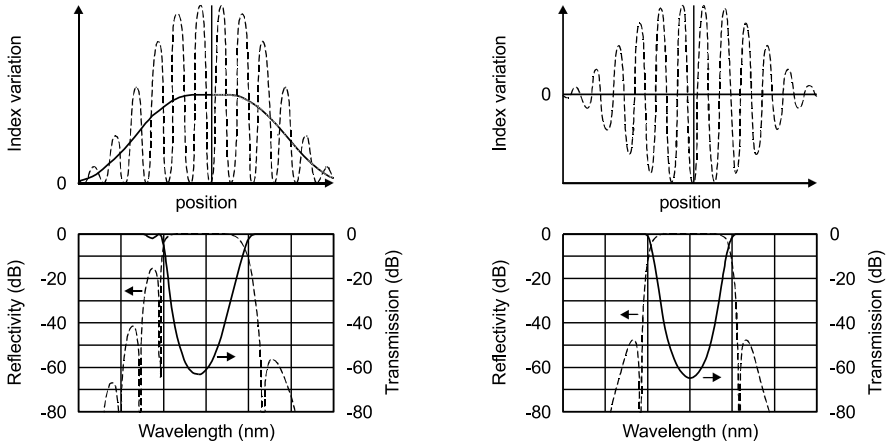


Fig. 9.17 Apodization of FBGs (schematic), with varying (*left*) and constant (*right*) average effective refractive index and corresponding reflectance spectra (after [147]). *Upper figures: dashed lines: local index variation, full lines: average refractive index*

9.7.4 Temperature and Strain Dependence

FBGs exhibit a temperature dependent shift of the reflection band of about 13 pm/K which is essentially due to the coefficient of thermal expansion of the glass forming the fibre core [142]. For telecom applications such a pronounced temperature-induced variation of the FBG channel wavelength(s) is unacceptable, and one straightforward means to suppress this shift is by fixing the FBG onto a submount which exhibits a negative CTE so that the resulting temperature variation is reduced. Typical residual temperature dependence is $<0.5 \dots 1$ pm/K for $-5^\circ\text{C} \leq T \leq +70^\circ\text{C}$ [50, 148–151].

On the other hand, the temperature-induced shift of the reflected wavelength is widely exploited for temperature sensing using FBGs. In a similar way, the reflectance peak of FBGs exhibits a pronounced change due to mechanical strain which is taken advantage of in FBG-based stress sensors.

9.7.5 Chirped Gratings

A chirped grating is an FBG with a refractive index continuously varying across the grating region for example as [142]

$$n(z) = n_{\text{eff}} + \Delta n_{\text{mod}} \times f_{\text{apod}}(z) \times \cos\left(\frac{2\pi}{\Lambda}z - \frac{\pi}{2n_{\text{eff}}\Lambda^2}\Lambda_{\text{ch}}z^2\right) \quad (9.36)$$

where $n(z)$ is the index variation along the fibre axis, Δn_{mod} is the index modulation amplitude, $f_{\text{apod}}(z)$ is the apodization function, and Λ_{ch} is the (dimensionless)

so-called chirp parameter (of the Bragg grating). Due to the variation of the pitch and/or the effective refractive index (characterized by Λ_{ch}) different wavelengths are reflected from different parts of the grating, and the choice of the chirp parameter determines whether a given grating compensates positive or negative (residual) dispersion. Dispersion compensating FBGs (DCG) are normally designed for simultaneously compensating the dispersion and the dispersion slope [152, 153]. The compensation of higher order dispersion derivatives is no issue for telecom applications while in chirped fibres designed for pulse compression higher order dispersion derivatives are being compensated as well.

9.7.6 Long-Period Fibre Bragg Gratings

Period lengths Λ of ‘standard’ FBGs (cf. (9.34)) are in the order of several 100 nm while the periodicity of long-period FBGs (LPG) is in the several 10 μm to several 100 μm range. Such long-range periodic index variations do not induce coupling of counter-propagating modes as ‘normal’ FBGs do, but they give rise to coupling between co-propagating modes [154]. In particular, the core-guided modes couple to forward propagating cladding modes and the latter experience pronounced attenuation due to absorption and scattering which can be observed as an attenuation of the transmitted intensity.

Depending on the details of the grating, coupling to different modes is supported. This is a strongly wavelength-dependent process and does correspondingly offer high design flexibility so that LPGs can be fabricated with essentially any spectral shape in transmission without creating any back reflected light.

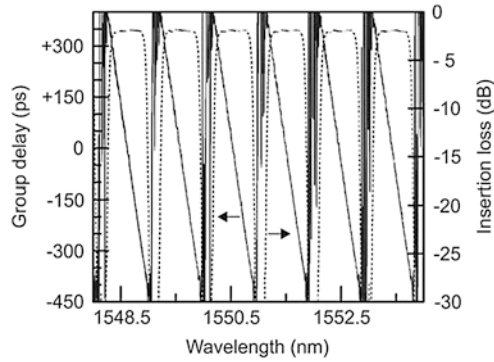
The coupling to different modes has also received specific attention with the recent rise of space division multiplexing (see Chap. 1) where long-period FBGs have been designed as mode converters or mode selectors [155] or for coupling between selected cores [156].

Telecom-applications of LPGs include their use as non-reflecting band rejection filters and as gain flattening filters for EDFAs and Raman amplifiers, in addition, they offer attractive characteristics for sensing applications [157, 158].

9.7.7 Commercially Available Devices

The most relevant commercial application of FBGs is using chirped gratings for dispersion compensation. An alternative solution for dispersion compensation has been (and still is) the use of dispersion compensating fibre (DCF). However, large strands of DCF (many km) are needed which makes this solution fairly bulky. In addition, due to the DCF’s small core dimensions nonlinear interactions (four-wave mixing, self-phase modulation, ...) introduce signal distortions, and DCFs do also add a significant amount of signal attenuation. FBG-based dispersion compensation,

Fig. 9.18 Close-up of channelized dispersion-compensating fibre Bragg grating (100 GHz channel spacing, selected part of 51 channel device, [50]). *Full curves: dispersion, dashed curves: transmission*



on the other hand, does not suffer from any of these shortcomings and thus it is the preferred choice.

DCGs are offered (i) in channelized versions, where the dispersion compensation is tailored to the ITU grid (50 GHz or 100 GHz are standard, but other separations such as 25 GHz or 33 GHz for example are available on customer demand), and these DCGs may cover the complete C-band (from 32 to about 50 channels). A close-up taken from a channelized dispersion compensating Bragg grating which covers the complete C-band (51 channels with 100 GHz separation) is shown in Fig. 9.18. (ii) DCGs are available for continuous dispersion compensation over a wider wavelength range, e.g. the full C-band, or (iii) they come as single channel tunable dispersion compensators. In the latter case the dispersion to be compensated may be as high as ± 3000 ps/nm, alternatively dispersion as low as 0.1 ps/nm can be compensated with high precision.

Fibre Bragg grating-based band filters are commercially available ranging from broadband (several 10 nm) down to very narrowband filters (about 20 pm), and they are also offered for channel selection (primarily for 50 GHz and 100 GHz but for 25 GHz channel separation as well). The separation of individual channels is by no means straightforward when FBGs are used: OADMs for handling a single channel can either be built using two optical circulators (which is a fairly expensive solution) or e.g. using a less expensive twin-core fibre based Mach-Zehnder interferometer design [147]. Therefore, as far as channel filtering is concerned, FBGs seem to be inferior from a cost point of view to thin film filters (for moderate channel counts or for stepwise upgrade of fibre optic systems) or to AWGs (for higher channel count).

Finally, FBGs are also available for locking the wavelengths of EDFA pump lasers or the emission wavelength of DFB lasers where they compete with Fabry-Pérot based solutions (see following paragraph).

9.8 Fabry-Pérot Interferometers

A Fabry-Pérot interferometer (FPI) or etalon consists of a transparent cavity bounded by two reflecting surfaces or by two parallel highly reflecting mirrors. To

be more precise, the former is an etalon and the latter represents an interferometer, but this distinction is not always made in the literature. The transmission spectrum of an FPI as a function of wavelength or frequency is characterised by peaks of large transmission corresponding to resonances of the FPI/etalon. The FPI is named after Charles Fabry and Alfred Pérot [159].

FPI filters have found widespread applications. They are used in order to ensure single mode operation of lasers, they enable spectroscopic applications with specific high demands on spectral resolution, they are used in astronomy for generating pictures at selected wavelengths, and they are found in fibre optic communication systems as well, e.g. for precise locking of laser emission wavelengths in DWDM and ultra DWDM transmitters, wavelength monitoring, laser stabilization for tunable laser modules, and for DWDM channel frequency and optical power monitoring.

9.8.1 Multiple-Reflection Cavities

The wavelength- (or frequency-) dependent transmission of an FPI is due to the interference of multiple reflections of the radiation between the two reflecting surfaces as illustrated schematically in Fig. 9.19.

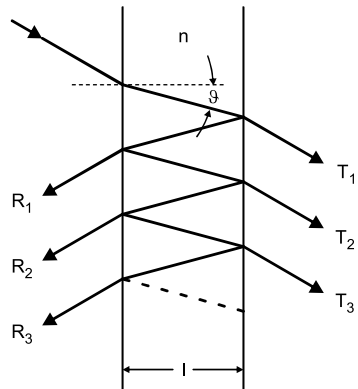
If the transmitted beams are in phase, constructive interference occurs which gives rise to transmission maxima, while low transmission is observed if the transmitted beams are out of phase.

The phase difference between subsequent reflections, δ , is given by

$$\delta = \left(\frac{2\pi}{\lambda}\right)2nl \cos \vartheta \tag{9.37}$$

where λ is the light wavelength in vacuum, ϑ is the angle between the light propagation direction and the normal to the reflecting planes within the cavity, l is the thickness of the cavity, and n is the refractive index of the material within the cavity.

Fig. 9.19 Fabry-Pérot etalon (schematic) illustrating multiple transmitted (T_i) and reflected (R_i) beams



The various transmitted beams constitute a geometrical series and can therefore be summed up easily. This is outlined in detail in numerous (text-) books (e.g. [61, Chap. 7.6] and [160]) and we will present here the final results only. If r and t represent, respectively, the electric field reflection and transmission factors of the mirror plates, and a represents the field attenuation factor of the light travelling through the medium between the mirrors, and with $R = |r|^2$, $T = |t|^2$, $A = |a|^2$ being the corresponding intensities, the transmitted intensity T_{FP} of the FPI is given by

$$T_{FP} = \frac{T_0}{1 + [\frac{2}{\pi} F_R \sin(\frac{\delta}{2})]^2} \quad (9.38)$$

where F_R is defined as

$$F_R = \frac{\pi \sqrt{AR}}{1 - AR} \quad (9.39)$$

and T_0 is given by

$$T_0 = \frac{AT^2}{(1 - AR)^2} = \frac{A(1 - R)^2}{(1 - AR)^2} \quad (9.40)$$

Losses are normally negligible in standard devices. For that reason we will assume zero loss (i.e. $A = 1$) in the following discussion in order to keep the formulae simpler.

9.8.2 Wavelength/Frequency Characteristics

According to (9.38) an FPI exhibits periodic spectral characteristics, and the separation between adjacent transmission peaks represents the free spectral range of the FPI. With λ_0 being the central wavelength of the FPI and c the vacuum speed of light, the FSR is given in terms of wavelength or frequency, respectively, by

$$FSR_\lambda = \frac{\lambda_0^2}{2nl \cos \vartheta + \lambda_0} \approx \frac{\lambda_0^2}{2nl \cos \vartheta} \quad \text{and} \quad FSR_\nu \approx \frac{c}{2nd \cos \vartheta} \quad (9.41)$$

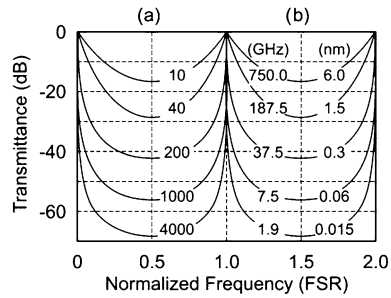
The ratio of the FSR to the full-width half-maximum of any of the transmission bands is called the finesse (FIN). For the wavelength domain we get

$$FIN = \frac{FSR_\lambda}{\Delta\lambda_{FWHM}} = \frac{\pi}{2\arcsin[(1 - R)/2\sqrt{R}]} \quad (9.42)$$

which can be approximated (for $R > 0.5$) by

$$FIN \approx \frac{\pi\sqrt{R}}{(1 - R)} \quad (9.43)$$

Fig. 9.20 (a) Spectral transmission characteristics of FPI filters with fixed FSR (60 nm) for different finesse values (ranging from 10 to 4000), and (b) corresponding 3 dB bandwidth, see [161]



It is worthwhile to note that the effective finesse of an FPI filter may be lower than given by (9.43), e.g. if the mirrors are not perfectly flat or not perfectly aligned, and the finesse is also lower than (9.43) in the presence of loss.

Another important performance parameter is the contrast factor C representing the ratio of maximum to minimum intensity transmission and given by

$$C = \frac{T_{FP,max}}{T_{FP,min}} = \left(\frac{1 + AR}{1 - AR} \right)^2 \tag{9.44}$$

The contrast factor C determines the maximum achievable crosstalk attenuation if an FPI is used for selecting a single channel wavelength out of different channels.

Typical transmission characteristics of FPI filters for different finesse values (or corresponding 3 dB bandwidth for fixed FSR) are illustrated in Fig. 9.20.

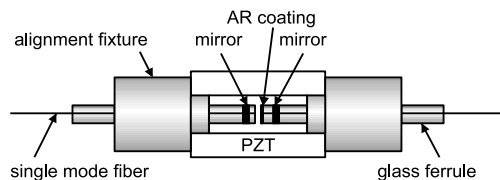
9.8.3 Implementations

Fabry-Pérot interferometers for telecommunication applications are normally made tunable over a reasonable spectral range by providing a means to vary the cavity length. An example of a piezoelectrically driven, tunable, lenseless all-fibre design is illustrated in Fig. 9.21 [161].

With passive temperature compensation the device operation temperature is in the range from $-20\text{ }^\circ\text{C}$ to $+80\text{ }^\circ\text{C}$.

The mirrors of FPI filters can either be metallic or alternatively dielectric multi-layer structures. In the latter case these constitute a special case of dielectric or thin-film multilayer filters/structures covered in more detail in Sect. 9.9.

Fig. 9.21 FPI filter (schematic, cf. [161])



A specific type of FP interferometer is the Gires-Tournois interferometer (GTI) [162]. As for the normal FPI, the cavity of the GTI consists of two parallel reflective plates, but only one of them being partly reflective while the other one is fully reflective so that the GTI can only work in the reflection mode. Apart from that a GTI behaves in the same way as an FPI does. An example of a telecom application is the insertion of a GTI into a Michelson interferometer in such a way that the combination serves as an optical channel interleaver (see Sect. 9.11).

9.8.4 Typical Performance Characteristics

Typical performance characteristics of FPI filters can be summarized as follows: FPI filters are commercially available covering the complete range of the O-, E-, S-, C-, and L-bands, i.e. the wavelength range from 1280 to 1620 nm which corresponds to an FSR of 340 nm or 51 THz. On the other hand, the FSR may be as small as 10 GHz (corresponding to 80 pm), and the full range in between is either covered by standard devices or ones built on customer demand. The finesse may be up to several 1000 or even beyond 10,000 on special request. The total insertion loss is typically between 1.5 and 3 dB, and the PDL is <0.2 dB.

9.8.5 Applications

9.8.5.1 Channel Selection

Tunable FP filters enable fast and precise channel selection in dynamic multi-wavelength systems. This can either simply be the selection of a single narrow-band channel or the dropping of selected channels in WDM networks. For these purposes the FSR should be larger than the wavelength band over which the channels are spread, and the finesse should be large enough for assuring sufficiently low crosstalk. As a rule of thumb this demand is fulfilled if the finesse is about three times the number of channels.

9.8.5.2 Optical Channel/Performance Monitoring

Continuously tuned FPI filters can be used for optical channel monitoring, and with appropriately chosen resolution up to 400 channels in the C-band can be supervised.

9.8.5.3 FP Etalons for Wavelength Locking

As channel spacings in DWDM systems get smaller and smaller, the requirements on wavelength stability, as far as wavelength sources are concerned, get more and

more demanding. For systems with 100 GHz channel separation a wavelength drift of $< |0.1|$ nm over the complete laser lifetime is acceptable and this can be ensured by current chip technology. However, if the channel spacing is reduced to 50 GHz, the maximum acceptable drift is $\pm 2.5 \dots 3$ GHz ($20 \dots 24$ pm) only, and this requires active wavelength locking which is typically implemented using an FP etalon as a reference. Any deviation of the laser emission from the resonance wavelength of the etalon causes an error signal and this is taken as an input for the wavelength control. Normally the laser operation temperature is adjusted in order to get the proper emission wavelength. Typical frequency stability achieved with wavelength lockers is about ± 2.5 GHz and it can be improved to about ± 1.25 GHz with more sophisticated designs.

9.9 Thin Film Filters

Thin-film filter technology started in the 1930s with the development of dielectric multilayer antireflective coatings for military purposes during World War II. Since then TFFs (also designated as dielectric multilayer filters) have been developed for applications in many different areas (e.g. aerospace, spectroscopy, microscopy, lasers) and TFFs have entered the field of fibre optic communication as well after they had reached a sufficient maturity in the 1990s. TFFs used in fibre optics include band-pass (single or multiple), short-pass, long-pass, and gain flattening filters, and these will be covered in more detail below. Properties of TFFs, which are particularly appreciated, include their proven reliability and long-term stability, and their excellent wavelength stability makes them even suitable for the stabilization of the emission wavelengths of wavelength sources (DFB lasers) [163].

TFFs do also enable the fabrication of non-resonant structures such as anti-reflection coatings/filters or beam splitters, but these will not be discussed here any further. A comprehensive and general treatment of TFFs can be found in [164, 165] for example, and more details with a particular focus on telecom applications are given in [163].

9.9.1 Generic Functionalities of TFFs

9.9.1.1 High Reflector Coatings

The generic structure of an HR coating is a sequence of alternating layers of two materials, one of which having a high and the other with a low refractive index. If the thickness of an individual layer made of high and low index material (and referred to as quarter-wave layer) is given by

$$H = \frac{\lambda_c}{4n_H} \quad \text{and} \quad L = \frac{\lambda_c}{4n_L} \quad (9.45)$$

respectively, with λ_c being the desired centre wavelength and n_H and n_L the refractive indices of the high and low index material, the basic HR design can be represented as [163]

$$HR \equiv \text{Substrate} | (HL)^p | \text{Ambient} \quad (9.46)$$

where the power p indicates how often the period is repeated. HR layers exhibit a reflection band (designated as ‘stop band’) around λ_c , the width of which depends on the contrast between n_H and n_L . Filters become more square-shaped as p gets larger, and the maximum reflection R_{max} of the stop band depends on both, the contrast between n_H and n_L and on the number of layer periods as well according to

$$R_{max} \cong 1 - 4 \left(\frac{n_L}{n_H} \right)^{2p} \frac{n_S}{n_A} \quad (9.47)$$

Here n_S and n_A are the refractive indices of the substrate and the ambient medium, respectively.

9.9.1.2 Band-Pass Filters

A thin-film band-pass filter is either simply a single thin-film FP filter or consists, in general, of several coupled thin-film FP filters. The generic structure of a TF FP filter is a central layer designated as *spacer* plus an HR structure on either side of the spacer. The thickness d_{sp} of the spacer is given by

$$d_{sp} = 2L = m \frac{\lambda_c}{2n_L} \quad (m = 1, 2, 3, \dots) \quad (9.48)$$

and the generic structure of a band-pass filter can be represented as

$$\text{Substrate} | (LH)^p (2L)^m (HL)^p | \text{Ambient} \quad (9.49)$$

For a first order filter ($m = 1$) the spacer thickness is one half-wave, for $m = 2$ it is two half-waves, etc. The band-pass filter shape is determined essentially by the reflectance of the HR structures and by the order m of the spacer, and band-pass filters get the more square shaped and flat top the higher m gets. Proper coupling of multiple FP filters is a critical issue and has received considerable attention by many research groups [163].

9.9.1.3 Band-Edge Filters

Band-edge filters can be fabricated according to two different approaches: The edge can either be one of the stop band edges of an appropriately designed HR structure. For example, a short-pass filter is obtained if the low-wavelength edge is aligned with the desired band edge (i.e. λ_c is moved to longer wavelengths). If needed, the

stopband width can be extended by cascading two (or more) HR structures with different centre wavelengths. Alternatively, one might design a sufficiently wide band-pass structure where the cut-on and cut-off features of the band-pass determine the edge.

9.9.1.4 Gain-Flattening Filters

Gain-flattening filters exploit the fact that it has become possible to model essentially any kind of TFF function and fabricate the corresponding very complex layer stacks with extremely high precision. Gain equalization using TFFs started in the 1990s for flattening the gain of EDFAs and has since then made significant progress so that TFF-based GFFs have become an attractive alternative to FBG-based GFFs (Sect. 9.7.6).

9.9.2 Fabrication of TFFs

9.9.2.1 Substrates

TFFs are normally fabricated on glass substrates which should be sufficiently stable (mechanically, environmentally), have a smooth surface (no defects as defects might grow larger during layer deposition), and should ensure good adhesion of the deposited layers. The size may be as large as 300 mm in diameter, and smaller dices are cut after the thin film layer stack has been deposited. If the temperature of a TFF is raised, the refractive index n and the effective layer thickness d_{sp} do normally increase which gives rise to a long wavelength shift of λ_c (according to (9.48)), and the shift amounts to about 10...15 pm/°C [163, 166]. However, it has been shown that this shift can successfully be suppressed by the use of substrates which have a coefficient of thermal expansion capable of counteracting the unwanted wavelength variation [167]. As the temperature increases, the substrate expands, stretches the filter layers and reduces the physical layer thickness. By proper substrate selection and overall device design the temperature-dependent variation of the optical path length $d_{sp} \times n$ can be made so small that this approach allows minimizing the temperature-induced shift to levels that meet typical specifications of ≤ 1 pm/°C for narrow channel filters (50, 100 GHz) and ≤ 3 pm/°C for CWDM or edge filters without need of any active control. Substrate materials meeting these demands are offered by various suppliers.

9.9.2.2 Materials

Thin film coatings should be highly durable, and one class of materials which perfectly meet this requirement are the refractory oxides, examples of which are

SiO₂, TiO₂, ZrO₂, HfO₂, Nb₂O₅, and Ta₂O₅. SiO₂ has a rather low refractive index ($n = 1.44 \dots 1.49$ at 1.5 μm [163, 168]) while the other oxides listed have significantly higher refractive indices. Therefore SiO₂ is generally used as the low-index material and it is frequently combined with Ta₂O₅ ($n = 2.10$ at 1.55 μm [168]) for the fabrication of wavelength filters.

9.9.2.3 Deposition Processes

Thin film layers are typically grown by physical vapour deposition (PVD) although chemical vapour deposition has also been reported for the fabrication of telecom filters [163]. The three PVD processes most widely used for TFF fabrication are ion-assisted deposition (IAD), ion beam sputtering (IBS) and reactive magnetron sputtering. Details of these processes are reported elsewhere (see [163] and references therein) and we will recall the most relevant requirements for these fabrication processes.

Demands on filter tolerances may be as high as ± 0.1 nm for the filter edge wavelength which corresponds to a maximum tolerable variation of the operation wavelength (1.55 μm range) of about 0.01%, and this requires both well defined layer thicknesses and non-porous layers with bulk-like density. These specifications have to be met over a sufficiently large substrate area in order to ensure acceptable overall yield, and this is normally enabled by fully automating the deposition process combined with optical in-situ monitoring. Based upon these developments single deposition runs may last up to multiple days (if required), and providing filters with correspondingly complex structure has become possible [163, 166].

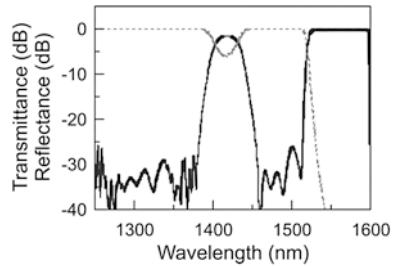
9.9.3 Filters for Telecom Applications

As already stated earlier, thin film filters used in fibre optic networks comprise band-pass-, multiple-band-, edge-, and gain flattening filters, and TFFs are used as wavelength lockers for DFB lasers as well.

9.9.3.1 Band-Pass Filters

TFF-based band-pass filters cover the complete range of filters from CWDM to (D)WDM applications, and as far as CWDM channels are concerned, TFFs are essentially the only solution with commercial relevance. For (D)WDM applications TFFs are typically offered for 100 GHz and 200 GHz channel spacings but are available for 50 GHz and 400 GHz channel separation as well. The clear channel passband of 100 GHz filters is typically about 25 GHz, but TFFs with 50 GHz clear channel passband are also available ('wide-top' filters). The latter tend to have

Fig. 9.22 Transmittance (grey, dotted curve) and reflection (full curve) characteristics of short-pass tri-band filter [170]



higher chromatic dispersion (e.g. 60 ps/nm) which is about twice the value of standard 100 GHz filters and therefore it is evident that filter dispersion has to be given proper attention with the deployment of 40 Gbit/s systems. More detailed information on dispersion is compiled in [163] e.g. or is given by the respective manufacturers.

CWDM filters are commercially available for single channels (and about 15 nm passband), but they are also available for numbers of adjacent channels, e.g. four or eight, and they are offered with various degrees of roll-off at the band edges [169].

9.9.3.2 Multiple-Band Filters

Multiple-band filters are filters designed for transmitting or reflecting more than one band or wavelength regime. For spectroscopy applications filters are offered with multiple blocking bands while developments for telecom applications include dual band filters (e.g. transmitting the O- and C-bands, and reflecting elsewhere), or transmitting two CWDM channels (1510 and 1570 nm) and reflecting all other channels. Tri-band filters are a variety for supporting the deployment of FTTx. One concept for bringing optical fibre to the residential customer are broadband passive optical networks (BPON, cf. 1st ed. of this book, Chap. 1, Sect. 1.5.1) with the 1260–1360 nm and 1480–1500 nm wavelength ranges reserved for digital upstream and digital downstream traffic, respectively, and the 1.55 μm band provided for downstream analogue signals. For use in such systems filters capable of handling three bands are commercially available either as long-pass- or short-pass (SP) tri-band filters [170], and an example of a corresponding SP filter, which reflects the 1550–1560 nm wavelength range and passes both, the 1260–1360 nm and the 1480–1500 nm ranges, is illustrated in Fig. 9.22.

Other commercially available triple band filters exhibit e.g. three arbitrarily chosen passbands which are one or several CWDM channels wide, while alternating pass/reflect bands constitute the key feature of so-called comb filters.

9.9.3.3 Edge Filters

Edge filters are commercially available both, as short-pass- and as long-pass filters (SPF, LPF), and they are essentially available for the separation of any wavelength

range into a reflected and a transmitted regime. The range between the reflected and the transmitted wavelengths, which cannot be used for transmission channels because neither the reflection nor the transmission are adequate, is typically a few nm wide. This is due to the fact that the roll-off of filters gets less steep as the filter bandwidth increases (and edge filters are in essence very broadband filters, as stated above).

9.9.3.4 Gain Flattening Filters

Commercially available GFFs are primarily designed for covering the C-band (1525 to 1565 nm), but are available for the S- and L-band as well. The output power/gain variation of an EDFA plus GFF cascade can be made <0.5 dB over the complete wavelength range specified, the difference between the designed transmission of a GFF and its actual value can be made as small as about ± 0.1 dB, and PDL is typically <0.1 dB [97, 163, 166, 170].

9.9.3.5 TFFs for Hybrid PLC Modules

Thin film filters have been used in hybrid PLC modules, e.g. for separating 1.3/1.55 μm wavelengths in FTTH transceivers, for a number of years already [171 and references therein] and a more recent variety are TFFs to be used with a polymer optical integration platform [172, 173], see also Chap. 13. Such a PLC platform is highly flexible and may be particularly suited for low cost optoelectronic modules to be used in access networks. The TFF elements can be designed with a wide range of application specific spectral characteristics, including CWDM filters, “triple play” filters, and reflectors for OTDR monitoring. In contrast to the common TFFs these PLC embedded TFFs have to be extremely thin (<20 to $25 \mu\text{m}$) to minimize optical excess loss. To this end they are deposited on a thin polymer “substrate” film using ion beam sputtering. If the same kind of polymer is used as for the PLC waveguides, unwanted residual reflection at the WG/TFF interfaces can be largely suppressed, and it is further improved by inserting the TFF under a small angle (e.g. 8°), so that better than -30 dB crosstalk levels can be achieved.

Polymer-based multilayer structures have also been designed for polarisation handling purposes, namely as polarization rotator and polarisation beam splitter. The former has proven to efficiently compensate for polarisation effects e.g. in AWGs whereas with the latter >20 dB discrimination between TE- and TM-polarized guided waves over the 1535–1600 nm wavelength range could already be demonstrated [173].

9.9.4 Filter Modules

As thin film filters have no wavelength-dispersive properties and can only discriminate between transmitted and reflected wavelengths, they are essentially three-port devices as illustrated in Fig. 9.23.

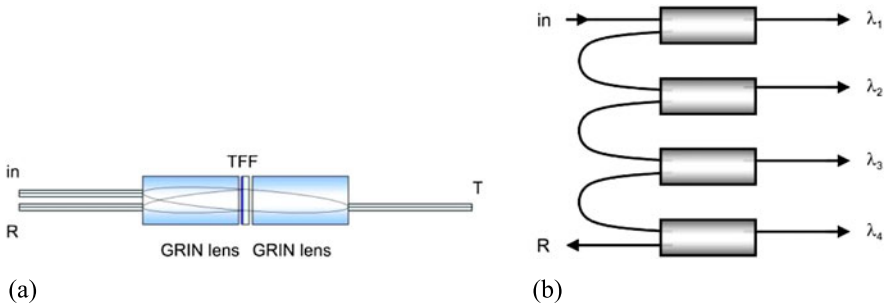


Fig. 9.23 Three-port TFFs (a) single device: in, T, R represent incoming, transmitted, and reflected signals, respectively. (b) Four-channel MUX/DEMUX: $\lambda_1, \dots, \lambda_4$ are transmitted via different output ports, any other wavelength is reflected (R)

In order to enable the spatial separation of the incoming and the reflected light without the need of an optical circulator, the incoming light hits the TFF at an angle. However, the characteristics of TFFs depend on the angle of incidence: (i) the transmission wavelength shifts to longer wavelengths with increasing incidence angle (which may be used for (fine-) tuning the centre wavelength if this is wanted or acceptable), and (ii) the characteristics get polarization dependent which is generally unwanted. As a consequence, TFFs are normally mounted under very small angles of incidence (around 1 degree). The beam shaping and focusing is typically achieved by using GRIN (gradient-index) lenses, but as outlined in [163], there are various additional restrictions and design considerations to be taken into account.

Optical add-drop multiplexers (OADM) are key building blocks in WDM networks, and they have to combine or separate larger numbers of wavelength channels. In order to accomplish that functionality using TFFs they have to be cascaded, and one corresponding option is illustrated in Fig. 9.23(b).

Different wavelength channels to be separated by a TFF-based DEMUX travel different paths and experience a different number of reflections until they are eventually transmitted (or leave by the reflection output port). Each reflection causes an average loss of typically 0.3 dB and as a consequence the overall attenuation of the wavelength transmitted first (λ_1) is correspondingly lower than that of the last wavelength transmitted (λ_4 in Fig. 9.23 or λ_n in general). One possibility to compensate this variation without significant effort is by using appropriate MUX and DEMUX pairs which have a complementary arrangement of the wavelengths so that the total loss for any channel is almost the same after one MUX/DEMUX pair has been traversed. Due to this inherent asymmetry of TFF-based MUX/DEMUXs, a standard cascade comprises a maximum of eight three-port devices, and MUX/DEMUXs for higher channel counts are a combination of such cascades with band splitting couplers or interleavers.

Another issue of cascaded TFFs is chromatic dispersion (CD) where each reflection and the final transmission contribute to the total CD of a channel. CD accumulation can be mitigated by choosing proper cascade architectures, and one example is the combination of a 3 dB coupler with two legs of interleaved channels [174]. As

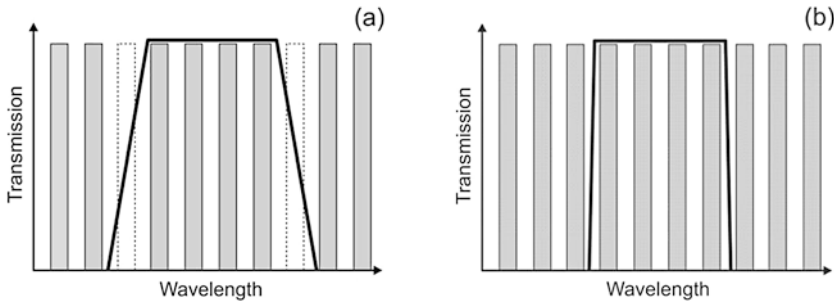
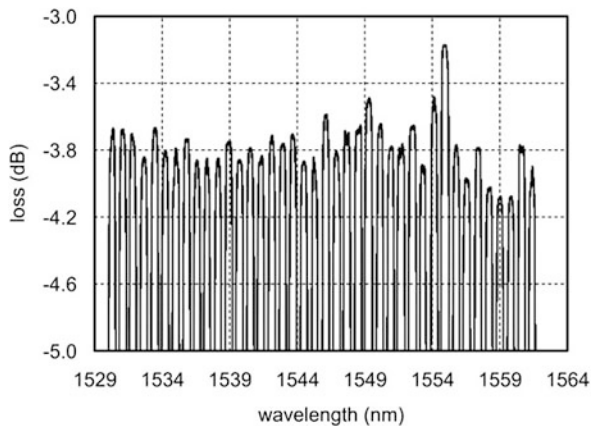


Fig. 9.24 Schematic representation of (a) 4-skip-1 and (b) 4-skip-0

the adjacent channel separation is doubled by the interleaver structure, the reflection CD is significantly reduced, however, at the expense of an extra 3 dB loss.

Band splitting couplers, (also designated as wave-band or wideband couplers), are TFF-based band filters with rather large bandwidth so that they can be used to transmit or reflect a number of WDM channels by one element, and they also support a “pay-as-you-grow” strategy. Such filters come in two varieties (cf. Fig. 9.24). Either all channels having the fundamental separation from each other are used (“ x -skip-0”), or n channels next to the edges of the banded filter are skipped (“ x -skip- n ”) with $n > 0$. The reason for using skip- n filters is the following: With increasing width of the transmission band it gets more and more difficult to ensure a sufficiently steep roll-off at the band edges of the filters so that the corresponding fabrication effort and related cost go up. At the same time detrimental effects of chromatic dispersion increase with steeper band edges (due to the fact that TFFs are minimum phase filters in transmission with transmission and phase response constituting a Hilbert transform pair, cf. Sect. 9.2.1). Compared to x -skip-0 filters x -skip- n solutions are beneficial in two respects: they allow for less steep filter edges, which reduces CD, and in addition, the maxima of CD can be moved further away from the band filter edges resulting in lower overall CD within the filter band [174].

Fig. 9.25 Channel dependent variation of insertion loss in a TFF-based 40-channel DEMUX [51]



The most common varieties are x -skip-1 and x -skip-2 filters, but e.g. 20-skip-4 devices are also commercially available (e.g. [97]). Based upon the concepts illustrated MUX/DEMUXs with a maximum channel count of 40 are offered from different manufacturers. Because the different channels traverse different filters, there is a certain variation of the individual channel's insertion loss as illustrated in Fig. 9.25.

Other approaches to build TFF-based MUX/DEMUXs have been reported in the literature [163, 175, 176], however, they have not yet found commercial relevance.

9.10 Microrings

Microring resonators (MRR) optically coupled to dielectric waveguides represent a class of filters with characteristics very similar to Fabry-Pérot filters. They are particularly easy to fabricate as no gratings, facets, or high-reflecting structures are needed for building the cavity. Ring radii may be as low as a few μm while typical dimensions are in the several 10 μm up to a few 100 μm range which allows for compact one- or two-dimensional arrays. MRRs enable a wide range of applications. Examples related to fibre optic communication include optical channel filtering [177], planar dispersion compensation [178], all-optical wavelength/frequency conversion [179, 180], all-optical switching [181, 182], and cascaded microring (MR) modulators for WDM optical interconnects [183]. Furthermore, higher-order MRR filters constitute a basis for on-chip WDM systems [184], and optical signal processing as an alternative to signal processing in the electrical domain in areas such as radar, photonic beam-steering of phased-array antennas, or radio-over-fibre in mobile communication systems is another topic which has received much attention during the last few years [185]. Key advantages of photonic (monolithic) microwave (RF) filters are wide bandwidth and passband centre wavelength tunability, reconfigurability, immunity to electromagnetic interference (EMI), low loss, low weight and low power consumption. Finally, MRRs are considered promising beyond telecom applications as well, and one particularly prominent area of current interest is sensing of (bio)molecules [158, 186, 187].

MRRs have been fabricated in various materials including SiON_x [178], SOI [181, 186], glass [177], or semiconductor material systems such as GaAIs [181] and GaInAsP [180].

9.10.1 Key Features of Microring Resonators

The most simple MRR configuration is a single microring coupled to a dielectric waveguide which represents an all-pass filter. The design can be horizontal (as illustrated in Fig. 9.26(left)) but vertical coupling, (where the MR and the feeding WG are vertically arranged in layers one on top of the other) is an equivalent option. Another generic MRR configuration is the add-drop multiplexer shown in Fig. 9.26(right) which consists of an MR coupled to two dielectric WGs.

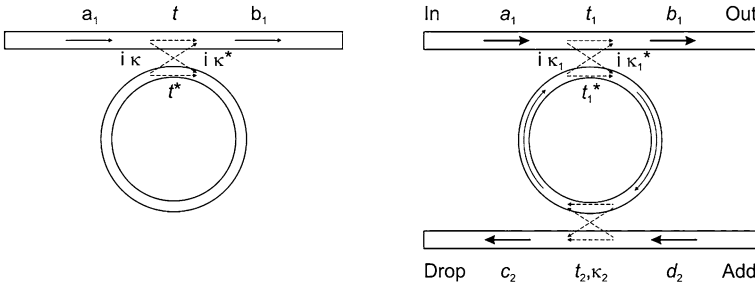


Fig. 9.26 Generic microring resonator structure (*left*) and principle of MR-based add-drop multiplexer (*right*)

The characteristics of waveguide-coupled microrings can be derived by different approaches. Details are given in various textbooks [7, 38] and the most relevant results are given below.

For the add-drop multiplexer illustrated in the right side of Fig. 9.26, the following relations hold:

$$T_{out} = \left| \frac{b_1}{a_1} \right|^2 = \frac{|t_1|^2 + |at_2|^2 - 2a|t_1t_2| \cos(\theta - \theta_{t_1} - \theta_{t_2})}{1 + |at_1t_2|^2 - 2a|t_1t_2| \cos(\theta - \theta_{t_1} - \theta_{t_2})} \tag{9.50}$$

$$T_{drop} = \left| \frac{c_2}{a_1} \right|^2 = \frac{(1 - |t_1|^2)(1 - |t_2|^2)a}{1 + |at_1t_2|^2 - 2a|t_1t_2| \cos(\theta - \theta_{t_1} - \theta_{t_2})} \tag{9.51}$$

where T_{out} and T_{drop} are the intensities at the (forward) output and the drop port, respectively, t_1 and t_2 characterize the fraction of light amplitude propagating along the straight WGs in the coupling regions, a represents the attenuation which the propagating fields experience after travelling once along the ring length L , and a is related to the field attenuation coefficient $\alpha/2$ by

$$a = \exp(-\alpha L/2) \tag{9.52}$$

i.e. $a = 1$ corresponds to zero loss. θ and θ_t are defined by

$$\theta = \frac{2\pi\nu}{c} n_{eff} L \quad \text{and} \quad t_j = |t_j| \exp(i\theta_{t_j}) \quad j = 1, 2 \tag{9.53}$$

respectively, where $\nu = c/\lambda$ is the frequency of the propagating wave. The coupling between the straight WGs and the MR is characterized by coupling constants κ_1 and κ_2 which satisfy the relation

$$|t_j|^2 + |\kappa_j|^2 = 1 \quad \text{with } j = 1, 2 \tag{9.54}$$

The behaviour of a microring coupled to a single WG only (Fig. 9.26, left) is obtained from (9.50) to (9.54) by setting $t_1 = t$, $t_2 = 1$, $\theta_{t_1} = \theta_t$, $\theta_{t_2} = 0$, $\kappa_1 = \kappa$, and $\kappa_2 = 0$.

The waveguide-coupled MRs characterized by (9.50) and (9.51) exhibit periodic characteristics, in particular periodic dips in the transmission spectra and corresponding maxima at the drop port in the case of the add-drop multiplexer according to

$$\theta - \theta_{t_1} - \theta_{t_2} = 2m\pi = \frac{2\pi\nu}{c} n_{eff} L - \theta_{t_1} - \theta_{t_2} = \beta L - \theta_{t_1} - \theta_{t_2} \quad (9.55)$$

with m being an integer and β the propagation constant (see (9.26)). Two adjacent transmission minima are given by

$$\begin{aligned} \theta - \theta_{t_1} - \theta_{t_2} &= 2m\pi = \beta L - \theta_{t_1} - \theta_{t_2} \quad \text{and} \\ \theta - \theta_{t_1} - \theta_{t_2} &= 2(m+1)\pi = (\beta + \Delta\beta)L - \theta_{t_1} - \theta_{t_2} \end{aligned} \quad (9.56)$$

Equation (9.56) yields

$$\Delta\beta L = 2\pi \quad (9.57)$$

and combining (9.24), (9.31), and (9.57) with keeping in mind that $\Delta\nu$ is equivalent to the FSR we get

$$FSR = \frac{c}{n_g L} \quad (9.58)$$

i.e. the free spectral range is determined by the ring dimension and the effective group refractive index n_g .

The intensity at the ‘through’ output port vanishes if

$$a = \left| \frac{t_1}{t_2} \right| \quad \text{or} \quad a = |t| \quad (9.59)$$

holds for the add-drop multiplexer or the MR coupled to a single WG, respectively. This condition is called “critical coupling”, and in this case light coupling back from the ring to the (‘through’) output waveguide is equal in amplitude but has opposite phase compared to the directly propagating light so that complete destructive interference occurs.

As far as phase effects are concerned, MRRs exhibit pronounced phase variations around the resonance, i.e. the group delay exhibits a peak at the resonance wavelength (see e.g. [7]).

9.10.2 Polarization-Dependent Effects

The effective refractive index n_{eff} of straight or bent waveguides is normally different for TE- and TM-polarized light and as a consequence the resonance frequencies and the FSR of MRRs are polarization dependent. But, more importantly, MRRs may also rotate the state of polarization so that an initially purely TE- (TM-) polarized wave launched into the feeding WG will leave the WG-coupled MR structure partly (or even completely) TM- (TE-) polarized [188]. The extent of polarization rotation depends on many parameters including WG geometry (cross sectional

shape and bend radius), refractive index contrast, degree of vertical asymmetry, MR loss, and wavelength (near resonance polarization rotation may be particularly pronounced) [189]. Bent WG and MRR designs exist which favour polarization rotation or even enable complete polarization conversion [190], but on the other hand, by proper design, polarization rotation can be suppressed to a large extent as well. As a consequence, polarization-dependent characteristics have to be taken into account in the design of MRR-based devices with sharp resonances while these effects tend to be less relevant in filters with fairly broad add-drop bands such as the higher order filters described below.

9.10.3 Higher Order Filters

Single microring resonators (MRRs) in an arrangement as shown in Fig. 9.26 are generally insufficient for more demanding filter applications but the monolithic integration of larger numbers of MRRs results in significantly more attractive filter characteristics, and due to their small size MRRs lend themselves particularly well to monolithic integration resulting in higher-order filter chips.

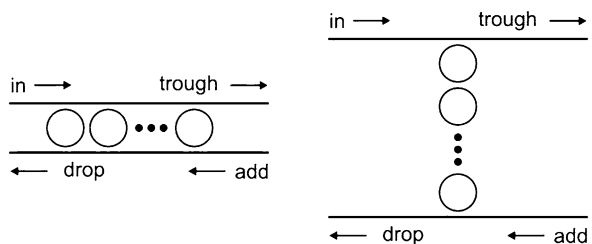
Two generic arrangements, parallel and serially cascaded MRs, are shown in Fig. 9.27 (see also [191, 192]).

In a parallel all-pass filter arrangement the phase characteristics of the individual rings add and this property can be exploited for the fabrication of MR-based dispersion compensators [178].

On the other hand, Fig. 9.28(right) illustrates how the passband shape gets more rectangular as the order (i.e. number of serially cascaded microrings) increases. These filters have been fabricated in a glass called Hydex[®], which is a high index material ($n = 1.7$) and offers the possibility to vary the index contrast between the core and the silica cladding in the range from 1 to 25% [193]. As a consequence tight bends with radii down to about 5 μm are possible, and this enables the fabrication of compact and complex microstructures.

A particularly high degree of design flexibility with the capability to approximate (essentially) any filter function is obtained if (1) the coupling strengths between the individual MRRs are made freely adjustable, (2) the MRRs include a phase shifting section, tuned either thermo-optically or by carrier injection, and (3) MZIs are added to MRRs within a basic filter unit cell, which enables the design of filters with independently chosen poles and zeros (within the Z-transform formalism, [7]).

Fig. 9.27 Parallel (*left*) and serially (*right*) cascaded MRs as generic building blocks for higher order filters



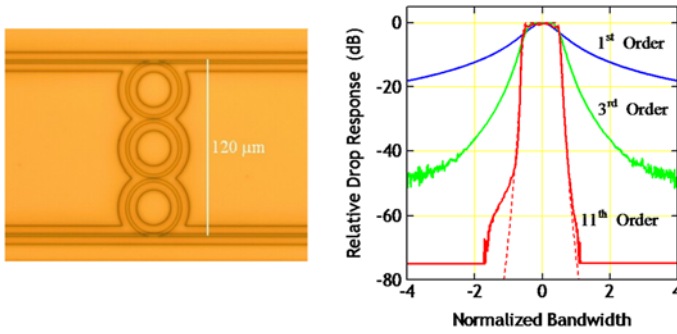


Fig. 9.28 Top view of 3-ring serially cascaded MR filter (left) and experimentally determined drop-response of serially cascaded microring filters with different numbers of MRs (right), all fabricated in Hydex® [177, 193]

Furthermore, for near-ideal filter approximations active filter designs are superior to purely passive ones, and this can be achieved by adding optical amplifiers to the filter structures, either by monolithic integration of SOAs in filters realized in III–V semiconductors, in particular in the InP/GaInAsP material system [194] or by hybridly integrating evanescent SOAs on a silicon platform [195]. With SOAs under forward bias overall zero-insertion loss filters can be made while biasing an appropriately located SOA in the reverse direction enables to switch of single optical paths. For completeness, one restriction with planar filter structures should be mentioned: they are generally polarization dependent although this limitation does not receive specific coverage in most reports on higher-order planar filters.

Flexibly configurable filters, implemented by cascading appropriate basic unit cells, have been fabricated in the SOI [184, 195–198] and the InP/GaInAsP material systems [194, 199], and one example is illustrated in Fig. 9.29.

Various key characteristics and features of such MRR filters have already been demonstrated, including tunable Q-factor [195], flat top passband, passband width

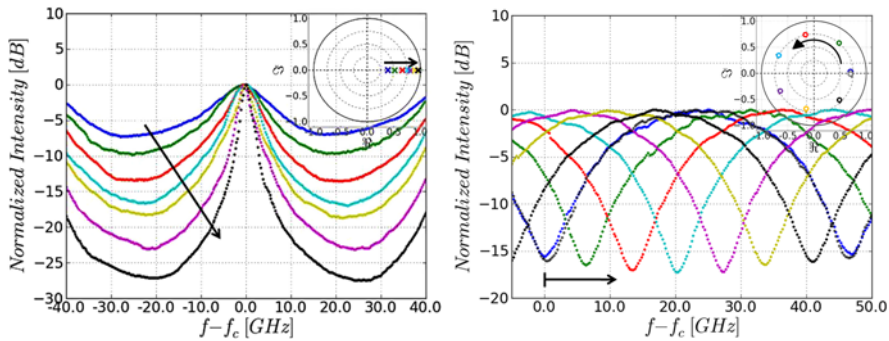


Fig. 9.29 Measured filter response of a single filter stage reconfigured (a) as a pole or (b) zero. Arbitrary placement of the pole/zero in the complex plane, demonstrated by independently adjusting the (a) magnitude and (b) phase (figure taken from [194], courtesy Eric Norberg)

tunability and fast roll-off [194, 199]. Extinction ratios exceeding 30 dB [194] or even up to 40 dB for a 3rd order filter [199] have already been achieved. Passband frequency/wavelength tunability is typically in the order of several 10 GHz within a single FSR, while placing the filter anywhere in the C-band has been shown by smooth tuning the filter across multiple FSRs [199]. Finally, dynamic change of the filter characteristics from pass-band to notch type filter has also been reported in [7, 194–197].

9.10.4 Microring-Based Filters with Extended FSR

For typical applications in fibre optic systems filters should have FSRs in the range of several 10 nm, i.e. comparable to the width of the C-band for example. This is not easy to accomplish as it is equivalent to rather low ring radii which is challenging from a technological point of view. A way to overcome these difficulties is the combination of MRs with different radii in such a way that resonances do only occur where the resonances of all individual MRs involved coincide (Vernier effect), and widely tunable lasers using MRRs with (slightly) different radii for mode selection have already been demonstrated (see Chap. 5, Sect. 5.4.4). Furthermore, a corresponding filter has been fabricated in the SiO₂/Si material system comprising two rings with 28.5 μm radius coupled to one ring with 39.3 μm. The FSRs of the individual rings have been 8 nm and 6 nm, respectively while the filter based upon the coupled rings exhibited about 20 nm FSR [200].

9.10.5 Prospects and Further Developments of MR-Based Filters

As illustrated above higher order MRR-based filter structures are highly promising as compact and versatile devices, both in III–V semiconductors (in particular GaInAsP) and in Silicon Photonics (see Chap. 14 and [201]), and it is expected that a number of corresponding devices will move from the R&D lab to the market in the next few years.

9.11 Interleavers

9.11.1 Operation Principle

Interleavers are used in wavelength routing and for (de)multiplexing and prefiltering as well, in particular for upgrading existing systems. The latter application is based upon the fact that an ongoing trend in the development of WDM systems is to locate transmission channels closer and closer to each other for making better use of

the transmission capacity of a single optical fibre. As a consequence, optical filters have to cope with ever decreasing channel separations which makes their fabrication more and more demanding. One smart and economic way to meet this challenge is the use of optical interleavers in combination with standard filters. In doing so, the interleaver is the only filter which has to separate (or recombine) channels with the smallest separation while all other filters or wavelength selective devices operate for larger channel separations and therefore have to meet less demanding specifications.

An interleaver operates as follows: If a stream of wavelength channels at carrier frequencies $\nu_1, \nu_2, \dots, \nu_n$ and constant channel separation $\Delta\nu$ enters a standard interleaver, frequencies $\nu_1, \nu_3, \nu_5, \dots$ exit from one port of the interleaver while frequencies $\nu_2, \nu_4, \nu_6, \dots$ come out from the other port. The frequency separation is $2\Delta\nu$ for the data streams at output ports 1 and 2. Interleavers can also be cascaded if even larger channel separations are required (a cascade of N interleaver stages splits the original data stream into 2^N channels with $2^N \Delta\nu$ channel separation).

If an interleaver is operated in the reverse direction, it can combine 2 (or 2^N , $N = 2, 3, \dots$) streams of frequency channels with channel separation of $2\Delta\nu$ ($2^N \Delta\nu$) into a single data stream with $\Delta\nu$ channel separation.

In principle, any kind of optical filter which exhibits a periodic response with respect to frequency may be used as an interleaver. However, for real applications there are additional requirements, in particular: flat top band shape, large channel width, high adjacent band isolation, low polarization dependence (i.e. low polarization dependent loss and low polarization dependence of the channel centre frequency/wavelength), low chromatic dispersion, and low overall insertion loss. Furthermore, the channel separation of the interleaver has to match the ITU grid with sufficient accuracy over the whole operation range, and interleavers meeting all these demands require careful design and mature manufacturing.

9.11.2 Interleaver Types

9.11.2.1 Functionality

Interleavers fall into different categories according to their functionality. The simplest design, designated as a 1:2 interleaver, separates the even and odd channels of an incoming wavelength comb (or combines these two groups of channels into a single one if operated in the reverse direction).

The next category are 1:2^N interleavers (i.e. cascades of N interleaver stages) which separate a single DWDM comb into 2^N data streams (or combine 2^N sequences of wavelength channels into a single data stream).

A third category are banded interleavers which separate (or combine) bands of channels. In this case it is particularly demanding to ensure a steep roll-off at the end of the bands to be separated over a wavelength interval corresponding to a single channel spacing (which is significantly narrower than the range covered by the individual bands).

Finally, interleavers may be asymmetric, i.e. they may single out one channel out of a larger number of channels N , or more generally speaking, they separate (or combine) channels with freely chosen passband width (e.g. 60%/40%, 70%/30%, ...).

9.11.2.2 Principles and Concepts

Interleavers also fall into different categories according to the physical principles they are based upon, and as outlined in detail in [202], an impressive number of interleaver variants have already been reported. They can be classified into three broad classes of filter technologies: (i) AWG routers operated as interleavers, (ii) Gires-Tournois (GT)-based Michelson interferometers, and (iii) lattice filters (i.e., cascades of differential-delay elements where the differential-delay of each element is an integral multiple of a unit delay and power is exchanged across paths between the elements [53, 202]).

AWG routers operated as interleavers [203] offer particular application potential as single-state $1:2^N$ interleavers, but they can also serve as single channel or banded filters [204], and still another application variety is polarization interleaving. Non-linear interactions such as cross-phase modulation (XPM) and four wave mixing (FWM) rely on parallel polarization, and therefore unwanted interactions between neighbouring channels are reduced considerably if they are orthogonally polarized [205]. In practice, even and odd channel polarizations are adjusted orthogonally with an AWG accomplishing their (de)interleaving.

Interleavers based upon Gires-Tournois (GT) interferometers can either be of interferometric [202, 206] or of birefringent type [202], and such interleavers have been implemented in free space optics, in combination with thin-film filter GT interferometers, as all-fibre solution with appropriately designed FBG as reflecting elements [207], or as planar devices. Examples include a particularly compact loop-mirror-based Michelson-Gires-Tournois interferometer structure implemented in SOI [208] or coupled microring resonator/Mach-Zehnder interferometer structures for applications in optical communication [209, 210] or related areas such as microwave photonics [211]. GT-based interleavers can be built as 1:2 or as asymmetric devices as well. Lattice filter based interleavers have e.g. been built in free space optics employing birefringent crystals [202, 210], or as cascaded Mach-Zehnder interferometers (MZI) with properly chosen delay and coupling between the individual MZIs, and the latter approach is particularly suited for planar light-wave technology [204, 212]. Lattice-filter based interleavers can be of 1:2 type but can be designed for banded applications as well.

A very good comparison of typical performance characteristics of a large number of interleaver types is given in [202].

9.11.3 Characteristics of Commercially Available Interleavers

Interleavers are fabricated by a number of suppliers and have been implemented using different technologies. These include designs using crystals, fibres (with cas-

Table 9.1 Typical performance data of commercially available 50/100 GHz interleavers

Parameter	Unit	Typical values
Wavelength accuracy	nm	0.02
Insertion loss	dB	≤2.0
0.5 dB passband width/Clear channel	GHz	20...30
Isolation/Crosstalk	dB	>20...25
Return loss	dB	>40
Directivity	dB	>45...55
Polarization dependent loss	dB	<0.2...0.5
Polarization mode dispersion	ps	<0.2...0.3
Chromatic dispersion	ps/nm	<±20...30

caded MZIs or FBGs for example), and planar lightwave circuits as well. In a number of cases suppliers do not disclose their concept and the technology used, and one can make guesses only. A comprehensive overview has been published some time ago [53] and the data are still relevant although one or the other supplier listed has since then discontinued its interleaver business.

Interleavers are primarily offered for 25/50 and 50/100 GHz channel spacings, but they are also available for 12.5/25 GHz [213] or 100/200 GHz operation, with asymmetric channel widths [213], with polarization-maintaining fibres as polarization interleaver [112] or as 1:4 interleavers [214]. Interleavers suited for channel spacings down to 6.25 GHz have been published in the literature (see [202]) and a commercial product had been available about a decade ago already (Essex Corp.), but production has been discontinued since then.

Interleavers typically cover the C- or the L-band with 80 channels for example in the case of 50/100 GHz interleavers.

A number of key performance parameters for commercially available 50/100 GHz are listed in Table 9.1. The parameter variations are partly due to different technologies and implementations, but also due to slightly different definitions of the parameters themselves.

The further improvement of interleavers is very likely to go on as interleavers represent an efficient means for upgrading the channel count of communication systems without the need to improve the performance of each individual wavelength filter.

9.12 Acousto-Optic Tunable Filters

Acousto-optic tunable filters (AOTF), sometimes also designated as acoustically tunable optical filters (ATOF), are passband transmission filters based upon the acousto-optic interaction inside an anisotropic medium. An applied radio-frequency causes acoustical vibrations in a corresponding crystal (e.g. TeO₂, LiNbO₃) and

creates a bulk transmission diffraction grating. AOTFs offer the unique property of multiple-band filtering by mixing multiple radio frequencies, and arbitrary wavelength selection can be accomplished within microseconds. AOTFs are available for operation within the visible or near/mid infra-red spectral region and have been developed for applications in fibre optic communication systems as well [215, 216]. However, they could not satisfactorily meet the demands of (D)WDM systems, and as there is no application where the unique properties of AOTFs can compensate their shortcomings, these filters are currently considered of essentially no relevance for fibre optic communication systems although AOTFs have found various other useful applications [217].

References

1. G. Bennett, K.-T. Wu, A. Malik, S. Roy, A. Awadalla, A review of high-speed coherent transmission technologies for long-haul DWDM transmission at 100 G and beyond. *IEEE Commun. Mag.* **52**(10), 102–110 (2014)
2. W.J. Tomlinson, Wavelength multiplexing in multimode optical fibers. *Appl. Opt.* **16**, 2180–2194 (1977)
3. K. Kobayashi, M. Seki, Microoptic grating multiplexers and optical isolators for fiber-optic communications. *IEEE J. Quantum Electron.* **QE-16**, 11–22 (1980)
4. T. Ohara, H. Takahara, T. Yamamoto, H. Masuda, T. Morioka, M. Abe, H. Takahashi, Over 1000 channel, 6.25 GHz-spaced ultra-DWDM transmission with supercontinuum multicarrier source, in *Opt. Fiber Commun. Conf. (OFC'05)*, Anaheim, CA, USA (2005), Techn. Digest, paper OWA6
5. B.J. Puttnam, R.S. Luís, W. Klaus, J. Sakaguchi, J.-M. Delgado Mendinueta, Y. Awaji, N. Wada, Y. Tamura, T. Hayashi, M. Hirano, J. Marcianti, 2.15 Pb/s transmission using a 22 core homogeneous single-mode multi-core fiber and wideband optical comb, in *Proc. 41st Europ. Conf. Opt. Commun. (ECOC'15)*, Valencia, Spain (2015), PDP.3.1
6. A. Turukhin, O.V. Sinkin, H. Batshon, H. Zhang, Y. Sun, M. Mazurczyk, C. Davidson, J.-X. Cai, M.A. Bolshtyansky, D. Foursa, A. Pilipetskii, Tb/s power-efficient transmission over 14,350 km using a 12-core fiber, in *Opt. Fiber Commun. Conf. (OFC'16)*, Anaheim, CA, USA (2016), Techn. Digest, paper Th4C.1
7. C.K. Madsen, J.H. Zhao, *Optical Filter Design and Analysis, a Signal Processing Approach* (Wiley, New York, 1999)
8. C. Peucheret, Phase characteristics of optical filters, in *Wavelength Filters in Fibre Optics*, ed. by H. Venghaus (Springer, Berlin, Heidelberg, 2006), Chap. 2
9. G. Lenz, B.J. Eggleton, C.R. Giles, C.K. Madsen, R.E. Slusher, Dispersive properties of optical filters for WDM systems. *IEEE J. Quantum Electron.* **34**, 1390–1402 (1998)
10. L. Poladian, Group delay reconstruction for fiber Bragg gratings in reflection and transmission. *Opt. Lett.* **22**, 1571–1573 (1997)
11. M. Tilsch, C.A. Hulse, F.K. Zernik, R.A. Modavis, C.J. Addiego, R.B. Sargent, N.A. O'Brien, H. Pinkney, A.V. Turukhin, Experimental demonstration of thin-film dispersion compensation for 50-GHz filters. *IEEE Photonics Technol. Lett.* **15**, 66–68 (2003)
12. B. Costa, D. Mazzoni, M. Puleo, E. Vezzoni, Phase shift technique for the measurement of chromatic dispersion in optical fibers using LED's. *IEEE J. Quantum Electron.* **QE-18**, 1509–1514 (1982)
13. G. Genty, T. Niemi, H. Ludvigsen, New method to improve the accuracy of group delay measurements using the phase-shift technique. *Opt. Commun.* **204**, 119–126 (2002)
14. S.E. Mechels, J.B. Schlager, D.L. Franzen, Accurate measurements of the zero-dispersion wavelength in optical fibers. *J. Res. Natl. Inst. Stand. Technol.* **102**, 333–347 (1997)

15. S.D. Dyer, K.B. Rochford, A.H. Rose, Fast and accurate low-coherence interferometric measurement of fiber Bragg grating dispersion and reflectance. *Opt. Express* **5**, 262–266 (1999)
16. C. Peucheret, F. Liu, R.J.S. Pedersen, Measurement of small dispersion values in optical components. *Electron. Lett.* **35**, 409–411 (1999)
17. K. Ogawa, Characterization of chromatic dispersion of optical filters by high-stability real-time spectral interferometry. *Appl. Opt.* **45**, 6718–6722 (2006)
18. D. Dai, W. Mei, S. He, Using a tapered MMI to flatten the passband of an AWG. *Opt. Commun.* **219**, 233–239 (2003)
19. M.G. Thompson, D. Brady, S.W. Roberts, Chromatic dispersion and bandshape improvement of SOI flatband AWG multi/demultiplexers by phase-error correction. *IEEE Photonics Technol. Lett.* **15**, 924–926 (2003)
20. H.-J. Deyerl, C. Peucheret, B. Zsigri, F. Floreani, N. Plougmann, S.J. Hewlett, M. Kristensen, P. Jeppesen, A compact low dispersion fiber Bragg grating with high detuning tolerance for advanced modulation formats. *Opt. Commun.* **247**, 93–100 (2005)
21. X.X. Zhang, Thin film optical filter—an enabling technology for modern optical communication systems. White paper. www.auxora.com
22. F. Havermeier, W. Liu, C. Moser, D. Psaltis, G.J. Steckman, Volume holographic grating-based continuously tunable optical filter. *Opt. Eng.* **43**, 2017–2021 (2004)
23. H. Chotard, Y. Painchaud, A. Mailloux, M. Morin, F. Trépanier, M. Guy, Group delay ripple of cascaded Bragg grating gain flattening filters. *IEEE Photonics Technol. Lett.* **14**, 1130–1132 (2002)
24. L. Poladian, Understanding profile-induced group-delay ripple in Bragg gratings. *Appl. Opt.* **39**, 1920–1923 (2000)
25. S. Jamal, J.C. Cartledge, Variation in the performance of multispan 10-Gb/s systems due to the group delay ripple of dispersion compensating fiber Bragg gratings. *J. Lightwave Technol.* **20**, 28–35 (2002)
26. L.-S. Yan, T. Luo, Q. Yu, Y. Xie, K.-M. Feng, R. Khosravani, A.E. Willner, Investigation of performance variations due to the amplitude of group-delay ripple in chirped fiber Bragg gratings. *Opt. Fiber Technol.* **12**, 238–242 (2006)
27. H. Geiger, M. Ibsen, Complexity limitations of optical networks from out-of-band dispersion of grating filters, in *Proc. 24th Europ. Conf. Opt. Commun. (ECOC'98)*, Madrid, Spain (1998), pp. 405–406
28. G. Castanon, T. Hoshida, Impact of filter dispersion slope in NRZ, CS-RZ, IMDPSK and RZ formats on ultra high bit-rate systems, in *Proc. 28th Europ. Conf. Opt. Commun. (ECOC'02)*, Copenhagen, Denmark (2002), vol. **4**, paper 9.6.1
29. M. Lee, N. Antoniadis, On the impact of filter dispersion slope on the performance of 40 Gbps DWDM systems and networks. *Photonic Netw. Commun.* **14**, 97–102 (2007). doi:10.1007/s11107-006-0051-0
30. M. Kuznetsov, N.M. Froberg, S.R. Henion, K.A. Rauschenbach, Power penalty for optical signals due to dispersion slope in WDM filter cascades. *IEEE Photonics Technol. Lett.* **11**, 1411–1413 (1999)
31. C. Riziotis, M.N. Zervas, Effect of in-band group delay ripple on WDM filter performance, in *Proc. 27th Europ. Conf. Opt. Commun. (ECOC'01)*, Amsterdam, The Netherlands (2001), pp. 492–493, paper Th.M.1.3
32. A. Dochhan, G. Göger, S. Smolorz, H. Rohde, W. Rosenkranz, The influence of FBG phase ripple distortions—comparisons of different modulation formats, in *Opt. Fiber Commun. Conf. and Nat. Fiber Opt. Eng. Conf. (OFC/NFOEC'2008)*, San Diego, CA, USA (2008), Techn. Digest, paper JWA60
33. V. Veljanovski, M. Alfiad, D. van den Borne, S.L. Jansen, T. Wuth, Equalization of FBG-induced group-delay ripples penalties using a coherent receiver and digital signal processing, in *Opt. Fiber Commun. Conf. and Nat. Fiber Opt. Eng. Conf. (OFC/NFOEC'2009)*, San Diego, CA, USA (2009), Techn. Digest, paper JThA40

34. A. Dochhan, S. Smolorz, H. Rohde, W. Rosenkranz, Electronic equalization of FBG phase ripple distortions in 43 Gb/s WDM systems, in *Proc. 10th ITG Topical Meeting Photon. Networks*, Leipzig, Germany, 04–05 May 2009, pp. 175–181
35. J.T. Mok, J.L. Blows, B.J. Eggleton, Investigation of group delay ripple distorted signals transmitted through all-optical 2R regenerators. *Opt. Express* **12**, 4411–4422 (2004)
36. D. Marcuse, *Theory of Dielectric Optical Waveguides*, 2nd edn. (Academic, New York, 1991)
37. H. Kogelnik, Theory of optical waveguides, in *Guided-Wave Optoelectronics*, ed. by T. Tamir (Springer, Berlin, Heidelberg, New York, 1988), Chap. 2
38. S.L. Chuang, *Physics of Photonic Devices*, 2nd edn. (Wiley, Hoboken, 2009)
39. K. Jędrezejewski, Biconical fused taper—a universal fibre devices technology. *Opto-Electron. Rev.* **8**, 153–159 (2000)
40. M. Rusu, O.G. Okhotnikov, Practical method for fabricating dense WDM fiber couplers with arbitrary wavelength channels, in *Advanced Topics in Optoelectronics, Microelectronics, and Nanotechnologies*, ed. by O. Iancu, A. Manea, D. Cojoc. Proc. SPIE, vol. **5227** (2003), pp. 402–409
41. www.foc-fo.de
42. J.H. Chang, B.G. Jeon, J.K. Kang, J.H. Jung, Y.K. Kim, Characteristics of optical fiber WDM with high isolation, in *Proc. 1999 IEEE Region 10 Conf.*, The Silla Cheju, Cheju Islands, Korea, Sept. 15–17, 1999
43. www.newport.com
44. www.itfoptical.com
45. H. Fukuda, K. Yamada, T. Tsuchizawa, T. Watanabe, H. Shinjima, S.-I. Itabashi, Ultrasmall polarization splitter based on silicon wire waveguides. *Opt. Express* **14**(25), 12401–12408 (2006)
46. D.W. Kim, M.H. Lee, Y. Kim, K.H. Kim, Planar-type polarization beam splitter based on a bridged silicon waveguide coupler. *Opt. Express* **23**(2), 998–1004 (2015)
47. D. Dai, J. Bauters, J.E. Bowers, Passive technologies for future large-scale photonic integrated circuits on silicon: polarization handling, light non-reciprocity and loss reduction. *Light Sci. Appl.* **1**(3), e1–e12 (2012)
48. www.photoline.ixblue.com
49. www.ntt-electronics.com/en/products/photronics
50. www.teraxion.com
51. www.oclaro.com
52. www.finisar.com
53. R.M. de Ridder, C.G.H. Roeloffzen, Interleavers, in *Waveguide Filters in Fibre Optics*, ed. by H. Venghaus (Springer, Berlin, Heidelberg, 2006), Chap. 9
54. L. Lu, L. Zhou, X. Sun, J. Xie, Z. Zou, X. Li, J. Chen, CMOS-compatible athermal tunable silicon optical lattice filters, in *Opt. Fiber Commun. Conf. and Nat. Fiber Opt. Eng. Conf. (OFC/NFOEC'13)*, Anaheim, CA, USA (2013), Techn. Digest, paper OTu3C.4
55. S. Takashia, Y. Mori, H. Hasegawa, K.-I. Sato, T. Watanabe, Low crosstalk wavelength tunable filter that utilizes symmetric and asymmetric Mach-Zehnder interferometers, in *Opt. Fiber Commun. Conf. and Nat. Fiber Opt. Eng. Conf. (OFC/NFOEC'14)*, San Francisco, CA, USA (2014), Techn. Digest, paper Th3F.6
56. T. Goh, Y. Hashizume, Completely cyclic flat-top multi/demultiplexer for multi-carrier transceiver, in *Opt. Fiber Commun. Conf. and Nat. Fiber Opt. Eng. Conf. (OFC/NFOEC'13)*, Anaheim, CA, USA (2013), Techn. Digest, paper OTu3C.1
57. H. Kouketsu, S. Kawasaki, N. Koyama, A. Takei, T. Taniguchi, Y. Matsushima, K. Utaka, High-speed and compact non-blocking 8×8 InAlGaAs/InAlAs Mach-Zehnder-type optical switch fabric, in *Opt. Fiber Commun. Conf. and Nat. Fiber Opt. Eng. Conf. (OFC/NFOEC'14)*, San Francisco, CA, USA (2014), Techn. Digest, paper M2K.3
58. L.B. Soldano, A.I. de Vreede, M.K. Smit, B.H. Verbeek, E.G. Metaal, F.H. Green, Mach-Zehnder interferometer polarization splitter in InGaAsP/InP. *IEEE Photonics Technol. Lett.* **6**(3), 402–405 (1994)

59. T.K. Liang, H.K. Tsang, Integrated polarization beam splitter in high index contrast silicon-on-insulator waveguides. *IEEE Photonics Technol. Lett.* **17**(2), 393–395 (2005)
60. D. Dai, Z. Wang, J. Peters, J.E. Bowers, Compact polarization beam splitter using an asymmetrical Mach-Zehnder interferometer based on silicon-on-insulator waveguides. *IEEE Photonics Technol. Lett.* **24**(8), 673–675 (2012)
61. M. Born, E. Wolf, *Principles of Optics*, 6th edn. (Pergamon, Oxford, 1980)
62. C. Palmer (ed.), *Diffraction Gratings Handbook*, 6th edn. (Newport Corp., Rochester, 2005), 1st edn.: E. Loewen (ed.)
63. J.P. Laude, Diffraction gratings WDM components, in *Wavelength Filters in Fibre Optics*, ed. by H. Venghaus (Springer, Berlin, Heidelberg, 2006), Chap. 3
64. www.senko.com
65. www.ibsen.com
66. www.kosi.com
67. www.wasatchphotonics.com
68. J.B.D. Soole, K.R. Poguntke, A. Scherer, H.P. LeBlanc, C. Chang-Hasnain, J.R. Hayes, C. Caneau, R. Bhat, M.A. Koza, Wavelength-selectable laser emission from a multistriple array grating integrated cavity laser. *Appl. Phys. Lett.* **61**, 2750–2752 (1992)
69. C. Cremer, N. Emeis, M. Schier, G. Heise, G. Ebbinghaus, L. Stoll, Grating spectrograph integrated with photodiode array in InGaAsP/InP. *IEEE Photonics Technol. Lett.* **4**, 108–110 (1992)
70. H. Jian-Jun, B. Lamontagne, A. Delage, L. Erickson, M. Davies, E.S. Koteles, Monolithic integrated wavelength demultiplexer based on a waveguide Rowland circle grating in InGaAsP/InP. *J. Lightwave Technol.* **16**, 631–638 (1998)
71. A. Densmore, V.I. Tolstikhin, K. Primenov, DWDM data receiver based on monolithic integration of an echelle grating demultiplexer and waveguide photodiodes. *Electron. Lett.* **41**, 766–767 (2005)
72. S. Janz, A. Balakrishnan, S. Charbonneau, P. Cheben, M. Cloutier, A. Delâge, K. Dossou, L. Erickson, M. Gao, P.A. Krug, B. Lamontagne, M. Packirisamy, M. Pearson, D.X. Xu, Planar waveguide echelle gratings in silica-on-silicon. *IEEE Photonics Technol. Lett.* **16**, 503–505 (2004)
73. J. Brouckaert, W. Bogaerts, P. Dumon, D. Van Thourhout, R. Baets, Planar concave grating demultiplexer fabricated on a nanophotonic silicon-on-insulator platform. *J. Lightwave Technol.* **25**, 1269–1275 (2007)
74. F. Horst, Silicon integrated waveguide devices for filtering and wavelength demultiplexing, in *Opt. Fiber Commun. Conf. (OFC/NFOEC' 10)*, San Diego, CA, USA (2010), Techn. Digest, paper OWJ3
75. S. Pathak, P. Dumon, D. Van Thourhout, W. Bogaerts, Comparison of AWGs and echelle gratings for wavelength division multiplexing on silicon-on-insulator. *IEEE Photonics J.* **6**(5), 4900109 (2014)
76. J. Brouckaert, W. Bogaerts, S. Selvaraja, P. Dumon, R. Baets, D. Van Thourhout, Planar concave grating demultiplexer with high reflective Bragg reflector facets. *IEEE Photonics Technol. Lett.* **20**, 309–311 (2008)
77. F. Horst, W.M.J. Green, B.J. Offrein, Y.A. Vlasov, Silicon-on-insulator echelle grating WDM demultiplexers with two stigmatic points. *IEEE Photonics Technol. Lett.* **21**, 1743–1745 (2009)
78. W. Bogaerts, S.K. Selvaraja, P. Dumon, J. Brouckaert, K. De Vos, D. Van Thourhout, R. Baets, Silicon-on-insulator spectral filters fabricated with CMOS technology. *IEEE J. Sel. Top. Quantum Electron.* **16**, 33–44 (2010)
79. R. März, *Integrated Optics—Design and Modeling* (Artech House Inc., Boston, 1994)
80. M.K. Smit, New focusing and dispersive planar component based on an optical phased array. *Electron. Lett.* **24**, 385–386 (1988)
81. H. Takahashi, S. Suzuki, K. Kato, I. Nishi, Arrayed-waveguide grating for wavelength division multi/demultiplexer with nanometer resolution. *Electron. Lett.* **26**, 87–88 (1990)

82. C. Dragone, An $N \times N$ optical multiplexer using a planar arrangement of two star couplers. *IEEE Photonics Technol. Lett.* **3**, 812–815 (1991)
83. J.S. Kee, D.P. Poenar, P. Neuzil, L. Yobas, Y. Chen, Design and fabrication of poly(dimethylsiloxane) arrayed waveguide grating. *Opt. Express* **18**(21), 21732–21742 (2010)
84. A. Malik, M. Muneeb, S. Pathak, Y. Shimura, J. Van Campenhout, R. Loo, G. Roelkens, Germanium-on-silicon mid-infrared arrayed waveguide grating multiplexers. *IEEE Photonics Technol. Lett.* **25**(8), 1805–1808 (2013)
85. J. Jiang, C.L. Callender, C. Blanchetiere, J.P. Noad, S. Chen, J. Ballato, D.W. Smith Jr., Arrayed waveguide gratings based on perfluorocyclobutane polymers for CWDM applications. *IEEE Photonics Technol. Lett.* **18**, 370–372 (2006)
86. B. Yang, Y. Zhu, Y. Jiao, L. Yang, Z. Sheng, S. He, D. Dai, Compact arrayed waveguide grating devices based on small SU-strip waveguides. *J. Lightwave Technol.* **29**(13), 2009–2014 (2009)
87. D. Dai, Z. Wang, J.F. Bauters, M.-C. Tien, M.J.R. Heck, D.J. Blumenthal, J.E. Bowers, Low-loss Si_3N_4 arrayed-waveguide grating (de)multiplexer using nano-core optical waveguides. *Opt. Express* **19**(15), 14130–14136 (2011)
88. H. Asakura, K. Nashimoto, D. Kudzuma, M. Hashimoto, H. Tsuda, 200-GHz spacing, 8ch, high-speed wavelength selective arrayed-waveguide grating using buried PLZT waveguides. *IEICE Electron. Express* **9**(7), 712–717 (2012)
89. C. van Dam, *InP-Based Polarization Independent Wavelength Demultiplexers* (Delft University of Technology, The Netherlands, 1997), PhD thesis, ISBN 90-9010798-3
90. X.J.M. Leijts, B. Kuhlow, M.K. Smit, Arrayed waveguide gratings, in *Wavelength Filters in Fibre Optics*, ed. by H. Venghaus (Springer, Berlin, Heidelberg, 2006), Chap. 4
91. M.K. Smit, C. van Dam, PHASAR-based WDM-devices: principles, design and applications. *IEEE J. Sel. Top. Quantum Electron.* **2**, 236–250 (1996)
92. D.C. Kim, H.M. Kim, J.S. Kim, H.R. Choo, J. Kim, K.E. Pyun, K.-H. Yoo, Fabrication of InP-based reflection type arrayed waveguide grating with metal coated reflection facet. *Jpn. J. Appl. Phys.* **40**(Part 2, 1A/B2), L36–L37 (2001)
93. D. Dai, X. Fu, Y. Shi, S. He, Experimental demonstration of an ultracompact Si-nanowire-based reflective arrayed-waveguide grating (de)multiplexer with photonic crystal reflectors. *Opt. Lett.* **35**(15), 2594–2596 (2010)
94. K. Okamoto, K. Ishida, Fabrication of silicon reflection-type arrayed-waveguide gratings with distributed Bragg reflectors. *Opt. Lett.* **38**(18), 3530–3533 (2013)
95. B.I. Akca, C.R. Doerr, G. Sengo, K. Wörhoff, M. Pollnau, R.M. de Ridder, Broad-spectral-range synchronized flat-top arrayed-waveguide grating applied in a 225-channel cascaded spectrometer. *Opt. Express* **20**(16), 18313–18318 (2012)
96. S. Pathak, M. Vanslebrouck, P. Dumon, D. Van Thourhout, W. Bogaerts, Optimized silicon AWG with flattened spectral response using an MMI aperture. *J. Lightwave Technol.* **31**(1), 87–93 (2013)
97. www.lumentum.com
98. T. Kamalakis, T. Sphicopoulos, D. Syvridis, An estimation of performance degradation due to fabrication errors in AWGs. *J. Lightwave Technol.* **20**, 1779–1787 (2002)
99. S. Day, J.P. Stagg, D. Moule, S.J. Clements, C. Rogers, S. Ojha, T. Clapp, J. Brook, J. Morley, The elimination of sidelobes in the arrayed waveguide WDM, in *Integrated Photonics Research* (Optical Society of America, Washington, 1996), p. IMC5
100. M. Kohtoku, T. Hirono Member, S. Oku, Y. Kadota, Y. Shibata, Y. Yoshikuni, Control of higher order leaky modes in deep-ridge waveguides and application to low-crosstalk arrayed waveguide gratings. *J. Lightwave Technol.* **22**, 499–508 (2004)
101. E. Kleijn, P.J. Williams, N.D. Whitbread, M.J. Wale, M.K. Smit, X.J.M. Leijts, Sidelobes in the response of arrayed waveguide gratings caused by polarization rotation. *Opt. Express* **20**, 22660–22668 (2012)
102. C.G.P. Herben, X.J.M. Leijts, D.H.P. Maat, H. Blok, M.K. Smit, Crosstalk performance of integrated optical cross-connects. *J. Lightwave Technol.* **17**, 1126–1134 (1999)

103. S. Das, B. Grek, J. Sun, M. Jain, L.G. Kazowski, MAWG: multicasting arrayed waveguide grating for WDM-PON applications, in *Opt. Fiber Commun. Conf. and Exp./Nat. Fiber Opt. Eng. Conf.* (OFC/NFOEC'08), San Diego, CA, USA (2008), Techn. Digest, paper JWA35
104. T. Niwa, H. Hasegawa, K.-I. Sato, T. Watanabe, H. Takahashi, M. Okuno, Novel wavelength filter offering multi-stage selection for colorless, directionless, and contentionless ROADMs. *IEICE Electron. Express* **9**(16), 1297–1303 (2012)
105. Y. Ikuma, H. Tsuda, AWG-based tunable optical dispersion compensator with multiple lens structure. *J. Lightwave Technol.* **27**(22), 5202–5207 (2009)
106. G. Kurczveil, M.J.R. Heck, J.D. Peters, J.M. Garcia, D. Spencer, J.E. Bowers, An integrated hybrid silicon multiwavelength AWG laser. *IEEE J. Sel. Top. Quantum Electron.* **17**(6), 1521–1527 (2011)
107. L. Chen, C.R. Doerr, P. Dong, Y.-K. Chen, Monolithic silicon chip with 10 modulator channels at 25 Gbps and 100-GHz spacing. *Opt. Express* **19**(26), B946–B951 (2011)
108. Y. Yin, R. Proietti, X. Ye, C.J. Nitta, V. Akella, S.J.B. Yoo, LIONS: an AWGR-based low-latency optical switch for high-performance computing and data centers. *IEEE J. Sel. Top. Quantum Electron.* **19**(2), 3600409 (2013)
109. K.-I. Sato, H. Hasegawa, T. Niwa, T. Watanabe, A large-scale wavelength routing optical switch for data center networks. *IEEE Commun. Mag.* **51**(9), 46–52 (2013)
110. Y. Hida, Y. Hibino, H. Okazaki, Y. Ohmori, 10 m-long silica-based waveguide with a loss of 1.7 dB/m, in *Integrated Photonics Research (IPR'95)*, Dana Point, CA, USA (1995), Techn. Digest, pp. 49–51
111. Y. Hibino, H. Okazaki, Y. Hida, Y. Ohmori, Propagation loss characteristics of long silica-based optical waveguides on 5-inch Si wafers. *Electron. Lett.* **29**, 1847–1848 (1993)
112. www.enablence.com
113. Y. Inoue, A. Kaneko, F. Hanawa, H. Takahashi, K. Hattori, S. Sumida, Athermal silica-based arrayed-waveguide grating multiplexer. *Electron. Lett.* **33**, 1945–1947 (1997)
114. A.J. Ticknor, B.P. McGinnis, T. Tarter, M. Yan, Efficient passive and active wavelength-stabilization techniques for AWGs and integrated optical filters, in *Opt. Fiber Commun. Conf. (OFC'2005)*, Anaheim, CA, USA (2005), Techn. Digest, paper NTHL3
115. www.neophotonics.com
116. Y. Hida, Y. Hibino, T. Kitoh, Y. Inoue, T. Shibata, A. Himeno, 400-channel 25-GHz spacing arrayed-waveguide grating covering a full range of C- and L-bands, in *Opt. Fiber Commun. Conf. (OFC'2001)*, Anaheim, CA, USA (2001), Techn. Digest, paper WB2
117. K. Takada, M. Abe, T. Shibata, K. Okamoto, 5 GHz-spaced 4200-channel two-stage tandem demultiplexer for ultra-multi-wavelength light source using supercontinuum generation. *Electron. Lett.* **38**, 572–573 (2002)
118. NTT Photonics Labs, Annual report, 2005
119. K. Takada, M. Abe, T. Shibata, K. Okamoto, 1-GHz-spaced 16-channel arrayed-waveguide grating for a wavelength reference standard in DWDM network systems. *J. Lightwave Technol.* **20**, 850–853 (2002)
120. M. Zirngibl, C. Dragone, C.H. Joyner, Demonstration of a 15×15 arrayed waveguide multiplexer on InP. *IEEE Photonics Technol. Lett.* **4**, 1250–1253 (1992)
121. M. Smit, X. Leijtens et al., An introduction to InP-based generic integration technology. *Semicond. Sci. Technol.* **29**, 083001 (2014)
122. R. Nagarajan, M. Smit, Photonic integration. *IEEE LEOS Newsl.* **21**, 4–10 (2007)
123. S. Chandrasekhar, M. Zirngibl, A.G. Dentai, C.H. Joyner, F. Storz, C.A. Burrus, L.M. Lunardi, Monolithic eight-wavelength demultiplexed receiver for dense WDM applications. *IEEE Photonics Technol. Lett.* **7**, 1342–1344 (1995)
124. M. Zirngibl, C.H. Joyner, C.R. Doerr, L.W. Stulz, H.M. Presby, An 18-channel multifrequency laser. *IEEE Photonics Technol. Lett.* **8**(7), 870–872 (1996)
125. L.H. Spiekman, M.R. Amersfoort, A.H. De Vreede, F.P.G.M. Van Ham, A. Kuntze, J.W. Pedersen, P. Demeester, M.K. Smit, Design and realization of polarization independent phased array wavelength demultiplexers using different array orders for TE and TM. *J. Lightwave Technol.* **14**(6), 991–995 (1996)

126. C.G.P. Herben, D.H.P. Maat, X.J.M. Leijtens, M.R. Leys, Y.S. Oei, M.K. Smit, Polarization independent diluted WDM cross-connect on InP. *IEEE Photonics Technol. Lett.* **11**(12), 1599–1601 (1999)
127. R. Stabile, A. Albores-Mejia, K.A. Williams, Monolithic active-passive 16×16 optoelectronic switch. *Opt. Lett.* **37**, 4666–4668 (2012)
128. B.W. Tilma, Y. Jiao, P.J. van Veldhoven, B. Smallbrugge, H.P.M.M. Ambrosius, P.J. Thijs, X.J.M. Leijtens, R. Nötzel, M.K. Smit, E.A.J.M. Bente, InP-based monolithically integrated tunable wavelength filters in the 1.6–1.8 μm wavelength region for tunable laser purposes. *J. Lightwave Technol.* **29**(18), 2818–2830 (2011)
129. S.C. Nicholes, M.L. Mašanovič, B. Jevremovič, E. Lively, L.A. Coldren, D.J. Blumenthal, The world's first InP 8×8 monolithic tunable optical router (MOTOR) operating at 40 Gbps line rate per port, in *Opt. Fiber Commun. Conf. and Nat. Fiber Opt. Eng. Conf. (OFC/NFOEC'09)*, San Diego, CA, USA (2009), Techn. Digest, paper PDP.B1
130. R. Nagarajan, M. Kato, S. Corzine, P. Evans, C. Joyner, R. Schneider, F. Kish, D. Welch, Monolithic, multi-channel DWDM transmitter photonic integrated circuits, in *21st IEEE Semicond. Laser Conf. (ISLC 2008)*, Sorrento, Italy (2008), Conf. Digest, paper MA3
131. www.infinera.com
132. K. Lawniczuk, C. Kazmierski, M.J. Wale, P. Szczepański, R. Piramidowicz, M.K. Smit, X.J.M. Leijtens, AWG-DBR-based transmitter fabricated in an InP generic foundry platform, in *Opt. Fiber Commun. Conf. and Nat. Fiber Opt. Eng. Conf. (OFC/NFOEC'14)*, San Francisco, CA, USA (2014), Techn. Digest, paper Tu3H.2
133. C.R. Doerr, L. Zhang, P.J. Winzer, Monolithic InP multiwavelength coherent receiver using a chirped arrayed waveguide grating. *J. Lightwave Technol.* **29**(4), 536–541 (2011)
134. L.A. Coldren, S.C. Nicoles, L. Johansson, S. Ristic, R.S. Guzzon, E.J. Norberg, U. Krishnamachari, High performance InP-based photonic ICs—a tutorial. *J. Lightwave Technol.* **29**(4), 554–570 (2011)
135. K. Okamoto, Wavelength-division-multiplexing devices in thin SOI: advances and prospects. *IEEE J. Sel. Top. Quantum Electron.* **20**(4), 8200410 (2014)
136. S. Pathak, D. Van Thourhout, W. Bogaerts, Design trade-offs for silicon-on-insulator-based AWGs for (de)multiplexer applications. *Opt. Lett.* **38**(16), 2961–2964 (2013)
137. J. Wang, Z. Sheng, L. Li, A. Pang, A. Wu, W. Li, X. Wang, S. Zou, M. Qi, F. Gan, Low-loss and low-crosstalk 8×8 silicon nanowire AWG routers fabricated with CMOS technology. *Opt. Express* **22**(8), 9395–9403 (2014)
138. S.T.S. Cheung, B. Guan, S.S. Djordjevic, K. Okamoto, S.J.B. Yoo, Low-loss and high contrast silicon-on-insulator (SOI) arrayed waveguide grating, in *Conf. Lasers Electro-Opt. (CLEO/QELS 2012)*, San Jose, USA (2012), Techn. Digest, paper CM4A.5
139. J. Zou, X. Xia, T. Lang, J.-J. He, Birefringence compensated arrayed waveguide grating, in *Optoelectronic Devices and Integration V*, ed. by X. Zhang, H. Ming, C. Yu. *Proc. SPIE*, vol. **9270** (2014), 92700Y
140. K.O. Hill, Y. Fujii, D.C. Johnson, B.S. Kawasaki, Photosensitivity in optical fiber waveguides: application to reflection filter fabrication. *Appl. Phys. Lett.* **32**, 647–649 (1978)
141. G. Meltz, W.W. Morey, W.H. Glenn, Formation of Bragg gratings in optical fibers by a transverse holographic method. *Opt. Lett.* **14**, 823–825 (1989)
142. A. Othonos, K. Kalli, *Fiber Bragg Gratings: Fundamentals and Applications in Telecommunications and Sensing* (Artech House, Boston, London, 1999)
143. R. Paschotta, *Encyclopedia of Laser Physics and Technology* (Wiley-VCH, Berlin, 2008)
144. P.St.J. Russell, J.L. Archambault, L. Reekie, Fiber gratings. *Phys. World* **October**, 41–46 (1993)
145. I. Riant, F. Haller, Study of the photosensitivity at 193 nm and comparison with photosensitivity at 240 nm influence of fiber tension: type IIA aging. *J. Lightwave Technol.* **15**, 1464–1469 (1997)
146. T. Erdogan, Fiber grating spectra. *J. Lightwave Technol.* **15**, 1277–1294 (1997)
147. A. Othonos, K. Kalli, D. Pureur, A. Mugnier, Fibre Bragg gratings, in *Wavelength Filters in Fibre Optics*, ed. by H. Venghaus (Springer, Berlin, Heidelberg, 2006), Chap. 5

148. www.gouldfo.com
149. www.broptics.com
150. www.aos-fiber.com
151. www.redferncomponents.com
152. M. Li, H. Li, Reflection equalization of the simultaneous dispersion and dispersion-slope compensator based on a phase-only sampled fiber Bragg grating. *Opt. Express* **16**, 9821–9828 (2008)
153. Y. Painchaud, A. Mailloux, H. Chotard, E. Pelletier, M. Guy, Multi-channel fiber Bragg gratings for dispersion and slope compensation, in *OSA Trends in Optics and Photonics (TOPS)*, vol. **70**, *Opt. Fiber Commun. Conf. (OFC/I/OOC'02)*, Anaheim, CA, USA (2002), Techn. Digest, pp. 581–582
154. A.M. Vengsarkar, P.J. Lemaire, J.B. Judkins, V. Bhatia, T. Erdogan, J.E. Sipe, Long-period fiber gratings as band-rejection filters. *J. Lightwave Technol.* **14**, 58–65 (1996)
155. I. Giles, A. Obeysekara, R. Chen, D. Giles, F. Poletti, D. Richardson, Fiber LPG mode converters and mode selection technique for multimode SDM. *IEEE Photonics Technol. Lett.* **24**(21), 1922–1925 (2012)
156. T. Almeida, A. Shahpari, A. Rocha, R. Oliveira, F. Guiomar, A. Pinto, A.L. Teixeira, P. André, R.N. Nogueira, Experimental demonstration of selective core coupling in multicore fibers of a 200 Gb/s DP-16QAM signal, in *Opt. Fiber Commun. Conf. (OFC'16)*, Anaheim, CA, USA (2016), Techn. Digest, paper Tu3I.4
157. S.W. James, R.P. Tatam, Optical fiber long-period grating sensors: characteristics and application. *Meas. Sci. Technol.* **14**, R49–R61 (2003)
158. X. Fan, I.M. White, S.I. Shopova, H. Zhu, J.D. Suter, Y. Sun, Sensitive optical biosensors for unlabeled targets: a review. *Anal. Chim. Acta* **620**, 8–26 (2008)
159. C. Fabry, A. Pérot, Théorie et applications d'une nouvelle méthode de spectroscopie interférentielle. *Ann. Chim. Phys.* **16**, 115–144 (1899)
160. T. Koonen, Fabry-Perot interferometer filters, in *Wavelength Filters in Fibre Optics*, ed. by H. Venghaus (Springer, Berlin, Heidelberg, 2006), Chap. 6
161. www.micronoptics.com
162. F. Gires, P. Tournois, Interféromètre utilisable pour la compression d'impulsions lumineuses modulées en fréquence. *C.R. Acad. Sci. Paris* **258**, 6112–6115 (1964)
163. M.K. Tilsch, R.B. Sargent, C.A. Hulse, Dielectric multilayer filters, in *Wavelength Filters in Fibre Optics*, ed. by H. Venghaus (Springer, Berlin, Heidelberg, 2006), Chap. 7
164. H.A. Macleod, *Thin Film Optical Filters* (Institute of Physics Publishing, Dirac House, Temple Back, Bristol, 2001)
165. A. Thelen, *Design of Interference Coatings* (McGraw-Hill, New York, USA, 1989)
166. A. Badeen, M. Briere, P. Hook, C. Montcalm, R. Rinfret, J. Schneider, B.T. Sullivan, Advanced optical coatings for telecom and spectroscopic applications, in *Proc. Conf. Opt. Systems Design*. Glasgow, UK. SPIE, vol. **7101** (2008), pp. 7101–7117
167. H. Takahashi, Temperature stability of thin-film narrow-bandpass filters produced by ion assisted deposition. *Appl. Opt.* **34**, 667–675 (1995). Note that the author's last name is misspelled as “Takashashi” in the article; the correct spelling is “Takahashi”
168. www.oxfordplasma.de
169. www.auxora.com
170. www.iridian.ca
171. N. Kawakami, J. Kobayashi, M. Hikita, A. Kudo, F. Yamamoto, S. Imamura, Filter-embedded four-channel WDM module fabricated from fluorinated polyimide. *J. Lightwave Technol.* **24**, 2388–2393 (2006)
172. N. Keil, Z. Zhang, C. Zawadzki, C. Wagner, A. Scheibe, H. Ehlers, D. Ristau, J. Wang, W. Brinker, N. Grote, Ultra low-loss 1×2 multiplexer using thin-film filters on polymer integration platform. *Electron. Lett.* **45**, 1167–1168 (2009)
173. N. Keil, C. Zawadzki, Z. Zhang, J. Wang, N. Mettbach, N. Grote, M. Schell, Polymer PLC as an optical integration bench, in *Opt. Fiber Commun. Conf. (OFC/NFOEC'11)*, Los Angeles, CA, USA (2011), Techn. Digest, paper OWM1

174. R.M. Fortenberry, M.A. Scobey, D.J. Derickson, L.F. Stokes, P.C. Egerton, Chromatic dispersion of thin film filters, in *Opt. Fiber Commun. Conf. (OFC'05)*, Anaheim, CA, USA (2005), Techn. Digest, paper OFL2
175. K. Nosu, H. Ishio, K. Hashimoto, Multireflection optical multi/demultiplexer using interference filters. *Electron. Lett.* **15**, 414–415 (1979)
176. Y. Okabe, H. Sasaki, A simple wide wavelength division multi/demultiplexer consisting of optical elements, in *Opt. Fiber Commun. Conf. (OFC/IOOC'02)*, Anaheim, CA, USA (2002), Techn. Digest, pp. 322–323
177. B.E. Little, S.T. Chu, P.P. Basil, J.V. Hryniewicz, F.G. Johnson, F. Seifert, D. Gill, V. Van, O. King, M. Trakalo, Very high-order microring resonator filters for WDM applications. *IEEE Photonics Technol. Lett.* **16**, 2263–2265 (2004)
178. G.L. Bona, F. Horst, R. Germann, B.J. Offrein, D. Wiesmann, Tunable dispersion compensator realized in high-refractive-index-contrast SiON technology, in *Proc. 28th Europ. Conf. Opt. Commun. (ECOC'02)*, Copenhagen, Denmark (2002), vol. **2**, paper 4.2.1
179. P.P. Absil, J.V. Hryniewicz, B.E. Little, P.S. Cho, R.A. Wilson, L.G. Joneckis, P.-T. Ho, Wavelength conversion in GaAs micro-ring resonators. *Opt. Lett.* **25**, 554–556 (2000)
180. M. Hamacher, U. Troppenz, H. Heidrich, D.G. Rabus, Active ring resonators based on InGaAsP/InP, in *Conf. Photonic Fabrication Europe*. Proc. SPIE, vol. **4947** (2003), pp. 212–222
181. V. Van, T.A. Ibrahim, K. Ritter, P.P. Absil, F.G. Johnson, R. Grover, J. Goldhar, P.-T. Ho, All-optical nonlinear switching in GaAs–AlGaAs microring resonators. *IEEE Photonics Technol. Lett.* **14**, 74–76 (2002)
182. V.R. Almeida, C.A. Barrios, R.R. Panepucci, M. Lipson, All-optical control of light on a silicon chip. *Nature* **431**, 1081–1084 (2004)
183. Q. Xu, B. Schmidt, J. Shakya, M. Lipson, Cascaded silicon micro-ring modulators for WDM optical interconnection. *Opt. Express* **14**, 9430–9435 (2006)
184. M.S. Dahlem, C.W. Holzwarth, A. Khilo, F.X. Kärtner, H.I. Smith, E.P. Ippen, Reconfigurable multi-channel second-order silicon microring-resonator filterbanks for on-chip WDM systems. *Opt. Express* **19**(1), 306–316 (2011)
185. J. Capmany, B. Ortega, D. Pastor, A tutorial on microwave photonic filters. *J. Lightwave Technol.* **24**(1), 201–229 (2006)
186. K. De Vos, I. Bartolozzi, E. Schacht, P. Bienstman, R. Baets, Silicon-on-insulator microring resonator for sensitive and label-free biosensing. *Opt. Express* **15**, 7610–7615 (2008)
187. A. Yalçın, K.C. Popat, J.C. Aldridge, T.A. Desai, J. Hryniewicz, N. Chbouki, B.E. Little, O. King, V. Van, S. Chu, D. Gill, M. Anthes-Washburn, M.S. Ünlü, B.B. Goldberg, Optical sensing of biomolecules using microring resonators. *IEEE J. Sel. Top. Quantum Electron.* **12**, 148–155 (2006)
188. W.W. Lui, T. Hirono, K. Yokohama, W.-P. Huang, Polarization rotation in semiconductor bending waveguides: a coupled-mode theory formulation. *J. Lightwave Technol.* **16**, 929–936 (1998)
189. F. Morichetti, A. Melloni, M. Martinelli, Effects of polarization rotation in optical ring-resonator-based devices. *J. Lightwave Technol.* **24**, 573–585 (2006)
190. C. van Dam, L.H. Spiekman, F.P.G.M. van Ham, G.H. Groen, J.J.G.M. van der Tol, I. Moerman, W.W. Pascher, M. Hamacher, H. Heidrich, C.M. Weinert, M.K. Smit, Novel compact polarization converters based on ultra short bends. *IEEE Photonics Technol. Lett.* **8**, 1346–1348 (1996)
191. Y.M.P. Chamorro-Posada, F.J. Fraile-Pelaez, F.J. Diaz-Otero, Micro-ring chains with high-order resonances. *J. Lightwave Technol.* **29**(10), 1514–1521 (2011)
192. S. Darmawan, Y.M. Landobasa, M.-K. Chin, Pole-zero dynamics of high-order ring resonator filters. *J. Lightwave Technol.* **25**(8), 1568–1575 (2007)
193. B.E. Little, A VLSI photonics platform, in *Opt. Fiber Commun. Conf. (OFC'03)*, Atlanta, GA, USA, (2003), vol. **2**, pp. 444–445, paper ThD1

194. E.J. Norberg, R.S. Guzzon, J. Parker, L.A. Johansson, L.A. Coldren, Programmable photonic microwave filters monolithically integrated in InP/InGaAsP. *J. Lightwave Technol.* **29**(11), 1611–1619 (2011)
195. H.-W. Chen, A. Fang, J.D. Peters, Z. Wang, J. Bovington, D. Liang, J. Bowers, Integrated microwave photonic filter on a hybrid silicon platform. *IEEE Trans. Microw. Theory Tech.* **58**(11), 3213–3219 (2010)
196. M.S. Rasras, D.M. Gill, S.S. Patel, K.-Y. Tu, Y.-K. Chen, A.E. White, A.T.S. Pomerene, D.N. Carothers, M.J. Grove, D.K. Sparacin, J. Michel, M.A. Beals, L.C. Kimerling, Demonstration of a fourth order pole-zero optical filter integrated using CMOS processes. *J. Lightwave Technol.* **25**(1), 87–92 (2007)
197. N.-N. Feng, P. Dong, D. Feng, W. Qian, H. Liang, D.C. Lee, J.B. Luff, A. Agarwal, T. Banwell, R. Menendez, P. Toliver, T.K. Woodward, M. Asghari, Thermally-efficient reconfigurable narrowband RF photonic filter. *Opt. Express* **18**(24), 24648–24653 (2010)
198. B. Guan, S.S. Djordjevic, N.K. Fontaine, L. Zhou, S. Ibrahim, R.P. Scott, D.J. Geisler, Z. Ding, S.J.B. Yoo, CMOS compatible reconfigurable silicon photonic lattice filters using cascaded unit cells for RF-photonic processing. *IEEE J. Sel. Top. Quantum Electron.* **20**(4), 8202110 (2014)
199. R.S. Guzzon, E.J. Norberg, J.S. Parker, L.A. Johansson, L.A. Coldren, Integrated InP–InGaAsP tunable coupled ring optical bandpass filters with zero insertion loss. *Opt. Express* **19**(8), 7816–7826 (2011)
200. Y. Yanagase, S. Suzuki, Y. Kokubun, S.T. Chu, Box-like filter response by vertically series coupled microring resonator filter, in *Proc. 27th Europ. Conf. Opt. Commun.* (ECOC'01), Amsterdam, The Netherlands (2001), vol. 4, pp. 634–635
201. L.C. Kimerling, L. Dal Negro, S. Saini, Y. Yi, D. Ahn, S. Akiyama, D. Cannon, J. Liu, J.G. Sandland, D. Sparacin, J. Michel, K. Wada, M.R. Watts, Monolithic silicon microphotonics, in *Silicon Photonics*, ed. by L. Pavesi, D.J. Lockwood (Springer, Berlin, Heidelberg, 2004), pp. 89–119
202. S. Cao, J. Chen, J.N. Damask, C.R. Doerr, L. Guiziou, G. Harvey, Y. Hibino, H. Li, S. Suzuki, K.-Y. Wu, P. Xie, Interleaver technology: comparisons and applications requirements. *J. Lightwave Technol.* **22**, 281–289 (2004)
203. D. Dai, S. He, Novel ultrasmall Si-nanowire-based arrayed-waveguide grating interleaver with spirals. *Opt. Commun.* **281**, 3471–3475 (2008)
204. C.R. Doerr, K. Okamoto, Advances in silica planar lightwave circuits. *J. Lightwave Technol.* **24**(12), 4763–4789 (2006)
205. G.P. Agrawal, *Lightwave Technology* (Wiley, New York, 2005), Chap. 9.5.3
206. B. Dingel, M. Izutsu, Multifunctional optical filter with a Michelson-Gires-Tournois interferometer for wavelength-division-multiplexed system applications. *Opt. Lett.* **23**, 1099–1101 (1998)
207. X. Shu, K. Sugden, I. Bennion, Flattop multi-passband filter based on all-fiber Michelson-Gires-Tournois interferometer, in *Proc. 30th Europ. Conf. Opt. Commun.* (ECOC'04), Stockholm, Sweden (2004), paper Tu1.3.1
208. X. Jiang, J. Wu, Y. Yang, T. Pan, J. Mao, B. Liu, R. Liu, Y. Zhang, C. Qiu, Y. Su, Compact silicon photonic interleaver using loop-mirror-based Michelson-Gires-Tournois interferometer, in *Opt. Fiber Commun. Conf.* (OFC'16), Anaheim, CA, USA (2016), Techn. Digest, paper Tu2F.5
209. M. Kohtoku, S. Oku, Y. Kadota, Y. Shibata, Y. Yoshikuni, 200-GHz FSR periodic multi/demultiplexer with flattened transmission and rejection band by using a Mach-Zehnder interferometer with a ring resonator. *IEEE Photonics Technol. Lett.* **12**, 1174–1176 (2000)
210. J. Song, Q. Fang, S.H. Tao, M.B. Yu, G.Q. Lo, D.L. Kwong, Passive ring-assisted Mach-Zehnder interleaver on silicon-on-insulator. *Opt. Express* **16**, 8359–8365 (2008)
211. L. Zhuang, W. Beeker, A. Leinse, R. Heideman, P. van Dijk, C. Roeloffzen, Novel wideband microwave polarization network using a fully-reconfigurable photonic waveguide interleaver with a two-ring resonator-assisted asymmetric Mach-Zehnder structure. *Opt. Express* **21**(3), 3114–3124 (2013)

212. H. Arai, H. Nonen, K. Ohira, T. Chiba, PLC wavelength splitter for a dense WDM transmission system. *Hitachi Cable Rev.* **21**, 11–16 (2002)
213. www.optoplex.com
214. www.hitachi-cable.co.jp
215. J.L. Jackel, M.S. Goodman, J.E. Baran, W.J. Tomlinson, G.-K. Chang, M.Z. Iqbal, G.H. Song, K. Bala, C.A. Brackett, D.A. Smith, R.S. Chakravarthy, R.H. Hobbs, D.J. Fritz, R.W. Ade, K.M. Kissa, Acousto-optic tunable filters (ATOF's) for multiwavelength optical cross-connects: crosstalk considerations. *J. Lightwave Technol.* **14**, 1056–1066 (1996)
216. M.K. Smit, T. Koonen, H. Hermann, W. Sohler, Wavelength-selective devices, in *Fibre Optic Communication Devices*, ed. by N. Grote, H. Venghaus (Springer, Berlin, Heidelberg, 2001), Chap. 7
217. www.goochandhousego.com/products/prod/16

Herbert Venghaus studied physics and earned a Ph.D. degree at the University of Hamburg. Subsequently he joined the Max-Planck-Institute for Solid State Research in Stuttgart and focused on optic and magneto-optic properties of III–V- and II–VI-semiconductors. In 1980 he started working at the Corporate Research Laboratories of Siemens AG (München and Erlangen) and in 1986 he joined the Heinrich-Hertz-Institute (Berlin), which has become a Fraunhofer Institute in 2003. His main responsibility as a department head at HHI has been the development of Indium Phosphide based optoelectronic integrated circuits (OEICs) with particular emphasis on monolithic integration. More recently he has shifted his primary interest on the identification of new, non-telecom applications of devices and technologies initially developed for fibre optic communication including, and these new topics included the development of THz systems based on telecom devices or biosensors based upon planar resonator structures. He has been actively involved in various European projects and has also been a member of the program committee of various international conferences. He holds several patents, has published more than 80 scientific papers, various book chapters and has been editor of three books as well.

Chapter 10

Optical Switches

Shifu Yuan and John E. Bowers

Abstract After a detailed introductory discussion of general concepts, which apply to optical switches regardless of their implementation technology, the following sections cover opto-mechanical switches and liquid crystal technologies for optical switching, including small matrix switches and wavelength selective switches. Planar lightwave circuit (PLC) based optical switch technologies constitute the topic of the next section, and the treatment includes switches in various material systems such as LiNbO₃, polymer, silicon-on-insulator (SOI), and switching by means of the electro-optic- or thermo-optic effect. The following, major part of the chapter covers MEMS-based switches including 2D and 3D switches, switching matrices and wavelength selective switches as well. The chapter concludes with a brief discussion of piezo-electric actuator-based matrix switches. The description of optical switches includes their fundamentals, including underlying physics, operation principles, and generic implementations, typical characteristics of commercially available devices, and recent developments of switches that are still in the R&D stage.

10.1 General Concepts of Optical Switching

10.1.1 Introduction

Optical switches are important devices for optical fiber communication systems where they are used for protection, restoration, wavelength routing, fiber-management, automatic patch panel, and in optical cross-connects [1–3]. As the majority of optical communication systems use single mode fibers (SMFs), we will focus on SMF optical switches in this chapter. An optical switch offers to optically switch fiber circuits without doing expensive optical-electronic-optical (OEO) con-

S. Yuan (✉)

Calient Technologies, 25 Castilian Drive, Goleta, CA 93117, USA

e-mail: syuan@calient.net

J.E. Bowers

Electrical and Computer Engineering Department, University of California, Santa Barbara, CA 93106, USA

e-mail: bowers@ece.ucsb.edu

versions. Such a switch is transparent to all protocols, data formats, and modulation formats since it only rearranges the physical fiber circuit.

The various classes of optical switches include 1×2 , 2×2 , $1 \times N$, and large scale $N \times M$ matrix switches, wavelength selective switches (WSSs), and multi-cast $N \times M$ switches. Each category of optical switches has different technologies for implementation including liquid crystal (LC), planar lightwave circuit (PLC), micro-electro-mechanical-system (MEMS), and piezo-electronic actuator based technologies.

Most optical switches use an electronically controlled mechanism to switch an optical signal into different directions. However, there are also all-optical switches that use optical signals to control switches [4] but these are beyond the scope of the present chapter. We will also not deal with optical switches that comprise optical gain elements (e.g. optical amplifiers) designated as active optical switches [5] but we will restrict ourselves to passive optical switches, and the present chapter will be organized as follows: Sect. 10.1 discusses general concepts that apply to optical switches regardless of their implementation technology. Section 10.2 discusses opto-mechanical switches, and Sect. 10.3 covers liquid crystal technologies for optical switching, including small matrix switches and wavelength selective switches. The topic of Sect. 10.4 are planar lightwave circuit based optical switch technologies, Sect. 10.5 is devoted to MEMS-based optical switches, including 2D MEMS switches, 3D MEMS switches, and MEMS-based WSSs, and Sect. 10.6 briefly discusses piezo-electric actuator-based matrix switches.

10.1.2 Basics

The most simple, generic switching elements are 1×2 and 2×2 switches. As illustrated in Fig. 10.1, a 2×2 switch can switch between its “bar” and “cross” state, and switching may be digital or continuous, depending on implementation of the switch. An illustration of a 2×2 switch using a digital actuator is also illustrated in Fig. 10.1. 1×2 and 2×2 switches can be devices in their own right (see Sect. 10.2) and they can be cascaded resulting in larger switching matrices.

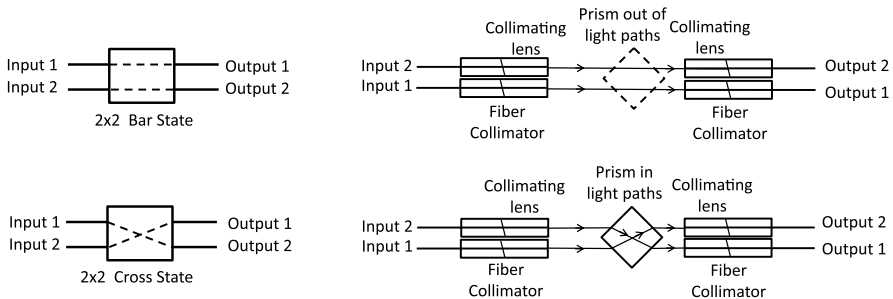


Fig. 10.1 Simple 2×2 optical switch, schematic (*left*) and mechanical switch using prism as digital actuator (*right*)

10.1.3 Optical Matrix Switches

10.1.3.1 General Aspects

An optical matrix switch [6] has input ports and output ports and the switch selectively sets up a connection between one input port i and one output port j which can be described as a pair of ports, e.g., (i, j) . When a connection is (not) set up, the connection is called in the on (off) state, and it might be worthwhile to note that a port can only be used in one connection at a given instant. Optical paths are essentially bidirectional so that a signal from port i to port j can equally propagate from port j to port i . However, if a switch has optical power monitoring for feedback control, the light propagation direction is important, and with respect to monitoring, such switches may be classified as unidirectional.

An optical matrix switch can be called an $M \times N$ optical switch with M input and N output ports. Telcordia definition GR-1073 [6] does not specify which ports are input and output ports since the switch is typically bidirectional. However, in order to avoid confusion, we will consider an $M \times N$ switch to have M input and N output ports with the understanding that the signal might be bidirectional.

An optical matrix switch should meet a number of requirements including: small insertion loss, low crosstalk, fast switching time, good directivity, and small footprint. In addition, non-blocking operation may also be required or may even be mandatory [6] where “non-blocking” includes the following variants:

Strict-sense non-blocking: it is possible to establish a new path from any unused input to any unused output port, no matter what paths are set already.

Wide-sense non-blocking: after connections have already been set, it is still possible to connect any unused input to any unused output using dedicated algorithms without interrupting the connections set-up already.

Re-arrangeably non-blocking: the switch enables any connection from inputs to outputs provided all connections to be made are known in advance. If connections have been made before, disconnecting and resetting existing connections may be required in order to make the new connections.

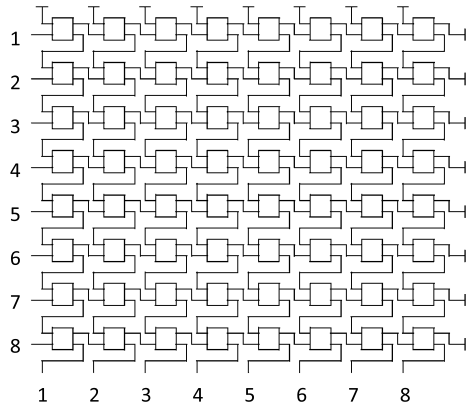
Blocking switch: new connections from free input to free output ports cannot be made at all once a certain number of connections have been set.

For most telecom applications switches need to be strict-sense or wide-sense non-blocking while blocking and re-arrangeable non-blocking switches are typically not acceptable.

10.1.3.2 Optical Matrix Switch Architectures

Optical Matrix Switches Using Digital Switching Elements Optical matrix switch architectures are essentially based upon two types of actuators: either digital actuators that switch/steer light paths digitally to the ‘on’ or ‘off’ position, or analogue actuators that enable directing optical signals to many positions

Fig. 10.2 Example of 8×8 crossbar switch using 2×2 optical switches [6]



continuously with an analogue driving signal. Larger digital switches can be implemented with multiple 2×2 (or 1×2) switches. Figure 10.2 shows an $N \times N$ crossbar switch architecture that uses 2×2 switches as basic switching elements, arranged in N horizontal lines and N vertical lines in a 2D plane. Each cross point has a switching element and in total N^2 switching elements are needed. A crossbar switch has intrinsic non-uniform insertion loss due to different path lengths and different numbers of switching elements for different connections.

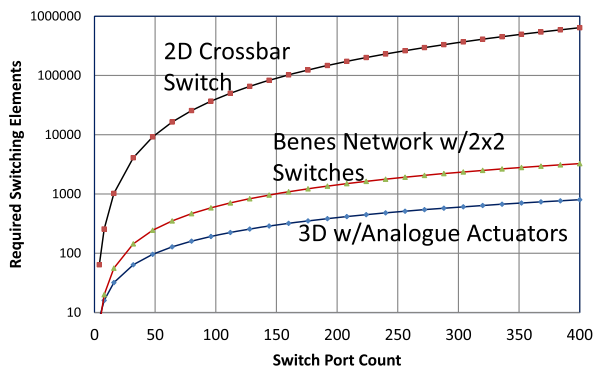
The 2×2 switches of an $N \times N$ crossbar architecture can also be arranged in such a way that light from any input to any output port passes N switching elements resulting in path-independent insertion loss (PI-IL) [7, 8]. Both, the general and the PI-IL crossbar switch architectures are strictly non-blocking. There are other architectures that use smaller numbers of switching elements, e.g. the Benes architecture [9] but depending on the structure of such switches these architectures may cause switches to be blocking. Larger switching matrices using digital actuators do generally suffer from higher insertion loss since IL increases proportionally to the amount of switching elements in the light path. In addition, crosstalk from each 2×2 switch accumulates in the case of multistage switches, which is another drawback.

Optical Switch Architectures Using Analogue Actuators Analogue actuators, including MEMS mirrors, liquid crystal devices, and piezo-electric actuators, can move an optical beam freely to multiple space positions so that a single actuator enables a $1 \times N$ optical switch.

With $2N$ $1 \times N$ optical switches arranged in an architecture proposed by Spanke a strictly non-blocking $N \times N$ switch can be achieved [10]: Each input port directs the incoming beam to the appropriate output $N \times 1$ switch which then switches the signal to the output port. Corresponding switches become complicated for large port numbers N since there are N^2 optical fibers to be physically interconnected. However, the design can be made better scalable if the interconnects are realized as free space $1 \times N$ and $N \times 1$ switches at the input and output, respectively, resulting in $2N$ actuating elements for an $N \times N$ switch with analogue actuators.

Since 2D analogue actuators can steer optical beams along two axes so that the optical beams are traveling in 3-dimensional space inside the switch, switches of this

Fig. 10.3 Required switching element number vs. switch port count for 3D switch architecture with analogue actuators, Benes network, and 2D crossbar switch



kind are typically called 3D optical switches. On the other hand, integrated crossbar switches using digital actuating elements are called 2D optical switches.

The number of required switching elements scales differently as the number of ports gets larger as illustrated in Fig. 10.3 for (i) 2D crossbar, (ii) Benes switches based upon 2×2 switches, and (iii) 3D analogue $N \times N$ switches, and the advantages of analogue actuators for larger $N \times N$ switching fabrics is obvious.

Clos architecture for Very Large Scale Optical Switches Clos proposed a scheme to build large scale non-blocking $N \times N$ switches by using multiple smaller switches in three stages and requiring fewer crosspoints than a complete crossbar [11]. Key features are: a first stage with $m = \frac{N}{n}$ non-blocking $n \times k$ switches (n inputs, k outputs), a second stage consisting of k crossbar switches of size of $m \times m$, and a third stage consisting of m non-blocking $k \times n$ switches with k inputs and n outputs.

A Clos network is a strict-sense non-blocking switch if $k \geq 2n - 1$, and it is re-arrangeably non-blocking if $k \geq n$. In addition, it can also be implemented in a folded architecture [12].

10.1.4 Wavelength Selective Switches (WSS)

10.1.4.1 General Aspects

A wavelength selective switch (WSS) [13–17] is a device capable to switch optical wavelengths between several optical fibers. Each fiber carries multiple DWDM wavelengths, and wavelength selective means selectively switching a particular wavelength between fibers. WSSs are blocking in the wavelength domain since there is no wavelength conversion inside the switch.

Being hitless is a feature required for most telecom systems [15]. Although the telecom system can use non-hitless WSSs to implement hitless operation, it is desirable for WSSs itself to be hitless. For a WSS that is non-hitless, the switched

wavelength may be swiping through (the) other un-intended channels shortly during the transient time of switching. For a hitless WSS, this does not happen. That means when switching a wavelength with the hitless WSS, only the specific wavelength in the present port and the target port are affected, while all the other wavelengths and other ports won't be affected.

Currently (most) optical transmission systems align operation wavelengths to the traditional ITU standard with 50 GHz and 100 GHz channel spacing. However, tighter channel spacing (25 GHz, 33 GHz) or 87.5 GHz instead of 100 GHz might enable higher total transmission rates per fiber [16], and in order to be compatible with such systems, flexible grid or gridless operation of WSSs has been proposed as a future proof technology. To enable gridless operation of a WSS, 12.5 GHz or 25 GHz granularity is required, and as a consequence much more actuators ($4\times$ for 12.5 GHz or $2\times$ for 25 GHz granularity) are needed for a WSS with 50 GHz channel spacing. Technologies like liquid crystal on silicon (LCoS) have no problem in offering more pixels but for others like MEMS it is difficult to do so. Currently, most WSSs are specified for operation at fixed ITU grid frequencies with either 50 GHz or 100 GHz channel separation. However, how important future proof flexible grid WSSs might be, is a matter of ongoing and controversial discussion.

10.1.4.2 Optical Architectures for $1 \times N$ WSSs

A $1 \times N$ WSS can be constructed with discrete components such as demultiplexers (demuxes), switches, and multiplexers (muxes), but such a switch will be bulky with hundreds of fiber terminations to interconnects. This is unfavorable for telecom applications, where device size, i.e. small WSS footprint, has become particularly important. Furthermore, cascading discrete demux/mux components narrows the device wavelength passband, which makes this approach even less attractive.

Currently most $1 \times N$ WSSs deployed in reconfigurable optical add-drop multiplexers (ROADMs) use diffraction grating-based free-space-optics coupled with an optical switching engine [16, 17]. The switching engine manipulates the particular wavelengths from one port to another by changing the phase, polarization, angle or position of a wavelength-dispersed optical beam. The switching engine can use digital or analogue actuation elements as described in Sect. 10.1.3.2.

The diffraction grating in a WSS is usually in the Bragg or Littrow configuration, where the diffraction angle of the -1 st order is equal to the incidence angle for the central wavelength [18], see also Chap. 9, Sect. 9.5. The diffraction grating for WSSs is designed to have maximum diffraction efficiency (e.g., $>90\%$) in the Bragg configuration.

In recent WSS designs, the ports are typically arranged as 1D arrays of fibers or fiber collimators at the input/output as shown in Fig. 10.4(a). These linear ports are arranged parallel to each other, and different wavelengths, after passing the optical lens, will be focused to different positions in the back plane of the optical lens where the optical switching elements are located. These switching elements redirect each individual input beam to the selected output port.

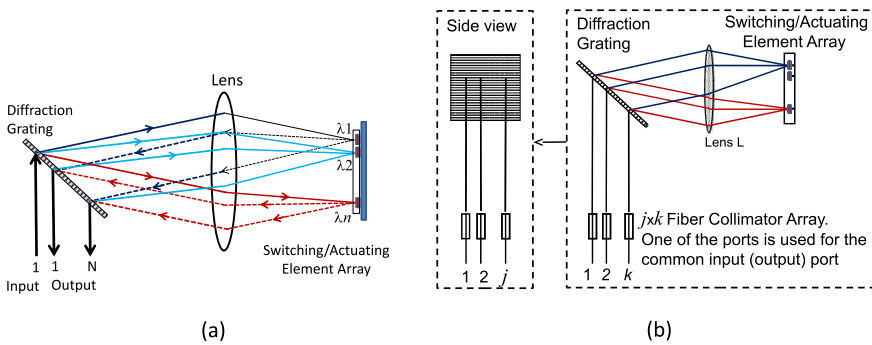


Fig. 10.4 $1 \times N$ WSS basic architecture. (a) Input/output ports in a 1D array, (b) input/output ports in a $j \times k$ 2D array

The direction of the port spreading may be either parallel or perpendicular to the direction of wavelength spreading produced by the grating (as shown in Fig. 10.4(a)). If it is parallel, then adding more ports increases the size of the optics in the wavelength dispersion direction and the optical design needs to consider the different path lengths. If it is perpendicular, which is more common in current WSS designs, then adding more ports increases the size of the optics perpendicular to the dispersion direction.

The switching elements can steer the beam in two axes, therefore it is possible to arrange the input/output fibers in 2 dimensions as $j \times k$, so that it is possible to increase the device size along two axes. Figure 10.4(b) shows the schematic of a $1 \times N$ WSS switch with an $j \times k$ 2D configuration for the input/output ports.

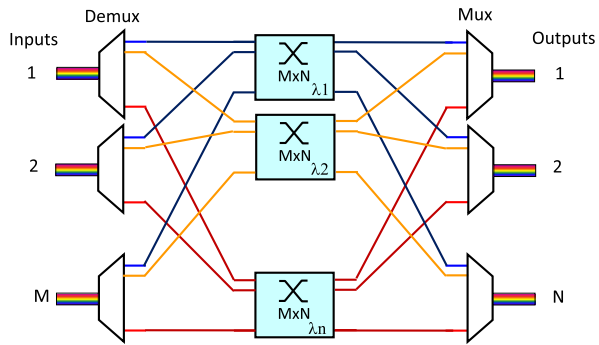
Switching/actuation of $1 \times N$ WSSs may be achieved by 1D arrays of MEMS mirrors, polarization-based liquid crystal arrays, or LCoS-based phase only spatial light modulators (SLM), or other types of actuating devices.

For 1×2 , 2×2 and some of the $1 \times N$ WSSs, digital switching elements like polarization liquid crystal cells or Texas Instruments digital micromirror devices (TI DMD), i.e. digital MEMS mirrors, can be used [19]. However, most of the $1 \times N$ switches use analogue switching elements such as 3D MEMS mirror arrays or LCoS phase only SLMs for optical beam steering.

10.1.4.3 $M \times N$ WSSs

An $M \times N$ WSS is also called a wavelength selective cross-connect (WSXC) [13, 14]. The designation $1 \times N$ or $M \times N$ refers to the fiber terminals and is essentially equivalent to the switch matrix size. A WSS can handle m DWDM wavelengths, e.g., $m = 40$ or 96 . These channels are separated by 50 GHz or 100 GHz according to the ITU grid. A 50 GHz channel spacing, n channel $M \times N$ WSS means (a) The WSS under consideration has M input fiber terminals and N output fiber terminals, (b) each WSS terminal fiber carries n DWDM wavelengths, (c) the WSS has $n M \times N$ switches, one switch for each wavelength, and (d) the DWDM wavelengths have a channel spacing of 50 GHz.

Fig. 10.5 $M \times N$ wavelength selective cross-connect with n wavelength



In principle, $M \times N$ WSSs can be built with the same grating technologies as $1 \times N$ WSSs to separate wavelengths in space while a 3D $M \times N$ switch architecture is used for space switching. It is highly desirable to build $M \times N$ integrated wavelength selective switches due to their low cost and low loss nature. The schematic of an $M \times N$ WSS capable of handling n wavelengths is shown in Fig. 10.5 [13–15], and a specific $M \times N$ optical wavelength selective (n wavelengths) optical cross-connect switch architecture as proposed by Solgaard [20] is illustrated in Fig. 10.6. This $M \times N$ switch uses 2D arrays of switching/actuating elements to implement

Fig. 10.6 $M \times N$ WSS.

- (a) Diffraction grating separating the wavelengths from multiple inputs into an $N \times n$ parallel beams.
- (b) $N \times N$ WSS architecture using two switching element arrays

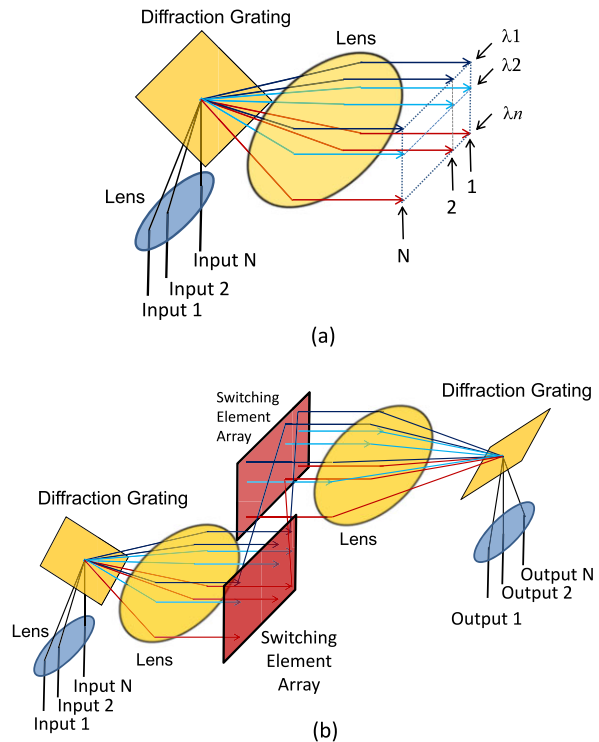
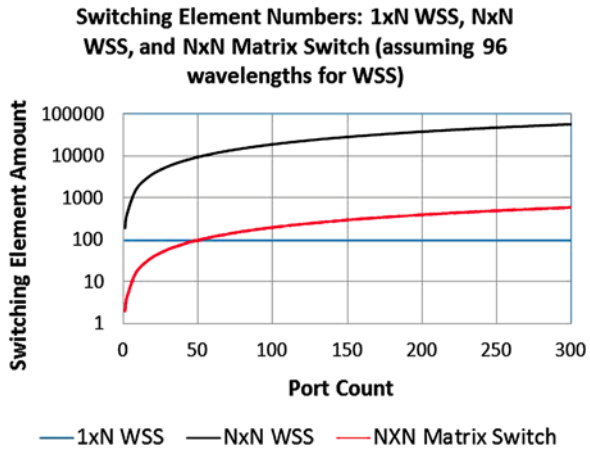


Fig. 10.7 Comparison of minimum switching elements needed to build $1 \times N$ WSS, $N \times N$ WSS, and $N \times N$ matrix switch (assuming $1 \times N$ and $N \times N$ WSSs to have 96 wavelength channels)



the full-functionality of $M \times N$ ports optical wavelength switching. Each connection (i, j, λ_k) needs two switching elements to steer an input beam to the output mirror and steer the output mirror to let the beam to point to the right output port. A diffraction grating separates the multi-wavelength signal into individual wavelength channels (Fig. 10.6) in such a way that different wavelengths are all spread in one direction, and light from different input fibers is spread perpendicularly to the wavelength spread direction. After the lens, wavelengths from one input fiber are separated vertically, and the same wavelengths from different input fibers are lined up horizontally.

Input and output fibers are arranged to have parallel demultiplexed beams (see Fig. 10.6(a)), and these are coupled with a matrix switching system using two switching element arrays (see Fig. 10.6(b)) so that a fully functional $M \times N$ WSS is obtained. The switching/actuation elements need to be analogue, and the total amount of required switching elements is $(M + N) \times n$. The switching elements can be 3D MEMS or LCoS. A comparison of the minimum number of switching elements needed for $1 \times N$ WSS, $N \times N$ WSSs and $N \times N$ matrix switches as shown in Fig. 10.7 demonstrates the difficulties in designing $N \times N$ WSSs because the number of required switching elements increases very rapidly with port count. Today’s largest commercially available optical matrix switch port count is 320×320 , which has about 640 switching elements [21], and for a 96 wavelength 4×4 WSS a total of 768 switching elements is required.

10.1.4.4 Multicast Optical Switches

An $M \times N$ multicast switch is a unidirectional switch that can route any input port to any one or to multiple (up to N) output ports [22, 23]. The operation principle is (i) splitting any incoming light at each input into N optical beams, (ii) connecting each split portion to a different $M \times 1$ switch, and (iii) setting each switch in such a way that the channel(s) wanted pass to the corresponding output. The output port count determines the splitting ratio, the typical number of output ports of this switch

varies from 4 to 24, and if the output port number is large, the IL is correspondingly high due to the high splitting ratio. This architecture is called Broadcast and Select, which we call multicast switch type “A”.

Another type of multicast switch (“type B”) uses a larger optical switch for optical switching and the splitting ratio can be customized to different ratios. For example, if we use $1 \times L$ splitters for the input ports, the multicast switch can only route at most L ($L < N$) ports to any L output ports, and in order to make type B multicast switches strictly non-blocking, an $(M \cdot L) \times N$ matrix switch is required.

Most currently available multicast switches are of type A and are based on PLC technologies. Switch sizes include 2×8 , 4×4 , 4×8 , 8×8 , 8×16 , and 8×24 [23]. Type B multicast switches offer better flexibility in fiber interconnects but need large-scale optical matrix switches.

10.2 Opto-Mechanical Switches

Small opto-mechanical 1×1 , 1×2 , 2×2 and $1 \times N$ switches have been widely used in telecom systems in central offices and in un-controlled environments. These optical switches have been among the first commercially available ones and have been widely deployed for protection and restoration and are widely used for optical testing for about 40 years [24].

The switching function of opto-mechanical switches relies on mechanical actuation [24], accomplished by mechanically moving or rotating fibers, prisms, or mirrors. Opto-mechanical switch design involves collimated optics, free space optics and fiber coupling, and specially designed optical components in a mechanical moving mechanism.

10.2.1 Fiber Collimators

Fiber collimators are used to either couple light from free space into an optical fiber or collimating light from a fiber to form a “collimated” optical beam. The basic structure of a fiber collimator consists (in most cases) of at least a lens and an optical fiber. Lenses which can be used include fiber lenses, ball lenses, aspherical lenses, spherical singlets and doublets, GRIN (GRaded INdex) lenses, microscope objectives, or cylindrical lenses. In the case of thermally expanded core (TEC) fiber no lens is needed at all. Lens materials vary from glass to silicon. Currently, most fiber collimators use GRIN lenses [25, 26] or so called C-lenses [27]. A C-lens is a miniature lens with similar performance as a GRIN lens but slightly better insertion loss, lower cost, and longer working distance compared to GRIN-lens collimators, so that C-lens fiber collimators are more popular for micro-optic devices.

Furthermore, collimators can be single fiber or multiple fiber collimators using a single lens or multiple fibers with multiple lenses to form a fiber collimator array. Their diameters can be as small as the fiber itself, for example $125 \mu\text{m}$, or as

large as tens or hundreds of millimeters, all depending on the optical design and purpose. Based on optical beam waist size and waist position the optimum working distance can be determined. Another important specification for fiber collimators is insertion loss, which is due to the lens and coupling imperfections. The alignment tolerance for insertion loss due to misalignment and beam spot size mismatch of two collimated Gaussian beams was treated in [28–30].

10.2.2 Opto-Mechanical Actuators

An opto-mechanical actuator controls or moves optical parts, and opto-mechanical switches require actuators. These may typically involve a relay, a solenoid, a drive motor, a deflection opto-mechanical scanner, or other mechanical rotation components or even a high precision mechanical robotic arm for larger switches [32–44]. The actuators under consideration here produce either linear (straight line), rotary (circular), or oscillatory motion and are typically driven with electric current. One important feature of an actuator is to have a latching mechanism which ensures that, after the end of the movement, the switch will remain in its actual status/position and does not need any additional power to hold the moveable part in position.

The opto-mechanical actuators most widely used for optical switches are solenoid relays and stepper motors, and their most important characteristics are accuracy, speed, and cost. Stepper motors can be used as a rotary actuator which can move around a rotational axis to multiple positions (degrees), but the rotation of stepper motors can also be translated into a linear movement.

10.2.3 1×1 , 1×2 , 2×2 and Small Port Count $N \times N$ Opto-Mechanical Switches

1×1 (on/off), 1×2 and 2×2 opto-mechanical switches were the first optical switches available and have been widely used for over 30 years. These 1×1 , 1×2 , and 2×2 opto-mechanical switches have about 1 dB insertion loss, very high isolation, low crosstalk, and a switching time between 5 ms to 20 ms. They use a digital actuator, such as a solenoid-based electro-mechanical relay. 1×1 on/off switches only require a light blocker to be moved in and out of the light path, and 1×2 or 2×2 switches most frequently use solenoid electro-mechanical relays as digital actuators.

A simple 2×2 opto-mechanical relay switch may use two dual fiber collimators with a glass ferrule with 250 or 127 μm separation, a common collimating lens, and a reflective mirror on a relay as actuator [32]. When the reflective mirror is moved into the light path by the solenoid electro-mechanical relay, the switch is changed from the bar to the cross state. The structure is robust and has good misalignment tolerance due to the very short free space path length. Another widely used variety of 1×2 and 2×2 switches uses prisms (see Fig. 10.1 and [33–35]). Moving the prism

into the light path changes the switch from the bar to the cross state due to refraction of the prism. The prism can be moved vertically or horizontally, and the architecture can also be used for 1×1 and 1×2 switches. The cube prism architecture is very robust, and an angular misalignment of the prism will only generate a small lateral beam offset. Another variant of a 1×2 prism switch uses a prism with specific shape and takes advantages of dual fiber collimators with shared collimating lens, so that the cost for alignment, assembly, and materials is lower and the light path is more robust [35].

For achieving larger than 2×2 switches with opto-mechanical actuators, several approaches using electro-mechanically driven prisms to deflect optical beams in free space have been proposed, and 4×4 and 8×8 switches have been demonstrated [36, 37].

10.2.4 $1 \times N$ Opto-Mechanical Switches

$1 \times N$ opto-mechanical switches with larger N are available from many vendors and have been widely deployed for protection, restoration, testing & measurement, and monitoring in telecom applications. Compared to other kinds of optical switches, a $1 \times N$ switch is particularly simple since the switch can be implemented with a single analogue controlling opto-mechanical actuator.

A straightforward way to build a $1 \times N$ opto-mechanical switch is using a linear actuator for fiber movement, either along one axis or along two axes. The basic principle is shown in Fig. 10.8 with the input fiber loaded in a movable stage. Index matching glue or gel between the interface of input and output fibers reduces back-reflections.

Since the moving parts are optical fibers, the accuracy requirements for this actuator type are as high $<0.5 \mu\text{m}$ in the linear moving direction and $<0.5 \mu\text{m}$ fiber position accuracy, which can be achieved by using V-grooves on silicon, Pyrex glass, or fused silica substrates [31]. Instead of using fiber to fiber direct coupling, similar $1 \times N$ switches can be built using fiber collimator arrays instead of fiber arrays, however, this adds cost and also increases insertion loss. On the other hand, a collimated beam greatly reduces the insertion loss sensitivity for the switch since the beam spot size for a fiber collimator is typically $100 \mu\text{m}$ (depending on design), compared to a single mode fiber core of about $10 \mu\text{m}$.

Although $1 \times N$ switches based upon moving fibers or collimators are simple, they exhibit several shortcomings: (a) the displacements required are large, which

Fig. 10.8 Basic architecture of a $1 \times N$ optical switch that moves the input fibers using a stepper motor linear actuator

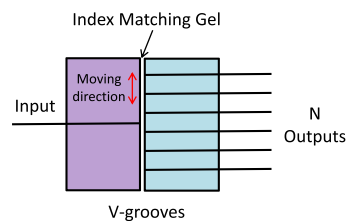
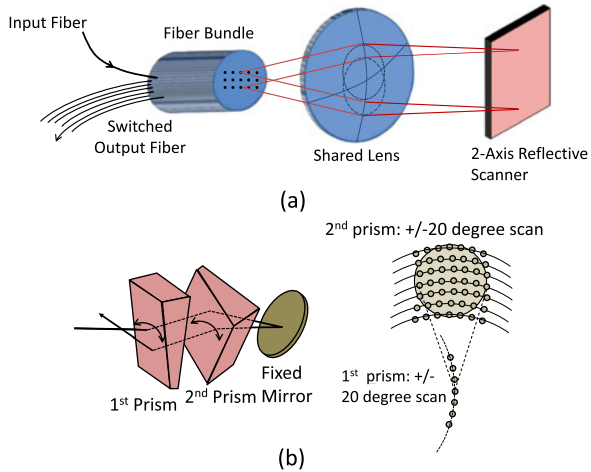


Fig. 10.9 Basic architecture of an $1 \times N$ optical fiber bundle switch by using a 2-axis reflective scanner [38, 39]. (a) Fiber bundle scanning switch architecture, (b) high-resolution scanner that enables beam deflection by two rotating prisms



ultimately limits the switch size, (b) switching time may not be uniform and depend on fiber position (c) moving fibers or fiber collimators may cause dynamic crosstalk. This might require special measures in order make switching to be hitless.

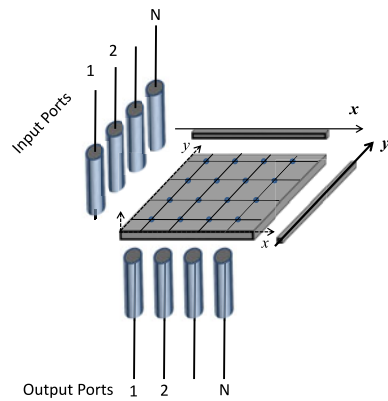
Ford and DiGiovanni have proposed a fiber bundle scanning switch, illustrated in Fig. 10.9(a), which offers a cost effective approach for large $1 \times N$ switches [38, 39]. The input and all output fibers are carried in one fiber bundle and share a single lens. A two axis moveable reflective scanner in the aperture stop back-reflects incoming light with an appropriate deflection angle so that it can be coupled into any output fiber. The cost of a fiber bundle switch is nearly independent of the number of outputs, in contrast to switches with individually lensed fibers, and the number of outputs is only limited by the scan area and the density of fibers held in the bundle.

Figure 10.9(b) shows a high-resolution scanner that enables beam deflection by two rotating prisms held between a lens and a fixed mirror. When one prism is rotated, the spot on the bundle is deflected along an arc whose radius is set by the prism wedge and the lens' focal length. By rotating both prisms, the spot can be positioned anywhere within a 2D area. The smaller the prism wedge angle, the smaller the arc swept out by the prism rotation so that the full angular excursion of a mechanical rotational actuator can be mapped into an arbitrarily small scan angle. With appropriate lens focal length and prism deflection, the full mechanical scan range matches the active area of the fiber bundle. Corresponding switches can have hundreds or even thousands of ports, e.g. 1×160 has been demonstrated and 1×4096 has been designed [38, 39].

10.2.5 Large Scale $N \times N$ Opto-Mechanical Switches with Robotic Arms

Robotic optical switches with large scale $N \times N$ non-blocking cross-connect functionality have been developed for quite some time [40–48]. Although there are ap-

Fig. 10.10 Schematic of $N \times N$ optical switch based on robotic motor arms, arms can move in/out fibers in x -direction and y -direction, respectively [45, 46]



proaches of using fiber collimators for non-contact robotic optical switching, typically the large scale $N \times N$ robotic switches physically connect two optical fibers together without mirrors, lenses, or collimators, in exactly the same way that fiber connectors mate. Instead of doing so manually, the mating is done by robotic motor driven arms.

The robotic $N \times N$ approach was first described by Sjolinder with opposing fiber connectors translating independently along separate, orthogonal, linear tracks in two separate parallel planes so that any input optical fiber and any output fiber can be coaxially aligned at an array of insertion points formed between the two planes, as shown in Fig. 10.10 [45]. Based on this concept, FiberZone developed a robotic optical switch based on a three-layer architecture with two active layers in which robotic motors position input (or source) and output (destination) fibers in an x - and y -plane, respectively, and a passive connection layer or adaptor layer where connections are latched in place [46]. After completing a latched connection, the switch systems are functionally equivalent to a manual patch panel with its purity of signal and low loss characteristics. Transmission of optical signals maintains full connection integrity, even if electrical power is lost.

Since each input and each output fiber is moved in a straight line, fiber entangling is no issue. However, because all input (output) fibers need to be arranged in a row (column), raising the switch size to more than 200×200 ports is difficult but 180×180 port switches are commercially available [47].

Kewitsch proposed another way to build large scale $N \times N$ switches using a robotic motor actuator offering 1000×1000 switching capacity. This architecture uses a single robotic motor actuator to do 3-axis pick-and-placement [48].

Based on this architecture, Telescent [49] developed an all-fiber, robotically re-configured cross-connect that is scalable up to a true non-blocking 1008×1008 switch, based upon 48 modules enabling a pay as you grow strategy. The insertion loss is identical to that of a manual patch panel by utilizing standard LC/PC, LC/UPC, or LC/APC connectors. This flexible patch-panel is a latching matrix switch.

The drawbacks of this flexible robotic $N \times N$ switch include: (a) switching time is slow, typically 1 minute per connection, (b) switching cannot be done in paral-

lel but in the 1 minute time frame one connection can be made only (c) it may be difficult to reduce cost since each port needs individual assembly (e) repeatability depends on cleanliness of connectors (which have to be cleaned), (f) mating durability is limited, connectors can be plugged in about 1000 times, after that reliability may degrade.

10.3 Liquid Crystal (LC)-Based Optical Switching

10.3.1 Operating Principles of Liquid Crystal Material for Optical Switches

Liquid crystals (LC) are rod-like molecules in a state of matter that goes from crystalline \rightarrow smectic \rightarrow nematic \rightarrow liquid as it is heated [50]. The optical properties (refractive index and birefringence) of LCs depend on molecular orientation [51, 52] and can be controlled by applying relative modest electric fields across LC cells, and the change of the optical properties can be exploited to build 1×2 , 2×2 , and larger $N \times N$ optical switches, and in particular, $1 \times N$ wavelength selective switches [52–54].

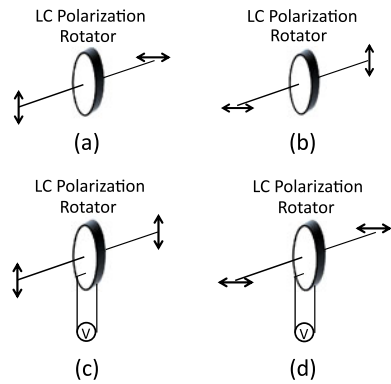
Liquid crystals are used in two ways for optical switching: (i) as programmable polarization rotator and acting as digital actuator [55], or (ii) as programmable spatial phase modulator for performing spatial beam steering and acting as analogue actuation element [56]. Both, operation in transmission or reflective configurations are possible. Depending on the alignment of the LC molecules (typically either parallel, vertical, or twisted), phase only, amplitude, or polarization of an incident light beam are modified. Currently the most frequently used liquid crystal types are parallel aligned nematic (PAN), twisted nematic (TN), and smectic liquid crystals.

Liquid Crystal Polarization Switching Principle Both parallel aligned nematic and twisted nematic liquid crystal cells can be used as a controllable polarization rotator. Without applied voltage such cells continuously rotate incoming linearly polarized by 90° , i.e., s-polarized light is rotated to p-polarized light while p-polarized light is rotated to s-polarization, as shown in Fig. 10.11(a) and (b). On the other hand, when an appropriate voltage is applied to the LC cell, it behaves like a piece of glass and both, s- and p-polarized light, keep their original polarization (Fig. 10.11(c) and (d)).

For polarization induced switching a half-wave retardance is required as a half-wave retarder can rotate the polarization of linearly polarized light to twice the angle between the retarder fast axis and the plane of polarization. Therefore, placing the fast axis of a half-wave retarder at 45° to the polarization plane results in a polarization rotation of 90° .

For switching the polarization state between two angles only, for example 0 and 90° , a twisted-nematic device is an excellent solution as it has a very simple driving scheme [55, 57]: a high voltage (e.g. above ~ 5 V) gives 0 rotation and a low voltage

Fig. 10.11 Functionality of LC polarization rotator



(e.g. below ~ 0.5 V) gives 90° rotation, so that no tight control of operation voltage is required nor are temperature changes an issue.

Multiple elements of TN or PAN LC polarization switches can be easily fabricated by appropriately patterning an indium tin oxide (ITO) film on top of the LC. ITO is transparent and electrically conducting and can be deposited as a thin film. With a specially patterned ITO layer containing multiple electrodes, the pixels can be controlled and switched (on/off) individually with an electric field.

Liquid Crystal Spatial Light Modulator Operating Principle A liquid crystal spatial light modulator (LC SLM) has a pixel array of LC cells [56]. Both PAN and TN LCs can be used for SLMs, and LC SLMs can be either transmissive or reflective. An example of an LC SLM is a transmission PAN liquid crystal display (LCD) SLM.

LCD SLMs based on transmissive LCD technology frequently have a small pixel fill factor (around 60%), and the relatively large amount of optically inactive space makes it difficult to achieve hitless and flexible passband operation. In addition, compared to reflective solutions, the thickness of the LC layer needs to be doubled.

Another important LC SLM technology is liquid crystal on silicon (LCoS) [58, 59]. LCoS technology has been developed for many years for image and video display applications. This technology combines the unique light-modulating properties of LC materials and the advantages of high-performance silicon complementary metal oxide semiconductor (CMOS) technology through dedicated LCoS assembly processes. An LCoS device is reflective. LCoS SLMs can be used to modulate the amplitude, phase, and/or polarization of optical beams with different configurations and LC alignments. The architecture of LCoS devices is similar to that of conventional LC devices except that a silicon backplane constitutes one of the substrates.

A schematic of an LCoS structure is shown in Fig. 10.12.

The silicon CMOS backplane comprises high-performance driving electronic circuitry, buried underneath the pixel array(s), which has (have) a very high fill factor ($>99\%$). The pixels are aluminum mirrors deposited on the surface of the silicon backplane, typical sizes are in the range of 3 to $32 \mu\text{m}$, and chips with XGA resolution have 1024×768 pixels, each with an independently addressable voltage so that

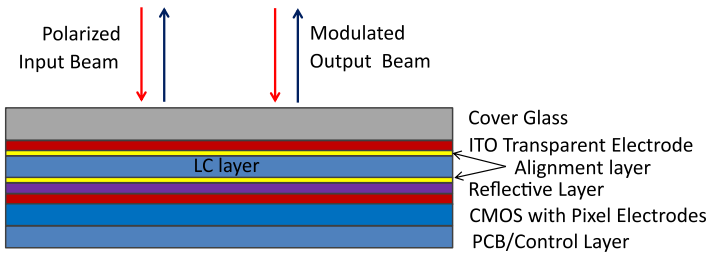


Fig. 10.12 Liquid crystal on silicon spatial light modulator basic structure [58, 59]

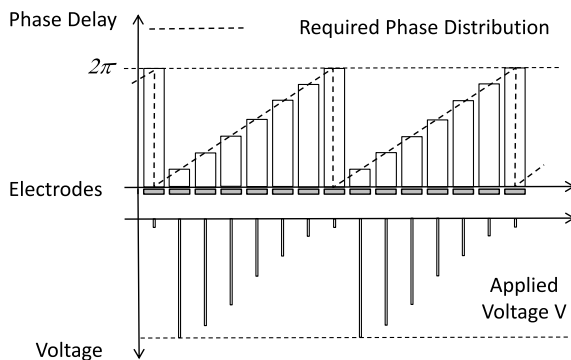
the phase retardation of each pixel can be controlled. Typical LCoS cell dimensions are: 1 to 3 cm² size, ~2 mm thickness, and a minimum pixel pitch of ~2.8 μm. A common voltage for all pixels is supplied by an ITO layer on the cover glass. The dimensions of the LCoS cell are determined by the pixel size and the pixel pitch.

For optical switching LCoSs are typically operated as spatial phase modulators, and both PAN and TN LC technology can be used for “phase only” LCoS SLMs. If the polarization of the incident light beam is parallel to the slow optical axis of a PAN LCoS device, and if an appropriate phase distribution has been generated across the pixels of the SLM, optical beam steering is achieved [60, 61]. For appropriate beam steering the phase modulation required is at least 2π in order to fully modulate the phase of each pixel.

The principle of optical beam steering using LCoS SLMs is the same as phased array beam steering. The diffractive optical phased array can be thought of as a quantized, programmable multiple level phase grating [60]. As illustrated in Fig. 10.13 each ramp comprises several LCoS pixels, each pixel with an increasingly larger phase delay, ranging from zero to 2π .

Detailed descriptions of the general characteristics of diffraction gratings can be found in physics or optics text books (see also Chap. 9, Sect. 9.5) and will not be repeated here. For beam steering the first diffraction order is usually chosen since it has the highest diffraction efficiency.

Fig. 10.13 Generating a digitized liquid crystal phase grating using spatial light modulation



The more phase levels are used in the array, the closer the ramp comes to an ideal ramp (instead of stair steps), and the higher the diffraction efficiency [60]. For example, a binary phase grating ideally provides a diffraction efficiency of 40.5% in each of the two first order diffracted beams. For a quantized phase grating using three phase levels/pixels the ideal first order diffraction efficiency is 68.4%, and it increases to 81% (87.5%, 94.9%) for 4 (5, 8) phase levels/pixels, respectively.

LCoS-based beam steering results in highly wavelength dependent switches in contrast to fairly wideband operation of TN LC polarization switching. Therefore optical space switches typically use TN LC polarization switching if wide passbands are required. On the other hand, WSSs do not require wide passbands and therefore LCoS beam steering is typically used for WSSs.

10.3.2 Liquid Crystal Optical Matrix Switch: 1×2 , 2×2 , $N \times N$ and $1 \times N$ Switches

1×2 Switches The basic principle of LC polarization-based optical switches [57, 62–67] is illustrated in Fig. 10.14 where PBS and PS represent a polarization beam splitter and a polarization switch, respectively. It is obvious, that this 1×2 LC switch is polarization dependent.

Polarization independent optical switching even with polarization dependent LC devices can be accomplished, and Fig. 10.15 illustrates one example of turning the polarization dependent 1×2 switch shown in Fig. 10.14 into a polarization independent 1×2 switch using polarization diversity optics. The beam displacing prism (BDP) separates the un-polarized light into s- and p-polarized beams. The p-polarized beam passes the half-wave plate (HWP) and is changed to an s-polarized

Fig. 10.14 Liquid crystal polarization switch-based 1×2 polarization dependent optical switch. (a) Switch to output 1, (b) Switch to output 2. PBS: polarization beam splitter, LC: liquid crystal, PS: polarization switch

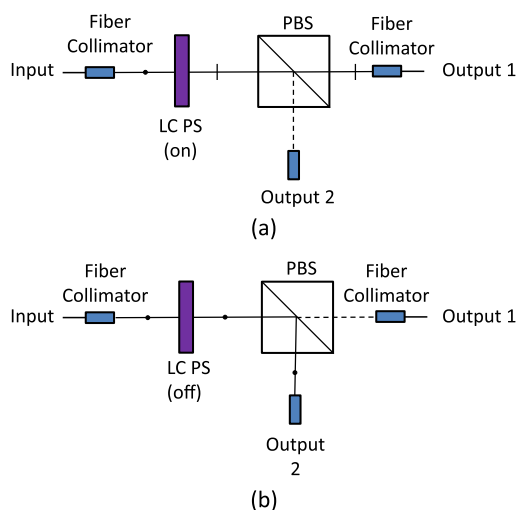
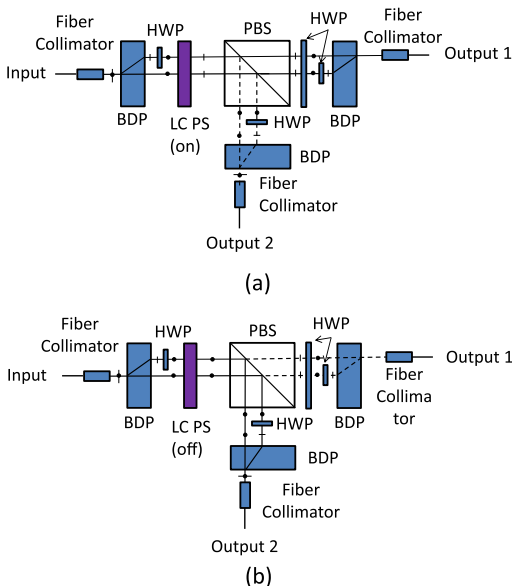


Fig. 10.15 Liquid crystal polarization switch-based 1×2 polarization independent optical switch using polarization diversity optics. (a) Switch to output port 1, (b) Switch to output port 2. BDP: beam displacing prism, HWP: half-wave plate, PBS: polarization beam splitter, LC: liquid crystal, PS: polarization switch



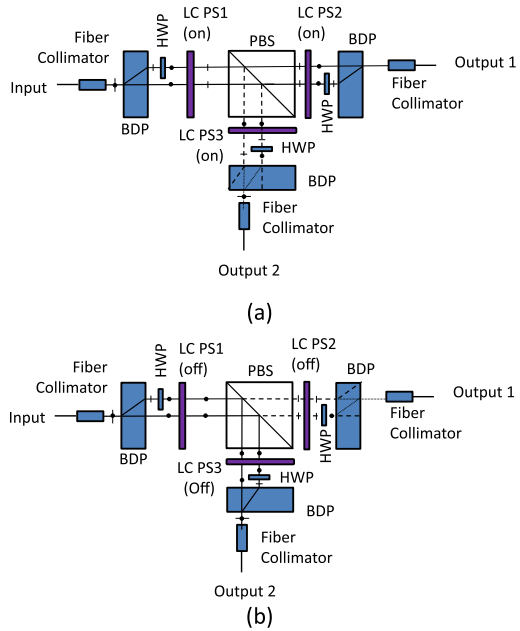
beam. When the PS is in its “on” state, both beams are switched to p-polarization and pass through the PBS and the HWP. After that both beams are changed to s-polarization, pass through the polarization combining optics and are coupled into output port 1 (Fig. 10.15(a)). When the LC PS is in its “off” state, both beams remain s-polarized, are reflected by the PBS, combined by the polarization combining optics and coupled into output port 2 (Fig. 10.15(b)).

LC polarization switching typically has a polarization extinction ratio of about 20 to 25 dB, which is generally insufficient to meet crosstalk requirements of optical switches. Double LC-PS elements in the light path enable to achieve double crosstalk rejection so that the crosstalk level can be improved significantly.

Figure 10.16 illustrates how first order crosstalk from the first LC-PS1 can be removed from the light path. When PS1 and PS2 are in the “on” state (Fig. 10.16(a)), the switch is in the $1 \rightarrow 1$ state. First order crosstalk from PS1 is s-polarized light. It is reflected by PBS to PS3 which is in its “on” state and changes the first order s-polarized light to p-polarization, and as a consequence it is directed to other spots instead of being coupled to output port 2. When PS1 and PS3 are in their “off” state (Fig. 10.16(b)), the switch is in the $1 \rightarrow 2$ state. First order crosstalk from PS1 is p-polarized light that passes through PBS to PS2, which is in its “off” state so that p-polarized light remains p-polarized and is directed out of the light path. By using this approach crosstalk of LC-PS-based optical switches can be improved to 40 to 50 dB.

In another configuration, but based upon the same principle, Fujii proposed to use PBS and BDP and four TN-LC devices to achieve low crosstalk 1×2 optical switching [65].

Fig. 10.16 Optical crosstalk reduction by using two LC-PS elements in a light path. (a) First order crosstalk removal in output port 2, (b) First order crosstalk removal in output port 1. HWP: half-wave plate, PBS: polarization beam splitter, BDP: beam displacing prism, LC: liquid crystal, PS: polarization switch



2×2 Polarization Independent Optical Switches LC-PS-based 2×2 optical switches with polarization diversity optics were reported by Wagner [62] and later by Soref [63, 64]. The 2×2 switch reported by Wagner used multi-mode fiber, but the switching architecture applies to single mode fiber switches as well. The schematic of the 2×2 optical switch, which uses a single LC-PS only, is shown in Fig. 10.17. When the LC-PS is in the “on” state (no voltage applied), the switch is in the bar state, i.e. $1 \rightarrow 1$ and $2 \rightarrow 2$ (Fig. 10.17(a)) while the “off” state (with voltage applied) to the LC-PS corresponds to the cross state of the switch, i.e. $1 \rightarrow 2$ and $2 \rightarrow 1$ (Fig. 10.17(b)). Since only one LC-PS cell is used, the crosstalk for this 2×2 switch structure is about 20 dB.

Polarization independent 2×2 switches with lower crosstalk, enabled by using four LC-PS elements, were reported in [66]. The concept is similar to that shown in Fig. 10.16 and ~ 40 dB interchannel crosstalk has been achieved.

Liquid Crystal-Based $1 \times N$ Optical Switches Both LC-PS and LCoS enable $1 \times N$ optical switches. LC-PS-based $1 \times N$ switches require multiple stages to enable multiple outputs. A total of $\log_2 N$ stages of LC-PS cascaded switching elements are required, and for the reduction of transient and static optical crosstalk another stage of LC-PS is needed to turn the target channel off before the actual signal is switched to that channel.

Figure 10.18 shows a 1×4 optical switch using three LC-PSs in two switching stages. The BDP1 and HWP are used for polarization diversity in the vertical direction. The BDP1 and HWP in the input side are used for separating the s- and p-polarized beams in the vertical direction (that is perpendicular to the paper sur-

Fig. 10.17 LC polarization switch-based 2×2 polarization independent optical switch using polarization diversity optics. (a) Bar state with LC-PS in off state, (b) cross state with LC-PS in on state. PBS: polarization beam splitter, TIR: total internal reflection prism

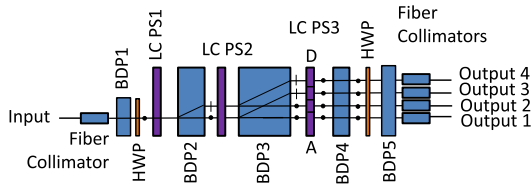
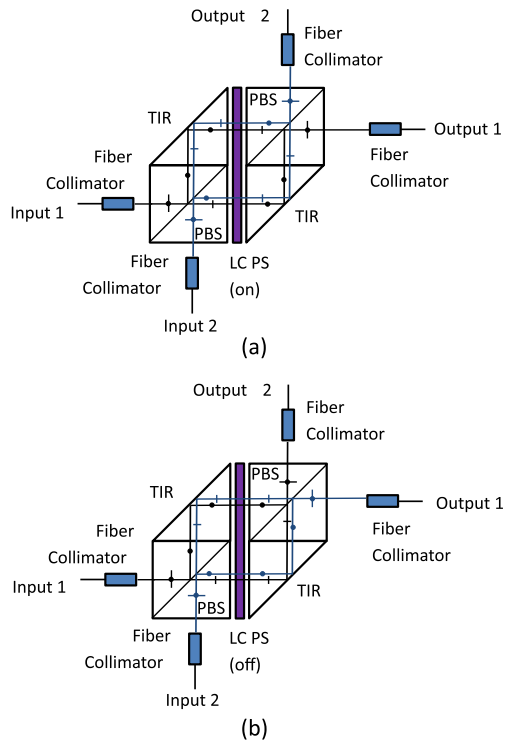


Fig. 10.18 Optical structure of the LC-PS-based 1×4 optical switch. LC PS: liquid crystal polarization switch; BDP: beam displacing prism; HWP: half-wave plate

face) and make both beams to have the same s-polarization direction. The HWP and BDP5 in front of the output ports are used for combining the two s-polarized beams in the vertical direction.

Recently, chiral smectic liquid crystals (SmC*) polarization insensitive binary phase gratings were reported. The LC is used as a programmable wave-plate and the advantage of this configuration is that it offers polarization insensitive binary phase modulators so that no polarization diversity is needed. Based on this, both $1 \times N$ and 8×8 switches were reported, however, with high IL [69–72].

Performance of Liquid Crystal-Based 1×2 , 2×2 , and $1 \times N$ Switches LC-PS-based 1×2 , 2×2 , and $1 \times N$ space switches have been developed and commer-

cialized in the past with reasonably good optical performance. These switches have typically less than 1.5 dB IL, about 45 dB optical crosstalk, 1 to 20 ms switching time, and they are very reliable with billions of switch cycles due to no moving parts. The switches operate over the whole 1.55 μm band but the passband is not as wide as that of opto-mechanical switches. In addition, LC-PS-based 1×2 , 2×2 , and $1 \times N$ optical switches require a large number of optical components and are more complicated than their opto-mechanical counterparts, which makes manufacturing more demanding. For this reason opto-mechanical or MEMS switches dominate the market for 1×2 , 2×2 , and $1 \times N$ optical switches.

Liquid Crystal-Based $N \times N$ Optical Switches There were some proposals of building $N \times N$ space switches using LC-PS activation elements [68]. Basically, the 1×2 switching elements shown in Fig. 10.14 to Fig. 10.16 can be used to build $N \times N$ optical switches with crossbar architecture (see Fig. 10.2). However, these approaches are not very practical due to high loss and difficulties in manufacturing and packaging.

10.3.3 Wavelength Selective Switches Using Liquid Crystal Techniques

The first liquid crystal-based 1×2 and 2×2 WSSs were developed and manufactured by Corning Inc. [54]. 1×1 , 2×2 , and $1 \times N$ WSSs using LC PS devices have found widespread use [73] and are currently commercially available from CoAdna Technologies [74]. The other kind of widely deployed liquid crystal $1 \times N$ WSSs uses LCoS SLMs and has become commercially available first from Finisar [75, 79] and now from many vendors. Since liquid crystals easily scale in pixel number, these WSSs can handle 96 or more DWDM wavelength channels and are operational with flexible grid.

Liquid Crystal Polarization Switching-Based 1×2 , 2×2 , and $1 \times N$ WSSs

The switching core of $1 \times N$ WSSs are multiple $1 \times N$ switches. One implementation, proposed by Kelly and coworkers, uses LC-PS and birefringent wedges to direct the input optical beam to two or more output directions controlled by LC polarization switches [76], as illustrated in Fig. 10.19. The birefringent wedge deflects s-polarized light at a larger angle than p-polarized light, the polarization of the light hitting the wedge is controlled by the voltage across the LC PS cell, and as a consequence the output beam can be switched between two different output directions (Fig. 10.19(a) and (b)).

$1 \times N$ switches can be obtained by cascading $\log_2 N$ stages of such LC-PS and birefringent wedge assemblies as shown in Fig. 10.19(c). Finally, Fig. 10.19(d) shows a 1×4 switch based on two LC-PS/birefringent wedge assemblies plus a regular wedge prism to adjust the deflection angles of the beams to be symmetric. The four possible output beams exhibit two different polarization directions

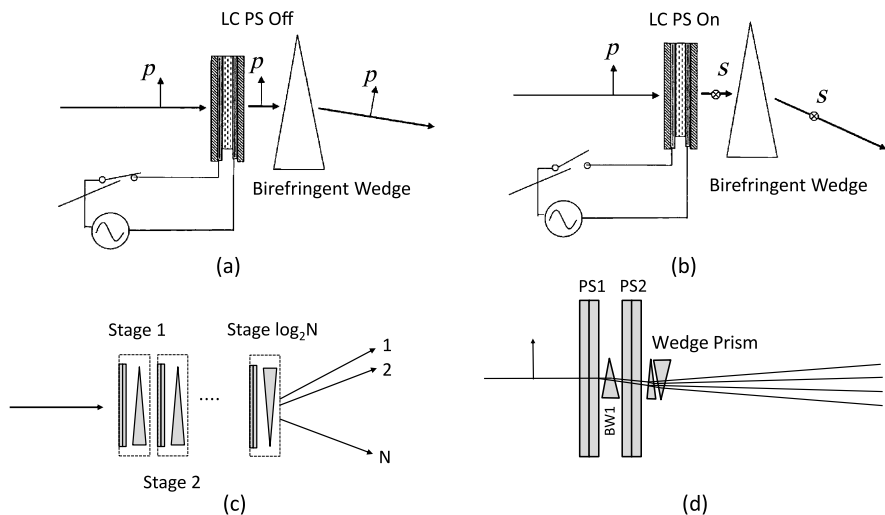


Fig. 10.19 Beam deflection by LC PS plus birefringent wedge(s) [76]. (a) Single LC PS stage in “off” state (voltage applied), (b) Single LC PS stage in “on” state (no voltage applied), (c) $1 \times N$ switch (schematic), (d) 1×4 LC PS switch with symmetric output

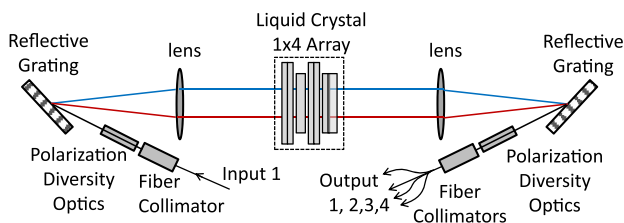


Fig. 10.20 Schematic illustration of 1×4 LC/wedge switching array-based WSS [76]

(Fig. 10.19(d)), and if that is not desirable, a third LC-PS may be added to manage the polarization directions so that all possible output beams have the same orientation of polarization.

Figure 10.20 shows an actual 1×4 LC/wedge switching array-based WSS. There are 1 input and 4 output fibers, and both input and output ports have fiber collimators and polarization diversity optics. A dispersive reflective grating separates the input beams into different angles according to the wavelengths.

The number of discrete wavelengths to be handled by a WSS determines the pixel number of the LC-PS array. A fixed (e.g. 50 GHz) channel spacing, 96 wavelength 1×4 WSS requires 96 pixels. For a flexible passband with 25 GHz resolution, the minimum number of pixels is 192.

LC-PS can operate either reflectively, transmissively or transfectively, but operating in reflective mode offers several advantages. A reflective device has a much smaller footprint and lower part count since a reflective device utilizes the same components for demultiplexing and multiplexing of the optical signals. In addition,

the optics of a reflective device is self-aligning in contrast to transmissive devices where the multiplexing optics must mirror the demultiplexing optics to a very high degree to obtain best performance. Also, double pass through the LC PS cell may improve the extinction ratio, the size of the channel blocking window, and switching speed.

There are many other kinds of $1 \times N$ WSS architectures using LC PS devices, however, the basic principle is still the same. Liquid crystal PS-based $1 \times N$ WSSs have been widely deployed for optical transport network and other applications. Commercially available $1 \times N$ WSSs have up to 30 output ports with variable attenuator function and packaged in a small package. Insertion loss is typically <5 dB with about 30 dB extinction ratio. These WSSs also offer flexible, flat top passband with 25 GHz resolution. Switching times are in the 1 ms to 100 ms range.

Liquid Crystal-on-Silicon-Based $1 \times N$ WSSs WSSs using LCoS switching elements rely on multiple phase gratings formed in LCoS technology where each phase grating is used for steering a particular wavelength to the output port wanted. The concept shown in Fig. 10.4 enables LCoS-based $1 \times N$ WSSs, however, due to various reasons these tend to be bulky and difficult to fit into a standard telecom shelf/blade and therefore alternative approaches are required.

Friskén proposed a modified LCoS-based $1 \times N$ WSS architecture that uses cylindrical lenses (CL) to handle the optics requirement of both the switching and wavelength axis [77]. Figure 10.21 shows a schematic of the $1 \times N$ WSS operating in reflective mode. The top view (Fig. 10.21(a)) shows the dispersion plane while the side view (Fig. 10.21(b)) shows the switching plane. The key points of this solution are: (i) CL1 and CL3 collimate light in the wavelength dispersion plane but do not affect light beams in the switching plane, while CL2 collimates light in the switching plane and does not affect light beams in the wavelength dispersion plane. (ii) The diffraction grating element (in transmissive mode) angularly separates the input wavelength channels into multiple channelized wavelength beams. (iii) The image of each of the spatially separated beams is a highly asymmetric ellipse ($\sim 700 \mu\text{m} \times 25 \mu\text{m}$) with its major axis in the switching plane, and the zones of the LCoS device match the elongated spatially separated wavelength bands.

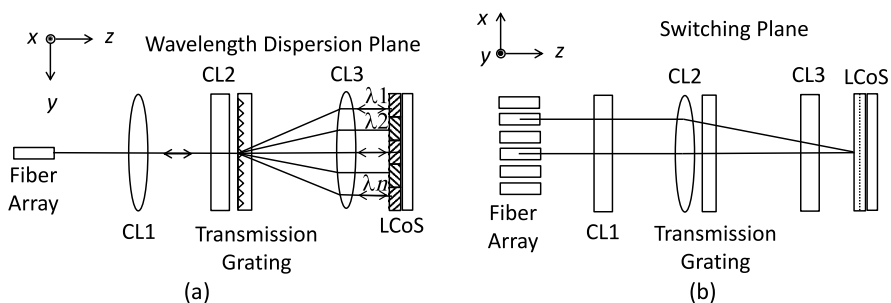
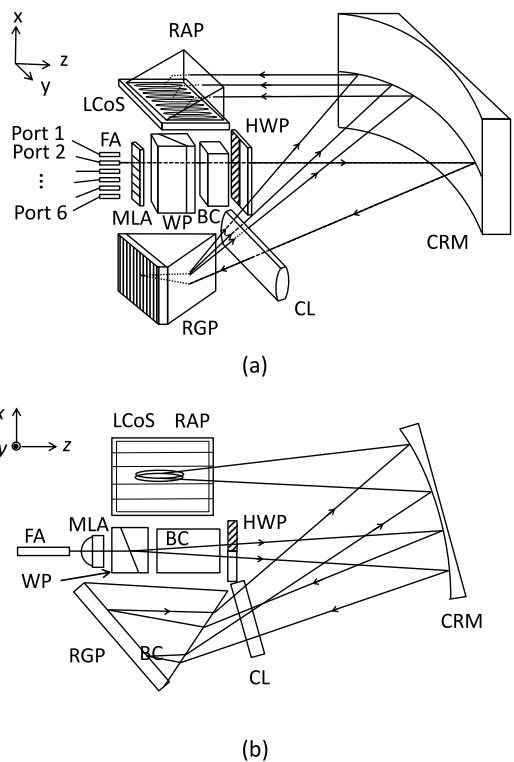


Fig. 10.21 Schematic representation of $1 \times N$ WSS operating in reflective mode (after [77]). (a) Top view illustrating wavelength dispersion plane, (b) side view illustrating switching plane. CL: cylindrical lens

Fig. 10.22 General concept of $1 \times N$ WSS using liquid crystal on silicon with polarization diversity optics, (a) perspective view, (b) top view [77]. FA: fiber array, MLA: micro-lens array, WP: Wollaston prism, BC: birefringent crystal, HWP: half-wave plate, CRM: cylindrical reflective mirror, RGP: reflective grating prism, RAP: right angle prism



LCoS SLM switches have a number of advantages compared to MEMS solutions such as large modulation depths, no moving parts, low power dissipation, potential for large aperture operation, and low cost. Nematic LCoS devices are used for commercially available $1 \times N$ WSSs from Meadowlark Optics [55], HOLOEYE Photonics AG [59], Hamamatsu [80], and others.

A compact polarization independent $1 \times N$ WSS switch using an LCoS and a reflective grating is shown in Fig. 10.22 [77]. The design has been widely used for commercially available $1 \times N$ WSSs offered by Finisar Corporation [78, 79]. In this approach light is dispersed and focused in one plane and collimated in the orthogonal plane so that the LCoS utilized for switching between input and output ports operates on one polarization state of light only and this polarization diversity scheme does not require two sets of switching elements for the two polarization split beams (Fig. 10.22(b)).

Operation of the device can be understood from Fig. 10.22(a) where the various sub-components of the switch are: fiber array (FA), micro-lens array (MLA), Wollaston prism (WP), birefringent crystal (BC) e.g., YVO_4 or calcite, half-wave ($\lambda/2$) plate (HWP) assembly, cylindrical reflective mirror (CRM), reflective grating prism (RGP), and right angle prism (RAP). Any port can be chosen to be the input port and all others are the output ports. The BC and the HWP can be im-

plemented in such a way that polarization dependent path length differences are reduced, and furthermore the CRM can include a conic term in the definition of its curvature (to produce a cylindrical mirror) as an additional means for equalization path length differences of differently polarized beams, and as a consequence the WSS will have low polarization mode dispersion. The top view (Fig. 10.22(b)) illustrates the polarization diversity operation. If light from differently polarized beams overlaps in the same LCoS region, the same grating can be used for redirecting both images, and this is possible if light paths have been equalized sufficiently. The phase shift applied by the LCoS determines to which output port the light is directed.

There are applications that require a certain amount of coupling between ports including less efficient “images” for optical signal attenuation or optical power splitting, and these demands can be met by many different algorithms. There are also other ways to do polarization diversity, e.g. using two different LCoS zones for the two orthogonal polarization directions. That will double the control complexity, but requires less strict optics.

LCoS $1 \times N$ WSSs have become a mature technology that has proven itself in current applications of 50 GHz multiport WSSs for ROADMs. The introduction of flexible grid for $1 \times N$ WSSs doesn't introduce any new hardware requirements to be qualified and can be implemented on existing optical hardware designs without compromising in any way the reliability of the devices. LCoS-based $1 \times N$ WSSs can offer about 12.5 GHz channel spacing and the flexible grid for the LCoS is intrinsic. LCoS-based $1 \times N$ WSSs typically have ~ 5 dB insertion loss and ~ 35 dB extinction ratio.

Recently, a WSS approach that uses a silica-based PLC-front end and LCoS has been proposed to achieve very high port count, in particular a corresponding 1×95 WSS [81].

Liquid Crystal-on-Silicon-Based $N \times N$ WSSs $N \times N$ WSS technologies are not mature enough for industry applications but have gained much research interest. One example are LCoS-based 2×2 , 3×3 , and 2×4 WSSs [77, 82]. Higher port count $N \times N$ WSSs are based so far on multiple $1 \times N$ WSSs using e.g. the Spanke architecture.

It has also been suggested to use the $1 \times N$ WSS architecture shown in Fig. 10.22 for making 2×2 or 3×3 WSSs by using a more complicated LCoS phase only SLM image, which is a programmable hologram that combines multiple deflection properties for different beams [77]. However, this method cannot scale to larger $N \times N$ WSSs with $N > 3$.

Recently Han et al. demonstrated a similar 2×4 WSS based on LCoS technology [82]. Optical beams from two input ports can be simultaneously switched on a 50 GHz grid to any one of the four output ports. The 2×4 WSS demonstrated has 8 dB insertion loss, ~ 25 dB isolation, it is polarization dependent, and the implementation of polarization diversity will significantly increase the overall system complexity. Based on these principles, Finisar introduced a 4×16 wavelength-selective optical switch covering the entire C-band that has a worst case 6.5 dB insertion loss [79].

10.4 Waveguide-Based Optical Switches

10.4.1 Generic Aspects

Waveguide-based optical switches enable the manipulation of light guided in interconnected planar waveguides based upon different activation mechanisms such as the electro-optic-, thermo-optic-, acousto-optic-, and the magneto-optic effect [2, 83]. There are also waveguide-based MEMS optical switches, which will be discussed in Sect. 10.5.2.2.

Waveguide-based optical switches are 2D devices, they constitute 1×2 or 2×2 switches in their own right but larger switching fabrics can also be built by cascading, and many different architectures have been proposed and realized already. The operating principle of generic planar 2×2 (or 1×2) switching structures is illustrated in Fig. 10.23 but there are quite a few other variants [2, 83].

Switching relies on the modification of the effective refractive index in one or both waveguide (WG) arms, which is accomplished by external means, in particular an applied voltage or heating, i.e. by exploiting the electro-optic- (see e.g. Chap. 8, Sect. 8.2.1.4) or the thermo-optic effect. The refractive index change introduces a phase change of the propagating wave and this modifies coupling between modes (a) or interference at the device output (b). Operation of a digital optical switch (DOS) relies on mode sorting in such a way that light propagating in the fundamental mode is directed to the arm with higher index of refraction, and the index difference required can be achieved electro- or thermo-optically [83, 84]. A DOS exhibits a step-like response once the WG asymmetry has become sufficiently large, and therefore DOSs are highly insensitive to wavelength, polarization, and other physical parameters that may normally affect device operation.

Microring resonators (MRR) are another generic element for the implementation of switches and switching matrices, and corresponding devices have been fabricated in III-V semiconductors (GaAs- and InP-based alloys) and in the SOI material system as well, and switching has been demonstrated thermo-optically [85] and by

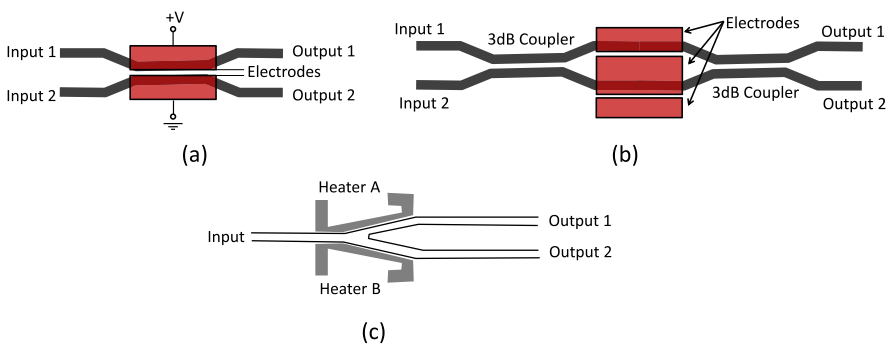


Fig. 10.23 Generic 2×2 electro-optic switch structures: (a) directional coupler (switch), (b) Mach-Zehnder interferometer switch, (c) digital optical switch

carrier injection also [86]. Switching based upon the resonance shift of a single MRR is of limited practical use as the resonance is rather narrow [87], but higher order MRR with multiple rings enable sufficiently broad pass bands, and an 8×4 TO switching matrix has already been demonstrated [85]. However, as it is a 2D switch architecture, the number of switching elements scales as N^2 for an $N \times N$ switch, which limits the fabrication and usefulness of larger MRR-based switching matrices. Switching power can be fairly low while the total insertion loss tends to be large due to the multi-stage cascade. A flexible-bandwidth WDM crossbar switch architecture suitable for use in high performance computing and data center applications has recently been proposed and analyzed [88]. Its capability ranges from static all-to-all wavelength connectivity to on-demand μs -scale dynamically allocated multiple-wavelength connectivity and its realization in silicon photonics is estimated to be quite feasible.

Altogether MRR-based switches have not yet achieved commercial relevance but are still in the R&D stage and will therefore not be treated in more detail in the present chapter.

10.4.2 Electro-Optic Waveguide Optical Switches

Electro-optic (EO) switches fall essentially into two categories: They either rely on the Pockels effect (see e.g. Chap. 8, Sect. 8.2.1.4), which modifies the material refractive index by an applied voltage (LiNbO_3 , III–V semiconductors), or on carrier injection in materials without Pockels effect (Si).

10.4.2.1 LiNbO_3 -Based Switches

LiNbO_3 (LN) exhibits a large electro-optic effect, high quality large wafers (>4 inch diameter) are readily available, waveguides can be fabricated by proven planar technologies (Ti diffusion or proton diffusion) [2, Chap. 2], and LN-based EO switches have been investigated and fabricated over the past 30 years [89–94].

LN-based EO switches are reliable, compact, and thermally stable. The underlying physics of EO switches offers switching times <1 ns although the capacitance of the electrodes renders this time somewhat longer in reality. Their drawbacks include relatively high insertion loss and crosstalk, and they may exhibit polarization dependence including PDL. Polarization independence is possible, but at the cost of higher driving voltage, which in turn limits the switching speed. LN EO switches are particularly attractive for high speed switching and small port counts.

Commercially available devices include 1×2 , 2×2 , 1×8 , 1×16 , and 8×8 optical switches [94]. They may have <10 ns switching time (sub-ns on request), about <4 dB insertion loss for a 1×2 or 2×2 , and <5 dB for a 1×8 switch, and driving voltages are typically several volts. Crosstalk is ~ 18 dB, which is fairly high compared to other kinds of optical switches, however, double-stage designs can

suppress the crosstalk to better than 30 dB. 1×2 and 2×2 switches do also find application as high speed modulators and are offered with >30 GHz bandwidth, suited for 40 Gbit/s modulation [94], and polarization switches are also commercially available. Higher port count switches are generally obtained by cascading 2×2 switches, and the accumulated loss essentially limits this approach to 1×16 switches. Operation wavelengths of LN switches do typically cover the C- and the L-band.

Digital optical switches have also been realized in LiNbO_3 beginning with the demonstration of the concept [84] and including a 1×32 switch matrix [95] or a 4×4 switch matrix [96]. For a detailed treatment of DOSs see e.g. [97, 98].

10.4.2.2 Electro-Optic Switches in SOI

Silicon photonics [99] (silicon-on-insulator (SOI) -based photonics) enables the monolithic integration of electro-optic switches or switching matrices with digital complementary metal-oxide-semiconductor (CMOS) drivers, and this is considered particularly promising [100, 101]. As there is no Pockels effect in silicon, EO switches operate with free carrier injection. SOI-based electro-optic switches have been demonstrated with both MRR [102, 103] and MZI [104–108] architectures. MRR architecture electro-optic switches typically have narrow wavelength pass-band while broad wavelength band switches have been achieved with MZI structures. The power consumption of such a switch is caused by the electro-optic modulation to attain a π -phase shift, and using longer modulation arms has been verified to have lower power consumption. A 2×2 switch element exhibited 0.6 mW power consumption and 6 ns switching time [106]. Another example of a device realized in SOI is a non-blocking 4×4 electro-optic switch matrix, which exhibits fairly low (routing state dependent) power consumption in the range for various states from about 2 mW to 24 mW and 5 to 6 ns switching time, enabled by 1.2-mm-long modulation arms [108].

Typically SOI electro-optic switches have switching times comparable to that of LN-based electro-optic devices but with sub-mW power consumption only. However, these switches still suffer from high IL and low extinction ratio and may only be used for building very small port count switches. The 2D nature of the underlying switch architecture limits scalability.

10.4.3 Waveguide-Based Thermo-Optic Switches

Thermo-optic (TO) switches have been realized both, as Y-branch (DOS) and as interferometric structures in various materials [83]. The main difference between EO and TO switches is the much longer switching time of TO switches, which ranges from sub-ms to tens of ms.

10.4.3.1 Silica-Based PLC Thermo-Optic Switches based on MZI Structures

Silica-based PLCs [109, 110] have been developed for many applications and with a multitude of subcomponents, including thermo-optic switches, e.g. for building wavelength selective switches and ROADMs. One important design parameter for WGs in PLCs is the index difference Δ between core and cladding. Typically $0.5\% \leq \Delta \leq 2\%$ is used as a compromise between sufficiently low loss (the smaller Δ the better) and compact PLC design (the larger Δ the better). Table 10.1 compares properties of silica WGs for $\Delta = 0.75\%$ and $\Delta = 1.5\%$ [111].

Additional aspects of silica-based PLC technology are covered in numerous publications (see e.g. [109, 110]) and will therefore not be repeated here.

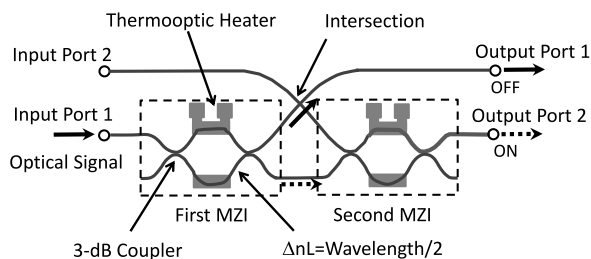
Single MZI 2×2 switches exhibit typical extinction ratios of about 25 to 35 dB. Improved optical crosstalk levels can be obtained using two cascaded MZIs for building a 2×2 cross-point switching unit (which is not a full 2×2 crossbar switch) as shown in Fig. 10.24. This double-MZI design achieves a particularly high extinction ratio in the bar-path because light power leaking from the first MZI is blocked by the second MZI in the off-state [110–114], and this property is important for matrix switches where the bar-path extinction ratio is more important than that of the cross-path [9, 111].

PLC-based thermo-optic $1 \times N$ switches and $N \times N$ switching matrices have been a research topic for many years [112–120], and $1 \times N$ thermo-optical switches have become commercially available with sizes up to 1×128 , to be used e.g. for sharing a single optical channel monitor in multiple channel power monitoring. PLC-based non-blocking switching matrices with port count up to 16×16 have been made commercially available also, serving as a compact, stable, and reliable solution for the implementation of optical cross connects [118]. Characteristics of the $1 \times N$ and $N \times N$ devices include <3 dB insertion loss (or <3.5 dB for switching matrices), loss uniformity <1 dB, PDL <0.4 dB (<0.5 dB for matrices), extinction ratio >40 dB, and <3 ms switching time. Total power consumption is <4.5 W (<9 W) for a 1×8 (1×128) switch or a 8×8 (16×16) switching matrix.

Table 10.1 Properties of Silica Waveguides

Waveguides	$\Delta = 0.75\%$	$\Delta = 1.5\%$
Propagation loss	3.5 dB/m	7.9 dB/m
Fiber coupling loss	0.4 dB	2.0 dB
Minimum bend radius	5 mm	2 mm

Fig. 10.24 Basic 2×2 cross-point switching unit with double-MZI switch configuration for crosstalk reduction



Larger switching matrices (32×32) have already been reported but are still in the R&D stage [119]. PLC-based switching matrices tend to be fairly large, e.g. a 16×16 matrix based upon WGs with $\Delta = 0.75\%$ and using double-MZI cross-point switching units has been reported to result in $100 \times 107 \text{ mm}^2$ chip dimensions so that the switch (just) fits into a 6 inch wafer [111–114] while a 1×128 switch using WGs with $\Delta = 1.5\%$ has been demonstrated on a 4 inch wafer [115].

10.4.3.2 Polymer-Based PLC Thermo-Optic Switches

Polymers on silicon constitute another highly mature materials platform (besides silica or SOI). It enables the fabrication of complex PLCs including thermo-optic switches, variable optical attenuators (VOA), and power taps, but it also serves as a platform for hybrid integration of passive and active elements (see Chap. 13).

The refractive index change of amorphous polymers is predominantly due to their density change, so that a high coefficient of thermal expansion (CTE) results in a large thermo-optic effect. Enablence [122] has developed polymers with $dn/dT \approx -4 \times 10^{-4}/^\circ\text{C}$, which is 40 times larger than the TO coefficient of silica, and 3 to 5 times larger than that of common optical polymers such as polymethylmethacrylate (PMMA) and polycarbonate. An important benefit is that power consumption of TO switches gets the lower the higher the EO coefficient is. Furthermore, organic polymers exhibit low insertion loss ($\leq 0.1 \text{ dB/cm}$ at all key communication wavelengths, i.e. 840 nm, 1310 nm, 1550 nm), low fiber to waveguide coupling loss ($< 0.3 \text{ dB}$), two orders of magnitude smaller birefringence than silica, wide controllability of refractive index contrast (maximum Δn is an order of magnitude larger than that achievable in silica), environmental stability, ease of hybridization, high yield, and low cost [122–124].

Polymer-based PLC TO switches include DOSs, a schematics of which has been shown in Fig. 10.23, and it should be added here that the angle of the Y-branch is very small, typically 0.1° [122]. The power consumption for such a switching unit (by heaters on top of the WG arms) is about 35 mW, which is much smaller than for TO switches in silica. Y-branch DOS units can be connected with bends and crossings to form $M \times N$ switching matrices, and a $1 \times N$ switch requires $(n - 1) 1 \times 2$ Y-branch switching units. A strictly non-blocking $N \times N$ switching matrix can be fabricated with $2N(N - 1) 1 \times 2$ switches using a recursive tree structure, as shown in Fig. 10.25. The total number of 1×2 DOSs needed for $N \times N$ non-blocking, recursive tree structure switches as a function of N is shown in Table 10.2.

Figure 10.26 shows a 2×2 (or cross-bar) DOS built with four 1×2 units. This switch operates in the bar state by powering the four inner electrodes while powering the four outer electrodes results in the cross state. Switch sizes from 2×2 , 4×4 , 8×8 , to 16×16 are currently commercially available. The 8×8 cross-bar switches exhibit 40 mW power dissipation per DOS (total $\sim 2 \text{ W}$), 3 dB insertion loss, and 45 dB extinction ratio, mainly limited by crosstalk at the crossings. Switching time is about 3 ms.

Fig. 10.25 Architecture of 8×8 DOS-based switching matrix based on recursive tree structure. Each box represents a 1×2 switch [122]

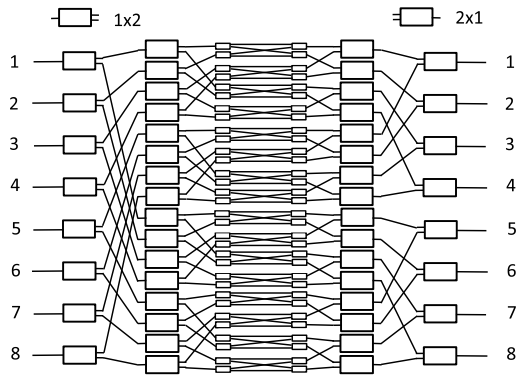
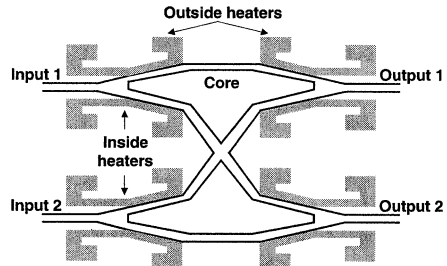


Table 10.2 Number of 1×2 switches needed in planar strictly non-blocking $N \times N$ switches using recursive tree structure [122]

N	Number of 1×2 switches
2	4
4	24
8	112
16	480
32	1,984
64	8,064
128	32,512
256	130,560
512	523,264
1024	2,095,104

Fig. 10.26 Schematic diagram of a 2×2 Y-branch digital thermo-optic switch [122]



Path-independent loss $N \times N$ architectures with twice the number of 1×2 DOSs are possible in the same way as for silica-based MZI switches. However, the larger number of 1×2 switches raises power consumption and insertion loss. On the other hand, silica-based MZI 16×16 switches cannot use a recursive tree structure since the number of electrodes in combination with the much higher power consumption per switching unit will result in unacceptably high total power consumption.

Concerning power consumption of switching matrices it is worthwhile to note that a single actuation unit in silica-based technology requires about 15 times more energy than a polymer Y-branch DOS unit. On the other hand, an asymmetric MZI switching unit does not need power when in the bar (off) state. As a result the total power consumption of 8×8 switches is comparable, no matter whether they are based on a silica MZI-switch or a polymer Y-branch DOS architecture.

The largest strictly non-blocking $N \times N$ switch fabricated so far has been 16×16 [122] while significantly larger devices have been designed and are in early development stages [125]. However, due to complexity, power consumption, and limited wafer size, building matrix switches larger than 32×32 using polymer WGs is still very challenging.

10.4.3.3 SOI-Based Thermo-Optic Switches

SOI-based thermo-optic switches [126] have also found an increasing interest recently, and silicon wire-based TO switches that use the large TO coefficient of silicon can be considered very promising. Table 10.3 gives a comparison of key characteristics of silica- and SOI-based PLCs [127]. The higher refractive index of Si enables very compact devices, which is favorable for the fabrication of larger switching fabrics, the significantly higher TO coefficient is particularly useful for TO switches in general, and switching matrices ranging from 2×2 to 32×32 have been reported [128–133].

One interesting proposal has been a silicon-silica hybrid TO switch architecture that integrates low power silicon optical switches in a hybrid silica structure so that the low-loss fiber chip coupling and the long term stability of silica PLCs is combined with a silicon low power consuming optical switch [127].

10.4.3.4 Thermo-Optic Switch-Based $1 \times N$ WSS

The integration of multiple wavelength demuxes/muxes plus a $1 \times N$ switch for each wavelength results in a $1 \times N$ WSS that can be realized on a single chip, and a corresponding 1×9 WSS with 8 wavelength channels has been demonstrated in [134]. The (potential) advantages of waveguide-based $1 \times N$ WSSs include low cost and

Table 10.3 Characteristics of silica-based PLC and silicon photonics [127]

Characteristics	Silica-based PLC	Silicon photonics
Refractive index	1.45	3.4
Core size ($\mu\text{m} \times \mu\text{m}$)	5×5	0.5×0.2
Fiber connection loss	Small	Large
Minimum bending radius (mm)	1	0.005
Thermo-optic coefficient (per $^{\circ}\text{C}$)	1×10^{-6}	18×10^{-6}

high reliability, but with respect to narrow passband, low channel count, and insertion loss these switches are inferior to alternative solutions, and as a consequence TO switch-based $1 \times N$ WSSs have not found as widespread use as LC-based $1 \times N$ WSSs.

10.4.3.5 Thermo-Optic Switch-Based $M \times N$ Multicast Switch

An optical multicast switch (MCS) is a compact and cost-effective optical switch with colorless, directionless, and contentionless functionality, which enhances the operational flexibility of multi-degree reconfigurable optical add/drop multiplexers [135–137]. Optical MCSs combine silica- or polymer-based PLCs, TO switches and splitters/couplers, integrated on a single chip.

An $M \times N$ multicast switch comprises M $1 \times N$ splitters as input units and N $M \times 1$ switches as output units, which are interconnected in between. An $M \times N$ MCS works as an MCS for optical signals propagating from one of the M inputs to the output ports. On the other hand, if an $M \times N$ MCS is operated in the backward direction, i.e. optical signals propagate from the N output ports to the M input ports, the switch works only as a select-and-combine optical switch without multicasting function. Depending on IL and isolation specifications, different structures of $M \times N$ MCS can be utilized. Figure 10.27 shows examples of TO 8×8 MCSs (for light propagation from right to left they represent an 8×8 MCS, while they constitute a 8×8 select-and-combine switch for light propagating from the right to the left). A conventional 8×8 MCS comprises 8-arrayed 1×8 splitters or couplers and 8-arrayed 8×1 switches, and those chips are separated and connected via a 64-fiber circuit sheet in order to avoid too many waveguide crossings on a PLC chip, as shown in Fig. 10.27(a). Corresponding chips were packaged into a $240 \text{ mm} \times 95 \text{ mm} \times 12.5 \text{ mm}$ module [135, 136]. A different circuit configuration that integrates the $1 \times M$ splitters and the TO switches into a single chip was proposed and fabricated to offer a smaller package and lower insertion loss [135, 137], as shown in Fig. 10.27(b). It should be pointed out that in references [135–137] the authors treated the 8×8 MCS as a select-and-combine switch from left to right and described it to have 8-arrayed 1×8 switches (comprising eight 1×2 switching elements cascaded serially, with a gate switch placed after each 1×2 switching element) and 8×1 combiners (comprising seven 2×1 coupler/combiner elements, placed between the stages of the switch elements). Considering signals propagating through the 8×8 MCS from right to left, the optical signal passes a 1×8 splitter and a 8×1 switch before it exits from one of the output ports. This circuit configuration reduces the maximum number of waveguide crossings by 75%, establishes an even number of crossings between the paths, and allows single chip integration of 8×8 multicast switches with $110 \text{ mm} \times 15 \text{ mm}$ chip size, and a fiber pigtailed module size of $150 \text{ mm} \times 45 \text{ mm} \times 13 \text{ mm}$.

Optical 4×8 , 8×8 , 8×16 , and 8×12 MCSs have been commercialized and are available from Enablence [121], Neophotonics [138] and other vendors with similar optical performance.

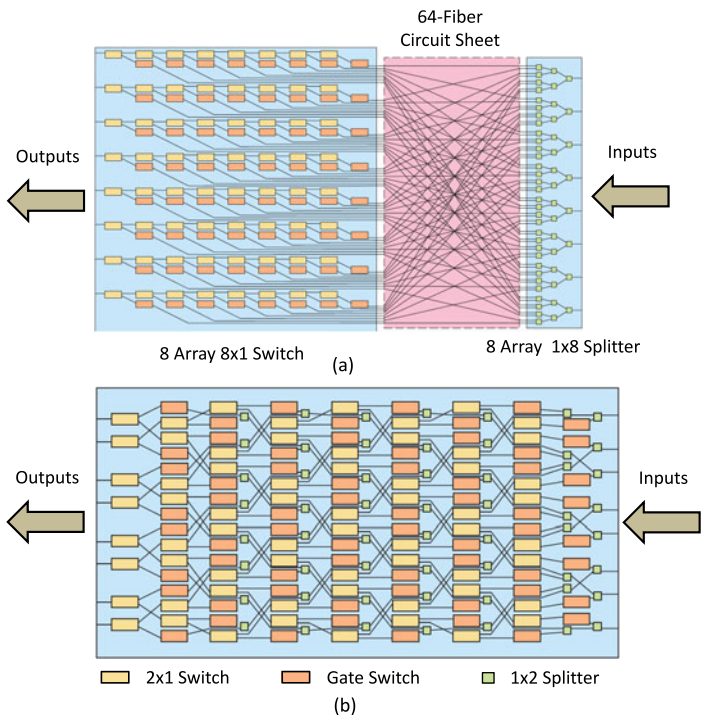


Fig. 10.27 (a) Conventional and (b) single chip circuit configuration of PLC-based multicast switch

10.5 MEMS-Based Optical Switch Technologies

10.5.1 Generic Aspects

One of the most promising technologies for optical switches with up to hundreds of ports is micro-electro-mechanical systems (MEMS) technology [139–144]. MEMS-based optical switches exhibit low loss, low crosstalk, low power consumption, small size, and reasonable speed adequate for most network reconfigurability requirements. Furthermore, MEMS fabrication techniques allow the integration of micro-optics, micro-actuators, complex micromechanical structures, and possibly microelectronics on the same substrate to realize integrated optical microsystems.

MEMS fabrication techniques utilize the mature fabrication technology of the Integrated Circuit (IC) industry. The fact that silicon is the primary substrate material used in IC circuitry and that it also exhibits excellent mechanical properties makes it the most popular micromachining material. MEMS optical switches can be fabricated using two popular micromachining technologies, surface micromachining and bulk micromachining, or a combination of both [141–143].

Bulk micromachining is the most mature and simple micromachining technology, sometimes called the etching/subtraction process as silicon is removed from

the bulk silicon substrate by etchants, anisotropic or isotropic ones. Anisotropic etchants etch different silicon orientation planes at different rates while isotropic etchants remove silicon evenly in all directions.

Surface micromachining is a more complex fabrication technique, and complex 3D mechanical structures can be created using alternate layers of sacrificial and structural materials. Free-standing 3D mechanical structures are formed by etching away the sacrificial layers. The patterned material is left as thin-film free-standing mechanical structures, suspended over the substrate according to the thickness of the etched sacrificial layer.

There are two approaches to implement MEMS optical switches: 2D and 3D MEMS switches that use digital or analogue actuators, respectively, and 2D MEMS switches can be classified into two types: 2D free-space MEMS switches and 2D MEMS waveguide switches. Furthermore, 3D MEMS can be arranged in arrays to realize multiple $1 \times N$ switches for switching individual wavelengths in WSSs.

10.5.2 2D MEMS Switches

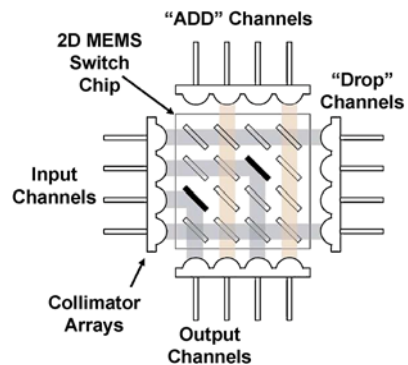
10.5.2.1 2D MEMS Free-Space Optical Switches

2D MEMS free-space switches use digital actuators/mirrors for switching and can be used to implement 1×2 , 2×2 , and $N \times N$ free-space optical switches.

Figure 10.28 shows a generic schematic of a 2D switch [139, 144] with vertical reflective “digital” mirrors: They reflect a light beam by 90° if they are in the light path, while light propagates straight if the mirrors are out of the light path. One micromirror only in a column and in a row can be activated to be in the reflection position during operation. Light propagates in free space, and collimation of light coming from and going to the fibers is accomplished by micro-lens arrays.

The first 2×2 MEMS switch was reported in 1996 [145], and 1×2 and 2×2 switches were subsequently commercialized for testing, measurement, and optical protection applications [34, 145–149]. Insertion loss was <0.6 dB and some the devices had latching functionality [149].

Fig. 10.28 Schematic of 2D MEMS optical switch [139, 144]



There are two basic ways for the actuation of 2D MEMS mirrors: (i) the mirrors are parallel to the substrate in the off position and, when actuated, are turned to the vertical (on) position by rotating the mirror by 90° [145, 150–152], (ii) the vertical micromirrors are moved in and out of the optical path vertically or laterally without changing the mirror angle [146, 147, 153–155]. 2D switches have been implemented by using both bulk-micromachining [145–147] and surface-micromachining technologies [150, 151, 153], and most approaches use electrostatic actuation but magnetic actuation has also been demonstrated [146, 151].

The (maximum possible) port count of free-space 2D MEMS switches is determined by various factors such as MEMS mirror size, fill factor (mirror width divided by unit cell width), mirror angle accuracy, beam spot size, and path length differences, which can be kept sufficiently small up to 64×64 switch size. Chip size may also be a limiting factor, but the main limitations for reaching large port count free-space 2D MEMS optical switches are not so much fundamental physical limits but rather related to the N^2 dependence of scalability, i.e. chip size, complexity, amount of mirrors, and control electrodes grow $\sim N^2$ for $N \times N$ port switches [156, 157]. This affects overall reliability and packaging so that the port count is essentially limited to $\sim 32 \times 32$ ports while 8×8 and 16×16 switches had become commercially available. Typical characteristics are < 3.5 dB insertion loss, switching time < 7 ms, crosstalk > 50 dB, and PDL can be managed to be sufficiently small (< 0.4 dB).

10.5.2.2 2D MEMS Waveguide Switches

2D MEMS waveguide switches use optical waveguides for beam propagation and MEMS actuators to enable switching. A corresponding solution implemented in the SOI materials platform with 50×50 ports and scaling potential to even 100×100 ports has been recently reported, a schematic and an SEM picture of the structure are shown in Fig. 10.29 [158–160].

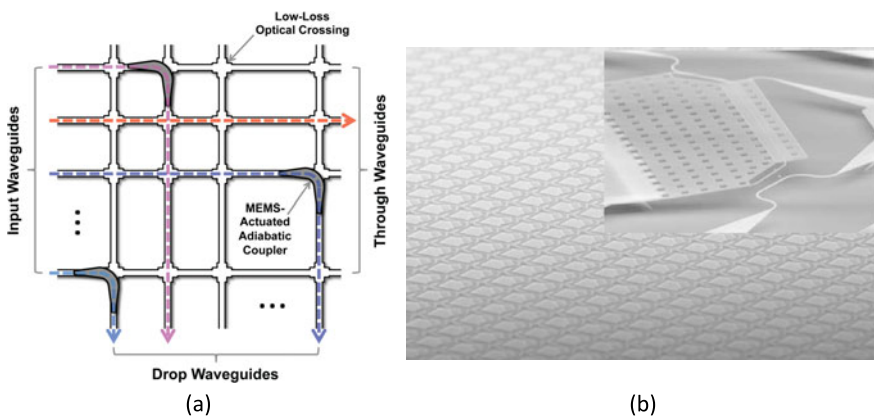


Fig. 10.29 (a) Schematic and (b) SEM picture of 2D MEMS waveguide optical switch in SOI materials platform [158–160]

The N^2 switching elements of this $N \times N$ switch are implemented as pairs of directional couplers with one arm of the directional coupler placed on a MEMS cantilever serving as activation element. In the off state the spacing between the two waveguides in the directional couplers is $> 1 \mu\text{m}$ preventing any light coupling. For the on state, the spacing is reduced to 250 nm so that light couples to the waveguide on the MEMS cantilever, is then turned by 90° through the waveguide, and finally couples back to the substrate waveguide through the second directional coupler.

The waveguides around the directional couplers have been made fully suspended by selectively etching the buried oxide and are anchored at the waveguide crossings. The size of the unit cell is $160 \times 160 \mu\text{m}^2$, and the reported 50×50 switch with 2,500 switching elements has a chip size of $7.6 \times 7.6 \text{ mm}^2$. The insertion loss of such $N \times N$ switches is determined by the waveguide propagation loss ($\sim 0.2 \text{ dB/cm}$), insertion loss due to waveguide crossings (0.01 dB/crossing , number of crossing passed varies between $N - 1$ and $2N - 1$), and the switching element loss (measured as 0.2 dB). The reported 50×50 switch has a maximum on chip insertion loss of 9.6 dB (8.8 dB loss for propagation through 98 cells and 0.8 dB loss for switching) and high extinction ratio ($> 50 \text{ dB}$). For a 100×100 switch the total on chip loss is estimated to be 10 dB [160]. Switch response times have been measured as $0.85 \mu\text{s}$ (on) and $0.47 \mu\text{s}$ (off), the fiber coupling loss from waveguide to standard single mode fiber is $\leq 6 \text{ dB/interface}$, and the adiabatic coupler switch ensures broadband operation (1400 to 1700 nm wavelength range).

10.5.3 3D MEMS Switches

10.5.3.1 General Aspects

3D MEMS mirrors switch a signal from one input fiber to a selected output fiber using a pair of MEMS mirrors and fiber collimators and applying analogue beam steering, and an $N \times N$ switch requires $2N$ switching elements [160, 161]. 3D MEMS constitutes one of the most promising concepts for achieving very large switching port counts (e.g. from 32 to 2000).

10.5.3.2 3D MEMS Mirror Arrays

The key building block of 3D MEMS switches are MEMS mirror arrays, and the relevant parameters include:

MEMS Mirror Size and Fill Factor: The typical size of MEMS mirrors for large scale optical switches is in the range from $100 \mu\text{m}$ to 2 mm . The mirror matrix can have a simple or an interleaved $j \times k$ design, and the mirror reflective surface can be round, elliptical, or square. Larger mirror size and higher fill factor enable better tolerance and shorter path lengths. However, high fill factors tend to raise static and dynamic crosstalk, and making mirrors too big increases the pitch resulting in greater path lengths or the need of higher deflection angles.

MEMS Mirror Deflection Angle: 3D MEMS mirrors deflect optical beams independently in both the x - and the y -axis direction. Higher deflection angles allow shorter optical path lengths, which make the overall system more compact and less sensitive to vibrations and improve insertion loss. On the other hand, high deflection angles reduce the reflectivity and raise polarization dependent loss.

MEMS Mirror Resonance Frequency and Driving Voltages: The MEMS mirror is a mechanical resonator and has an intrinsic resonance frequency, and this is a very important characteristics as well as the Q factor. The relationship between deflection angle and driving voltage is also important in designing the driving circuit and the feedback control loop.

MEMS Mirror Reflectivity, Flatness, and Curvature: The MEMS mirror reflective surface is typically coated with a layer of aluminum or gold, resulting in high reflectivity over a wide wavelength range (92% and >95% reflectivity, respectively) from 1260 nm to 1700 nm. Flatness requirement is typically $< \lambda/10$ at 632.8 nm and the mirror curvature radius should be >0.5 m.

MEMS Stability, Angular Drift, and Control Systems: Stability of the mirror plays a critical role in the complexity of the control schemes and the reliability of the overall system. MEMS switches need to have a life time of longer than 10 years, and in order to assure low insertion loss over its life time, some sort of power monitoring and feedback control is needed but even under these circumstances the long or short term drift of MEMS deflection angles is typically required to be <0.1 degree.

Yield of MEMS Mirror Arrays: A proven concept for assuring high yield of MEMS mirror arrays comprising large numbers of mirrors is designing the mirror array with an appropriate number of spare mirrors [161].

10.5.3.3 Examples of MEMS Mirror Arrays

Surface-micromachined two-axis mirror arrays for building MEMS $N \times N$ switches with N of the order of 100s were reported in [162–164], and one early example of such a mirror that was used for the Lucent/Agere WaveStar™ LambdaRouter™ switch, is shown in a scanning electron microscope micrograph in Fig. 10.30 [162–164].

The basic element is a 500 μm -diameter round gimbal-mounted reflective mirror suspended from a fixed frame using a gimbal ring and four torsional springs, two for each axis. The MEMS mirror is attached to the ring by a second set of assemblies and can rotate with respect to the ring around a second orthogonal axis, thus achieving two degrees of freedom of tilt. The MEMS mirrors are arranged in an array with 1 mm pitch. The mirrors are tilted by applying voltages to fixed electrodes located underneath the mirror and the gimbal ring and have a mechanical deflection angle of about 6.5° . Two electrodes per axis are necessary because of the attractive nature of the electrostatic force. The electrostatic actuator is effectively a capacitor with negligible steady-state power consumption and no heat dissipation on chip, allowing for densely integrated arrays of many hundreds of micromirror devices.

Fig. 10.30 Surface-micromachined beam-steering micromirror [163]

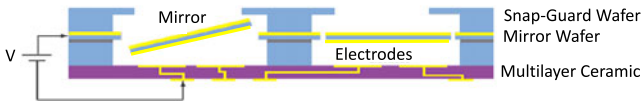
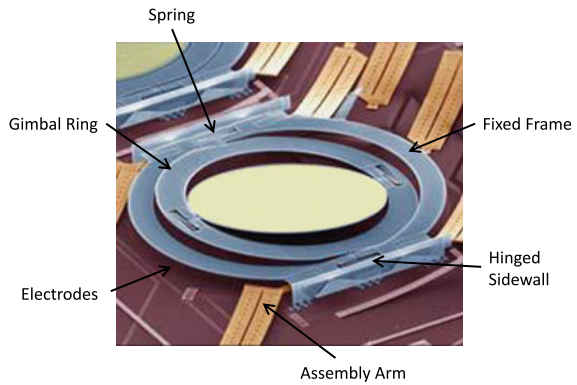


Fig. 10.31 Bulk-micromachined single crystal MEMS micromirror structure with simple parallel plates [165]

Another bulk-micromachined single crystal MEMS design with simple parallel plates was developed by GlimmerGlass Inc. [165]. A multilayer ceramic substrate was used for the driving electrodes, routing, and sealing, and provided the mechanical support for MEMS mirrors and drivers. The mechanical mirror structure is fabricated separately, and the two parts are bonded to form a parallel-plate electrostatic actuated 3D-MEMS mirror array, as shown in Fig. 10.31. The gimbaled mirror array was micromachined into the device layer of an SOI wafer. An SOI handling layer provided mechanical support and separation between mirrors and electrodes. The parallel plate is prone to intrinsic snap down resulting in unstable MEMS mirror operation, and in order to prevent electrostatic snap down failure, a third, snap guard layer was bonded to the top of the MEMS mirror layer, serving as a mechanical hard stop for the mirror movement. The mechanical deflection angle of these mirrors is typically $<4.5^\circ$.

The other kind of MEMS mirrors use vertical comb drive actuators, also based on electrostatic actuation, was first reported in [166], and [167], and several variations of vertical comb drive mirrors have been reported subsequently, including self-aligned vertical combs, angular vertical combs, electrostatically assembled vertical combs, and thick vertical combs ($100\ \mu\text{m}$) attached to mirror edges on double sided SOI wafers [167–174]. Bulk micromachined micromirrors with vertical comb drive actuators do not have the snap-down failure effect, which increases both the stability of such MEMS structures and the actual deflection angles. In addition, compared to parallel plate structures, micromirrors with vertical comb drive offer much larger torques so that the operating voltage can be smaller and the resonance frequency can

be higher. At the same time vertical comb drive offers much higher deflection angles, which is particularly advantageous for 3D MEMS switch applications. Calient has been using vertical comb drive actuators to fabricate 2-axis MEMS mirror arrays reliably since 2000 with mirrors having high mechanical deflection angles of more than 20° [175, 176].

10.5.3.4 2D High Port Count High Precision Fiber Collimator Arrays

Fiber collimator arrays containing an array of optical fibers and a corresponding array of micro-lenses constitute another key element of 3D MEMS-based switches. An important characteristics of fiber collimator arrays is their beam pointing error, which has been confirmed to be <1 mrad for 98% of the beams, and this can be achieved if the fiber position accuracy is $\pm 1 \mu\text{m}$ and the micro-lens pitch error and focal length variations of the micro-lens array are sufficiently small: A wave front aberration of a tenth of a wavelength may cause the path to have observable IL penalty already.

Micro-lens arrays need to be monolithically integrated and can be manufactured in high volume. So far refractive micro-lenses are the best choice for large port count MEMS optical switches since they offer low loss performance over a broad wavelength range. In contrast, diffractive lenses have high chromatic aberration that causes high wavelength-dependent loss so that they should be used for narrowband designs only. Both silicon and glass micro-lenses can be used for the telecom wavelength range (1260 nm–1650 nm). The lens shape is typically spherical, and for the same insertion loss target, lens shape accuracy requirements vary for different materials as a function of refractive index. For example, comparable radius curvature non-uniformity causes much more focal length variations for glass than for silicon lenses. The lens shape accuracy and the radius of curvature uniformity specifications for glass lenses are 5 times higher than those for silicon lenses so that silicon micro-lens arrays [179] are better suited for the applications under consideration here. A $\pm 1\%$ focal length uniformity over the complete lens array guarantees sufficiently uniform optical spot sizes, and a pair of fiber collimator arrays will typically have about 0.4 to 0.6 dB IL.

10.5.4 3D MEMS $N \times N$ Optical Switches

10.5.4.1 3D MEMS Switch Architectures, General Aspects

Various 3D MEMS optical switch architectures have been proposed and realized during the past 20 years with different switch port count, mirror deflection angle, pitch, fill factor, MEMS mirror stability, path-length, total packaging size, and optical performance such as insertion loss and crosstalk. For all these architectures, the input and output fibers are either arranged in the same or in two fiber collimator

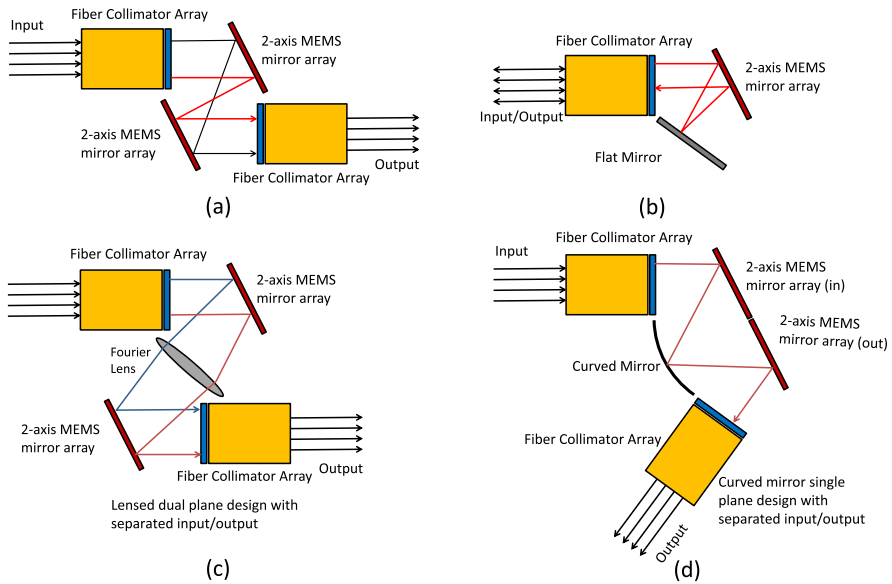


Fig. 10.32 Different 3D MEMS switch architectures, (a) parallel dual plane design [162, 163, 175], (b) flat mirror single plane design [165], (c) dual plane design with separated input/output and Fourier lens [184–186], (d) curved mirror single plane design with separated input/output [182]

2D array(s), and the optical beams are steered in three dimensions by two stages of 2-axis micromirrors. The two MEMS mirror arrays (for both, inputs and outputs) can be in one chip or in two chips.

The most relevant designs are:

- (a) Parallel dual plane design [162, 163, 175], as shown in Fig. 10.32(a)
- (b) Flat mirror single plane design [165] that uses a fiber collimator array that has both inputs and outputs (Fig. 10.32(b))
- (c) Dual plane design with separated input/output and Fourier lens [184–186] (Fig. 10.32(c))
- (d) Curved mirror single plane design with separated input/output [182] (Fig. 10.32(d))
- (e) Roof-type mirror single plane design [189]
- (f) 4F design with separated input/output [187]

Four examples of the architectures are shown in Fig. 10.32. The parallel dual plane design, as illustrated in Fig. 10.32(a), constitutes one of the most important and widely used structures [161–163], and the Calient switch as well as various implementations by Lucent Technologies, discussed in more detail below, are based upon this design. It has been demonstrated that optical switches with port count up to thousands are possible with this architecture, however, larger maximum deflection angles are required in order to keep the path lengths short [198, 199].

10.5.4.2 Calient 3D MEMS Switches

Calient developed a 384×384 non-blocking optical switch with very good optical performance based on the configuration shown in Fig. 10.32(a) [175, 176]. Due to the symmetrical design, both input and output mirrors require the same maximum deflection angles (up to $\pm 20^\circ$). The MEMS array is shown in Fig. 10.33(a). The typical relationship between the driving voltage and the mechanical deflection angle is shown in Fig. 10.33(b). The optical path length is 46 mm to 55 mm, with an average mirror-mirror separation of 26.9 mm.

Large scale optical switches with 3D MEMS mirrors generally need a feedback control system so that time and/or temperature dependent variations of (a) MEMS deflection angles (b) high voltage driver output voltages, and (c) mechanical alignments can be compensated by fine-tuning the MEMS mirrors.

Switch feedback control can be implemented either as a direct or an indirect monitoring system, and direct monitoring can be implemented in several ways, e.g. using the customer input light and tap couplers or internal light of an un-used band and wavelength division multiplexing. A 3D MEMS optical switch architecture with direct power monitoring (similar to the one used by Calient) is shown in Fig. 10.34. Each input/output fiber has a 1×2 beam splitting coupler to tap a small portion of the power, which enables the switch path insertion loss to be measured.

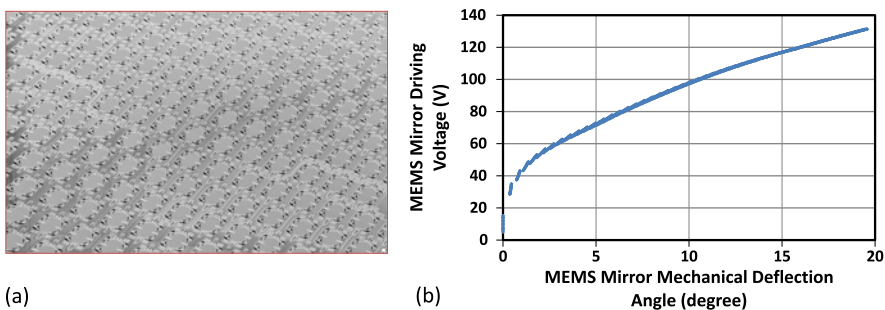
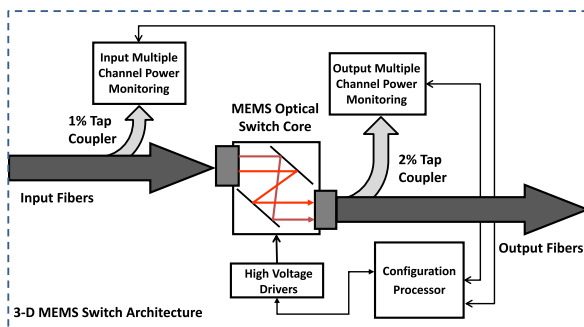


Fig. 10.33 (a) 400 mirror 3D MEMS array, (b) relationship between driving voltage and mechanical deflection angle for MEMS mirrors as shown in (a)

Fig. 10.34 3D MEMS switch system architecture with optical power monitoring functions



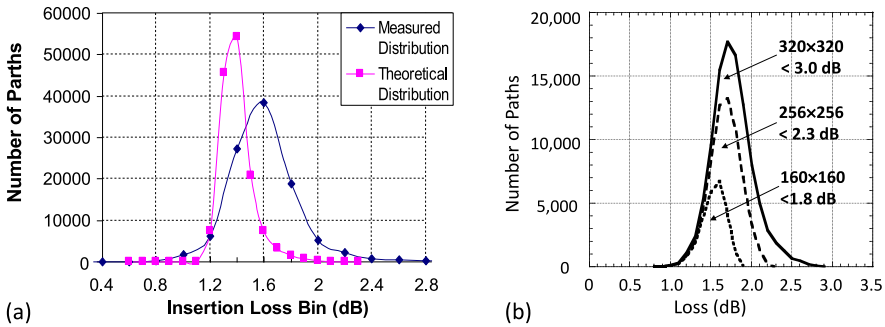


Fig. 10.35 Insertion loss performance of Calient 3D MEMS switch. (a) Theoretical and measured insertion loss distribution for a 360×360 switch, (b) insertion loss distribution for different switch sizes, all data for $1.55 \mu\text{m}$

The insertion loss for each path of an optical switch can be calculated by using fiber collimator measurement data and taking the optical configuration into account. Calculated and measured overall system insertion loss values at 1550 nm for all $129,600$ paths of a 360×360 optical switch are shown in Fig. 10.35(a). The measured overall system insertion loss includes switch core loss and loss of connectors and the power monitoring unit. Compared to the modeling the experimentally determined loss is slightly higher and has a wider distribution, which is partly due to connector variations. Furthermore, insertion loss gets larger as shown in Fig. 10.35(b), where the measured insertion loss from an actual switch is shown for different port counts.

The wavelength dependent loss variation for the O-, S-, C-, and L-bands are very small ($< 0.8 \text{ dB}$), with 1550 nm insertion loss typically larger than loss at 1310 nm (in agreement with theoretical calculations). The E-band exhibits about 1 dB additional wavelength dependent loss due to the water peak of the fiber couplers. This peak can be removed by using water-peak removed fiber couplers.

Other critical optical parameters of 3D MEMS switches are return loss, directivity, polarization dependent loss, crosstalk, and switching time. The return loss is dominated by the return loss of the fiber collimators, and measured values vary from 42 dB to 55 dB with typical values of 46 dB . The directivity is about 70 dB . Different paths of a switch have different PDL, measured values are $< 0.2 \text{ dB}$ and typical PDL is 0.05 dB .

Static crosstalk is measured to be better than 60 dB and it is primarily due to adjacent ports while non-neighboring ports have typically 80 dB static crosstalk. Dynamic crosstalk occurs only when a new connection is set up, and worst values observed during beam scanning amount to 30 dB . Switching time for Calient MEMS switches is $< 50 \text{ ms}$. The resonance frequencies of the MEMS mirrors are of the order of 400 to 600 Hz . Moving the mirrors too rapidly excites the resonant mode of the mirror and causes ringing of the optical signal, but a special voltage or driving profile to control the movement of MEMS mirrors assures low ringing of the optical signal and fast switching time. The feedback control of the 3D MEMS switches

may cause signal fluctuations during active control cycles and therefore the MEMS mirror movement steps have to be carefully chosen in order to ensure small optical signal fluctuations.

Finally it should be mentioned that the Calient 3D MEMS switch discussed so far can be scaled to more than 1000×1000 ports with reasonably low optical insertion loss with the same kind of MEMS mirrors and similar optical design [177].

10.5.4.3 Miscellaneous 3D MEMS Switches

Glimmerglass 3D MEMS Switches The flat mirror single plane design developed by Glimmerglass and illustrated in Fig. 10.32(b) [165, 178] uses a fiber collimator array that has both input and output ports and a MEMS mirror array in a single plane, serving as both input and output MEMS mirrors. A flat mirror reflects the optical paths back to the MEMS mirror array. In this design, any port can be used as input or output port, any port can be switched to any port, and a non-symmetric number of input and output ports is possible. For example, if the total switch has 192 mirrors, the switch size can be 1×191 , 96×96 , 32×160 , etc. as long as the input port count and output port count make the total amount of 192. Glimmerglass offers a 96×96 switch based upon the flat mirror single plane design (Fig. 10.32(a)) and uses a dual plane design for its 192×192 3D MEMS switch (Fig. 10.32(c)). The switch uses bulk-micromachined parallel plate beam-steering micromirrors (see Fig. 10.31) with about $<4^\circ$ deflection angle [165]. The 192×192 switch has a typical (maximum) insertion loss of 1.7 (3.7) dB, 20 ms switching time, 70 dB crosstalk, and offers direct optical power monitoring and feedback control loops.

Fujitsu 80 \times 80 Switch Fujitsu has proposed and implemented a roof-type mirror single plane design for an 80×80 switch, which uses two-axis tilt comb-driven 2D MEMS mirror arrays with V-shaped torsion bars for the 3D MEMS switch [188]. The MEMS mirrors have maximum deflection angles of $\pm 5^\circ$. Mean insertion loss amounts to 2.6 dB with a variation from 1.5 to 4.0 dB. Another characteristic feature is the fact that input and output ports are pre-assigned [189].

Lucent Technologies 3D MEMS Switches Lucent Technologies has reported 3D MEMS switches with different architectures, and the 3D MEMS switch commercialized first was the “LambdaRouter” using the parallel dual plane design (see Fig. 10.30 and Fig. 10.32(a)) [162–164, 180, 181]. The low deflection angles of the MEMS mirrors used resulted in long optical paths and high insertion loss.

Lucent also demonstrated 238×238 , 256×256 , and 1100×1100 3D MEMS switches using a lensed dual plane design, i.e. a structure with a Fourier lens between the two MEMS mirrors [184–186] (see Fig. 10.32(c)). The Fourier lens enables lower total insertion loss even if low deflection angles of the MEMS mirror array (about 5° mechanical deflection angle on both axes) are used. The 238×238 switch exhibited 1.33 dB mean insertion loss with a loss variation from 0.8 dB to

2 dB [184] while a mean fiber-to-fiber insertion loss of 2.1 dB and maximum insertion loss of 4.0 dB across all possible connections were reported for the 1100×1100 switch [186]. This is the largest 3D MEMS switch demonstrated so far and clearly demonstrates the potential of the Fourier lens in improving the insertion loss.

The 4F design with separated input/output is another concept developed by Lucent Technologies and implemented for a 100×100 switch [187]. Its key features are two 4F imaging systems, which make the design rather complex. It has been demonstrated that the 4 F imaging system is more than ten times less sensitive to microlens-to-fiber misalignment, however, the insertion loss (2.9 dB mean, variation from 1.4 to 4.5 dB) is higher than observed for switches using similar MEMS mirrors with comparable port count but alternative design. Altogether the performance of these switches did not meet expectation and the concept does not appear to be particularly promising.

In general Lucent Technologies MEMS switches include integrated power monitoring for each fiber and feedback control [183], however, switch systems with open-loop control were also reported [184].

NTT MEMS Switch NTT fabricated silicon single crystal 1024 channel parallel plate MEMS mirrors for 3D MEMS switch applications [190], and also developed a 100×100 switch and a fully functional 128×128 switching system with mean loss of 2.6 dB and insertion loss variations from 0.6 to 4.8 dB [191–193]. NTT also demonstrated a 512×512 optical switch based upon a curved mirror design that also has two separated MEMS planes with separated inputs/outputs. The design exhibits characteristics essentially similar to that of the design with flat mirror but offers reduced deflection angles and smaller beam spot size on the mirrors, which improves clipping loss. The 512×512 switch exhibited a mean insertion loss of ~ 5 to 6 dB and variations from 2 to 11 dB [194].

3D MEMS Switch with Indirect Monitoring An interesting variant of the 3D MEMS architecture that uses the flat mirror single plane design and indirect optical monitoring was proposed and demonstrated in [195]. The goal of the architecture is to offer a cost effective feedback loop to control MEMS mirror movement without directly monitoring the optical power inside an optical fiber. Out-of-band light is injected along each of the beam paths and imaging sensors are used to monitor the beams deflected from the MEMS mirrors so that the mirror position can be monitored and direct feedback control for the MEMS mirrors is possible. The advantages of this indirect optical monitoring include compact design with dark fiber connection ability. The feedback control system can track and correct MEMS mirror drift and driver voltage drift, however, it cannot track mechanical structure changes of the many optical components, so that the optimized position from the feedback control system may not be the best position for the switch to have lowest insertion loss. Since the optical power from the fibers is not directly monitored, the feedback control system may have tracking errors.

Concluding Remark There are other approaches that seek to build modular MEMS optical switches [196], which do not use monolithic but smaller MEMS

mirror chips in a modular way so that the switch size can be enlarged by adding switching modules.

The Clos architecture can be used for the implementation of much larger port counts, however, due to the three stage switching architecture, insertion loss increases considerably.

Altogether, MEMS optical switches have matured in the past, commercial products have become available, and MEMS optical switches have been deployed for lab automation, telecom applications, and recently in data centers. Scaling 3D MEMS optical switches from about 360×360 , which represents the current state-of-the-art (see, however, the section on Lucent switches above), to extreme large port counts in the range of several thousands is possible and corresponding research and development is ongoing [197–199].

10.5.5 3D MEMS-Based Wavelength Selective Switches

10.5.5.1 3D MEMS-Based $1 \times N$ Wavelength Selective Switches

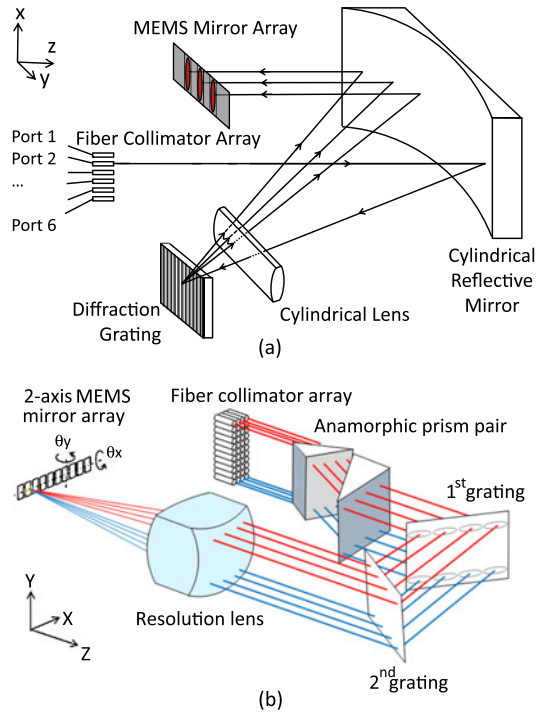
The first MEMS-based WSS built was a wavelength blocker for an ROADM, which is a 1×1 WSS [200–205]. Wavelength blockers use a 1D array of MEMS mirrors with one axis of deflection to achieve the attenuation/blocking function on each wavelength channel. A wavelength blocker is simpler than a $1 \times N$ WSS, but the basic principle is the same.

A 3D MEMS-based $1 \times N$ WSS can be designed according to the generic illustration in Fig. 10.4 (with a 3D MEMS mirror array with multiple mirrors in a 1D array taken as optical switching element) [206–211]. Incoming light is angularly separated by the transmission grating, a collimating lens transfers the angularly dispersed wavelengths to different MEMS mirrors which can pivot in both x - and y -directions, and redirect each wavelength slice to the corresponding output port through the diffraction grating.

For hitless operation, the 2-axis MEMS mirror movements have to follow a special pattern to avoid unwanted leakage. Sometimes one axis is used for switching only and the other is used for switching and attenuation. Wavelength selective switches should be compact so that the package fits into a blade space of a telecom rack, and reflective grating-based $1 \times N$ WSS designs are favorable in this respect as reflective gratings fold the optical light path resulting in compact design. A corresponding 1×4 WSS was demonstrated by Lucent Technologies [207], and Wu et al. reported a 1×32 WSS [208–211].

The WSSs reported in [207–211] have circular optical beams. However, since the MEMS mirrors can be rectangular or elliptical, the optical beam must not necessarily be circular. If the beam is elliptical and the long direction is aligned to the grating dispersion direction, a better wavelength resolution can be achieved while the short extension in the other direction keeps the height of the optics small.

Fig. 10.36 $1 \times N$ WSS schematic using elliptical beams. (a) Schematic optical setup of $1 \times N$ WSS with cylindrical lens and cylindrical reflective mirror, (b) schematic optical setup of a 1×43 WSS with anamorphic prism pair [213]



Two corresponding architectures have been proposed already, one of them using a cylindrical lens and a cylindrical reflector (see Fig. 10.36(a)), the other one using an anamorphic prism pair (see Fig. 10.36(b)). In Fig. 10.36(a), the reflective grating is used to disperse different wavelength beams to different MEMS mirrors in the wavelength dispersive plane while the cylindrical lens combines the beams in the switching plane. This way the beam in the x -direction is much bigger than in the y -direction on the MEMS mirrors, and the beams in y -direction are much larger than in x -direction on the diffractive grating surface. This architecture is used to build many commercially available $1 \times N$ WSSs [212]. In Fig. 10.36(b), the same principal was implemented by an anamorphic prism pair. Based on this architecture, a 1×43 WSS with 40 channels at 100 GHz channel spacing was demonstrated [213].

The performance of the MEMS micromirror array has a significant influence on the performance of the WSS [214]. Micromirror arrays used in $1 \times N$ WSSs include electro-magnetic or electrostatic actuations. The most important parameters are high deflection angles, high fill factor, low angle drift, mirror size, and pitch to match the grating dispersion. Most mirror arrays have a pitch of about $100 \mu\text{m}$ with a fill factor of $>98\%$. The total mirror number in a row is typically the same as the channel number. However, in order to enable flexible passbands, a larger number of mirrors (e.g. twice the channel number or even more) is needed, and that makes the design of corresponding $1 \times N$ WSSs difficult as flexible passbands require smaller pitch and larger numbers of MEMS mirrors to be actuated.

10.5.5.2 3D MEMS-Based $N \times N$ Wavelength Selective Switches

Making $N \times N$ WSSs is a very challenging task. $N \times N$ WSSs have $N \times m$ MEMS mirrors where m is the total wavelength channel number. For an 8×8 WSS with 40 channels, each MEMS array has 320 mirrors. Furthermore, 100% MEMS mirror yield is required, the MEMS mirror size is very small, it should have $>92\%$ fill factor, and should be arranged in a 2D array with about 10 degree deflection angle, which is also challenging.

The majority of $N \times N$ WSSs are constructed with multiple $1 \times N$ WSSs in a Spanke configuration, and due to the availability, reliability, and modularity of $1 \times N$ WSSs such $N \times N$ WSSs have been widely used in ROADMs.

However, there is research directed toward building integrated $N \times N$ MEMS WSSs. One example of an $N \times N$ all optical wavelength selective optical cross-connect switch architecture was proposed by O. Solgaard et al. [20]. This approach uses an array of MEMS mirrors for the full functionality of $N \times N$ port optical wavelength switching. It requires two MEMS mirror arrays to steer different wavelengths to different ports, and the wavelength selective routing apparatus uses a diffraction grating to separate the multi-wavelength signals to individual wavelength channels.

Another concept to build an $N \times N$ WSS has been proposed and demonstrated by integrating AWG devices with MEMS mirrors [215–217], which resulted in particularly narrow passbands [217].

More recently, an experimental 5×5 WSS with 46 wavelength channels and 100 GHz spacing has been demonstrated [218]. The two MEMS arrays used as switching engines are composed of 46×5 micromirror arrays monolithically integrated on each MEMS chip. The reported insertion loss is 35 dB with a 15 dB extinction ratio.

A 4×4 WSS for 8 CWDM wavelength channels using a monolithic SOI chip comprising four 4×1 MEMS wavelength-selective switches and four 1×4 passive splitters, together with a 4×4 waveguide shuffle network is another reported approach [219]. An 8-element micromirror array matching the CWDM (1470 to 1610 nm) grid with 20-nm spacing was integrated in the waveguide, and the MEMS mirror is actuated by a rotary comb-drive actuator. The demonstrated 4×4 WSS has 24 dB insertion loss with 25 dB crosstalk.

All experimentally demonstrated $N \times N$ WSSs discussed above have very high loss, and significant additional effort is needed in order to make these $N \times N$ WSSs suited for system applications.

An alternative approach to build an $N \times N$ WSS is to use individual wavelength demux/mux and a large port count optical switch to integrate them together. Using Calient's S320 320×320 switch, 8 demux and 8 mux, an 8×8 WSS with 40 channels and 100 GHz channel spacing has been implemented [220]. The WSS had about 11 dB total IL and is a low cost solution. The drawback is the narrow passband due to cascading individual mux and demux.

10.6 Piezoelectric Optical Switches

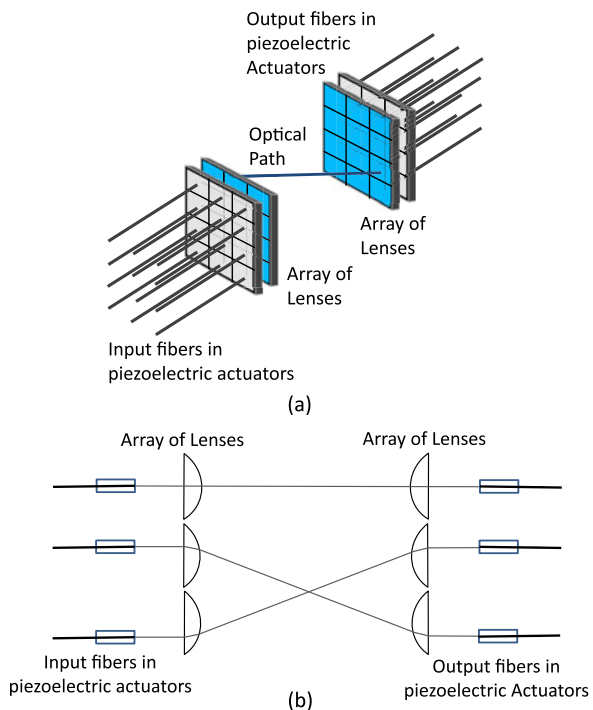
Other variants of optical switches include piezoelectrically actuated optical switches developed by Polatis [221–224]. Unlike 3D MEMS mirrors, the piezoelectric actuators are used as the switching elements that steer the optical beams in free space from input ports to output ports.

Two approaches for piezoelectric-actuator-based $N \times N$ switches have been implemented by Polatis. One approach uses piezoelectric-actuators for moving the tip of the fiber to steer the beam, as shown in Fig. 10.37. The lateral movement in x - and y -direction is translated to the deflection angle of the optical beam through a lens. Each fiber is associated with a lens for this purpose. The lens also collimates the light signal from the fiber to a collimated beam. The optical signal passes directly from the input to the output fibers in free space through two lenses. The design of the switch is highly depending on how small the fiber/actuator assembly and the maximum displacement of the piezoelectric actuator are. An alternative approach uses a piezoelectric actuator to move a fiber collimator assembly as a whole unit and making the connection [221–224].

Comparing the two approaches shows that moving fibers requires smaller displacement while the loss is higher since the fiber is off the center of the lens, which causes aberration induced insertion loss.

Polatis offers optical switches based on piezoelectric beam steering technology from 4×4 to 192×192 , with a recent announcement of 384×384 switches. The ad-

Fig. 10.37 Schematic of piezoelectric $N \times N$ optical switch [221–224]



vantages of these switches are their low insertion loss (minimum 0.4 dB, worst case 2.8 dB not including connectors), modularity, and insertion loss stability. Disadvantages include higher cost and difficulties in packaging density and displacement of the piezoelectric elements.

10.7 Summary and Outlook

Optical switches continue to improve in performance with lower loss, lower back-reflection, better spectral characteristics. Integration continues to expand, resulting in lower cost, smaller size and higher reliability. Telecom and datacom networks continue to increase in capacity, which drives the demand for high capacity optical switching rather than electrical switching. The integration of optical amplifiers allows such switching networks to scale to larger sizes, although with some drawbacks. The optimum switch architecture depends on the application, and consequently, a wide range of switch technologies and architectures continue to be researched and commercialized.

References

1. R. Ramaswami, K. Sivarajan, *Optical Networks: A Practical Perspective* (Morgan Kaufmann, New York, 1998)
2. T.S. El-Bawab, *Optical Switching* (Springer, New York, 2006)
3. G.I. Papadimitriou, C. Papazoglou, A.S. Pomportsis, *Optical Switching* (Wiley-Interscience, Hoboken, 2007)
4. C. Li, *Principles of All-Optical Switching* (Wiley/Science Press, Beijing, 2015)
5. G.A. Fish, B. Mason, L.A. Coldren, S.P. DenBaars, Compact, 4×4 InGaAsP-InP optical crossconnect with a scaleable architecture. *IEEE Photonics Technol. Lett.* **10**(9), 1256–1258 (1998)
6. Generic requirements for singlemode fiber optic switch, Telcordia Technologies Generic Requirements, GR-1073-Core (Piscataway, NJ, 2011)
7. T. Shimoe, K. Hajikano, K. Murakami, Path-independent insertion loss optical space switch, in *Opt. Fiber Commun. Conf. (OFC'87)*, Reno, NV, USA (1987), Techn. Digest, paper WB2
8. T. Nishi, T. Yamamoto, S. Kuroyanagi, A polarization-controlled free-space photonic switch based on a PI-loss switch. *IEEE Photonics Technol. Lett.* **5**, 1104–1106 (1993)
9. K. Padmanabhan, A.N. Netravali, Dilated networks for photonic switching. *IEEE Trans. Commun.* **COM-35**(12), 1357–1365 (1987)
10. R.A. Spanke, Architectures for large nonblocking optical space switches. *IEEE J. Quantum Electron.* **QE-22**(6), 964–967 (1986)
11. C. Clos, A study of non-blocking switching networks. *Bell Syst. Tech. J.* **32**, 406–424 (1953)
12. M.L. Heitner, J.J. Song, R. Vianna, Folded Clos architecture switching, US patent number 6696917 (2000)
13. W.T. Anderson, J. Jackel, G.K. Chang, H. Dai, W. Xin, M. Goodman, C. Allyn, M. Alvarez, O. Clarke, A. Gottlieb, F. Kleytman, J. Morreale, V. Nichols, A. Tzathas, R. Vora, L. Mercer, H. Dardy, E. Renaud, L. Williard, J. Perreault, R. McFarland, T. Gibbons, The MONET project—a final report. *J. Lightwave Technol.* **18**(12), 1988–2009 (2000)

14. K.S. Jepsen, U. Gliese, B.R. Hemenway, S. Yuan, K.S. Cheng, J.E. Hurley, L. Guiziou, J.W. McCamy, N. Boos, D.J. Tebben, B. Dingel, M.J. Li, S. Gray, G.E. Kohnke, L. Jiang, V. Srikant, A.F. Evans, J.M. Jouanno, Network demonstration of $32\lambda \times 10$ Gb/s across 6 nodes of 640×640 WSXCs with 750 km Raman-amplified fiber, in *Opt. Fiber Commun. Conf. (OFC'2000)*, Baltimore, MD, USA (2000), Techn. Digest, paper PD35
15. M. Adams, ROADM and wavelength selective switches perspectives for fiber optic manufacturing test engineering, JDSU Technical White Paper (2008)
16. Finisar Corporation, Wavelength selective switches for ROADM applications, Finisar Corporation WSS ROADM Product Guide (2011)
17. P. Wall, P. Colbourne, C. Reimer, S. McLaughlin, WSS switching engine technologies, in *Opt. Fiber Commun. Conf. and Nat. Fiber Opt. Eng. Conf. (OFC/NFOEC'08)*, San Diego, CA, USA (2008), Techn. Digest, paper OWC1
18. E.G. Loewen, E. Popov, *Diffraction Gratings and Applications* (Marcel Dekker, New York, 1997)
19. J.L. Wagener, T.A. Strasser, Multiple function digital optical switch, US Patent No. 8,086,080 (2011)
20. O. Solgaard, J.P. Heritage, A.R. Bhattarai, Multi-wavelength cross-connect optical switch, US Patent 6,374,008 (2002)
21. Calient Technologies, S-320 optical circuit switch datasheet. <http://www.calient.net/products/s-series-photonic-switch/> (2013)
22. B.C. Collings, Advanced ROADM technology and architecture, in *Opt. Fiber Commun. Conf. (OFC'15)*, Los Angeles, CA, USA (2015), Techn. Digest, paper Tu3D.3
23. www.enablence.com, Enablence technologies, Inc., iMS™ $M \times N$ Multicast switch modules (2010)
24. P.G. Hale, R. Kompfner, Mechanical optical fibre switch. *Electron. Lett.* **12**(15), 388 (1976)
25. W.J. Tomlinson, Application of GRIN-rod lenses in optical fiber communication systems. *Appl. Opt.* **19**, 1127–1138 (1980)
26. SELFOC Product Guide, manufacturer's literature on fiber collimators, NSG America Inc., NJ, USA (1997)
27. CASIX Inc, Technical specifications for C-lens. <http://www.casix.com/products/glass-optics/telecom-optics/c-lens.shtml>
28. S. Yuan, N.A. Riza, General formula for coupling-loss characterization of single-mode fiber collimators by use of gradient-index rod lenses. *Appl. Opt.* **38**, 3214–3222 (1999)
29. D. Marcuse, Loss analysis of single-mode fiber splices. *Bell Syst. Tech. J.* **56**, 703–719 (1977)
30. H. Kogelnik, Coupling and conversion coefficients for optical modes, in *Proceed. Symp. Quasi-Optics*, ed. by J. Fox. Polytechnic Brooklyn, Brooklyn, NY, USA. Polytechnic Institute Microwave Research Institute Symposia Series, vol. 14, pp. 335–347 (1964)
31. www.senko.com, Senko advanced components, fiber array and V-groove (2013)
32. P.M. Garel-Jones, M.R. Harman, T.P. Cutts, Opto-mechanical device having optical element movable by twin flexures, US Patent No. 5594820 (1995)
33. H.-S. Lee, Miniaturization of gradient index lens used in optical components, US Patent No. 6088166 (2000)
34. www.diconfiberoptics.com
35. W.-Z. Li, Q. Shao, Mechanical optical switching device, US Patent No. 6215919 (1999)
36. Y. Fujii, J. Minowa, T. Aoyama, K. Doi, Low loss 4×4 optical matrix switch for fiber-optic communications. *Electron. Lett.* **15**(14), 427–428 (1979)
37. J. Minowa, Y. Fujii, Y. Nagata, T. Aoyama, K. Doi, Nonblocking 8×8 optical matrix switch for fibre-optic communications. *Electron. Lett.* **16**(11), 422–423 (1980)
38. J.E. Ford, D.J. DiGiovanni, D.J. Reiley, $1 \times N$ fiber bundle scanning switch, in *Opt. Fiber Commun. Conf. (OFC'98)*, San Jose, CA, USA (1998), Techn. Digest, pp. 143–144
39. J.E. Ford, D.J. DiGiovanni, $1 \times N$ fiber bundle scanning switch. *IEEE Photonics Technol. Lett.* **10**(7), 967–969 (1998)

40. M. Mizukami, M. Makihara, S. Imagaki, K. Sasakura, 200×200 automated optical fiber cross-connect equipment using a fiber-handling robot for optical cabling systems, in *Opt. Fiber Commun. Conf. (OFC'15)*, Los Angeles, CA, USA (2015), Techn. Digest, paper OFP5
41. K. Saito, M. Nishimura, T. Yamanishi, H. Koboyashi, T. Katagiri, M. Tachikura, Optical fiber switching device having one of a robot mechanism and an optical fiber length adjustment unit, US Patent No. 5613021 (1995)
42. N. Tamaru, Y. Nishida, T. Kanai, J. Yamaguchi, T. Shoji, Optical fiber cross connection apparatus and method, US Patent No. 5784515 (1998)
43. J. Arol, Z. Ganor, Self-aligning opto-mechanical crossbar switch, US Patent No. 6859575 (2005)
44. K. Goossen, Robotic optical cross-connect, US Patent No. 6307983 (2001)
45. S. Sjolinder, Mechanical optical fibre cross connect, in *Proc. Photon. Switching*, Salt Lake City, UT, USA (1995), paper PFA4
46. B. Phini, Z. Ganor, R. Cohen, M. Eizenshtat, Optical crossbar switch, US Patent No. 8107779 (2007)
47. www.fiberzone-networks.com
48. A.S. Kewitsch, Large scale, all-fiber optical cross-connect switches for automated patch-panels. *J. Lightwave Technol.* **27**(15), 3107–3115 (2009)
49. www.telescent.com/tswitch
50. www.emd-performance-materials.com/en/display/lc_materials/lc_phases/lc_phases.html
51. P. Yeh, C. Gu, *Optics of Liquid Crystal Displays*, 2nd edn. Wiley Series in Pure and Applied Optics, vol. 1 (Wiley, Hoboken, 2010)
52. R.A. Soref, Low-cross-talk 2×2 optical switch. *Opt. Lett.* **6**, 275–277 (1981)
53. J. Prisco, A low-crosstalk liquid crystal optical switch. *J. Lightwave Technol.* **LT-3**, 37–38 (1985)
54. J. Kondis, B.A. Scott, A. Ranalli, R. Lindquist, Liquid crystals in bulk optics-based DWDM optical switches and spectral equalizers, in *IEEE/LEOS Internat. Conf. Opt. MEMS*, Piscataway, NJ, USA (2001), Techn. Digest, pp. 292–293
55. Meadowlark product catalogue 2009–2010, www.meadowlark.com, pp. 45–62 (2010)
56. An introduction to spatial light modulators. http://laser.physics.sunysb.edu/~melia/SLM_intro.html#4.7
57. Y. Fujii, Low-crosstalk 2×2 optical switch composed of twisted nematic liquid crystal cells. *IEEE Photonics Technol. Lett.* **5**, 715–718 (1993)
58. G. Lazarev, A. Hermerschmidt, S. Krüger, S. Osten, in *LCOS Spatial Light Modulators: Trends and Applications*, ed. by W. Osten, N. Reingand. Optical Imaging and Metrology: Advanced Technologies (Wiley-VCH, Weinheim, 2012)
59. Holoeye Systems Inc, <http://www.holoeyesystems.com/lcos-microdisplays/>
60. Beam steering using liquid crystals. White Paper, Boulder Nonlinear Systems (2001)
61. M. Johansson, S. Hard, B. Robertson, I. Manolis, T. Wilkinson, W. Crossland, Adaptive beam steering implemented in a ferroelectric liquid crystal spatial-light-modulator free-space, fiber-optic switch. *Appl. Opt.* **41**, 4904–4911 (2002)
62. R.E. Wagner, J. Cheng, Electrically controlled optical switch for multimode fiber applications. *Appl. Opt.* **19**(17), 2921–2925 (1980)
63. R.A. Soref, D.H. McMahon, Total switching of unpolarized fiber light with a four-port electro-optic liquid-crystal device. *Opt. Lett.* **5**(4), 147–149 (1980)
64. R.A. Soref, Low-cross-talk 2×2 optical switch. *Opt. Lett.* **6**, 275–277 (1981)
65. Y. Fujii, Low-crosstalk 1×2 optical switch composed of twisted nematic liquid crystal cells. *IEEE Photonics Technol. Lett.* **5**, 206–208 (1993)
66. N.A. Riza, S. Yuan, Reconfigurable wavelength add-drop filtering based on a Banyan network topology and ferroelectric liquid crystal fiber-optic switches. *J. Lightwave Technol.* **17**(9), 1575–1584 (1999)
67. N.K. Shankar, J.A. Morris, C.P. Yakymyshyn, C.R. Pollock, A 2×2 fiber optic switch using chiral liquid crystals. *IEEE Photonics Technol. Lett.* **2**, 147–149 (1990)

68. S. Yuan, N.A. Riza, Low interchannel crosstalk high speed fiber optic $N \times N$ crossconnect switch using polarization optics and ferroelectric liquid crystals, in *Ann. Meeting IEEE Lasers & Electro-Optics Soc. (LEOS'98)*, Orlando, FL, USA (1998), Techn. Digest, vol. 2, pp. 415–416
69. P. Gravey, J.L. de Bougrenet de la Tocnaye, B. Fracasso, N. Wolffer, A. Tan, B. Vinouze, M. Razzak, A. Kali, Liquid crystal-based optical space switches for DWDM networks. *Ann. Télécommun.* **58**(9), 1378–1400 (2003)
70. P. Berthel , B. Fracasso, J.L. de Bougrenet de la Tocnaye, Design and characterization of a LC SLM for a polarization-insensitive optical space-switch. *Appl. Opt.* **37**, 5461–5468 (1998)
71. B. Fracasso, L. Noirie, J.L. de Bougrenet de la Tocnaye, M. Razzak, E. Daniel, Performance assessment of a liquid crystal multichannel photonic space-switch, in *Proc. Photon. Switching*, Monterey, CA, USA (2001), pp. 24–26, paper PThB3
72. N. Wolffer, B. Vinouze, R. Lever, P. Gravey, L. Bramerie, 8×8 holographic liquid crystal switch, in *Proc. 26th Europ. Conf. Opt. Commun. (ECOC'2000)*, Munich, Germany (2000), pp. 275–276
73. J. Kelly, Application of liquid crystal technology to telecommunication devices, in *Opt. Fiber Commun. Conf. and Nat. Fiber Opt. Eng. Conf. (OFC/NFOEC'07)*, Anaheim, CA, USA (2007), Techn. Digest, paper NThE1
74. www.coadna.com
75. S. Frisken, Advances in liquid crystal on silicon wavelength selective switching, in *Opt. Fiber Commun. Conf. and Nat. Fiber Opt. Eng. Conf. (OFC/NFOEC'07)*, Anaheim, CA, USA (2007), Techn. Digest, paper OWV4
76. J.R. Kelly, M. Cui, D. Heineman, H. Washbur, M. Xue, Apparatus and method for optical switching with liquid crystals and birefringent wedges. US Patent 7499608 (2009)
77. S.J. Frisken, G.W. Baxter, H. Zhou, D. Abakoumov, Wavelength selective reconfigurable optical cross-connect. US Patent No. 7787720 B2 (2010)
78. G. Baxter, S. Frisken, D. Abakoumov, H. Zhou, I. Clarke, A. Bartos, S. Poole, Highly programmable wavelength selective switch based on liquid crystal on silicon switching elements, in *Opt. Fiber Commun. Conf. (OFC'06)*, Anaheim, CA, USA (2006), Techn. Digest, paper OTuF2
79. www.finisar.com/roadms-wavelength-management/10wsaaxfll
80. www.hamamatsu.com
81. K. Suzuki, Y. Ikuma, E. Hashimoto, K. Yamaguchi, M. Itoh, T. Takahashi, Ultrahigh port count wavelength selective switch employing waveguide-based I/O frontend, in *Opt. Fiber Commun. Conf. (OFC'15)*, Los Angeles, CA, USA (2015), Techn. Digest, paper Tu3A.7
82. T. Han, J. Plumridge, S. Frisken, G. Baxter, LCOS-based matrix switching for 2×4 WSS for fully flexible channel selection, in *Proc. Photon. Switching*, Ajaccio, France (2012), paper Th-S23-005
83. G.I. Papadimitriou, C. Papazoglou, A.S. Pomportsis, Optical switching: switch fabrics, techniques, and architectures. *J. Lightwave Technol.* **21**(2), 384–405 (2003)
84. Y. Silberberg, P. Perlmutter, J.E. Baran, Digital optical switch. *Appl. Phys. Lett.* **51**, 1230–1232 (1987)
85. P. DasMahapatra, R. Stabile, K.A. Williams, Multiple input to multiple output switching in an 8×4 optical crosspoint matrix, in *Proc. 40th Europ. Conf. Opt. Commun. (ECOC'14)*, Cannes, France (2014), paper P.4.18
86. M.R. Watts, W.A. Zortman, D.C. Trotter, R.W. Young, A.L. Lentine, Vertical junction silicon microdisk modulators and switches. *Opt. Express* **19**(22), 21989–22003 (2011)
87. V.R. Almeida, C.A. Barrios, R.R. Panepucci, M. Lipson, All-optical control of light on a silicon chip. *Nature* **431**, 1081–1084 (2004)
88. A.S. Khope, A.A. Saleh, J.E. Bowers, R.C. Alferness, Elastic WDM crossbar switch for data centers, in *Proc. IEEE Opt. Interconn. Conf. (OI)*, San Diego, CA, USA (2016), paper TuP7
89. G. Singh, R.P. Yadav, V. Janyani, Ti indiffused Lithium Niobate (Ti: LiNbO₃) Mach-Zehnder interferometer all optical switches: a review, in *New Advanced Technologies*, ed. by A.

- Lazinica (InTech, 2010). www.intechopen.com. Chap. 2. ISBN 978-953-307-067-4
90. N. Agrawal, C.M. Weinert, H.-J. Ehrke, G.G. Mekonnen, D. Franke, C. Bornholdt, R. Langenhorst, Fast 2×2 Mach-Zehnder optical space switches using InGaAsP-InP multi quantum-well structures. *IEEE Photonics Technol. Lett.* **7**(6), 644–645 (1995)
 91. D.H. Yoon, W.S. Yang, J.M. Kim, H.D. Yoon, Fabrication and properties of a 4×4 LiNbO₃ optical matrix switch. *Mater. Trans.* **43**(5), 1061–1064 (2002)
 92. E.J. Murphy, C.T. Kemmerer, D.T. Moser, M.R. Serbin, J.E. Watson, P.L. Stoddard, Uniform 8×8 lithium niobate switch arrays. *J. Lightwave Technol.* **13**(5), 967–970 (1995)
 93. H. Nishinoto, M. Iwasaki, S. Suzuki, M. Kondo, Polarization independent LiNbO₃ 8×8 matrix switch. *IEEE Photonics Technol. Lett.* **2**(9), 634–636 (1990)
 94. Eospace Inc, Technical specifications of custom high-speed lithium niobate electro-optic switches. www.eospace.com
 95. A.C. O'Donnell, Polarisation independent 1×16 and 1×32 lithium niobate optical switch matrices. *Electron. Lett.* **27**(25), 2349–2350 (1991)
 96. H. Okayama, M. Kawahara, Ti: LiNbO₃ digital optical switch matrices. *Electron. Lett.* **29**(9), 765–766 (1993)
 97. R. Krähenbühl, M.M. Howerton, J. Dubinger, A.S. Greenblatt, Performance and modeling of advanced Ti: LiNbO₃ digital optical switches. *J. Lightwave Technol.* **20**(1), 92–99 (2002)
 98. M. Iodice, G. Mazzi, L. Sirtleto, Thermo-optical static and dynamic analysis of a digital optical switch based on amorphous silicon waveguide. *Opt. Express* **14**(12), 5266–5278 (2006)
 99. R.A. Soref, The past, present and future of silicon photonics. *IEEE J. Sel. Top. Quantum Electron.* **12**, 1678–1687 (2006)
 100. L.C. Kimerling, D. Ahn, A.B. Apsel, M. Beals, D. Carothers, Y.K. Chen, T. Conway, D.M. Gill, M. Grove, C.Y. Hong, M. Lipson, J. Liu, J. Michel, D. Pan, S.S. Patel, A.T. Pomerene, M. Rasras, D.K. Sparacin, K.Y. Tu, A.E. White, C.W. Wong, Electronic-photonics integrated circuits on the CMOS platform. *Proc. SPIE* **6125**, 6–15 (2006)
 101. B. Jalali, M. Paniccia, G. Reed, Silicon photonics. *IEEE Microw. Mag.* **7**, 56–68 (2006)
 102. Q. Huang, X. Zhang, J. Xia, J. Yu, Systematic investigation of silicon digital 1×2 electro-optic switch based on a microdisk resonator through carrier injection. *Appl. Phys. B* **105**(2), 353–361 (2011)
 103. L. Liu, G. Roelkens, T. Spuesens, R. Soref, P. Regreny, D. Van Thourhout, R. Baets, Low-power electro-optical switch based on a III–V microdisk cavity on a silicon-on-insulator circuit, in *Optoelectronic Materials and Devices IV*, Shanghai, China (2009), *Proc. SPIE* **7631**, 7631 0P (2009)
 104. A. Biberman, H.L.R. Lira, K. Padmaraju, N. Ophir, M. Lipson, K. Bergman, Broadband CMOS-compatible silicon photonic electro-optic switch for photonic networks-on-chip, in *Conf. Lasers Electro-Opt. (CLEO/QELS 2010)*, San Jose, CA, USA (2010), Techn. Digest, paper CPDA11
 105. J. van Campenhout, W.M. Green, S. Assefa, Y.A. Vlasov, Low-power, 2×2 silicon electro-optic switch with 110-nm bandwidth for broadband reconfigurable optical networks. *Opt. Express* **17**, 24020–24029 (2009)
 106. P. Dong, S. Liao, H. Liang, R. Shafiqi, D. Feng, G. Li, X. Zheng, A.V. Krishnamoorthy, M. Asghari, High-speed and broadband electro-optic silicon switch with submilliwatt switching power, in *Opt. Fiber Commun. and Nat. Fiber Opt. Eng. Conf. (OFC/NFOEC'11)*, Los Angeles, CA, USA (2011), Techn. Digest, paper OWZ4
 107. W.M.J. Green, M. Yang, S. Assefa, J.V. Campenhout, B.G. Lee, C.V. Jahnes, F.E. Doany, C.L. Schow, J.A. Kash, Y.A. Vlasov, Silicon electro-optic 4×4 non-blocking switch array for on-chip photonic networks, in *Opt. Fiber Commun. and Nat. Fiber Opt. Eng. Conf. (OFC/NFOEC'11)*, Los Angeles, CA, USA (2011), Techn. Digest, paper OTHM1
 108. J. Xing, P. Zhou, Y. Gong, Z. Li, M. Tan, Y. Yu, J. Yu, Nonblocking 4×4 silicon electro-optic switch matrix with low power consumption. *IEEE Photonics Technol. Lett.* **27**(13), 1434–1436 (2015)
 109. K. Okamoto, Planar lightwave circuits (PLC's), in *Photonic Networks*, ed. by G. Prati (Springer, London, 1997), pp. 118–132

110. A. Himeno, K. Kato, T. Miya, Silica-based planar lightwave circuits. *IEEE J. Sel. Top. Quantum Electron.* **4**(6), 913–924 (1998)
111. T. Goh, M. Yasu, K. Hattori, A. Himeno, M. Okuno, Y. Ohmori, Low loss and high extinction ratio strictly nonblocking 16×16 thermo-optic matrix switch on 6-in wafer using silica-based planar lightwave circuit technology. *J. Lightwave Technol.* **19**(3), 371–379 (2001)
112. T. Goh, A. Himeno, M. Okuno, H. Takahashi, K. Hattori, High-extinction ratio and low-loss silica-based 8×8 strictly nonblocking thermo-optic matrix switch. *J. Lightwave Technol.* **17**(7), 1192–1199 (1999)
113. T. Goh, A. Himeno, M. Okuno, H. Takahashi, K. Hattori, High extinction ratio and low loss silica-based 8×8 thermo-optic matrix switch. *IEEE Photonics Technol. Lett.* **10**, 358–360 (1998)
114. T. Goh, M. Yasu, K. Hattori, A. Himeno, Y. Ohmori, Low loss and high extinction ratio silica-based strictly nonblocking 16×16 thermo-optic matrix switch. *IEEE Photonics Technol. Lett.* **10**, 810–812 (1998)
115. T. Watanabe, T. Goh, M. Okuno, S. Sohma, T. Shibata, M. Itoh, M. Kobayashi, M. Ishii, A. Sugita, Y. Hibino, Silica-based PLC 1×128 thermo-optic switch, in *Proc. 27th Europ. Conf. Opt. Commun.* (ECOC'01), Amsterdam, The Netherlands (2001), pp. 134–135, paper Tu.L.1.2
116. M. Okuno, N. Takato, T. Kitoh, A. Sugita, Silica-based thermo-optic switches. *NTT Rev.* **7**, 57–63 (1995)
117. T. Nishi, T. Yamamoto, S. Kuroyanagi, A polarization-controlled free-space photonic switch based on a PI-LOSS switch. *IEEE Photonics Technol. Lett.* **5**, 1104–1106 (1993)
118. www.ntt-electronics.com/en/products/photronics/nxn_n_o_m_s.html
119. S. Sohma, T. Watanabe, N. Ooba, M. Itoh, T. Shibata, H. Takahashi, Silica-based PLC type 32×32 optical matrix switch, in *Proc. 32nd Europ. Conf. Opt. Commun.* (ECOC'06), Cannes, France (2006), paper OThV4
120. K. Watanabe, Y. Hashizume, Y. Nasu, M. Kohtoku, M. Itoh, Y. Inoue, Ultralow power consumption silica-based PLC-VOA/switches. *J. Lightwave Technol.* **26**(14), 2235–2244 (2008)
121. Enablence Inc, Technical specifications, www.enablence.com
122. L. Eldada, R. Gerhardt, J. Fujita, T. Izuhara, A. Radojevic, D. Pant, F. Wang, C. Xu, Intelligent optical cross-connect subsystem on a chip, in *Opt. Fiber Commun. Conf.* (OFC'05), Anaheim, CA, USA (2005), Techn. Digest, paper NTuL2. See also: Enablence technical white paper at www.enablence.com
123. E.L.W. Rabbering, J.F.P. van Nunen, L. Eldada, Polymeric 16×16 digital optical switch matrix, in *Proc. 27th Europ. Conf. Opt. Commun.* (ECOC'01), Amsterdam, The Netherlands (2001), paper PD.B.1.6
124. L. Eldada, R. Norwood, R. Blomquist, L.W. Shacklette, M.J. McFarland, Thermo-optically active polymeric photonic components, in *Opt. Fiber Commun. Conf.* (OFC'2000), Baltimore, MD, USA (2000), Techn. Digest, vol. 2, pp. 124–126
125. J. Fujita, T. Izuhara, A. Radojevic, R. Gerhard, L. Eldada, Ultrahigh index contrast planar polymeric strictly non-blocking 1024×1024 cross-connect switch matrix, in *Integr. Photon. Res.* (IPR), San Francisco, CA, USA (2004), Techn. Digest, paper IThC3
126. T. Tsuchizawa, K. Yamada, H. Fukuda, T. Watanabe, S. Uchiyama, S. Itabashi, Low-loss Si wire waveguides and their application to thermo-optic switches. *Jpn. J. Appl. Phys.* **45**(8B), 6658–6662 (2006)
127. K. Watanabe, R. Kasahara, Y. Hashizume, Extremely-low-power-consumption thermo-optic switch with silicon-silica hybrid structure. *NTT Tech. Rev.* **8**(2), 1–5 (2010)
128. K. Tanizawa, K. Suzuki, M. Toyama, M. Ohtsuka, N. Yokoyama, K. Matsumaro, M. Seki, K. Koshino, T. Sugaya, S. Suda, G. Cong, T. Kimura, K. Ikeda, S. Namiki, H. Kawashima, Ultra-compact 32×32 strictly-non-blocking Si wire optical switch with fan-out LGA interposer. *Opt. Express* **23**(13), 17599–17606 (2015)
129. K. Tanizawa, K. Suzuki, M. Toyama, M. Ohtsuka, N. Yokoyama, K. Matsumaro, M. Seki, K. Koshino, T. Sugaya, S. Suda, G. Cong, T. Kimura, K. Ikeda, S. Namiki, H. Kawashima, 32×32 strictly non-blocking Si-wire optical switch on ultra-small die of $11 \times 25 \text{ mm}^2$, in

- Opt. Fiber Commun. Conf. (OFC'15)*, Los Angeles, CA, USA (2015), Techn. Digest, paper M2B.5
130. S. Nakamura, S. Takahashi, M. Sakauchi, T. Hino, M. Yu, G. Lo, Wavelength selective switching with one-chip silicon photonic circuit including 8×8 matrix switch, in *Opt. Fiber Commun. Conf. and Nat. Fiber Opt. Eng. Conf. (OFC/NFOEC'11)*, Los Angeles, CA, USA (2011), Techn. Digest, paper OTuM2
 131. L. Chen, Y.K. Chen, Compact, low-loss and low-power 8×8 broadband silicon optical switch. *Opt. Express* **20**(17), 18977–18985 (2012)
 132. K. Suzuki, K. Tanizawa, T. Matsukawa, G. Cong, S.-H. Kim, S. Suda, M. Ohno, T. Chiba, H. Tadokoro, M. Yanagihara, Y. Igarashi, M. Masahara, S. Namiki, H. Kawashima, Ultra-compact 8×8 strictly-nonblocking Si-wire PILOSS switch. *Opt. Express* **22**(4), 3887–3894 (2014)
 133. K. Suzuki, G. Cong, K. Tanizawa, S.-H. Kim, K. Ikeda, S. Namiki, H. Kawashima, Ultra-high-extinction ratio 2×2 silicon optical switch with variable splitter. *Opt. Express* **23**, 9086–9092 (2015)
 134. C.R. Doerr, L.W. Stulz, D.S. Levy, M. Cappuzzo, E. Cben, L. Gomez, E. Laskowski, A. Wong-Foy, T. Murphy, Silica-waveguide 1×9 wavelength-selective cross connect, in *Opt. Fiber Commun. Conf. (OFC/IOOC'02)*, Anaheim, CA, USA (2002), Techn. Digest, PDP FA3
 135. T. Watanabe, K. Suzuki, T. Takahashi, Multicast switch technology that enhances ROADM operability. *NTT Tech. Rev.* **12**(1), 1–5 (2014)
 136. H. Takahashi, T. Watanabe, M. Okuno, Y. Hibino, T. Goh, Silica waveguide-based optical switches for photonic networks. *Techn. Rep. of IEICE* **103**(68), 1–6 (2003), CS2003-9 (in Japanese)
 137. T. Watanabe, K. Suzuki, T. Goh, K. Hattori, A. Mori, T. Takahashi, T. Sakamoto, K. Morita, S. Sohma, S. Kamei, Compact PLC-based transponder aggregator for colorless and directionless ROADM, in *Opt. Fiber Commun. and Nat. Fiber Opt. Eng. Conf. (OFC/NFOEC'11)*, Los Angeles, CA, USA (2011), Techn. Digest, paper OTuD3
 138. Neophotonics Inc., www.neophotonics.com/solutions/
 139. M.C. Wu, O. Solgaard, J.E. Ford, Optical MEMS for lightwave communication. *J. Lightwave Technol.* **24**, 4433–4454 (2006)
 140. L.Y. Lin, E.L. Goldstein, R.W. Tkach, Free-space micromachined optical switches for optical networking. *IEEE J. Sel. Top. Quantum Electron.* **5**(1), 4–9 (1999)
 141. S.S. Lee, L.Y. Lin, M.C. Wu, Surface-micromachined free-space fibre-optic switches. *Electron. Lett.* **31**, 1481–1482 (1995)
 142. R.S. Muller, K.Y. Lau, Surface-micromachined microoptical elements and systems. *Proc. IEEE* **86**, 1705–1720 (1998)
 143. W. Piyawattanametha, P.R. Patterson, D. Hah, H. Toshiyoshi, M.C. Wu, Surface- and bulk-micromachined two-dimensional scanner driven by angular vertical comb actuators. *J. Microelectromech. Syst.* **14**, 1329–1338 (2005)
 144. P.D. Dobbelaere, K. Falta, L. Fan, S. Gloeckner, S. Patra, Digital MEMS for optical switching. *IEEE Commun. Mag.* **40**(3), 88–95 (2002)
 145. H. Toshiyoshi, H. Fujita, Electrostatic micro torsion mirrors for an optical switch matrix. *J. Microelectromech. Syst.* **5**, 231–237 (1996)
 146. R.A. Miller, Y.C. Tai, G. Xu, J. Bartha, F. Lin, An electromagnetic MEMS 2×2 fiber optic bypass switch, in *Proc. Int. Conf. Solid-State Sensors and Actuators*, Chicago, IL, USA (1997), paper 1A4
 147. C. Marxer, N.F. de Rooij, Micro-opto-mechanical 2×2 switch for single-mode fibers based on plasma-etched silicon mirror and electrostatic actuation. *J. Lightwave Technol.* **17**(1), 2–6 (1999)
 148. R.T. Chen, H. Nguyen, M.C. Wu, A high-speed low-voltage stress induced micromachined 2×2 optical switch. *IEEE Photonics Technol. Lett.* **11**, 1396–1398 (1999)
 149. W. Noell, P.A. Clerc, F. Dupont, C. Marxer, N. de Rooij, Novel process-insensitive latchable 2×2 optical cross connector for single and multimode optical MEMS fiber switches,

- in *IEEE/LEOS Internat. Conf. Opt. MEMS*, Piscataway, NJ, USA (2003), Techn. Digest, pp. 49–50
150. L.Y. Lin, E.L. Goldstein, R.W. Tkach, Free-space micromachined optical switches with sub-millisecond switching time for large-scale optical crossconnects. *IEEE Photonics Technol. Lett.* **10**, 525–527 (1998)
 151. B. Behin, K.Y. Lau, R.S. Muller, Magnetically actuated micromirrors for fiber-optic switching, in *Solid-State Sensor and Actuator Workshop* Cleveland, OH, USA (1998), Techn. Digest, pp. 273–276
 152. R.L. Wood, R. Mahadevan, E. Hill, MEMS 2D matrix switch, in *Opt. Fiber Commun. Conf. (OFC/IOOC'02)*, Anaheim, CA, USA (2002), Techn. Digest, vol. 1, pp. 91–92
 153. L. Fan, S. Gloeckner, P.D. Dobbelaere, S. Patra, D. Reiley, C. King, T. Yeh, J. Gritters, S. Gutierrez, Y. Loke, M. Harburn, R. Chen, E. Kruglick, M. Wu, A. Husain, Digital MEMS switch for planar photonic crossconnects, in *Opt. Fiber Commun. Conf. (OFC/IOOC'02)*, Anaheim, CA, USA (2002), Techn. Digest, vol. 1, pp. 93–94
 154. P.M. Dobbelaere, S. Gloeckner, S.K. Patra, L. Fan, C. King, K. Falta, Design, manufacture and reliability of 2-D MEMS optical switches. *Proc. SPIE* **4945**, 39–45 (2003)
 155. J.-N. Kuo, G.-B. Lee, W.-F. Pan, A high-speed low-voltage double switch optical cross-connect using stress-induced bending micromirrors. *IEEE Photonics Technol. Lett.* **16**(9), 2042–2044 (2004)
 156. L.-Y. Lin, E.L. Goldstein, R.W. Tkach, On the expandability of free-space micromachined optical cross connects. *J. Lightwave Technol.* **18**, 482–489 (2000)
 157. M.C. Wu, P.R. Patterson, Free-space optical MEMS, in *MEMS: A Practical Guide to Design, Analysis, and Applications*, ed. by J.G. Korvink, O. Paul, (William Andrew, Norwich, 2005), pp. 345–402
 158. S. Han, T.J. Seok, N. Quack, B.-W. Yoo, M.C. Wu, Monolithic 50×50 MEMS silicon photonic switches with microsecond response time, in *Opt. Fiber Commun. Conf. (OFC'14)*, San Francisco, CA, USA (2014), Techn. Digest, paper M2K.2
 159. T.J. Seok, N. Quack, S. Han, M.C. Wu, 50×50 digital silicon photonic switches with MEMS-actuated adiabatic couplers, in *Opt. Fiber Commun. Conf. (OFC'15)*, Los Angeles, CA, USA (2015), Techn. Digest, paper M2B.4
 160. M.C. Wu, S. Han, T.J. Seok, N. Quack, Large-port-count MEMS silicon photonics switches, in *Opt. Fiber Commun. Conf. (OFC'15)*, Los Angeles, CA, USA (2015), Techn. Digest, paper M2B.3
 161. R. Helkey, S. Adams, J. Bowers, T. Davis, O. Jerphagnon, V. Kaman, A. Keating, B. Liu, C. Puserla, Y. Xu, S. Yuan, X. Zheng, Design of large scale, MEMS based photonic switches. *Opt. Photonics News* **13**, 40–43 (2002)
 162. D.J. Bishop, C.R. Giles, G.P. Austin, The lucent LambdaRouter: MEMS technology of the future here today. *IEEE Commun. Mag.* **40**(3), 75–79 (2002)
 163. V.A. Aksyuk, F. Pardo, D. Carr, D. Greywall, H.B. Chan, M.E. Simon, A. Gasparyan, H. Shea, V. Lifton, C. Bolle, S. Arney, R. Frahm, M. Paczkowski, M. Haeueis, R. Ryf, D.T. Neilson, J. Kim, C.R. Giles, D. Bishop, Beam-steering micromirrors for large optical crossconnects. *J. Lightwave Technol.* **21**, 634–642 (2003)
 164. D.T. Neilson, V.A. Aksyuk, S. Arney, N.R. Basavanahally, K.S. Bhalla, D.J. Bishop, B.A. Boie, C.A. Bolle, J.V. Gates, A.M. Gottlieb, J.P. Hickey, N.A. Jackman, P.R. Kolodner, S.K. Korotky, B. Mikkelsen, F. Pardo, G. Raybon, R. Ruel, R.E. Scotti, T.W. Van Blaricum, L. Zhang, C.R. Giles, Fully provisioned 112×112 micro-mechanical optical cross connect with 35.8 Tb/s demonstrated capacity, in *Opt. Fiber Commun. Conf. (OFC'2000)*, Baltimore, MD, USA (2000), Techn. Digest, vol. 4, pp. 202–204
 165. A. Fernandez, B.P. Staker, W.E. Owens, L.P. Muray, J.P. Spallas, W.C. Banyai, Modular MEMS design and fabrication for an 80×80 transparent optical cross-connect switch. *Proc. SPIE* **5604**, 208–217 (2004)
 166. Z.J. Yao, N.C. MacDonald, Single crystal silicon supported thin film micromirrors for optical applications. *Opt. Eng.* **36**(5), 1408–1413 (1997)

167. R.A. Conant, J.T. Nee, K.Y. Lau, R.S. Muller, A flat high frequency scanning micromirror, in *Solid-State Sensor and Actuator Workshop*, Cleveland, OH, USA (2000), Techn. Digest, pp. 6–9
168. J.-L.A. Yeh, J. Hongrui, N.C. Tien, Integrated polysilicon and DRIE bulk silicon micro-machining for an electrostatic torsional actuator. *J. Microelectromech. Syst.* **8**(4), 456–465 (1999)
169. D.S. Greywall, C.-S. Pai, S.-H. Oh, C.-P. Chang, D.M. Marom, P.A. Busch, R.A. Cirelli, J.A. Taylor, F.P. Klemens, T.W. Sorsch, J.E. Bowers, W.-C. Lai, H.T. Soh, Monolithic fringe field-activated crystalline silicon tilting-mirror devices. *J. Microelectromech. Syst.* **12**(5), 702–707 (2003)
170. D.S. Greywall, P.A. Busch, F. Pardo, D.W. Carr, G. Bogart, H.T. Soh, Crystalline silicon tilting mirrors for optical cross-connect switches. *J. Microelectromech. Syst.* **12**, 708–712 (2003)
171. O. Tsuboi, Y. Mizuno, N. Kouma, H. Soneda, H. Okuda, S. Ueda, I. Sawaki, F. Yamagishi, Y. Nakamura, A 2-axis comb-driven micromirror array for 3-D MEMS optical switch. *Trans. Inst. Electron. Eng. Jpn.* **123-E**, 398–402 (2003)
172. J. Kim, D. Christensen, L. Lin, Monolithic 2-D scanning mirror using self-aligned angular vertical comb drives. *IEEE Photonics Technol. Lett.* **17**(11), 2307–2309 (2005)
173. D. Hah, H.S.-Y. Huang, J.-C. Tsai, J.-C. Toshiyoshi, M.C. Wu, Low-voltage, large-scan angle MEMS analog micromirror arrays with hidden vertical comb-drive actuators. *J. Microelectromech. Syst.* **13**, 279–289 (2004)
174. N. Kouma, O. Tsuboi, Y. Mizuno, H. Okuda, X. Mi, M. Iwaki, H. Soneda, S. Ueda, I. Sawaki, A multi-step DRIE process for a 128×128 micromirror array, in *IEEE/LEOS Internat. Conf. Opt. MEMS*, Piscataway, NJ, USA (2003), Techn. Digest, pp. 53–54
175. X. Zheng, V. Kaman, S. Yuan, Y. Xu, O. Jerphagnon, A. Keating, R.C. Anderson, H.N. Poulsen, B. Liu, J.R. Schemit, C. Pusarla, R. Helkey, D.J. Blumenthal, J.E. Bowers, Three-dimensional MEMS photonic cross-connect switch design and performance. *IEEE J. Sel. Top. Quantum Electron.* **9**, 571–578 (2003)
176. J.E. Bowers, Low power 3D MEMS optical switches, in *IEEE/LEOS Internat. Conf. Opt. MEMS Nanophoton.* (OPT MEMS), Clearwater, FL, USA (2009), Techn. Digest, paper ThB1
177. S. Yuan, C. Lee, Scaling optical switches to 100 Tb/s capacity, in *Integr. Photon. Res., Silicon Nanophoton. Photonics in Switching*, Monterey, CA, USA (2010), OSA Techn. Digest, paper PWB3
178. www.glimmerglass.com
179. L. Erdmann, D. Efferenn, Technique for monolithic fabrication of silicon microlenses with selectable rim angles. *Opt. Eng.* **36**(4), 1094–1098 (1997)
180. J. Kim, A.R. Papanian, R.E. Frahm, J.V. Gates, Performance of large scale MEMS-based optical crossconnect switches, in *15th Ann. Meeting IEEE Lasers & Electro-Optics Soc.* (IEEE/LEOS), Glasgow, Scotland, UK (2002), Techn. Digest, vol. 2, pp. 411–412
181. R. Ryf, J. Kim, J.P. Hickey, A. Gnauck, D. Carr, F. Pardo, C. Bolle, R. Frahm, N. Basavanhally, C. Yoh, D. Ramsey, R. Boie, R. George, J. Kraus, C. Lichtenwalner, R. Papazian, J. Gates, H.R. Shea, A. Gasparyan, V. Muratov, J.E. Griffith, J.A. Prybyla, S. Goyal, C.D. White, M.T. Lin, R. Ruel, C. Nijander, S. Arney, D.T. Neilson, D.J. Bishop, P. Kolodner, S. Pau, C.J. Nuzman, A. Weis, B. Kumar, D. Lieuwen, V. Aksyuk, D.S. Greywall, T.C. Lee, H.T. Soh, W.M. Mansfield, S. Jin, W.Y. Lai, H.A. Huggins, D.L. Barr, R.A. Cirelli, G.R. Bogart, K. Teffeau, R. Vella, H. Mavoori, A. Ramirez, N.A. Ciampa, F.P. Klemens, M.D. Morris, T. Boone, J.Q. Liu, J.M. Rosamilia, C.R. Giles, 1296-port MEMS transparent optical crossconnect with 2.07 petabit/s switch capacity, in *Opt. Fiber Commun. Conf. (OFC'01)*, Anaheim, CA, USA (2001), Techn. Digest, paper PD28-1-3
182. M. Kozhevnikov, N.R. Basavanhally, J.D. Weld, Y.L. Low, P.R. Kolodner, C.A. Bolle, R. Ryf, A.R. Papazian, A. Olkhovets, J. Kim, D.T. Neilson, V.A. Aksyuk, J.V. Gates, Compact 64×64 micromechanical optical cross-connect. *IEEE Photonics Technol. Lett.* **15**(7), 993–995 (2003)

183. A. Olkhovets, P. Phanaphat, C. Nuzman, D.J. Shin, C. Lichtenwalner, M. Kozhevnikov, J. Kim, Performance of an optical switch based on 3-D MEMS crossconnect. *IEEE Photonics Technol. Lett.* **16**(3), 780–782 (2004)
184. V.A. Aksyuk, S. Arney, N.R. Basavanhally, D.J. Bishop, C.A. Bolle, C.C. Chang, R. Frahm, A. Gasparyan, J.V. Gates, R. George, C.R. Giles, J. Kim, P.R. Kolodner, T.M. Lee, D.T. Neilson, C. Nijander, C.J. Nuzman, M. Paczkowski, A.R. Papazian, F. Pardo, D.A. Ramsey, R. Ryf, R.E. Scotti, H. Shea, M.E. Simon, 238×238 micromechanical optical cross connect. *IEEE Photonics Technol. Lett.* **15**, 587–589 (2003)
185. D.T. Neilson, R. Frahm, P. Kolodner, C.A. Bolle, R. Ryf, J. Kim, A.R. Papazian, C.J. Nuzman, A. Gasparyan, N.R. Basavanhally, V.A. Aksyuk, J.V. Gates, 256×256 port optical crossconnect subsystem. *J. Lightwave Technol.* **22**, 1499–1509 (2004)
186. J. Kim, C.J. Nuzman, B. Kumar, D.F. Lieuwen, J.S. Kraus, A. Weiss, C.P. Lichtenwalner, A.R. Papazian, R.E. Frahm, N.R. Basavanhally, D.A. Ramsey, V.A. Aksyuk, F. Pardo, M.E. Simon, V. Lifton, H.B. Chan, M. Haueis, A. Gasparyan, H.R. Shea, S. Arney, C.A. Bolle, P.R. Kolodner, R. Ryf, D.T. Neilson, J.V. Gates, 1100×1100 port MEMS-based optical crossconnect with 4-dB maximum loss. *IEEE Photonics Technol. Lett.* **15**(11), 1537–1539 (2003)
187. M. Kozhevnikov, R. Ryf, D.T. Neilson, P. Kolodner, C.A. Bolle, A.R. Papazian, J. Kim, J.V. Gates, Micromechanical optical crossconnect with 4-F relay imaging optics. *IEEE Photonics Technol. Lett.* **16**(1), 275–277 (2004)
188. Y. Mizuno, O. Tsuboi, N. Kouma, H. Soneda, H. Okuda, Y. Nakamura, S. Ueda, I. Sawaki, F. Yamagishi, A 2-axis comb-driven micromirror array for 3D MEMS switches, in *IEEE/LEOS Internat. Conf. Opt. MEMS*, Lugano, Switzerland (2002), Techn. Digest, pp. 17–18
189. M. Yano, F. Yamagishi, T. Tsuda, Optical MEMS for photonic switching—compact and stable optical crossconnect switches for simple, fast, and flexible wavelength applications in recent photonic networks. *IEEE J. Sel. Top. Quantum Electron.* **11**(2), 383–394 (2005)
190. R. Sawada, J. Yamaguchi, E. Higurashi, A. Shimizu, T. Yamamoto, N. Takeuchi, Y. Uenishi, Single Si crystal 1024-ch MEMS mirror based on terraced electrodes and a high-aspect ratio torsion spring for 3-D cross-connect switch, in *Ann. Meeting IEEE Lasers & Electro-Optics Soc. (LEOS)*, Piscataway, NJ, USA (2003), Digest Int. Conf. Opt. MEMS, pp. 11–12
191. T. Yamamoto, J. Yamaguchi, N. Takeuchi, A. Shimizu, E. Higurashi, R. Sawada, Y. Uenishi, A three-dimensional MEMS optical switching module having 100 input and 100 output ports. *IEEE Photonics Technol. Lett.* **15**, 1360–1362 (2003)
192. J. Yamaguchi, T. Sakata, N. Shimoyama, H. Ishii, F. Shimokawa, T. Yamamoto, High-yield fabrication methods for MEMS tilt mirror array for optical switch. *NTT Tech. Rev.* **5**(10), 1–6 (2007)
193. M. Mizukami, J. Yamaguchi, N. Nemoto, Y. Kawajiri, H. Hirata, S. Uchiyama, M. Makihara, T. Sakata, N. Shimoyama, H. Ishii, F. Shimokawa, 128×128 3D-MEMS optical switch module with simultaneous optical paths connection for optical cross-connect systems, in *Proc. Photon. Switching*, Pisa, Italy (2009), pp. 247–248
194. Y. Kawajiri, N. Nemoto, K. Hadama, Y. Ishii, M. Makihara, J. Yamaguchi, T. Yamamoto, 512×512 port 3D MEMS optical switch module with toroidal concave mirror. *NTT Tech. Rev.* **10**(11), 1–6 (2012)
195. E. Korevaar, Y. Taketomi, T. Barrott, H. Tigli, M. Last, L. Dirvscio, E. Davis, Optical switch module. US Patent No. 7,734,127 (2007)
196. J.I. Dadap, P.B. Chu, I. Brener, C. Pu, C.D. Lee, K. Bergman, N. Bonadeo, T. Chau, M. Chou, R. Doran, R. Gibson, R. Harel, J.J. Johnson, S.S. Lee, S. Park, D.R. Peale, R. Rodriguez, D. Tong, M. Tsai, C. Wu, W. Zhong, E.L. Goldstein, L.Y. Lin, J.A. Walker, Modular MEMS-based optical cross-connect with large port-count optical switch. *IEEE Photonics Technol. Lett.* **15**, 1773–1775 (2003)
197. P.M. Hagelin, U. Krishnamoorthy, J.P. Heritage, O. Solgaard, Scalable optical cross-connect switch using micromachined mirrors. *IEEE Photonics Technol. Lett.* **12**, 882–884 (2000)
198. R.R.A. Syms, Scaling laws for MEMS mirror-rotation optical cross connect switches. *J. Lightwave Technol.* **20**, 1084–1094 (2002)

199. W.M. Mellette, J.E. Ford, Scaling limits of MEMS beam-steering switches for data center networks. *J. Lightwave Technol.* **33**(15), 3308–3318 (2015)
200. J.E. Ford, J.A. Walker, Dynamic spectral power equalization using micro-opto-mechanics. *IEEE Photonics Technol. Lett.* **10**, 1440–1442 (1998)
201. H. Venghaus, A. Gladisch, B.F. Joergensen, J.-M. Jouanno, M. Kristensen, R.J. Pedersen, F. Testa, D. Trommer, J.P. Weber, Optical add/drop multiplexers for WDM communication systems, in *Opt. Fiber Commun. Conf. (OFC'97)*, Dallas, TX, USA (1997), Techn. Digest, vol. 4, pp. 280–281
202. J.E. Ford, V.A. Aksyuk, D.J. Bishop, J.A. Walker, Wavelength add-drop switching using tilting micromirrors. *J. Lightwave Technol.* **17**(5), 904–911 (1999)
203. R. Ryf, Y. Su, L. Möller, S. Chandrasekhar, X. Liu, D.T. Neilson, C.R. Giles, Wavelength blocking filter with flexible data rates and channel spacing. *J. Lightwave Technol.* **23**, 54–60 (2005)
204. D.T. Neilson, H. Tang, D.S. Greywall, N.R. Basavanhally, L. Ko, D.A. Ramsey, J.D. Weld, Y.L. Low, F. Pardo, D.O. Lopez, P. Busch, J. Prybyla, M. Haueis, C.S. Pai, R. Scotti, R. Ryf, Channel equalization and blocking filter utilizing micro electro mechanical mirrors. *IEEE J. Sel. Top. Quantum Electron.* **10**, 563–569 (2004)
205. N.A. Riza, M.J. Mughal, Broadband optical equalizer using fault-tolerant digital micromirrors. *Opt. Express* **11**, 1559–1565 (2003)
206. D.M. Marom, D.T. Neilson, D.S. Greywall, C.-S. Pai, N.R. Basavanhally, V.A. Aksyuk, D.O. López, F. Pardo, M.E. Simon, Y. Low, P. Kolodner, C.A. Bolle, Wavelength-selective $1 \times K$ switches using free-space optics and MEMS micromirrors: theory, design, and implementation. *J. Lightwave Technol.* **23**, 1620–1629 (2005)
207. D.M. Marom, D.T. Neilson, D.S. Greywall, N.R. Basavanhally, P.R. Kolodner, Y.L. Low, C.A. Bolle, S. Chandrasekhar, L. Buhl, S.-H. Oh, C.-S. Pai, K. Werder, H.T. Soh, G.R. Bognart, E. Ferry, F.P. Klemens, K. Teffeau, J.F. Miner, S. Rogers, J.E. Bowers, R.C. Keller, W. Mansfield, Wavelength selective 1×4 switch for 128 WDM channels at 50 GHz spacing, in *Opt. Fiber Commun. (OFC/IOOC'02)*, Anaheim, CA, USA (2002), Techn. Digest, pp. 857–859
208. J. Tsai, S.T.-Y. Huang, D. Hah, M.C. Wu, $1 \times N^2$ wavelength selective switch with two cross-scanning one-axis analog micromirror arrays in a 4-f optical system. *J. Lightwave Technol.* **24**(2), 897–903 (2006)
209. J. Tsai, S. Huang, D. Hah, H. Toshiyoshi, M.C. Wu, Open-loop operation of MEMS-based $1 \times N$ wavelength-selective switch with long-term stability and repeatability. *IEEE Photonics Technol. Lett.* **16**, 1041–1043 (2004)
210. J. Tsai, M.C. Wu, A high port-count wavelength-selective switch using a large scan-angle, high fill-factor, two-axis MEMS scanner array. *IEEE Photonics Technol. Lett.* **18**(13), 1439–1441 (2006)
211. J.-C. Tsai, L. Fan, C.-H. Chi, D. Hah, M.C. Wu, A large port-count 1×32 wavelength-selective switch using a large scan-angle, high fill factor, two-axis analog micromirror array, in *Proc. 30th Europ. Conf. Opt. Commun. (ECOC'04)*, Stockholm, Sweden (2004), vol. 2, pp. 152–153
212. www.lumentum.com/en/products/1x9-100-ghz-wss-mini
213. Y. Ishii, K. Hadama, J. Yamaguchi, Y. Kawajiri, E. Hashimoto, T. Matsuura, F. Shimokawa, MEMS-based 1×43 wavelength-selective switch with flat passband, in *Proc. 35th Europ. Conf. Opt. Commun. (ECOC'09)*, Vienna, Austria (2009), PDP, session 1
214. W.P. Taylor, J.D. Brazzle, A.B. Osenar, C.J. Corcoran, I.H. Jafri, D. Keating, G. Kirkos, M. Lockwood, A. Pareek, J.J. Bernstein, A high fill factor linear mirror array for a wavelength selective switch. *J. Micromech. Microeng.* **14**, 147–152 (2004)
215. D.T. Fuchs, C.R. Doerr, V.A. Aksyuk, M.E. Simon, L.W. Stulz, S. Chandrasekhar, L.L. Buhl, M. Cappuzzo, L. Gomez, A. Wong-Foy, E. Laskowski, E. Chen, R. Pafchek, A hybrid MEMS-waveguide wavelength selective cross connect. *IEEE Photonics Technol. Lett.* **16**, 99–101 (2004)

216. R. Ryf, P. Bernasconi, P. Kolodner, J. Kim, J.P. Hickey, D. Carr, F. Pardo, C. Bolle, R. Frahm, N. Basavanthally, C. Yoh, D. Ramsey, R. George, J. Kraus, C. Lichtenwalner, R. Papazian, J. Gates, H.R. Shea, A. Gasparyan, V. Muratov, J.E. Griffith, J.A. Prybyla, S. Goyal, C.D. White, M.T. Lin, R. Ruel, C. Nijander, S. Arney, D.T. Neilson, D.J. Bishop, S. Pau, C. Nuzman, A. Weis, B. Kumar, D. Lieuwen, V. Aksyuk, D.S. Greywall, T.C. Lee, H.T. Soh, W.M. Mansfield, S. Jin, W.Y. Lai, H.A. Huggins, D.L. Barr, R.A. Cirelli, G.R. Bogart, K. Teffeau, R. Vella, H. Mavoori, A. Ramirez, N.A. Ciampa, F.P. Klemens, M.D. Morris, T. Boone, J.Q. Liu, J.M. Rosamilia, C.R. Giles, Scalable wavelength-selective crossconnect switch based on MEMS and planar waveguides, in *Proc. 27th Europ. Conf. Opt. Commun. (ECOC'01)*, Amsterdam, The Netherlands (2001), vol. 6, PDP, pp. 76–77
217. S. Yuan, N. Madamopoulos, R. Helkey, V. Kaman, J. Klingshirn, J. Bowers, Fully integrated $N \times N$ MEMS wavelength selective switch with 100% colorless add-drop ports, in *Opt. Fiber Commun. and Nat. Fiber Opt. Eng. Conf. (OFC/NFOEC'08)*, San Diego, CA, USA (2008), Techn. Digest, paper OWC2
218. K. Sorimoto, H. Uetsuka, M. Tachikura, H. Kawashima, M. Mori, T. Hasama, H. Ishikawa, N.A. Idris, H. Tsuda, Compact 5×5 wavelength-selective cross connect using integrated 2-D MEMS mirror arrays, in *18th Microopt. Conf. (MOC'13)*, Tokyo, Japan (2013), Techn. Digest, pp. 55–57
219. C.-H. Chi, J.-C. Tsai, D. Hah, S. Mathai, M.-C.M. Lee, M.C. Wu, Silicon-based monolithic 4×4 wavelength-selective cross connect with on-chip micromirrors, in *Opt. Fiber Commun. and Nat. Fiber Opt. Eng. Conf. (OFC/NFOEC'06)*, San Francisco, CA, USA (2014), Techn. Digest, paper OTuF
220. V. Kaman, X. Zheng, S. Yuan, J. Klingshirn, C. Pusarla, R.J. Helkey, O. Jerphagnon, J.E. Bowers, A 32×10 Gb/s DWDM metropolitan network demonstration using wavelength-selective photonic crossconnects and narrow-band EDFAs. *IEEE Photonics Technol. Lett.* **17**, 1977–1979 (2005)
221. www.polatis.com
222. A.N. Dames, J.H. James, Optical fiber switching assembly. US patent No. US 7,106,925 B2 (2006)
223. A.N. Dames, Piezo-electric actuator, US Patent No. US 7,026,745 B2 (2006)
224. A.N. Dames, Beam steering arrangement and optical switches. US Patent No. US 7,095,915 (2006)

Shifu Yuan received the B.S. degree in Applied Physics, M.S., and Ph.D. degrees in Optics, all from the Harbin Institute of Technology, Harbin, China in 1988, 1991, and 1994, respectively. In 1994, he joined the Department of Precision Instruments, Tsinghua University, Beijing China, as a post-doctoral research associate and then an Associate Professor, where he had been engaged in the research and development of photonic information processing and optical image processing and recognition. From 1996 to 1998, he was a post-doctoral research associate with CREOL/School of Optics, University of Central Florida, where he was engaged in the research and development of liquid crystal based optical switch, fiber optics and photonic delay line. In 1998, He joined Chorum Technologies, Richardson, TX, working on liquid crystal based optical switches and birefringent crystal based optical interleavers. In 1999, he joined Corning Inc, Corning, New York, where he had been involved in the research and development of optical networking architectures and applications of wavelength selective switch. In 2000, he joined CALIENT Technologies as a Sr. Optical Engineer and since 2010, he has been the Chief Technology Officer of Optical Technologies at CALIENT. He had been leading the technical team at CALIENT in development of large scale 3-D MEMS optical switches and bringing the largest port count optical switch from design to high volume production.

John E. Bowers holds the Fred Kavli Chair in Nanotechnology, and is the Director of the Institute for Energy Efficiency and a Professor in the Departments of Materials and Electrical and Computer Engineering at UCSB. He is a cofounder of Aurrion, Aerius Photonics and Calient Networks. Dr.

Bowers received his M.S. and Ph.D. degrees from Stanford University and worked for AT&T Bell Laboratories and Honeywell before joining UC Santa Barbara. Dr. Bowers is a member of the National Academy of Engineering, a fellow of the IEEE, OSA and the American Physical Society, and a recipient of the OSA Tyndal Award, the OSA Holonyak Prize, the IEEE LEOS William Streifer Award and the South Coast Business and Technology Entrepreneur of the Year Award. He has published eight book chapters, 600 journal papers, 900 conference papers and has received 54 patents. He and coworkers received the EE Times Annual Creativity in Electronics (ACE) Award for Most Promising Technology for the hybrid silicon laser in 2007.

Chapter 11

Passive Devices

Wolfgang Coenning and François Caloz

Abstract The chapter presents devices which ensure the following generic functionalities: (i) physically connecting devices, (ii) splitting and coupling of light, (iii) separating and redirecting light travelling into opposite directions (optical circulators), and (iv) isolating light travelling into one direction from light travelling into the reverse direction (optical isolators). The coverage includes theoretical aspects, standardisation issues, and typical characteristics of fibres and fibre-optic cables. The treatment of optical circulators and isolators includes their fundamental principles, polarisation-independent 3D (free space) implementations, and planar integrated waveguide-based solutions as well.

Fibre optic networks have experienced tremendous growth during the last few years, starting with backbone or long haul networks over Metro nets and having reached to the residential area more recently. The enabling components for this development include lasers, modulators, detectors for example, but passive devices as well and the latter will be the topic of this chapter. The most relevant functionalities of passive devices are (i) physically connecting devices, (ii) splitting and coupling, but also (iii) separating and redirecting light travelling into opposite directions (optical circulators), and (iv) isolating light travelling into one direction from that travelling into the reverse direction (optical isolators), and corresponding solutions will be covered in the subsequent paragraphs.

W. Coenning (✉)
Hochschule Esslingen, Flandernstraße 101, 3732 Esslingen, Germany
e-mail: wolfgang.coenning@hs-esslingen.de

F. Caloz
Diamond SA, via dei Patrizi 5, 6616 Losone, Switzerland
e-mail: francois.caloz@diamond-fo.com

11.1 Optical Connectors

11.1.1 Introduction

The optical fibre connecting devices most widely used are splices and connectors. Splices are permanent connections; they may be fusion splices, where the two fibres are fused together or mechanical splices, where the fibres are mechanically positioned in a semi-permanent way. Optical connectors are passive optical components designed to connect two or more optical fibres in a non permanent way that may be easily detached and reconnected several times.

Requirements on optical connectors are increasing steadily in parallel with the improvement of fibre optic technologies. Main technical requirements are low insertion loss, low return loss, stable performance with respect to temperature and during mechanical stress as well as after disconnecting and re-establishing the connection. In addition, connectors have to be reliable, safe and easy to use, and small. They should offer dust protection and protection against wrong handling, and last but not least, the price of optical connectors should be low since that may have a significant influence on the overall price of the system as large quantities of connectors are used in modern fibre optic networks.

11.1.2 Connecting Different Types of Fibres

The main challenge for optical connectors' manufacturers is related to the dimension of the optical fibre and its core since the role of an optical connection is to align the cores of the fibres to be connected. Dimensions of fibre cores range from a few micrometres up to hundreds of micrometres, and as a consequence the requirements on precision of the mechanical alignment range from a few tens of nanometres to tens of micrometres, depending on the fibre type.

Since most of the applications covered by this book are based on single-mode (SM) optical fibre designed to be operated in the wavelength range between 1200 nm and 1650 nm, we will primarily concentrate on this type of fibre in this chapter. Examples of connector applications using other types of fibres are discussed in Sect. 11.1.9.

Fibres to be connected have to be aligned properly but a number of alignment errors may negatively affect the performance of the optical connection, and Fig. 11.1 illustrates the most relevant alignment errors: An air gap, fibre core offset and angular misalignment are extrinsic parameters and may be corrected by using the right positioning technology. Mode field diameter mismatch is due to fabrication tolerances of optical fibres, this parameter is intrinsic and can not be corrected by aligning the fibres.

The two key performance parameters that characterise any optical connection are attenuation and return loss. Both place different physical demands on the positioning of the optical fibre in the optical connection interface.

Fig. 11.1 Main alignment errors affecting performances of fibre optical connections

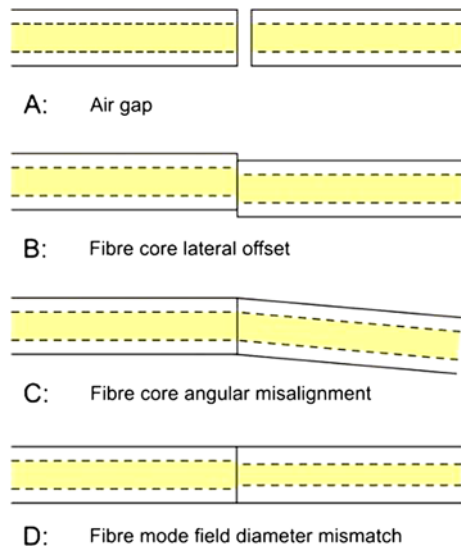
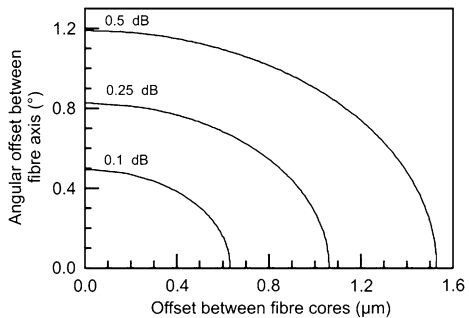


Fig. 11.2 Lines of equal attenuation of two coupled standard single-mode fibres as a function of lateral and angular offset for 1310 nm operation wavelength



Return loss is primarily affected by end face separation, lateral offset and angular misalignment. Figure 11.2 illustrates the dependence of the coupling loss on lateral and angular offset of two standard non-dispersion shifted single-mode fibres operated at 1310 nm. The curves are obtained under the assumption that both, input and output fibres, are in physical contact (no air gap between the fibres).

The most significant parameters affecting return loss are end face separation, end face high index layer conditions (high index layer thickness and index of refraction) and end face condition.

Environmental conditions may also affect the characteristics of the optical interface, and as a consequence connectors are specified for working under different physical and mechanical conditions including device classes which assure that specified performance is guaranteed even under extreme environmental conditions (see Sect. 11.1.4).

11.1.3 Basics of FO-Connectors

Since fibre dimensions are small (125 μm diameter in the case of standard telecom fibre), they are difficult to handle, process, polish and align. The most common way of solving these difficulties is to fix the fibre in an object of larger dimensions (ferrule) prior to proceed to any further handling of the fibre.

Ferrules are high precision tubes with outer diameter controlled with sub-micron precision and a hole in the centre which has a diameter of the optical fibre cladding, and they are available for one single fibre only or up to 72 fibres being handled. In this chapter, we will mainly focus on single fibre connectors.

So far three different types of ferrules are standardised:

- Mono-bloc ferrules, that are one material (ceramics) ferrules, usually referred to as full zirconium ferrule (IEC 61755-3-1/IEC 61755-3-2)
- Multi-material ferrules, which are composed by an outer ceramic tube with a Cu/Ni metallic insert in the centre. These ferrules are referred to as composite ferrules (IEC 61755-3-5/IEC 61755-3-6)
- Multi-material ferrules, which are composed by an outer ceramic tube with a titanium metallic insert in the centre. These ferrules are referred to as composite ferrules (IEC 61755-3-7/IEC 61755-3-8)

Single fibre connectors usually rely on cylindrical ferrules with diameters ranging from 1.25 mm up to 3.2 mm (the most frequently used ferrule diameters are 2.5 and 1.25 mm). The fibre is fixed in the ferrule hole, and the end faces of the ferrules are then polished in order to enable physical contact between the two fibres to be connected. Two ferrules are then brought into contact through a precision sleeve which has the role of guiding them one in front of the other, as illustrated in Fig. 11.3. The other reference surface for the alignment is the outer diameter of the ferrule. Therefore, if the fibre cores are positioned exactly in the centre of the ferrules, aligning the two ferrules' outer diameters will perfectly align the two fibre cores.

The ferrule is then assembled into a connector body which has the function of guiding the ferrules' axial positions as well as to orientate them, in order to bring them into the right position and to guarantee the necessary compression force. Most of the optical connections have a plug-adapter-plug design, where the spring-loaded ferrules are assembled in the plug-part (also called "connector"), whereas the alignment sleeve is contained in the adapter.

Polishing of the ferrule end face may be straight or angled, depending on the optical performance requirement and particularly the return loss.

Fig. 11.3 Simplified (schematic) scheme of an optical connection

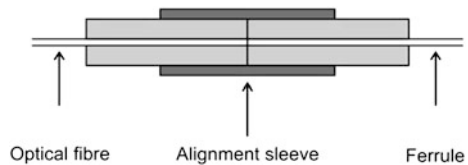


Table 11.1 Examples of performance categories (IEC 61753 standard series)

Category	Environment	Operating conditions
C	Indoor controlled	Operating temperature: $-10\text{ °C} \leq T \leq +60\text{ °C}$ Relative humidity: 5%–93%
U or O	Outdoor uncontrolled	Operating temperature: $-40\text{ °C} \leq T \leq +75\text{ °C}$ Relative humidity: 0%–100%
I	Industrial	Operating temperature $-40\text{ °C} \leq T \leq +70\text{ °C}$ Relative humidity 0%–95%
E	Extreme	Proposal: $-45\text{ °C} \leq T \leq +85\text{ °C}$

11.1.4 Relevant Standards for Optical Connectors

Different standard series have been developed by international standardisation bodies (IEC, CENELEC, TIA, . . .) to specify optical connectors, in particular their optical and mechanical characteristics as well as performance, reliability and test and measurement procedures in order to determine these quantities. The main purpose of these standards is to ensure that products conforming to the standard will work together repeatedly to a known level of optical performance without the need for compatibility testing or cross checking, and this has to be true for the combination of any products from any manufacturer.

The optical interface standard (IEC 61753-series) defines the location of the fibre core in relation to the datum target and the following key parameters: lateral offset, end face separation, end face angle, end face high index layer condition. If these requirements are met, (in particular) attenuation and return loss performance in a randomly mated pair of fibres of the same type will be within the appropriate specifications.

Performance standards (IEC 61753-series) describe different service environments in which connectors may be used as illustrated in Table 11.1. Connectors are generally designed for operation in specific categories, and materials may also be suitable for specific categories only. For example, zirconium ferrule material is suited for all environmental categories, while the polymer material specified for some rectangular ferrules may only be applicable for controlled indoor environment.

The categories given in Table 11.1 are related to the following typical environments:

- C: Office, equipment room, telecommunication centre or building, not subjected to condensed water.
- U or O: Outdoors but enclosed or covered. Locations: shacks, lofts, telephone booths, street cabinets, garages, cellars, building entrances and unattended equipment stations. Subject to condensed water and limited wind driven precipitation, in close proximity of sand or dust.
- I: Automation islands.
- E: Outside plants with direct exposure of components to the environment.

Finally, there exist reliability and test standards similar to the ones for other OEICs as well and these will not be described in more detail here.

Table 11.2 Attenuation grades for single-mode fibre optical connectors (IEC 61755-1)

Attenuation Grade	Attenuation ($\geq 97\%$) ^a	Average	Note
A	–	–	Reserved for future applications
B	≤ 0.25 dB	≤ 0.12 dB	
C	≤ 0.5 dB	≤ 0.25 dB	
D	≤ 1 dB	≤ 0.5 dB	

^a The probability of a random mated connector set of meeting or exceeding the specified level of attenuation will be $\geq 97\%$. This performance is reached considering a statistical distribution of connectors' parameters (MFD, eccentricity and tilt angle) and using a nominal value for the wavelength

11.1.5 Optical Requirements for Single-Mode FO-Connectors

11.1.5.1 Insertion Loss and Alignment Requirements

Connectors fall into different attenuation grade categories as illustrated in Table 11.2 and applicable to any pair of randomly mated connectors. For example, any grade B connector mated with any other grade B connector will have an insertion loss smaller than 0.25 dB with a probability of better than 97%.

The achievable insertion loss (attenuation) for fibre optic connectors is directly related to the precision of the alignment of the two connecting fibres.

Ferrule hole concentricity and diameter, fibre cladding diameter and fibre core concentricity are the main contributions to the eccentricity of the fibre core position relative to the centre of the ferrule. The sum of all these tolerances usually leads to overall values for fibre eccentricity in the order of typically 1 to 2 μm . However, dedicated composite ferrule technology allows centring of the fibre core by deformation of a metallic insert in such a way that the residual fibre core eccentricity is lower than 0.1 μm and therefore high performance, low loss connectors become possible (see [1]).

Figure 11.4 displays a ferrule with an eccentric connector core, and a solution, which enables to experimentally determine the eccentricity, is illustrated in Fig. 11.5.

During the measurement the fibre core is illuminated and the ferrule is rotated in a precision sleeve in front of a microscope and a CCD camera. The fibre core concentricity is defined as the diameter of the circular trajectory of the fibre core image. The position of the fibre core is then corrected using a special crimping tool. Using this technology, Diamond was able to develop a low loss connector class that was named "0.1 dB", allowing reaching random attenuation values smaller than 0.1 dB [1].

11.1.5.2 Return Loss and End Face Geometry Requirements for Contacting Fibres

In order to achieve stable optical connection, physical contact between the input and output fibres is needed. Lack of optical contact would result in high and instable

Fig. 11.4 Sketch of a ferrule with off-centred fibre, in comparison with an ideally perfect “reference connector”

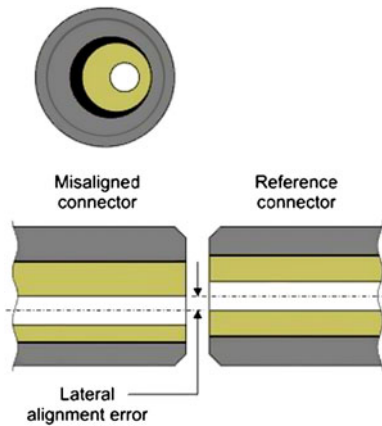


Fig. 11.5 Schematic sketch of a ferrule concentricity measurement instrument

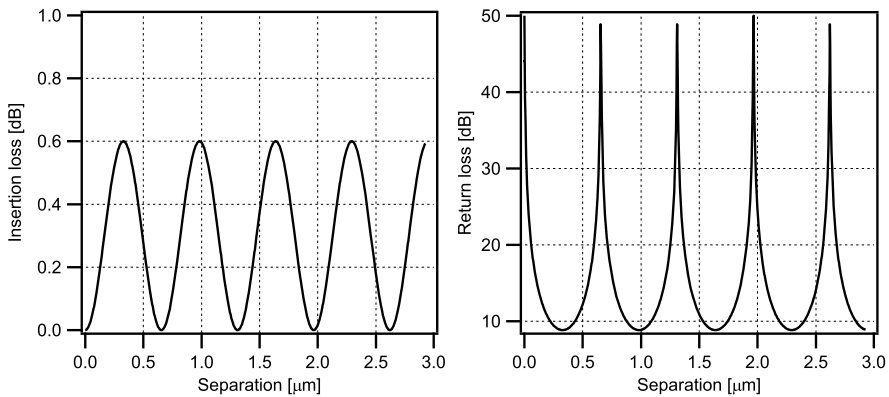
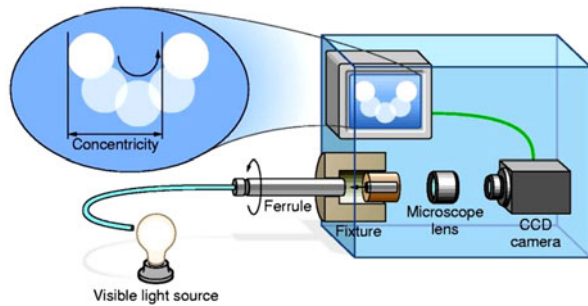
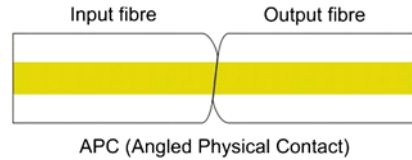


Fig. 11.6 Calculated induced insertion loss and return loss for two perfectly aligned fibres separated by an air gap

insertion loss of the connection, and it would have an even larger effect on the return loss (see Fig. 11.6). As a consequence, it is essential to avoid any air gap between the two connected fibres. This can be accomplished by spherically polishing of the

Fig. 11.7 Scheme of APC-polished connector end face



two ferrules and pressing them together in an optical connection so that an elastic deformation of the spherical ferrules leads to physical contact of the two fibres.

11.1.5.3 PC- and APC-Polished Connectors

In the previous discussion we only mentioned physical-contact (PC)-polished connectors, where the fibre is polished 90° towards its axis. In order to reduce reflections at the connection interface, the connector industry developed the so-called angled PC (APC) connectors, which are polished with a tilt of 8° , as displayed in Fig. 11.7.

In APC-connectors the input and output fibres have to be in physical contact, exactly in the same way as for PC connectors. The additional angle allows a reduction of the amount of reflected light which is coupled back into the input optical fibre by several orders of magnitudes. APC connectors' return loss (RL)-values are specified in the standards to be below -65 dB. In reality well polished APC connectors reach RL-values well below -100 dB!

11.1.6 Mechanical and Climatic Requirements for FO-Connectors

Ideal optical connectors provide stable and repeatable alignment between fibres which must be detachable and repeatable over hundreds or even thousands of connection cycles without deterioration. Handling by operators may include pulling, torsion, twisting, etc., and the optical connection may not only be placed in air-conditioned rooms, but in unprotected locations as well, which may exhibit extreme variations in temperature and humidity. Appropriate (long-term) operation under all these conditions is assured by test standards (e.g. IEC 61300-2-xx) which connectors have to pass.

11.1.7 Available Standard Connector Types

Standard connector types to be mentioned are based on three different ferrule types:

- Cylindrical 2.5 mm ferrules (E-2000, FC, SC, LSA, ...)
- Cylindrical 1.25 mm ferrules (LC, F-3000, MU, LX.5)



Figure	Connector Name	Mechanical interface standard
	E-2000	IEC 61754-15
	F-3000 LC compatible	IEC 61754-20
	SC	IEC 61754-4
	MPO (Multi-fiber connector using rectangular MT ferrule technology)	IEC 61754-7
	FC	IEC 61754-13

Fig. 11.8 Examples of most frequently used fibre optic connectors (courtesy Diamond SA [1])

- Rectangular multi-fibre ferrule, ranging from 2 to 12 fibres (MT, MT-RJ, MPO, MF ...)

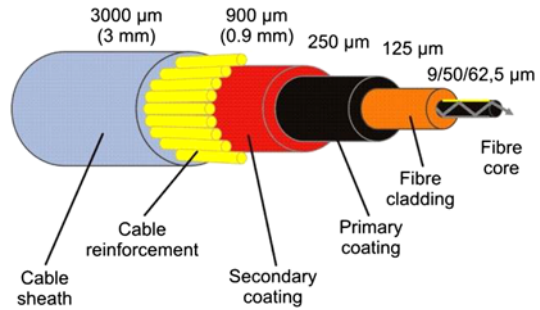
Figure 11.8 shows a few examples of some of the most frequently used connector types.

Recently developed connectors usually use a push pull latching mechanism as opposed to a screw coupling nut, allowing better accessibility, space reduction and therefore higher connection density.

Standard connections may be simplex, allowing connecting an input and one output connector. Duplex connections, where the number of input and output connectors is two, are often used in the case where there is a downstream and an upstream fibre to be connected.

Backplane connectors are used in interconnect systems for connecting printed circuit boards or electro-optic circuit boards to backplanes. Depending on the construction, they may range from one connection up to 6 connections. When using MT-ferrule technology (see beginning of this section), one backplane connection is capable to interconnect up to several tens of fibres.

Fig. 11.9 Typical simplex patch cord cable construction



11.1.8 FO-Cables for Patch Cords

Cord is a general term for a terminated cable assembly, whatever the expected use is. Examples of cords are equipment cord, work area cord or patch cords. Equipment cords are cords connecting equipment to a distributor. Patch cord (see Fig. 11.9) is a cord used within cross-connect implementations at distributors. A work area cord is a cord connecting the telecommunications outlet to the terminal equipment.

Cords represent a very important product family in which optical connectors are used. They often are assemblies of connectors and cable which are not produced by the same manufacturer. In many cases both, cable and connector, are qualified products performing well separately, but as soon as the two are combined into a patch cord, problems may appear:

- Problems may be caused by the fact that connectors are two fixed points in a patch cord, therefore not allowing the cable sheath or other polymer layers to shrink or move as a function of temperature, thus leading to bending of the fibre in the cable causing high attenuation variations.
- Connector ferrules are usually spring loaded. In a connector assembly the fibre (including primary and secondary coating) is fixed to the ferrule, and the cable reinforcement and sheath are fixed to the connector body. In a connection cycle the two ferrules come into contact and push each other back into the connector body. This movement is pushing back the fibre whereas the other cable layers are fixed. In some cable constructions, this movement of the fibre is not allowed due to dimensions or to friction. In this case the fibre usually bends within the connector body, causing high attenuation.

For the reasons mentioned above, terminated patch cords need to be qualified as such. The connector and the cable used in the assembly have to be qualified products, and the subsequent patch cord qualification is a repetition of selected tests used for the connector testing. (Patch cord performance standards: e.g. IEC 61753-121 document series.)

11.1.9 Connectors for Special Fibres or Special Use

So far the discussion was focused on connectors for standard single-mode fibres, the most widely used fibre for telecom applications. However, there are also connectors for other types of fibres (polarisation maintaining, specialty fibres at shorter wavelengths), for special applications such as very high optical power or particularly harsh environment requiring a hardened connector design.

11.1.9.1 Polarisation-Maintaining Connectors

Standard single-mode fibres do not maintain a well-defined state of polarisation (SOP) of the light because many effects including reflection from surfaces, stress within the transmitting media (due to moving the fibre or temperature variations), or magnetic fields can affect the polarisation of the propagating light.

On the other hand, many systems such as fibre interferometers and sensors, fibre optic gyroscopes, fibre lasers and electro-optic modulators depend on a well-defined SOP, which can be assured by polarisation maintaining (PM) fibre plus corresponding connectors and a careful overall assembly so that polarisation-dependent losses, which normally degrade system performance, can be avoided.

In response to these requirements several manufacturers have developed polarisation-maintaining fibres which exhibit birefringence within the core that is characterised by two orthogonal axes corresponding to different propagation constants of light polarised parallel to these axes (frequently designated as fast and slow axis, respectively). If the input light into a PM fibre is linearly polarised and orientated along one of these two axes, the output light from the fibre will remain linearly polarised and parallel to the principal axis, even when subjected to external stress.

Birefringence within a PM fibre is obtained by breaking the circular symmetry, and this can either be done by forming a non-circular fibre core (shape induced birefringence), or by inducing constant stress within the fibre (stress induced birefringence) by fabricating the fibre with two highly doped regions located on opposite sides of the core. Corresponding examples are illustrated in Fig. 11.10. The currently

Fig. 11.10 Examples of polarisation-maintaining fibres: (a) elliptical-cladding-, (b) PANDA-, (c) “bow-tie”-, (d) elliptical-core-, (e) double-core-, and (f) elliptical-core circular-cladding fibre

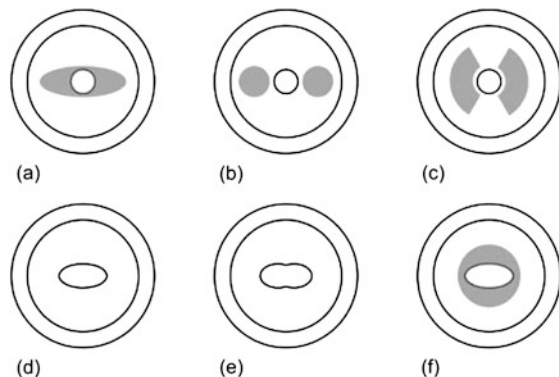
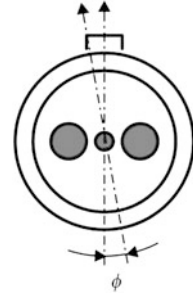


Fig. 11.11 For FO connectors assembled on PM-fibre the orientation of the birefringence axes is a key parameter



most popular SM fibre is the so-called PANDA fibre (where PANDA stands for ‘polarisation-maintaining and absorption-reducing’) which relies on stress-induced birefringence. One particular advantage of PANDA fibres compared to most other variants is the fact that the PANDA core size and numerical aperture are compatible with regular single-mode fibre. This ensures minimum loss in devices using both types of fibre.

While one can produce perfectly linearly polarised light in theory, this is not the case in practice. Instead, there is always some residual polarisation (random or elliptical) present in the output beam, and a measure of beam quality is its polarisation extinction ratio (PER). The extent to what a fibre maintains polarisation depends on the input launch conditions, in particular on the alignment between the polarisation axes of the light and the fibre principal axes.

If a perfectly polarised beam is launched into an ideal fibre misaligned by an angle ϕ with respect to the slow (fast) axis of the fibre (see Fig. 11.11), this misalignment causes a small amount of light being transmitted along the fast (slow) axis of the fibre and consequently degrades the PER of the output beam.

The optimum achievable value of the output extinction ratio (ER) is thus limited by

$$ER \leq -10 \cdot \log(\tan^2 \phi) \quad (11.1)$$

Thus to achieve output extinction ratios better than 20 dB, the angular misalignment must be less than 6 degrees. For 30 dB extinction ratio, the angular misalignment must be less than 1.8 degrees.

As a consequence, in PM connector assemblies it is not only important to align fibre cores but also to orient the fibre axes (see Fig. 11.11), so that in a connection, both fibres have their main axes aligned. In addition, since most PM fibres are stress-induced high birefringence fibres, care should be taken not to excessively stress them because this would decrease their efficiency in maintaining polarisation states.

For these connectors orientation of fibre concentricity, as described in Sect. 11.1.5.1, is no longer possible because priority has to be given to the principle axis orientation. Therefore, this type of fibre is most conveniently terminated using centred technology connectors, which allow both, to position the fibre core in the centre of the ferrule and then to orient the fibre axis.

Very often, PM-applications also require shorter wavelengths, usually related to smaller fibre core and mode field diameter as compared to standard single-mode

fibre. For these applications the alignment of the fibre core is even more challenging. A general rule of thumb is that if the mode field diameter is two times smaller, the same offset error is leading to a 4 times larger attenuation in a connection. The only possible way of manufacturing low loss PM-connectors on small core fibres is by using centring technology, as developed by Diamond SA (see Sect. 11.1.5.1).

11.1.9.2 High Power Connectors

The transmission of high power signals through single-mode fibres raises new challenges not only for the fibre manufacturers but for the in-line components manufacturers as well. Within the core of the fibres and in the areas where the light beam is focused, the power density can reach more than 10 GW/m^2 (as a reference, this is more than hundred times the power density dissipated on the surface of the sun). This can have catastrophic consequences for materials that cannot withstand such a high power density.

One very critical component is the single-mode connector. Good connectors provide only a much reduced hindrance to the transmitted signal (the best connectors guarantee a maximum attenuation as low as 0.1 dB). These small losses are mostly induced by a mismatch of the fibre core parameters (numerical aperture, diameter) or a lateral and angular misalignment, and the energy that gets lost this way is not a threat to the connector reliability as it is dissipated through the fibre cladding.

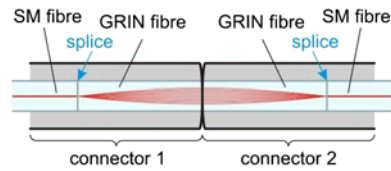
Problems arise when the connectors are not perfectly clean. Contamination particles that are located at the connector interface can absorb part of the transmitted energy and convert it into heat. When the heat produced this way is high enough, the temperature of the fibre can rise over the melting point of silica, causing the collapse of the connection.

To avoid these problems, a connector that has to bear high power signals must ensure perfect cleanliness conditions. A visual inspection of the ferrule's end face before every mating is essential. There shouldn't be any metallic wear parts; metal sleeves and threads are to be avoided. When the connectors are unmated, there must be a protection cap for the ferrules in order to avoid any contamination on the fibre. The mating adapter must also have a protection cap to prevent dust particles to enter the sleeve, and connectors exhibiting all these features are commercially available already [1].

Cleanliness and the above mentioned features may still not be sufficient to guarantee a flawless functioning of the connectors as small particles that may be overlooked with a field inspection microscope could still cause the connector to fail. The only way to eliminate this risk is to reduce the power density at the connector interface, i.e. to enlarge the beam diameter. For this reason connector manufacturers propose a connector design based on expanded beam technology.

Expanded beam connectors that use collimating lenses have been on the market for many years. They are constructed for use in harsh environments, so they usually have rugged bodies and provide higher insertion loss values. Some manufacturers offer expanded beam connectors as high power connectors based on the use of a piece of gradient index fibre instead of an external lens to collimate the light beam.

Fig. 11.12 High power connector based on grin lens design using gradient index fibre



This way the expanded beam system can be integrated in a standard cylindrical ferrule (2.5 mm or 1.25 mm), as illustrated in Fig. 11.12.

The GRIN fibre is spliced to a standard SM fibre and cut at the right length in order to achieve the desired focal length. At the connector interface, the beam is collimated and has a large mode field diameter dependent on the magnification of the GRIN fibre (typical magnification factors 4 to 5, leading to a power density decrease of a factor 16 to 25). In the other connector, the second GRIN fibre focuses the beam back into the SM fibre.

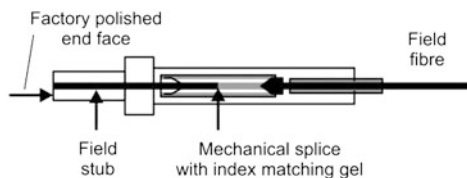
It has been demonstrated that connectors based on the design described above can withstand high power signals (up to 1 W) under standard contamination conditions (same cleaning procedure and same inspection procedure) and show low insertion loss values (similar to standard SM connectors). This technology may be coupled to the E-2000™ connector body offering a good protection of the ferrule from the environment thanks to its protection cap.

11.1.9.3 Field Termination

Most of the fibre optic connectors are assembled in the factory and then spliced (pigtail) or patched in the field, but there are applications where it is needed to assemble the connector in the field. Since connector assembly requires specialised tools and skills, it is usually not possible to assemble connectors in the field using the same technologies as in the factory. Therefore, alternative solutions have been developed for field terminations:

- Optimised, “quick assembly” tools, which allow the field assembly of standard connectors.
- Field termination connectors based on mechanical splices: A connector assembly that is factory terminated and polished may be field terminated on a cable end. The connection to the cable fibre is accomplished through a mechanical splice (see Fig. 11.13).
- Field termination connectors based on fusion splices: The principle is similar to the termination mentioned above with the difference that the mechanical splice

Fig. 11.13 Schematics of a field termination based on mechanical splice



is replaced by a fusion splice which increases performance and reliability of the termination. Some manufacturers offer this kind of solution with similar performance as for standard connectors. Usual installations rely on a 1–3 m pigtail which is spliced to the cable end, but in the case of a fusion field termination the pigtail is significantly shorter (10–20 mm) and the connector housing integrates splice protection features. This makes this solution very similar in performance to what is usually achieved with factory-assembled connectors.

11.1.10 Cleaning and Inspection

A single particle mated into the core of a fibre can cause significant back reflection, insertion loss, and equipment damage. If high optical power is involved, contamination may even cause a permanent damage. As a consequence, it is of high importance to prevent contamination of connector end faces which may be due to:

- Mishandling such as accidental touching of connector end faces or inappropriate cleaning
- Connectors left open for a while and subject to dust or other environmental contaminations
- Travelling contamination where one contaminated connector used for measurements on a patch panel may contaminate a large series of initially clean connectors
- Contaminated connector adapters where contamination is usually not bound to the adapter parts

Accessible connector end faces (when the connector can be hold in a hand) may be cleaned using fabric and/or composite material wipes which combine mechanical action and absorbency to remove contamination. Wipes should be used with a resilient pad in order avoid potential scratching of the connector end face and assist the cleaning material in conforming to the connector end-face geometry, and wipes should be lint free and non-debris producing.

The use of a solvent with a dry wipe is advantageous for various reasons: it adds chemical action to the mechanical function of the wipe which increases its cleaning ability. In addition, the use of a static dissipative solvent eliminates the problem that dry wipes may leave a static charge on the end face of connectors which can subsequently attract particulate contamination.

If the connector end face is assembled in a port, it can only be accessed through the adapter aperture, and in such cases purpose-built swabs or mechanical port cleaning devices provide mechanical action and absorbency to remove contamination. Again, the cleaning end of the swab or cleaning material used in the port-cleaning device should be lint free and non-debris generating. Particular care has to be taken that saturating the connector interface is avoided when solvents are used.

Cleaning of connector end faces and adapters is a process which usually does not have 100% yield and may therefore require several iterations, which require

observation of the end faces with an adequate inspection microscope. Today's microscopes usually use a CCD camera and may be connected to measurement instruments (e.g. OTDR, power meter), to a computer or a portable screen, and in some cases image analysis is used to facilitate the detection of any defect or contamination.

11.2 Fibre Optical Couplers

11.2.1 Introduction

Routing signals to their appropriate destination is one important functionality in communication networks, and combining, distributing or tapping optical channels is equally important. Passive optical couplers offer this functionality (see Fig. 11.14) and are therefore widely used in fibre optic networks.

Some designs are inherently directional, such as couplers where several fibres are fused in the middle, routing signals from a group of input fibres to a separate group of output fibres. Others are not directional, taking inputs from all fibres and distributing them among all fibres. Therefore $2 \times N$ couplers and $1 \times N$ couplers (tree couplers) are special cases of star couplers. In the four-port directional coupler, an incoming signal at each of the input ports 1 or 2 reaches both output ports 3 and 4; otherwise an incoming signal from each of the output ports 3 or 4 and propagating in the opposite direction reaches both input ports 1 and 2.

The behaviour of these coupler structures is the result of reciprocity. Reciprocity is essential for the correct interpretation of incoming signals at the output ports. We will see that using fused-fibre technology, a T-coupler is nothing more than a directional coupler terminating the second input fibre. Fused-fibre couplers may be further characterised by the wavelength dependence of coupling. In this chapter we will only discuss power splitters with a wavelength-independent behaviour over a specified wavelength range and not wavelength-selective splitters (filters). Such devices are discussed in Chap. 9.

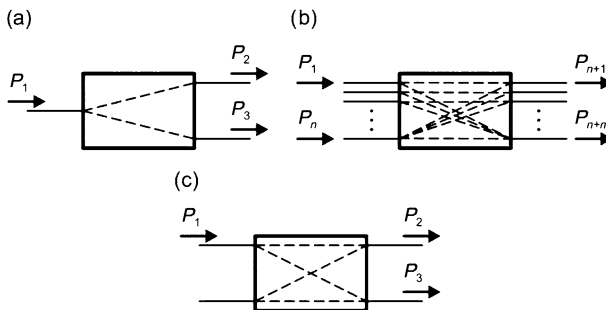
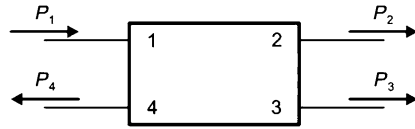


Fig. 11.14 Coupler types: (a) T- or Y-coupler, (b) star coupler, (c) directional coupler

Fig. 11.15 4-Port model of a directional coupler



11.2.2 Modelling of Optical Directional Couplers/Power Splitters

A generic model of a directional coupler, which is independent of the coupler type, is shown in Fig. 11.15 with ports numbered 1, 2, 3, and 4.

Based upon this model, the directional coupler can be characterised by a scattering matrix. The scattering matrix is commonly used in the field of microwave technology [2], and it is also used with the same definitions in fibre optics. Two complex quantities, a_i and b_i , associated with each port i , represent the complex amplitudes for the input and the reflected light waves, respectively. The relation between the input and the reflected light waves is given by

$$\mathbf{b} = \mathbf{S}\mathbf{a} \quad (11.2)$$

with vectors $\mathbf{a} = [a_1, a_2, a_3, a_4]$ and $\mathbf{b} = [b_1, b_2, b_3, b_4]$ and the scattering matrix \mathbf{S} given by

$$\mathbf{S} = \begin{bmatrix} s_{11} & s_{12} & s_{13} & s_{14} \\ s_{21} & s_{22} & s_{23} & s_{24} \\ s_{31} & s_{32} & s_{33} & s_{34} \\ s_{41} & s_{42} & s_{43} & s_{44} \end{bmatrix} \quad (11.3)$$

all corresponding to the 4-port case. If the coupler is made of identical fibres,

$$s_{ij} = s_{ji} \quad (i, j = 1, 2, 3, 4) \quad (11.4)$$

holds due to geometric symmetry and reciprocity of the device. Therefore we get for the scattering matrix:

$$\mathbf{S} = \begin{bmatrix} s_1 & s_2 & s_3 & s_4 \\ s_2 & s_1 & s_4 & s_3 \\ s_3 & s_4 & s_1 & s_2 \\ s_4 & s_3 & s_2 & s_1 \end{bmatrix} \quad (11.5)$$

with

$s_1 = s_{11} = s_{22} = s_{33} = s_{44}$: self-reflection coefficient

$s_2 = s_{12} = s_{21} = s_{34} = s_{43}$: transmission coefficient

$s_3 = s_{13} = s_{31} = s_{24} = s_{42}$: coupling coefficient

$s_4 = s_{14} = s_{41} = s_{23} = s_{32}$: blocking coefficient.

For an ideal directional coupler with no reflections and no loss, the corresponding scattering matrix \mathbf{S}_{ideal} is known to be a unitary matrix given by

$$\mathbf{S}_{ideal} = \begin{bmatrix} 0 & c_1 & ic_2 & 0 \\ c_1 & 0 & 0 & ic_2 \\ ic_2 & 0 & 0 & c_1 \\ 0 & ic_2 & c_1 & 0 \end{bmatrix} \quad (11.6)$$

where c_1 and c_2 are real constants and

$$c_1^2 + c_2^2 = 1 \quad (11.7)$$

holds.

In the following paragraph we will show how the scattering matrix formalism can be applied to the description of (biconical fused) fibre couplers (see also Sects. 11.2.3 and 11.2.4).

The coupling region can support two fundamental modes, the even and the odd one, which are characterised by different propagation constants β_{even} and β_{odd} , given by

$$\beta_{even} = \frac{2\pi n_{even}}{\lambda} \quad \text{and} \quad \beta_{odd} = \frac{2\pi n_{odd}}{\lambda} \quad \text{with} \quad \frac{\beta_{even} + \beta_{odd}}{2} = \beta_{av} \quad (11.8)$$

with n_{even} and n_{odd} being the effective refractive indices of the even and odd modes, respectively, and λ the vacuum wavelength of the wave under consideration. A plane electromagnetic wave propagating into the z -direction is represented by

$$E(z, t) = E_0 \exp[-i(\beta z - \omega t)] \quad (11.9)$$

with $\omega = 2\pi c/\lambda$ and c being the vacuum speed of light. Light propagating in the odd mode will travel faster in the coupling area because its electrical field extends further into the low-index cladding of the fibre. As a consequence a phase difference as given by (11.10) accumulates between the even and odd modes as they propagate a distance L along the coupler.

$$\varphi = L(\beta_{even} - \beta_{odd}) = \frac{2\pi L}{\lambda}(n_{even} - n_{odd}) \quad (11.10)$$

If a common phase delay of both modes, i.e. $\exp(-i\beta_{av}L)$, is neglected, the total electrical fields at the output arms 2 and 3 are given by

$$\begin{aligned} E_2 &= \frac{E}{2} + \frac{E}{2} \exp(i\varphi) = \frac{E}{\sqrt{2}} \sqrt{1 + \cos \varphi} \exp\left(\frac{i\varphi}{2}\right) \\ E_3 &= \frac{E}{2} + \frac{E}{2} \exp(i\varphi) = \frac{E}{\sqrt{2}} \sqrt{1 + \cos \varphi} \exp\left(\frac{i\varphi}{2} - \frac{i\pi}{2}\right) \end{aligned} \quad (11.11)$$

Equation (11.11) demonstrates that the output of arm 3 is always delayed by 90° with respect to arm 2. This behaviour is independent of the coupling length and the strength of the coupling mechanism and therefore independent of the coupling factor.¹ Another important result is that the angle φ determines the coupling ratio of the coupler where the following cases are of particular relevance: $\varphi = 0$ corresponds to no coupling at all, $\varphi = 90^\circ$ characterises a splitting ratio of 50%, i.e. this represents an ideal 3 dB coupler, and $\varphi = 180^\circ$ is equivalent to a splitting ratio of 100%, i.e. 100% of the input power appears in arm 3 and no power is observed in arm 2. According to (11.10) and (11.11), for a given set of fibre parameters, the periodic exchange of the output power between the arms 2 and 3 depends only on the length of the coupling region. Neglecting the common phase shift (i.e. $\exp(i\varphi/2)$), we get:

$$\begin{aligned} E_2 &= c_1 E_1 + i c_2 E_4 \\ E_3 &= i c_2 E_1 + c_1 E_4 \end{aligned} \quad (11.12)$$

The quadratic terms c_1^2 and c_2^2 represent the power coupling coefficients between connected or coupled arms.

Directional couplers can also be analysed using the coupled mode theory, as outlined in Chap. 9, Sect. 9.3.1.

If ports 2, 3 and 4 are terminated without any reflection, the power P_i at each port can easily be calculated using the incoming wave a_1 at port 1 and the outgoing waves b_2 , b_3 and b_4 at the other ports which leads to

$$\begin{aligned} P_1 &= |a_1|^2 \\ P_2 &= |b_2|^2 = |s_2|^2 |a_1|^2 \\ P_3 &= |b_3|^2 = |s_3|^2 |a_1|^2 \\ P_4 &= |b_4|^2 = |s_4|^2 |a_1|^2 \end{aligned} \quad (11.13)$$

Besides the coupling ratio CR there are three other parameters which characterise the behaviour of a coupler and which are usually expressed in units of dB: the excess loss EL , the return loss RL , and the directivity D , and these four key parameters are given by

¹It might be worthwhile to note that the sign of the phase change of the wave leaving the coupler via the cross port depends on the sign in the exponent of (11.9). Conventions using positive or negative sign for the wave propagation are both found in the literature giving rise to different signs of the phase change, which might raise confusion.

$$\begin{aligned}
 CR &= -10 \log\left(\frac{P_3}{P_1}\right) = -20 \log(|s_3|) \\
 EL &= -10 \log\left(\frac{P_2 + P_3}{P_1}\right) = -10 \log(|s_2|^2 + |s_3|^2) \\
 RL &= -10 \log\left(\frac{P_r}{P_1}\right) \\
 D &= -10 \log\left(\frac{P_4}{P_1}\right) = -20 \log(|s_4|)
 \end{aligned}
 \tag{11.14}$$

where P_r results from the outgoing wave at port 1 due to internal reflections in the coupling zone. In general, EL , RL , and D result from internal imperfections of the device because there are no incoming waves except at port 1. Other figures of merit, which are relevant for the characterisation of couplers, are independence (or negligible residual dependence) on fibre modes and on the state of polarisation. The first is a very important requirement for multimode couplers because different excitation conditions can often result in a large change of the coupling ratio. Polarisation independence is naturally a topic for single-mode couplers only. One rule of thumb is that the shorter the tapered zone of the fibres the larger the residual polarisation dependence. As a consequence, the overall size of couplers should not be reduced too much.

11.2.3 Fibre Coupler Technologies

The most common type of fibre coupler is the evanescent field coupler which uses a narrow spacing between two adjacent fibre cores. Because the electromagnetic field extends beyond the cores, coupling between the cores happens. Fibre-based couplers are produced using essentially two different techniques. Most popular is the fused biconical taper technique, producing fused biconical couplers (FBCs). Two fibres are fused together and stretched at high temperature. To achieve an approach of the fibre cores due to a force, the fibres must be twisted in- or outside the coupling area. The stretching decreases the diameter of the fibres and therefore, proportionally, the diameter and the distance of the cores. At the beginning and at the end of the coupling zone a tapered zone occurs. This causes an extension of the electromagnetic field and therefore the possibility of coupling. The coupling length is the major parameter to define the coupling ratio. Fused biconical couplers are primarily used as power splitters for telecommunication applications but they also serve as wavelength division multiplexers and demultiplexers. The other popular approach to fabricate fibre couplers relies on polishing the fibres. The two fibres, which will build the coupler, are first embedded into a glass plate and then polished down to the cores. Joining the glass plates brings the cores into proximity. The lateral spacing can be freely chosen which allows the definition of essentially any coupling ratio wanted. Due to a perfectly manageable polishing process it is

easier and more repeatable to create couplers using different fibre types with different diameters. Therefore this technique is very important for the fabrication of couplers which use special fibres, for example, for high power or sensors applications.

11.2.4 Classification

By appropriate design of the manufacturing process and pre-treatment of the fibres, which constitute the coupler, it is possible to create couplers with different coupling ratio and transmission characteristics, and the following categories can be distinguished:

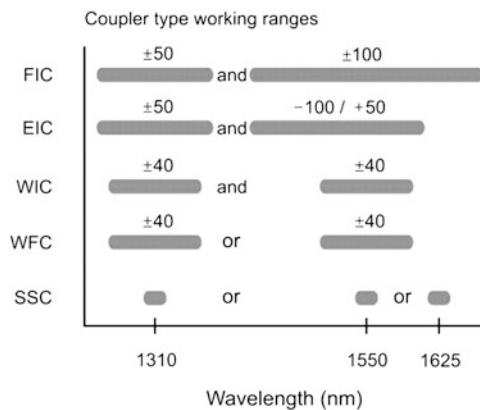
- Standard single-mode couplers (SSCs), specified for one wavelength and a (small) bandwidth of typically ± 5 nm
- Wavelength flattened couplers (WFCs), specified for one wavelength and a (wider) bandwidth of typically ± 40 nm
- Wavelength independent couplers (WICs), specified for two wavelengths (for example: 1310 nm and 1550 nm) and for a bandwidth of typically ± 40 nm at each wavelength
- Extended wavelength independent couplers (EIC), specified for two wavelengths and larger unequal bandwidths of typically ± 50 nm and -100 nm/ $+50$ nm
- Full range wavelength independent couplers (FIC), specified for two wavelengths and large equal bandwidths of typically ± 50 nm and ± 100 nm

These fibre coupler categories are illustrated in Fig. 11.16.

Due to the coupling principle it is not possible to narrow the gap between the two transmission windows to less than 75 nm because a smaller separation would at the same time narrow the transmission windows themselves which is not acceptable.

The typical coupling behaviour of fused biconical couplers using standard single-mode fibres or pre-treated fibres as a function of pull length during the pulling process is illustrated in Fig. 11.17.

Fig. 11.16 Fibre coupler categories [3]



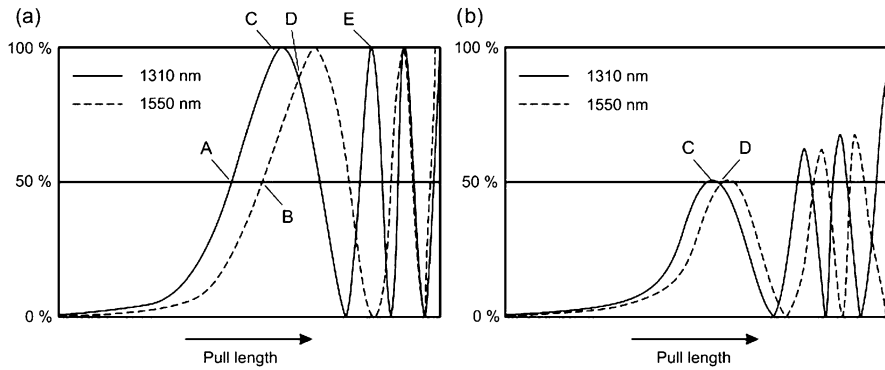


Fig. 11.17 Coupling behaviour of fused biconical couplers made of identical fibres (*figure on the left*) and different fibres (*figure on the right*) [3]

Continuous monitoring of the power at the output ports enables to stop the pulling process at the desired pull length in order to get the requested coupling behaviour. For example, point A and B indicate pull lengths representing a 50/50%-power splitting for 1310 nm or 1550 nm. At point D the power splitting is 80/20% for both wavelengths. In the case of identical fibres (Fig. 11.17, left part) the coupling ratio exhibits a large wavelength dependence due to the steep slopes of the curves. If different fibre types are used (Fig. 11.17, right part), the wavelength dependence is significantly lower. Finally, the same basic structure could also be used as a wavelength multiplexer as point E in (Fig. 11.17, left part) illustrates.

Typical and best performance values of the different fibre coupler types and for various splitting ratios are compiled in Table 11.3.

11.2.5 Star Couplers

Multiport couplers can – in theory – be made by fusion of many fibres. Large variations of the power distribution at the different outputs and an often poor repeatability of the manufacturing processes have prevented the commercial implementation of the theoretic concepts so far. In practice the manufacturing process has acceptable yield for a maximum of four fibres or even less. Therefore transmissive star couplers, which are key devices for star-type networks, are mostly built by a cascade of equal or different T-couplers. One particular advantage of this approach is the flexibility to create individual power distributions at the output ports, and lower cost is an additional argument in favour of this approach. There is only one shortcoming of transmissive star couplers which favours the use of fused couplers with more than two fibres: the latter require less space. Figure 11.18 shows a drawing of a transmissive 1×8 star coupler, built from 1×2 couplers with different coupling ratios.

Table 11.3 Typical values of input power degradation as observed at output port 2 and 3 for the coupling ratios indicated. Numbers, given in dB, represent total attenuation due to splitting plus internal coupler losses [3]

	FIC		EIC		WIC		WFC		SSC	
Wavelength [nm]	1310 ± 50 and 1550 ± 100		1310 ± 50 and 1550 + 50/ - 100		1310 ± 40 and 1550 ± 40		1310 ± 40 or 1550 ± 40, and 1625 ± 40		1310 ± 5, 1550 ± 5, or 1625 ± 5	
Coupling ratio	Output port									
	O2	O3	O2	O3	O2	O3	O2	O3	O2	O3
50/50%	4.2	4.2	4.0	4.0	3.6	3.6	3.4	3.4	3.4	3.4
60/40%	3.2	5.4	3.0	5.2	2.7	4.7	2.5	4.3	2.5	4.3
67/33%	2.7	6.4	2.5	6.2	2.2	5.6	2.0	5.2	2.0	5.2
70/30%	2.4	7.0	2.2	6.8	2.0	6.1	1.8	5.6	1.8	5.6
80/20%	1.7	9.2	1.5	9.0	1.4	8.4	1.1	7.4	1.1	7.4
90/10%	1.1	13.0	0.9	12.8	0.8	11.7	0.6	10.6	0.6	10.6
95/05%	0.8	16.8	0.6	16.6	0.5	15.3	0.4	13.8	0.4	13.8
99/01%	0.1	24.7	0.4	24.5	0.2	23.1	0.2	22.0	0.2	22.0
Minimum directivity [dB]					55 for 1 × 2, 60 for 2 × 2					
Minimum return loss [dB]					55 for 1 × 2, 60 for 2 × 2					
Polarisation dependent loss ^{a,b} [dB]	typical 0.05									

^a Maximum 0.1 dB for port O2 and maximum 0.2 dB for port O3

^b FIC, EIC: measured at 1310 nm and 1550 nm, WIC, WFC, SSC: measured at central wavelength of wavelength range

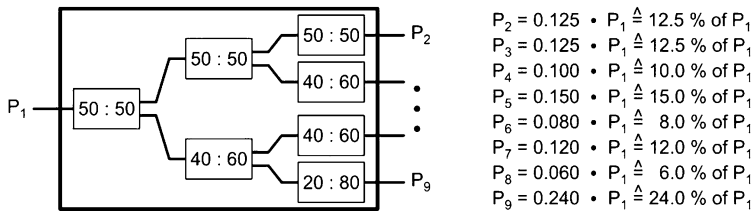


Fig. 11.18 Drawing of a 1 × 8 star coupler and output power distribution

11.3 Optical Circulators

An optical circulator is a nonreciprocal, passive multiport device, and its key functionality is directing light sequentially from port to port which results in the separation of signals which travel along an optical fibre in opposite directions. Sub-components optical circulators are assembled from are a selection from polarising beam splitters, phase shifters, Faraday rotators, optical isolators, walk-off polarisers, prisms, and lenses.

Fig. 11.19 Functionality of an “ideal” 4-port optical circulator (schematic)

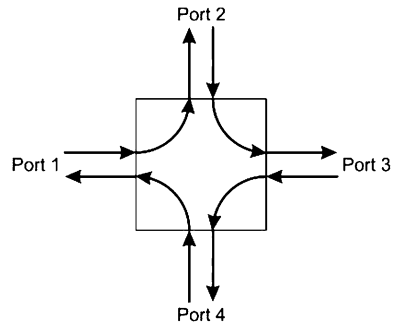
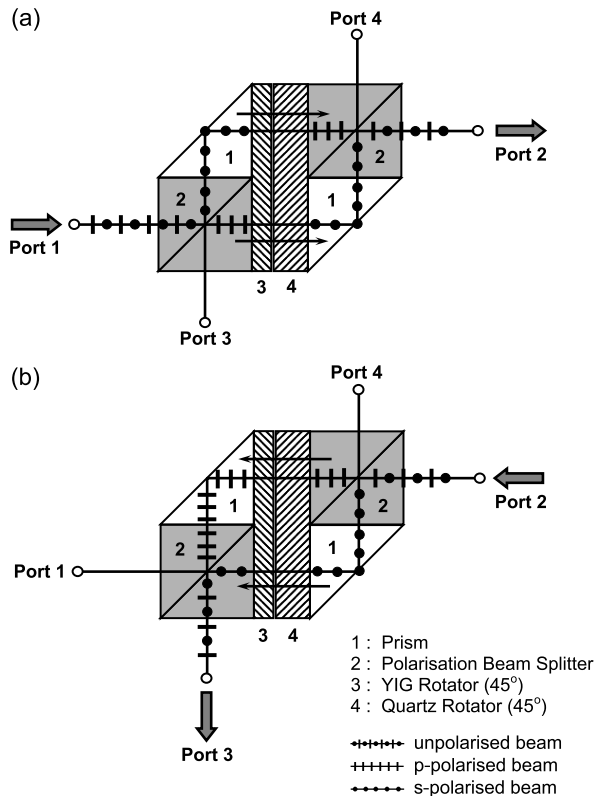


Fig. 11.20 Design example of an “ideal” 4-port optical circulator [4]



Optical circulators are typically 3- or 4-port devices, and an “ideal” 4-port circulator is schematically illustrated in Fig. 11.19 where “ideal” means that light may enter by any input and is routed to the subsequent port in all cases.

Various implementations of optical circulators have been published starting in the late 70-ies and early 80-ies of the last century and continuing since then including different “ideal” 4-port circulators [4–7] and one design is illustrated in Fig. 11.20.

Table 11.4 Typical characteristics of commercially available optical circulators. Numbers given apply to 3-port and 4-port circulators as well (for the former case all entries containing “4” should be removed)

Wavelength ranges	1310 ± 30 nm
	1525–1565 nm
	1570–1610 nm
Insertion loss (1 → 2, 2 → 3, 3 → 4)	0.8 ... 1.2 dB
Channel isolation (2 → 1, 3 → 2, 4 → 3)	
peak:	> 50 dB
complete operation range	> 40 dB
Directivity (1 → 3, 2 → 4)	> 50 dB
Return loss	> 55 dB
Polarisation-dependent loss (PDL)	< 0.1 ... 0.15 dB
Polarisation mode dispersion (PMD)	0.06 ... 0.1 ps
Wavelength-dependent loss (WDL)	0.15 ... 0.2 dB
Polarisation extinction ratio ^a	20 ... 23 dB

^a Applies for polarisation-maintaining circulators

Typical characteristics of these early devices were about 2 dB insertion loss, 25 to 35 dB isolation (sometimes <25 dB), and the operation wavelength was typically around 1.3 μm.

In practice the full functionality of an “ideal” circulator requires a very sophisticated and complex design. However, this is not generally needed, and as a consequence optical circulators are normally offered with reduced functionality [8]. In the case of 4-port circulators the corresponding routing characteristics can be represented by 1 → 2, 2 → 3, 3 → 4, i.e. port 1 is an input port only, ports 2 and 3 serve as input and output ports while port 4 is an output-only port. 3-port circulators do in general correspond to 1 → 2, 2 → 3 routing, i.e. they have one input-only port (1), one output-only port (3) while port 2 serves both, as an input and an output port.

Commercially available optical circulators are essentially all mini bulk assemblies packed with fibre pigtails, and typical parameters of circulators for operation at telecom wavelengths are compiled in Table 11.4.

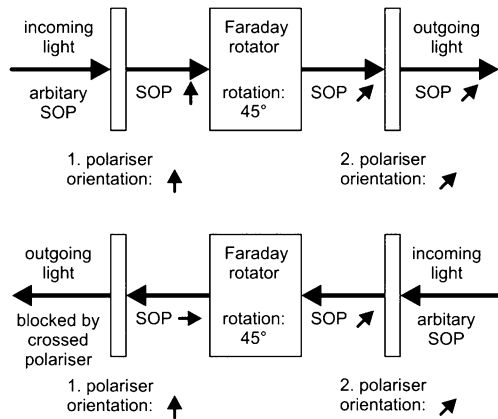
The wavelength ranges over which optical circulators are specified may vary by several nm, and there are also products on the market which cover the complete C+L bands. Dimensions of typical circular modules are about 5.5 mm in diameter and 60 ... 65 mm length.

11.4 Optical Isolators

11.4.1 General Characteristics

Optical isolators transmit light in one direction only. They play an important role in fibre optic systems by preventing back-reflected and scattered light from reaching

Fig. 11.21 Generic set-up and operation of a polarising optical isolator. *Upper part* illustrates light transmission, *lower part* corresponds to blocking



the sensitive cavity of transmitter lasers, which might otherwise strongly affect the performance of lasers, and optical isolators assure stable performance of EDFAs. An isolator is a two-port optical circuit and its behaviour can be characterised by a scattering matrix according to

$$\mathbf{S} = \begin{bmatrix} s_{11} & s_{12} \\ s_{21} & s_{22} \end{bmatrix} \tag{11.15}$$

An in-depth treatment of the fundamentals is given e.g. in [9] and the implementations of a large number of different variants of optical isolators are also presented. Optical isolators fall essentially into one of two categories: polarising isolators which are polarisation-dependent and reject the unwanted polarisation which counter propagates to the transmitted beam, and polarisation-independent isolators, in which the unwanted polarisation appears spatially displaced and is blocked at the output of the isolator.

Key elements of a polarising optical isolator (as illustrated in Fig. 11.21) are a pair of linear polarisers separated by a Faraday rotator, which shifts the plane of polarisation by 45°. The polarisers are orientated in such a way that their planes of polarisation differ by 45°.

The functionality of the polarisation dependent optical isolator shown in Fig. 11.21 can be understood as follows: Light coming from the left in the example shown will pass the first polariser (provided their polarisations match while any polarisation mismatch leads to extra insertion loss (cf. also Sect. 11.4.2). Next the light enters the Faraday rotator (usually a yttrium-iron-garnet = YIG or a terbium-gallium-garnet = TGG) material which rotates the light polarisation by 45°. At the output the light beam passes the second polariser which is intended to operate as an analyser and which is orientated at an angle of 45° with respect to the first polariser.

Light coming from the right can only pass the second polariser if the light polarisation and the optical axis of the polariser are parallel. Reciprocity would now demand that the polarisation of the backward passing light were changed to the polarisation of the input polariser. However, the Faraday rotator rotates the polari-

sation of the back-travelling beam by another 45° , which results in an overall rotation of 90° compared to the first polariser so that the back-travelling light beam is blocked by the polariser. It is easy to understand that the performance of an isolator is primarily defined by the quality of the two polarisers although the quality of the antireflection-coating of each surface inside the isolator is another important issue.

It might be worthwhile to mention that a Faraday rotator could not be replaced by an optically active or liquid-crystal polarisation rotator because in those devices the sense of rotation is such that the polarisation of the reflected wave retraces that of the incident wave so that the reflected wave is transmitted back through the polariser to the entrance of the device.

Figures of merit which essentially characterise isolators are isolation I and insertion loss IL , which are related to the scattering parameters s_{11} and s_{12} by

$$\begin{aligned} I &= -10 \log(|s_{12}|^2) \\ IL &= -10 \log\left(\frac{|s_{21}|^2}{1 - |s_{11}|^2}\right) \end{aligned} \quad (11.16)$$

11.4.2 Polarisation-Independent Optical Isolators

One serious drawback of optical isolators using polarisers and a Faraday rotator is their polarisation dependence which increases the insertion loss. Therefore implementations of optical isolators without polarisation dependence are very interesting for future transmission systems.

Isolators with polarisation-independent characteristics have been implemented so far according to two different concepts: They are either deflection-type devices, where the birefringence of prisms causes a polarisation-dependent deflection with free space propagation at different angles, or displacement-type isolators where birefringent crystals split and laterally shift the two polarisations while the free space propagation is collinear [9].

For the first time a polarisation-independent (deflection-type) isolator was proposed in 1979 [10]. The configuration of the suggested fibre-based isolator is shown in Fig. 11.22.

The device uses two birefringent plates with equal thickness, a Faraday rotator and a compensating plate which shifts the phase of the light by $\lambda/4$. The light beam with two orthogonal polarisations propagates in the directions indicated by the solid and dotted lines in the figure. The birefringent plates produce a spatial separation for the orthogonally polarised components of the light. In case of the forward travelling light, these parts of light interchange their polarisation before the second birefringent plate and then they are combined at the second fibre. In the case of backward travelling light, the two orthogonally polarised components of light do not change their polarisation due to the nonreciprocal characteristics of a Faraday rotator. Therefore, they are not combined by the birefringent plate and consequently also not coupled into the input fibre (fibre 1). The principle used in this configuration

Fig. 11.22 Configuration and behaviour of a polarisation-independent isolator after [10]

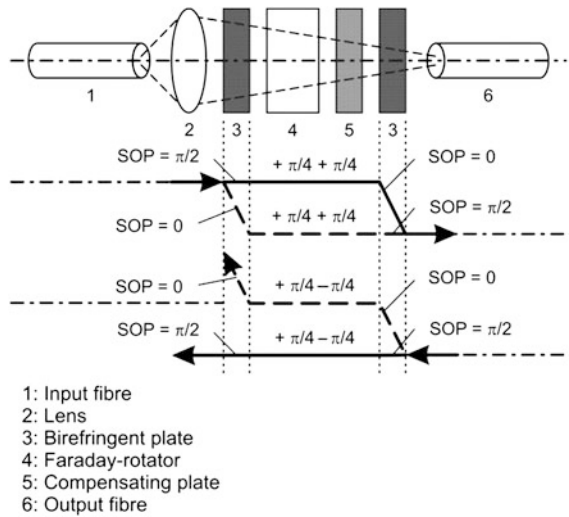
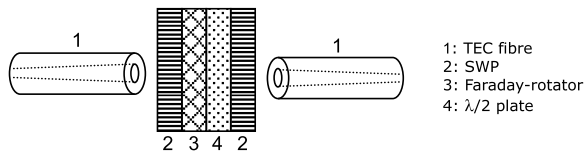


Fig. 11.23 Setup of a polarisation-independent optical isolator after [11]



is that the backward travelling light is focused on points with a spatial offset with respect to the core of fibre 1. Based on the same principle, a very small fibre-embedded polarisation-independent isolator has also been fabricated [11]. This configuration is shown in Fig. 11.23.

An isolator chip is inserted between TEC (thermal expanded core) fibres. The chip consists of spatial walk-off polarisers (SWP), a half-wave plate ($\lambda/2$ -plate) and a Faraday rotator. Rutile plates were used as an SWP and a garnet crystal of $(\text{YbTbBi})_3\text{Fe}_5\text{O}_{12}$ was used as a Faraday rotator. The isolator exhibited about 2.5 dB insertion loss and over 40 dB of isolation at $\lambda = 1550 \text{ nm}$.

Another type of polarisation-independent isolator has been proposed which is based upon a polarisation-dependent isolator, two SWPs, and two half-wave plates [12], see Fig. 11.24. Forward travelling light with orthogonal polarisations is separated by the first SWP and then set to the same polarisation using a half-wave plate in one path before the light passes through the polarisation-dependent isolator.

Fig. 11.24 Polarisation-independent optical isolator after [12]

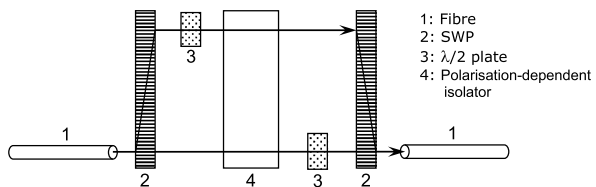
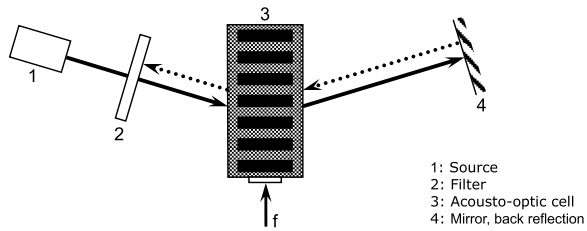


Fig. 11.25 Polarisation-independent optical isolator using an acousto-optic cell after [13]



Then one of the light beams is rotated again by a half-wave plate before the second SWP will combine the two beams. Backward travelling light is blocked completely by the polarisation-dependent isolator because after travelling through the SWP and through the half-wave plate both light beams have the same polarisation orientation which is blocked by the isolator.

An acousto-optic cell as illustrated in Fig. 11.25 can serve as an isolator without the drawback of exact positioning several elements. The optical signal transmitted from a laser or travelling in the transmission system is frequency-up-shifted by the acousto-optic modulator and Bragg-diffracted. Coming to a reflection face part of the light is reflected onto itself and traces its path back into the cell. The backward-travelling light undergoes a second Bragg diffraction accompanied by a second frequency up-shift. Since the frequency of the returning light differs from that of the original light by twice the acoustic frequency used in the cell, a filter may be used to block it. Depending to the acoustic frequency used to modulate the light, even without a filter, the laser will be insensitive to the frequency-shifted light.

11.4.3 Two-Stage Isolators

The performance of isolators is limited by the temperature- and wavelength-dependent characteristics of all optical elements, furthermore the magnetic field strength decreases with increasing temperature and the same holds for the Verdet constant (of the Faraday rotator material). Fabrication tolerances and errors represent another limiting effect. As a consequence the peak isolation of single-stage isolators is limited to about 40 dB and about 30 dB isolation is typically specified over moderate wavelength and temperature operation ranges. One widely adopted means towards improved performance are two-stage isolators, which enable higher peak isolation (~ 60 dB) and a less pronounced frequency- and temperature dependent roll-off of the isolation [9, Chap. 6].

11.4.4 Commercially Available Optical Isolators

Commercially available optical isolators fall essentially into two categories, free space, bulk optics isolators and fibre optic isolators, where commercially available fibre optic isolators are in fact mini free space isolators packaged with fibre pigtailed.

11.4.4.1 Free-Space Optical Isolators

Free space optical isolators are commercially available for selected wavelengths or wavelength bands ranging from the UV (<400 nm) to the near IR (>2 μm), including 980 nm and the 1.3, and 1.55 μm telecom wavelengths. Single-stage isolators may reach peak isolation better than 40 dB but isolation is typically specified ≥ 30 dB over ± 10 nm from the centre wavelength. Fixed narrowband isolators are offered both, polarisation dependent and polarisation independent while wavelength adjustable/tunable or broadband isolators are polarisation dependent. Double-stage isolators enable >60 dB peak isolation with all other parameters comparable to those of single-stage isolators. Power rating depends on the polariser type used [14] and is typically in the 25 W/cm² to 500 W/cm² range but may amount to even a few 10 kW/cm² (e.g. 1064 nm isolators), and 1.3 μm and 1.55 μm isolators may be capable to handle 1 W of total power. The overall insertion loss of single- and double stage isolators is in the few 0.1 dB range, and apertures are typically a few mm.

Finally, optical isolators exhibit a polarisation mode dispersion (PMD) of typically 0.1 ps (which is in fact rather a differential-group delay (DGD) as explained in detail in [9]), and the residual polarisation dependent loss (PDL) of polarisation independent isolators is <0.1 dB.

11.4.4.2 Fibre Optic Isolators

Fibre optic isolators are commercially available for a number of selected wavelengths or wavelength regimes including the 1310 nm, 1480 nm, 1550 nm and 1585 nm telecom wavelengths [15, 16]. Figure 11.26 illustrates the typical wavelength dependent performance of a two-stage isolator for different temperatures (data from [15]).

The figure clearly demonstrates that the minimum isolation depends significantly on the wavelength- and temperature operation ranges. This has to be kept in mind if the specifications of different isolators are compared, and this is also reflected in Table 11.5 which compiles typical performance data of devices from two different manufacturers.

Fig. 11.26 Isolation of a two-stage fibre optical isolator as a function of deviation from the centre wavelength for 3 different temperatures (*full line*: 10 °C, *dashed line*: 23 °C, *dash-dotted line*: 55 °C), after [15]

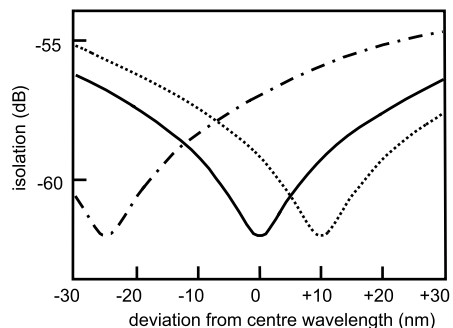


Table 11.5 Characteristics of single- and two-stage fibre optic isolators of two different manufacturers

	[16]		[15]	
	Single-stage	Dual-stage	Single-stage	Dual-stage
Operation wavelength (nm)	1310, 1550	1310, 1550	1310, 1480, 1550, 1590	1310, 1480, 1550, 1590
Wavelength range (nm)	±30	±30	±10	±10
Peak isolation (dB)	42	58	45	65
Minimum isolation (dB)	32	45	40	55
Typical insertion loss (dB)	0.3	0.7	0.5	0.6
Crosstalk (dB).5	>65	>60	55	55
PDL (dB)	0.05	0.1	0.1	0.1
PMD (ps) ^a	0.2 (0.05)	0.1 (0.05)		
Power handling (W)	0.3	0.3	0.3...5	0.3...5
Operation temperature (°C)	−20 to +70	−20 to +70	0 to +70	0 to +70

^a More correctly: differential group delay (see [9])

As the fibre optic isolators discussed here are mini assemblies of bulk components (as mentioned already), it is not surprising that the performance of free space and fibre optic isolators is essentially similar.

11.4.4.3 All-Fibre Optical Isolators

True all-fibre isolators have not yet received a greater amount of attention, although 17 dB isolation have already been demonstrated for an optical isolator building upon Faraday rotation in a highly terbium-doped fibre [17] additional designs have been suggested but not yet implemented [18].

11.5 Planar Integrated Waveguide-Based Optical Isolators and Circulators

11.5.1 Planar Integrated Optical Isolators

In addition to optical isolators as stand-alone devices, planar isolators and/or solutions which are suited for incorporation into optoelectronic integrated circuits (OEICs) have been a research topic for several decades already, see e.g. the reviews by M. Levy [19] or by B.J.H. Stadler et al. [20].

Planar waveguide optical isolators are predominantly designed using magneto-optical (MO) material but can be based upon non-magnetic concepts as well. If OEICs are to be developed, solutions of the former type require the combination

of MO and semiconductor layers and corresponding materials development started with III–V QWs directly grown on garnet [21], followed by wafer bonding of garnet layers onto III–V semiconductors [22] as a next step. In 1997 Yokoi and Mizumoto proposed [23] and in 2000 demonstrated [24] WGs in III–V material and using the MO material as a cladding layer, and this approach has since then been widely adopted and used with SOI WGs as well, e.g. using MZI- [25] or ring resonator based designs [26].

11.5.1.1 TE-TM Conversion-Based Isolators

Early isolator concepts aimed at adapting the Faraday rotation scheme to WG isolators which is equivalent to TE-TM conversion. This approach requires phase matching between the TE and TM modes, and this is technologically highly demanding due to shape birefringence and growth induced stress/strain birefringence. Nevertheless, as outlined in detail in [19] different groups have successfully adopted various strategies to achieve efficient TE-TM conversion. Isolation ratios exceeding 30 dB have been demonstrated, however in a YIG waveguide structure only [27] which is incompatible with monolithic OEIC fabrication. Building upon TE-TM conversion, only hybrid isolators using WG Faraday rotators or planar hybrid isolator assemblies [28] have been fabricated so far while corresponding monolithically integrated isolators are still lacking.

11.5.1.2 Nonreciprocal Phase Shift-Based Isolators

A technologically less demanding planar WG isolator solution is based on a nonreciprocal phase shift. Designs based upon MZI structures have been suggested about 40 years ago [29, 30]. A magnetically active material, e.g. YIG variants, placed on top of the arms of an MZI plus a magnetic field applied with opposite orientation for the interferometer arms, give rise to a nonreciprocal phase shift for the forward and backward travelling TM-polarised waves. By proper adjustment of the relevant magneto-optic parameters and interferometer geometry constructive interference in the forward- and destructive interference in the backward direction can be achieved (see e.g. [20, 24]).

Corresponding devices have been realised in the InP material system [31] and on SOI [25, 32, 33] with >20 dB optical isolation over 8 nm bandwidth reported. Moreover, advanced devices have been proposed, including polarisation independent designs [34–37] and a wideband isolator (1.25 to 1.65 μm) with calculated >35 dB isolation [38].

Another variant of this isolator type is a nonreciprocal ring (or racetrack) resonator with a magneto-optic layer (e.g. Ce:YIG) on top of the ring. Using an axially magnetised neodymium cylinder magnet on the top of the ring resulted in about 20 dB isolation in the telecom regime [39, 40]. In a more recent variant the external magnet is replaced by a metal wire ring on top of the garnet. A current through this

wire gives rise to a radial magnetic field which induces different phase shifts for the clockwise and counter-clockwise propagating modes resulting in optical isolation, and 32 dB isolation and 2.3 dB excess loss only have been reported [41]. Corresponding isolators can be made very compact and are consequently promising for monolithic integration. On the other hand, due to the generic characteristics of ring resonators (see Chap. 9, Sect. 9.10.1), the achievement of high isolation over wider wavelength ranges is a very challenging task.

11.5.1.3 Isolators Exploiting Nonreciprocal Loss

Nonreciprocal loss in semiconductor optical amplifier (SOA) structures combined with a ferromagnetic layer magnetised parallel to the light propagation direction enables the fabrication of monolithic integrated isolators. If the ferromagnetic layer is placed on top of the WG, such devices operate for TM polarisation [42, 43] while a ferromagnetic layer at the SOA sidewall acts as an isolator for TE-polarised waves. Results achieved so far include 10 dB/mm isolation over the complete C-band (1530–1560 nm) and a peak TE-mode nonreciprocal attenuation of 14.7 dB/mm [44], or the monolithic integration with a laser diode, however, with lower optical isolation [45]. SOA-based isolators lend themselves to integration on GaAs- or InP-basis while their implementation would be much more demanding on an SOI platform. On the other hand, one inherent and serious shortcoming of this approach is the power needed for compensating the large optical losses induced by the ferromagnetic layer.

11.5.1.4 Nonmagnetic Solutions

A rather different approach uses RF modulation which gives rise to direction dependent propagation characteristics while no magneto-optic materials are used at all. Various concepts have been proposed and implemented already [46–49], but further improvements are needed before such devices will become competitive with existing solutions.

It might be worthwhile to note here that device concepts have also been claimed to exhibit nonreciprocal light propagation characteristics and were consequently suited for making optical isolators which, however, did not have an asymmetric scattering matrix (as required for a true optical isolator). This topic is discussed in depth in [50], the authors give reference to papers with unjustified claims, and an overview of various viable optical isolator concepts published so far is also included.

11.5.2 Planar Optical Circulators

Optical circulators constitute a generic building block for complex OEICs, one well known application example is their combination with Bragg gratings used as

wavelength (de)multiplexers or in sensing applications as well. Therefore, planar waveguide-based optical circulators have been a research topic for several decades already although with lower overall effort than that spent on the development of planar optical isolators. Most circulator designs under investigation in the past are similar to corresponding isolator concepts, they rely on the same technology and exhibit comparable performance. Up to now only a limited number of circulators have already been realised with quite a few more having been suggested but not yet implemented so far.

11.5.2.1 Planar Hybrid Circulators

Hybrid 4-port polarisation independent waveguide optical circulators are early examples of fabricated circulators. Based upon a nonreciprocal Mach-Zehnder interferometer structure and including quarter-wave plates and Faraday rotators [51, 52], such circulators exhibited a forward to reverse isolation of 14.0 to 23.7 dB and 3.0 to 3.3 dB insertion loss at $\lambda = 1.55 \mu\text{m}$ [51] or 16.2 to 29.8 dB isolation and 8.8 to 9.4 dB insertion loss [52], respectively, with a completely alignment-free waveguide-embedding configuration demonstrated in the latter case.

11.5.2.2 Nonreciprocal Phase Shift-Based Circulators

Mach-Zehnder interferometers with a nonreciprocal phase shift section do also enable the design of planar optical circulators (similar to corresponding optical isolators). Such circulators are polarisation-dependent (TM polarisation operation only) and 3-port- as well as 4-port-circulator structures, fabricated in the SOI material system, have been reported [53–55]. Maximum isolation achieved has been in the 10 to 20 dB regime, and the total device insertion loss amounted to about 10 dB plus significant fibre-chip coupling losses in the absence of optical tapers. Finally it is worthwhile to note that these circulators exhibit appropriate performance at selected wavelengths only due to the generic characteristics of MZIs in combination with fairly small free spectral ranges (12 or 20 nm, respectively).

11.5.2.3 Miscellaneous Planar Circulator Concepts

Various additional optical circulator designs have been proposed in the literature the implementation of which is still pending. Examples include circulators based on ring resonators [56], ring cavities [57], resonators in 2D photonic crystals [58], and nonmagnetic circulators based on photonic transitions [59]. Most of the circulators are polarisation dependent once again, while a polarisation independent circulator is suggested in [60]. However, the concept requires Faraday rotators and half-wave plates so that it lends itself to a hybrid rather than a monolithically integrated realisation.

References

1. www.diamond-fo.com
2. R.E. Collin, *Foundations of Microwave Engineering*, 2nd edn. (Wiley, Hoboken, 2001), ISBN 978-0-7803-6031-0
3. www.foc-fo.de
4. H. Iwamura, H. Iwasaki, K. Kubodera, Y. Torii, J. Noda, Simple polarisation-independent optical circulator for optical transmission systems. *Electron. Lett.* **15**, 830–831 (1979)
5. T. Matsumoto, Polarisation-independent optical circulator coupled with multimode fibres. *Electron. Lett.* **16**, 8–9 (1980)
6. Y. Fujii, Polarisation-independent optical circulator having high isolation over a wide wavelength range. *IEEE Photonics Technol. Lett.* **4**, 154–156 (1992)
7. J.-H. Chen, D.-C. Su, J.-C. Su, Holographic spatial walk-off polarizer and its application to a 4-port polarisation-independent optical circulator. *Opt. Express* **11**, 2001–2006 (2003)
8. W.L. Emkey, A polarisation-independent optical circulator for 1.3 μm . *J. Lightwave Technol.* **LT-1**, 466–469 (1983)
9. J.N. Damask, *Polarisation Optics in Telecommunications* (Springer, New York, 2005)
10. T. Matsumoto, Polarisation-independent isolators for fiber optics. *Trans. IECE Japan* **E62**, 516–517 (1979)
11. K. Shiraishi, T. Chuzenji, S. Kawakami, Polarisation-independent in-line optical isolator with lens-free configuration. *J. Lightwave Technol.* **10**, 1839–1842 (1992)
12. K. Shiraishi, New configuration of polarisation-independent isolator using a polarisation-dependent one. *Electron. Lett.* **27**, 302–303 (1991)
13. B.E.A. Saleh, M.C. Teich, *Fundamentals of Photonics*, 3rd edn. (Wiley, Hoboken, 2007), ISBN 0471358320
14. www.thorlabs.com
15. www.ozoptics.com
16. www.fiberer.com
17. L. Sun, S. Jiang, J.D. Zuegel, J.R. Marciano, All-fiber optical isolator based on Faraday rotation in highly terbium-doped fiber. *Opt. Lett.* **35**(5), 706–708 (2010)
18. M. Berent, A.A. Rangelov, N.V. Vitanov, Broadband optical isolator in fibre optics. *J. Opt.* **15**, 085401 (2013)
19. M. Levy, The on-chip integration of magneto-optic waveguide isolators. *IEEE J. Sel. Top. Quantum Electron.* **8**(6), 1300–1306 (2002)
20. B.J.H. Stadler, T. Mizumoto, Integrated magneto-optical materials and isolators: a review. *IEEE Photonics J.* **6**(1), 0600215 (2014)
21. M. Razeghi, P. Meunier, P. Maurel, Growth of GaInAs–InP multiquantum wells on garnet ($\text{GGG} = \text{Gd}_3\text{Ga}_5\text{O}_{12}$) substrate by metalorganic chemical vapor deposition. *J. Appl. Phys.* **59**(6), 2261–2263 (1986)
22. H. Yokoi, T. Mizumoto, K. Maru, Y. Naito, Direct bonding between InP and rare earth iron garnet grown on $\text{Gd}_3\text{Ga}_5\text{O}_{12}$ substrate by liquid phase epitaxy. *Electron. Lett.* **31**(18), 1612–1613 (1995)
23. H. Yokoi, T. Mizumoto, Proposed configuration of integrated optical isolator employing wafer-direct bonding technique. *Electron. Lett.* **33**(21), 1787–1788 (1997)
24. H. Yokoi, T. Mizumoto, N. Shinjo, N. Futakuchi, Y. Nakano, Demonstration of an optical isolator with a semiconductor guiding layer that was obtained by use of a nonreciprocal phase shift. *Appl. Opt.* **39**(33), 6158–6164 (2000)
25. S. Ghosh, S. Keyvavinia, W. Van Roy, T. Mizumoto, G. Roelkens, R. Baets, Ce:YIG/Silicon-on-Insulator waveguide optical isolator realized by adhesive bonding. *Opt. Express* **20**(2), 1839–1848 (2012)
26. K. Shang, S. Cheung, B. Li, R.P. Scott, Y. Takamura, S.J.B. Yoo, On-chip optical isolators based on a ring resonator with bismuth-iron-garnet overcladding, in *Conf. Lasers Electro-Opt. (CLEO'14)*, San Jose, CA, USA (2014), Techn. Digest, paper SM1H.6

27. R. Wolfe, J.F. Dillon, R.A. Lieberman, V.J. Fratello, Broadband magneto-optic waveguide isolator. *Appl. Phys. Lett.* **57**(10), 960–962 (1990)
28. N. Sugimoto, H. Terui, A. Tate, Y. Katoh, Y. Yamada, A. Sugita, A. Shibukawa, Y. Inoe, A hybrid integrated waveguide isolator on a silica-based planar lightwave circuit. *J. Lightwave Technol.* **14**, 2537–2546 (1996)
29. S. Yamamoto, T. Makimoto, Circuit theory for a class of anisotropic and gyrotropic thin-film optical waveguides and design of nonreciprocal devices for integrated optics. *J. Appl. Phys.* **45**(2), 882–888 (1974)
30. F. Auracher, H.H. Witte, A new design for an integrated optical isolator. *Opt. Commun.* **13**(4), 435–438 (1975)
31. Y. Sobu, Y. Shoji, K. Sakurai, T. Mizumoto, GaInAsP/InP MZI waveguide optical isolator integrated with spot size converter. *Opt. Express* **21**(13), 15373–15381 (2013)
32. Y. Shoji, M. Ito, Y. Shirato, T. Mizumoto, MZI optical isolator with Si-wire waveguides by surface-activated direct bonding. *Opt. Express* **20**(16), 18440–18448 (2012)
33. Y. Shoji, Y. Shirato, T. Mizumoto, Silicon Mach-Zehnder interferometer optical isolator having 8 nm bandwidth for over 20 dB isolation. *Jpn. J. Appl. Phys.* **53**(2), 022202 (2014). doi:[10.7567/JJAP.53.022202](https://doi.org/10.7567/JJAP.53.022202)
34. O. Zhuromskyy, M. Lohmeyer, N. Bahlmann, H. Dötsch, P. Hertel, A.F. Popkov, Analysis of polarisation independent Mach-Zehnder-type integrated optical isolator. *J. Lightwave Technol.* **17**(7), 1200–1205 (1999)
35. O. Zhuromskyy, H. Dötsch, M. Lohmeyer, L. Wilkens, P. Hertel, Magneto-optical waveguides with polarisation-independent nonreciprocal phase shift. *J. Lightwave Technol.* **19**(2), 214–221 (2001)
36. J. Fujita, M. Levy, R.M. Osgood Jr., L. Wilkens, H. Dötsch, Polarisation-independent waveguide optical isolator based on nonreciprocal phase shift. *IEEE Photonics Technol. Lett.* **12**, 1510–1512 (2000)
37. Y. Shoji, I.-W. Hsieh, R.M. Osgood, T. Mizumoto, Polarisation-independent magneto-optical waveguide isolator using TM-mode nonreciprocal phase shift. *J. Lightwave Technol.* **25**(10), 3108–3113 (2007)
38. Y. Shoji, T. Mizumoto, Ultra-wideband design of waveguide magneto-optical isolator operating in 1.31 μm and 1.55 μm band. *Opt. Express* **15**(2), 639–645 (2007)
39. M.-C. Tien, T. Mizumoto, P. Pintus, H. Kromer, J.E. Bowers, Silicon ring isolators with bonded nonreciprocal magneto-optic garnets. *Opt. Express* **19**(12), 11740–11745 (2011)
40. L. Bi, J. Hu, P. Jiang, D.-H. Kim, G.F. Dionne, L.C. Kimerling, C.A. Ross, On-chip optical isolation in monolithically integrated non-reciprocal optical resonators. *Nat. Photonics* **5**, 758–762 (2011)
41. D. Huang, P. Pintus, C. Zhang, Y. Shoji, T. Mizumoto, J.E. Bowers, Silicon microring isolator with large optical isolation and low loss, in *Opt. Fiber Commun. Conf. (OFC'16)*, Anaheim, CA, USA (2016), Techn. Digest, paper Th1K.2
42. W. Zaets, K. Ando, Optical waveguide isolator based on nonreciprocal loss/gain of amplifier covered by ferromagnetic layer. *IEEE Photonics Technol. Lett.* **11**, 1012–1014 (1999)
43. M. Vanwolleghem, P. Gogol, P. Beauvillain, W. Van Parys, R. Baets, Design and optimization of a monolithically integratable InP-based optical waveguide isolator. *J. Opt. Soc. Am. B* **24**, 1–12 (2007)
44. H. Shimizu, Y. Nakano, Fabrication and characterization of an InGaAsP/InP active waveguide optical isolator with 14.7 dB/mm TE mode nonreciprocal attenuation. *J. Lightwave Technol.* **24**, 38–43 (2006)
45. H. Shimizu, Y. Nakano, Monolithic integration of a waveguide optical isolator with a distributed feedback laser diode in the 1.5- μm wavelength range. *IEEE Photonics Technol. Lett.* **19**, 1973–1975 (2007)
46. S. Bhandare, S.K. Ibrahim, D. Sandel, H. Zhang, F. Wüst, R. Noé, Novel nonmagnetic 30-dB traveling-wave single-sideband optical isolator integrated in III/V material. *IEEE J. Sel. Top. Quantum Electron.* **11**, 417–421 (2005)

47. H. Lira, Z. Yu, S. Fan, M. Lipson, Electrically driven nonreciprocity induced by interband photonic transition on a silicon chip. *Phys. Rev. Lett.* **109**, 033901 (2012)
48. C.R. Doerr, N. Dupuis, L. Zhang, Optical isolator using two tandem phase modulators. *Opt. Lett.* **36**, 4293–4295 (2011)
49. C.R. Doerr, L. Chen, D. Vermeulen, Tandem-phase-modulator-based optical isolator in silicon, in *Proc. 39th Europ. Conf. Opt. Commun.* (ECOC'13), London, UK (2013), paper PD2.D.1
50. D. Jalas, A. Petrov, M. Eich, W. Freude, S. Fan, Z. Yu, R. Baets, M. Popović, A. Melloni, J.D. Joannopoulos, M. Vanwolleghem, C.R. Doerr, H. Renner, What is – and what is not – an optical isolator. *Nat. Photonics* **7**, 579–582 (2013)
51. N. Sugimoto, T. Shintaku, A. Tate, H. Terui, M. Shimokozono, E. Kubota, M. Ishii, Y. Inoue, Waveguide polarisation-independent optical circulator. *IEEE Photonics Technol. Lett.* **11**, 355–357 (1999)
52. N. Hanashima, K. Hata, R. Mochida, T. Oikawa, T. Kineri, Y. Satoh, S. Iwatsuka, Hybrid optical circulator using garnet–quartz composite embedded in planar waveguides. *IEEE Photonics Technol. Lett.* **16**, 2269–2271 (2004)
53. S. Ghosh, S. Keyvaninia, W. Van Roy, T. Mizumoto, G. Roelkens, R. Baets, Adhesively bonded Ce:YIG/SOI integrated optical circulator. *Opt. Lett.* **38**(6), 965–967 (2013)
54. K. Mitsuya, Y. Shoji, T. Mizumoto, Demonstration of a silicon waveguide optical circulator. *IEEE Photonics Technol. Lett.* **25**(8), 721–723 (2013)
55. K. Mitsuya, Y. Shoji, T. Mizumoto, The first demonstration of silicon waveguide optical circulator, in *Opt. Fiber Commun. Conf. and Nat. Fiber Opt. Eng. Conf.* (OFC/NFOEC'13), Anaheim, CA, USA (2013), Techn. Digest, paper JTh2A.25
56. D. Jalas, A.Y. Petrov, M. Eich, Optical three-port circulators made with ring resonators. *Opt. Lett.* **39**, 1425–1428 (2014)
57. W. Śmigaj, L. Magdenko, J. Romero-Vivas, S. Guenneau, B. Dagens, B. Gralak, M. Vanwolleghem, Compact optical circulator based on a uniformly magnetized ring cavity. *Photonics Nanostruct. Fundam. Appl.* **10**, 83 (2012)
58. W. Śmigaj, J. Romero-Vivas, B. Gralak, L. Magdenko, B. Dagens, M. Vanwolleghem, Magneto-optical circulator designed for operation in a uniform external magnetic field. *Opt. Lett.* **35**, 568–570 (2010)
59. Z. Yu, S. Fan, Integrated nonmagnetic optical isolators based on photonic transitions. *IEEE J. Sel. Top. Quantum Electron.* **16**(2), 459–466 (2010)
60. T. Zaman, X. Guo, R. Ram, Proposal for a polarisation-independent integrated optical circulator. *IEEE Photonics Technol. Lett.* **18**(12), 1359–1361 (2006)

Wolfgang Coenning was born in Reutlingen, Germany, in 1962. He received his diploma degree in electrical communication engineering and Ph.D. from the University of Stuttgart, Germany, in 1987 and 1995, respectively. From 1987 to 2001 he was with the Institute of Electrical and Optical Communication Engineering of the University of Stuttgart working on optoelectronic devices and optical communication systems. From 2001 to 2006 he has with Diamond GmbH in Leinfelden-Echterdingen, Germany, a subsidiary of Diamond SA in Losone, Switzerland. He has been responsible for research and development of customized optical systems in different areas as well as for production of these devices. Further he established the training center “Glasfaserschule” at Diamond GmbH for internal and external education in optics. In 2008 he finished off an additional training in scientific teaching and is since 2008 with the University of Applied Sciences Esslingen, Germany.

François Caloz received a diploma in applied physics from the Swiss Federal Institute of Technology in Zurich in 1991 and a Ph.D. in physical chemistry from the Swiss Federal Institute of Technology in Lausanne in 1997. From 1997–1999 he was a post-doctoral fellow at the Jet Propulsion Laboratory (Pasadena, Los Angeles, CA), and since 1999 he is with Diamond SA, a worldwide leader in developing and supplying passive fibre optic components and high precision fibre optic solutions. François Caloz has been employed by Diamond SA as the fibre optic laboratory

manager, where he was mainly involved in the development, test and measurement of passive optical components, as well as in the implementation and development of new test and measurement equipment. He is currently involved in the standardization of fibre optic connectors in IEC 86B committee “Fibre optic interconnecting devices and passive components”, which is responsible for the preparation of international standards for fibre optic interconnecting devices and passive components, related test and measurement methods and functional interfaces, including all mechanical, environmental and optical requirements to ensure interoperability and reliable performance of fibre optic interconnecting devices and passive components.

Chapter 12

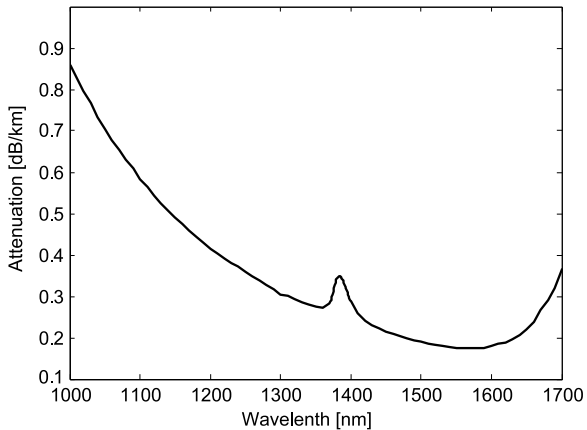
Fiber Amplifiers

Karsten Rottwitt

Abstract The chapter provides a discussion of optical fiber amplifiers and through three sections provides a detailed treatment of three types of optical fiber amplifiers, erbium doped fiber amplifiers (EDFA), Raman amplifiers, and parametric amplifiers. Each section comprises the fundamentals including the basic physics and relevant in-depth theoretical modeling, amplifiers characteristics and performance data as a function of specific operation parameters. Typical applications in fiber optic communication systems and the improvement achievable through the use of fiber amplifiers are illustrated.

Since the early days of optical communication there has been a strong effort in making optical fibers with as low an intrinsic attenuation as possible. State-of-the-art high capacity transmission optical fibers have a minimum attenuation close to 0.2 dB/km at the wavelength 1555 nm. Figure 12.1 illustrates the at-

Fig. 12.1 The attenuation in a standard single-mode optical fiber versus wavelength. Data adapted from [1]



K. Rottwitt (✉)
DTU Fotonik, Department of Photonics Engineering, Technical University of Denmark, DTU,
2800 Kgs. Lyngby, Denmark
e-mail: karo@fotonik.dtu.dk

tenuation as a function of wavelength in a state-of-the-art high capacity optical fiber.

For wavelengths in the range from 500 nm to 1550 nm the attenuation is mainly due to Rayleigh scattering whereas the loss at wavelengths beyond 1550 nm is mainly due to infrared absorption [1].

Even though 0.2 dB/km is a very low attenuation, it is obvious that there is a need for optical amplification when transmitting an optical signal over long distances. For this reason the development of the erbium doped fiber amplifier (EDFA) led to huge progress within the field of optical communication. It may be fair to state that the EDFA enabled tremendous progress in the field of optical communication, progress, which emphasized the need for more and more bandwidth. This together with the availability of high power fiber lasers, powered by EDFAs, led to the interest in Raman amplifiers which again enabled further increase in the capacity of optical communication systems. Even though the Raman amplifier has proven strong benefits, it appears to be a safe statement that the EDFA will continue to be one of the most important components within optical communication systems.

The continued search for optical communication systems that support more and more capacity has seeded a strong interest in novel modulation schemes and space division multiplexing and consequently also a search for optical fiber amplifiers which may assist in improved system performance. Such amplifiers may be parametric amplifiers which in addition to being able to amplify an optical signal also enable phase sensitive amplification and further signal processing such as regeneration or wavelength conversion of a signal.

In the following chapter, the three types of optical fiber amplifiers are discussed in individual sections. Section 12.1 is dedicated to the EDFA, Sect. 12.2 to the fiber Raman amplifier, and Sect. 12.3 to the fiber optical parametric amplifier. The chapter is concluded in Sect. 12.4 with a short summary of the three methods of optical amplification.

12.1 The EDFA

In the EDFA the core of the optical fiber is co-doped with erbium ions. These have energy levels separated by energies corresponding to optical frequencies. The energy levels are defined by the angular momentum of the electrons of the ions together with their spin. When an ion makes a transition between two energy levels, light may be emitted. This together with the fact that the host fiber is a silica based optical fiber makes an EDFA an obvious component to splice to passive fibers for achieving amplification.

The EDFA has numerous advantages of which the most important ones are listed below:

- gain at 1555 nm coinciding with the loss minimum of optical fibers
- large gain, and large gain efficiency, tens of dB per mW of pump power

- low noise figure, 3 dB at high gain
- low polarization dependence
- low channel to channel crosstalk

The EDFA was heavily researched in the late 1980s and in the early 1990s, see for example [2–4]. The EDFA may be one of the most important inventions for optical communication, and it is for example less likely that we would have trans-oceanic transmission links employing wavelength division multiplexed signals, nor metro/access networks, without the EDFA.

12.1.1 Energy Levels

The erbium-ion may be described using a simplified energy level diagram as depicted in Fig. 12.2. When optically pumped at 980 nm, the EDFA acts as a 3-level laser system which means that the Er^{3+} ion is excited from the ground state level ${}^4I_{15/2}$ to the third energy level ${}^4I_{11/2}$ with rate W_{PA} (index *PA* indicates absorption at pump wavelength) from which it rapidly, considered instantaneous in the figure, decays to the upper laser level ${}^4I_{13/2}$ where the ion exists for a finite time (approx. 10 ms). On the other hand, the erbium ion may also decay to the ground state energy level with rate W_{PE} (index *PE* indicates emission at pump wavelength). While in the ${}^4I_{13/2}$ state, the erbium ion may decay back to the ground state level either in a spontaneous process with rate $1/\tau_{21}$ (τ_{21} is the lifetime of the energy level ${}^4I_{13/2}$) or stimulated by a signal with rate W_{SE} (index *SE* indicates emission at signal wavelength). The signal may also cause the erbium ion to change energy level from ${}^4I_{15/2}$ to ${}^4I_{13/2}$ with rate W_{SA} (index *SA* indicates absorption at signal wavelength).

It is noted that one may also pump the EDFA using light at 1480 nm in which case the Er^{3+} ions are excited directly into the upper laser level ${}^4I_{13/2}$.

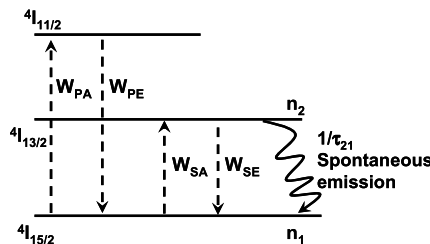


Fig. 12.2 The energy levels of Er^{3+} are characterized by quantum numbers for the orbital momentum L and spin-momentum S . For Er^{3+} $L = 6$ and $S = 3/2$. Thus, the total angular momentum, J , varies between $L - S = 9/2$ and $L + S = 15/2$ [3, 4], the latter being the ground state level. The energy of one electron is changed between the different energy levels either by pumping or due to emission. An electron may exist in the ${}^4I_{13/2}$ level up to about 10 ms. The notation for the energy levels are: ${}^{2S+1}L_J$, where L is quoted with a letter rather than a number (J represents the value 6)

12.1.2 Rate Equations

In any practical case the population levels at the relevant energy levels are determined from rate equations. Assuming that the decay from ${}^4I_{11/2}$ to ${}^4I_{13/2}$ is instantaneous or that one is pumping using the pump wavelength at 1480 nm, the rate equation for the population of ions in the lower energy level $n_1(r, \phi, z)$ is

$$\frac{dn_1(r, \phi, z)}{dt} = -[W_{SA}(r, \phi, z) + W_{PA}(r, \phi, z)]n_1(r, \phi, z) + \left[W_{SE}(r, \phi, z) + W_{PE}(r, \phi, z) + \frac{1}{\tau_{21}} \right] n_2(r, \phi, z), \quad (12.1)$$

where the rates W_{SE} , W_{SA} , W_{PE} , W_{PA} and $1/\tau_{21}$ are as described in Fig. 12.2, $n_2(r, \phi, z)$ is the ion population level in the upper energy level, and (r, ϕ, z) is the position in the fiber. A similar rate equation exists for the population of ions in the upper energy level. When evaluating the steady state case, i.e. $dn_1/dt = 0$ and $dn_2/dt = 0$, the population level in the excited state, $n_2(r, \phi, z)$, has the solution

$$n_2 = \rho(W_{SA} + W_{PA}) / (W_{SE} + W_{SA} + W_{PE} + W_{PA} + 1/\tau_{21}), \quad (12.2)$$

where $\rho = n_1 + n_2$ is the total erbium concentration level of the fiber. A rate equation for n_1 is easily found using the figure or simply by using $n_2 = \rho - n_1$. The number of excited Er-ions relative to the total number of ions, i.e. here: $x = n_2 / (n_1 + n_2)$, also referred to as the *inversion*, is a very important parameter that determines evolution of the signal but also spontaneous emission, which is equivalent to the signal gain and the noise performance. In the following, equations for the evolution of signal and pump power are described together with their solutions.

As discussed above, the two wavelengths used for pumping are 1480 nm or 980 nm, respectively. When pumping at 1480 nm, the EDFA acts as a two-level laser system and the inversion can not exceed a maximum level of 70%. If instead erbium is pumped at 980 nm, the rate W_{PE} approximates zero and consequently the maximum inversion may be 100%.

12.1.3 Signal Propagation

In the signal mode the power may be separated into a sum of pure signal and spontaneous emission. The evolution of the pure signal power P_s , is governed by

$$\frac{dP_s}{dz} = [\gamma_e(\nu_s, z) - \gamma_a(\nu_s, z)]P_s, \quad (12.3)$$

where ν_s is the frequency of the signal and z the position coordinate. The emission and absorption factors γ_e and γ_a are defined through the material emission and

absorption cross sections ($\sigma_e(\nu)$, $\sigma_a(\nu)$), together with the overlap integrals between the population levels n_1 and n_2 and the transverse signal mode $I_s(r)$:

$$\gamma_e(\nu, z) = \sigma_e(\nu) 2\pi \int_0^{a_d} n_2(r, z) I_s(r) r dr, \quad (12.4)$$

$$\gamma_a(\nu, z) = \sigma_a(\nu) 2\pi \int_0^{a_d} n_1(r, z) I_s(r) r dr, \quad (12.5)$$

where a_d is the radius of the rare earth doping. It is noted that the signal is assumed to be in the fundamental fiber mode, the LP₀₁ mode. Since this mode does not vary in the angular coordinate, the integration over the angular coordinate ϕ equals 2π . The intrinsic fiber loss is omitted in the propagation equation (12.3) but may be included as an additional term $-\alpha_s P_s$, on the right hand side of equation (12.3) where α_s is the loss rate.

The intensity of the electric field representing the signal is

$$I_s(r, \phi, z) = P_s(z) |E_s^{01}(r, \phi)|^2, \quad (12.6)$$

where $P_s(z)$ is the signal power, and the index '01' on $E_s^{01}(r, \phi)$ shows that the transverse distribution of the electrical field of the signal is in the fundamental mode, i.e. the electrical field is normalized according to

$$\int_0^{2\pi} \int_0^b |E_s^{01}(r, \phi)|^2 r dr d\phi = 1, \quad (12.7)$$

where b is the radius of the cladding of the optical fiber. The solution to the propagation equation for the signal is:

$$P_s(z) = P_s(z=0) \exp \left\{ \int_0^z (\gamma_e(\nu_s, x) - \gamma_a(\nu_s, x)) dx \right\} = P_s(z=0) G. \quad (12.8)$$

Equation (12.8) defines the signal gain G as the output signal power relative to the input signal power.

In analogy to the propagation equation for the signal, a similar propagation equation exists for the pump power, i.e.

$$\frac{dP_p}{dz} = [\gamma_e(\nu_p, z) - \gamma_a(\nu_p, z)] P_p, \quad (12.9)$$

where γ_e and γ_a are now determined by replacing the signal frequency by the pump frequency and by replacing the signal intensity distribution by the pump intensity distribution in (12.4) and (12.5), using as above that the intensity of the pump is

$$I_p(r, \phi, z) = P_p(z) |E_p^{01}(r, \phi)|^2, \quad (12.10)$$

where $P_p(z)$ is the pump power which, like the signal, is in the fundamental fiber mode.

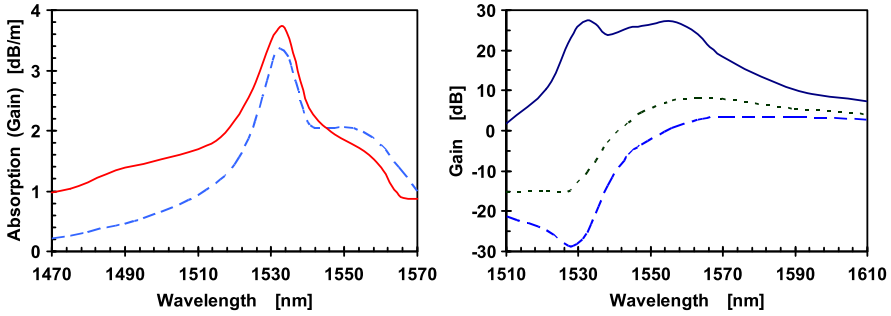


Fig. 12.3 *Left:* Absorption (solid) and gain (dashed) spectra in an Al:Ge erbium doped fiber versus wavelength [5]. *Right:* Gain as a function of wavelength for different average levels of inversion: upper trace 63%, middle trace 45%, lower trace 38%, data are a courtesy of OFS Fitel Denmark. Both figures are for aluminum-germanium-doped silica fibers

12.1.4 Emission and Absorption Cross Sections

Rather than using the comprehensive model described above, which requires numerical analysis, alternative semi-analytical models have found their use to predict amplifier gain, gain saturation, and noise properties [5–7]. In this model the gain per unit length is given as

$$\frac{G(\lambda)}{L} = [g^*(\lambda) + \alpha(\lambda)]Inv - \alpha(\lambda), \quad (12.11)$$

where $\alpha(\lambda) = \sigma_a(\lambda)\Gamma(\lambda)\rho$ is the absorption per unit length with no inversion, ρ is the total erbium concentration and $\Gamma(\lambda)$ is the overlap between the fiber mode and the transverse distribution of the erbium ions. The gain per unit length with full inversion is $g^*(\lambda) = \sigma_e(\lambda)\Gamma(\lambda)\rho$, and Inv is the average inversion of ions in the amplifier when operating under signal induced gain compression, i.e. $Inv = \frac{1}{L} \int_0^L x dz$, where $x(z) = n_2/\rho$ is the local inversion as described in the text following (12.2) L the physical fiber length. Figure 12.3(left) shows examples of absorption and gain per unit length for a specific fiber, and Fig. 12.3(right) shows gain as a function of average inversion level as obtained in an EDFA.

Material Systems A silica based optical fiber consists of a core surrounded by a silica cladding. The core material is silica to which a codopant is added to raise the refractive index. In standard passive fibers, germanium is typically used as codopant, however, in erbium doped fibers aluminum is a commonly used codopant material. The reason is that the wavelength dependent absorption and emission cross sections in (12.4), (12.5), and displayed in Fig. 12.3(left), depend on the core material, and it has been found that by using aluminum it is possible to obtain advantages with respect to the spectral properties of the amplifier.

In erbium doped fibers, the fiber is co-doped with erbium in addition to the index raising dopant, i.e. germanium/aluminum. With this material system amplification around 1555 nm is demonstrated. The erbium doped fiber is pumped with

either 1480 nm or 980 nm. Other active materials including ytterbium, neodymium, praseodymium or thulium may also be used. All of these have been demonstrated for applications at different wavelengths. As it is of relevance to this chapter, it is noted that ytterbium may be used in combination with erbium, referred to as Er:Yb. The resulting fiber is pumped using 980 nm, and the pump energy is first used to excite the ytterbium system and then energy is transferred to the erbium system. This material combination offers much higher pump absorption per unit length, and the constructed amplifier may provide more gain per unit length as compared to a fiber where erbium is the only rare earth dopant.

Fibers doped solely with ytterbium are often used to obtain very high output power amplifiers. The ytterbium system is pumped at 980 nm and provides gain from 1000 nm to 1100 nm. For further details regarding different material systems see e.g. [3, 4].

12.1.5 Characteristics

Polarization Dependence The polarization dependence of EDFAs is very weak, and as noted in [2] only becomes significant when many amplifiers are cascaded. The polarization dependent gain manifests itself when a signal with a well defined state of polarization saturates the amplifier. The spontaneous emission in the polarization state orthogonal to the polarization state of the signal then experiences a gain higher than the signal and the ASE in the same state of polarization as the signal. Consequently, the spontaneous emission in the orthogonal state increases faster than the spontaneous emission in the same state of polarization as the signal. A polarization dependent gain of 0.01 dB was reported by V.L. Mazurczyk and coworkers [8].

Time Response The response time of erbium is defined by the lifetime of the excited state ${}^4I_{13/2}$ in Fig. 12.2. This is a metastable state and has a rather long lifetime of approximately 10 ms, which is much longer than the time for one bit in a communication signal, for example a 40 Gb/s non return to zero signal where a bit slot equals 25 ps. Consequently, the performance of an amplifier is well predicted by considering the signal as a continuous wave. An additional benefit of the long lifetime of the metastable state is that the pump source may be rather noisy without any transfer of noise from the pump to the signal, assuming that the frequency of the pump noise exceeds the kHz response time of the erbium system, defined by the metastable lifetime.

It is noted that in a long chain of amplifiers, as for example used to amplify a WDM signal in a long haul communication system, the dynamic behavior may create transients that potentially could create detrimental power spikes [9].

Dispersion Whenever a material has a significant absorption or gain peak in the wavelength space, it may also have significant group velocity dispersion. This could

impact propagation of short pulses through the material. In addition, when designing a fiber laser aiming at a high repetition rate, the fiber length is critical. Consequently, in such amplifiers, a high erbium concentration is desired. In relation to this, it is noted that the erbium concentration has an upper limit due to effects such as clustering which results in reduced gain efficiency [10]. In [10] B. Pálsdóttir has reported concentration levels as high as 5×10^{25} ions/m³ to 10×10^{25} ions/m³ (corresponding to 75 to 150 dB/m absorption at 1530 nm).

Most often erbium doped fibers have normal group velocity dispersion (GVD) and can be used to compensate for anomalous dispersion in standard single mode fibers used in laser cavities. However, when the level of inversion changes in a pumped EDFA, the dispersion changes. In an example in [10], an un-pumped erbium doped fiber with an NA of 0.27, and a GVD equal to -40 ps/nm/km at 1550 nm, almost independent of wavelength from 1520 nm to 1620 nm is considered. When the fiber is pumped, the GVD changes significantly and may even be normal or anomalous, depending on the used pump power, for further details the reader is referred to [10].

12.1.6 Amplifier Performance

Amplified Spontaneous Emission A signal may be amplified in an EDFA only because of stimulated emission. However, stimulated emission is accompanied by spontaneous emission. The spontaneous emission propagates in both directions of the optical fiber. Obviously, the spontaneous emission generated in the first infinitesimal section of the optical fiber is amplified in the succeeding fiber sections. Thus, the power of the spontaneous emission at the output of the amplifier is referred to as amplified spontaneous emission (ASE). In the following, the forward propagating ASE is denoted ASE⁺ whereas the backward propagating ASE is denoted ASE⁻.

Compared to the equation for the signal, the propagation equation for spontaneous emission includes a source term. The propagation equations for forward and backward propagating ASE powers are:

$$\frac{dP_{ASE^\pm}}{dz} = \pm 2h\nu\gamma_e(\nu, z)B_0 \pm [\gamma_e(\nu_s, z) - \gamma_a(\nu_s, z)]P_{ASE^\pm}, \quad (12.12)$$

where $h\nu B_0$ is the power of one photon per unit bandwidth accumulated within bandwidth B_0 . By solving the propagation equation (12.12), the power of the ASE may be predicted.

Noise Figure The performance of an amplifier is characterized by its gain but equally important also by its noise performance. It is customary to quantify the noise performance of an amplifier by its degradation of the signal-to-noise ratio when the signal is amplified by the amplifier. The degradation of the signal-to-noise ratio is called the noise figure [3, 4]. The signal-to-noise ratio is defined as the squared mean

photon number $\langle n \rangle^2$ relative to the variance of the photon number V_n . At the output of an EDFA the mean photon number and the variance in photon number are:

$$\begin{aligned}\langle n \rangle &= Gn_0 + M\tilde{n}, \\ V_n &= G^2(V_0 - n_0) + Gn_0(2\tilde{n} + 1) + M\tilde{n}(\tilde{n} + 1),\end{aligned}\quad (12.13)$$

where G is the gain of the amplifier and n_0 is the mean signal photon number at launch. \tilde{n} is the noise photon number in the signal mode while M is the number of signal modes the detector is sensitive to, and V_0 the variance of the photon number at launch [3, 4]. Assuming the signal is monochromatic with frequency ν_s , the noise power in the signal mode is related to the noise photon number through $\tilde{P} = h\nu_s\tilde{n}B_0$, where B_0 is the bandwidth of the signal. It is noted that for the signal mode B_0 equals $1/T$, where T is the time duration of the signal. Assuming furthermore that $V_0 = n_0$, i.e. an input with a Poissonian probability distribution as for example a coherent state, then the electrical signal-to-noise ratio is given by

$$SNR_e = \frac{Gn_0}{2\tilde{n} + 1 + \frac{M\tilde{n}}{Gn_0}(\tilde{n} + 1)} \approx \frac{Gn_0}{2\tilde{n} + 1} \approx \frac{Gn_0}{2\tilde{n}}. \quad (12.14)$$

The first approximation is valid when the noise power is much less than the signal power, i.e. $Gn_0/M\tilde{n} \gg 1$, whereas the second approximation is valid when the added spontaneous emission is significant, i.e. $\tilde{n} \gg 1/2$. The ratio $\frac{Gn_0}{\tilde{n}}$ represents the optical signal-to-noise ratio at the output of the amplifier.

When the input signal is shot-noise limited and therefore has Poissonian statistics i.e. $V_0 = n_0$, the noise figure equals

$$F = \frac{SNR_{in}}{SNR_{out}} = \frac{2\tilde{n} + 1 + \frac{M\tilde{n}}{Gn_0}(\tilde{n} + 1)}{G} \approx \frac{2\tilde{n} + 1}{G}. \quad (12.15)$$

The approximation is valid if the output signal power exceeds the noise power, i.e. $Gn_0/M\tilde{n} \gg 1$, which is true in almost all cases. Expressing the added noise in terms of power, the noise figure in (12.15) may be rewritten as

$$F = \frac{2\tilde{P}}{Gh\nu B_0} + \frac{1}{G}, \quad (12.16)$$

where \tilde{P} is the spontaneously emitted power within the bandwidth B_0 and in the signal polarization, i.e., more specifically, \tilde{P} is the spontaneously emitted power in the signal mode.

Amplifier Efficiency The EDFA is characterized by its high gain efficiency of several dB of gain per mW of pump power. In addition, this high gain efficiency is obtained in amplifiers that are only tens of meters long. Moreover, the EDFA is also characterized by noise figures close to 3 dB for high gain amplifiers. Consequently, the EDFA is ideal as discrete amplifier, and a large effort has been made

to optimize such amplifiers by including ASE suppression filters, optical isolators [11], and dividing the amplifier into different wavelength bands, C band amplifiers, L band amplifiers etc. [12].

Optimum Length If the case is considered where the pump power is given and the signal power is fixed, then the signal gain increases as the fiber length increases, starting from very short lengths. However, for long lengths the inversion level can not be maintained and the gain drops because of absorption by the erbium as well as the intrinsic fiber loss, at the signal wavelength. Consequently, there exists an optimum length, see for example [3, 13].

Depletion For a given amplifier design, i.e. for an amplifier with a fixed length and a fixed pump power, the gain is constant for low input signal power levels. However, as the input signal power increases, the gain decreases and the output signal power approaches a constant value. When this happens, the amplifier is saturated. The input signal power level where the gain has dropped by 3 dB, is referred to as the saturation power level. This power level increases linearly with pump power and inversely with the emission cross section at the signal wavelength [2].

When the amplifier is operated in depletion, the inversion level drops and consequently the noise performance of the amplifier worsens. Figure 12.4 illustrates the noise figure of an amplifier as a function of input signal power. Two graphs are shown, the dashed curve is a simple amplifier design whereas the solid curve illustrates the noise figure obtained if additional noise reduction filters/isolators are inserted into the amplifier [11].

The spectral gain profile, which in effect is determined by the level of inversion of the amplifier, also depends on the input signal power level. Considering a fixed fiber length and a fixed pump power level, the level of inversion changes as the signal input power level increases because an increased signal power level uses the pump power over a shorter distance compared to the undepleted power level. As

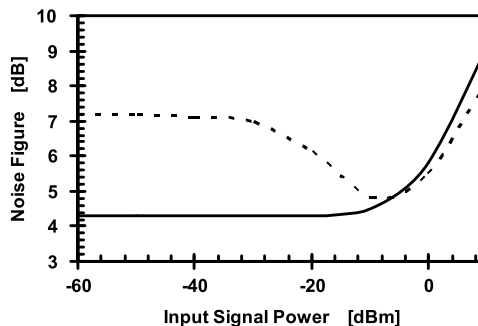


Fig. 12.4 Noise figure as a function of input signal power for a saturated amplifier. The signal wavelength is 1550 nm whereas the pump is at 1470 nm and a pump power of 60 mW has been assumed. The *dashed line* characterizes an amplifier without components to reduce ASE, the *solid line* represents the case with an isolator in the amplifier. Data adopted from [11]

a consequence of the change in inversion level, the spectral shape of the gain is modified.

12.1.7 Recent Applications

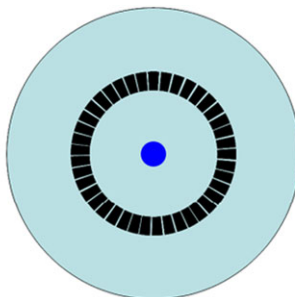
The EDFA has proven itself to be one of the most important components within optical communication systems. The amplifier is commercially available and applied in almost all optical communication system architectures, and most research on this type of commodity amplifiers is directed toward production parameters such as uniformity and consistency during fabrication and splicing to other fibers [10].

In addition to being used as an amplifier in communication systems, the EDFA is also widely used in fiber lasers. In the mid nineties of the last century focus was directed toward low power fiber lasers, including single frequency or narrow linewidth fiber lasers. However, within the last decade focus has been directed toward high power fiber lasers, continuous wave as well as short pulsed lasers, and new fibers for these applications are still being researched. These fibers include fibers that may handle high powers for example for high power delivery or fibers that may be used for pulse compression. Examples of such fibers include so called air clad fibers, higher order mode fibers, and rod like fibers. In the following a short description of the state-of-the-art regarding such erbium doped fibers is provided.

Air Clad Fibers In order to increase the output power of an EDFA it has been suggested to use a so-called air clad fiber, see Fig. 12.5 [10]. This fiber type consists of an inner core highly doped with erbium and surrounded by a cladding, defining an active single mode fiber for the signal. The cladding is surrounded by an additional cladding which is a ring of air holes. This defines a multimode waveguide with a high NA of 0.5 to 0.6 for the pump beam.

In [14] F. Koch and coworkers demonstrated a 30 dBm output power amplifier providing 40 dB gain from 1530 nm to 1568 nm. The result was achieved by combining a preamplifier pumped by 750 mW of pump power at 974 nm followed by an air clad erbium doped fiber pumped by 8 W at 976 nm. The length of the air clad fiber was 20 m.

Fig. 12.5 Illustration of an air clad fiber. In [14] the pump guide is 50 μm , with a cladding defined by a ring of air holes. The single mode core has a mode field diameter of 10 μm . The outer diameter of the fiber is 125 μm



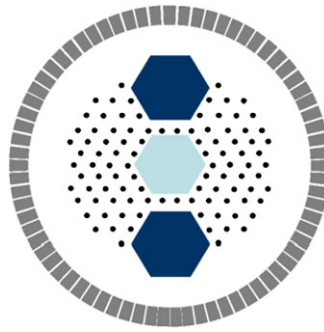


Fig. 12.6 Illustration of cross section of PM rod type fiber. The center of the fiber has a hexagonal structure of Yb/Al doping with a corner to corner distance of $70\ \mu\text{m}$. The pump waveguide has a diameter of $200\ \mu\text{m}$ and is surrounded by 90 air holes which define the cladding for the pump. Two stress zones, top and bottom, of the microstructured area, enable the polarization state of the light to be maintained during propagation [15]

Rod Type Amplifiers Air clad fibers may also be achieved with microstructuring of not only the air clad but also of the cladding of the single mode fiber [15]. By using microstructuring of the fiber it has been possible to enlarge the core as well as the cladding region and consequently increase the pump absorption.

In 2008 O. Schmidt and coworkers demonstrated an ytterbium doped polarization maintaining (PM) rod type amplifier [16]. A figure of the fiber cross section is shown in Fig. 12.6.

The center of the fiber had a hexagonal structure of Yb/Al doping with a corner to corner distance of $70\ \mu\text{m}$ resulting in a mode field area of $2300\ \mu\text{m}^2$. The pump waveguide had a diameter of $200\ \mu\text{m}$ and was surrounded by 90 air holes which defined the cladding for the pump. This resulted in an NA for the pump waveguide of 0.6 at $976\ \text{nm}$. The ratio of the pump waveguide cross sectional area to the active cross sectional area led to a small signal absorption of $30\ \text{dB/m}$ at $976\ \text{nm}$. The air clad was surrounded by a $1.5\ \text{mm}$ outer cladding. By using the rod type amplifier an output power of $163\ \text{W}$, with a degree of polarization of 85%, was reported [16].

Higher Order Mode (HOM) Fibers To achieve very high output power fiber lasers including high energy pulsed fiber lasers, a significant effort has been made to make large mode area fibers, for example using microstructured fibers. Such a fiber allows mitigation of nonlinear effects such as Raman scattering, Brillouin scattering, self phase modulation, and four wave mixing. Another promising approach relies on using HOMs in the optical fiber. Mode areas up to $3200\ \mu\text{m}^2$ at $1600\ \text{nm}$ have been demonstrated [17].

In 2007 S. Ramachandran and coworkers made a first demonstration of amplification in higher order mode fibers [18]. In their experiment they propagated a signal in the LP_{07} mode with an effective mode area of $2040\ \mu\text{m}^2$. The HOM fiber was doped with Yb and the signal was at $1083\ \text{nm}$ while the amplifier was pumped using conventional pumps at $975\ \text{nm}$ launched into the cladding surrounding the inner

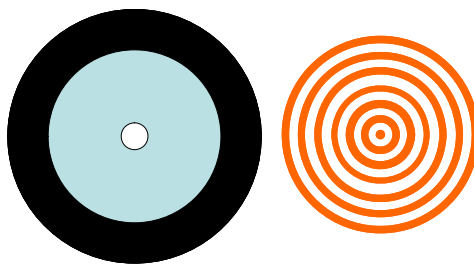


Fig. 12.7 *Left:* Cross section of HOM fiber used in [18], *right:* illustration of intensity distribution of the LP₀₇ mode propagating in the fiber. The fiber consists of a single-mode-like central core surrounded by a 40 μm inner cladding doped with Yb. Finally, this structure is surrounded by an outer cladding. In [18] the length of the HOM fiber was 4.75 m

core, see Fig. 12.7. A signal gain of 3.9 dB with a slope efficiency (rate of change of output power per absorbed pump power) of 62% was achieved for an input power of 6 W, while a signal gain of 8.2 dB and a slope efficiency of 48% were obtained for an input power of 1 W.

A significant challenge when working with high power lasers and amplifiers, for example in large mode area fiber amplifiers, is reported to be instability of the output beam [19, 20]. The reason for this is explained by thermal heating caused by the mismatch between the energy level to which the active material is excited by the pump and the energy level from which the active material emits a desired photon. The thermal heating causes mode coupling, and consequently the output beam jumps between different modes at the output. The threshold for the instability has been reported to be in the range from 100 W to 2500 W, and has been described by various research groups [13, 19–21].

In 2012 K.R. Hansen, M.M. Johansen, and coworkers provided a model for the instability [22–24]. They related the thermally induced mode coupling directly to the gain obtained in the active fiber. K.R. Hansen and co-workers reported a threshold for a 1030 nm signal to be around 400 W, independent of pump direction, core, and cladding size. They demonstrated that an efficient way to increase the threshold for thermal mode coupling is by reducing the diameter of the doping relative to the core diameter. In one example the threshold was increased from around 450 W to 1000 W by using a core diameter of 40 μm and a doping diameter of 20 μm .

Space Division Multiplexing Space division multiplexing (SDM) has been suggested as a means to increase the information capacity carried by individual fibers in optical communication systems, see Chap. 1. This has seeded a strong interest in multimode optical fiber amplifiers, erbium as well as Raman amplifiers. In SDM most attention has been devoted to the application of linearly polarized modes (LP-modes). However, using vectorial modes has also been suggested as a way to enhance the capacity carried by an optical communication system [25].

Extending the application of optical fiber amplifiers to SDM systems poses significant challenges, of which the most significant ones include mode dependent gain

and enhanced signal power fluctuations at the output of the amplifier. The latter is caused by random coupling among the propagating modes, for example as a result of bending and twisting of the fiber. This undesired mode coupling may be counteracted by the use of so-called MIMO equalization (Chap. 1). However, the MIMO equalization is associated with added complexity and requires complicated decoding techniques. Consequently, there is a strong incentive to design HOM amplifiers free of spatial mode dependent gain and free of mode coupling.

In 2012 Neng Bai [26] presented a wavelength division multiplexed SDM transmission experiment over 50-km few-mode fiber using the fiber's LP_{01} and two degenerate LP_{11} (LP_{11a} , LP_{11b} , respectively) modes. A few-mode EDFA was used to boost the power of the output signal before a few-mode coherent receiver. Neng Bai used a 6×6 time-domain MIMO equalizer to recover the transmitted data.

An in-line HOM EDFA was demonstrated in 2012 by Sleiffer et al. [27]. The authors demonstrated a capacity of 73.7 Tb/s, more specifically 57 Tb/s capacity plus overhead for forward-error correction. In the experiment, the information was transmitted through 119 km of few-mode fiber with a multimode EDFA after the first 84 km of transmission. The signal comprised 96 WDM channels each carrying 200 Gb/s. The few-mode fiber supported three spatial modes, the fundamental LP_{01} mode and two degenerate LP_{11} modes, LP_{11a} and LP_{11b} , and the inline multimode EDFA provided 18 dB gain per mode. The spectral efficiency was 12 b/s/Hz.

In 2015 R. Ryf and coworkers [28] demonstrated error free transmission of an SDM signal consisting of six spatial modes (LP_{01} , LP_{11a} , LP_{11b} , LP_{21a} , LP_{21b} , and LP_{02}). The total information, equal to 72 Tb/s, was transmitted over a distance of 179 km using an all-fiber span including three sections of passive fibers and two cladding pumped multimode-erbium doped fiber amplifiers. The work represented a first time demonstration of SDM transmission through multiple all-fiber amplified transmission spans.

As mentioned above, one of the major challenges when designing an HOM amplifier is that the gain for each mode differs. To circumvent this mode dependent gain Kang et al. in 2014 proposed a theoretical fiber design of an HOM EDFA, that provides gain for six modes all getting the same gain within 0.5 dB [29]. The fiber design is based upon a ring core multimode fiber which results in a large effective refractive index difference between the adjacent linearly polarized (LP) mode groups. This results in an efficient suppression of mode coupling. In [29] it is demonstrated that for a fiber length of 5 m, the maximum gain difference among the six mode groups is only 0.6 dB for the straight fiber, and 1.5 dB for a fiber with a bend radius of 5 cm. The predictions were shown for wavelengths in the range from 1530 nm to 1565 nm.

In 2015 C. Simonneau and coworkers [30] demonstrated a five mode amplifier (the LP_{01} , the degenerate mode-pair LP_{11a} and LP_{11b} , and the degenerate mode pair LP_{21a} and LP_{21b}). An average gain of 16.3 dB was achieved with a differential modal gain close to 5 dB. A noise figure of 5 dB for the best performing mode was achieved and a noise figure close to 8.8 dB for the worst performing mode. An intermodal crosstalk less than -8.9 dB between any two modes was reported.

To lift the degeneracy between the LP_{11a} , LP_{11b} and the LP_{21a} , LP_{21b} modes, J.-B. Trinel and coworkers demonstrated amplification in a few-mode EDFA [31].

An elliptical core was used to lift the degeneracy among modes belonging to the same mode group. An average gain of 18.6 dB was reported with 3.44 dB differential modal gain. A global modal crosstalk less than -9.4 dB (between any two modes) was obtained.

Finally, general aspects of few mode EDFAs with particular emphasis on crosstalk issues including a good compilation of work related to few mode EDFAs reported during the last few years is given in [32].

12.2 Raman Amplifiers

Within optical communication, Raman scattering in optical fibers may be applied to obtain amplification. This is achieved by simultaneously launching light at two frequencies separated by a frequency difference corresponding to the energy of phonons in the glass fiber. Hereby light is transferred from the high frequency beam, the pump, to the low frequency beam, the signal. The benefits of Raman amplification include:

- *Gain at any wavelength:* The Raman scattering process only depends upon the frequency shift between pump and signal, i.e. the phonon energy. In silica glass, this is 13 THz. Thus, the maximum signal gain is obtained 13 THz from the pump wavelength.
- *Wide bandwidth:* By launching multiple pump wavelengths a composite gain spectrum is obtained. In this way it is possible to broaden the gain bandwidth [33].
- *Distributed gain medium:* The Raman gain per unit length is relatively weak. Hence it is possible to counterbalance the loss along the transmission fiber. This distributed amplification has unique noise properties [34].
- *Intrinsic to silica:* Silica has a Raman efficiency that is sufficient to achieve gain such that a transmission fiber may be turned into an amplifier in itself, i.e. no special doping is necessary [35].

Figure 12.8 displays a generic design of a fiber Raman amplifier.

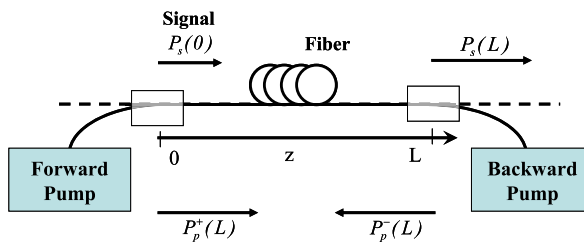


Fig. 12.8 Generic set-up of Raman amplifier. Forward and backward pump coupled together with the signal in wavelength dependent couplers. The signal is propagating in one direction only. Bi-directional signal transmission is not considered in detail in this chapter

In the simplest configuration only one pump is used and the amplifier is either forward or backward pumped. In short discrete amplifiers the amplifier may consist of multiple stages, gain equalization filters, isolators etc.

The amplifier fiber is characterized with respect to its Raman gain coefficient and the attenuation of the fiber at the pump and signal wavelengths. Finally, the dispersion properties may also be important for the amplifier performance when using multiple pump wavelengths, due to cross-coupling among pumps and between pumps and signals.

12.2.1 Propagation Equations

In the following an approach is presented which enables the prediction of the performance of a Raman amplifier based on the evolution of optical power. By neglecting spontaneous Raman scattering [36, 37] the propagation equation of the signal power is

$$\frac{dP_s}{dz} = g_R P_p P_s - \alpha_s P_s, \quad (12.17)$$

where g_R is the Raman gain coefficient, i.e. the difference between stimulated emission and absorption, P_p and P_s are the power of the pump and signal, respectively. P_p may be a sum of a forward P_p^+ and a backward propagating P_p^- pump beam. Finally, α_s is the intrinsic loss at the wavelength of the signal. In (12.17) the first term on the right hand side represents the difference between stimulated emission and absorption while the second term represents the intrinsic loss.

The equation for the forward and the backward propagating pump power is

$$\pm \frac{dP_p^\pm}{dz} = -\frac{v_p}{v_s} g_R P_p^\pm P_s - \alpha_p P_p^\pm, \quad (12.18)$$

where the first term on the right hand side represents depletion due to the signal and the second term on the right hand side describes the attenuation at the pump wavelength described by α_p .

Equation (12.17) may be solved analytically, and the signal gain, i.e. the signal output power relative to the signal input power, at the output end of a fiber of length L is

$$G(L) = \exp\left(\int_0^L g_R P_p(z) dz - \alpha_s L\right). \quad (12.19)$$

Assuming that the pump is independent of the signal and determined solely by the intrinsic fiber loss, i.e. the pump decays exponentially with the intrinsic fiber loss, the gain may be evaluated analytically. This situation is referred to as the undepleted pump regime. When the pump propagates in the positive z direction, the pump power is simply described through

$$P_p(z) = P_p^0 \exp(-\alpha_p z), \quad (12.20)$$

where P_p^0 is the launched pump power. In (12.20) the pump power is launched from the signal input end, and it is referred to as the co-pumped or the forward pumped Raman amplifier. Alternatively, if the pump power P_p^L is launched from the signal output end of the fiber, then the pump propagates according to

$$P_p(z) = P_p^L \exp(-\alpha_p(L - z)). \quad (12.21)$$

In (12.21) the pump propagates in the negative z direction or opposite to the signal, referred to as the counter-pumped, or the backward pumped Raman amplifier.

The signal gain in the undepleted forward-pumped Raman amplifier is given by

$$G(L) = \exp(g_R L_{eff} P_p^0) \exp(-\alpha_s L), \quad (12.22)$$

where L_{eff} is the effective fiber length for the Raman amplifier, in the following referred to as the Raman effective length, given by

$$L_{eff} = \frac{1 - \exp(-\alpha_p L)}{\alpha_p}. \quad (12.23)$$

In a typical transmission fiber, the loss at the pump wavelength is ~ 0.25 dB/km, and therefore the Raman effective length is about 17 km for a very long fiber. The gain of the undepleted backward pumped Raman amplifier is identical to the gain in (12.22) only with P_p^0 replaced by P_p^L .

Equation (12.22) shows that the gain in decibels increases linearly with the pump power in Watts. For a typical dispersion-shifted transmission fiber (with $A_{eff} \approx 75 \mu\text{m}^2$) and an optical fiber much longer than the effective length, the Raman gain is approximately 55 dB/W when the intrinsic signal loss is neglected and an unpolarized pump is assumed. This number represents a typical value for the gain efficiency of Raman amplifiers.

The undepleted pump approximation is very powerful and may be used to estimate the levels of gain and spontaneous emission, which we return to in Sect. 12.2.4. The criterion for validity of the undepleted model is that the loss rate of the pump should be dominated solely by the intrinsic loss [36], i.e.:

$$\frac{\nu_p}{\nu_s} g_R P_s \ll \alpha_p. \quad (12.24)$$

In a typical dispersion-shifted fiber with $\alpha_p \approx 0.057 \text{ km}^{-1}$ ($= 0.25$ dB/km) and $g_R \approx 0.7 \text{ (Wkm)}^{-1}$, the undepleted pump approximation is valid for $P_s \ll 80$ mW at any position along the fiber amplifier. It is noted that in (12.24) depletion due to spontaneous emission is neglected which is a valid approximation since the signal is typically orders of magnitude higher than the spontaneous emission.

The Raman gain is often quoted in terms of the On-Off Raman gain which is the ratio of the signal output power with the pump on to the signal output power with the pump off. The On-Off Raman gain is easily calculated in the undepleted pump regime by omitting the factor $\exp(-\alpha_s L)$ in (12.22).

Multiple Pump Wavelengths One of the advantages of the Raman amplifier is that pump sources at different wavelengths may be combined to form an amplifier with a wide bandwidth. In one example, gain over 92 nm was achieved in a 45 km long dispersion shifted fiber by combing a pump at 1453 nm (206 mW) with a pump at 1495 nm (256 mW) [33]. This property of the Raman process may be utilized not only to achieve a wide bandwidth amplifier but equally well to achieve a flat gain spectrum [37] or a flat noise spectrum [38].

When multiple pumps propagate together, the propagation gets slightly more complicated compared to the case when only one pump beam propagates since all pump and signal waves interact mutually with each other through Raman scattering. However, mathematically the propagation equations are easily extended to multiple pumps as described in [37]. In general, the Raman process transfers energy from shorter to longer wavelengths. As a consequence, to achieve a gain spectrum as wide and as flat as possible by using multiple pumps, more pump power should be launched within the shorter wavelengths of a pump spectrum. For the signals in a wideband amplifier the transfer of energy from shorter to longer wavelengths also impacts the signal-to-noise ratio differently from shorter toward longer wavelengths. In general longer signal wavelengths are favored compared to shorter signal wavelengths.

12.2.2 The Raman Gain Coefficient

From the previous discussion it is obvious that the Raman gain coefficient g_R is of key importance. Figure 12.9 displays the Raman gain coefficient for different fiber types. All have been measured using unpolarized pump light at a wavelength of 1453 nm. The pure silica fiber, labeled Pure-silica, which has a fiber core of silica and a cladding with a lower refractive index, displays the lowest gain coefficient of approximately 0.5 (W km)^{-1} at its peak. The dispersion compensating fiber, labeled

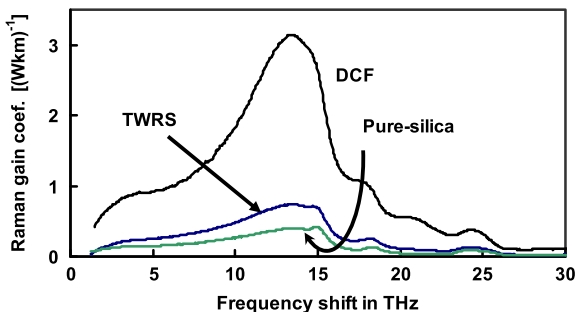


Fig. 12.9 Raman gain coefficient versus frequency shift between pump and signal for different fiber types. In the dispersion compensating fiber, DCF, the germanium content is higher and the effective area less than in the high capacity transmission fiber, the TrueWave Reduced Slope fiber, TWRS. The pure-silica fiber has no germanium in the core (data adopted from [36])

DCF, which has a small core area, a silica cladding, and a core of silica glass heavily doped with germanium, displays the largest Raman gain coefficient of approximately 3 (W km)^{-1} at its peak. The higher gain coefficient compared to the silica core fiber is caused by the germanium content and the effective area of the fiber [35, 39]. In typical high capacity transmission fibers, in Fig. 12.9 exemplified by an OFS TrueWave Reduced Slope fiber, labeled TWRS, the gain coefficient is close to 0.7 (W km)^{-1} at its peak. This fiber has a lower concentration of germanium compared to the dispersion compensating fiber and an effective area of approximately $75 \times 10^{-12} \text{ m}^2$.

The composite spectrum of any germano-silicate fiber with moderate fractional germanium concentration (less than 50%) [35], may be predicted and scaled according to the operating wavelength [39]. The gain coefficient depends on the wavelength and the spatial overlap between the pump and signal wave which vary with wavelength and the spatial power distribution of the pump and the signal, i.e. their mode profiles.

12.2.3 Characteristics

Raman Induced Kerr Effect In the Raman scattering process energy is not only transferred from the short wavelength beam, the pump, to the long wavelength beam, the signal, the pump also induces a phase shift of the signal with a wavelength dependence as shown in Fig. 12.10(right). The induced refractive index change is evaluated using the Kramers Kronig relation which is also valid in the case of Raman scattering, even though the scattering is a nonlinear phenomenon [40]. The reason for this is that the Raman scattering from the signal point of view may be considered as an effective first order nonlinearity.

Time Response Since the Raman scattering is an interaction between the pump, the signal, and molecular vibrations, the response time is not instantaneous. By taking the inverse Fourier transform of the frequency domain response, i.e. the gain spectrum as the imaginary part and the Raman induced refractive index as the real part, the Raman response in the time domain may be predicted. From this it is derived that the Raman response is in the order of a hundred femtoseconds [40].

Polarization Dependence The Raman gain spectrum of silica depends on the relative polarization state of the pump and signal beams. When they are co-polarized, the peak gain is approximately 10 times higher than when they are orthogonally polarized, see Fig. 12.10(left). This may cause a polarization dependent gain (PDG), which may lead to transmission impairments, for example, amplitude fluctuations, if the relative polarization of the pump and signal vary randomly. However, the small amount of PDG produced in Raman amplifiers consisting of long lengths of fibers is typically not as large as in bulk samples because of intrinsic polarization

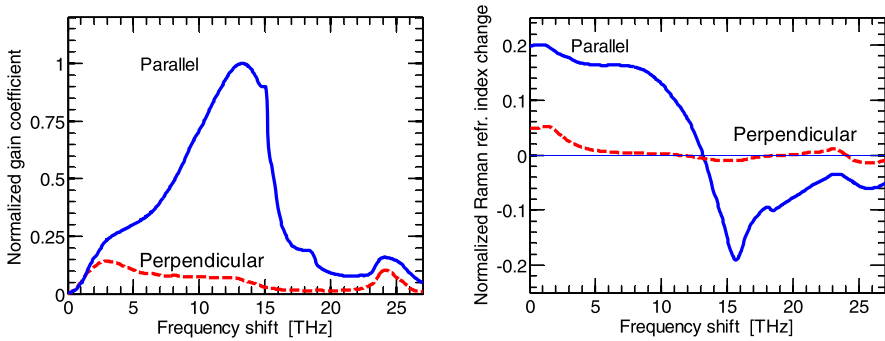


Fig. 12.10 *Left*: Raman gain coefficient, *right*: corresponding Raman induced refractive index change, both sets of curves as a function of the frequency shift between the pump and the signal. The data are from [41] using values for fused quartz. In *both figures two curves* are displayed, one labeled ‘parallel’, which is recorded by measuring the scattered light in the same linear state of polarization as the launched light, and one labeled ‘perpendicular’, which is recorded by measuring the scattered light in a state of polarization perpendicular to the launched light. The *curves* of the Raman gain coefficient are normalized to the peak gain coefficient for the parallel measurement whereas the Raman induced refractive index change is normalized relative to the intensity dependent refractive index of pure silica [42]

mode dispersion (PMD) of fibers. Even when the pump and signal polarizations are aligned at the input, PMD causes both polarizations to evolve differently and consequently changing the strength of the Raman coupling along the fiber. This produces an averaging effect that is larger if the pump and signals propagate in opposite directions [42–44]. Consequently, Raman amplifiers are typically backward pumped.

In [44] Lin and Agrawal consider a 10 km long forward, respectively backward, pumped Raman amplifier using 1 W of pump power. An average gain of 8 dB is achieved in the forward as well as the backward pumped amplifiers for a large PMD and assuming an unpolarized pump. If the pump and signal are polarized, the gain depends on the polarization states of the pump and the signal. In the absence of PMD the pump and the signal maintain their state of polarization. The intrinsic fiber loss is 2 dB, and the signal experiences a maximum gain of 17.6 dB, that is 19.6 dB On-Off Raman gain if the pump and the signal are copolarized. On the contrary, the signal experiences a loss of 1.7 dB when the pump and the signal are orthogonally polarized, corresponding to an On-Off Raman gain of 0.3 dB.

PMD has the effect of making PDG vanish as a consequence of averaging of Raman gain. This averaging is weaker in a forward pumped amplifier compared to a backward pumped amplifier. The reason for this is that in the forward pumped amplifier the pump and signal propagate along with each other whereas in the counter-pumped amplifier the pump and signal propagate toward each other and one time sequence of the signal experiences many different time sequences of the pump which leads to strong averaging. As a consequence there is a significant benefit in using a backward pumped amplifier configuration. In the latter case a PMD of $0.001 \text{ ps}/(\text{km})^{1/2}$ is sufficient to essentially eliminate the impact of PDG while under forward pumping conditions a PMD of $0.01 \text{ ps}/(\text{km})^{1/2}$ is needed for the sup-

pression of unwanted PDG effects [44]. However, the suggestion to increase the PMD leads to a trade-off since a significant amount of fiber PMD may in itself directly impair the signal transmission. Thus, other methods should be considered to reduce PDG. This includes simple measures to depolarize the pump light such as polarization-multiplexing two independent pump lasers emitting pump light at the same wavelength [45].

12.2.4 Amplifier Performance

Spontaneous Raman Scattering The signal gain is determined by stimulated emission and absorption. However, stimulated emission is accompanied by spontaneous emission which leads to a significant signal distortion. In the simplest model, propagation of amplified spontaneous emission within bandwidth B_0 is governed by:

$$\pm \frac{dP_{ASE^\pm}}{dz} = g_R P_p P_{ASE^\pm} + h\nu B_0 (1 + n_\nu) g_R P_p - \alpha_{ASE} P_{ASE^\pm}, \quad (12.25)$$

where P_{ASE^+} and P_{ASE^-} characterize the amplified spontaneous emission co-propagating or counter-propagating with the signal, respectively. h is Planck's constant, ν the frequency of the signal, B_0 the bandwidth of the signal, P_p , g_R the Raman gain coefficient, P_p the pump power, and $(1 + n_\nu)$ the thermal phonon population number. At room temperature $(1 + n_\nu) \approx 1.14$ [39], the sign (\pm) in front of $\frac{dP_{ASE^\pm}}{dz}$ in (12.25) accounts for power propagating in the forward (+) and backward (-) direction, respectively. The first term on the right hand side represents amplification of spontaneous emission, the second term represents generation of spontaneous emission, and the last term is the fiber attenuation at the wavelength of the ASE power described by the attenuation coefficient α_{ASE} .

It is noted that a factor of 2 may be included in the spontaneous emission (second term in (12.25)) to account for the fact that the signal typically occupies one state of polarization whereas the spontaneous emission is equally generated in both polarizations guided by single mode optical fibers.

At the signal output end ($z = L$) the noise power P_{ASE^+} , propagating with the signal in the signal polarization state, is given by

$$P_{ASE^+}(L) = G(L)(1 + n_\nu)h\nu_s B_0 g_R \int_0^L \frac{P_p(z)}{G(z)} dz, \quad (12.26)$$

where $G(L)$ is the Raman gain, i.e. the signal output power relative to the input power (see (12.22)).

The design of broadband amplifiers suitable for WDM applications requires consideration of several factors including interactions among multiple pumps, Rayleigh backscattering, and spontaneous Raman scattering [37].

Noise Figure The noise figure of the Raman amplifier is in general given by

$$F = \frac{2\tilde{n} + 1}{G}, \quad (12.27)$$

where $\tilde{n} = P_{ASE}/(h\nu B_0)$ is the number of ASE photons emitted into the signal mode, and G is the signal gain i.e. the signal output power relative to the signal input power.

When Raman scattering is used to convert a fiber into a distributed amplifier where the signal is amplified as it propagates through the transmission fiber, the degradation of the signal-to-noise ratio is typically much larger than the degradation produced by a discrete amplifier with a gain comparable to the On-Off gain of the Raman amplifier. That is, the noise figure of the pumped transmission span may be many dB worse than the noise figure of a typical discrete amplifier. However, the pumped transmission span is kilometers long. Thus, for comparative purposes the concept of an effective discrete amplifier with an effective noise figure and effective gain has been introduced [46] as outlined below.

Effective Noise Figure To understand the concept of an effective noise figure, the noise performance of the distributed amplifier is represented as the signal-to-noise ratio performance of a passive fiber of the same length as the distributed amplifier, followed by a discrete amplifier with a noise figure equal to the effective noise figure.

The effective noise figure, F_{eff} , is then $F_{eff} = F/T_{sp}$, where T_{sp} is the transmission loss through the passive fiber span from the signal input to the point where the effective discrete amplifier is located. For example, in a 100 km long fiber with an intrinsic loss of 0.2 dB/km, the effective noise figure in decibels is $F_{eff} \text{ (dB)} = F \text{ (dB)} - 20 \text{ dB}$.

When evaluating a distributed Raman amplifier, for example by comparing it with a discrete amplifier, it is important to make the comparison based on the same transmission length, and furthermore the comparison should be based on the same path average power for the signal and hence (presumably) equal nonlinear impairments. For these conditions it has been shown that the distributed Raman amplifier performs better than any other solution with discrete amplifiers. This is a very important result [36].

Pump Depletion In many realistic Raman amplifiers the rate at which pump power is lost exceeds the exponential decay rate originating from the intrinsic fiber loss. This pump depletion occurs when a significant fraction of the pump power is transferred to the signal via Raman amplification. Examples are the amplification of a large number of signal channels, the amplification of a very high power signal, or an amplifier providing a very high gain. Under such conditions the simple model described above is not appropriate.

If the effects of depletion cannot be ignored, the differential equations (12.18), which describe the propagation of the pump including depletion, need to be solved.

Neglecting spontaneously emitted Raman light the coupled propagation equations for the signal and pump are

$$\frac{dP_s}{dz} = g_R(P_p^+ + P_p^-)P_s - \alpha_s P_s, \quad (12.28)$$

$$\pm \frac{dP_p^\pm}{dz} = \frac{v_p}{v_s} g_R P_p^\pm P_s - \alpha_p P_p^\pm. \quad (12.29)$$

The ratio $\frac{v_p}{v_s}$ in the first term on the right-hand side of (12.29) accounts for the energy lost to the fiber in the form of phonons when pump light scatters to signal light. The sign accounts for the forward and backward propagating pump power, respectively.

The coupled equations in (12.28) and (12.29) may only be solved numerically. However, considering only the forward pumped amplifier and assuming that the losses at the signal and pump wavelengths are identical, the coupled equations may be solved by counting photons rather than calculating power. From this, the number of signal photons, n_s , is

$$n_s(z) = n_s(z=0) \frac{1+r}{r + G_R^{-(1+r)}} \exp(-\alpha z), \quad (12.30)$$

where r is the ratio of signal to pump photons at launch $r = n_s(z=0)/n_p(z=0)$, and G_R the undepleted On-Off Raman gain [47, 48].

Using real values for the intrinsic fiber loss, the effects of depletion must be evaluated numerically. Figure 12.11(left) illustrates the effect of pump depletion in a counter-pumped fiber Raman amplifier. In the figure the On-Off Raman gain versus signal input power is shown. The figure shows three curves, each calculated for fixed launched pump powers of 150 mW, 300 mW, and 600 mW. Figure 12.11(right) illustrates the effective noise figure corresponding to the cases in Fig. 12.11(left).

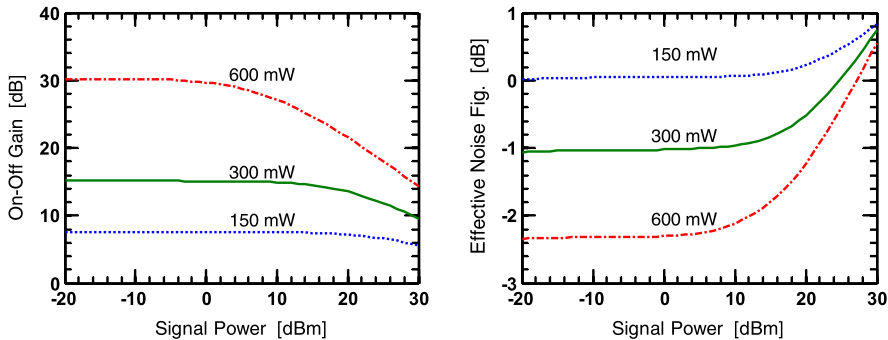


Fig. 12.11 On-Off Raman gain versus input signal power for three different pump power levels (*left*) and corresponding effective noise figures as a function of input signal power (*right*). Each data point is calculated for a 100 km long counter-pumped Raman amplifier. The signal wavelength is 1555 nm and the pump wavelength is 1455 nm. The loss coefficient at the pump wavelength is 0.25 dB/km creating an effective Raman length of 17 km, and the Raman gain coefficient is 0.7 (W km)^{-1} . Adapted from [36]

Figure 12.11(left) illustrates that the On-Off Raman gain decreases as the launched signal becomes sufficiently powerful. This is explained by the rate of loss of the pump. At any position along the fiber, the intrinsic fiber loss and the product of the signal power and the Raman gain coefficient determine the rate of loss of the pump. The latter describes the transfer of energy from the pump to the signal, i.e. the depletion of the pump due to the signal. For a sufficiently powerful signal, the rate of pump loss is enhanced by the depletion of the pump due to Raman interaction between pump and signal. As the pump is more quickly attenuated, the effective length of the Raman interaction is reduced, leading to a reduction in the On-Off Raman gain.

From Fig. 12.11(right) it is seen that the noise figure of the Raman amplifier increases as the pump is depleted. This is explained by the enhanced decay of the pump power due to pump depletion. As the length of the Raman interaction is reduced, the signal power is allowed to drop to a lower minimum value within the span, resulting in a higher span noise figure.

12.2.5 System Considerations

The Raman amplifier is a distributed amplifier in the sense that its efficiency is very low, and Raman amplification occurs in silica based transmission fibers without additional doping. It is in fact this distributed gain that enables improved noise properties since the gain is pushed into a transmission span, and consequently the signal power does not drop as much as it otherwise would have done if there were no amplification. However, the distributed gain also causes the average path signal power to be higher than in a system without distributed gain.

In typical high-capacity digital transmission systems, the signal power launched into a fiber span is adjusted to minimize the bit-error rate (BER) of the received signal. Often the BER does not only worsen at lower launched signal power due to accumulation of spontaneous emission, but also at higher launched signal power due to optical nonlinear impairments, including pulse distortion from self- and cross-phase modulation in addition to generated four-wave mixing waves and subsequent depletion of the generating waves. In general, the launched power is adjusted until the complicated interplay between the various sources of noise and pulse distortion results in a minimum BER [49].

In [34] K. Rottwitt and coworkers and in [49] J. Stark and coworkers demonstrated that the linear accumulation of spontaneous emission is worse in a discretely amplified system compared to a distributedly amplified system. However, the nonlinear impairments are slightly worse in a Raman amplified system compared to a discretely amplified system. The balance between the accumulated linear noise and the nonlinear noise defines the maximum achievable spectral efficiency which turns out to be higher in a distributed Raman amplified system compared to a lumped amplified system.

Impact of Rayleigh Scattering A major fraction of the intrinsic loss in an optical fiber is due to Rayleigh scattering. In this process light is scattered and a fraction of the optical power is lost. However, a small part of the scattered light is recaptured, half of which propagates in the same direction as the signal and the other half propagates in the opposite direction. In a Raman amplifier this causes a severe penalty as the signal and the backward propagating spontaneous emission are reflected figuratively an even or an odd number of times, respectively. Especially the Rayleigh reflected signal may cause a severe penalty because it appears as an echo of the signal exactly at the signal frequency. In distributed amplifiers the effect due to Rayleigh reflections may be more significant relative to what is found in a discretely amplified system because of the long distances over which gain is accumulated.

Rayleigh Reflected ASE When the Raman gain approaches 25 dB, the Rayleigh reflected ASE is comparable to the forward propagating ASE giving rise to a 3 dB increase in the total spontaneous emission in the signal mode [38]. Consequently, the electrical signal-to-noise ratio is expected to increase until it is impacted by Rayleigh reflections when the On-Off Raman gain exceeds 25 dB. At the same time the system performance is expected to degrade due to an increase in the signal effective length when more and more Raman gain is applied.¹ Thus, a Raman amplifier improves the system performance up to an upper limit in the On-Off Raman gain. In [38] the electrical signal-to-noise ratio is predicted in a 100 km long backward pumped Raman amplifier as a function of the On-Off Raman gain, and the optimum gain is shown to be close to 20 dB where the difference between the improvement due to an increased signal-to-noise ratio including Rayleigh reflected ASE and the increased signal effective length is close to 6.4 dB.

Rayleigh Reflected Signal The Rayleigh reflected signal power at $z = L$, denoted P_{dbr} , relative to the transmitted signal power $P_T = G(L)P_s^0$, is [36, 50]

$$\frac{P_{dbr}(L)}{P_T} = (B_R\alpha_s^R)^2 \int_0^L \frac{1}{G^2(\bar{z})} \int_{\bar{z}}^L G^2(x) dx d\bar{z}, \quad (12.31)$$

where $G(x)$ is the net gain and not the On-Off Raman gain, and $B_R\alpha_s^R$ is the recapture fraction of the fiber times the Rayleigh backscatter coefficient. Figure 12.12 illustrates the ratio of the double-reflected signal power, P_{dbr} , relative to the unscattered signal at the output-end of the transmission fiber, $P_T = G(L)P_s^0$.

The double reflected signal power is critical to the performance of a system applying distributed Raman amplifiers. One way to reduce the double Rayleigh scattering is to apply bidirectional pumping. In effect this splits the gain into two sections, one close to the input end and one close to the output end with a loss element in between. In an example of a 100 km long distributed Raman amplifier pumped to

¹The signal length L_{eff}^s is defined through the relation $P_s^0 L_{eff}^s = \int_0^L P_s(z) dz$, where P_s^0 is the signal power at $z = 0$. In the absence of gain and assuming that the loss rate at the signal and pump wavelength are identical, the signal effective length equals the Raman effective length in (12.23).

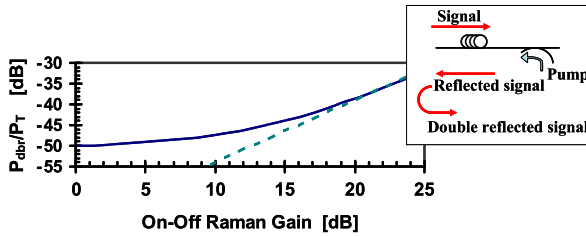


Fig. 12.12 Ratio of double reflected signal power to forward propagating signal power versus On-Off Raman gain in a 100 km long fiber. A peak Raman gain coefficient of 0.7 (W km)^{-1} and a loss coefficient for the signal and pump of $\alpha_s = 0.2 \text{ km}^{-1}$ and $\alpha_p = 0.25 \text{ km}^{-1}$ were used. The *dashed line* has the slope corresponding to a $G_R^{3/2}$ dependence. Data from [36]

transparency, this may lead to an improvement of 7 dB in the ratio of Rayleigh reflected power relative to the signal output power [36]. However, the use of forward pumping is accompanied by a noise contribution originating from coupling of noise in the pump to noise on the signal [51]. Consequently, most system demonstrations using Raman amplifiers have been based on backward pumped amplifiers only.

In the treatment above all considerations regarding polarization have been neglected. However, assuming that the distance between two successive reflections is long, the reflected power, that beats with the signal, needs to be multiplied by $5/9$ [52] to take the polarization dependence into account.

12.2.6 Recent Applications

Some of the first long haul transmission experiments were performed using Raman gain to counterbalance the intrinsic fiber losses. In 1988 Mollenauer and Smith used Raman gain to counterbalance the loss in a 4000 km transmission experiment [53]. The experiment was carried out in a loop configuration where each roundtrip in the loop was in fact a 41.7 km long Raman amplifier. The pump laser was a color center laser and the required pump power was 300 mW.

Due to the poor pump power efficiency work on Raman amplifiers was abandoned when the EDFA matured. However, in the mid to late 1990's high power fiber lasers became available and the interest in Raman amplifiers was renewed.

High Capacity Transmission The Raman amplifier applied as a distributed amplifier has proven its capabilities and found its way into applications, e.g. commercial 40 Gb/s products [54]. However, research on Raman assisted high capacity optical communication systems continues and has most recently been directed toward space division multiplexed systems.

In 2005 G. Charlet and coworkers demonstrated a 6 Tb/s experiment over a transatlantic transmission distance of 6120 km [55]. The capacity was obtained by

multiplexing 149 channels each carrying 42.7 Gb/s. The modulation format was differential phase shift keying. A spectral efficiency of 0.8 b/s/Hz was achieved. The repeaters in their experiment were based on distributed backward pumped Raman amplifiers each being 65 km long which was claimed to be the optimum length. 16 dB of Raman gain was provided by five pump sources operated at the wavelengths 1429 nm, 1439.5 nm, 1450 nm, 1461 nm, and 1493 nm.

In a system experiment a capacity of 25.6 Tb/s was demonstrated by A.H. Gnauck et al. [56] in 2008. In this experiment 160 channels, each containing two polarization multiplexed 85.4 Gb/s signals, were transmitted over 240 km. The experiment demonstrated a spectral efficiency as high as 3.2 b/s/Hz. The 240 km transmission was made up of three 80 km fiber spans. Raman amplification was added together with EDFAs to counterbalance loss from 1530 nm through 1600 nm. Each span included a dispersion-compensating fiber. Consequently, the Raman amplification enabled an increase in the received optical signal-to-noise ratio, and in addition, the Raman amplification was also used to simplify the design of the optical repeaters.

In 2009 G. Charlet and coworkers demonstrated a record in capacity times distance product of 41.8 Pb/s km [57]. The system capacity was 16.4 Tb/s obtained through wavelength multiplexing of 164 channels each carrying 100 Gb/s. The modulation format was 50 Gb/s polarization division multiplexed quadrature phase-shift keying. The signals were transmitted in a loop experiment, and after a total distance of 2550 km a BER better than 10^{-13} (using forward error correction) was achieved. Each loop contained a 65 km long bidirectionally pumped Raman amplifier using 25% forward and 75% backward pumping.

Space Division Multiplexing Like EDFAs, Raman amplifiers also hold great promise for application in SDM systems. The challenges in EDFAs related to mode dependent gain and mode coupling also exist when considering Raman amplifiers. However, the problem differs in the sense that the Raman amplification results from a direct overlap between the spatial modes of the pump and the signal, respectively. In 2011, Ryf and coworkers were the first to demonstrate mode-equalized optical amplification in few-mode fiber using Raman gain among multiple modes [58]. The Raman amplifier used was capable of providing 8 dB of gain with a gain variation among the 6 spatial signal modes of less than 0.5 dB. The signals were transmitted through 137 km few-mode fiber. One challenge described was to ensure an amplifier design with a minimum mode-dependent gain. In 2012 Ryf and coworkers demonstrated an improved transmission distance of 209 km using 10 dB of Raman gain, with focus on conditions for minimal mode-dependent gain in a few-mode fiber Raman amplifier [59]. They achieved a mode dependent gain less than 0.5 dB. Ryf and coworkers also predicted an optimum design of a multimode Raman amplifier providing 10 dB of Raman gain with a mode dependent gain less than 0.13 dB [60].

D. Jia and coworkers compared in 2012 the mode dependent gain in a Raman amplifier to that of an EDFA [61]. They demonstrated a smaller mode dependent Raman gain compared to a few-mode EDFA. Recently, 2014, J. Zhou presented an analytical model for minimizing the mode dependent gain in a multimode fiber Raman amplifier [62].

The issue of mode coupling in SDM systems has been addressed by various research groups, for example Winzer and Foschini [63] and Keang-Po Ho and co-workers [64]. Significant attention has been given to predictions of system performance in the presence of mode-dependent loss and distributed optical noise. The issue of mode coupling was also discussed in [65], where a theoretical model of a higher order mode Raman amplifier model was presented. The model included random mode coupling among spatial modes, and the impact of the number of the random couplings was described. Having a large number of random couplings, resulted in a maximum ratio of the squared mean modal signal output power relative to the variance in the modal signal output power.

Even though it is challenging to apply forward pumping, it is essential in bidirectional pumping/bidirectional transmission [66]. Demonstrations of bidirectional transmission using distributed Raman amplification has been demonstrated by employing single mode fibers [66], and recently also by using few-mode fibers. In 2015 Ryf and coworkers presented a first time demonstration of bidirectionally pumped Raman amplifier supporting 3 spatial modes (LP₀₁, LP_{11a}, LP_{11b}) [67]. They obtained a peak gain of 16 dB using 1.2 W of pump power, 6 dB from the pump propagating in the same direction as the signal and 10 dB from the pump propagating in the opposite direction relative to the signal. The fiber used was 70 km long and a mode dependent gain of 2 dB was achieved. The pump power was launched into the LP₁₁ mode. Error free transmission was obtained, with a Q larger than 7 dB for all 60 WDM channels from 1546 nm to 1562 nm, through a total transmission length of 1050 km.

Silicon Raman Photonics In addition to silica based fiber Raman amplifiers, Raman gain in silicon waveguides has attracted significant interest. In 2003 R. Claps and coworkers demonstrated amplification and lasing in silicon waveguides [68]. Since then the topic has attracted much attention. The reason for this is the fact that the Raman cross section is three to four orders of magnitude higher in silicon compared to silica. In addition, the effective area of the waveguide is about 100 times smaller in a silicon waveguide compared to a silica based fiber. In [68] a gain coefficient of 2×10^{-8} cm/W at a pump wavelength of 1427 nm was demonstrated. This should be compared with a gain coefficient for silica of $\sim 10^{-13}$ m/W. However, it is noted that the two gain coefficients just quoted for silicon and silica do not include the effective waveguide area. Finally, it is further noted, that in silicon the gain peak occurs at a frequency shifted by 15.6 THz and with a bandwidth of 105 GHz in contrast to a frequency shift (at maximum gain) of 13 THz for silica and a bandwidth of several THz.

Dimitropoulos and coworkers calculated the noise figure of silicon Raman amplifiers in the presence of nonlinear losses [69] and predicted a noise figure close to 4 dB. This result was obtained considering a 1 cm long waveguide pumped with 200 MW/cm², a gain coefficient of 15 cm/GW, and a nonlinear absorption of 0.7 m/GW. One of the main challenges is the nonlinear optical loss that competes with the Raman gain. Besides competing with the Raman gain, the nonlinear loss also affects the signal-to-noise ratio.

12.3 Parametric Amplifiers

Parametric amplification is based on four wave mixing which is a mutual interaction of four waves through the intensity dependent refractive index, also referred to as the optical Kerr effect. In a degenerate case the process involves three waves only [48]. The effect may classically be described as a third order nonlinear process as it depends on the electrical field raised to the third power [70]. The efficiency of the four wave mixing relies heavily on phase matching and thus the group velocity dispersion properties of the optical fiber are as important as the nonlinear strength of the fiber.

The development of high power lasers and highly nonlinear optical fibers with tailored group velocity dispersion properties have seeded renewed interest in fiber devices based on parametric processes. These devices include regenerators, wavelength converters and amplifiers, phase-sensitive as well as phase-insensitive ones.

In this section the focus is directed toward a general discussion of fiber optical parametric amplifiers (FOPAs). The section also includes a subsection on recent applications.

12.3.1 Propagation Equations

In the degenerate parametric amplifier, gain is obtained by transfer of energy between three propagating waves, the signal, the pump, and the so-called idler. That is, the energy goes from the pump to the signal and the idler. If the fiber is too long, the energy eventually goes back to the pump.

The propagation of signal, pump, and idler is governed by three coupled differential equations. If the amplitude of the signal power is A_s in units \sqrt{W} and likewise the amplitude of the pump is A_p and that of the idler is A_i , then the coupled equations are [48]

$$\begin{aligned}\frac{dA_p}{dz} &= \gamma [(|A_p|^2 + 2(|A_s|^2 + |A_i|^2))A_p + 2A_s A_i A_p^* \exp\{i\Delta\beta z\}], \\ \frac{dA_s}{dz} &= \gamma [(|A_s|^2 + 2(|A_i|^2 + |A_p|^2))A_s + A_i^* A_p^2 \exp\{-i\Delta\beta z\}], \\ \frac{dA_i}{dz} &= \gamma [(|A_i|^2 + 2(|A_s|^2 + |A_p|^2))A_i + A_s^* A_p^2 \exp\{-i\Delta\beta z\}],\end{aligned}\quad (12.32)$$

where the nonlinear strength γ is related to the intensity dependent refractive index, n_2 , and the effective area of the mode, A_{eff} , through $\gamma = 2\pi n_2 / (\lambda A_{eff})$, and where $\Delta\beta = \beta(\omega_s) + \beta(\omega_i) - 2\beta(\omega_p)$ is the linear phase mismatch between the three waves. The frequency of the pump, ω_p , signal, ω_s , and idler ω_i , waves are related through energy conservation. In the case of degenerate four wave mixing this is: $2\omega_p = \omega_s + \omega_i$. All three equations (12.32) are weighted by the same nonlinear strength. This is an approximation which is valid under the assumption that the

amplifier is operated at wavelengths where the idler, the pump as well as the signal are in the fundamental fiber mode and with a modest wavelength separation. In addition, the amplitude equations are all scalar which emphasizes the assumption that the signal, pump, and idler are all launched in the same state of polarization and remain in the same state of polarization throughout propagation through the amplifier. Finally, the nonlinearity is assumed to be instantaneous and only CW beams are considered. The amplitude equations (12.32) may be rewritten as power equations:

$$\begin{aligned}
 \frac{dP_p}{dz} &= -4\gamma P_p \sqrt{P_s P_i} \sin \theta, \\
 \frac{dP_s}{dz} &= 2\gamma P_p \sqrt{P_s P_i} \sin \theta, \\
 \frac{dP_i}{dz} &= 2\gamma P_p \sqrt{P_s P_i} \sin \theta, \\
 \frac{d\theta}{dz} &= \Delta\beta + \gamma(2P_p - P_s - P_i) \\
 &\quad + \gamma(P_p \sqrt{P_s/P_i} + P_p \sqrt{P_i/P_s} - 4\sqrt{P_s P_i}) \cos \theta,
 \end{aligned} \tag{12.33}$$

where $\theta = \Delta\beta z - 2\phi_p(z) + \phi_s(z) + \phi_i(z)$, with $\phi_p(z)$ being the phase of the pump, $\phi_s(z)$ the phase of the signal, and $\phi_i(z)$ the phase of the idler, while P_p , P_s , and P_i are the power levels of the pump, signal, and idler, respectively. By having a signal, idler, and pump present at the fiber input, and by adjusting the relative phase between them it is possible to control whether the signal is amplified or attenuated – this gives a possibility to create a phase sensitive amplifier. However, if the idler is zero at the input, then $\theta = \pi/2$ may be assumed since there is always a zero point field that satisfies this condition. Note, in (12.33) a zero point field is required if the idler is zero at the input, otherwise (12.33) is not capable of predicting any changes in power levels. In the absence of an idler the amplification becomes phase in-sensitive, and the gain defined as the output signal power relative to the input signal power may be expressed as:

$$G = 1 + \left(\gamma P_p L \frac{\sinh(gL)}{gL} \right)^2, \tag{12.34}$$

where L is the fiber length and g a phase parameter that describes the phase matching condition between the pump, idler, and signal according to

$$g^2 = [(\gamma P_p)^2 - (\kappa/2)^2] \quad \text{with } \kappa = \Delta\beta + 2\gamma P_p. \tag{12.35}$$

In (12.34) it is assumed that there is no pump depletion, and that there is no intrinsic fiber attenuation. The contribution $\Delta\beta$ to κ reflects the linear phase matching whereas the contribution $2\gamma P_p$ represents the nonlinear contribution to the phase matching, assuming that the pump power is much larger than both the power in the idler and the signal.

The gain exhibits a maximum when g is maximum, that is when $\kappa = 0$. At this point

$$G = 1 + (\sinh(\gamma P_p L))^2 \approx \exp(2\gamma P_p L)/4. \quad (12.36)$$

This gives a gain efficiency of: $G = 8.7\gamma P_p L - 6$, when the gain is measured in dB. For state-of-the-art highly nonlinear fibers a nonlinear strength γ of 11 (W km)^{-1} is realistic, and for a 500 m long fiber this gives a gain efficiency of $G = 47.9P_p - 6 \text{ dB}$ where G is in dB and P_p in units of W.

12.3.2 Amplifier Gain Spectrum

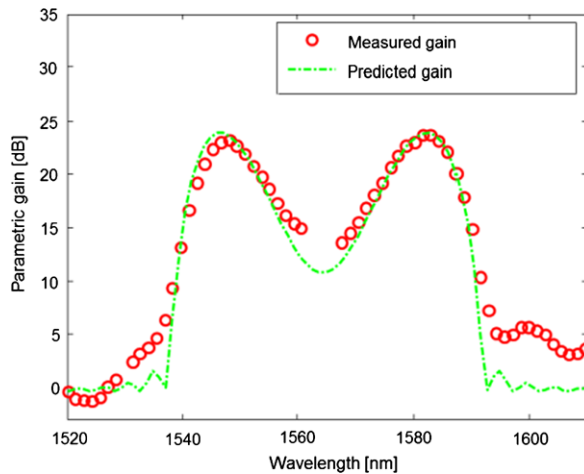
The operation wavelength and the bandwidth of the amplifier are related to each other through the group velocity dispersion properties of the optical fiber that is used in the amplifier. The reason for this is that the pump wavelength has to be chosen slightly longer than the wavelength where the group velocity dispersion of the amplifier fiber equals zero, and the bandwidth of the amplifier is determined by the phase-matching of the interacting waves. Mathematically this is seen from (12.34) and (12.35) in which the parameter κ may be expressed through the slope of the group velocity dispersion S at the wavelength where the group velocity dispersion equals zero, λ_0 , as:

$$\kappa = -(2\pi c/\lambda_0^2)S(\lambda_p - \lambda_0)(\lambda_p - \lambda_s)^2 + 2\gamma P_p, \quad (12.37)$$

where λ_s is the signal wavelength, and λ_p the pump wavelength.

Figure 12.13 illustrates the gain spectrum of a parametric amplifier. The fiber used was 500 m long with a zero dispersion wavelength at 1561 nm, a dispersion slope of $0.015 \text{ ps}/(\text{nm}^2 \text{ km})$, and a pump power of 29 dBm at 1564 nm. The fiber

Fig. 12.13 Parametric gain as a function of wavelength. Circles are measured data, the symmetric green line represents predicted data using (12.32)



had a nonlinear strength of 12.5 (W km)^{-1} . The figure illustrates measured as well as predicted data. The predicted data are found by solving the coupled amplitude equations as in (12.32).

By considering the bandwidth of the amplifier as the distance between the gain peaks, i.e. where $\kappa = 0$, it is evident, that the bandwidth of the amplifier is determined by the slope of the group velocity dispersion with respect to wavelength, the lower the slope the larger the bandwidth. In addition, the bandwidth does also depend on the nonlinear strength and the pump power.

12.3.3 Characteristics

Group Velocity Dispersion Fluctuations As described above the group velocity dispersion is a key parameter in four wave mixing that determines the efficiency and bandwidth of the four wave mixing. Fluctuations in the group velocity dispersion, caused for example by variations in the core diameter of the fiber, limit the parametric interactions. Several research groups have discussed the impact of fluctuations in the group velocity dispersion on the amplifier performance, and methods to measure the fluctuations have been proposed, direct measurements [71] as well as indirect ones [72].

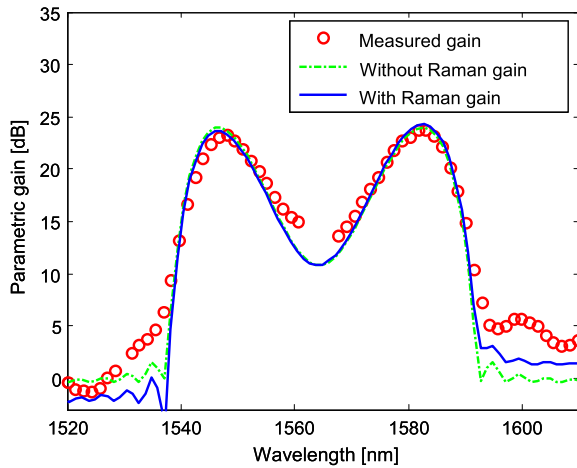
One approach to mitigate the effect of fluctuations in group velocity dispersion is to modify the fiber design. Bill P.-P. Kuo and coworkers demonstrated in 2012 [73] a dispersion stabilized design of a highly nonlinear fiber that enabled a first time demonstration of a parametric oscillator in the short wavelength near infrared wavelength band.

Response Time The response time is defined by the nonlinearity and hence for all practical purposes instantaneous. However, a small contribution to the nonlinearity comes from Raman scattering. This is not included in the propagation equations (12.32) and is typically neglected. However, since a strong pump is used to achieve amplification, Raman scattering does impact the gain spectrum. Figure 12.14 illustrates the impact due to Raman gain in the amplifier configuration used in Fig. 12.13.

Polarization Dependence The parametric interaction between the pump, the signal, and the idler is strongly polarization dependent. To get the maximum (degenerate) four wave mixing, the state of polarization of the pump, the signal, and the idler need to be aligned to each other. If they are orthogonal to each other, the (degenerate) four wave mixing is minimized. Experimentally, the polarization states of the beams may be aligned by adjusting the input state of polarization for maximum output signal power. However, if the state of polarization does not remain aligned during propagation, the efficiency is reduced.

Different approaches have been pursued to mitigate the polarization dependence, see for example M.E. Marhic [75]. In one approach the signal is split into a horizontal and a vertical component, and both components are then amplified equally in the

Fig. 12.14 Parametric gain as a function of wavelength, as in Fig. 12.13. Circles are measured data, the *symmetric green line* represents predicted data without taking Raman scattering into account, and the *blue unsymmetrical curve* represents predictions when Raman scattering is included [74]



designed FOPA. In another approach pump power at two different wavelengths are combined and the polarization state of each pump laser is orthogonal to each other.

12.3.4 Amplifier Performance

Spontaneous Emission Optical amplification is always accompanied by spontaneous emission and as a general rule, the signal-to-noise ratio can never be improved while the signal is being amplified. This is also the case for a parametric amplifier. However, since the amplifier may be operated as a phase sensitive amplifier, it may not be sufficient to characterize the amplifier based on its noise figure, as done for the EDFA and Raman amplifier, but it may also require information describing the phase change of the signal experienced during propagation.

The spontaneous emission in a parametric amplifier is more complicated to predict than the spontaneous emission in an EDFA or a Raman amplifier. One reason for this is the fact that the four wave mixing is described as an interaction between electrical fields and the intensity dependent refractive index, and consequently the phases of the interacting fields are important. In addition, Raman scattering may be important to include in the description, since spontaneous Raman scattering may seed spontaneous emission in four wave mixing. To predict the spontaneous emission in four wave mixing, one therefore has to use a numerical approach as for example described by S.M.M. Friss and coworkers [76]. However, by applying various approximations as for example neglecting Raman scattering and/or depletion it is possible to derive analytical results as described for example by Marhic [75], Voss [77], and McKinstrie [78].

Noise Figure McKinstrie and coworkers have calculated the noise figure of a degenerate (single-pumped) as well as a double-pumped parametric amplifier under

the assumption that the amplifier is unsaturated. McKinstrie et al. [78] have shown that the noise figure for a phase-insensitive parametric optical fiber amplifier equals

$$F = \frac{\langle n_0 \rangle (G^2 \langle n_0 \rangle + G(G - 1)(\langle n_0 \rangle + 1))}{(G \langle n_0 \rangle + (G - 1))^2}, \tag{12.38}$$

where G is the gain of the parametric amplifier and $\langle n_0 \rangle$ the mean number of input signal photons. For a high gain and a large signal input photon number the noise figure approximates

$$F = \frac{2G - 1}{G} \tag{12.39}$$

i.e a lower limit of 3 dB.

The phase sensitive parametric optical fiber amplifier is more interesting since it has a noise figure with a lower limit of 0 dB. However this is very difficult to achieve experimentally as for example spontaneous Raman scattering [78] seed undesired spontaneous emission and fluctuations in the pump power couple directly to the signal [79] causing detrimental impact on the amplifier performance. These issues have hindered an experimental demonstration of noise free amplification. However, in 2011 D.J. Blessing and coworkers demonstrated experimentally a noise figure of 1.1 dB [80].

Saturation Performance The results in Fig. 12.13 were obtained using a very low input signal power level of -30 dBm. As the signal input power is increased, the transfer of energy from the pump to the signal and idler happens over shorter distances and the analytical expression in (12.34) is no longer valid. However, the coupled equations (12.32) are still valid and may be used to predict the saturation behavior of the parametric amplifier numerically.

Using the same amplifier configuration as in Fig. 12.13, the saturation performance illustrated in Fig. 12.15 is found.

Fig. 12.15 Parametric gain versus wavelength shift between the pump and signal. The fiber was 500 m long with a zero dispersion wavelength at 1561 nm, a dispersion slope of $0.015 \text{ ps}/(\text{nm}^2 \text{ km})$, and a nonlinear strength γ of 11.5 (W km)^{-1} . A pump power of 29 dBm at 1564 nm was used. From [81]

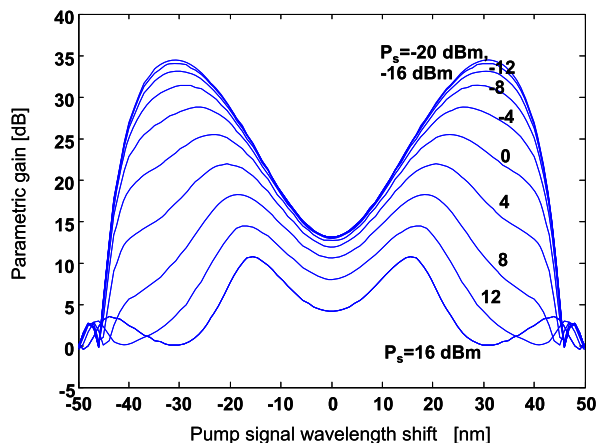
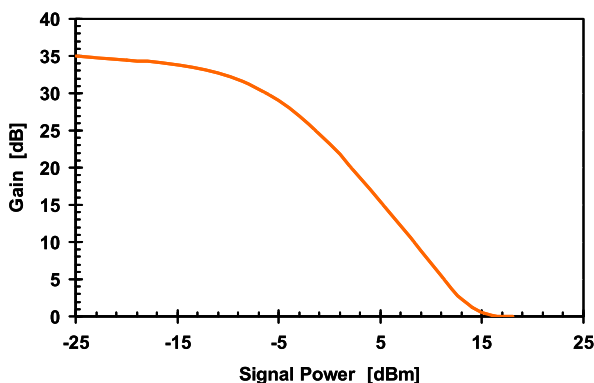


Fig. 12.16 Gain of parametric amplifier as a function of input signal power. The amplifier configuration is as in Fig. 12.13. From [81]



When the parametric amplifier is operated in depletion, its performance gets complicated. The spectral shape changes which is in contrast to the Raman amplifier. In addition, the bandwidth of the amplifier generally reduces.

Figure 12.16 shows the gain as a function of signal power. The calculations are performed for a 500 m long highly nonlinear fiber using $\gamma = 11.5 \text{ (W km)}^{-1}$ and a dispersion slope of $0.015 \text{ ps}/(\text{nm}^2 \text{ km})$, similar to Fig. 12.13 through Fig. 12.15. The signal wavelength is chosen where the undepleted gain is maximum. At low signal power levels the gain is constant whereas the gain has dropped by 3 dB for a signal input power of approximately -7 dBm . As the input signal power is increased further, the gain eventually drops to the background loss of the fiber.

12.3.5 Application Issues

Forward Pumping The only viable configuration for a parametric amplifier is as a forward pumped amplifier. Since its response time, for all practical purposes, is instantaneous, intensity fluctuations of the pump are transferred to the signal. In [82] it is shown that the noise figure may be dominated by contributions from pump-signal crosstalk. However, it is also shown that the ratio of pump induced noise and spontaneous emission depends on the FOPA gain and the signal power level.

Brillouin Scattering Due to the low efficiency of the parametric process, high pump power with a well-defined phase is required. This leads to the onset of Brillouin scattering and consequently limits the maximum achievable gain, see for example [83]. Various methods have been proposed to mitigate the impact of stimulated Brillouin scattering (SBS) including fiber designs with other index raising codopants, for example aluminum instead of germanium, the use of phase modulation, applying a strain along the fiber or applying a temperature gradient along the fiber. To date the most frequently applied SBS suppression method is to apply a phase modulation of the pump.

Fig. 12.17 Output power as a function of input power through a 500 m long fiber of the same type as in Fig. 12.13. The circles represent measurements applying 4 tone phase modulation (see details in the main text) to suppress Brillouin scattering while the diamonds represent the case when no phase modulation is applied, adapted from [84]

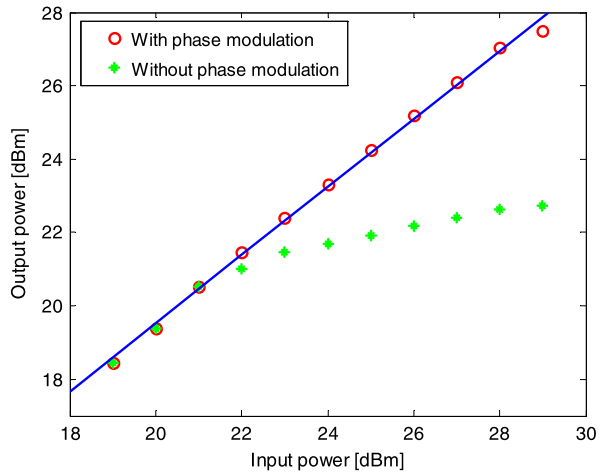


Figure 12.17 shows measurements of transmitted power through 500 meters of highly nonlinear fiber: When no measure has been taken to suppress SBS, the maximum input power is limited to approximately 22 dBm before the onset of SBS. However, when applying a phase modulation consisting of four tones (100 MHz, 330 MHz, 1 GHz, and 3 GHz), the onset of SBS is strongly reduced and only appears as the input pump power exceeds 30 dBm.

12.3.6 Recent Applications

The topic of parametric amplification has attracted more and more interest within recent years. This has been spurred by demonstrations of various applications and the development of high power fiber lasers and specifically tailored highly nonlinear, dispersion engineered optical fibers. The FOPA is an attractive device since it does not only provide phase-insensitive amplification but also phase-sensitive amplification, wavelength conversion, and has an almost instantaneous response as well. Some of the recent demonstrations of applications are highlighted below.

Wavelength Conversion Parametric amplifiers have great potential as devices for wavelength conversion since a signal is copied by nature to the idler as it propagates through the parametric fiber amplifier.

In 2008 J.M. Chavez Boggio and coworkers demonstrated a conversion over 700 nm [85]. In their experiment a 15 m long highly nonlinear fiber with very low fourth order dispersion was used. The nonlinear strength γ was 11.5 (W km)^{-1} , the wavelength of zero dispersion of the fiber was at 1582.8 nm, and the dispersion slope was $0.027 \text{ ps}/(\text{nm}^2 \text{ km})$. The third and fourth order dispersion coefficients were $0.038 \text{ ps}^3/\text{km}$ and $1.4 \times 10^{-5} \text{ ps}^4/\text{km}$, respectively. To achieve the wavelength conversion a pulsed pump was used. The peak power of each pump pulse was 200 W.

In one example a signal at 1312.6 nm was converted to 1999 nm with a conversion efficiency of 30 dB.

Waveform Sampling Another application of the parametric process is as sampling of a signal. To this end, in principle, a wavelength converter is designed, however, with the only purpose of generating an idler, which is a sample of the signal. The power generated in the idler is proportional to the power of the signal. P. Andrekson and coworkers have demonstrated this approach and have shown high resolution optical waveform sampling for example of a 640 Gb/s RZ data stream. The method may be further extended to include phase information in constellation diagrams [86, 87].

Broadband Amplification One of the benefits of parametric amplifiers is that their bandwidth is determined by the fiber design, more specifically, by the slope of the group velocity dispersion with respect to wavelength, and the available pump power. In addition, their operation wavelength is determined by the wavelength of zero group velocity dispersion around which the gain is symmetrically centered.

In 2008 Chavez Boggio and coworkers demonstrated a parametric amplifier providing gain over 81 nm [88]. The amplifier was a 2 pump configuration where each pump wavelength was located symmetrically around the zero dispersion wavelength of the fiber which was measured to be 1561.9 nm, with a dispersion slope of 0.025 ps/(nm² km). One pump wavelength was at 1511.29 nm while the other was at 1613.85 nm. Approximately 1 W of pump power was used in each of the two pump beams. The fiber in their experiment was 350 m long with a nonlinear strength $\gamma = 14$ (W km)⁻¹.

Regeneration Application of advanced modulation formats such as phase shift keying have proven superior transmission properties and enabled record high capacity transmission. However, one of the limiting factors in such high capacity communication links is signal distortion due to the nonlinear phase shift accumulated during transmission. Due to intensity fluctuations of the signal, a phase shift keyed signal may be distorted significantly since the induced nonlinear phase shift fluctuates in accordance with the intensity of the signal. However, by employing a method to reduce the intensity fluctuations, the phase distortion may be reduced leading to a further improved transmission capacity if phase shift keyed signals are used.

Such limiting capabilities may be obtained by the parametric amplifier. This is explained by the fast response time of the amplifier. By operating the amplifier in depletion, it is capable of acting as a limiter which means that the amplitude of individual pulses are nearly identical after propagation through the amplifier. As a consequence the accumulation of nonlinear phase shift on each pulse is the same, and each bit have less phase noise.

In 2009 C. Peucheret and coworkers [89] demonstrated experimentally that a parametric amplifier may be used as a limiter and consequently mitigate the accumulated phase penalties. In [89] the dynamic range of a 40 Gb/s return to zero differential phase shift keyed (RZ-DPSK) signal was enhanced. An optical signal-to-noise ratio penalty of 3.5 dB was reduced to 0.2 dB by using a single pumped

Table 12.1 Main characteristics of different types of fiber amplifiers

	EDFA	Raman	FOPA
Efficiency	dB per mW	60 dB/W	40 dB/W
Time response	10 ms	100 fs	instantaneous
Pump configuration	co/counter; arbitrary	(co) counter	co
Length	meters	kilometers	hundreds of meters
Operation wavelength	1530–1610 nm	13 THz separation between pump and signal	pump close to the wavelength of zero dispersion
Bandwidth	100 nm	13 THz +	(tens to hundreds of nm) depends on dispersion-slope and pump power
Polarization dependence	very weak	strong but mitigated when counter pumped	strong

FOPA with a 22 dB small signal gain. The improvement in the optical signal-to-noise ratio was experimentally found through BER measurements.

12.4 Conclusion

Optical fiber amplifiers are one of the most important fiber devices if not the most important ones. They have played a significant role in the evolution that has led to the high capacity optical communication systems which constitute one of the most important carriers in today's information society where fiber to the home is now becoming a reality around the globe.

This chapter has discussed (i) the EDFA which has been a research topic throughout the late 1980s but is still subject to research with respect to specific applications including high power amplifiers and amplifiers for space division multiplexed systems; (ii) the Raman amplifier which attracted significant research interest in the late 1990s of the last century which still continues with a particular focus on novel fiber types, novel materials, and systems applications incl. space division multiplexed systems, and finally (iii) the parametric amplifier which is currently a topic of research in many research groups around the world.

The aim of the chapter has been to highlight the fundamental physical mechanism of each amplifier type including a brief discussion of the important amplifier properties such as gain, noise performance, and noise sources, and finally to illustrate some of the most recent results with respect to the three amplifier types covered.

A short summary of the main characteristics of the discussed amplifiers is shown in Table 12.1.

References

1. A.T. Pedersen, L. Grüner-Nielsen, K. Rottwitt, Measurement and modeling of low wavelength losses of silica fibers and their impact at communication wavelengths. *J. Lightwave Technol.* **27**, 1296–1300 (2009)
2. P.C. Becker, N.A. Olson, J.R. Simpson, *Erbium-Doped Fiber Amplifiers, Fundamentals and Technology* (Academic Press, San Diego, 1999)
3. E. Desurvire, *Erbium Doped Fiber Amplifiers, Principles and Applications* (Wiley, New York, 1994)
4. M.J.F. Digonet, *Rare-Earth-Doped Fiber Lasers and Amplifiers*, 2nd edn. (Marcel Dekker, New York, 1993)
5. C.R. Giles, E. Desurvire, Modeling erbium-doped fiber amplifiers. *J. Lightwave Technol.* **9**, 271–283 (1991)
6. Y. Sun, J.L. Zyskind, A.K. Srivastava, Average inversion level, modeling, and physics of erbium-doped fiber amplifiers. *IEEE J. Sel. Top. Quantum Electron.* **3**, 991–1007 (1997)
7. P.F. Wysocki, J.R. Simpson, D. Lee, Prediction of gain peak wavelength for Er-doped fiber amplifiers and amplifier chains. *IEEE Photonics Technol. Lett.* **6**, 1098–1100 (1994)
8. V.L. Mazurczyk, J.L. Zyskind, Polarization dependent gain in erbium doped-fiber amplifiers. *IEEE Photonics Technol. Lett.* **6**, 616–618 (1994)
9. J. Nagel, The dynamic behaviour of amplified systems, in *Opt. Fiber Commun. Conf. (OFC'98)*, San Jose, CA, USA (1998), Techn. Digest, paper ThO3
10. B. Pálsdóttir, Erbium doped AirClad fibers for high power broad band amplifiers and single mode erbium doped fibers for high performance amplifiers and lasers, in *Opt. Fiber Commun. Conf. and Nat. Fiber Opt. Eng. Conf. (OFC/NFOEC'08)*, San Diego, CA, USA (2008), Techn. Digest, paper OTuJ1
11. O. Lumholt, J.H. Povlsen, K. Schüsler, A. Bjarklev, S. Dahl-Pedersen, T. Rasmussen, K. Rottwitt, Quantum limited noise figure operation of high gain erbium doped fiber amplifiers. *J. Lightwave Technol.* **11**, 1344–1352 (1993)
12. Y. Sun, A.K. Srivastava, J. Zhou, J.W. Sulhoff, Optical fiber amplifiers for WDM networks. *Bell Labs Tech. J.* **4**, 187–206 (1999)
13. M.N. Zervas, R.I. Laming, D.N. Payne, Efficient erbium-doped fiber amplifiers incorporating an optical isolator. *IEEE J. Quantum Electron.* **31**(3), 472–480 (1995)
14. F. Koch, B. Palsdóttir, J.O. Olsen, T. Veng, B. Flintham, R. Keys, 30 dBm wideband air-clad EDFA using two pump lasers, in *Opt. Fiber Commun. Conf. and Nat. Fiber Opt. Eng. Conf. (OFC/NFOEC'08)*, San Diego, CA, USA (2008), Techn. Digest, paper OWU3
15. K.P. Hansen, J. Broeng, P.M.W. Skovgaard, J.R. Folkenberg, M.D. Nielsen, A. Petersson, T.P. Hansen, C. Jakobsen, H.R. Simonsen, J. Limpert, F. Salin, High-power photonic crystal fiber lasers: design, handling and subassemblies, in *Fiber Lasers II: Technology, Systems and Applications*, San Jose, CA, USA (2005), Proc. SPIE, vol. 5709, pp. 273–283
16. O. Schmidt, J. Rothhardt, T. Eidam, F. Röser, J. Limpert, A. Tünnermann, K.P. Hansen, C. Jakobsen, J. Broeng, Single-polarization ultra-large-mode-area Yb-doped photonic crystal fiber. *Opt. Express* **16**, 3918–3923 (2008)
17. S. Ramachandran, J.W. Nicholson, S. Ghalmi, M.F. Yan, P. Wisk, E. Monberg, F.E. Dimarcello, Light propagation with ultralarge modal areas in optical fibers. *Opt. Lett.* **31**, 1797–1799 (2006)
18. S. Ramachandran, K. Brar, S. Ghalmi, K. Aiso, M. Yan, D. Trevor, J. Flemming, C. Headley, P. Wisk, G. Zyzdik, M. Fisteyn, E. Monberg, F. Dimarcello, High-power amplification in a 2040 μm^2 higher order mode, in *Photonics West*, San Jose, CA, USA (2007), Techn. Digest, PDP LBN-7
19. T. Eidam, C. Wirth, C. Jauregui, F. Stutzki, F. Jansen, H.-J. Otto, O. Schmidt, T. Schreiber, J. Limpert, A. Tünnermann, Experimental observations of the threshold-like onset of mode instabilities in high power fiber amplifiers. *Opt. Express* **19**(14), 13218–13224 (2011)

20. M. Karow, H. Tünnermann, J. Neumann, D. Kracht, P. Weßels, Beam quality degradation of a single-frequency Yb-doped photonic crystal fiber amplifier with low mode instability threshold power. *Opt. Lett.* **37**, 4242–4244 (2012)
21. A.V. Smith, J.J. Smith, Influence of pump and seed modulation on the mode instability threshold of fiber amplifiers. *Opt. Express* **20**, 24545–24558 (2012)
22. K.R. Hansen, T.T. Alkeskjold, J. Broeng, J. Lægsgaard, Thermally induced mode coupling in rare-earth doped fiber amplifiers. *Opt. Lett.* **37**, 2382–2384 (2012)
23. K.R. Hansen, T.T. Alkeskjold, J. Broeng, J. Lægsgaard, Theoretical analysis of mode instability in high-power fiber amplifiers. *Opt. Express* **21**(2), 1944–1971 (2013)
24. M.M. Johansen, K.R. Hansen, M. Laurila, T.T. Alkeskjold, J. Lægsgaard, Estimating modal instability threshold for photonic crystal rod fiber amplifiers. *Opt. Express* **21**(13), 15409–15417 (2013)
25. N. Bozinovic, Y. Yue, Y. Ren, M. Tur, P. Kristensen, H. Huang, A.E. Willner, S. Ramachandran, Terabit-scale orbital angular momentum mode division multiplexing in fibers. *Science* **340**(6140), 1545–1548 (2013)
26. N. Bai, E. Ip, Y.-K. Huang, E. Mateo, F. Yaman, M.-J. Li, S. Bickham, S. Ten, J. Liñares, C. Montero, V. Moreno, X. Prieto, V. Tse, K.M. Chung, A.P.T. Lau, H.-Y. Tam, C. Lu, Y. Luo, G.-D. Peng, G. Li, T. Wang, Mode-division multiplexed transmission with inline few-mode fiber amplifier. *Opt. Express* **20**(3), 2668–2680 (2012)
27. V.A.J.M. Sleiffer, Y. Jung, V. Veljanovski, R.G.H. van Uden, M. Kuschnerov, H. Chen, B. Inan, L. Grüner-Nielsen, Y. Sun, D.J. Richardson, S.U. Alam, F. Poletti, J.K. Sahu, A. Dhar, A.M.J. Koonen, B. Corbett, R. Winfield, A.D. Ellis, H. de Waardt, 73.7 Tb/s ($96 \times 3 \times 256$ -Gb/s) mode-division-multiplexed DP-16QAM transmission with inline MM-EDFA. *Opt. Express* **20**(26), B428–B438 (2012)
28. R. Ryf, N.K. Fontaine, H. Chen, A.H. Gnauck, Y. Jung, Q. Kang, J.K. Sahu, S.U. Alam, D.J. Richardson, Y. Sun, X. Jiang, L. Grüner-Nielsen, R.V. Jensen, R. Lingle Jr., 72 Tb-s transmission over 179-km all-fiber 6 mode span with two cladding pumped in-line amplifiers, in *Proc. 41st Europ. Conf. Opt. Commun.* (ECOC'15), Valencia, Spain (2015), paper ID 0634
29. Q. Kang, E. Lim, Y. Jun, X. Jin, F.P. Payne, S. Alam, D.J. Richardson, Gain equalization of a six-mode-group ring core multimode EDFA, in *Proc. 40th Europ. Conf. Opt. Commun.* (ECOC'14), Cannes, France (2014), paper P.1.14
30. C. Simonneau, P. Genevaux, G. Le Cocq, Y. Quiquempois, L. Bigot, A. Boutin, M. Bigot-Astruc, P. Sillard, G. Charlet, 5-Mode amplifier with low modal crosstalk for spatial mode multiplexing transmission with low signal processing complexity, in *Proc. 41st Europ. Conf. Opt. Commun.* (ECOC'15), Valencia, Spain (2015), paper ID 0131
31. J.-B. Trinel, Y. Quiquempois, A. Le Rouge, L. Garcia, J.-F. Morizur, G. Labroille, L. Bigot, Optical amplifier sharing for single mode fibers: amplification of 5 non-degenerate modes in an elliptical-core FM-EDFA, in *Proc. 41st Europ. Conf. Opt. Commun.* (ECOC'15), Valencia, Spain (2015), paper ID:0522
32. P. Genevaux, C. Simonneau, G. Charlet, Challenges in the design of few mode EDFAs, in *Opt. Fiber Commun. Conf.* (OFC'16), Anaheim, CA, USA (2016), Techn. Digest, paper Tu2I.2
33. K. Rottwitz, H.D. Kidorf, A 92 nm bandwidth Raman amplifier, in *Opt. Fiber Commun. Conf.* (OFC'98), San Jose, CA, USA (1998), Techn. Digest, post-deadline paper PD6
34. K. Rottwitz, J.H. Povlsen, A. Bjarklev, O. Lumholt, B. Pedersen, T. Rasmussen, Noise in distributed erbium doped fibers. *IEEE Photonics Technol. Lett.* **5**, 218–221 (1993)
35. J. Bromage, K. Rottwitz, M.E. Lines, A method to predict the Raman gain spectra of germanosilicate fibers with arbitrary index profiles. *IEEE Photonics Technol. Lett.* **14**, 24–26 (2002)
36. K. Rottwitz, A. Stentz, Raman amplification in lightwave communication systems, in *Optical Fiber Telecommunication IVA*, ed. by I. Kaminov, T. Li (Academic Press, San Diego, 2002). Chap. 5
37. H. Kidorf, K. Rottwitz, M. Nissov, M. Ma, E. Rabarrijoana, Pump interactions in a 100 nm bandwidth Raman amplifier. *IEEE Photonics Technol. Lett.* **11**, 530–532 (1999)

38. K. Rottwitz, Distributed Raman amplifiers, in *Raman Amplification*, ed. by G. Agrawal, C. Headley (Academic Press, San Diego, 2005). Chap. 3
39. K. Rottwitz, J. Bromage, A.J. Stentz, L. Leng, M.E. Lines, H. Smith, Scaling the Raman gain coefficient: applications to germanosilicate fibers. *J. Lightwave Technol.* **21**, 1652–1663 (2003)
40. K. Rottwitz, J.H. Povlsen, Analyzing the fundamental properties of Raman amplification in optical fibers. *J. Lightwave Technol.* **23**, 3597–3605 (2005)
41. R.W. Hellwarth, Third-order optical susceptibilities of liquids and solids. *Prog. Quantum Electron.* **5**(1), 1–68 (1977)
42. S. Popov, E. Vanin, G. Jacobsen, Influence of polarization mode dispersion value in dispersion-compensating fibers on the polarization dependence of Raman gain. *Opt. Lett.* **27**, 848–850 (2002)
43. Q. Lin, G.P. Agrawal, Statistics of polarization-dependent gain in fiber-based Raman amplifiers. *Opt. Lett.* **28**, 227–229 (2003)
44. Q. Lin, G.P. Agrawal, Vector theory of stimulated Raman scattering and its application to fiber-based Raman amplifiers. *J. Opt. Soc. Am. B* **20**, 1616–1631 (2003)
45. J. Bromage, Raman amplification for fiber communication systems. *J. Lightwave Technol.* **22**, 79–93 (2004)
46. P.B. Hansen, L. Eskildsen, A.J. Stentz, T.A. Strasser, J. Judkins, J.J. DeMarco, R. Pedrazzani, D.J. Digiiovanni, Rayleigh scattering limitations in distributed Raman pre-amplifiers. *IEEE Photonics Technol. Lett.* **10**, 159–161 (1998)
47. J. Auyeng, A. Yariv, Spontaneous and stimulated Raman scattering in long low loss fibers. *IEEE J. Quantum Electron.* **QE-14**, 347–352 (1978)
48. G.P. Agrawal, *Nonlinear Fiber Optics*, 3rd edn. (Academic Press, San Diego, 1995)
49. J. Stark, P. Mitra, A. Sengupta, Information capacity of nonlinear wavelength division multiplexing fiber optic transmission line. *Opt. Fiber Technol.* **7**, 275–288 (2001)
50. M. Nissov, K. Rottwitz, H. Kidorf, F. Kerfoot, Rayleigh crosstalk in long cascades of distributed unsaturated Raman amplifiers. *Electron. Lett.* **35**, 997–998 (1999)
51. C.R.S. Fludger, V. Handerek, R.J. Mears, Pump to signal RIN transfer in Raman fiber amplifiers. *J. Lightwave Technol.* **18**, 1140–1148 (2001)
52. M.O. van Deventer, Polarization properties of Rayleigh backscattering in single-mode fibers. *J. Lightwave Technol.* **11**, 1895–1899 (1993)
53. L.F. Mollenauer, K. Smith, Demonstration of soliton transmission over more than 4000 km in fiber with loss periodically compensated by Raman gain. *Opt. Lett.* **13**, 675–677 (1988)
54. D. Fishman, W.A. Thompson, L. Vallone, LambdaXtreme transport system; R&D of a high capacity system for low cost ultra long haul DWDM transport. *Bell Labs Tech. J.* **11**, 27–53 (2006)
55. G. Charlet, E. Corbel, J. Lazaro, A. Klekamp, R. Dischler, P. Tran, W. Idler, H. Mandoyan, A. Konczykowska, F. Jorge, S. Bigo, WDM transmission at 6 Tbit/s capacity over transatlantic distance, using 42.7-Gb/s differential phase-shift keying without pulse carver. *J. Lightwave Technol.* **23**, 104–107 (2005)
56. A.H. Gnauck, G. Charlet, P. Tran, P.J. Winzer, C.R. Doerr, J.C. Centanni, E.C. Burrows, T. Kawamishi, T. Sakamoto, K. Higuma, 25.6 Tb/s WDM transmission of polarization multiplexed RZ-DQPSK signals. *J. Lightwave Technol.* **26**, 79–84 (2008)
57. G. Charlet, J. Renaudier, H. Mardoyan, P. Tran, O.B. Pardo, F. Verluise, M. Achouche, A. Boutin, F. Blache, J.-Y. Dupuy, S. Bigo, Transmission of 16.4 bit/s capacity over 2550 km using PDM QPSK modulation format and coherent receiver. *J. Lightwave Technol.* **27**, 153–157 (2009)
58. R. Ryf, A. Sierra, R.-J. Essiambre, S. Randel, A. Gnauck, C.A. Bolle, M. Esmaelpour, P.J. Winzer, R. Delbue, P. Pupalakakis, A. Sureka, D. Peckham, A. McCurdy, R. Lingle, Mode-equalized distributed Raman amplification in 137-km few-mode fiber, in *Proc. 37th Europ. Conf. Opt. Commun.* (ECOC'11), Geneva, Switzerland (2011), PDP Th.13.K5
59. R. Ryf, R.-J. Essiambre, J. von Hoyningen-Huene, P.J. Winzer, Analysis of mode-dependent gain in Raman amplified few-mode fiber, in *Opt. Fiber Commun. Conf. and Nat. Fiber Opt.*

- Eng. Conf. (OFC/NFOEC'12)*, Los Angeles, CA, USA (2012), Techn. Digest, paper OW1D.2
60. R. Ryf, M.A. Mestre, S. Randel, C. Schmidt, A.H. Gnauck, R. Essiambre, P.J. Winzer, R. Delbue, P. Pupalaiakis, A. Sureka, Y. Sun, X. Jiang, D.W. Peckham, A. McCurdy, R. Lingle, Mode-multiplexed transmission over a 209-km DGD-compensated hybrid few-mode fiber span. *IEEE Photonics Technol. Lett.* **24**(21), 1965–1968 (2012)
 61. D. Jia, H. Zhang, Z. Ji, N. Bai, G. Li, Optical fiber amplifiers for space-division multiplexing. *Front. Optoelectron.* **5**(4), 351–357 (2012)
 62. J. Zhou, An analytical approach for gain optimization in multimode fiber Raman amplifiers. *Opt. Express* **22**(18), 21393–21402 (2014)
 63. P.J. Winzer, G.J. Foschini, Outage calculations for spatially multiplexed fiber links, in *Opt. Fiber Commun. Conf. and Nat. Fiber Opt. Eng. Conf. (OFC/NFOEC'11)*, Los Angeles, CA, USA (2011), Techn. Digest, paper OThO5
 64. K.-P. Ho, J.M. Kahn, Mode-dependent loss and gain statistics effects on mode-division multiplexing. *Opt. Express* **19**(17), 16612–16635 (2011)
 65. K. Rottwitz, K. Nielsen, S.M.M. Friis, M.A.U. Castaneda, Challenges in higher order mode Raman amplifiers, in *Opt. Fiber Commun. Conf. (OFC'15)*, Los Angeles, CA, USA (2015), Techn. Digest, paper Tu3C.6
 66. J. Bromage, J.-C. Bouteiller, H.J. Thiele, K. Brar, L.E. Nelson, S. Stulz, C. Headley, R. Boncek, J. Kim, A. Klein, G. Baynham, L.V. Jørgensen, L. Grüner-Nielsen, R.L. Lingle Jr., D.J. DiGiovanni, WDM transmission over multiple long spans with bidirectional Raman Pumping. *J. Lightwave Technol.* **22**(1), 225–231 (2004)
 67. R. Ryf, M. Esmaeelpour, N.K. Fontaine, H. Chen, A.H. Gnauck, R.-J. Essiambre, J. Toulouse, Y. Sun, R. Lingle Jr., Distributed Raman amplification based transmission over 1050 km few mode-fiber, in *Proc. 41st Europ. Conf. Opt. Commun. (ECOC'15)*, Valencia, Spain (2015), paper ID 0760
 68. R. Claps, D. Dimitropoulos, V. Raghunathan, Y. Han, B. Jalali, Observation of stimulated Raman amplification in silicon waveguides. *Opt. Express* **11**, 1731–1739 (2003)
 69. D. Dimitropoulos, D.R. Solli, R. Claps, O. Boyraz, B. Jalali, Noise figure of silicon Raman amplifiers. *J. Lightwave Technol.* **26**, 847–852 (2008)
 70. K. Rottwitz, P. Tidemand-Lichtenberg, *Nonlinear Optics, Principles and Applications* (CRC Press, Boca Raton, 2015)
 71. E. Myslivets, N. Alic, S. Radic, High resolution measurement of arbitrary-dispersion fibers: dispersion map reconstruction techniques. *J. Lightwave Technol.* **28**(23), 3478–3487 (2010)
 72. L.S. Rishøj, A.S. Svane, T. Lund-Hansen, K. Rottwitz, Quantitative evaluation of standard deviations of group velocity dispersion in optical fibre using parametric amplification. *Electron. Lett.* **50**(3), 199–200 (2014)
 73. B.P.-P. Kuo, J.M. Fini, L. Grüner-Nielsen, S. Radic, Dispersion-stabilized highly-nonlinear fiber for wideband parametric mixer synthesis. *Opt. Express* **20**(17), 18611–18619 (2012)
 74. D. Noordegraaf, M. Lorenzen, C.V. Nielsen, K. Rottwitz, Brillouin scattering in fiber optical parametric amplifiers, in *Proc. 9th Internat. IEEE Conf. Transparent Optical Netw. (ICTON'07)*, Rome, Italy (2007), vol. 1, pp. 197–200
 75. M.E. Marhic, *Fiber Optical Parametric Amplifiers, Oscillators and Related Devices* (Cambridge Univ. Press, Cambridge, 2008)
 76. S.M.M. Friis, K. Rottwitz, C.J. McKinstrie, Raman and loss induced quantum noise in depleted fiber optical parametric amplifiers. *Opt. Express* **21**(24), 29320–29331 (2013)
 77. P.L. Voss, K.G. Köprülü, P. Kumar, Raman-noise-induced quantum limits for $\chi^{(3)}$ nondegenerate phase-sensitive amplification and quadrature squeezing. *J. Opt. Soc. Am. B* **23**(4), 598.610 (2006)
 78. C.J. McKinstrie, S. Radic, M.G. Raymer, Quantum noise properties of parametric amplifiers driven by two pump waves. *Opt. Express* **12**, 5037–5066 (2004)
 79. Z. Tong, A. Bogris, M. Karlsson, P.A. Andrekson, Full characterization of the signal and idler noise figure spectra in single-pumped fiber optical parametric amplifiers. *Opt. Express* **18**(3), 2884–2893 (2010)

80. D.J. Blessing, C.J. McKinstrie, Z. Tong, C. Lundstrom, P. Andrekson, M. Karlsson, E. Tip-suwannakul, L. Gruner-Nielsen, H. Toda, B.J. Puttnam, Towards ultrasensitive optical links enabled by low-noise phase-sensitive amplifiers. *Nat. Photonics* **5**(7), 430–436 (2001)
81. K. Rottwitt, M.R. Lorenzen, D. Noordegraaf, C. Peucheret, Gain characteristics of a saturated fiber optic parametric amplifier, in *Proc. 10th Internat. IEEE Conf. Transparent Optical Netw. (ICTON'08)*, Athens, Greece (2008), vol. 1, pp. 62–64, paper Mo.D1.1
82. P. Kylemark, P.O. Hedekvist, H. Sunnerud, M. Karlsson, P.A. Andrekson, Noise characteristics of fiber optical parametric amplifiers. *J. Lightwave Technol.* **22**, 409–416 (2004)
83. J. Hansryd, P.A. Andrekson, M. Westlund, J. Li, P.-O. Hedekvist, Fiber-based optical parametric amplifiers and their applications. *IEEE J. Sel. Top. Quantum Electron.* **8**(3), 506–520 (2002)
84. M. Lorenzen, D. Noordegraaf, C.V. Nielsen, O. Odgaard, L. Gruner-Nielsen, K. Rottwitt, Brillouin suppression in a fiber optical parametric amplifier by combining temperature distribution and phase modulation, in *Opt. Fiber Commun. Conf. and Nat. Fiber Opt. Eng. Conf. (OFC/NFOEC'08)*, San Diego, CA, USA (2008), Techn. Digest, paper OML1
85. J.M. Chavez Boggio, J.R. Windmiller, M. Knutzen, R. Jiang, C. Bres, N. Alic, B. Stossel, K. Rottwitt, S. Radic, 730-nm optical parametric conversion from near- to short-wave infrared band. *Opt. Express* **16**, 5435–5443 (2008)
86. P.A. Andrekson, M. Westlund, H. Sunnerud, High resolution optical waveform sampling using fiber-optic parametric amplifiers, in *Proc. 2008 IEEE/LEOS Winter Topical Meeting*, Sorrento, Italy (2008), pp. 55–56, paper MB3
87. P.A. Andrekson, M. Westlund, Nonlinear optical fiber based high resolution all-optical waveform sampling. *Laser Photonics Rev.* **1**, 231–248 (2007)
88. J.M. Chavez Boggio, C. Lundström, J. Yang, H. Sunnerud, P.A. Andrekson, Double-pumped FOPA with 40 dB flat gain over 81 nm bandwidth, in *Proc. 34th Europ. Conf. Opt. Commun. (ECOC'08)*, Brussels, Belgium (2008), paper 3B5
89. C. Peucheret, M. Lorenzen, J. Seonne, D. Noordegraaf, C.V. Nielsen, L. Gruner-Nielsen, K. Rottwitt, Amplitude regeneration of RZ-DPSK signals in single pump fiber optic parametric amplifiers. *IEEE Photonics Technol. Lett.* **21**, 872–874 (2009)

Karsten Rottwitt received the M.Sc. degree in electrical engineering in 1990 from the Technical University of Denmark and in 1993 he received the Ph.D. degree also from the Technical University of Denmark. His Ph.D. was on soliton propagation through distributed erbium doped fiber amplifiers. After he finished his Ph.D. he continued in a Post Doc position until 1995, where he then moved to AT&T Bell Labs, NJ, USA. Here he worked within the Submarine Systems department. In 1998 Karsten Rottwitt joined the Fiber Research department within Lucent Technologies, Bell Labs, where he worked on Raman amplifiers. In 2000 Karsten Rottwitt moved back to Denmark, and from 2000 to 2002 he was at the University of Copenhagen. In 2002 he got a position as associated Professor at the Technical University of Denmark, where he is now heading activities in fiber optics, including fiber devices and nonlinear effects in fibers. He has been involved with organizing several international conferences including program chair for the OSA topical meeting on Nonlinear Photonics and general chair of the OSA Topical meeting on Sensors. He holds several patents, has authored and co-authored more than 140 journal and conference papers, and two book chapters.

Chapter 13

Hybrid Photonic Integration: Components and Technologies

Ziyang Zhang and Arne Leinse

Abstract This chapter introduces the background and the significance of the technology developed for the hybrid photonic integration. Two platforms are chosen as representative examples, i.e., the polymer motherboard integration platform (Polyboard) and the silicon nitride/silicon dioxide (TriPleX™) PLC platform. On these platforms, both the individual components and the hybrid integration technology have witnessed fast advancement in the last decade, complementing the well-established InP-monolithic platform and the silicon-on-insulator (SOI) platform by providing pragmatic, flexible and cost-effective solutions to various challenges in the photonic applications. Starting from the basic waveguides and related passive elements, the chapter goes on to discover the unique coupling/bonding methods with fibers, light sources and photo detectors. In the end, optical assemblies and modules are demonstrated in application areas covering Telecom, Datacom, microwave photonics and bio-medical sensing, wherein the technology for the hybrid photonic integration technology is well proven and validated.

13.1 Introduction

Photonic integration endeavors to bring multiple optical functions into a compact device with small footprint, lower power consumption and reliable performance, analogous to electronic integration. However, contrary to the situation in the electronic industry where silicon CMOS dominates, photonic devices nowadays do not tend to converge and to rely only on one material system. Light sources are mostly realized using III–V semiconductor-related materials. Modulators have been dominated by lithium niobate (LiNbO₃), but gradually overtaken by InP and silicon-

Z. Zhang (✉)

Leibniz Institute for Astrophysics (AIP), An der Sternwarte 16, 14482 Potsdam, Germany
e-mail: zzhang@aip.de

A. Leinse

LioniX BV, P.O. Box 456, 7500 AL, Enschede, The Netherlands
e-mail: a.leinse@lionixbv.nl

on-insulator (SOI) based platforms. Detectors are fabricated using III–V semiconductors and Si–Ge materials. Waveguide networks, filters, and other passive optical functions can be realized in low-cost platforms such as polymer, silica and silicon nitride planar lightwave circuits (PLCs). To pursue a general and pragmatic approach, hybrid photonic integration attempts to select individual components that are designed, fabricated and optimized on their best-suited material platforms and assemble them in a common motherboard. These components can be tested prior to the assembly. In this way, high freedom of device performance and yield optimization can be realized, leading to a relatively high cost-efficiency. With the help of automatic alignment tools and machine-assisted assembly equipment, hybrid integration can offer the benefits of micro-optical packaging at reduced costs, potentially higher overall module performance and higher reliability. Its versatility makes it particularly useful for low to medium production volumes.

This chapter introduces the background of the hybrid photonic integration technology, focusing on a polymer and a silicon nitride/silicon dioxide (TriPleX™) PLC based platform, respectively. The waveguides, passive components and coupling methods with fibers, light sources and photo detectors are presented, followed by the demonstration of various optical assemblies and modules, including passive wavelength multiplexers, optical line terminals (OLT) for wavelength division multiplexed passive optical networks (WDM-PON), optical network unit (ONU), colorless dual-polarization coherent receiver, as well as miniaturized optical beam forming networks for microwave photonics and optical assemblies for medical sensing applications.

13.2 Passive Photonic Components

13.2.1 Polymer Waveguides

A typical buried polymer channel waveguide is shown in Fig. 13.1(a). The refractive index of core and cladding material usually features values from 1.4 to 1.7, depending on the material compositions. To avoid geometrical birefringence effects, the waveguide core is kept as a square shape ($W = H$). The TE mode field (E_x) is shown in Fig. 13.1(b). The typical mode field diameter (MFD) can range from a few to over 10 μm , depending on the waveguide refractive index contrast. Since polymer materials in general possess a strong thermo-optic effect and at the same time very low thermal conductivity, they are ideal candidates for realizing power-efficient thermo-optic tunable devices [1–3]. The heater electrode placed beneath the waveguide can provide more uniform heating conditions in the waveguide region but also protect the electrode from environmental disturbances that can lead to electrical failure [4–6]. In addition, air trenches can be added as extra thermal buffers to isolate the thermal energy, reduce the thermal crosstalk and improve the tuning efficiency of the targeted device. Studies have shown that the air trenches are also helpful in

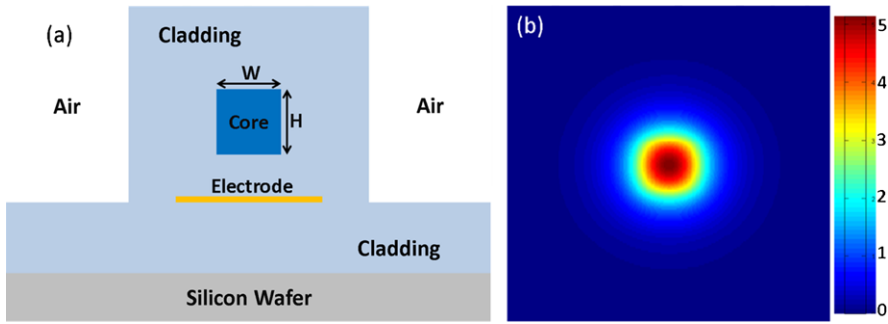


Fig. 13.1 (a) Schematic of buried polymer channel waveguide with imbedded electrode and air trenches, (b) TE waveguide mode profile (E_x field component)

suppressing stray light in the circuit, i.e., the optical crosstalk can also be reduced [7, 8].

The fabrication follows a typical “bottom-up” approach in the standard wafer production. Silicon wafers are usually taken as substrate, though the technology is also applicable on glass plates, ceramic and InP wafers, and others. The substrate surface is first primed with a proper adhesion promoter. A layer of polymer cladding material is then spin-coated on top and cured under strong UV illumination. The thickness of the cladding can be controlled by the spin-coating conditions such as rotation speed and time. To reach a precision of a few nanometers, subsequent low-rate reactive ion etching can be used.

Metal can be deposited directly on top of the polymer cladding by sputtering or thermal evaporation. A positive lithography process followed by wet chemical etching can be used to structure the metal. With subsequent spin-coating and curing processes, the metal stripes are imbedded inside the polymer.

To pattern the waveguide core, photo resist can be used as etching mask. However, since the main plasma chemistry for polymer etching is oxygen based, the photo resist mask will also be consumed. To improve the etching selectivity, defined as the ratio between the etching rate of the polymer material and that of the mask, a metal layer can be patterned on top of the waveguide core by a “lift-off” process.

During the “lift-off” process, metal is first deposited on top of the patterned photo resist, which is then washed away by an organic solvent such as Acetone and 1-Methyl-2-Pyrrolidone (NMP). Only the metal that is deposited in the openings remains. This process requires that the polymer material beneath must be chemically resistant against the organic solvent and that its chemical, physical and optical properties should not be adversely affected.

With pure oxygen plasma etching and metal masks such as nickel, chromium or titanium, the etching selectivity can reach values beyond 500. Trenches and slots with 50- μm depth can therefore be etched in polymer by using a thin layer of metal that is only 100 nm thick.

Once the waveguide core is etched, the metal mask can be removed by selective wet chemistry, dry plasma etching, or ion milling. A scanning electron microscopy

Fig. 13.2 SEM image of polymer waveguide core, etched by pure oxygen plasma

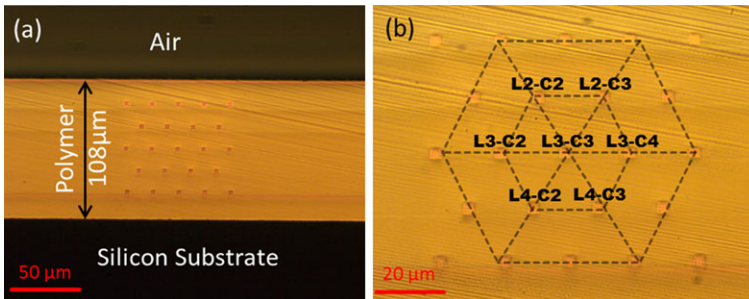
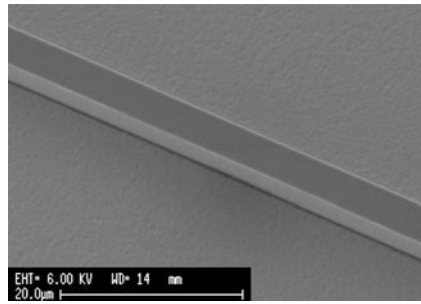


Fig. 13.3 Microscope images of 5-layer multi-core polymer waveguides, illuminated through cross-section: (a) broader view showing total thickness of polymer layers on silicon substrate, (b) detailed view showing alignment of waveguides on the lattice

(SEM) image of an etched polymer waveguide core is shown in Fig. 13.2. To finish the waveguide structure, the second cladding layer is spin-coated on top and cured. The wafer can be further structured by using a metal mask, and deep trenches can be etched.

The fabrication process can be repeated to stack up the polymer waveguide layers into a multi-core structure [9], as shown in Fig. 13.3, for realizing high density, three-dimensional photonic integrated circuits (PICs). The total thickness of the polymer layers is measured to be 108 μm , within which the bottom cladding is 20 μm directly above the silicon substrate, the inter-waveguide-layer distance is 17.3 μm (4 times), and the upper cladding is around 15.7 μm below air. The waveguide loss among all 5 layers is below 1 dB/cm, and the crosstalk between the waveguides at the 20- μm hexagonal lattice is better than 40 dB after a propagation distance of 3.8 cm.

To increase the waveguide index contrast and bring down the device footprint, amorphous silicon nitride (SiN_x) can be deposited on polymer cladding by low-temperature plasma enhanced chemical vapor deposition (PECVD) as waveguide cores [4, 10–12], and SiN_x /polymer heterogeneous waveguides can then be created. Figure 13.4 shows a widely tunable filter based on a grating-assisted co-directional coupler comprising two parallel asymmetric waveguides, one with SiN_x core and the other with polymer core [12]. Long-period gratings are formed along the SiN_x

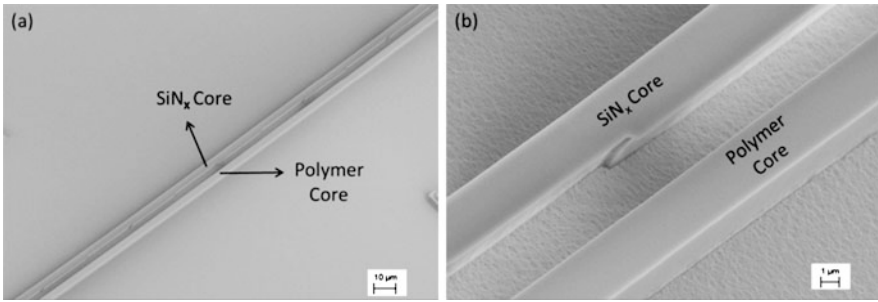


Fig. 13.4 SEM photos of heterogeneous waveguide coupler: (a) far view and (b) detailed view showing grating

waveguide to provide phase matching and wavelength filtering. The coupler is differentially thermally tunable. The temperature gradient distribution, introduced by a pair of offset micro-heaters, can either red- or blue-shift the filter curve, depending on which waveguide appears “hotter”. A total tuning range of 82 nm has been experimentally demonstrated [12].

13.2.2 TriPleX Waveguides

The TriPleX technology which is described in detail also in [13] is based on alternating and highly stable silicon oxide (SiO_2) and silicon nitride (Si_3N_4) layers [14, 15] and offers extremely low propagation loss and a very broad wavelength window for linear and non-absorbing transmission. The layers are precisely controlled to ensure reliable and accurate waveguide properties and modal shapes. The fabrication equipment and materials are CMOS-compatible. The TriPleX platform is ready for foundry services which enable low-cost and high-volume production.

The well-established low-pressure chemical vapor deposition (LPCVD) technology is applied to generate highly transparent crystalline films. The transparency window of both materials allows for the realization of low-loss waveguides over a wide wavelength range (405 nm to 2.35 μm). Propagation losses as low as 5×10^{-4} dB/cm have been reported. A specific tapering technology is developed for on-chip, low-loss (<0.1 dB) spot size converters, allowing for combining efficient fiber to chip coupling with high-contrast waveguides required for increased functional complexity as well as for hybrid integration with other photonic platforms such as InP and SOI.

TriPleX technology combines good integration potential with high design flexibility, allowing for the tailoring of waveguide properties [16]. Three commercially available basic waveguide geometries are provided which can be obtained by modifying individual steps in the generic fabrication flow [17]. The geometries are categorized by their shape: box shell (I), double stripe (II), and filled box (III). Type II

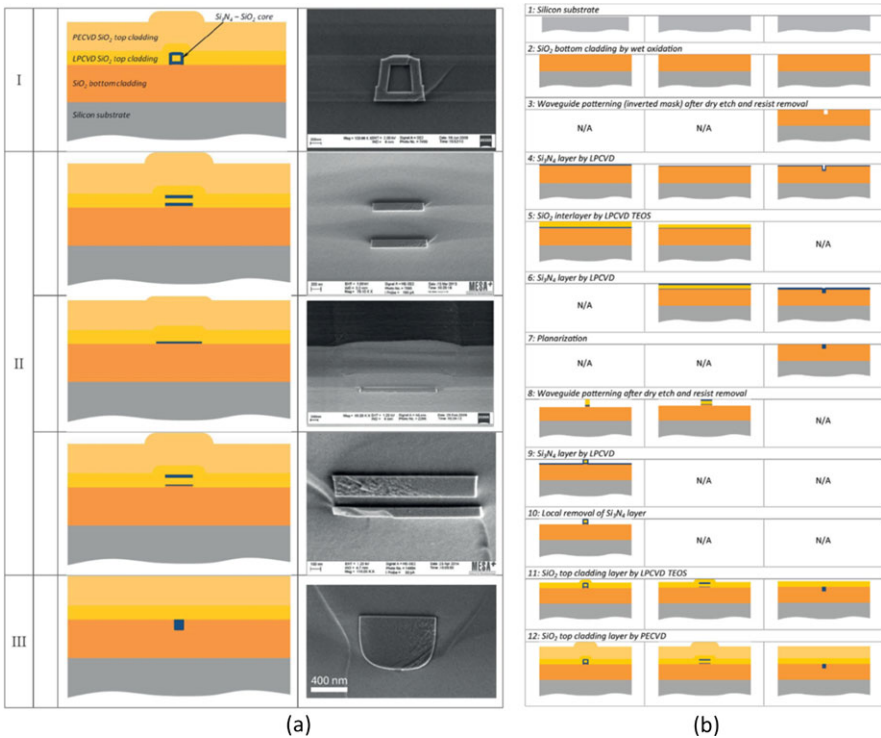


Fig. 13.5 (a) Schematic layout of TriPleX geometries and SEM images of realized structures: box shell (I), symmetric double-strip (IIa), single stripe (IIb), asymmetric double stripe (IIc), filled box (III). (b) generic process flow for fabrication of the three basic TriPleX geometries

is further subdivided into three groups: the symmetric double stripe (IIa), the asymmetric double stripe (IIc), and the single stripe (IIb) which is a special case of (IIc). The schematic layouts of the geometries and SEM micrographs of realized structures are depicted in Fig. 13.5(a). The generic process flow covering the fabrication steps of all TriPleX types is given in Fig. 13.5(b).

While the overall geometrical dimensions of the waveguide cores of these shapes are typically in the order of $1 \mu\text{m}^2$, their waveguide characteristics and potential application areas differ greatly.

The box shell layout is highly suited for telecom applications: due to its symmetrical shape, the polarization dependence is largely reduced [18]. The box shell is available in a low [15] and high [19] index contrast variant based on different ratios of the Si₃N₄ and SiO₂ thicknesses in the core region. In the low contrast version, a $1 \times 1 \mu\text{m}^2$ SiO₂ core is surrounded by 50-nm-thick Si₃N₄, while the high contrast is achieved with SiO₂ and Si₃N₄ core dimensions of $0.5 \times 0.5 \mu\text{m}^2$ and 170 nm, respectively. The waveguide propagation loss of the high-contrast box shell geometry is below 0.2 dB/cm (minimal bend radius < 150 μm) and reduces to 0.06 dB/cm for the low-contrast variant (minimal bending radius $\sim 500 \mu\text{m}$) [20].

The symmetric double stripe layout is typically applied in components requiring tight bending radii and large polarization birefringence. The optimized geometry is composed of two 170-nm-thick and 1.2- μm -wide Si_3N_4 layers separated by a 500-nm-thick SiO_2 interlayer. The effective index of the waveguide mode at 1.55 μm wavelength and the group index are 1.535 and 1.72, respectively, while the waveguide birefringence is 5.3×10^{-2} . The waveguide attenuation is ≤ 0.1 dB/cm [21]. Waveguide propagation loss as low as 0.095 dB/cm was measured in optical ring resonator (ORR) structures with a bending radius down to 70 μm [21]. The circular mode of this waveguide geometry has a mode field diameter (MFD) of ~ 1.5 μm . To enable low-loss coupling to standard single-mode fibers (SMF28), both Si_3N_4 stripes are adiabatically tapered in the vertical direction. At an optimized thickness of 35 nm for both tapered Si_3N_4 layers and a taper length of 600 μm , fiber-chip coupling losses of < 0.5 dB were demonstrated.

The asymmetric double-stripe geometry is particularly suited for combining regions with low and high effective indices of the mode on a single chip. In a realized example of this geometry type, a 40-nm-thick low-contrast Si_3N_4 stripe is separated in the vertical direction by a 100-nm SiO_2 interlayer from the 175-nm-thick high-contrast Si_3N_4 channel [22]. An adiabatic transition is made between both contrast regions by tapering the thicker layer to zero. In the high-contrast region the channel width is set to 1.5 μm , while the width in the low contrast area is variable. The high contrast waveguide exhibits a MFD of 1.7 μm and 1.3 μm in the in-plane and out-of-plane directions, respectively. The waveguide birefringence is in the order of 5×10^{-2} . Demonstrated loss values for the low and high modal confinement areas on the same chip were 0.015 dB/cm and 0.15 dB/cm, respectively.

The single stripe geometry is applied when extremely low optical losses are required: as explained, the single stripe can be converted from the asymmetric double stripe by locally removing the high-contrast waveguide. By optimization of the channel fabrication process and replacement of the upper PECVD SiO_2 cladding layer by a bonded thermal SiO_2 film, the waveguide propagation has been reduced to a record-low level of below 5×10^{-4} dB/cm at 1.58 μm wavelength on 40-nm \times 13- μm and 50-nm \times 6.5- μm multimode stripe waveguides [23].

Finally, the filled-box geometry was developed for applications requiring ultra-high confinement of the modal field in the core layer. In this geometry, core widths of 0.8 to 1.0 μm and thicknesses varying from 0.8 to 1.2 μm were realized [24]. The waveguide channel is multimode: up to three modes exist. For 1.55- μm wavelength and TE-polarized light the corresponding effective index of the mode and the MFD of the fundamental mode (TE_{00}) are around 1.79 and 1 μm , respectively. A minimum bending radius of 12.5 μm was calculated for the TE_{00} mode taking 0.01 dB/cm as the loss criterion. As stoichiometric LPCVD Si_3N_4 films exhibit high tensile stress, the layer thickness growth is limited to < 500 nm. Therefore, trench etching (into the thermal oxide layer) and trench filling (by LPCVD Si_3N_4 deposition) in combination with chemical mechanical polishing (CMP) was applied for the fabrication of crack-free waveguides (see also Fig. 13.5). The optical propagation loss of these waveguides at 1.55 μm wavelength was 0.4 dB/cm [24].

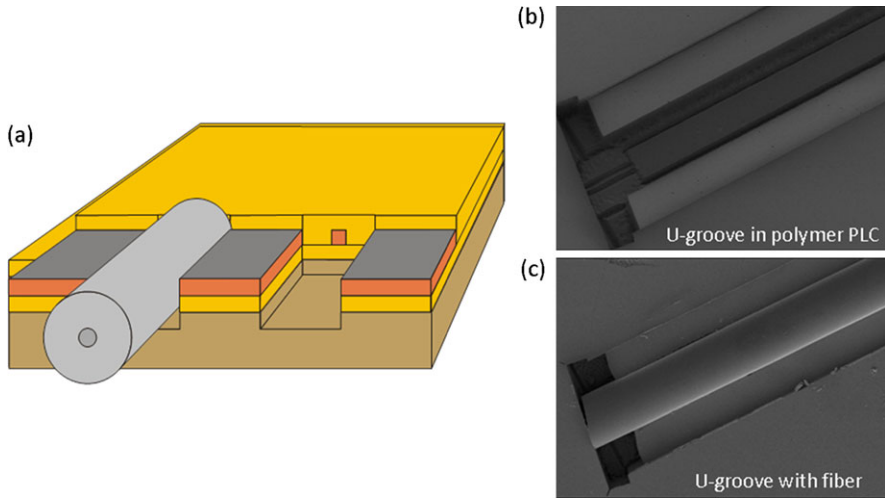


Fig. 13.6 (a) Schematic layout of fiber attachment with a U-groove, (b) SEM photo of empty U-groove, (c) SEM photo of fiber with 8° facet cut, attached inside the U-groove

13.2.3 Fiber Attachment Grooves (U-Grooves)

Low-loss and low-reflection fiber-to-waveguide coupling has been challenging for planar lightwave circuits (PLCs) due to the refractive index and/or mode mismatch between the two light-guiding media. The coupling issue becomes more serious with high-index contrast PLCs, based on e.g. silicon (SOI) and III–V semiconductors. Solutions are either expensive (with nano spot size converters) or bulky (with vertical grating couplers) [25, 26]. For low-index contrast PLCs, such as silica or SiN_x platforms, the coupling issue is less severe and can be solved by butt-joint coupling with the aid of anti-reflection coatings. An additional sub-mount is often needed to hold the fiber in place.

On the polymer platform, passive fiber/waveguide coupling can be achieved by means of on-chip fiber grooves, as shown in Fig. 13.6, denoted as U-grooves [3, 27]. The U-groove depth guarantees that once the fiber is pressed inside, the fiber core and the waveguide center are aligned vertically. Horizontally, they are positioned to the respective waveguides in a self-aligned manner, thus providing virtually perfect lateral adjustment. The width of the U-groove is designed to be a few micrometers narrower than the diameter of the fiber. Since the polymer material provides certain flexibility, the fiber can be pressed, and the side walls of the U-groove clamp the fiber in place. Additionally, in an attempt to suppress back reflections, the fiber and waveguide interface can be angled at 8° . The fiber can first be cut at this angle and then attached in the U-groove.

The U-groove can be etched by standard oxygen reactive ion etching (RIE) or inductively coupled plasma etching (ICP), utilizing a metal mask. Depending on the

technology, the uniformity achieved across a whole 4-inch wafer can well fall into the deviation range of less than 1% from the designed values, for both the groove width and the etching depth.

With proper index-matching glue and waveguide tapering for mode matching the typical loss per-facet for the U-groove based fiber/waveguide coupling is as low as 0.25 dB over a broad spectral range from 1300–1600 nm. An automated “pick-and-place” fiber attachment process for purely passive and high-throughput assembly is feasible and was already implemented as a demonstrator version.

13.3 New Hybrid Assembly Approach

In an EU-FP7 project (PHASTFlex) a new disruptive packaging approach has been developed to enable low-cost and high-accuracy packaging of hybrid combinations of InP and TriPleX waveguides [28]. A long-standing problem in the deployment of optical circuits based on InP materials has been the small size of the optical waveguides compared to the standard transmission medium, i.e. glass optical fibers. High-precision, sub-micron alignments are often needed. The packaging process is then made rather expensive by the time-consuming active and manual aligning process. The PHASTFlex project focuses specifically on finding a solution to this technical issue. PHASTFlex proposes the development of a fully automated, high-precision, cost-effective assembly technology for next generation hybrid photonic packages. In hybrid packages multiple photonic integrated circuits (PIC) can be assembled, combining the best of different material platforms for a wide range of applications and performance. In PHASTFlex, InP PICs with active functions will be combined with passive TriPleX PICs on a ceramic carrier as shown schematically in Fig. 13.7. The most demanding assembly task for the multi-port PICs is the high-precision ($\pm 0.1 \mu\text{m}$) alignment and fixing of the optical waveguides. The PHASTFlex consortium has proposed an innovative concept in which the waveguides in the TriPleX PIC are released during fabrication to make them movable. A two-stage assembly process is envisaged, in which a passive placement and bonding stage is followed by an active fine alignment stage using integrated MEMS functions on the TriPleX chip. Thereafter the waveguides can be locked in position. Actuators and fixing functions, integrated in the same PIC, place and fix the flexible waveguides in the optimal position at the peak out-coupled power with the accuracy required. The PHASTFlex project focuses on the development of a complete assembly process and the necessary tooling to implement this concept, including pre-assembly using solder reflow and automated handling, and on-chip micro-fabricated fine-alignment and fixing functions.

The first MEMS functionality has been realized in the TriPleX waveguides. A picture of these free-hanging MEMS waveguides is shown in Fig. 13.8.

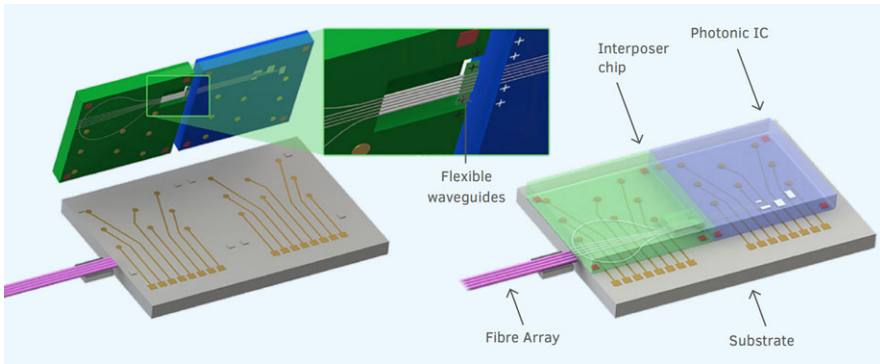
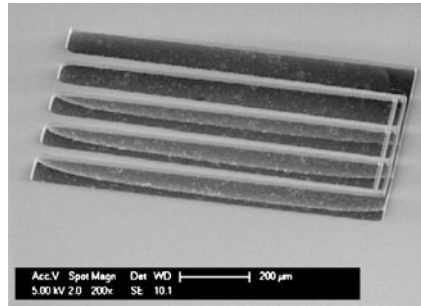


Fig. 13.7 Schematic representation of PHASTFlex packaging concept

Fig. 13.8 Free-hanging waveguide in TriPleX platform



13.4 Thin Film Elements

13.4.1 Wavelength Filters

Optical filters are key components in optical networks employing multiple operating wavelengths. The implementations of filter functions can be realized in the form of thin film filters (TFF), or, in general, thin film elements (TFE). Depending on the applications and spectral requirements, the thickness of the TFEs ranges from a few μm up to a few tens of μm . The lateral size can extend to several hundreds of μm . Some examples of TFEs are shown in Fig. 13.9. They are fabricated on a full wafer using a high-precision ion beam sputtering process, in which at least two dielectrics of different indices are deposited in an interleaved and often periodic manner to achieve certain spectral characteristics. The dielectric films are formed on a thin polymer layer which again is spun onto a Si substrate; the latter is finally removed. The wafer is cut into small pieces by an excimer laser.

TFEs can be vertically inserted into dedicated slots crossing the PLC waveguides. The slots are deep-etched using oxygen reactive ion etching in conjunction with a thin metal mask, similar to the U-groove fabrication process. The slots may also be formed by applying a dicing saw, subject to the wafer and chip layout. The width of

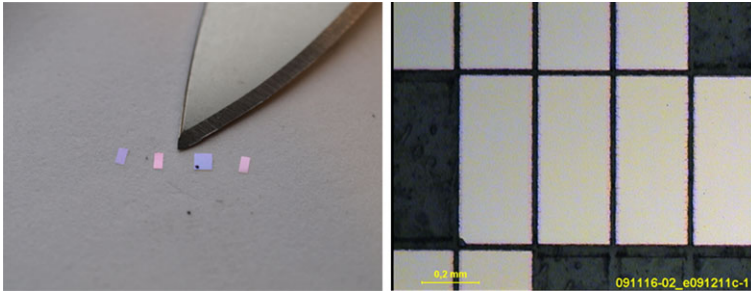


Fig. 13.9 Photographs of TFEs after laser cutting (developed and fabricated in collaboration of Laser Zentrum Hannover, Hanover, Germany and Fraunhofer HHI)

the slot needs to be well adjusted to the thickness of the TFE platelet. The vertical tilt angle of the mounted TFE and its thickness are important parameters determining the excess losses.

The U-grooves and TFEs can be combined to realize various devices. As an example, a 1×2 wavelength (de)multiplexer is demonstrated [27]. The device is designed to split and combine signals at 1310 nm and 1490 nm (or 1550 nm) in optical networks. The schematic layout and a device photograph are shown in Fig. 13.10. The device contains three U-grooves for fiber attachment, a central slot for TFE insertion, and the interconnecting polymer waveguides. The total chip made on a Si substrate measures 5 mm by 1.3 mm. The input signals at wavelengths 1310 nm (λ_1) and 1490 nm (or 1550 nm) (λ_2) are launched into the input port. Using a long-wavelength pass filter (LWPF), signals at wavelength 1490 nm/1550 nm will be guided to output port 2, whereas signals at 1310 nm get reflected by the TFE to output port 1.

Measurement results are shown in Fig. 13.11, displaying the filter performance of the LWPF. At 1310 nm, the fiber-to-fiber insertion loss at output port 1 is around 1.2 dB. The other channel at 1550 nm exhibits an even lower loss of 1.0 dB. The crosstalk suppression is larger than 30 dB. Across the entire wavelength range, the back reflection into the input fiber (optical return loss) is suppressed by more than 50 dB. When the loss from the fiber connectors is subtracted and only the net insertion loss from the input fiber to the output fiber is considered, the chip itself features a loss well below 1 dB. The maximum polarization dependent loss is below 0.5 dB.

Optical time-domain reflectometry (OTDR) represents a powerful means to remotely monitor the connectivity and termination status of optical networks. It is used to identify with high spatial resolution any point of failure that may degrade transmission performance. With conventional OTDR, optical reflections of a sequence of test pulses generated from broken or disconnected fiber parts are exploited. However, the reflected signals are often weak, noisy and hard to interpret. To gain accurate information about the fiber termination at reduced cost and effort, e.g. at the subscriber site, a dedicated integrated optical element is required as an edge filter that is transparent for the normal operating wavelengths but reflects almost 100% of the dedicated OTDR wavelength set away from the communication band (e.g.

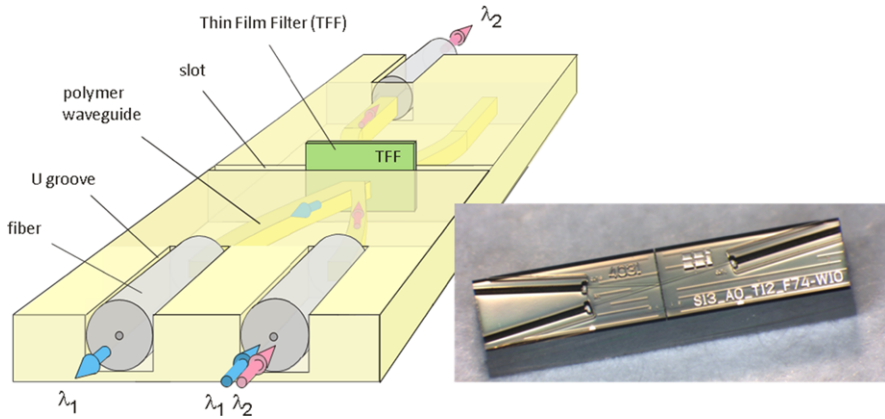
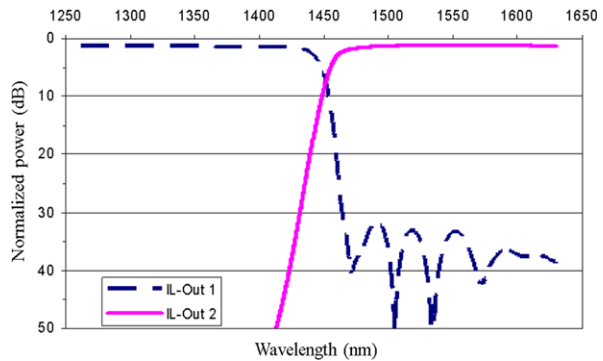


Fig. 13.10 Schematic layout and device photograph of 1×2 wavelength (de)multiplexer

Fig. 13.11 Measured characteristics of 1×2 wavelength (de)multiplexer



beyond the L band). Low excess loss, low device cost and simple installation are the principal demands posed on such network elements which have the potential of becoming a high-volume product when widely installed at subscriber terminals.

A simple and highly compact implementation of such an OTDR device can be realized on the polymer platform. The TFE is essentially a band pass filter designed to exhibit a spectral band edge at 1610 nm which is suitable for reflecting OTDR signals at 1625 nm or above as “ping” wavelength while letting the telecommunication wavelengths passing through.

The OTDR reflector is essentially comprised of two parts, the polymer base chip and the integrated TFE. The polymer base chip, as sketched in Fig. 13.12(a), contains two U-grooves for in-out fiber attachment, a single mode waveguide, and a central slot intercepting the waveguide. The assembled chip, shown in Fig. 13.12(b), measures only 3 mm (length) by 0.7 mm (width).

The characteristics of such a 1×1 OTDR device across the wavelength range from 1260 nm to 1630 nm are displayed in Fig. 13.13. The filter exhibits flat transmission from 1260 nm to 1580 nm, and at wavelengths > 1610 nm the filter behaves like a 100% reflection mirror. The crosstalk suppression is better than 23 dB which

Fig. 13.12 (a) Schematic layout and (b) photograph of 1×1 OTDR device

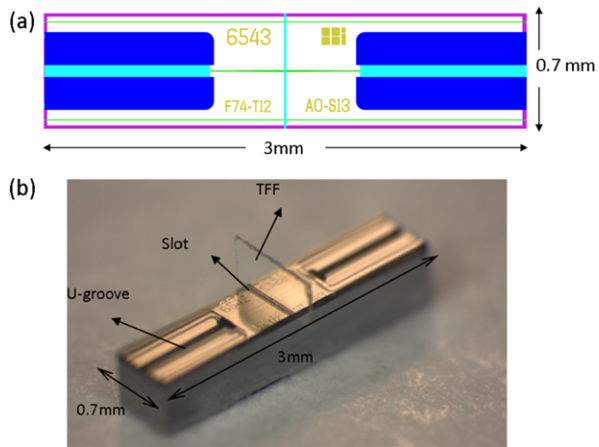
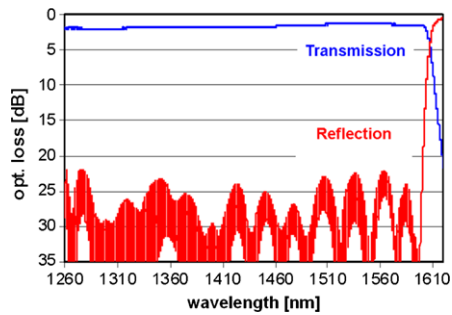


Fig. 13.13 Transmission/reflection characteristics of 1×1 OTDR device



can be further improved by fine-tuning the TFF layer deposition process. The insertion loss is below 2 dB over the 1260 nm to 1580 nm wavelength range, with a minimum value of 1.8 dB around 1550 nm. The reflected signal at 1625 nm exhibits a loss of less than 1.0 dB. The insertion loss originates mainly from the fiber-to-waveguide coupling, the coupling between the waveguide and the TFF, and additional loss from the TFF itself. By optimizing the waveguide taper design at the slot interfaces, the insertion loss may be further reduced.

13.4.2 Polarization Handling TFEs

Polarization handling is another key function in PLC devices to offer either polarization insensitive or polarization multiplexed/diversified operation. In many applications, the TE and TM components need to be separated and their imbalance needs to be kept minimal. Polarization dependence in PLC is mostly caused by the waveguide geometries, the material birefringence, non-linear processes, confinement issues, and so on. Passive polarization control implemented on waveguides usually involves complicated designs to compensate the different propagation constants of

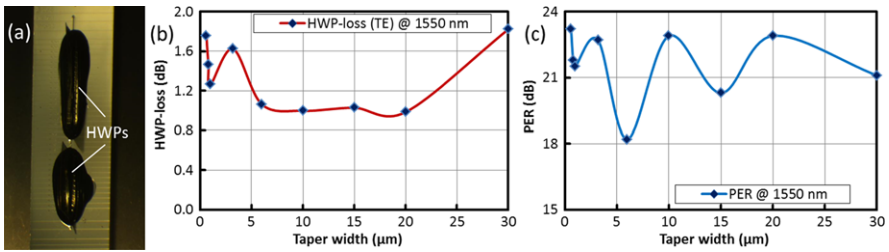


Fig. 13.14 (a) Photograph of polymer waveguide chip with vertically inserted HWPs, (b) HWP induced loss versus polymer waveguide taper width, (c) PER versus polymer waveguide taper width

the TE and TM modes. This often raises stringent challenges on the fabrication process and may lead to considerable extra loss.

On the polymer platform, a wave plate in the form of a TFE can be inserted to intercept the waveguides and rotate the polarization state of the light. Commonly used is a half-wave plate ($\lambda/2$ plate, HWP) that converts the TE and TM light components. Figure 13.14(a) shows a polymer waveguide chip with vertically inserted HWPs. To limit the beam divergence in the non-guided HWP region, the waveguides at the slot facets are tapered resulting in a broader mode field diameter and reduced scattering losses at the waveguide/HWP interface. Figure 13.14(b) indicates the effect of the polymer waveguide taper width on the HWP-induced loss. For a waveguide refractive index contrast of 1.48 (core): 1.45 (cladding) and a thickness of 3.2 μm , a taper width of 10 μm can help to bring the HWP-induced loss down to ~ 1.0 dB. The polarization conversion efficiency is evaluated by the TE/TM polarization extinction ratio (PER) of the output light. The results in Fig. 13.14(c) show that a high PER of ~ 23 dB can be achieved with the same taper width of 10 μm .

A TFE can also be designed to separate the polarization components of the incoming light in the waveguide. The schematic architecture of such a polarization beam splitter (PBS) is shown in Fig. 13.15. Depending on the characteristics of the polarization splitting TFE, one polarization (TM) will be reflected to output 1 and the other will pass through to output 2 (TE). The incident angle from the waveguide to the polarization splitting thin film element (PSTFE), i.e. the half-angle between the two waveguides, can be varied to optimize the splitting ratio for a desired bandwidth.

Figure 13.16 shows the spectra for the TE and TM signals at the two outputs. Across the telecommunication C-band (from 1535 nm to 1575 nm), the splitting ratios at both outputs are larger than 25 dB. The insertion loss is ~ 0.6 dB for the reflected and 1.3 dB for the transmitted path. The performance in terms of insertion loss, polarization splitting ratio and bandwidth can be further improved by optimizing the TFE layers as well as by carefully designing the waveguide/TFE interface so that the deflected beams are better collected.

The simplicity and high efficiency of TFE based polarization handling open up new possibilities in realizing polarization insensitive and multiplexed devices on the

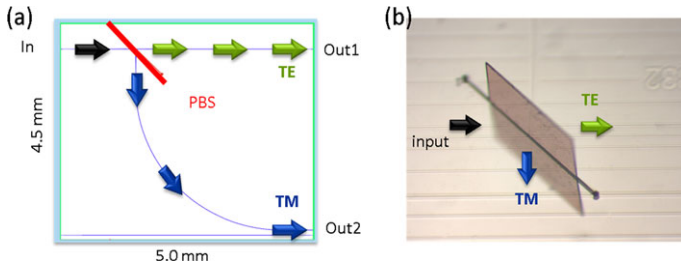


Fig. 13.15 (a) Schematic layout and (b) photograph of TEE-based polarization splitter on polymer platform

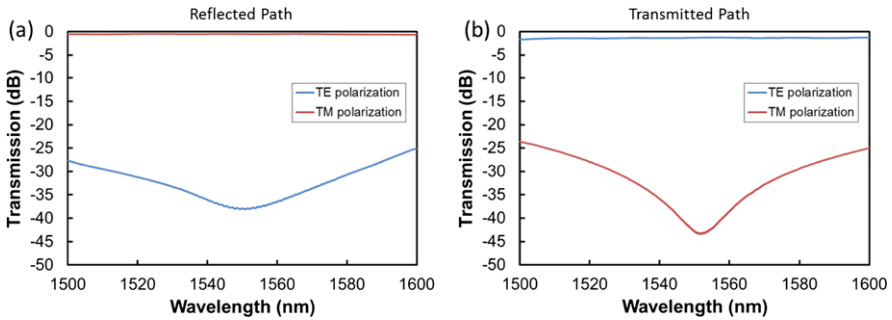


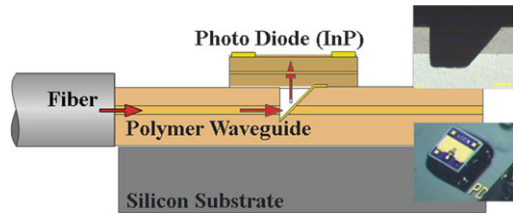
Fig. 13.16 Wavelength dependent transmission of TFE-based polarization beam splitter on polymer platform

polymer integration platform, such as polarization-multiplexed modulators, dual-polarization optical 90° hybrids, and coherent receivers.

13.5 Hybrid Integration with Active Components

Monolithic integration technologies based on InP material and SOI have evolved into foundry services over the last decade. However, the service has not yet ultimately proven to be highly cost-effective. The complexity in the design and fabrication increases almost exponentially with the number of integrated device functionalities. Very often trade-offs in the device performance need to be made in order to meet a reasonable yield. On the other hand, the fabrication of single components such as laser and photodiodes has matured in the last years. Many of the active components are available on the market, and it is practical to integrate these components in a hybrid manner onto a suitable versatile motherboard platform. Some technologies have been developed to facilitate the integration.

Fig. 13.17 Coupling of planar PD to polymer optical motherboard via integrated 45° mirror



13.5.1 Planar Photodiode Integration via 45° Mirrors

Optoelectronic devices such as laser diodes and photo diodes can be assembled on a polymer waveguide network via the conventional butt-joint method in which an extra sub-mount for the active component is necessary. Alternatively, the integration can be done vertically via a 45° mirror which eliminates the need for the extra sub-mount and enables passive, automatic on-wafer assembly using a fine placer.

On the polymer platform, 45° facets can be created by applying a fast-rotating angled dicing blade and sawing through the polymer chip [3]. The surface roughness can be minimized by the intrinsic “polishing” during sawing by choosing the right diamond concentration on the blade tip, the optimal blade rotation speed and the feeding speed. To improve the reflectivity, the 45° surface should be coated with a thin layer of metal, typically Ti and Au, by directed metal evaporation.

Apart from the design and processing simplicity, such 45° deflection mirrors offer much broader coupling bandwidth, less polarization sensitivity, and less beam divergence compared to vertical grating couplers. The 45° groove is usually filled with index matching epoxy so that the back reflection on the straight facet can be avoided and the beam divergence in the free space be reduced.

Figure 13.17 shows the vertical coupling scheme for a bottom illuminated PD coupled to the polymer optical motherboard via an integrated 45° mirror. Also shown are the side view of such a mirror and the top view of a mounted PD. The PD is placed on top of the polymer chip, in a purely passive way, by a state-of-art bonder with positioning precision of $\sim 1 \mu\text{m}$. The PD is fixed by UV glue with adequate index matching to suppress back reflections. Shear force tests have shown that the critical bonding values can reach up to 10 N/mm^2 . The backside of the PD is anti-reflection (AR) coated against the glue which completely fills the mirror trench. The mirror loss measured by means of a multi-mode fiber is around 1 dB. The actual mirror loss also depends on the diameter of the PD active area, its central position, and how it matches the actual beam spot. Using a 25 Gb/s capable PD with an active diameter of $20 \mu\text{m}$, an insertion loss of 1.8 dB is obtained, including the mirror coupling loss, fiber waveguide coupling loss via a U-groove and the propagation loss of a 3-mm-long polymer waveguide.

The bottom illuminated PD is designed with a full p-metal contact on its top side which facilitates uniform current flow and serves as optical reflector for light to double-pass the absorbing layer. This is beneficial regarding achievable responsivity particularly for very high-frequency PDs, the absorption layer thickness of which is limited by the transit time to below $1 \mu\text{m}$. On the other hand, the back-illuminated

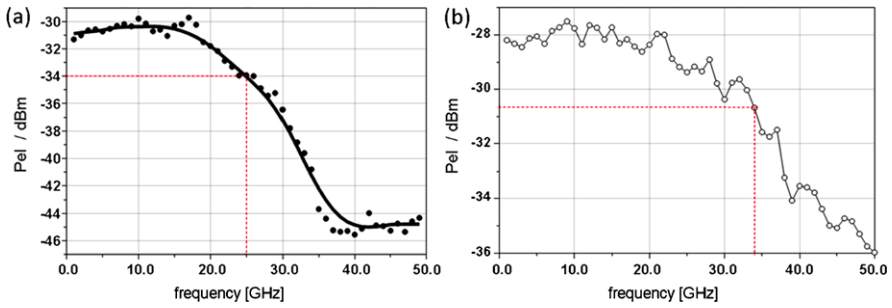
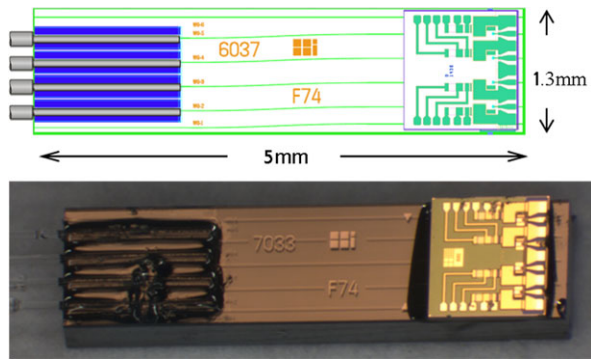


Fig. 13.18 Frequency response of a mounted PD (a) without impedance matching and (b) with 50 Ω impedance matching

Fig. 13.19 Four-channel fiber-waveguide-detector array



PD is more sensitive to beam divergence because of the longer optical path of the beam between the waveguide output and the active PD region. By using adequate designs the effective beam diameter at the active PD area can be kept as small as $\sim 10 \mu\text{m}$ ($1/e^2$). This value is well below the active diameter of PDs suitable for 25 Gb/s reception, a bit rate which is in the focus for 100 Gb/s transmission applications such as the 4×25 Gb/s wavelength multiplexed or differential quaternary phase shift keying (DQPSK) schemes.

Figure 13.18 shows the small signal frequency response of a mounted PD chip. The measurement was performed directly on the chip using a suitable RF probe head. Without extra electronics for 50 Ω impedance matching the 3 dB bandwidth is around 25 GHz, as shown in Fig. 13.18(a). By applying impedance matching and some compromises regarding responsivity, the bandwidth can be increased to as high as 34 GHz, as shown in Fig. 13.18(b).

PD arrays can be mounted on top of the mirror in a similar fashion. A 4-channel PD array coupled to the Polyboard is shown in Fig. 13.19. The optimal coupling position is firstly calculated in terms of waveguide position, cladding/core layer thickness and the mirror opening width. The PD array (with bias-T) is then mounted on top of the 45° mirror at the proper location and fixed with UV curing glue. Finally the fiber array is plugged in and glued for the measurements.

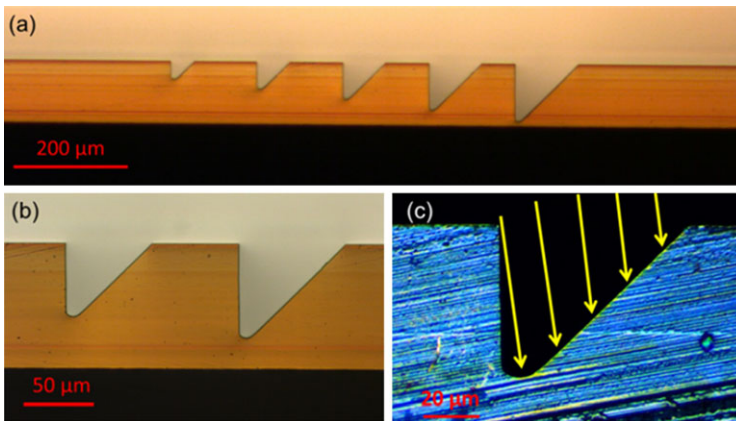


Fig. 13.20 Microscope images of 5-step 45° mirrors: (a) broader view and (b) detailed view showing placement of mirrors backside illuminated through the polymer, before the mirror surface metallization. (c) detailed view illuminated from the top, revealing correct metallization area. *Arrows* indicate 10° angle under which the metal vapor comes

The measured responsivities vary between 0.3 A/W to 0.4 A/W, and the highest value is 0.43 A/W. Since the responsivity, measured using a fiber illuminated directly on the PD, is 0.65 A/W, the lowest insertion loss has been derived to be 1.8 dB. The static crosstalk ranges from 28 dB to 30 dB, for any two PDs within the array, suggesting stray light to be the limiting factor. The polarization dependent loss is around 0.6 dB, of which ~ 0.5 dB is attributed to the metallized mirror itself. The optical return loss into the launching fiber (back-reflection) is better than 35 dB.

In 3-dimensional waveguide structures, such as shown in Fig. 13.3, the 45° mirrors can be arrayed by varying the dicing depths to tap out light from each of the multi-layer waveguide cores separately [9], as indicated in Fig. 13.20. The fabrication of the multi-step mirror array, however, raises two additional challenges. The first challenge is that the depth of the mirrors must be calculated and well controlled so that the tip reaches, in the ideal case, the middle point between the two core layers. Light from each layer can then be subsequently extracted by the mirror array. The blade tip can be first referenced to the top surface of the polymer chip and then be adjusted to the specified depths calculated from the layer thickness. The dicing saw equipment should be capable of controlling the vertical placement of the blade with an accuracy of $1\ \mu\text{m}$. The lateral distance between the mirrors can be adjusted to allow relaxed attachment of either linear planar PD arrays or an adapted 2D PD array chip.

The second challenge is that the metal coating must reach the very bottom of the deep mirror where the light spot from the bottom waveguide is expected, while staying clear from the straight waveguide facet. Thermal evaporation with well-defined deposition directivity must be used, and the tilt angle must be carefully calculated.

Fig. 13.21 Photograph of 1-cm long multilayer waveguides and multi-step mirrors under test. Optical input (*left*): lensed fiber; electrical output (*right*): planar PD array with needle contacts

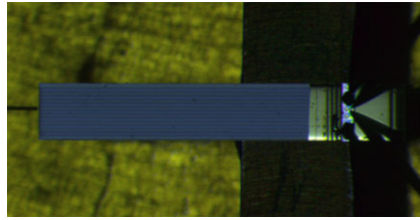
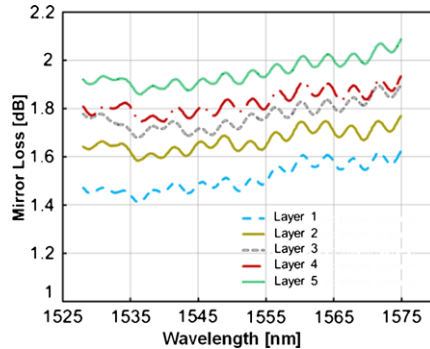


Fig. 13.22 Mirror loss from each waveguide layer extracted from PD responsivity measurement and normalized with respect to corresponding waveguide loss. Mirror loss increases slightly with deeper mirrors due to larger free-space beam divergence, enhanced scattering and absorption

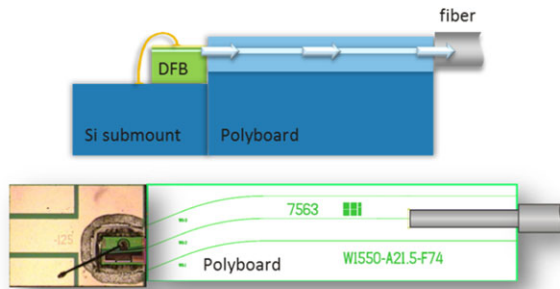


Microscope images of fabricated mirrors are shown in Fig. 13.20. The chip is flipped sideways and backside illuminated in Fig. 13.20(a) and (b). The uncoated multi-step mirror structures are revealed along with the individual polymer layers. In Fig. 13.20(c) the chip is topside illuminated where the coated metal line can be seen on the 45° surface (20 nm Ti + 80 nm Au) and the arrows indicate the direction, with 10° tilting, from which the metal vapor impinges.

For testing of the mirrors, light from a tunable laser source is launched via a lensed fiber into the 1-cm long multicore waveguide chip and collected from the corresponding mirrors by a PD array. The measurement setup is shown in Fig. 13.21. Index matching oil is used to fill the mirror groove to limit the beam divergence as well as to reduce the back reflection at the PD surface. The PD has an active area diameter of $\sim 50 \mu\text{m}$ and offers a broadband responsivity of around 1.1 A/W. The mirror loss can be extracted from the photocurrent by referencing to the straight waveguide loss of the same length.

The multi-step mirror losses are displayed in Fig. 13.22, ranging from 1.5 dB to 1.9 dB at 1550 nm. The wavelength dependence can be attributed to the PD responsivity characteristics. The bottom mirrors gradually suffer more loss, caused by the longer free space beam propagation distance and the associated larger beam divergence, more severe scattering, and more material absorption in the coupling oil-filled region. The slight ripples are caused by the Fabry-Pérot effect from the 1-cm long waveguide facets as no index matching oil is applied on the input fiber side. The mirror loss can be further reduced by applying proper waveguide tapers to limit the free-space beam divergence and by optimizing the dicing parameters to achieve a smoother mirror surface.

Fig. 13.23 Butt-joint coupling of curved stripe DFB laser to polymer waveguide chip



13.5.2 Butt-Joint Laser Diode Integration

Laser diode (LD) and waveguide coupling is challenging in three aspects: (a) LDs mostly possess a near-field mode field diameter of only a few micrometers. The waveguide mode must be tailored to match the laser mode size. (b) The coupling is very sensitive to any spatial misalignment. A positioning inaccuracy of $\sim 1 \mu\text{m}$ in the lateral and/or vertical dimension may lead to an extra coupling loss of more than 1 dB. (c) Optical feedback (back reflection) must be suppressed. If scattered light finds its way back into the laser cavity, the stable-state laser oscillation may be disturbed, causing ripples in the laser spectrum. In severe cases, the lasers can become multimode and the performance, in terms of line-width and directivity, will be seriously degraded. The LD output facet needs to be AR coated to suppress back reflections.

Though it is feasible to couple an edge-emitting LD or a VCSEL via a 45° mirror to the polymer waveguide with the help of a micro lens, it is more straightforward to use the conventional butt-joint method, as illustrated in Fig. 13.23. The DFB LD is first placed on a submount with predefined contact pads. This submount can be a silicon die with an oxide insulating layer or a ceramic piece for faster heat dissipation. Some high-end LDs require a diamond submount, which offers the highest thermal conductivity among the conventional materials to cool the LDs efficiently. For high frequency applications, the metal pads on the submount must be carefully designed as part of the impedance-matched transmission line. To facilitate the assembly process at a later stage, the thickness of the submount is adjusted by backside polishing to reach a similar height level as the Polyboard.

The LD in Fig. 13.23 features a curved stripe (CS) design which proves to be more robust against external feedback and offers higher single-mode yield [29]. The output of the laser is AR coated with respect to the polymer material and the beam shape is adjusted to obtain low divergence for optimal coupling with the buried polymer waveguide. The incident angle to the polymer waveguide is 21.6° for the 1490 nm lasing wavelength. The polymer waveguide bends further to suppress the back-reflection into the laser. At the output side, a single-mode fiber is attached in the U-groove. The position of the LD is fine-tuned until the maximal output power at a certain drive current is reached in the fiber. The LD is then fixed on the facet of the Polyboard by UV curing glue to complete the assembly process.

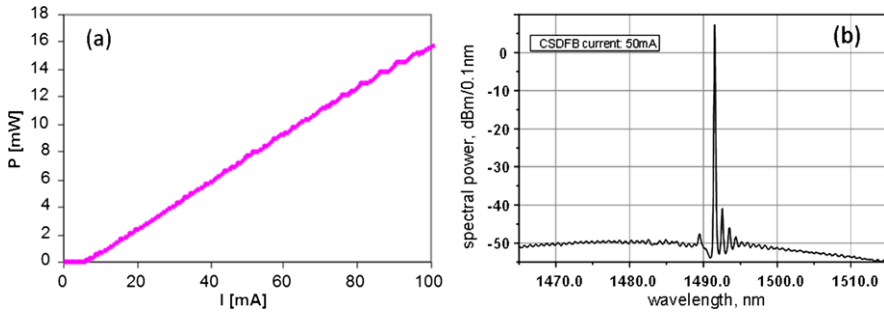


Fig. 13.24 CSDFB laser P – I curve at (a) room temperature, (b) laser spectrum, both are measured at the fiber output in the U-groove

Figure 13.24 shows the output characteristics of a LD-Polyboard subassembly measured from the fiber output at room temperature. The laser diode used here is a DFB laser with a curved stripe design (CSDFB). The threshold current is 7.2 mA and at 100 mA the output power reaches 16 mW. The spectrum of the laser shows a distinct single mode emission with the side-mode-suppression ratio (SMSR) being larger than 45 dB.

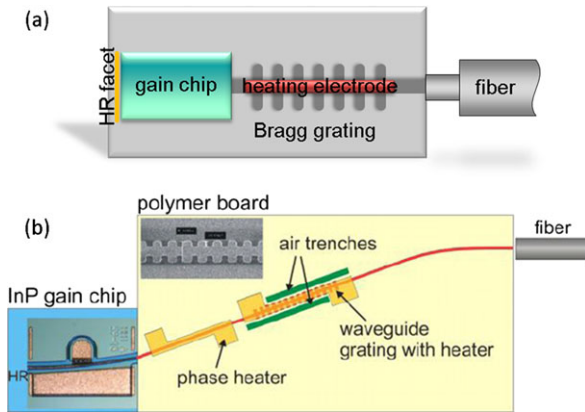
A LD array can be integrated on the Polyboard in a similar way. One concern is the bending of the LD array (or a bar) in the vertical dimension, e.g., the bowing effect. The LD array must be handled by pick-up tools with uniformly distributed holding force and placed on a submount with matched thermal expansion coefficient, and the angular alignment between the LD array and the polymer chip must be carefully adjusted. When a small walk-off angle exists, a severe power imbalance among the channels may occur.

13.5.3 Gain Chip Integration

A gain chip (GC) is a mandatory building block for the construction of any external cavity laser. A GC is similar to a LD except that the internal optical feedback loop is intentionally removed. At least one facet of a gain chip is AR coated against air or other media to eliminate internal lasing and enhance light emission. It usually employs a multi-quantum well design that enhances output power and may broaden the gain bandwidth.

A GC can be butt-joint coupled to a tunable polymer Bragg grating and thereupon built into an external cavity tunable laser. Schematic layouts of such structures are illustrated in Fig. 13.25. The basic layout in Fig. 13.25(a) consists of a GC with high-reflection (HR) coating at the rear facet, a thermally tunable polymer waveguide Bragg grating with a heater electrode, and a fiber. The grating functions as a wavelength selective reflector and together with the HR coating on the other side of the gain chip a cavity for laser oscillation is formed. When the threshold is reached, the laser emits into the fiber.

Fig. 13.25 Schematic layout of tunable external cavity laser. **(a)** basic layout: Straight facet gain chip coupled to tunable Bragg grating. **(b)** advanced layout: Curved stripe gain chip coupled to tunable Bragg grating with optimized heater conditions and additional phase electrode



A more advanced structure as shown in Fig. 13.25(b) includes a curved stripe GC, which, similar to the curved stripe DFB LD, makes the laser more robust against optical feedback. The polymer waveguide is accordingly bent with the right coupling angle to the GC. During thermal tuning, the central wavelength of the Bragg reflector shifts toward shorter wavelength due to the thermally induced negative refractive index change in the polymer waveguide. At the same time, however, the roundtrip phase reappearing condition in the laser oscillation is inevitably altered. Since the longitudinal mode spacing of such external cavity lasers is usually narrower than the Bragg grating spectrum width, a jump in the longitudinal mode number may occur as the laser mode readjusts itself to match the phase reappearing condition. This phenomenon is called “mode hopping”. When not treated properly, mode hopping can cause discontinuities in the laser’s $P-I$ curve and lead to significant drop of the single-mode yield, i.e., degradation of the side-mode-suppression ratio. To address this issue, an additional phase electrode is added in order to compensate the phase shift during thermal tuning.

$P-I$ curves of the laser with the advanced layout are shown in Fig. 13.26. Assuming that the HR coating provides $\sim 90\%$ broadband reflection, the optimal Bragg grating reflectivity can be derived from the rate equations once the gain coefficient and the roundtrip loss of the cavity are known. A batch of such lasers with various Bragg grating reflectivities has been experimentally characterized. Thanks to the high power efficiency of the GC as well as the low coupling loss to the polymer waveguide, the Bragg grating needs to provide a fractional reflectivity of only 13% for the laser to emit an output power larger than 12 mW at a driving current of 100 mA.

The output power of the tunable laser has been measured at different heating powers. The drive current of the gain chip was chosen to be 50 mA. The results are summarized in Fig. 13.27. A total tuning range in excess of 50 nm from 1560 nm to 1509 nm is achieved. The heating power needed for such a tuning range is ~ 161 mW. The degradation of the laser output power across such a tuning range amounts to less than 2 dB, indicating a flat broadband gain spectrum of the GC as well as fairly good thermo-optic linearity and thermal stability of the polymer ma-

Fig. 13.26 Laser $P-I$ curves for Bragg gratings with different reflectivities

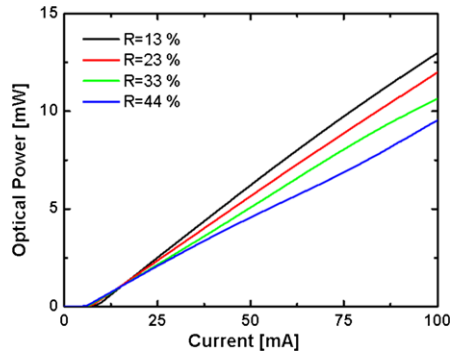
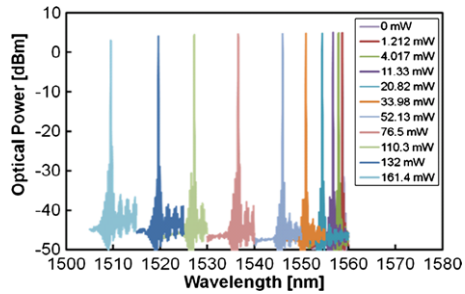


Fig. 13.27 Tunable laser spectra at various heating powers



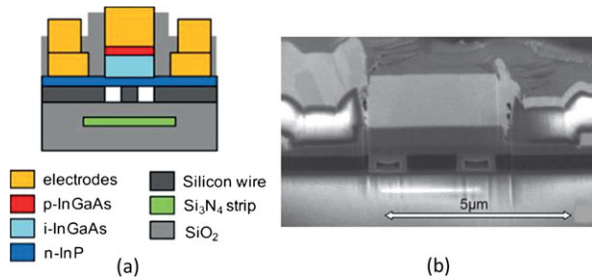
terial, at least at the lab demonstration stage. The SMSR remains larger than 26 dB which can certainly be improved by adjusting the phase electrode to avoid mode-hopping.

Latest research results have shown that direct laser modulation at 10 Gb/s can be achieved by adopting a GC design with low parasitic capacitance, shortened polymer waveguide and Bragg-grating length, and further improved facet coupling [30–32]. On the other hand, with increased waveguide and Bragg-grating length, a narrow laser line-width of less than 200 kHz has been demonstrated [33, 34].

13.5.4 TriPleX Hybrid Integration Method

The high design flexibility provided by the TriPleX platform is a prerequisite to boosting photonic integration. The availability of low- and high-contrast regions on a single chip easily enables interposer functionality in photonic assemblies. The large freedom in pitch and mode size conversion is, for example, utilized in low-loss connections between optical fiber arrays and high-confinement waveguide technologies such as InP or SOI [13]. In return, active functionality (light generation, detection, and modulation) available on the latter platforms is efficiently joined with the TriPleX circuitry. The proposed integration concepts for silicon nitride waveguides with the silicon photonic platform are based on a hybrid bonding process utilizing a

Fig. 13.28 (a) Concept of TriPleX integration with SOI and III/V semiconductors, (b) SEM micrograph of integration cross section [35]



SiO₂ interface layer with a controlled thickness [35]. The integration concept and a SEM micrograph of a fabricated device are shown in Fig. 13.28.

Currently, a novel assembly concept for integrating InP and TriPleX chips on a carrier platform is being developed [28]. Besides addressing low-cost, high-volume assembly, the approach focuses on bridging the gap between typical flip-chip placement accuracies ($\leq 1 \mu\text{m}$) and the sub-100-nm alignment precision required by high-contrast coupling interfaces by monolithically integrated MEMS-based fine tuning structures.

On-chip adiabatic tapering sections are key elements for many integration aspects. Therefore, the optimization of the taper design and technology was emphasized. Vertical tapers are usually fabricated by standard lithography and isotropic etching of the silicon nitride layers. Measurements of propagation loss through such tapering sections resulted in ≤ 0.5 dB per taper [22]. The most critical part of the tapering path is at the starting position of the taper (thin side) where the propagation of the weakly confined mode is extremely sensitive to any geometrical changes. To address this issue, a novel ultra-taper procedure has been developed in which the shape of the tapering section can be controlled by the design rather than solely by the process-specific etch profile [36]. The preliminary results based on insertion loss measurements of waveguides with multiple tapering sections indicate a taper loss reduction by about one order of magnitude.

Last but not the least, the TriPleX platform is also well suited for lab-on-a-chip applications. The microfluidic channels are defined in a fused silica wafer and then bonded on the optical TriPleX wafer, as indicated in Fig. 13.29(a) and (b). Light sources, fiber array and fluidic vessels are then integrated in a hybrid manner [17, 37]. A photograph of the lab-on-a-chip assembly is shown in Fig. 13.29(c).

13.6 Optical Subassemblies and Modules

By combining the polymer motherboard technology and the hybrid integration method with InP active components various optical subassemblies and modules can be realized. For the WDM-PON technology, optical line terminals (OLT) and optical network units (ONU) are key components in the network infrastructure. The hybrid integration approach allows high-performance and cost-effective OLTs to be

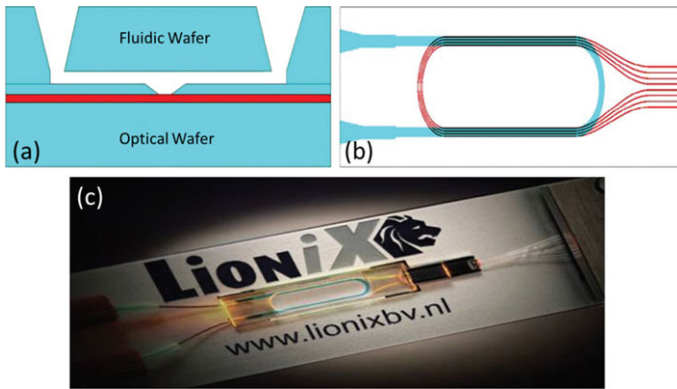


Fig. 13.29 Concept of integrating optical circuits with microfluidic channels: (a) cross-section and (b) top view. (c) picture of component sub-assembly with attached VCSELs, optical fibers and fluidic vessels [37]

assembled using polymer arrayed waveguide gratings (AWGs) for wavelength multiplexing (MUX) and de-multiplexing (DMX), InP LD arrays as directly modulated transmitters (Tx) and planar PD arrays as receivers (Rx). Furthermore, a colorless ONU is demonstrated on the polymer motherboard platform utilizing the full flexibility that the platform offers: an on-chip U-groove allows for submount-free fiber pigtailling, an on-chip 45° mirror enables vertical light detection by planar back-side illuminated photodetectors (PDs), and a vertically inserted TFE (de)multiplexes wavelengths from the C band (~ 1528 nm to ~ 1568 nm) and the L band (~ 1568 nm to ~ 1610 nm) [8, 30]. The integrated tunable laser on the ONU can be directly modulated at 10 Gb/s data rate. Optimized thermo-optic design can make the wavelength tuning extremely efficient. The PDs can be chosen to cover a large range of bandwidths from 2.5 GHz to 30 GHz. Deep-etched air trenches can be introduced without any extra fabrication steps to block stray light in the optical circuit and thus suppress optical cross-talk.

To improve the spectral efficiency of the WDM system and the total capacity of the optical networks, coherent optical transmission technologies have been developed such as polarization-multiplexed quadrature phase-shift keying (DP-QPSK), dual-polarization 16-quadrature amplitude modulation (16-QAM), and higher order modulation formats up to 128-QAM (see also Chap. 8). A tunable laser source that can switch its emission polarization state is needed [33, 38]. On the coherent receiver side, an optical 90° hybrid is required as the frontend to convert the phase modulated signal into amplitude modulation detectable by photodiodes. A PLC-based 90° hybrid with integrated polarization elements, variable optical attenuators, and a low-cost wavelength-tunable local oscillator (LO) is highly desired to bring down the device cost and footprint. On the polymer motherboard such an optical 90° hybrid can be realized by using low-loss polymer 2×4 MMIs as phase mixers, 1×1 thermally tunable MMIs as VOAs, and TFEs as polarization splitter (PS) and rotator. Furthermore, an on-chip tunable local oscillator can be integrated that allows colorless detection in the C-band [34].

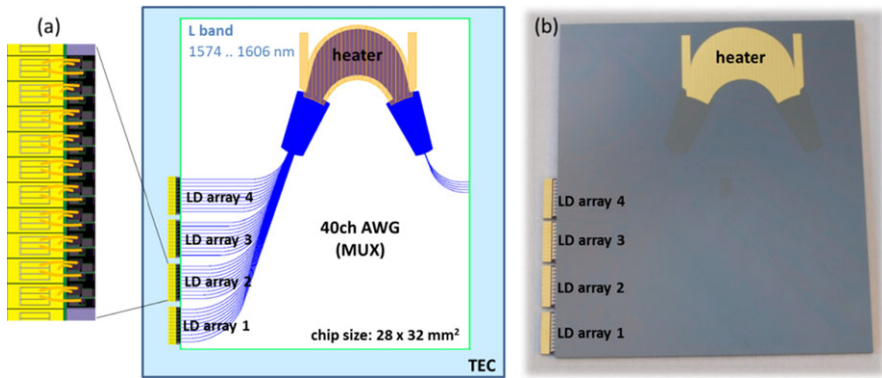


Fig. 13.30 40-channel OLT-Tx based on 4×10 direct-modulated LD arrays butt-joint coupled to a thermally tunable polymer AWG: (a) schematic layout and (b) photograph of assembly. The heater on the AWG-chips allows for some spectral fine-tuning of the AWG channel

13.6.1 Polymer AWG-Based OLTs

An OLT-component for operation at the transmitter side is shown in Fig. 13.30(a) and (b). This device consists of four InP-based 10-channel DFB LD arrays first placed on a Si submount and then butt-joint coupled to a polymer MUX AWG. The complete device, combining the AWG and the LD arrays, is 29 mm long and 30 mm wide. The 40-channel MUX AWG is based on a polymer waveguide with square cross-section of $3.5 \mu\text{m} \times 3.5 \mu\text{m}$ and a refractive index contrast of 1.47:1.45. It is designed to cover the L-band (1568 nm to 1610 nm) with 100 GHz channel spacing. The spectral characteristic of the AWG channels is of Gaussian type with a 1-dB width of 0.25 nm. A heater electrode placed on top of the arrayed waveguide region can be biased to thermally adjust the AWG central wavelength to match the ITU-grid [39].

Figure 13.31(a) shows the overlaid spectra of the AWG at different heater powers. Figure 13.31(b) illustrates the central wavelength during thermal tuning. At ~ 900 mW, the tuning range exceeds the channel spacing of ~ 0.8 nm. The schematic layout of the InP LD array is shown in Fig. 13.31(c). Each single element comprises a 150- μm -long DFB section and a 250- μm -long optical gain region. The emission wavelength for each individual LD is defined by e-beam lithography to match the 100-GHz channel spacing. A heater electrode is included in the DFB section by which up to 3-nm tuning can be thermally realized, in order to pin-point the wavelength at the ITU grid. The emitting wavelengths of different LDs on the array are listed in Fig. 13.31(d). Four 10-channel LD arrays with finely adjusted emission wavelengths provide 40 channels in the L-band. The LD arrays are first mounted on the Si-submounts with pre-defined RF lines and then butt-joint coupled to the polymer-based AWG. The arrays have been HR coated on the back side against air, whereas the front facet has an AR coating against polymer to avoid back reflections. Index-matching epoxy is first applied to secure the optical coupling, followed by a mechanical fixing epoxy to support the large array.

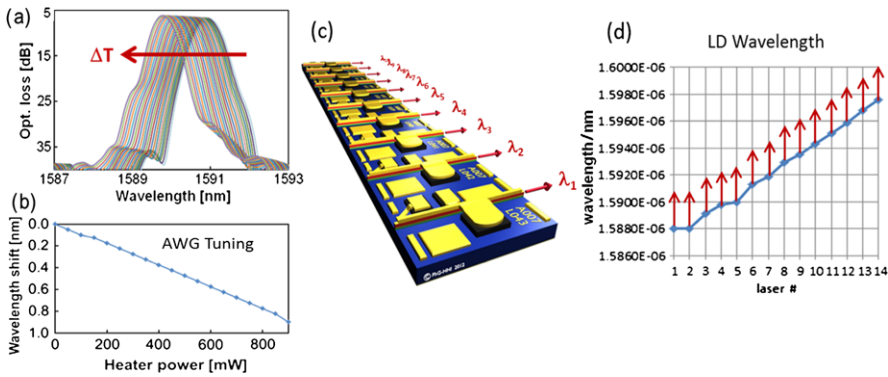
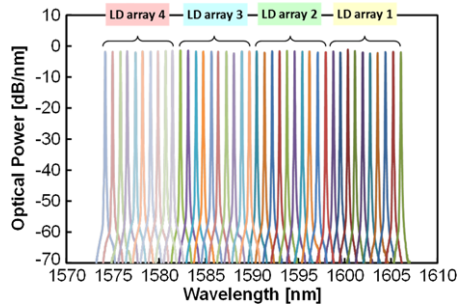


Fig. 13.31 (a) Overlaid AWG spectra at different heater powers, (b) AWG central wavelength as function of heater power, (c) schematic layout of multi-wavelength LD array, (d) measured emission wavelengths

Fig. 13.32 Multiplexed transmission spectra at output of OLT-Tx



The assembled OLT-Tx is placed on a thermo-electric cooler (TEC) which stabilizes the assembly temperature at 25 °C. The performance is illustrated in Fig. 13.32, where the spectra of the 40 channels are measured at the output of the MUX AWG. Each LD and the AWG itself are independently adjusted to match the channel wavelengths at the ITU-grid. An optical output power larger than 0 dBm can be obtained in the fiber by increasing the injection current of the LD to ~120 mA. The matched spectra from the LDs and the AWG lead to a stunning SMSR of >70 dB for all 40 channels. The LDs can be directly modulated up to 25 Gb/s, resulting in a total data rate of 1 Tb/s at the OLT-Tx.

The corresponding OLT-Rx is shown in Fig. 13.33(a) and (b). Four InP planar PD arrays are vertically coupled to the polymer DMX AWG by integrated 45° mirrors. The 40-channel polymer DMX AWG is designed to operate at 100-GHz channel spacing over the C-band (1528 nm to 1568 nm). A $\lambda/2$ plate can be inserted in the middle of the arrayed waveguide region to eliminate residual polarization dependence.

Figure 13.34 shows the responsivities of the OLT-Rx. The PDs have an intrinsic responsivity of 1.1 A/W, while an effective responsivity of ~0.22 A/W is measured for the OLT. The device insertion loss, including the fiber coupling, mirror coupling

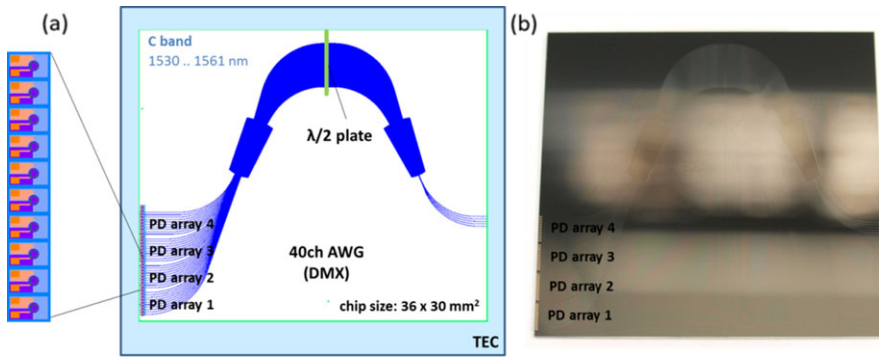
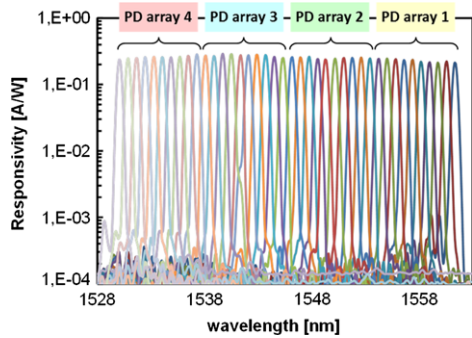


Fig. 13.33 40-channel OLT-Rx based on 4×10 planar PD arrays vertically coupled to polymer AWG via integrated 45° mirrors: (a) schematic layout and (b) photograph of assembly

Fig. 13.34 Measured responsivities of PD arrays on OLT-Rx



and the polymer AWG itself, is then calculated to be ~ 7.5 dB. As discussed in Sect. 13.5.1, the PD bandwidth can be extended to over 30 GHz at the cost of reduced responsivity, allowing each channel to reach a direct detection rate > 25 Gb/s, and a total data rate > 1 Tb/s can be received with such an OLT-Rx.

13.6.2 TriPleX AWGs

As discussed in Sect. 13.2.2, TriPleX waveguides with the single-stripe geometry exhibit extremely low propagation loss [23], and the same waveguide geometry can be used to realize highly transparent AWGs. One of the AWG designs from the University of California Santa Barbara [40] is shown in Fig. 13.35. The measurement results in Fig. 13.36 show that the 16-channel 200-GHz AWG has a very low loss of ~ 0.4 to 0.8 dB spanning across the 1310-nm and 1550-nm wavelength windows. The crosstalk suppression between adjacent and non-adjacent channels is better than 30 dB and 40 dB, respectively. Since the majority of light field lies in the SiO_2 cladding for this type of single-stripe Si_3N_4 waveguide, the AWG also

Fig. 13.35 Layout of AWG (de)multiplexer based on single-stripe TriPleX waveguide [40]

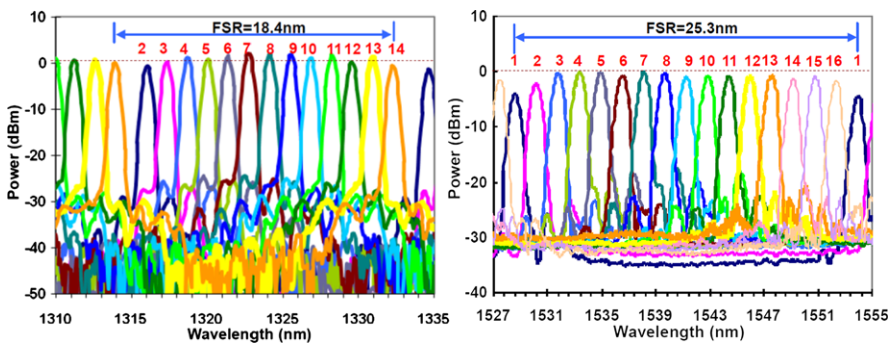
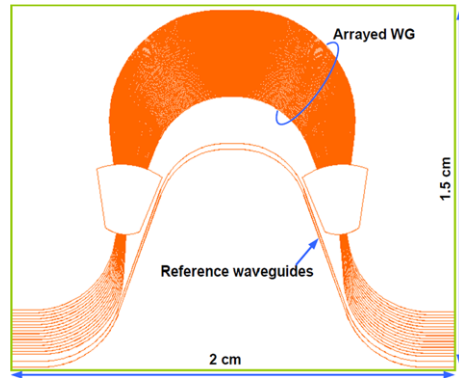


Fig. 13.36 Spectral characteristics of TriPleX AWG at two wavelength windows [40]

features a low temperature dependence of about $0.011 \text{ nm}/^\circ\text{C}$, a value that is very close to a pure SiO_2 AWG device. Coupled with LD/PD arrays, the TriPleX AWGs can be adopted as low-loss OLTs in the WDM-PON. They can also be used as mini-spectrometers for sensing systems.

13.6.3 Colorless ONU

Over the last few years wavelength division multiplexing-passive optical network (WDM-PON) technology has witnessed rapid development in response to the exponentially growing demand on end-user access bandwidth. Within this technology, a colorless optical network unit (ONU) supporting all wavelength channels is needed to simplify network operation, reduce inventory and installation costs, and to keep maintenance efforts sufficiently low [8, 30].

The schematic layout and a photograph of an assembled ONU implemented on the polymer platform are shown in Fig. 13.37. The polymer chip measures 5.6 mm (L) by 2.4 mm (W), and with the butt-joint coupled InP GC array the assembly size increases to 6.5 mm (L) by 2.5 mm (W).

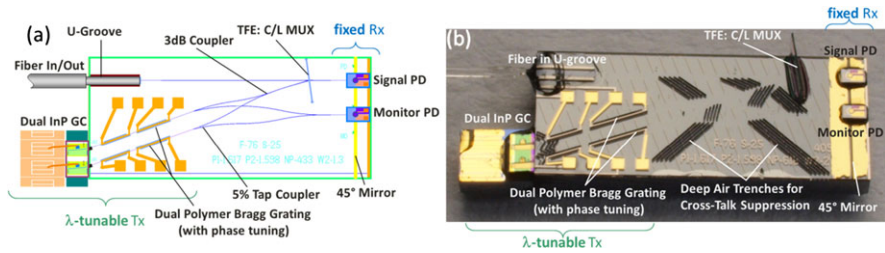


Fig. 13.37 ONU assembled on polymer-based hybrid integration platform, (a) schematic layout and (b) photograph of assembly

An array of two identical GC elements is first placed and wire-bonded onto an RF-submount and then butt-joint coupled to the dual-channel polymer Bragg gratings. Together they form a tunable transmitter (Tx). To relieve the thermal strain from a single polymer Bragg grating, the C-band wavelength tuning is split between two paths, with one of the two GCs directly modulated at a time. 5% of the Tx power is tapped out via a pair of asymmetric Y-couplers to be received by the monitor PD. The TFE-based C/L-band filter reflects the Tx signal, which further propagates through the polymer waveguide into the single mode fiber.

On the receiver side, the incoming optical signal at any wavelength within the L-band goes through the same fiber into the polymer waveguide. The TFE passes the signal through to the receiver side of the ONU, where an on-chip 45° mirror deflects the light and feeds it to the high-speed planar PDs mounted on top.

A series of air trenches are etched on the polymer chip simultaneously with the U-groove and the TFE slot. The air trenches provide many optical interfaces and deliberately scatter the stray light in the polymer slab in directions away from the location where the Rx PD and the monitor PD are mounted.

The TFE is a key element performing the C/L-band wavelength (de)multiplexing. It consists of alternating layers of sputtered SiO₂ and TiO₂ films on a thin polymer substrate, as already outlined above. The total thickness of the filter adds up to 24 μm. The fabrication (performed at Laser Zentrum Hannover) is done on a standard 3-inch silicon wafer. After sputtering, the TFE is cut by an excimer laser into desired dimensions. A photograph of the TFE after cutting is shown in Fig. 13.38(a). The TFE is generally characterized by single-mode fiber measurements prior to the integration into the Polyboard. The reflection/transmission spectra are displayed in Fig. 13.38(b). The TFE introduces an insertion loss <2 dB. Due to the band-edge effect, however, the transition slope between 1562 nm to 1572 nm cause signals at these wavelengths to suffer from extra attenuation. Filters with steeper band-edges at reasonable thickness are being investigated.

After the assembly, the ONU is first characterized on the Tx side. The drive current for the GCs is set to 50 mA. The lower arm of the tunable laser path offers a tuning range from 1525 nm to 1548 nm (see Fig. 13.39(a)) and the upper arm from 1545 nm to 1568 nm (see Fig. 13.39(b)). The side-mode suppression ratio is larger than 40 dB and the combined tuning range of 43 nm appropriate for the C-band. The dropping of the laser output power at wavelengths above 1560 nm is evidently

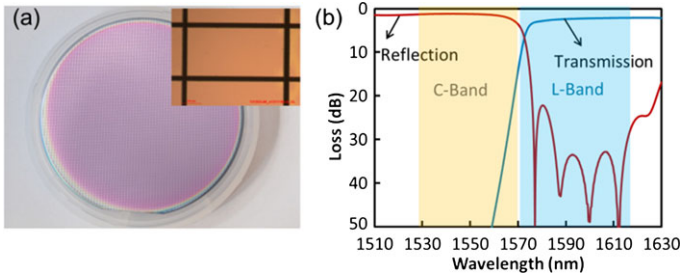


Fig. 13.38 (a) Microscope image of C/L band filter after laser cutting. (b) Reflection and transmission spectra of TFE-based filter

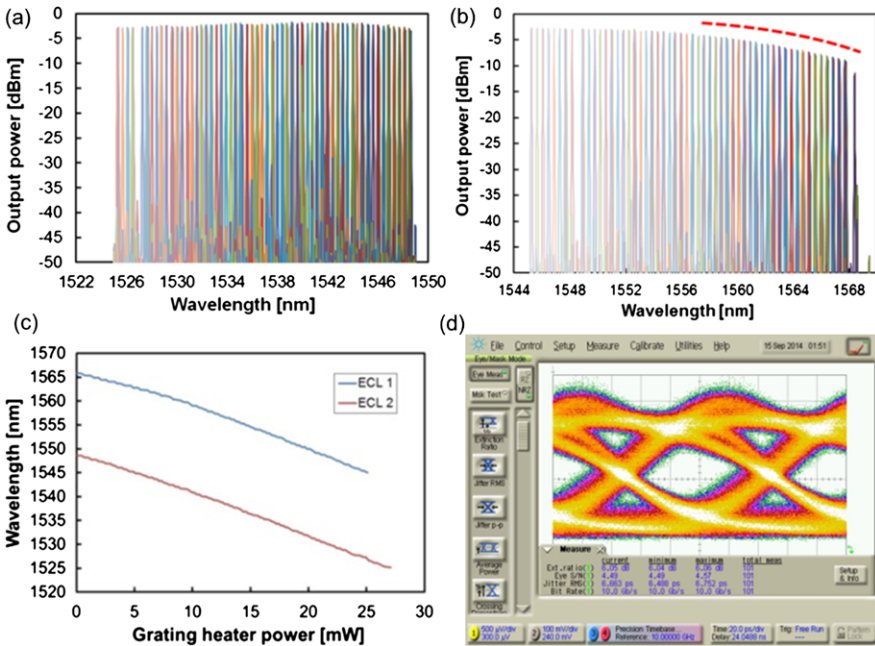
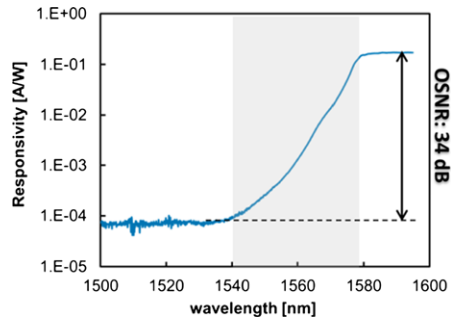


Fig. 13.39 Tx characteristics of ONU: (a) tuning spectra of lower arm laser, (b) tuning spectra of upper arm laser, (c) total tuning range and efficiency of both lasers, (d) eye diagram at 10 Gb/s data rate after 11.3-km-long standard single-mode fiber transmission

due to the band-edge in the reflection spectrum from the TFE, as indicated by the dashed curve in Fig. 13.39(b). The transmitter loss away from the band-edge region is around 7 dB from the GC to the fiber, including the 3-dB intrinsic loss of the Y-branch.

Both laser branches show almost identical thermal tuning behavior; the related efficiencies are plotted in Fig. 13.39(c). In order to reach 23 nm wavelength tuning, only ~26 mW heater power is needed for each laser. The thick polymer bottom

Fig. 13.40 Responsivity measurement of the ONU chip at different wavelengths



cladding and the deep-etched air trenches surrounding the buried heater electrodes function as effective thermal buffers [5] so that the tuning efficiency reaches a value of only 0.88 nm/mW.

The Tx laser can be directly modulated via the GC at 10 Gb/s data rate. The eye diagram after transmission along an 11.3-km-long standard single-mode fiber is shown in Fig. 13.39(d). The signal-to-noise ratio is 5.85 dB and the bit error rate is lower than 1×10^{-13} . No band-pass filter is used in the experiment.

As to the Rx side, the signal PD responsivity is shown in Fig. 13.40, measured by launching light from a broadband tunable laser into the input/output waveguide via a fiber. Above 1580 nm, the PD responsivity remains at 0.14 A/W, corresponding to a receiver loss of ~ 7 dB from the fiber to the PD. The mirror loss amounts to ~ 1 dB, the fiber/waveguide coupling and the waveguide propagation loss add up to ~ 2 dB. The rest is attributed to (1) the TFE loss, which amounts to ~ 2 dB as concluded from the measurement using fibers, and (2) the associated scattering loss at the TFE/waveguide interface in the slot. The scattering loss is caused by the non-optimal wave-front matching from the free-space region (TFE and excess slot width) to the receiving waveguide, i.e., the mismatch between the broadened beam (location and size) and the near-field mode profile of the waveguide. This loss may still be reduced by introducing proper tapers and waveguide offsets at the slot region. The optical signal-to-noise ratio (OSNR) is measured to be 34 dB at 1580 nm and 1540 nm.

13.6.4 Dual-Polarization Switchable Tunable Laser

Tunable Bragg gratings, polarization handling devices and thermo-optic switches (TOS) can be combined in the Polyboard to build up more advanced components, such as a wavelength tunable external cavity laser with switchable dual-polarization emission [38]. Generally, it proves difficult to fabricate LDs with TM-polarized output. Proper epitaxial strain has to be introduced to suppress the preferred TE mode in distributed feedback LDs [41]. On the Polyboard, however, such lasers can be assembled rather straightforwardly [33]. In Fig. 13.41(a), a TE-emitting InP-based multi-quantum-well GC is butt-coupled to the Polyboard. Again, the left facet of the

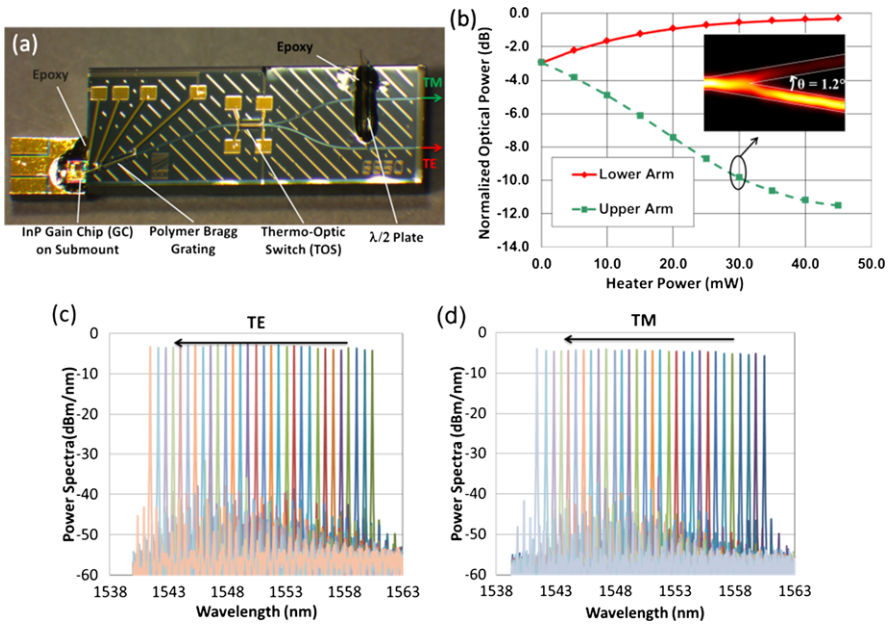


Fig. 13.41 (a) Photograph of polarization switchable external cavity laser. An InP GC and a $\lambda/2$ plate are secured by epoxies on the passive Polyboard. (b) simulated TOS characteristics, and laser wavelength tuning characteristics for the (c) TE and (d) TM path [38]

GC is high-reflection coated against air and the right facet is anti-reflection coated against polymer, the thermally tunable polymer Bragg grating functions as the front reflector, and the GC and the polymer Bragg grating together form the laser oscillator region. A 1-mm long waveguide buffer is reserved to prevent optical feedback from the TOS back into the oscillator to ensure stable single-mode operation. The laser emission is then split into two outputs: in the lower path the TE polarization is maintained while the light in the upper path goes through a half-wave ($\lambda/2$) plate and gets its polarization state rotated to TM. The TOS can steer the paths either for two balanced outputs or for a preferred output at one polarization.

The TOS is, in essence, a polymer waveguide Y-branch with heater electrodes placed off the Y-center to generate a temperature gradient and drive the adiabatic transformation of the eigenmode into the switched path [38]. The performance of the TOS is evaluated by numerical simulations as displayed in Fig. 13.41(b), in good agreement with the experimental results.

The switching behavior is identical for the TE and the TM path, as plotted in Fig. 13.41(c)–(d). When the heater electrode power increases to 20 mW, the wavelength shifts continuously from 1561 nm to 1541 nm, i.e., 20 nm wavelength tuning range is achieved with a tuning efficiency of 1 nm/mW. The SMSR is larger than 35 dB for all wavelengths obtained and can be further enhanced to above 40 dB by adjusting the phase electrode to avoid the mode hopping positions. The presence of the $\lambda/2$ -plate introduces a 1.4-dB output power drop in the TM path. This loss may

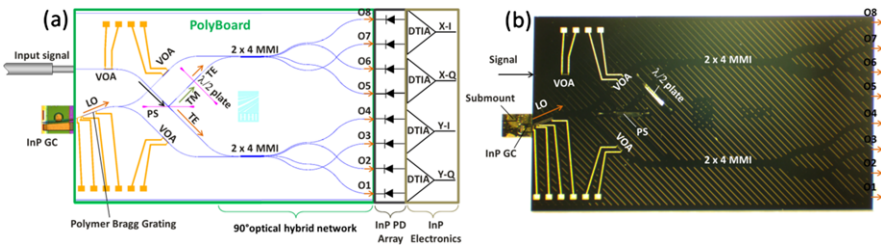


Fig. 13.42 (a) Schematic layout of the polymer-based coherent receiver and (b) photograph of the assembled 90° hybrid with LO integrated [34]

be minimized to below 1 dB by applying proper waveguide tapers to reduce light scattering in the non-confined slot region.

Such lasers may be adopted as low-cost local oscillators for dual-polarization, colorless coherent receivers. They may also trigger designs of other novel, polarization-diversity, multi-flow lasers and directly modulated transmitters for various Telecom and Datacom, and sensors applications.

13.6.5 Colorless Dual-Polarization 90° Hybrid

The exponential growth of Internet traffic is pushing the optical fiber technology from the current 112 Gb/s links based on the DP-QPSK coherent transmission scheme to 400 Gb/s and further beyond 1 Tb/s using higher order modulation formats up to 128-QAM. On the coherent receiver side, an optical 90° hybrid is required as the frontend to convert the phase modulated signal into amplitude modulation detectable by PDs. In order to reduce device cost, footprint, and power consumption, an integrated laser source acting as local oscillator (LO) is highly desired. For colorless operation under the WDM scheme, the optical 90° hybrid must be able to handle a broad wavelength range, e.g. the C-band, and accordingly the LO should be tunable over that same range [34].

The schematic layout of a hybrid coherent receiver is displayed in Fig. 13.42(a), and a photograph of an assembled colorless dual-polarization 90° hybrid as the coherent receiver frontend is shown in Fig. 13.42(b). The Polyboard measures 14 mm (length) by 7.8 mm (width). The output waveguides are arranged with 1 mm spacing in order to match the pitch size of the high-speed InP waveguide-based 8-PD array and the following electronic components.

The input signal from the fiber is first regulated by an variable optical amplifier (VOA) and reaches the TFE-based polarization splitter. The TE component propagates through to the lower 2 × 4 MMI (lower Rx, TE, O1–O4) while the TM component gets reflected and further passes through a half-wave ($\lambda/2$) plate serving as a polarization rotator. The TM light is then converted into TE polarization and reaches the upper 2 × 4 MMI (upper Rx, TM, O5–O8). An InP GC with high-power gain

spectrum is coupled to the polymer Bragg grating to form the tunable LO, the TE-polarized LO is split into two paths by a Y-branch, and both paths go through a VOA before reaching the corresponding 2×4 MMIs. In this configuration the MMI and the PDs only need to be optimized for TE polarization. It is worth noting that the PS usually causes higher loss for the transmitted TE path (~ 1.3 dB) than the reflected TM path (~ 0.5 dB). The addition of the $\lambda/2$ plate on the TM path introduces an extra loss of ~ 1 dB which balances out this PS-caused loss imbalance and helps to generate more uniformly distributed output power among the two mixer MMIs.

The tunable polymer Bragg grating and the VOAs are thermally driven. Heater electrodes are added with extension pads arranged on the upper- and lower-left corners of the Polyboard to facilitate wire bonding during packaging. Since the VOAs (1×1 MMIs) are compact with low insertion loss (< 0.5 dB), they are added both in the signal and the LO path to provide extra flexibility in handling signals with potentially large amplitude variations.

The PS and the $\lambda/2$ plate are passively inserted into the slots with the help of a vacuum tool and secured by index-matching UV curing epoxy. The slots are ~ 0.5 μm wider than the thickness of the TFE to ease mounting while keeping the excess slot loss as low as possible. The GC is first placed on a submount and then actively coupled to the Polyboard using an automatic alignment setup. Once a stable lasing point is reached, the facet is fixed by the index-matching and mechanically supporting epoxies. For high-power applications, the optical subassembly needs to be placed on a holder with sufficient cooling capability.

After assembly, the device is first characterized on the signal side. Broadband light with controlled polarization is injected as input. The polarization state is aligned to the TE and TM direction, respectively, and the outputs from O1 to O8 are analyzed in terms of the total optical loss, imbalance, and polarization extinction ratio (PER). The results are displayed in Fig. 13.43(a) and (b). Both the upper and lower Rx appear to have similar performance with an average insertion loss of ~ 13.3 dB at 1530 nm and 15.5 dB at 1565 nm, including 6 dB MMI intrinsic loss, 1.5 dB fiber coupling loss (both facets), 3 dB waveguide loss (propagation + bending), 1.5 dB TFE loss (PS + $\lambda/2$ plate), 0.5 dB VOA loss, and 0.8 to 3 dB MMI excess loss across the C-band (1535 nm to 1575 nm). The power imbalance among

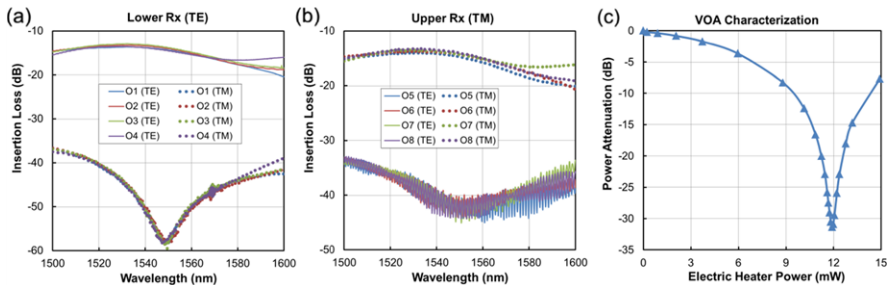


Fig. 13.43 Insertion loss of (a) the lower receiver Rx O1–O4, (b) the upper receiver Rx O5–O8, and (c) power attenuation of the on-chip VOA

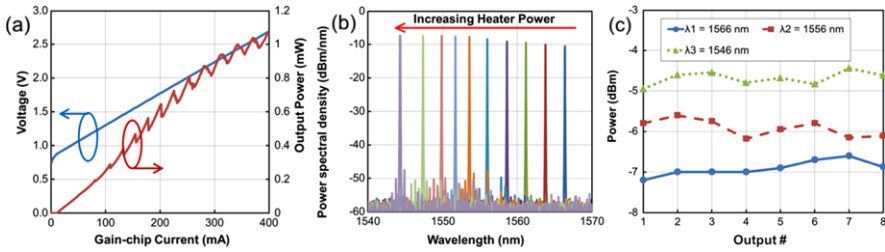


Fig. 13.44 (a) P - I and V - I curve of LO, (b) overlaid spectra of LO during tuning, and (c) LO power comparison at all eight outputs at three different wavelengths

all eight outputs is below 1 dB and the PER is larger than 25 dB across the C-band. The characterization results of the on-chip VOA are shown Fig. 13.43(c). At 12 mW electric heater power the VOA reaches an attenuation level of 32 dB.

The P - I and V - I characteristics of the LO are shown in Fig. 13.44(a), measured from the fiber at O1. The initial wavelength (without tuning) is 1566 nm. The output power reaches more than 1 mW at ~ 400 mA gain current. The ripples in the P - I curve are caused by mode-hopping and can be compensated by adjusting the phase-electrode included in the laser cavity. The LO can be continuously tuned over 22 nm, as demonstrated in Fig. 13.44(b). The side-mode-suppression ratio is larger than 40 dB. The power imbalance among the 8 outputs is evaluated at three wavelengths, as illustrated in Fig. 13.44(c). The power fluctuations among these three different wavelengths agree well with the 2×4 MMI measurements from the signal path and can be minimized by adjusting the MMI structural parameters. At the same wavelength, the power imbalance remains below 1 dB. The typical linewidth of the LO is ~ 200 kHz, but < 100 kHz may be achievable with further optimization.

13.6.6 TriPleX Microwave Beam-Former Assembly

Low-loss TriPleX waveguides have been implemented in many passive optical components for communication applications, including high-Q micro-ring resonators (MRRs), add-drop filters, AWG-based (de)multiplexers and so on. Another highly interesting area in communications is microwave photonics (MWP), an interdisciplinary field investigating the techniques for generation, transmission, processing, and analyzing of RF/microwave signals using photonic devices or subsystems [42, 43].

In recent years, a number of RF/microwave functionalities have been demonstrated using on-chip MWP signal processing in TriPleX technology [44–48]. The optical components are based on optical MRRs, and tuning and bandwidth reconfiguration in the order of a few GHz can be easily implemented. Squint-free performance and seamless beam steering for broadband applications can be achieved. For the utilization of optical beam-forming networks (OBFNs) in satellite-tracking

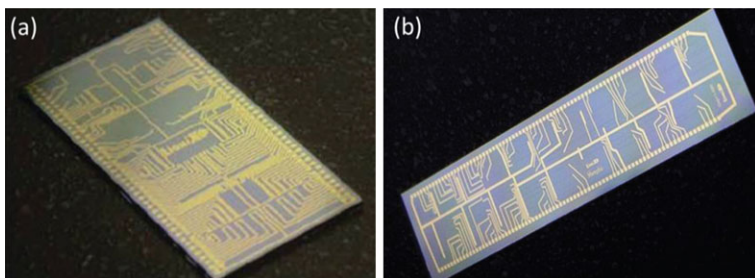


Fig. 13.45 Pictures of (a) 16×1 single-wavelength OBFN chip [43] and (b) 16×16 multi-wavelength OBFN chip [49]

phased array antenna systems operating in the Ku-band (10.7 to 12.75 GHz), delay lengths in the order of tens of centimeter are required. Consequently, low loss and compact waveguide configurations are essential for meeting performance and cost requirements. Therefore, the double stripe TriPleX geometry enabling MRRs with $125 \mu\text{m}$ radius is a very promising approach.

To date, three different types of optical beam-formers have been implemented with the TriPleX technology: single-wavelength, multi-wavelength, and multi-beam [50]. A realized chip of a 16×1 single-wavelength OBFN component is shown in Fig. 13.45(a). On the $7 \text{ mm} \times 22 \text{ mm}$ chip area, a tunable time delay (TTD) unit with 40 MRRs, splitters/combiners, and an optical sideband filter are included [51, 52]. Delays of 650 ps over 4.5-GHz bandwidth were measured.

By introducing a novel hardware architecture [49] based on parallelism, a 16×16 multi-wavelength OBFN could be realized on chip real estate as small as $36 \times 8 \text{ mm}^2$. Besides delay units and combiners, this chip, shown in Fig. 13.45(b), contains optical phase shifters, carrier tuners, and (de)multiplexers. A continuously tun-

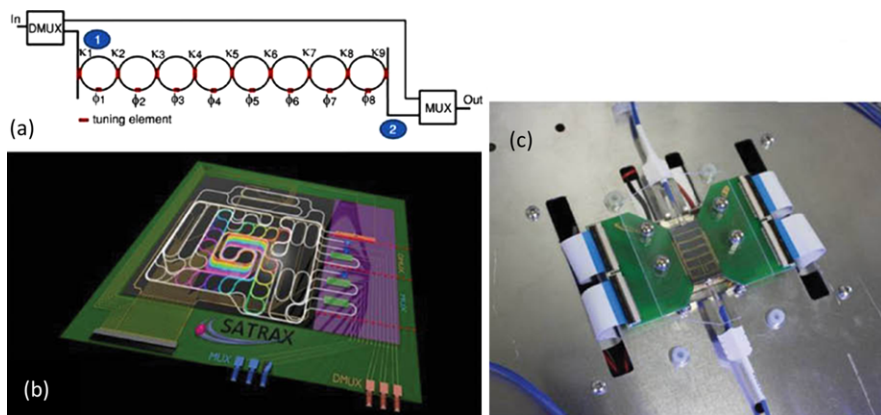


Fig. 13.46 (a) Schematic of fully tunable RF filter [54], (b) artist's impression of chip layout on circuit board, (c) fabricated chip assembly

able delay of up to 140 ps was measured over an instantaneous bandwidth from 2 to 10 GHz.

Further developments toward a fully integrated and low-cost MWP beam-former system exploit the large-scale integration potential of the TriPleX technology. Simultaneous implementation of components operating with phase modulation and direct detection [53] has been reported, and fully tunable RF filters have been implemented [54]. The various stages of the MPW beam-former system—from the filter schematic to the fabricated chip assembly—are illustrated in Fig. 13.46(a)–(c).

13.6.7 TriPleX Optical Coherence Tomography Assembly

Integrated photonics solutions become increasingly important for bio-medical applications and have started to enter fields like optical coherence tomography (OCT), Raman spectroscopy, and flow cytometry, and TriPleX-based photonics technology has been applied for a range of novel, miniaturized bio-medical components.

OCT is a widely applied noninvasive medical imaging technique for 3-D biological tissue investigation. The technique is based on low-coherence interferometry from scattering media. Operation in the 800-nm to 1300-nm wavelength range enables up to several millimeter penetration depth in the tissue. Utilization of wide spectral ranges (>100 nm) results in sub-micrometer resolution. For OCT in the spectral domain, two basic data acquisition modes can be distinguished: the swept-source OCT and the spectrometer-based OCT.

An integrated design for the swept-source OCT operating with an external swept source at 1300 nm was developed [55], and the corresponding circuit design is displayed in Fig. 13.47(a). The TriPleX chip functionality is designed in the single-stripe TriPleX geometry (50 nm × 3.4 μm) and has a chip footprint of 4 mm

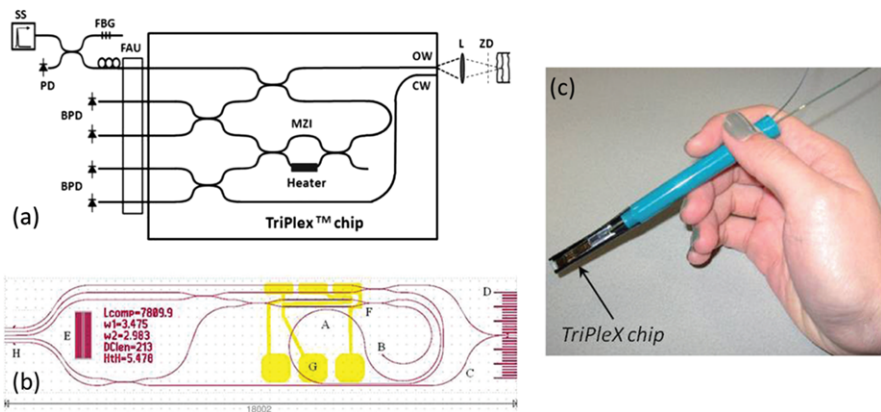


Fig. 13.47 (a) Schematic layout of swept-source OCT setup, (b) design of TriPleX chip layout, (c) example of handheld OCT probe (courtesy 2M)

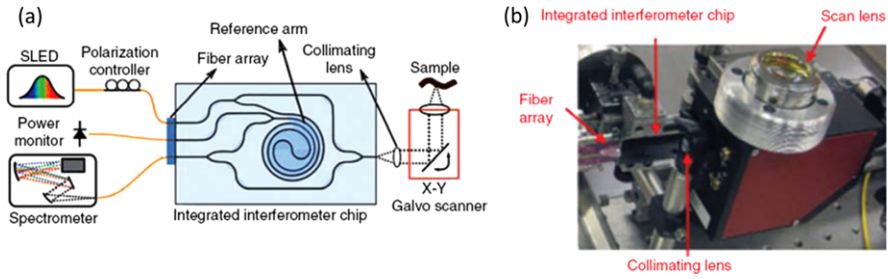


Fig. 13.48 (a) Schematic layout of OCT setup with integrated TriPleX-based interferometer chip and (b) photograph of test setup with fiber array, integrated interferometer chip and scan lens [20]

$\times 18$ mm, as shown in Fig. 13.47(b). The final packaged module is shown in Fig. 13.47(c). Component characterization resulted in a lateral resolution of $21 \mu\text{m} \pm 1 \mu\text{m}$, 80 dB sensitivity, and a maximum imaging depth of ~ 5 mm. The axial resolution of $12.7 \pm 0.5 \mu\text{m}$ is in good agreement with the bandwidth-limited resolution.

Based upon the TriPleX box shell geometry, an integrated interferometer chip was developed for a spectrometer-based OCT [20]. The design supports both polarizations and combines several Y-branches with a 190-mm-long reference arm at a footprint of only $10 \text{ mm} \times 33 \text{ mm}$, as sketched in Fig. 13.48(a). Under the test setup, shown in Fig. 13.48(b), the axial resolution of the system was measured to be $14 \mu\text{m}$. The sensitivity measured at 0.25 mm depth and 0.1 mW optical power on the sample was 65 dB. Comparison with the response of a fiber-based system showed good agreement in performance.

13.7 Conclusion

In this chapter, hybrid photonic integration technology is reviewed, focusing on the polymer and the TriPleX™ platforms. Diverse waveguide types are provided to address very specific problems in photonic applications. Multicore polymer waveguides with matched 45° mirror array can be used to build compact 3D photonic integrated circuits or connector devices with multicore fibers with matched pitch size. Polymer/inorganic heterogeneous waveguides can largely increase the choice of materials and their optical properties in constructing lightwave circuits. On the TriPleX™ platform, the single-stripe, double-stripe, and box-like silicon nitride waveguides buried in silicon dioxide can offer great flexibility in the PLC design: One can choose either extremely low transmission loss, high-quality-factor resonators or sharp bending corners and polarization independent devices.

Various optical assemblies and modules have been demonstrated, including passive waveguide splitters, polarization controllers, OLTs, ONU and coherent receiver for optical communications, but also miniaturized optical beam forming networks for microwave photonics and OCT devices for medical sensing applications. With

technologies advancing to integrate trans-platform components in a compact, three-dimensional way, hybrid photonic integration is expected to bring photonic device functionalities to a new, unprecedented level.

References

1. H. Ma, A.K.Y. Jen, L.R. Dalton, Polymer-based optical waveguides: materials, processing, and devices. *Adv. Mater.* **14**, 1339–1365 (2002)
2. G. Coppola, L. Sirlito, I. Rendina, M. Iodice, Advance in thermo-optical switches: principles, materials, design, and device structure. *Opt. Eng.* **50**(7), 071112 (2011)
3. Z. Zhang, N. Metzbach, C. Zawadzki, J. Wang, D. Schmidt, W. Brinker, N. Grote, M. Schell, N. Keil, Polymer-based photonic toolbox: passive components, hybrid integration and polarization control. *IET Optoelectron.* **5**(5), 226–232 (2011)
4. Z. Zhang, D. Liu, D. Felipe, A. Liu, N. Keil, N. Grote, Polymer embedded silicon nitride thermally tunable Bragg grating filters. *Appl. Phys. Lett.* **102**(18), 181105 (2013)
5. A. Liu, Z. Zhang, D. Felipe, N. Keil, N. Grote, Power-efficient thermo-optic tunable filters based on polymeric waveguide Bragg gratings. *IEEE Photonics Technol. Lett.* **26**(3), 313–315 (2014)
6. D. Felipe, Z. Zhang, W. Brinker, M. Kleinert, A. Maese-Novo, C. Zawadzki, M. Moehle, N. Keil, Polymer-based external cavity lasers: tuning efficiency, reliability and polarization diversity. *IEEE Photonics Technol. Lett.* **26**(14), 1391–1394 (2014)
7. P. Kersten, G. Schreiber, Stray light suppression structures using a waveguide and angled, deep etched trenches filled with an absorbing material. WO Patent 2004023179, March 18 (2004)
8. Z. Zhang, D. de Felipe, W. Brinker, M. Kleinert, A. Maese-Novo, M. Moehle, C. Zawadzki, N. Keil, C/L-band colorless ONU based on polymer bi-directional optical subassembly. *J. Lightwave Technol.* **33**, 1230–1234 (2015)
9. Z. Zhang, M. Kleinert, A. Maese-Novo, G. Irmscher, E. Schwartz, C. Zawadzki, N. Keil, Multicore polymer waveguides and multi-step 45° mirrors for 3D photonic integration. *IEEE Photonics Technol. Lett.* **26**(19), 1986–1989 (2014)
10. D. Liu, Z. Zhang, N. Keil, N. Grote, Thermally tunable silicon nitride sampled gratings in polymer. *IEEE Photonics Technol. Lett.* **25**(17), 1734–1736 (2013)
11. Z. Zhang, A. Novo, D. Liu, N. Keil, N. Grote, Compact and tunable silicon nitride Bragg grating filters in polymer. *Opt. Commun.* **321**, 23–27 (2014)
12. Z. Zhang, G. Genrich, N. Keil, N. Grote, Widely tunable grating-assisted heterogeneous silicon nitride/polymer waveguide coupler. *Opt. Lett.* **39**(1), 162–165 (2014)
13. K. Wörhoff, R.G. Heideman, A. Leinse, M. Hoekman, TriPleX: a versatile dielectric photonic platform. *Adv. Opt. Technol.* **4**(2), 189–207 (2015)
14. R.G. Heideman, J.A. Walker, Surface waveguide technology for telecom and biochemical sensing, in *Photonics West'06*. Proc. SPIE, vol. 6125, San Jose, CA, USA (2006), paper 021
15. F. Morichetti, A. Melloni, M. Martinelli, R.G. Heideman, A. Leinse, D.H. Geuzebroek, A. Borreman, Box-shaped dielectric waveguides: a new concept in integrated optics? *J. Lightwave Technol.* **25**(9), 2579–2589 (2007)
16. W. Hoving, D. Geuzebroek, R. Heideman, Designing a next-generation waveguide by geometry. *SPIE Newsroom* (2008). doi:10.1117/2.1200806.1166; <http://www.spie.org/x25303.xml?pf=true&highlight=x2414>
17. R.G. Heideman, M. Hoekman, E. Schreuder, TriPleX-based integrated optical ring resonators for lab-on-a-chip and environmental detection. *IEEE Sel. Top. Quantum Electron.* **18**(5), 1583–1596 (2012)
18. R.G. Heideman, A. Melloni, M. Hoekman, A. Borreman, A. Leinse, F. Morichetti, Low loss, high contrast optical waveguides based on CMOS compatible LPCVD processing: technology

- and experimental results, in *IEEE/LEOS Benelux Chapter 2005 Ann. Symp.*, Mons, Belgium Dec. 1–2, 2005, pp. 71–74
19. D.A.I. Marpaung, C.G.H. Roeloffzen, A. Leinse, M. Hoekman, A photonic chip based frequency discriminator for a high performance microwave photonic link. *Opt. Express* **18**, 27359–27370 (2010)
 20. G. Yurtsever, B. Považay, A. Alex, B. Zabihian, W. Drexler, R. Baets, Photonic integrated Mach-Zehnder interferometer with an on-chip reference arm for optical coherence tomography. *Biomed. Opt. Express* **5**, 1050–1061 (2014)
 21. L. Zhuang, D. Marpaung, M. Burla, W. Beeker, A. Leinse, C. Roeloffzen, Low-loss, high-index-contrast Si₃N₄/SiO₂ optical waveguides for optical delay lines in microwave photonics signal processing. *Opt. Express* **19**, 23162–23170 (2011)
 22. D.T. Spencer, M.J.R. Heck, R. Moreira, J. Bovington, J.E. Bowers, A. Leinse, H.H.v.d. Vlekkert, R.G. Heideman, M. Hoekman, T.T. Veenstra, Integrated single and multi-layer Si₃N₄ platform for ultra-low loss propagation and small bending radii, in *Opt. Fiber Commun. Conf. (OFC'14)*, San Francisco, CA, USA (2014), Techn. Digest, paper Th1A.2
 23. J.F. Bauters, M.J.R. Heck, D.D. John, J.S. Barton, C.M. Bruinink, A. Leinse, R.G. Heideman, D.J. Blumenthal, J.E. Bowers, Planar waveguides with less than 0.1 dB/m propagation loss fabricated with wafer bonding. *Opt. Express* **19**, 24090–24101 (2011)
 24. J.P. Epping, M. Hoekman, R. Mateman, A. Leinse, R.G. Heideman, A. Rees, P. Slot, C.J. Lee, K.J. Boller, High confinement, high yield Si₃N₄ waveguides for nonlinear optical applications. *Opt. Express* **23**, 642–648 (2015)
 25. V. Almeida, R. Panepucci, M. Lipson, Nanotaper for compact mode conversion. *Opt. Lett.* **28**, 1302–1304 (2002)
 26. G. Roelkens, D. Van Thourhout, R. Baets, High efficiency grating coupler between silicon-on-insulator waveguides and perfectly vertical optical fibers. *Opt. Lett.* **32**, 1495–1497 (2007)
 27. N. Keil, Z. Zhang, C. Zawadzki, C. Wagner, A. Scheibe, H. Ehlers, D. Ristau, J. Wang, W. Brinker, N. Grote, Ultra low-loss 1 × 2 multiplexer using thin-film filters on polymer integration platform. *Electron. Lett.* **45**(23), 1167–1168 (2009)
 28. EU FP7 project PHASTFlex (<http://www.phastflex.eu/>)
 29. M. Möhrle, W. Brinker, C. Wagner, G. Przyrembel, A. Sigmund, W.D. Molzow, First complex coupled 1490 nm CSDFB lasers: high yield, low feedback sensitivity, and uncooled 10 Gb/s modulation, in *Proc. 35th Europ. Conf. Opt. Commun. (ECOC'09)*, Vienna, Austria (2009), paper 8.1.2
 30. Z. Zhang, D. Felipe, W. Brinker, M. Kleinert, A. Maese-Novo, C. Zawadzki, M. Moehrle, N. Keil, Bi-directional, crosstalk-suppressed, 40-nm wavelength tuneable colourless ONU on polymer platform, in *Proc. 40th Europ. Conf. Opt. Commun. (ECOC'14)*, Cannes, France (2014), paper Mo. 4.4.4
 31. H. Klein, C. Wagner, W. Brinker, F. Soares, D. de Felipe, Z. Zhang, C. Zawadzki, N. Keil, M. Möhrle, Hybrid InP-polymer 30 nm tunable DBR laser for 10 Gbit/s direct modulation in the C-band, in *Internat. Conf. Indium Phosphide Relat. Mater. (IPRM'12)*, Santa Barbara, CA, USA (2012), pp. 20–21, Techn. Digest
 32. D. Felipe, C. Zawadzki, Z. Zhang, W. Brinker, H. Klein, M. Möhrle, N. Keil, N. Grote, M. Schell, 40 nm tuneable source for colourless ONUs based on dual hybridly integrated polymer waveguide grating lasers, in *Proc. 39th Europ. Conf. Opt. Commun. (ECOC'13)*, London, UK (2013), pp. 189–191
 33. D. Felipe, Z. Zhang, W. Brinker, M. Kleinert, A. Maese-Novo, C. Zawadzki, M. Moehrle, N. Keil, Polymer-based external cavity lasers: tuning efficiency, reliability and polarization diversity. *IEEE Photonics Technol. Lett.* **26**(14), 1391–1394 (2014)
 34. Z. Zhang, A. Maese-Novo, A. Polatynski, T. Mueller, G. Irmscher, D. de Felipe, M. Kleinert, W. Brinker, C. Zawadzki, N. Keil, Colorless, dual-polarization 90° hybrid with integrated VOAs and local oscillator on polymer platform, in *Opt. Fiber Commun. Conf. (OFC'15)*, Los Angeles, CA, USA (2015), Techn. Digest, paper Th1F.3
 35. M. Piels, J.F. Bauters, M.L. Davenport, M.J.R. Heck, J.E. Bowers, Low-loss silicon nitride AWG demultiplexer heterogeneously integrated with hybrid III–V/silicon photodetectors.

- J. Lightwave Technol. **32**, 817–823 (2014)
36. R.G. Heideman, M. Hoekman, Two-dimensional tapered coupler (nonlinear taper), U.S. Patent Application No.: 14/270,014
 37. J. Yue, F.H. Falke, J.C. Schouten, T.A. Nijhuis, Microreactors with integrated UV/vis spectroscopic detection for online process analysis under segmented flow. *Lab Chip* **13**, 4855–4863 (2013)
 38. T. Mueller, A. Maese-Novo, Z. Zhang, A. Polatynski, D. de Felipe, M. Kleinert, W. Brinker, C. Zawadzki, N. Keil, Switchable dual-polarization external cavity tunable laser. *Opt. Lett.* **40**, 447–450 (2015)
 39. D. Felipe, C. Zawadzki, Z. Zhang, A. Maese-Novo, M. Wenzel, H. Li, G. Przyrembel, A. Sigmund, M. Möhrle, N. Keil, N. Grote, M. Schell, Hybrid InP/polymer optical line terminals for 40-channel 100-GHz spectrum-sliced WDM-PON, in *Proc. 39th Europ. Conf. Opt. Commun. (ECOC'13)*, London, UK (2013), pp. 237–239
 40. D. Dai, Z. Wang, J.F. Bauters, M. Tien, M. Heck, D.J. Blumenthal, J.E. Bowers, Low-loss Si₃N₄ arrayed-waveguide grating (de)multiplexer using nano-core optical waveguides. *Opt. Express* **19**, 14130–14136 (2011)
 41. S.C. Nicholes, J.W. Raring, M. Dummer, A. Tauke-Pedretti, L.A. Coldren, High-confinement strained MQW for highly polarized high-power broadband light source. *IEEE Photonics Technol. Lett.* **19**(10), 771–773 (2007)
 42. J. Capmany, D. Novak, Microwave photonics combines two worlds. *Nat. Photonics* **1**, 319–330 (2007)
 43. D. Marpaung, C. Roeloffzen, R. Heideman, A. Leinse, S. Sales, J. Capmany, Integrated microwave photonics. *Laser Photonics Rev.* **7**, 506–538 (2013)
 44. L. Zhuang, W.P. Beeker, A. Leinse, R.G. Heideman, C.G.H. Roeloffzen, Novel wideband microwave polarization network using a fully-reconfigurable photonic waveguide interleaver with a two-ring resonator-assisted asymmetric Mach-Zehnder structure. *Opt. Express* **21**, 3114–3124 (2013)
 45. L. Zhuang, M.R. Khan, W.P. Beeker, A. Leinse, R.G. Heideman, C. Roeloffzen, Novel microwave photonic fractional Hilbert transformer using a ring resonator-based optical all-pass filter. *Opt. Express* **20**, 26499–26510 (2012)
 46. M. Burla, D.A.I. Marpaung, L. Zhuang, C.G.H. Roeloffzen, M.R. Khan, A. Leinse, M. Hoekman, R. Heideman, On-chip CMOS compatible reconfigurable optical delay line with separate carrier tuning for microwave photonic signal processing. *Opt. Express* **19**, 21475–21484 (2011)
 47. D. Marpaung, L. Chevalier, M. Burla, C.G.H. Roeloffzen, Impulse radio ultrawideband pulse shaper based on a programmable photonic chip frequency discriminator. *Opt. Express* **19**, 24838–24848 (2011)
 48. D. Marpaung, B. Morrison, R. Pant, C. Roeloffzen, A. Leinse, M. Hoekman, R. Heideman, B.J. Eggleton, Si₃N₄ ring resonator-based microwave photonic notch filter with an ultrahigh peak rejection. *Opt. Express* **21**, 23286–23294 (2013)
 49. M. Burla, D. Marpaung, L. Zhuang, M. Khan, A. Leinse, W. Beeker, M. Hoekman, R.G. Heideman, C. Roeloffzen, Multiwavelength-integrated optical beamformer based on wavelength division multiplexing for 2-D phased array antennas. *J. Lightwave Technol.* **32**, 3509–3520 (2014)
 50. C. Roeloffzen, R. Oldenbeuving, R.B. Timens, P. van Dijk, C. Taddei, A. Leinse, M. Hoekman, R.G. Heideman, L. Zhuang, D. Marpaung, M. Burla, Integrated optical beamformers, in *Opt. Fiber Commun. Conf. (OFC'15)*, Los Angeles, CA, USA (2015), Techn. Digest, paper Tu3F.4
 51. C.G.H. Roeloffzen, L. Zhuang, C. Taddei, A. Leinse, R.G. Heideman, P. Dijk, R.M. Oldenbeuving, D. Marpaung, M. Burla, K.J. Boller, Silicon nitride microwave photonic circuits. *Opt. Express* **21**, 22937–22961 (2013)
 52. L. Zhuang, C.G.H. Roeloffzen, A. Meijerink, M. Burla, D.A.I. Marpaung, A. Leinse, M. Hoekman, R.G. Heideman, W. Etten, Novel ring resonator-based integrated photonic beamformer for broadband phased array receive antennas—Part II: Experimental prototype. *J. Lightwave Technol.* **28**, 19–31 (2010)

53. L. Zhuang, M. Hoekman, C. Taddei, A. Leinse, R.G. Heideman, A. Hulzinga, J. Verpoorte, R.M. Oldenbeuving, P. Dijk, K.J. Boller, C. Roeloffzen, On-chip microwave photonic beamformer circuits operating with phase modulation and direct detection. *Opt. Express* **22**, 17079–17091 (2014)
54. C. Taddei, L. Zhuang, M. Hoekman, A. Leinse, R. Oldenbeuving, P. Dijk, C. Roeloffzen, Fully reconfigurable coupled ring resonator-based bandpass filter for microwave signal processing, in *Proc. Internat. Top. Meeting Microwave Photon./The 9th Asia-Pacific Microwave Photon. Conf. (MWP/APMP' 14)*, Sapporo, Japan (2014), pp. 44–47, paper TuC-4. doi:[10.1109/MWP.2014.6994485](https://doi.org/10.1109/MWP.2014.6994485)
55. V.D. Nguyen, N. Weiss, W. Beeker, M. Hoekman, A. Leinse, R.G. Heideman, T.G. van Leeuwen, J. Kalkman, Integrated-optics-based swept-source optical coherence tomography. *Opt. Lett.* **37**, 4820–4822 (2012)

Ziyang Zhang received his Master of Science degree in 2004 and Ph.D. in 2008, both from the Royal Institute of Technology (KTH), Sweden. Subsequently he spent eight years with Fraunhofer Heinrich Hertz Institute (HHI), Berlin, as a senior scientist and then moved to Leibniz-Institute for Astrophysics Potsdam (AIP) as head of the Astrooptics group. His research experience covers silicon-based photonic devices, polymer photonics and hybrid photonic integration, from optical circuit design, numerical simulations, nano-fabrication technology, to module assembly, packaging and further to device characterization. He has been heavily engaged in Telecom/Datacom industry solutions and lead the EU FP-7 projects ICT-POLYSYS and ICT-PANTHER. He has also worked as an expert in the EU FP-7 project ICT-ACTPHAST and organized a special issue of “Optics Communications” dedicated to polymer photonics. He has authored and co-authored more than 40 articles in SCI-indexed journals, plus over 60 contributions in international conferences.

Arne Leinse is Project-/account Manager & Vice President of LioniX BV. He received an M.Sc. degree from the University of Twente in the Integrated Optical Microsystems group in 2001. In this same group he started his Ph.D. work on the topic of active microring resonators for various optical applications, carried out in the framework of a European project (IST 2000–28018 “Next generation Active Integrated optic Subsystems”) and his thesis was titled: “Polymeric micro-ring resonator based electro-optic modulator”. In 2005 he joined LioniX BV where he was involved in the invention and development of the TriPleX™ platform from the very beginning of concept development until exploitation. He is a member of the management team and involved in a variety of (integrated optical) projects including the strategic roadmap of technology and LioniX as well.

Chapter 14

Silicon Photonic Integrated Circuits

Roel Baets, Wim Bogaerts, Bart Kuyken, Abdul Rahim, Günther Roelkens, Thijs Spuesens, Joris Van Campenhout, and Dries Van Thourhout

Abstract The chapter covers fundamentals of Silicon Photonic ICs including the driving forces, basic physics, technological implementations, current state of the art, ongoing R&D and trends for future research. The treatment includes all relevant devices excluding Silicon Photonics based sources. The chapter comprises specific sections on wavelength selective devices such as delay-line based- and ring resonator-based spectral filters, and covers grating couplers, waveguide-integrated germanium photodetectors, and optical isolators as well. Nonlinear optic devices constitute a more advanced topic, and its coverage includes fundamental aspects and a number of corresponding devices including wavelength converters, all optical amplifiers, phase sensitive amplifiers, and a section on the design of complex Silicon Photonic ICs.

R. Baets · W. Bogaerts · B. Kuyken · A. Rahim · G. Roelkens · T. Spuesens (✉) ·
D. Van Thourhout

Ghent University – imec, Photonics Research Group, Center of Nano- and Biophotonics
(NB-Photonics), iGent Tower – Department of Information Technology (INTEC), Ghent
University, Technologiepark-Zwijnaarde 15, 9052 Gent, Belgium
e-mail: thijs.spuesens@intec.UGent.be

R. Baets
e-mail: roel.baets@intec.ugent.be

W. Bogaerts
e-mail: wim.bogaerts@intec.UGent.be

B. Kuyken
e-mail: bart.kuyken@intec.UGent.be

A. Rahim
e-mail: abdul.rahim@intec.UGent.be

G. Roelkens
e-mail: gunther.roelkens@intec.UGent.be

D. Van Thourhout
e-mail: driesvt@intec.UGent.be

J. Van Campenhout
imec, Kapeldreef 75, 3001 Heverlee, Belgium
e-mail: joris.vancampenhout@intec.ugent.be

14.1 Silicon Photonics as a Generic Photonic Integrated Circuit Platform

In September 1969 the Bell System Technical Journal published a paper by Stewart Miller entitled “Integrated Optics: An Introduction” [1]. This paper is widely considered to be the seminal paper that launched the field of photonic integration (or integrated optics, as it was called for several decades). The abstract of Miller’s paper reads: *“This paper outlines a proposal for a miniature form of laser beam circuitry. Index of refraction changes of the order of 10^{-2} or 10^{-3} in a substrate such as glass allow guided laser beams of width near 10 microns. Photolithographic techniques may permit simultaneous construction of complex circuit patterns. This paper also indicates possible miniature forms for a laser, modulator and hybrids. If realized, this new art would facilitate isolating the laser circuit from thermal, mechanical, and acoustic ambient changes through small overall size; economy should ultimately result.”* This paper clearly hints at the benefits of integrating photonic functions on a chip in terms of reliability and cost advantage and at the use of technologies to achieve this integration that, back then, had already become indispensable for the manufacturing of electronic integrated circuits. Interestingly the first CMOS integrated circuits had been made by RCA only a year earlier, in 1968, by a group led by Albert Medwin.

The field of electronic integrated circuits has obviously grown exponentially since the 1960s. Already in 1965 Gordon Moore, co-founder of the INTEL corporation, predicted this exponential growth, with the forecast that the number of transistors on an integrated circuit would double approximately every two years. This trend, coined as Moore’s law, has had a dramatic impact on the development of digital electronics and on the world economy as a whole. The field of photonic integrated circuits (PICs) however did largely stay in the research labs for the rest of the twentieth century (at least if discrete photonic components made by wafer-scale technologies are not taken into account). One can argue that was the case both because of the lack of a substantial market pull and because of the difficulty to implement a variety of key photonic functions in a single material system and technology platform. It was very difficult to identify large volume markets that would necessitate the integration of a large number of photonic components in a circuit. Furthermore a challenging feature of photonic integrated circuits is the fact that there is a broad variety of photonic building blocks: light emitters and light detectors, light modulators, devices that manipulate light in the spatial, spectral or polarization domain, optical isolators, etc. This is obviously very different from the situation in electronics where transistors are the predominant building block. The diversity in photonic building blocks has led to the development of a broad variety of material platforms for photonic integration, each with advantages for specific building blocks but rarely with a broad set of assets for all important building blocks. On top of this there is the richness of many different wavelength bands, but again few materials fit all possible wavelength bands. As a result of all of this the investments in PIC-technologies have been diluted over many different material systems, contrary to

the case of electronic ICs where the vast majority of investments went into silicon technology, in particular silicon CMOS technology.

Apart from being the ubiquitous material in electronics, silicon is being used in large volume for opto-electronic applications in the visible and near infrared (below 1.1 μm) wavelength bands. In particular silicon's excellent absorption properties turn it into an excellent material for conversion of light signals into electric signals. Mainstream examples include photodiodes for 850 nm optical interconnect systems, CCD and CMOS image sensors and solar cells. But for a long time silicon was not considered to be an attractive material for PICs, mostly since it seemed impossible to combine light emission, light guiding, light modulation and light detection on a silicon platform. In 1985 Richard Soref and Joseph Lorenzo published their seminal paper on the use of silicon as a material for PICs [2]. They demonstrated light guiding at 1.3 μm in a silicon waveguide with vertical confinement provided by weak carrier-induced refractive index contrast. This waveguide is schematically illustrated in Fig. 14.1(a). They also proposed the use of carrier injection to create a silicon-based optical modulator. In a later theoretical paper [3] Soref and Bennett predicted that carrier-induced silicon optical modulators would have practical lengths of about 1 mm for a carrier concentration change of the order of $1 \times 10^{-18} \text{ cm}^{-3}$ while keeping the free carrier absorption losses relatively modest.

The field of silicon photonics gained momentum only after the year 2000. Three mutually strengthening drivers can be pinpointed for the rapidly growing scientific and industrial interest between 2000 and 2010. These will be called hereafter the market driver, the physical driver and the technology driver.

14.1.1 The Market Driver: Short Reach Data Links

The rapid growth in Internet traffic is driving the need for high data capacity interconnect solutions at all distance levels, all the way from sub-mm-level connections within computer chips to multi-mm-level connections between continents. Interestingly the two extremes in this range are served by technological solutions that, at least for now, can keep up with the increasing market demand. Long-distance communication is very well addressed by the astounding capacity of fiber-optic networks through the use of a plethora of multiplexing techniques and advanced modulation formats. Very short distance interconnect is served well by electrical copper wiring, even if this happens at a considerable price in terms of power dissipation, certainly within chips where the copper wire cross-section is very small. But at the intermediate level – with distances in the range of 1 to 100 m – the challenges are enormous. Electrical interconnect is not practical and would lead to enormous power dissipation, large cable size and cost. Optical interconnect would be too expensive and too bulky if the solutions deployed in long-distance communication would be re-used without modification. There is a dramatic need for solutions that combine high data capacity with low power consumption, small form factor, excellent reliability and low cost. Two types of solutions have been developed in the past

decade. The first is based on multimode optical fiber in combination with low cost 850 nm VCSELs and silicon detectors. The second is based on single mode fiber in combination with silicon photonics transceivers and a 1.3 or 1.55 μm laser diode. This is what drives the field of silicon photonics.

The emergence of a supply chain for silicon photonics PICs leads people to be creative and come up with new applications for this technology, and thereby new markets. This is for example the case for advanced coherent receivers for long-distance optical communication. But a very important high-volume market may be the sensors market. Silicon photonics technology allows to manufacture PICs with advanced sensing functions at a very low cost, possibly even so low that the chip may become a use-once disposable chip, as in the case of biosensors for protein or DNA detection. Most of these applications operate in the typical telecom 1.3–1.55 μm bands, but a lot of research is being conducted to explore other wavelength bands – both longer and shorter wavelengths – and adapt the silicon photonics platform to these bands.

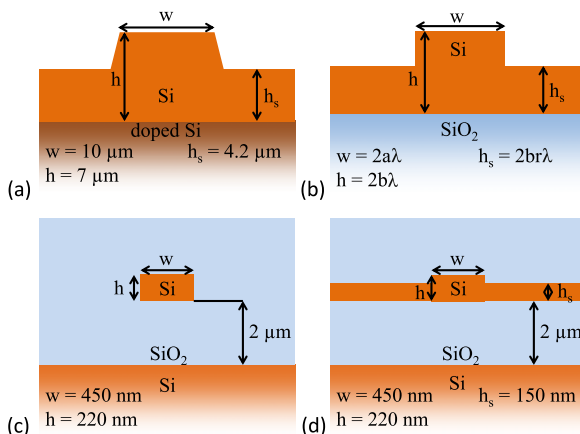
14.1.2 The Physical Driver: High Index Contrast

The name of the game in silicon photonics is high index contrast. While the early silicon waveguide of Soref and Lorenzo [2] was based on weak index contrast between undoped and doped silicon, it did not take long before one realized that a better option was to use silicon-on-insulator (SOI) wafers, consisting of a thin crystalline silicon layer on a silica (SiO_2) buffer layer on a silicon substrate. With this structure one can form waveguides, the core of which is silicon (refractive index $n = 3.5$), the bottom cladding is silica ($n = 1.5$) and the upper cladding is silica or air. The high vertical index contrast can be complemented by high horizontal index contrast by etching the silicon layer down to the buffer. Depending on the depth of etching the in-plane index contrast can be chosen to be low or high. There is not one possible choice here and various actors in the field have opted for different strategies, as illustrated in Fig. 14.1. Given the high index contrast it is logical that the cross-sectional dimensions of the waveguide need to be sufficiently small to achieve single mode operation. Surprisingly however, the “large” rib waveguide shown in Fig. 14.1(b) – with a width and a thickness of several microns – can be single-moded if the waveguide dimensions and the rib etch depth in particular are chosen appropriately, i.e. the following relation should hold:

$$\frac{a}{b} \leq 0.3 + \frac{r}{\sqrt{1-r^2}} \quad (14.1)$$

where a is a constant for the rib width, b is a constant for the rib height (see Fig. 14.1) and r is the fractional height of the slab with respect to the rib height [4]. However, it is not possible with this large rib waveguide to design very compact circuitry. The fully etched silicon waveguide of Fig. 14.1(c) – the structure with the highest index contrast all around – has become a more prominent choice. It is often

Fig. 14.1 Waveguide variants: (a) the first silicon waveguide demonstrated by Soref and Lorenzo in 1985 employing a carrier induced vertical index contrast [2]; (b) large silicon on silica rib waveguide that is single moded under specific dimensional conditions [4], see also (14.1); (c) a thin SOI waveguide with full etch; (d) a thin SOI waveguide with partial etch



called a (nano) photonic wire or strip waveguide. In order to remain single-moded this waveguide needs to have dimensions of the order of the wavelength of light in silicon, both vertically and horizontally. A typical silicon layer thickness is in the range 200 to 400 nm and a typical waveguide width is in the range 400 to 800 nm, for operation at $1.55 \mu\text{m}$. A variant of the photonic wire is the structure shown in Fig. 14.1(d), in which the silicon layer is not fully etched, thereby creating somewhat weaker lateral confinement. This structure is very important in optical modulators in order to provide electrical access to the waveguide core through the electrically conducting slab to the left and the right of that core. It also has lower waveguide losses than the photonic wire in view of reduced scattering losses at the etched sidewalls. In many circuits it is sensible to combine the wires of type Fig. 14.1(c) and those of type Fig. 14.1(d) and include adiabatic transitions between both types. The remainder of this chapter mostly focuses on thin SOI-waveguides of those two types.

High index contrast waveguides such as photonic wires have important assets. They allow for very sharp bends with radii of curvature down to a few microns, thereby enabling high density PICs. More generally, many basic component types can be scaled down in length or in area because of the high index contrast. Furthermore, high index contrast is also at the basis of more advanced waveguiding concepts such as photonic crystal waveguides which can enable amongst others propagation of light at low group velocity. Another important feature of high index contrast is that the waveguide mode is as tightly confined as it can possibly be in dielectric structures. This means that the electric field strength is as high as it can get for a given optical power. This implies that the light-matter interaction is maximized. This is of particular importance in sensing devices as well as in nonlinear optical devices.

But high index contrast also comes at a price. The propagation constant and effective index of photonic wires are extremely sensitive to small deviations in the dimensions – thickness and width – of the waveguide. In wavelength selective devices based on interferometric mechanisms, such as ring resonators, the spectral

response will critically depend on the guided mode effective index and therefore on the waveguide dimensions. As a rule of thumb one can often write:

$$\frac{\Delta\lambda_c}{\lambda_c} \approx \frac{\Delta d}{d} \quad (14.2)$$

where λ_c is a characteristic wavelength of the spectral response and $\Delta\lambda_c$ its deviation as a result of a deviation Δd in waveguide width or thickness d . Since this thickness or width is of the order of the wavelength itself, the rule of thumb often translates to:

$$\Delta\lambda_c \approx \Delta d \quad (14.3)$$

This equation illustrates the dramatic need for accuracy in silicon photonic wires: for a deviation in width or thickness of the silicon core of 1 nm, there will be a wavelength shift in the spectral behavior of the order of 1 nm! Therefore silicon photonics is only possible when one uses a technology with very high geometric accuracy and reproducibility.

Another challenge of photonic wires is their polarization sensitivity: the quasi-TE mode has an effective index that differs strongly from that of the quasi-TM mode. Again this is the consequence of high index contrast. In principle a square silicon waveguide surrounded by silica would be polarization insensitive but any nm-level deviation from the square cross-section would lead to substantial polarization mode dispersion. Therefore it is more usual to live with the strong polarization dependence and use the silicon PICs for single polarization optical signals. In cases where the input light signal has an unpredictable polarization state – as is the case for the receiver end in fiber optic links – one can choose to split the two polarizations and process them in separate circuits. In less tightly confined silicon waveguides, such as the rib structure in Fig. 14.1(b), the waveguide geometry can be optimized for polarization insensitivity.

A further consequence of high index contrast is strong dispersion. The effective group index of a photonic wire mode can differ substantially from its phase index. This is not necessarily a problem for circuits that operate over a relatively narrow spectral band, but it turns the design of wideband devices into a real challenge. Furthermore in nonlinear optical devices the dispersion plays an important role for efficient phase matching. Here the strong index contrast can be turned into a blessing in the sense that the waveguide cross-section can be tailored relatively easily to achieve specific dispersion properties, e.g. zero group velocity dispersion at a predetermined wavelength. But again, all of this works only if geometry can be controlled down to nanometer accuracy.

A final challenge of silicon photonic wires is their scattering-induced optical loss. Given the strong field confinement, the electric field is relatively strong at the silicon-silica and silicon-air interfaces. Any roughness of these high-index-contrast interfaces will then lead to strong scattering. This is not so much a problem for the horizontal interfaces, which are the result of polishing processes and are almost atomically smooth. But the vertical sidewalls are the result of a lithographic process and a subsequent dry etching process. Unless the interface roughness is limited to a

few nanometer, the scattering losses will be unacceptably high. Again this calls for fabrication accuracy with nanometer-level precision.

14.1.3 The Technology Driver: The CMOS Fab

The fact that the technology portfolio in a CMOS fab can be put to use for silicon-based PICs is an enormous driver for the field since the cost of investment into the fab can be shared with other and larger users. The legacy of the microelectronics industry is enormous. Anno 2014 there is infrastructure worldwide capable of manufacturing very large scale CMOS ICs with smallest dimensions down to 14 nm and do so in very high volume and with very high yield. Quite obviously this goes beyond the smallest dimensions that one will typically find in PICs with waveguide widths of the order of 500 nm and perhaps gaps or slots between waveguides down to 100 nm. But as was emphasized earlier, photonics needs accuracy: as an example one may want 450 nm wide photonic wires with a standard deviation across the wafer of 5 nm and an RMS roughness of 2 nm. The accuracy provided by the process portfolio in a CMOS fab scales together with the resolution and the smallest feature. Therefore, it makes sense to use the most advanced CMOS-node that is accessible and affordable for silicon photonic circuitry.

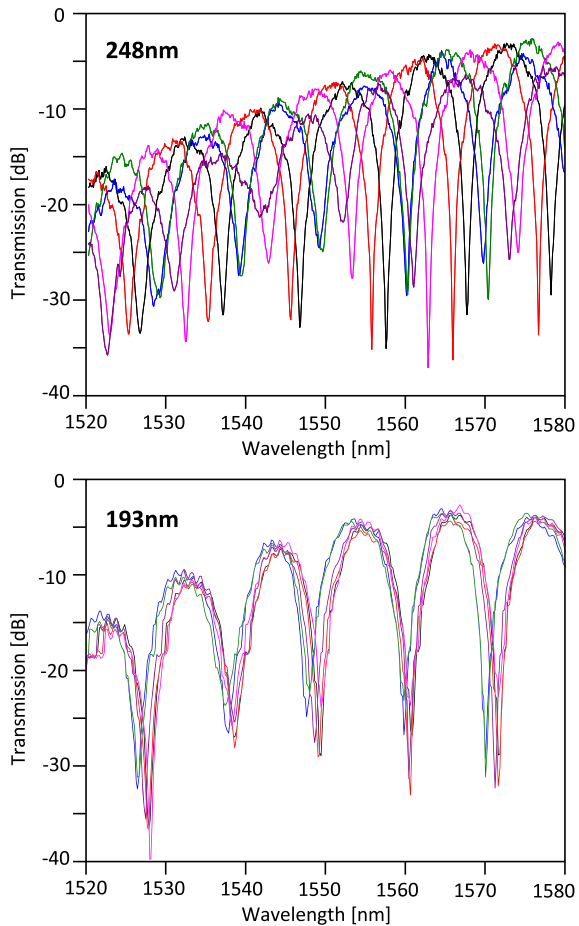
In order for silicon photonics to make use of CMOS-technology there needs to be some degree of compatibility, i.e. “CMOS-compatibility”. The term CMOS-compatibility has many meanings and is therefore somewhat ambiguous. Roughly speaking one can distinguish three levels of compatibility:

1. CMOS-wafer compatibility: the silicon photonics functionality can be integrated in the process flow for electronic CMOS circuitry, thereby enabling co-integration of electronics and photonics in a single chip.
2. CMOS-fab compatibility: the silicon photonics wafers can be manufactured with the set of tools and processes available in a CMOS fab without disturbing the capability to manufacture electronic ICs in that same fab.
3. CMOS-tool capability: the silicon photonics wafers can be manufactured with a set of tools that were developed (and perhaps formerly used) for CMOS technology.

Most fabrication of silicon PICs is happening at the second level, but there are also examples at the first and at the third level. One may think that the possibility of co-integrating photonics with electronics in a single chip is an important driver for the field. This may be the case for a subset of applications of silicon photonics, but this co-integration is not very flexible since it implies that both the electronics and the photonics need to be manufactured at the same “CMOS-node”. This is often not desirable from an economic point of view: the electronics part of a high data rate transceiver may require a very advanced CMOS-node where the cost/mm² is very high. The photonic circuitry is often more area consuming than the electronic circuitry and therefore it is often not affordable to manufacture the photonics part in the most advanced CMOS-node.

The workhorse for patterning circuits in a CMOS fab is the deep-UV step-and-scan lithography system. The three latest lithography generations used in volume CMOS-manufacturing have made use of a wavelength of exposure of first 248 nm, then 193 nm, followed by the same with water immersion between the imaging lens and the silicon wafer. These consecutive generations have allowed to scaling down the minimum feature size in CMOS circuits from 130 nm down to an amazing 22 nm and even 14 nm, in just over 10 years. The silicon photonics community largely started research on 248 nm systems [5] and gradually switched to 193 nm [6] and even 193 nm with immersion [7]. This has resulted in a gradual decrease of the scattering-induced losses of photonic wires and a continuous improvement of the uniformity and the reproducibility of the spectral response of interferometric devices. This is illustrated in Figs. 14.2 and 14.3. Figure 14.2 shows the improvement in uniformity as a result of the transition from a 248 nm to a 193 nm lithography platform, both on 200 mm wafers [8].

Fig. 14.2 Transmission of 6 nominally identical Mach-Zehnder interferometers revealing the improvement in uniformity as a result of the transition from a 248 nm (*top*) to a 193 nm (*bottom*) lithography platform, both on 200 mm wafers (reprinted from [8])



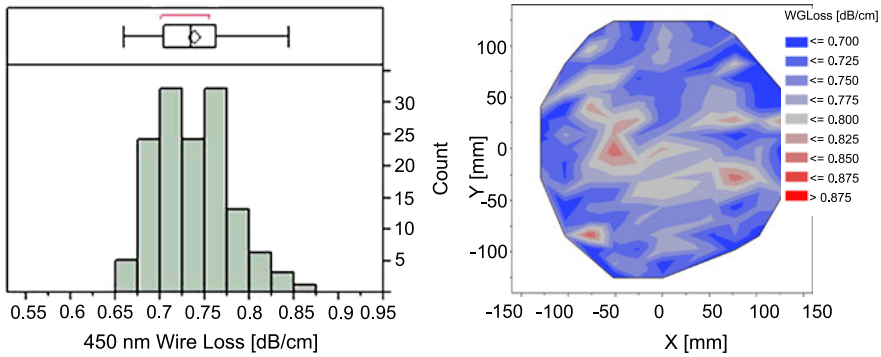


Fig. 14.3 Photonic wire losses and their uniformity obtained on a 193 nm immersion lithography system on 300 mm wafers (reprinted from [7])

Figure 14.3 shows the low photonic wire losses and their uniformity obtained on a 193 nm immersion lithography system on 300 mm wafers [7]. The average loss obtained on a 450 nm wide photonic wire was about 0.75 dB/cm, to be compared with the typical values between 2 and 3 dB/cm obtained for 193 nm dry lithography on 200 mm wafers.

One of the important challenges specific to the field of silicon photonics is that access to a CMOS-facility is non-trivial and that the calibration of processes for photonic components is expensive in such an environment. For this reason multi-project-wafer services have been set up by a variety of organizations, with the purpose to lower these barriers and create access mechanisms to CMOS fabs with standardized process modules for silicon photonics in a shared-cost mode and with a variety of supporting tools and services, such as design tools, process design kits (PDKs), access to standardized packaging approaches etc. [9, 10].

14.2 Basic Properties of Silicon High-Index-Contrast Waveguides

In the following section we will give a brief overview of the basic properties of some common silicon waveguide structures. We will discuss strip waveguides with air and oxide cladding, rib waveguides with oxide cladding and slot waveguides with oxide cladding.

While slab modes can be strictly TE or TM polarized, this is not true for channel waveguide modes. Strictly speaking, modes in channel waveguides are hybrid modes and therefore not truly TE or TM polarized. However, because the polarization is nearly linear in these structures the modes are often referred to as TE-like and TM-like modes and can be very well approximated as if they were really TE/TM polarized which is advantageous from a computational point of view.

14.2.1 Strip Waveguides

Figure 14.4(a) shows the geometry of a strip waveguide with oxide cladding. The simulation domain is indicated by the dashed box. The waveguide has a width of 450 nm and a height of 220 nm. The buried oxide layer (BOX) has a thickness of 2 μm . This strip waveguide has symmetry in both the x and y direction, where x is defined as being parallel to the substrate.

The electric field components are shown in Fig. 14.4(b) for both the fundamental TE-like and TM-like mode at a wavelength of 1550 nm. The dominant field component for the TE-like mode is E_x , while for the TM-like mode it is the E_y component. The other field components are much weaker but not zero and reveal the hybrid nature of these modes. Note that the field profiles are symmetric in this case, which is to be expected because of the symmetry in the waveguide structure. In most numerical mode solvers, symmetry can be exploited to reduce the simulation time.

By having a closer look at the E_x field component of the TE-like mode, it becomes clear that there is a discontinuity in the field at the sidewalls and that the field is strong near these interfaces. Any imperfection in the sidewalls will therefore have a strong impact on TE-like polarized modes. Sidewall roughness will induce loss and also back reflections while inaccuracies in width will have impact on the effective index of the mode. This can cause serious problems for the design of e.g. delay based optical filters [11]. Tight width and height control and smooth sidewalls are therefore of prime importance and put stringent requirements on the fabrication technology.

For the TM-like mode the main field component (E_y) is strong at the top and bottom interfaces of the waveguide. As no etching process is involved in these interfaces, distributed back-reflections due to roughness are less of a problem in this case. However, any variations in width and height will have a strong impact on the effective index.

The effective indices of the fundamental TE-like and TM-like mode are plotted as function of wavelength in Fig. 14.4(c). Both, the TE-like and TM-like modes are guided in the wavelength range of 1 to 2 μm when the cladding material is oxide. The significant difference in effective index for these modes indicates that there is large birefringence. Also note that at a wavelength of 2 μm the effective index of the TM-like mode is very close to the refractive index of silicon oxide and hence the mode is only weakly guided at this wavelength and very close to cut-off.

The group velocity (or second order) dispersion of the fundamental TE-like and TM-like modes is shown in Fig. 14.4(d) as a function of wavelength. The simulation is set up to include material dispersion also, but this influence is quite small for the wavelength range considered here. Dispersion is therefore dominated by waveguide dispersion and can thus be engineered.

For the particular waveguide dimensions used here, the dispersion is positive (anomalous) in the wavelength range of 1.15 to 1.6 μm with a maximum of 760 ps/nm/km for the TE-like mode. The TM-like mode on the other hand has positive dispersion below a wavelength of 1.15 μm and negative dispersion up to a wavelength of at least 2 μm .

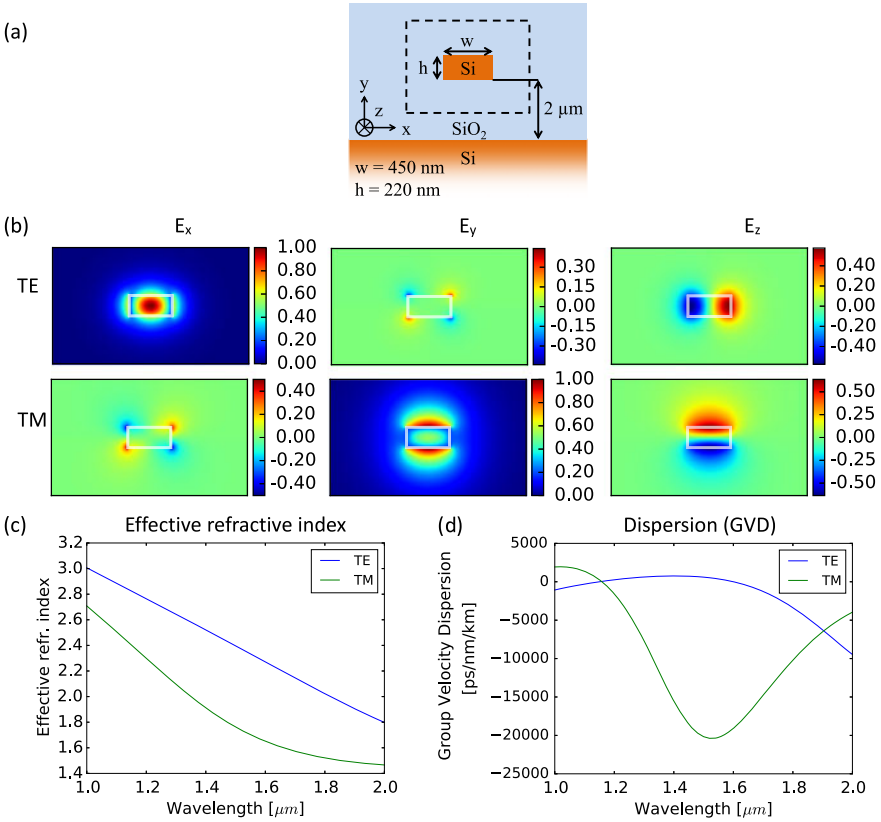


Fig. 14.4 Basic properties of a silicon strip waveguide with oxide cladding. (a) Schematic representation of the geometry, (b) electric field components, colors represent relative electric field strengths according to color bar, (c) effective index versus wavelength, and (d) group velocity dispersion versus wavelength for the fundamental TE-like and TM-like modes

Figure 14.5(a) shows again the geometry of a strip waveguide, but in this case with an air cladding instead of oxide cladding. The waveguide dimensions are kept the same ($450 \times 220 \text{ nm}^2$). The structure now still has symmetry along the x -direction, but the symmetry along the y -direction is broken. The electric field components are again plotted for the fundamental TE-like and TM-like mode in Fig. 14.5(b). The field components of the TE-like mode are very similar as compared to the case of the strip waveguide with oxide cladding. The field components of the TM-like mode on the other hand, are different and no longer symmetric along the y -axis. Because the refractive index contrast is higher at the silicon/air interface compared to the silicon/silicon oxide interface, the confinement near the top of the waveguide is higher.

At short wavelengths the effective index of the TM-like mode in an air cladded waveguide follows the same trend as that of a TM-like mode in an oxide cladded waveguide as can be seen in Fig. 14.5(c). At a wavelength of approximately 1680 nm

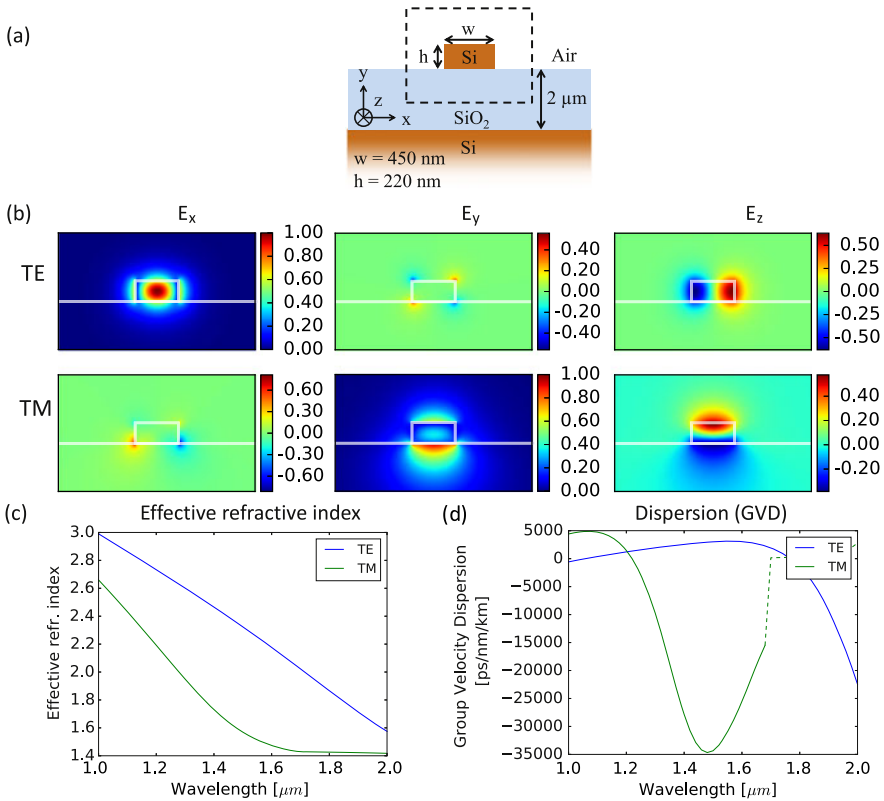


Fig. 14.5 Basic properties of a silicon strip waveguide with air cladding. (a) Schematic representation of the geometry, (b) electric field components, colors represent relative electric field strengths according to color bar, (c) effective index versus wavelength, and (d) group velocity dispersion versus wavelength for the fundamental TE-like and TM-like modes

however, the TM-like mode goes into cut-off and is no longer guided by the air cladded waveguide. The TE-like mode remains guided in the wavelength range of $1\text{--}2 \mu\text{m}$.

Because the effective index as function of wavelength is comparable to the case of oxide cladded strip waveguides, also the GVD curves show similar behavior up to a wavelength of 1680 nm where the TM-like mode goes into cut-off as can be seen from Fig. 14.5(d).

14.2.2 Rib Waveguides

In this section we will discuss some typical properties of rib waveguides. The geometry of the simulated rib waveguide is shown in Fig. 14.6(a). The height of the rib

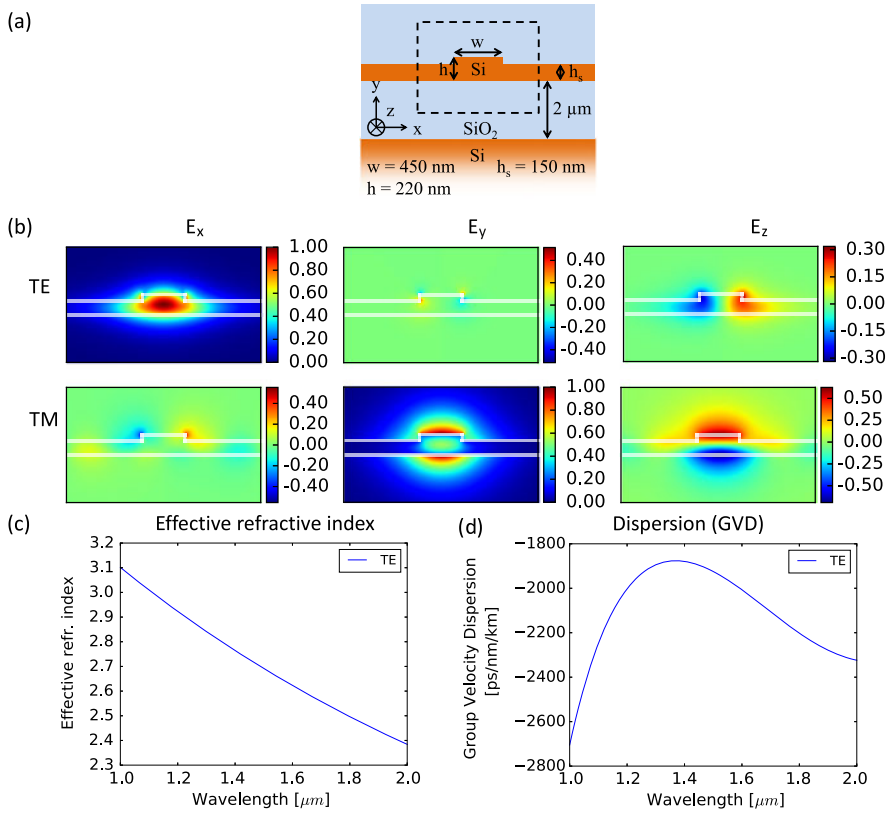


Fig. 14.6 Basic properties of a silicon rib waveguide with oxide cladding. (a) Schematic representation of the geometry, (b) electric field components, colors represent relative electric field strengths according to color bar, (c) effective index versus wavelength, and (d) group velocity dispersion versus wavelength for the fundamental TE-like and TM-like modes

is 220 nm and the rib width is 450 nm. The slab region has a thickness of 150 nm. There is symmetry along the x -axis for this structure.

As can be seen from Fig. 14.6(b) the TE-like mode is confined near the rib but extends laterally into the slab region. The E_x component of the electric field has a strong intensity near the rib edge, just as in the case of a strip waveguide. However, as the area of the sidewall is smaller in a rib configuration, the impact of sidewall roughness is reduced resulting in lower propagation losses and lower distributed backscattering. Lateral confinement on the other hand, is lower compared to strip waveguides and therefore bend radii are larger. To reduce the bend radii the rib width is often slightly increased, but care has to be taken if single mode operation is required.

Although the field profiles shown in Fig. 14.6(b) for the TM-like mode seem to indicate that this mode is guided, this appears to be not true. TM-like modes in rib waveguides are inherently leaky and this has also been experimentally verified [12].

The reason for this is that the effective index of the TM-like mode is in the same range as the effective index of TE slab modes. At the rib edge, mode conversion will take place and guided TM-like modes will couple into TE slab modes that can propagate under any arbitrary angle in the slab and can therefore be phase matched to the guided TM-like mode in the propagation direction. By careful rib width control this effect can be mitigated to some extent, but in general it is assumed that TM-like modes are not guided in these rib waveguides. For this reason only the effective index and GVD of the TE-like mode are plotted in Fig. 14.6(c) and (d).

Because the TE-like mode is more confined in silicon in rib waveguides compared to strip waveguides, the effective index is larger as can be seen in Fig. 14.6(c).

The dispersion for the fundamental TE-like mode is plotted in Fig. 14.6(d). As can be seen the dispersion is negative (normal) between 1 and 2 μm . This is the opposite of the case of strip waveguides and shows that strong dispersion engineering is possible.

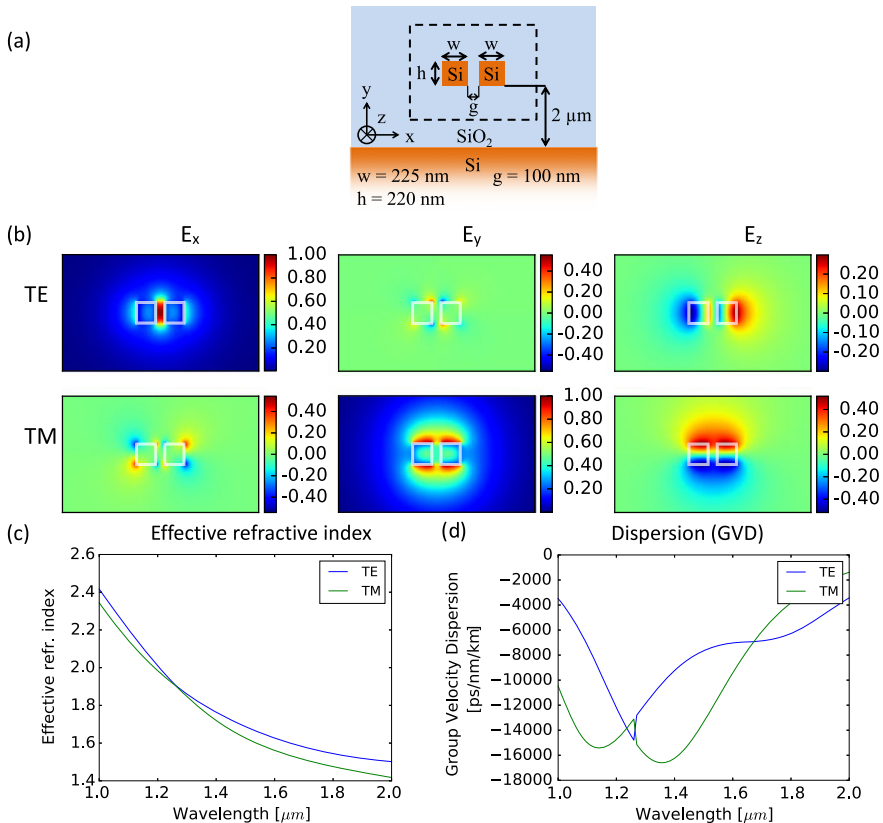


Fig. 14.7 Basic properties of a silicon slot waveguide with oxide cladding. (a) Schematic representation of the geometry, (b) electric field components, colors represent relative electric field strengths according to color bar, (c) effective index versus wavelength, and (d) group velocity dispersion versus wavelength for the fundamental TE-like and TM-like modes

14.2.3 Slot Waveguides

The last geometry we discuss here is the slot waveguide which is shown in Fig. 14.7(a). In a slot waveguide two silicon wires are brought close together. For the simulation results discussed here, the width of the two silicon wires is 225 nm and the gap is 100 nm, while the height is still 220 nm. Here we assume there is oxide cladding and therefore, there is symmetry along the x -axis and y -axis. As can be seen in Fig. 14.7(b) this slot waveguide structure supports a TE-like mode that is highly confined in the gap in between the two silicon wires, while it also still supports a TM-like mode. Because the electric field is strongly confined outside the silicon wires, slot waveguides are of particular interest to sensing applications [13]. When the slot waveguides have no oxide cladding but are rather exposed to a certain liquid or gas, a strong shift in effective index can be expected.

The effective index as function of wavelength is shown in Fig. 14.7(c) for both the fundamental TE-like and TM-like mode. In this configuration the effective indices are quite similar in contrast to the strip waveguides discussed above. Obviously, if the wavelengths are short enough, the structure will support guided modes in the silicon wires and thus transfer into a directional coupler.

The dispersion as function of wavelength is shown in Fig. 14.7(d). The dispersion is negative (normal) for both the TE-like and TM-like mode over the wavelength range considered here.

14.3 Wavelength-Handling Components in Silicon Photonics

14.3.1 Introduction

A wavelength selective filter is a device that can separate individual wavelengths from a waveguide on which multiple wavelengths are propagating (see also Chap. 9). If the filter has a reciprocal behavior, then the same device can be used to add multiple wavelengths propagating on different waveguides to a single waveguide. Traditionally wavelength selective devices have been used in optical communication. More recently such filters are sought for optical spectroscopic applications as well.

In optical tele- and data communication, wavelength selective filters are used to (de) multiplex Wavelength Division Multiplexed (WDM) signals. WDM is a technique to efficiently utilize the enormous bandwidth of an optical channel which can either be an optical fiber for long haul optical telecommunication or an integrated photonic waveguide for on-chip optical data communication. On the transmitter side of a WDM system, information signals are multiplexed using different carrier wavelengths before transmission over the optical channel. On the receiver side, these multiplexed channels are separated by a wavelength selective device ensuring that the correct wavelength is guided to the photodetector before opto-electric conversion. A wavelength selective filter is, hence, required both on the transmitter and

the receiver side to perform the multiplexing and demultiplexing operation, respectively.

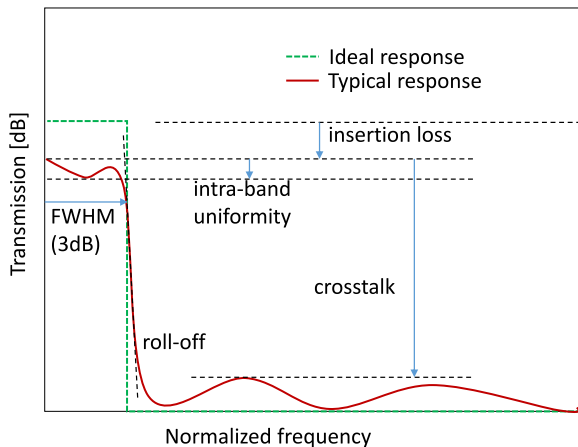
Recently wavelength selective devices are also used for spectral sensing or spectroscopy. The light from a broad band source is resolved after interaction with the material to be studied into its spectral components using a wavelength selective device. Afterwards these spectral components are photo detected to determine the spectral fingerprint of samples such as gases and complex molecules. Apart from that, optical sensors which use wavelength shifts to sense a certain physical quantity (i.e., biosensors to sense bacteria, chromatographs to sense liquids or stress sensors) also utilize wavelength filters.

Implementing the wavelength selective devices on a silicon photonic platform has the potential to provide mass-scale fabrication of small form factor devices [14]. Moreover, at telecom wavelength of 1550 nm or 1310 nm, the power consumed by the integrated photonic wavelength selective devices in general and silicon photonic devices in particular is independent of the data rates. The large thermo-optic coefficient of silicon paves the way to implement adaptively tunable spectral filters requiring moderate electrical power. At spectroscopic wavelengths of 2.5 μm to 8 μm , the absorption cross-section of molecules to be sensed becomes stronger resulting in enhanced sensitivity of the spectrometer [15].

The specifications for wavelength filters are determined by their application. For example, the requirements for a wavelength filter for spectroscopy are different from that of wavelength filters for WDM applications. Important attributes for any wavelength selective filter are (1) small footprint with ease of scalability to achieve enhanced spectral resolution, (2) low power operation, (3) small insertion loss with low crosstalk and (4) large fabrication tolerance for easier manufacturability. The functional performance specifications of a typical wavelength selective device are shown in Fig. 14.8.

The two basic architectures for wavelength selective filters are Finite Impulse Response (FIR) or Infinite Impulse Response (IIR) filters [17]. In integrated optics

Fig. 14.8 Functional performance specifications of a wavelength selective filter [16]



FIR filters typically use a delay line configuration, hence termed as delay line filters. Building blocks such as (a) power splitting/combining couplers, (b) waveguide grating routers or (c) echelle (planar concave) gratings have been used for the implementation of delay line FIR filters. For IIR filter implementations, resonant devices such as ring resonators are used.

14.3.2 Delay Line Based Spectral Filters

An asymmetric MZI is the simplest possible coherently connected delay line based feed-forward spectral filter. A schematic representation of a 2×2 asymmetric MZI is shown in Fig. 14.9. It is composed of two coupling devices which are connected by a pair of waveguides termed as delay lines due to their relative length difference ΔL . An input signal is split by the first coupler into two components. They travel on the delay lines connecting the two couplers. The delay length ΔL produces a time delay τ resulting in a relative phase shift of

$$\Delta\varphi = n_{eff} \cdot \frac{2\pi}{\lambda} \cdot \Delta L \quad (14.4)$$

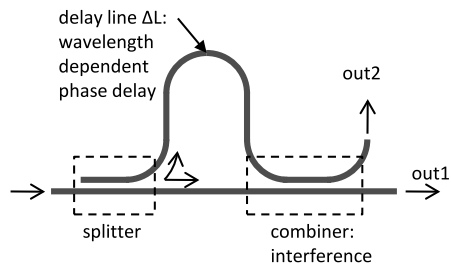
Due to the wavelength dependence of $\Delta\varphi$, the two components interfere either constructively or destructively when recombined in the second coupler resulting in a periodic frequency response with periodicity or Free Spectral Range (*FSR*)

$$FSR = \frac{1}{\tau} = \frac{c}{n_g \cdot \Delta L} \quad (14.5)$$

where c is the speed of light and n_g the group index.

Although in its stand-alone form a 2×2 asymmetric MZI acts as a wavelength filter and is used for bandpass filtering and sensing, its unity order (single zero) is not sufficient to deliver complex transfer functions required for spectroscopic or optical communication applications. However, it can be used as a building block to conceive higher order wavelength filters. A typical example is a *lattice filter*, shown in Fig. 14.10, in which 2×2 MZIs are concatenated coherently. By an appropriate choice of the coupling coefficients of the coupling elements any desired spectral response can be achieved. In [18] an 8th order lattice filter in an SOI material platform

Fig. 14.9 Asymmetric MZI as a simple FIR filter



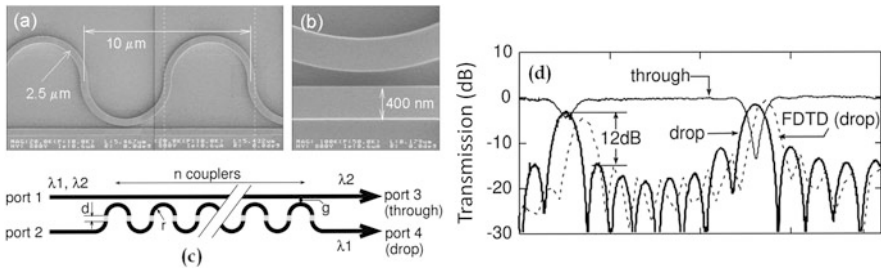


Fig. 14.10 (a) SEM image of section of a lattice filter, (b) directional coupler, (c) N th order lattice filter, (d) transmission of a single channel of an 8th order lattice filter [18]

with an FSR of 80 nm for channel dropping applications has been demonstrated. The device had a channel dropping bandwidth of 10 nm, insertion loss of 2 dB, and side lobe suppression of 10 dB.

It is also possible to concatenate 2×2 asymmetric MZIs incoherently in a *tandem lattice filter* configuration, as shown in Fig. 14.11. This approach provides an athermal spectral filter due to its flat pass band. Figure 14.11(a) shows the configuration of a three-stage 8 channel device and its measurement results are shown in Fig. 14.11(b). It can be seen that the filter has a flat pass band for over 50% of the channel spacing, insertion loss of 1.6 dB, pass band uniformity of 0.7 dB, and 18 dB of extinction at the center wavelength of the channel [19].

When implemented on high index contrast materials such as SOI, small fabrication imperfections such as gap width variations of directional couplers and waveguide width variations result in degraded performance (i.e., insertion loss, crosstalk, channel uniformity) of the lattice-based wavelength selective devices. The former leads to changes in the coupling coefficients and the latter induce phase errors on the delay lines. The problem of phase errors on delay lines is further compounded by factors such as mask discretization, waveguide roughness, and non-uniformity

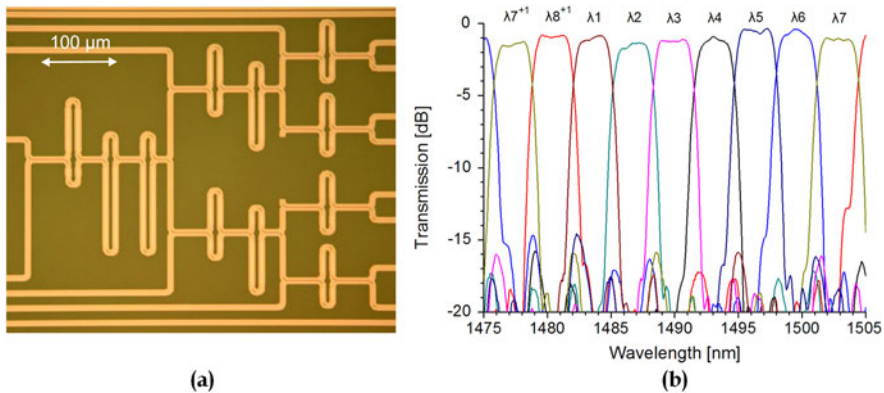


Fig. 14.11 (a) Microscopic image of tandem lattice filter, (b) flat passband transmission of tandem lattice filter shown in (a) [19]

of silicon layer thickness in SOI. These errors can be minimized by increasing the width of the delay line waveguides. Active trimming of wavelength selective filters for the compensation of phase errors is possible by including heater elements to exploit the thermo-optic effect which will consume power and is not always sufficient due to a limited tuning range. In some implementations of lattice filters, tunable couplers and delay lines with embedded phase shifting elements are used not only for trimming the phase errors but also to enhance the degree-of-freedom (DoF) to achieve a tunable spectral response. Any change in the coupling coefficients due to gap variations in the directional coupler cannot be directly compensated. A possibility is to use multimode interference couplers which are based on the self-imaging principle. In comparison to directional couplers they are more tolerant to fabrication errors. Furthermore it is also possible to use higher order MMI couplers in each stage of the filter to reduce the overall waveguide length and hence the phase errors induced on the delay lines. Using such an approach the so-called “*parallel-serial*” filter has been demonstrated [20] to demultiplex eight spectrally overlapping channels which are 12.5 GHz apart and have an interchannel crosstalk of -20 dB.

A fully “parallel” approach of implementing spectral filters is by using *Arrayed Waveguide Gratings* (AWGs) which are also designated Waveguide Grating Routers (WGR) or Phased Arrays (PHASAR), see also Chap. 9, Sect. 9.6. A simplified schematic of an AWG is shown in Fig. 14.12. Unlike MZI based spectral filtering which relies on temporal multi-beam interference, an AWG uses spatial dispersion for wavelength filtering.

An AWG comprises two Free Propagation Regions (FPR) which are connected by an array of delay lines called waveguide gratings. Like in a 2×2 MZI, the unit delay length ΔL determines the FSR of the spectral response. The spectral resolution of an AWG is determined by the number of grating arms. As an approximate rule of thumb, to pack N channels in an FSR requires three to four times the number of grating arms.

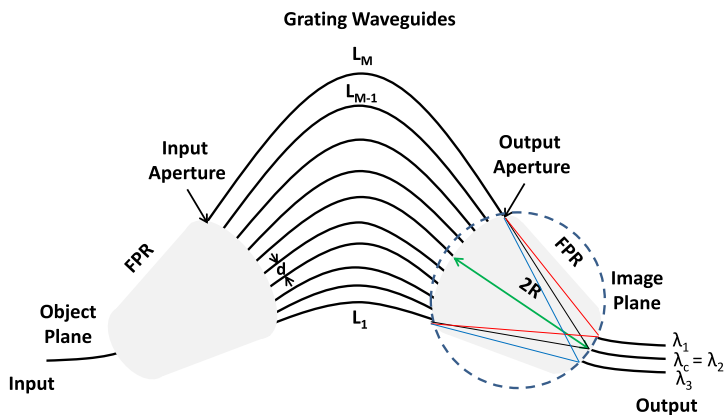


Fig. 14.12 Simplified schematic of an AWG

The wavelength selectivity of the AWG has the following principle: light is guided through the input waveguide to the first FPR where the lateral confinement of light vanishes and it diffracts. This diffracted light is coupled to the M waveguides of the AWG which are arranged on a circle of radius R . The combination of an input waveguide with an FPR and a waveguide grating effectively constitutes a $1 \times N$ star coupler. The waveguides in the waveguide grating have a linear incremental optical path length difference ΔL which is equal to an integer multiple of the center wavelength λ_c . As a result the light in the waveguide grating will arrive with an equal phase shift at the output aperture. The field distribution at the input aperture (see Fig. 14.12) is reproduced at the output aperture with an amplitude and phase distribution equal to that of the input field. Therefore, after interference in the second FPR, the input field at the object plane (see Fig. 14.12) is reproduced at the image plane, which follows a circular path with radius R , on which the output waveguides are arranged.

For input light at $\lambda \neq \lambda_c$, the phase difference $\Delta\varphi$ produced by the wavelength dependent optical path length difference ΔL introduces a tilt of the outgoing beam from the waveguide grating. This leads to a wavelength dependent shift of the focal point (image) formed on the image plane, where it can be guided out by an output waveguide. This spatial dispersion produced by the AWG is the underlying principle of wavelength selectivity in AWGs.

Depending on the application, an AWG can have any arbitrary number of input and output ports (i.e., an $M \times N$ configuration is possible). For example, a $1 \times N$ AWG filter acts as a multiplexer. An $M \times N$ AWG is used to route one wavelength on the N th input to any other output waveguide M . Due to the parallel architecture of the AWG, it provides potential for scaling to higher numbers of channels while ensuring a compact footprint.

A fully passive AWG (without any compensation for phase errors on the waveguide grating) operating in the C-band has been demonstrated [21] with an exceptionally low loss of only 1.1 dB and very low crosstalk of -25 dB. The device has a small footprint of $200 \times 350 \mu\text{m}^2$. Another 8×800 GHz C-band AWG based wavelength filter has been demonstrated in [22] with a loss of 1.86 dB and interchannel crosstalk of -27.3 dB. For mid-infrared spectroscopy, a 6×200 GHz AWG at a wavelength of $3.8 \mu\text{m}$ with an insertion loss of only 1 dB and crosstalk of -25 dB has been demonstrated [15]. Figure 14.13 shows an L-band AWG device for the demultiplexing of 32×10 Gbit/s channels with a spacing of 200 GHz [23]. The device showed an insertion loss of 2.5 dB, crosstalk of -18 dB and channel uniformity of 3 dB for all channels. A very ambitious design for a 512×512 AWG with channel spacing of 25 GHz has been reported in [24] however, with a very high crosstalk of -4 dB.

Like lattice filters, AWG based wavelength filters are sensitive to the non-uniformity of waveguide dimensions. This results in phase errors on the grating waveguides due to variation of the effective index and consequently results in increased insertion loss, crosstalk and reduced channel uniformity. Other factors which influence the performance of AWG based wavelength selective filters are the pitch between the adjacent waveguides of an AWG and the imperfect imaging of the

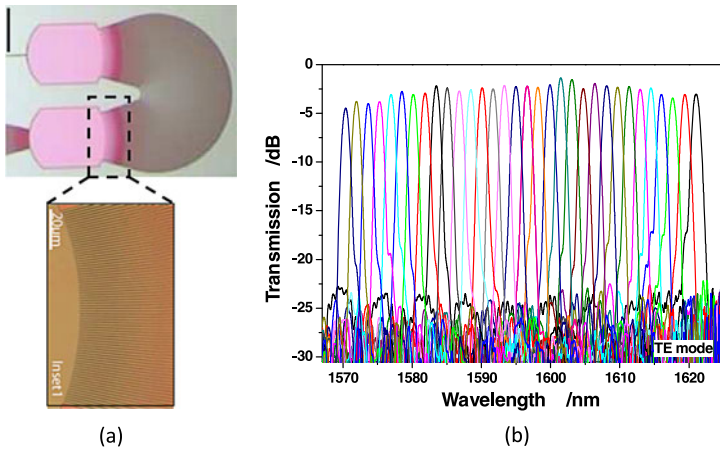


Fig. 14.13 (a) Microscopic images of a 32 channel AWG with *inset* showing the access to the grating waveguides, (b) measured transmission response of the AWG [23]

refocused light. The former causes phase errors due to evanescent coupling between waveguides and the latter causes phase errors due to different paths followed by the light traveling in the free propagation region. Smarter design and routing techniques can be employed to reduce the effect of phase errors on the delay line. For example, in [22] it has been shown that a “U” shaped AWG design gives improved crosstalk compared to an “S” shaped AWG design. Similarly, in [25] it has been shown that the insertion loss of the AWG can be decreased by reducing the pitch of the arm apertures resulting in improved imaging at the output plane of the AWG. Techniques such as wider waveguides in the delay section and thermal trimming are also possible to compensate phase errors in the delay lines of an AWG.

Typically an increase of grating order, which is required to enhance the spectral resolution of the filter, leads to degraded crosstalk due to an increased average waveguide length leading to larger phase errors. *Reflective AWG* configurations can significantly reduce the average waveguide length. This does not only improve the crosstalk but makes the footprint of the device more compact. Furthermore, the grating section is composed of only straight waveguides resulting in decreased variations in effective index, hence improving the crosstalk even further. Figure 14.14(a) shows the configuration of an AWG in reflective configuration with its microscopic image shown in Fig. 14.14(b). A second order DBR is used at the end of each grating arm for reflections [26] and a 1×1 MMI coupler is used to suppress higher order modes for the rib waveguides used to access the slab region of the AWG. As presented in Fig. 14.14(c), the device presented in [26] has shown an on-chip insertion loss of 3 dB and interchannel crosstalk of -20 dB. Another reflective approach uses echelle gratings also known as a *Planar Concave Grating* (PCG) or etched diffraction gratings.

Figure 14.15 shows the configuration of an echelle-grating based wavelength selective filter. The light from an input waveguide, which along with output wave-

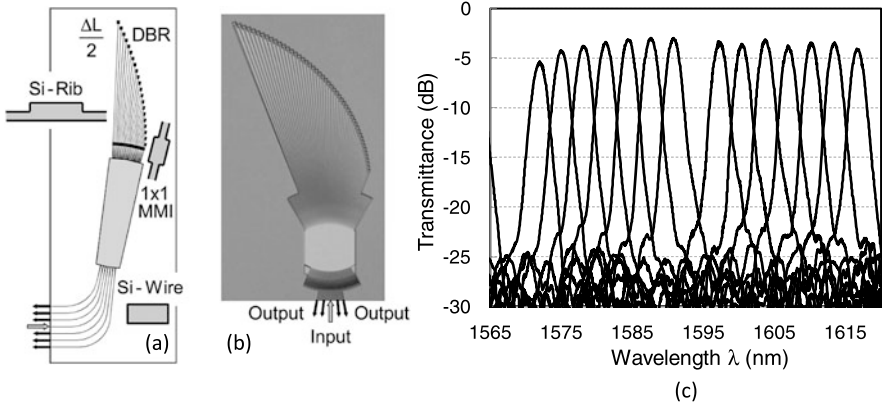
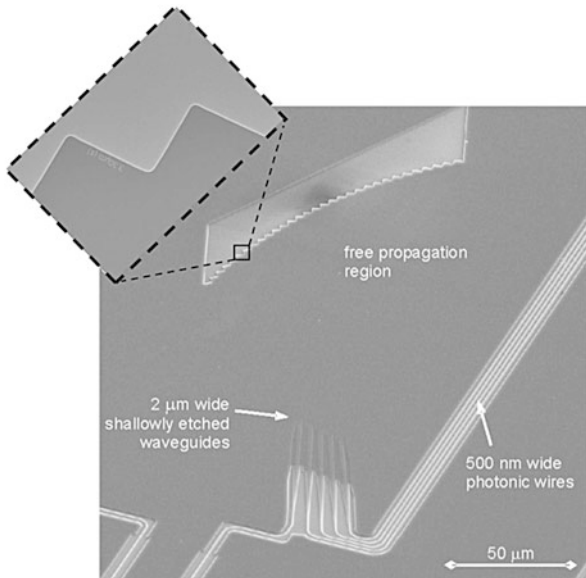


Fig. 14.14 (a) Configuration of an AWG in reflective configuration with *insets* showing geometry of waveguides used and position of 1×1 MMI coupler, (b) microscopic image of reflective AWG [27], (c) transmission response of a 14 channel reflective AWG with channel spacing of 400 GHz

Fig. 14.15 Configuration of an echelle grating based wavelength selective device. Different sections are labeled with *inset* showing a typical echelle grating facet [28]



guides are placed on a circle with radius R , terminate in an unetched slab region, forming an FPR, where it diverges. At the end of the slab region the divergent light is reflected and focused onto the output waveguides by a concave grating formed by an array of mirrors which are placed along the perimeter of a circle with radius $2R$. The reflected beams interfere in such a way that different wavelengths are focused on different output waveguides, resulting in wavelength selectivity.

The principle of AWGs and PCGs is the same as both use spatial dispersion for wavelength filtering. But unlike an AWG, in a PCG the delay lines are introduced in the FPR. Due to lack of lateral confinement in the FPR fabrication induced phase errors due to waveguide roughness and core size variation are minimized. Moreover due to its reflective configuration the effect of phase errors induced by the difference in the propagation direction of the light is effectively averaged out. Thanks to the enhanced tolerance to phase errors, PCGs are known for providing low crosstalk wavelength selective devices. A C-band 1×4 PCG with crosstalk of -30 dB for a channel separation of 20 nm and an on-chip normalized insertion loss of 7.5 dB is reported in [28], which was the pioneering work to demonstrate a PCG in thin film SOI. Later on, in [29], an eight channel PCG is demonstrated as a wavelength demultiplexer operating in the C-band. For 3.2 nm channel spacing, the insertion loss of the device is 3.5 dB with 3 dB bandwidth of 2.4 nm and inter-channel crosstalk of -16 dB. In [15] a design of a 1×8 PCG operating around a mid-infrared wavelength of $3.8 \mu\text{m}$ is demonstrated with normalized insertion loss of 1.63 dB and a crosstalk of -20 dB.

The crosstalk of the PCG based wavelength selective devices is influenced by the channel spacing. It has been demonstrated in [24] that the crosstalk decreases as the channel spacing is increased. For example, the crosstalk of a four channel PCG deteriorates from 24.2 dB to -18.7 dB when the channel spacing is decreased from 10 nm to 6.4 nm. The increase in crosstalk is attributed to the phase errors induced in the larger FPR required to pack the same number of channels into a smaller FSR.

The insertion loss of the PCG is mainly influenced by the non-verticality of the grating facets due to fabrication process limitations. This leads to reflection of light into the substrate. Moreover, the scattering from the grating facets is another contributing factor. The major fraction of insertion loss comes from the Fresnel loss due to the index discontinuity in the grating facets [28]. In [30] it has been reported that the Fresnel loss can be reduced by replacing the grating facet with a 2nd order Distributed Bragg Reflector (DBR) resulting in the reduction of insertion loss for a 1×4 PCG from 7.5 dB to 1.9 dB. Using the same principle of using a DBR at the facets of the PCG, a 1×30 PCG (see Fig. 14.16(a)) with a channel spacing of 400 GHz has been reported in [21]. The device has an insertion loss of 3 dB and interchannel crosstalk of -15 dB (see Fig. 14.16(b)).

14.3.3 Spectral Filters Using Ring Resonators

A ring resonator comprises a waveguide folded to itself called the ring, which is coupled to a waveguide called the bus waveguide. The coupling between ring and bus waveguide is typically achieved by using a directional coupler. Figure 14.17(a) shows the configuration of a *ring resonator*. The ring will be resonant for the wavelengths that can fit an integer number of times in the optical path length of the ring,

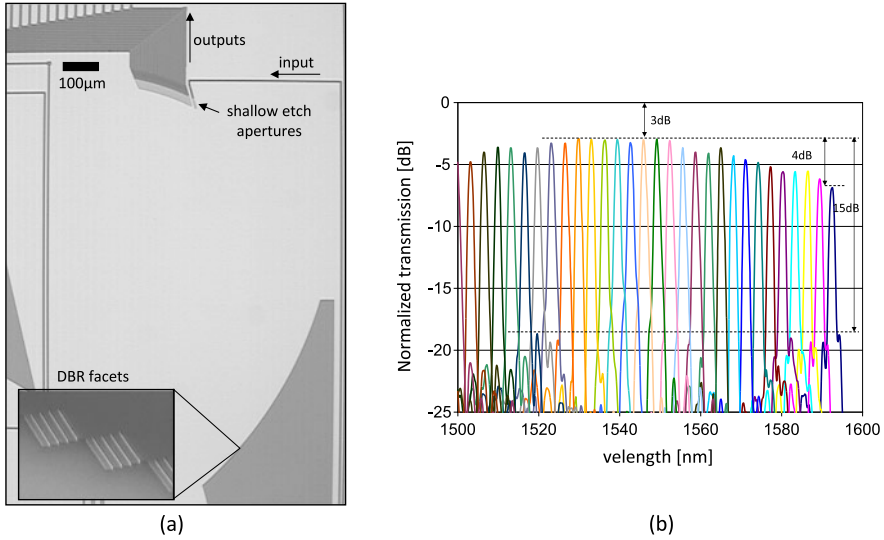


Fig. 14.16 (a) SEM image of 1×30 echelle grating for channel spacing of 400 GHz, (b) measurement result for 30 channel PCG [21]

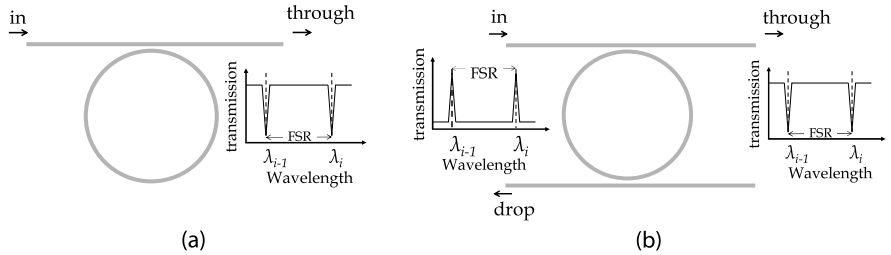


Fig. 14.17 (a) Configuration of ring resonator, (b) ring resonator based add-drop filter

manifested as a periodic dip in the transmission response of the ring. This periodicity represents the FSR of the ring resonator and is determined by the radius R of the ring and is given by

$$FSR = \lambda^2 / n_g 2\pi R \tag{14.6}$$

Apart from the wavelengths for which the ring is resonant, all other wavelengths will go through. Therefore, ring resonators are also referred to as “all-pass” filters. The wavelengths trapped in the ring can be dropped when a second bus waveguide is coupled to the ring. Due to reciprocity it can also be used to add a wavelength. Figure 14.17(b) shows the configuration of a ring based add-drop filter. For this single ring based add-drop filter configuration, the pass band of the dropped channel is very narrow making it very sensitive to a shift in the resonance wavelength either due to ambience (i.e., change of temperature) or to fabrication variations. By

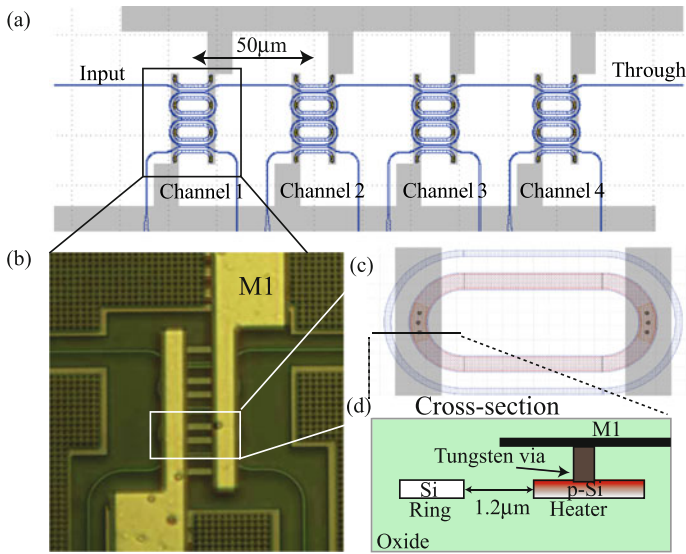


Fig. 14.18 (a) Bank of four 2nd order ring based wavelength filters, (b) microscope image of the fabricated device, (c) single ring waveguide with a p-doped heater for trimming, (d) waveguide and heater cross-section [31]

sandwiching multiple rings, which determine the order of the filter, between the two bus waveguides the width of the pass band can be increased and adaptively tuned by controlling the inter-resonator coupling coefficients. Furthermore, the filter response becomes tolerant to spectral shifts [31]. A bank of several rings can be placed side-by-side on a single bus waveguide to demultiplex wavelengths traveling on the bus waveguide, as shown in Fig. 14.18. The implementation of ring resonator based spectral filters in high index contrast SOI material allows to deliver very small footprint wavelength selective filters.

In [31], as shown in Fig. 14.18, a four channel demultiplexer is demonstrated for an FSR of 300 GHz using 2nd order ring-resonator filters in each stage with a crosstalk of -18 dB and an insertion loss of 1.5 dB. A 3rd order ring resonator filter has been demonstrated in [32] to demultiplex 16 channels of a 100 GHz WDM system. Each channel has a 1 dB passband width of 37.5 GHz while ensuring an interchannel crosstalk of -20 dB. The device has a relatively large insertion loss of 5 dB. A 5th order filter with a very high out-of-band rejection ratio of 40 dB, pass bandwidth of 310 GHz and insertion loss of 1.8 dB is demonstrated in [33]. The SEM images and measurement results are shown in Fig. 14.19(a) and (b), respectively. A 2nd order *counter propagating ring resonator* based spectral filter is demonstrated in [34] to demultiplex 20 channels spaced 124 GHz apart while ensuring an inter-channel crosstalk of -45 dB and 3 dB bandwidth of 20 GHz.

In contrast to delay line filters, where the spectral response depends on the relative optical path length difference, the spectral response of the ring resonator is dependent on the absolute optical round trip length (perimeter) of the ring. This makes

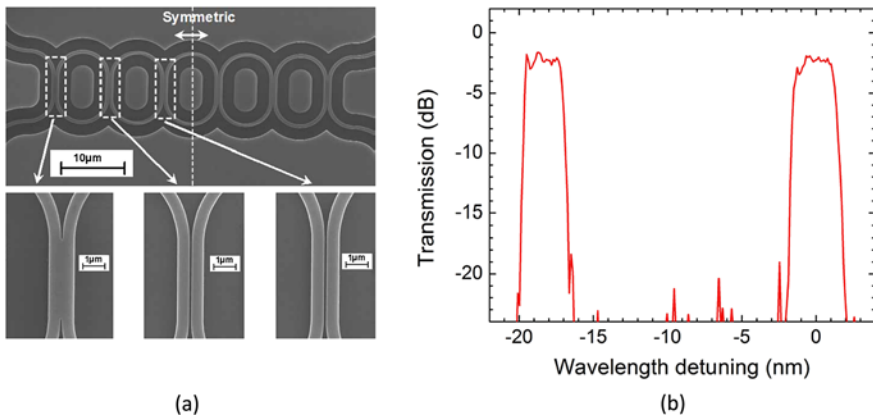


Fig. 14.19 (a) SEM image of 5th order ring based wavelength filter and (b) its measured spectral response with a low passband ripple of only 0.4 dB [32]

the resonance frequency of the ring resonator very sensitive to refractive index variations due to fabrication induced changes in the geometry of the ring waveguide or changes in the cladding material. This can be compensated by thermal trimming techniques at the cost of energy efficiency. On the other hand, this strong sensitivity makes ring resonators ideal candidates for the sensing of physical, chemical or biological properties. Another critical factor that impacts the response of a ring resonator based wavelength selective filter is the requirement to have a very good control on the gap between the bus and the ring waveguide, for which thermal trimming is not possible.

14.4 Grating Coupling for Silicon Photonics

While silicon photonic integrated circuits allow high performance optical functions with a compact footprint, the high refractive index contrast makes efficient optical interfacing with standard single mode (low index contrast) fibers challenging. The most common solutions for coupling are *in-plane* coupling, also often referred to as *edge coupling* (discussed in the next section), and *grating couplers*, which enable the coupling of light from the surface of the chip. These two solutions are schematically represented in Fig. 14.20.

In electronics, the standard way to contact the electrical circuits is through metal pads on the top surface of the chip. This allows for wafer-scale testing by probing the individual chips on the wafer or even the entire wafer itself without need for intermediate packaging or post-processing steps. For photonics a similar strategy is needed that allows vertical coupling of light to and from the chip. This will enable wafer-scale testing. Also, surface couplers introduce several other advantages: The density of optical ‘pins’ can be much higher: The couplers can be positioned any-

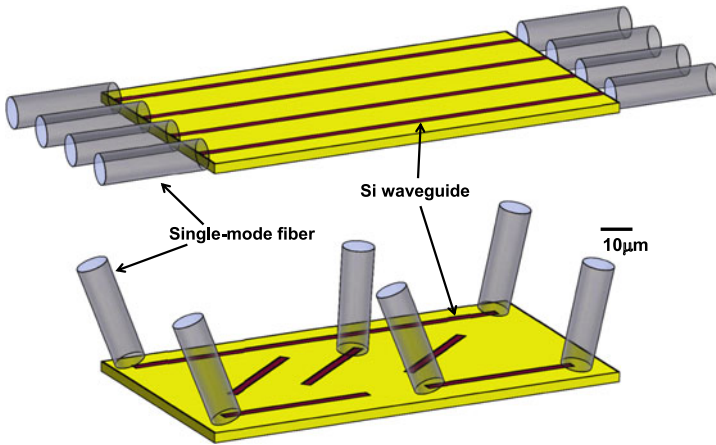


Fig. 14.20 The two most common coupling solutions: in-plane couplers (*top*), out-of-plane couplers (*bottom*)

where on the chip (especially those for testing) and do not need to be routed to the edge. Chips can be probed with fibers oriented at an angle close to the vertical.

A grating coupler consists of a periodic refractive index modulation in or close to the waveguide core (implemented as grooves [35], metal lines [36] or sub-wavelength [37] structures). Every such modulation of the refractive index acts as a scatterer for incident light. While individual scatterers emit light quasi-isotropically, their periodic arrangement causes the generation of a directional beam, the angle of which is determined by the Bragg condition, as graphically illustrated in Fig. 14.21, where Λ is the period of the grating and β is the propagation constant of the optical mode in the grating. By positioning the fiber under the appropriate angle efficient fiber-to-chip coupling can be realized.

The efficiency of the fiber-chip coupling depends on the directivity of the grating (i.e. the fraction of light that is coupled towards the fiber), the field profile of the diffracted light, and on the polarization and wavelength of the incident light. High directivity can be obtained by optimization of the grating shape [38] as shown in

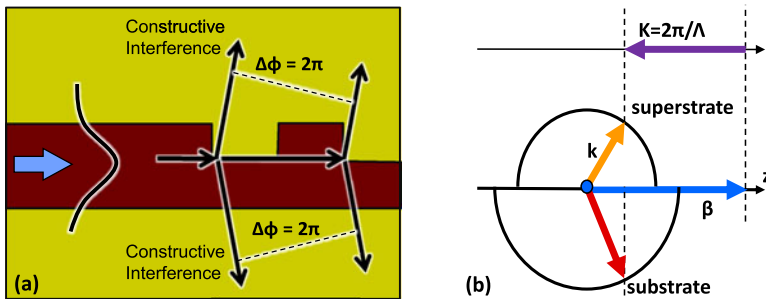


Fig. 14.21 Operation principle of a waveguide coupled diffraction grating

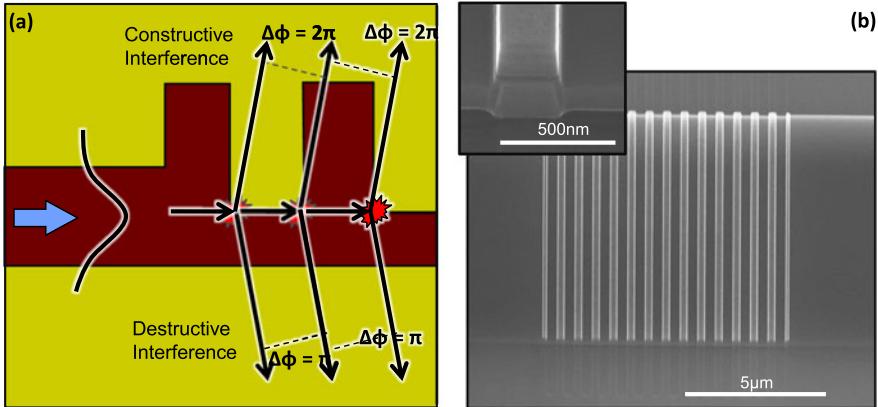


Fig. 14.22 Improving the directionality by optimizing the grating profile [38], (a) principle, (b) fabricated grating

Fig. 14.22, or by implementing a bottom mirror at the correct distance from the grating in order to ‘recycle’ the downwards diffracted light, as shown in Fig. 14.23 [39, 40]. The field profile of the diffracted light can be properly matched to that of the Gaussian fiber mode by stepping away from a perfectly periodic grating structure [41], as shown in Fig. 14.24.

Using these techniques fiber-to-chip grating coupling efficiencies better than -2 dB are obtained [38, 40]. The 1 dB bandwidth of the fiber-to-chip coupling is typically 30 nm for coupling to standard single mode fiber, but can be increased by using High NA (HNA) fiber.

So far we have only discussed single polarization operation. Due to the strong birefringence of silicon high-index-contrast waveguide structures, one-dimensional grating structures are strongly polarization dependent. In many applications however, the polarization of the light traveling in the fiber is unknown and varying, requiring a different grating coupling structure to cope with this. This can be realized using a two-dimensional grating structure, which can be seen as the superposition of two orthogonal one-dimensional grating couplers. Such a structure couples the two orthogonal polarizations in the fiber into identically polarized modes in two (nearly) orthogonal waveguides. This way, a polarization diversity approach can be applied to render the silicon waveguide circuits polarization independent. In such an approach two identical silicon waveguide circuits need to be integrated, so that each can process one of the orthogonal fiber polarizations. The two dimensional grating coupler performs at the same time the function of the fiber/chip coupler, polarization splitter and rotator. The two-dimensional grating coupler and the polarization diversity scheme are shown in Fig. 14.25. Similar techniques as for the one-dimensional grating case can be used to increase the efficiency of two-dimensional grating couplers [42].

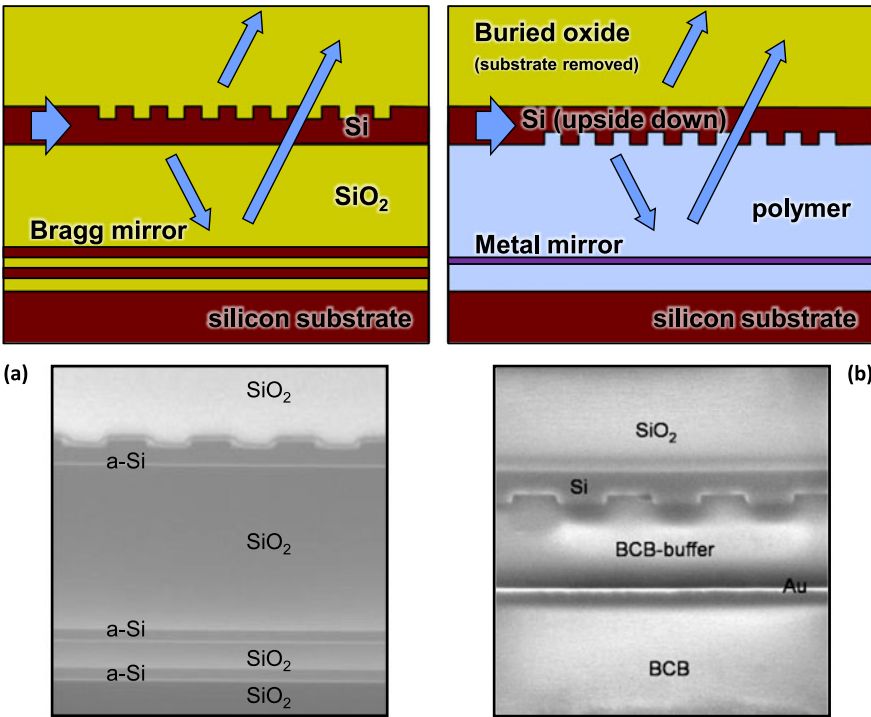


Fig. 14.23 Grating couplers with bottom mirror. (a) Grating coupler in amorphous silicon deposited on top of a DBR mirror stack [39], SEM picture courtesy Shankar Kumar Selvaraja, (b) Bonded grating with gold ‘bottom’ mirror [40], SEM picture courtesy Frederik Van Laere

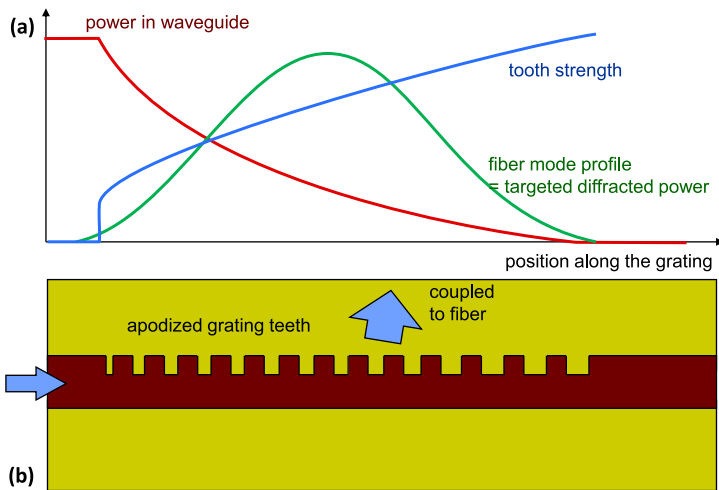


Fig. 14.24 Optimizing modal overlap by apodizing the grating [41]. (a) Optimizing the scattering profile, (b) schematic drawing of apodization by changing the trench width

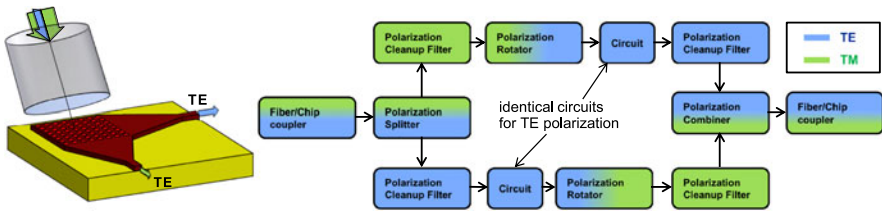


Fig. 14.25 (Left) Two-dimensional grating coupler: operation principle; (Right) polarization diversity approach

14.5 Edge Coupling for Silicon Photonics

While grating couplers are very popular for coupling light to and from silicon nanophotonic ICs, edge couplers sometimes are still preferred. When well-designed, they operate over a broad wavelength range, up to several 100 nm, with low coupling loss and in some cases even with low PDL (polarization dependent loss). However, when a highly confined single mode silicon waveguide is simply cleaved and coupled to an optical fiber, the loss can be prohibitively large (around 8 dB for coupling to a lensed fiber with 2 μm mode field, around 30 dB to a standard single mode fiber). However, by increasing the mode field diameter of the waveguides this coupling loss can be improved considerably. From inspecting Fig. 14.26, which plots the effective mode width and height for a 220 nm thick silicon waveguide, there are two possible routes to enlarging the mode size. The most straightforward approach is to increase the width of the waveguide. While simple from a technological point of view, this only increases the lateral mode size. The mismatch in vertical direction remains strong, however. Increasing the size of the waveguide also in the

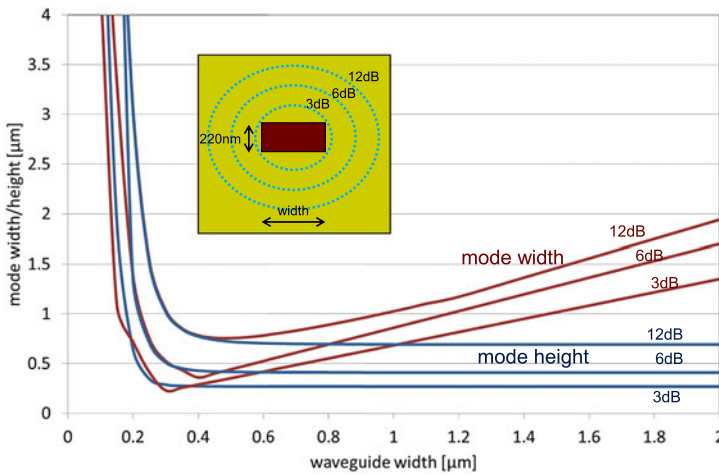


Fig. 14.26 Effective mode width and height for a standard 220 nm silicon strip waveguide embedded in silica, from [43]

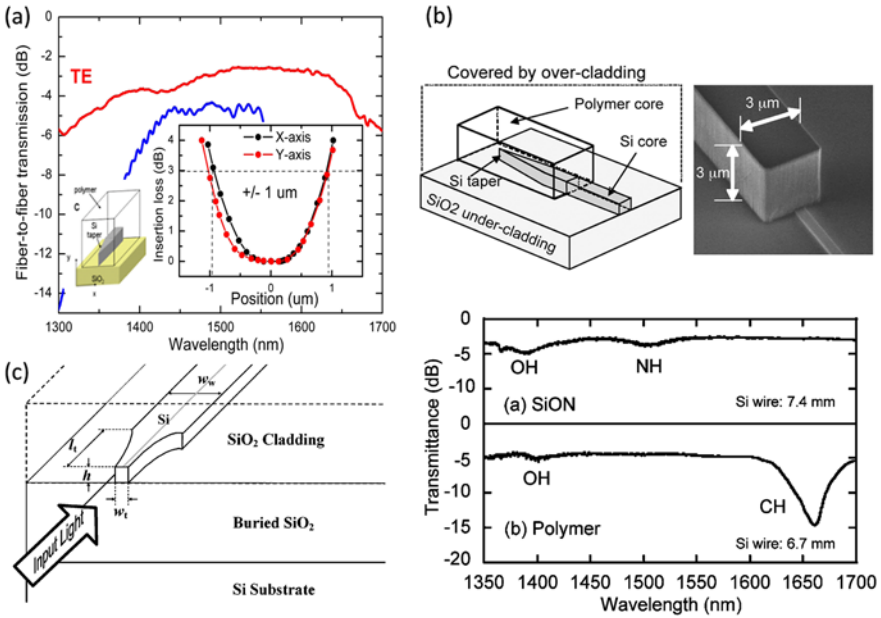
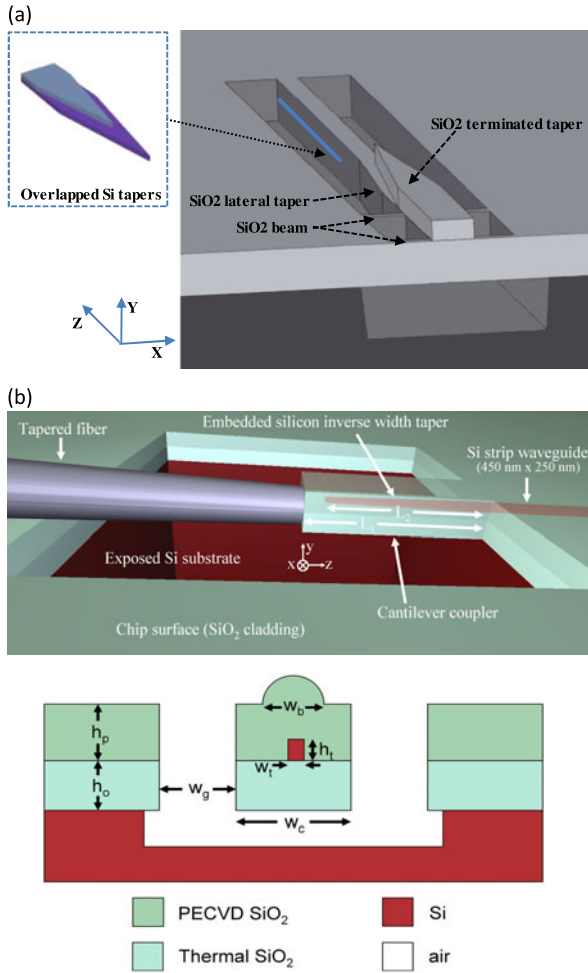


Fig. 14.27 Early demonstrations of inverted taper couplers, (a) Inverted taper with polymer overlay, *inset* shows alignment tolerance (from [44]), (b) Comparison between polymer and SiON overlay (from [45]), (c) Nanotaper without overlay (from [46])

vertical direction is possible, e.g. through the deposition of poly-silicon and gray-scale lithography to form a taper, but it is technologically challenging. The fact, that this large waveguide supports higher order modes and exhibits high reflection at the interface, are other drawbacks. Therefore another approach, originally used for realizing spot-size converters made in III–V laser diodes and amplifiers, is typically preferred. As also visible in Fig. 14.26, the mode size increases exponentially when the width of the waveguide decreases. Note that in this case the mode size increases not only laterally but also vertically. The most important limitation here is the narrowest waveguide width that can be reliably patterned using the lithography tool employed (electron beam lithography for lab demonstrations, 248 nm or 193 nm deep UV lithography for commercial applications).

Figure 14.27 shows some early demonstrations of such fiber-chip couplers. Figure 14.27(a) shows the fiber to fiber transmission for TE- and TM-polarized light, for a straight waveguide connected to 150 μm long inverse tapers covered with a 2 μm × 2 μm polymer [44]. Narrowing down the silicon waveguide (80 nm taper tip) pushes the light out to the polymer overlay waveguide which then determines the shape of the mode coupled to the tapered fiber. In this case most of the loss actually stems from the waveguide loss and the actual fiber-chip coupling loss was determined to be lower than 0.5 dB/connection. The inset of the graph shows the alignment tolerance as function of horizontal and vertical offset. A ±1 μm 3 dB alignment tolerance is obtained in both directions. Figure 14.27(b) compares an

Fig. 14.28 (a) Cantilever coupler for edge coupling (from [51]), (b) Cantilever designed for use within wafer testing [52, 53]



SiON and a polymer overlay waveguide whereby the dips in the coupling efficiency reflect different absorption peaks for the respective materials used [45]. Similar efficiencies were obtained in both cases (taper length 300 μm , taper tip 80 nm, overlay 3 $\mu\text{m} \times 3 \mu\text{m}$). Figure 14.27(c) shows an example of a coupler where no overlay waveguide is used [46]. In this case the light is pushed out to the silica top and bottom cladding layers. This simplifies the processing but, to avoid excessive coupling to the high index silicon substrate, the taper has to be kept as short as possible and the chip needs to be cleaved directly at the end of the taper (taper length 40 μm , taper tip 100 nm).

These early results were quickly picked up by the silicon photonics community and the inverted taper rapidly became the favorite coupling strategy in cases where edge coupling is preferred over grating coupling. Several groups reported variants and improvements. Roelkens et al. showed that separating the silicon inverted taper

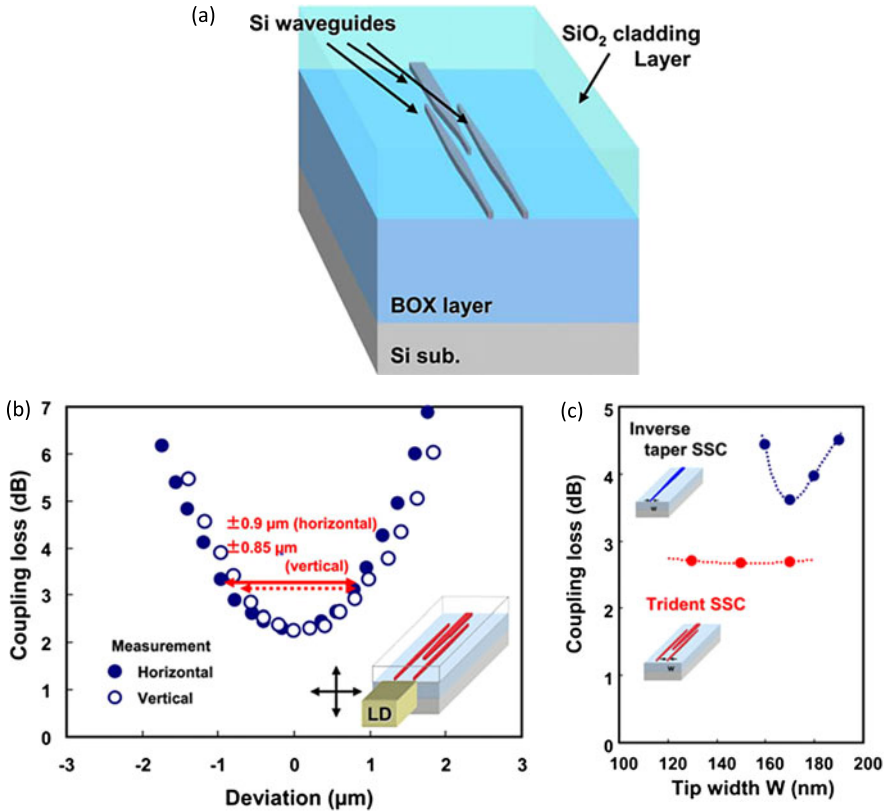


Fig. 14.29 Trident edge coupler optimized for coupling to a laser diode (from [54])

waveguide from the low index overlay waveguide by a low index dielectric layer relaxes the requirements on the width of the taper tip [47]. This allowed increasing the taper tip to 175 nm, a value obtainable with 248 nm DUV lithography, albeit at the cost of an increase in the length of the taper (to 175 μm). Now, 193 nm DUV lithography is becoming more and more the standard tool in silicon photonics manufacturing, allowing for taper tips in the range of 120 nm to 150 nm. Using immersion lithography, even narrower taper tips are feasible. These might be required when trying to reduce also the losses for TM-polarized light (e.g. see [48]). In [49], silicon rich SiO_x was used instead of polymer or SiON to define the low index overlay. Introducing a more complex structure in the overlay waveguide allows to reduce the length of the taper [50].

More recently a novel type of inverted taper based couplers was developed whereby the silicon beneath the edge coupler is removed. This allows to define the low index waveguide by structuring the silica bottom and top cladding layers without risking leakage to the high index silicon substrate. In [51] this approach was used to define a classical edge coupler with coupling loss ~2 dB/facet to a 5 μm mode field lensed fiber (Fig. 14.28(a)). In [52, 53] a taper that can be addressed

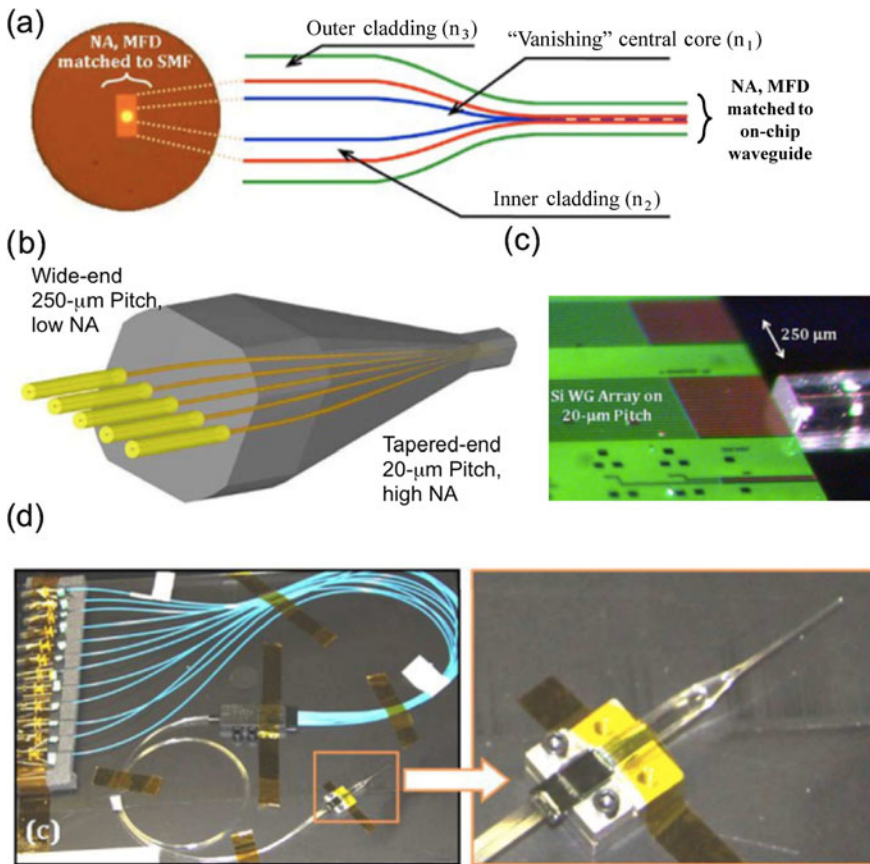


Fig. 14.30 Coupling from array of inverted tapers to fiber array. The fiber array contains a taper structure, which transforms light from standard single mode fibers at 250 μm pitch to high numerical aperture fibers with 20 μm pitch [55], (a) schematic representation of a spot size converter interconnecting a fiber and a waveguide, (b) 3D illustration of multichannel taper coupler based on the spot size converter shown in (a), (c) image of multichannel taper coupler interfacing an array of silicon waveguides, (d) image of fiber pigtailed multichannel taper coupler with breakout to PM fibers

anywhere on the wafer is demonstrated and provides an alternative route towards waferscale testing (Fig. 14.28(b)).

With the increasing maturity of inverted taper based edge couplers, several research groups started investigating reliable packaging approaches involving these tapers. In [54] the inverted taper was optimized for co-packaging with a laser diode. To increase the robustness and tolerance to variations in the taper tip width a novel taper structure—the trident spot size converter (SSC)—was developed (Fig. 14.29). In [55] a novel type of fiber array was demonstrated, which tapers the light from standard single mode fibers at 250 μm pitch to high numerical aperture fibers with 20 μm pitch (Fig. 14.30). This array was then attached to an array of silicon in-

verted tapers with low index overlay. Another promising approach towards low cost packaging was proposed in [56, 57]. In this work, an array of silicon inverted tapers is impressed in an array of polymer waveguides with identical pitch on a separate substrate (rigid or flexible). The polymer waveguides thereby serve as the low index overlay. This approach ensures automatic vertical alignment and provides large tolerance in the lateral and longitudinal directions.

14.6 Waveguide Ge Photodetectors on Si

14.6.1 Introduction

Photodetectors are a key element for the majority of electro-optical applications due to their ability to convert light signals into the electrical domain. In the past decades, impressive progress in Si photodiodes has enabled the ubiquitous deployment of low-cost image sensors and solar cells. In the field of data communications, high-speed surface-illuminated photodetectors based on group III–V semiconductors have been an essential building block, enabling multi-Gbit/s optical interconnects over multi-mode fiber in combination with VCSEL light sources operating at 850 nm.

Over the past 15 years, substantial R&D efforts have been directed at exploiting CMOS processing infrastructure for the fabrication of optical components. The adoption of Ge as a material for photodetection at near-infrared wavelengths has strongly accelerated, following tremendous progress in hetero-epitaxial growth of high-quality Ge on Si substrates. Free-space p–i–n Ge-on-Si photodetectors have been demonstrated with responsivities and detection speeds rivaling their III–V counterparts. In addition, surface illuminated Ge–Si avalanche photodetectors (APD) have been developed enabling receiver sensitivities *beyond* group III–V APDs at 10 Gbit/s, leveraging the superior noise characteristics of carrier multiplication in Si as compared to group III–V semiconductors [58]. Consequently, Ge photodetectors are currently competing with III–V photodetectors for market share in short-reach optical communications.

Perhaps even more important in the longer term, significant progress in *selective-area* epitaxial growth of high-quality Ge on Si has led to the development of high-performance *waveguide* Ge photodetectors. In such waveguide photodetectors, the Ge layer essentially forms a waveguide structure that enables longer absorption length in a compact footprint and small layer thickness which can be exploited for achieving superior performance in terms of bandwidth, response, and dark current. In the next paragraphs, we will discuss design and integration aspects, as well as give an overview of the state of the art in high-performance Ge waveguide photodetectors.

14.6.2 Design Aspects

The desired performance metrics for Ge waveguide photodetectors for optical interconnect applications typically include:

- High responsivity in the communication bands of interest: > 1 A/W in the O-band, C-band and/or L-band
- High 3-dB opto-electrical bandwidth: 20 GHz for 25 Gbit/s, and 40 GHz for 50 Gbit/s
- Low dark current: below 100 nA
- Low capacitance: below 20 fF
- Low bias voltage: below 2 V

In order to meet this set of specifications, a comprehensive and combined optimization of device design and process integration flow is a key necessity. In this effort, several conflicting requirements need to be addressed.

14.6.2.1 High Responsivity

Obtaining high responsivity requires among others efficient *optical coupling* from the input Si or SiN waveguide into the Ge waveguide. Direct *butt coupling* is the most efficient approach, but may pose integration challenges as in this case the Ge waveguide needs to have largely similar lateral dimensions as the Si waveguide to limit radiation losses and coupling to higher-order modes at the Ge/Si interface. *Evanescent coupling* is often a good alternative, but achieving high responsivity in this case typically requires the use of longer detectors and a more intricate metal contacting layout. Efficient *carrier generation* upon optical illumination is another key aspect for efficient detectors, requiring that the majority of photons is absorbed in the Ge material and converted into electron-hole pairs that subsequently contribute to the light current. In order to achieve this goal, photon losses due to optical scattering at waveguide discontinuities, as well as spurious optical absorption at metals and in highly doped areas need to be suppressed as much as possible, especially for wavelengths beyond 1550 nm where the absorption coefficient of Ge drops rapidly. Finally, efficient *carrier collection* needs to be achieved, such that the majority of generated charge can be converted into light current. This is typically obtained by creating a sufficiently strong electric field across the Ge structure, such that generated carriers can drift out of the absorbing layer and be collected at the electrodes before recombining. The electric field is typically achieved in a reverse biased p-i-n diode where the absorbing Ge layer is preferentially located in the intrinsic region of the diode.

14.6.2.2 High Bandwidth

The opto-electrical bandwidth of a photodetector depends both on the *carrier transit time* as well as on the *RC response time* [59]. In order to reduce the carrier transit time, the distance between the collecting electrodes should be made as small as possible, leading to thin or narrow Ge structures. This requirement typically represents a trade-off with obtaining high responsivities. RC time reduction can be obtained by lowering the contact resistance of the metal electrodes which typically necessitates

the use of highly-doped Ge or Si regions. In addition, the photodetector capacitance can be reduced by reducing the detector length. Again, these design choices can in some cases lead to reduced responsivity.

14.6.2.3 Low Dark Current

Low dark current is essential to enable optical receivers with high sensitivity. In most photodetectors based on p–i–n diodes, the dark current density is mostly driven by the material quality of the Ge layer and highly related to the Ge deposition process, as will be discussed below. However, design choices can also affect dark current performance. Smaller Ge regions and lower electric fields in defect-rich Ge regions will typically result in lower dark current. However, such design choices and operation conditions may result in reduced responsivity or lower bandwidth.

14.6.2.4 Low Capacitance

Low capacitance is essential to enable high-speed optical receivers with high sensitivity and low power consumption. Owing to their compact footprint, Ge waveguide photodetectors typically exhibit capacitance values below 50 fF, and often less than 10 fF for compact devices.

14.6.2.5 Low Bias Voltage

Sufficiently low bias voltage (<2 V) is essential for compatibility with low-power receiver amplifier circuits implemented in scaled CMOS technology. In addition, as explained above, low bias voltage can also help to reduce dark current. Ge waveguide photodetectors based on p–i–n diodes often support low-bias voltage operation owing to the large built-in field in the sub-micrometer Ge waveguides.

14.6.3 Integration Aspects

14.6.3.1 Germanium Deposition

Most demonstrations of Ge waveguide photodetector integration in Si PIC platforms involve selective epitaxial growth of Ge on silicon using chemical-vapor deposition (CVD) reactors. Typically, such selective Ge growth is carried out in etched openings in an SiO₂ masking layer. In order to minimize the density of defects in the Ge crystal, mostly in the form of threading dislocations originating from the lattice constant mismatch between Ge and Si, a thin intermediate Ge buffer layer is often

grown at lower temperatures of around 250 °C, followed by the main growth at temperatures as high as 600 °C [59]. In some cases, in-situ doping is added during the epitaxial growth to engineer the electric field profile in the Ge layer.

At imec [60], standard reduced-pressure CVD (RPCVD) production systems are used for Ge epitaxial growth on Si. These tools are horizontal, cold wall, single wafer, load locked reactors with a lamp-heated graphite susceptor in a quartz tube. Before initiating Ge epitaxial growth, the native oxide is removed by a wet-chemical treatment in HF. After loading into the epitaxial reactor, the wafers receive a pre-epi bake in H₂. Ge is subsequently epitaxially grown on Si substrates at a typical growth temperature of 450 °C, using GeH₄ as Ge precursor and H₂ as carrier gas at atmospheric pressure. A post-growth annealing step is added to reduce the dislocation density. In this annealing step, the reduction in threading dislocation density of the grown Ge layer largely depends on the Ge thickness [61]. For Ge layers grown more than 1 μm thick, the threading dislocation density can typically be reduced to less than 10⁸ cm⁻².

Finally, a chemical-mechanical polishing (CMP) step is often added after growth and annealing, before proceeding to the back-end-of-line processing steps, to create a planarized surface with the desired Ge thickness. Typical final Ge layer thicknesses for waveguide Ge photodetectors are in the range 200 to 1000 nm.

14.6.3.2 Junctions and Contacts

For the formation of p-i-n diodes in the Ge (and Si) layers, standard CMOS ion implantation processes can be utilized. Both boron and phosphorous implant species are frequently used, as p-type and n-type dopants, respectively. Activation of the dopants typically requires an additional annealing step. As has been shown in several reports, CMOS-like contact modules can be used to implement the metal contacts to Ge photodetectors. Standard Ti/TiN metal layers can be used to form low-resistance Ohmic contacts to Ge, provided the active doping level in the Ge layer, especially for n-type Ge, is sufficiently high.

14.6.4 State of the Art

An excellent overview of the state of the art in Ge-on-Si photodetectors up to 2010 has been described by Michel et al. [59], highlighting waveguide Ge PDs with bandwidth up to 30 GHz, responsivities in the range 0.9 A/W to 1.1 A/W, and room-temperature dark currents in the μA range. More recent work has targeted improved responsivity and higher bandwidth in addition to further reductions in the dark current levels. A non-exhaustive overview of some of the recent progress is described in the following section.

In 2011, DeRose et al. [62] reported a Ge-on-Si waveguide photodetector combining a bandwidth of 45 GHz with 0.8 A/W responsivity at 1500 nm wavelength

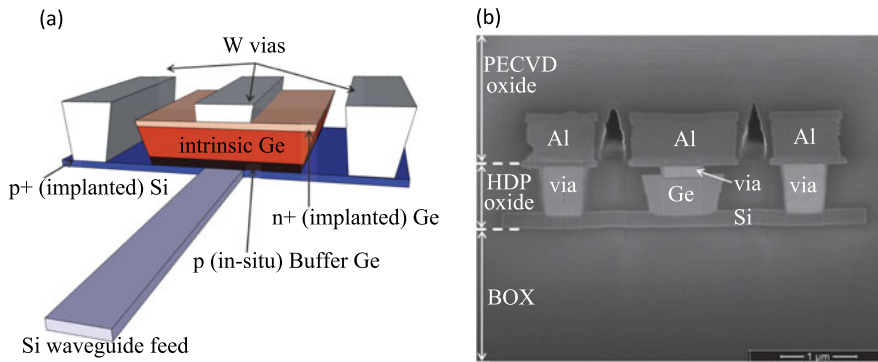


Fig. 14.31 (a) Schematic representation of a germanium waveguide n-i-p photodiode, (b) SEM cross-section of final selective area epitaxially grown Ge photodiode [62]

and a low dark current of just 3 nA. The photodetector was implemented as a vertical Ge/Si n-i-p diode. This photodiode was implemented in Sandia's CMOS compatible silicon photonics process flow, using Ge selective epitaxial growth followed by a Ge CMP step. The final Ge thickness was 600 nm, which allowed for decent responsivities with an evanescent coupling scheme despite the presence of the metal contact of top of the Ge. The use of CMOS like Ti/TiN Ohmic electrical contacts further supported high-speed operation. A schematic and an SEM cross-section of the fabricated device are shown in Fig. 14.31.

Using a similar approach as [62], Liao et al. [63] reported a Ge PD with 36 GHz bandwidth and 0.95 A/W responsivity. In this work, a 900 nm thick Ge layer was used which helped to achieve high responsivity.

In 2012, Vivien et al. [64] demonstrated a butt-coupled photodetector based on a lateral Ge p-i-n diode implemented in a 400 nm thick Ge layer. The detector had a responsivity of 0.8 A/W and supported 40 Gbit/s operation at zero bias. Furthermore, a bandwidth substantially beyond 50 GHz, and possibly as high as 120 GHz was estimated at a reverse bias of 2 V. The dark current, however, was relatively high at about 4 μ A at a reverse bias of 1 V which was attributed either to higher than expected defect levels in the epitaxially grown germanium layer or due to dopant diffusion during thermal annealing.

Also in 2012, Li et al. [65] suggested several design improvements to improve the performance of Ge photodetectors integrated in a 130 nm CMOS logic process. A distributed Bragg reflector (DBR) was implemented behind the detector to reflect any non-absorbed light back into the detector and increase the responsivity, especially for short detectors. In addition, the location of the metal electrodes on the Ge was optimized to reduce undesired absorption. A "fingered" metal contact layout was adopted, placing the contacts on the Ge only in regions with low optical intensity instead of using a single continuous metal electrode. A schematic representation of these design improvements is shown in Fig. 14.32(a). With these improvements a responsivity beyond 0.8 A/W was obtained in the entire C-band. However, the bandwidth of these detectors was less than 20 GHz and the dark current was rela-

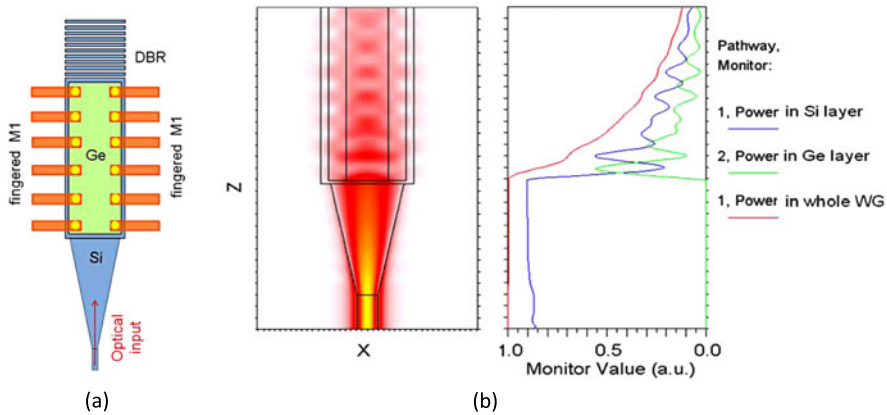
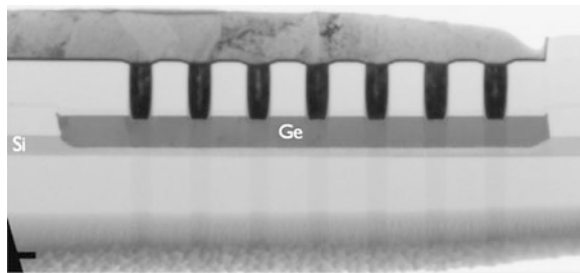


Fig. 14.32 Design optimization of Ge PDs [65]. (a) Schematic top view of the improved Ge PD design, with a DBR and fingered M1 electrodes. (b) Simulated optical power versus position in the PD

Fig. 14.33 Longitudinal TEM cross section of imec's 50 GHz Ge/Si p-i-n waveguide photodetector



tively high at ~ 300 nA at room temperature, in part arising from the limited process options available for direct monolithic integration with CMOS logic.

In 2014, imec realized waveguide Ge PDs with bandwidth beyond 50 GHz at -1 V bias, responsivity higher than 0.8 A/W in the C-band, and dark current below 50 nA [66]. The devices were implemented as vertical p-i-n (VPIN) Ge/Si structures, and were co-integrated with high-speed Si depletion modulators, thermo-optic devices, and various passive devices in imec's 200 mm Si photonics platform. A longitudinal TEM cross section of this photodetector is shown in Fig. 14.33.

In a latest development, Ge-on-Si photodetectors without direct metal contact to the Ge material have been developed [67, 68] as illustrated in Fig. 14.34. In these devices, the Ge is grown on top of a lateral p-i-n (LPIN) diode in Si, and carrier collection from the Ge is realized by the fringe field generated by the underlying p-i-n structure in silicon. Owing to the absence of metal contacts on the Ge and highly doped areas in the Ge, responsivities in excess of 1 A/W can be achieved. In addition, despite the presence of a highly defective layer between the Ge and Si, very low dark currents of only a few nA can be obtained [68]. Furthermore, reported bandwidths for such devices are sufficient for operation at 28 Gbit/s to 40 Gbit/s.

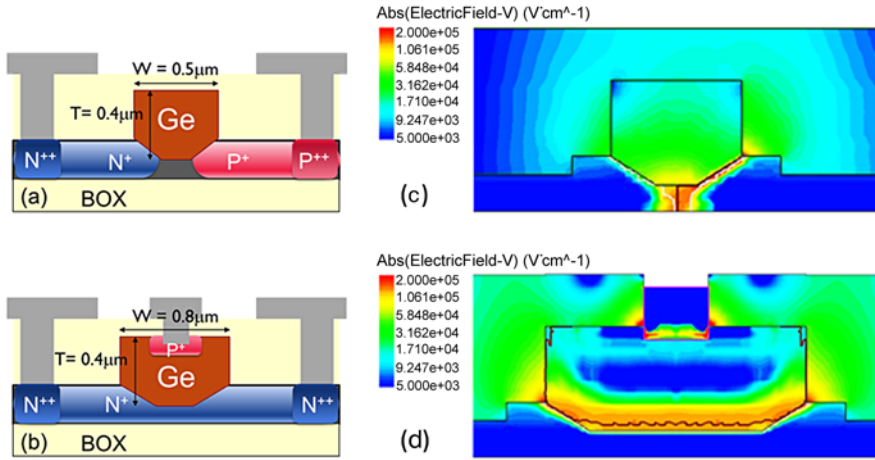


Fig. 14.34 (a) Schematic cross-section of a silicon contacted Ge waveguide PD, (b) a VPIN p-i-n Ge waveguide PD, (c) electric field simulation of a silicon contacted Ge waveguide PD, (d) a VPIN p-i-n Ge waveguide PD at -1 V bias [68]

The lower process complexity for fabricating such devices is an additional benefit compared to more traditional Ge PD designs.

An overview of the performance of the described Ge PDs is shown in Table 14.1.

14.6.5 Impact and Outlook

The development of Ge waveguide photodetectors has complemented the silicon photonic integration platform with a monolithically integrated high-performance photodetector covering the telecommunication bands in the near-infrared, thereby strongly propelling the field of silicon photonics. Waveguide-integrated Ge photodetectors on Si enable single-mode optical receivers with substantially increased functionality and performance as compared to their free-space counterparts. By combining an array of waveguide-integrated Ge photodetectors with wavelength or polarization de-multiplexing circuits implemented in silicon or silicon-nitride waveguides, advanced high-capacity receivers can be constructed on a single chip. One example are coherent optical transceivers targeting metro data links as described in [69] where an array of eight high-speed Ge waveguide photodetectors is combined with passive Si photonic circuitry to enable a coherent receiver bandwidth capacity of 100 Gbit/s. Furthermore, the integration of Ge waveguide photodetectors with wavelength-selective filters enables silicon-based optical receivers capable of wavelength-division multiplexing (WDM) [70]. Such architectures may in the near future enable WDM single-mode intra-data center interconnects at 100GbE, 400GbE and beyond. Silicon PICs offer a clear path for scaling the bandwidth density of single-mode optical transceivers while reducing cost and energy per transmitted bit. The Ge waveguide-integrated photodetector has been a key building block

Table 14.1 Overview of state-of-the-art germanium photodiodes on silicon

Ref.	Institute/company	Ge PD type	Responsivity (A/W)	Wavelength (nm)	Bias Voltage (V)	Bandwidth (GHz)	Dark Current (nA)	Capacitance (fF)
[62]	Sandia/MIT	Ge/Si VPIN	0.85	1500	-1	~41	~5	2.4 ^a
[63]	Kotura/Oracle	Ge/Si VPIN	0.95	1550	-1	~36	~2.6	8.5
[64]	CEA-LETI/IEF	Ge LPIN	0.8	1550	-1	>67	~4000	n/a
[65]	Luxtera/Oracle	Ge LPIN	0.9	1550	-0.5	14–19	~300	7
[66]	imec	Ge/Si VPIN	0.85	1550	-1	>50	~30	<10 ^a
[67]	IME/U Delaware	Si contacted	1.14	1550	-4	~20	~120	n/a
[68]	imec	Si contacted	1	1550	-1	~20	~3	<10 ^a

^a= estimated

in unlocking this scaling potential and will remain an essential component for Si PICs in the foreseeable future.

14.7 Optical Isolators Integrated on a Silicon Photonics Platform

It is well known that any time-independent linear system, described by a symmetric electric permittivity tensor and a symmetric magnetic permeability tensor, is reciprocal, in the sense that its scattering matrix is symmetrical. This is the case for linear, time-independent circuits implemented in silicon which implies that in such systems it is fundamentally impossible to create optical isolators. Therefore, three routes can be envisioned to realize optical isolation within silicon photonic integrated circuits: the integration of nonreciprocal materials such as magneto-optic garnets [71–75], the use of time-dependent silicon photonic circuits [76–78] or the use of nonlinear optical functions [79]. While nonlinear optical functions can be implemented relatively easily on a silicon photonic IC, due to the strong light confinement and high third order nonlinear coefficient and high thermo-optic coefficient of silicon, such isolators are not ‘general purpose’ since they will only operate in a limited range of optical input powers and levels of feedback. Therefore, for practical applications both the magneto-optic devices and optical modulation-based devices are of most interest. One issue with the latter approach is the power consumption associated with driving the modulator structures while in the first case the issues are more related to the integration of the magneto-optic materials within the silicon photonics process flow.

A conventional optical isolator is based on the principle of nonreciprocity induced by a ferromagnetic/ferrimagnetic garnet under the influence of an external magnetic field. Ferrimagnetic garnets are unique materials with strong magneto-optical properties (or Faraday rotation coefficient) and low optical absorption at telecom wavelengths. In spite of possessing very good material properties for magneto-optical applications the main hurdle is the difficulty of incorporating garnet materials on a semiconductor platform. Different strategies have been pursued, classified into two broad categories: bonding [71–74] and deposition [75]. Deposition is a wafer scale process but it suffers from degraded material properties as compared to its single crystalline form. On the other hand bonding envisages an opportunity to incorporate excellent epitaxially grown magneto-optic material on the waveguide but it is intrinsically a die-to-wafer technique which limits the scaling of the integration. Bonding can be performed in two ways: by means of surface activated direct molecular bonding or by means of adhesive bonding.

While bulk optical isolators rely on the nonreciprocal polarization rotation (Faraday effect), waveguide-based isolators based on this principle (and definitely when implemented in silicon) would suffer from the strong birefringence, limiting the obtainable degree of isolation. Therefore, waveguide based optical isolators are based on the magneto-optic Kerr effect, resulting in a nonreciprocal phase delay for light passing through the magneto-optic/silicon hybrid waveguide in opposite directions (when the light propagation is perpendicular to the magnetization

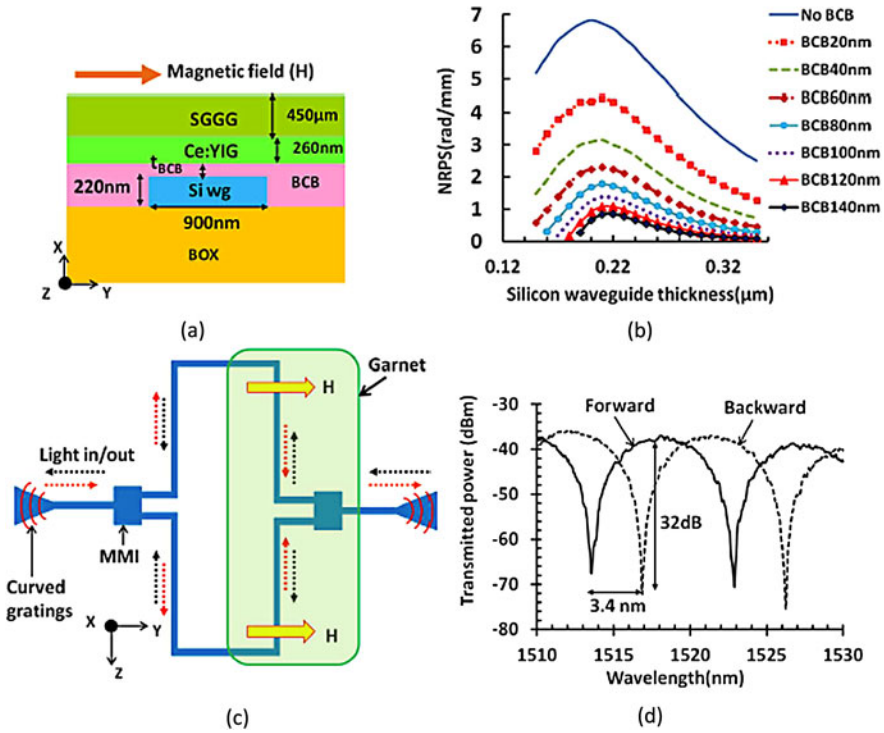


Fig. 14.35 (a) Schematic diagram of a garnet bonded waveguide cross-section; (b) non-reciprocal phase shift (NRPS) vs. silicon waveguide thickness; (c) schematic drawing of a push-pull MZI type isolator; (d) measured spectra for forward and backward propagations [71]

in the magneto-optic material, the so-called Voigt-configuration). As an example, in Fig. 14.35(a) a schematic cross-section of a hybrid magneto-optic/silicon waveguide is shown. The magneto-optic material is a Ce substituted Yttrium Iron Garnet (Ce:YIG) on a (Ca, Mg, Zr) Substituted Gadolinium Gallium Garnet (SGGG) substrate. The Faraday rotation coefficient of the Ce:YIG is about 4500°/cm at 1550 nm wavelength. The non-reciprocal phase shift (NRPS) is proportional to

$$NRPS \propto \frac{g_{xz} \iint_{Ce:YIG} E_x E_z dx dy}{\iint [E_x H_y - H_x E_y] dx dy} \tag{14.7}$$

with g_{xz} the gyro-magnetic constant, when a magnetic field is applied along the y-axis as indicated in Fig. 14.35(a) [71].

As the NRPS is proportional to the product of E_x and E_z , a strong NRPS can be expected only for the TM-polarized mode in this waveguide configuration. The calculated NRPS as a function of the separation between the magneto-optic material and the silicon waveguide layer and as a function of the silicon waveguide layer thickness

is shown in Fig. 14.35(b), assuming a BCB adhesive bonding layer in between the magneto-optic material and the silicon waveguide layer [71].

In order to translate the nonreciprocal phase shift into a nonreciprocal power transmission, the hybrid magneto-optic/silicon waveguide structure can be incorporated into an interferometric structure, such as the Mach-Zehnder interferometer as depicted in Fig. 14.35(c). By making the device layout as shown in Fig. 14.35(c), push-pull operation can be realized using a uni-directional magnetization. As illustrated in Fig. 14.35(b), the required nonreciprocal waveguide length can be made short (< 1 mm) for optimal Si waveguide layer thickness (~ 220 nm) and a small separation between silicon and the magneto-optic material. Figure 14.35(d) then shows a typical measurement result where the transmission of the (unbalanced) Mach-Zehnder interferometer in forward and backward direction is plotted. As can be seen, > 30 dB isolation can be obtained using such structures. However, one issue with these isolator structures still is their relatively large insertion loss, on the order of 7 dB. While the example presented was based on adhesive bonding, other demonstrations have been made either using molecular bonding [72] or by sputter deposition [75] on silicon ring resonators.

As already mentioned above, nonreciprocal optical functions can also be realized using time-dependent systems, such that one doesn't have to rely on nonreciprocal materials. Various implementations of such schemes have been presented in recent years. In Fig. 14.36, two examples are given.

In the first configuration a bimodal silicon waveguide is used. In part of the waveguide structure, a traveling wave refractive index modulation is applied, as shown in Figs. 14.36(b) and (c). This refractive index modulation can scatter the incident fundamental mode to the first order mode (resulting in an interband transition), provided that the period and the frequency of the refractive index modulation matches with the frequency and phase mismatch between the fundamental and first order mode. This will only occur in one propagation direction as indicated in Fig. 14.36(a), thereby resulting in nonreciprocal transmission through such a structure. Since the bands shown in Fig. 14.36(a) are largely parallel, wide optical bandwidth operation can be obtained. An alternative structure, as illustrated in Fig. 14.36(b), relies on the cascading of two phase modulators, which are driven in quadrature. The idea behind this type of structure is that a delay line is introduced in between the modulators, such that the phase modulation imprinted by the second phase modulator either cancels that of the first modulator and therefore the transmission is 1 (e.g. from left to right) or the two phase modulators reinforce each other (e.g. from right to left) and thereby suppress the optical carrier. Perfect suppression of the carrier can be obtained for a particular phase modulation index. In this case all optical power is translated to the sidebands in the simple configuration of Fig. 14.36(d) which for broadband operation also need to be suppressed. This can be realized by arranging parallel arrays of such tandem phase modulators and by varying the phase of the driving signals in the different arms as shown in Fig. 14.36(e) and 14.36(f). While being an attractive approach for realizing silicon photonics process flow compatible optical isolators, these devices still suffer from relatively high insertion loss and power consumption associated with driving the modulators.

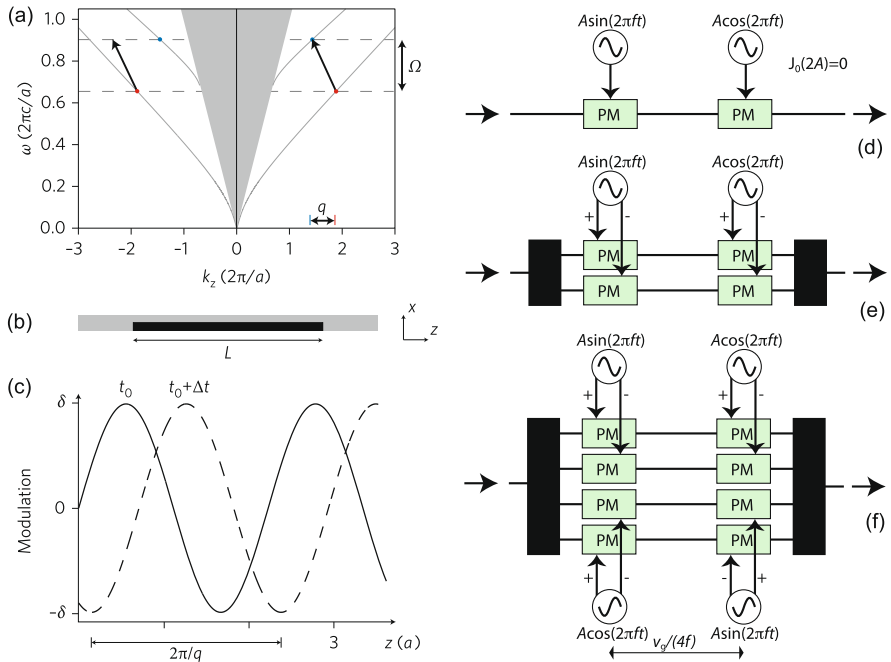


Fig. 14.36 (a) Optical isolation based on inter-band photonic transitions (from [77]), (b) optical isolation based on cascaded phase modulators (from [76])

14.8 Nonlinear Optics Based on Silicon Photonics

14.8.1 Introduction

Silicon photonic nanowires exhibit a number of properties which enhance nonlinear interactions drastically and make them an ideal candidate as a platform for doing nonlinear optics. First, the strong confinement available on the platform induces, even at moderate powers, large electric fields inside the waveguide. Secondly, the nonlinear index of silicon is very high: it is two orders of magnitude higher than the value found in silica and one order of magnitude higher than the value found in other CMOS compatible materials such as e.g. aluminum nitride or silicon nitride. Lastly, the high confinement in the waveguides allows one to tune the geometric dispersion of the waveguide. By controlling the dispersion it is possible to phase match the different waves in the nonlinear process and enhance the efficiency. By exploiting these three advantages, researchers have made a lot of progress in integrating nonlinear optical functions on a silicon chip.

This section starts with a brief introduction into the field of nonlinear optics, specifically addressing the most important nonlinear interactions in silicon. Hereafter some state of the art demonstrations will be discussed. Lastly, the nonlinear absorption in silicon is known to limit the efficiency of nonlinear interactions at

telecom wavelengths. This fundamental problem will be addressed as well and some solutions will be put forward. The section will be concluded with some important results obtained in other CMOS compatible materials which suffer less or do not suffer from any two-photon absorption at all.

14.8.2 Nonlinear Optical Interactions and Nonlinear Optical Materials

In a nonlinear optical material the polarization is a nonlinear function of the electric field. As such the nonlinear polarization can be expanded in a Taylor series with respect to the electric field:

$$P(E) = \varepsilon_0(\chi^{(1)}E + \chi^{(2)}E^2 + \chi^{(3)}E^3 + \dots) \quad (14.8)$$

Here, ε_0 is the susceptibility of vacuum, $\chi^{(1)}$ the linear susceptibility of the material, and $\chi^{(2)}$ and $\chi^{(3)}$ are the second and third order nonlinear susceptibility, respectively. It can be shown that in a centro-symmetric material, such as silicon, the even terms vanish [80]. For silicon, the strongest nonlinear term in (14.8) will be proportional to E^3 . As a consequence, the refractive index will be intensity dependent [80]. The refractive index in a third order nonlinear material is given by

$$n = n_0 + n_2 I \quad (14.9)$$

where n_0 and n_2 are the linear and the nonlinear refractive index, respectively, and I is the intensity. The third order nonlinear process is sometimes referred to as the optical Kerr effect, as opposed to the electrical Kerr effect where an electrical field changes the refractive index, it is here the optical intensity which changes the refractive index.

The nonlinearity, at least the one addressed in this section, comes from the nonlinear polarization of the electron cloud and is extremely fast (< 10 fs response time). As a result, the effect is also very broadband. Since the nonlinear refractive index n_2 is proportional to the third order susceptibility, it is used as a defining parameter for the third order nonlinearity of the material. In Table 14.2, the nonlinear refractive indices for selected materials are given.

In a waveguide configuration, the intensity scales as $\frac{P}{A_{eff}}$, where P is the incident power and A_{eff} is the effective area of the waveguide. For this reason the nonlinear

Table 14.2 Nonlinear indices of a set of common materials given along with the typical nonlinear parameter for a waveguide fabricated in the material at a wavelength of 1550 nm

	n_2 (10^{-20} m ² /W)	γ (W ⁻¹ m ⁻¹)
Crystalline silicon [81]	650	450 (real part)
Silicon nitride [82]	24	1.5
Hydex glass [83]	11.5	0.233
Silica [80]	2.7	10^{-3}

parameter, defined as

$$\gamma = \frac{n_2 \omega}{A_{eff} c}, \quad (14.10)$$

which is inversely proportional to the mode area and proportional to the nonlinear refractive index, is used for quantifying the nonlinearity of a waveguide. Here ω is the frequency of light, and c is the speed of light in vacuum. The nonlinear parameter for typical waveguides can be found in Table 14.2. As shown in the table, the nonlinear parameter of silicon is five orders of magnitude larger than the one found in a single mode optical fiber.

14.8.2.1 Degenerate Four Wave Mixing

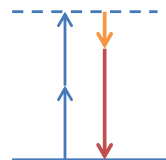
The nonlinear polarization acts as a source term for the Maxwell equations. It can be shown that in a nonlinear waveguide [80] the following equation holds

$$\nabla^2 E - \frac{\partial^2 E}{c^2 \partial t^2} = \mu_0 \frac{\partial^2 P_L}{c^2 \partial t^2} + \mu_0 \frac{\partial^2 P_{NL}}{c^2 \partial t^2} \quad (14.11)$$

where P_L and P_{NL} are the linear and the nonlinear polarization, respectively, and all other parameters have their usual meaning. Indeed, the right hand side of the equation acts as a source term for the wave equation. The nonlinear polarization term makes the wave equation a nonlinear equation. This has two important consequences. First, different fields present in a nonlinear medium will be coupled. Energy can be transferred between the electric fields, e.g. one field can be amplified by another electric field. As a second consequence, there is nonlinear mixing of the waves, such that new optical frequencies, initially not present in the medium, are generated. The coupled wave equations can be solved numerically and lead to a whole set of interactions and processes [80]. The most interesting one is the process of degenerate four wave mixing. As in any third order process, there are four fields interacting. However, one field is degenerate in the process. A quantum mechanical scheme of degenerate four wave mixing interaction is shown in Fig. 14.37. As can be seen in the figure, two photons are annihilated in the process while two other photons are created.

In such a case, the photons which are annihilated are mostly referred to as pump photons, while the created photons are called the signal and idler photons. The process can be used to amplify and convert photons. In such an approach a waveguide is fed with a strong pump and a weak signal. At the output of the waveguide an

Fig. 14.37 Quantum mechanical picture of the degenerate four-wave mixing process



amplified signal appears as well as the converted idler signal. The degenerate four wave mixing process is the working horse of most of the applications discussed in the following section.

As is evident from Fig. 14.37, the four wave mixing process conserves energy. No energy is transferred to the material. The energy is transferred only by the interacting signals, here from the pump waves to the idler and signal waves. Alike the energy transfer, there is also a momentum transfer from the pump to the signal and the idler wave. Since the impulse needs to be conserved, the following relations hold [80]:

$$\hbar\omega_p + \hbar\omega_p = \hbar\omega_i + \hbar\omega_s \quad (14.12a)$$

$$\Rightarrow \Delta\omega = \pm(\omega_s - \omega_p) = \pm(\omega_p - \omega_i) \quad (14.12b)$$

where $+$ ($-$) holds for $(\omega_s - \omega_p)$ and $(\omega_p - \omega_i) > (<) 0$

$$\beta_p + \beta_p = \beta_i + \beta_s + 2\gamma P \quad \Rightarrow \quad \beta_p = \frac{\beta_i + \beta_s}{2} + \gamma P \quad (14.13)$$

Here β_p , β_s and β_i are the propagation constants of the pump, the signal, and the idler wave, respectively, γ is the nonlinear parameter of the waveguide, and P the power of the pump wave. The correction factor $2\gamma P$ takes into account the intensity dependent refractive index and as such the nonlinear phase shift. When working in the vicinity of the pump, the propagation constants can be written as a Taylor expansion with respect to the detuning $\Delta\omega$ of the signal and idler

$$\beta_j = \beta(\omega_j) = \beta(\omega_p \pm) \quad (14.14a)$$

$$\beta_j = \beta(\omega_p) \pm \frac{d\beta}{d\omega}(\omega_p)\Delta\omega + \frac{1}{2} \frac{d^2\beta}{d\omega^2}(\omega_p)\Delta\omega^2 \pm \dots \quad (14.14b)$$

$$\beta_j = \beta_p \pm \frac{d\beta_p}{d\omega} \Delta\omega + \frac{1}{2} \frac{d^2\beta_p}{d\omega^2} \Delta\omega^2 + \dots \quad (14.14c)$$

where $j = s, i$, correspond to the signal and the idler, respectively, and $+$ or $-$ depend on the relative frequencies of pump, signal, and idler.

Substituting (14.14c) into (14.13) results in

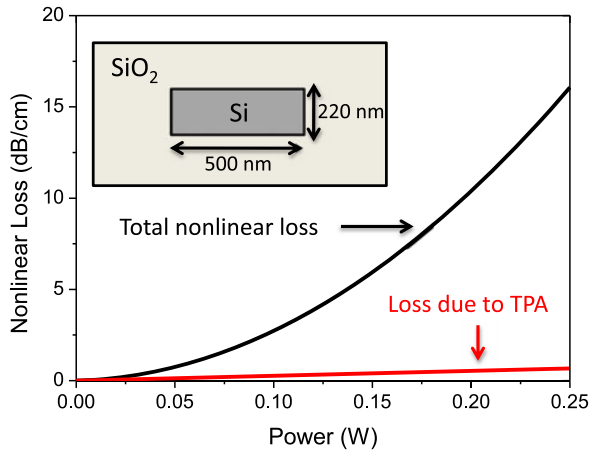
$$\frac{d^2\beta_p}{d\omega^2} \Delta\omega^2 = -2\gamma P \quad (14.15)$$

which indicates that the second derivative has to be negative, or the group velocity has to be anomalous in the waveguide in order to achieve phase matching (provided the nonlinear parameter is positive. Because the dispersion of a waveguide depends to a large extent on the geometry of the cross section of the waveguide, it can be satisfied by changing the geometry.

14.8.2.2 Nonlinear Absorption in Silicon Photonic Wire Waveguides

Silicon has a bandgap of -1.1 eV and is therefore transparent for the telecom wavelength window (~ 0.8 eV). However, at high intensities, the nonlinear absorption

Fig. 14.38 Simulated nonlinear loss in a typical silicon waveguide when exposed to a high continuous wave power. The carrier lifetime is assumed to be 1 ns



of photons, namely two photon absorption becomes more likely. Since the process involves two photons, it is a nonlinear process. The higher the intensities, the more photons, the more likely absorption becomes. The nonlinear absorption as a result of pure two photon absorption is given by

$$\alpha = \alpha_0 + \alpha_2 I \quad (14.16)$$

Here is α_0 the linear absorption coefficient, and α_2 the two-photon absorption coefficient, and I the average intensity of the optical wave. However, the nonlinear absorption of photons in silicon excites carriers from the valence band into the conduction band which causes additional absorption. The total nonlinear absorption is mostly dominated by free carrier absorption and it can be shown that free carrier absorption (FCA) scales with the square of the intensity. It is given by

$$\alpha = \alpha_0 + \alpha_2 I + \alpha_{FCA} \frac{\alpha_2 \tau \lambda}{2hc} I^2 \quad (14.17)$$

Here α_{FCA} is the free carrier absorption coefficient ($1.45 \times 10^{-21} \text{ m}^2$ in silicon at 1550 nm), h Planck's constant, τ the carrier lifetime, c the vacuum speed of light, and α_0 , α_2 and I are as defined before (see (14.16)). Figure 14.38 shows the nonlinear absorption of a typical waveguide. The nonlinear absorption can be significantly reduced by reducing the carrier lifetime and sweeping out the carriers out of the waveguide in a pin structure. This can be accomplished by using short pulses, or by using another CMOS compatible material which does not show significant nonlinear absorption.

14.8.3 Applications and Demonstrations

The applications discussed below take advantage of the very fast, and thus very broadband nature of the Kerr effect.

14.8.3.1 Wavelength Converters

One of the first demonstrations of nonlinear optical interactions in a silicon waveguide was the conversion of a continuous wave signal [84], where a signal at one wavelength has been converted to another wavelength. The conversion efficiency was rather low in the first experiments because of the two photon absorption and reached a level of -9.6 dB in a 4 cm long waveguide when pumped with several hundreds of mW. However, by using pin diodes (see Fig. 14.39) the conversion efficiency has been boosted close to the transparency level [85]. A pin diode allows to sweep out the carriers generated by the two-photon absorption process. As a consequence the effective carrier lifetime can be reduced. As an example (see [86]), the effective carrier lifetime measured as a function of the voltage across the pin junction is shown in Fig. 14.40. Lower carrier lifetimes, down to 12.2 ps can be achieved, meaning less nonlinear absorption. It also needs to be noted that the bandwidth over which conversion can take place, can span several 100's of nm due to the broadband nature of the Kerr effect.

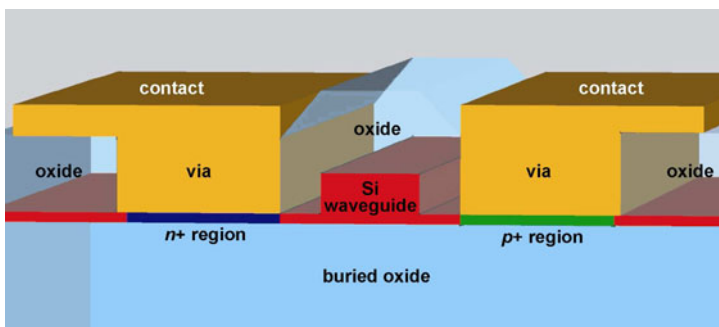
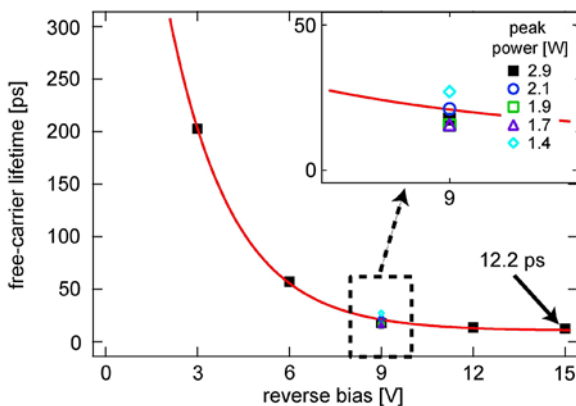


Fig. 14.39 Cross section of pin diode to extract the generated carriers in a silicon waveguide [86]

Fig. 14.40 Carrier lifetime as a function of reverse bias. The carrier lifetime was measured in a pump probe setup, it does not depend on the pump power (shown in the inset). The carrier lifetime can be reduced to 12.2 ps



14.8.3.2 All Optical Amplifiers

A second set of devices related to wavelength converters are all optical amplifiers. They take advantage of the enormous broadband response of the Kerr effect to amplify over a broad wavelength band. However, due to the high nonlinear absorption in silicon no one has been able to demonstrate a true continuous wave amplifier. The only approach which can show true net gain is when two synchronized picosecond pulses are used [87]. One pulse amplifies the other, the probe pulse, by a couple of dB.

14.8.3.3 Phase Sensitive Amplifiers

The nonlinear interactions are phase sensitive, which means that the efficiency and the direction of the process are dependent on the phase relation between the waves. This property is exploited in a phase sensitive amplifier. Depending on the phase of the incoming signal, the amplifier will amplify or attenuate the signal. Figure 14.41 shows the amplification or attenuation as a function of the relative phase between the waves. Corresponding amplifiers [88] can potentially work with very low noise figures, and the amplifiers can for example be used to regenerate optical signals because noise with unwanted phase is de-amplified. In silicon, phase sensitive amplification of a continuous wave signal modulated at 10 Gbit/s bit rate was realized [89]. Again a pin diode is needed to reduce the nonlinear losses. In another experiment [90], phase sensitive amplification was demonstrated in a short ($\sim 200 \mu\text{m}$) long photonic crystal waveguide. This experiment used picosecond pulses and no pin diode.

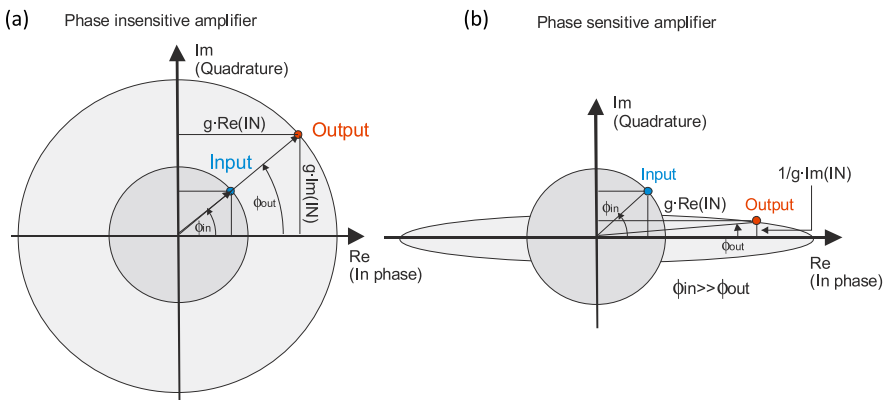


Fig. 14.41 Phase (in)sensitive amplification. (a) When a signal is amplified insensitive to its phase, the amplification is constant as a function of phase, (b) When the amplification is phase sensitive, the signal will be amplified or attenuated depending on the signals input phase. From [88]

14.8.3.4 Quantum Mechanics: Entangled Photon Pairs

In quantum communication networks entangled photon pairs are used to securely communicate between a transmitter and a receiver. The degenerate four wave mixing process can be used to generate such entangled photon pairs or as a repeater. Indeed, in the spontaneous regime, at moderate pump powers and without a seed the four wave mixing process will generate spontaneously idler and signal photons which share unique information. There have been various demonstrations in silicon waveguides and silicon resonators where the efficient generation of entangled photons has been demonstrated [91].

14.8.3.5 An Ultra-High Resolution All-Optical Sampler

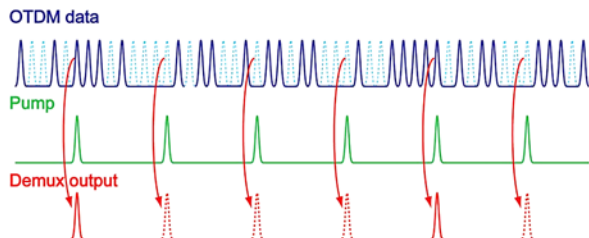
Sampling an optical signal with a photo-diode is limited by the intrinsic speed of the electrical read-out circuit. An all-optical sampling scheme, based on the ultrafast Kerr effect, can be much faster. In a typical optical sampling scheme, the sampling resolution is limited by the pulse duration of an ultrafast mode-locked laser. The pulse duration of such a mode-locked laser can be lower than 1 ps and allows to obtain a very high resolution.

Here, the pulses generated by the mode-locked laser are used as the pump photons in the four-wave mixing process. The data signal, that needs to be sampled, acts as the signal in the four wave mixing process. When the data signal and the pump pulse temporally overlap, the data signal will be converted to an idler wavelength. The idler wavelength is isolated in a wavelength demultiplexer and sent to a (slow) photodiode. The area of the (long) electrical pulse is proportional to the intensity of the sampled signal. In an experiment by the group of Oxenløwe [92], for example, a 1.28 Tbit/s signal was successfully sampled. A result which surpasses the speed of a typical electrical photodiode by an order of magnitude.

14.8.3.6 A Wavelength Demultiplexer

An all-optical wavelength demultiplexer can be constructed by using almost the same sampling setup. Here, the optical pump is a fast repetition rate pulsed laser which samples and converts parts of the signal to another wavelength band. As can be seen in Fig. 14.42, this has been used to demultiplex a 160 Gbit/s signal to a 10 Gbit/s signal [93].

Fig. 14.42 Ultrafast optical sampling scheme/demultiplexer. The sampled or demultiplexed signal is converted to another wavelength in the presence of the pump pulses [93]



14.8.3.7 Results in Other CMOS Compatible Materials

There have been impressive demonstrations of nonlinear optics in other CMOS compatible materials (silicon nitride [94], Hydrex [94], aluminum nitride [95], a-Si:H [96–99]). For example, it has been found that hydrogenated amorphous silicon (a-Si:H) has a smaller two photon absorption coefficient than crystalline silicon. Additionally it has a higher nonlinear refractive index. Although the results depend on the fabrication technique, the material seems to be a promising candidate for doing nonlinear optics and several impressive results have been obtained, for example all optical amplification [96] and ultra-low power continuous wave conversion [99]. The latter examples have been shown to work with a much higher efficiency than in crystalline silicon.

Another platform for doing nonlinear optics is silicon nitride which has a band-gap energy of 5 eV and does not suffer from two photon (or even three or four photon) absorption at telecom wavelengths. However, due to its lower nonlinear parameter, resonators have to be used to obtain the power levels needed for the nonlinear process. The resonators can have a very high Q factor (up to a million [100]), which reduces the threshold for nonlinear interactions significantly. When these ring resonators are optically pumped, the resonators do not only enhance the pump power, but also give feedback to the amplified signals. As a consequence, very similar as in a laser, there can be oscillations when the optical parametric gain is stronger than the optical losses. At that point sidebands will be generated. Through cascaded four wave mixing new lines are generated and at significant high powers a whole set of lines, i.e. a comb, is generated. Remarkable progress has been achieved in understanding these processes. The integration of these nonlinear optical functions on a chip allows integrating a WDM source pumped by a single bonded laser [101]. The output spectrum of a silicon ring resonator pumped by a single frequency continuous wave laser is shown in Fig. 14.43. It has to be added that similar results have been obtained in other material systems which lack two photon absorption in the telecom band such as aluminum nitride [95] and hydrex glass [94].

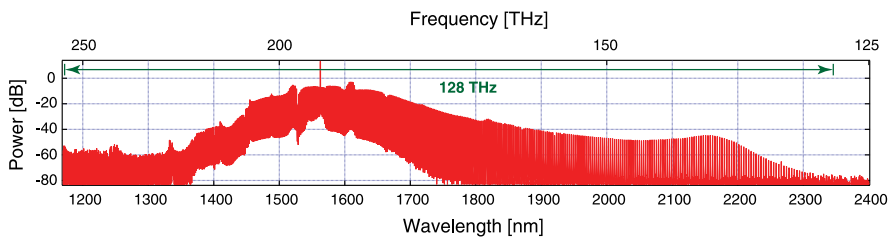


Fig. 14.43 The comb like output spectrum of a silicon nitride ring resonator acting as a parametric oscillator (figure from [102])

Fig. 14.44 Strain induced by a silicon nitride layer on top of a silicon waveguide breaks the symmetry, introducing a second order nonlinearity in the waveguide (figure from [103])

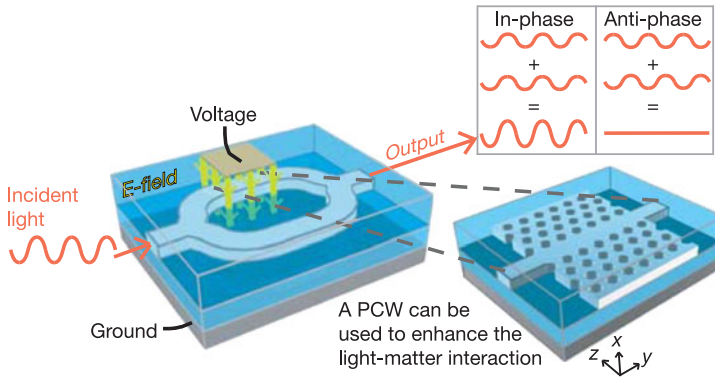
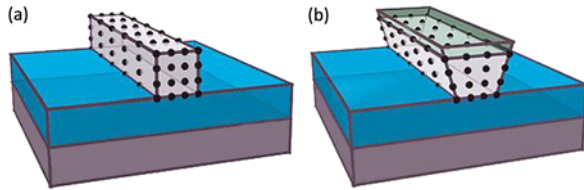


Fig. 14.45 Working principle of Pockels type modulator in silicon (figure from [103])

14.8.3.8 Non-Kerr Effect Processes in Silicon Waveguides

Some other techniques have been used to introduce non-Kerr like processes in silicon waveguides. There has been quite some effort in introducing a second order nonlinear effect in the waveguides. This was achieved by breaking the centro-symmetry of the waveguide by straining the material. This is mostly done by covering the waveguide with a strained silicon nitride layer (Fig. 14.44). The introduction of a second order nonlinear response opens the door for new applications, and the most important ones are Pockels effect based modulators. The Pockels effect, a second order effect, allows a very fast change of the refractive index of the material by applying a DC electric field and enables building corresponding modulators (Fig. 14.45). If the interaction is even more enhanced by using a sort of slow light photonic crystal waveguide, such modulators can be made very short.

14.9 Design of Complex Silicon Photonic Integrated Circuits

Silicon photonics, as the first optical integration technology with sub-micrometer waveguides, introduces a number of design challenges that are not found in lower-contrast optical waveguides [104]. First of all, the miniature dimensions allow for much smaller components, and therefore for a much larger number of components within a circuit. This enables unparalleled circuit complexity. This complexity also

introduces the need for active control of the circuits, which requires a close integration with electronics, both in the design as in the technology. Finally, the high index contrast makes the waveguides exceptionally sensitive to small geometric variations [105], which raises the question of fabrication and operational tolerances and circuit yield.

These challenges need to be addressed at the design stage: complex circuits need to be designed to specification, including the electronic control and read-out functions, and they need to be designed for manufacturing, guaranteeing sufficient yield of the final device.

Photonic design has been largely a domain of physical simulation. While optical circuit simulators have been around for some time, they are mostly used for system exploration. Most photonic on-chip devices are still designed using full-vectorial electromagnetic solvers based on finite difference time domain (FDTD) or eigenmode propagation. For larger circuits, this approach becomes impractical, and optical circuit design needs to be separated from the physical design of the individual functional blocks [106]. The result of the physical design of a building block is then encoded into a behavioral model (or compact model) that describes the block's behavior within a certain approximation. This method is similar to the approach used in electronic design.

Practices from electronic design automation (EDA) are being adopted for silicon photonic design [107]. In a typical EDA flow, we discern several design stages [108]:

1. Front-end design: defining the 'logical' circuit based on the desired functionality,
2. Back-end design: translating the logical circuit into a physical layout for fabrication,
3. Verification: validating that the layout corresponds to the desired functionality and that it meets the standards of the manufacturer.

In the front-end design stage, the circuit functionality is captured in a *schematic*, which interconnects the functional building blocks in a hierarchical circuit. This representation of the circuit does not yet take into account the actual placement and physical implementation of the building blocks, but rather describes the blocks purely on a functional basis. The functionality of the circuit can then be simulated using an optical circuit simulator, either in the time domain or the frequency domain [109–112]. Design becomes more complex when designing a mixed optical/electrical circuit. At that point, the most widely used approach is to simplify the optical circuit functionality such that it can be handled by an electronic simulator. The optical models are then represented in SPICE or Verilog-A, an analog electronics modeling language. This, however, introduces limitations in the optical functionality that can be accurately modeled: multiple wavelength channels, polarization and fast nonlinearities are very difficult to capture in such models, while, on the other hand, specialized optical circuit simulators can handle these phenomena. A future solution would be a mixed-signal co-simulation strategy, similar as that used for analog-digital circuits.

Once the basic functionality is captured, the challenge is to optimize the design for yield. Silicon waveguides are especially susceptible to any change in the geometry, and the variations will be cumulative throughout larger circuits. While some Monte-Carlo techniques exist to run a simple yield analysis of optical circuits, there is still a lot of room for innovative research, such as the use of statistical variability analysis techniques [113]. This is because photonic variability is truly a multi-dimensional problem, where the slow/fast corner approach used in electronics is not always applicable.

Once the circuit functionality is satisfactory, it has to be transferred to an actual layout that can be sent to the fab for fabrication. In a cell-based approach, the information from the schematic can be used as a starting point for the layout, replacing the logical building blocks by their layout counterparts. However, the functionality of the layout can be significantly different from what was originally designed: the actual placement can impact phase delays between components.

Circuit-based design usually uses pre-defined (parametric) building blocks [114] but it is also possible to incorporate full-custom blocks. For these, it is important that the layout generates the desired geometry. Lithographic processes tend to deform the original patterns, and compensation in the form of optical proximity corrections (OPC) need to be applied [115]. Some design tools incorporate a lithography simulator to enable litho-friendly designs [116].

To guarantee that the mask patterns can actually be fabricated, most fabrication services require that the design passes a design rule check (DRC) which inspects the design for features that cannot be fabricated: too small line widths, periods, layers that are incompatible, sharp angles, etc.

If those checks have been passed, the design should also be checked for functional integrity: does the mask layout correspond to the functional schematic that was composed in the front-end design phase? This layout-versus-schematic check is now commonplace in electronic design, but the techniques for photonics are only in a rudimentary stage [115]. Also, during this stage the layout could be analyzed for parasitics: unwanted optical coupling, scattering or absorption [117].

A design flow like this is very similar to a full-custom analog electronics design flow. Therefore, it requires a similar support from the tools. Integration of photonics design in EDA tools is emerging [118, 119], and also the first mature *process design kits* (PDK) are being released by various fabs. A PDK is a combination of design rules, documentation and a verified component library that can be used by the designer as a basis for his circuit. Through the PDK, a designer can reuse trusted components with guaranteed performance and focus on the functionality of the circuit rather than the building blocks. For the fab, the designs that are sent in for fabrication are less complex and contain less unknown geometries that could lead to manufacturing problems.

Silicon photonics is changing the way photonic designers approach photonic integrated circuits. Smaller features, larger complexity and small fabrication tolerances are gradually pushing the photonics community towards an EDA-style design flow. Still, there are significant open challenges, especially with photonic-electronic co-simulation and verification.

References

1. S.E. Miller, Integrated optics: an introduction. *Bell Syst. Tech. J.* **48**(7), 2059–2069 (1969)
2. R.A. Soref, J.P. Lorenzo, Single-crystal silicon: a new material for 1.3 and 1.6 μm integrated-optical components. *Electron. Lett.* **21**, 953–955 (1985)
3. R.A. Soref, B.R. Bennett, Electrooptical effects in silicon. *IEEE J. Quantum Electron.* **23**, 123–129 (1987)
4. R.A. Soref, J. Schmidtchen, K. Petermann, Large single-mode rib wave-guides in GeSi–Si and Si-on-SiO₂. *IEEE J. Quantum Electron.* **27**(8), 1971–1974 (1991)
5. W. Bogaerts, R. Baets, P. Dumon, V. Wiaux, S. Beckx, D. Taillaert, B. Luyssaert, J. Van Campenhout, P. Bienstman, D. Van Thourhout, Nanophotonic waveguides in silicon-on-insulator fabricated with CMOS technology. *J. Lightwave Technol.* **23**(1), 401–412 (2005)
6. S. Selvaraja, P. Jaenen, W. Bogaerts, P. Dumon, D. Van Thourhout, R. Baets, Fabrication of photonic wire and crystal circuits in silicon-on-insulator using 193 nm optical lithography. *J. Lightwave Technol.* **27**(18), 4076–4083 (2009)
7. S. Selvaraja, P. De Heyn, G. Winroth, P. Ong, G. Lepage, C. Cailler, A. Rigny, K. Bourdelle, W. Bogaerts, D. Van Thourhout, J. Van Campenhout, P. Absil, Highly uniform and low-loss passive silicon photonics devices using a 300 mm CMOS platform, in *Opt. Fiber Commun. Conf.*, (OFC'14), San Francisco, CA, USA (2014), Techn. Digest, paper Th2A.33
8. W. Bogaerts, P. Dumon, S.K. Selvaraja, D. Van Thourhout, R. Baets, Silicon nanophotonic waveguide circuits and devices, in *LEOS Annual Meeting*, Newport Beach, CA, USA (2008), paper TuU1
9. P. Dumon, W. Bogaerts, R. Baets, J.-M. Fedeli, L. Fulbert, Towards foundry approach for silicon photonics: silicon photonics platform ePIXfab. *Electron. Lett.* **45**(12), 581–582 (2009)
10. P. Dumon, A. Khanna, Foundry technology and services for Si photonics, in *Proc. 18th OptoElectron. Commun. Conf. and Photonics in Switching (OECC/PS)*, Kyoto, Japan (2013), paper TuN2-3
11. F. Morichetti, A. Canciamilla, C. Ferrari, M. Torregiani, A. Melloni, M. Martinelli, Roughness induced backscattering in optical silicon waveguides. *Phys. Rev. Lett.* **104**(3), 033902 (2010)
12. M.A. Webster, R.M. Pafchek, A. Mitchell, T.L. Koch, Width dependence of inherent TM-mode lateral leakage loss in silicon-on-insulator ridge waveguides. *IEEE Photonics Technol. Lett.* **19**(6), 429–431 (2007)
13. F. Dell'Olio, V.M. Passaro, Optical sensing by optimized silicon slot waveguides. *Opt. Express* **15**(8), 4977–4993 (2007)
14. R. Soref, The past, present, and future of silicon photonics. *IEEE J. Sel. Top. Quantum Electron.* **12**(6), 1678–1687 (2006). doi:[10.1109/JSTQE.2006.883151](https://doi.org/10.1109/JSTQE.2006.883151)
15. M. Muneeb, X. Chen, P. Verheyen, G. Lepage, S. Pathak, E. Ryckeboer, A. Malik, B. Kuyken, M. Nedeljkovic, J. Van Campenhout, G. Mashanovich, G. Roelkens, Demonstration of silicon-on-insulator mid-infrared spectrometers operating at 3.8 μm . *Opt. Express* **21**, 11659–11669 (2013)
16. W. Bogaerts, S. Pathak, A. Ruocco, S. Dwivedi, Silicon photonics non-resonant wavelength filters: comparison between AWGs, echelle gratings, and cascaded Mach-Zehnder filters, in *Integrated Optics: Devices, Materials, and Technologies XIX* (2015). Proc. SPIE, vol. 9365, 93650H
17. C.K. Madsen, J.H. Zhao, *Optical Filter Design and Analysis: A Signal Processing Approach* (Wiley, New York, 1999). ISBN 978-0-471-18373-0
18. K. Yamada, T. Shoji, T. Tsuchizawa, T. Watanabe, J. Takahashi, S. Itabashi, Silicon-wire-based ultrasmall lattice filters with wide free spectral ranges. *Opt. Lett.* **28**, 1663–1664 (2003)
19. F. Horst, W.M.J. Green, S. Assefa, S.M. Shank, Y.A. Vlasov, B.J. Offrein, Cascaded Mach-Zehnder wavelength filters in silicon photonics for low loss and flat pass-band WDM (de-)multiplexing. *Opt. Express* **21**(10), 11652–11658 (2013)

20. A. Rahim, S. Schwarz, J. Bruns, K. Voigt, G. Winzer, L. Zimmermann, C.G. Schaffer, K. Petermann, Silicon photonic implementation of a scalable O-OFDM demultiplexer. *IEEE Photonics Technol. Lett.* **25**(20), 1977–1980 (2013)
21. W. Bogaerts, S.K. Selvaraja, P. Dumon, J. Brouckaert, K. De Vos, D. Van Thourhout, R. Baets, Silicon-on-insulator spectral filters fabricated with CMOS technology. *IEEE J. Sel. Top. Quantum Electron.* **16**(1), 33–44 (2010)
22. S. Pathak, P. Dumon, D. Van Thourhout, W. Bogaerts, Comparison of AWGs and echelle gratings for wavelength division multiplexing on silicon-on-insulator. *IEEE Photonics J.* **6**(5), 4900109 (2014)
23. Q. Fang, T.-Y. Liow, J.F. Song, K.W. Ang, M.B. Yu, G.Q. Lo, D.-L. Kwong, WDM multi-channel silicon photonic receiver with 320 Gbps data transmission capability. *Opt. Express* **18**(5), 5106–5113 (2010)
24. S. Cheung, S. Tiehui, K. Okamoto, S.J.B. Yoo, Ultra-compact silicon photonic 512×512 25 GHz arrayed waveguide grating router. *IEEE J. Sel. Top. Quantum Electron.* **20**(4), 310–316 (2014)
25. S. Pathak, D. Van Thourhout, W. Bogaerts, Design trade-offs for silicon-on-insulator-based AWGs for (de)multiplexer applications. *Opt. Lett.* **38**, 2961–2964 (2013)
26. K. Okamoto, K. Ishida, Fabrication of silicon reflection-type arrayed-waveguide gratings with distributed Bragg reflectors. *Opt. Lett.* **38**, 3530–3533 (2013)
27. K. Okamoto, Wavelength-division multiplexing devices in thin SOI: advances and prospects. *IEEE J. Sel. Top. Quantum Electron.* **20**(4), 248–257 (2014)
28. J. Brouckaert, W. Bogaerts, P. Dumon, D. Van Thourhout, R. Baets, Planar concave grating demultiplexer fabricated on a nanophotonic silicon-on-insulator platform. *J. Lightwave Technol.* **25**(5), 1269–1275 (2007)
29. F. Horst, W.M.J. Green, B.J. Offrein, Y.A. Vlasov, Silicon-on-insulator echelle grating WDM demultiplexers with two stigmatic points. *IEEE Photonics Technol. Lett.* **21**(23), 1743–1745 (2009)
30. J. Brouckaert, W. Bogaerts, S. Selvaraja, P. Dumon, R. Baets, D. Van Thourhout, Planar concave grating demultiplexer with high reflective Bragg reflector facets. *IEEE Photonics Technol. Lett.* **20**(4), 309–311 (2008)
31. P. De Heyn, J. De Coster, P. Verheyen, G. Lepage, M. Pantouvaki, P. Absil, W. Bogaerts, J. Van Campenhout, D. Van Thourhout, Fabrication-tolerant four-channel wavelength-division-multiplexing filter based on collectively tuned Si microrings. *J. Lightwave Technol.* **31**(16), 2785–2792 (2013)
32. S. Park, K. Kim, I. Kim, G. Kim, Si micro-ring MUX/DeMUX WDM filters. *Opt. Express* **19**, 13531–13539 (2011)
33. F. Xia, M. Rooks, L. Sekaric, Y. Vlasov, Ultra-compact high order ring resonator filters using submicron silicon photonic wires for on-chip optical interconnects. *Opt. Express* **15**, 11934–11941 (2007)
34. M. Dahlem, C. Holzwarth, A. Khilo, F. Kärtner, H. Smith, E. Ippen, Reconfigurable multi-channel second-order silicon microring-resonator filterbanks for on-chip WDM systems. *Opt. Express* **19**, 306–316 (2011)
35. A. Mekis, S. Gloeckner, G. Masini, A. Narasimha, T. Pinguet, S. Sahni, P. De Dobbelaere, A grating-coupler-enabled CMOS photonics platform. *IEEE J. Sel. Top. Quantum Electron.* **17**(3), 597–608 (2011)
36. S. Scheerlinck, D. Taillaert, D. Van Thourhout, R. Baets, Flexible metal grating based optical fiber probe for photonic integrated circuits. *Appl. Phys. Lett.* **92**(3), 031104 (2008)
37. R. Halir, P. Cheben, S. Janz, D.-X. Xu, Í. Molina-Fernández, J.G. Wangüemert-Pérez, Waveguide grating coupler with subwavelength microstructures. *Opt. Lett.* **34**(9), 1408–1410 (2009)
38. D. Vermeulen, S. Selvaraja, P. Verheyen, G. Lepage, W. Bogaerts, P. Absil, D. Van Thourhout, G. Roelkens, High-efficiency fiber-to-chip grating couplers realized using an advanced CMOS-compatible silicon-on-insulator platform. *Opt. Express* **18**(17), 18278–18283 (2010)

39. S.K. Selvaraja, D. Vermeulen, M. Schaekers, E. Sleenckx, W. Bogaerts, G. Roelkens, P. Dumon, D. Van Thourhout, R. Baets, Highly efficient grating coupler between optical fiber and silicon photonic circuit, in *Conference on Lasers and Electro-Optics (CLEO) Held in Conjunction with the Quantum Electronics and Laser Science Conference (QELS)* (2009), paper CTuC6
40. F. Van Laere, G. Roelkens, M. Ayre, J. Schrauwen, D. Taillaert, D. Van Thourhout, T.F. Krauss, R. Baets, Compact and highly efficient grating couplers between optical fiber and nanophotonic waveguides. *J. Lightwave Technol.* **25**(1), 151–156 (2007)
41. D. Taillaert, P. Bienstman, R. Baets, Compact efficient broadband grating coupler for silicon-on-insulator waveguides. *Opt. Lett.* **29**(23), 2749–2751 (2004)
42. L. Caroll, D. Gerace, I. Cristiani, S. Menezo, L.C. Andreani, Broad parameter optimization of polarization-diversity 2D grating couplers for silicon photonics. *Opt. Express* **21**(18), 21556–21568 (2013)
43. W. Bogaerts, D. Vermeulen, Off-chip coupling, in *Handbook of Silicon Photonics*, ed. by L. Vivien, L. Pavesi (CRC–Press, Boca Raton, 2013), pp. 97–138
44. S. McNab, N. Moll, Y. Vlasov, Ultra-low loss photonic integrated circuit with membrane-type photonic crystal waveguides. *Opt. Express* **11**(22), 2927–2939 (2003)
45. T. Tsuchizawa, K. Yamada, H. Fukuda, T. Watanabe, J. Takahashi, T. Shoji, E. Tamechika, S. Itabashi, H. Morita, Microphotonics devices based on silicon microfabrication technology. *IEEE Sel. Top. Quantum Electron.* **11**(1), 232–240 (2005)
46. V.R. Almeida, R.R. Panepucci, M. Lipson, Nanotaper for compact mode conversion. *Opt. Lett.* **28**(15), 1302–1304 (2003)
47. G. Roelkens, P. Dumon, W. Bogaerts, D. Van Thourhout, R. Baets, Efficient silicon-on-insulator fiber coupler fabricated using 248-nm-deep UV lithography. *IEEE Photonics Technol. Lett.* **17**(12), 2613–2615 (2005)
48. B. Ben Bakir, A.V. De Gyves, R. Orobtcouk, P. Lyan, C. Porzier, A. Roman, J.M. Fedeli, Low-Loss (<1 dB) and polarization-insensitive edge fiber couplers fabricated on 200-mm silicon-on-insulator wafers. *IEEE Photonics Technol. Lett.* **22**(11), 739–741 (2010)
49. M. Pu, L. Liu, H. Ou, K. Yvind, J.M. Hvam, Ultra-low-loss inverted taper coupler for silicon-on-insulator ridge waveguide. *Opt. Commun.* **283**(19), 3678–3682 (2010)
50. A. Khilo, M.A. Popović, M. Araghchini, F.X. Kärtner, Efficient planar fiber-to-chip coupler based on two-stage adiabatic evolution. *Opt. Express* **18**(15), 15790–15806 (2010)
51. Q. Fang, T.-Y. Liow, J.F. Song, C.W. Tan, M. Bin Yu, G.Q. Lo, D.-L. Kwong, Suspended optical fiber-to-waveguide mode size converter for silicon photonics. *Opt. Express* **18**(8), 7763–7769 (2010)
52. P. Sun, R.M. Reano, Cantilever couplers for intra-chip coupling to silicon photonic integrated circuits. *Opt. Express* **17**(6), 4565–4574 (2009)
53. M. Wood, P. Sun, R. Reano, Compact cantilever couplers for low-loss fiber coupling to silicon photonic integrated circuits. *Opt. Express* **20**(1), 739–741 (2012)
54. N. Hatori, T. Shimizu, M. Okano, M. Ishizaka, T. Yamamoto, Y. Urino, M. Mori, T. Nakamura, Y. Arakawa, A hybrid integrated light source on a silicon platform using a trident spot-size converter. *J. Lightwave Technol.* **32**(7), 1329–1336 (2014)
55. F.E. Doany, B.G. Lee, S. Assefa, W.M.J. Green, M. Yang, C.L. Schow, C.V. Jahnes, S. Zhang, J. Singer, V.I. Kopp, J.A. Kash, Y.A. Vlasov, Multichannel high-bandwidth coupling of ultradense silicon photonic waveguide array to standard-pitch fiber array. *J. Lightwave Technol.* **29**(4), 475–482 (2011)
56. T. Barwicz, Y. Taira, Low-cost interfacing of fibers to nanophotonic waveguides: design for fabrication and assembly tolerances. *IEEE Photonics J.* **6**(4), 6600818 (2014)
57. I.M. Soganci, A. La Porta, B.J. Offrein, Flip-chip optical couplers with scalable I/O count for silicon photonics. *Opt. Express* **21**(13), 16075–16085 (2013)
58. M. Morse, T. Yin, Y. Kang, O. Dosunmu, H.D. Liu, M. Paniccia, G. Sarid, E. Ginsburg, R. Cohen, Y. Saado, R. Shnaiderman, M. Zadka, State of the art Si-based receiver solutions for short reach applications, in *Opt. Fiber Commun. Conf. and Nat. Fiber Opt. Eng. Conf. (OFC/NFOEC'09)*, San Diego, CA, USA (2009), Techn. Digest, paper OMR5

59. J. Michel, J. Liu, L.C. Kimerling, High performance Ge-on-Si photodetectors. *Nat. Photonics* **4**(8), 527–534 (2010)
60. www2.imec.be
61. R. Loo, G. Wang, L. Souriau, J.C. Lin, S. Takeuchi, G. Brammertz, M. Caymax, High quality Ge virtual substrates on Si wafers with standard STI patterning. *J. Electrochem. Soc.* **157**(1), H13–H21 (2010)
62. C.T. DeRose, D.C. Trotter, W.A. Zortman, A.L. Starbuck, M. Fisher, M.R. Watts, P.S. Davids, Ultra compact 45 GHz CMOS compatible Germanium waveguide photodiode with low dark current. *Opt. Express* **19**, 24897–24904 (2011)
63. S. Liao, N.-N. Feng, D. Feng, P. Dong, R. Shafiiha, C.-C. Kung, H. Liang, W. Qian, Y. Liu, J. Fong, J.E. Cunningham, Y. Luo, M. Asghari, 36 GHz submicron silicon waveguide germanium photodetector. *Opt. Express* **19**, 10967–10972 (2011)
64. L. Vivien, A. Polzer, D. Marris-Morini, J. Osmond, J.M. Hartmann, P. Crozat, E. Cassan, C. Kopp, H. Zimmermann, J.-M. Fédéli, Zero-bias 40 Gbit/s germanium waveguide photodetector on silicon. *Opt. Express* **20**, 1096–1101 (2012)
65. G. Li, Y. Luo, X. Zheng, G. Masini, A. Mekis, S. Sahni, H. Thacker, J. Yao, I. Shubin, K. Raj, J.E. Cunningham, A.V. Krishnamoorthy, Improving CMOS-compatible germanium photodetectors. *Opt. Express* **20**, 26345–26350 (2012)
66. P.P. Verheyen, M. Pantouvaki, J. Van Campenhout, P.P. Absil, H. Chen, P. De Heyn, G. Lepage, J. De Coster, P. Dumon, A. Masood, D. Van Thourhout, R. Baets, W. Bogaerts, Highly uniform 25 Gb/s Si photonics platform for high-density, low-power WDM optical interconnects, in *Proc. Adv. Photon. Commun.*, San Diego, CA, USA (2014), paper IW3A.4
67. Y. Zhang, S. Yang, Y. Yang, M. Gould, N. Ophir, A.E.-J. Lim, G.-Q. Lo, P. Magill, K. Bergman, T. Baehr-Jones, M. Hochberg, A high-responsivity photodetector absent metal-germanium direct contact. *Opt. Express* **22**, 11367–11375 (2014)
68. H.-T. Chen, P. Verheyen, P. De Heyn, G. Lepage, J. De Coster, P. Absil, G. Roelkens, J. Van Campenhout, High-responsivity low-voltage 28-Gb/s Ge p-i-n photodetector with silicon contacts. *J. Lightwave Technol.* **33**(4), 820–824 (2015)
69. C.R. Doerr, L. Chen, D. Vermeulen, T. Nielsen, S. Azemati, S. Stulz, G. McBrien, X. Xu, B. Mikkelsen, M. Givehchi, C. Rasmussen, S.Y. Park, Single-chip silicon photonics 100-Gb/s coherent transceiver, in *Opt. Fiber Commun. Conf. (OFC'14)*, San Francisco, CA, USA (2014), Techn. Digest, PDP Th5C.1
70. M. Rakowski, M. Pantouvaki, P. De Heyn, P. Verheyen, M. Ingels, H.-T. Chen, J. De Coster, G. Lepage, B. Snyder, K. De Meyer, M. Steyaert, N. Pavarelli, J.S. Lee, P. O'Brien, P. Absil, J. Van Campenhout, 22.5 a 4 × 20 Gb/s WDM ring-based hybrid CMOS silicon photonics transceiver, in *Proc. IEEE Internat. Solid-State Circ. Conf. (ISSCC)*, San Francisco, CA, USA (2015), pp. 408–409
71. S. Ghosh, S. Keyvaninia, W. Van Roy, T. Mizumoto, G. Roelkens, R. Baets, A Ce:YIG/silicon-on-insulator waveguide optical isolator realized by adhesive bonding. *Opt. Express* **20**(2), 1839–1848 (2012)
72. M.-C. Tien, T. Mizumoto, P. Pintus, H. Kroemer, J.E. Bowers, Silicon ring isolators with bonded nonreciprocal magneto-optic garnets. *Opt. Express* **19**(12), 11740–11745 (2011)
73. Y. Shoji, T. Mizumoto, H. Yokoi, I.-W. Hsieh, R.M. Osgood, Magneto-optical isolator with silicon waveguides fabricated by direct bonding. *Appl. Phys. Lett.* **92**(7), 071117 (2008)
74. Y. Shoji, M. Ito, Y. Shirato, T. Mizumoto, MZI optical isolator with Si-wire waveguides by surface-activated direct bonding. *Opt. Express* **20**(16), 18440–18448 (2012)
75. L. Bi, J. Hu, P. Jiang, D.H. Kim, G.F. Dionne, L.C. Kimerling, C.A. Ross, On-chip optical isolation in monolithically integrated non-reciprocal optical resonators. *Nat. Photonics* **5**, 758–762 (2011)
76. C. Doerr, L. Chen, D. Vermeulen, Silicon photonics broadband modulation-based isolator. *Opt. Express* **22**(4), 4493–4498 (2014)
77. Z. Yu, S. Fan, Complete optical isolation created by indirect interband photonic transitions. *Nat. Photonics* **3**, 91–94 (2009)

78. C. Galland, R. Ding, N. Harris, T. Baehr-Jones, M. Hochberg, Broadband on-chip optical non-reciprocity using phase modulators. *Opt. Express* **21**(12), 14500–14511 (2013)
79. B. Peng, S. Ozdemir, F. Lei, F. Monifi, M. Gianfreda, G. Long, S. Fan, F. Nori, C. Bender, L. Yang, Parity-time-symmetric whispering-gallery microcavities. *Nat. Phys.* **10**, 394–398 (2014)
80. G.P. Agrawal, *Nonlinear Fiber Optics*, 3rd edn. (Academic Press, San Diego, 2001)
81. R.M. Osgood Jr., N.C. Panou, J.I. Dadap, X. Liu, X. Chen, I.-W. Hsieh, E. Dulkeith, W.M. Green, Y.A. Vlasov, Engineering nonlinearities in nanoscale optical systems: physics and applications in dispersion-engineered silicon nanophotonic wires. *Adv. Opt. Photonics* **1**(1), 162–235 (2009)
82. D.T.H. Tan, K. Ikeda, P.C. Sun, Y. Fainman, Group velocity dispersion and self phase modulation in silicon nitride waveguides. *Appl. Phys. Lett.* **96**(6), 061101 (2010)
83. D.J. Moss, R. Morandotti, A.L. Gaeta, M. Lipson, New CMOS-compatible platforms based on silicon nitride and Hydex for nonlinear optics. *Nat. Photonics* **7**, 597–607 (2013)
84. M.A. Foster, A.C. Turner, R. Salem, M. Lipson, A.L. Gaeta, Broad-band continuous-wave parametric wavelength conversion in silicon nanowaveguides. *Opt. Express* **15**, 12949–12958 (2007)
85. A. Gajda, L. Zimmermann, M. Jazayerifar, G. Winzer, H. Tian, R. Elschner, T. Richter, C. Schubert, B. Tillack, K. Petermann, Highly efficient CW parametric conversion at 1550 nm in SOI waveguides by reverse biased p–i–n junction. *Opt. Express* **20**, 13100–13107 (2012)
86. A.C. Turner-Foster, M.A. Foster, J.S. Levy, C.B. Poitras, R. Salem, A.L. Gaeta, M. Lipson, Ultrashort free-carrier lifetime in low-loss silicon nanowaveguides. *Opt. Express* **18**, 3582–3591 (2010)
87. M.A. Foster, A.C. Turner, J.E. Sharping, B.S. Schmidt, M. Lipson, A.L. Gaeta, Broad-band optical parametric gain on a silicon photonic chip. *Nature* **441**, 960–963 (2006)
88. R. Slavík, F. Parmigiani, J. Kakande, C. Lundström, M. Sjödin, P.A. Andrekson, R. Weerasuriya, S. Sygletos, A.D. Ellis, L. Grüner-Nielsen, D. Jakobsen, S. Herstrom, R. Phelan, J. O’Gorman, A. Bogris, D. Syvridis, S. Dasgupta, P. Petropoulos, D.J. Richardson, All-optical phase and amplitude regenerator for next-generation telecommunications systems. *Nat. Photonics* **4**, 690–695 (2010)
89. F.D. Ros, D. Vukovic, A. Gajda, K. Dalgaard, L. Zimmermann, B. Tillack, M. Galili, K. Petermann, C. Peucheret, Phase regeneration of DPSK signals in a silicon waveguide with reverse-biased p–i–n junction. *Opt. Express* **22**, 5029–5036 (2014)
90. Y. Zhang, C. Husko, J. Schröder, S. Lefrancois, I. Rey, T. Krauss, B.J. Eggleton, Record 11 dB phase sensitive amplification in sub-millimeter silicon waveguides, in *Conf. Lasers Electro-Opt. Pacific Rim (CLEO-PR)*, Kyoto, Japan (2013), Techn. Digest, paper PD1b-3
91. S. Clemmen, K. Phan Huy, W. Bogaerts, R.G. Baets, Ph. Emplit, S. Massar, Continuous wave photon pair generation in silicon-on-insulator waveguides and ring resonators. *Opt. Express* **17**(19), 16558–16570 (2009)
92. L.K. Oxenløwe, H. Ji, M. Galili, M. Pu, H. Hu, H.C.H. Mulvad, K. Yvind, J.M. Hvam, A. Clausen, P. Jeppesen, Silicon photonics for signal processing of Tbit/s serial data signals. *IEEE J. Sel. Top. Quantum Electron.* **18**(2), 996–1005 (2012)
93. F. Li, M. Pelusi, D.X. Xu, A. Densmore, R. Ma, S. Janz, D.J. Moss, Error-free all-optical demultiplexing at 160Gb/s via FWM in a silicon nanowire. *Opt. Express* **18**, 3905–3910 (2010)
94. D.J. Moss, R. Morandotti, A.L. Gaeta, M. Lipson, New CMOS-compatible platforms based on silicon nitride and Hydex for nonlinear optics. *Nat. Photonics* **7**, 597–607 (2013)
95. H. Jung, C. Xiong, K.Y. Fong, X. Zhang, H.X. Tang, Optical frequency comb generation from aluminum nitride microring resonator. *Opt. Lett.* **38**, 2810–2813 (2013)
96. B. Kuyken, S. Clemmen, S.K. Selvaraja, W. Bogaerts, D. Van Thourhout, P. Emplit, S. Massar, G. Roelkens, R. Baets, On-chip parametric amplification with 26.5 dB gain at telecommunication wavelengths using CMOS-compatible hydrogenated amorphous silicon waveguides. *Opt. Lett.* **36**(4), 552–554 (2011)

97. K. Narayanan, S.F. Preble, Optical nonlinearities in hydrogenated-amorphous silicon waveguides. *Opt. Express* **18**(9), 8998–9005 (2010)
98. Y. Shoji, T. Ogasawara, T. Kamei, Y. Sakakibara, S. Suda, K. Kintaka, H. Kawashima, M. Okano, T. Hasama, H. Ishikawa, M. Mori, Ultrafast nonlinear effects in hydrogenated amorphous silicon wire waveguide. *Opt. Express* **18**(6), 5668–5673 (2010)
99. K.-Y. Wang, A.C. Foster, Ultralow power continuous-wave frequency conversion in hydrogenated amorphous silicon waveguides. *Opt. Lett.* **37**(8), 1331–1333 (2012)
100. A. Gondarenko, J.S. Levy, M. Lipson, High confinement micron-scale silicon nitride high Q ring resonator. *Opt. Express* **17**(14), 11366–11370 (2009)
101. J.S. Levy, A. Gondarenko, M.A. Foster, A.C. Turner-Foster, A.L. Gaeta, M. Lipson, CMOS-compatible multiple wavelength oscillator for on-chip optical interconnects. *Nat. Photonics* **4**(1), 37–40 (2010)
102. Y. Okawachi, K. Saha, J.S. Levy, Y.H. Wen, M. Lipson, A.L. Gaeta, Octave-spanning frequency comb generation in a silicon nitride chip. *Opt. Lett.* **36**(17), 3398–3400 (2011)
103. R.S. Jacobsen, K.N. Andersen, P.I. Borel, J. Fage-Pedersen, L.H. Frandsen, O. Hansen, M. Kristensen, A.V. Lavrinenko, G. Moulin, H. Ou, C. Peucheret, B. Zsigri, A. Bjarklev, Strained silicon as a new electro-optic material. *Nature* **411**, 199–202 (2006)
104. W. Bogaerts, M. Fiers, P. Dumon, Design challenges in silicon photonics. *IEEE J. Sel. Top. Quantum Electron.* **20**(4), 8202008 (2014)
105. S.K. Selvaraja, W. Bogaerts, P. Dumon, D. Van Thourhout, R. Baets, Subnanometer linewidth uniformity in silicon nanophotonic waveguide devices using CMOS fabrication technology. *IEEE J. Sel. Topics Quantum Electron.* **16**(1), 316–324 (2010)
106. C. Arellano, S. Mingaleev, I. Koltchanov, A. Richter, J. Pomplun, S. Burger, F. Schmidt, Efficient design of photonic integrated circuits (PICS) by combining device-and circuit-level simulation tools. *Proc. SPIE* **8627**, 862711 (2013)
107. L. Chrostowski, M. Hochberg, *Silicon Photonics Design* (Cambridge University Press, Cambridge, 2015)
108. L.-T. Wang, Y.-W. Chang, K.-T.T. Cheng, *Electronic Design Automation: Synthesis, Verification, and Test* (Morgan Kaufmann, San Mateo, 2009)
109. D. Melati, F. Morichetti, A. Canciamilla, D. Roncelli, F. Soares, A. Bakker, A. Melloni, Validation of the building-block-based approach for the design of photonic integrated circuits. *J. Lightwave Technol.* **30**(23), 3610–3616 (2012)
110. M. Fiers, T. Van Vaerenbergh, K. Caluwaerts, D. Vande Ginste, B. Schrauwen, J. Dambre, P. Bienstman, Time-domain and frequency-domain modeling of nonlinear optical components at the circuit-level using a node-based approach. *J. Opt. Soc. Am. B* **29**(5), 896–900 (2012)
111. C. Arellano, S. Mingaleev, E. Sokolov, I. Koltchanov, A. Richter, Time-and-frequency-domain modeling (TFDM) of hybrid photonic integrated circuits. *Proc. SPIE* **8265**, 82650K (2012)
112. P. Gunupudi, T. Smy, J. Klein, Z. Jakubczyk, Self-consistent simulation of opto-electronic circuits using a modified nodal analysis formulation. *IEEE Trans. Adv. Packaging* **33**(4), 979–993 (2010)
113. T. Weng, Z. Zhang, Z. Su, Y. Marzouk, A. Melloni, L. Daniel, Uncertainty quantification of silicon photonic devices with correlated and non-Gaussian random parameters. *Opt. Express* **23**(4), 4242–4254 (2015)
114. M. Fiers, E. Lambert, S. Pathak, P. Dumon, B. Maes, P. Bienstman, W. Bogaerts, Improving the design cycle for nanophotonic components. *J. Comput. Sci.* **4**(5), 313–324 (2013)
115. W. Bogaerts, P. Dumon, D. Taillaert, V. Wiaux, S. Beckx, B. Luyssaert, J. Van Campenhout, D. Van Thourhout, R. Baets, SOI nanophotonic waveguide structures fabricated with deep UV lithography. *Photonics Nanostruct. Fundam. Appl.* **2**(2), 81–86 (2004)
116. X. Wang, W. Shi, M. Hochberg, K. Adam, E. Schelew, J.F. Young, N.A.F. Jaeger, L. Chrostowski, Lithography simulation for the fabrication of silicon photonic devices with deep-ultraviolet lithography, in *9th IEEE Conf. Group IV Photonics*, San Diego, CA, USA (2012), paper ThP17

117. E. Kleijn, M. Smit, X. Leijtens, Analysis of parasitic effects in PICs using circuit simulation. *Proc. SPIE* **8781**, 878104 (2013)
118. A. Mekis, S. Abdalla, D. Foltz, S. Gloeckner, S. Hovey, S. Jackson, Y. Liang, M. Mack, G. Masini, M. Peterson, T. Pinguet, S. Sahni, M. Sharp, P. Sun, D. Tan, L. Verslegers, B.P. Welch, K. Yokoyama, S. Yu, P.M. De Dobbelaere, A CMOS photonics platform for high-speed optical interconnects, in *IEEE Photon. Conf (IPC)*, San Francisco, CA, USA (2012), pp. 356–357
119. J. Pond, C. Cone, L. Chrostowski, J. Klein, J. Flueckiger, A. Liu, D. McGuire, X. Wang, A complete design flow for silicon photonics. *SPIE Photonics Eur.* **9133**, 913310 (2014)

Roel Baets is full professor at Ghent University (UGent). He is also associated with IMEC. He received an M.Sc. degree in Electrical Engineering from Ghent University in 1980 and a second M.Sc. degree from Stanford University in 1981. He received a Ph.D. degree from Ghent University in 1984. From 1984 till 1989 he held a postdoctoral position at IMEC (with detachment to Ghent University). Since 1989 he has been a professor in the Faculty of Engineering and Architecture at UGent where he founded the Photonics Research Group. From 1990 till 1994 he has also been a part-time professor at the Delft University of Technology and from 2004 till 2008 at the Eindhoven University of Technology. Roel Baets has mainly worked in the field of integrated photonic components. He has made contributions to research on semiconductor laser diodes, guided wave and grating devices and to the design and fabrication of photonic ICs, both in III–V semiconductors and in silicon. His current interests include silicon and silicon nitride based photonic ICs for life science applications. Roel Baets is also director of the multidisciplinary Center for Nano- and Biophotonics (NB Photonics) at UGent, founded in 2010. Roel Baets was co-founder of the interuniversity UGent-VUB M.Sc. programme in Photonics and of the international Erasmus Mundus M.Sc. programme in Photonics. Roel Baets is a grant holder of the Methusalem programme of the Flemish government and of the European Research Council (ERC advanced grant). He is a Fellow of the IEEE and a member of the Royal Flemish Academy of Sciences of Belgium.

Wim Bogaerts is professor in the Photonics Research Group at Ghent University – imec. He received his Ph.D. in the modeling, design and fabrication of silicon nanophotonic components at Ghent University in 2004. During this work, he started the first silicon photonics process on imec’s 200 mm pilot line, which formed the basis of the multi-project-wafer service ePIXfab. Wim’s current research focuses on the design challenges for silicon photonics: large-scale integration, circuit complexity, tolerances, parasitics and multiphysics, and their use in reconfigurable photonic circuits. In June 2014, Wim co-founded Luceda Photonics, a spin-off company of Ghent University, IMEC and the University of Brussels (VUB). Luceda Photonics develops unique software solutions for silicon photonics design, using the IPKISS design framework. Wim has a strong interest in telecommunications, information technology and applied sciences. He is a member of IEEE, Optical Society of America (OSA) and SPIE.

Bart Kuyken received the B.S. degree in electrical engineering and physics in 2006 and 2008 from Ghent University where he also obtained the M.Sc. degree in electrical engineering in 2008. He received an additional M.Sc. degree from Stanford University in 2009. In 2013, he received a Ph.D. degree from Ghent University at the Department of Information Technology. He has been a visiting scientist at the IBM TJ Watson Research Center (US) in 2011 and at the Max Planck Institut for Quantum Optics (D) in 2013 and 2015. He is currently working as a postdoctoral fellow in the Photonics Research Group at Ghent University. His current research interests include the integration of nonlinear optical function in silicon photonics waveguides exploiting its high Kerr nonlinearity.

Abdul Rahim is a postdoctoral researcher at the Photonics Research Group of Ghent University. He received his Bachelors degree in Electrical Engineering from University of Engineering and Technology (Lahore) and Erasmus Mundus joint Masters degree in Electrical Engineering with emphasis on Photonics from Royal Institute of Technology (Sweden) and Ghent University (Belgium). He worked on the topic of micro-photon filters for residual dispersion compensation to

receive a Ph.D. degree from Technische Universitaet Berlin (Germany). His research interests include Silicon Photonics and its large scale integration for optical communication applications.

Gunther Roelkens received the Ph.D. degree in Photonics from Ghent University in 2007. Currently he is a tenure track professor in the Photonics Research Group and an assistant professor at the Eindhoven University of Technology, working on the realization of complex active/passive photonic integrated circuits for communication and sensing applications. He was a visiting scientist at the IBM TJ Watson research center in New York. He is currently coordinating the activities of a group of 25 people, has published about 400 papers in international conferences and journals, of which about 125 A1 papers. He won the Andreas de Leenheer award for his Ph.D. research. He has been involved in 4 FP7 European research projects. In the last 5 years he has delivered about 15 invited lectures on various international meetings. His research interests include the heterogeneous integration of III–V semiconductors on top of silicon-on-insulator waveguide circuits and the realization of highly integrated transceivers on the silicon waveguide platform. He holds a European Research Council starting grant on the exploration of mid-IR photonic integrated circuits for life sciences and environment.

Thijs Spuesens received the M.Sc. degree in electrical engineering from Eindhoven University of Technology, Eindhoven, The Netherlands, in 2008. Later that year he joined the Photonics Research Group at INTEC, Ghent University, Ghent, Belgium, where he received a Ph.D. degree in Photonics in 2014. For his Ph.D. he worked on the realization of compact on chip optical interconnects by heterogeneous integration of III–V on silicon. He has been involved in European projects FP7 WADIMOS and FP7 HISTORIC. Currently he is working as a postdoctoral researcher in the Photonics Research Group. His current research interests are in the field of Silicon Photonics platform development and integrated Laser Doppler Vibrometry.

Joris Van Campenhout is program director of the Optical I/O industry-affiliation program at imec (Belgium), which targets the development of a scalable and industrially viable short-reach optical interconnect technology based on silicon photonics. Prior to joining imec in 2010, he was a post-doctoral researcher at IBM's TJ Watson Research Center (USA), where he developed silicon electro-optic switches for chip-level reconfigurable optical networks. He obtained a Ph.D. degree in Electrical Engineering from Ghent University (Belgium) in 2007, for his work on hybrid integration of electrically driven III–V microdisk lasers on silicon photonic waveguide circuits. Joris received the IEEE Photonics Society Graduate Student Fellowship (USA) in 2007 and the Scientific Prize Alcatel Lucent Bell (Belgium) in 2008. He holds 3 patents and has authored or co-authored over 100 papers in the field of silicon integrated photonics.

Dries Van Thourhout received the M.Sc. degree in engineering physics and the Ph.D. degree from Ghent University, Ghent, Belgium in 1995 and 2000 respectively. From Oct. 2000 to Sep. 2002 he was with Lucent Technologies, Bell Laboratories, New Jersey, USA, working on the design, processing and characterization of InP/InGaAsP monolithically integrated devices. In Oct. 2002 he joined the Department of Information Technology, Ghent University, Belgium. Since 2008 he has a position as full time research professor focusing on the design, fabrication and characterization of integrated photonic devices. Main topics involve Silicon nanophotonic devices and the integration of novel materials (III–V, graphene, ferro-electrics, quantum dots, . . .) on these waveguides to expand their functionality. He is working on applications for telecom, diatom, optical interconnect and sensing. He has submitted 14 patents, has authored and coauthored over 180 journal papers and has presented invited papers at all major conferences in the domain. He is member of IEEE Photonics Society and has been associate editor for IEEE Photonics Technology Letters. He has coordinated several European Projects (FP6 PICMOS, FP7 WADIMOS, FP7 SMARTFIBER), contributed in many more and is holder of an ERC Grant (ULPPIC). He received the prestigious "Laureaat van de Vlaamse Academie Van België" prize in 2012.

Chapter 15

Silicon Lasers and Photonic Integrated Circuits

Sudharsanan Srinivasan, Alan Y. Liu, Di Liang, and John E. Bowers

Abstract This chapter discusses photonic integration on silicon from the material property, device as well as photonic circuit point of view. The progressive growth of silicon-based electronic integrated circuits (ICs) has followed Moore's Law and has been driven by the roadmap of conventional electronic ICs. Silicon is arguably the primary host material platform for future photonic integrated circuits (PICs) as well, particularly for applications beyond conventional fiber-optical telecommunications. Until recently, the lack of a laser source on silicon has been seen as the key hurdle limiting the usefulness and complexity of silicon photonic integrated circuits. In this chapter, we review the numerous efforts including bandgap engineering, Raman scattering, monolithic heteroepitaxy and hybrid integration to realize efficient light emission, amplification and lasing on silicon. The state-of-the-art integration technologies for narrow linewidth lasers and high-speed modulators are also discussed.

15.1 Silicon as a Platform for PICs

An integrated circuit (IC) is a miniaturized electronic circuit that consists of a large number of individual components, fabricated side-by-side on a common substrate

S. Srinivasan (✉)

Aurion Inc., 6868, Cortona Drive, Suite C, Goleta, CA 93117, USA
e-mail: sudha.srinivasan@aurion.com

A. Y. Liu

Materials Department, University of California, Santa Barbara, CA 93106, USA
e-mail: Alanyoungliu@gmail.com

D. Liang

Hewlett Packard Labs in Hewlett Packard Enterprise (HPE), 1501 Page Mill Road, MS 1123, Palo Alto, CA 94304, USA
e-mail: di.liang@hp.com

J.E. Bowers

Electrical and Computer Engineering Department, University of California, Santa Barbara, CA 93106, USA
e-mail: bowers@ece.ucsb.edu

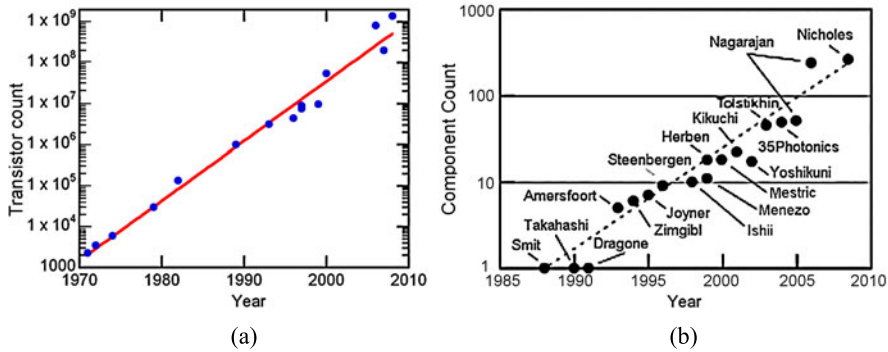


Fig. 15.1 (a) Electronic [1] and (b) Photonic integrated circuit evolution [5, 7]

and wired together to perform a particular task. In 1943, the first working transistor was demonstrated [1], and eleven years later, the invention of the IC began a new era. The inherent advantages in *cost and performance* have been the driving force in the IC industry since then. Moore's Law has set the progressive pace in these advances. Gordon Moore foresaw exponential growth, with the number of transistors on an IC doubling approximately every two years [2], as illustrated in Fig. 15.1(a). Large-scale integration and mass production also resulted in the enormous reduction of the chip size and system cost and tremendous improvement in performance and applications. The first UNIVAC computer in 1951 weighed 13 metric tons and occupied more than 35 m² of floor space with a clock speed of 2.25 MHz [3]. Sixty-five years later, a personal computer now easily delivers 1000× faster speed and is small and light enough to fit into a shirt pocket. Moore's Law was actually the fifth paradigm to provide accelerating price-performance [4]. The exponential technology advance in computing devices (computing speed per unit cost) has existed for the entire past century. Integration is the leading driver in the semiconductor world in the 20th and 21st centuries, both technologically and economically.

While the term IC generally refers to microelectronics, the analogous term photonic integrated circuit (PIC), also sometimes referred to as planar lightwave circuits, offers functionality of information signals imposed on an optical carrier ranging from the ultraviolet to near infrared. Though the growth of PICs can also be depicted and predicted by a photonic "Moore's Law" [5, 6], several figures of merit including critical dimensions, integration scale, complexity of function, and cost per unit component show that present PICs are many generations behind electronic ICs. PICs appeared much later than ICs and have grown more slowly (Fig. 15.1(b)). The reasons that PIC integration advances have occurred more slowly are partially market based, partially technology based, and partially the result of the choice of host material. Most telecom devices are based on Indium Phosphide (InP) substrates, which have required custom fabrication lines dedicated to InP photonics.

The first transistor and one of the first two ICs were demonstrated on germanium (Ge), but silicon (Si) quickly became the dominant host material for electronic ICs. Si is the second most abundant element on earth, but more importantly, Si has out-

performed Ge and even many compound semiconductors from the early stage of IC development due to large bandgap and thermal conductivity, stable and high crystal quality/purity, excellent mechanical properties and an ideal native oxide, SiO_2 . Unlike Si-dominated electronic ICs, PICs have been fabricated in a variety of host material systems, including element semiconductors (Si- and Ge-related), compound semiconductors (InP- and Gallium Arsenide (GaAs)-based), dielectrics (SiO_2 and SiN_x -related), polymers and crystalline materials (e.g. LiNbO_3). The material properties of different material systems place them into desirable but discrete functionality regimes. For example, InP and GaAs are flagship materials for light sources, while silica- and Si-based waveguides exhibit more than an order of magnitude lower propagation loss than III–V counterparts with the same dimensions.

Material incompatibility between different material systems has been the largest barrier to singling out a unitary host material for large-scale PICs. Analogous to a long-term debate in electronic ICs about whether to integrate high-performance electronics on Si, InP or GaAs, the same question surfaced lately in the PIC community. This debate did not shake the dominance of Si in electronic ICs, though several successful compound semiconductor-based IC chip companies, such as Vitesse, RF Micro Devices, Skywork solutions, and Broadcom, etc., were successful in target markets. The success of Si-based electronic ICs proves the wisdom in determination of a primary host material, which is reflected by the International Technology Roadmap for Semiconductors (ITRS) [8]. The solidification of silicon's role resulted in rational technology development and deployment, drastically reducing the uncertainties in investments, critical research directions and resource allocations. The past half-century technology revolution in design tools, circuit architecture, substrate manufacturing and epitaxy, device processing, packaging, testing and quality control led to the present Si IC industry with about 200 billion U.S. dollars in revenue per year [9]. The annual research and development investment in electronic ICs, particularly in device innovation, is about \$45 billion/year. This level of R&D spending is unaffordable for the PIC industry due to a much smaller volume and revenue.

It is therefore important to determine the primary host material for PICs. InP-based compound semiconductors and Si compete for the mainstream adoption as the host material for future PICs. A 40 Gb/s InP-based single-chip all-photonic transceiver has been demonstrated [10]. It includes a high-gain, high-saturation power semiconductor optical amplifier-uni-traveling receiver and a widely tunable transmitter that combines a sampled grating distributed Bragg reflector (DBR) laser with an electroabsorption modulator (EAM) [10, 11]. The first InP monolithic tunable optical router with error-free 40 Gb/s operation per port was demonstrated successfully by Nicholes et al. [7]. The device has eight wavelength converters and an 8×8 arrayed-waveguide grating router (see Sect. 9.6), yielding more than 200 on-chip functional elements. InP chip maker Infinera has introduced two new PICs: the sliceable ePIC-500 (supports a 500 Gb/s super-channel) and the application-optimized oPIC-100 (supports one wavelength channel at 100 Gb/s), for terabit scale metro and regional DWDM networks. This new coherent PIC technology integrates over 600 optical functions into just two optical chips. Infinera also sees a technology pathway that will allow their future PICs to scale and support 2 Tb/s, 4 Tb/s and

even greater capacity per line card in the future. Luxtera, now acquired by Molex, is an industry leader in complementary metal oxide semiconductor (CMOS) photonics and have developed a four channel 25 Gb/s product for the 100 Gb/s Ethernet and InfiniBand markets. PICs are presently moving forward on parallel Si and III–V platforms, but the future requirement for higher capacity, lower power on-chip and off-chip *optical* interconnects in microprocessors may tilt the balance. Larger bandwidth, lower power consumption (i.e., lower heat dissipation), smaller interconnect delays, and better resistance to electromagnetic interference are attractive advantages over the conventional Cu and Al electrical interconnects [12]. By leveraging the mature CMOS technology along with low-cost and high-quality Si substrates, redundant investments in money and time for fundamental research, infrastructure, and business model development can be largely reduced. With the compensation and assistance of mature electronic ICs, Si PICs are able to tolerate more error, lowering the design and fabrication criteria. Furthermore, the potentially enormous volume of optical interconnects (on-chip, inter-chip, rack-to-rack) is several orders of magnitude larger than the sum of conventional PIC markets. Exciting results in CMOS optical components, such as continuous-wave (cw) Si Raman lasers, modulators, detectors, optical buffers and switches, have been demonstrated in succession in university and industrial labs in the past few years. The basic operation principles of key devices for transmitters are discussed in the following sections, starting from a major question still being investigated: how to deploy a high-performance electrically-driven cw light source on Si?

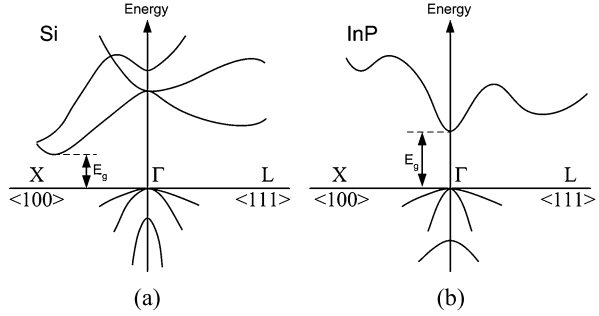
15.2 Lasers (Emitters) and Amplifiers on Silicon

As discussed in Sect. 15.1, GaAs- and InP-based III–V materials have been dominant candidates for semiconductor light emitting devices for nearly half a century. Si has not been widely used because it has an indirect bandgap, and hence is a poor light emitting material. The band structure for Si is shown in Fig. 15.2(a) where it can be seen that free electrons tend to reside at the X valley, which is the lowest point in the conduction band. However, the X valley doesn't align with the peak of the valence band where holes find their lowest energy to stay. This momentum mismatch determines that free electrons have to bridge to the Γ valley through phonons in order to recombine with holes in the valence band *radiatively*. This transition has a low probability, resulting in a long radiative lifetime of \sim milliseconds. Meanwhile, these free carriers (electrons and holes) can recombine *nonradiatively*, resulting in extremely poor internal quantum efficiency η_i of light emission in Si, which is in the order of 10^{-6} and is defined as [13]

$$\eta_i = \frac{\tau_{nonrad}}{\tau_{nonrad} + \tau_{rad}} \quad (15.1)$$

where τ_{nonrad} and τ_{rad} are recombination lifetimes for nonradiative and radiative processes, respectively.

Fig. 15.2 Energy band diagrams of (a) Si and (b) InP at 300 K



The band diagram of InP is shown in Fig. 15.2(b), and has a direct bandgap, which means electrons and holes can recombine radiatively with high efficiency ($\eta_i \sim 1$).

A major source of nonradiative recombination in processed Si is trap recombination. Another major nonradiative process is Auger recombination where an electron (or hole) is excited to a higher energy level by absorbing the released energy from an electron-hole recombination. The Auger recombination rate R increases with injected free carrier density ΔN and is inversely proportional to the bandgap. Since the Auger recombination is a three-particle process, the Auger recombination rate for high-level carrier injection with $\Delta N \approx \Delta P$ is proportional to ΔN^3

$$\tau_a = N/R = N/C_a \Delta N^3 \approx 1/C_a \Delta N^2 \quad (15.2)$$

where C_a is the ambipolar Auger coefficient around $10^{-30} \text{ cm}^6/\text{s}$ [14]. It is the dominant recombination mechanism for high-level carrier injection ($\Delta N \sim 10^{19} \text{ cm}^{-3}$) in Si.

Free carrier absorption represents another hurdle to realizing lasing in Si. The free electrons in the conduction band can jump to higher energy levels by absorbing photons. This process leads to higher optical loss as governed by (15.3) [15],

$$\alpha_f = \frac{q^3 \lambda_0^2}{4\pi^2 c^3 n \varepsilon_0} \left(\frac{N_e}{m_{ce}^{*2} \mu_e} + \frac{N_h}{m_{ch}^{*2} \mu_h} \right) \quad (15.3)$$

where q is the electronic charge, λ_0 is the vacuum wavelength, n is the refractive index of Si, ε_0 is the permittivity of free space, $N_e(N_h)$ is the free electron (hole) concentration, and $\mu_e(\mu_h)$ is the electron (hole) mobility. In high-level carrier injection devices (e.g. lasers and amplifiers) or heavily-doped situations, free carrier loss is orders of magnitudes higher than the material gain [15]. It explains why intrinsic or lightly-doped Si is used as low-loss waveguide material, but excessively high free carrier absorption stands as another major limitation for achieving lasing in heavily doped cases.

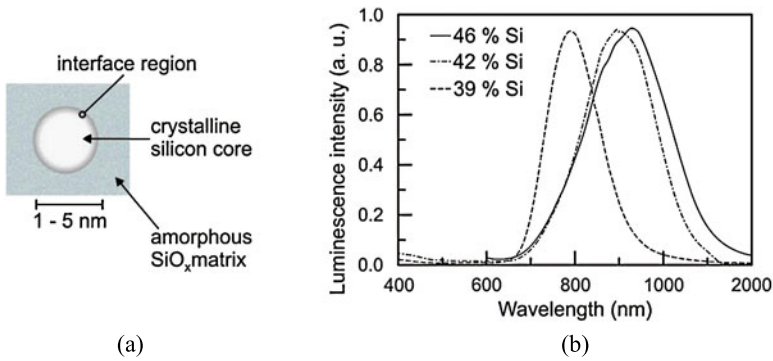


Fig. 15.3 (a) TEM cross-section of a typical Si-nc embedded in the SiO_x dielectric. (Courtesy Lorenzo Pavesi, University of Trento, Italy.) (b) Luminescence spectrum of Si-nc in dielectric [16]

15.2.1 Low-Dimensional Silicon Approaches

Recently, a number of groups have reported enhanced light-emitting efficiency in low-dimensional (i.e. in the order of the de Broglie wavelength) Si including porous Si [17–20], Si nanocrystals [21, 22], SOI superlattices [23], and Si nano-pillars [24, 25]. The motivation is to achieve the quantum confinement of excitons in a nanometer-scale crystalline structure [22]. In the meantime, the spatial localization of carriers by dielectrics also decreases the probability of nonradiative recombination with defects or trap centers, i.e. increases nonradiative recombination lifetime τ_{nonrad} and subsequently internal quantum efficiency η_i , and form radiative states [26].

For the first time Pavesi et al. reported the observation of optical net gain and modal gain in Si nanoclusters (Si-nc) dispersed in a silica matrix [27]. The Si-nc can be formed by introducing Si nanoparticles into ultra-pure quartz, thermal SiO_2 or plasma-enhanced chemical vapor deposition (PECVD) SiO_2 , etc. by deposition, sputtering, ion implantation, cluster evaporation, etc. The excess Si (excess with respect to the SiO_2 stoichiometric quantity) clusterizes after a thermal annealing process ($\sim 1100^\circ\text{C}$) which leads to phase separation. The thermal process and the starting excess Si content determine the final sizes of the clusters and the Si-nc crystalline nature. As shown in Fig. 15.3(a), the Si-nc embedded in an amorphous SiO_x matrix have a core-shell structure with a crystalline Si core (1–5 nm) and a thin (~ 0.5 nm) transition layer of a suboxide (Si-nc interface) [28]. Figure 15.3(b) shows luminescence spectra of Si-nc for various Si concentrations [16]. As can be seen the emission shifts to shorter wavelengths with decreasing Si concentration which goes along with a smaller mean Si-nc radius. Furthermore, the width of the luminescence bands gets narrower and the luminescence intensity increases as the Si-nc size decreases [16]. It is believed that the luminescence comes from confined exciton recombination in the Si-nc at around 800 nm [29] and radiative interface states around 700 nm [30]. The luminescence spectral broadening is intrinsic in nature [27].

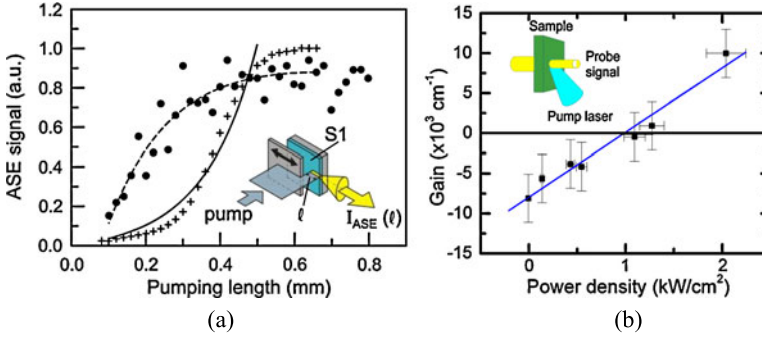


Fig. 15.4 ASE vs. pumping length of Si-nc for pump powers of 10 W/cm^2 [16] and 1 kW/cm^2 [31]. (a) Corresponding modal gain at 800 nm : $g = -20 \text{ cm}^{-1}$ and $g = 100 \text{ cm}^{-1}$, respectively, (b) dependence of material gain on pump power density geometry. Insets: (a) Schematic of variable stripe length (VSL) method and (b) pump-probe measurement geometry (Courtesy Lorenzo Pavesi, University of Trento, Italy)

The optical gain from Si-nc formed by many different techniques was measured by the variable stripe length method (VSL) [16] and the pump-probe technique [31], as shown schematically in Figs. 15.4(a), inset and (b), inset, respectively. VSL measures the amplified spontaneous emission (ASE) signal coming out of an edge of a waveguide with a Si-nc-rich core. Figure 15.4(a) shows the ASE signal intensity I_{ASE} vs. pump length l for Si-nc formed by PECVD. The ASE signal intensity increases sublinearly with the pumping length when the pump power ($\lambda = 390 \text{ nm}$) is lower than threshold. But when the pump power is above this threshold and net modal gain becomes positive, the ASE signal increases more than exponentially, which can be fitted with [27]:

$$I_{ASE}(l) = \frac{I_{sp}(\theta) \cdot l}{g_{mod}} (g_{mod}l - 1) \quad (15.4)$$

$$g_{mod} = \Gamma g - \alpha \quad (15.5)$$

where I_{sp} is the spontaneous emission intensity emitted within the observation angle (θ) per unit length, α is the overall loss coefficient, Γ is the optical confinement factor in the active layer, and g is the net material gain. A modal gain g_{mod} of -20 cm^{-1} at 800 nm emission wavelength was deduced when the pump power was 10 W/cm^2 , while 1 kW/cm^2 pump power leads to 100 cm^{-1} modal gain. For pump length $l > 0.5 \text{ mm}$, I_{ASE} saturates as expected for any finite power supply amplification mechanism.

The pump-probe transmission measurement (Fig. 15.4(b), inset) involves the use of an intense laser pump beam (390 nm in this case [27]) to excite the Si-nc to reach population inversion while a weak probe signal at $\sim 800 \text{ nm}$ simultaneously passes through the sample with active region thickness d . The Si-nc in the quartz substrate are formed by negative ion implantation and thermal anneal [27]. In the presence (absence) of a sufficiently strong pump beam the probe signal is amplified

(absorbed). Figure 15.4(b) shows the net material gain extracted from (15.6) as a function of pump power.

$$I_{tr} = I_{in}e^{(g-\alpha)d} \quad (15.6)$$

where I_{tr} and I_{in} refer to transmitted and incident probe beam intensities, respectively. Up to $10,000 \text{ cm}^{-1}$ average material gain is obtained, comparable to that of self-assembled quantum dots made of III–V semiconductors [32]. No change in probe signal intensity is observed when the same measurement is performed on an identical quartz sample without Si-nc. A four-level system model has been proposed to interpret the population inversion scheme in Si-nc. A more detailed discussion can be found in [13].

Several approaches have been demonstrated lately to achieve electrically-injected light emission, including a light-emitting diode (LED) structure [33] and a field-effect LED [34, 35] with the demonstration of 1 MHz direct modulation speed [36]. The critical design element of all is to embed Si-nc into an ultrathin dielectric layer which is sandwiched by a poly-Si layer and a single crystalline Si substrate to allow efficient carrier injection by tunneling. A large amount of effort is focused on reducing leakage current in the dielectric and achieving high enough current density without excessive device heating and premature failure for amplifiers and lasers. Another intrinsic limitation for Si-nc-based emitters is the difficulty of integration with conventional SOI waveguides due to emission around 800 nm.

Incorporating rare earth doping (e.g. Er, Tb, Yb, Gd) into Si-nc is a way to shift emission to the important communication wavelengths of 1.3–1.6 μm [37]. Following the revolution that the Er-doped fiber amplifier (EDFA) led in fiber optic telecommunications, research in Si emitters has been concentrated to doping Si with rare earth elements [38, 39]. However, it has been shown that Si is not a good host material to accommodate rare earth elements. Dopant clustering and back transfer of energy from the rare earth element are main obstacles to obtaining high emission efficiency [40]. SiO_2 dielectric with Si-nc therefore seems a better host choice for Er^{3+} [37] because the SiO_2 environment is an excellent natural host material for Er^{3+} , and Si-nc are shown to act as a good sensitizer as well [37, 41]. The energy of excitons excited by optical or electrical pumping from Si-nc is transferred to Er^{3+} ions which are coupled to adjacent Si-nc. Up to 70% energy transfer efficiency has been reported from Si-nc to Er^{3+} [42]. By employing a light-emitting device structure with 5.5 A/cm^2 injection current density in Fig. 15.5(a), room-temperature electroluminescence (EL) at $1.54 \mu\text{m}$, corresponding to typical Er first-excited multiplet $^4I_{13/2}$ to the ground state $^4I_{15/2}$ transitions, is demonstrated [40]. Two metal rings provide the electrical contacts to the n-type poly-Si and to the p-type Si substrate. Emission is detected from the metal-free central area. The disappearance of the intrinsic EL peak around 800–900 nm for Si-nc in Er-doped Si-nc samples clearly proves the efficient energy transfer from excitons formed in Si-nc to the rare earth ions.

However, significant light emission diminishes quickly from low temperature (30 K) to room temperature under electrical pumping, a much faster decay than in the case of optical pumping [40]. Studies of PL (488 nm, 10 mW) under different

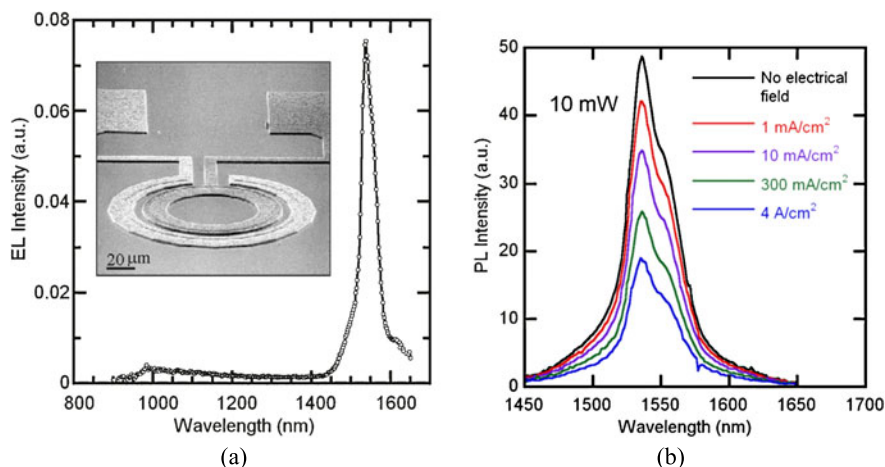


Fig. 15.5 (a) EL spectrum of a device based on Er-doped Si-nc obtained at room temperature under forward bias conditions with a current density of 5.5 A/cm^2 . *Inset*: SEM image of an LED device structure with ring-type electrodes. (b) PL spectra of a device based on Er-doped amorphous Si-nc for the unbiased device (*black line*) and in the presence of different current densities flowing through the device (Courtesy Fabio Iacona, Center of Materials and Technologies for Information and Communication Science (MATIS CNR-INFN), Catania, Italy)

electrical biases have been performed to investigate the effect of injected carriers on the luminescence properties. Figure 15.5 shows the PL spectra with the device under different forward bias, compared with that of the unbiased case. A clear quenching of the PL signal with increasing electrical pumping is noticed, indicating the new possible nonradiative paths with the presence of electrically-injected carriers. Iacona et al. [40] believe that independent but unbalanced electron and hole injection causes the Auger de-excitation of Er ions. For the conventional PL, on the other hand, electron-hole pairs are generated simultaneously in the active region and then undergo a rapid recombination with subsequent Er excitation. For electrical pumping, measurements suggest that more electrons than holes are injected into the active region in these devices. It results in wasting a certain amount of current since they do not recombine with holes and cause the Auger de-excitation of Er ions [40]. In addition to the major challenge of increasing the injection current density in all Si-nc-based light emitting devices, how to overcome the EL efficiency degradation with increasing injected current density is a problem for Er-doped devices.

In another promising experiment, utilizing low-dimensional Si, Cloutier et al. observed optical gain and stimulated emission in nanopatterned crystalline Si [43]. Figure 15.6, inset, is an SEM side-view of periodic nanopatterned Si with a highly ordered array of holes in the top Si layer of a conventional SOI wafer. The top Si is about 100 nm thick with 3 μm buried oxide underneath. An anodic aluminum oxide nanopore membrane serves as a mask for patterning holes with 60 nm diameter and 110 nm center-to-center spacing in $\text{Cl}_2\text{-BCl}_3$ plasma dry etch. Figure 15.6(a) shows the edge emission from a cw optically-pumped sample at 10 K. In the spectrum of

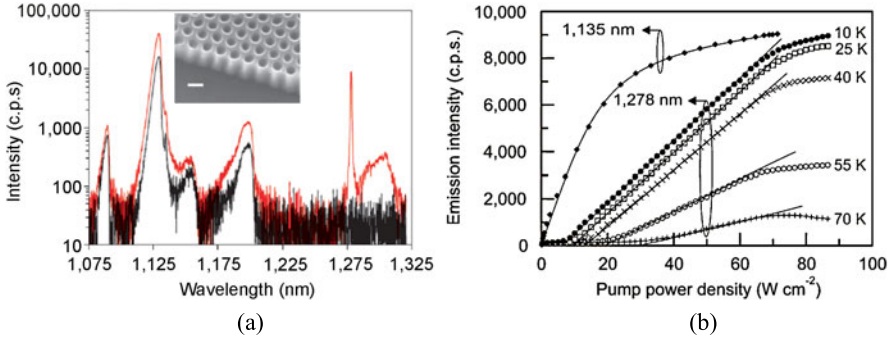


Fig. 15.6 (a) Edge-emission spectra from cleaved nanopatterned (red) and unpatterned (black) samples at 10 K. *Inset:* Side-view SEM image of nanopatterned Si; scale bar: 100 nm. (b) Evolution of the edge-emission intensity of the 1278 nm line as a function of pump power at 10, 25, 40, 55 and 70 K temperatures. The evolution of the 1135 nm phonon-assisted free-exciton line at 10 K is shown for comparison. Its intensity has been divided by 7 to plot all curves on the same scale (reproduced from [43] under permission of Macmillan Publishers Ltd.)

this gain-guided slab waveguide, a sharp peak at 1278 nm is observed and remains detectable till 80 K. The other emission bands in the spectrum below 1250 nm, believed to be emission from the crystalline Si substrate, are similar to the classical spontaneous PL emission bands of an unpatterned reference SOI sample. The temperature-dependent 1278 nm-peak intensity vs. cw pump power density characteristic is shown in Fig. 15.6(b). Transition from spontaneous to stimulated emission is observed in the 10–70 K range. Linewidth narrowing after passing pump power threshold presented additional evidence of stimulated emission. The phonon-assisted free-exciton recombination PL band at 1135 nm is also plotted to show no stimulated emission observable at this wavelength. The optical gain in nanopatterned Si is measured with the variable stripe length method discussed previously. Modal gains g_{mod} of 260, 247, 230, 165, and $88 \pm 5 \text{ cm}^{-1}$ [44] are measured at 10, 25, 40, 55 and 70 K, respectively, with a fixed pump power density of 65 W/cm^2 . In contrast, a modal loss of $-31 \pm 5 \text{ cm}^{-1}$ at 10 K is measured when the pump power density is only 8 W/cm^2 , i.e. below pump threshold [43].

The optical gain and stimulated emission in nanopatterned Si is attributed to the bistable carbon-substitutional-carbon-interstitial ($C_s C_i$) complex known as the *G-center* [44]. It is well-known that substitutional carbon (C_s) atoms occur naturally in Si wafers at concentrations between 10^{15} and 10^{17} cm^{-3} depending on the crystal growth technique [45], and are necessary for *G-center* formation. A *G-center* is created when a mobile interstitial carbon atom (C_i) binds with a substitutional carbon atom (C_s), a consequence of a damage event and following $C_s\text{-Si}_i$ exchange (where Si_i represents a Si interstitial) [46]. The density of *G-centers* depends on the densities of C_s in the lattice and introduced $C_s\text{-Si}_i$. Recent studies show that nanopatterned carbon-rich Si generates higher gain. Figure 15.7(a) exhibits a $33\times$ enhancement in the PL intensity at 25 K for a nanopatterned Si with $\sim 10^{19} \text{ cm}^{-3}$ carbon atoms implanted (background carbon concentration: $2.5 \times 10^{16} \text{ cm}^{-3}$), compared

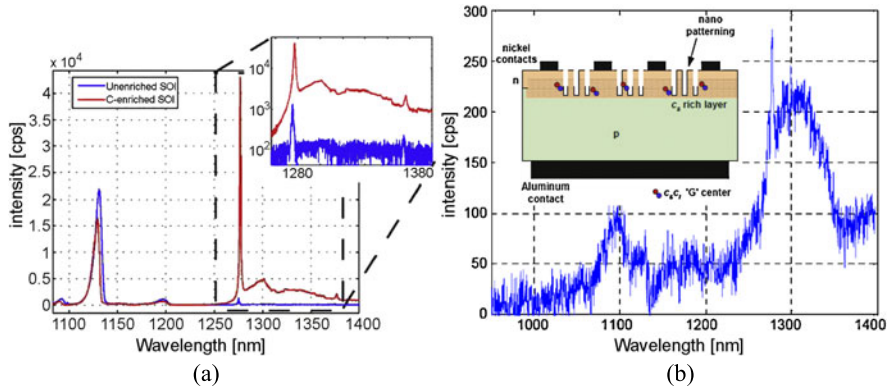


Fig. 15.7 (a) Photoluminescence spectrum at 25 K of nanopatterned Si and nanopatterned C-enriched Si. The *inset* shows a semi-logarithmic plot of the region containing the G line and phonon replicas. (b) Electroluminescence spectrum of *G-center* LED at 60 K and a current of 50 mA. *Inset*: Schematic of the *G-center* LED in nanopatterned Si (reproduced from [44] under the permission of American Institute of Physics)

with the PL response from a base-line nanopatterned SOI sample with background carbon concentration. These results confirm that the carbon in the silicon crystal is responsible for the creation of *G-centers*, rather than the dry etching process [44]. It also provides a path for increasing the efficiency and gain of this material. Electroluminescence at 1287 nm is demonstrated in the nanopatterned Si pn junction with a 100 nm-thick carbon-rich layer at the junction interface (Fig. 15.7(b), inset) [44]. Figure 15.7(b) shows the electroluminescence from the device at 60 K with a current of 50 mA. The mechanism of the electroluminescence can be described briefly in the following way: the *G-center* is bistable and can be excited below 50 K. The excited/injected carriers occupy the *G-center*-induced acceptor and donor states existing inside the conventional Si bandgap, resulting in a sub-bandgap of 0.97 eV. The trapped electrons and holes can recombine directly producing a phonon-less emission at 1278 nm, or indirectly producing an emission band extending from 1250 nm to 1350 nm. However, emission is quickly diminished at higher temperatures when carriers in the *G-center*-induced states move back to the conduction and valence bands [44].

With the availability of nanotechnology, the phonon-selection rule can be relaxed or broken by crystal-symmetry breaking or phonon localization; however, it still remains challenging to achieve room-temperature cw lasing based on these temperature-dominated processes presently.

15.2.2 Raman Effect

Raman scattering is an inelastic scattering mechanism where photons propagating through the medium give up energy or gain energy from surrounding opti-

cal phonons. This results in a frequency shifted output photon of -15.6 THz and $+15.6$ THz in bulk silicon for the Stokes and anti-Stokes, respectively [47]. The anti-Stokes can typically be neglected over the Stokes under equilibrium temperature conditions and no external crystal phonon excitation due to Boltzmann statistics.

Spontaneous Raman emission occurs in a linear regime where the scattered light intensity is linearly proportional to the pump light intensity. Above a certain threshold this interaction is no longer linear and Stimulated Raman Scattering (SRS) occurs. The SRS relation for the change in Raman power can be written as:

$$\frac{dP_R}{dz} = g_R \cdot P_R \cdot P_P \quad (15.7)$$

where P_R is the power of the Raman signal at the Stokes wavelength, P_P is the pump power, and g_R is the SRS gain coefficient. The Raman gain coefficient is [47]:

$$g_R = \frac{8\pi c^2 \omega_p}{\hbar \omega_s^4 n_s^2 \omega_s (N+1) \Delta \omega_s} S \quad (15.8)$$

where ω_p and ω_s are the frequencies of the pump and Stokes wavelengths, respectively. n_s , N , and $\Delta \omega_s$ are the index of refraction at the Stokes wavelength, the Bose occupation factor (0.1 at room temperature), and the full-width-half-maximum of the spontaneous Raman spectrum, respectively. S is the spontaneous scattering efficiency.

Although the 1.3 and 1.5 μm operating wavelengths are well below the bandgap energy of silicon and single photons are not absorbed, two photon absorption (TPA) still occurs. TPA is a nonlinear loss mechanism that increases as the number of photons increases in a waveguide. During TPA, two photons are absorbed by an electron in the valence band, exciting it as a free carrier into the conduction band. The free carriers generated through TPA add an additional carrier induced loss, free carrier absorption (FCA), discussed previously, to the signal [48].

The first demonstration of a pulsed silicon Raman laser [49] overcame TPA by using a long delay within the laser cavity (an 8 m long cavity), and a short optical pulse such that the carriers generated during TPA would recombine prior to the next pass of the optical pulse (Fig. 15.8(a)). The experimental light output versus pump light ($L-L$) characteristic is shown in Fig. 15.8(b). Most demonstrations in silicon have been conducted with a pump wavelength of ~ 1550 nm and a lasing wavelength near 1690 nm.

In order to achieve net gain under continuous wave operation, the conduction band carrier lifetime needs to be reduced. This can be achieved in a few ways. One method is to reduce the volume-to-surface ratio of the waveguide in order to increase the surface recombination rate of the carriers. Imbedding a p-i-n structure into the waveguide to sweep carriers away [52] resulted in the first cw demonstration of a silicon Raman laser [50] and is the approach most widely used [53]. Figure 15.9(a) shows the cross section of a waveguide with an imbedded p-i-n structure, along with the first cw $L-L$ curve [50]. Although the p-i-n structure reduces the carrier lifetime to achieve lasing, TPA and FCA increase the cavity loss at higher pump powers leading to compression of the $L-L$ curve (Fig. 15.9(b)).

Fig. 15.8 (a) Experimental setup and (b) laser light vs pump light from the first pulsed silicon Raman laser [49] (reproduction under permission of the Optical Society of America)

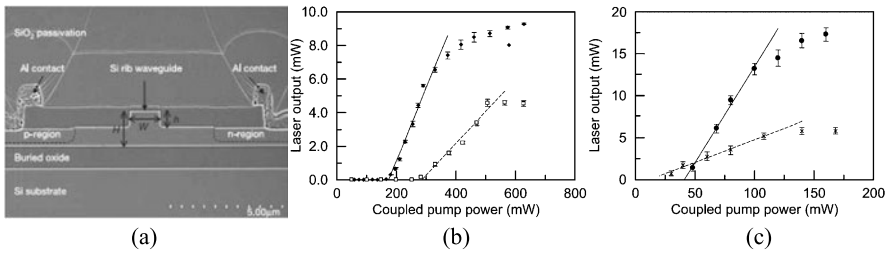
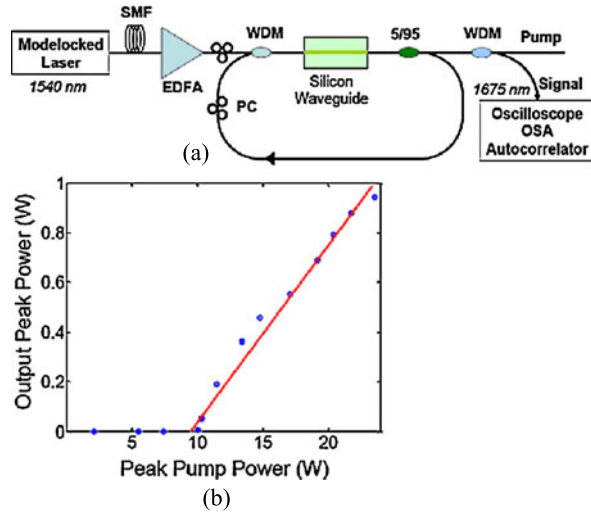


Fig. 15.9 (a) Waveguide cross section with imbedded p-i-n cross section for carrier lifetime reduction. (b) $L-L$ curve of first continuous wave silicon Raman laser [50]. (c) $L-L$ curve of racetrack Raman laser [51] (reproduction under permission of Macmillan Publishers Ltd. and American Institute of Physics)

Further improvements in laser performance have been made by utilizing a specially designed ring cavity that enhances the pump wavelength in the cavity while still allowing power at the lasing wavelength to efficiently exit the cavity [53]. This has led to a reduction in threshold pump power from 200 mW to 20 mW while increasing the maximum laser output power from 10 mW to 18 mW (Fig. 15.9(c)). Another configuration of this ring has been used to generate lasing at longer wavelengths (1848 nm) not typically accessible by InP or GaAs based semiconductor lasers [51]. The cavity of this cascaded Si Raman laser is designed such that lasing at 1680 nm acts as a pump for second order lasing at 1848 nm. Figure 15.10 shows the spectra of the pump, the first order lasing mode, and the second order lasing mode.

Silicon Raman amplifiers and lasers are unlikely to be integrated with CMOS chips due to the optical pump sources required. However, their excellent wavelength purity and emission wavelength are of interest in medical or sensing applications.

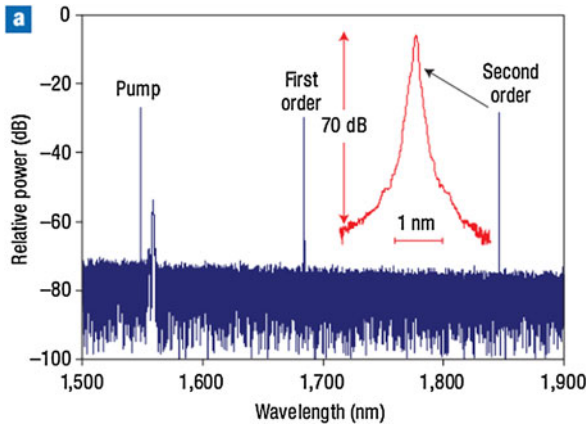


Fig. 15.10 Cascaded silicon Raman laser output spectrum measured with a grating-based optical spectrum analyser with a resolution of 0.01 nm, showing three peaks corresponding to the pump, the first- and the second-order laser outputs. *Inset*: high-resolution scan of the second-order lasing peak, showing 70 dB side-mode suppression ratio (SMSR) [51] (reproduction under permission of Macmillan Publishers Ltd.)

Table 15.1 Linear thermal expansion coefficients and bandgaps (300 K) of selected important semiconductors as a function of their lattice constants (300 K)

Semi-conductor	Lattice constant (nm)	Lattice mismatch to Si (%)	Bandgap (eV)	Linear TEC ($10^{-6}/\text{K}$)	Linear TEC (relative)
GaN	0.3189	-41.2815	3.20	3.17	1.22
Si	0.5431	0.0000	1.12	2.60	1.00
GaP	0.5451	0.3683	2.26	4.65	1.79
Ge	0.5646	3.9588	0.66	5.90	2.27
GaAs	0.5653	4.0876	1.42	5.73	2.20
InP	0.5869	8.0648	1.35	4.60	1.77
InAs	0.6058	11.5448	0.36	4.52	1.74

15.2.3 Monolithic Integration Approaches

An on-going effort for nearly four decades has been to achieve epitaxially grown compound direct bandgap materials on Si substrates. However, overcoming the mismatch in lattice constant and thermal expansion coefficient is a major challenge to achieving sufficiently low threading dislocation density [54]. Table 15.1 compares these two parameters of several important semiconductors. GaAs and InP have a lattice (thermal expansion coefficient) mismatch of 4.1% (120.4%) and 8.1% (76.9%), respectively. Thus, they lead to 10^8 – 10^{10} cm^{-2} threading or misfit dislocation density when GaAs or InP is grown on Si substrates [55]. Numerous approaches including special surface treatment [56], strained superlattices [57, 58], low-temperature buffers [59] and growth on patterned substrates [60] have been employed to re-

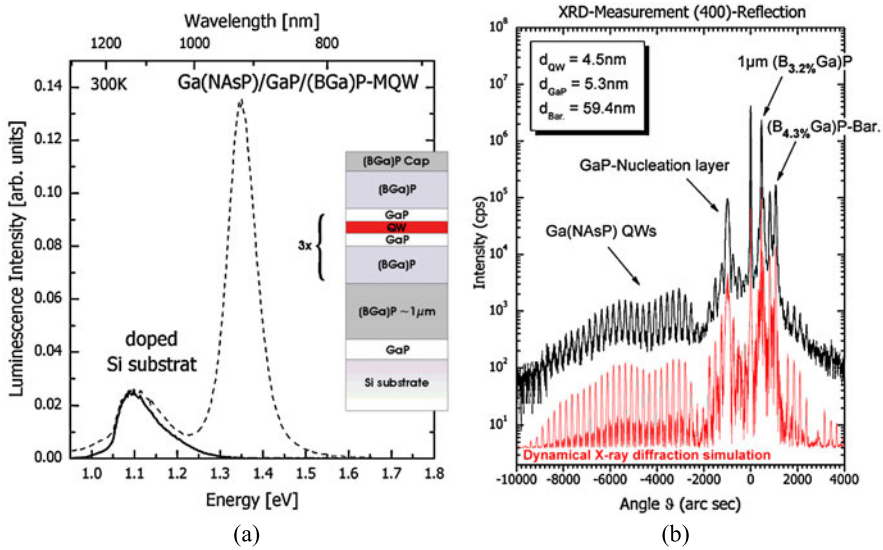
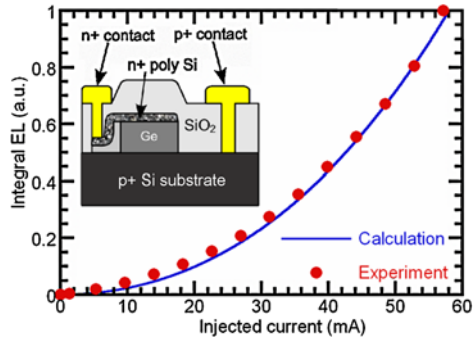


Fig. 15.11 (a) Room temperature PL spectrum of Ga(NAsP)/GaP/(BGa)P MQW structure (*dashed line*) in comparison to a doped Si substrate (*solid line*). *Inset*: Epitaxial layer structure. (b) High-resolution XRD pattern around the (400)-reflection of Si (*upper trace*: experimental, *lower trace*: modeling by dynamical X-ray diffraction theory) [61] (Courtesy Wolfgang Stolz, Philipps-Universität Marburg, Germany)

duce the dislocation density to around 10^5 – 10^6 cm^{-2} , still two orders of magnitude higher than the typical number ($< 10^4$ cm^{-2}) in InP- or GaAs-based epitaxial wafers used to achieve room-temperature cw lasers. In this section we discuss several pertinent approaches to achieve high-quality heteroepitaxy thin films for Si photonics applications.

GaP is the binary compound semiconductor with smallest lattice mismatch with Si. Kunert et al. have demonstrated the monolithic integration of a Ga(NAsP)-based multiple quantum well (MQW) active region on Si with a (BGa)P/GaP buffer layer [61]. Ga(NAsP) pseudomorphically grown on GaP substrates has been introduced as a direct bandgap material [62]. By incorporating small percentages of N or B into GaP, it is also possible to adjust the lattice constant to match with Si. Tensile (BGa)P was selected to be the buffer and barrier material to balance the compressive strain of Ga(NAsP) quantum wells. The inset in Fig. 15.11(a) shows the MQW structure with a 100 nm GaP nucleation layer on (001) Si, followed by a 1 μm ($\text{B}_{0.0032}\text{Ga}$)P buffer. Each 4.5 nm Ga(NAsP) quantum well (QW) is sandwiched by a 5 nm GaP intermediate layer to avoid the formation of N–B bonds and a 60 nm ($\text{B}_{0.0043}\text{Ga}$)P barrier layer. Figure 15.11(a) shows the room-temperature PL spectrum of the sample, exhibiting a strong peak at 930 nm originating from the active region in addition to a broad peak at the Si bandgap. The relative intensity of the peak at 930 nm from 13 nm quantum wells is a good sign of appreciable material gain. High-resolution X-ray diffraction (XRD) is employed to probe the dislocation-induced MQW satellite fringe shifting or broadening. The good agreement between

Fig. 15.12 Integral EL intensity of a $20\ \mu\text{m} \times 100\ \mu\text{m}$ 0.2% tensile-strained Ge/Si p-i-n LED increases superlinearly with injected current, which agrees with theoretical calculations. *Inset:* Schematic cross-section of the Ge/Si LED [66] (courtesy Xiaochen Sun, MIT, Cambridge, MA, USA)



experimental and simulated data in Fig. 15.11(b) indicates excellent integrity of the active region. It is promising to obtain high-quality active region growth on a Si substrate when utilizing quaternary or even higher order compound semiconductor material systems, which give more freedom to compensate lattice-mismatched and thermal expansion- mismatched materials. More recently, demonstrations of lasing from an InGaAs/GaAs QW grown on GaP/Si template [63], as well as experiments on cryogenic laser operation using GaNAsP lattice matched to silicon [64] have been published and are relevant papers suggested for further reading.

Since the debut of the first transistor and integrated circuits on Ge, Ge(SiGe)-on-Si heteroepitaxy is of great interest for building light emitters on a Si substrate. Compatibility with modern CMOS technology and potential $\sim 1.55\ \mu\text{m}$ emission from direct band-to-band transitions (0.8 eV) are important reasons for corresponding research. Crystalline Ge is an indirect bandgap material with a minimum bandgap energy of 0.66 eV, close to the direct transition band. Theoretically, a 2% tensile strain is required for converting Ge into a direct bandgap material, while experiment shows a large emission wavelength red shift to $2.5\ \mu\text{m}$ (0.5 eV) [65], which is of less interest for optical interconnects and telecommunications.

Strain engineering and heavy n-type doping were used to achieve room-temperature direct bandgap electroluminescence [66, 67]. Sun et al. selectively grew Ge on p^+ Si substrates and with moderate tensile strain of 0.2%–0.25% to reduce the direct bandgap between the minimum of the direct Γ valley and the maximum of the light-hole band to 0.76 eV [66]. Heavily doped poly-Si was used for the electrode, resulting in a p-i-n diode structure as shown schematically in Fig. 15.12, inset. Figure 15.12 demonstrates a superlinear relationship between the integral direct bandgap room-temperature electroluminescence intensity and the injected current. The electroluminescent intensity is proportional to both the total injected carrier concentration and the fraction of electrons scattered to the direct Γ valley. A model based on the Fermi-Dirac distribution has been developed to fit the experimental data very well [66]. An important question is whether the relatively high threading dislocation density of around $1.7 \times 10^7\ \text{cm}^{-2}$ could be a major hurdle to realizing diode lasers on this Ge-on-Si substrate.

Another room-temperature Ge LED has been demonstrated by n-type heavy doping, resulting in the Fermi level above the indirect L valley and good electron occu-

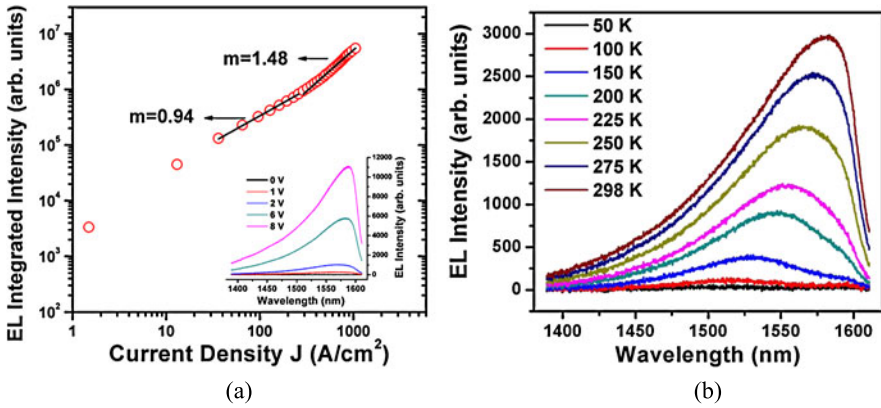


Fig. 15.13 (a) Integrated luminescence vs. current density ($L-J^m$) characteristics of a Ge LED. *Inset*: Electroluminescence spectra of the Ge LED under different applied biases. (b) EL spectra measured at various temperatures. Better radiative efficiencies are observed for higher temperatures (courtesy Szu-Lin Cheng, Stanford University, Stanford, CA, USA)

pation of the direct Γ valley of Ge [67]. An n^+/p Ge homojunction LED structure (300 μm in diameter) on a Si substrate is employed. The doping concentrations of phosphorous and boron are $7.5 \times 10^{18} \text{ cm}^{-3}$ and $3.6 \times 10^{17} \text{ cm}^{-3}$, respectively, achieved by in-situ doping to achieve an abrupt junction profile. Room temperature EL spectra of the Ge LED under different applied biases (Fig. 15.13(a), inset) show the EL peak located near 1.6 μm , indicating emission from the direct bandgap of Ge. The onset of the EL is at 0.75 V, closely matching the indirect bandgap (0.66 eV) of Ge. The corresponding injected current density vs. EL intensity in Fig. 15.13(a) exhibits a superlinear current density-EL intensity dependence and a fitting exponent m of 1.48 is observed for currents greater than 300 A/cm^2 . This implies that the device is more effective when operating under high current, contrary to typical LEDs which suffer from low radiative efficiency at higher injection current levels due to enhanced Auger recombination. The hypothesis of this enhanced EL intensity is Joule heating-induced larger overlap of the Fermi-Dirac distribution of the carriers in the Γ valley, which is confirmed by temperature-dependent EL in Fig. 15.13(b). The wavelength peak shifts towards longer wavelength due to the shrinkage of the direct bandgap. The observation of this band filling effect in Ge LEDs is inverse to the EL quenching in devices which rely on quantum confinement effects like Si-Ge quantum-dot and quantum-well devices [68] and those discussed in Sect. 15.2.1, giving an edge to achieve room temperature lasing in the future. The use of high Q ring cavities together with these structures holds promise for room temperature lasing.

In 2012, electrically pumped room temperature lasing from a Ge-on-Si heterostructure was demonstrated [69]. This was achieved by doping Ge with phosphorous with concentrations in excess of $4 \times 10^{19} \text{ cm}^{-3}$. A gain spectrum of 200 nm width and an output power of 1 mW were measured. More recently, lasing in a direct bandgap GeSn alloy grown on Ge/Si virtual substrate was reported [70]. The lasing

wavelength is closer to 2 μm and required cryogenic cooling. Surface passivation and design optimization regarding doping, optical mode confinement and carrier injection is expected to increase the operation temperature as well as decrease the threshold excitation density.

Another exciting approach is the epitaxial growth of direct gap III–V semiconductors directly on silicon substrates [96, 97] with the use of epitaxial lateral overgrowth (ELO) to achieve high quality III–V layers. More recently, Z. Wang et al. showed an optically pumped InP based laser grown on (001) silicon operating at room temperature [98]. This novel epitaxial technology suppresses threading dislocations and anti-phase boundaries to a less than 20 nm thick layer not affecting the device performance. Future advances in these technologies can make them a competing platform for realizing lasers on silicon.

In the next section, we show recent results of quantum dot (QD) growth on silicon substrates using molecular beam epitaxy (MBE) and review laser performance to date using this approach.

15.2.4 Quantum Dot and Quantum Well Lasers on Silicon

InAs/GaAs quantum dot lasers emitting around 1.3 μm are the best studied semiconductor quantum dot system, and will be the primary focus of this section. Such quantum dot lasers have demonstrated the lowest threshold current densities and highest lasing temperatures of any semiconductor laser emitting in the telecom range [71, 72], making them an attractive candidate to meet low power consumption and athermal performance demands for silicon photonics devices/packages. Here, we review various methods to integrate self-assembled quantum dot lasers with silicon photonic devices, focusing on epitaxial growth of such laser structures directly onto silicon substrates.

The approach that is closest to commercial deployment is integration of quantum dot lasers via flip chip bonding and butt coupling onto ‘silicon optical interposer’ chips consisting of spot size converters, optical modulators, photodetectors, and power splitters. Such transceivers have demonstrated error free operation at 20 Gbit/s from 25 to 125 $^{\circ}\text{C}$ without active adjustment of the quantum dot laser, modulator, or photodiode [73]. Another approach to take advantage of the inherent benefits of quantum dot lasers for silicon photonics is the proposal of using a highly efficient temperature stable quantum dot comb laser as an external dense wavelength-division-multiplexing (DWDM) light source coupled into a silicon photonics chip for modulation and multiplexing [74].

InAs quantum dot lasers have also been integrated with silicon by wafer bonding. Using direct fusion bonding at 300–500 $^{\circ}\text{C}$, broad area lasers (2.1 mm \times 100 μm) with current injection across the bonded GaAs/Si interface show room temperature pulsed lasing thresholds of 205 A/cm² [75]. A pulsed lasing temperature up to 110 $^{\circ}\text{C}$ was reported by bonding p-doped quantum dot lasers in a later report [76]. Although the previous two structures were bonded on pure silicon wafers, wafer

bonded quantum dot lasers on SOI waveguides have also been demonstrated (with the optical mode still confined in the III–V layers), paving the way for future integration with silicon waveguides [77].

Direct growth of quantum dot lasers onto silicon substrates represents another exciting approach for integration onto silicon. Historically, the primary focus of monolithic integration by epitaxy has been to achieve good laser performance by minimizing the number of generated dislocations as much as possible. Despite significant reductions in dislocation density to 10^5 – 10^6 cm^{-2} , dislocation densities near native substrate levels ($\sim 10^4$ cm^{-2}) appear difficult to achieve. One approach to further reduce the negative effects of residual dislocations on laser performance is to substitute QW active regions by three dimensional quantum dots. Physically, efficient capture and tight spatial confinement of injected carriers by individual quantum dots reduces total carrier migration and subsequent non-radiative recombination at dislocation cores. Because individual quantum dots are essentially independent of each other, the effect of threading dislocations in the active layer is greatly diluted if the quantum dot density is much higher than the dislocation density.

The prospect of using semiconductor quantum dots and their associated three-dimensional potential wells to reduce the effects of dislocations was proposed as early as 1991 [86]. Early explorations of this idea culminated in room temperature pulsed lasing at 1.1 μm or shorter, summarized in Table 15.2. For integra-

Table 15.2 Summary of In(Ga)As self-assembled quantum dot lasers epitaxially grown on silicon

Year	I_{th} (mA)/ J_{th} (A cm^{-2})	Max lasing temp ($^{\circ}\text{C}$)	Device size (μm^2)	λ (μm)	PL linewidth (meV)	Ref.
1999	788/3850 (Pulsed 80 K)	–	800×50	1 (80 K)	49 (17 K)	[78]
2005–2009	500/900 (Pulsed)	95 (Pulsed)	600×80 (lowest threshold) 800×8 (highest temperature)	1	51	[79–81]
2011	1087.5/725 (Pulsed)	42 (Pulsed)	3000×50	1.3	37	[82]
2012	45/64.3 (Pulsed) 114/163 (cw)	84 (Pulsed) 30 (cw)	3500×20 (lowest threshold) 3000×20 (highest temperature)	1.26	38	[83]
2014	150/200 (Pulsed)	111 (Pulsed)	3000×25	1.25	37	[84]
2014	16/430 (cw)	119 (cw), > 130 (Pulsed)	$(700\text{--}1200) \times$ $(4\text{--}12)$	1.25	37	[85]

tion with silicon waveguides and/or transmission through silica fiber, longer wavelengths are desirable to minimize propagation loss. The first 1.3 μm InAs/GaAs quantum dot laser epitaxially grown on silicon was reported in 2011 [82]. The epitaxial structure comprised a GaAs buffer directly nucleated on a (001) silicon substrate off-cut 4 degrees from the [110] direction, followed by $\text{In}_{0.15}\text{Ga}_{0.85}\text{As}/\text{GaAs}$ strained layer superlattice dislocation filter layers and another $\text{GaAs}/\text{Al}_{0.4}\text{Ga}_{0.6}\text{As}$ short-period superlattice. Following the buffer a conventional GaAs/AlGaAs separate confinement heterostructure (SCH) laser structure was grown with five layers of InAs/GaAs dot-in-a-well layers as the active region. Cleaved facet broad area lasers 3 mm long and 50 μm wide with Ti/Au p-contacts on the III–V epitaxial layer side and Cr/Au n-contact on the bottom silicon substrate showed room temperature pulsed lasing with a threshold current density of 725 A/cm^2 . Lasing was limited to $\leq 42^\circ\text{C}$, and a maximum room temperature output power of 26 mW was reported.

By using $\text{In}_{0.15}\text{Al}_{0.85}\text{As}/\text{GaAs}$ strained layer superlattices in place of $\text{In}_{0.15}\text{Ga}_{0.85}\text{As}/\text{GaAs}$ strained layer superlattices for improved dislocation filtering, as well as employing a top-top contact geometry to avoid current injection through the dislocated GaAs/Si interface as was done previously, the pulsed lasing threshold for a 3 mm \times 25 μm broad area laser was reduced to 200 A/cm^2 [84]. Room temperature output powers above 100 mW have been obtained from a single cleaved facet, and the maximum lasing temperature under pulsed operation was simultaneously increased up to 111 $^\circ\text{C}$ [84]. Continuous-wave (cw) performance has not been reported for this device.

Previously, cw lasing of InAs/GaAs quantum dot lasers grown on a germanium substrate was demonstrated with comparable performance to those grown on GaAs substrates [87]. As mentioned above, epitaxial growth of germanium on silicon is a mature CMOS technology, and Ge/Si templates are now widely commercially available. Since Ge is nearly lattice matched to GaAs (0.08% lattice mismatch), growth of GaAs on Ge/Si substrates allows for decoupling of the lattice mismatch and polarity mismatch issues into separate interfaces (i.e. lattice mismatch is treated at the Ge/Si interface while polarity mismatch is treated at the GaAs/Ge interface, as opposed to dealing with both at the same interface which is the case with direct growth of GaAs on Si).

Continuous wave lasing of InAs/GaAs quantum dot lasers epitaxially grown on silicon was first achieved using such an intermediate Ge buffer approach [83]. The same InAs/GaAs quantum dot laser structure grown on Ge/Si substrates with a 2 μm Ge buffer but without strained superlattice dislocation filtering layers exhibits much-improved lasing characteristics compared to direct nucleation of GaAs on Si with very low room temperature pulsed lasing threshold of 64 A/cm^2 , as well as room temperature cw lasing thresholds of 163 A/cm^2 . Maximum cw output power at room temperature (RT) is 3.7 mW from both facets for a 3.5 mm long cavity with a 20 μm wide ridge. cw operation was sustained up to 30 $^\circ\text{C}$ in a 3 mm long device.

Further improvement in cw performance soon followed. InAs/GaAs quantum dot lasers grown on Ge/Si substrates with thresholds of 16 mA and 50 mW output power for small cavities have been demonstrated, while larger cavities have yielded up to

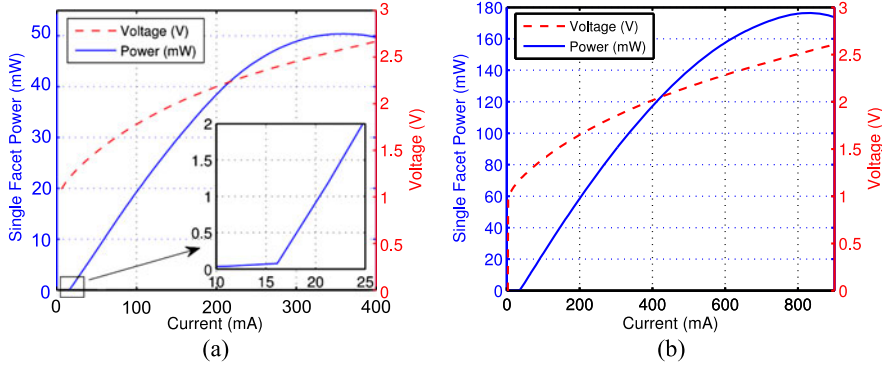


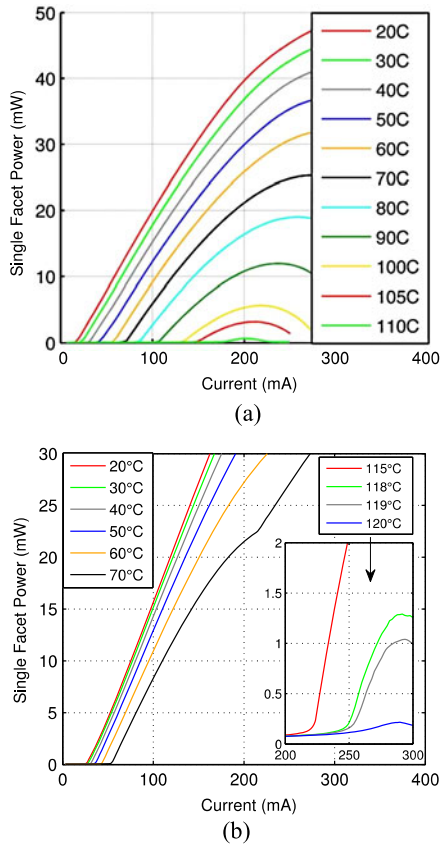
Fig. 15.14 (a) Room temperature cw light-current-voltage (LIV) plot of 7-layer quantum dot laser epitaxially grown on Ge/Si substrate with 95% HR coating on one facet, $937 \times 4 \mu\text{m}^2$ device size, 16 mA threshold current, 50 mW output power. (b) Characteristics of larger ($1130 \times 10 \mu\text{m}^2$) but otherwise similar laser; 38 mA threshold current, 176 mW maximum output power [85]

176 mW output power so far with 38 mA threshold current (see Fig. 15.14) [85]. These devices employed seven dot layers for the active region and 95% dielectric high reflection (HR) coating on one facet. Modulation p-doping the GaAs barriers between the quantum dot layers can improve the laser characteristic temperature (T_0) to the 100–200 K range and cw lasing up to 119 °C (see Fig. 15.15). Analysis of >300 devices on two different wafers from separate growth runs exhibited similar characteristics with an average threshold current density of 500 A/cm^2 and minimum values as low as 250 A/cm^2 (see Fig. 15.16). A summary of the progress made with self-assembled quantum dot lasers epitaxially grown on Si or Ge/Si is presented in Table 15.2.

Reliable performance of epitaxially grown III–V lasers on silicon has been a major challenge. This is particularly true for GaAs/AlGaAs based lasers, which are susceptible to recombination enhanced defect reactions [88]. Reported lifetimes for GaAs based QW lasers epitaxially grown on silicon have ranged from a few seconds to 200 hours at room temperature (see Table 15.3). For example, GaAs/AlGaAs QW laser grown on Ge/Ge_xSi_{1-x}/Si substrates reported a cw lifetime at room temperature of around 4 hours under a constant applied current density of 270 A/cm^2 prior to catastrophic failure [94]. The dislocation density measured at the surface of the SiGe buffer in the aforementioned work was reported to be $2 \times 10^6 \text{ cm}^{-2}$. In comparison, GaAs/AlGaAs quantum dot laser diodes epitaxially grown on Ge/Si substrates have surpassed 2100 hours of cw operation at 30 °C under an applied current density of 2 kA/cm^2 before the aging process was stopped for characterization (see Fig. 15.17) [95].

Table 15.3 summarizes some representative lifetime data that have been reported for GaAs based lasers grown on silicon to date. Compared to previous GaAs based QW lasers, InAs/GaAs quantum dot lasers show significantly longer lifetimes at harsher operating conditions, despite having a higher dislocation density compared to some of the QW devices. The improved lifetime is attributed to the same princi-

Fig. 15.15 (a) Room temperature cw light-current (LI) plots of the device in Fig. 15.14(a) at various stage temperatures showing lasing up to 110 °C. (b) LI-plot of a similar sized device ($993 \times 5 \mu\text{m}^2$) but with p-doped active region, demonstrating lasing up to 119 °C [85]



ple that enables the operation of quantum dot lasers despite high defect/dislocation densities, namely that once carriers are captured by a quantum dot they become localized and can no longer diffuse laterally toward dislocations, unlike the QW case. If the dot density significantly exceeds the dislocation density, then the capture cross-section of individual dislocations or defects acting as non-radiative recombination centers is reduced due to competing radiative transitions of the quantum dot ensemble. The net result is a reduction of the non-radiative recombination rate resulting in improved device lifetime. Further, the strain field of the InAs quantum dots presents an additional mechanical barrier for the propagation of growing dislocation loops, and some loops may become pinned by the dots [89]. We expect that future work combining state-of-the-art dislocation reduction techniques, as well as improved uniformity and density of the quantum dot active region, will result in significantly improved laser performance and in particular improved laser reliability.

The following two sections describe more mature technologies, to fabricate high performance transmitters on silicon, which have advanced closer to production and anticipated to appear in the telecom/datacom market in the next few years.

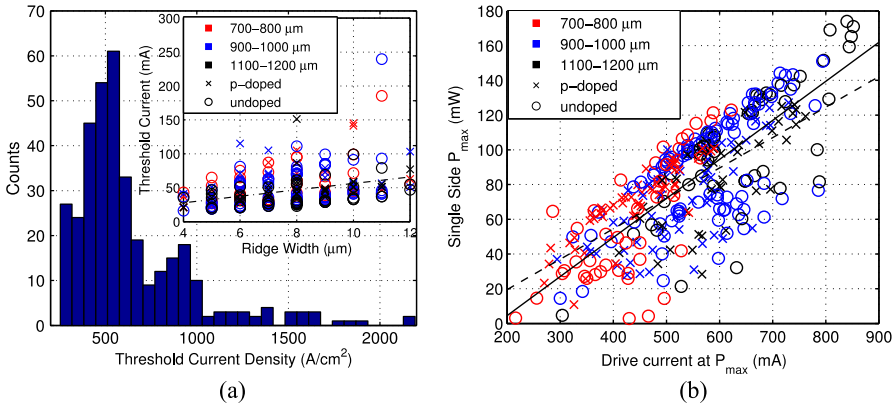


Fig. 15.16 (a) Histogram of cw threshold current density at 20 °C for 7-layer quantum dot lasers epitaxially grown on Ge/Si substrates with 95% HR coating on one facet with either intrinsic or p-doped active regions. *Inset*: corresponding threshold currents plotted against ridge width, the *dashed* best fit line has a slope of 4.75 mA/µm. (b) Maximum cw output power at 20 °C versus corresponding drive current. *Solid* and *dashed* lines are best fits for the undoped and p-doped devices with slopes of 22.52 and 17.52 W/A, respectively [85]

Table 15.3 Summary of representative lifetime data for GaAs based lasers grown on silicon

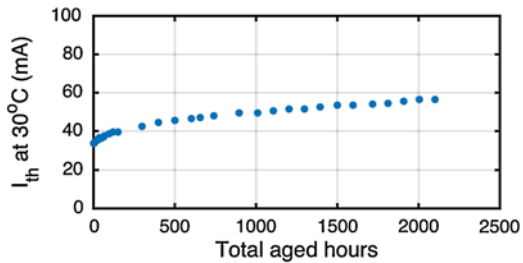
Year	Description	Aging condition	$J(0)/P(0)$	Dislocation density (method used)	Longest time to failure ^a	Ref.
1987	GaAs/AlGaAs SQW	RT APC	~2 mW	10^7 cm^{-2} (-)	<10 s	[90]
1991	In _{0.05} Ga _{0.95} As/AlGaAs SQW	RT APC	~2000 A/cm ² / 2 mW	–	10 hours	[91]
2000	In _{0.2} Ga _{0.8} As “quantum dot like” active region	RT APC	1320 A/cm ² / 0.5 mW	–	80 hours ^b	[92]
2001	GaAs/AlGaAs SQW on ELO stripe	RT APC	810 A/cm ² / 1 mW	$2 \times 10^6 \text{ cm}^{-2}$ (etch pits)	200 hours	[93]
2003	GaAs/AlGaAs SQW on Ge _x Si _{1-x} /Si	RT ACC	270 A/cm ² / <1 mW	$2 \times 10^6 \text{ cm}^{-2}$ (PVTEM + etch pits)	4 hours ^b	[94]
2014	InAs QDs on Ge/Si	30 °C ACC	2000 A/cm ² / 16.6 mW	$2 \times 10^8 \text{ cm}^{-2}$ (PVTEM)	4600 hours (extrapolated).	[95]

^aTime to failure is defined either by 2× increase in drive current in APC mode, 2× increase in threshold in ACC mode

^bActual catastrophic failures [95]

Acronyms: ACC: automatic current control, APC: automatic power control, PVTEM: plain-view TEM

Fig. 15.17 Threshold current (I_{th}) at 30 °C aging temperature of versus aging time for one of the InAs quantum dot lasers epitaxially grown on Ge/Si substrates reported in [85]



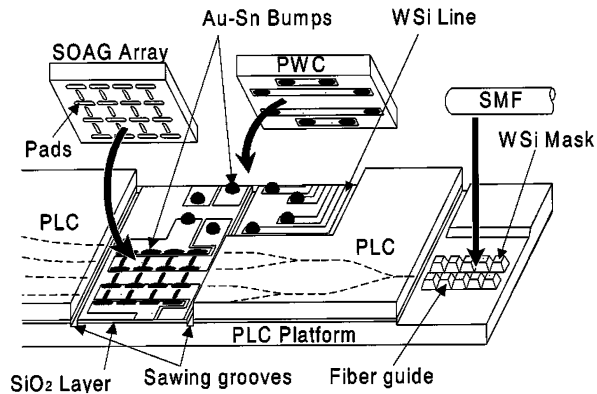
15.2.5 Hybrid (Assembly-Level) Integration

In Sects. 15.2.1–15.2.2 we reviewed a few of the major efforts to make silicon lase by manipulating the material properties of silicon or by utilizing other physical mechanisms to obtain optical gain. Recent progress in monolithic integration of direct bandgap materials on Si substrates is also highlighted in Sect. 15.2.3, though the lasing efficiency requires significant improvement. Although much progress has been made in this area and optically pumped Si Raman lasers have been demonstrated, room temperature electrically pumped lasers with useful powers for optical communication applications have not been demonstrated. Hybrid integration is a promising approach where III–V compound semiconductors are used to provide electrically pumped gain and are coupled into passive lightwave circuits on silicon.

The traditional approach to hybrid integration is to take prefabricated III–V lasers and amplifiers and die bond these elements onto a passive planar lightwave circuit (PLC). Since the waveguides on the host substrate, the PLC, and the laser die are already defined, the alignment accuracy during placement needs to be a fraction of the mode width. This is typically within a few hundred nanometers for silicon waveguides, making alignment a challenge for high volume manufacturing and leading to substantial variation in coupling power and back reflections between the two waveguides. Efforts have been made to reduce the sensitivity of this coupling by increasing the mode size through spot size converters [99]. Precision cleaving the III–V active die and creating a perfectly matched trench in the PLC host substrate have been explored in order to create assembly methods that allow for self alignment of the optical modes [100].

Figure 15.18 illustrates a PLC utilizing hybrid integration for switching [101]. In this work, self alignment with $\pm 1 \mu\text{m}$ precision is achieved by placing solder-wettable pads on both the host PLC substrate and the III–V chips. During bonding, the surface tension of the Au–Sn solder bumps pulls the two chips into alignment. This demonstration yielded coupling losses of $4 \sim 5$ dB when used with spot size converters. However, the production efficiency and chip yield result in expensive integration cost. Another noteworthy tunable laser demonstration using this technique was published by NEC recently [102]. The laser included individual InP and Si chips assembled to achieve gain and filtering/tuning functionality, respectively. The laser had full C-band tunability with fiber coupled output power in excess of 100 mW. The linewidth across the entire wavelength range was around 15 kHz.

Fig. 15.18 Schematic of proposed hybrid integration scheme for switching [101]. SOAG: semiconductor optical amplifier gate, PWC: printed wiring chips (reproduction under the permission of Institute of Electrical and Electronic Engineers)



The following section includes a wide variety of high performance photonic devices, which were demonstrated by bonding III–V layers onto SOI prior to laser fabrication.

15.2.6 Heterogeneous (Wafer-Scale) Integration

A new heterogeneous integration methodology is the transfer of thin crystalline III–V films onto an SOI host substrate. The silicon is typically patterned prior to the transfer, and the III–V films are processed after transfer allowing for the use of standard lithography-based patterning techniques used to fabricate III–V lasers. The alignment of the optical modes is determined by the lithography, which allows for an extremely repeatable fabrication process and coupling efficiencies near ~ 1 dB between the III–V regions and the passive silicon regions as demonstrated by Park et al. [103]. The following section will focus on the new heterogeneous platforms and devices.

Direct wafer bonding is commonly used to mate lattice mismatched semiconductors such as AlGaAs and GaP for high power LEDs, InGaAsP, AlAs and GaAs for improved mirror reflectivity in long wavelength VCSELs, and InGaAsP and AlGaAs for high characteristic temperature T_0 lasers [104]. This process consists of a thorough cleaning of the sample surface to remove all semiconductor particles that were generated during dicing or cleaving as well as all organics on the surface. Next a chemical surface treatment is employed to remove any surface native oxides or other stable surface states. The samples are then placed in physical contact with each other and undergo spontaneous bonding and are held together with Van der Waals forces. This bond is relatively strong, depending on the two material systems being bonded, but is further strengthened through a high temperature anneal (typically 600 °C or higher) while applying pressure on the bonded sample. The high temperature anneal results in the formation of covalent bonds at the bonded interface, while the pressure on the sample compensates for any waviness or surface roughness and ensures greater surface area contact between the two materials.

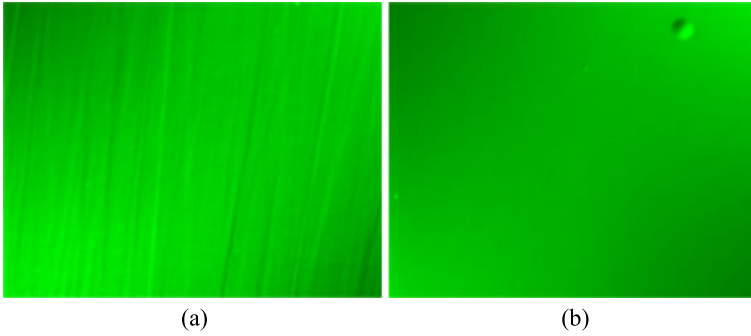


Fig. 15.19 Nomarski microscope images, showing the surface roughness of the transferred III–V surface at bonding temperatures of (a) 600 °C and (b) 250 °C

The substrate of one of the material systems is then removed by using a wet etch resulting in the transfer of one epitaxial layer structure to another.

The difference in the thermal expansion coefficient of silicon ($\alpha_{Si} = 2.6 \times 10^{-6}/\text{K}$) and InP ($\alpha_{InP} = 4.8 \times 10^{-6}/\text{K}$, cf. Table 15.1), thermal damage, and doping diffusion pose a large challenge for achieving high quality with active region transfer to silicon through direct wafer bonding. As samples cool down from 600 °C to room temperature, the InP begins to fracture since the thermal stress built up was larger than the fracture energy of the InP. Mild success in preserving the III–V material can be achieved by thinning the substrate of the InP to $\sim 150 \mu\text{m}$ between the spontaneous bonding step and high temperature anneal steps. The thinned III–V materials conform more easily to the silicon without accumulating enough stress to fracture the III–V but show cross hatching and material waviness in the transferred III–V materials (Fig. 15.19(a)). Figure 15.19(b) shows a Nomarski mode microscope image of the top surface of an InAlGaAs active region layer structure transferred to silicon after 250 °C anneal. The Nomarski mode of the microscope shows the polarization dependence of the surface reflection and is useful for seeing surface particles and roughness.

The thermal mismatch stress σ of the bonded wafers is given by:

$$\sigma = \frac{E}{1 - \nu^2} \left(\frac{\frac{E_{InP}}{1 - \nu_{InP}^2} \alpha_{InP} h_{InP} + \frac{E_{Si}}{1 - \nu_{Si}^2} \alpha_{Si} h_{Si}}{\frac{E_{InP}}{1 - \nu_{InP}^2} h_{InP} + \frac{E_{Si}}{1 - \nu_{Si}^2} h_{Si}} - \alpha \right) \Delta T \quad (15.9)$$

where α is the thermal expansion coefficient, h is the thickness of the substrate, E is Young's modulus, ν is Poisson's ratio, and ΔT is the difference between the bonding temperature and room temperature. The critical stress $\tau_{critical}$ required to generate dislocations in InP is empirically formulated by Pasquariello et al. using the theory of stress induced dislocation generation [105] as:

$$\tau_{critical} = 898 \exp\left(\frac{5934}{T}\right) \quad (15.10)$$

Fig. 15.20 Critical dislocation generation stress in InP and shear stress between InP bonded to silicon vs. temperature [106] (reproduction under permission of the Institute of Electrical and Electronic Engineers)

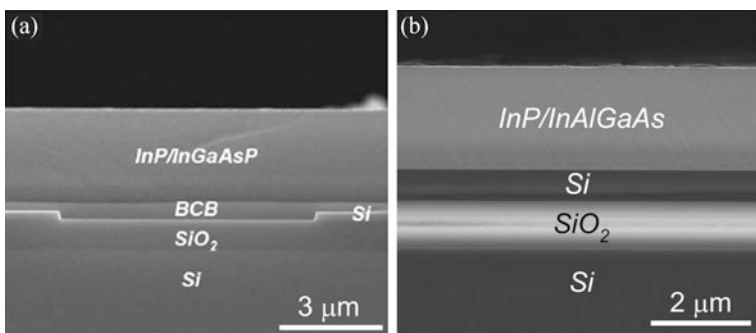
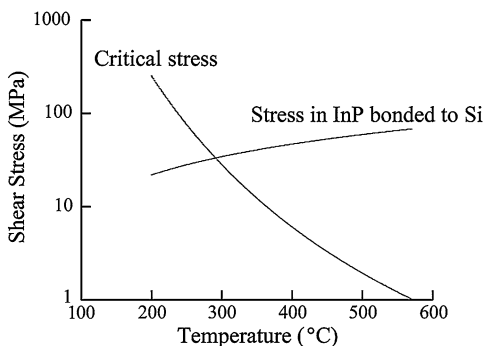


Fig. 15.21 SEM cross-sectional images of (a) DVS-BCB [107] and (b) LTOPA [108] bonding to integrate InP thin epitaxial films on an SOI substrate

Figure 15.20 shows a plot of the critical stress and the shear stress as a function of temperature. In order to prevent the generation of dislocations in the InP, the bonding temperature must be kept below 300 °C. Two low-temperature III–V film transfer approaches have been used to yield electrically pumped lasers on silicon. The first uses polymers such as divinyl-tetramethyldisiloxane-benzocyclobutene (DVS-BCB) as a 300 nm thin adhesive layer between the III–V region and the waveguide as shown in Fig. 15.21(a) [107], and the second uses low-temperature oxygen plasma-assisted (LTOPA) wafer bonding where the interfacial oxide with around 15 nm thickness is too thin to be seen in the SEM image of Fig. 15.21(b) [108]. Detailed studies of polymer-based and LTOPA bonding can be found in [109] and [110], respectively. The transferred InP-based epitaxial thin film acts as a gain medium to generate photons when carriers are injected optically or electrically. Then the light can be evanescently coupled into the SOI waveguide underneath as long as the interface material (i.e. polymer or oxide) is sufficiently thin.

Figures 15.22(a) and (b) are the LTOPA wafer bonding-based heterogeneous silicon evanescent platform (HSEP) cross-sectional schematic and SEM image, showing a heterogeneous waveguiding structure formed by bonding III–V epitaxial layers onto the SOI substrate. The typical anneal temperature is kept at 300 °C in all devices made on this platform and discussed in this section. The small index differ-

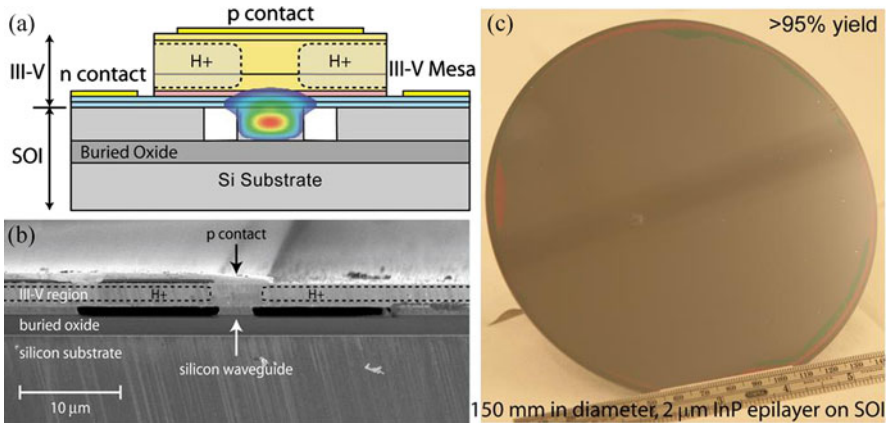


Fig. 15.22 (a) Cross-sectional schematic and (b) SEM image of heterogeneous Si evanescent platform [108]; (c) 150 mm diameter, 2 μm thick InP epitaxial transfer on SOI with >95% yield [112]

ence between Si and III–V materials enables a large freedom in manipulating modal confinement in Si and the III–V semiconductor, which is realized by adjusting the III–V layer thickness, the SOI waveguide dimension [111], and the rib etch depth. The large index contrast for SOI waveguides can tremendously reduce the chip size and power consumption and enhance the integration complexity and yield. Unlike the conventional flip-chip die bond to place discrete active components on passive chips, HSEP eliminates effort and loss in alignment and modal mismatch and literally millions of devices can be made with one bond. Proton implantation in III–Vs creates a current flow channel resulting in good gain and optical mode overlap. Scale-independent integration [110] is demonstrated up to the presently largest InP substrates of 150 mm in diameter in Fig. 15.22(c) [112]. No degradation in bonding quality or increase of processing complexity was observed as the process was scaled up to 150 mm, indicating the possibility for low-cost mass production. Bonding and III–V device back-end processing, both conducted at temperatures less than 350 $^{\circ}\text{C}$, are completely CMOS-compatible.

Since the first demonstration of epitaxial III–V layer transfer onto SOI, there have been several lasers fabricated with various designs for different applications. Distributed feedback (DFB) lasers [113–115], distributed Bragg reflector (DBR) lasers [116, 117], microring/microdisk lasers [118, 119], arrayed waveguide grating (AWG) multi-wavelength lasers [120, 121], and tunable lasers [122, 123] are some of the prominent laser designs demonstrated in this platform. Figure 15.23 shows an SEM image of an electrically pumped heterogeneous silicon DFB laser along with its optical spectrum. A recent result [124] showed a 200 μm long DFB laser with low threshold current of 8.8 mA and achieved 12.5 Gb/s data transmission using direct modulation. A more compact DFB laser design, using hyperbolic materials, for optical interconnect applications is discussed in [125]. Microring lasers with 50 μm diameter and threshold current <5 mA have also been reported [126], and sub-mA threshold operation has been demonstrated in a DVS-BCB (divinylsiloxane-bis-

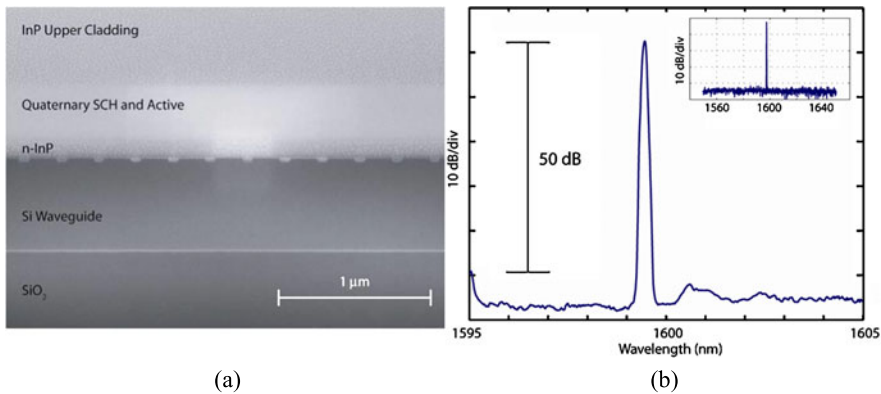


Fig. 15.23 (a) SEM image of longitudinal cross-section of heterogeneous Si DFB laser; (b) optical spectrum showing 50 dB of side-mode suppression. *Inset* illustrates single mode lasing over 100 nm span [113]

benzocyclobutene) bonded disk laser with 7.5 μm disk diameter by Van Campenhout et al. [119]. All these results show promise of dense on-chip laser integration for high bandwidth intra-chip communication with low power consumption.

Heterogeneous integration on the one hand helps to reduce the cost of an individual laser due to increased wafer size, and on the other hand can also enable novel laser designs that use more than one photonic element to improve the laser characteristics for a specific application. The photonic circuit techniques described here can evolve in parallel with material advancements and can be optimized separately. We will discuss one example of such a circuit technique to reduce the laser linewidth. The linewidth of a semiconductor laser can be reduced significantly by reducing the loss of the optical cavity and by reducing the confinement factor, which is defined as the ratio of the carrier confined volume to the volume occupied by the photons in the laser cavity. The confinement factor can be further approximated as a product of confinement factors for each of the laser dimensions, viz. lateral, transverse and longitudinal confinement factor.

A narrow linewidth heterogeneous DFB laser on silicon was recently realized by reducing the loss and transverse confinement factor of the optical mode. This was achieved by designing a high-Q hybrid resonator with a grating in silicon to reduce the optical losses so that very little modal overlap with the pumped quantum wells was needed to provide gain. The high-Q silicon resonator is fashioned from a silicon waveguide patterned with a 1D grating (see Fig. 15.24(a)). Coupling to radiation modes is minimized via a bandgap-modulated defect section in the middle, over a spatial width marked as L_d in Fig. 15.24(a), with uniform grating reflectors of length L_m on either side. The defect is designed directly in the frequency domain by parabolically modulating the lower-frequency band edge of the grating as a function of position localizing a resonant mode with a Lorentzian profile in both real and reciprocal space along the resonator (Fig. 15.24(b)). The lowest measured linewidth reported for this laser structure is 18 kHz, as shown in Fig. 15.24(c) [127].

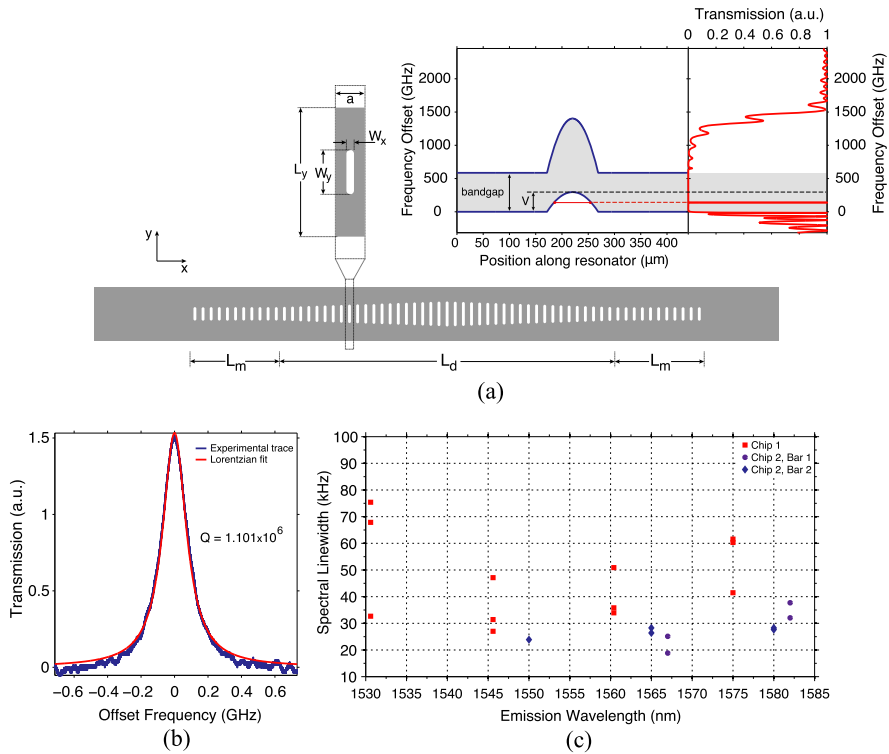
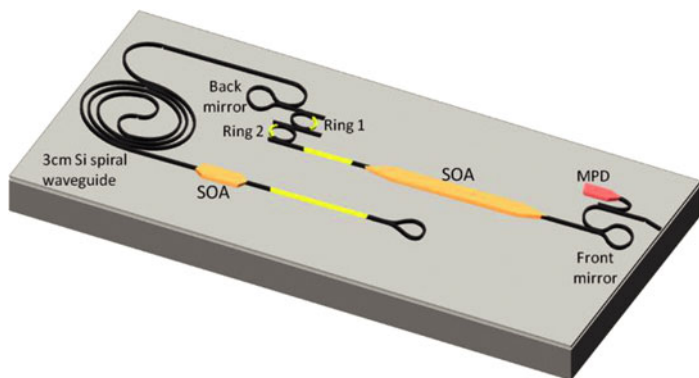


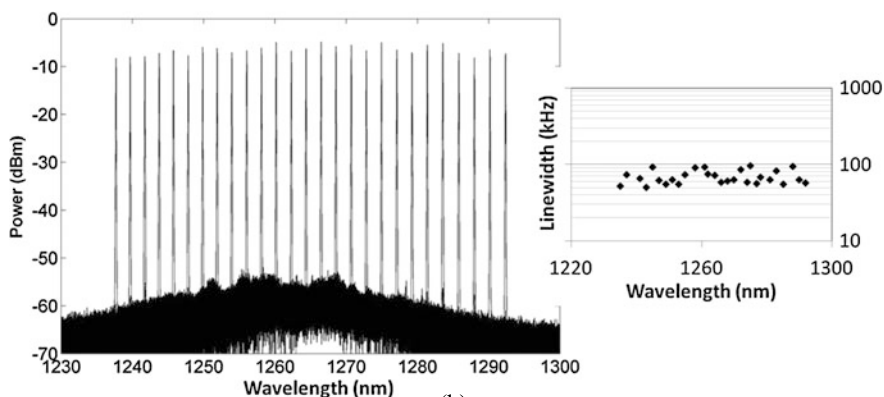
Fig. 15.24 (a) Schematic top view of grating in silicon along with spatial band structure of high-Q hybrid resonator plotted against simulated transmission spectrum. (b) Experimental trace and Lorentzian fit of transmission resonance of high-Q silicon resonator. (c) Distribution of spectral linewidths of high-Q hybrid lasers as a function of emission wavelength [127]

It is expected that this linewidth can be improved even more by further reduction of the transverse confinement factor by lowering the number of quantum wells and/or increasing the spacer oxide thickness between the III–V epitaxial layers and silicon.

Linewidth reduction of tunable lasers can also be achieved by decreasing the longitudinal confinement factor (as detailed in [128]). One corresponding implementation consists of a short active section coupled to a longer passive section by a semitransparent mirror (e.g. 60% reflectance), where wavelength tuning is achieved using two silicon waveguide based cascaded ring resonators with slightly different diameters. This monolithic tunable diode laser showed a linewidth < 100 kHz over 54 nm tuning range near the O-band (see Fig. 15.25(b)) [128]. Further optimization of the filter design and the back mirror reflectivity can improve the linewidth even further. Altogether, these heterogeneous integration schemes show great promise with respect to realizing novel photonic integrated circuits which offer superior laser characteristics combined with small size, low weight, low power consumption and attractive cost.



(a)



(b)

Fig. 15.25 (a) Schematic view of tunable laser design with integrated external cavity. Tuners are *yellow* (two phase sections and two rings for wide tuning), and SOAs are *orange* (one is the laser active section, and one is used as an ON/OFF switch or to control the level of feedback). The monitor photodiode (MPD) is used to measure the laser output power for adjustment of laser parameters. (b) Overlapping spectra showing >54 nm tuning range with SMSR >45 dB (resolution bandwidth: 0.02 nm \cong 2.5 GHz) along with the corresponding measured linewidth [128]

15.2.7 Industrial Development and Commercialization

While it has been a research interest to enable a Si-based light source in academia for decades, industry has sped up the pace in R&D and commercialization over the past 15 years, aiming to progress along the lines of Moore’s law. In this section, we review the mainstream technology, near-future and long-term trends and highlight some related recent research results to enable an on-chip Si laser for datacom and telecom applications.

The first successful commercialization route was to take prefabricated III–V lasers, either edge-emitters or VCSELs, and amplifiers and die bond these elements onto a passive planar lightwave circuit (PLC), e.g., silica-based PLC initially and

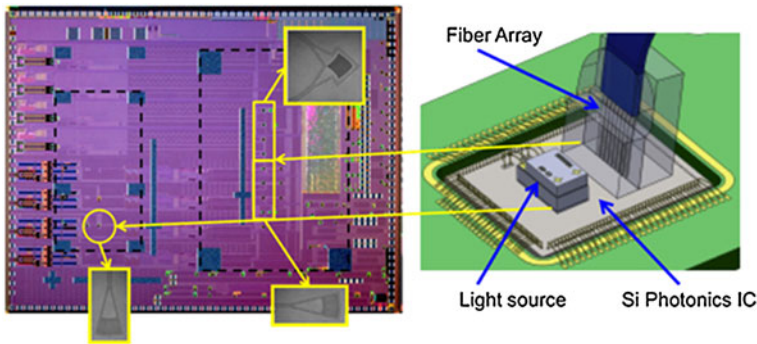
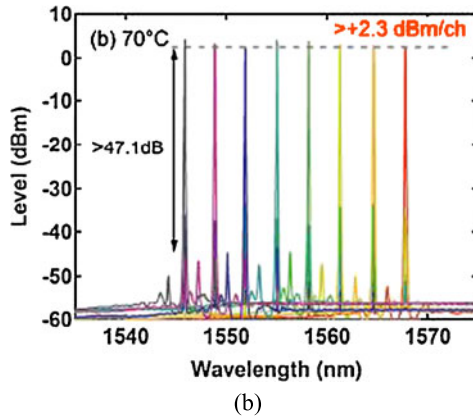
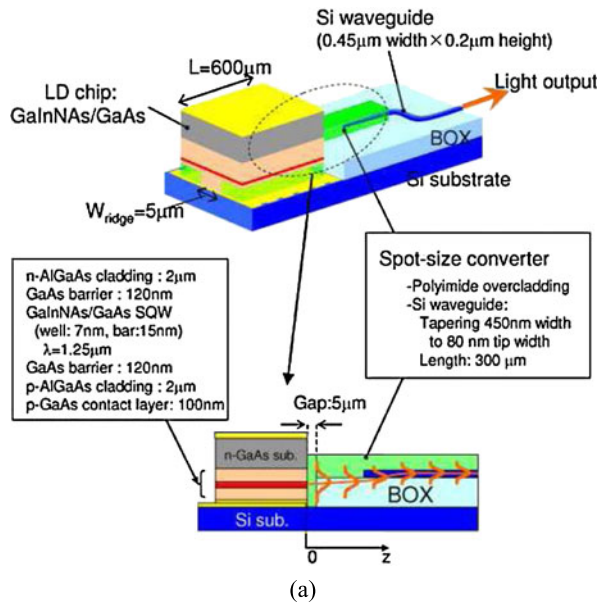


Fig. 15.26 Luxtera Si photonic transceiver chip photograph and packaging cartoon with laser module and optical fiber assembly attached to the top surface of Si CMOS photonics die [129]. Courtesy of Luxtera

shifting to CMOS Si PLCs right now. This solution provides an optical carrier with high power capability and state-of-the-art performance with low threshold current, low relative intensity noise (RIN) and high wall-plug efficiency [130, 131]. It also relies on mature devices and allows the prescreening of the lasers before assembly to ensure good reliability. Therefore, it has been the mainstream approach for photonic interconnect products in the current market. Figure 15.26 are a photograph of a Luxtera's 40 Gbit/s transceiver product chip and packaging cartoon showing a cw DFB laser module flip-chip bonded on a Si CMOS photonic chip [129]. The cw laser output is sent into the CMOS photonic chip through near-vertical couplers based on diffraction gratings, and split into 4 streams to feed 4 independent MZI modulators. The company's newest 4×26 Gbit/s transceiver module still employs a similar architecture as the previous 4×10 and 4×14 Gbit/s products, showing data handling expandability [132].

In addition to grating couplers, edge coupling via a spot size converter is another popular approach. Though it takes more fabrication effort to make a spot size converter than a grating coupler, a spot size converter has the advantage of a much larger optical bandwidth than a grating coupler. Figure 15.27(a) shows the schematic of a III–V diode laser die flip-chip bonded onto the Si substrate of an SOI wafer and output aligned with a spot size converter in the Si waveguide [133]. The 600 μm -long FP laser cavity is defined by two as-cleaved facets. In order to keep the excess loss within 1 dB, the offset in the lateral direction needs to be less than $\pm 0.9 \mu\text{m}$. This value can be improved up to $\pm 1.5 \mu\text{m}$ by tapering the overcladding layer to an input width of 8 μm . In the vertical direction, the offset has to be less than $\pm 0.4 \mu\text{m}$, which leads to a tight control of III–V substrate and AuSn thickness. The reported throughput is about 60 chips/hour [133]. Taking account of the alignment accuracy of the flip-chip bonding machine, the coupling efficiency is estimated to be 35% in the worst case and 85% in the best case based upon a theoretical investigation, similar to the efficiency of grating couplers. However, this integration scheme gains an advantage in better thermal management. As reported in the literature and to be

Fig. 15.27 (a) Schematic illustration of laser diode chip integrated on Si waveguide with spot-size converter [133]. (b) 8- λ superimposed spectrum of flip-chip bonded AlGaInAs DFB laser array under 100 mA \times 8 channel simultaneous operation at 70 °C [136]



discussed in more detail later in this section [134, 135], heat dissipation in III–V-on-SOI structures is a serious problem for device performance and can pose a reliability issue as well. The thick BOX layer blocks the heat from the III–V junction, so TEC cooling at the Si substrate is of very little use. By partially removing the top Si layer and the BOX layer, the III–V die can get direct contact with the Si substrate through a thin AuSn layer which ensures efficient heat dissipation. An impressive characteristic temperature (T_0) of 132 K was therefore obtained from a GaInNAs-based QW structure with 1250 nm emission wavelength [133]. Very recently an 8-channel multi-wavelength hybrid laser array was also demonstrated based upon the same platform (Fig. 15.27(b)) [136]. Benefiting from high-performance InAlGaAs-based

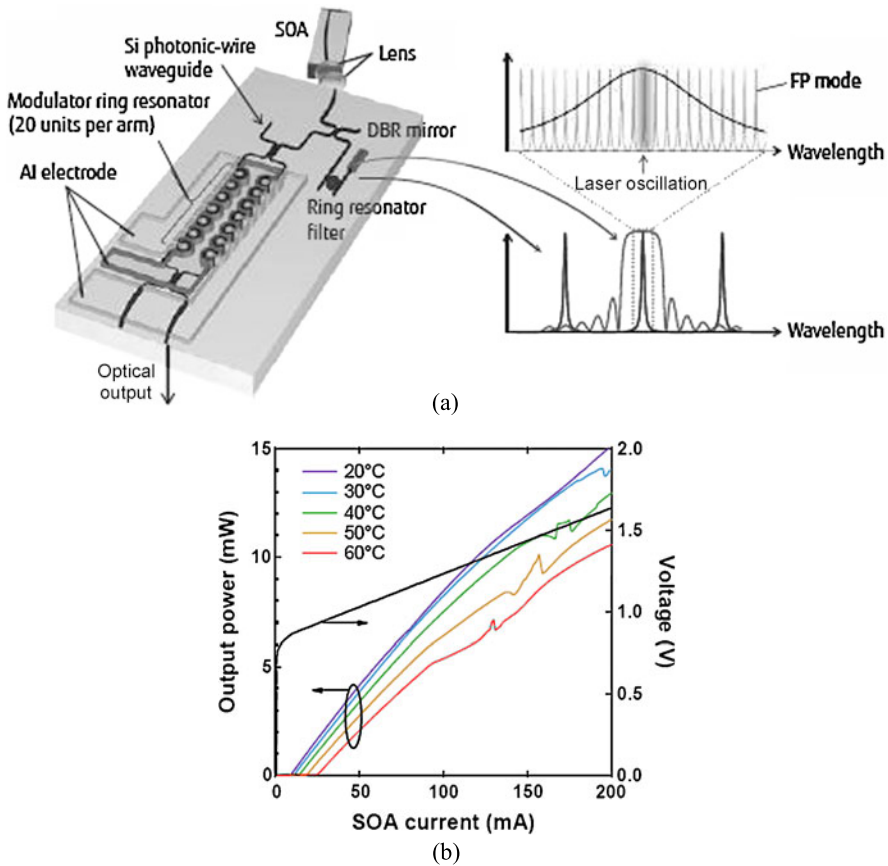


Fig. 15.28 (a) Structure of integrated optical transmitter and laser wavelength selection mechanism [137], (b) temperature-dependent light-current-voltage (LIV) characteristics of Si hybrid laser [138]

DFB laser arrays, the lasing wavelength is pushed to the 1550 nm window, and the hybrid chip shows excellent spectral characteristics even at 70 °C.

Figure 15.28 illustrates a similar design which takes advantage of the same good heat dissipation principle, however, the III–V part is only an SOA which provides optical gain, and a FP laser cavity is defined by the high-reflection facet of the SOA and a Si DBR mirror in order to achieve single wavelength emission and wavelength tunability [137, 138]. As Fig. 15.28(a) shows, a properly designed DBR limits the reflector bandwidth to less than a FSR of the microring resonator so that single-wavelength emission is assured, and also allows some microring resonance shift due to fabrication imperfection and environment change. Furthermore, since both the DBR and the microring are pure Si components and in close physical proximity, the temperature shift tends to move the DBR reflection band and ring resonance by about the same amount, so that only very little (or even zero) tuning effort is

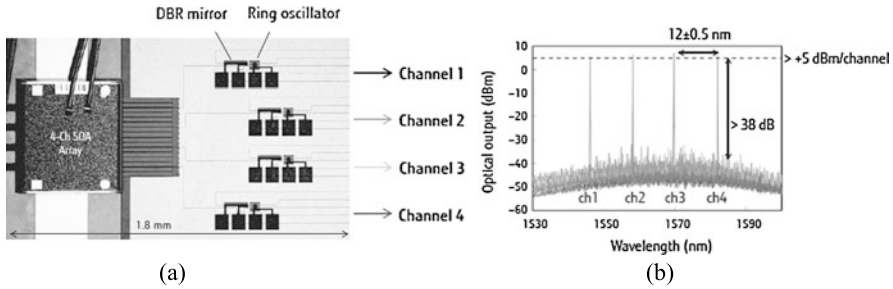


Fig. 15.29 (a) Microscopic image of a fabricated 4-ch Si hybrid laser array, (b) spectrum of 4-ch Si hybrid laser array [137]

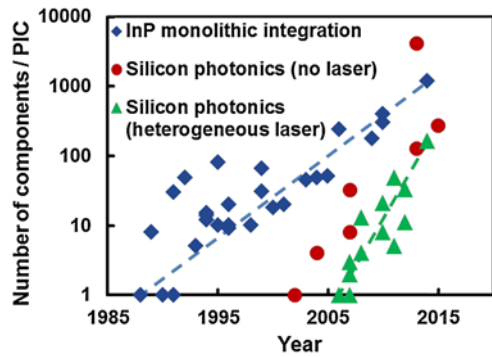
required. The coupling between the SOA die and the Si waveguide does also rely on a spot size converter. Si waveguide components have typically lower loss than III–V counterparts, so they can be fabricated in well-controlled CMOS technology, and as a consequence can lower the laser’s cost. Figure 15.28(b) shows the temperature-dependent LIV characteristics of this flip-chip bonded Si hybrid laser [138]. The threshold current is as low as 9.4 mA at 20 °C and 25 mA at 70 °C, and a good wall-plug efficiency (WPE) from 7.6 to 4.5% in this temperature range is also achieved.

A hybrid CWDM laser array was also demonstrated recently based upon a large gain bandwidth SOA chip [137]. Figure 15.29(a) shows the fabricated 4-channel device with an SOA size of $1.8 \times 1.1 \text{ mm}^2$. The same microring resonator is used for each channel and their FSR is designed to be around 12 nm. Each Si DBR is designed differently so that each Bragg wavelength coincides with one of the consecutive microring resonances. Figure 15.29(b) demonstrates the lasing spectra showing four well-defined lasing peaks with over 5 dBm output for each channel and 38 dB side-mode suppression ratio [137].

Besides Luxtera, Acacia Communications is another company employing the external coupling approach for 100G+ metro solutions. Their transceivers consist of a coherent silicon photonic integrated circuit, which is co-packaged with a low power ASIC/DSP chip and an external laser. The laser serves as the input to the modulators and as the local oscillator for the receiver as well [139]. The company has been shipping 100G C form-factor pluggable (CFP) PM-QPSK transceivers with total power consumption of <24 W for the whole package and has recently announced a new 400G transceiver module set to ship later in 2015.

Since CMOS foundries normally do not allow any non-CMOS compatible (“exotic”) materials into their fabrication line, packaging III–V dies, either fabricated lasers or optical gain chips, with a Si photonic chip in the backend process is a logical first step to realize a reliable silicon photonics light source. However, inevitable loss and reflection at the coupling interfaces, moderate fabrication efficiency, considerable cost of the chip alignment step, and conflicting demands of small dimensions of the III–V material based devices vs. minimum III–V chip size required for reliable handling during packaging (resulting in inefficient III–V real estate usage) all limit the long-term competitiveness of this approach in the fast

Fig. 15.30 Development of chip complexity measured by the number of components per chip for InP-based photonic integrated circuits (blue) and silicon based integration distinguishing PICs with no laser (red) or with heterogeneously integrated lasers (green), which fit to exponential growth curves (dashed) [145]

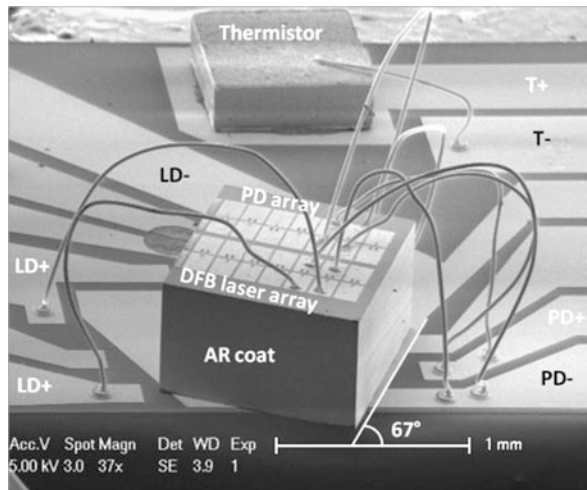


growing Si photonics market. The new heterogeneous approach discussed earlier in this chapter (see Sect. 15.2.6), which is based upon the transfer of a III–V epitaxial layer onto a Si photonic chip by direct wafer bonding and subsequent definition of the device structure, is a more attractive solution [107, 108, 140, 141]. Among industrial companies Intel had taken a leading position in the execution of early advanced research and later product commercialization. In 2010 Intel demonstrated a 50 Gbit/s heterogeneous transceiver based on 4-transmitter channels with 12.5 Gbit/s Si MZI modulators fed by four heterogeneously integrated DBR lasers, and four Ge-based photodetectors in the receiver [142]. Three years later, Intel announced engineered samples of 100 Gbit/s Si photonics modules with heterogeneously integrated lasers [143]. HP recently launched a program called “The Machine”, in which photonic interconnects will eventually replace conventional copper cable and provide low-power consumption, high-speed data transmission between a new generation of computing cores and memories [144]. Heterogeneously integrated Si lasers are likely to serve as the optical engines in this photonic interconnect system.

Since the first demonstration of the heterogeneous device platform in 2005 [146], there has been an extremely fast progression in both advanced research and product engineering [141]. Figure 15.30 indicates that the growth of the number of components/PIC in the heterogeneous Si platform doubles every year compared to 2.6 years for InP PICs [145]. The mature CMOS technology and profound knowledge database accumulated during decades of research on PICs for telecom applications fuel the acceleration in device design and fabrication. Highly improved yield, scaling potential and shorter processing time as demonstrated by recent studies of III–V-to-Si direct wafer bonding have paved the way for efficient mass production [110, 147]. Reliability has remained the last major concern, but fortunately, encouraging results were recently demonstrated from UCSB [148].

In the UCSB study, heterogeneously integrated Si DFB lasers similar to previously demonstrated DFB devices [113] were used. As it is known that superlattices can serve as effective buffer to block the propagation of threading dislocations in III–V-on-Si heteroepitaxy [58, 59, 149], similar superlattice structures were designed in the bonding III–V epitaxial layers. In order to the study whether potential bonding-induced defects at the III–V/Si interface would cause reliability issues,

Fig. 15.31 Side-view SEM image of complete carrier used in aging test [148]



three epitaxial structures (A, B or C) with the following key characteristics (full details are given in [148])

- A: unstrained superlattice layers close to the bonding interface
- B: strained (-1% well, 1% barrier) superlattice layers close to the bonding interface
- C: control design with thicker n-InP layer to obtain similar heterogeneous optical mode profile

were transferred to pre-patterned SOI chips, and a total of 3000 laser diodes were characterized. Each laser diode was integrated with an on-chip photodetector to screen out defective lasers. The dimensions of a single die, comprising 300 laser diodes each, were $8\text{ mm} \times 8\text{ mm}$. Fourteen typical devices of each epitaxial structure were selected for aging tests. For that purpose the initial dies were further diced into smaller chips, each comprising of two lasers with the same grating design, waveguide facets were polished and AR coated, and a 7° angle for the output Si waveguide was chosen to minimize reflections. The dies were placed on ceramic sub-mounts using silver epoxy for good thermal contact. In order to collect light from a surface normal detector the dies were mounted at a 23° angle from normal using the flip-chip bonder. The devices were wire-bonded to the pads on the sub-mount alongside a thermistor. An SEM image of a complete carrier is shown in Fig. 15.31 [148].

The aging tests were done at five different temperatures, viz. 25°C , 50°C , 60°C , 70°C and 85°C while the devices were driven with 80 or 100 mA. Room temperature (25°C) LI curves were taken at certain intervals during the aging test. The threshold current during the period of aging, at different bias conditions and temperature, is shown in Figs. 15.32(a)–(f). Regardless of design and aging conditions, most devices exhibited no significant degradation in this time period. Only two devices showed increased threshold with time at 70°C . With 50% increase in threshold

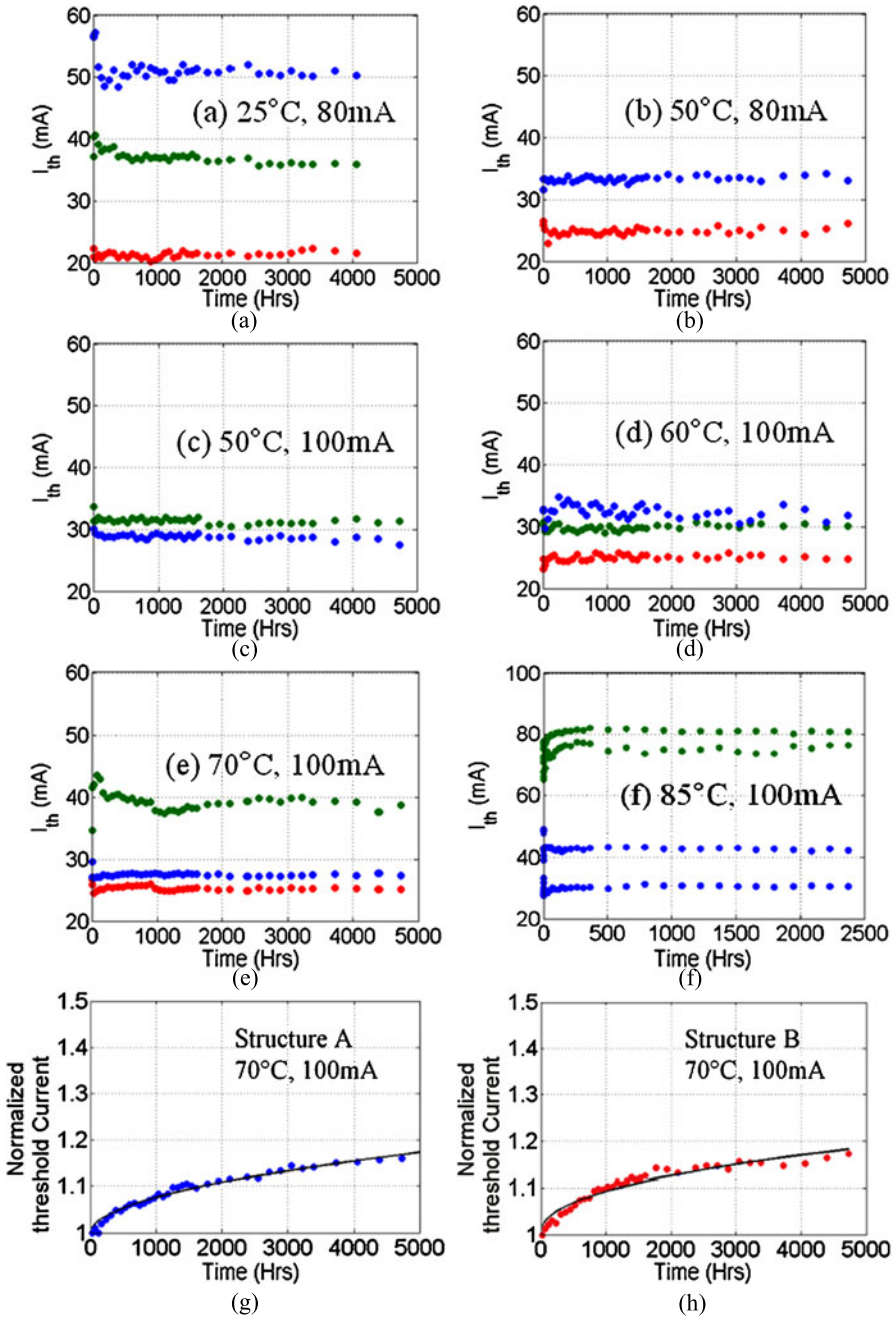


Fig. 15.32 (a)–(f) Threshold current of devices under various aging conditions—Structure A (blue), structure B (red) and structure C (green). (g), (h) Degradation data for two structures along with the sub-linear fit (black)

as failure criterion, the two equations below are used for a sub-linear fit to evaluate the mean time to failure (MTTF):

$$I_{th}/I_{th}(0) = 1 + at^m \quad (15.11)$$

$$MTTF = \left(\frac{0.5}{a}\right)^{1/m} \quad (15.12)$$

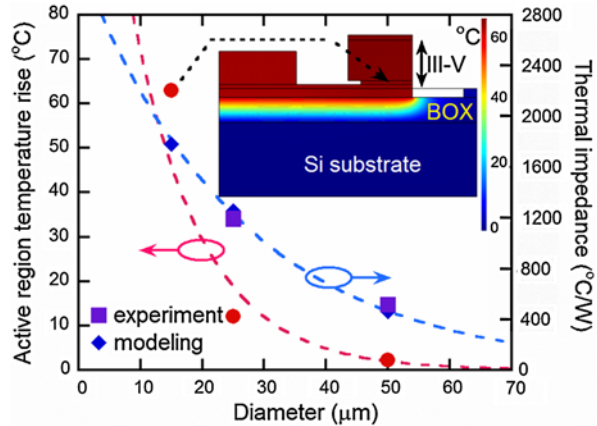
where I_{th} and t are threshold current and aging time, respectively. The values for the fitting parameters a and m for the data shown in Figs. 15.32(g) and (h) are as follows: Structure A: $a = 0.004678$, $m = 0.43$ and structure B: $a = 0.002215$, $m = 0.51$. This corresponds to MTTF values, at 70 °C, of 49,000 hrs and 40,000 hrs for structures A and B, respectively. Due to insufficient lifetime of devices with structure C corresponding laser lifetimes could not be determined [148].

A subsequent TEM study on one of the failed devices did not reveal any sign of defect propagation towards the MQW active region, indicating that another failure mechanism, e.g., metal-semiconductor contact degradation, dielectric failure, etc. limits the lifetime of the selected device [148]. Additionally, no visible dark line defects were observed in a separate electroluminescence experiment. The reliability study is a necessary requirement en route to commercialization of heterogeneously integrated PICs and we conclude that the technology is suitable for making reliable active optical devices with lifetimes on par with commercially available semiconductor active devices.

High temperature performance of the laser is important, because operation at elevated temperatures cause a shift of the lasing wavelength, lowers the device efficiency, and limits the direct modulation bandwidth. The thermal resistance is strongly influenced by the thick (typically 800 nm or more) buried-oxide layer (BOX) that is required to prevent optical leakage to the Si substrate. While Si with a thermal conductivity of 130 W/mK is one of the semiconductor materials with the best thermal conductivity, SiO₂ is 100× worse in this respect which makes it a thermal bottleneck [134, 135]. Compact device structures, e.g. heterogeneous Si microring lasers, are likely to have higher series resistance and subsequently higher thermal impedance and are more sensitive to thermal issues [150]. Figure 15.33 represents the simulated temperature rise in the heterogeneous microring laser active region at threshold and corresponding thermal impedance values as a function of ring diameter [150]. A finite element method was employed, but simulation is based on experimentally determined device series resistance and threshold current. The predicted temperature increase in the active region is 2.5 °C for $D = 50 \mu\text{m}$ device and it grows exponentially to 63 °C for $D = 15 \mu\text{m}$, which prevents cw lasing for smaller ring diameters [150].

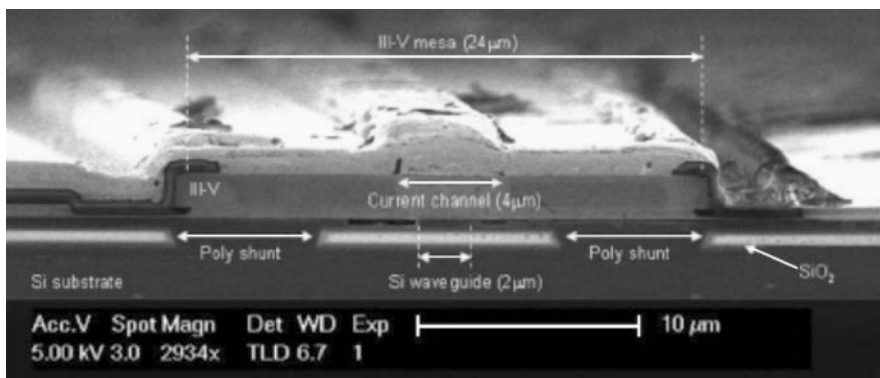
A thermal shunt approach was developed to overcome the heat blocking in the BOX layer [151–153]. The idea was to etch a number of trenches through top Si and the BOX layers within or around the III–V mesa, and then fill the trenches with highly thermal conductive materials. Figure 15.34(a) is an SEM cross-sectional image showing a heterogeneously integrated laser with two thermal shunts composed of poly-Si underneath the III–V mesa [151]. The poly-Si shunts are formed before the bonding process by first etching the trenches, and then backfilling the

Fig. 15.33 Calculated active region temperature rise at threshold and experimental and modeling data for thermal impedance as a function of ring laser diameter. *Inset:* Temperature profile of ring laser ($D = 15 \mu\text{m}$) at threshold (9.4 mA) obtained by FEM modeling [150]

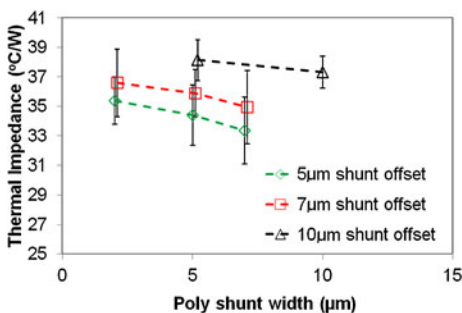


etched region with amorphous silicon, followed by an anneal at 900°C for one hour. Figure 15.34(b) is the measured thermal impedance as a function of poly-Si thermal shunt width and offset from the shunt edge to the Si waveguide center. Wider shunts that are close to the silicon waveguide show the largest decrease in thermal impedance Z_t . A $7\text{-}\mu\text{m}$ -wide block of poly-Si that is $5 \mu\text{m}$ from the center of the Si waveguide reduces the average Z_t of an $800\text{-}\mu\text{m}$ -long FP laser from 41.5 to $33.5^{\circ}\text{C}/\text{W}$. Narrower shunts provide less benefit, as they have a smaller cross section through which heat can flow from the upper Si epitaxial layer into the Si substrate [151].

A more effective thermal management by another thermal shunt design has been implemented in heterogeneous microring lasers [152, 153]. Figure 15.35(a) shows the 3D schematic of such a heterogeneously integrated microring laser whose p-type contact and III–V-on-Si mesa are mostly surrounded by a Au layer, and this Au layer extends to and has contact with the Si substrate after the top Si and BOX layers have been locally removed. The n-type contact inside the mesa is also connected to the Si substrate through another Au thermal shunt. This double metal shunt design enables the Joule heat from the III–V mesa to be effectively “grounded” to the Si substrate through the Au shunts [153]. Figures 15.35(b) and (c) are stage temperature-dependent LI curves for $D = 50 \mu\text{m}$ ring lasers with and without thermal shunts. The first sudden increase in output power (just above 10 mA) corresponds to the threshold. The kinks in the curves, above threshold, correspond to switching in lasing direction. When the stage temperature was at 20°C , both devices exhibited the same threshold current around 12.3 mA. The device without thermal shunt had earlier thermal roll-over in the output power (L – I) curves, and its maximum cw lasing temperature was about 70°C . The device with double thermal shunts, in contrast, was able to lase cw up to 105°C . The L – I curves show a slower thermal roll-over at the same stage temperature while the output power is 8 to 10 dB higher. With the help of this thermal shunt design, the measured thermal impedance of ring lasers with 50 , 30 and $20 \mu\text{m}$ diameter is reduced from 580 , 1031 and $1591^{\circ}\text{C}/\text{W}$ to 364 , 652 , and $1105^{\circ}\text{C}/\text{W}$, respectively. Clearly, 30% to 40% improvement in thermal



(a)



(b)

Fig. 15.34 (a) SEM cross section of heterogeneous silicon FP laser with 5 μm wide poly-Si thermal shunt. The shunts are used to bypass the low thermal conductivity of the SiO₂, and channel heat away from the III–V mesa into the Si substrate, (b) thermal impedance of heterogeneous Si lasers including poly-Si thermal shunts between 2 and 5 μm wide and that are between 5 and 10 μm away from the center of the silicon waveguide [151]

impedance was achieved for the devices with thermal shunts, and the maximum cw lasing temperatures could be raised by more than 35 °C [153]. Cu, instead of Au, can also be used and may lead to even better results due to its higher thermal conductivity compared to Au. Furthermore, Cu is preferred in CMOS processing.

In addition to integrating thermal shunts with heterogeneously integrated devices in order to minimize the BOX layer-induced thermal barrier effect, a more advanced approach is to replace the entire BOX layer by another material which can conduct heat much better and has proper optical properties (e.g., refractive index, absorption coefficient, etc.). Diamond is a good candidate because (i) it exhibits the highest bulk thermal conductivity of all materials found in nature, (ii) has excellent optical properties, and (iii) is CMOS compatible. A recent demonstration of Si-on-diamond (SOD) substrate fabrication and low-loss SOD waveguides constitutes a promising start [154]. However, open questions associated with diamond growth, wafer bonding and device fabrication require additional studies.

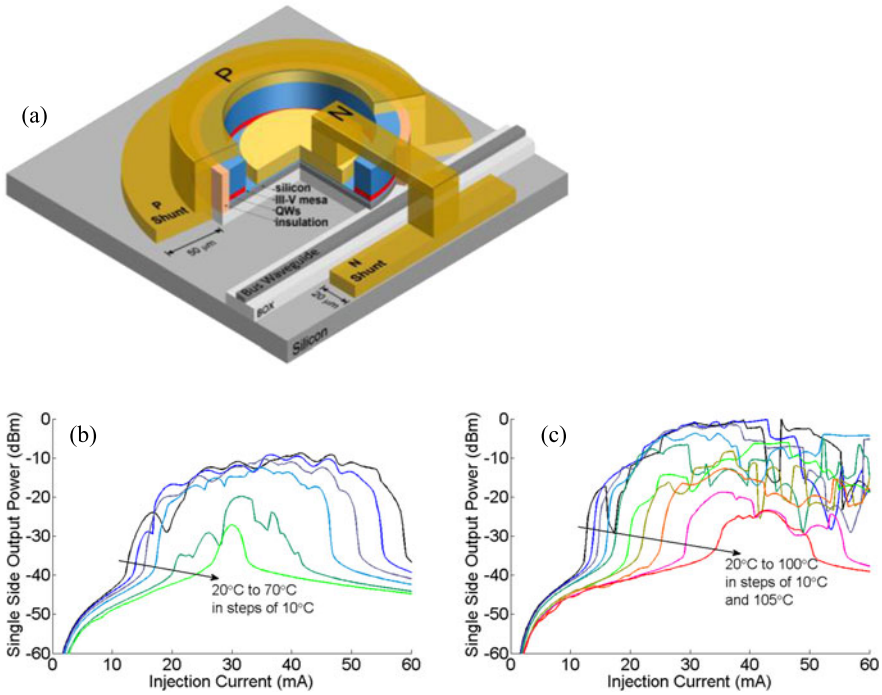


Fig. 15.35 (a) Illustration of heterogeneous Si microring laser with thermal shunts, and *LI* curve of 50 μm in diameter heterogeneous Si microring lasers (b) without and (c) thermal shunt design

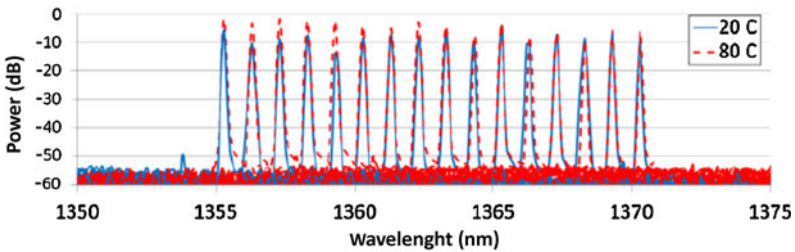


Fig. 15.36 16 wavelength array with 200 GHz spacing, wavelength stabilized at 20 °C and 80 °C [155]

In cases where emission wavelengths have to be locked to a given grid, such as in telecom applications, wavelength tuning and a feedback loop are typically required. Aurrion recently demonstrated an impressive 16-wavelength heterogeneous laser spectra from two adjacent 8-channel, 200 GHz channel spacing arrays [155]. The wavelengths are locked in a range of 20–80 °C (see Fig. 15.36). The output power exceeds 30 mW at RT and exceeds 15 mW at 80 °C, and the SMSR at all

wavelengths of operation exceeds 40 dB. The corresponding diode efficiencies for 20 °C and 80 °C were 17% and 7%, respectively [155].

Without any doubt, the III–V-on-Si heterogeneous integration technology overcomes the fundamentally poor light emission efficiency in Si, and it offers promising CMOS compatibility and good robustness for a wide range of devices. As discussed in Sect. 15.2.4, the recent breakthrough in high-quality QD heteroepitaxy on Si substrates will make the monolithic approach significantly more competitive. As soon as the defect density can be reduced by factor of 10 the number of hours of operation can be increased to a level acceptable for commercialization, and thereafter will be an attractive long-term solution because of its scalability, lower cost and superior device performance. Regardless of which approach is adopted as the final solution for a Si-based light source, the photonic community is looking forward to the vision of photonics-microelectronics integration becoming a reality in the near future with additional market opportunities for the entire semiconductor industry.

15.3 High-Speed Signal Processing in Silicon

The progress in high-speed silicon modulators has been extraordinary in the past decade. Though conventional electro-optic effects are either unavailable (i.e. the Pockels effect [156]), or weak (i.e. the Kerr and Franz-Keldysh effects) in silicon, the free carrier plasma effect has been successfully employed to provide index changes Δn in the order of 10^{-4} – 10^{-3} with reasonable applied voltages. The change of free carrier concentration not only causes the loss variation as according to (15.3), but also determines the index change as given by (15.13) [157].

$$\Delta n = \frac{-q^2 \lambda_0^2}{8\pi^2 c^2 n \epsilon_0} \left(\frac{N_e}{m_{ce}^*} + \frac{N_h}{m_{ch}^*} \right) \quad (15.13)$$

Soref et al. derived the useful empirical equations (15.14)–(15.17) to relate the free carrier plasma effect to the change of index Δn and absorption loss $\Delta \alpha$ in the telecommunication windows at 1.31 and 1.55 μm .

At $\lambda_0 = 1.31 \mu\text{m}$:

$$\Delta n = \Delta n_e + \Delta n_h = -6.2 \times 10^{-22} \Delta N_e - 6.0 \times 10^{-18} (\Delta N_h)^{0.8} \quad (15.14)$$

$$\Delta \alpha = \Delta \alpha_e + \Delta \alpha_h = 6.0 \times 10^{-18} \Delta N_e + 4.0 \times 10^{-18} \Delta N_h \quad (15.15)$$

At $\lambda_0 = 1.55 \mu\text{m}$

$$\Delta n = \Delta n_e + \Delta n_h = -8.8 \times 10^{-22} \Delta N_e - 8.5 \times 10^{-18} (\Delta N_h)^{0.8} \quad (15.16)$$

$$\Delta \alpha = \Delta \alpha_e + \Delta \alpha_h = 8.5 \times 10^{-18} \Delta N_e + 6.0 \times 10^{-18} \Delta N_h \quad (15.17)$$

where ΔN_e and ΔN_h are the respective concentration changes of electrons and holes. Please note the $(\Delta N)^{0.8}$ dependence for holes in the refractive index calculation [157]. An appreciable index change $\Delta n > 1 \times 10^{-3}$ is readily achievable by a moderate doping of about $5 \times 10^{17} \text{ cm}^{-3}$, making the plasma effect the primary phase modulation mechanism in silicon. A more detailed derivation of carrier

change-induced index and absorption variations from the Kramers-Kronig relations can be found in [158], followed by an excellent review of the history of silicon modulator development. The following sections highlight a few of the most recent innovative high-speed optical modulators on a Si substrate.

15.3.1 Silicon Optical Modulators

The first two silicon modulators passing the 10 Gb/s data transmission benchmark utilized a forward-biased MOS capacitor structure, and a ring-resonator p-i-n diode structure, respectively [159, 160]. Further improvement in bandwidth in the former case is limited by large capacitances in MOS capacitors, while the latter case suffered from slow minority carrier generation and/or recombination [161].

A p-n diode-based Mach-Zehnder interferometer (MZI) design demonstrated 50 Gb/s data transmission and more than 40 GHz bandwidth [162]. The device operates in a carrier depletion mode (i.e. reverse-biased), so the depletion region, whose width is W_D , replaces the MOS capacitor separation, resulting in a reduction of device capacitance [163]. W_D is given by

$$W_D = \sqrt{\frac{2\varepsilon_0\varepsilon_r(V_{Bi} + V)}{qN_A}} \quad (15.18)$$

where ε_r , V_{Bi} , V and N_A are the low-frequency relative permittivity of silicon, the built-in voltage, applied reverse bias voltage, and acceptor concentration respectively. The change of depletion region width leads to a change of free carrier concentration and to a related change of the refractive index as well. This subsequently results in an optical phase change $\Delta\phi$

$$\Delta\phi = \frac{2\pi \Delta n_{eff} L}{\lambda_0} \quad (15.19)$$

where Δn_{eff} and L are the effective modal index and the device length, respectively. The MZI geometry converts the phase modulation into an optical intensity modulation.

Figure 15.37(a) is a cross-sectional schematic view of the phase shifter, showing a 0.4 μm -wide p-doped rib waveguide. A special doping profile is designed to place the pn junction in an optimal position for good optical mode overlap and results in the highest depletion in a p-doped rib because the hole density change gives rise to a large index change as described by (15.14) and (15.16). The traveling wave electrode design based on a coplanar waveguide structure is utilized to overcome the RC limitation on modulation bandwidth. The phase modulators were incorporated into an asymmetric MZI structure with an arm length mismatch of 180 μm to convert a phase variation into an intensity modulation. A phase efficiency $V_\pi L_\pi \sim 2.8$ V-cm is obtained in a 1 mm-long phase shifter. Figure 15.37(b) shows the eye diagram of this modulator's optical output at a bit rate of 50 Gb/s. The extinction ratio is

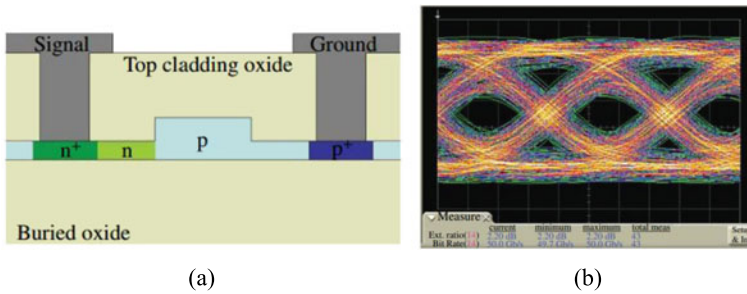


Fig. 15.37 (a) Cross-sectional view of phase modulator (schematic). (b) 50 Gb/s optical eye diagram obtained at 1551.75 nm [162]

measured to be 2.2 dB and was limited by the noise from the EDFA. The eye diagram shows that the modulator is capable of transmitting data at 50 Gb/s, which is consistent with a 3 dB bandwidth >40 GHz. A polarization diversity scheme was realized by modifying the doping profile in the rib waveguide enabling modulators that can operate at 40 Gb/s for both TE and TM polarization [164].

The same research group has also demonstrated ring resonator modulators showing open eyes for data rates up to 40 Gb/s [165]. At this high bit rate the extinction ratio was 1.1 dB only, and this has been attributed to the imperfect electrical signal feeding the device which does not completely reach the 1 and 0 levels during switching. This result is particularly interesting for two reasons. First, ring resonators occupy a very small area and hence allow for dense integration, lowering cost. Second, the small size reduces the device capacitance and hence the power consumption for the modulator is <100 fJ/bit. Furthermore, the total power consumption for ring modulators including the driver can be made as low as a few pJ/bit [166].

15.3.2 Hybrid Silicon Modulators

A similar carrier depletion-mode modulator has also been implemented based on the heterogeneous integration platform discussed in Sect. 15.2.6. The III–V MQW epitaxial layer is transferred onto the SOI waveguide and the carrier density is modulated by a reverse bias. Once the MQWs are in a carrier depletion state, several physical effects, such as band-filling-, plasma-, Pockels-, and Kerr effect, all contribute to the index change. Among all of them, the Pockels effect is the only phenomenon which is sensitive to crystal orientation. In other words, this effect can be additive to the other effects if the optical signal propagates along the right direction, or it can reduce the overall index change otherwise (see also Chap. 8, Sect. 8.2.1.4). On the hybrid silicon platform, the direction of patterned silicon waveguides needs to be aligned to the [011] direction of the III–V material so that the phase shift is maximized, or under the correct angle to make it polarization independent. Figure 15.38 shows simulation results with consideration of all these effects [167]. As can be

Fig. 15.38 Estimated index shift (TE polarization) of a carrier depletion InAlGaAs MQW phase modulator [167]

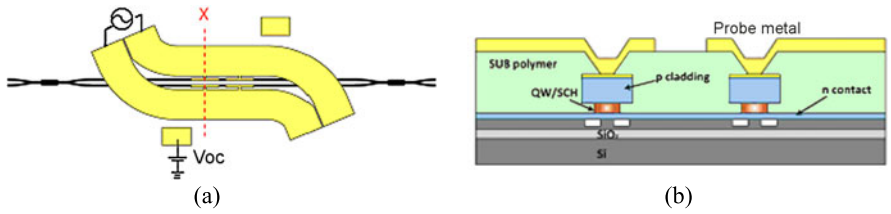
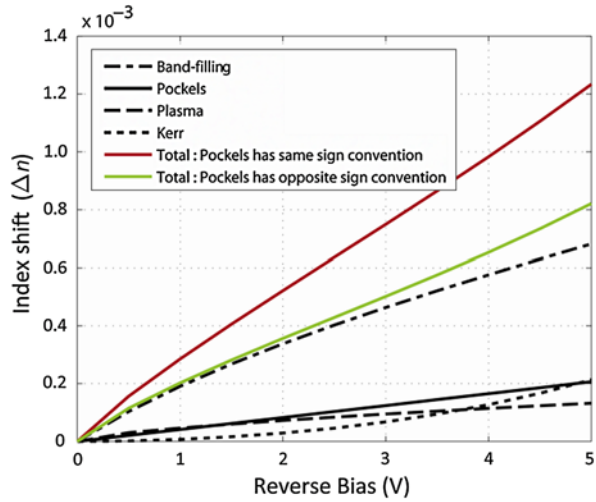


Fig. 15.39 (a) Top view of a device with a CL-slotline electrode. (b) Cross section (along x) of the hybrid waveguide [169]

seen, the index change is proportional to the magnitude of the reverse bias. Moreover, the introduced index shift in the case of orientation match is approximately 1.5 times larger than in the mismatch case.

Targeting MQWs the same reverse-bias operation, a 16-period MQW active region has been designed with a PL peak at $1.36 \mu\text{m}$ in order to achieve high optical confinement in the MQWs and low absorption at $1.55 \mu\text{m}$ [168]. Both, the top SCH layer and the MQWs, are n-type doped in order to introduce free carriers. The thickness and doping of the top SCH layer are carefully designed to result in complete depletion of this layer at zero bias. Thus, all applied bias voltage will be used to deplete the MQW region only. As shown in Fig. 15.39(a), a capacitively loaded (CL) traveling wave electrode (TWE) based on a slotline architecture is adopted to prevent the electrical field from overlapping with the doped semiconductor underneath the metal electrode. This reduces the microwave propagation losses and allows for longer modulators and higher bandwidth. The dimensions on the slotline can also be adjusted for matching the optical group velocity and the microwave phase velocity which also improves the bandwidth.

The device capacitance is reduced by half by using a push-pull scheme because the two diodes on both arms are in series [169]. The cross section of the loaded

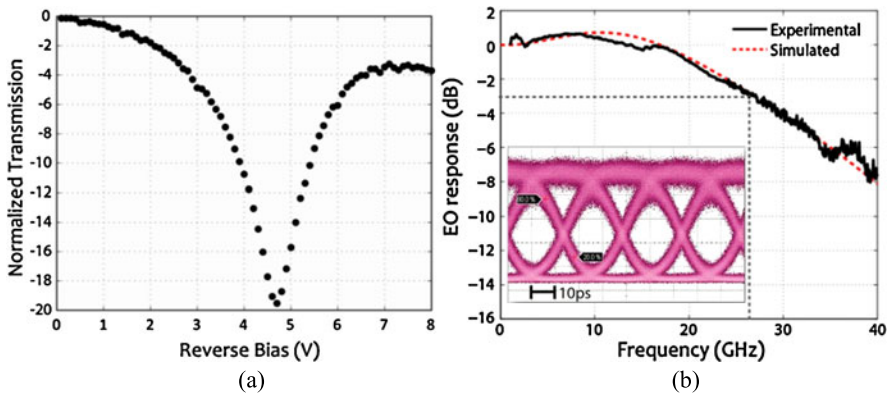


Fig. 15.40 (a) Normalized transmission as a function of reverse bias at 1550 nm for a 500 μm long MZM device. (b) Modulation bandwidth measured at -3 V with 25Ω termination. *Inset*: Eye diagram at 40 Gb/s with 11.4 dB extinction ratio [170]

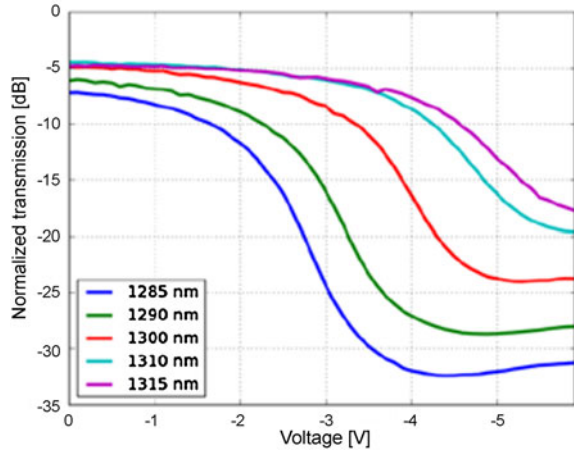
region is depicted in Fig. 15.39(b). The signal and ground of the slotline are on top of each arm, respectively. The two arms have a common ground formed by connecting the n-contact layers together. The cladding mesa is 4 μm wide, and the active region is intentionally under-cut to 2 μm to reduce the device capacitance. The silicon waveguides have a height of 0.47 μm , a slab height of 0.2 μm , and a width of 1 μm . Figure 15.40(a) shows the normalized transmission of a 500 μm long MZM device as a function of reverse bias.

As can be seen, the V_π of a 500 μm long modulator is 4.7 V. This is equivalent to a voltage length product of 2.4 V mm with a static ER of 20 dB. The frequency response of the modulator with -3 V bias across the diode and 25Ω termination is shown in Fig. 15.40(b). The transmission curve indicates a 3 dB cutoff frequency around 27 GHz. There is good agreement between the measured and expected bandwidth. The inset of Fig. 15.40(b) shows open eyes at 40 Gb/s modulation speed with 11.4 dB extinction ratio [170].

In another approach the PL peak of an InAlGaAs-MQW based electroabsorption modulator (EAM) is shifted closer to the operation wavelength which results in a strong quantum confined Stark effect (QCSE) and consequently a high ER. The MQW section of a realized 1.3 μm EAM contained 12 wells and 13 barriers with a PL peak at 1247 nm. This design assured sufficiently low optical absorption, and making the both, the top and bottom SCH undoped, resulted in a reduced overall device capacitance.

The bias dependent optical waveguide transmission curves of the InAlGaAs-MQW EAM measured at different wavelengths are shown in Fig. 15.41. The active section, which has the same cross-sectional geometry as the MZM described earlier, has a 100 μm long effective absorber length with a three level taper design to transfer the mode into and out of the silicon waveguide with an insertion loss <0.5 dB per taper [172]. The total device insertion loss is 4.9 dB for wavelengths greater

Fig. 15.41 Bias dependent transmission curves of InAlGaAs-MQW based electroabsorption modulator at different input wavelengths [171]



than 1300 nm. The static extinction ratio for a 2 V bias change is between 10 dB and 20 dB.

The electrode design is very important for an electroabsorption modulator. It affects the modulation bandwidth, the microwave reflection and the modulation efficiency. Figures 15.42(a) and (b) show the schematic structure and an SEM image of a modulator which uses a traveling wave segmented electrode design with a low impedance 100 μm active modulation segment and a high impedance 160 μm passive transmission line segment in cascade to improve the overall device modulation bandwidth. An undercut process based on selective wet etching was adopted to narrow the intrinsic layer width down to 2.35 μm while keeping the p-InP mesa width of 4 μm as defined by dry etching. A small silicon ridge width of 1 μm was chosen to keep the main part of the optical mode confined in the intrinsic region, giving a confinement factor of 24% in the MQWs. Figure 15.42(c) shows the measured and calculated electro-optical (E/O) modulation response using a 50 Ω off-chip termination at the electrical output of the device. Only a 2 dB drop was observed up to 67 GHz, which was the upper limit of the lightwave component analyzer used. The extrapolation based on simulation (assuming an intrinsic RC time constant of 1.3 ps) gives a 3 dB bandwidth of ~ 74 GHz. With such a large bandwidth, this device is theoretically able to support a non-return-to zero (NRZ) transmission bit rate close to 100 Gb/s [171].

Large signal transmission experiments have been carried out at 50 Gb/s under a bias of -4 V. $2^{31} - 1$ NRZ pseudorandom bit sequence (PRBS) patterns were amplified to a level of around $2.2 V_{pp}$ and applied to the modulator. The input wavelength was set to 1300 nm and the optical power reaching the modulator was around 4 dBm. Figure 15.43 shows the transmission eye diagrams measured for a back-to-back (B2B) configuration and a 16 km long single mode fiber (SMF) link, respectively. All of these diagrams demonstrate widely opened eyes, and correspond to more than 9 dB dynamic extinction ratio [171].

A similar device with a lumped electrode design showed good temperature stability, with open eyes at 40 Gb/s from 20 $^{\circ}\text{C}$ to 80 $^{\circ}\text{C}$ [172]. The peak-to-peak voltage

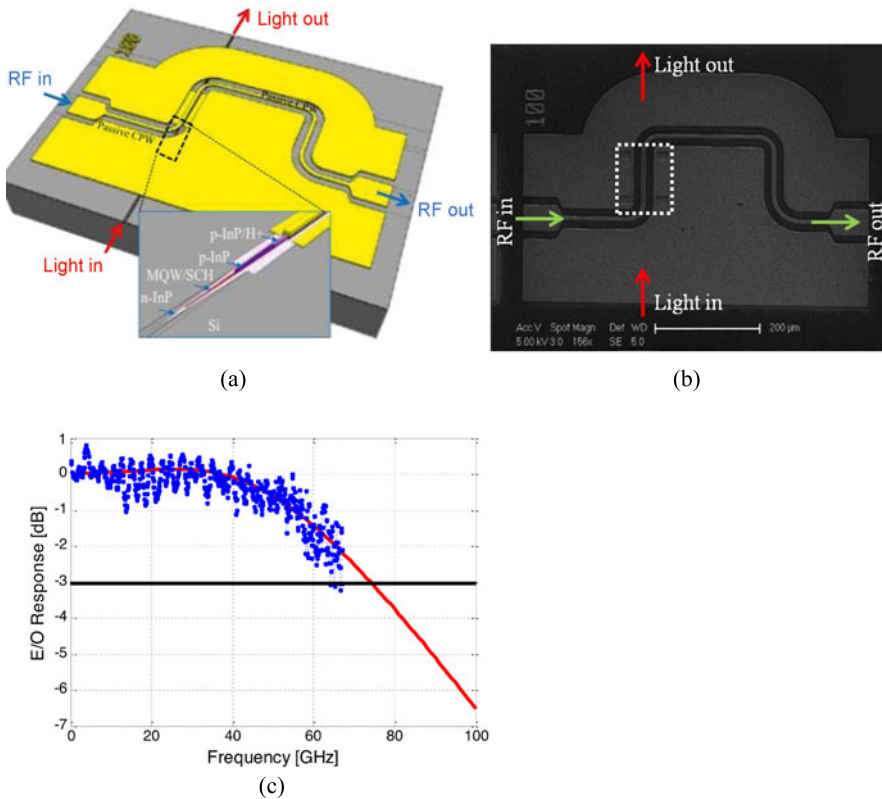


Fig. 15.42 (a) Schematic of heterogeneous distributed silicon modulator. *Inset*: enlarged taper part without the probe metal. (b) Top-view SEM image of the final device. (c) The measured and calculated modulation response for the modulator [171]

applied was only 1 V and the modulator consumed around 112.5 fJ/bit. There have also been recent efforts to incorporate CVD graphene on silicon to potentially fabricate a broadband temperature insensitive modulator. Reference [173] shows the demonstration of a 10 Gb/s graphene-Si electroabsorption modulator operating between 20 °C and 50 °C, in the C band.

The QCSE has also been utilized in strained Ge/SiGe MQW structures monolithically integrated on Si substrates, though the absorption coefficient in SiGe MQWs is still lower than in InP-based materials [174]. Furthermore, it has been reported that strained silicon also exhibits a linear electro-optic refractive index modulation [175]. More recently, there has been an interest in integrating LiNbO₃ on silicon to realize highly linear modulators for analog applications. However, the modulation bandwidth achieved needs much improvement before such devices can be incorporated into large scale systems. In summary, we believe that each of these integrated modulator solutions will soon find its appropriate role in a variety of applications.

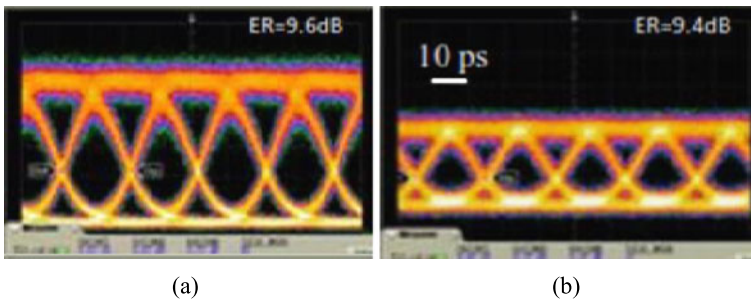


Fig. 15.43 Measured $2^{31} - 1$ PRBS NRZ eye diagrams at 50 Gb/s for (a) a back to back configuration and (b) after 16 km SMF transmission. The modulator under test was biased at -4 V with the input wavelength set at 1300 nm [171]

15.4 Summary

The roadmap of the microelectronics industry development indicates that Si is unlikely to be replaced by other materials. The urgent need to break the “brick wall” of interconnect bandwidth and power consumption in microprocessors plus emerging markets (e.g. fiber-to-the-home) should be a compelling force to make Si the primary host material for PICs as well. Equipped with the recently developed Si lasers, modulators and photodetectors, plus other necessary components demonstrated already or under development, sophisticated Si PICs should become widespread.

Acknowledgements The authors thank DARPA MTO, Intel, Hewlett Packard, and Google for supporting this research.

References

1. J.D. Plummer, M.D. Deal, P.B. Griffin, *Silicon VLSI Technology: Fundamentals, Practice, and Modeling* (Prentice Hall, New York, 2000)
2. G.E. Moore, Cramming more components onto integrated circuits. *Electronics* **19**, 114–117 (1965)
3. http://en.wikipedia.org/wiki/UNIVAC_I
4. <http://www.kurzweilai.net/articles/art0134.html?printable=1>
5. M.K. Smit, Past and future of InP-based photonic integration, in *LEOS Annual Meeting*, Newport Beach, CA, USA (2008), paper MF1
6. L. Thylen, A Moore’s law for photonics, in *Intern. Symp. Biophoton., Nanophoton. Metamater.*, Hangzhou, China (2006), pp. 256–263
7. S.C. Nicholes, M.L. Maanovi, B. Jevremovi, E. Lively, L.A. Coldren, D.J. Blumenthal, The world’s first InP 8×8 monolithic tunable optical router (Motor) operating at 40 Gbps line rate per port, in *Opt. Fiber Commun. Conf. and Nat. Fiber Opt. Eng. Conf. (OFC/NFOEC’09)*, San Diego, CA, USA (2009), Techn. Digest, PDPB1
8. <http://www.itrs.net/>
9. <http://www.eetimes.com/showArticle.jhtml?articleID=214502894>
10. J.W. Raring, L.A. Coldren, 40-Gb/s widely tunable transceivers. *IEEE J. Sel. Top. Quantum Electron.* **13**, 3–14 (2007)

11. L.A. Coldren, InP-based photonic integrated Circuits, in *Conf. Lasers Electro-Opt. (CLEO/QELS'08)*, San Jose, CA, USA (2008), Techn. Digest, paper CTuBB1
12. D. Liang, A.W. Fang, H.-W. Chen, M. Sysak, B.R. Koch, E. Lively, Y.-H. Kuo, R. Jones, J.E. Bowers, Hybrid silicon evanescent approach to optical interconnects. *Appl. Phys. A* **95**, 1045–1057 (2009)
13. L. Pavesi, Optical gain and lasing in low dimensional silicon: the quest for an injection laser, in *Device Applications of Silicon Nanocrystals and Nanostructures*, ed. by N. Koshida (Springer, New York, 2009). Chap. 4
14. P. Jonsson, H. Bleichner, M. Isberg, E. Nordlander, The ambipolar Auger coefficient: measured temperature dependence in electron irradiated and highly injected n-type silicon. *J. Appl. Phys.* **81**, 2256–2262 (1997)
15. R. Soref, J.P. Lorenzo, All-silicon active and passive guided-wave components for $\lambda = 1.3$ and $1.6 \mu\text{m}$. *IEEE J. Quantum Electron.* **QE-22**, 873–879 (1986)
16. L. Dal Negro, M. Cazzanelli, N. Daldosso, Z. Gaburro, L. Pavesi, F. Priolo, D. Pacifici, G. Franzo, F. Iacona, Stimulated emission in plasma-enhanced chemical vapour deposited silicon nanocrystals. *Physica E* **16**, 297–308 (2003)
17. U. Gösele, V. Lehmann, Light-emitting porous silicon. *Mater. Chem. Phys.* **40**, 253–259 (1995)
18. L.T. Canham, Silicon quantum wire array fabrication by electrochemical and chemical dissolution of wafers. *Appl. Phys. Lett.* **57**, 1046–1048 (1990)
19. A.G. Cullis, L.T. Canham, Visible light emission due to quantum size effects in highly porous crystalline silicon. *Nature* **353**, 335–338 (1991)
20. K.D. Hirschman, L. Tsybeskov, S.P. Duttagupta, P.M. Fauchet, Silicon-based visible light-emitting devices integrated into microelectronic circuits. *Nature* **384**, 338–341 (1996)
21. W.L. Wilson, P.F. Szajowski, L.E. Brus, Quantum confinement in size-selected, surface-oxidized silicon nanocrystals. *Science* **262**, 1242–1244 (1993)
22. O. Bisi, S. Ossicini, L. Pavesi, Porous silicon: a quantum sponge structure for silicon based optoelectronics. *Surf. Sci. Rep.* **38**, 1–126 (2000)
23. Z.H. Lu, D.J. Lockwood, J.M. Baribeau, Quantum confinement and light emission in SiO_2/Si superlattices. *Nature* **378**, 258–260 (1995)
24. A.G. Nassiopoulos, S. Grigoropoulos, D. Papadimitriou, Electroluminescent device based on silicon nanopillars. *Appl. Phys. Lett.* **69**, 2267–2269 (1996)
25. A. Malinin, V. Ovchinnikov, S. Novikov, C. Tuovinen, A. Hovinen, Fabrication of a silicon based electroluminescent device. *Mater. Sci. Eng. B* **74**, 32–35 (2000)
26. M.V. Wolkin, J. Jorne, P.M. Fauchet, G. Allan, C. Delerue, Electronic states and luminescence in porous silicon quantum dots: the role of oxygen. *Phys. Rev. Lett.* **82**, 197–200 (1999)
27. L. Pavesi, L. Dal Negro, C. Mazzoleni, G. Franzo, F. Priolo, Optical gain in silicon nanocrystals. *Nature* **408**, 440–444 (2000)
28. A. Zimina, S. Eisebitt, W. Eberhardt, J. Heitmann, M. Zacharias, Electronic structure and chemical environment of silicon nanoclusters embedded in a silicon dioxide matrix. *Appl. Phys. Lett.* **88**, 163103 (2006)
29. J. Heitmann, F. Müller, L. Yi, M. Zacharias, D. Kovalev, F. Eichhorn, Excitons in Si nanocrystals: confinement and migration effects. *Phys. Rev. B* **69**, 195309 (2004)
30. K. Leonid, R. Markku, N. Sergei, K. Olli, S. Juha, Raman scattering from very thin Si layers of Si/SiO_2 superlattices: experimental evidence of structural modification in the 0.8–3.5 nm thickness region. *J. Appl. Phys.* **86**, 5601–5608 (1999)
31. L. Dal Negro, M. Cazzanelli, B. Danese, L. Pavesi, F. Iacona, G. Franzo, F. Priolo, Light amplification in silicon nanocrystals by pump and probe transmission measurements. *J. Appl. Phys.* **96**, 5747–5755 (2004)
32. C. Lingk, G.v. Plessen, J. Feldmann, K. Stock, M. Arzberger, G. Böhm, M.C. Amann, G. Abstreiter, Dynamics of amplified spontaneous emission in InAs/GaAs quantum dots. *Appl. Phys. Lett.* **76**, 3507–3509 (2000)

33. S. Fujita, N. Sugiyama, Visible light-emitting devices with Schottky contacts on an ultra-thin amorphous silicon layer containing silicon nanocrystals. *Appl. Phys. Lett.* **74**, 308–310 (1999)
34. R.J. Walters, G.I. Bourianoff, H.A. Atwater, Field-effect electroluminescence in silicon nanocrystals. *Nat. Mater.* **4**, 143–146 (2005)
35. R.J. Walters, J. Carreras, F. Tao, L.D. Bell, H.A. Atwater, Silicon nanocrystal field-effect light-emitting devices. *IEEE J. Sel. Top. Quantum Electron.* **12**, 1647–1656 (2006)
36. C. Josep, J. Arbiol, B. Garrido, C. Bonafos, J. Montserrat, Direct modulation of electroluminescence from silicon nanocrystals beyond radiative recombination rates. *Appl. Phys. Lett.* **92**, 091103 (2008)
37. F. Minoru, Y. Masato, K. Yoshihiko, H. Shinji, Y. Keiichi, 1.54 μm photoluminescence of Er^{3+} doped into SiO_2 films containing Si nanocrystals: evidence for energy transfer from Si nanocrystals to Er^{3+} . *Appl. Phys. Lett.* **71**, 1198–1200 (1997)
38. G. Franzò, F. Priolo, S. Coffa, A. Polman, A. Carnera, Room-temperature electroluminescence from Er-doped crystalline Si. *Appl. Phys. Lett.* **64**, 2235–2237 (1994)
39. G. Franzò, S. Coffa, F. Priolo, C. Spinella, Mechanism and performance of forward and reverse bias electroluminescence at 1.54 μm from Er-doped Si diodes. *J. Appl. Phys.* **81**, 2784–2793 (1997)
40. F. Iacona, A. Irrera, G. Franz, D. Pacifici, I. Crupi, M.P. Miritello, C.D. Presti, F. Priolo, Silicon-based light-emitting devices: properties and applications of crystalline, amorphous and Er-doped nanoclusters. *IEEE J. Sel. Top. Quantum Electron.* **12**, 1596–1606 (2006)
41. G. Franzò, V. Vinciguerra, F. Priolo, The excitation mechanism of rare-earth ions in silicon nanocrystals. *Appl. Phys. A* **69**, 3–12 (1999)
42. D. Pacifici, G. Franzò, F. Priolo, F. Iacona, L. Dal Negro, Modeling and perspectives of the Si nanocrystals-Er interaction for optical amplification. *Phys. Rev. B* **67**, 245301 (2003)
43. S.G. Cloutier, P.A. Kosyrev, J.M. Xu, Optical gain and stimulated emission in periodic nanopatterned crystalline silicon. *Nat. Mater.* **4**, 887–891 (2005)
44. E. Rotem, J.M. Shainline, J.M. Xu, Enhanced photoluminescence from nanopatterned carbon-rich silicon grown by solid-phase epitaxy. *Appl. Phys. Lett.* **91**, 051127 (2007)
45. G. Davies, The optical properties of luminescence centres in silicon. *Phys. Rep.* **176**, 83–188 (1989)
46. G.D. Watkins, Defects in irradiated silicon: EPR and electron-nuclear double resonance of interstitial boron. *Phys. Rev. B* **12**, 5824–5839 (1975)
47. R. Claps, D. Dimitropoulos, V. Raghunathan, Y. Han, B. Jalali, Observation of stimulated Raman amplification in silicon waveguides. *Opt. Express* **11**, 1731–1739 (2003)
48. T.K. Liang, H.K. Tsang, Role of free carriers from two-photon absorption in Raman amplification in silicon-on-insulator waveguides. *Appl. Phys. Lett.* **84**, 2745–2747 (2004)
49. O. Boyraz, B. Jalali, Demonstration of a silicon Raman laser. *Opt. Express* **12**, 5269–5273 (2004)
50. H. Rong, R. Jones, A. Liu, O. Cohen, D. Hak, A.W. Fang, M.J. Paniccia, A continuous-wave Raman silicon laser. *Nature* **433**, 725–728 (2005)
51. H. Rong, S. Xu, Y.-H. Kuo, V. Sih, O. Cohen, O. Raday, M.J. Paniccia, Low-threshold continuous-wave Raman silicon laser. *Nat. Photonics* **1**, 232–237 (2007)
52. R. Jones, H. Rong, A. Liu, A.W. Fang, M.J. Paniccia, D. Hak, O. Cohen, Net continuous wave optical gain in a low loss silicon-on-insulator waveguide by stimulated Raman scattering. *Opt. Express* **13**, 519–525 (2005)
53. S. Fathpour, K.K. Tsia, B. Jalali, Energy harvesting in silicon Raman amplifiers. *Appl. Phys. Lett.* **89**, 061109 (2006)
54. C.P. Kuo, S.K. Vong, R.M. Cohen, G.B. Stringfellow, Effect of mismatch strain on bandgap in III–V semiconductors. *J. Appl. Phys.* **57**, 5428–5432 (1985)
55. H. Kawanami, Heteroepitaxial technologies of III–V on Si. *Sol. Energy Mater.* **66**, 479–486 (2001)
56. Y.H. Xie, K.L. Wang, Y.C. Kao, An investigation on surface conditions for Si molecular beam epitaxial (MBE) growth. *J. Vac. Sci. Technol. A* **3**, 1035–1039 (1985)

57. K. Samonji, H. Yonezu, Y. Takagi, K. Iwaki, N. Ohshima, J.K. Shin, K. Pak, Reduction of threading dislocation density in InP-on-Si heteroepitaxy with strained short-period superlattices. *Appl. Phys. Lett.* **69**, 100–102 (1996)
58. Y. Masafumi, S. Mitsuru, I. Yoshio, Misfit stress dependence of dislocation density reduction in GaAs films on Si substrates grown by strained-layer superlattices. *Appl. Phys. Lett.* **54**, 2568–2570 (1989)
59. K. Nozawa, Y. Horikoshi, Low threading dislocation density GaAs on Si(100) with In-GaAs/GaAs strained-layer superlattice grown by migration-enhanced epitaxy. *Jpn. J. Appl. Phys.* **30**, L668–L671 (1991)
60. E. Yamaichi, T. Ueda, Q. Gao, C. Yamagishi, M. Akiyama, Method to obtain low-dislocation-density regions by patterning with SiO₂ on GaAs/Si followed by annealing. *Jpn. J. Appl. Phys.* **33**, L1442–L1444 (1994)
61. B. Kunert, S. Zinnkann, K. Volz, W. Stolz, Monolithic integration of Ga(NAsP)/(BGa)P multi-quantum well structures on (001) silicon substrate by MOVPE. *J. Cryst. Growth* **310**, 4776–4779 (2008)
62. B. Kunert, K. Volz, J. Koch, W. Stolz, Direct-bandgap Ga(NAsP)-material system pseudomorphically grown on GaP substrate. *Appl. Phys. Lett.* **88**, 182108 (2006)
63. X. Huang, Y. Song, T. Masuda, D.-H. Jung, M. Lee, InGaAs/GaAs quantum well lasers grown on exact GaP/Si (001). *Electron. Lett.* **50**(17), 1226–1227 (2014)
64. S. Liebich, M. Zimprich, A. Beyer, C. Lange, D.J. Franzbach, S. Chatterjee, N. Hossain, S.J. Sweeney, K. Volz, B. Kunert, W. Stolz, Laser operation of Ga(NAsP) lattice-matched to (001) silicon substrate. *Appl. Phys. Lett.* **99**, 071109 (2011)
65. V.G. Talalaev, G.E. Cirlin, A.A. Tonkikh, N.D. Zakharov, P. Werner, Room temperature electroluminescence from Ge/Si quantum dots superlattice close to 1.6 μm . *Phys. Status Solidi A* **198**, R4–R6 (2003)
66. X. Sun, J. Liu, L.C. Kimerling, J. Michel, Room-temperature direct bandgap electroluminescence from Ge-on-Si light-emitting diodes. *Opt. Lett.* **34**, 1198–1200 (2009)
67. S.-L. Cheng, J. Lu, G. Shambat, H.-Y. Yu, K. Saraswat, J. Vuckovic, Y. Nishi, Room temperature 1.6 μm electroluminescence from Ge light emitting diode on Si substrate. *Opt. Express* **17**, 10019–10024 (2009)
68. L. Tsybeskov, E.-K. Lee, H.-Y. Chang, D.J. Lockwood, J.-M. Baribeau, X. Wu, T.I. Kamins, Silicon-germanium nanostructures for on-chip optical interconnects. *Appl. Phys. A* **95**, 1015–1027 (2009)
69. R. Camacho-Aguilera, Y. Cai, N. Patel, J. Bessette, M. Romagnoli, L. Kimerling, J. Michel, An electrically pumped germanium laser. *Opt. Express* **20**, 11316–11320 (2012)
70. S. Wirths, R. Geiger, N. von den Driesch, G. Mussler, T. Stoica, S. Mantl, Z. Ikonik, M. Luysberg, S. Chiussi, J.M. Hartmann, H. Sigg, J. Faist, D. Buca, D. Grützmacher, Lasing in direct-bandgap GeSn alloy grown on Si. *Nat. Photonics* **9**, 88–92 (2015)
71. D. Bimberg, U.W. Pohl, Quantum dots: promises and accomplishments. *Mater. Today* **14**, 388–397 (2011)
72. T. Kageyama, K. Nishi, M. Yamaguchi, R. Mochida, Y. Maeda, K. Takemasa, Y. Tanaka, T. Yamamoto, M. Sugawara, Y. Arakawa, Extremely high temperature (220 °C) continuous-wave operation of 1300-nm-range quantum-dot lasers, in *Europ. Conf. Lasers Electro-Opt. and XIIIth Europ. Quant. Electron. Conf. (CLEO®/Europe-EQEC'11)*, Munich, Germany (2011), Techn. Digest, paper PDP A1
73. Y. Urino, N. Hatori, K. Mizutani, T. Usuki, J. Fujikata, K. Yamada, T. Horikawa, T. Nakamura, Y. Arakawa, First demonstration of athermal silicon optical interposers with quantum dot lasers operating up to 125 °C. *J. Lightwave Technol.* **33**(6), 1223–1229 (2014)
74. D. Livshits, A. Gubenko, S. Mikhlin, V. Mikhlin, C.H. Chen, M. Fiorentino, R. Beausoleil, High efficiency diode comb-laser for DWDM optical interconnects, in *IEEE Opt. Interconn. Conf.*, San Diego, CA, USA (2014), Techn. Digest, paper TuB6
75. K. Tanabe, K. Watanabe, Y. Arakawa, III–V/Si hybrid photonic devices by direct fusion bonding. *Sci. Rep.* **2**, 1–6 (2012)

76. K. Tanabe, T. Rae, K. Watanabe, Y. Arakawa, High-temperature 1.3 μm InAs/GaAs quantum dot lasers on Si substrates fabricated by wafer bonding. *Appl. Phys. Express* **6**, 082703 (2013)
77. K. Tanabe, Y. Arakawa, 1.3 μm InAs/GaAs quantum dot lasers on SOI waveguide structures, in *Conf. Lasers Electro-Opt. (CLEO/QELS'14)*, San Jose, CA, USA (2014), Techn. Digest, paper JThA31
78. K.K. Linder, J. Philips, O. Qasaimeh, X.F. Liu, S. Krishna, P. Bhattacharya, J.C. Jiang, Self-organized $\text{In}_{0.4}\text{Ga}_{0.6}\text{As}$ quantum-dot lasers grown on Si substrates. *Appl. Phys. Lett.* **74**, 1355–1357 (1999)
79. Z. Mi, P. Bhattacharya, J. Yang, K.P. Pipe, Room-temperature self-organised $\text{In}_{0.5}\text{Ga}_{0.5}\text{As}$ quantum dot laser on silicon. *Electron. Lett.* **41**(13), 742–744 (2005)
80. J. Yang, P. Bhattacharya, Z. Mi, High-performance $\text{In}_{0.5}\text{Ga}_{0.5}\text{As}$ quantum-dot lasers on silicon with multiple-layer quantum-dot dislocation filters. *IEEE Trans. Electron Devices* **54**, 2849–2855 (2007)
81. Z. Mi, J. Yang, P. Bhattacharya, G. Qin, Z. Ma, High-performance quantum dot lasers and integrated optoelectronics on Si. *Proc. IEEE* **97**, 1239–1249 (2009)
82. T. Wang, H. Liu, A. Lee, F. Pozzi, A. Seeds, 1.3 μm InAs/GaAs quantum-dot lasers monolithically grown on Si substrates. *Opt. Express* **19**, 11381–11386 (2011)
83. A. Lee, Q. Jiang, M. Tang, A. Seeds, H. Liu, Continuous-wave InAs/GaAs quantum-dot laser diodes monolithically grown on Si substrate with low threshold current densities. *Opt. Express* **20**, 22181–22187 (2012)
84. S. Chen, M. Tang, J. Wu, Q. Jiang, V. Dorogan, M. Benamara, Y. Mazur, G. Salamo, A. Seeds, H. Liu, 1.3 μm InAs/GaAs quantum-dot laser monolithically grown on Si substrates operating over 100 $^{\circ}\text{C}$. *Electron. Lett.* **50**, 1467–1468 (2014)
85. A.Y. Liu, C. Zhang, J. Norman, A. Snyder, D. Lubyshev, J.M. Fastenau, A.W.K. Liu, A.C. Gossard, J.E. Bowers, High performance continuous wave 1.3 μm quantum dot lasers on silicon. *Appl. Phys. Lett.* **104**, 041104 (2014)
86. J.M. Gerard, C. Weisbuch, Semiconductor structure for optoelectronic components with inclusions, US Patent 5,075,742 (1991)
87. H. Liu, T. Wang, Q. Jiang, R. Hogg, F. Tutu, F. Pozzi, A. Seeds, Long-wavelength InAs/GaAs quantum-dot laser diode monolithically grown on Ge substrate. *Nat. Photonics* **5**, 416–419 (2011)
88. L.C. Kimerling, Recombination enhanced defect reactions. *Solid-State Electron.* **21**, 1391–1401 (1978)
89. R. Beanland, A.M. Sanchez, D. Childs, K.M. Groom, H.Y. Liu, D.J. Mowbray, M. Hopkinson, Structural analysis of life tested 1.3 μm quantum dot lasers. *J. Appl. Phys.* **103**, 0141931 (2008)
90. J.P. van der Ziel, R.D. Dupuis, R.A. Logan, C.J. Pinzone, Degradation of GaAs lasers grown by metalorganic chemical vapor deposition on Si substrates. *Appl. Phys. Lett.* **51**, 89–91 (1987)
91. H.K. Choi, C.A. Wang, N.H. Karam, GaAs-based diode lasers on Si with increased lifetime obtained by using strained InGaAs active layer. *Appl. Phys. Lett.* **106**, 024502 (2015)
92. Z.I. Kazi, T. Egawa, T. Jimbo, M. Umeno, First room-temperature continuous-wave operation of self-formed InGaAs quantum dot-like laser on Si substrate grown by metalorganic chemical vapor deposition. *Jpn. J. Appl. Phys.* **39**, 3860–3862 (2000)
93. Z.I. Kazi, P. Thilakan, T. Egawa, M. Umeno, T. Jimbo, Realization of GaAs/AlGaAs lasers on Si using epitaxial lateral overgrowth by metalorganic chemical vapor deposition. *Jpn. J. Appl. Phys.* **40**, 4903–4906 (2001)
94. M.E. Groenert, A.J. Pitera, R.J. Ram, E.A. Fitzgerald, Improved room-temperature continuous wave GaAs/AlGaAs and InGaAs/GaAs/AlGaAs lasers fabricated on Si substrates via relaxed graded $\text{Ge}_x\text{Si}_{1-x}$ buffer layers. *J. Vac. Sci. Technol. B* **21**, 1064–1069 (2003)
95. A.Y. Liu, R.W. Herrick, O. Ueda, P.M. Petroff, A.C. Gossard, J.E. Bowers, Reliability of InAs/GaAs quantum dot lasers epitaxially grown on silicon. *J. Sel. Top. Quantum Electron.* **21**, 1900708 (2015)

96. F. Olsson, M. Xie, S. Lourduoss, I. Prieto, P.A. Postigo, Epitaxial lateral overgrowth of InP on Si from nano-openings: theoretical and experimental indication for defect filtering throughout the grown layer. *J. Appl. Phys.* **104**, 093112 (2008)
97. M. Deura, T. Hoshii, T. Yamamoto, Y. Ikuhara, M. Takenaka, S. Takagi, Y. Nakano, M. Sugiyama, Dislocation-free InGaAs on Si(111) using micro-channel selective-area metal-organic vapor phase epitaxy. *Appl. Phys. Express* **2**, 011101 (2009)
98. Z. Wang, B. Tian, M. Pantouvaki, W. Guo, P. Absil, J. Van Campenhout, C. Merckling, D. Van Thourhout, Room temperature InP DFB laser array directly grown on (001) silicon. [arXiv:1501.03025](https://arxiv.org/abs/1501.03025)
99. Y. Liu, Y. Li, Z. Fan, B. Xing, Y. Yu, J. Yu, Fabrication and optical optimization of spot-size converters with strong cladding layers. *J. Opt. A* **11**, 085002 (2009)
100. E.E.L. Friedrich, M.G. Oberg, B. Broberg, S. Nilsson, S. Valette, Hybrid integration of semiconductor lasers with Si-based single-mode ridge waveguides. *J. Lightwave Technol.* **10**, 336–340 (1992)
101. J. Sasaki, M. Itoh, T. Tamanuki, H. Hatakeyama, S. Kitamura, T. Shimoda, T. Kato, Multiple-chip precise self-aligned assembly for hybrid integrated optical modules using Au–Sn solder bumps. *IEEE Trans. Adv. Packaging* **24**, 569–575 (2001)
102. N. Kobayashi, K. Sato, M. Namiwaka, K. Yamamoto, S. Watanabe, T. Kita, H. Yamada, H. Yamazaki, Silicon photonic hybrid ring-filter external cavity wavelength tunable lasers. *J. Lightwave Technol.* **33**(6), 1241–1246 (2015)
103. H. Park, A.W. Fang, S. Kodama, J.E. Bowers, Hybrid silicon evanescent laser fabricated with a silicon waveguide and III–V offset quantum wells. *Opt. Express* **13**, 9460–9464 (2005)
104. A. Black, A.R. Hawkins, N.M. Margalit, D.I. Babic, A.L. Holmes Jr., Y.L. Chang, P. Abraham, J.E. Bowers, E.L. Hu, Wafer fusion: materials issues and device results. *IEEE J. Sel. Top. Quantum Electron.* **3**, 943–951 (1997)
105. D. Pasquariello, M. Camacho, F. Ericsson, K. Hjort, Crystalline defects in InP-to-silicon direct wafer bonding. *Jpn. J. Appl. Phys.* **40**, 4837–4844 (2001)
106. D. Pasquariello, K. Hjort, Plasma-assisted InP-to-Si low temperature wafer bonding. *IEEE J. Sel. Top. Quantum Electron.* **8**, 118–131 (2002)
107. G. Roelkens, D. Van Thourhout, R. Baets, R. Nötzel, M.K. Smit, Laser emission and photo-detection in an InP/InGaAsP layer integrated on and coupled to a silicon-on-insulator waveguide circuit. *Opt. Express* **14**, 8154–8159 (2006)
108. A.W. Fang, H. Park, O. Cohen, R. Jones, M.J. Paniccia, J.E. Bowers, Electrically-pumped hybrid AlGaInAs-silicon evanescent laser. *Opt. Express* **14**, 9203–9210 (2006)
109. I. Christiaens, G. Roelkens, K. De Mesel, D. Van Thourhout, R. Baets, Thin-film devices fabricated with benzocyclobutene adhesive wafer bonding. *J. Lightwave Technol.* **23**, 517–523 (2005)
110. D. Liang, J.E. Bowers, Highly efficient vertical outgassing channels for low-temperature InP-to-silicon direct wafer bonding on the silicon-on-insulator (SOI) substrate. *J. Vac. Sci. Technol. B* **26**, 1560–1568 (2008)
111. H. Park, A.W. Fang, O. Cohen, R. Jones, M.J. Paniccia, J.E. Bowers, Design and fabrication of optically pumped hybrid silicon-AlGaInAs evanescent lasers. *IEEE J. Sel. Top. Quantum Electron.* **12**, 1657–1663 (2006)
112. D. Liang, J.E. Bowers, D.C. Oakley, A. Napoleone, D.C. Chapman, C.-L. Chen, P.W. Juodawlkis, O. Raday, High-quality 150 mm InP-to-silicon epitaxial transfer for silicon photonic integrated circuits. *Electrochem. Solid-State Lett.* **12**, H101–H104 (2009)
113. A. Fang, E. Lively, Y. Kuo, D. Liang, J.E. Bowers, A distributed feedback silicon evanescent laser. *Opt. Express* **16**, 4413–4419 (2008)
114. S. Stankovic, R. Jones, M.N. Sysak, M.J. Heck, G. Roelkens, D. Van Thourhout, Hybrid III–V/Si distributed-feedback laser based on adhesive bonding. *IEEE Photonics Technol. Lett.* **24**(23), 2155–2158 (2012)
115. T. Maruyama, T. Okumura, S. Sakamoto, K. Miura, Y. Nishimoto, S. Arai, GaInAsP/InP membrane BH-DFB lasers directly bonded on SOI substrate. *Opt. Express* **14**, 8184–8188 (2006)

116. A.W. Fang, B.R. Koch, R. Jones, E. Lively, D. Liang, Y.-H. Kuo, J.E. Bowers, A distributed Bragg reflector silicon evanescent laser. *IEEE Photonics Technol. Lett.* **20**(20), 1667–1669 (2008)
117. G.-H. Duan, C. Jany, A. Le Liepvre, A. Accard, M. Lamponi, D. Make, P. Kaspar, G. Levaufré, N. Girard, F. Lelarge, J.-M. Fedeli, A. Descos, B. Ben Bakir, S. Messaoudene, D. Bordel, S. Menezo, G. de Valicourt, S. Keyvaninia, G. Roelkens, D. Van Thourhout, D.J. Thomson, F.Y. Gardes, G.T. Reed, Hybrid III–V on silicon lasers for photonic integrated circuits on silicon. *IEEE J. Sel. Top. Quantum Electron.* **20**(4), 158–170 (2014)
118. D. Liang, M. Fiorentino, T. Okumura, H.-H. Chang, D.T. Spencer, Y.-H. Kuo, A.W. Fang, D. Dai, R.G. Beausoleil, J.E. Bowers, Electrically-pumped compact hybrid silicon microring lasers for optical interconnects. *Opt. Express* **17**, 20355–20364 (2009)
119. J. Van Campenhout, P. Rojo Romeo, P. Regreny, C. Seassal, D. Van Thourhout, S. Verstuyft, L. Di Cioccio, J.-M. Fedeli, C. Lagahe, R. Baets, Electrically pumped InP-based microdisk lasers integrated with a nanophotonic silicon-on-insulator waveguide circuit. *Opt. Express* **15**, 6744–6749 (2007)
120. G. Kurczveil, M.J.R. Heck, J.D. Peters, J.M. Garcia, D. Spencer, J.E. Bowers, An integrated hybrid silicon multiwavelength AWG laser. *IEEE J. Sel. Top. Quantum Electron.* **17**(6), 1521–1527 (2011)
121. S. Keyvaninia, S. Verstuyft, S. Pathak, F. Lelarge, G. Duan, D. Bordel, J. Fedeli, T. De Vries, B. Smalbrugge, E. Geluk, J. Bolk, M. Smit, G. Roelkens, D. Van, Thourhout, III–V-on-silicon multi-frequency lasers. *Opt. Express* **21**, 13675–13683 (2013)
122. J. Hulme, J. Doyle, J.E. Bowers, Widely tunable Vernier ring laser on hybrid silicon. *Opt. Express* **21**, 19718–19722 (2013)
123. A. Le Liepvre, C. Jany, A. Accard, M. Lamponi, F. Poingt, D. Make, F. Lelarge, J.-M. Fedeli, S. Messaoudene, D. Bordel, G.-H. Duan, Widely wavelength tunable hybrid III–V/silicon laser with 45 nm tuning range fabricated using a wafer bonding technique, in *9th IEEE Conf. Group IV Photonics*, San Diego, CA, USA (2012), pp. 54–56
124. C. Zhang, S. Srinivasan, Y. Tang, M. Heck, M. Davenport, J.E. Bowers, Low threshold and high speed short cavity distributed feedback hybrid silicon lasers. *Opt. Express* **22**, 10202–10209 (2014)
125. O. Bondarenko, C.-Y. Fang, F. Vallini, J.S.T. Smalley, Y. Fainman, Extremely compact hybrid III–V/SOI lasers: design and fabrication approaches. *Opt. Express* **23**(3), 2696–2712 (2015)
126. D. Liang, M. Fiorentino, S. Srinivasan, J.E. Bowers, R.G. Beausoleil, Low threshold electrically-pumped hybrid silicon microring lasers. *IEEE J. Sel. Top. Quantum Electron.* **17**(6), 1528–1533 (2011)
127. C.T. Santis, S.T. Steger, Y. Vilenchik, A. Vasilyev, A. Yariv, High-coherence semiconductor lasers based on integral high-Q resonators in hybrid Si/III–V platforms. *Proc. Natl. Acad. Sci.* **111**(8), 2879–2884 (2014)
128. T. Komljenovic, S. Srinivasan, E. Norberg, M. Davenport, G. Fish, J.E. Bowers, Widely-tunable narrow-linewidth monolithically-integrated external-cavity semiconductor lasers. *IEEE Sel. Top. Quantum Electron.* **21**(6), 1–9 (2015)
129. C.R. Doerr, Silicon photonic integration in telecommunications. *Front. Phys.* **3**, 37 (2015)
130. T. Pinguet, P.M. De Dobbelaere, D. Foltz, S. Gloeckner, S. Hovey, L. Yi, M. Mack, G. Masini, A. Mekis, M. Peterson, S. Sahni, J. Schramm, M. Sharp, D. Song, B.P. Welch, K. Yokoyama, Y. Shuhuan, Silicon photonics multicore transceivers, in *IEEE Photon. Soc. Summer Top. Meeting* Seattle, WA, USA (2012), pp. 238–239, Techn. Digest
131. S. Romero-Garcia, B. Marzban, S. Sharif Azadeh, F. Merget, B. Shen, J. Witzens, Misalignment tolerant couplers for hybrid integration of semiconductor lasers with silicon photonics parallel transmitters, in *Proc. SPIE, Silicon Photonics and Photonic Integrated Circuits IV*, vol. 9133 (2014), 91331A
132. P. de Dobbelaere, A. Narasimha, A. Mekis, B. Welch, C. Bradbury, C. Sohn, D. Song, D. Foltz, D. Guckenberger, G. Masini, J. Schramm, J. White, J. Redman, K. Yokoyama, M. Harrison, M. Peterson, M. Mack, M. Sharp, R. LeBlanc, S. Abdalla, S. Gloeckner, S. Hovey,

- S. Jackson, S. Sahni, S. Yu, T. Pinguet, Y. Liang, Silicon photonics for high data rate optical interconnect, in *IEEE Opt. Interconn. Conf.*, Santa Fe, NM, USA (2012), pp. 113–114
133. K. Ohira, K. Kobayashi, N. Iizuka, H. Yoshida, M. Ezaki, H. Uemura, A. Kojima, K. Nakamura, H. Furuyama, H. Shibata, On-chip optical interconnection by using integrated III–V laser diode and photodetector with silicon waveguide. *Opt. Express* **18**, 15440–15447 (2010)
134. M.N. Sysak, H. Park, A.W. Fang, J.E. Bowers, R. Jones, O. Cohen, O. Raday, M.J. Paniccia, Experimental and theoretical thermal analysis of a hybrid silicon evanescent laser. *Opt. Express* **15**, 15041–15046 (2007)
135. M.N. Sysak, D. Liang, R. Jones, G. Kurczveil, M. Piels, M. Fiorentino, R.G. Beausoleil, J.E. Bowers, Hybrid silicon evanescent laser technology: a thermal perspective. *IEEE J. Sel. Top. Quantum Electron.* **17**, 1490–1498 (2011)
136. S. Tanaka, T. Matsumoto, T. Kurahashi, M. Matsuda, A. Uetake, S. Sekiguchi, Y. Tanaka, K. Morito, Flip-chip-bonded, 8-wavelength AlGaInAs DFB laser array operable up to 70 °C, in *Proc. 40th Europ. Conf. Opt. Commun.* (ECOC'14), Cannes, France (2014), paper Tu.1.1.4
137. S. Tanaka, T. Akiyama, S. Sekiguchi, K. Morito, Silicon photonics optical Tx technology for Tbps class I-O co-packaged with CPU. *Fujitsu Sci. Tech. J.* **50**, 123–131 (2014)
138. S. Tanaka, S.-H. Jeong, S. Sekiguchi, T. Kurahashi, Y. Tanaka, K. Morito, High-output-power, single-wavelength silicon hybrid laser using precise flip-chip bonding technology. *Opt. Express* **20**, 28057–28069 (2012)
139. C. Doerr, L. Chen, D. Vermeulen, T. Nielsen, S. Azemati, S. Stulz, G. McBrien, X.M. Xu, B. Mikkelsen, M. Givehchi, C. Rasmussen, S.Y. Park, Single-chip silicon photonics 100-Gb/s coherent transceiver, in *Opt. Fiber Commun. Conf.* (OFC'14), San Francisco, CA, USA (2014), Techn. Digest, PDTh5C.1
140. M.J.R. Heck, H.-W. Chen, A.W. Fang, B.R. Koch, D. Liang, H. Park, M.N. Sysak, J.E. Bowers, Hybrid silicon photonics for optical interconnects. *IEEE J. Sel. Top. Quantum Electron.* **17**, 333–346 (2011)
141. M.J.R. Heck, J.F. Bauters, M.L. Davenport, J.K. Doylend, S. Jain, G. Kurczveil, S. Srinivasan, T. Yongbo, J.E. Bowers, Hybrid silicon photonic integrated circuit technology. *IEEE J. Sel. Top. Quantum Electron.* **19**, 6100117 (2013)
142. A. Alduino, L. Liao, R. Jones, M. Morse, B. Kim, W. Lo, J. Basak, B. Koch, H. Liu, H. Rong, M. Sysak, C. Krause, R. Saba, D. Lazar, L. Horwitz, R. Bar, S. Litski, A. Liu, K. Sullivan, O. Dosunmu, N. Na, T. Yin, F. Haubensack, I. Hsieh, J. Heck, R. Beatty, H. Park, J. Bovington, S. Lee, H. Nguyen, H. Au, K. Nguyen, P. Merani, M. Hakami, M. Paniccia, Demonstration of a high speed 4-channel integrated silicon photonics WDM link with hybrid silicon lasers, in *Integrated Photonics Research, Silicon and Nanophotonics and Photonics in Switching*, Monterey, CA, USA (2010), p. PDIW15
143. <http://www.eetimes.com/showArticle.jhtml?articleID=214502894>
144. <http://www.hpl.hp.com/research/systems-research/themachine/>
145. M.J.R. Heck, M.L. Davenport, J.E. Bowers, Progress in hybrid-silicon photonic integrated circuit technology. SPIE News Room (2013). doi:10.1117/2.1201302.004730
146. H. Park, A. Fang, S. Kodama, J.E. Bowers, Hybrid silicon evanescent laser fabricated with a silicon waveguide and III–V offset quantum wells. *Opt. Express* **13**, 9460–9464 (2005)
147. D. Liang, A.W. Fang, J.E. Bowers, D.C. Oakley, A. Napoleone, D.C. Chapman, C.-L. Chen, P.W. Juodawlkis, O. Raday, 150 mm InP-to-silicon direct wafer bonding for silicon photonic integrated circuits. *ECS Trans.* **16**, 235–241 (2008)
148. S. Srinivasan, N. Julian, J. Peters, D. Liang, J.E. Bowers, Reliability of hybrid silicon distributed feedback lasers. *IEEE J. Sel. Top. Quantum Electron.* **19**, 1501305 (2013)
149. D. Liang, S. Srinivasan, J. Peters, A.W. Fang, J.E. Bowers, Demonstration of enhanced III–V-on-silicon hybrid integration by using a strained superlattice as a defect blocking layer. *ECS Trans.* **33**(4), 421–426 (2010)
150. D. Liang, M. Fiorentino, S. Srinivasan, S.T. Todd, G. Kurczveil, J.E. Bowers, R.G. Beausoleil, Optimization of hybrid silicon microring lasers. *IEEE Photonics J.* **3**, 580–587 (2011)
151. M.N. Sysak, H. Park, A.W. Fang, O. Raday, J.E. Bowers, R. Jones, Reduction of hybrid silicon laser thermal impedance using poly Si thermal shunts, in *Opt. Fiber Commun. Conf.*

- and Nat. Fiber Opt. Eng. Conf. (OFC/NFOEC'11)*, Los Angeles, CA, USA (2011), Techn. Digest, paper OWZ6
152. D. Liang, S. Srinivasan, M. Fiorentino, G. Kurczveil, J.E. Bowers, R.G. Beausoleil, A metal thermal shunt design for hybrid silicon microring laser, in *IEEE Opt. Interconn. Conf.*, Santa Fe, NM, USA (2012), paper TuD2
 153. C. Zhang, D. Liang, G. Kurczveil, J.E. Bowers, R.G. Beausoleil, Thermal management of hybrid silicon ring lasers for high temperature operation. *IEEE J. Sel. Top. Quantum Electron.* **21**(6), 1–7 (2015)
 154. D. Liang, M. Fiorentino, S.T. Todd, G. Kurczveil, R.G. Beausoleil, J.E. Bowers, Fabrication of silicon-on-diamond substrate and low-loss optical waveguides. *IEEE Photonics Technol. Lett.* **23**, 657–659 (2011)
 155. B.R. Koch, E.J. Norberg, K. Byungchae, J. Hutchinson, S. Jae-Hyuk, G. Fish, A. Fang, Integrated silicon photonic laser sources for telecom and datacom, in *Opt. Fiber Commun. Conf. and Nat. Fiber Opt. Eng. Conf. (OFC/NFOEC'13)*, Anaheim, CA, USA (2013), Techn. Digest, paper PDP5C.8
 156. G.T. Reed, A.P. Knights, *Silicon Photonics: An Introduction* (Wiley, Chichester, 2004)
 157. R. Soref, B. Bennett, Electrooptical effects in silicon. *IEEE J. Quantum Electron.* **QE-23**, 123–129 (1987)
 158. G.T. Reed, *Silicon Photonics: The State of the Art* (Wiley, Chichester, 2008)
 159. A. Liu, R. Jones, L. Liao, D. Samara-Rubio, D. Rubin, O. Cohen, R. Nicolaescu, M.J. Paniccia, A high-speed silicon optical modulator based on a metal-oxide-semiconductor capacitor. *Nature* **427**, 615–618 (2004)
 160. Q. Xu, B. Schmidt, S. Pradhan, M. Lipson, Micrometre-scale silicon electro-optic modulator. *Nature* **435**, 325–327 (2005)
 161. J. Basak, L. Liao, A. Liu, D. Rubin, Y. Chetrit, H. Nguyen, D. Samara-Rubio, R. Cohen, N. Izhaky, M.J. Paniccia, Developments in gigascale silicon optical modulators using free carrier dispersion mechanisms. *Adv. Opt. Technol.* **2008**, 678948 (2008). doi:[10.1155/2008/678948](https://doi.org/10.1155/2008/678948)
 162. D.J. Thomson, F.Y. Gardes, J.-M. Fedeli, S. Zlatanovic, Y. Hu, B.P.P. Kuo, E. Myslivets, N. Alic, S. Radic, G.Z. Mashanovich, G.T. Reed, 50-Gb/s silicon optical modulator. *IEEE Photonics Technol. Lett.* **24**(4), 234–236 (2012)
 163. A. Liu, L. Liao, D. Rubin, H. Nguyen, B. Ciftcioglu, Y. Chetrit, N. Izhaky, M.J. Paniccia, High-speed optical modulation based on carrier depletion in a silicon waveguide. *Opt. Express* **15**, 660–668 (2007)
 164. F.Y. Gardes, D.J. Thomson, N.G. Emerson, G.T. Reed, 40 Gb/s silicon photonics modulator for TE and TM polarisations. *Opt. Express* **19**(12), 11804–11814 (2011)
 165. D.J. Thomson, F.Y. Gardes, D.C. Cox, J.-M. Fedeli, G.Z. Mashanovich, G.T. Reed, Self-aligned silicon ring resonator optical modulator with focused ion beam error correction. *J. Opt. Soc. Am. B* **30**, 445–449 (2013)
 166. P. Dong, R. Shafiqi, S. Liao, H. Liang, N.-N. Feng, D. Feng, G. Li, X. Zheng, A.V. Krishnamoorthy, M. Asghari, Wavelength-tunable silicon microring modulator. *Opt. Express* **18**(11), 10941–10946 (2010)
 167. H.-W. Chen, Y. Kuo, J.E. Bowers, Hybrid silicon modulators. *Chin. Opt. Lett.* **7**, 280–285 (2009)
 168. H.-W. Chen, Y.-H. Kuo, J.E. Bowers, A hybrid silicon–AlGaInAs phase modulator. *IEEE Photonics Technol. Lett.* **20**, 1920–1922 (2008)
 169. H.-W. Chen, Y.-H. Kuo, J.E. Bowers, High speed Mach-Zehnder silicon evanescent modulator using capacitively loaded traveling wave electrode, in *6th IEEE Conf. Group IV Photonics*, San Francisco, CA, USA (2009), paper FC4
 170. H.-W. Chen, J.D. Peters, J.E. Bowers, Forty Gb/s hybrid silicon Mach-Zehnder modulator with low chirp. *Opt. Express* **19**, 1455–1460 (2011)
 171. Y. Tang, J.D. Peters, J.E. Bowers, Over 67 GHz bandwidth hybrid silicon electroabsorption modulator with asymmetric segmented electrode for 1.3 μm transmission. *Opt. Express* **20**, 11529–11535 (2012)

172. Y. Tang, J.D. Peters, J.E. Bowers, Energy-efficient hybrid silicon electroabsorption modulator for 40-Gb/s 1-V uncooled operation. *IEEE Photonics Technol. Lett.* **24**(19), 1689–1692 (2012)
173. Y.T. Hu, M. Pantouvaki, S. Brems, I. Asselberghs, C. Huyghebaert, M. Geisler, C. Alessandri, R. Baets, P. Absil, D. Van Thourhout, J. Van Campenhout, Broadband 10 Gb/s graphene electro-absorption modulator on silicon for chip-level optical interconnects, in *60th IEEE Internat. Electron Devices Meeting (IEDM'14)*, San Francisco, CA, USA (2014), Techn. Digest, 5.6.1–5.6.4
174. J.E. Roth, O. Fidaner, R.K. Schaevitz, Y.-H. Kuo, T.I. Kamins, J.S. Harris, D.A.B. Miller, Optical modulator on silicon employing germanium quantum wells. *Opt. Express* **15**, 5851–5859 (2007)
175. R.S. Jacobsen, K.N. Andersen, P.I. Borel, J. Fage-Pedersen, L.H. Frandsen, O. Hansen, M. Kristensen, A.V. Lavrinenko, G. Moulin, H. Ou, C. Peucheret, B. Zsigri, A. Bjarklev, Strained silicon as a new electro-optic material. *Nature* **441**, 199–202 (2006)

Sudharsanan Srinivasan is a photonics system engineer at Aurrion Inc., Goleta, CA. He received his Bachelors degree with specialization in Engineering Physics from Indian Institute of Technology, Madras, India (July 2009). He received a Ph.D. on heterogeneous integration for silicon photonics at the University of California, Santa Barbara in June 2015. His research interests are in Silicon Photonics. He was President of the Santa Barbara chapter of the IEEE Photonics Society.

Alan Y. Liu received his B.S. in Physics and Mathematics with a minor in Business from Tulane University in 2011, and a Ph.D. in Electronic and Photonic Materials in 2016. He is currently a postdoctoral scholar with Prof. John Bowers' silicon photonics group at the University of California, Santa Barbara. His research interests include quantum dot optoelectronics and silicon photonics.

Di Liang is currently a research scientist at HP Labs (Palo Alto, CA). He received his B.S. degree in Optical Engineering from the Zhejiang University, Hangzhou, China in 2002, and his M.S. and Ph.D. degrees in Electrical Engineering from the University of Notre Dame, Indiana, USA in 2004 and 2006, respectively. His research interests include III–V and silicon photonics, particular in diode lasers, modulators and photodiodes, microring resonators, hybrid integration and nanofabrication technology. He has authored and coauthored over 120 journal and conference papers, three book chapters, and was granted by two US/international patents with another 27 pending. He received American Vacuum Society 35th PCSI-Young Scientist Award and Best Paper Award of The 214th Electrochemical Society Meeting both in 2008, Optical Society of America New Focus/Bookham Student Award in 2006, and Newport/Spectra-Physics Research Excellence Award in 2005.

John E. Bowers holds the Fred Kavli Chair in Nanotechnology, and is the Director of the Institute for Energy Efficiency and a Professor in the Departments of Materials and Electrical and Computer Engineering at UCSB. He is a cofounder of Aurrion, Aerius Photonics and Calient Networks. Dr. Bowers received his M.S. and Ph.D. degrees from Stanford University and worked for AT&T Bell Laboratories and Honeywell before joining UC Santa Barbara. Dr. Bowers is a member of the National Academy of Engineering, a fellow of the IEEE, OSA and the American Physical Society, and a recipient of the OSA Tyndal Award, the OSA Holonyak Prize, the IEEE LEOS William Streifer Award and the South Coast Business and Technology Entrepreneur of the Year Award. He has published eight book chapters, 600 journal papers, 900 conference papers and has received 54 patents. He and coworkers received the EE Times Annual Creativity in Electronics (ACE) Award for Most Promising Technology for the hybrid silicon laser in 2007.

Chapter 16

Photonic Integrated Circuits on InP

Norbert Grote, Moritz Baier, and Francisco Soares

Abstract This chapter is devoted to photonic integrated circuits (PIC) on InP semiconductor basis. This materials platform is capable of monolithically integrating not only passive optical waveguide and receiver (Rx) devices but also transmitter (Tx) type structures, in particular optical amplifiers and lasers. In the first part the principal integration approaches of these diverse device structures will be addressed: vertical integration schemes relying on evanescent optical coupling between vertically stacked device levels; and lateral integration schemes exploiting in-plane optical coupling of the optical devices. In the latter case, butt-joint coupling, selective-area-growth, and quantum-well intermixing are being used, all of them geared to accomplish lateral band gap engineering. In the following section, recent examples of PICs based on proprietary technology solutions will be given. The second part of this chapter discusses generic photonic integration copying the foundry model successfully established in the electronics world. In this model, using defined building blocks, PIC design and manufacturing are strictly separated, thereby facilitating open access to this technology. As an example of such a generic platform, the TxRx technology developed by Fraunhofer HHI will be outlined. Selected building blocks will be described, and representative PICs made on multi-project wafer runs will be shown highlighting the viability of the foundry approach. In addition, the supply chain required for successful adoption of the foundry model will be briefly covered, including the design software environment, testing and wafer validation capabilities, and also generic packaging.

N. Grote (✉) · M. Baier · F. Soares

Photonic Components Dept., Fraunhofer Institute for Telecommunications,
Heinrich-Hertz-Institute, Einsteinufer 37, 10587 Berlin, Germany
e-mail: norbert.grote@hhi.fraunhofer.de

M. Baier

e-mail: moritz.baier@hhi.fraunhofer.de

F. Soares

e-mail: francisco.soares@hhi.fraunhofer.de

16.1 Introduction

Monolithic photonic integration follows the same fundamental idea as the micro-electronic integrated circuits technology, but in the optical domain: to combine a number of the same and/or different device structures in one chip to implement complex optical functionalities in the form of photonic integrated circuits. The motivations for this approach are manifold: lower packaging costs by reduced number of fiber ports; defined optical phase conditions within the optical circuit as required, for instance, with coherent technology; enhanced opto-mechanical stability of optical connections, hence superior reliability; reduced optical coupling losses; lower cooling power consumption; and miniaturization to meet the desire of more and more shrinking the form factor of modules.

The vision to create monolithic photonic integrated circuits (PIC) using InP was already conceived [1] shortly after the emergence of the first semiconductor lasers on InP in the mid of the 1970's [2]. At that time and during the following decade III–V technology, and InP technology in particular, was generally in an infant state, and all but viable to support the implementation of this concept. Amongst others, extremely well controllable epitaxial growth techniques, providing compositions and thicknesses and doping concentrations of InP and the related composite InGaAsP and InGaAlAs layers with ultra-high precision, are key to successful realization of any InP photonic device, and this is by far even more true for monolithic integration. Until the second half of the 1980's, Liquid Phase Epitaxy (LPE) was still prevailing, which was not capable of meeting those demands. Advanced growth techniques like Metalorganic Vapour Phase Epitaxy (MOVPE) and Molecular Beam Epitaxy (MBE) that are commonly used nowadays were only in an early development stage with InP materials. Nonetheless, even during that period, basic integration approaches were already successfully investigated and simple integrated device structures accomplished, and in the late 1980's and 1990's those studies led to remarkable early demonstrations of extended PICs, e.g. [3–5]. Despite steady progress, however, interest in monolithic photonic integration drastically lost importance during the last decade of the past century because of a growing economic pressure on components developers to focus on more mature and deployable components, meaning to give priority to simpler, essentially discrete devices. It also happened at that time that quite a few big companies worldwide abandoned investing in InP technology and closed or spun off their respective departments. Many of them reappeared as new but smaller companies for which risky PIC technology expectedly was not among their primary business goals. Moreover, hybrid integration was seen as a viable alternative.

The situation changed with the US company Infinera (www.infinera.com), founded in 2000 under the previous name Zeptron Networks, which deserves the credit of having re-energized InP PIC technology by identifying and establishing it as a key enabler for future fiber communication systems. This commercial development raised a lot of awareness for PICs, and in the following period of time a strong increase of respective activities occurred having led to more and more enhanced PIC capabilities.

InP did not remain the only materials option for PICs but silicon-on-insulator (cf. Chaps. 14, 15) emerged as a competing platform. There is a fundamental difference however: InP technology is unique in that it supports monolithic integration also of light-amplifying and light-emitting devices, namely gain elements/optical amplifiers and lasers which are of crucial importance for a wide range of photonic applications.

Until recently the dominant working method in integrated photonics has been to develop optimized chip designs and fabrication processes for each and every application, starting from the specifications of the envisaged product. As a result of this approach, a broad range of different and proprietary PIC technologies has been created. Due to this huge fragmentation in relation to the associated market sizes, the cost price per PIC chip has been high, likely too high, for a successful and sustainable introduction into products. In particular, the cost of entry is too high for most businesses. To mitigate this issue research and development activities have been commenced recently to adopt the foundry model which has been extremely successful in the microelectronics industry for decades. This generic approach makes use of a set of defined building blocks which are offered to designers to create their individual integrated photonic chips. The cost advantages of this method are evident. In particular, many different circuit designs can be accommodated on the same wafer and made in the same fabrication run so that prototyping costs can be shared by many users. Compared to electronics, however, transfer of this approach to photonics is substantially more demanding due to the diversity of building blocks and associated device structures.

In this chapter we will first address key technologies involved in InP based photonic integration, followed by examples of state-of-the art integrated components. In the second part we will focus on the generic integration approach.

16.2 Key Technological Challenges of Photonic Integration

The InP class of materials (InGaAsP, InGaAlAs) offers to implement an unrivaled range of different functionalities: “receiver” devices, especially pin photodiodes; optical waveguides and passive optical devices built on them, like directional and multi-mode interference (MMI) couplers, AWG filters, ring filters, polarization splitters and converters; thermo-optic phase shifters and electro-optic modulators, and others; and above all “transmitter” devices including (wavelength tunable) DFB and DBR lasers, semiconductor optical amplifiers (SOA) and the structurally related electro-absorption modulator (EAM) devices. Even more, also electronic devices may be incorporated for which InP materials are particularly qualified when ultra-high speed applications are envisaged.

The various devices to be integrated rely on different “active” band gaps and layer structures. At a given operating wavelength, waveguides need to be optically transparent (i.e. high band gap) and photodiodes absorptive. The gain spectrum of laser and SOA diodes should be centered around the operating wavelength for optimum

gain performance whereas the band-edge of EAM elements has to be distinctly detuned. Therefore, the fundamental challenge with monolithically integrating those devices to create photonic circuits is how to realize the associated very diverse structures on the same wafer and how to accomplish optical connections between them – as loss-less and reflection-less as possible. Not to forget electrical connections as well as thermal issues. In the following main approaches will be described.

16.2.1 Vertical Integration

Dual-Waveguide Structures In adjacent waveguides with overlapping mode profiles guided light is well known to be transferred from one waveguide to the other by evanescent coupling. This basic mechanism has been efficiently exploited to connect different optical devices in a vertical configuration. The main advantage of this scheme is the fact that the layer structures of the individual devices can be sequentially grown in one epitaxial step.

Waveguide-Photodiode Integration The most common application of the vertical coupling scheme has been the optical connection of a pin photodiode to a passive waveguide, as illustrated in Fig. 16.1(a) (and described in more detail in Chap. 6). In essence, the pin layer stack of the photodiode which can be seen as an absorbing waveguide is placed on top of a waveguide. Due to the higher refractive index of the intrinsic absorption layer the light is gradually extracted from the waveguide along its propagation direction to create a vertical flow of photo-generated electrons and holes across the pin junction. This way the traveling distance of the carriers determining the transit time is decoupled from the absorption length, and ultra-high bandwidth (even > 100 GHz [6]) can be achieved without sacrificing responsivity. When building such structures on semi-insulating substrates and using semi-insulating waveguide materials to provide efficient electrical isolation between different photodiodes, extended integrated receiver components (referred to as Rx-PIC) can readily be designed and fabricated incorporating e.g. balanced detectors or arrays of photodiodes in conjunction with other optical waveguide devices. Prominent examples of Rx-PICs are amongst others receivers for phase- or quadrature-modulated transmission systems (e.g. [7], see also Sect. 3); and for wavelength-division-multiplexing (WDM) detection schemes (e.g. [8–10]).

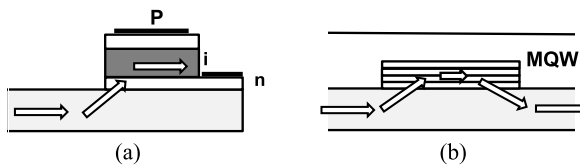


Fig. 16.1 (a) Schematic of vertical waveguide-photodiode integration employing evanescent coupling, and (b) passive-active waveguide integration using “offset” MQWs

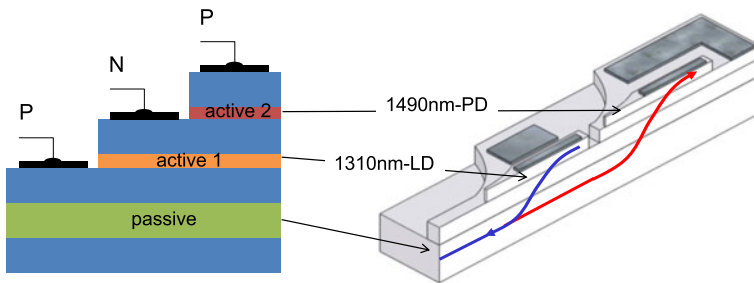


Fig. 16.2 Optical duplexer PIC relying on multi-guide vertical integration: (*left*) principal layer stack comprising two different active waveguides for the photodiode and the laser diode; (*right*) 3D-sketch of the structure with the *blue line* indicating the 1310 nm output laser beam and the *red one* the incoming 1490 nm light (adapted from [12])

Off-Set Quantum Well Configuration A similar coupling technique which is especially employed with combinations of active-passive waveguides is presented in Fig. 16.1(b). Here, an active MQW layer region (called “offset quantum-well”) is placed on top of a passive waveguide with a bulk core layer (but may also consist of another MQW region). The upper MQW is to form the active region of devices like lasers, SOAs, and EAMs and will be removed outside the active area by a suitable etching process. As with the photodiode integration, light guided in the bottom waveguide will be “drawn” into the higher-index MQW stack to get amplified (in SOA structures) and to generate lasing (in the presence of a feedback mechanism). At the active-passive interfaces the propagating lightwave experiences an unavoidable discontinuity of the refractive indices of the waveguide materials which induces optical interface losses and back-reflections. To mitigate these detrimental effects slanted and tilted structures are most helpful. A less challenging overgrowth step covering the full wafer is finally required to create the upper cladding layer structure, including an InGaAs Ohmic contact cap layer.

Multi-Guide Vertical Integration Recently the vertical integration technique has been largely generalized by the Canadian company OneChip Photonics (www.onechipphotonics.com) towards multi-functional PICs by placing a series of functional optical waveguide levels on top of each other. Such a technology has recently been made available on a foundry basis [11]. As outlined above, light is propagating between the different levels by stepwise vertical twin-guide coupling. With an input/output waveguide placed at the bottom the different levels are arranged such that the associated waveguide band gap wavelengths are increasing upwards. All of the waveguides feature a ridge design, and lateral tapers are formed at each guiding level to enable smooth optical transition of the coupled light-waves. The principle is exemplified in Fig. 16.2 on an optical duplexer chip comprising a transmitter laser diode (1310 nm emission) and a photodiode tailored for 1490 nm detection [12]. In this structure the bottom waveguide is designed such that it provides a wavelength splitting function for the transmitter and receiver wavelengths by properly adjusting its ridge width.

Fig. 16.3 Schematic of an electro-absorption modulated transmitter laser PIC incorporating a DFB laser diode (DFB-LD); electro-absorption modulator (EAM); and passive waveguides (PWG) with spot-size converters (SSC); N, P = electrical contacts (courtesy of OneChip Photonics)

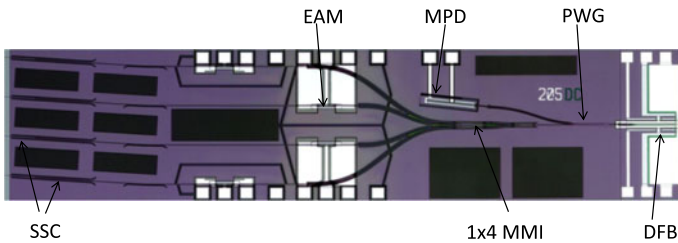
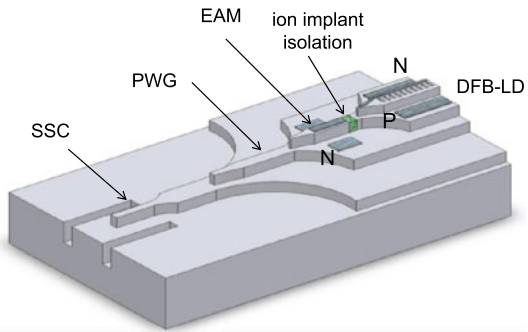


Fig. 16.4 Image of 4×25 Gb/s SDM transmitter PIC implemented on a multi-guide vertical integration platform [13]; MMI = multimode interference coupler; for other acronyms refer to Fig. 16.3

Another example is an electro-absorption modulated laser (EML) represented in Fig. 16.3. Here, an electro-absorption modulator (EAM) is placed below the laser level carrying the DFB seed laser. From the EAM the emitted light is again coupled downwards into the output waveguide which exhibits a spot-size converter at its end to provide low-loss and alignment-tolerant coupling to a single-mode fiber.

Building on the multi-guide vertical integration technology various advanced PIC components have been demonstrated recently: The transmitter structure shown in Fig. 16.3 was extended into a four-channel transmitter PIC designed for 4×25 Gb/s space-division multiplexing applications (Fig. 16.4, [13]). It comprises one DFB laser (1303 nm) with a surface-etched Bragg-grating to feed four EAMs (3-dB bandwidth measured to be 24 GHz) via an 1×4 beam splitter composed of cascaded 1×2 MMI couplers. A photodiode allows for monitoring the launched optical laser power. The output waveguides feature spot-size converters to provide efficient output coupling to the four parallel single-mode fibers (PSM4). A matching 4×25 Gb/s receiver PIC has been reported in [14], along with a similar device designed for use in wavelength-division-multiplexing systems. The optical demultiplexer in the latter device was implemented as an etched diffractive echelle grating. Further, a dual-polarization QPSK coherent receiver to operate at a symbol rate of 32 GBaud and capable of 112 Gb/s detection in total was demonstrated [15].

The main advantage of vertical integration is the fact that it needs only one epitaxial step for the entire layer structure. Thus, subsequent and potentially more risky

regrowth processes, as crucial with lateral integration and addressed in the following section, are avoided. Along with this, epitaxy and wafer processing may be strictly separated in the supply chain. On the other hand, this scheme requires highly sophisticated epitaxial structure design with typically ~ 100 individual layers demanding particularly precise thickness and composition/refractive index control because these parameters largely affect the optical coupling conditions inside the stack. Furthermore, depending on the number of device levels a particularly large number of corresponding lithographic masks may be involved in wafer fabrication.

16.2.2 Lateral Integration

The opposite scheme to vertical integration is lateral integration where the functional elements are arranged in the same plane. Here, the light in the PIC propagates horizontally from one waveguide into another – active or passive – across optical interfaces that need to be formed so as to provide minimal optical coupling losses and back-reflections. In fact, lateral integration configurations are most commonly used even though, in practice, a mixture with vertically integrated structures is used. This is particularly true when photodiodes are involved for which the evanescent coupling scheme, as outlined in Sect. 2.1, represents the perfect solution.

Butt-Joint Coupling The most flexible lateral integration method is butt-coupling (Fig. 16.5(a)) which allows combining waveguides of fairly different designs: active/active and active-passive; quantum-well and bulk layers; widely differing band gaps; weakly and strongly guidance; ridge and buried-heterostructures (see also Chap. 3, Fig. 3.4). To enable smooth optical transitions tapered interface regions are incorporated. An example is sketched in Fig. 16.5(b) which refers to semi-insulating (Fe-doped) butt-joint ridge waveguides with a shallow (200 nm, loss < 0.5 dB/cm) and a deep ridge (1700 nm, ~ 2 dB/cm), respectively, as used on Fraunhofer HHI's PIC platform [16]. Respective measurements (conducted at Politecnico di Milano)

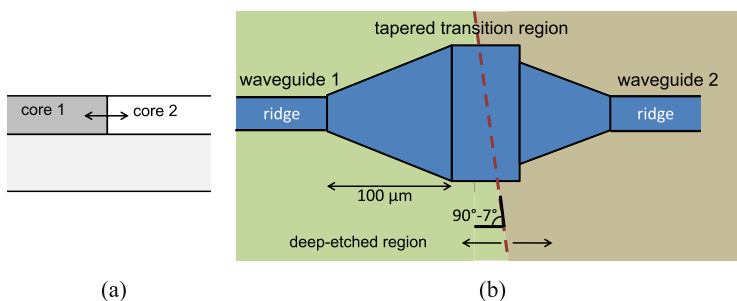


Fig. 16.5 (a) Basic vertical cross-section of butt-coupled ridge-waveguides represented by the two core layers 1 and 2; (b) example of tapered transition (top view) between a shallow (200 nm ridge height) and deep ridge waveguide (1700 nm) of $2 \mu\text{m}$ width [16]

have indicated a typical coupling loss of some 0.2 dB, and back-reflections well below -50 dB. Comparable values (0.19 dB and < -50 dB, respectively) were obtained on related active-passive butt-joint structures [17] suggesting such data to be representative for what may be reliably achievable.

Butt-Joint Regrowth Implementation of the butt-coupling principle inevitably demands epitaxial regrowth at defined areas on the wafer. The key word here is selective-area-epitaxy (SAE) which has been studied and applied for more than 30 years, and published in numerous papers (e.g. [18, 19]). A widely established application is the formation of current-blocking layers in buried-heterostructure laser diodes (see Chap. 3, Fig. 3.4).

SAE refers to a growth process where the wafer to be regrown is partially covered by a dielectric masking film (usually made of SiO_2 or Si_3N_4) which is etched away in those areas where epitaxial growth is to occur. For implementing butt-joint structures this process is followed by etching of the underlying semiconductor layers to create the exposed mesa grooves in which to selectively fill in the regrown layers. Using “chemical” epitaxy techniques, MOVPE and also MOMBE (metalorganic MBE), no deposition occurs on the mask material under defined growth conditions; in a limited space of relevant growth parameters (temperature, reactor pressure, III/V ratio, etc.) it takes place only in the exposed regions. At typical MOVPE growth temperatures (for InP materials around 600°C), the constituent species generated by pyrolysis of the MOVPE precursors cannot be adsorbed on the amorphous mask material. Rather, as illustrated in Fig. 16.6, they diffuse in the vapor phase and migrate on the mask surface towards the growth area near the mask edge where they additionally contribute to the wanted layer deposition. However, this occurrence along with mesa sidewall effects is associated with irregular local growth behavior characterized by enhanced growth rates, different crystal planes and also – in the case of ternary and quaternary materials – stoichiometric deviations.

The MOVPE growth habit near the mesa edge is affected by a range of parameters including process parameters, mask dimensions, and materials involved. Slightly overhanging masks are particularly effective in suppressing excess edge deposition. Figure 16.7 shows a scanning electron microscope (SEM) photograph of

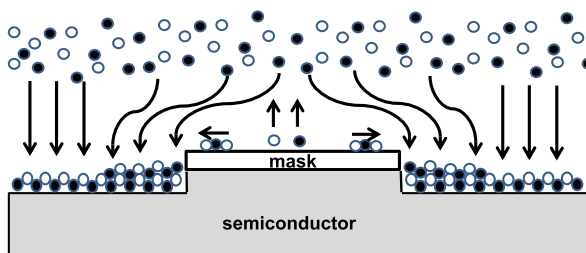


Fig. 16.6 Simplified basic mechanisms of selective-area-MOVPE, illustrated for the butt-joint growth case: diffusion in the gas phase and on the mask material, and desorption from the mask surface; *open and full circles* symbolize two representative growth species

Fig. 16.7 SEM photo of a cleaved butt-joint active (laser)-passive waveguide layer structure grown by MOVPE (Fraunhofer HHI)

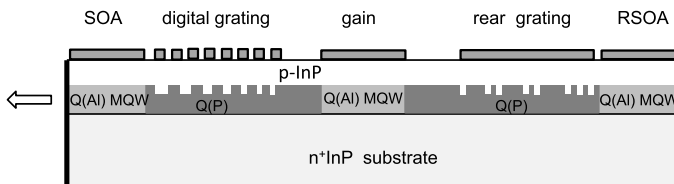
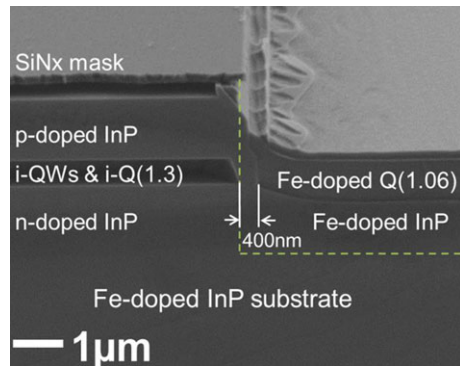


Fig. 16.8 Cross-section of a tunable laser diode, called digital supermode distributed Bragg reflector (DSDBR) laser, featuring four butt-joint interfaces (adapted from [20]); Q(P) = InGaAsP, Q(AI) = InGaAlAs

cleaved cross-section of a real waveguide-waveguide structure made by butt-joint regrowth. The perturbed region can be seen to stretch out only over a few micrometers, thus not largely affecting optical coupling.

In earlier days butt-joint growth was regarded as an integration technique that would be extremely difficult to control and might inherently entail reliability risks. Nowadays, however, such concerns have been eliminated, and butt-joint growth has become a widely established processing step. This is exemplarily illustrated on the widely-tunable laser structure sketched in Fig. 16.8, which combines gain and amplifier sections, a phase section and tunable gratings [20]. The fabrication of this device, which can be considered a PIC in itself and meanwhile has reached product status, involves no less than four regrowth interfaces. Even more, the structure involves butt-joint interfaces of InGaAsP/InGaAlAs layers which are particularly challenging because of the known Al-oxide issue (see also Chap. 3, Sect. 3.3.2).

Selective-Area-Growth Based Integration A variant of selective epitaxy is known under the name Selective-Area-Growth, SAG. This technique aims at creating spatial band gap variations of a given layer structure on the wafer whilst avoiding butt-joint regrowth. Employing SAG, devices with different active regions can be implemented that may be connected in series or configured as a parallel array, for example to build a coarse-wavelength-division multiplexing (CWDM) transmitter. Using the traditional channel spacing of 20 nm an 8-channel CWDM array requires a set of laser diodes emitting over a wavelength span of 140 nm which is not achiev-

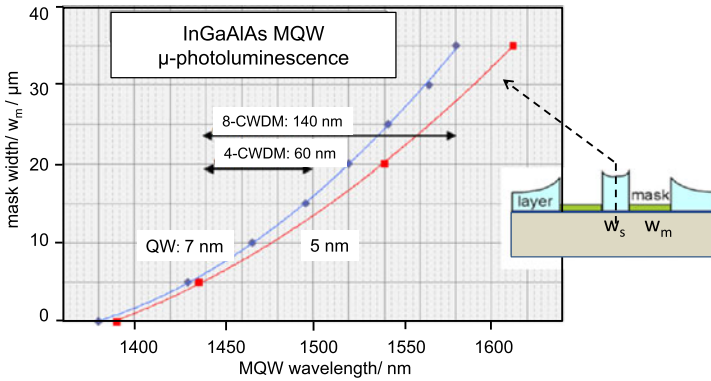


Fig. 16.9 Relationship between mask width, w_m , and InGaAlAs MQW peak wavelength as measured by micro-photoluminescence (spatial resolution: $\sim 2 \mu\text{m}$) in the middle of the SAG stripe (width $w_s = 20 \mu\text{m}$). The *insert* schematically depicts the thickness profile. Reference QW thicknesses for large-area deposition ($w_m = 0$) are 7 nm (blue curve) and 5 nm (red curve), respectively. The *inserted arrows* indicate the wavelength region covered by 4 and 8 coarse-wavelength-division multiplex (CWDM, 20 nm spacing) channels, respectively (work of III–V Lab, France)

able with the same active layer. Furthermore, SAG allows for regrowth-free gradual – ideally adiabatic – transitions between waveguides of different effective band gaps.

SAG deliberately makes use of the growth enhancement effect encountered with SAE in that it locally generates increased layer thickness. When applied to QW layers this increase directly leads to an increase of the associated QW transition wavelengths. Indeed, SAG is essentially employed in conjunction with QW structures to exploit the large wavelength dependence on well thickness, d_w , which is well known to follow a $\Delta E_g \sim 1/d_w^2$ relationship (with ΔE_g denoting the band gap increase). This effect is not present in bulk layers. Another reason for this restriction is the fact that the SAG related growth rate enhancement effect comes along with a change in layer composition, caused by different diffusion and decomposition rates of the group (III) components. This occurrence is commonly subcritical with MQW stacks but may be not in the case of thicker ternary and quaternary layers where the induced strain tends to degrade the crystalline quality. Nonetheless, SAG has been successfully applied to fabricate spot-size converters involving tapered InGaAsP bulk layers, namely in MZ modulator devices [21].

Practically, SAG structures are fabricated under similar conditions as butt-joint regrowth (see Fig. 16.6); the main difference is that the growth process generally takes place on planar rather than etched wafers. SAG thickness control is accomplished by elaborate designs of the mask (SiO_2 ; Si_3N_4) that is deposited on the wafer prior to the SAG growth process. Usually a pair of stripes is involved the area between which is utilized for the actual SAG devices. The inset in Fig. 16.9 shows a schematic cross-section. The SAG effect is predominantly determined by the geometric dimensions of the mask, that is the width of the parallel mask stripes and the distance between them. However, the overall mask lay-out also plays a role

(“loading effect”), and dummy masks may be useful to achieve a uniform as possible distribution of patterned and non-patterned areas on the wafer. As represented in Fig. 16.9 the SAG effect on the MQW band gap, here expressed by the inverse wavelength, is really huge indeed. Increasing the mask width, w_m , from zero (= large-area growth) to 35 μm causes a wavelength “red-shift” of some 200 nm, slightly dependent on the starting thickness of the well layer in the MQW stack. Decreasing the gap width, w_s , instead has a similar effect. The data of Fig. 16.9 were obtained from micro-photoluminescence scans (spatial resolution of some 2 μm) perpendicular to the mask stripes across the non-uniform gap (w_s) and were taken in the middle of that gap.

Smooth optical transitions between different MQW waveguide sections can be easily achieved by properly shaping the mask geometry along the longitudinal direction. Tapering w_m gradually over a distance in the 100 μm to 200 μm range may be sufficient to reach adiabatic behavior. The same SAG technique can be employed for implementing BH-MQW laser diodes with integrated spot-size conversion functionality by tapering the active MQW layer [22].

In principle SAG can be used with both the InGaAsP and InGaAlAs material system. Most of the published studies relate to the former one (e.g. [23]). However, InGaAlAs is not only known for its advantageous “inverted” band structure (see Chap. 3) but also benefits from the presence of only one group (V) element. This feature leaves, in a fairly linear fashion, growth rate and composition control solely to the group (III) species which considerably eases predicting SAG results. In fact, efficient modeling tools [24] have been developed in conjunction with InGaAlAs allowing for simulating the impact of mask patterns on spatial (QW)-layer properties (thickness, band gap, strain) and eventually for designing the SAG mask lay-out for a complete PIC design. SAG process modeling has been relying on simplified diffusion mechanisms in the MOVPE gas phase but more recently it has been refined taken into account additional effects, like the overgrowth at mask edge and migration on the mask surface [25]. In any case, to transfer SAG simulation results to real structures a range of experimental fitting parameters are required that are specific to the individual MOVPE growth reactor used. SAG transfer from one epitaxial reactor to another still demands considerable recalibration work. For experimental evaluations there is a particular need for measurement techniques featuring high spatial resolution, such as micro-photoluminescence, micro-focus high-resolution X-ray diffraction (HR-XRD), and synchrotron based XRD [26]. Optical interference microscopy and mechanical profiling are employed for thickness measurements.

Recently, various world-class PIC devices relying on SAG technology have been successfully demonstrated, particularly by researchers of III–V Lab, France. Figure 16.10 shows the emission spectra of a parallel 8-array of InGaAlAs MQW ridge-waveguide DFB lasers, each of them butt-joined to a passive InGaAsP waveguide at either side. The mask width, w_m , was varied between 6 μm and 30 μm , whereas the gap between the masks, w_s , into which the laser material was grown was kept at 20 μm . The pitch of the array was 250 μm . As can be seen, the lasers cover a total spectral range of more than 140 nm, with a fairly equal wavelength spacing of nominally 20 nm. Typical threshold currents of these devices were well around 20 mA,

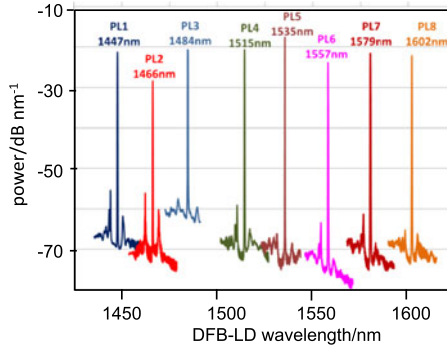


Fig. 16.10 Emission spectra of an 8-CWDM DFB InGaAlAs MQW laser array fabricated by SAG. Each DFB laser device is 400 μm long with a 200 μm long centered DFB grating and is integrated with butt-joined passive input and output waveguides (collaborative work of III–V Lab and Fraunhofer HHI conducted in the framework of the European project PARADIGM [27])

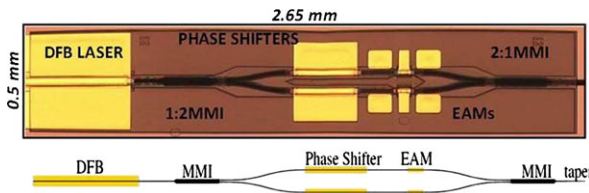


Fig. 16.11 Fabricated transmitter PIC for complex modulation schemes based on SAG technology: chip photograph (*top*) and device architecture (adapted from [30]). The *black stripes* indicate the waveguides (MQW wavelength ~ 1390 nm), and the *yellow patterns* the various electrical contacts of the DFB laser and of the EAMs (active MQW wavelength: ~ 1550 nm and ~ 1530 nm). The 50 μm long EAM elements exhibit a dynamic extinction ratio of up to 18 dB and a modulation bandwidth of >20 GHz

and the optical output power measured at the passive waveguide output varied from 7–10 mW at 100 mA drive current.

A “serial” SAG based PIC is depicted in Fig. 16.11. It represents a compact transmitter device that can be used for generating complex amplitude and phase modulation formats [28, 29]. Essentially, it comprises a DFB source laser and a Mach-Zehnder (MZ) interferometer structure each arm of which incorporates a current-injection phase shifter and an electro-absorption modulator to provide push-pull operation. In the MZ 1:2 and 2:1 MMI structures serve as input and output couplers, the latter terminated by a spot-size converter accomplished by simultaneous lateral and vertical tapering. Whereas the passive waveguide sections including the MMIs have been grown in mask-free areas the band gaps of the laser diode and the EAMs, and also of the SSC, are adjusted by adjacent SAG masks, as introduced above.

The structure shown in Fig. 16.11 has been extended into a significantly more complex transmitter enabling polarization-diversity QPSK transmission. Apart from

quadrupling the number of EAMs and phase shifters that device additionally integrated variable optical attenuators (VOA) and optical amplifiers (SOA) altogether requiring five different band gaps [31].

Quantum-Well Intermixing Quantum-well intermixing (QWI) is a technique that relies on a compositional modification of hetero-interfaces. To create a sizeable band gap effect, it is only applicable to quantum-well structures, as the name suggests. The underlying physical effect is the natural tendency of different materials to interdiffuse, and this phenomenon is deliberately enhanced by suitable QWI processes which can be locally applied on a device wafer. The interdiffusion of atoms tends to change abrupt interfaces into compositionally graded ones, and in QW layers this affects the position of the QW energy levels and hence the band gap wavelength, as sketched in Fig. 16.12.

In various investigations the QWI process was identified to be related to the presence of impurities and defects in the vicinity of the QW structure. Even without special measures annealing processes tend to cause intermixing of atoms across the QW interfaces, the rate depending on temperature (typically above some 600 °C) and time, and a range of structural parameters; even the substrate properties (defect density, doping) seems to have an impact [32]. The intermixing effect appears to be mostly related to the group (V) elements, and consequently InGaAsP-QWs were found to be more prone to this effect than comparable (In)GaAlAs structures [33]. Note that the latter features a uniform group (V), i.e. arsenic, concentration profile across the QW barriers and wells.

QWI procedures are used to largely accelerate the intermixing process by introducing additional point defects. This can be done in selected, lithographically defined areas on the wafer, thus making local band gap engineering feasible. Different QWI variants have been developed, including impurity-induced disordering; impurity-free vacancy-enhanced disordering; photoabsorption-induced disordering; and implantation-enhanced interdiffusion. Here we will briefly address the latter approach [34, 35]. A comprehensive overview on the three former techniques may be found in [36].

Ion implantation is employed to introduce point defects in a controllable way using phosphorus anions (P^+). These are not directly implanted into the QW layer

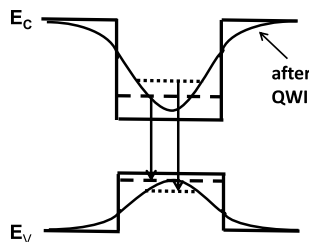
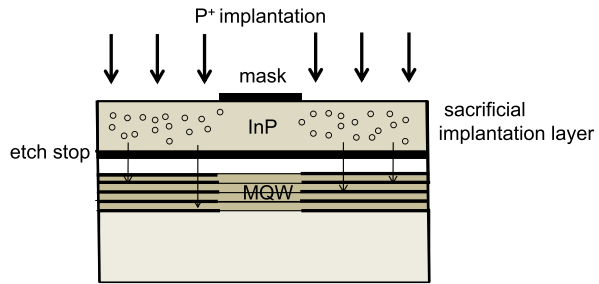


Fig. 16.12 Schematic representation of QWI effect on composition and effective band gap (arrows) of a QW layer; conduction and valence band energy levels of an abrupt QW are indicated by the broken lines, and those after QWI processing by the dotted ones

Fig. 16.13 Schematic of ion implantation based QWI. Ions are implanted into an upper InP buffer layer to create point defects that diffuse into the QW region upon high-temperature annealing. Spatial selectivity is achieved through implantation masks



stack but in a buffer layer on top of it (Fig. 16.13). Upon thermal annealing at high temperatures, typically above 600 °C for InGaAsP based structures, the generated point defects diffuse into the QW region to induce the intermixing mechanisms. The strength of this effect is determined by a number of structural and process parameters, such as layer thicknesses, compositions and doping; implantation energy and dose; annealing ambient; time and temperature. It is obvious that for each particular device structure the QWI process has to be carefully adapted and recalibrated. Areal selectivity is achieved by masks on the wafer surface. To create different band gaps there are two choices, that is employing sequential implantation with different ion energies and doses followed by a common annealing step, or alternatively a common implantation step and stepwise annealing including sequential etching of the previously annealed buffer layer region. The latter option is certainly more economical since the expensive implantation process has to be used only once. Parameters reported in [35] for P⁺-ion implantations were: energy of 100 keV and a dose of $5 \times 10^{14} \text{ cm}^{-2}$.

A prerequisite is, however, that the preceding intermixing steps remain unaffected by the subsequent anneals. This is in fact the case as becomes apparent from Fig. 16.14 depicting the QW wavelength shift in dependence of the annealing time (RTA = rapid thermal annealing). Once an implanted region is removed the PL peak wavelengths of the underlying QW regions behave stable.

The question as to how QWI may affect optical device properties is exemplarily highlighted in Fig. 16.15 showing results of electro-absorption measurements performed on as-grown samples and samples subject to ion-implantation based QWI treatment. The excitonic absorption characteristics can be seen to be well retained despite the intermixing processes evidencing QWI not to distinctly degrade the crystalline integrity.

Exploiting QWI technology various integrated devices, especially combinations of lasers and electro-absorption modulators (EAM), have been successfully demonstrated recently, notably at the University of California Santa Barbara. As shown above EAMs are particularly predestined for utilizing QWI because it provides the required band gap “blue”-shift in relation to the laser band gap, unlike SAG which is a “red-shift” technology. Integration with widely-tunable SG-DBR lasers and with DBR lasers have been reported in [37] and [38], respectively. Another application is wavelength converters [35]. In one architecture, a widely tunable laser diode (SG-DBR) was integrated with a SOA based Mach-Zehnder interferometer exploiting

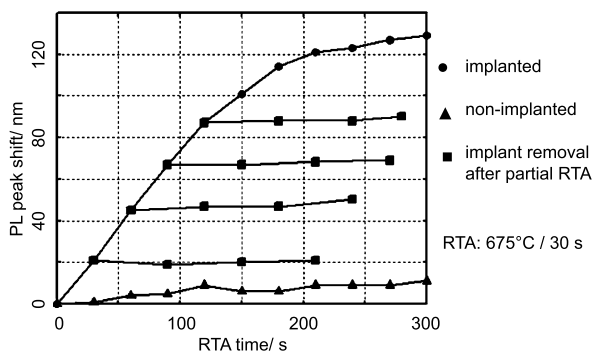
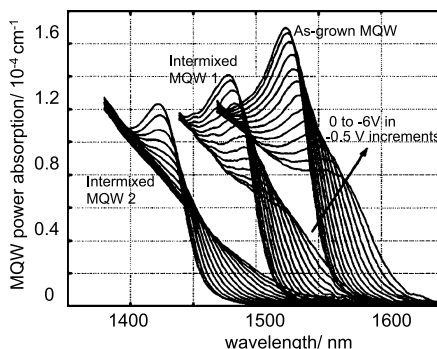


Fig. 16.14 Effect of rapid thermal annealing (RTA) time on QWI wavelength shift in a 7-QW InGaAsP/InGaAsP ($PL_{peak} = 1560$ nm) sample capped with an 450 nm thick phosphorus implanted InP layer; The measured photoluminescence peak wavelength shifts towards shorter wavelengths (“blue” shift) but remains fairly stable after removal of the implanted region (after [37])

Fig. 16.15 Photocurrent spectroscopy measurements on reverse-biased InGaAsP based MQW pin mesa structures. The exciton peaks are still clearly visible after QWI shifting the band edge towards shorter wavelengths [37]



cross-phase modulation. Employment of QWI successfully helped optimize active-passive waveguide transitions and reduce the carrier lifetime in the QW-SOA resulting in wavelength conversion over the full C-band at 10 Gb/s data rates [39]. The QWI technique is not restricted to InP materials but is likewise applicable to other semiconductor systems. In [40] GaAs-GaAlAs based photonic integrated circuits for sensing applications have been reported the fabrication of which involved QWI, in this case in the form of vacancy-enhanced disordering, for the integration of DBR lasers, photodetectors, phase modulators and passive waveguide elements.

16.3 Recent Achievements

In this section examples of InP PIC achievements will be presented to highlight the current state-of-the-art in this field. We will focus on most recent implementations essentially relying on application specific fabrication approaches. Comprehensive overviews of previous developments may be found in [41, 42].

Fig. 16.16 Evolution of InP based monolithic photonic integration by number of components per chip [42]

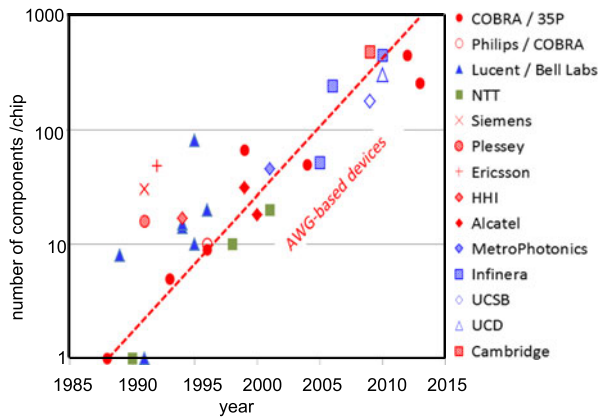
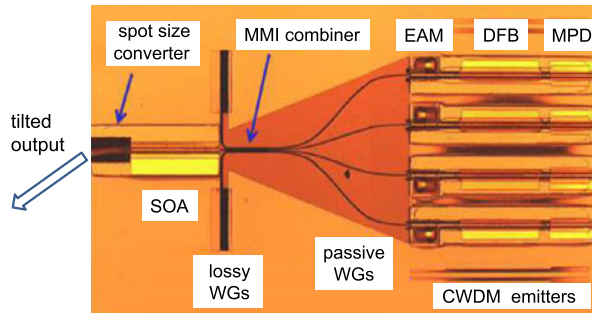


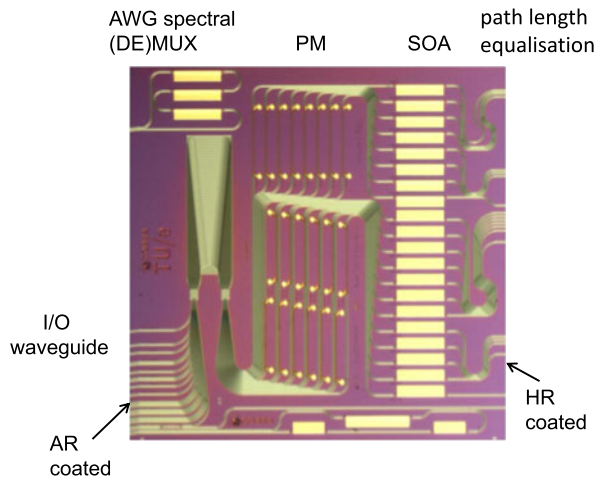
Fig. 16.17 Chip photograph of a monolithic CWDM transmitter PIC made by SAG technology (III-V Lab; after [43])



As mentioned in the introduction photonic integration started already in the 1980's. Since then steady progress has been made despite fluctuating attention over the years. The worldwide evolution of InP based photonic integration from 1990 until today is depicted in Fig. 16.16. As an indicator of complexity the number of devices integrated on the same chip has been taken which can be seen to have reached a level of the order of > 500 . Such large-scale (on a photonic scale) PICs are now being commercially deployed in optical communications systems. Predicting the future evolution in InP PIC technology is naturally rather speculative, however, unless a truly disruptive integration technology will emerge the count of integrated devices per chip may not exceed a some ten thousand even in the long run owing to limitations in functionality and fabrication yield.

Exploiting the SAG integration approach which has been shown in Sect. 2.2 to be particularly useful for covering a wide operational wavelength range a 4-channel CWDM transmitter PIC has been realized. A photograph of a respective chip is displayed in Fig. 16.17. The actual transmitter in each channel consists of a DFB laser modulated by an electro-absorption modulator (EAM) at 10 Gb/s. At the backside the laser diode is connected with a monitor photodiode (MPD). The signals, spaced by 20 nm in wavelength, are multiplexed by a 4×1 MMI combiner the inherent losses of which are compensated by a common SOA placed in the output waveguide which again is terminated by a spot size converter [43].

Fig. 16.18 Microscope image of a pulse-shaper PIC for chirp compensation; chip size: $6 \times 6 \text{ mm}^2$; PM = phase modulator (TU Eindhoven, The Netherlands; [45])



The PIC shown in Fig. 16.18 is targeting optical signal processing, namely optical pulse shaping which in general means synthesizing a defined output waveform from a given optical input pulse (for further reading on this topic see [44]). The particular chip shown uses optical pulse shaping to perform dispersion compensation for highly chirped optical pulses. The device integrates a 20-channel arrayed waveguide grating with 20 electro-optic phase modulators and 20 semiconductor optical amplifiers on a single chip of $6 \times 6 \text{ mm}^2$. The light from an optical pulse source is launched into the chip (AR-facet) and passes through an AWG to be decomposed into its spectral components which again propagate through the phase modulators and SOAs. These are used to manipulate their spectral phase and amplitude. After back-reflection at the HR-facet the individual components are recombined in the AWG to finally exit the chip through the common input/output waveguide [45].

Optical switches are particularly suited for monolithic integration given the large number of optical interconnects in matrices. There is currently much interest in energy efficient switching solutions for use within ICT equipment, both in datacenters as well as in the wider Internet. Fast optical switches, based on InP semiconductor optical amplifiers (SOAs) are attractive solutions because SOAs not only enable fast switching speed along with large dynamic on-off ratios but also allow for compensation of optical insertion losses. The switch shown in Fig. 16.19 is an 8×8 port optical switch based on the Clos architecture, altogether incorporating 64 SOAs. This $6 \times 4 \text{ mm}^2$ PIC has 8 input ports next to 8 output ports, located for ease of access on the same facet of the PIC. The switch uses four 2×2 port broadcast and select stages, followed by two 4×4 port and a further four 2×2 port stages to achieve its functionality. All of the switch stages are connected by low-loss passive waveguides. All of the optical paths through the switch exhibit on-chip gain between 4 dB and 8 dB. The performance of the switch is characterized by an input power dynamic range (IPDR) of 9.5 dB for a 1 dB OSNR penalty and has a minimum OSNR penalty of 0.65 dB for 10 Gb/s data streams. Simulations have been used to predict the performance of this switch design when extended to a larger number of

Fig. 16.19 An 8×8 port fast optical switch PIC using SOAs as switching elements interconnected by passive waveguides (Cambridge University/Oclaro, UK)

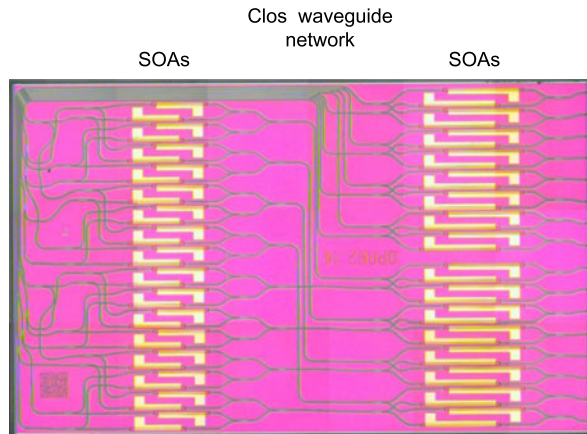
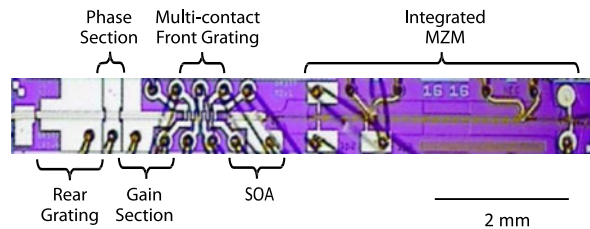


Fig. 16.20 Transmitter PIC incorporating a widely tunable DSDBR laser diode (>40 nm) and a Mach-Zehnder modulator (Oclaro, UK; [47])



input and output ports. It is predicted that a 64×64 port switch is feasible, with an IPDR of 6 dB for a 2 dB penalty [46].

Mach-Zehnder modulators in conjunction with CW driven lasers are attractive sources to generate ultra-high data rates using IQ modulation formats. While comparable with EMLs regarding potential electrical bandwidth they offer distinct advantages with respect to the optical operational bandwidth which can readily span over >40 nm, thus being predestined for WDM systems. Single-mode source lasers, with a fixed emission wavelength or wavelength-tunable, can be either co-packaged or monolithically integrated, the latter rendering possible very small-form factor modules. Figure 16.20 shows a monolithic chip that integrates a widely-tunable DSDBR laser diode, as already sketched in Fig. 16.8, with a ~ 2 mm long MZM. Such PICs, assembled in an SFP⁺ module, have recently been successfully tested as colorless transmitters in WDM configured passive-optical networks (PON) covering the full C-band [47].

Phase-shift keying has emerged as a highly efficient modulation method to enable 100–1000 Gb/s transmission systems. To this end, coherent receivers (CRx) have evolved into key devices for the demodulation of those phase-sensitive optical data signals. Such CRx components have been developed recently in different configurations by a number of companies and other organizations (e.g. [7, 48–51]). In essence, these chips comprise a 90° optical hybrid, made of a 4×4 MMI or a combination of 2×2 ones, providing output signals with the necessary phase relations to detect the in- and quadrature phase with a pair of terminating high-speed (balanced)

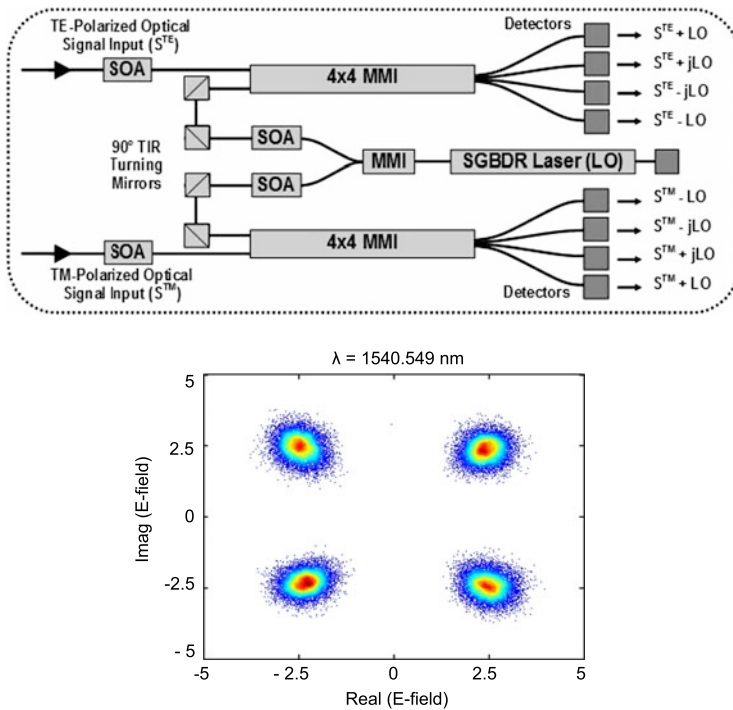


Fig. 16.21 Circuit diagram of recently developed monolithic dual-polarization coherent receiver chip including a wavelength-tunable laser diode (SGBDR) as local oscillator (*top*) and constellation diagram measured on a real chip (Freedom Photonics, USA; [51])

photodiodes, with or without on-chip electrical impedance matching. This circuitry is fed through two input waveguides for the input signal (with defined polarization) and the local oscillator reference signal. For exploiting both polarizations TE and TM (dual-polarization, DP) to double the aggregated bit rate this design is basically duplicated on the chip. Extensions have included variable optical attenuators [50] and polarization beam splitters [7]. Even more, in [51] a dual-polarization coherent receiver chip is presented that also incorporates a wavelength-tunable laser diode serving as local oscillator and additional optical amplifiers. The photonic circuit diagram of the latter device is depicted in Fig. 16.21, together with a measured constellation diagram. Most recently, coherent receiver PICs for symbol rates of 100 Gbaud have been successfully realized [52].

Corresponding optical transmitters are again based on Mach-Zehnder modulators (MZM) as their central components. For higher-order quadrature phase-shift keying modulation (QPSK, QAM) so-called IQ modulators are used the core of which consists of two data encoding MZ modulators nested in both arms of an outer MZM structure (schematic illustrated in Fig. 16.23). Such transmitter components are being available today from various vendors for use in long-haul and increasingly also metro networks.

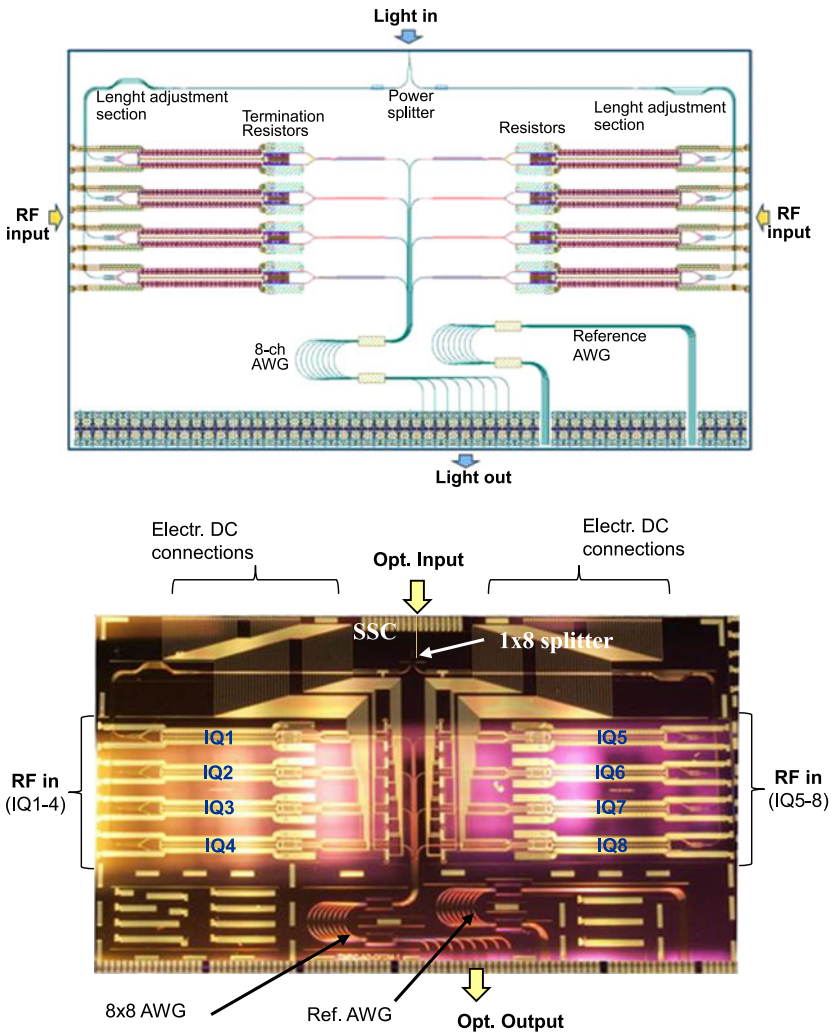


Fig. 16.22 Schematic (*top*) and microscope image (*bottom*) of a monolithic 8×25 Gb/s all-optical OFDM/Nyquist-WDM transmitter PIC having a footprint of $15.5 \times 28 \text{ mm}^2$ (Fraunhofer HHI, Germany, [53])

For WDM schemes multiple IQ structures have to be combined which is practically only feasible by photonic integration. Figure 16.22 shows a respective InP transmitter PIC which has been realized for all-optical 8×25 Gb/s OFDM/Nyquist-WDM data transmission (OFDM = orthogonal frequency division multiplexing) in the framework of the European project ASTRON [53]. Coherent optical orthogonal frequency division multiplexing (OFDM) and Nyquist-wavelength division multiplexing (Nyquist-WDM) are considered promising approaches for future flexible optical networks to generate spectrally efficient superchannels with

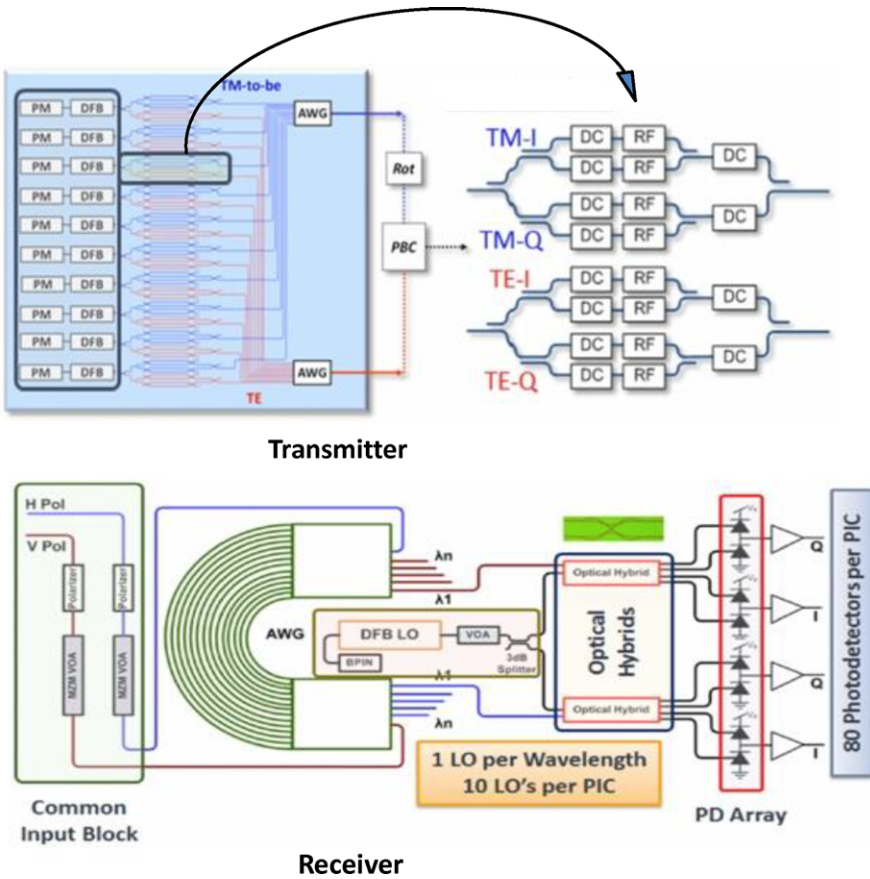


Fig. 16.23 Architectural diagram (*top*) of a PM-QPSK (polarization-multiplexed QPSK) transmitter PIC, capable of 500 Gb/s data generation, integrating >450 functional elements (in the *blue part*), including 10 tunable DFB lasers, monito photodiodes, 40 MZMs in total, and various sensing and control functions; (*bottom*) photonic circuit of the corresponding coherent receiver involving a local oscillator DFB laser for each wavelength channel (Infinera, USA; adapted from [55])

data bit rates up to several Tb/s. The entire chip measuring $15.5 \times 28 \text{ mm}^2$ encompasses eight IQ modulators involving MZMs with periodically capacity-loaded traveling-wave electrodes. These structures are integrated with a 1×8 splitter and combiner, respectively, and specially designed 8×8 arrayed-waveguide grating (AWG) devices to enable direct/inverse discrete Fourier transforms of the signals directly in the optical domain [54]. Additional optical and electrical elements including spot size converters, phase shifters, monitoring diodes, electrical RF GSG/GS converters and 50Ω RF termination resistors are incorporated in order to provide low optical fiber-chip coupling, easy IQ MZM operating point settings, and proper RF performance bringing the number of integrated components to a total of 155.

A related integrated transmitter architecture, which is likely to represent the InP PIC with the highest device count made to date, is schematically displayed in Fig. 16.23 [55]. It represents a 10-wavelength dual-polarization QPSK transmitter comprised of 10 pairs of IQ modulators wavelength-multiplexed by means of an AWG combiner for each polarization path. Each of these channels is fed by a DFB laser diode which is tunable over a narrow band to allow for fine wavelength adjustment. Their rear side is waveguide-connected to a monitor photodiode. Altogether such a chip has been reported to include more than 450 integrated functions, including control functions. Such PICs have been assembled into modules which have been demonstrated to be capable of providing 500 Gb/s data traffic each [56]. The corresponding coherent receiver chip is also shown in Fig. 16.23. Again this PIC integrates 10 DFB lasers serving as local oscillator, similar to the one of Fig. 16.21.

16.4 Open Access to Integration Platforms: Adoption of Foundry Model

Until recently InP PIC achievements have exclusively been relying on dedicated integration technologies, and the industrial developments were to a large extent geared towards in-house exploitation. Even if access to this technology would be provided to external clients, many potential users, in particular small companies, can hardly afford investing in a PIC development for their specific products, given the fact that it may easily cost several hundreds of thousands of USD to up into the million USD range only for getting proof-of-concept chips. Chip designers are required to have an intimate knowledge of the proprietary technology utilized, including epitaxy related material data, detailed fabrication process features and process flow. This information is generally not disclosed by chip manufacturers to external parties. To overcome these hurdles which are all but conducive to a wider-spread use of PIC technology, adoption of a generic foundry model appears to be a natural way [57].

In the electronics industry the generic foundry business has already been successfully used for decades. The key characteristics of such a generic model are: use of a frozen technology; owned by the chip manufacturer; suited for many different PIC designs; strict separation of PIC design and chip fabrication; technology-blind circuit design made from a set of defined device building blocks; availability of a “process design kit” (PDK) providing all the information needed by a designer; and thanks to the generic nature different PIC designs can be accommodated on a wafer and fabricated in the same multi-project wafer run. The foundry concept not only helps overcome the afore-mentioned restrictions regarding open access to design and manufacturing but also provides substantial advantages with respect to cost-effectiveness: wafer run costs can be shared by MPW users; development costs are minimized by process standardization; repeating the same processes run by run enhances fabrication reliability; and testing and qualification can also be performed in a generic manner.

Clearly, adopting the foundry approach in photonics is more demanding than it is in electronics due to the larger variety of basic active and passive optical device functions and building blocks, and the enormous space of optical and electrical parameters associated with them. Not surprisingly, there was a great deal of skepticism that a generic foundry model would be applicable at all in the photonics arena, and it was only less than a decade ago that serious initiatives were launched to transfer this concept to InP photonics. Europe has taken the lead here, particularly through the two major R&D projects EuroPIC [58] and PARADIGM [27] funded by the European Community. The goal of these projects was not only to develop the technology of generic InP based integration platforms but beyond that to establish a full ecosystem for generic InP PIC fabrication including an integrated design environment (circuit design and simulation tools, mask layout software, design rule checking), involvement of design houses, testing and to a certain extent generic packaging, and even brokerage activities for MPW services.

As a result of those projects open access MPW services were launched recently on a pre-commercial basis by three European entities – UK based Oclaro, Fraunhofer HHI of Germany, and Smart Photonics in The Netherlands, the latter exploiting the technology of the COBRA institute of Eindhoven Technical University. All of these PIC platforms are capable of serving a wide variety of applications. There are, however, special differences in the technology and building block offerings. Even in the longer run full convergence in capabilities may not be anticipated – similar to Si electronics where foundries are also not compatible with each other in all respects. In the next section the integration platform of Fraunhofer HHI will be described in some more detail.

16.4.1 A Generic TxRx PIC Platform

Technological Platform Implementation Starting from a Rx platform development which basically integrated a high-speed (40 GHz bandwidth) photodiode with a range of passive optical waveguide functions, Fraunhofer HHI's platform has been substantially extended recently by adding laser type building blocks and further elements so as to provide full TxRx capability, with Tx denoting transmitter and Rx receiver functionalities [59, 60]. The technological implementation of this platform is illustrated in Fig. 16.24.

The entire epitaxial PIC structure is built on a semi-insulating (Fe doped) substrate which not only allows for true electrical isolation of the integrated active elements but is likewise essential for achieving high electrical bandwidth. To this end, all of the passive waveguides used in the platform are made of Fe doped material which has the added benefit of eliminating optical losses induced by free carrier absorption. The bottom of the PIC layer stack is formed by a fairly thick diluted waveguide structure from which the optical input/output waveguides of the PIC chip are made. Terminated by vertically tapered spot-size converters they provide optimized optical coupling to standard single mode fibers with less than 2 dB coupling efficiency. On top of this Fe doped waveguide the “half” structure of the laser

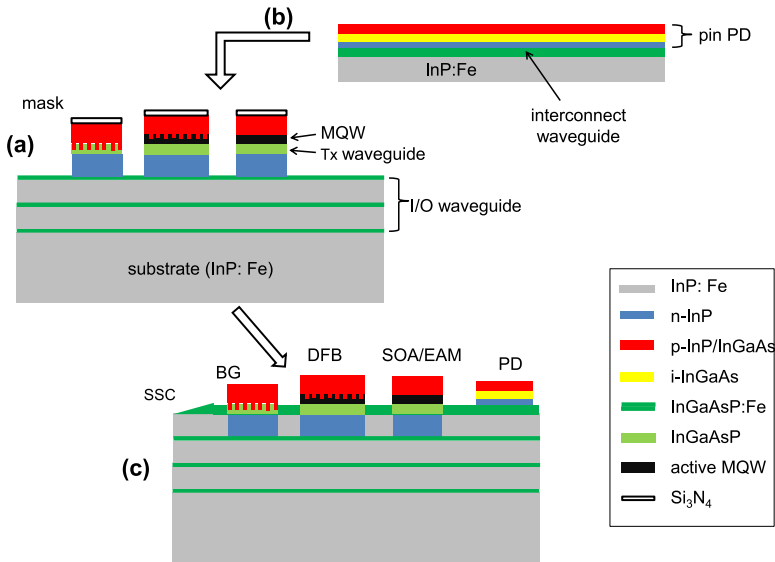


Fig. 16.24 Schematic of generic InP PIC platform as developed at Fraunhofer HHI (BG = Bragg grating; PD = photodiode; DFB = DFB laser; EAM = electro-absorption modulator; SOA = semiconductor optical amplifier)

building block designed for C-band operation is deposited. As its core it embodies a thin quaternary bulk waveguide layer on top of which the active region in form of an InGaAsP/InGaAsP offset multi-quantum well stack is placed. This stack is used to implement laser gain blocks/SOAs and electro-absorption modulators. It should be noted that the performance of the EA modulator is somewhat limited because of the use of a common active medium; employment of SAG technology will help overcome this limitation. At places where DFB laser elements are to be positioned 1st-order complex-coupled DFB gratings are patterned involving electron-beam lithography and reactive ion etching. In the same way tunable gratings, used as building block for instance for DBR lasers, are realized after locally etching off the active MQW material. Omitting the grating here, current-injection based phase shifters can be made. Following these processing steps the wafer is overgrown with the upper p-InP cladding and contact layer structure. Subsequently, the individual Tx building blocks are mesa-structured down to the bottom waveguide layer to complete the Tx level.

The next major fabrication stage encompasses the integration of the Rx level consisting of the layers of the evanescently coupled pin photodiode (refer to Fig. 16.1) and of the access waveguide which again is made semi-insulating. This waveguide simultaneously interconnects the Tx elements to which it is butt-coupled. The key technology used for this is selective-area-epitaxy, as described in Sect. 2.2. Outside the photodiode areas the pin PD layers are removed. In the final wafer processing stage all of the different functional building blocks on the PIC wafer are laterally structured into ridge-waveguide devices. To this end the same mask is used for the

passive waveguides and the Tx elements thus ensuring optimal lateral alignment. Passive-active butt-coupling efficiency amounts to <1 dB/interface and is primarily determined by the precision in vertical alignment. Due to the use of a semi-insulating substrate both the metal n- and the p-contacts are required to be formed on the surface side of the structure.

The entire process requires (only) three epitaxial growth steps, including base wafer growth, and about 25 lithographic mask levels. An attractive feature of the developed platform is the fact that the Tx and the Rx level are structurally largely separated such that they may also be implemented as separate sub-platforms, yet using the same design manual and PDK.

Building Blocks The principal physical functions that are required to create a generic TxRx capable photonic integration platform are: single-mode guiding of light; optical amplification; manipulation of optical phase; and absorption of light. These functions lead to the key basic building blocks (BB): passive optical waveguide; gain/optical amplifier element; phase shifter; and optical detector. In principle, these elements would suffice for a designer to create a wide range of integrated photonic devices and circuits. In practice, however, the PIC manufacturer – the foundry – will offer more complex building blocks composed of the elemental functions to avoid an excessive number of design interfaces which would multiply technology and performance risks. The building blocks are owned by the foundry, and as rule of the game their technological implementations are usually not disclosed to designers.

The building blocks which are presently (at the time of writing) provided on Fraunhofer's PIC platform as illustrated in Fig. 16.24, are compiled in Table 16.1.

Performance characteristics and all the lay-outing information required by designers are described in a comprehensive design manual. Here a selection of exemplary BBs will be given along with keys device parameters. In Fig. 16.25 the structure of the passive waveguides is represented featuring a rib design with three different rib heights, h , (200; 600; and 1700 nm) and thus index contrasts. The latter parameter immediately determines the minimum bend radius ensuring negligible radiation loss. It also largely impacts the overall chip size of a PIC. Sidewall roughness and free carrier absorption are the principal sources for the optical losses. The latter one is essentially eliminated because of the use of Fe doped waveguide material, as already noted above. Typical propagation losses measured on these waveguides range from ~ 0.5 dB/cm for the low-index and about 2 dB/cm for the high-index structure, with losses for TE polarized light being consistently lower than for TM polarization. To couple optical signals between the different waveguides transition elements are available as a separate building block exhibiting losses of some 0.2 dB, as already outlined in Sect. 2.2.

Figure 16.26 refers to a gain element which represents a fundamental building block to generate and amplify light. As such it can be used as an optical amplifier as well as a central part of any laser structure. On the platform these devices are parameterized, that is their length can be chosen by the designer from 100 μm to the mm-range. Achievable gain and spectral bandwidth are key device parameters. For

Table 16.1 List of building blocks offered on Fraunhofer HHI’s InP PIC platform (F = fixed design; P = parameterized)

Building block	Design	Building block	Design
<i>Passive optical and electrical BBs</i>		<i>Tx-related BBs</i>	
Waveguide (three different Δn)	P	Gain element/SOA	P
Waveguide transitions	F	DFB laser diode (25 G)	P
Waveguide crossings	F	Tunable Bragg grating (5 nm)	P
Waveguide circular arc	P	DBR laser	P
Input/output spot size converter	F	Phase shifter (current injection)	P
MMI (1×2 ; 2×2)	F	EA modulator (40 G, under development)	P
Directional coupler	P	P-isolation section	P
AWG	P	<i>Rx-related BBs</i>	
Phase shifter (thermo-optic)	P	pin-PD (40 G and <10 G)	F
Polarization converter	F	Balanced pin-PD (40 G)	F
Polarization beam splitter	F	Pin-PD impedance matching RC	
Metal interconnects incl. waveguide crossover	F		
RF lines	F		

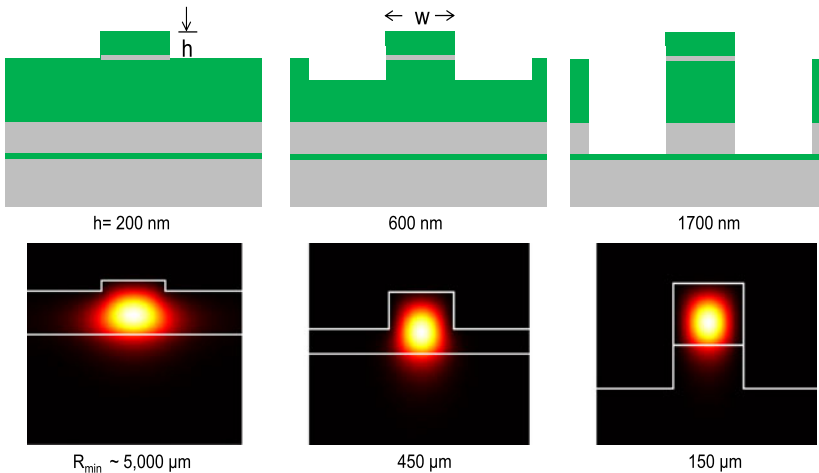


Fig. 16.25 Cross-sections and simulated mode profiles of the three rib waveguide types used on Fraunhofer HHI’s PIC platform. The waveguides consist of semi-insulating InP and InGaAsP layers of $1.06 \mu m$ material wavelength (compare to Fig. 16.24). The rib width, w , amounts to some $2 \mu m$. The rib height, h , determines the index contrast and correspondingly the minimum bend radius, R_{min}

the given active 8-QW stack typical characteristic SOA figures are: 3–4 dB/100 μm gain per length and 3-dB spectral bandwidth of 40 nm around 1550 nm. Technological modifications to the platform are underway to locally adjust the QW number

Fig. 16.26 Gain vs current characteristics of a 500 μm long gain block (SOA) measured in fiber-to-fiber (SSMF) configuration. The gain device was butt-coupled to 1 mm long input and an output shallow-ridge ($h = 200$ nm) waveguides terminated by a spot-size converter at either end

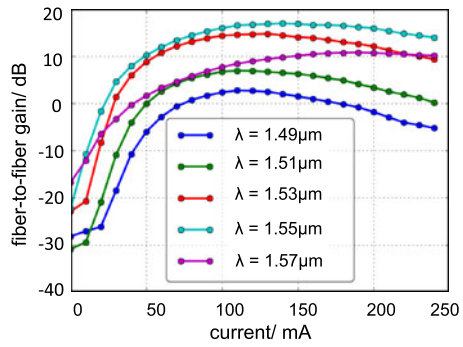
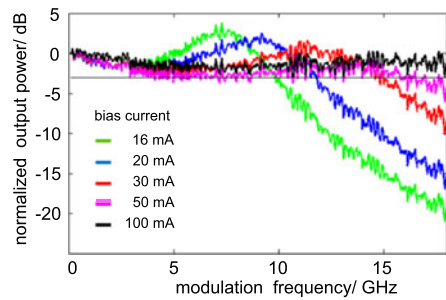


Fig. 16.27 Small-signal response curves of the 200 μm long DFB laser building block in dependence of bias current (incl. threshold current). At 100 mA a 3-dB bandwidth of >18 GHz is achieved. The devices under test were butt-coupled to 500 μm long waveguide sections at both sides

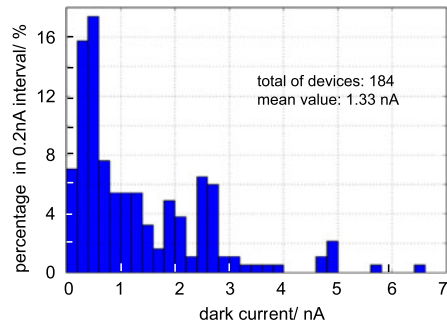


in the SOA regions for optimizing specific properties separately from the other Tx devices.

The standard laser source on the platform is a complex-coupled DFB laser. As opposed to the DBR laser building block where the length of the gain and the grating section can be set by the designer a fixed cavity length of 200 μm has been chosen for the DFB laser building block supporting high modulation bandwidth up to around 20 GHz, as evidenced in Fig. 16.27, which is adequate for ~ 25 Gb/s operation. Recently, using such devices 56 Gb/s transmission experiments were successfully conducted using 4-level amplitude modulation (PAM4) at a symbol rate of 28 Gbaud [61]. While the geometrical parameters are fixed the emission wavelength can be adjusted across the C-band. Extension to cover also the L-band is being investigated. Typical threshold currents for the 200 μm long lasers amount to 8–10 mA, and the ex-waveguide optical output power to ~ 5 mW at 100 mA, measured at room temperature on waveguide integrated structures similar to the afore-mentioned gain blocks.

For light detection waveguide-integrated photodiodes are offered with two sizes. The high-speed version exhibits a 3-dB bandwidth of >30 GHz suitable for receiving 40 Gb/s data signals. Mean values of the dark current of these devices are around 1 nA at -2 V bias. Figure 16.28 shows a respective distribution that was collected from a receiver chip comprising 100 photodiodes [10] and from test structures with another 84 devices in total, all of them made on the same wafer. An electrical passive on-chip biasing circuit is available for impedance matching, and a pair of balanced photodiodes is provided as a separate building block.

Fig. 16.28 Dark current distribution of 40 Gb/s capable waveguide-integrated pin photodiodes taking into account 184 devices on the same wafer



Polarization components are of paramount importance for photonic integrated circuits for handling optical signals of arbitrary polarization. Whereas light emitted from laser diodes is commonly strongly TE polarized the polarization state of light received e.g. through an optical fiber is generally unknown and may vary with time. Polarization diversity is an effective scheme to cope with this issue: The lightwave is split into its optical TE and TM component by means of a polarization beam splitter (PBS), then separately processed and finally recombined optical signal in the electrical domain. However, various optical circuit elements like SOAs, electro-absorption and Mach-Zehnder modulators are only sensitive to TE modes. To overcome this restriction, TM polarized light is transferred into the TE state using a so-called polarization converter (PC). The PBS building block implemented on the platform relies on a thermo-optically adjustable asymmetric Mach-Zehnder interferometer structure which enables polarization extinction ratios of >25 dB [62]. For integratable waveguide based PC devices a common approach makes use of a 2-section slanted waveguide structure achieved by wet chemical etching [63]. However, to accomplish optimum TE/TM conversion of >20 dB the waveguide width ($\sim 1.2 \mu\text{m}$) with previous designs was found to demand extremely tight fabrication tolerances of <100 nm. Applying an optimized set of design parameters simulation studies have indicated more relaxed tolerances of >200 nm which significantly eases reliable fabrication even using state-of-the art optical lithography. Figure 16.29 shows respective simulation [64] and preliminary experimental results [65].

Multi-Project Wafer Foundry Runs As outlined above the principle of the generic platform approach is the separation of PIC design and PIC fabrication. The different users on a multi-project wafer (MPW) run are responsible for designing their PICs but may hire a specialized design house for this purpose. The designs are transferred into mask files using dedicated software tools (see next section) and eventually submitted to the foundry where the final wafer lay-out is made. A broker organization may be involved here – a role that for InP PICs has been assumed by the European organization JePPIX [66]. On the HHI platform the standard user cell measures $4 \times 12 \text{ mm}^2$ which the user is free to divide into sub-cells of 2×4 , 4×4 , and $6 \times 4 \text{ mm}^2$. Sticking to a constant width, here 4 mm, is essential to facilitate bar cleaving. Following the lay-out process the physical masks are made and the wafer processing started. At Fraunhofer HHI all the masks are made in-house employing

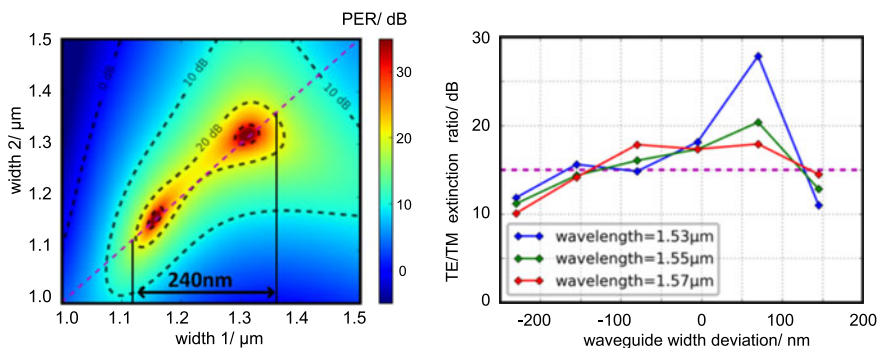


Fig. 16.29 Performance of polarization converter building block consisting of a 2-section slanted waveguide structure as reported in [64]: (*left*) simulated polarization extinction ratio (PER) as a function of waveguide top widths of the two sections (*dashed curves*: 10 dB- and 20 dB iso-PER contour lines); (*right*) measurement results of TE/TM extinction as a function of deviation from nominal width ($=1.2 \mu\text{m}$) [65]

electron-beam lithography. Before dicing the bars into the individual chips the input/output facets are usually anti-reflection coated with dielectric materials utilizing an ion beam sputtering process. Figure 16.30 displays the lay-out of a completed wafer along with examples of fabricated (and published) PIC designs.

Top left: Multichannel AWG based colliding pulse mode-locked laser on which generation of 12.7 GHz optical pulse trains with 17–19 ps pulse widths was demonstrated: The chip incorporates an 4-array of $700 \mu\text{m}$ long SOAs, a set of passive optical waveguide delay lines to equalize the optical path lengths of the four wavelength channels, an AWG serving as 4×1 wavelength combiner, a common $100 \mu\text{m}$ long saturable absorber section and a $400 \mu\text{m}$ SOA section in the SSC terminated output waveguide [67].

Top right: 8-channel WDM transmitter structure incorporating a directly modulated DFB laser and a monitor photodiode in each channel. The lasers merge into a common output waveguide with spot-size converter using multimode interference (MMI) couplers in different architectures (8×1 and cascaded 2×1 and 4×1 designs). The DFB laser diodes can be thermally tuned over a few nanometers by integrated heaters to adjust the channel wavelengths (spacing: 100 GHz) [68].

Middle left: Chip with flip-flop (FF) for all-optical static-random-access-memory (SR-FF). The FF circuit (two ones shown on chip) is based on coupled SOA-MZI switches arranged in "master-slave" architecture and features eight input/output waveguides with spot-size converters. In each of the four MZIs a 1 mm long SOA is integrated in one arm, and a current-injection phase shifter in the other one. MMI structures are used as couplers in the MZIs. Each FF chip measures $6 \times 2 \text{ mm}^2$. Read/write operation at 5 Gb/s was demonstrated [69].

Middle right: The chip represents a test structure for assessing stray light which may have adverse effects (optical crosstalk) in any integrated photonic device and need to be suppressed to lowest possible levels. In the middle a DFB laser is placed that is connected to a passive waveguide with a reference photodiode on top. Stray

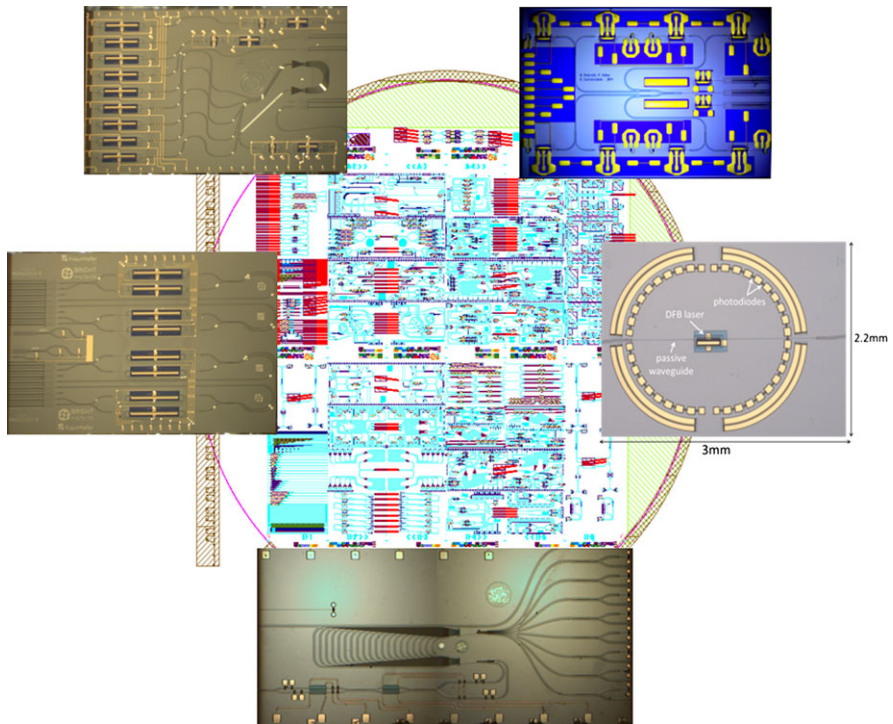


Fig. 16.30 Floorplan of a full Multi-Project-Wafer and selection of four exemplary TxRx-type PICs (photographs of chip surface)

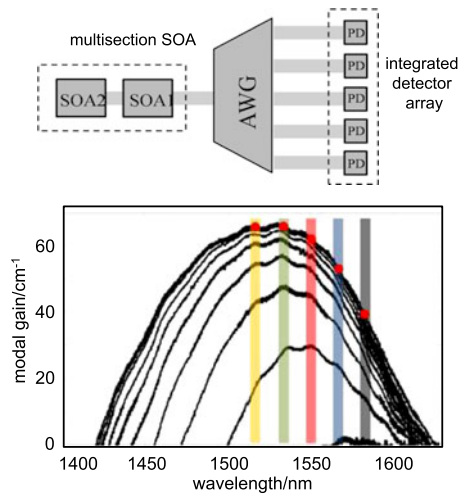
light generated at the butt-coupling interfaces is captured and monitored by a surrounding ring of photodiodes to give an indication of relative power levels and spatial distribution. Without applying “light blocking” structures (trenches, absorbers) measured values were down to the -40 dB level [59].

Bottom: The photo shows an 8-channel demultiplexer PIC for simultaneous mode-division-multiplex and wavelength-division-multiplex transmission over “few-mode” fibers. This Rx-type PIC can handle two spatial fiber modes and four wavelength channels. In essence, it is comprised of a balanced Mach-Zehnder coupler with integrated thermo-optical phase shifters and an 8-channel AWG (50 GHz channel spacing; 400 GHz free spectral range) with integrated photodiodes [70].

16.4.2 Testing of PICs

How can the proper function of the chips be verified? Naturally, the separated responsibilities for design and fabrication impede cause analysis if the chip performance does not meet expectations. The foundry does not measure the real PIC

Fig. 16.31 On-wafer modal gain measurement using a wavelength demultiplexer to sample gain at various wavelengths: schematic of test structure (*top*) and measurement results. The *five colored bars* indicate the passbands of the AWG (*bottom*) [75]



devices because generally it is design-agnostic, and beyond that may not be expected to have at its disposal all the dedicated measurement equipment needed for the different specific applications. Instead, wafers are released on validation measurements against specifications set for agreed parameters of building blocks and/or test structures, and also structural parameters like waveguide width. These validation measurements can be very comprehensive, time consuming and thus expensive. Automated and standardized optical on-wafer measurements requiring vertical on-chip tapping structures are highly desirable; even more methods that are capable of characterizing optical device properties solely by electrical measurements.

An example of the latter is a “non-invasive” capacitive technique that allows for light detection in waveguides with fairly simple-to-measure variations in electrical conductivity of the waveguide core, induced by surface-state carrier generation effects [71]. This approach, referred to as CLIPP (contactless integrated photonic probe), can be exploited for on-chip measurements of waveguides losses by applying multiple CLIPP structures. It is likewise promising for monitoring the state (i.e. working points) of photonic circuits [72] as well as for active fiber alignment applications using CLIPP structures as on-chip optical power monitors [73].

Use of “smart” integrated test structures, accommodated on the wafer specifically for validation purposes, is a more general approach which still opens up wide opportunities for introducing innovative ideas. On-wafer measurement schemes are applicable by making use of the integrated light sources and detectors. For instance, waveguide propagation losses have been measured employing ring resonator structures integrated with a laser and detector [74]. Another example along this line is a test structure for modal gain characterization, as depicted in Fig. 16.31. It consists of a SOA with two or more sections (at least one pair) of different lengths the modal gain of which is to be determined. An AWG spectrally resolves the amplified spontaneous emission (ASE) from the SOA, and the photocurrents of the corresponding photodetectors provide a measure for the spectral gain values [75].

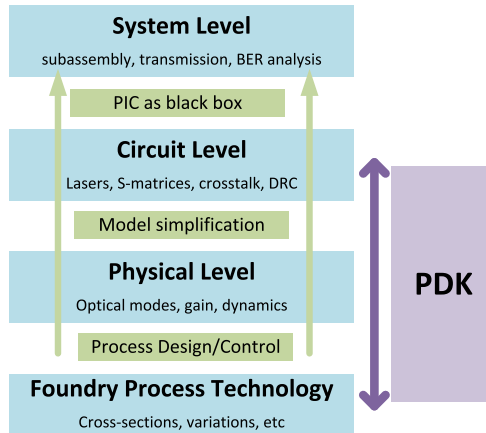


Fig. 16.32 Schematic illustration of three important layers of abstraction above a foundry's integration technology: physical, circuit and system level. The process design kit (PDK) contains information on the technology and physical parameters, like the relevant material parameters. It further contains circuit level models of the BBs and important boundary conditions such as crosstalk and design rule checks (DRC). This data together with a given design can be used to perform full system simulations

16.4.3 Design Environment

Just as photonics emerged as a technology for discrete devices, the tools used for designing and simulating them were also focused on discrete device structures. As such, those tools gained a lot of depth for specific applications, but not necessarily a lot of breadth. With the emergence of PICs, however, this paradigm is bound to change, as it is highly impractical for a PIC designer to adopt a different solution for each component he uses in his design [76].

It is useful to think of PIC design in terms of a hierarchy of abstraction layers, see Fig. 16.32. To assess the performance of a complex PIC, it evidently makes little sense to try and solve Maxwell's equations in the optical domain on an area of several mm^2 in size. If one further thinks of electro-optic or thermal effects and their interrelation, it becomes obvious that abstraction is key. In the following the three main abstraction levels with respect to PIC design are briefly addressed.

Physical Simulations The relevant physics in PICs is vast, and as such there is no "definite solver" for all problems. The main areas that usually are to be simulated are Maxwell's equations for optical- and RF waves, the Poisson equation for charge distributions, the heat equation for thermal simulations, and models for semiconductor physics. More and more tools actually offer co-simulation of the various physical aspects involved to allow for coupling of different effects. Simulating charge effects and optical waves simultaneously, for example, enables thorough simulation of the dynamics of electro-optic modulators.

Maxwell's equations are usually solved in two dimensions to calculate the modes that can propagate in a given cross-section, as already illustrated in Fig. 16.25. To propagate those modes, specialized uni- or bidirectional methods are typically used [77, 78]. In some cases, this mixed approach is insufficient, and Maxwell's equations have to be solved in a three-dimensional space, predominantly using the finite difference time domain (FDTD) method [79]. Examples for such challenging devices include grating couplers or nano-lasers.

For most active devices, models of electronic bands of the semiconductor as well as a set of rate equations are to be solved simultaneously. For field effects, the (dynamic) charge distribution is also of importance. All of those physics usually take place in optical cavities supporting a set of transversal and longitudinal modes, making the simulation of active devices very challenging. Many simulators rely on mixed models where some effects are defined phenomenologically, such as the logarithmic gain-current dependence in quantum wells.

All of the above generally depends on temperature. For high optical powers, optical nonlinearities come into play. Hence, the models obtained in physical simulations will generally rely on electrical current or voltage, temperature and optical power. From those dependencies, simplified phenomenological models can be derived and can then be fed up to the circuit simulator. The easiest example for such a simplification is the scattering matrix of an optical waveguide. Once the losses and group indices and their dispersion are known for all modes of a waveguide, this data can be encapsulated into a simple matrix.

Circuit Simulations With the more phenomenological models obtained from physical simulations, circuit level simulations can be conducted to provide information of the performance of composite building blocks and eventually of a complete photonic circuit. Passive components can easily be modeled with scattering matrices in frequency domain. Active components can only be modeled non-linearly in frequency domain, as fully physical models for those mostly rely on time domain. For efficient simulation, however, frequency domain models are essential. Hence, circuit level simulators mostly rely on fits of experimental data or phenomenological models for active components. Examples for this are effective noise figures of SOAs or the chirp parameter of a laser. Electro-optic effects can often be sufficiently modeled with a static model plus a small-signal response. Recently design capabilities for assessing the impact of fabrication tolerances on functional PIC performance using Monte-Carlo simulations have been incorporated in a circuit simulator tool [80]. An illustration is depicted in Fig. 16.33.

System Simulations From a system perspective, an individual PIC, as complex as it might be, is only a small piece of a much larger puzzle. Hence, to perform system level simulations, the PIC has to be reduced to a simple (preferable frequency domain) model with a set of electrical and optical I/Os. This kind of model is exactly the end result of circuit simulators. System simulation tools that started pushing towards inclusion of PIC models are available from various vendors: TransmissionMaker from VPI Photonics [81], PICWave from PhotonDesign [82] and Interconnect from Lumerical [83]. Those tools are all capable of simulating complex

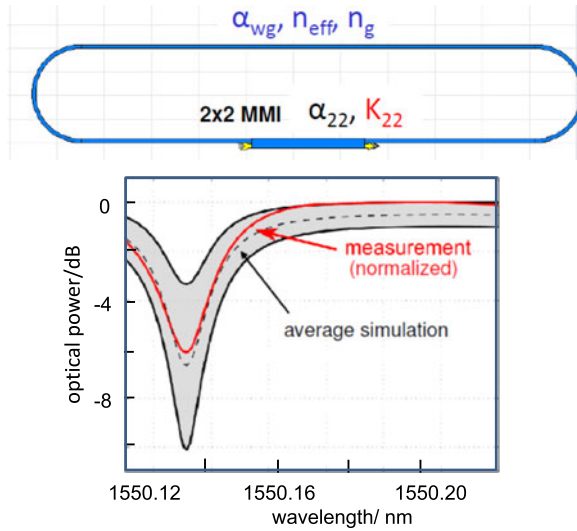


Fig. 16.33 (Top) Ring resonator as modeled in ASPIC [80]. The loss of the 2×2 MMI, α_{22} , and its coupling ratio, K_{22} , are modeled statistically using the Monte-Carlo method. For the purpose of this simulation, the waveguide parameters have no statistical distribution. (Bottom) normalized transmission of the ring filter. The transmission has a certain average and standard deviation, depending on the statistics of the MMI. The circuit was fabricated in HHI's platform, from which the parameters were taken. The measurement is within the predicted deviation (grey) from the ideal transmission curve (courtesy of Politecnico di Milano/Filarete)

electro-optical transmission links as deployed in the field. Their toolboxes for PICs now also enable simulating the performance of a newly designed PIC in a given system before starting its actual fabrication.

Process Design Kits and Layout To achieve the afore-mentioned level of abstraction, foundries typically supply their users with so-called process design kits (PDK). The PDK contains detailed data on both performance and layout of all BBs. It further contains cross-sectional data to enable the designer to carry out simulations on the physical level. The BBs are characterized by models which are fed by the foundry's experimental data. The layout part of a PDK contains information on geometry and electrical and optical connections. It further contains a set of design rules, e.g. to make sure the bend radius of a waveguide is not too tight. Figure 16.34 shows an example where all this information in the PDK is used for circuit simulations and then to directly generate a layout from the circuit simulator.

Typically, the PDK of a foundry is accompanied by a design manual. This is a document that describes the PDK's content and gives some insight into the foundry's technology but without disclosing proprietary details. It is also intended to give a complete documentation of all BBs inside the PDK, including design examples and experimental data.

The assembly of the final mask set for an MPW wafer is commonly done in a fully automated fashion. The foundry inserts the private content of its BB into the

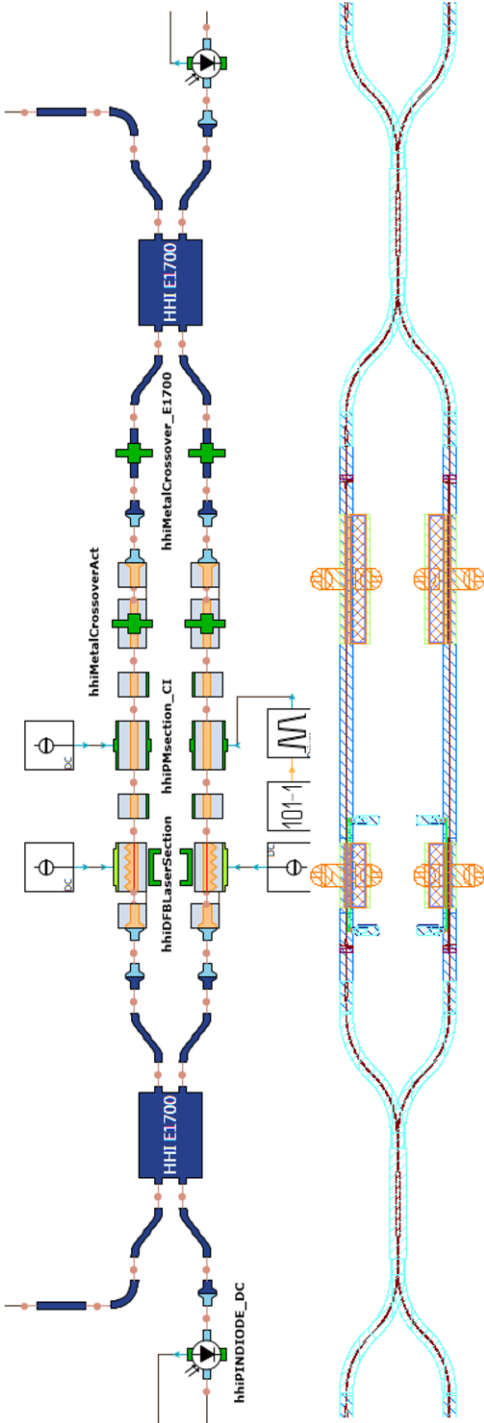


Fig. 16.34 Design flow taking an integrated THz source [84] as example: (*Top*) schematic in a circuit/system simulator (VPI TransmissionMaker). (*Bottom*) layout generated directly from the simulated schematic. Specialized layout software such as Phoenix’ OptoDesigner [85] facilitates the mask design specifically for PICs. In contrast to ASICs, bends for example play a much more important role. This makes it that routing is much more challenging in photonic ICs than in their electronic counterparts. With increasing PIC complexity design rule checks (DRC) are becoming more and more important but differ from the electronics world

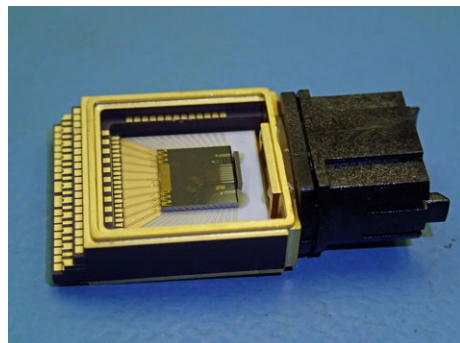
locations specified by the users' designs. This private content in turn is adapted to the parameters set by the user. For example, a designer may have used a parameterized DFB laser building block and specified its wavelength with a certain value. The wafer layout tool at the foundry will use this wavelength to calculate the correct grating period and inserts this grating automatically into the BB.

To ensure the interoperability of the various tools used in modern PIC design, the PDAFlow foundation was created [86]. This consortium encompasses all the aforementioned software companies. Within the foundation, a continuing effort towards standardization of all aspects of PIC design is made.

16.4.4 Generic Packaging

In addition to design and fabrication, packaging capabilities are crucial because bare chips are in fact of only minor value for users. Generic packages that are compatible with a broad range of PICs are therefore of utmost importance to allow for rapid prototyping and for packaging of smaller volumes for which expensive customized developments are hardly affordable. Notwithstanding that with large volumes customized packages may be the preferred solution. In the already mentioned PARADIGM project steps were taken to create a generic package for PICs. An outcome of those activities is shown in Fig. 16.35. This particular built has been designed to be capable of supporting up to 12 single-mode fiber connections to the PIC via a lens array. Electrically, it supports 10 high-speed connections (25 GHz), and 36 slow-speed/DC electrical connections implemented by electrical interposers. Further, two high-current DC connections are available for the thermoelectric cooler enabling precise temperature control of the PIC chip. Thermal materials have been included in the design which is also capable of being hermetically sealed where reliability and environmental conditions require it. The package style has been specifically designed to fit within one of the most common transceiver platforms in use today; the XFP platform. It should be emphasized that the generic packaging approach demands optical and electrical interfaces on the chip to be compliant with the design constraints imposed by the standard package.

Fig. 16.35 Generic package for InP PICs as developed in the PARADIGM project under the responsibility of the consortium partner Gooch & Housego (courtesy of B. Musk, Entropix Ltd, UK)



Despite this early generic development a bottleneck with PIC packaging is continuing to exist, and in response to this in 2016 the European Commission has launched a call for proposals under the HORIZON 2020 program aiming at establishing a pilot line for PIC packaging in Europe building on existing expertise.

Successful commercialization of any product demands a complete supply chain to be in place. For foundry-type manufacturing of InP PICs, as outlined above, the major links of this chain have been successfully established on the R&D level in recent years, encompassing a design platform with interoperability of different design tools; PIC processing and testing; and packaging. Pre-commercial foundry operations have been commenced including involvement of professional design houses and brokerage activities. Currently, in terms of manufacturing readiness level, MRL (scale: 1–10), this technology area may be characterized by MRL 3–5, depending on the specific disciplines. For the years to come, it will be decisive for sustainable growth and for acceptance in diverse potential application areas to steadily progress to higher levels.

References

1. P.K. Tien, Integrated optics and new wave phenomena in optical waveguide. *Rev. Mod. Phys.* **49**, 361–420 (1977)
2. J.J. Hsieh, Room temperature operation of InGaAsP/InP double heterostructure diode lasers emitting at 1.1 μm . *Appl. Phys. Lett.* **28**, 283–285 (1976)
3. T.L. Koch, U. Koren, R.P. Gnall, F.S. Choa, F. Hernandez-Gil, C.A. Burrus, M.G. Yung, M. Oron, B.I. Miller, GaInAs/GaInAsP multi-quantum-well integrated heterodyne receiver. *Electron. Lett.* **25**, 1621–1623 (1989)
4. R. Kaiser, D. Trommer, F. Fidorra, H. Heidrich, S. Malchow, D. Franke, W. Passenberg, W. Rehbein, H. Schroeter-Janssen, R. Stenzel, G. Unterboersch, Monolithically integrated polarization diversity heterodyne receivers on GaInAsP/InP. *Electron. Lett.* **30**, 1446–1447 (1994)
5. M.G. Young, U. Koren, B.I. Miller, M. Chien, T.L. Koch, D.M. Tennant, K. Feder, K. Dreyer, G. Raybon, Six wavelength laser array with integrated amplifier and modulator. *Electron. Lett.* **31**, 1835–1836 (1995)
6. P. Runge, G. Zhou, F. Ganzer, S. Mutschall, A. Seeger, Waveguide integrated InP-based photo-detector for 100 Gbaud applications operating at wavelengths of 1310 nm and 1550 nm, in *41st European Conference on Optical Communication (ECOC'15)*, Valencia, Spain (2015), Tu.1.1.3
7. R. Zhang, P. Runge, G. Zhou, R. Klötzer, D. Pech, H.-G. Bach, D. Perez-Galacho, A. Ortega-Murnox, R. Halir, I. Molina-Fernandez, 56 Gbaud DP-QPSK receiver module with a monolithic integrated PBS and 90° hybrid InP chip, in *Proc. 26th Internat. Conf. Indium Phosphide Relat. Mater. (IPRM'14)*, Montpellier, France (2014), paper We-B1-4
8. J.B.D. Soole, M.R. Amersfoot, H.P. Blanc, N.C. Andreakis, A. Rajhel, C. Caneau, Polarization-independent monolithic eight-channel 2 nm spacing WDM detector based on compact arrayed waveguide demultiplexer. *Electron. Lett.* **31**, 1289–1291 (1995)
9. S. Chandrasekhar, M. Zirngibl, A.G. Dentai, C.H. Joyner, F. Storz, C.A. Burrus, L.M. Lunardi, Monolithic eight-wavelength demultiplexed receiver for dense WDM applications. *IEEE Photonics Technol. Lett.* **7**, 1342–1344 (1995)
10. M. Baier, R. Broeke, F. Soares, M. Gruner, A. Seeger, M. Moehrle, N. Grote, M. Schell, 100-channel WDM Rx-type PIC for use of low cost and low power consumption electronics, in *40th European Conference on Optical Communication (ECOC'14)*, Cannes, France (2014), We.2.4.5

11. www.gcsincorp.com; S. Wang, Can foundries underpin the success of the PIC? Presentation given at *PIC International Conference*, Brussels, 1–2 March 2016
12. V. Tolstikhin, Regrowth-free multi-guide vertical integration in InP for optical communications, in *Proc. 23rd Internat. Conf. Indium Phosphide Relat. Mater. (IPRM'11)*, Berlin, Germany (2011), pp. 363–366
13. V. Tolstikhin, S. Ristic, K. Pimenov, C. Watson, M. Florjanczyk, 100 Gb/s multi-guide vertical integration transmitter PIC in InP for fiber-optics interconnects, in *39th European Conference on Optical Communication (ECOC'13)*, London, UK (2013), Th.2.B.3
14. V. Tolstikhin, F. Wu, Y. Logvin, S. Ristic, Y. Tang, K. Pimenov, A. Khajooezadeh, 100 Gb/s receiver photonic integrated circuits in InP for applications in fiber-optics interconnects, in *Proc. OSA Conf. on Integrated Photonics Research, Silicon and Nano-Photonics (IPR'13)*, Rio Grande, Puerto Rico (2013), IW5A.4
15. S. Ristic, M. Florjanczyk, M. Lebbby, Optoelectronic integrated circuits (OEICs) for 100G Ethernet and coherent networks based on multi-guide vertical integration platform, in *Opt. Fiber Commun. Conf. (OFC'14)*, San Francisco, CA, USA (2014), Techn. Digest, paper Tu3H.6
16. F.M. Soares, K. Janiak, J. Kreissl, M. Moehrle, N. Grote, Semi-insulating substrate based generic InP photonic integration platform, in *Proc. SPIE 8767, Integrated Photonics: Materials, Devices, and Applications II*, May 22, 2013, 87670M. doi:[10.1117/12.2017431](https://doi.org/10.1117/12.2017431).
17. Y. Barbarin, E.A.J.M. Bente, T. de Vries, J.H. den Besten, P.J. Veldhoven, M.J.H. Sander-Jochem, E. Smalbrugge, F.W.M. van Otten, E.J. Geluk, M.J.R. Heck, X.J.M. Leijtens, J.G.M. van der Tol, F. Karouta, Y.S. Oei, R. Nötzel, M.K. Smit, Butt-joint interfaces in InP/InGaAsP waveguides with very low reflectivity and low loss, in *Proc. Symp. IEEE/LEOS Benelux Chapter*, Mons, Belgium (2005), pp. 89–92
18. J. Wallin, G. Landgren, K. Streubel, S. Nilsson, M. Öberg, Selective area regrowth of butt-joint coupled waveguides in multi-section DBR lasers. *J. Cryst. Growth* **124**, 741–746 (1992)
19. H. Roehle, H. Schroeter-Janssen, R. Kaiser, Large- and selective-area LP-MOVPE growth of InGaAsP-based bulk and QW layers under nitrogen atmosphere. *J. Cryst. Growth* **170**, 109–112 (1997)
20. S.C. Davies, R.A. Griffin, A.J. Ward, N.D. Whitbread, I. Davies, L. Langley, S. Fourte, J. Mo, Y. Xu, A. Carter, Narrow linewidth, high power, high operating temperature digital supermode distributed Bragg reflector laser, in *39th European Conference on Optical Communication (ECOC'13)*, London, UK (2013), Th.1.B.3
21. I.B. Betty, Strongly-guided InP/In_xGa_{1-x}As_yP_{1-y} Mach-Zehnder modulator for optical communications. Ph.D thesis, University of Waterloo, Ontario, Canada (2005); see also: K. Anderson, I. Betty, Indium phosphide MZ chips are suited to long-reach metro, *LaserFocus-World* 03/01/2003
22. H. Kobayashi, M. Ekawa, N. Okazaki, O. Aoki, S. Ogita, H. Soda, Tapered thickness MQW waveguide BH MQW lasers. *IEEE Photonics Technol. Lett.* **6**, 1080–1081 (1994)
23. M.S. Kim, C. Caneau, E. Colas, R. Bhat, Selective area growth of InGaAsP by OMVPE. *J. Cryst. Growth* **123**, 69–74 (1992)
24. J. Décobert, N. Dupuis, P.Y. Lagrée, N. Lagay, A. Ramdane, A. Ougazzaden, F. Poingt, C. Cuisin, C. Kazmierski, Modelling and characterization of AlGaInAs and related materials using selective area growth by metal-organic vapor-phase epitaxy. *J. Cryst. Growth* **298**, 28–31 (2007)
25. J. Decobert, G. Binet, A.D.B. Maia, P.Y. Lagree, C. Kazmierski, AlGaInAs MOVPE selective area growth for photonic devices. *Adv. Opt. Techn.* **4**, 167–177 (2015)
26. R. Guillamet, N. Lagay, C. Mocuta, G. Carbone, P.Y. Lagrée, J. Decobert, Analysis and optimization by micro-beam X-ray diffraction of AlGaInAs heterostructures obtained by Selective Area Growth for optoelectronic applications, in *Proc. 23rd Internat. Conf. Indium Phosphide Relat. Mater. (IPRM'11)*, Berlin, Germany (2011), pp. 386–389
27. <http://www.paradigm.jepix.eu>, newsletter#4
28. C. Kazmierski, D. Carrara, K. Lawniczuk, G. Aubin, J.G. Provost, R. Guillamet, 12.5 GB operation of a novel monolithic 1.55 μm BPSK source based on prefixed optical phase switch-

- ing, in *Opt. Fiber Commun. Conf. (OFC'13)*, Anaheim, CA, USA (2013), Techn. Digest, paper OW4J.8
29. C. Kazmierski, N. Chimot, F. Jorge, A. Konczykowska, F. Blache, J. Decobert, F. Alexandre, A. Garreau, R. da Silva, 80 Gb/s multi-level BPSK experiment with an InP monolithic source based on prefixed optical phase switching, in *Proc. 26th Internat. Conf. Indium Phosphide Relat. Mater. (IPRM'14)*, Montpellier, France (2014), Th-B2-1
 30. H. Mardoyan, O. Bertran-Pardo, P. Jennev , G. de Valicourt, M.A. Mestre, S. Bigo, C. Kazmierski, N. Chimot, A. Steffan, J. Honecker, R. Zhang, P. Runge, A. Richter, C. Arelano, A. Ortega-Mo ux, I. Molina Fernandez, PIC-to-PIC experiment at 130 Gb/s based on a monolithic transmitter using switching of prefixed optical phases and a monolithic coherent receiver, in *Opt. Fiber Commun. Conf. (OFC'14)*, San Francisco, CA, USA (2014), Techn. Digest, post-deadline paper Th5C
 31. J. Decobert, G. Binet, A.D.B. Maia, P.Y. Lagree, C. Kazmierski, AlGaInAs MOVPE selective area growth for photonic devices. *Adv. Opt. Techn.* **4**, 167–177 (2015)
 32. R.W. Glew, A.T.R. Briggs, P.D. Greene, E.M. Allen, The influence of the substrate on the thermal stability of InGaAs/InGaAsP quantum wells, in *Proc. 4th Internat. Conf. Indium Phosphide Relat. Mater. (IPRM'92)*, Newport, USA (1992), pp. 234–237
 33. N. Grote, The III–V materials for Infra-red devices, in *Materials for Optoelectronics*, ed. by M. Quillec (Kluwer Academic, Norwell, 1996), p. 173. ISBN 0-7923-9665-0
 34. S. Charbonneau, E. Kotels, P. Poole, J. He, G. Aers, J. Haysom, M. Buchanan, Y. Feng, A. Delage, F. Yang, M. Davies, R. Goldberg, P. Piva, I. Mitchell, Photonic integrated circuits fabricated using ion implantation. *IEEE J. Sel. Top. Quantum Electron.* **4**, 772–793 (1998)
 35. E.J. Skogen, J.W. Raring, G.B. Morrison, C.S. Wang, V. Lal, M.L. Masanovic, L. Coldren, Monolithically integrated active components: a quantum-well intermixing approach. *J. Sel. Top. Quantum Electron.* **11**, 343–355 (2005)
 36. J.H. Marsh, Quantum well intermixing. *Semicond. Sci. Technol.* **8**, 1136–1155 (1993)
 37. J.W. Raring, L.A. Johansson, E.J. Skogen, M.N. Sysak, H.N. Poulsen, S.P. DenBaars, L.A. Coldren, 40-Gb/s widely tunable low-drive-voltage electro-absorption-modulated transmitter. *J. Lightwave Technol.* **25**, 239–248 (2007)
 38. C. Wang, E. Skogen, J. Raring, G. Morrison, L. Coldren, Short-cavity 1.55 μm DBR lasers integrated with high-speed EAM modulators, in *Proc. 19th IEEE Semiconductor Laser Conf.*, Matsueshi, Japan (2004)
 39. V. Lal, M.L. Masanovic, E.J. Skogen, J. Raring, J.A. Summers, L.A. Coldren, Quantum-well-intermixed monolithically integrated widely tunable all-optical wavelength converter operating at 10 Gb/s. *IEEE Photonics Technol. Lett.* **17**, 1689–1691 (2005)
 40. D. Hofstetter, B. Maisenh lder, H.P. Zappe, Quantum-well intermixing for fabrication of lasers and photonic integrated circuits. *IEEE J. Sel. Top. Quantum Electron.* **4**, 794–802 (1998)
 41. L.A. Coldren, S.C. Nicholes, L. Johansson, S. Ristic, R.S. Guzzon, E.J. Norberg, U. Krishnamachari, High performance InP-based photonic ICs – a tutorial. *J. Lightwave Technol.* **29**, 554–570 (2011)
 42. M. Smit, X. Leijtens, H. Ambrosius, E. Bente, J.v.d. Tol, B. Smalbrugge, T. de Vries, E.J. Geluk, J. Bolk, R. van Veldhoven, L. Augustin, P. Thijs, D. d'Agostino, H. Rabbani, K. Lawniczuk, S. Stopinski, S. Tahvili, A. Corradi, E. Kleijn, D. Dzibrou, M. Felicetti, E. Bitincka, V. Moskalenko, J. Zhao, R. Santos, G. Gilardi, W. Yao, K. Williams, P. Stabile, P. Kuindersma, J. Pello, S. Bhat, Y. Jiao, D. Heiss, G. Roelkens, M. Wale, P. Firth, F. Soares, N. Grote, M. Schell, H. Debregeas, M. Achouche, J.L. Gentner, A. Bakker, T. Korthorst, D. Gallagher, A. Dabbs, A. Meloni, F. Morichetti, D. Melati, A. Wonfor, R. Penty, R. Broeke, B. Musk, D. Robbins, An introduction to InP based generic integration technology. *Semicond. Sci. Technol.* **29**, 083001 (2014)
 43. H. Debregeas, J. Decobert, N. Lagay, R. Guillamet, D. Carrara, O. Patard, C. Kazmierski, R. Brenot, Selective-area-growth technology for flexible active building blocks, in *Conf. on Integrated Photonics Research, Silicon and Nano-Photonics (IPR'12)*, Colorado Springs, USA (2012), OSA Techn. Dig., paper IM2A.3

44. A.M. Weiner, Ultrafast optical pulse shaping: a tutorial review. *Opt. Commun.* **294**, 3669–3692 (2011)
45. M.S. Tahvili, S. Latkovski, E. Smalbrugge, X.J.M. Leijtens, P.J. Williams, M.J. Wale, J. Parra-Cetina, R. Maldonado-Basilio, P. Landais, M.K. Smit, E.A.J.M. Bente, InP-based integrated optical pulse shaper: demonstration of chirp compensation. *IEEE Photonics Technol. Lett.* **25**, 450–453 (2013)
46. Q. Cheng, M. Ding, A. Wonfor, J. Wei, R.V. Penty, I.H. White, The feasibility of building a 64×64 port count SOA-based optical switch, in *Proc. Photonics in Switching 2015*, Florence, Italy (2015), pp. 199–201
47. J. Zhu, S. Pachnike, M. Lawin, S. Mayne, A. Wonfor, R.V. Penty, R. Cush, R. Turner, P. Firth, M. Wale, I.H. White, J.P. Elbers, First demonstration of a WDM-PON system using full C-band tunable SFP⁺ transceiver modules. *J. Opt. Commun. Netw.* **7**, A28–A36 (2015)
48. S. Farwell, P. Aivaliotis, Y. Qian, P. Bromley, R. Griggs, J. Ng Yew Hoe, C. Smith, S. Jones, InP coherent receiver chip with high performance and manufacturability for CFP2 modules, in *Opt. Fiber Commun. Conf. (OFC'14)*, San Francisco, CA, USA (2014), Techn. Digest, paper W11.6
49. Y. Tang, F. Wu, Y. Logvin, J. Lei, G. Liu, K. Luo, C. Watson, K. Pimenov, Y. Bai, D. Masson, V. Tolstikhin, H. Xie, Y. Hua, High performance DP-QPSK receiver module incorporating InP-based Integrated coherent detection chip, in *Opt. Fiber Commun. Conf. (OFC'15)*, Los Angeles, CA, USA (2015), Techn. Digest, paper M3C.3
50. P. Runge, S. Schubert, A. Seeger, K. Janiak, J. Stephan, D. Trommer, N.L. Nielsen, Monolithic InP receiver chip with a variable optical attenuator for colorless WDM detection. *IEEE Photonics Technol. Lett.* **26**, 349–351 (2014)
51. M.L. Masanovic, Integrated photonic coherent receivers, in *Opt. Fiber Commun. Conf. (OFC'14)*, San Francisco, CA, USA (2014), Techn. Digest, paper W1J.4
52. P. Runge, G. Zhou, F. Ganzer, S. Seifert, S. Mutschall, A. Seeger, Polarization insensitive coherent receiver PIC for 100 Gbaud communication, in *Opt. Fiber Commun. Conf. (OFC'16)*, Anaheim, CA, USA (2016), Techn. Digest, Tu2D.5
53. <http://www.ict-astron.eu>
54. S. Shimizu, G. Cincotti, N. Wada, Demonstration and performance investigation of all-optical OFDM systems based on arrayed waveguide gratings. *Opt. Express* **20**, B525–B534 (2012)
55. R. Nagarajan, M. Kato, D. Lambert, P. Evans, S. Corzine, V. Lal, J. Rahn, A. Nilsson, M. Fisher, M. Kuntz, J. Pleumeekers, A. Dentai, H.-S. Tsai, D. Krause, H. Sun, K.-T. Wu, M. Ziari, T. Butrie, M. Reffle, M. Mitchell, F. Kish, D. Welch, Terabit/s class InP photonic integrated circuits. *Semicond. Sci. Technol.* **27**, 094003 (2012)
56. F. Kish, M. Reffle, T. Butie, M. Ziari, P. Evans, S. Corzine, H.S. Tsai, D. Pavinski, J. Zhang, J. Tang, A. Dentai, R. Muthiah, J. Pleumeekers, D. Lambert, M. Missey, V. Lal, M. Fisher, S. Murthy, R. Salvatore, S. Demars, A. James, J. Rahn, S. Kumar, M. Mitchell, J. Zhang, T. Liu, R. Nagarajan, D. Welch, 500 Gb/s and beyond photonic integrated circuit module, in *Opt. Fiber Commun. Conf. (OFC'15)*, San Francisco, CA, USA (2014), Techn. Digest, paper W3I.1
57. M. Smit, X. Leijtens, E. Bente, J. van der Tol, H. Ambrosius, D. Robbins, M. Wale, N. Grote, M. Schell, Generic foundry model for InP-based photonics. *IET Optoelectron.* **5**, 187–194 (2011)
58. <http://www.europic.jeppix.eu>
59. F.M. Soares, M.F. Baier, M. Moehrle, N. Grote, Technology platform for transmit and receive type photonic integrated circuits, in *Proc. 26th Internat. Conf. Indium Phosphide Relat. Mater. (IPRM'14)*, Montpellier, France (2014), Mo-B1-5
60. F.M. Soares, M. Baier, T. Gaertner, D. Franke, M. Moehrle, N. Grote, Development of a versatile InP-Based photonic platform based on butt-joint integration, in *Conference on Lasers and Electro-Optics/Pacific Rim*, Busan, S. Korea (Optical Society of America, Washington, 2015), paper 26J2_1
61. M.F. Baier, F.M. Soares, T. Gaertner, M. Moehrle, N. Grote, C. Meuer, 50 Gbit/s PAM-4 transmission using a directly modulated laser made on generic InP integration platform, in *Proc.*

- 27th Internat. Conf. Indium Phosphide Relat. Mater. (IPRM'15), St. Barbara, USA (2015), paper WE2O7.3
62. M. Baier, F.M. Soares, W. Passenberg, T. Gaertner, M. Moehrle, N. Grote, Polarization beam splitter building block for InP based generic photonic integrated circuits, in *Proc. 26th Internat. Conf. Indium Phosphide Relat. Mater. (IPRM'14)*, Montpellier, France (2014), Tu-D3-4
 63. D.O. Dzibrou, J.J.G.M. van der Tol, M.K. Smit, Improved fabrication process of low-loss and efficient polarization converters in InP-based photonic integrated circuits. *Opt. Lett.* **38**, 1061–1063 (2013)
 64. M. Baier, F.M. Soares, M. Moehrle, N. Grote, M. Schell, A new approach to designing polarization rotating waveguides, in *18th Europ. Conf. on Integrated Optics (ECIO'16)*, Warsaw, Poland (2016), paper o-37
 65. M. Baier, F.M. Soares, T. Gaertner, R. Weiser, M. Moehrle, N. Grote, M. Schell, Highly fabrication tolerant polarization converter for generic photonic integration technology, in *Proc. 28th Intern. Conf. Indium Phosphide Rel. Mat. (CSW/IPRM'16)*, Toyama, Japan (2016), paper MoC3-6
 66. <http://www.jeppix.eu>
 67. S. Liu, D. Lu, L. Zhao, D. Zhou, W. Wang, R. Broeke, C. Ji, Synchronized operation of a monolithically integrated AWG-based multichannel harmonically mode-locked laser, in *Opt. Fiber Commun. Conf. (OFC'16)*, Anaheim, CA, USA (2016), paper W4H.4
 68. N. Andrioli, P. Velha, P. Tommasino, M. Chiesa, M.B. Preve, A. Trifiletti, M. Romagnoli, G. Contestabile, An InP monolithically integrated multiwavelength transmitter with direct modulation, in *21st Optoelectron. and Commun. Conf. (OECC'16)*, Niigata, Japan (2016), paper ThE1-3
 69. S. Pitris, C. Vagionas, G.T. Kanellos, R. Kisacik, T. Tekin, R. Broeke, N. Pleros, Optical Static RAM cell using a monolithically integrated InP Flip-Flop and wavelength-encoded signals, in *Opt. Fiber Commun. Conf. (OFC'16)*, Anaheim, CA, USA (2016), Tu2K
 70. D. Melati, A. Alippi, A. Annoni, N. Perserico, A. Melloni, Integrated 8-channel mode and wavelength demultiplexer for MDM and WDM transmission over few-mode fibers, in *42nd Europ. Conf. Optical Commun. (ECOC'16)*, Duesseldorf, Germany (2016), paper SC2.10
 71. F. Morichetti, S. Grillanda, M. Carminati, G. Ferrari, M. Sampietro, M.J. Strain, A. Melloni, Non-invasive on-chip light observation by contactless waveguide conductivity monitoring. *IEEE J. Sel. Top. Quantum Electron.* **20**, 8201710 (2014)
 72. D. Melati, M. Carminati, S. Grillanda, G. Ferrari, F. Morichetti, M. Sampietro, A. Melloni, Contactless integrated photonic probe for light monitoring in indium phosphide-based devices. *IET Optoelectron.* (2015). doi:[10.1049/iet-opt.2014.0159](https://doi.org/10.1049/iet-opt.2014.0159)
 73. M. Carminati, S. Grillanda, P. Ciccarella, G. Ferrari, M.J. Strain, M. Sampietro, A. Melloni, F. Morichetti, Fiber-to-waveguide alignment assisted by a transparent integrated light monitor. *IEEE Photonics Technol. Lett.* **27**, 510–513 (2015)
 74. E. Bitincka, G. Gilardi, M. Smit, On-wafer optical loss measurements using ring resonators with integrated sources and detectors. *IEEE Photonics J.* **6**, 1–12 (2014)
 75. E. Bitincka, Generic testing of photonic ICs. Doctoral thesis, Techn. Univ. Eindhoven, The Netherlands (2014)
 76. T. Korthorst, R. Stoffer, A. Bakker, Photonic IC design software and process design kits. *Adv. Opt. Techn.* **4**, 147–155 (2015)
 77. D.F.G. Gallagher, Eigenmode expansion methods for simulation of optical propagation in photonics – pros and cons. *Proc. SPIE* **4987**, 69–82 (2003)
 78. L. Thylén, The beam propagation method: an analysis of its applicability. *Opt. Quantum Electron.* **15**, 433–439 (1983)
 79. K. Yee, Numerical solution of initial boundary value problems involving Maxwell's equations in isotropic media. *IEEE Trans. Antennas Propag.* **14**, 302–307 (1966)
 80. <http://www.aspicdesign.com/>
 81. <http://www.vpiphotonics.com/>
 82. <https://www.photond.com/>
 83. <https://www.lumerical.com/>

84. F.M. Soares, J. Kreissl, M. Theurer, E. Bitincka, T. Goebel, M. Moehrl, N. Grote, Transmitter PIC for THz applications based on generic integration technology, in *Proc. 25th Intern. Conf. on Indium Phosphide and Rel. Mat.* (IPRM'13), Kobe, Japan (2013), paper TuD4-4
85. <http://www.phoenixbv.com/>
86. <http://www.pdaflow.org/>

Norbert Grote received the Dipl. Phys. and Dr. degree in physics from the Technical University of Aachen (RWTH), Germany, in 1974 and 1977, respectively. At the RWTH he was working on III–V (GaInP, GaAlP) based light emitting diodes and GaAs DFB lasers and related liquid phase epitaxial growth processes. In 1980 he joined the Heinrich-Hertz-Institut in Berlin where he was among the first to help establish the Integrated Optics Division having the mission of developing components for optical telecommunication systems. He was engaged with InP epitaxy and the development of various photonic and also electronic (HBT) devices on InP basis. Until mid of 2015, he was deputy head of the Photonic Components department, renamed after HHI became a member institute of the Fraunhofer Association in 2003. In this position he was supervising different R&D groups working on InP materials technology, laser devices, and polymer based waveguide devices. In recent years his R&D focus was mainly on photonic integration encompassing both monolithic InP photonic integrated circuits and hybrid integration technology on a polymer platform. Currently he is working for HHI in an advisory position. Over the years he was extensively involved in the initiation and coordination of public and industrial R&D programmes/projects. Amongst others, he coordinated the EC funded FP6 project MEPHISTO, and was engaged with the FP7 IP projects EuroPIC and PARADIGM, both addressing generic monolithic optical integration technology and photonic integrated circuits. He is (co)author of more than 140 papers and conference contributions. He (co)-chaired various national and European workshops, and in 2011 he was Conference Chair of the prestigious “International Conference on Indium Phosphide and Related Materials” (23rd IPRM) for which he subsequently served as chairman of the International Steering Committee from 2011–2013.

Moritz Baier received his M.Sc. at KIT, Karlsruhe, Germany in 2013 where he worked on IQ modulators in silicon. His studies in the framework of the ERASMUS program Europhotonics included semesters in Marseille, France, and Barcelona, Spain. He consecutively did internships at the Institute for Microstructure Technology and the Institute for Photonics and Quantum Electronics, both at KIT. He joined the Photonic Components Department of the Fraunhofer Heinrich-Hertz Institute in 2013 where he is currently working on InP based generic photonic integrated circuits for telecommunications. In this field he is working towards a doctoral thesis as Ph.D. student of the TU Berlin.

Francisco Soares received his M.Sc. degree in Electrical Engineering from the Delft University of Technology in The Netherlands in the year 2000, and subsequently his Ph.D. degree in the year 2006 from the Eindhoven University of Technology. After his Ph.D., he worked 4 years as a Post-Doctoral Researcher at the University of California, Davis in the USA, where he continued his research on the design, fabrication, and characterization of InP-based photonic integrated circuits. He joined the Photonic Components Department of the Fraunhofer Heinrich-Hertz Institute in the year 2010, where he has been doing research and development of large-scale-, and high-level-integration of InP-based photonic devices.

Index

Symbols

2D optical switch, 487
2nd order grating, 143
3 dB bandwidth, 250, 251
3D optical switch, 487
 α -parameter for modulators, 172
 α parameter (of fibre), 62
 $\lambda/4$ phase shift, 120
 $\kappa \cdot L$ product, 122
 Q -factor, 252

A
Acousto-optic modulator, 575
Acousto-optic tunable filter, 471
Active layer etching, 122
Actuator, opto-mechanical~, 493
ADC architectures, flash~, pipeline~, serial ripple~, 340, 341
ADC, time-interleaved SAR--, 342
ADC concepts, 342
AlAsSb, 134
Aliasing, 339
All optical amplifier, 724
All-optical wavelength demultiplexer, 725
All-pass filter, 419
Amplified spontaneous emission, 592, 745
Analogue actuator, 486
Angled facet, 117
Apodization, 447, 701
Apodized fibre Bragg grating, 422
Arrayed waveguide grating, 436, 691, 693
Arrayed waveguide grating, reflective~, 693
Asymmetric Mach-Zehnder interferometer, 689
Asymmetric waveguide, 116
Au heatsink, 136

Auger recombination, 743
Avalanche photodiode, 257

B

Back facet phase, 123
Balanced receiver, 400, 403, 405
Band gap shrinkage, 213
Band-edge filter, 456
Band-pass filter, 418, 456, 458
Bandwidth efficiency, 313
Bend loss (fibre), 60
Bend-optimized fibre, 71, 74
Benes switch, 487
Binary phase plate, 12
Binary-weighted DAC, 337
Bit error ratio (formula), 304
Blaze angle, 432
Blaze wavelength, 432
Block turbo code, 327
Box shell layout, 634
Bragg condition, 121
Bragg fibre, 83
Brillouin scattering, 619
Broad-area device, 116
Broadcast and Select, 492
Building blocks of PICs, 823
Buried oxide layer (BOX), 682
Buried ridge stripe laser, 108
Buried tunnel junction, 135
Buried-heterostructure, 107
Butt coupling, 708
Butt-joint coupling, 805
Butt-joint integration, 169, 648
Butt-joint method, 648
Butt-joint regrowth, 806

C

Cantilever coupler, 704
 Capacitively loaded electrode, 383
 Carrier density pulsation, 231
 Carrier frequency recovery, 332, 334
 Carrier phase recovery, 334
 Carrier transit time, 251, 708
 Cascaded microring filter, 467
 Cascaded microring modulator, 466
 Characteristic temperature, 115
 Chirp, 125, 158, 172, 360, 363–365, 367–371, 388, 392, 394, 397, 398
 Chirp, facet-reflection induced~, 173
 Chirp, static~, 173
 Chirp parameter, 360, 361, 363, 368–370
 Chirped grating, 448
 Chirped optical pulses, 815
 Chromatic dispersion, 57, 362, 364, 370, 395, 397, 398, 402
 Chromatic dispersion coefficient, 360, 361, 370
 Chromatic dispersion compensation, 333
 Circuit simulation, 831
 Client data framer, 299
 Clos architecture, 487
 CMOS-compatibility, 679
 Coarse-wavelength-division multiplexing, 807
 Code, low-density parity-check~, 328
 Code, turbo block~, 327
 Code overhead, 301
 Coded modulation, 301
 Coherent detection, 297
 Coherent receiver, 296, 309
 Coherent receiver frontend, 345
 Coherent transceiver, 299
 Colourless AWG, 442
 Complex coupling, 121
 Compressive strain, 110
 Conduction band discontinuity, 111
 Connector, high power~, 559
 Connector, multi-core fibre~, 28
 Connector, polarisation-maintaining~, 557
 Constant chirp parameter approximation, 369
 Constant modulus algorithm, 333
 Constellation diagram, 302
 Constellation size, 300
 Contactless integrated photonic probe, 829
 Contrast factor, 453
 Cost-efficiency, 4
 Counter propagating ring resonator, 697
 Coupled mode theory, 425
 Coupling coefficient, 122
 Coupling efficiency, 115
 Coupling length, 427

Critical coupling, 465

Crossbar switch, 486

Current tuning, 138

Curved stripe DFB laser, 127

CWDM transmitter, 814

D

DAC, binary-weighted~, segmented~, 337
 DAC, resistor ladder~, thermometer-coded~, 336

DAC architectures, 340

DAC resolution, 335

Dark current, 251, 709

Data converter, 300, 334

Data mapping, 330

DBR (coarse, fine) tuning, 216

DBR laser, 214

Degenerate four wave mixing, 720

Detection limit, 253

DFB grating, 120

Dielectric DBR, 136

Dielectric multilayer filter, 455

Differential drive, 367, 368, 388, 391, 397

Differential gain, 125

Differential mode attenuation, 60

Differential mode delay, 59

Diffraction grating, 431, 491

Diffraction order, 432

Digital equalization, 330

Digital optical switch, 513

Digital signal processing, 28, 299

Digital supermode DBR laser, 225

Diluted nitrogen containing InGaAs, 134

Direct modulation, 361, 362

Directional coupler, 428

Discrete mode laser, 129

Dispersion equalizer, 332

Dispersion slope, 420

Dispersion tolerance, 361, 363, 364, 371, 402

Dispersion-compensating fibre, 74

Dispersion-tailored fibre, 69, 72

Distributed Bragg reflector, 132, 214

Distributed feedback, 120

Double stripe layout, asymmetrical~, 635

Double-heterostructure, 106

DPSK modulation, 398

Drude model, 372

DSDBR laser, 394, 816

Dual carrier FDM, 317

Dual polarization I/Q modulator, 343

Dual polarization operation, 307

Dual-depletion region photodiode, 263

Dual-polarization QPSK, 804

Dual-waveguide structure, 802

Duobinary encoded signal, 396, 397
 Duobinary encoding, 396
 Duplexer, ~chip, ~PIC, 803

E

Echelle grating, 435, 689, 693, 694, 696
 EDFA, 21, 586
 Edge coupler, 702
 Edge filter, 459
 Effective number of bits, 336
 Electrical signal-to-noise ratio, 593
 Electro-absorption modulated laser, 804
 Electro-optic effect, 374
 Electro-optic switch, 510
 Electroabsorption, 373
 Electroabsorption (EA) modulator, 169, 363, 374
 Electrostatic deflection, 139
 Emission and absorption cross sections, 589, 590
 Emission spectrum, 114
 Energy efficiency, 4
 Entangled photon pairs, 725
 Equalization functions, 329
 Equalizer, 333
 Erbium doped fibre amplifier, 21, 586
 Erbium energy level diagram, 587
 Etalon, 450
 Etched slot, 129
 Evanescent coupling, 708, 802
 Evanescently-coupled WGPLD, 268
 Excitonic absorption, 812
 External cavity tunable laser, 234, 649
 External quantum efficiency, 249
 External slope efficiency, 123
 Eye opening penalty, 363, 364, 369, 370

F

Fabry-Pérot interferometer, 450
 Fabry-Pérot laser, 113
 Far Nyquist DWDM, 312, 313
 Far-field, 115
 Faraday effect, 715
 Fast optical switching, 119
 FDM frontend, 346
 FEC decoding, 334
 FEC encoding, 330
 Feedback sensitivity, 127
 Ferrimagnetic garnet, 715
 Ferromagnetic garnet, 715
 Ferrule, 550
 Few-mode fibre, 6
 Fibre and planar directional coupler, 425
 Fibre attachment groove, 636

Fibre attenuation, 585
 Fibre bundle, 16
 Fibre bundle scanning switch, 495
 Fibre collimator, 492
 Fibre collimator array, 523
 Fibre coupler, 562, 566
 Fibre coupler categories, 567
 Fibre dispersion, 56
 Fibre fabrication, 54
 Fibre loss, 55, 60
 Fibre response method, 363
 Fibre splicer, 28
 Fibre-chip coupler, 703
 Filled-box geometry, 635
 Filter, finite impulse response~, 688
 Filter dispersion, 420
 Finesse, 452
 Finite difference time domain, 831
 Finite impulse response filter, 688
 Flame hydrolysis, 440
 Flash ADC, 340
 Flexible grid, 488
 Forward error correction, 299, 326
 Forward error correction, hard decision~, 326
 Forward error correction, soft decision~, 327
 Foundry model, 820
 Franz-Keldysh effect, 363, 372, 374
 Free carrier absorption, 211, 372, 743
 Free propagation region, 691
 Free spectral range, 215, 227ff., 236ff., 393, 438, 452, 465, 580, 689ff., 828
 Frequency offset compensation, 334
 Frequency-dependent gain, 257
 Frontend correction, 332, 333
 Fused biconical coupler, 566

G

G-center, 748
 GaAs-based QD lasers, 112
 Gain chip, 117
 Gain flattening filter, 460, 457
 GaInNAs quantum well, 141
 GaSb-based VCSEL, 135
 GCSR laser, 224
 Ge photodetector, 707
 Gires-Tournois interferometer, 454
 Graded-index few-mode fibre, 7
 Graded-index multimode fibre, 61
 Grating coupler, 698, 701
 Gray mapping, 300
 Gridless operation (of wavelength selective switch), 488
 Group delay, 420, 421
 Group delay ripple, 423

Group velocity dispersion, 591
 Growth enhancement effect, 808
 Guided mode, 52

H

Half-wavelength voltage, 368, 391, 393, 400, 403
 Heterodyne receiver, 296
 Heteroepitaxy, 753
 Heterogeneous (wafer-scale) integration, 763
 High index contrast waveguide, 677
 High temperature (laser) operation, 125
 High-contrast grating, 139
 High-pass filter, 419
 High-power laser diodes, 116
 High-temperature (laser) performance, 111
 Higher order filter, 466
 Hitless wavelength selective switch, 488
 Homodyne receiver, 296
 Horizontal cavity surface emitting laser, 142
 Hybrid assembly, 637
 Hybrid dielectric/gold back reflector, 136

I

Impact ionization engineering, 261
 Implantation-enhanced interdiffusion, 811
 In-plane coupler, 699
 Index contrast, 823
 Index ellipsoid, 374–376
 Index-coupled DFB laser, 121
 Infinite impulse response filter, 688
 InGaAlAs material family, 105
 InGaAlAs-BH laser, 108
 Integratable discrete mode laser, 129
 Integrated modulator, 240
 Integration platform, 820, 821
 Interdiffusion, 811
 Interleaver, 468
 Intermodal dispersion, 56
 Internal loss (of laser), 132
 Internal quantum efficiency, 742
 Intervalence band absorption, 379
 Intra-modal dispersion, 57
 Intracavity contacting scheme, 140
 Intradyn receiver, 296
 Inversion, 588
 Inverted taper, 703, 704
 Ion implantation, 811
 IQ modulator, 342ff., 403ff., 817
 IQ modulator structure, 344

K

Kerr effect, 375
 Kramers-Kronig relations, 373

L

Large-signal analysis, 156
 Laser diode structures, 106
 Latching mechanism, 493
 Lateral integration, 805
 Lattice filter, 689
 Leaky mode, 53
 Least-mean-squares algorithm, 333
 Lens integrated surface emitting laser, 143
 LIDAR, 116
 Lift-off process, 631
 Linear phase mismatch, 613
 Linewidth characteristics, 131
 Linewidth enhancement factor, 158, 361
 Liquid crystal based switch, 497
 Liquid crystal on silicon, 498
 Littrow configuration, 432
 Long-cavity (laser) design, 136
 Long-period FBG, 449
 Low-density parity-check code, 328
 Low-pass filter, 419
 Lumped electrode (structure), 365, 379

M

Mach-Zehnder delay interferometer, 400
 Mach-Zehnder interferometer, 366, 429, 717
 Mach-Zehnder interferometer modulator, 366
 Mach-Zehnder modulator, nested~, 309
 Mach-Zehner interferometer, asymmetric~, 689
 Magneto-optic Kerr effect, 715
 Mask set, 832
 Maxwell's equations, 51, 720, 831
 MEMS switch, 518
 MEMS waveguide switch, 519
 Micro-electro-mechanical system mirror, 139
 Micro-photoluminescence, 809
 Micro-structured optical fibre, 82
 Micro-electro-mechanical systems (MEMS), 517
 Microring resonator, 463, 509
 Microstrip line, 388
 Microwave beam-former, 664
 Minimum-phase filter, 420
 Mirror, 644
 Mirror loss, 164
 Modal bandwidth, 58
 Modal differential group delay, 7
 Modal theory of light propagation, 51
 Mode selection, 214
 Mode-hop free (laser) operation, 130
 Mode-selective excitation, 12
 Modified uni-travelling-carrier photodiode, 265

- Modulation, coded~, 301
 - Modulation bandwidth, 126
 - Modulation decoding, 334
 - Modulation efficiency, 301
 - Modulation encoding, 330
 - Modulator, 118, 169–175, 180, 183–191, 197, 240, 308, 330, 343–345, 359ff., 498, 511, 718, 727, 781–788, 804, 810, 815, 816
 - Monte-Carlo simulation, 831
 - Moore's law, 740
 - MQAM transmitter, 309
 - MSM photodetector, 255
 - Multi species gas detection, 130
 - Multi-core fibre, 88
 - Multi-core fibre connector, 28
 - Multi-core structure, 632
 - Multi-guide vertical integration, 803
 - Multi-modulus algorithm, 333
 - Multi-project wafer, 820, 826
 - Multicast optical switch, 491, 516
 - Multilayer DBR, 133
 - Multimode fibre, 50, 57, 63
 - Multiple carrier I/Q modulator, 345
 - Multiple-band filter, 459
 - Multiple-quadrature-amplitude-modulation, 301
- N**
- (nano) photonic wire, 677
 - Nanopatterned crystalline Si, 747
 - Near Nyquist DWDM, 312, 313, 331
 - Nematic liquid crystal cell, 497
 - Nested Mach-Zehnder modulator, 309
 - Net coding gain, 327
 - Noise figure, 592, 593, 606, 607
 - Nonlinear K -factor, 154
 - Notch filter, 419
 - Nyquist DWDM, 312
 - Nyquist pulse shaping, 331
- O**
- Off-center phase shift, 123
 - Off-set quantum well configuration, 803
 - Ohmic tunnel junction, 135
 - On-wafer measurement, 829
 - On-wafer testability, 132
 - Optical amplifier, 20
 - Optical beam steering, 499
 - Optical circulator, 569, 570, 579, 580
 - Optical connector, 548
 - Optical frontend, 300
 - Optical gain, 164
 - Optical isolator, 571ff., 573, 575–579, 715
 - Optical loss, 823
 - Optical nonlinearity, 831
 - Optical receiver frontend, 345
 - Optical receiver, 257
 - Optical switch, 483ff., 815
 - Opto-mechanical actuator, 493
 - Opto-mechanical switch, 492–495
 - Out-of-plane coupler, 699
 - Outdiffusion, 107
 - Over-filled launch, 58
- P**
- P–i–n photodiode, 253
 - Packaging, 834
 - Parabolic index profile, 51
 - Parallel-serial filter, 691
 - Partially-depleted-absorber photodiode, 265
 - Passive-optical network, 816
 - Patch cord, 556
 - Path-independent insertion loss, 486
 - Pattern effect, 362, 400
 - Phase effect, 419
 - Phase recovery, 332
 - Phase sensitive amplifier, 724
 - Phase velocity, 383
 - Phase-shift method, 421
 - Photodiode, modified uni-travelling-carrier~, 265
 - Photodiode, side-illuminated waveguide~, 266
 - Photonic lantern, 17
 - Photonic switch array, 119
 - Pipeline ADC, 340
 - Pixel fill factor, 498
 - Planar concave grating, 693
 - Plasma effect, 361, 372
 - Plastic optical fibre, 64
 - PMD compensation, 333
 - Pockels effect, 374–378
 - Polarization beam splitter, 430, 826
 - Polarization controller, 641
 - Polarization diversity, 700
 - Polarization division multiplexing, 298, 307
 - Polarization independent optical switch, 502
 - Polarization recovery, 332, 333
 - Polarization rotator, 497
 - Polymer waveguide, 630
 - Power splitter, 428
 - Power-equalization filter, 419
 - Pre-FEC bit error rate, 328, 329
 - Preform, 54
 - Prism switch, 494
 - Process design kit, 832
 - Propagation equation, 589, 592, 600, 607

Propagation loss, 829
 Pulse shaping, 325
 Pump depletion, 606
 Push-pull operation, 367, 717

Q

QD-based VCSEL, 141
 Quadrature amplitude modulation, 301
 Quadrature phase-shift keying modulation, 817
 Quantization error, 339
 Quantum dash, 113
 Quantum dot, 112
 Quantum dot laser, 756, 758
 Quantum efficiency, external-, 249
 Quantum-confined Stark effect, 169, 363, 373
 Quantum-well intermixing, 811
 Quantum-well structures, 109

R

R-EAM-SOA, 118
 Radiation caustic, 74
 Raised-cosine filter, 331
 Raman amplifier, 599ff.
 Raman gain coefficient, 602
 Raman scattering, 618, 749
 Rate equations, 153, 361, 362, 588
 Rayleigh scattering, 609
 Reach penalty, 319
 Receiver sensitivity, 253
 Receiver signal processing, 332
 Reconfigurable optical add-drop multiplexer, 488
 Recursive tree structure, 513
 Reflection coating, 114
 Reflective AWG, 693, 694
 Reflective defects, 129
 Reflective SOA, 118
 Refractive index variation, 213
 Relative confinement factor, 133
 Relaxation oscillation (frequency), 153, 362
 Resistor ladder DAC, 336
 Resolving power, 433
 Resonance frequency, 137
 Responsivity, 250, 254, 708
 Rib waveguide, 684
 Ridge waveguide, 107
 Ring based add-drop filter, 696
 Ring based wavelength filter, 698
 Ring resonator, 695
 Robotic optical switch, 495
 Root raised cosine filter, 331
 Round trip condition, 133

S

Sampled grating, 219
 Saturated amplifier, 594
 Scattering loss, 129
 Scattering matrix, 563, 831
 Schottky electrode, 378, 383
 Segmented DAC, 337
 Segmented electrode, 383, 395
 Selective-area-epitaxy, 806
 Selective-area-growth, 169, 807
 Self-assembled quantum dot laser, 757
 Semiconductor optical amplifier, 117
 Serial ripple ADC, 340
 SFP+, 816
 SG-DBR laser, 220, 221
 Shannon capacity (limit), 303
 Shannon-Hartley theorem, 303
 Short cavity design, 136
 Short-cavity edge-emitting laser, 165
 Short-wavelength Bragg mode, 128
 Shot noise, 252
 Si nanoclusters, 744
 Side-illuminated waveguide-photodiode, 266
 Side-mode suppression, 123
 Signal-to-noise ratio, 252, 400, 592
 Signal-to-noise ratio, electrical-, 593
 Signal-to-noise-and-distortion ratio, 336, 339
 Signal-to-quantization-noise ratio, 339
 Silica dispersion, 57
 Silicon Raman laser, 750, 752
 Silicon-on-insulator, 676ff.
 Single stripe geometry, 635
 Single-mode aperture, 137
 Single-mode fibre, 66
 Single-mode yield, 123
 Slot waveguide, 687
 Small-signal frequency response, 153
 Small-signal modulation, 126, 153
 Soft decision FEC, 327
 Space (spatial) division multiplexing, 1ff., 597, 804
 Spanke architecture, 486
 Spatial beam steering, 497
 Spatial hole burning, 122
 Spatial light modulator, 498
 Spatial multiplexer, 9
 Spatial phase modulator, 497
 Spectral efficiency, 310, 312
 Spectral pre-shaping, 331
 Split step Fourier method, 360
 Spot-based spatial multiplexer, 10, 12
 Spurious free dynamic range, 336
 SSG-DBR laser, 223
 Standard, optical connectors, 551

Standard single-mode fibre, 69
 Standardization, 65, 68
 Standing-wave effect, 133
 Star coupler, 568
 Stark shift, 373
 Steam oxidation, 134
 Step index profile, 51
 Step-index few-mode fibre, 7
 Step-index multimode fibre, 61
 Stimulated Raman scattering, 750
 Strained QW, 110
 Strip waveguide, 682, 683
 Successive approximation register ADC, 340
 Super-structure grating, 223
 Supermode, 17
 Surface relief grating, 433
 Surface relief transmission grating, 434
 Surface-emitting laser diodes, 131
 Symbol error probability, 304
 Symbol rate, 301
 System simulation (tools), 831

T

Tandem lattice filter, 690
 Tap coupler, 428
 Tapered laser, 115
 Tapered transition, 805
 Tensile strain, 111
 Thermal noise, 252
 Thermo-optic switch, 511, 513
 Thermometer-coded DAC, 336
 Thin film element, 638
 Thin-film filter, 455
 Threshold gain, 122
 Time-interleaved SAR-ADC, 342
 Timing recovery, 332
 Transceiver package, 152
 Transit time-limited bandwidth, 251
 Transmission grating, 433
 Transmission line, 380
 Transmissive star coupler, 568
 Transmitter, 309
 Transmitter, MQAM-, 309
 Transmitter building blocks, 330
 Travelling wave electrode, 405
 Travelling-wave structure, 379
 Trench assisted structure (of UMCF), 63

TriPleX waveguide, 633
 Tunable twin guide (TTG) laser, 228, 229
 Tunable vertical cavity surface emitting laser, 234
 Tuning map of SG-DBR, 222
 Tunnel junction, 135
 Turning mirror, 142
 Twisted nematic liquid crystal cell, 497
 Two photon absorption, 750
 Two-stage isolator, 575

U

U-groove, 636
 Uncooled EA/DFB laser, 185
 Uncooled laser operation, 124
 Uni-travelling-carrier photodiode, 263

V

Valence band discontinuity, 112
 Vernier effect, 221, 224, 244, 468
 Vertical integration, 802
 Vertical-cavity surface-emitting laser, 131
 Volume-phase holographic grating, 434

W

Wafer bonding, 140, 756, 763, 764
 Wannier exciton, 373
 Wave equation, 52
 Waveguide coupled diffraction grating, 699
 Waveguide dispersion, 57
 Waveguide Ge photodetector, 707
 Waveguide-photodiode integration, 802
 Wavelength and power locker, 227
 Wavelength converter, 723
 Wavelength detuning, 125
 Wavelength selective filter, 687, 688
 Wavelength selective switch, 25, 487, 497, 529, 531
 Wavelength-division-multiplex, 124
 Weakly-coupled (SDM) fibre, 85
 Weakly-guiding approximation, 52
 White Gaussian noise, 303
 Widely tunable laser, 219

Y

Y-laser, 224